GEOPHYSICAL CONSTRAINTS ON UPPER CRUSTAL STRUCTURE IN THE MIDLAND VALLEY OF SCOTLAND

MICHAEL C. DENTITH

Thesis submitted for the degree of Philosophiae Doctorem at the University of Glasgow, 1987.

VOL. I

DECLARATION

I declare that the contents of this thesis are the results of my own work, have not been accepted in substance or in part for any other degree, and are not currently being submitted for any other degree.

All other works referred to in this thesis have been acknowledged.

M. C. Dentith

J. Hall
(Supervisor)

J. J. Doody
(Supervisor)

Department of Geology,
University of Glasgow,
Glasgow.

ACKNOWLEDGEMENTS

This project was completed under the supervision of Jeremy Hall and Ben Doody whose help throughout this period, and during the completion of this thesis, is gratefully acknowledged. I should also like to express my gratitude to Prof. Bernard Leake for allowing me the use of the facilities of the Department of Geology at Glasgow during this research.

The MAVIS project was financed by the Tricentrol Oil Corporation. Their assistance throughout the project made the work considerably easier. I would particularly like to thank Andy Spencer, Steve Hacker and Marion Merryweather for their help.

Virtually all the staff, post-graduates and undergraduates of the Geology Department assisted with the acquisition of the MAVIS I and II data. The assistance of Allan Trench, Bob Cumberland, Mark Wood, Steve Hay, Innes Ferguson, Graeme Johnson, Gill Whelan, Pat Bradshaw, Eddie Speirs and Ben Doody in collecting the quarry blast and Vibroseis data made the work considerably easier.

This project would not have been completed without the co-operation of numerous land and quarry owners whose generousity is gratefully acknowledged.

The contributions of Andy Conway and Maggie Fleming, whilst employed as research assistants at Glasgow, were essential to the success of MAVIS.

My thanks go to the technical staff at Glasgow, especially George Gordon for the design and maintenance of the recording equipment and Roddy Morrison for provision of large quantities of draughting film. I should particularly like to express my gratitude to Bob Cumberland. This project would not have been completed without his considerable patience and efficient organisation of the geophysical data at Glasgow.

The MAVIS shots were fired by Ritchies Equipment Limited. The Forth Ports Authority and Royal Navy co-operated in the firing of shots in the Firth of Forth from the MV Strathyre owned by Captain Andrew Murdoch of Port Seton.

I should like to acknowledge the assistance of the Glasgow University computing service, who consistently lost plots, failed to prevent the mainframe computer from crashing, and published statistics claiming 90% reliability throughout the course of this project.

I should like to thank Colin Farrow for assistance with the departmental computing facilities, the efficiency of which provide an interesting contrast with the above.

This project benefited considerably from discussions with Jeremy Hall, Ben Doody, Graham Durant, Pete Haughton, Brian Bluck, Kenny Davidson, Mark Wood, Colin Davenport and Allan Trench.

Douglas McLean, Bob Cumberland and Mark Wood helped considerably with the figures.

Discussions and provision of data by Bill Read (University of Nottingham), Mike Browne and Colin MacBeth (both

British Geological Survey) assisted in the interpretation of the MAVIS data.

The financial support and encouragement of my parents were essential to the completion of this project.

This work was carried out whilst in receipt of a NERC (CASE) research studentship with the Tricentrol Oil Corporation. This award is gratefully acknowledged.

I should like to mention the role of the Curlers Bar in the completion of this work.

Finally, I should like to mention Lisa Davies who proof read the manuscript and considerably improved the grammar.

CONTENTS (Vol I)

CONTENTS (Vol II - List of Figures)

CHAPTER 4 - SEISMIC VELOCITY DETERMINATION AND INTERPRETATION

CHAPTER 5 - INTERPRETATION OF SEISMIC DATA

APPENDIX 1 (Figs in Vol. I)

SUMMARY

The Midland Valley Investigation by Seismology (MAVIS) consists of three refraction lines of c. 80 km length across the Carboniferous basins of the Midland Valley of Scotland. Two lines trend approximately east-west (MAVIS I north and south), the latter crossing a major gravity and magnetic anomaly near Bathgate. The third line (MAVIS II) trends north-south, crossing the MAVIS I lines and Bathgate anomaly and extends into Lower Old Red Sandstone outcrop to the north and south of the Ochil and Wilsontown Faults respectively. These data are supplemented by lines recorded using quarry-blast sources. Two profiles trend east-west across the Bathgate anomaly (Sola north and south). A third profile (MAVIS III) trends north-south across the Lothian oil-shale fields.

Three refractors are recognised defining four crustal layers. The first layer has velocities between 3.0 and 5.0 km/s and extends to depths between 0.5 and 3.0 km. This layer is interpreted as the Carboniferous and Upper Old Red Sandstone. The second layer has velocities between 5.3 and 5.9 km/s and occurs between depths of 0.5 to 3.0 km and 4.0 to 6.0 km. This layer is interpreted as the Lower Old Red Sandstone and Lower Palaeozoic. Therefore, the topmost refractor is interpreted as the unconformity between the Upper and Lower Old Red Sandstone mapped at the surface in the Midland Valley. The third layer occurs at between 4.0 to 6.0 and 7.0 and 8.5 km depth with velocities between 6.0 and 6.1 km/s. This layer is interpreted as crystalline basement. The deepest layer occurs at depths greater than 7.0 to 8.5

km and is interpreted as a higher velocity crystalline basement. The interface between the two basement layers may mark the transition from amphibolite to granulite facies metamorphism.

Velocity data from layer 1 show Poisson's ratio for this layer to be 0.29 +/- 0.06, and the ratio of horizontal to vertical P-wave velocity to be 1.15 +0.12 -0.15. Both values are consistent with the sandstone/limestone/shale sequence mapped at the surface.

The Bathgate gravity anomaly was modelled within the constraints imposed by the seismic data. The results of earlier magnetic modelling were confirmed, with deep and shallow end members of a series of possible solutions being modelled. The shallow model satisfies the anomaly with a thickened sequence of Carboniferous lavas within the seismic layer 1. The deep model is for a gabbroic intrusion within the crystalline basement extending from 10 to 15 km depth. Gravity modelling across the Ochil Fault show this fracture to dip to the south.

Relief on the Old Red Sandstone unconformity is found to mirror structures mapped at the surface, whilst the underlying basement is virtually planar. A detachment is postulated between these horizons with the surface structures forming by thin-skinned tectonic processes. The detachment horizon is probably either within the Lower Palaeozoic sequence of seismic layer 2, or at the ductility contrast to be anticipated at the interface between Lower Palaeozoic and crystalline rocks. A detailed structural interpretation of the Lothian oil-shale fields suggests there may be several levels of such detachment with the Midland Valley. A model is presented for the development of the Ochil fault as an en echelon fracture resulting from reactivation of a basement lineament.

INTRODUCTION

The Midland Valley of Scotland is considered prospective by a number of oil companies, a play involving a Dinantian oil-shale source with reservoirs in overlying sandstone bodies being envisaged. The Tricentrol Oil Corporation hold exploration licences in the area and financed the MAVIS (Midland Valley Investigation by Seismology) seismic refraction project as part of their exploration effort in this region. The data were intended to:

[1] Act as a framework for reflection data and provide additional velocity information.

[2] Map the depth to two refractors interpreted as the unconformity between the Upper and Lower ORS and top of crystalline basement. Since the potential source rocks are of Carboniferous age, the thickness of these strata are limited by the depth to the former, whilst the relationship between surface and basement structures allows constraints to be placed on structural styles within the region.

[3] To provide data on the sources of a major gravity and magnetic "high" centred around Bathgate and a gravity "low" near Alloa.

[4] Extend the models of upper crustal structure provided by Davidson (1986) and Sola (1985) across the southern Midland Valley.

This thesis describes the acquisition and processing of the MAVIS data, and the re-interpretation of the quarry-blast data of Sola (1985). Gravity modelling within the constraints provided by the seismic data was also undertaken. Methods and their application to the data are described in chapters 3 to 6. The geological interpretation of these data are discussed in chapter 7. Figures are in volume II.

CHAPTER 1 - BACKGROUND GEOLOGY

1.1. Introduction

A bewildering number of tectonic models for the evolution of the Scottish Caledonides have been published. Early interpretations in terms of a destructive plate boundary (Dewey 1971) have been modified to include strike-slip (usually sinistral) and terrane tectonics (Bluck 1985, Hutton 1987). Tectonic models of the Variscides are slightly less common but concentrate on evidence to the south of the Midland Valley. A detailed review of these models is not attempted here. Instead, the major stratigraphic units within the Midland Valley are described and their tectonic setting briefly reviewed. The geological significance of the MAVIS data is discussed in Chapter 7.

1.2. Pre-Palaeozoic Basement

There is no pre-Palaeozoic basement exposed in the Midland Valley and tectonic models for the evolution of the region predict a wide variety of basement types, e.g. Dalradian rocks (Yardley et al. 1982), oceanic crust (Mitchell & McKerrow 1975), a pre-Dalradian block (Kennedy 1958, George 1960).

Indirect evidence of basement type is available from three sources:

[1] Provenance studies based on clasts in Lower Palaeozoic conglomerates

[2] Geophysical measurements, e.g. Poisson's ratio

[3] Xenoliths from volcanic vents

Conglomerates in the Lower Palaeozoic strata exposed near Girvan and in a series of inliers in the southern Midland Valley (see section 1.3) contain numerous igneous clasts of acid to basic composition. Bluck (1983, 1984) suggests that the source of these clasts was a volcanic-plutonic arc massif in the Midland Valley and Southern Uplands. A Midland Valley basement of such acid-intermediate composition is in agreement with the velocities described by Hall et al. (1983) and Davidson et al. (1984) (Figs.2.6 and 2.8) for the LISPB "Lower Palaeozoic" layer.

The seismic model of Midland Valley crustal structure is described in section 2.2. Measurements of P- and S-wave velocities of Lewisian rocks (Hall & Al-Haddad 1976, Hall & Simmons 1979) and the calculation of Poisson's ratio by comparison of LISPB P- and S-wave data (Assumpcao & Bamford 1978) suggest that the LISPB 6.4 km/s "pre-Caledonian basement" is composed of intermediate granulite gneiss similar to that exposed in the Lewisian complex to the northwest. Powell (1978), from magnetic evidence, suggests that the layer has been affected by retrogressive metamorphism. The 7.0 km/s lower crustal layer is probably basic igneous rocks metamorphosed to garnet granulite facies and gradational between gabbro and eclogite.

Xenoliths from the Midland Valley and adjoining regions have been described by Upton et al. (1976), Graham & Upton (1978) and Upton et al. (1983). Upton et al. (1984) integrate these data with the seismic evidence (Fig.1.1).

Xenoliths of foliated quartzo-feldspathic granulitic gneisses and unfoliated plutonic rocks are correlated with the LISPB 6.4 km/s pre-Caledonian layer whilst basic granulitic meta-igneous examples are assigned to the 7.0 km/s lower crustal layer. Mantle material is represented by foliated peridotites and other unfoliated ultra-mafics.

The absence of greenschist or amphibolite facies xenoliths, together with the sedimentary and geophysical evidence, suggests that the Midland Valley basement consists of an island arc igneous complex overlying granulite facies metamorphics. It should be remembered that the Midland Valley basement may not be a homogeneous unit, the techniques described cannot distinguish between similar juxtapositioned basement blocks.

1.3. Lower Palaeozoic

Lower Palaeozoic rocks are not well exposed in the Midland Valley (Fig.1.2). Ordovician strata are exposed at Girvan and at the Highland Border. Silurian rocks outcrop at Girvan and in a series of inliers in the southern Midland Valley. Downtonian rocks unconformably succeed the Highland Border Complex at Stonehaven. There is evidence that some of the Lower Old Red Sandstone (ORS) may be of Silurian age but these rocks will be considered separately (see section 1.4). General descriptions of the Lower Palaeozoic rocks are given by Cameron & Stephenson (1985) and, to a lesser extent, by Walton (1983).

In the southwest Midland Valley the rocks of the Ballantrae Ophiolite Complex record a history of subduction on the southern margin of the Laurentian continent. Following early Ordovician obduction, the complex was unconformably overlain by a conglomeratic and turbiditic sequence of Llanvirn-Ashgillian age deposited in a series of fault bounded basins (Williams 1962). Clast provenance studies in the conglomerates suggest them to have been produced by the erosion of the Ballantrae Complex and a plutonic arc (Longman et al. 1979). Bluck (1983) interprets the Girvan sequence as having formed in a proximal fore-arc setting and postulates the presence of a major arc massif to the north and a fore-arc basin to the south. The fore-arc is envisaged as lying beneath the allochtonous accretionary prism sequence of the Southern Uplands which has been thrust to the north, effectively eliminating the arc-trench gap.

The rocks of the Highland Border Complex occur as a series of discontinuous outcrops along the Highland Border. Curry et al. (1984) show the complex to range from pre-Arenig to late Caradoc age. The complex is unconformably overlain by Downtonian strata at Stonehaven and by the Lower ORS at Loch Lomond. The Dalradian is reverse faulted against the complex. Therefore, these rocks may be considerably more extensive at depth than suggested by their surface outcrop. Bluck (1984) postulates deposition in a marginal basin. By comparison of their geological history with that of the Dalradian he demonstrates that the two crustal blocks were not adjacent at this time. The Highland Boundary Fault (HBF) is considered to mark a terrane boundary with juxtapositioning of the two blocks probably occurring during the late Silurian, with final docking by thrusting probably in Upper

Devonian times. The tectonic evolution of the Midland Valley region through the Ordovician is shown in Fig.1.3.

The Silurian strata exposed around Girvan and in the southern Midland Valley inliers show a transition from marine turbidites, shales and conglomerates up into terrestrial conglomerates and sandstones. Clast provenance and palaeoflow studies suggest deposition in an inter-arc basin, with a source in a volcanic terrane to the south (Bluck 1983). The tectonic setting in Silurian times is summarised in Fig.1.4.

1.4. Old Red Sandstone (ORS)

The ORS of the Midland Valley has been described by Mykura (1983) and Cameron & Stephenson (1985). The tectonic setting during deposition has been described by Bluck (1983, 1984). A two-fold division of the ORS is recognised in the Midland Valley with a thick Lower ORS sequence unconformably overlain by a thinner Upper ORS succession. Radiometric evidence suggests much of the Lower ORS to be of Silurian age (Thirlwall 1983), whilst poor biostratigraphic constraint on the Upper ORS means much of this succession could be of Carboniferous age. ORS outcrop in the Midland Valley is shown in Fig.1.5.

The Lower ORS rests unconformably on the Lower Palaeozoic in the Pentland Hills (Mykura 1960) and at Girvan (Cocks & Toghill 1973), though the contact may be conformable at Lesmahagow and in the Hagshaw Hills (Rolfe 1961) (see Fig.1.2 for locations). Near Stonehaven, rocks of Downtonian age are succeeded conformably by the Lower ORS.

Terrestrial clastic sediments dominate the succession with coarse conglomerates common. Igneous rocks of Lower ORS age include andesitic, basaltic and rhyolitic extrusives with intrusive felsites and dolerites. The succession to the north of the Ochil Fault is folded into the asymmetric Strathmore Syncline and parallel Ochil-Sidlaw Anticline (Armstrong & Paterson 1970, Francis et al. 1970). In the southern Midland Valley poorly exposed, heavily faulted, outcrops extend from the Ayrshire coast to the Pentland Hills (Mykura 1960).

Using palaeoflow and clast provenance data Bluck (1983, 1984) suggests that the Lower ORS was deposited in two basins; the Lanark and Strathmore Basins, within a volcanic chain formed of the Lower ORS igneous rocks (Fig.1.6). Deposition is envisaged as having occurred within a volcanic arc during the closing stages of the Caledonian Orogeny.

Earth movements preceding the deposition of the Upper ORS are associated with sinistral transpression along the Highland Border. Sinistral movements of this age are described from faults within the Dalradian block, e.g the Loch Tay Fault (Smith 1961), in clast fractures from within Lower ORS conglomerates (Ramsay 1962) and in fault patterns along the Highland Border and in the Ochil Hills (see section 7.3).

The Upper ORS was deposited on the eroded surface of the Lower ORS. This sequence is also composed of terrestrial clastic sediments, though the Upper ORS is more mature and generally finer than the Lower. There are no volcanic rocks within the succession. Exposure is poor and correlation between outcrops difficult. Bluck (1980) interprets the conglomeratic succession in the northwest Midland Valley as having been deposited in a series of pull-apart basins resulting from sinistral movements along the HBF. No detailed interpretation is available to explain deposition elsewhere in the Midland Valley.

1.5. Carboniferous

1.5.1. Introduction

Extensive reviews of the Carboniferous of Scotland, and of the Midland Valley, are provided by Francis (1983a, 1983b) and Cameron & Stephenson (1985) respectively.

The Carboniferous of the Midland Valley conformably succeeds the Upper ORS. There is a transition from terrestrial red beds to a fluvio-deltaic and shallow marine sequence, but this change is diachronous and a significant part of the Upper ORS may be of Carboniferous age. The stratigraphic subdivisions of the Midland Valley Carboniferous are shown in Fig.1.7. Red beds reappear at the end of the Westphalian heralding a return to arid conditions in the Permian.

1.5.2. Structure

In the Midland Valley, as in the Carboniferous of England and Ireland, sedimentation and volcanism were influenced by contemporaneous tectonics. The major structural elements in the Midland Valley are shown in Fig.1.8.

Hall (1971, 1974) recognises two zones of differing structural style separated by the north-south trending "Lanark Line". To the east of this line north-south folds cut by east-west normal faults and dykes predominate. To the west, east-west faulting is less apparent with northwest trending folds and faults more important. Both patterns are superimposed on an older northeast-southwest "Caledonian" grain within the pre-Carboniferous basement. Northeast-southwest trending linear volcanic vent systems also suggest basement structures of this trend. During the Carboniferous, the influence of northeast-southwest and east-west structures was gradually superceded by those of northwest-southeast trend which controlled Permian deposition in the Midland Valley, and to a lesser extent, in England (see section 1.6).

The nature of the HBF during Carboniferous times is poorly constrained due to lack of outcrop, though Carboniferous sediments cross the fault near Loch Lomond suggesting little or no relief on the fault line. The Southern Uplands Fault (SUF) was down-thrown to the northwest in Carboniferous times with the Southern Uplands forming an area of positive relief which was gradually overstepped by the Carboniferous and Permian succession.

The Pentland Fault is mapped offshore in the Firth of Forth (Thomson 1978) and extends southwest to the SUF. Near Edinburgh the fault juxtaposes the Lower ORS volcanics of the Pentland Hills and the Carboniferous strata of the Midlothian Coalfield. The fault is reversed since a bore within the volcanics penetrated Carboniferous strata.

Further south, near West Linton, the fault changes its down-throw from southeast to northwest. The fracture can be traced, probably without interruption, to the point where it joins the SUF, down-throwing southeast at Tinto but changing to northwest again further south (Fig.1.8). The Pentland Fault was probably active as a strike-slip fault during the post-Lower pre-Upper ORS deformation and may have originated in an earlier period. The relationships of the strata along the Pentland Fault between Midlothian and Douglas suggest that several reversals of the direction of throw may have occurred during its history.

Faults sub-parallel to the SUF are mapped in Ayrshire, increasing in frequency adjacent to this fault. Stratigraphic units abruptly change thickness across these fractures indicating syn-depositional movements. There is stratigraphic and geophysical evidence that, like the Pentland Fault, the Straiton and Dusk Water Faults have undergone changes in their direction of throw.

Further to the east, east-west trending faults are common, though throws are comparatively small except in the case of the Ochil and Campsie Faults (Anderson 1951). The throw on the former is estimated at over 3 km. In the Lothian oil-shale fields six east-west trending faults with throws of up to 0.5 km dominate the structure. Francis & Walker (1986) present evidence that faults of this trend were active during the Carboniferous. They certainly existed by late Carboniferous times when dykes of the Midland Valley Sill Complex (see section 1.5.4) are mapped as intruding along such fault planes.

Northwest-southeast trending faults are mapped geophysically in the Firth of Clyde (McLean & Deegan 1978) and are also present within the Midland Valley. Individual throws on these faults are relatively minor.

The two largest folds in the Carboniferous of the Midland Valley are the north-south to northeast-southwest trending Central Coalfield and Fife-Midlothian Synclines. The former appears to have originated as the depositional Kincardine Basin, though the axes of the two structures are offset by a few kilometres. The latter is cut by the Pentland Fault, movements on which are probably responsible for the marked asymmetry of the Midlothian Syncline. Strata are inverted adjacent to the fault in this area (Tulloch & Walton 1958). Smaller scale folding along northeast-southwest trends controlled sedimentation in Fife, e.g the Balmule Anticline, and to a lesser extent further west. Folds of north-south to northeast-southwest trend are especially common in the Lothian oil-shale fields (Mitchell & Mykura 1962). In the west, less persistent folds of northwest-southeast to east-west trend occur, e.g the Mauchline Basin, whilst folds of northeast-southwest trend are associated with the faults of this trend, e.g. the Dailly Syncline (Mykura 1967).

There is disagreement as to the tectonic framework into which the Carboniferous of the Midland Valley is best fitted. Tectonic models can be broadly divided into those advocating pure shear in a east-west stress field (Russell 1971, Hazeldene 1987), pure shear in a north-south stress field (Leeder 1976, Bott et al. 1984) and dextral strike-slip models (Dewey 1982, Read 1987a). The complex history of reactivated structures and syn-depositional movements is probably best explained by dextral strike-slip in response to an approximately north-south oriented stress field, i.e. a transtensional regime. This explains the movements on east-west and northeast-southwest faults with simultaneous folding along north-south to northeast-southwest lines (Read 1987a).

1.5.3. Sedimentation

In addition to syn-depositional folding and faulting, sedimentation was controlled by the topography of contemporaneous lava piles. Also, there is evidence of regional increases in sediment thickness to the northeast or north in several stratigraphic groups. Consequently, isopach maps are the products of several interfering influences. Fig.1.9 demonstrates a pattern of sedimentation which continued throughout virtually the entire Carboniferous, though as regional subsidence continued the influence of the structures shown diminished. A shelf area in Ayrshire is separated by a lava pile from two major basins; in the centre of the Midland Valley and in Fife and Midlothian. These basins are separated by a complex zone of small scale folding. Smaller basins occur around Douglas and in central Fife. Fig.1.10 illustrates the effect of syn-depositional tectonics on the thickness of the Limestone Coal Group.

The Calciferous Sandstone Measures (CSM) in the Midland Valley show extreme lateral facies changes. The group includes large volumes of basic igneous rocks and records an increasing marine influence on sedimentation.

In the western Midland Valley the Cementstone Group consists of argillaceous limestones interbedded with mudstones and sandstones of probable lagoonal origin (Freshney 1961). In Renfrewshire, and further east, the succession is overlain by the lavas of the Clyde Plateau, dividing the CSM into Lower and Upper Sedimentary Groups (Richey et al. 1930). The Upper Sedimentary Group rests unconformably on the lava pile, the topography of which controlled its distribution (Whyte 1981). Lithologies include sandstones, mudstones, and coals with marine limestones near the top of the sequence, e.g. the Hollybush Limestone.

In West and Midlothian the CSM consist of a Cementstone Group overlain by the Lower and Upper Oil-Shale Groups. The CSM reach their maximum thickness of around 2 km in this area. The Cementstone Group is similar to that in the west but, in contrast, igneous rocks are rare. The Lower Oil-Shale Group contains few well-developed oil-shales and consists of a sequence of shales and sandstones with some coals and freshwater limestones. The Upper Oil-Shale Group contains nine to ten oil-shale seams, up to 5 m thick, interbedded with argillaceous strata, plus marine horizons, coals and marls (Mitchell & Mykura 1962).

In East Lothian igneous strata are again well developed. Sediments are mainly argillaceous and include cementstones near the base and a series of marine bands higher up the succession.

In East Fife the CSM are represented by sandstones, mudstones and siltstones with impersistent coals and dolomitic limestones. The sequence contains several marine horizons, especially near the top, e.g. the Ardross Limestones (Forsyth & Chisholm 1977).

The increasing marine influence seen in the upper part of the CSM continues into the Lower Limestone Group (LLG). The group consists of a cyclic succession of sandstones, mudstones, limestones and coals with basaltic lavas and tuffs north of Bathgate. The coals have been worked in parts of the Central Coalfield and in Midlothian and Fife.

The Limestone Coal Group (LCG) contains many workable coals within a sequence of deltaic sandstones, siltstones and shales. Paradoxically, the group contains no limestones except for rare freshwater examples. Two important marine bands; the Johnstone Shell Bed and the Black Metals, can be traced over nearly all the Midland Valley. Phreatic volcanic activity occurred at this time in Ayrshire and Fife with rare localised lava flows in the latter. Basalt lavas continued to be deposited north of Bathgate where virtually all of the group is volcanic.

The Upper Limestone Group (ULG) is lithologically similar to the LLG. Several well-developed limestones provide useful marker horizons, though sandstones and mudstones are more common. Coals are generally poorly developed. Minor unconformities within the group are also mapped. Volcanic strata are restricted to ash horizons in Fife and Ayrshire.

The Passage Group (PG) is poorly defined stratigraphically. The group consists mainly of sandstones with locally thick beds of clay rocks. Erosive bases to the sandstone horizons are responsible for many non-sequences. Marine bands and coals are thin and impersistent except at Westfield in Fife. In Ayrshire, basaltic lavas separate two sedimentary groups, the upper of which contains bauxitic clays. The lavas are overstepped by the Coal Measures and, in places, rest unconformably on the ULG. Sedimentation continued to follow approximately the pattern established in the Dinantian, though distorted in Ayrshire by the lava pile.

The Lower and Middle Coal Measures (LCM, MCM) consist of cycles of coal, mudstone, sandstone and seat clay. Reddening of the strata occurs near the top of the MCM extending down from the Upper Coal Measures (UCM) and Permian. The UCM are mainly red sandstones, though grey beds occur in Ayrshire and Douglas with thick coals in the latter.

1.5.4. Igneous Activity

The Carboniferous succession in the Midland Valley contains large volumes of intrusive and extrusive igneous rocks (Fig.1.11). Most are of alkaline affinity. In addition, there are tholeiitic sills and dykes (the Midland Valley Sill Complex) emplaced during the late Carboniferous.

The distribution in time and space of this activity is shown in Fig.1.12. The greatest volume of lavas was produced during the Dinantian, the bulk of later activity being phreatic, though more widespread.

Thick lava sequences occur in the CSM of East Lothian and in the western Midland Valley where the Clyde Plateau Lavas outcrop to the north, west and south of Glasgow. It is possible that the two areas are the remnants of a virtually continuous lava field which covered the Midland Valley in the early Visean (De Souza 1979). The lavas of the Clyde Plateau frequently show well-developed boles indicative of contemporaneous sub-aerial weathering (MacDonald 1973). The flows probably originated from the many associated vents, though fissure eruption has been suggested due to the lateral persistence of some flows (up to 6 km) (Francis et al. 1970).

Towards the end of the Dinantian activity became concentrated around Bathgate and near Burntisland (Allan 1924). The Bathgate Lavas probably overlap those of the Clyde Plateau (Anderson 1963) (Fig.6.7), whilst plugs and vents in the West Lothian oil-shale fields suggest a former eastward extension of these lavas.

Silesian igneous activity is characterised by phreatic explosive eruptions from a large number of vents. However, the lavas of the Bathgate Hills continue into the Silesian, interbedding with sedimentary horizons, whilst basaltic lavas in the Passage Group of Ayrshire reach 160 m in thickness. There are also a series of lava flows at Westfield in Fife. In the Westphalian, activity was concentrated in the Firth of Forth where the LCM are entirely volcanic.

There are many alkaline sills of Silesian age within the Midland Valley. This may be due to the inability of thick piles of unlithified Carboniferous sediments to support a magma column. This caused sill emplacement to replace surface extrusion (Francis 1968).

The late Carboniferous tholeiitic activity resulted in a large number of east-west trending dykes which acted as feeders to the extensive Midland Valley Sill Complex. The structure of the intrusion is complicated; the sill changes stratigraphic horizon and is found to be thickest in basinal areas. Francis (1982) describes the mechanism of intrusion of the complex.

1.6. Permian

Permian outcrop in the Midland Valley is restricted to Arran and around Mauchline. There are also isolated outliers in the Southern Uplands. The rocks are mainly red sandstones and mudstones with basaltic lavas, indicating a terrestrial environment (Lovell 1983, Cameron & Stephenson 1985).

The succession in the Mauchline basin consists of up to 300m of basaltic lava flows with thin intercalated sediments, overlain by aeolian sandstones reaching 450m in thickness (Mykura 1967).

Many vents mapped in the Midland Valley as cutting Carboniferous strata are assumed to be of Permian age, suggesting the Mauchline Lavas to be a remnant of a far more extensive igneous province.

Probable Permian rocks are mapped in the Firth of Clyde based on geophysical evidence and limited sampling (McLean & Deegan 1978). The succession is assumed to be similar to that exposed around Mauchline and on Arran.

Understanding the tectonic environment in Permian times is difficult due to lack of outcrop. Mykura (1967) describes northwest trending fractures which controlled deposition in the Mauchline basin. Hall (1974) suggests such structures originated in the Carboniferous, becoming more important throughout this period, and traces the system into the Southern Uplands and Vale of Eden. McLean (1978) includes this, together with the offshore east Arran basin and a linear system extending from Stranraer to the Cheshire Basin, as evidence of the importance of north-west trending structures at this time.

1.7. Post-Palaeozoic

No sediments or extrusive volcanics of post-Permian age occur in the Midland Valley. However, Tertiary dolerite dykes associated with the Arran and Mull igneous centres are relatively abundant in the west of the region, whilst doleritic sills of similar age occur in Ayrshire. Faults of northwest trend, common in the western Midland Valley, are assumed to be of Tertiary age (Anderson 1951), though Mykura (1967) and Hall (1974) show structures of this trend to have been active in the late Carboniferous and Permian.

1.8. Summary

Clearly the Midland Valley has undergone a complex tectonic history. The interpretation of geophysical data will be complicated by the structural complexity of the region and its wide variety of rock types. Some ambiguity of interpretations is inevitable and geological and geophysical data must be integrated to reduce these to a minimum.

CHAPTER 2 - PREVIOUS GEOPHYSICAL RESEARCH

2.1. Introduction

A considerable amount of geophysical work has been undertaken in the Midland Valley and adjacent regions. Data from the Firth of Clyde are summarised by McLean & Deegan (1978). More recently, Davidson et al. (1984) review results mainly from the central and western Midland Valley. Hall (1984) outlines geophysical constraints on the structure of the Dalradian block to the north. Unfortunately there is no equivalent review for the Southern Uplands.

2.2. Seismic Refraction

Upper crustal and whole crustal seismic refraction data are available from the Midland Valley and adjoining areas.

Crampin et al. (1970) describe the Lowlands Seismological Network (LOWNET), an array of seven radio linked seismometers in the central and eastern Midland Valley (Fig.2.1a). Analysis of quarry blasts and natural seismic events produced a preliminary model of a three layered upper crust (Fig.2.1b). Layers 1 and 2 have velocities of 3 and 5.65 km/s respectively, though the former is seen only as a time delay on later arrivals. These layers are interpreted as Palaeozoic sedimentary sequences. A refractor of velocity 6.45 km/s occurring at 7-8 km depth is interpreted as crystalline basement.

The north-south trending Lithospheric Profile in Britain (LISPB) crosses the Midland Valley near Edinburgh (Fig.2.2). The experiment is been described by Bamford et al. (1976, 1977, 1978), Kaminski et al. (1976) and Assumpcao & Bamford (1978). A concise summary is given by Bamford (1979).

The four layer crustal model defined for northern Britain is shown in Fig.2.3. The layers are interpreted as:

[1] A superficial layer of Upper Palaeozoic and younger sediments. The geometry of this layer is poorly constrained and based mainly on geological evidence.

[2] In the Highlands this layer has velocities of 6.1-6.2 km/s and is interpreted as a combination of Caledonian metasediments and intrusions. South of the Highland Border the layer has a velocity of 5.8-6.0 km/s and is interpreted as a Lower Palaeozoic succession.

[3] North of the SUF this layer has a velocity of 6.48 km/s and is interpreted as the Caledonian foreland. South of the SUF the layer has a velocity of 6.28 km/s. This difference is considered significant by Bamford (1979) though no geological interpretation is suggested.

[4] A lower crustal layer, poorly constrained to the south of the SUF, with a velocity of 7.0 km/s.

Crustal thickness varies from 25 km at the northern end of the LISPB profile to more than 30 km beneath the Midland Valley. The mantle has a uniform velocity of 8.0 km/s. Good shear waves were recorded from several shots. Comparison of P- and S-wave velocities and travel times enabled Assumpcao & Bamford (1978) to compute Poisson's ratio along the profile (Fig.2.4).

The LISPB interpretation suggests that the SUF is a fundamental element in the British Caledonides since it separates two types of pre-Caledonian basement (layer 3). LISPB was a large scale experiment with shots tens of kilometres apart and receivers spaced at intervals of several kilometres. Therefore, correlation of surface structures with those mapped seismically may be incorrect.

Hall et al. (1983) re-interpret the LISPB data from the Southern Uplands. The data are combined with data from quarry blasts recorded at the U.K. Atomic Energy Authority seismic arrays at Eskdalemuir and Broughton and the results from the Southern Uplands Seismic Profile (SUSP), a refraction seismic profile along the strike of the Southern Uplands. (Fig.2.5). SUSP predicts P-wave velocities of 6.0 km/s at a depth of about 1 km, increasing to 6.3 km/s at 3-4 km depth. Apparent velocities measured at the Broughton array, located on the SUSP line, confirm these velocities from sources to the north-east and south-west (along strike), and from the Midland Valley to the north-west. From the south and east, however, apparent velocities are lower, being typically 5.6-5.8 km/s. This suggests that the high velocity crust recognised by LISPB in the Midland Valley continues beneath the Southern Uplands, but deepens to the south-east of SUSP and Broughton. Data recorded at the Eskdalemuir array show high apparent velocities along strike to the north-east and south-west, with lower velocities across strike to the north-west and south-east. These data can be explained in terms of a high velocity block, 10-20 km wide, occurring beneath Eskdalemuir and extending along strike.

Re-examination of the LISPB data from the region shows that the time-distance data can be interpreted in terms of a series of low and high velocity segments of about 5.6 and 6.0 km/s (Hall et al. 1983). The original interpretation assumed these effects to be due to refractor relief. Fig.2.6a shows how a model of upper crustal blocks can satisfy the data. The lithological implications of the velocity data are shown in Fig.2.6b (see Hall et al. 1983 for sources of data). Field and laboratory measurements of the velocities of greywackes and crystalline rocks of granitic to dioritic composition are plotted. It is concluded that the high velocities are due to crystalline rocks of granodioritic to dioritic composition, whilst the lower velocities are from greywackes. Oliver et al. (1984) have suggested that the observed velocities are due to a transition from poorly foliated prehnite-pumpellyite facies greywackes to well foliated greenschist facies quartzo-feldspathic schists. It is unlikely, however, that such a transition would be sharp enough to explain the data.

The LISPB model of Midland Valley upper crustal structure is shown in Fig.2.7. The interpretation of arrivals from the uppermost crustal layer is clearly a poor fit to the data. Fig.2.9a shows a series of short to medium range seismic refraction profiles recorded to refine the LISPB model in the Midland Valley (Davidson et al. 1984, Sola 1985, Davidson 1986). Fig.2.8 includes P-wave velocity data from different groups of rocks from within the Midland Valley, plus velocity-depth models from a number of sources (see Davidson et al. 1984 for sources). The Carboniferous and Upper ORS sediments are of distinctly lower velocity than the Lower ORS and Lower Palaeozoic sediments. Velocities encountered at shallow depth are acceptable for Lower Palaeozoic and Lower ORS rocks, but layer 2 velocities are comparable to those of quartzo-feldspathic gneisses. As in the Southern Uplands, the interpretation of LISPB layer 2 as a Palaeozoic sedimentary sequence is probably incorrect.

The time-distance data described by Davidson et al. (1984) show a sharp change in apparent velocity, from velocities attributable to the Carboniferous and Upper ORS, to those characteristic of the Lower ORS and Lower Palaeozoic, at a depth of about 2 km. This suggests the unconformity between the Upper and Lower ORS, mapped at the surface in the Midland Valley, is a refractor, and allows the subdivision of LISPB layer 1. The data from lines 1 and 2 (Fig.2.9a) presented by Davidson et al. have been reinterpreted and are described in chapters 5 and 7. The line 3 profile trends approximately east-west from the Ayrshire coast to the Southern Uplands (Fig.2.9a). Where the line crosses outcrops of Lower Palaeozoic rocks velocities are found to increase gradually with depth before a sharp increase to 6.0-6.1 km/s at about 3 km. This velocity is comparable to that of the LISPB "Lower Palaeozoic" layer 2. Clearly this refractor cannot be the top of a Lower Palaeozoic sequence and so supports the interpretation of this layer as basement. Fig.2.8 shows the velocity of this refractor to plot within the field for acid-intermediate gneisses, confirming the presence of crystalline rocks at a depth of about 3 km.

Based on these data a revised crustal model may be constructed, Table 2.1.

Table 2.1. Crustal Model for the Midland Valley of Scotland.

Layer	Velocity (km/s)	Approximate Depth (km)	Interpretation
1	2.5-3.5	0-3	Carboniferous and Upper ORS
2	4.0-5.5	3-6	Lower ORS and Lower Palaeozoic
3	5.9-6.2	3-8	Crystalline basement (6.0 km/s)
4	6.4	8-20	Crystalline basement (6.4 km/s)
5	7.0	20-35	Lower crust
		35	Moho

MacBeth & Burton (1985) describe surface wave data obtained in the Midland Valley and adjacent regions. Arrivals from the Kintail earthquake, recorded during the LISPB experiment, were inverted to provide regionalised shear wave velocity profiles. Seven regions of relatively homogeneous velocity are recognised with resolution to 17 km depth. Velocities in the topmost 2 km are consistently low with an average velocity of 3.15 km/s. Lower layers have a mean velocity of 3.60 km/s and show a consistent velocity gradient between limiting values of 3.4-3.8 km/s. The low near surface velocities represent an average of the topmost 2 km and are probably caused by a superficial weathered layer and open cracks in the upper few hundred metres. MacBeth & Burton (1986) refine the model for the Midland Valley using marine shots fired in the Firth of Forth and recorded by the LOWNET array. Shear wave velocity profiles were constructed for the uppermost 2 km of the Midland Valley (Fig.2.10). There is reasonable agreement between five of the eight profiles with velocities grouped around 1.45 km/s at the surface, increasing to between 1.9 and 3.5 km/s at 2 km depth. The velocities from the DU and ELO profiles are seen to be anomalously high with surface velocities of about 2.1 km/s. This is because the ray-paths from shot to receiver are mostly through Lower ORS, whilst the remaining data are mainly from lower velocity Carboniferous strata.

2.3. Seismic Reflection

Commercial seismic reflection data and deep reflection profiles obtained for academic purposes have been recorded within the Midland Valley and its offshore continuations.

Hall (1971, 1974) describes the results from a small scale seismic reflection survey in the western and central Midland Valley. Reflection profiles and velocity data were used to determine the thickness of igneous rocks in these areas.

Vibroseis reflection data, recorded to 6.0 s two way time (TWT) for the Tricentrol Oil Corporation, have been studied by the author though a detailed interpretation was not attempted. Limited data, recorded for the British Geological Survey (BGS) during the Tricentrol survey, show coherent events to around 2 km depth (Penn et al. 1984). This is typical of reflection profiles from within the Midland Valley which rarely image structures below refraction layer 1 (Carboniferous and Upper ORS), i.e. below about 2 km depth. This lack of penetration is probably due to mining out of coal seams in the Carboniferous strata, plus the complex faulting and geology of the sequence. In addition, the

WINCH data suggest that the underlying Devonian sequence may be seismically transparent (see below).

Data recorded to 15 s TWT across the offshore continuations of the Midland Valley have been obtained by the British Institutions Reflection Profiling Syndicate (BIRPS). The Western Isles North Channel (WINCH) profile (Brewer et al. 1983) extends from the Outer Hebrides to the Irish Sea (Fig.2.2). Hall et al. (1984) describe a detailed interpretation of this line where it crosses the offshore continuations of the Midland Valley and bounding Dalradian and Southern Upland terranes. Fig.2.11 shows a line drawing of this section of the profile. Lines represent coherent events within the data. From the surface, the dotted horizons are; top of crystalline basement, top of the reflective lower crust, base of the crust (Moho) and a mantle reflector.

The Carboniferous and Permo-Triassic sediments of the Firth of Clyde basin are seen to be about 2.0 and 1.5 km thick respectively. Since the profile crosses a northwest trending basin, similar to the Mauchline Basin of the Midland Valley, these thicknesses can only be extrapolated along strike with caution, though they are comparable to onshore estimates. The underlying basement is characterised by a lack of coherent signals and occurs at around 3-4 km, shallowing towards the Midland Valley margins. Reflective lower crust is less well-developed beneath the Midland Valley than to the north and south. This may be a function of the data processing since higher background noise levels have been shown to disguise deep crustal reflectivity (Klemperer pers. comm.). A change in crustal character associated with major strike-slip movements does, however, remain a possibility.

The Moho occurs at about 10 s TWT, equivalent to approximately 30 km depth. To the north, the Moho shallows to about 8 s TWT near Islay, whilst beneath the Southern Uplands it probably remains at about 10 s TWT.

The data provide little insight as to the nature of the Midland Valley bounding fractures. High-angled structures would not be imaged, but there is no evidence of a change in seismic character correlatable with the surface faults, though Hall et al. (1983) suggest no major structure should be anticipated at the SUF. Data from the Highland Border are confused by shallow diffractions, but Hall et al. (1984) suggest a high-angled fault is more likely than a major thrust.

The Northeast Coast (NEC) line (Fig.2.2), also recorded by BIRPS to 15 s TWT, runs sub-parallel to WINCH off the east coast of the Midland Valley and Southern Uplands (Klemperer & Matthews 1987). Where the line crosses the eastward extrapolation of the Midland Valley and SUF virtually no upper crustal structure is imaged. Reflective lower crust occurs at about 7.0 s TWT and the Moho at about 10.0 s TWT, corresponding to depths of approximately 20 and 30 km respectively. Again, reflective lower crust is less well-developed beneath the Midland Valley than in other parts of the profile.

2.4. Gravity and Magnetics

Fig.2.12 shows two north-south trending gravity profiles across the Midland Valley (Hipkin & Hussain 1983). The effects of known sedimentary layers have been removed to highlight anomalies of deeper origin. The LISPB experiment predicts a layer of velocity 6.4 km/s to occur at about 7 km depth beneath the Midland Valley terminating at the SUF and falling to about 15 km depth some 20 km north of the HBF (Fig.2.3). This would result in a positive anomaly of 20-30 mgal in the Midland Valley relative to the areas to the north and south. The required change in gravity is observed to the north and seems to coincide with the Moine-Dalradian contact mapped at the surface. No equivalent change is observed to the south. (The "low" immediately to the south of the SUF is interpreted as a granitic body beneath the Southern Uplands (Lagios & Hipkin 1979)). Hipkin & Hussain (1983) assume the LISPB model of the SUF to be correct and suggest that lower crustal/mantle mixing is compensating for its predicted gravitational effects in this region. Several independent lines of evidence (Hall et al. 1983, Upton et al. 1983, Al-Mansouri 1986, Davidson 1986) suggest that the LISPB model is incorrect and that the Midland Valley basement continues under the Southern Uplands. Such a model requires no gravity gradient in the region of the SUF.

The regional aeromagnetic map of the Midland Valley (Fig.2.9c) shows anomalies which correlate with exposed basic igneous rocks, and linear features associated with the SUF and the HBF (BGS 1972, Hall & Dagley 1970). Hipkin & Hussain (1983) describe the regional Bouguer gravity map covering northern Britain. The part of this map covering the Midland Valley is shown in Fig.2.9b.

The regional gravity and magnetic maps highlight a number of local anomalies. Modelling of these anomalies is hindered by a lack of geological control and usually only provides a series of models of possible sources.

Anomalies associated with the Inchgotrick, Kerse Loch and Southern Uplands Faults are modelled by McLean (1966). Modelling changes in thicknesses of stratigraphic units across these faults enables syn-depositional movements to be estimated, e.g. 800m for the Inchgotrick Fault during the Carboniferous.

Qureshi (1970) considered the anomalies associated with the HBF. The models used are over simplified, e.g. basement of uniform density is assumed and the effects of the Highland Border Complex are ignored. These models suggest the Lower ORS to be around 1.5 km thick in this region.

A gravity "low" centred around Hamilton was modelled by Alomari (1980) as either a Lower Old Red Sandstone basin up to 10 km thick, or an acidic pluton extending from about 4 to 12 km depth.

The gravity and magnetic "high" centred around Bathgate was modelled by Hossain (1976). Two models were produced (Fig.2.13), representing the shallow and deep extremes of a series of possible solutions. The shallow model consists of a cone of lavas, identical to those outcropping in the Midland Valley, extending to a depth of 5 km. The second model consists of a deep (10-14 km) ultra-basic intrusion. For this model the magnetic anomaly was smoothed by calculating the effects of increasing the flight height by 2 km. This removes high frequency effects due to near surface features.

The abundance of igneous rocks in the Midland Valley make gravity and magnetic modelling without good geological/geophysical control unreliable. Much of the earlier gravity and magnetic work needs re-assessing in the light of the MAVIS data and is discussed in sections 6.3 and 7.5.

2.5. Electrical Methods

The electrical conductivity of the crust beneath Scotland and northern England has been investigated by several magneto-telluric surveys. Jones & Hutton (1979a, 1979b) describe data mainly from the Southern Uplands, though two stations are within the Midland Valley. One-dimensional inversion of these data suggests there is a conductive zone beneath the Midland Valley between about 12 and 44 km depth. In addition, the Carboniferous sediments may form a superficial conducting layer, though such shallow structure is not well resolved. Beneath the Southern Uplands there is a zone of similar conductivity between depths of about 28 and 70 km. Jones & Hutton (1979b) suggest that these layers are the same because of their similar resistivities.

Hutton et al. (1980) extend this work with thirty new stations, forming a traverse approximately coincident with the LISPB profile. One-dimensional inversion at each site was combined to form a two-dimensional profile. This model is poorly constrained in the Midland Valley. Ingham &

Hutton (1982a, 1982b) extend the data into the Midland Valley (Fig.2.14). Agreement between this model and LISPB is not necessarily to be expected, but there are some correlations, e.g. between the depth to the lower crust on LISPB and a decrease in resistivity. In addition, changes in depths to crustal layers are seen to occur at the SUF in both cases. It is not clear to what extent the LISPB model was used to constrain the magnetotelluric interpretation. South of the Ochil Fault (station KRS, Fig.2.14) "Carboniferous sediments" are shown as about 2 km thick with a similarly resistive layer at about 5 km. This is in agreement with the seismic models of Davidson et al. (1984), though such shallow structure is poorly constrained by the electrical data.

2.6. Summary

Geophysical work in the Midland Valley can be divided into large scale experiments to examine deep crustal structure and small scale investigations of near surface features. The smaller scale experiments have shown some of the results from the larger to be incorrect. However, their localised nature makes them of limited use. The intermediate scale of the MAVIS experiment enables the results of these surveys to be better integrated and upper crustal structure to be mapped across much of the southern and central Midland Valley.

CHAPTER 3 - DATA ACQUISITION AND PROCESSING

3.1. Introduction

Acquisition of controlled source MAVIS data was in two phases. MAVIS I was recorded in the summer of 1984 and consisted of two, sub-parallel, east-west trending lines. The MAVIS I south line involved five shots, at Trearne, Drumgray, Avonbridge, Oxcars and Methil. The MAVIS I north line also had five shots, at Ballikinrain, North Third, Cattlemoss, Westfield and Methil. Subsequently, an additional north-south trending line (MAVIS II) was recorded in the autumn of 1985, with shots at Aberuthven, Dollar, Longannet, Avonbridge and Blairhill. A further line (MAVIS III) was recorded using the quarries at Cruiks, Hillwood and Kaimes as sources. Data from quarries at Cairnyhill, Tamsloup, Headless Cross and Cairngryffe were used to supplement MAVIS II. Quarry-blast data obtained from sources at Tamsloup and Kaimes (Sola south line), and Medrox and Craigpark (Sola north line) by Sola (1984), were re-interpreted. The locations of these seismic lines are shown in Fig.3.1., Appendix 2 and in Appendix 2 of Sola (1984).

3.2. Data Acquisition

The MAVIS I data acquisition and initial interpretation were undertaken by A.Conway whilst employed as a research assistant at Glasgow. M.Fleming was similarly employed for the MAVIS II experiment. Thus much of what is described in this section is their work.

The line lengths required for the MAVIS I experiment were estimated using an upper crustal model (Fig.3.2b) similar to that described by Davidson et al. (1984). The time-distance graph predicted by the model is shown in Fig.3.2a. Cross-over distances of 7, 33 and 82 km are obtained for first arrivals from the three refractors. Clearly, to obtain first arrivals from all four layers, a line length in excess of 80 km is required. Line lengths of 81, 107 and 49 km were used for the MAVIS I north and south lines and the MAVIS II line respectively. The shorter line length in the latter case meant that first arrivals from the deepest refractor were not anticipated.

Five approximately equally spaced shots were fired on each line. Shot details are given in Table 3.1. The larger end shots were designed to penetrate to the deeper layers, whilst smaller within line shots were intended to provide reversal of the shallower refractors (Fig.3.3).

During the planning of MAVIS I quarry owners were approached to fire the shots. However, the shot sizes were unacceptably large since their maximum instantaneous charge was 75 kg. Mindful of public relations they were reluctant to detonate larger charges. Private landowners proved to be more helpful. Permitting problems caused the MAVIS I south line east end shot to be moved from off the East Lothian coast, to the site used for the north line end shot near Methil. This has the advantage of providing a location common to both lines for comparison of delay times etc. In permitting the MAVIS II line the opposite was found to be true. The extremely wet summer of 1985 meant that crops were still in the field in November and that the ground was

Table 3.1a. MAVIS Customised Shot Details.

LOCATION	GRID REFERENCE km E	km N	DATE	TIME (BST)	SHOT DETAILS	DETECTED TO:
MAVIS I (South Line)						
TREARNE	237.28	653.27	26.5.84	09 39 56.05	2 X 150 kg Plaster Gelatine in two 50 m holes	85 km
DRUMGRAY	277.26	670.02	26.5.84	11 49 56.79	100 kg Plaster Gelatine in one 50 m hole	45 km
AVONBRIDGE OPENCAST	291.33	673.87	26.5.84	15 04 55.57	100 kg Plaster Gelatine in one 50 m hole	50 km
OXCARS	323.77	680.80	26.5.84	11 13 15.33	5 X 100m 200 grain Superflex on sea bed in 10 m of water	50 km
METHIL	336.70	692.00	26.5.84	13 42 47.25	200 kg Plaster Gelatine on sea bed in 30 m of water	110 km

Table 3.1b. MAVIS Customised Shot Details.

LOCATION	GRID REFERENCE km E	km N	DATE	TIME (BST)	SHOT DETAILS	DETECTED TO:
MAVIS I (North Line)						
BALLIKINRAIN	255.79	686.93	4.7.84	15 34 56.94	1 X 150 kg + 3 X 50 kg Plaster Gelatine in one 50 m and three 20 m holes	65 km
NORTH THIRD	274.93	688.19	29.5.84	19 22 36.44	150 kg Plaster Gelatine in one 50 m hole	45 km
CATTLE MOSS	299.43	691.53	29.5.84	15 44 54.21	150 kg Plaster Gelatine in one 50 m hole	45 km
WESTFIELD OPENCAST	321.11	698.90	29.5.84	15 17 25.01	3 X 50 kg Ammonium Nitrate slurry in three 15 m holes	25 km
METHIL	336.70	692.00	29.5.84	13 47 23.81	200 kg Plaster Gelatine on sea bed in 30 m of water	85 km

Table 3.1c. MAVIS Customised Shot Details.

LOCATION	GRID REFERENCE km E	km N	DATE	TIME (BST)	SHOT DETAILS	DETECTED TO:
MAVIS II						
ABERUTHVEN	297.75	712.74	17.11.85	12 05 05.26	2 X 150 kg Plaster Gelatine in two 50m holes	50 km
DOLLAR	296.92	696.10	17.11.85	12 35 38.82	2 X 100 kg Plaster Gelatine in two 30m holes	30 km
LONGANNET QUARRY	296.48	685.98	17.11.85	14 07 42.74	2 X 100 kg Plaster Gelatine in two 30 m holes	25 km
AVONBRIDGE OPENCAST	291.03	673.82	17.11.85	14 25 06.06	2 X 100 kg Plaster Gelatine in two 30 m holes	40 km
BLAIRHILL QUARRY	288.64	665.94	17.11.85	14 45 04.82	2 X 150 kg Plaster Gelatine in two 50 m holes	50 km

frequently waterlogged. Consequently, landowners were reluctant to allow drilling rigs onto their land. In the event four quarries were used, with the remaining shot (Dollar) on farmland. A further problem with this line was that commercial seismic reflection crews working in the area had acquired a reputation for damaging crops etc. The different nature of the MAVIS survey did not convince some landowners that things would be any different and they refused to co-operate. One landowner was wise to the potential profit to be made from charging for access to his land during seismic experiments. The line was moved to avoid his property.

Before undertaking the MAVIS I experiment background noise levels were investigated using data from the LOWNET seismological array (see section 2.2). The major source of noise was found to be the weather, particularly strong winds which increased noise levels ten-fold. Industrial and urban noise were only locally significant and substantially reduced at weekends. For this reason, whenever possible, the data were recorded at the weekend. Wind noise was virtually eliminated during the recording of MAVIS II by sheltering exposed geophones beneath a plastic bucket.

Experiments, prior to MAVIS I, to find the best form of geophone to ground coupling showed that a single vertical 4.5 Hz L15B Mark Products geophone waxed to rock gave a higher signal to noise ratio than an array spiked and buried in drift. For this reason rock sites were used wherever possible. For MAVIS II lack of exposure made drift sites unavoidable. However this, and subsequent quarry-blast work, showed that carefully selected drift sites can yield good data. Particular sources of noise are structures extending underground which are liable to move in the wind, e.g. fences and trees. In one instance during MAVIS II, and several times during quarry-blast recording, geophones were waxed to man-made structures, usually concrete floors. Good data were obtained in all cases.

Geophones were spaced at regular intervals (typically 1.5 km) between shots. Spacings were greater in urban areas where suitable sites are rare, e.g. where the MAVIS I south line passes through Glasgow. For the MAVIS II line receivers were placed up to 1 km off line to avoid the built up Grangemouth-Polmont area. Land shot and receiver sites were located, where possible, to within 10 m using Ordnance Survey maps. Marine shots were located using the firing ship's radar location system. Larger uncertainties in location were accounted for by assigning larger travel-time errors, based on predicted apparent velocity of the arrival and the location uncertainty. Ranges were calculated from national grid co-ordinates.

To record the MAVIS lines fifty FM seismographs were designed and built at the Department of Geology, University of Glasgow. These "Mark 2" instruments were developed from prototypes built in 1981 and were designed to be a cheap, portable and easy to use alternative to the NERC Geostore equipment. The recorders use a standard stereo cassette tape in conjunction with a four track recording head, i.e four tracks are recorded on the two-sided two-track (stereo) tape. Use of a C120 tape allows an hour long window to be recorded. Two tracks of seismic data were recorded from the single vertical component geophone on a 3 kHz carrier; a high gain channel selectable in 6 dB steps over a range of 88-118 dB, and a low gain channel set 18 dB down from the selected high gain. The remaining channels record the 60 kHz MSF time signal broadcast from Rugby and any auxiliary data. A remote starting facility on the instruments allows recording to begin up to twenty-four hours after deployment. This facility is particularly useful for recording quarry blasts, where there is usually only limited time and assistance for deployment. Recorder specifications are given in Appendix 1.

Recorder gains for MAVIS I were estimated from a 50 kg test shot recorded to 20 km. Fig.3.4 shows gain setting as a function of range and shot size, based on this data set. The ranges reached by the MAVIS I shots were variable (Table.3.1) depending on shot type and position within the line. The Westfield shot reached only 25 km, probably due to poor confinement in shallow holes and the use of a lower velocity slurry explosive. In contrast, the Methil (south line) shot was recorded along all 110 km of the line. The shorter line length and previous experience of gain setting and shot size and type, meant all shots were recorded along the entire MAVIS II line. For quarry-blast recording a source equivalent to 150 kg instantaneous charge was assumed in gain estimation. This was because charge delays and sizes are usually determined by the quarry on the day of the blast. Therefore, these could not be ascertained until arrival at the quarry to record the shot instant. Data were recorded at ranges of up to 25 km, the maximum attempted.

The MAVIS I south line was recorded on Saturday 26th May, the north line on Tuesday 29th May 1984. The mid-week recording was necessary because MSF transmission was due to stop on the 30th May for three weeks maintenance. Drilling problems with the north line Ballikinrain shot prevented it being fired at the required time. This shot was recorded one month later when the MSF transmitter was working again. The MAVIS II line was recorded on Sunday 17th November 1985. Recording of the MAVIS lines was undertaken with the assistance of the staff and students from the Geology Department. University and hired vehicles were used with, if possible, each driver experienced in the use of the sets. Recorders were operated manually during pre-arranged recording windows with gain settings changed as appropriate. The simplicity of operating the seismographs is reflected in the high success rate in obtaining recordings.

All drilling and shot firing was sub-contracted to Ritchies Equipment Ltd of Dunblane. Following the drilling problems that delayed the Ballikinrain shot on MAVIS I, wherever possible holes were drilled in advance for MAVIS II. Explosives had to be loaded on the day of firing, however, to comply with legal requirements. Shot times were obtained from "shot boxes" or recorders placed close to the shots, with a correction applied for shot depth and distance from the hole. Velocities were taken from Hall (1970). For the Dollar shot of MAVIS II the recorder malfunctioned and the shot instant was calculated from the two nearest recorder sites (both at ranges of about 1 km).

Seismic data were successfully recorded at about 90% of sites during all phases of MAVIS. The few failures were due to non-operation of the remote triggering system, or not being on site at the correct time. By far the largest cause of data loss was non-reception, or poor recording, of the MSF time signal preventing accurate measurement of arrival time. This reduced the quantity of useful data to between 70 and 80%. Future sets will include a synchronised internal clock to overcome this problem. Initial trials with this improvement have proved successful.

The use of quarry-blasts as seismic sources has been discussed by Davidson (1986) and Sola (1985). They conclude that quarries are reasonable sources of P-wave first-break data, but second arrivals are obscured by the length of the first-break wavetrain, typically 500 ms in duration. This duration is due to the quarry-blast, consisting of a series of time-delayed charges in closely spaced holes, creating a long source waveform. This type of blast is used because it fragments the maximum volume of rock whilst reducing vibration outside the quarry. This means the effective seismic source is the first hole detonated. In spite of these problems, Davidson (1986) was able to successfully discriminate S-wave energy by filtering. A further problem with quarry sources is that they are designed to send energy upwards. Holes are typically about 10 m from the quarry face, the blast being intended to collapse the rock between the shots and the face. This limits the amount of energy passing down into the Earth. Despite these limitations, the overwhelming advantage of quarry-blast sources over customised shots is cost, the former are free. Details of quarry-blast sources are given in Table 3.2.

When recording quarry-blasts, two operators usually set up the recorders relying on the remote starting facility. Data were typically recorded at about ten locations. Lack of recorders required that the earlier work that has been reinterpreted was built up piece-meal, recording each blast at perhaps two or three sites.

Locating the shot position within a quarry is difficult. Ordnance Survey maps are not sufficiently up to date to be of use. Also, for environmental reasons, quarries usually have a narrow entrance widening where the face is being worked. This screens the view outside from within the quarry, making positioning using back-bearings virtually impossible. This problem was partially overcome by recording the travel time to a reference site from a located shot point. All subsequent origin times were calculated relative to this travel time. This meant small movements of shot location were unimportant.

Limited recording of the Compagnie Generale Geophysique (CGG) Vibroseis source, being used by the Saxon Oil Company (now part of Enterprise Oil) for seismic reflection work near Hamilton, was also undertaken. Fig.3.5 shows the only successful recording, made at a range of a few 100 m. Failure to record the signal was partly because the vibrators were not powerful enough to be detected at useful refraction survey ranges, and partly because the sweep frequencies (about 20-80Hz) were somewhat high for the recorders to detect.

Table 3.2. MAVIS Quarry-Blast Details.

LOCATION	GRID REFERENCE km E	km N	DATE	TIME (BST)	SHOT DETAILS	DETECTED TO:
MAVIS II						
CAIRNYHILL QUARRY	284.84	666.20	16.7.86	13 10 37.68	16 holes 66 ft deep 14 fit spacing, 160 kg per hole single row pattern, 25 ms delay between charges.	15 km
CAIRNYHILL QUARRY	284.85	666.20	23.9.86	13 07 47.13	17 holes 64 ft deep 2400 kg.	10 km
MAVIS III						
CRUIKS QUARRY	313.01	681.70	18.9.86	12 46 01.20	Unknown	25 km
CRUIKS	--	--	23.10.86	12 46 09.16	12 holes 66-80 ft deep	10 km
HILLWOOD QUARRY	313.02	671.78	4.9.86	16 09 20.58	Unknown	10 km
KAIMES QUARRY	313.22	666.44	4.9.86	16 00 12.46	10 holes 46 ft deep 75 kg each hole 25 ms delay between holes	10 km
KAIMES QUARRY	--	--	26.6.86	16 03 54.72	Unknown	15 km
KAIMES QUARRY	--	--	17.10.86	16 00 43.91	7 holes 70 kg each	20 km

3.3. Initial Processing and Digitisation

The playback and digitising system used is shown schematically in Fig.3.6. The recordings obtained from the seismometers were played back using an analogue playback facility and then converted to digital form. The Glasgow system consists of a tape-head similar to that of the recorders, i.e. four track, but wired to playback rather than record. The recording is passed through a demodulator and then analogue filters, usually set to pass frequencies between 3 and 40 Hz. These filters were adjusted to assist in the detection of arrivals on noisy traces. The output is then amplified and passed to a UV Oscillograph. This instrument has the facility to run at a variety of paper speeds, whilst adjustment of the amplifier gain allows the amplitude of the trace to be varied. The MSF signal is also demodulated, but is passed directly to the amplifier and then oscillograph, after cleaning via a Schmidt trigger if required. This signal is also passed to a decoder which displays the time of recording to assist in the location of arrivals.

Arrivals were picked from the analogue playbacks and arrival times calculated using the MSF pulses as a time scale (Fig.3.7). Some data were repicked when digitised data became available. Good first arrivals were considered accurate to +/- 0.03 s. This is the sum of errors attributable to; 1), variations in playback speed, 2), uncertainties in site location, and 3), apparently different arrival times on the two seismic channels. When the MSF signal was poor the time scale was extrapolated from areas of good reception and a larger error in travel time (+/- 0.05 s) assigned. Where data were noisy an error encompassing the uncertainty in arrival time was added to these figures. Second arrivals were picked from the playbacks after digital processing of the data. These arrival times are less reliable since constructive/destructive interference may distort the waveform. A good arrival was assumed to be timed to +/- 0.05 s with larger errors assigned according to the quality of the data.

The analogue data were converted to digital form using a Programmable Data Processor (PDP) 11/23 PLUS micro-computer and software configured by R.T.Cumberland. The same playback system is used with the output passing through 3-40 Hz anti-aliasing analogue filters. An ADV11-C analogue input board accepts sixteen single ended bipolar inputs sampling the data at 200 samples/second. Variation in tape speed causes this sampling rate to vary by less than 2%. Offset binary data are output. The internal programmable gain is set to 8 for the MAVIS data, corresponding to variation of +/- 1.25 volts.

Table 3.3. Relationship Between Input Signal and Digital Output.

Input (Volts)	Output
+1.25	4095
0.00	2048
-1.25	0

Table 3.3 shows the relationship between the digital output (expressed in decimal form) and the input signal. (Note that

because the data are in offset binary form an input of 0.0 volts corresponds to an output of 2048.

For the MAVIS data, the program was configured to receive three input channels and digitise 10 s of data for recordings at less than 20 km range, 15 s at 20-60 km range and 20 s for ranges greater than 60 km. These lengths allowed the digitisation of all useful arrivals for a minimum amount of data storage. Program MSFPLOT, written by R.Reid, was then used to relate the start time of the digital data file to the shot instant, for plotting and digital processing of the data. The program plots the two seismic channels and the MSF channel relative to a time scale. The recognition of a known MSF pulse allows the time and, therefore, number of samples, between the shot and file start time to be calculated. Fig.3.8 shows an example of this calculation. When MSF reception was poor at the time of an arrival and the digitisation window did not include any second pulses, the first arrival, determined from the analogue play-back by extrapolation from areas of good MSF, was used to calculate the file start time. An identical method was used in several examples where the MSF signal did not digitise correctly. The cause of this problem has not yet been determined. These data, plus site range and recorder gain, are included in a header to the digital file. This integer file is then converted to binary form and transferred to floppy disc or the VAX-750 for digital processing.

3.4. Principles and Application of Digital Processing

3.4.1. Principles of Frequency Filtering

Digital processing of seismic data has been described by numerous authors, e.g Robinson & Treitel (1980), Hatton et al. (1986). Only a brief summary of the principles involved is given here.

Any periodic waveform may be expressed in terms of wave amplitude as a function of time (i.e in the time domain), or as a function of frequency by the amplitude and phase of a finite number of sine waves (i.e. in the frequency domain). Seismic waveforms are transient (non-periodic), but may be thought of as periodic with an infinitely long period. Rather than being constituted of discrete frequency components of given amplitudes and phases, they have continuous amplitude and phase spectra, i.e. they have an infinite number of sine wave components. To deal with such waves the amplitude and phase spectra are subdivided into a number of discrete slices. This expression of the continuous spectra in terms of a finite number of discrete frequency components provides an approximation in the frequency domain of what is a transient waveform in the time domain. This concept is illustrated in Fig.3.9. The continuous amplitude and phase spectra in (A) have been divided into sixteen components represented by the sinusoidal waves of different frequency and phase (B). The waveform shown in (C) is the sum of these waves. Thus the time function (C) and the frequency function (A) are seen to be equivalent.

Fourier transformation is used to convert a time function, g(t), into its amplitude, A(f), and phase spectra,

$\theta(f)$, or into the frequency spectrum $G(f)$ such that

$$G(f) = A(f)e^{i\theta(f)} \tag{3.1}$$

$g(t)$ and $G(f)$, the time and frequency domain representations of the waveform, are known as a Fourier pair and are interchangeable, such that each is the Fourier transform of the other.

Frequency filtering provides a means of discriminating against unwanted seismic energy (noise), where its frequency differs from that of the desired seismic waveforms. A seismogram is modified by the suppression of frequency components specified by their amplitude or phase. The effect of a filter is defined by its impulse response, i.e. its output when a spike function is input (Fig.3.10). The Fourier transform of the impulse response is known as the transfer function and specifies the amplitude and phase response of the filter. Mathematically, the effect of the filter is described by the convolution of the input signal, $g(t)$, with the impulse response, $f(t)$, of the filter.

Consider a low-pass frequency filter with cut-off frequency f_c. The ideal output of the filter is represented by the amplitude spectrum shown in Fig.3.11a. The amplitude of frequencies greater than f_c is zero, and is a constant unit amplitude below f_c. This represents the transfer function of the ideal low-pass filter. Fourier transformation of this function into the time domain gives the impulse response shown in Fig.3.11b. Unfortunately this impulse response is infinitely long and therefore of no practical use. Truncation is necessary to produce a realisable filter operator of finite length. Fig.3.11c shows the frequency response of such an operator, shown in Fig.3.11d. Convolution of this filter operator with some input waveform results in low-pass filtering, but with the more gradual cut-off apparent in Fig.3.11c.

Filters can be designed by specifying a transfer function in the frequency domain, this being used to design an impulse response of finite length in the time domain. The truncation of the operator is an important control on the characteristics of the filter. Multiplication with a rectangular (square wave) function of appropriate length does not produce good frequency cut-off (see Fig.3.16). A more useful approach is to gradually truncate the operator by multiplication with a window function. Fig.3.12 illustrates this operation for a 40 Hz cut-off low-pass filter. The window function consists of one cycle of a cosine wave with its trough raised slightly greater than zero. This is known as a Hamming window. The infinitely long operator is multiplied by this window function to produce an operator of length, in this case, 0.25 s and the amplitude spectrum shown in the figure. The now inclined cut-off is centred at 40 Hz. This inclination is controlled by the width of the truncation window, the longer the filter operator the sharper will be the cut-off at the desired frequency.

Frequency filters are often either minimum or zero phase. Assume t0 is some point on the input waveform during the convolution operation such that t<0 represents the future and t>0 the past segment of this waveform. Minimum phase filters have a memory component only and thus operate on the present and past of the waveform, with all values for $t<0 = 0$. This means the output waveform has no phase shift relative to the input. In contrast, zero phase filters have anticipation and memory, the operator being symmetrical about a point t, equal to half the operator length. This has the advantage of more of the input waveform being considered during each convolution operation, but results in a phase shift equal to t/2 relative to the input waveform.

3.4.2. Computer Program

Program PLOT, written by R.Reid and K.Davidson, was used to process the data. The program is still being developed and is not listed here. Spectral analysis and frequency filtering were available for the processing of the MAVIS data. The program will plot unfiltered and filtered seismic data and frequency spectra. As the program and the data in digital form were not available until late in this project, only initial processing of the data has been completed. Improvements to the processing program and more detailed analysis of the data should lead to an improved interpretation.

Low-pass, high-pass, band-pass and band-stop filters are available with rectangular, triangular, Hamming, generalised Hamming, Hanning, Kaiser(I0-sinh) and Chebyshev windows. Filters may be minimum or zero phase and of variable length. Filters are designed using the program FWFIR. This program also allows the plotting of the impulse and amplitude (frequency) responses of the filter designed.

3.4.3. Filter Design and Application

Time precluded an extensive analysis to determine the most appropriate filters. However, initial tests were carried out to determine the most effective combination of filter type and length, and whether minimum or zero phase. The data recorded south from the Aberuthven shot were selected for testing. Strong shear wave arrivals are seen in the unfiltered data between 5 and 15 km range (Fig.3.13). Filter parameters were adjusted to ascertain the best combination for the discrimination of these, and other less obvious, shear wave arrivals.

Spectral analysis of the P- and S-wave data show the former to have frequencies mostly higher than 6 Hz, and the latter to have dominant frequencies of less than 6 Hz (Fig.3.14). A 6 Hz low-pass filter was used for the tests. The impulse and frequency responses of rectangular, Hamming, generalised Hamming(α = 0.50) and Hanning windowed filters (zero phase, 0.5 s operator length) are shown in Figs.3.15 to 3.18. Since the difference between P- and S-wave frequencies is about 2 Hz a sharp cut-off is desirable. The frequency response of the rectangular window suggests discrimination between frequencies will be poor. The frequency response of the Hamming, generalised Hamming and Hanning windows are virtually identical. As expected, qualitative testing of these filters produced very similar results. In the event the Hamming window was used for all processing. Fig.3.19 shows the same data for the Hamming window but with minimum phase. Note the sharper cut-off with the zero phase filter and the greater attenuation of frequencies outside the pass band. This difference is evident in Figs.3.20 and 3.21 where the zero phase filter has been considerably more successful in discriminating against unwanted frequencies. Figs.3.21 to 3.24 illustrate the effects of altering operator length. Lengths of 0.25, 0.50, 1.00 and 2.00 s were tested. Filter length does not appear to greatly affect data quality, though there is slight smearing of the data with increased length.

Filtering was intended to; 1), improve P-wave data quality (particularly second arrivals) by the suppression of background noise and S-wave energy 2), improve S-wave data quality by suppression of background noise and P-wave arrivals. The windowing function in the program PLOT allowed spectral analysis of specified parts of each seismic trace. Spectra were obtained from; 1), the pre-first break part of any trace 2), the first break plus 0.5 to 1.0 s (depending on the length of this wavetrain) and 3), suspected S-wave arrivals. The frequency content of these data was ascertained and filter cut-offs assigned accordingly. It should be remembered that the frequency spectra obtained in (2) are for P-wave signal and noise and in (3) are for S-wave signal, noise and P-wave coda.

3.5. Data Presentation and Analysis

The data are presented in Figs.3.25 to 3.50. Where possible the following seismograms are shown; a), unfiltered data, b), unfiltered data with P- and S-wave picks c), data filtered to enhance P-wave arrivals d), data filtered to enhance S-wave arrivals (if any were identified). All traces are normalised with respect to the maximum amplitude within the trace. Also shown are; E), time-distance graphs of the P-wave arrivals and, where appropriate, F), time-distance graphs of the S-wave arrivals. All are plotted at a reduction velocity of 6.0 km/s, except (D) and (F) which are at 3.5 km/s. Picks in (B) are labelled based on the results of ray-trace modelling (see chapter 5) and the ray-path classification in Table 5.1. Unlabelled picks are those which were not successfully modelled. When data are not available in digital form, i.e. the quarry-blast data, only the P-wave time-distance graphs are shown. P- and S-wave arrival times are listed in Appendix 3.

The digitised data show the first arrival signal to noise ratio to be generally quite good, especially on MAVIS II. As a result, filtering to enhance P-wave arrivals makes little difference to the first break, except where sites are extremely noisy, e.g. trace X on the Trearne and Drumgray seismograms. The discrimination against S-wave energy enhances P-wave second arrivals as expected, e.g. the "a6" reflections on the Oxcars and Avonbridge (MAVIS II) data. Several examples of clipping can be seen, especially on the Trearne data, though this is not a widespread problem. Also, a few traces show evidence of poor coupling to the ground, e.g. trace Y of the Trearne data, the first break is detected, but later (weaker) arrivals are poorly detected. Again, this not a common problem.

Filtering to enhance S-wave energy is reasonably successful. Note that areas where sites were located on drift (see Appendix 2) produce significantly poorer shear arrivals. Compare the S-waves detected to the north of the Dollar shot where all sites are on rock, to those to the south where all sites are on drift. Ranges reached by S-waves are considerably less than the P-waves. The cause may be the similarity of the S-wave and noise frequency spectra. Fig.3.51 shows a typical noise spectra (from the Cattle Moss data). Compare this with the S-wave spectra shown in Fig.3.14. The frequency spectra of the noise is seen to span the S-wave frequencies. It is possible that as range increases the signal to noise ratio for the S-wave arrivals is too low to allow their discrimination.

Shear waves were not detected from the three marine shots. Since all three sources were on the sea-bed this cannot be attributed to the water layer. Fig.3.51 shows the frequency spectra for the Methil (north line) shot of MAVIS I. Note that there is no evidence of a decrease in dominant frequency with range, as might be expected as higher frequencies suffer greater absorption. The P-wave arrivals are of lower frequency than those from the land shots, as can be seen by inspection of the Methil seismogram and comparison of Fig.3.51 and Fig.3.14. The dominant frequency is about 6 Hz. This is similar to the land shot S-wave frequencies shown in Fig.3.14. If the marine shot S-wave frequencies are similar to those recorded from land shots, i.e. there is no decrease in frequency similar to that seen with for the P-waves, then filtering will not allow the discrimination of the S-wave arrivals. Alternatively, the poor S-wave data may be a function of the sea bed detonation instead of within holes.

CHAPTER 4 - SEISMIC VELOCITY DETERMINATION AND INTERPRETATION

4.1. Introduction

In order to interpret arrivals from crustal reflectors and refractors it is important to quantify the velocity variation in the overlying layers. In the Midland Valley there are large volumes of intrusive and extrusive igneous rocks. Failure to detect the resulting variation in seismic velocity could lead to inaccurate estimates of interface depth.

A further cause of such errors is seismic anisotropy.

The SEIS81 ray-tracing package (see chapter 5) does not allow for velocity anisotropy. Most ray paths modelled are sub-horizontal and therefore so are the model velocities. Critical rays travelling at perhaps 40° would travel at lesser velocities in an anisotropic section. The result would be an over-estimate in refractor depth.

Davis & Clowes (1986) describe the results of seismic reflection and refraction work in the Winoma Basin, Western Canada. This basin consists of a sequence of Pleistocene turbidites. Comparison of refraction derived velocity-two way time models with reflection sections from the basin show "basement" velocities (i.e. 4.1 and 5.4 km/s) to occur within the stratified part of the reflection section. Davis & Clowes explain the velocities in terms of a seismically anisotropic sedimentary section. Since the interpretation of the crustal layers detected by the MAVIS experiment depends on their velocities (see section 7.1) it is important to ascertain whether these velocities are the result of anisotropic effects.

An attempt was made to quantify the seismic anisotropy within the MAVIS layer 1 using two separate methods:

[1] Comparisons of velocities derived by different methods.

[2] Mathematical modelling of the anisotropy of stratigraphic sections using data from velocity logs.

Three main sources of velocity data are available; 1), velocities derived from refraction time-distance graphs 2), velocity data summarised in the CDP tables of the Tricentrol reflection sections and 3), limited data from boreholes within the region. These sources measure different velocities; the first can be considered as horizontal velocities whilst the latter two are sub-vertical and vertical velocities respectively. By comparison of these velocities the degree of anisotropy within the Midland Valley can be estimated. Anisotropy may also be estimated by using the interval velocities obtained from velocity logs to construct velocity-depth sections, the anisotropy of which may be calculated.

The derivation and interpretation of the velocity data is described and the significance of the results discussed.

4.2. Velocities from Refraction Measurements

4.2.1. Introduction

Arrivals from the fifteen customised MAVIS shots, combined with the nine quarry sources, provide a large amount of data suitable for modelling the variation in seismic velocity with depth through the topmost crustal layers.

In the Midland Valley the direct arrival segments of time-distance graphs are usually curved (Davidson 1986, Sola 1985). This progressive variation in observed velocity with range is due to velocity varying with depth and/or laterally. Two techniques were used for the inversion of time-distance data to velocity-depth data:

[1] The Wiechert-Herglotz-Bateman method (Grant & West 1965)

[2] The tau-p method (Diebold & Stoffa 1981).

4.2.2. Wiechert-Herglotz-Bateman Method

The Wiechert-Herglotz-Bateman (WHB) method allows the direct inversion of time-distance data to velocity-depth data by means of the solution of the integral

$$Z(V) = \frac{1}{\pi} \int_{x=0}^{x=X} \cosh^{-1} (V\ dt/dx)\ dx \qquad (4.1)$$

where

$$V = (dx/dt)_{x=X}$$

where the velocity is derived at depth Z, Z being the turning point of a ray arriving at the surface at a range X from the source (Fig 4.1). The method is only applicable for situations where there are no velocity inversions and assumes no lateral velocity variation.

4.2.3. Tau-P Method

Several authors have discussed the mapping of time-distance data into the tau-p plane, for example Bessonova et al. (1974), Kennett (1976).

Diebold & Stoffa (1981) show that travel time can be expressed in terms of the horizontal (p) and vertical (q) components of wave slowness

$$\Delta T = p\Delta X = q\Delta Z \qquad (4.2)$$

where

$$p = \frac{\sin i}{V} \quad \text{and} \quad q = \frac{\cos i}{V}$$

V = velocity of medium
i = direction of ray path

Wave slowness, u, is given by

$$u = 1/V = (p^2 + q^2)^{1/2} \qquad (4.3)$$

For a series of horizontal homogeneous layers a refracted ray has travel time

$$T = pX + 2\sum_{j=1}^{n} qj\ Zj \qquad (4.4)$$

(Note that as p is a constant for horizontal layers only the single term pX is required).

This equation defines a straight line tangential to the time-distance curve at the point (T,X) with a gradient p and an intercept on the time axis of tau (τ).

Inversion to velocity-depth data depends on the representation of the time-distance curve as a series of straight lines, and the calculation of depth using planar layer equations for intercept time (see section 5.1.1 and Dobrin (1983)).

When the source-receiver offset is small, u1 (the slowness in the topmost layer) can be taken as equal to p1 and hence

$$u1 = \frac{1}{Vapp1} \tag{4.5}$$

Assuming a series of planar layers

$$Z1 = \frac{\tau(p2)/2}{(u1^2 - p1^2)^{1/2}} \tag{4.6}$$

allowing the use of the expression

$$Zk = \frac{\tau(pk+1)/2 - \sum_{j=1}^{k-1} Zj\,(uj^2 - pk+1^2)^{1/2}}{(uk^2 - pk+1^2)^{1/2}} \tag{4.7}$$

for inversion of the tau-p data to the velocity depth plane.

4.2.4. Application and Reliability of Inversion Methods

Both techniques were applied to the data using a modified version of the program WHB written by J. Hall and modified by K. Davidson. This version of the program, WHB10, is listed in Appendix 6. The program was originally designed to take smoothed time-distance data sampled at regular intervals from the shot-point. The smoothed curve must contain no decrease in its gradient, i.e. no velocity inversions.

Applying the techniques to the direct arrival segments allows near surface velocity variation to be estimated. However, direct arrival segments of time-distance graphs are not always well constrained, due to factors such as recorder failure, noisy traces etc. In order to reflect the degree of constraint on the input curve the program was amended to read data at irregular intervals, thus ensuring that the velocity-depth data would be well constrained where the time-distance data were similarly constrained. The resulting velocity-depth curve is extremely sensitive to the shape of the smoothed curve. Using the estimated error in arrival time (see section 3.3) five curves were input for each shot point (Fig.4.2). The curves were intended to produce the maximum variation in velocity-depth curves obtainable within the errors of the data. One curve (A) represents what is considered to be the best fit to the data, i.e. passing through the maximum number of points within their errors. The remaining four curves represent the straightest (B), most curved (C), and maximum (D) and minimum (E) time curves. In practice, there is a varying amount of scatter on the arrivals and the choice of curves is somewhat subjective. Points plotting well away from adjacent points (i.e. implying unrealistic velocities) were assumed to be the result of local static effects or mis-picks and were ignored.

The program WHB10 uses the resulting velocity-depth curves to determine maximum and minimum values for a given data point, and plots appropriate "error bars" centred on the point derived from the best fit curve. The "error bars" define an envelope of possible velocity-depth curves, but are not true error bars since the position of any point on the velocity-depth curve is dependent on the position of the preceding points. The envelope can be thought of as confidence limits on the velocity-depth data. Note the large velocity ranges obtained even when the data shows no scatter (Fig.4.2).

The reliability of the velocity-depth curves obtained from the above techniques was tested on model time-distance data generated using the SEIS81 ray-tracing program (see section 5.1.3). An aim of the velocity analysis was to provide an initial model of near surface velocity variation for refining by ray-tracing. Therefore, it was desirable that the time-distance data should invert to a velocity-depth model as similar as possible to the model input to the ray-tracing program.

A model was set up based on previous ray-tracing undertaken as part of the initial interpretation of the MAVIS data (Conway et al. 1987). The velocity-depth function was considered to be a realistic estimate of that to be found in the Midland Valley. No lateral velocity variation was included in the model. Twenty stations were modelled at 1 km intervals, with centre and end shots. The ray paths and resulting time-distance graphs are shown in Fig.4.3. Computed travel times to a given range are identical to within 0.01 s in all cases. The five smoothed curves were fitted to the data assuming an error of 0.03 s in arrival time. The WHB and tau-p derived velocity-depth curves are shown in Fig.4.4 with the model curve for comparison. In all cases the curve derived using the WHB method is an extremely good fit to the data. This fit is reflected in Fig.4.5, where the model and depth section derived from the WHB data are seen to be virtually identical. The model curve also lies within the confidence limits of the tau-p curve, though there is a general tendency to overestimate velocity at a given depth.

Fig.4.6 compares the velocity-depth curves derived from the source two data obtained to the west and east, for each inversion technique. The differences between the data sets are an expression of the differences in the smoothed curves fitted to the data. These are seen to be small and well within the confidence limits, though data points derived from stations at identical ranges rarely plot at identical co-ordinates within the velocity-depth plane.

A further problem with the tau-p method is the necessity to know the velocity at the surface. The assumption that u1=1/Vapp1 is often invalid since short offset receivers are frequently absent. The program allows a parameter V0 to be input, but this can only be estimated since the necessary data is rarely available. The effect of using different values is illustrated in Fig.4.7 using data from source 1. As expected, increasing the surface velocity causes a given velocity to be predicted at a greater depth. In the absence of surface velocities this variation is another source of inaccuracy in the tau-p interpretation. The data show that a surface velocity of 3.0 km/s produces the most reasonable results as expected from the model. Underestimating V0 causes overestimation of velocity at a given depth, whilst overestimation distorts the shape of the velocity-depth curve near the surface.

The time-distance curves from the field data vary greatly in the extent to which they are defined, due to varying receiver spacing and geometry. This problem has been partly overcome by adapting the program to take irregularly spaced data. However, the effects on the derived velocity-depth curves must also be considered. Fig.4.8 illustrates the WHB and tau-p derived velocity-depth curves compared to the model curve for various receiver spacings. The data are those from source 2 (E). Doubling the receiver spacing does not alter the WHB curve to any extent. However, the tau-p curve is again affected, with velocities near the surface predicted to occur at a greater depth. This is a function of the need to amend V0 rather than an improvement in the tau-p estimate. The influence of the V0 parameter increases with the offset of the first receiver, representing an increasingly thick "surface" layer. The effects on the tau-p data are similar and greater with a 3 km spacing and the WHB curve is also slightly affected. Despite this the true curve is easily within the confidence limits.

Fig.4.9 illustrates the effects of identical receiver spacing but varying receiver geometry, using source 1 data. For a given method and spacing, the different geometries tested produced virtually identical velocity-depth curves, i.e. the different geometries are less important than the actual spacing. Fig.4.10 illustrates the relative positions of points derived for different receiver spacings, again with the model curve for comparison. The WHB is seen to be little affected though the increased spacing causes a slight decrease in velocity at a given depth. The same is true for tau-p.

The effects of very closely spaced receivers were also considered (Fig.4.11). The data are those obtained from source 2(E) with the extra receivers at a ranges between 3 and 5 km. Again the WHB method provides a good estimate of the true curve. The tau-p curve is seen to trend towards the true curve when receiver spacing is reduced.

This work shows the WHB method to be more useful than the tau-p method (at least in terms of predicting ray-traced models). This is due to the tau-p method approximating the curved ray path by straight line segments, i.e. a continuous function is represented by a discrete set of points (Vera 1987). The problem is particularly acute due to the scarcity of data points compared to the marine refraction data with which the technique is most commonly used. Where receiver spacing is small the straight ray paths are closer to the curved path and hence the two methods yield similar results.

Both techniques suffer from a serious limitation when applied to data from the Midland Valley. In an area of steep dips, rapid lateral facies changes, heavy faulting and where igneous rocks are common, it is very unlikely that velocity will vary only with depth. Lateral velocity variation has to be considered the rule rather than the exception, and therefore, before analysis of real data the model was extended to evaluate such effects. Reference to initial ray-tracing models suggested that a lateral velocity variation of up to about 0.05 s-1 was possible in the region. The model was adjusted such that the velocities below source 2 were unaltered, but this amount of lateral variation was introduced. The resulting time-distance data and ray paths are shown in Fig.4.12. The variation in the shape of the resulting time-distance curves is entirely due to lateral velocity effects. Data recorded in the direction of lateral increase show considerably higher apparent velocities than those, from the same part of the model, recorded against the increase. The curvature of the time-distance segment is therefore a function of both lateral and vertical velocity variation. A single time-distance curve cannot discriminate the two effects and could be produced by an infinite number of combinations of the two.

Fig.4.13 illustrates the velocity-depth curves obtained using both the WHB and tau-p methods, and the model curves below each source. As expected, data recorded in the direction of lateral velocity increase predict higher velocities at a given depth than occur below the source location. Note the better agreement between the two methods for data recorded in the direction of lateral increase.

Obviously it is desirable to derive the true velocity-depth curve from the two curves obtained. This may be done if either reversed or split spread data are available. The method assumes that the vertical velocity gradient is identical along the line of the profile. This is reasonable in the Midland Valley where adjacent sources are usually within 20 km of each other. Also, it is assumed that the degree of velocity variation is constant both laterally and vertically. Fig.4.14a illustrates the method for split spread data using the WHB inversion. Due to the difficulty of comparing curves where there is not a regular spacing of data points, the obtained curves are approximated by third-degree polynomials obtained by curvilinear regression using the "S" package on the Geology Department VAX 750, or second-degree where there a few data points. These are represented by the dashed lines (A and B) passing through the two sets of data. These curves are derived from the similarly labelled time-distance data. The middle line (C) is obtained by taking the average of these two functions. Again the model velocity-depth curves beneath the three sources are shown. Figs.4.14b and 4.14c illustrate the case for reversed data. The same procedure is used, the averaged curve representing the true vertical variation half-way between the two shot points. Thus, simple averaging of the two data point curves is seen to be a good approximation of the vertical velocity variation beneath a point half-way between the two sources, or beneath a source recorded in two directions. Unfortunately the method only allows velocity-depth data to be extended to depths reached by both curves, i.e the depth reached by the curve recorded in the direction of lateral velocity increase.

Averaging is successful because of the small "apparent-dips" of the velocity contours, i.e.

$$V \text{ up dip} = V/\sin(\theta + \text{dip})$$
$$V \text{ down dip} = V/\sin(\theta - \text{dip})$$

where θ is the angle of emergence of the ray

This difference is small enough that the circular nature of the sine function is unimportant.

Fig.4.15a illustrates the velocity structure of the model incorporating lateral velocity variation. The depth section in Fig.4.15b is from WHB data ignoring lateral effects. The section shown in Fig.4.15c uses the method described to remove them. Note the loss of coverage inherent in the method.

Sources of error in the derived curves are the result of; 1), poor constraint of the time-distance data from which the curves are obtained 2), to derive the true velocity-depth curve a pair of curves must be recorded exactly parallel to lateral velocity change.

4.2.5. Field Velocity Determinations

Figs.4.16 to 4.49 show the WHB derived velocity-depth curves with polynomials fitted to the data. Where shear wave data are available Vp/Vs and Poisson's ratio are also plotted (see section 4.2.6)

The effects of lateral velocity variation were removed using the data pairs listed in Table 4.1. (Where ray paths were expected to pass through layer 2, e.g the Dollar north-Aberuthven south data and the Kaimes data, no average curve was calculated). The P-wave results are found to sèparate into two groups with different surface velocities and velocity-depth gradients. The curves converge at approximately 1 km depth (Fig.4.50). The exception is curve 4 which appears anomalously low. The cause of this is is unknown. In the case of the higher velocity group half the receivers (and sometimes the source) are on igneous rocks. The higher near surface velocities are an average of the igneous and sedimentary surface velocities. The "non igneous" data (numbers 7,8,9,10,13) are all from areas where Upper Carboniferous sediments (Coal Measures) outcrop. Best-fit and confidence limit curves are derived from these data by regressing the appropriate curves (Fig.4.51). These data are taken as representative of the P-wave velocity-depth variation through an Upper Carboniferous sedimentary pile.

Table 4.1. Sources used in WHB Inversion.

No.	Source 1	Source 2	Geology At/Between Shots
1	Ballikinrain	North Third W	Lower Carboniferous volc'
2	North Third W	North Third E	Lower Carboniferous volc'
3	North Third E	Cattle Moss W	Carboniferous sed's/volc'
4	Cattle Moss W	Cattle Moss E	Lower Carb' sed's/volc'
5	Cattle Moss E	Westfield	Carboniferous sed's/volc'
6	Trearne	Drumgray W	Carboniferous sed's/volc'
7	Drumgray W	Drumgray E	Upper Carboniferous sed's
8	Drumgray E	Avonbridge W	Upper Carboniferous sed's
9	Avonbridge W	Avonbridge E	Upper Carboniferous sed's
10	Dollar S	Longannet N	Upper Carboniferous sed's
11	Avonbridge N	Avonbridge S	Upper Carb' sed's/volc'
12	Avonbridge S	Blairhill N	Upper Carb' sed's/volc'
13	Headless X N	Headless X S	Upper Carboniferous sed's
14	Medrox E	Craigpark W	Carboniferous sed's/volc'
15	Cruiks S	Hillwood N	Carboniferous sed's/volc'
16	Cairnyhill N	Cairnyhill S	Upper Carb' sed's/volc'

In order to calculate an equivalent S-wave curve two methods were used. Firstly, only the data from the non-igneous sources were used, except those from Headless Cross where S-wave data are not available, and from Dollar and Longannet which are affected by the abnormally low P-wave velocity close to the surface near Dollar. Fig.4.52 shows these curves and the best fit curves. The calculation of Vp/Vs and Poisson's ratio curves was based on the comparison of the representative P- and S-wave curves (Fig.4.53). Though this is a small data set the method has the advantage over the second method, which compares all P- and S-wave data available, that unknown affects due to igneous strata can be disregarded. If the high velocity surface strata affected both types of waves to the same degree their presence could be ignored since the Vp:Vs ratio would be unaffected. Since the data show P- and S-wave velocity gradients to be different and igneous strata are relatively thin (less than 0.5 km thick) this is unlikely. Fig.4.54 shows the Vp/Vs and Poisson's ratio curves derived by comparison of all available P- and S-wave data with best fitted curves.

4.2.6. Vp/Vs and Poisson's Ratio

Poisson's ratio (σ) is defined as the ratio of strain normal to strain parallel to a uniaxial stress applied to a unit cube of rock. Values vary from 0.0 to 0.5. The ratio can be obtained from Vp and Vs using the expression

$$\sigma = \frac{0.5\,(Vp/Vs)^2 - 1}{(Vp/Vs)^2 - 1} \qquad (4.8)$$

The variation of Vp/Vs and Poisson's ratio with depth obtained, using both methods to determine Vs, is shown in

Fig.4.55. The determination based on the four "non-igneous" curves obtains a Vp:Vs ratio of about 2.0 at the surface decreasing to an average of 1.84 +/- 0.19 below 0.5 km. This corresponds to a Poisson's ratio of 0.29 +/- 0.06. The best-fit curve shows the expected decrease, although this is less than the errors. Also, the data are unstable with the best fit curve varying within the limiting curves. The data based on all Vp and Vs data available are more stable despite the reservations expressed above. Limiting values of 1.84 +/- 0.18 and 0.29 +/- 0.06 are reached below about 0.8 km. The curves show a more marked decrease near the surface and the error curves reflect best-fit shape better. These figures are very similar, though the errors are large, and in good agreement with Assumpcao & Bamford (1978) who quote values of 0.27 and 0.33 for the LISPB layer 1 in the Midland Valley (Fig.2.4). The interpretation of these results is discussed in section 7.1.3.

4.3. Velocities from Reflection Measurements

4.3.1. Introduction

Several phases of Vibroseis sourced reflection data have been acquired by Tricentrol in their exploration blocks. Most of the data are concentrated around their well site, but there are sufficient data adjacent to the MAVIS shot points at Dollar, Longannet, Blairhill, Avonbridge, Drumgray, Tamsloup and Cairnyhill (Fig.3.1) for velocities derived from both techniques to be compared. The reflection velocities are derived from CDP tables on the reflection sections. The tables list two-way time, root mean square velocity, interval velocity and depth (see below).

4.3.2. Application and Reliability of Inversion Technique

Velocities derived from reflection work are obtained by analysis of moveout using simplified models of velocity variation and reflector geometry. The following is largely taken from the review of velocity determination from reflection data published by Al-Chalabi (1979).

For a single reflector below a constant velocity layer the two-way travel time (Tx) is obtained from the equation

$$Tx^2 = T0^2 + \frac{X^2}{V^2} \qquad (4.9)$$

Where T0 is the two way travel time at zero offset, X is the source receiver offset and V is the layer velocity. When there are several such layers of differing velocity rays are refracted at each interface rendering the above equation invalid. Dix (1955) showed that the effect of this is to replace the average velocity to the refractor by its root mean square value defined as

$$Vrms^2 = \frac{\sum_{k=1}^{n} Vk^2 \; Tk^2}{T0} \qquad (4.10)$$

Where Vk and Tk are the velocity and two-way travel time within the kth layer and T0 is the zero offset reflection time, i.e. $T0 = \sum_{k=1}^{n} Tk$

For reasons of simplicity most velocity analysis algorithms assume a hyperbolic time-distance relationship. These techniques depend upon measuring the velocity which produces maximum coherency of traces (Vmcs) when moveout is compensated for. Moveout is defined as the shift applied to reflection times at an offset X to reduce the time to that which would have been recorded at zero offset. Obtaining Vrms from the velocity producing maximum coherency involves many corrections. The Vmcs invariably exceeds Vrms with the error increasing with ground heterogeneity (g) and ray parameter, i.e. with increasing refraction. (g is a function of layer thicknesses and velocities, see Al-Chalabi p.10). Vrms can be thought of as the limit to which Vmcs tends as spread length diminishes. For identical spreads however, it cannot always be said that bias decreases with depth as ray parameter decreases, since this improvement can be overwhelmed by a large increase in heterogeneity. In general Vrms is assumed to equal Vmcs.

The average velocity along a ray path is given by the equation

$$Va = \frac{1}{T}\int_0^T Vins(t)\,dt \qquad (4.11)$$

where Vins is the instantaneous velocity, i.e. the velocity over an infinitesimally small interval, and T is the total travel time. The average and rms velocities are related in terms of the heterogeneity factor (g) by

$$\frac{Vrms}{Va} = (1 + g)^{1/2} \qquad (4.12)$$

Hence in multi-layer ground Vrms exceeds Va, the difference depending on g.

The velocity over a given interval (Vint) is defined using the relation

$$Vint = \frac{VbTb - VaTa}{Tb - Ta} \qquad (4.13)$$

where Va and Vb are the average velocities at the top and base of the interval and Ta and Tb are the corresponding normal incident times, i.e. using average velocities. In reflection work Vint is computed from Vrms and hence the obtained velocity is the Vrms over the interval (Fig.4.56).

$$Vint = \left[\frac{Vb^2 Tb - Va^2 Ta}{Tb - Ta}\right]^{1/2} \qquad (4.14)$$

where Va and Vb are Vrms for the top and bottom of the layer. Intervals are commonly selected between prominent reflectors or over geologically significant intervals. Individual units will tend to be of fairly uniform velocity and hence the obtained Vrms velocity in the interval will be a close approximation to the average velocity within the interval.

Al-Chalabi lists seven main sources of error in velocity determination. These are readily divided into errors due to assumptions, e.g no refraction at interfaces, and those due to the limitations of the seismic reflection technique, e.g. absorption. These limitations mean that the there will be inaccuracies even if the ground were "ideal".

[1] Acquisition errors. Most errors of this type are in

ascertaining the relative and absolute positions of source and receivers. Such errors are larger in marine work and should be small for land surveys.

[2] Processing errors. Examples include those due to data normalisation and correction to datum.

[3] Errors due to noise. Noise events that are non-hyperbolic are discriminated against in the velocity analysis process, and hence should not significantly effect the analysis. Thus, the effect of random noise is found to be minimal even when signal to noise ratio is low.

[4] Errors related to wavelet form. Such errors are usually less than 1%. Examples include the effects of absorption of higher frequencies by the Earth and the errors in estimating onset of the wavelet.

[5] Errors related to wavelet propagation. Such errors are the result of assuming simple models to approximate the real Earth, e.g. the assumption of hyperbolic moveout, effects due to multiples and diffractions, anisotropy and reflector dip. These errors are discussed in more detail below.

The assumption of planar horizontal layers in the velocity analysis is an obvious source of error. Where there is reflector dip below an overlying constant velocity (V) layer, Vmcs will equal

$$\mathrm{Vmcs} = \frac{V}{\cos\alpha} \qquad (4.15)$$

where α is the angle of dip in the direction of the profile. The situation is more complex with several layers and effects are evaluated by stripping off successive layers.

Another source of error is velocity anisotropy. In stratified rocks the horizontal (parallel to bedding) velocity frequently exceeds the vertical (normal to bedding) velocity. For small angles of incidence and a horizontal reflector

$$Tx^2 = \left[\frac{D}{V}\right]^2 + \left[\frac{X}{AV}\right]^2 \qquad (4.16)$$

where D is the depth to the reflector, V the vertical velocity and A is the ratio of the horizontal axis to the vertical axis of an ellipsoid best fitted to the wavefront. (As will be considered in more detail later, the wavefront in an anisotropic media is not actually an ellipse but may be approximated by one at high angles of incidence, or if anisotropy is small). Therefore the Vmcs is an estimate of AV.

Levin (1978, 1979, 1980), Radovich & Levin (1982) and Crampin & Radovich (1982) published a series of papers on the estimation of velocities in anisotropic media based on analysis of moveout. A single anisotropic layer was modelled and $T^2 - X^2$ plots produced. When such plots are not linear it is a measure of the non-elliptical nature of the moveout. The line fitted to the data depends on spread length. Levin concludes that for <15% anisotropy (see below) the plot is essentially linear with the velocity obtained lying between the vertical and horizontal velocity of the layer. When the spread length is such that rays emerge at angles of less than 20°, the velocity derived is the vertical velocity, provided Poisson's ratio is the same for all the layers. The Tricentrol spread length is such that this angle is not exceeded by deeper reflections, but when reflections are at shallower depths the velocities will include a significant horizontal component. Fig.4.55 shows Poisson's ratio to be approximately constant at depths greater than about 0.5 km.

The remaining sources of error are:

[6] Errors due to velocity and structural effects of the ground. Though Al-Chalabi considers these separately from errors due to wavelet propagation the two are essentially the same. The obvious example of such effects are errors in static corrections. A further example is velocity heterogeneity within individual layers.

[7] Subjective errors. Examples include the interpretation of the velocity spectra. Such errors are impossible to quantify, though Al-Chalabi suggests a figure of less than 3% unless there is a significant mis-interpretation.

Clearly the Vrms derived is imprecise and the errors are passed into the estimates of the interval velocities. Consider the case where Vint is being determined from equation (4.14). Let Ea and Eb be the errors in Va and Vb respectively. Assume that both are known to be overestimates or underestimates. Such a situation arises when, for instance, the effect of reflector dip is removed. The error in Vint (ϵ) is given by

$$\epsilon \simeq \frac{EbvbTb - EaVaTa}{(Tb - Ta)\ Vint} \qquad (4.17)$$

i.e.

$$\epsilon \simeq \frac{DbEb - DaEa}{H} \qquad (4.18)$$

where Da and Db are the depth to the top and bottom of the interval and H is the thickness of the interval. Because some components of Ea and Eb are common to both top and bottom of the interval, e.g refraction, statics, these components will be of the same sense and so will tend to cancel each other out. When

$Ea \simeq Eb \simeq E$

$$\epsilon \simeq \frac{E\ (Db - Da)}{H} \simeq E \qquad (4.19)$$

This is a relatively small error in Vint.

Al-Chalabi shows that if

$$\sigma_{int} = \frac{(\sigma a^2\ Va^2\ Ta^2 + \sigma b^2\ Vb^2\ Tb^2)^{1/2}}{(Tb - Ta)\ Vint} \qquad (4.20)$$

where the standard errors in Va and Vb are σa and σb, then

$$\sigma int \simeq \frac{1.4\ \sigma\ D}{H} \qquad (4.21)$$

where D is the average depth of the interval, σint is the standard error in Vint and H is the thickness of the interval.

Equation (4.21) shows the error in Vint to be proportional to the interval depth ratio. Where this is small the error is large. It is important to note that a Vint derived from equation (4.20) is independent of errors in velocity estimation in the other layers.

Since there are few data available to judge the reliability of the interval velocities the only way to treat errors is to assume them to be random. By considering a large amount of data it is hoped that the errors will cancel, and a good estimate of velocity variation with depth obtained. Errors in processing and in model assumptions will affect all the reflection data and, as shown above, should not affect the calculation of interval velocity. Errors due to structure should be random and so not affect the derived velocity-depth curve.

4.3.3. Field Velocity Determinations

Fig.4.57 shows the distribution of CDP gathers. Data were input in the form of interval velocity versus depth to mid-point of the interval. The two quantities were regressed to obtain velocity as a function of depth in the form of a third-degree polynomial (Fig.4.58). Points were weighted according to the square root of fold of stack below the CDP gather, since resolution, and hence coherence of events, increases proportionally with increase in the square root of the fold of stacking. The maximum fold of stack is 48 for most of the data though that from the most recent phase reaches a maximum of 60 fold. Data were only used where coherent events were recognisable on the reflection profiles, since velocity estimation producing reasonable coherency was likely to be more reliable. This assumes the events to be primary reflections from within the plane of the section.

The estimation of the errors in the velocity-depth curve presented some difficulties, since very little was know about the method used to calculate the velocities. The method adopted was based on the comparison of velocity-depth variation obtained from CDP gathers within a restricted area. Six areas, each 2 km square, were selected to enclose the maximum number of CDP gathers (Fig.4.57). The velocity-depth curves from square 2 are shown in Fig.4.59. Errors were estimated by measuring the spread of the data at 0.5 km intervals. The outer two curves were ignored and the spread of the rest of the data measured. This was first done to measure velocity spread, and then repeated to measure the depth variation at the centre of the velocity spread. The resulting spreads in velocity and depth from all the squares, were then averaged, and curves fitted to the data. These curves are plotted on Fig.4.58, and are taken as estimates of the possible deviation from the best fit curve due to errors described above.

4.4. Velocities from Well Measurements

4.4.1. Introduction

Velocity logs are available from three boreholes in the Midland Valley. However, only Tricentrol's Inch of Ferryton bore reaches a reasonable depth. The locations of the Spilmersford (Allsop 1974) and Glenrothes (Browne et al. 1986) boreholes are shown in Fig.3.1.

4.4.2. Velocity Logging

Velocity logs record the travel time of compressional waves emitted every 0.1 s from two transmitters set above and below two pairs of receivers on the sonde (Fig 4.60). The transmitters are pulsed alternatively. The integrated travel time is recorded on the log as a series of "pips". Each "pip" represents an increase of 1 ms in total travel time, whilst a larger "pip" is recorded every 10 ms. Interval velocities can be calculated by recording the depths of the "pips" and an interval velocity-depth curve constructed.

4.4.3. Well Shooting

Well shoots are usually undertaken for the calibration of velocity logs. The method involves recording a source using a geophone at various depths in the well. These depths usually correspond to important geological horizons or strong reflectors. The shoot may also involve sources at increasing offset from wellhead (Fig.4.61). The travel times to the geophone are used in the correlation of the velocity log with the reflection sections. Only the Inch of Ferryton log appears to have been calibrated. The well survey recorded a source near wellhead at seventy-one positions with the geophone at approximately 80 ft intervals between 7000 and 800 ft. The source was moved slightly mid-way through the survey. The Tricentrol data is in the form of interval velocities and depths, with the effects of oblique ray-paths and refraction between interfaces having been compensated for using the velocity log.

4.4.4. Field Velocity Determinations

The velocity-depth curves obtained from the three velocity logs, for the topmost 1 km, are show in Fig.4.62 with those obtained from the reflection (A) and refraction (B) data. There is considerable scatter in all cases. The high velocity areas are due to igneous strata encountered in the wells, but the velocities appear comparable at other depths.

4.5. Velocity Anisotropy

4.5.1. Introduction

The anisotropic nature of rocks has been recognised since at least the 1930's (McCollum & Snell 1932, Weatherby et al. 1934). In stratified rocks this takes the form of velocity parallel to bedding differing from that perpendicular to bedding. In crystalline rocks a fabric may produce a similar effect. Aligned fractures may produce additional anisotropy in both cases.

Three scales of anisotropy are generally recognised (Al-Chalabi 1979, Uhrig & Van Melle 1955), (Fig.4.63):

[1] Micro-anisotropy. Anisotropy is observed within individual layers. Such layers are described as transversely anisotropic or intrinsically anisotropic. This is the result of preferential alignment of minerals grains and/or pores.

[2] Macro-anisotropy. A medium comprised of a series of planar parallel isotropic layers with different physical properties will respond as an intrinsically aniso-

tropic medium when the seismic wavelength greatly exceeds the thickness of the individual layers. Such a medium is referred to as a transversely isotropic media (TIM) and may be analogous to a sedimentary pile.

[3] Quasi-anisotropy. Refraction occurs at interfaces between layers thick relative to the seismic wavelength when there is a contrast in the seismic velocity of the layers. The deviation of the ray-path from a straight line depends on the angle of incidence, increasing with this angle. Consequently the more oblique the ray-path through the layers the greater the deviation from a straight line and hence the greater the travel time.

The three types of anisotropy will be considered separately in greater detail.

It is convenient at this stage to consider definitions of anisotropy. Some authors simply define an "anisotropy factor", usually "K" or "A", as the ratio of velocity parallel to bedding (or layering) to that perpendicular to bedding (or layering) e.g. Donoyer de Segonzac & Laherrere (1959), Kleyn (1956), Uhrig & Van Melle (1955) and Vander Stoep (1966). These values are often termed Vh and Vv respectively.

Levin (1979) prefers to express anisotropy as a percentage

$$A\% = \frac{100\ (Vh - Vv)}{Vv} \qquad (4.22)$$

Carlsen & Christensen (1979) define anisotropy in terms of the percentage velocity difference from the mean velocity

$$A\% = \frac{200\ (Vh - Vv)}{(Vh + Vv)} \qquad (4.23)$$

Levin (1980) points out that anisotropy can defined in terms of the elastic constants of a TIM though such a definition has little practical value since these are rarely known.

The definition of anisotropy in terms of the ratio Vh:Vv will be used since it gives an immediate "feel" for the anisotropy present.

It is difficult to make generalisations about what is the major control on anisotropy. Dunoyer de Segonzac & Laherrere (1959) consider lithology to be the major control. This is probably correct though the ranges they quote for different rock types are probably unreliable. The actual anisotropy of a sandstone would be affected by, for instance, whether there were shale horizons within the sequence. When estimating the anisotropy of a stratigraphic section all three scales of anisotropy described above must be considered.

It should be noted that both P- and S-waves are subject to anisotropy. The latter usually exhibit greater effects, but will not be considered here since most of the data available is for P-waves.

4.5.2. Micro-Anisotropy

Studies of micro-anisotropy are based on velocity measurements on cores. Most of the work has been done on cores collected as part of the Deep Sea Drilling Project.

Carlson & Christensen (1979) studied velocity variation in samples of calcareous deep sea sediments at varying confining pressures. The data showed anisotropy at a given pressure to increase with density, average velocity and depth of burial of the sample. Pressure does not appear to be a direct control. Vh:Vv ratios quoted range from about 1.05 (limestone) to about 1.18 (marly limestone). These data show the cause of anisotropy to a be a fabric within the samples, since cracks would close as pressure increased, and hence anisotropy would decrease. Carlsen & Christensen explain their data in terms of either preferred micro-fossil orientation, calcite recrystallisation or epitaxial growth of aligned calcite, i.e. anisotropy is controlled by the degree of fabric development. The degree of fabric development due to the latter two mechanisms would be a function of diagenetic alteration. Sample density and velocity, both affected by reduction in porosity, would be similarly controlled. This alteration would increase with depth of burial and the resulting rise in confining pressure. However, in the rocks of the Midland Valley, the time since deposition is sufficient to have equalised out such effects and anisotropy is probably not depth related.

Bachman (1979, 1983) compiled velocity data from marine calcareous, silt clay, siliceous, marly and sandy sediment and rock. Linear regression lines were fitted to plots of Vv versus Vh, the lines being forced to coincide at what were considered reasonable sea-floor values. This assumes no anisotropy due to depositional factors such as grain or pore alignment. The data, however, are probably not applicable to the Midland Valley being based mainly on recent deposits.

The core derived data suggests micro-anisotropy to be a function of fabrics of depositional or diagenetic origin. The applicability of these studies to the Midland Valley is unclear since most of the work is on young rocks.

4.5.3. Macro-Anisotropy

The stratified nature of rocks suggests the modelling of anisotropy in terms of a transversely isotropic medium (TIM). A TIM consists of alternating planar parallel layers of isotropic material with different densities and elasticities and therefore velocities, i.e. the material has identical physical properties in any plane perpendicular to a single axis of symmetry.

Postma (1955) showed that when the layer thickness is small relative to the seismic wavelength the medium will react as a single transversely anisotropic medium. Backus (1962) described "small" as being much less than "k", the distance over which displacement due to a seismic wave varies appreciably. Helbig (1984) considers this point in more detail.

Three types of wave are propagated by a TIM; P (compressional) waves, SV and SH (shear) waves. SV-waves are polarised in the vertical plane (assuming the axis of the media to be vertical) whilst SH-waves are polarised in the horizontal plane. These terms are strictly only applicable to waves travelling parallel or perpendicular to the axis of symmetry of the medium. In all other cases the particle motion is not completely parallel (P-waves) or perpendicular (S-waves) to the direction of propagation. Postma showed that the velocities of the waves varied with direction of propagation. The actual amount of anisotropy depends on the contrast in the physical properties of the component media and their relative thicknesses.

When velocity is plotted as a function of direction an ellipse is only defined for SH-waves. This is not the case for SV- and P-waves. The deviation from an ellipse for P-waves has been considered by several authors (Helbig 1983, Krey & Helbig 1956, Levin 1979, Uhrig & Van Melle 1956). The P-wave surface is found to a slightly squashed ellipse, though many authors ignore this and assume an elliptical distribution with the major axis the horizontal velocity (Vh) and the minor axis the vertical velocity (Vv). Thus, in three-dimensions an ellipsoid of revolution is defined about the axis of symmetry of the TIM. This axis is usually assumed to be vertical on the grounds that it will lie perpendicular to stratification, and that the beds will have negligible dip. Crampin (1986) discusses the assumption of a vertical axis and suggests the term "vertical transverse anisotropy" for such media.

Melia & Carlson (1984) carried out experimental studies on samples of laminated glass and epoxy to test these theoretical studies. They concluded that there is "no statistically significant difference between observation and theory".

Levin (1979) shows how to model transverse anisotropic media composed of component media with known velocities and densities, using the equations of Backus (1962). Only the equations for P-waves will be described here. As previously described the velocity of a wave through a TIM depends on the direction of travel, consequently the wavefront is not spherical. Two types of wave surface must be considered; the plane wave surface and the wave surface from a point source. Since plane waves cannot be generated within the Earth the first is of interest only as an aid to computation of the other surface. White (1965) gives the following equations for the generation of P-wave plane wave surfaces in TIM

$$2pV^2 = 2L + (A-L)\sin^2(\theta) + (C-L)\cos^2(\theta) + (((A-L)\sin^2(\theta)$$
$$+ (C-L)^2\cos^2(\theta))^2 + ((F+L)^2 - (A-L)(C-L))\sin^2(2\theta))^{1/2} \quad (4.24)$$

Theta is measured relative to the vertical axis of symmetry. A,C,F,L, and N are the five elastic constants necessary to define a TIM and p is density. For compressional waves

$$Vh = (A/p)^{1/2} \quad (4.25)$$

$$Vv = (C/p)^{1/2} \quad (4.26)$$

Assume

$$(A/L)^{1/2} = P \quad (4.27)$$

$$(C/L)^{1/2} = Q \quad (4.28)$$

$$(F/L)^{1/2} = R \quad (4.29)$$

$$(N/L)^{1/2} = S \qquad (4,30)$$

and

$$((R^2 + 1)^2 - (P^2 - 1)(Q^2 - 1))^{1/2} = \Delta \qquad (4,31)$$

equation (1) becomes

$$2V^2 = 2 + (P^2 - 1)\sin^2(\theta) + (Q^2 - 1)\cos^2(\theta) + (((P^2 - 1)\sin^2(\theta) + (Q^2 - 1)\cos^2(\theta))^2 + \Delta^2 \sin^2 2\theta)^{1/2} \qquad (4,32)$$

where V is the plane wave velocity

normalised with respect to $(L/p)^{1/2}$

The ray surfaces are derived using the equations of Krey & Helbig (1956)

$$X = V\sin\theta + (dV/d\theta)\cos\theta \qquad (4,33)$$

and

$$Z = V\cos\theta - (dV/d\theta)\sin\theta \qquad (4,34)$$

where

$$dV/d\theta = (\sin 2\theta/4V)\,(P^2 - Q^2 + ((P^2 - 1)\sin^2(\theta) + (Q^2 - 1)\cos^2(\theta) + 2\Delta^2\cos 2(\theta)) / (((P^2 - 1)\sin^2(\theta) + (Q^2 - 1)\cos^2(\theta))^2 + \Delta^2\sin^2(2\theta))^{1/2})) \qquad (4,35)$$

The surface is derived by incrementing θ for given P, Q, R, and S.

Where θ is equal to 0

$$X = dV/d\theta = 0 \qquad (4.36)$$

$$Z = V$$

where $\theta = \pi/2$

$$X = V$$

$$Z = -dV/d\theta = 0 \qquad (4.37)$$

therefore the ray surface is coincident with the plane wave surface at these points. Since velocity data from the Midland Valley is scarce there is little point in calculating the ray surface, since it is very similar to the plane wave surface. Instead, simple elliptical anisotropy will be assumed based on the horizontal and vertical velocities. The equation of the ellipse is

$$V^2(\theta) = (VvVh)^2 / (Vv^2 \sin^2(\theta) + Vh^2 \cos^2(\theta)) \qquad (4.38)$$

Backus (1962) shows how to combine transversely isotropic components with constants a, c, f, n and l to form a TIM

$$A = \langle a - f^2 (1/c) \rangle + (1/\langle 1/c \rangle)\langle f(1/c) \rangle^2 \qquad (4.39)$$

$$C = 1/\langle 1/c \rangle \qquad (4.40)$$

$$F = (1/\langle 1/c \rangle)\langle f(1/c) \rangle \qquad (4.41)$$

$$N = \langle n \rangle \qquad (4.42)$$

and

$$L = (1/\langle 1/l \rangle) \qquad (4.43)$$

$\langle\rangle$ indicate averages such that for a TIM with x1 parts of component 1 and x2 parts of component 2 such that x1+x2=1

$$N = x1n1 + x2n2 \qquad (4.44)$$

The above equations allow the combination of any number of transversely isotropic media, or combinations of isotropic and anisotropic media. When the components are isotropic

$$a = c = p(Vp^2) \tag{4.45}$$

$$l = n = p(Vs^2) \tag{4.46}$$

$$f = p(Vp^2 - 2Vs^2) \tag{4.47}$$

where Vp and Vs are the P and S wave velocities of the component.

Equations 4.39 to 4.43 become

$$A = \langle 4p(Vs^2)[1-(Vs^2/Vp^2)]\rangle + \langle 1-(2Vs^2/Vp^2)\rangle^2/\langle 1/(pVp^2)\rangle \tag{4.48}$$

$$C = 1/\langle 1/(pVp^2)\rangle \tag{4.50}$$

$$F = \langle 1-(2Vs^2/Vp^2)\rangle/\langle 1/(pVp^2)\rangle \tag{4.51}$$

$$N = \langle pVs^2\rangle \tag{4.51}$$

and

$$L = 1/\langle 1/(pVp^2)\rangle \tag{4.52}$$

where a component is intrinsically anisotropic

a not equal c

l not equal n

for instance

$$a = pVp(horizontal) \tag{4.53}$$
$$c = pVp(vertical) \tag{5.54}$$

Unfortunately Backus does not describe what values to assign Vs (horizontal) and Vs (vertical). This is problem since the shear waves will have split and there will be two horizontal velocities. Levin (1980) solves this problem by increasing the horizontal velocity of the TIM by 10% for P-waves and 30% for S-waves, without justifying his actions. A better solution is to adjust the velocities of the component before combining into the media. This is how intrinsically anisotropic layers were modelled. In fact, the actual value of S-wave "anisotropy" has very little effect on the models generated, since only P-wave anisotropy is being modelled and the TIM velocities are calculated from "A" and "C". "A" is not calculated using "l" and "n" and the "f" term of the equation for "C", though a square, is in combination with "a" and "c".

When forming a TIM composed of isotropic components equations 4.48 to 4.52 are used. When components were anisotropic equations 4.39 to 4.43 are used. A computer program TIMPROG was written (see Appendix 6) which enabled TIM based on Midland Valley stratigraphic sections to be formed, and their anisotropy factor quantified.

4.5.4. Quasi-Anisotropy

The affects of quasi-anisotropy are small and have little relevance to the velocity data available from the Midland Valley. A short description is included here for completeness.

A lot of early work on anisotropy was based on data from well shooting, based on the comparison of the velocities obtained with those derived seismically (Cholet & Richard 1954, Hagedoorn 1954, Uhrig & Van Melle 1955, Kleyn

1956, Dunoyer de Segonzac & Laherrere 1959, Vander Stoep 1966)

In a well survey a surface source is recorded by a geophone at selected depths in the well. This process is repeated for sources at increasing offsets from wellhead. As the offset increases the ray path between source and receiver becomes increasingly oblique to the layering, assuming the latter to be approximately horizontal. Refraction at the interfaces is increased, deviation from a straight line is greater and consequently travel time is also greater. Uhrig & Van Melle (1955) show the affects of such anisotropy to be small.

The well survey at the Inch of Ferryton bore involved sources at two small offsets with quasi-anisotropy compensated for using the velocity log. Consequently little can be discovered about the effects of this kind of anisotropy in the Midland Valley, though the effects of anisotropy on refraction and ray geometry will be considered in more detail in the section on ray-tracing.

4.5.5. Estimation of Velocity Anisotropy in the Midland Valley

Before the errors in refractor depth obtained from ray-tracing can be estimated, the amount of anisotropy within the Midland Valley must be quantified. Two methods of estimation are described. Firstly, anisotropy is estimated by comparison of "vertical" and "horizontal" velocities. The second method involves the modelling of TIM based on boreholes from the Midland Valley using velocities from logs and densities, with S-wave velocities derived from these.

Banik (1984) estimated anisotropy in the North Sea basin by comparison of log and stacking velocities. Anisotropy in the Midland Valley can be estimated in a similar manner.

The derivation of third-order polynomials representing refraction and reflection velocity-depth curves was described in sections 4.2 and 4.3. Fig.4.64 shows these curves. The two best-fit lines were compared and the errors on this line found by comparing the maximum WHB and minimum interval velocity limits and vice-versa. Averaging the resulting lines gives

Vwhb/Vint = Vh/Vv = 1.15 +0.12, -0.15.

This spread covers most values quoted in the literature. 1.20 is a typical shale value, whilst the lower limit corresponds to Vh/Vv=1.0, i.e. isotropy. These results must be considered as an underestimate of anisotropy since Vint contains a horizontal component. The "best-fit" value of 1.15 is reasonable for a sedimentary sequence consisting of little or no shale. Note that there is little variation with depth, as predicted by the laboratory measurement of cores, i.e. cracks are not a significant cause of the anisotropy.

Fig.4.62 shows the reflection and refraction derived curves in relation to the log derived velocity-depth curves. There is considerable scatter in the log data, but most falls within the limits of the reflection derived curve. This is expected since log velocities are vertical velocities. However, because of the horizontal component in the shallower interval velocities, it would be expected that the log velocities would be lower at shallow depths.

Stratigraphic sections from boreholes at Glenrothes, Spilmersford and Inch of Ferryton were modelled and anisotropy calculated (Figs.4.65 and 4.66). The Inch of Ferryton data is not shown due to its confidentiality. The borehole velocity data allowed interval velocities and interval thicknesses to be calculated. These layers were combined to form the TIM. Vp was taken directly from the velocity logs. Vs and density are also required in the calculation of the Vh:Vv ratio of the media. In sediments Vp/Vs ranges between about 1.6 to 1.9 (Castagna 1985, Domenico 1984, Pickett 1963, Tatham 1982, Wilkens et al 1984), this includes the ratio of 1.84 obtained in section 4.2.6. The ratio was varied between these limits in modelling. Density was also estimated based on Vp. Barton (1986) has considered the relationship between these two properties. The results of Nafe & Drake (1970) were used to estimate the range of possible densities for a given velocity (Fig.4.67). The data presented were regressed between 2.5 and 6.0 km/s to define third-order polynomials, used to obtain best fit, maximum and minimum density for a layer of given Vp. The three functions obtained are listed below

1. $\text{Density} = 0.006Vp^3 - 0.086Vp^2 + 0.557Vp + 1.132$ (4.55)

2. $\text{Density} = 0.007Vp^3 - 0.122Vp^2 + 0.767Vp + 0.677$ (4.56)

3. $\text{Density} = -0.006Vp^3 + 0.062Vp^2 - 0.009Vp + 2.029$ (4.57)

These three functions were written into the program TIMPROG and used in combination with the possible Vp/Vs to provide a range of Vh/Vv ratios for the TIM. Layers were assumed to be isotropic. The results are summarised in Table 4.3 (the Spilmersford velocity log was recorded in three parts and each has been considered individually)

Table 4.3. Anisotropy in Midland Valley Boreholes from Velocity Logs.

Density Function	Vp/Vs	Glenr Vh/Vv	Spilm1 Vh/Vv	Spilm2 Vh/Vv	Spilm3 Vh/Vv	I of F Vh/Vv
1	1.6	1.10	1.03	1.05	1.10	1.16
1	1.7	1.10	1.03	1.05	1.10	1.16
1	1.8	1.09	1.03	1.04	1.09	1.15
1	1.9	1.09	1.03	1.04	1.09	1.14
2	1.6	1.10	1.03	1.05	1.09	1.16
2	1.7	1.09	1.03	1.05	1.09	1.15
2	1.8	1.09	1.03	1.04	1.08	1.15
2	1.9	1.08	1.03	1.04	1.08	1.14
3	1.6	1.10	1.03	1.05	1.10	1.16
3	1.7	1.10	1.03	1.05	1.10	1.15
3	1.8	1.09	1.03	1.05	1.09	1.15
3	1.9	1.09	1.02	1.04	1.09	1.14
Average		1.09	1.03	1.05	1.09	1.15

These values fall within the limits of that derived by comparison of velocities. The values are lower than the best-fit value, except in the case of Inch of Ferryton where the value is identical. This is encouraging since the velocity derived value was for the same stratigraphic sequence (i.e. Coal Measures downwards) as occurs in the Inch of Ferryton bore. The Glenrothes and Spilmersford bores are both through older strata and are atypical sections due to their high sandstone and igneous contents respectively.

4.5.6. Effects of Anisotropy on Ray-Traced Models

Several authors have considered ray paths through anisotropic media. Most concentrate on reflected rays where the effects of anisotropy are generally small due to the steep ray-paths, e.g. Vander Stoep (1966).

Since there are relatively large errors in the estimated anisotropy, with isotropy falling within the errors, a detailed consideration of the effects of anisotropy on ray-tracing is not considered worthwhile. It is worth noting, however, that Kleyn (1956) shows the thickness of a planar constant velocity layer "computed neglecting anisotropy, equals the true thickness of this velocity layer times it's anisotropy factor...". For a 2 km thick layer with the calculated anisotropy factors this represents a depth of 1.74 +0.26, -0.17.

Inputting typical velocities for MAVIS layers 1 (4.6 km/s) and 2 (5.3 km/s) and a delay of 0.05 s into the equation to convert delay time to depth for planar layers (equation 5.6) produces a value of 0.23 km, i.e. +/- 0.12. This shows the depth errors due to anisotropy to increase uncertainty in refractor depth by between 0.05 and 0.14 km. This is not significant when the uncertainties due to assuming constant velocity planar layers in the calculation, and the frequently greater than 0.05 s scatter of the data, are considered.

CHAPTER 5 - INTERPRETATION OF SEISMIC DATA

5.1. Methods

5.1.1. Principles of Seismic Refraction Interpretation

When a seismic ray is incident on an interface between two media of different velocity the transmitted ray is refracted according to Snell's Law (Fig.5.1)

$$\frac{\sin i}{\sin r} = \frac{V1}{V2} \qquad (5.1)$$

where

sin i = the sine of the incidence angle
sin r = the sine of the transmission angle
V1 = velocity in media 1
V2 = velocity in media 2

Consider the ray paths shown in Fig.5.2. All layers have constant velocity and are separated by planar horizontal interfaces. The direct ray travels horizontally through layer 1 at a velocity V1. The resulting travel-time curve is a straight line of slope 1/V1. The angle θ is such that the ray AB is critically refracted, i.e. the ray is refracted so that it is transmitted at 90° to the normal and runs along the interface between the two layers. Therefore, sin r is equal to 1. Consider the path of the ray ABCD critically refracted at the interface between layers 1 and 2. The travel time, T(AD), along this path is

$$T(AD) = T(AB) + T(BC) + T(CD) \qquad (5.2)$$

$$= \frac{Z1}{V1 \cos\theta} + \frac{X - 2Z1 \tan\theta}{V2} + \frac{Z}{V1 \cos \theta} \qquad (5.3)$$

since sin r = 90°

$$\sin\theta = V1/V2 \text{ (Snell's Law)} \tag{5.4}$$

$$\cos\theta = \left[1 - \frac{V1^2}{V2^2} \right]^{1/2} \tag{5.5}$$

and equation 5.3 may be rewritten as

$$T(AD) = \frac{X}{V2} + \frac{2Z\,(V2^2 - V1^2)^{1/2}}{V1\ V2} \tag{5.6}$$

Therefore, on the time-distance plot, the intercept on the time axis (the intercept time, Ti1) is given by

$$Ti1 = \frac{2Z\,(V2^2 - V1^2)^{1/2}}{V1\ V2} \tag{5.7}$$

and therefore

$$Z1 = \frac{Ti1\ V1\ V2}{2\,(V2^2 - V1^2)^{1/2}} \tag{5.8}$$

Thus, the intercept time may be used in conjunction with V1 and V2 to determine the depth to layer 2.

The depth to layer 3 may also be obtained when V3 is also known.

$$Z2 = 0.5 \left[Ti2 - 2\ Z1 \frac{(V3^2 - V1^2)^{1/2}}{V3\ V1} \right] \frac{V3\ V2}{(V3^2 - V2^2)^{1/2}} \tag{5.9}$$

When interfaces are not horizontal, the velocity obtained from the time-distance plot is not the true refractor velocity and is known as an apparent velocity (Fig.5.3). When the data are recorded from a shot at A, in the direction of dip, the critical rays returning to the surface must pass through increasing thicknesses of layer 1. This results in the apparent velocity (Vd) being less than the true refractor velocity. The reverse is true for data recorded from a shot at B, in the "up dip" direction (Vu). Thus the equations given above are invalid. Since refractor dip is to be expected and constant velocity layers are unlikely, more sophisticated interpretational techniques must be utilised.

5.1.2. Plus-Minus and Delay-Time Methods

The plus-minus method (Hagedoorn 1959) involves the calculation for each receiver of a "plus time", analogous to an intercept time, for conversion to refractor depth, and a "minus time" for the estimation of refractor velocity. Reversed data are required and refractor topography is assumed to be such that cos(dip) is approximately equal to 1 (i.e. dips of less than about 5°). Consider the spread geometry in Fig.5.4.

The plus time is the sum of the travel-times to a receiver from the two sources, S1 and S2, minus the travel-time between S1 and S2 (T(S1S2)). For a receiver K

$$Tplus(K) = T(S1K) + T(S2K) - T(S1S2) \tag{5.10}$$

$$= (T(S1R) + T(RZ) + T(ZK)) + (T(S2W) + T(WT) + T(TK)) - (T(S1R) + T(RW) + T(S2W)) \tag{5.11}$$

$$= T(ZK) + T(TK) + T(RZ) + T(WT) - T(RW) \tag{5.12}$$

$$= T(ZK) + T(TK) - T(ZT) \tag{5.13}$$

This is the same as the intercept time (Tint) for a shot fired at K. Therefore the refractor depth below K, Z(K), is given by

$$Z(K) = \frac{Tplus(K) \quad V2\ V1}{2\ (V2^{2} - V1^{2})^{1/2}} \qquad (5.14)$$

V2 is obtained from the minus times. The minus time is defined as the difference in travel-time between refracted arrivals from sources S1 and S2 arriving at a receiver K.

$$Tminus(K) = T(S1K) - T(S2K) \qquad (5.15)$$

$$= (T(S1R) + T(RZ) + T(ZK)) - (T(S2W) + T(WT) + T(TK)) \qquad (5.16)$$

since refractor relief is assumed to be negligible between Z and T

$\angle KPZ = \angle KPT = 90^{\circ}$

$KZ = KT$

therefore

$$Tminus(K) = (T(S1R) + T(RZ)) - (T(S2W) + T(WT)) \qquad (5.17)$$

similarly

$$Tminus(L) = (T(S1R) + T(RU)) - (T(S2W) + T(WV)) \qquad (5.18)$$

Plotting minus time against receiver position gives a straight line with a gradient equal to half the refractor velocity

$$Gradient = \frac{X}{Tminus(L) - Tminus(K)} \qquad (5.19)$$

$$= \frac{X}{T(S1R)+T(RU)-T(S2W)-T(WV)-T(S1R)-T(RZ)+T(S2W)+T(WT)} \quad (5.20)$$

$$= \frac{X}{T(RU) - T(WV) - T(RZ) + T(WT)} \quad (5.21)$$

$$= \frac{X}{T(ZU) + T(VT)} \quad (5.22)$$

For low relief ZU = VT = KL = X

and therefore

$$T(ZU) + T(VT) = \frac{2X}{V2} \quad (5.23)$$

and hence the gradient of a minus time graph can be expressed as

$$\text{Gradient} = \frac{V2}{2} \quad (5.24)$$

Where a refractor is not reversed (i.e. for ranges S1C1 and S2C2) plus times can be estimated by extrapolation of the time-distance branches. Time-distance curves of velocity V2 are drawn starting at the outermost reversed points (at ranges C1 and C2), and continuing to ranges S1 and S2 respectively. An estimate of the plus-time of the unreversed points is obtained by doubling the difference between the observed arrival time and the time-distance curve and adding this to the plus time obtained at C1 or C2.

Where only a short length of reversal occurs, e.g. on the MAVIS II line, an adaptation of the plus-minus method was employed. A delay time (Td), equivalent to half a plus time, is calculated:

$$Td = Tarr - \frac{X}{Vref} - \frac{Tint}{2} \qquad (5.25)$$

Tarr = travel time
X = receiver range
Vref = refractor velocity
Tint = intercept time

Vref is the average of the apparent velocities of the appropriate time-distance branches. The delay time was then converted to depth using the formula

$$Z1 = \frac{Td\ V1\ V2}{(V2^2 - V1^2)^{1/2}} \qquad (5.26)$$

5.1.3. Ray-Tracing Method

The plus-minus interpretation was refined using the SEIS81 ray-tracing package (Cerveny & Psencik 1981). This package consists of the ray-tracing and plotting program SEIS81, plus the programs SYNTPL and SEISPL which, respectively calculate and plot, synthetic seismograms based on the output of SEIS81. The ray-tracing section of the program traces rays through two-dimensional laterally inhomogeneous media and can handle curved interfaces, block structures, vanishing layers and isolated bodies.

The ability to model complex interface structure and lateral velocity variations was essential, the latter having been demonstrated in section 4.2. In the program a ray-path is defined and travel times computed from the source to a specified receiver geometry. The "shooting method" is used with rays leaving the source between specified angles. Each ray is traced through the model, following (if possible) the specified ray path, back to the surface. When successive rays terminate at the surface at locations on either side of a receiver an iterative process is initiated which selects an intermediate initial angle and traces this ray through the model. This process is repeated a specified number of times, or until the ray terminates within a specified distance of the receiver.

The program uses a ray-tracing method described by Cerveny et al. (1974). The path of a seismic ray through a two-dimension medium with a continuous velocity function may be expressed by three equations

$$\frac{dx}{dt} = v \sin D \tag{5.27}$$

$$\frac{dz}{dt} = v \cos D \tag{5.28}$$

$$\frac{dD}{dt} = \frac{-\partial y}{\partial x} \cos D + \frac{\partial v}{\partial z} \sin D \tag{5.29}$$

where

x = horizontal direction
z = vertical direction
D = declination from the horizontal
t = arrival time at a point in the model
$\partial v/\partial x$ = partial derivative of velocity with respect to x
$\partial v/\partial z$ = partial derivative of velocity with respect to z

The ray is traced by integrating each formula over a given time interval using the Runge-Kutta method.

Velocities within each layer are input as a grid. A continuous velocity function is obtained by either fitting bicubic splines to these data or, alternatively, by linear interpolation between grid points. The latter was found to significantly reduce the number of rays successfully traced from the source to the receivers and the former was used throughout. At an interface between layers the velocity function may be discontinuous, allowing refraction and reflection to occur in accordance with Snell's Laws.

No amplitude modelling was undertaken for reasons of time, though synthetic seismograms were generated using SYNTPL and SEISPL to assist in the assigning of second arrivals picked on the digitised data.

5.2. Results

5.2.1. Plus-Minus and Delay-Time Results

The plus-minus method was applied to the MAVIS data by A Conway. The interpretation was based on the recognition of a consistent set of four time-distance branches. Criteria used in their recognition were; 1), sharp changes in apparent velocity 2), preconceptions of Midland Valley crustal structure (see Fig.3.2) and 3), satisfying the reciprocal time rule. The four branches are:

[A] Direct arrivals through layer 1. Time-distance branches are curved with apparent velocities of 3.0 to 4.5 km/s. The curvature is a function of both vertical and lateral velocity variation (see section 4.2).

[B] Refractions from layer 2 usually with apparent velocities between 5.0 and 5.8 km/s. When layer 2 reaches the surface, (Aberuthven and Cairngryffe shots), or approaches the surface, (Trearne and Kaimes shots), the branch is curved as in (A) with apparent velocities between 4.0 and 5.0 km/s.

[C] Refractions from layer 3 with apparent velocities between 5.9 and 6.1 km/s.

[D] Where arrivals are recorded at ranges greater than about 50 km refractions from a fourth layer with apparent velocities of about 6.4 km/s are observed.

The time-distance branches used in the plus-minus and delay-time interpretations are shown in Figs.5.5 to 5.7.

MAVIS I plus times are listed in Appendix 4. When converting to depth, the vertical and lateral velocity variations, highlighted by WHB inversion of the direct arrival data, were taken into account (section 4.2). The layer 1 velocity structure was approximated by a series of linear velocity-depth functions. For three or four trial locations on each line the depth to layer 2 was then calculated. For other locations on the line this procedure was approximated by estimating the velocity of an equivalent constant velocity layer, and converting to depth using this velocity. For deeper horizons constant velocity layers based on minus time velocities were used in conjunction with standard multi-layer formulae (see section 5.1.1).

The plus-minus interpretations of the MAVIS I lines are shown in Fig.5.8. The crossing of the two uppermost refractors at the eastern ends of the two lines is probably the result of the mis-identification of time-distance branches in the Methil data. On the Fig.5.8b the velocities of 5.50

and 5.24 km/s refer to the second layer. The velocity of 5.99 km/s is for the third layer. The dashed line between the two crossed interfaces represents their average depth. This interpretation suggests layer 2 to be very thin or absent. The lateral velocity variations observed in layers 2 and 3 are also the result of the mis-assignment of time-distance branches, e.g beneath Trearne, where the curved nature of the time-distance segment was not recognised. An erroneous apparent velocity of 5.56 km/s was assigned to layer 2, branch B on Fig.5.5. Subsequent ray-trace modelling of the data (see section 5.2.2) allowed the removal of these variations. The higher velocity of layer 2 on the MAVIS I north line relative to the south line is retained in the ray-traced model and is discussed in section 7.2. Ray-tracing of the data also allowed the small layer 3 lateral velocity variation to be removed. The depth to layer 4 was calculated assuming a velocity of 6.4 km/s, as seen on LISPB (Bamford et al. 1978), and for a velocity of 6.53 km/s, as obtained from the modest reversal of this refractor on the southern line. The two velocities make little difference to the structure obtained.

Very little reversal of refractors occurs on the MAVIS II line due to its shorter length and the Ochil Fault bringing layer 2 to the surface in the north. Where plus times could be calculated (stations 26, 27, 33, and 34 using the Blairhill and Dollar shots) the depths obtained to layer 2 were comparable to those obtained for MAVIS I. To overcome the lack of reversal the adaptation of the plus-minus method, described in section 5.1.2, was carried out M. Fleming, assuming velocities of 5.43 and 6.00 km/s for layers 2 and 3 respectively. The results of the delay-time conversion to depth are not reproduced here. The profiles showed excessive scatter (greater than 1 km for the first interface and greater than 2 km for the second) due to the scatter on the travel-time data and the use of an average refractor velocity

5.2.2. Ray-Traced Profiles

When ray-tracing the MAVIS I data the initial model was based on velocities derived from the WHB inversion, and the interface geometry and velocities determined by the plus-minus interpretation. Problems applying the delay time method to the MAVIS II data necessitated the use of an initial model based on WHB velocities, and velocities and interface depths determined from the MAVIS I data. An identical procedure was used for the MAVIS III quarry-blast line. The MAVIS I and II models were extended below layer 4 using the LISPB models of the Midland Valley. Quarry-blast data reinterpreted from Sola (1985) were modelled based on modified versions of his interpretation. The ray-tracing program requires velocity gradients within all layers and models refracted rays as diving rays. A velocity gradient of 0.05 s^{-1} is assumed for layer 2 and 0.03 s^{-1} for layers 3 and 4.

Several problems were encountered during ray-tracing. Surface obstacles and logistical constraints meant that it was not possible to place shots and receivers precisely on straight lines. In constructing the models for ray-tracing, shot point ranges were calculated from some origin (the easternmost shot on east-west trending lines and the northernmost shot on north-south trending lines). The receivers were positioned with respect to each calculated shot point. Since the receivers do not lie on a straight line between any two shots the sum of the ranges from these two shots does not equal the range between the shots. Therefore, in the two-dimensional profile to be ray-traced, the position of any receiver will be different for different shots. Usually the difference is less than 10 m, the error in locating the receiver. However, where the shots are more than a few kilometres off line, e.g the Westfield to Methil section of the MAVIS I north line, receiver locations can differ by up to 2 km. Since the velocity grid is poorly defined, and assumed to be uniform in this region, even this discrepancy will have little effect on travel-times.

Further problems were encountered in constructing the ray-tracing model in the Bathgate region where data from several quarry sources are combined. Fig.5.9 illustrates the relative positions of the sources in this region. Using the Aberuthven shot point as an origin the ranges of Blairhill and Cairnyhill are almost identical. However, the data cannot be satisfied because quartz-dolerite sills are the dominant control on travel time within the first 10 km of a shot, and the quarries are situated at differing distances from the sill margins. For this reason, in locating Cairnyhill on the ray-tracing model, the sill margin to the south east of Cairnyhill was assumed to coincide with the sill margin to the south of Tamsloup, and the source located accordingly. Because the receivers to the north of Cairnyhill are not on a sill, unlike those to the north of Tamsloup and Blairhill, the modelled travel times are consistently fast.

The ray-traced depth sections, observed and calculated travel-times and ray diagrams are shown in Figs.5.10 to 5.74. Observed and calculated P-wave travel times are listed in Appendix 3. The ray path classification used is shown in Table 5.1 .

Table 5.1 Ray-Path Classification.

Code	Wave Path
a1	Direct arrivals through layer 1
a2	Reflections from the top of layer 2
a3	Refractions through the top of layer 2
a3(d)	Direct arrivals through layer 2 (for shots in layer 2)
a4	Reflections from the top of layer 3
a5	Refractions through the top of layer 3
a6	Reflections from the top of layer 4
a7	Refractions through the top of layer 4
a8	Reflection from the top of layer 5
a9	Refractions through the top of layer 5
a10	Reflections from the top of layer 6 (Moho reflections)

The data allow the generation of a consistent set of ray-traced profiles. The topmost layer shows considerable velocity variation and varies between 0.5 and 2.5 km in thickness. North of the Ochil Fault and south of the Wilsontown Fault (see Fig.1.8) the second layer reaches the surface. The underlying layers show no lateral velocity change and are separated by interfaces with relief of less than a kilometre. Where the different lines intersect, depths to interfaces agree to within 0.5 km. This corresponds to a time difference of about 0.07 s for the first two interfaces, and about 0.05 s for the third interface. The scatter of the data frequently exceeds these amounts.

Observed data show a scatter about a number of best-fit velocity segments. Where possible during ray-tracing this scatter was modelled. However, calculated times are often obtained by "threading" through the observed arrivals, the discrepancy between individual observed and calculated times frequently exceeding the timing error. This scatter is illustrated by arrivals recorded at stations 41 to 50 from the Aberuthven shot of MAVIS II (Fig.5.36). (These stations are the "Blairhill/Avonbridge" receiver locations between these two sources in Fig.5.9). Since these are all sites located on rock outcrop near surface delays related to drift are not present. Also, the data are of good quality so mis-picks are unlikely. Elevation varies from 0.14 to 0.24 km AOD, equivalent to a time difference through quartz-dolerite of about 0.02 s. Scatter is about 0.06 s and the modelled data are threaded to pass through as many error bars as possible. This amount of scatter is presumably the result of complex velocity structure within the sub-surface delaying the seismic waves, and perhaps attenuating, some phases more than others. Constructive/destructive interference between different arrivals, especially at ranges where refracted and reflected arrivals have similar travel times, may be responsible for some scatter. The causes of scatter are considered to be below the resolution of the modelling program and are of secondary importance in comparison to the overall agreement achieved in modelling arrivals from all of the shots.

When modelling the data, well defined segments were fitted as closely possible at the expense of more scattered data originating from the same area of the model. Where scatter affected good data, the choice of which points were modelled depended on the fitting of data from other sources originating from the same part of the model. Finally, the observed data do not always reverse exactly, presumably due to errors in calculating the shot instant. Since the modelled data will always do so, this too affected which data points were modelled.

Problems were encountered in ray-tracing the data recorded from both Methil shots. Figs.5.19 and 5.32 show intercept times for time-distance branches from these sources to be typically 0.5 s greater than their equivalents from other shots. Possible causes include a positional error or an undetected low-velocity layer beneath the shot point. A delay of 0.5 s requires a positional error of about 2 km. This is not possible since positioning was by the radar location system of the firing ship. Further, if the delay was due to a positional error time-distance segments of different apparent velocity would be delayed by differing amounts. Alternatively, a thick basin containing low velocity Permo-Triassic sediments could explain the delay.

However, Thomson (1978) shows that Westphalian strata underlie the shot point. Since the refracted arrivals from layer 2 are subject to this delay, in the case of the north line shot, the cause must lie above this horizon. The BGS isopach maps (Browne et al. 1985) show a thick Carboniferous basin in the Methil area. Inclusion of this basin in the ray-traced model will not completely explain the delay. A further, but unlikely, possibility is that a zone of very low velocity Carboniferous rocks occurs beneath the shotpoint area. The Methil shots were offset from the nearest receivers by over 10 km to achieve the desired line length. Therefore, shallow structure is poorly constrained in their vicinity and the nature of the delay cannot be definitely asserted.

There are some significant differences between the final ray-traced models and the preliminary interpretation described by Conway et al. (1987). Layer 1 velocities are lower, in better agreement with those quoted by Davidson et al. (1984) for Carboniferous rocks. The depth to layer 2 is less at the western ends of the lines which is in accordance with the depths predicted from the surface geology. This is partly due to the lower velocities in layer 1 and partly due to the reassignment of arrivals from the Trearne shot from layer 1 to layer 2. The depth to this layer is deeper in the east to agree with the isopach data of Browne et al. (1985), and shallower beneath Westfield on the northern line due to the reassignment of arrivals from the this source. The depth to layer 3 is largely unaltered, but at the western end of the northern line the layer no longer deepens to over 7 km. Again, this is partly due to lower layer 1 velocities, and partly to reassignment of data. The depths to layer 4 are fairly similar. Differences in layer velocities have been reduced and lateral variations eliminated.

The ray-traced models of the lines originally interpreted by Sola (1985) do not include the refractor interpreted as the top of the Carboniferous lavas. Sola's inclusion of this horizon is based on data from Tamsloup where there is evidence for a velocity inversion. The incorporation of the lava horizon is not considered to be justified since arrivals from this layer are not observed from Sola's Medrox source, or from the appropriate MAVIS shots. Apart from this difference the models are not dissimilar, though the deepening of layer 2 to the west of Kaimes has been correlated with surface faults rather than being modelled as a gradual deepening with no surface geological expression.

Integration with geological data (see section 7.2) raises a number of points regarding the validity of the ray-tracing technique. Firstly, geological data suggest layer 1 to be considerably thinner at the western end of the MAVIS I north line than in the ray traced model. This appears to be due to overestimation of layer 1 velocities. Obviously, these velocities are constrained by the direct arrivals through layer 1. However, experiments show the data can be satisfied with many velocity distributions. The key point on the velocity grid is that just before the turning point of the ray. The effect of adjusting the velocity here is far greater than at any other point along the ray path. This point controls the velocity gradient and hence the turning point depth. This means great care has to be taken to keep velocity gradients as smooth as possible. This leads to a further point. The velocity grid used has a vertical spacing of 0.5 km. The lavas in this area are about 0.5 km thick. In order to satisfy the travel time of rays in the topmost 0.5 km the velocity at 0.5 km depth has to be a "lava" velocity. However, because of the grid spacing, the "lava" velocity also applies, at least in part, to depths between 0.5 and 1.0 km. Consequently, rays passing through this layer must be refracted at deeper interfaces to satisfy their travel times. These points highlight the problem of to what extent geological control influences the velocity model and, in turn, what is a reasonable velocity grid spacing. A spacing fine enough to resolve the inversion predicted below the lava pile implies a far greater degree of geological control than is actually present. The depth to the inversion can only be estimated, a velocity model including this would be over modelling. Also, a closely spaced near surface grid with large velocity variations, hinders the successful tracing of direct arrival rays back to the surface. The program has a tendency to "reflect" the rays off this area of high velocity gradients, before tracing them back to the surface. A similar problem applies to layer 2. In the model of the MAVIS I north line this layer has a higher velocity than elsewhere. As discussed in section 7.2, this is attributed to ORS lavas. However, layer 2 is interpreted as both Lower ORS and Lower Palaeozoic. It would be expected that the velocity at the base of the layer would be similar for all the data. Because a uniform velocity gradient is assumed for layer 2 (0.05 s^{-1}) this is not the case. This poses the problem of whether a different velocity gradient, or an inversion should modelled in this area. If the latter is undertaken, knowledge of the depth to the inversion is implied. Clearly these problems are not resolvable with the MAVIS data set and the limitations implied for the geological interpretations discussed in section 7.2 should not be forgotten.

CHAPTER 6 - GRAVITY MODELLING

6.1. Introduction

The gravity and magnetic fields in the Midland Valley and their geological interpretation have been extensively studied at Glasgow (McLean 1961, 1966, Cotton 1968, Qureshi 1970, Hossain 1976, Alomari 1980). This work has created a large database of rock density measurements. Two-dimensional gravity modelling has been undertaken based on these data using the MAVIS seismic profiles to constrain possible models. The aims of the modelling were to:

[1] Further constrain structures mapped seismically.

[2] Re-assess previous models of gravity and magnetic anomalies developed before the MAVIS experiment.

6.2. Method

Program MD2D was written to undertake this modelling (Appendix.9.6). The program calculates the two-dimensional gravity and magnetic effects of a series of n-sided polygons. The gravity part of the program was adapted from program T2D, written by W.T.C.Sowerbutts, and the magnetic part is an adaptation of the program MAGNET, written by D.R.Watts. The input to the two programs was standardised and the magnetic program altered to allow multiple bodies to be modelled. In the event, no magnetic modelling was undertaken due to lack of time. Observed data are input in the form of a grid reference and reading. The program then extrapolates the data on to a profile defined by the grid references of its end points. The capacity to remove a regional gradient is included. GHOST graphics routines allow the plotting of the model, or models, and the calculated and observed anomalies, or any combination thereof. A map of the stations and their extrapolated positions on the profile may also be plotted.

The gravity part of the program uses the method of Talwani et al. (1959). Consider the body approximated by the n-sided polygon in Fig.6.1. Hubbert (1948) showed that the gravity effect of this section is equal to a line integral around the perimeter such that

$$g = 2Gp \oint Z \, d\theta \qquad (6.1)$$

where

G = universal constant of gravitation
p = density

Assume P to be the origin of an XZ coordinate system. For some arbitrary point R (Fig.6.1)

$$Z = X \tan\theta = (X - Ai) \tan\phi i = \frac{Ai \tan\theta \tan\phi}{\tan\phi i - \tan\theta} \qquad (6.2)$$

The line integral for the side BC

$$\int_{BC} Z d\theta = \int_{B}^{C} \frac{Ai \tan\theta \tan\phi i}{\tan\phi i - \tan\theta} d\theta = Zi \qquad (6.3)$$

$$g = 2Gp \sum_{i=1}^{n} Zi \qquad (6.4)$$

In the most general case

$$Zi = Ai \sin\phi i \cos\phi i \quad (\theta i - \theta i+1) + \tan\phi i \log_e \frac{\cos\theta i \ (\tan\theta i - \tan\phi i)}{\cos\theta i+1 \ (\tan\theta i+1 - \tan\phi i)} \qquad (6.5)$$

$$\theta i = \tan^{-1} \frac{zi}{xi} \qquad (6.6)$$

$$\phi_i = \tan^{-1} \frac{z_{i+1} - z_i}{x_{i+1} - x_i} \qquad (6.7)$$

$$A_i = x_{i+1} + z_{i+1} \frac{x_{i+1} - x_i}{z_i - z_{i+1}} \qquad (6.8)$$

The procedure is repeated for different locations along the X axis and different bodies. The gravitation attractions from each body at a given point are then summed.

The density data used in modelling are listed in Table 6.1.

Table 6.1. Density Data.

Lithology	Density (g/cm3)
Carboniferous sediments	2.54
Carboniferous lavas	2.72
ORS sediments	2.61
ORS lavas	2.66
Basement (Vp=6.0 km/s)	2.69
Basement (Vp=6.4 km/s)	2.76
Basic intrusive	3.25

The two basement densities are taken from Bott et al. (1972). Note that there is a density contrast between the Lower ORS and the Lower Palaeozoic (density 2.71 g/cm3). However, this was ignored since this interface is not mapped seismically. The whole of layer 2 was modelled as ORS sediments on all profiles except G3 where ORS lavas were assumed as suggested by the higher velocity of layer 2 on the MAVIS I north line (see section 7.2). This was preferred to the assumption of a completely Lower Palaeozoic layer because the seismic results suggest that the layer 1-2 interface has the greatest relief. In addition, the effects of the quartz-dolerite Midland Valley sill (density 2.90 g/cm3) had to be ignored due to lack of constraint on its structure.

Fig.6.2. illustrates the anomalies modelled and the locations of the gravity and seismic profiles. Clearly these anomalies are three-dimensional. However, the extent of the seismic coverage and the limitations, mentioned above, of any models were not thought to justify a detailed three-dimensional interpretation. Instead, three orthogonal two-dimensional profiles were modelled. This geometry allows the recognition of any significant sources of anomaly located outwith any two-dimensional profile. Lines were placed so they symmetrically traverse the anomalies to reduce such effects to a minimum. The anomalies do not necessarily coincide exactly with surface structures. For example, the Alloa "low" lies several kilometres to the east of the structural basin of the Central Coalfield Syncline, and there is no surface expression of the Bathgate "high" (Fig.6.3). Further, the gravity and magnetic "highs" around Bathgate are not coincident, the latter being dis- placed a few kilometres south-west of the former.

Initial models were based on the MAVIS profiles and the isopach maps of Browne et al. (1985). These models were then refined until they fit the observed data to within 1 mgal. Where the source of anomaly is known to lie out of the plane of the profile these residuals are larger.

6.3. Results

6.3.1. Bathgate Anomaly

The MAVIS profiles show there to be no relief on any of the interfaces mapped that can be correlated with the Bathgate "high". Therefore, the source is likely to be a body of extrusive and/or intrusive igneous rocks. Powell (1970) suggests that the magnetic anomaly is due to a body 16 km in diameter, at a depth of 4.8 km, of relatively dense, magnetic Lewisian rocks of granulite facies. An alternative interpretation of the north-south profile across the magnetic anomaly is a body 10 km across, extending from 9.9 to 23 km depth (Gunn 1975). More detailed work by Hossain (1976) modelled the Bathgate magnetic "high" in terms of two extremes; a shallow "lava" model, and a deep "intrusive" model (see section 2.4 and Fig.2.13.). The shallow source requires lavas to extend to a depth of about 4 km. The MAVIS data shows the Carboniferous and Upper ORS to be close to 2 km thick in the Bathgate area. It may be possible, however, to model the anomaly as a thinner body if the top surface, modelled by Hossain at a depth of up to 1 km, is brought closer to the surface. Alternatively, the deeper part of the body could be an intrusion.

Fig.6.4 shows the key to the gravity models described below. The two gravity profiles (G1 and G2) show the anomaly can be modelled, as with the magnetics, in terms of two end member models. The shallow gravity model satisfies the anomaly with a thickened sequence of Carboniferous lavas (Figs.6.5 & 6.6). Such lavas are exposed at the surface to the north of Bathgate and a thick lava sequence, interpreted as the overlap of the Bathgate lavas with those of the Clyde Plateau to the west, is described from the Rashiehill borehole (Anderson 1963) (Fig.6.7). Note that the outcrop of the Bathgate lavas is to the east of the north-south G1 profile across the anomaly. This indicates that the north-south shallow model of the profile will not satisfy the observed anomaly. Figs.6.8 and 6.9 illustrate the deep intrusive model. The density of the intrusion, 3.25 g/cm3, is high in the range quoted by Telford et al. (1976) for gabbro. In this case the source of the anomaly must be a combination of this intrusion and the lavas mapped at the surface.

Gravity modelling across the Bathgate "high" has confirmed the range of possible sources determined in earlier potential field investigations. The geological implications of these interpretations is discussed in section 7.5.

6.3.2. Alloa and Ochil Fault Anomalies

The Alloa "low" coincides with the known depositional Kincardine Basin. The isopachs of Browne et al. (1985) show this basin to lie a few kilometres east of the present structural basin (the Central Coalfield Syncline). This is in agreement with the MAVIS I north line which shows the synclinal structure of ORS unconformity to be offset to the east of the synclinal axes (see section 7.2). This is confirmed by the gravity model of the G3 profile (Fig.6.10). Again, the source of the gravity "low" is not symmetrical about the north-south profile (G1). For this reason the "low" is not completely modelled along this line (Figs.6.6 and 6.9). Both models of the G1 profile confirm the southward dip of the Ochil Fault. The data cannot be satisfied by a vertical or reversed fault even when the unconstrained thickness of the ORS lavas of the Ochil Hills is adjusted. The nature of the Ochil Fault is discussed in more detail in section 7.3.

6.3.3. Hamilton Anomaly

The gravity "low" centred around Hamilton is not crossed by a refraction line, though the MAVIS profiles pass to the north and east, and the refraction profile described by Davidson (1986) lies to the south. Browne et al. (1987a) have recently published an interpretation of the anomaly (Fig.6.11, profile G4 on Fig.6.2). The anomaly is modelled as a 2.5 km thick Carboniferous basin. Note the slightly different densities used. In the model the Lower ORS and Lower Palaeozoic are shown as being at a depth of only about 0.5 km, with the Clyde Plateau Lavas providing additional density contrast to the west. The basin margins coincide with the surface expressions of the Dechmont Fault and a splay from the Wilsontown Fault. The thin Carboniferous sequence to the north of the Wilsontown Fault is not supported by the seismic evidence. Since the anomaly is subcircular this model ought to be an approximation of the north-south structure. A sub-circular "caldera" type basin is not likely, but more importantly, Fig.6.3 and the MAVIS I lines show there to be a thick Carboniferous sequence to the north. Therefore, a different source of density contrast is required to that used in modelling the east-west profile of the anomaly by Browne et al.. This implies the anomaly to be the result of several geological features. The validity of the basalt wedge on the west side of the basin beneath the Upper ORS is also somewhat suspect geologically.

Alomari (1980) produced two models to explain this anomaly (see section 2.4). A thick ORS basin is considered unlikely, since adjacent seismic lines show basement to be consistently far shallower than is required. For this reason his model of a granite intrusion is considered the most likely.

CHAPTER 7 - GEOLOGICAL INTERPRETATION AND DISCUSSION

7.1. Crustal Structure in the Midland Valley: Interpretation and Comparison with Previous Results

7.1.1. P-Wave Data

Fig.7.1 shows a representative MAVIS P-wave velocity-depth curve, based on the velocity analysis described in Chapter 4 and the ray-traced models. Similar curves obtained from LOWNET and LISPB for the Midland Valley are also plotted (see section 2.2). The MAVIS curve consists of a 2 km thick layer 1 of velocity 3.0-5.0 km/s overlying a layer 2 of similar thickness and velocity 5.4 km/s. Layer 3 has a velocity of 6.04 km/s and thickness of 3 km. Layer 4 has a velocity of 6.43 km/s. Velocity gradients are 0.05 s-1 for layer 2 and 0.03 s-1 for layers 3 and 4.

The MAVIS data allow the refinement of the LISPB and LOWNET crustal models. The thickness of the "superficial" LISPB layer 1 is essentially confirmed, though with a somewhat high velocity. Since this layer was based on surface geology, rather than seismic data, the agreement is remarkably good. The "Lower Palaeozoic" layer 2 of LISPB can be subdivided into the two layers with velocities of about 5.4 and 6.0 km/s. There is reasonable agreement for the depth and velocity of the 6.4 km/s "Caledonian foreland" layer 3 of LISPB. The LOWNET 5.65 km/s layer appears to be the product of the 5.4 and 6.0 km/s layers of MAVIS. Again there is reasonable agreement as to the depth and velocity of the LISPB layer 3.

Fig.7.2 is a compilation of velocity data gathered by Hall et al. (1983), Davidson et al. (1984) and Sola (1985). Velocities of Carboniferous rocks are significantly lower than those of Lower ORS and Lower Palaeozoic rocks which are, in turn, less than those of crystalline rocks. The MAVIS velocity-depth curve from Fig.7.1 is also shown. Based on this velocity data the geological interpretation of the MAVIS layers is:

Layer 1 Carboniferous and Upper ORS

Layer 2 Lower ORS and Lower Palaeozoic

Layer 3 Crystalline basement

Layer 4 Higher velocity crystalline basement.

This is in agreement with Davidson (1986) and Sola (1985). The higher velocity velocity-depth curve labelled "A" is from the Aberuthven shot of MAVIS II and illustrates the increase in velocity with depth for the Lower ORS lavas of layer 2 exposed at the surface to the south of this shot. The layer 2 curve labelled "B" is taken from the ray-traced model of the MAVIS I north line which has higher velocities than elsewhere.

7.1.2. S-Wave Data

Fig.7.3 compares the S-wave velocity-depth curves from MAVIS with those obtained in the Midland Valley by MacBeth & Burton (1986). Their data are based on the detection, using the LOWNET array, of surface waves generated by a source in the Firth of Forth. They divide the Midland Valley into four regions containing; A), ORS lavas B), ORS sediments C), Carboniferous sediments and D), the Firth of Forth estuary.

The latter is included to ascertain the effects of the water and recent sediments. The distribution of the receivers is such that five of the eight propagation paths are mainly through the Carboniferous. These velocity-depth data are therefore comparable with those from MAVIS layer 1. S-wave velocity varies between 1.4 and 2.1 km/s in the upper 400 m of the crust and between 1.9 and 3.5 km/s in the deepest layers. The MAVIS curve is seen to fall within these ranges, though there is a tendency to predict higher velocities at a given depth. This is probably due to the effects of the water and recent sediments on the surface wave data. The three remaining paths (AB, ELO and DU) pass through a significant proportion of Lower ORS strata. The latter two give similar results, though AB is anomalously low. The velocities predicted are seen to be greater by about 0.5 km/s than those obtained from the Carboniferous ray paths. This is as expected from the MAVIS P-wave models. S-wave velocity-depth data obtained from Aberuthven compare favourably with those from ELO and DU. This is somewhat unexpected since the MAVIS data is based on a single shot recorded through an ORS lava sequence with no allowance made for lateral velocity variations (see section 4.2), whilst the surface wave data is for a combination of ORS sediments and lavas and the Carboniferous.

7.1.3. Vp/Vs and Poisson's Ratio

Pickett (1963) demonstrates that Poisson's ratio, or just Vp/Vs, can be used as a lithological discriminator (Fig.7.4a,b and Table 7.1).

Table 7.1. Vp/Vs and Poisson's Ratio for Different Lithologies.

Lithology	Vp/Vs	Poisson's Ratio
Sandstone	1.6-1.75	0.18-0.26
Dolomite	1.8	0.28
Limestone	1.9	0.31

Fig.7.4c, based on the data of Birch (1966) and Christensen (1982), shows these differences to be related to mineralogy, particularly quartz content. Calcite, dolomite and feldspar (not shown) have Vp/Vs ratios of between 1.8 and 2.0 whilst quartz has a value of 1.5. Also shown on Fig.7.4c is the extrapolation to 100% clay and 0% porosity of Tosaya's (1982) empirical relation for Vp and Vs in shaly rocks. The actual location of the "clay point" depends on the clay mineralogy, but is included to illustrate the ratio for clay lithologies. The measurements in Fig.7.4c are on individual crystals and represent rocks consisting of an isotropic aggregate of such crystals. In reality, the physical properties measured in a sedimentary rock with finite porosity are the bulk physical properties of a two phase system of matrix and pore saturant. These properties are also a function of pore and crack geometry. Tatham (1982) concludes that the latter have a greater influence on Vp/Vs than matrix mineralogy, and that distinctive Vp/Vs is a function of lithological control of pore and crack shape rather than the lithology itself.

In spite of this, Wilkens et al. (1984) demonstrate that Vp/Vs can be used to measure the quartz content of siliceous limestones, where Vp/Vs varies four times as much due to this effect than due to porosity effects.

The Poisson's ratio and Vp/Vs curves obtained from the MAVIS data are for variation with depth and therefore with confining pressure. Several authors have studied the variation in Vp/Vs with pressure using laboratory measurements on cores and mathematical models of crack behaviour. Domenico (1984) plots reciprocal velocity and reciprocal velocity difference versus differential pressure (the difference between overburden pressure and pore pressure) for a series of sandstone and limestone cores of varying porosities (Fig.7.5). Fig.7.5 shows Vp/Vs to be greatest at the surface, decreasing with depth to an approximately constant value as increasing pressure closes cracks and pores. This decrease is greater in sandstones than in limestones, and is a function of sandstone Vs variation with porosity being more than twice that of sandstone Vp and limestone Vp and Vs. The depth at which the near constant value is achieved increases with porosity.

Castagna et al. (1985) show that in both saturated and dry samples of clastic sediments Vs is approximately linearly related to Vp. The Vp/Vs ratio is slightly larger when the samples contain mudrocks. For dry sandstones Vp/Vs is constant, but for wet sandstones Vp/Vs decreases as Vp increases. Both velocities increase with pressure. This is in agreement with the results of Toksov et al. (1976) and O'Connell & Budiansky (1974) who show Vp/Vs to decrease as dry crack density increases, but to increase when the cracks are saturated.

All authors agree that porosity and, sometimes, matrix lithology control Vp/Vs and Poisson's ratio. In the Midland Valley the Carboniferous sequence is mainly clastic sediments with mudrocks and subordinate limestones. Assuming the sequence to be saturated, it is expected that Vp/Vs, and to a lesser extent Poisson's ratio, will decrease with depth tending towards a constant value as increasing confining pressure closes most pores and cracks.

Fig.7.6 shows the MAVIS results (see section 4.2.6) to lie within the limestone field when plotted on a graph of Poisson's ratio versus Vp/Vs. This is unexpected but is probably the result of clay rocks within the sequence, since the Vp/Vs ratios of these can exceed 2.0. The effect of clays on sandstone Vp/Vs is discussed by Castagna et al. (1985). They show that the Vp/Vs ratio is less sensitive to clay content than to porosity, but the range of variation due to clay may be larger. "Thus Vp/Vs can be grossly dependent on clay content". Fig.7.7 shows Vp/Vs as a function of depth for shales and clean porous sandstones from the Gulf Coast of America. Note the increase in Vp/Vs near the surface. Shale velocity ratios are about 10% higher than the sandstones at a given depth, and thus in a sand-shale (clay) sequence, the observed Vp/Vs will be higher than for just a sand succession.

The large errors on the values obtained from MAVIS make further interpretation of the data unworthwhile and work in this area was abandoned at this stage.

7.1.4. Summary

The P-wave velocity data confirm the results of Davidson et al. (1984) who refine the LISPB crustal model and predict crystalline basement at about 4 km depth in the Midland Valley. S-wave velocities are in reasonable agreement with those obtained from surface wave studies, though the scatter on the data is large. Poisson's ratio obtained from these data is reasonable for a sandstone/limestone/ shale sequence, though poorly constrained.

7.2. Geological Implications of Ray-Traced Models

The geological interpretation of the ray-traced profiles (Figs.5.10 to 5.74) is based on the geometry of the interfaces and the velocities within the layers.

Figs.7.8 to 7.10 are three of a series of isopach and contour maps for various stratigraphic horizons and subdivisions within the Midland Valley presented by Browne et al. (1985). The first shows the depth to the base of the Upper Carboniferous, the second the depth to the base of the Carboniferous and the third is an isopach map of the Upper ORS Kinnesswood Formation and underlying Stratheden Group. The second and, particularly, the third are extremely speculative being based on very little data. These maps are combined to produce the sections along the MAVIS I and II lines shown in Fig.7.11, (the Upper ORS is not subdivided on the sections), for comparison with the depth to the base of the Upper ORS obtained from MAVIS. Agreement between the two data sets is surprisingly good. Most discrepancies can be accounted for by the thickness of Upper ORS assumed by

Browne et al. The exception is between 0 and 20 km from the western end of the MAVIS I north profile. The seismic data is of good quality in this region, but it is suspected that layer 1 velocities used in the ray-traced model may be somewhat high. This would result in an overestimate of the depth to the first interface (see section 5.2.2).

Surface geology is reflected by the velocity structure within layer 1. Areas of high velocity between 0 and 20 km on the MAVIS I lines (Figs.5.10, 5.23 and 5.35) correspond to the outcrop of the Carboniferous lavas, whilst the area of higher velocities at about 60 km on the north profile corresponds with a zone of surface intrusions and fold structures. Velocity "lows" at 35 km and between 20 and 40 km, on the MAVIS I south line and north line respectively, correspond with the Central Coalfield Syncline. Similar "lows" at the eastern ends of these lines are due to the Fife-Midlothian Syncline.

Surface structure is reflected in the geometry of the ORS unconformity interface. Layer 1 is thickest beneath the Central Coalfield and Fife-Midlothian Synclines and thins where older strata are exposed at the surface. On the MAVIS I north line, the increased thickness of layer 1 actually occurs a few kilometres to the east of the axis of the Central Coalfield Syncline. This offset is confirmed by gravity modelling (section 6.3.2). This is due to the axis of the depositional Kincardine Basin not coinciding with the modern structural basin (Francis et al. 1970). This is apparent in the isopach maps of Browne et al. (1985). The thickening at the eastern ends of the MAVIS I lines is poorly constrained, due to lack of reversed data, and is included to explain the large delay of the Methil arrivals. This is in agreement with Browne et al.'s isopach data which show such a structure. Abrupt changes in the thickness of layer 1 on the MAVIS III and Sola south lines coincide with faults mapped at the surface in the Lothian oil-shale fields. The density of refraction lines in this area allow the structure to be determined in some detail (see section 7.4)

Velocities within layer 2 are consistent (5.4 km/s at about 3 km depth) except for the MAVIS I north line where the velocity is 5.8 km/s. This is probably due to the interface being composed of Lower ORS lavas in this area. These velocities suggest that the northern and southern Midland Valley outcrops of ORS lavas are not continuous. Where layer 2 reaches the surface north of the Ochil Fault and south of the Wilsontown Fault, or approaches the surface, velocities are variable and poorly constrained. Those based on the Kaimes and Trearne data are primarily a function of the geometry of the top of the layer. Data from the Aberuthven shot are most reliable, but are for an ORS lava sequence. Similar data from Cairngryffe are based on only four arrival times.

In contrast to the first MAVIS interface, the second (top of crystalline basement) shows very little relief, especially on the MAVIS I south line. The preliminary MAVIS interpretation (Conway et al. 1987) shows the depth to the horizon increasing to over 7 km at the western end of the MAVIS I north line. The reduced velocities within layer 1 in the new interpretation and slight reassignment of time-distance segments based on second arrival data do not require this structure. There is, however, still some relief on the interface at about 40 km range. There is also relief on the interface at 15 km range on MAVIS II, in the region of the Ochil Fault. The two are probably related and may be a basement expression of a fracture related to the Ochil Fault. This is discussed in detail in section 7.3. The low relief of the basement, compared to near surface structure and the ORS unconformity, suggest the overlying structures to be the product of thin-skinned deformation. A detachment is envisaged between the two interfaces or, perhaps, at the ductility contrast to be anticipated at the top of crystalline basement.

The third interface is also virtually planar and follows the LISPB interpretation in shallowing to the south. The nature of this horizon is enigmatic, though Davidson (1986) suggests it coincides with a change from amphibolite to granulite facies rocks.

The ray-tracing models were extended to the base of the crust, based on the LISPB model. Poorly constrained Moho reflections from the Trearne shot suggest the crust to be about 35 km thick. This compares well with the results from LISPB (see Fig.2.3).

7.3. Nature of the Ochil Fault

The Ochil Fault extends east-west across the Midland Valley from the Fife coast to west of Stirling. It occurs as either a single fracture or a belt of faulting, separating the Lower ORS to the north from the Carboniferous to the south (Fig.1.8). The fault has its maximum downthrow at Alva where Geike (1900) estimated a throw to the south of greater than 3 km, an estimate accepted by Francis et al. (1970). A series of bores and some largely unsuccessful geophysical work by the BGS enabled the fault to be traced across the carse of Stirling to near Kippen, about 13 km west of Stirling (Francis et al. 1970). Here the fault ceases to be a major structure, and is seen only as a small fault in the Lower ORS, or as a fault or fold running west-southwest in the Upper ORS. It may be significant that there is a belt of relatively steep dipping strata in the Upper ORS Gargunnock Sandstone running west-southwest to the southwest of Kippen.

The fault is interesting for two reasons:

[1] At Alva the throw is in excess of 3 km, but the fault appears to die out about 13 km west of Stirling, i.e. only about 20 km from Alva.

[2] The direction of fault plane dip is unclear. This is critical in evaluating the history of the fault. A high-angle reverse fault would be indicative of a reactivated Caledonian wrench structure, whilst a normal fault could have a common origin with the late Carboniferous east-west normal faults seen to the south.

A feature of the Ochil Fault is the fault-plane intrusion of late Carboniferous quartz-dolerite described by Haldane (1927). The intrusion is chilled against the contact with the fault plane and so post-dates the fault rather than being tectonically emplaced. However, signs of subsidiary fractures affecting the intrusion and the country rock are common, indicating some post-intrusive movements. Haldane reports the fault plane as dipping between 63° and 72° to the south at thirty-two localities. This is not reliable evidence since it is the dip of the intrusive contact that is being measured. This dip is localised and variable. For instance, Francis et al. (1970) report that at Castle Craig Quarry, Tillicoultry, the plane of the fault is distorted by the intrusion and the contact sigmoidal.

The evidence from local mining operations is also inconclusive with all workings ceasing at the "troubled zone". This belt of disturbed strata is encountered south of the outcrop of the fault, but could be very wide, and so is not a reliable indicator of fault hade.

The Carboniferous to the south of the Ochil Fault is heavily faulted, the faults being of predominantly of east-west trend and southerly downthrow. Francis & Walker (1986) describe Namurian sills whose emplacement was controlled by similar fractures, and suggest these fractures to be Carboniferous growth faults. If these faults are assumed to have a common origin to the Ochil Fault a Carboniferous age and southerly dip are to be expected for the latter.

Such a fault geometry is in agreement with the seismic and gravity models described in sections 5.2.2 and 6.3.2.

Davison (1924) describes over two-hundred earthquakes originating in the region of the Ochil Fault. Fig.7.12 shows the distribution of isoseismal lines and known epicentres for a series of these earth tremors. Davison ascribes the shocks to a northward dipping Ochil Fault because; 1), the average trend of the long axis of the isoseismal lines is parallel to the surface expression of the fault 2), the spacing of isoseismal lines is less to the south and 3), known epicentres lie to the north of the fault forming a band, approximately 14 km in length parallel to the fault, extending from a few kilometres north-east of Tillicoultry to a short distance west of Bridge of Allan.

Clearly, there is a conflict of geological and geophysical evidence. Haldane (1927) suggests three solutions to the problem. Firstly, that the fault plane is normal near the surface and reverses at depth. Secondly, that the earthquakes originate on another fault, possibly one which is too small to be detected at the surface or else intersects the Ochil Fault at depth. Thirdly, the source of the tremors could be movements on the north-northwest trending faults adjacent to the Ochil Fault on its northern side (see later). The fact that these smaller faults are most common in the area of maximum seismic activity may be of significance.

To the north of the Ochil Fault the Lower ORS lavas and sediments of the Ochil Hills are cut by a series of faults (Fig.7.13). Francis et al. (1970) consider them to be of pre-Upper ORS age. These faults have three major trends; NW-SE, NNW-SSE and NE-SW. There is also a subordinate group with an east-west trend, but these are almost certainly contemporaneous with those of Carboniferous age mapped to the south. Most of the known faults in the Lower ORS strata of the northern Midland Valley are recognised in the lavas of the Ochil Hills. This is probably the result of the easier recognition of faults in an area of high relief and good exposure. It may be significant that in the area of the MAVIS II Aberuthven shot, where exposure is good and there are distinctive acid lavas, a number of faults have also been recognised. However, faults are rare in the well exposed sediments of the northwest limb of the Strathmore Syncline. The proximity of the Ochil Fault may also be a factor in the greater density of faulting.

The faults trending northwest, north-northwest and northeast can be dated by their association with local dykes contemporaneous with Lower ORS diorites. The dykes form a radial pattern around the diorites, but there is a tendency for preferred orientation along north-northwest and north-northeast trends. Since this coincides with the major fault trend it is likely that the fractures formed either before or during diorite emplacement. This would explain why such faults are seldom traceable northwards and westwards into the overlying sediments. The most likely explanation is that since the faults are not radial they were not associated with emplacement of the diorite. Rather, the dykes made use of pre-existing fault planes.

Around Blairlogie a group of north-northwest and northwest trending faults is well exposed. The largest is seen in Blairlogie Burn and has a throw of about 250 m decreasing to the north and northwest. Between Menstrie and Balquhan there are also northwest and north-northwest trending faults, the flanking fractures of which downthrow around

75-100 m to the west, the throw decreasing to the north. The northwest trending fault at Alva downthrows 60 m to the west, but dies out before reaching the Ochil Fault. The faults in Silver Glen probably only involved small amounts of movement. Further east, the northeast trending faults are more important with two examples being particularly prominent. The amounts of displacement are unknown but in both cases the fault planes dip to the southeast and associated small parallel faults have been mapped. The central part of the Ochil Hills is characterised by a group of northwest trending faults, the vertical component of which appears to have been small.

All the fault sets are mineralised. Those of north-northwest trend are characterised by copper mineralisation with minor iron, in a gangue composed mainly of barytes with calcite and sub-ordinate quartz. The northeast trending fractures are associated with dominantly iron and silver with minor cobalt, lead and copper in a gangue of mainly calcite with subordinate quartz and barytes. MacGregor (1944) considered the northeast trending faults to have been mineralised in one or more phases between Middle Carboniferous and Permian times. The dominant barytes mineralisation with subordinate copper of the north-northwest set is considered to be as late as Tertiary in age. The time of mineralisation is not significant to the age of faulting. Mineralisation depends on the fractures being open, and will not necessarily occur even if a particular fault set is already in existence. There was a significant amount of mining in the Ochil Hills, this is a useful source of structural data, allowing the orientation of fault planes to be established (Francis et al. 1970). The data suggest that, as well as normal faults, there are some steeply dipping reversed faults, assuming that the mineralised breccias described are either the faults marked on the map or parallel the local fractures. Examples include:

[1] at Allan Water a breccia (presumably the fault marked on the map) trends W.10°N. and dips 70°S. On the map the fault is shown as downthrowing to the north, i.e the fault is reversed.

[2] A mineralised breccia at Pendreich trends N.10°W. and dips 70° E. This suggests adjacent faults of similar trend, downthrowing to the northwest, are normal.

[3] At Airthrey the fault trend is W.10° .N and the dip 10° N, i.e. a reverse fault.

[4] The mineralised fault in the Second Inchna Burn dips and downthrows west and so is normal.

[5] The Myreton Hill Fault dips 80° S and downthrows northwest and so is reversed.

[6] The major northwest fault in the Balquhan Burn dips northeast at 70° but downthrows southwest and so is reversed.

[7] A W.15°.S trending mineralised fault at Alva dips south at 80° suggesting that the NE trending set maybe normal.

[8] This is is supported by the 80°S dip of the S.50° .W

trending

fault in Daiglen Burn.

All these throws may have been altered as a result of drag by the reactivated Ochil Fault.

The curvature of the north-northwest and northwest faults is typical of that seen in Harding's (1974) model for a sinistral wrench zone (Fig.7.13). The nature of the other fault sets can also be fitted into this model. The northeast faults are the en echelon normal set, and the north-northwest and northwest set the antithetic wrench faults. This is consistent with the observed fault plane dip in the northeast trending set, and the lack of vertical displacement in the northwest trending set in areas away from the Ochil Fault. The northwest faults adjacent to the Ochil Fault, whose throws decrease rapidly to the north, could be the result of drag as the Ochil Fault underwent the large degree of vertical displacement seen today. The north-northwest and northwest trending faults tend to have small components of vertical movement except near to the Ochil Fault. The significance of these faults is hard to evaluate, since subsequent movement on the Ochil Fault would probably have reactivated them, but it is interesting to note that similar faults are described from California by Sylvester & Smith (1976) from a known wrench environment. Their steeply dipping fault planes, and combination of normal and reversed geometries, support the interpretation of these faults as wrench faults. The reversed fault in Allan Water also fits the sinistral model of Harding (1974) as a "thrust or reverse fault".

Francis et al. (1970) consider that not all the displacement on the Ochil Fault is post-Carboniferous. They suggest the fault originated prior to the deposition of the Upper ORS and acted "in the form of a monoclinal fold, as a control on subsidence and deposition during much of the Carboniferous". The Central Coalfield Syncline was in the process of formation in Upper Carboniferous times and, at least, the later stages of the Lower Carboniferous, initiating as the depositional Kincardine Basin in Lower Limestone Group times (Francis 1956). North of the Ochil Fault there is no evidence of this structure. This, and the rapid decrease in throw to the east and west, suggests that the fault separated a positive area of slow, and possibly intermittent, subsidence to the north from an area of greater and continued subsidence to the south.

As stated previously, seismic and gravity modelling suggest that the fault dips to the south, and soles out in, or at the base of, the MAVIS layer 2 (Lower ORS and Lower Palaeozoic). There is also a thicker Carboniferous (and Upper ORS) sequence adjacent to the fault (Fig.5.35). Isopach evidence is insufficient to ascertain if this is a roll-over structure associated with a listric normal fault. However, Browne et al. (1987b) describe a sandstone body, interpreted as a channel within an argillaceous sequence, from the stratigraphic interval between the Upper Hirst Coal and the Calmy Limestone (i.e within the Upper Limestone Group). The channel trends north and west adjacent to the Ochil and Arndean Faults and may be a roll-over river. The palaeoflow directions implied by this channel suggest the conventional circular isopach pattern for the Kincardine Basin, based on little evidence from adjacent to the Ochil Fault, is incorrect. If the pattern was correct palaeoflow would be expected to be into the basin and not around its edge.

The surface expression of the fault coincides with the basement structure mapped on the MAVIS II line. There is also basement relief on the MAVIS I north line to the west. It is possible that this is a basement structure that was reactivated during the Carboniferous. The same structure could be responsible for the linear vent system mapped along the north-western margin of the Campsie Hills (Fig.1.8). Also, sedimentological work in the Lower ORS suggests the presence of a major wrench fault in this region (Haughton 1987). A north-south oriented Carboniferous extensional stress field (see section 1.5) may have caused reactivation of this fracture as a dextral wrench fault. The east-west trending Ochil Fault formed en echelon to this fracture, developing into a listric structure soling on to the proposed detachment surface at between 2 and 4 km depth. This is in agreement with the evidence of Francis & Walker (1986) for a Carboniferous origin for structures of this trend.

Fig.7.14 shows a schematic section across the Ochil Fault. The fault is shown as a listric normal fault dipping to the south. The model explains the channel paralleling the Ochil and Arndean Faults and, more importantly, the lateral decrease in throw, and thickening of the MAVIS layer 1 (interpreted as a roll-over structure). The detachment predicted by the seismic data is also incorporated. Fig.7.15 shows a model for the schematic evolution of this and the adjacent Campsie Fault. The model agrees with that of Francis et al. (1970), since fault data from the area to the north of the fault imply a proto-Ochil Fault during Lower ORS times. Note how both faults change trend to parallel the postulated basement fracture. The channel shown parallel to the Campsie Fault is in the Passage Group (Read 1987b) and is possibly also a roll-over river.

7.4. Structure of the Lothian Oil-Shale Fields

Fig.7.16 shows the distribution of MAVIS refraction lines in the region of the Lothian oil-shales fields, this being the most intensely covered area of the Midland Valley. The line separation allows a more detailed interpretation of the structure of this region to be attempted.

The structure of the oil-shale fields has been described by Carruthers et al. (1927) , Richey (1942), Anderson (1942), Kennedy (1943), Mitchell & Mykura (1962) and Cameron & McAdam (1978). The strata have a regional dip to the west, being overlain to the west by the Lower Limestone Group, and are folded into a series of minor domes and basins trending north-south to northeast-southwest. These folds are cut by a series of east-west to northeast-southwest trending faults. Of the six largest, the northernmost three, the Rosyth, Ochiltree and Winchburgh Faults, downthrow to the south. The other three, the Middleton Hall, Murieston and Calder Faults, all downthrow to the north. Horizontal slickensides are not uncommon in the region but unequivocal lateral movements can be rarely proven. Fig.7.17 shows a contour map for the Burdiehouse Limestone (the base of which is the boundary between the Upper and Lower Oil Shale Groups). The fold structures are clearly seen with axes apparently displaced across the Winchburgh, Middleton Hall and Uphall Faults. Kennedy (1944) describes lateral movement on the latter, showing the fault to hade to the south with an approximately 180 m component of sinistral horizontal displacement (Fig.7.16, inset).

The ray-traced sections of the MAVIS III and Sola south lines show an abrupt change in the depth to the ORS unconformity approximately coincident with the surface expression of the Calder-Murieston Fault zone (Figs.5.67 and 5.61). In contrast, there is no relief on this horizon elsewhere in the area, even where the MAVIS III line crosses the other faults described above.

Fig.7.18 shows the MAVIS III profile and its interpretation. The major east-west faults are envisaged as listric, soling out at shallow depth, and forming a flower structure across which there is a downthrow to the north associated with the Calder-Murieston Fault zone. This explains the lack of displacement of the ORS unconformity associated with the faults further north. Fig.7.19 shows a series of cross sections across the region (see Fig.7.16 for their locations). The sections show parallel (concentric) folding. It is not clear how well constrained these sections are in terms of fold geometry, but Cater (1987) describes structures interpreted as the result of bedding parallel shear (as predicted by this style of folding) from the Lower Oil-

Shale Group at Granton near Edinburgh. The geometry of parallel folds is such that a space problem is created due to the common centre of curvature of the beds. A detachment is required below this level, as suggested by the seismic data. The development of such a detachment in a predominantly shale sequence is to be expected and is in agreement with Cater (1987), who suggests deformation by bedding parallel stepped listric normal faulting, to account for deformation in the Lower Oil- Shale Group. The flower structure interpretation and the field evidence of lateral fault movements suggest a strike-slip origin for the structures mapped in the oil-shale fields, with the dome and basin structures forming en echelon in an approximately north-south oriented stress field.

7.5. Source of the Bathgate Gravity and Magnetic Anomaly

The MAVIS data do not allow the recognition of the source of the Bathgate anomaly. However, they do permit some potential sources to be discounted. There is no evidence for relief on any of the seismically defined interfaces being responsible for the anomaly. Therefore, the most likely source is either intrusive or extrusive igneous rocks, or some combination of these.

It might be possible to detect the extent of a shallow lava source by the velocity anomaly it would be expected to cause within Layer 1. Assessment of the extent of this anomaly might allow differentiation between the two gravity models. However, ray-traced profiles across the anomaly show this not to be the case (Figs.5.10, 5.35, 5.55 and

5.61). Horizontal velocities, calculated through the igneous and sedimentary sequences penetrated by the Spilmersford and Glenrothes boreholes (Figs.4.65 and 4.66) are found to differ only by about 0.20 km/s. This is because of the low velocity boles and sedimentary intercalations common within Carboniferous lava piles (Anderson 1963, MacDonald 1973, Francis 1983b). Such a velocity difference is below the resolution of the SEIS81 ray-tracing program.

Since the source of the anomaly lies, at least in part, within Layer 1, but is not exposed at the surface, it is likely that the lavas would be of early Visean age. Evidence for igneous activity in this area at this time are the tuff horizons in the Lower Oil-Shale Group, particularly in the west of the oil-shale basin, e.g. the Seafield Deans Ash (Fig.7.20). In addition, there are also "marl" horizons, produced by the sub-aerial erosion of basic lavas, within the Upper Oil-Shale Group. These horizons are similar to the Dykebar Marl of the Glasgow district which was derived from the adjacent Clyde Plateau Lavas.

Topography on contemporaneous lava piles is known to have controlled Carboniferous sedimentation in the Midland Valley (section 1.5). Even after being totally submerged the lavas continued to influence sedimentation due to differential compaction. Therefore, if Carboniferous lavas are indeed responsible for the Bathgate anomaly, their presence could be indicated by their effect on sediment thickness in the area and should be reflected in isopach geometry. Unfortunately the isopach data are not sufficiently constrained to provide a definitive answer. However, sedimentation is known to have been concentrated in the Central Coalfield and Fife-Midlothian regions at this time (Fig.1.9). The source of the Bathgate anomaly may have formed part of the watershed separating these two regions. Detailed studies of variations in lithology and thickness across the Bathgate area may enable any topographic "high" of igneous origin to be identified.

Fig.7.20 illustrates the spatial and temporal distribution of the Permo-Carboniferous igneous rocks of the Midland Valley of Scotland. Clearly the greatest volume of lavas was produced in the Visean. De Souza (1979), on radiometric evidence, proposed a virtually continuous basaltic lava field over much of the Midland Valley at this time. Francis (1983b), however, notes variations in thickness and composition, indicating that there were several eruptive centres. The interpretation of a Visean lava pile near Bathgate is compatible with the suggestions of De Souza and Francis. These lavas are probably from a source near Bathgate, since the nature of the anomaly suggests their thickness decreases rapidly away from this area. They could well be continuous with those of the Clyde Plateau to the west, Rashiehill in the north and Arthurs Seat to the east. Their relationship to the other Permo-Carboniferous igneous rocks in the Midland Valley is shown in Fig.7.20.

If this interpretation is correct the importance of Bathgate as an igneous centre within the Midland Valley has been underestimated. The presence of a thick Lower Carboniferous lava pile, younger lavas of up to Namurian age to the north, and the Midland Valley Sill to the east, would make this area one of the major igneous centres in the region. This would remain true even if part of the anomaly is due to basic intrusions associated with such a centre. Cotton (1968) describes an anomaly at Waterhead in the Campsie Hills which is attributed to such a source.

An alternative source for the Bathgate "high" is an intrusion of Lower ORS age. Most of the igneous rocks of this age in the Midland Valley are of intermediate or acid composition. There are, however, large basic intrusions in the Sidlaw Hills to the north and numerous smaller dykes and sills across the whole Midland Valley. A further possibility is the presence of a deep basic intrusion within the crystalline basement. A deep source such as this is unlikely to be detected seismically. The intrusion is at a depth greater than the deepest interface mapped from refractions and reflections are unlikely to be detected since the the body is of only limited lateral extent. Further, very little velocity contrast is to be expected between the basement and the intrusion.

Interpretation of seismic reflection data from the Bathgate area might allow confirmation of a Carboniferous lava source. Confirmation of the other possibilities would require a deep, expensive and extremely unlikely borehole.

7.6. Tectonic Implications of the MAVIS data

The resolution of the seismic refraction profiles is insufficient to constrain detailed structural interpretations. However, the tight grid of refraction lines in West Lothian has allowed the presence of a shallow detachment horizon (at less than 2 km depth) to be postulated. On a larger scale, the relief on the ORS unconformity is seen to reflect structures mapped at the surface, in contrast to the top of crystalline basement, which is found to be nearly planar. A detachment between these two horizons, i.e. between about 2 and 4 km depth, is postulated and used to explain the structures mapped in the region of the Ochil Fault.

Thin-skinned tectonic processes with multiple detachment levels have been postulated for the region by Gibbs (1984) who suggests a dextral strike-slip environment during Carboniferous times. The MAVIS data appear to confirm this hypothesis, though the resolution of the experiment cannot preclude other interpretations. Similar results have been described by Davidson (1986), who maps a planar crystalline basement horizon beneath the Lower Palaeozoic inlier at Lesmahgow (Fig.1.2) and across the outcrop of the Inchgotrick and Kerse Loch Faults (Fig.1.8).

Clearly, the conventional structural model of the Midland Valley where Caledonian basement fractures are reactivated to control Carboniferous sedimentation and volcanicity (Francis 1983) must now be treated with caution. Such control probably did exist in some areas, e.g. the Campsie-Ochil fault belt, but may have been less ubiquitous than previously thought.

7.7. Summary

[1] The MAVIS experiment successfully mapped the upper crustal layers recognised by Davidson et al. (1984) across

most of the Carboniferous outcrop of the Midland Valley of Scotland. The Carboniferous and Upper ORS layer varied between 0.5 and 3.0 km thick depending on surface geology and structure. The Lower ORS and Lower Palaeozoic layer extends from between 0.5 and 3.0 km to between 4.0 and 6.0 km depth. The layer appears uniform except in the area of the MAVIS I north line, where ORS igneous rocks are postulated as causing a higher velocity than elsewhere. Basement varies in depth between 4.0 to 6.0 and 7.0 to 8.5 km. There is little relief on the top of the layer except at the northern end of the MAVIS II line and the western end of the MAVIS I north line. A basement fracture of probable Caledonian age is postulated in this region. The 6.4 km/s layer and Moho depths are between 7.0 and 8.5 km and at 35 km respectively, in agreement with the LISPB interpretation. These results are summarised in Figs.7.21 to 7.23.

[2] Velocity studies based on reflection data and comparison of P- and S-wave data provided interesting, though poorly constrained, results.

[3] Gravity modelling within the framework of the seismic data was partially successful, enabling the nature of the Ochil Fault to be better understood. Modelling of the Bathgate gravity anomaly merely confirmed the results of the magnetic modelling (Hossain 1976) and, as such, can only be regarded as partially successful. There appears to be little alternative to drilling to resolving this problem, unless commercial seismic

reflection data are released which image a source within their limited depth of penetration.

[4] The data provide some insight into the tectonic evolution of the Midland Valley, particularly where line density is high, e.g. in the Lothian oil-shale fields. A detailed structural model for this area and the Ochil Fault, plus comparison of ORS unconformity and basement relief, suggest thin-skinned tectonic processes with detachments at several levels to have controlled deformation in the region.

Thus, the MAVIS experiment successfully achieved its major objectives of mapping the ORS unconformity and crystalline basement horizons across the Midland Valley. This was the reason for Tricentrol funding the project and always the major priority.

7.8. Recommendations for Further Work

The MAVIS experiment was the first of a scale that allowed Midland Valley crustal structure to be mapped on more than a localised level. As such, the experiment was, in some ways, a reconnaissance to highlight areas where more detailed work would be rewarding. Such work was completed in West Lothian and adjacent to the Ochil Fault, due to the availability of the Glasgow seismic recorders, which allowed rapid data acquisition. This facility, plus the large number of potential quarry sources, will permit an extensive refraction line network to be established in the Midland Valley, potentially the most intense in the U.K..

To make the maximum use of these data, however, the affects of igneous strata and complex velocity structure on travel times and amplitudes must be further understood by intensive studies in areas of known geology. Also, since at present quarry-blast sources are useful only in the generation of first arrival data, a further understanding of the complex source wavelet, and its conversion to a more ideal source, would greatly increase the usefulness of data obtained in this way.

The estimation of seismic anisotropy and Poisson's ratio from velocity data were interesting exercises, but emphasised the need to better understand the velocity data obtained, since errors were frequently too large to make the results useful. In the latter case this is partly due to the S-wave interpretation. Time precluded a detailed study of these arrivals and future work, including digital processing, may yield more reliable data and interpretations. S-wave arrivals from the basement would be particularly interesting in the light of recent work on the mineralogy of crystalline rocks from P- and S-wave studies (Hall & Ali 1985).

Areas of potential interest for future work include the basement features identified in the northwest of the survey area. The data need to be extended to the north to better constrain the structure. The nature of the Ochil Fault was quite well constrained by integration of the seismic data with gravity modelling. The complex nature of the Midland Valley geology make such integrated studies preferable to isolated work using a single geophysical technique.

Potential targets include the Pentland Fault, no data has been acquired in East Lothian, the Southern Uplands Fault and the northeast-southwest trending faults in Ayrshire. Small amounts of data suggest crystalline basement to be continuous beneath these structures, despite a complex history of movements in the overlying cover. These ?high-angled structures are ideal for potential field modelling in conjunction with the seismic work. The postulated Carboniferous basin east of Methil is a more difficult potential target due to its offshore location.

REFERENCES

AL-CHALABI, M. 1979. Velocity Determination from Seismic Reflection Data. In: Fitch, A. A. (Ed), Developments in Geophysical Exploration Methods - 1. Applied Applied Science Publishers Ltd.

AL-MANSOURI, D. 1986. Seismological Studies of Upper Crustal Structure in the Vicinity of the Girvan-Ballantrae Area, SW Scotland. Ph.D thesis (unpubl), University of Glasgow.

ALLAN, D. A. 1924. The Igneous Geology of the Burntisland District. Trans. R. Soc. Edin. v 53, pp 479-501.

ALLSOP, J. M. 1974. Geophysical Surveys at the Spilmersford Borehole, East Lothian, Scotland. Bull. Geol. Surv. G.B. No. 45, pp 63-72.

ALOMARI, M. I. 1980. Geological Interpretations of the Gravity Field of the Western Midland Valley of Scotland. Ph.D thesis (unpubl), University of Glasgow.

ANDERSON, E. M. 1951. The Dynamics of Faulting. 2nd Ed. Oliver & Boyd.

ANDERSON, F. W. 1963. The Geological Survey Bore at Rashiehill, Stirlingshire (1951). Bull. Geol. Surv. G.B. 20, pp 43-106.

ANDERSON, J. G. C. 1942. The Oil-Shales of the Lothians- Structure-Area II. Pumpherston. Geol. Surv. Wartime Pamphlet No. 27.

ANSTEY, N. A. 1970. Signal Characteristics and Instrument Specifications. Vol 1 of Seismic Prospecting Instruments. Borntraeger.

ARMSTRONG, M. and PATERSON, I. B. 1970. The Lower Old Red Sandstone of the Strathmore Region. Rep. Inst. Geol. Sci. No.70/12.

ASSUMPCAO, M. and BAMFORD, D. 1978. LISPB - V. Studies of Crustal Shear Waves. Geophys. J. R. Astr. Soc. v 54, pp 61-73.

BACHMAN, R. T. 1979. Acoustic Anisotropy in Marine Sediments and Sedimentary Rocks. J. Geophys. Res. v 84, pp 7661-7663.

----- 1983. Elastic Anisotropy in Marine Sedimentary Rocks. J. Geophys. Res. v 88, pp 539-545.

BACKUS, G. E. 1962. Long-wave Elastic Anisotropy Produced by Horizontal Layering. J. Geophys. Res. v 67, pp 4427-4440.

BAMFORD, D. 1979 Seismic Constraints on the Deep Geology of the Caledonides of Northern Britain. In: HARRIS, A. L., HOLLAND, C. H. and LEAKE, B. E. (Eds), The Caledonides of the British Isles - Reviewed. Spec. Publ. Geol. Soc. Lond. 8 p 323-337.

------- , FABER, S., JACOB, B, KAMINSKI, W., NUNN, K., PRODEHL, C., FUCHS, K., KING, R. and WILLMORE, P. 1976. A Lithospheric Seismic Profile in Britain - I. Preliminary Results. Geophys. J. R. Astr. Soc. v 44, pp 145-160.

------- NUNN, K., PRODEHL, C. and JACOB, B. 1977. LISPB - III. Upper Crustal Structure of Northern Britain. J. Geol. Soc. Lond. v 133, pp 481-488.

------- NUNN, K., PRODEHL, C. and JACOB, B. 1978. LISPB

- IV. Crustal Structure of Northern Britain. Geophys. J. R. Astr. Soc. v 54, pp 43-60.

BANIK, N. C. 1984. Velocity Anisotropy of Shales and Depth Estimation in the North Sea Basin. Geophysics v 49, pp 1411-1419.

BARTON, P. J. 1986. The Relationship between Seismic Velocity and Density in the Continental Crust - a Useful Constraint? Geophys. J. R. Astr. Soc. v 87, pp 195-208.

BESSONOVA, E. N., FISHMAN, V. M., RYABOYI, V. Z. and SITNIKOVA, G. A. 1974. The Tau method for inversion of travel-times - 1. Deep Seismic Sounding Data. Geophys. J. R. Astr. Soc. v 36, pp 377-398.

BIRCH, F. 1966. Compressibility; Elastic Constants, In: CLARK, S. P. (Ed), Handbook of Physical Constants. Geol. Soc. Amer. Mem. 97, pp 97-174.

BLUCK, B. J. 1980 Evolution of a Strike-Slip Fault Controlled Basin, Upper Old Red Sandstone, Scotland. In: BALLANCE, P. F. and READING, H. G. (Eds), Sedimentation in an Oblique Slip Mobile Zones. Spec. Publ. Int. Ass. Sedim. 4, pp 7-26.

----- 1983. Role of the Midland Valley of Scotland in the Caledonian Orogeny. Trans. R. Soc. Edin. (Earth Sciences), v 74, pp 119-136.

----- 1984. Pre-Carboniferous History of the Midland Valley of Scotland. Trans. R. Soc. Edin. Earth Sci. v 75, pp 275-295.

----- 1985. The Scottish Paratectonic Caledonides. Scott. J. Geol. v 21, pp 437-464.

BOTT, M. H. P., HOLLAND, J. G., STORRY, P. G. and WATTS, A. B. 1972. Geophysical Evidence Concerning the Structure of the Lewisian of Sutherland, N.W. Scotland. J. Geol. Soc. Lond. v 128, pp 599-612.

---- SWINBURNE, P. M. and LONG, R. E. 1984. Deep Structure and Origin of the Northumberland and Stainmore Troughs. Proc. Yorks. Geol. Soc. v 44, pp 479-495.

BREWER, J. A., MATTHEWS, D. H., WARNER, M. R., HALL, J. and SMYTHE, D. K. 1983. BIRPS Deep Seismic Reflection Studies of the British Caledonides. Nature v 305, pp 206-210.

BRITISH GEOLOGICAL SURVEY. 1972. Aeromagnetic Map of Great Britain, Sheet 1.

BROWNE, M. A. E., HALLEY, D. N. and McMILLAN, M. M. 1986. The Stratigraphy of the Glenrothes Borehole. British Geological Survey.

------ HARGREAVES, R. L. and SMITH, I. F. 1985. Investigation of the Geothermal Potential of the U.K., The Upper Palaeozoic Basins of the Midland Valley of Scotland. British Geological Survey.

------ ROBINS, N. S., EVANS, R. B., MONRO, S. K. and ROBSON, P. G. 1987a. Investigation of the Geothermal Potential of the U.K., The Upper Devonian and Carboniferous Sandstones of the Midland Valley of Scotland.

------ ROBINS, N. S., EVANS, R. B., MONRO, S. K. and ROBSON, P. G. 1987b. Investigation of the Geothermal Potential of the U.K., The Upper Devonian and Carboniferous Sandstones of the Midland Valley of Scotland. Supplement: The Application of Computer Techniques to the Identification of sandstone Bodies.

CAMERON, I. B. and McADAM, A. D. 1978. Oil-Shales of the Lothians, Scotland: Present Resources and Former Workings. Rep. Inst. Geol. Sci., No. 78/28.

------- and STEPHENSON, D. 1985. British Regional Geology: The Midland Valley of Scotland. 3rd Ed. BGS

CARLSON, R. L. and CHRISTENSEN, N. I. 1979. Velocity Anisotropy in Seim-Indurated Calcareous Deep Sea Sediments. J. Geophys. Res. v 84, pp 205-211.

CARRUTHERS, R. G., CALDWELL, W., BAILEY, E. M. and CONACHER, H. R. J. 1927. The Oil-Shales of the Lothians. 3rd Ed. Mem. Geol. Surv.

CASTAGNA, J. P., BATZLE, M. L. and EASTWOOD, R. L. 1985. Relationships Between Compressional-Wave and Shear-Wave Velocities in Clastic Silicate Rocks. Geophysics v 50, pp 571-581.

CATER, J. M. L. 1987. Sedimentology of Part of the Lower Oil-Shale Group (Dinantian) Sequence at Granton, Edinburgh, Including the Granton "Shrimp Bed". Trans. Trans. R. Soc. Edin. (Earth Sci) v 78, pp 29-40.

CERVENY, V., LANGER, J. and PSENCIK, I. 1974. Computation of Geometric Spreading of Seismic Body Waves in Laterally Inhomogeneous Media with Curved Interfaces. Geophys. J. R. Astr. Soc. v 38, pp 9-20.

------- and PSENCIK, I. 1981. 2-D Seismic Package. Research Report, Institute of Geophysics, Charles University, Prague.

CHOLET, J. and RICHARD, H. 1954. A Test on Elastic Anisotropy Measurement at Berriane (North Sahara). Geophys. Prosp. v 2, pp 232-246.

CHRISTENSEN, N. J. 1982. Seismic Velocities. In: CARMICHAEL, R. S., (Ed), Handbook of Physical Properties of Rocks II, pp 2-227. CRC Press Inc.

COCKS, L. R. M. and TOGHILL, P. 1973. Biostratigraphy of the Silurian of Girvan. Quart. J. Geol. Soc. Lond. v 129, pp 209-243.

CONWAY, A., DENTITH, M. C., DOODY, J. J. and HALL, J. 1987. Preliminary Interpretation of Upper Crustal Structure Across the Midland Valley of Scotland from Two East-West Seismic Refraction Profiles. J. Geol. Soc. Lond. v 144, pp 865-870.

COTTON, W. R. 1968. A Geophysical Survey of the Campsie and and Kilpatrick Hills. Ph.D thesis (unpubl), University of Glasgow.

CRAMPIN, S. 1986. Anisotropy and Transverse Isotropy. Geophys. Pros. v 34, pp 94-99.

------- JACOB, A. W. B., MILLER, A. and NEILSON, A. 1970. The LOWNET Radio-Linked Seismometer Network in Scotland. Geophys. J. R. Astr. Soc. v 21, pp 207-216.

------- and RADOVICH, B. J. 1982. Interpretation of Synthetic Common-Depth-Point Gathers for a Single Anisotropic Layer. Geophysics v 47, pp 323-335.

CURRY, G. B., BLUCK, B. J., BURTON, C. J. INGHAM, J. K., SIVITER, D. J. and WILLIAMS, A. 1984. Age Evolution and Tectonic History of the Highland Border Complex, Scotland. Trans. R. Soc. Edin. Earth Sci. v 75, pp 113-133.

DAVIDSON, K. A. S., 1986. Seismological Studies of Upper

Crustal Structure of the Southern Midland Valley of Scotland. Ph.D thesis (unpubl), University of Glasgow.

-------- SOLA, M. A., POWELL, D. W., and HALL, J. 1984. Geophysical Model for the Midland Valley of Scotland. Trans. R. Soc. Edin. Earth Sci. v 75, pp 175-181.

DAVIS, E. E, and CLOWES, R. M. 1986. High Velocities and Seismic Anisotropy in Pleistocene Turbidites off Western Canada. Geophys. J. R. Astr. Soc. v 84, pp 381-399.

DAVISON, C. 1924. A History of British Earthquakes. Cambridge.

DE SOUZA, H. A. F. 1979. The Geochronology of Scottish Carboniferous Volcanism. Ph.D thesis, (unpubl), University of Edinburgh.

DEWEY, J. F. 1971. A Model for the Lower Palaeozoic Evolution of the Southern Margin of the Southern Caledonides of Scotland and Ireland. Scott. J. Geol. v 7, pp 219-240.

----- 1982. Plate Tectonics and the Evolution of the British Isles. J. Geol. Soc. Lond. v 139, pp 371-414.

DIEBOLD, J. B. and STOFFA, P. L. 1981. The Traveltime Equation, Tau-P Mapping, and Inversion of Common Midpoint Data. Geophysics v 46, pp 238-254.

DIX, C. H. 1955. Seismic Velocities from Surface Measurements. Geophysics v 16, pp 68-86.

DOBRIN, M. B. 1983. Introduction to Geophysical Prospecting. 3rd Ed. Mcgraw-Hill

DOMENICO, S. N. 1984. Rock Lithology and Porosity Determination from Shear and Compressional Wave Velocity. Geophysics v 49, pp 1188-1195.

DUNOYER DE SEGONZAC, Ph and LAHERRERE, J. 1959. Application of the Continuous Velocity Log to Anisotropy Measurements in Northern Sahara; Results and Consequences. Geophys. Prosp. v 7, pp 202-217.

FORSYTH, I. H. and CHISHOLM, J. I. 1977. The Geology of East Fife. Mem. Geol. Surv. G.B.

FRANCIS, E. H. 1956. The Economic Geology of the Stirling and Clackmannan Coalfield, Scotland: Area North of the River Forth. Coalfld Pap. Geol. Surv. No. 1.

------- 1968. Effect of Sedimentation on Volcanic Processes, Including Neck-Sill Relationships in the British Carboniferous. Rep. 23rd Int. Geol. Congr., Prague, v 2 pp 163-174.

------- 1982. Emplacement Mechanism of Late Carboniferous Tholeiite Sills in North Britain. J. Geol. Soc. Lond. v 139, pp 1-20.

------- 1983a. Carboniferous. In: CRAIG, G. Y. (Ed), Geology of Scotland, pp 253-296. Scottish Academic Press.

------- 1983b. Carboniferous-Permian Igneous Rocks. In: CRAIG, G. Y. (Ed), Geology of Scotland, pp 297-324. Scottish Academic Press.

------- FORSYTH, I. H., READ, W. A. and ARMSTRONG, M. 1970. The Geology of the Stirling District. Mem. Geol. Surv. G.B.

------- and WALKER, B. H. 1986. Emplacement of Alkali-Dolerite Sills Relative to Extrusive Volcanism and Sedimentary Basins in the Carboniferous of Fife, Scotland. Trans. R. Soc. Edin. (Earth Sciences) v 77, pp 309-323.

FRESHNEY, E. C. 1961. The Cementstone Group of the West Midland Valley of Scotland. Ph.D thesis, (unpubl), University of Glasgow.

GEIKE, A. 1900. The Geology of Central and Western Fife and Kinross. Mem. Geol. Surv. G.B.

GEORGE, T. N. 1960. The Stratigraphical Evolution of the Midland Valley. Trans. Geol. Soc. Glasg. v 24, pp 33-107.

GIBBS, A. D. 1984. Structural Interpretation with Emphasis on Extensional Tectonics, Part 2. J.A.P.E.C. Course Notes No. 28.

GRAHAM, A. M. and UPTON, B. G. J. 1978. Gneisses in Diatremes, Scottish Midland Valley: Petrology and and Tectonic Implications. J. Geol. Soc. Lond. v 135, pp 219-228.

GRANT, F. S. and WEST, G. F. 1965. Interpretation Theory in Applied Geophysics. McGraw-Hill.

GUNN, P. J. 1975. Interpretation of the Bathgate Magnetic Anomaly, Midland Valley, Scotland. Scott. J. Geol. v 11, pp 263-266.

HAGEDOORN, J. G. 1954. A Practical Example of an Anisotropic Velocity Layer. Geophys. Prosp. v 2, pp 52-60.

--------- 1959. The Plus-Minus Method of Interpreting Seismic Refraction Sections. Geophys. Prosp. v 7, pp 158-183.

HALDANE, D. 1927. The Ochil Fault and its Dolerite Intrusion. Mem. Geol. Surv. Summ. Prog. for 1926, pp 147-153.

HALL, D. H. and DAGLEY, P. 1970. Regional Magnetic Anomalies: an Analysis of the Smoothed Aeromagnetic Map of Great Britain and Northern Ireland. Rep. Inst. Geol. Sci. 70/10.

HALL, J. 1970. The Correlation of Seismic Velocities with Formations in the South-West of Scotland. Geophys. Prosp. v 18, pp 134-148.

---- 1971. A Preliminary Seismic Survey Adjacent to the Rashiehill Borehole near Slamannan, Stirlingshire. Scott. J. Geol. v 7, pp 170-174.

---- 1974. A Seismic Reflection Survey of the Clyde Plateau Lavas in north Ayrshire and Renfrewshire. Scott. J. Geol. v 9, pp 254-279.

---- 1984. Geophysical Constraints on Crustal Structure in the Dalradian Region of Scotland. J. Geol. Soc. Lond. v 142, pp 149-156.

---- and AL-HADDAD, F. M. 1976. Seismic Velocities in the Lewisian Metamorphic Complex, North-West Britain - 'In Situ' Measurements. Scott. J. Geol. v 12, pp 305-314.

---- and ALI, M. 1985. Shear Waves in a Seismic Survey of Lewisian Basement an Extra Control on Lithological Variation and Porosity. J. Geol. Soc. Lond. v 142, pp 677-688.

---- , BREWER, J. A., MATTHEWS, D. H. and WARNER, M. R. 1984. Crustal Structure Across the Caledonides from the WINCH Seismic Reflection Profile: Influences on the Evolution of the Midland Valley of Scotland. Trans. R. Soc. Edin. Earth Sci. v 75, 97-109.

---- , POWELL, D. W., WARNER, M. R., EL-ISA, Z. M. H., ADESANYA, O. and BLUCK, B. J. 1983. Seismological Evidence of Shallow Crystalline Basement in the Southern Uplands of Scotland. Nature v 305, pp 418-420.

---- and SIMMONS, G. 1979. Seismic Velocities of Lewisian Metamorphic Rocks at Pressures to 8 kilo-bars: Relationship to Crustal Layering in North Britain. Geophys. J. R. Astr. Soc. v 58, pp 337-347.

HARDING, T. P. 1974. Petroleum Traps Associated with Wrench Faults. Amer Assoc. Petrol. Geol. Bull. v 58, pp 1290-1304.

HATTON, L., WORTHINGTON, M. H. and MAKIN, J. 1986. Seismic Data Processing Theory and Practice. Blackwell Scientific Publications.

HAUGHTON, P. W. 1987. Complex Control of Vertical Cycles in Recycled and Mixed Source Lower Old Red Sandstone Conglomerates, Kincardineshire, Scotland. (In prep).

HAZELDENE, R. S. 1987. British Isles Carboniferous Sediments Viewed in an Atlantic rift Setting. In: KELLING, G. and BESLEY, B. M. (Eds), Sedimentation in a Syn-orogenic Basin Complex: the Upper Carboniferous of North-West Europe. (In press) Blackie.

HELBIG, K 1983. Elliptical Anisotropy - its Significance and Meaning. Geophysics v 48, pp 825-832.

----- 1984. Anisotropy and Dispersion in Periodically Layered Media. Geophysics v 49, pp 364-373.

HIPKIN, R. G. and HUSSAIN, A. 1983. Regional Gravity Anomalies, 1. Northern Britain. Rep. Inst. Geol. Sci. 82/10.

HOSSAIN, M. M. A. 1976. Analysis of the Major Gravity and Magnetic Anomalies Centred Around Bathgate, Central Scotland. M.Sc Thesis (unpubl), University of Glasgow.

HUBBERT, M. K 1948. A Line-Integral Method of Computing the Gravimetric Effects of Two-Dimensional Masses. Geophysics v 13, pp 215-225.

HUSSAIN, A. and HIPKIN, R. G. 1981. Regional Gravity Map of the British Isles, Northern Sheet. University of Edinburgh.

HUTTON, V. R. S., INGHAM, M. R. and MBIPOM, E. W. 1980. An Electrical Model of the Crust and Upper Mantle in Scotland. Nature v 287, pp 30-33.

HUTTON, D. H. W. 1987. Strike-Slip Terranes and a Model for the Evolution of the British and Irish Caledonides. Geol. Mag. v 124, pp 405-425.

INGHAM, M. R. and HUTTON, V. R. S. 1982a. Crustal and Upper Mantle Electrical Conductivity Structure in Southern Scotland. Geophys. J. R. Astr. Soc. v 69, pp 579-594.

----- 1982b. The Interpretation and Tectonic Implications of the Geoelectric Structure of Southern Scotland. Geophys. J. R. Astr. Soc. v 69, pp 595-606.

JONES, A. G. and HUTTON, V. R. S. 1979a. A Multi-station Magnetotelluric Study of Southern Scotland - I. Fieldwork, Data Analysis and Results. Geophys. J. R. Astr. Soc. v 56, pp 329-349.

----- 1979b. A Multi-station Magnetotelluric Study of Southern Scotland - II. Monte-Carlo Inversion of the Data and its Geophysical and Tectonic Implications. Geophys. J. R. Astr. Soc. v 56, pp 351-368.

KAMINSKI, W., BAMFORD, D., FABER, S., JACOB, B., NUNN, K., and PRODEHL, C. 1976. A Lithospheric Seismic Profile in Britain - II. Preliminary Report on the Recording of a Local Earthquake. J. Geophys. v 42, pp 103-110.

KEAREY, P. and BROOKS, M. 1984. An Introduction to Geophysical Exploration. Blackwell Scientific Publications.

KENNEDY, W. Q. 1943. The Oil-Shales of the Lothians-Structure-Area IV. Philpstoun. Geol. Surv. Wartime Pamphlet No. 27.

-------- 1944. Transcurrent Movement Exemplified by a Fault in the West Lothian Oil-Shale Field. Trans. Geol. Soc. Glasg. v 20, pp 287-290.

-------- 1958. The Tectonic Evolution of the Midland Valley of Scotland. Trans. Geol. Soc. Glasg. v 23, pp 106-133.

KENNETT, B. L. N. 1976. A Comparison of Travel-Time Inversion. Geophys. J. R. Astr. Soc. v 44, pp 517-536.

KLEMPERER, S. L. and MATTHEWS, D. H. 1987. Iapetus Suture Located Beneath the North Sea by BIRPS Deep Reflection Profiling. Geology v 15, pp 195-198.

KLEYN, A. H. 1956. On Seismic Wave Propagation in Anisotropic Media with Applications in the Betun Area, South Sumatra. Geophys. Prosp. v 9, pp 56-69.

KREY, Th. and HELBIG, K. 1956. A Theorem Concerning Anisotropy of Stratified Media and its Significance for Reflection Seismics. Geophys. Prosp. v 4, pp 294-302.

LAGIOS, E. and HIPKIN, R. G. 1979. The Tweeddale Granite - a Newly Discovered Batholith in the Southern Uplands. Nature v 280, pp 672-675.

LEEDER, M. R. 1976. Sedimentary Facies and the Origin of Basin Subsidence Along the Northern Margins of the Supposed Hercynian Ocean. Tectonophysics v 36, pp 167-179.

LEWIN, F. K. 1978. The Reflection, Refraction and Diffraction of Waves in Media with an Elliptical Velocity Dependence. Geophysics v 43, pp 528-537.

-------- 1979. Seismic Velocities in Transversely Isotropic Media. Geophysics v 44, pp 918-936.

-------- 1980. Seismic Velocities in Transversely Isotropic Media II. Geophysics v 45, pp 3-17.

LONGMAN, C. D., BLUCK, B. J. and van BREEMAN, O. 1979. Ordovician Conglomerates and the Evolution of the Midland Valley. Nature v 280, pp 578-581.

LOVELL, J. P. B. 1983. Permian and Triassic. In: CRAIG, G. Y. (Ed), Geology of Scotland. Scottish Academic Press.

LUDWIG, J. W., NAFE, J. E. and DRAKE, C. L. 1970. Seismic Refraction. In: MAXWELL, A. E (Ed), The Sea, v 4, pp 53-84. Wiley, New York.

MacBETH, C. D. and BURTON, P. W. 1985. Upper Crustal shear Velocity Models from Higher Mode Rayleigh Wave Dispersion in Scotland. Geophys. J. R. Astr. Soc. v 83, pp 519-540.

-------- -------- 1986. Propagation of 0.7-2.5 Hz Rayleigh Waves in Scotland. Geophys. J. R. Astr. Soc. v 84, pp 101-120.

McCOLLUM, B. and SNELL, F. A. 1932. Asymmetry of Sound Velo-

ical and Tectonic Implications. Geophys. J. R. Astr. Soc. v 56, pp 351-368.
KAMINSKI, W., BAMFORD, D., FABER, S., JACOB, B., NUNN, K., and PRODEHL, C. 1976. A Lithospheric Seismic Profile in Britain - II. Preliminary Report on the Recording of a Local Earthquake. J. Geophys. v 42, pp 103-110.
KEAREY, P. and BROOKS, M. 1984. An Introduction to Geophysical Exploration. Blackwell Scientific Publications.
KENNEDY, W. Q. 1943. The Oil-Shales of the Lothians-Structure-Area IV. Philpstoun. Geol. Surv. Wartime Pamphlet No. 27.
------- 1944. Transcurrent Movement Exemplified by a Fault in the West Lothian Oil-Shale Field. Trans. Geol. Soc. Glasg. v 20, pp 287-290.
------- 1958. The Tectonic Evolution of the Midland Valley of Scotland. Trans. Geol. Soc. Glasg. v 23, pp 106-133.
KENNETT, B. L. N. 1976. A Comparison of Travel-Time Inversion. Geophys. J. R. Astr. Soc. v 44, pp 517-536.
KLEMPERER, S. L. and MATTHEWS, D. H. 1987. Iapetus Suture Located Beneath the North Sea by BIRPS Deep Reflection Profiling. Geology v 15, pp 195-198.
KLEYN, A. H. 1956. On Seismic Wave Propagation in Anisotropic Media with Applications in the Betun Area, Southern Sumatra. Geophys. Prosp. v 9, pp 56-69.
KREY, Th. and HELBIG, K. 1956. A Theorem Concerning Anisotropy of Stratified Media and its Significance for Reflection Seismics. Geophys. Prosp. v 4, pp 294-302.
LAGIOS, E. and HIPKIN, R. G. 1979. The Tweedale Granite - a Newly Discovered Batholith in the Southern Uplands. Nature v 280, pp 672-675.
LEEDER, M. R. 1976. Sedimentary Facies and the Origin of Basin Subsidence Along the Northern Margins of the Supposed Hercynian Ocean. Tectonophysics v 36, pp 167-179.
LEVIN, F. K. 1978. The Reflection, Refraction and Diffraction of Waves in Media with an Elliptical Velo--city Dependence. Geophysics v 43, pp 528-537.
----- 1979. Seismic Velocities in Transversely Isotropic Media. Geophysics v 44, pp 918-936.
----- 1980. Seismic Velocities in Transversely Isotropic Media II. Geophysics v 45, pp 3-17.
LONGMAN, C. D., BLUCK, B. J. and van BREEMAN, O. 1979. Ordovician Conglomerates and the Evolution of the Midland Valley. Nature v 280, pp 578-581.
LOVELL, J. P. B. 1983. Permian and Triassic. In: CRAIG, G. Y. (Ed), Geology of Scotland. Scottish Academic Press.
LUDWIG, J. W., NAFE, J. E. and DRAKE, C. L., 1970. Seismic Refraction. In: MAXWELL, A. E (Ed), The Sea, v 4, pp 53-54. Wiley, New York.
MacBETH, C. D. and BURTON, P. W. 1985. Upper Crustal shear Velocity Models from Higher Mode Rayleigh Wave Dispersion in Scotland. Geophys. J. R. Astr. Soc. v 83, pp 519-540.
------- ------ 1986. Propagation of 0.7-2.5 Hz Rayleigh Waves in Scotland. Geophys. J. R. Astr. Soc. v 84, pp 101-120.
McCOLLUM, B. and SNELL, F. A. 1932. Asymmetry of Sound Velo-

city in Stratified Formations. In: Early Geophysical Papers, S.E.G., Tulsa.

MacDONALD, J. G. 1973. The Campsie and Lennoxtown district. In: BLUCK, B. J. (Ed), Excursion Guide to the Geology of the Glasgow District, pp 60-65. Geological Society of Glasgow.

MacGREGOR, A. G. 1944. Barytes in Central Scotland. Wartime Pamphlet Geol. Surv. No. 38.

McLEAN, A. C. 1961. Density Measurements of rocks in South-West Scotland. Trans. R. Soc. Edin. v 68, pp 103-111.

------- 1966. A Gravity Survey in Ayrshire and its Geological Interpretation. Trans. R. Soc. Edin. v 66, pp 239-265.

------- 1978. Evolution of Fault controlled Ensialic Basins in North-Western Britain. In: BOWES, D. R. and LEAKE, B. E. (Eds), Crustal Evolution of North-Western Britain and Adjacent Regions. Geol. J. Spec. Issue No. 10.

------- and DEEGAN, C. E. 1978. The Solid Geology of the Clyde Sheet. Rep. Inst. Geol. Sci. 78/9.

MELIA, P. J. and CARLSON, R. L. 1984. An Experimental Test of P-Wave Anisotropy in Stratified Media. Geophysics v 49, pp 374-378.

MITCHELL, A. H. G. and McKERROW, W. S. 1975. Analogous Evolution of Burma Orogen and the Scottish Caledonides. Bull. Geol. Soc. Amer. v 86, pp 305-315.

MITCHELL, G. H. and MYKURA, W. 1962. The Geology of the Neighbourhood of Edinburgh. 3rd Ed. Mem. Geol. Surv. G.B.

MYKURA, W. 1960. The Lower Old Red Sandstone Rocks of the Pentland Hills. Bull. Geol. Surv. G.B. 16, pp 131-155.

------ 1967. The Upper Carboniferous rocks of South-West Ayrshire. Bull. Geol. Surv. G.B. 26, pp 23-98.

------ 1983. Old Red Sandstone. In: CRAIG, G. Y. (Ed), Geology of Scotland, pp 205-251. Scottish Academic Press.

NAFE, J. E. and DRAKE, C. L. 1957. Variation with Depth in and Shallow and Deep Water Marine Sediments of Porosity, Density and the Velocities of Compressional and Shear Waves. Geophysics. v 22, pp 523-552.

O'CONNELL, R. J. and BUDIANSKY, B. 1974. Seismic Velocities in Dry and Saturated Cracked Solids. J. Geophys. Res. v 79, pp 5412-5426.

OLIVER, G. J. H., SMELLIE, J. L., THOMAS, L. J., CASEY, D. M., KEMP, A. E. S., EVANS, L. J., BALDWIN, J. R. and HEPWORTH, B. C. 1984. Early Palaeozoic Metamorphic History of the Midland Valley, Southern Uplands-Longford-Down Massif and the Lake District, British Isles. Trans. R. Soc. Edin. (Earth Sci.) v 75, pp 245-258.

PENN, I. E., SMITH, I. F. and HOLLOWAY, S. 1984. Interpretation of a Deep Seismic Reflection Profile in the Glasgow Area. Geothermal Resources Programme, British Geological Survey.

PETERSON, R. A. and DOBRIN, M. B. 1966. A Pictorial Digital Atlas, United Geophysical Corp.

PICKETT, G. R., 1963. Acoustic Character Logs and their Application in Formation Evaluation. J. Petr. Tech.

v 15, pp 659-667.
POSTMA, G. W. 1955. Wave Propagation in a Stratified Medium. Geophysics v 20, pp 780-806.
POWELL, D. W. 1970. Magnetised rocks within the Lewisian of Western Scotland and Under the Southern Uplands. Scott. J. Geol. v 6, p 353-369.
------ 1978. Gravity and Magnetic Anomalies Attributable to Basement Sources Under Northern Britain. In: BOWES, D. R. and LEAKE, B. E. (Eds), Crustal Evolution in North-Western Britain and Adjacent Regions. Geol. J. Spec. Issue, 10, pp 107-114.
QURESHI, I. R. 1970. A Gravity Survey of a Region of the Highland Boundary Fault Scotland. J. Geol. Soc. Lond. v 125, pp 481-502.
RADOVICH, B. J. and LEVIN, F. K. 1982. Instantaneous Velocities and Reflection Times for Transversely Isotropic Solids. Geophysics. v 47, pp 316-322.
RAMSAY, D. M. 1962. Deformation of Pebbles in Lower Old Red Sandstone Conglomerates Adjacent to the Highland Boundary Fault. Geol. Mag. v 101, pp 228-248.
READ, W. A. 1987a. Controls on Silesian Sedimentation in the Midland Valley of Scotland. In: KELLING, G. and BESLEY, B. M. (Eds), Sedimentation in a Synorogenic Basin Complex: the Upper Carboniferous of North-West Europe. Blackie (in press).
---- 1987b. The Interplay of Sedimentation, Volcanicity and Tectonics in the Passage Group (Arnsbergian, E2 to Westphalian A) in the Midland Valley of Scotland. (In press).
RICHEY, J. E. 1942. The Oil-Shales of the Lothians-Structure-Area I. West Calder. Geol. Surv. Wartime Pamphlet No. 27.
------ ANDERSON, E. M. and MacGREGOR, A. G. 1930. The Geology of North Ayrshire. Mem. Geol. Surv.
ROBINSON, E. A. and TREITAL, S. 1980. Geophysical Signal Analysis. Prentice-Hall.
ROLFE, W. I. D. 1961. The Geology of the Hagshaw Hills Silurian Inlier, Lanarkshire. Trans. Edin. Geol. Soc. v 18, pp 240-269.
RUSSELL, M. J. 1971. North-South Geofractures in Scotland and Ireland. Scott. J. Geol. v 8, pp 75-84.
SMITH, D. I. 1961. Patterns of Minor Faulting in the South Central Highlands of Scotland. Bull. Geol. Surv. G.B. 17, pp 145-152.
SOLA, M. A. 1985. The Seismic Structure Under the Central Midland Valley from Refraction Measurements. Ph.D thesis, (unpubl), University of Glasgow.
SYLVESTER, A. G. and SMITH, R. 1976. Tectonic Transpression and Basement Controlled Deformation in San Andreas Fault Zone, Salton Trough, California. Amer. Ass. Petrol. Geol. Bull. v 60, pp 2081-2102.
TALWANI, J., WORZEL, J. L. and LANDISMAN, M. 1959. Rapid Gravity Computations for Two-dimensional Bodies With Application to the Mendocino Fracture Zone. J. Geophys. Res. v 64, pp 49-59.
TANER, M. T. and KOEHLER F. 1969. Velocity Spectra - Digital Computer Derivation and Applications of Velocity Functions. Geophysics, v 34, pp 859-881.
TATHAM, R. H. 1982. Vp/Vs and Lithology. Geophysics v 47, pp

336-344.
TELFORD, W. M., GELDART, L. P., SHERIFF, R. E. and KEYS, D. A. 1976. Applied Geophysics. C.U.P.
THOMSON, M. E. 1978. I.G.S. Studies of the Geology of the Firth of Forth and its Approaches. Rep. Inst. Geol. Sci. No.77/17.
THIRLWALL, M. F. 1983. Discussions on Implications for Caledonian Plate Tectonic Models of Chemical Data from Volcanic Rocks of the British Old Red Sandstone. J. Geol. Soc. Lond. v 140, pp 315-318.
TOKSOV, M. N., CHENG, C. H. and TIMUR, A. 1976. Velocities of Seismic Waves in Porous Rocks. Geophysics v 41, pp 621-645.
TOSAYA, C. A. 1982. Acoustic Properties of Clay-Bearing Rocks. Ph.D thesis, (unpubl), Stanford University.
TULLOCH, W. and WALTON, H. S. 1958. The Midlothian Coalfield. Mem. Geol. Surv. G.B.
UHRIG, L. F. and VAN MELLE, F. A. 1955. Velocity Anisotropy in Stratified Media. Geophysics v 20, pp 774-779.
UPTON, B. G. J., ASPEN, P., GRAHAM, A. M. and CHAPMAN, N. A. 1976. Pre-Palaeozoic Basement of the Scottish Midland Valley. Nature v 260, pp 517-518.
----- ASPEN, P., and CHAPMAN, N. A. 1983. The Upper Mantle and Crust Beneath the British Isles: Evidence from Inclusion Suites in Volcanic Rocks. J. Geol. Soc. Lond. v 140, pp 105-122.
----- ASPEN, P. and HUNTER, R. H. 1984. Xenoliths and their Implications for the Deep Geology of the Midland Valley and Adjacent Regions. Trans. R. Soc. Edin. Earth Sci. v 75, pp 65-70.
VANDER STOEP, D. M. 1966. Velocity Anisotropy in Wells. Geophysics v 31, pp 900-916.
VERA, E. E. 1987. On the Connection Between the Herglotz-Wiechert-Bateman and Tau-Sum Inversions. Geophysics v 52, pp 568-570.
WALTON, E. K. 1983. Lower Palaeozoic - Stratigraphy. In: CRAIG, G. Y. (Ed), Geology of Scotland, pp 105-137. Scottish Academic Press.
WATERS, K. H. 1978. Reflection Seismology. Wiley.
WEATHERBY, B. B., BORN, W. T. and HARDING, R. L. 1934. Granite and Limestone Velocity Determinations in Arbuckle Mountains, Oklahoma. Bull. A.A.P.G. v 18, pp 106-118.
WHITE, J. E. 1965. Seismic Waves. McGraw-Hill.
WHYTE, M. A. 1981. The Upper Brigantian (Lower Carboniferous) of Central Strathclyde. Scott. J. Geol. v 17, pp 227-246.
WILLIAMS, A. 1962. The Barr and Lower Ardmillan Series (Caradoc) of the Girvan District, South-West Ayrshire. Mem. Geol. Soc. Lond. 3.
WILKENS, R., SIMMONS, G and CARUSO, L. 1984. The Ratio Vp/Vs as a Discriminant of Composition for Siliceous Limestones. Geophysics v 49, pp 1850-1860.
YARDLEY, B. W. D., VINE, F. J. and BALDWIN, C. T. 1982. The Plate Tectonic Setting of NW Britain and Ireland in Late Cambrian and Early Ordovician Time. J. Geol. Soc. Lond. v 139, pp 455-463.

APPENDIX 1. GLASGOW FM SEISMIC RECORDER SPECIFICATIONS

Detector	: Mark Products L15B 4.5 Hz geophones with 600 coil, or alternative.
Amplifier Gain	: adjustable 88-118 db in 6 db steps; second output at 18 db lower than first; clipped 10 V p-p (less for better linearity). Input resistance of 4.7 $k\Omega$ for 0.65 of critical damping of L15B geophones.
Modulator	: centre frequency is 2 KHz; frequency deviation for 10 V p-p input is +/- 100%; current output is 250 μA.
Recording	: saturation.
Demodulator	: produces 2 V output for maximum modulator input (10 V); 14 db loss reduces overall system gain to the range 56-104 db (including both gain outputs).
System Frequency Response	: see Figs.A1, A2 and A3; 3 db down points indicate bandwidth of 2.5-55 Hz.
Noise and Distortion	: system noise limits dynamic range to 46 db at maximum gain, increasing to 60 db with decrease in gain. Distortion is less than 1% at 70% of clipping level. Wow and flutter (record and playback) is less than 0.25%.
Power Requirements	: during recording, 115 mA at 18V.

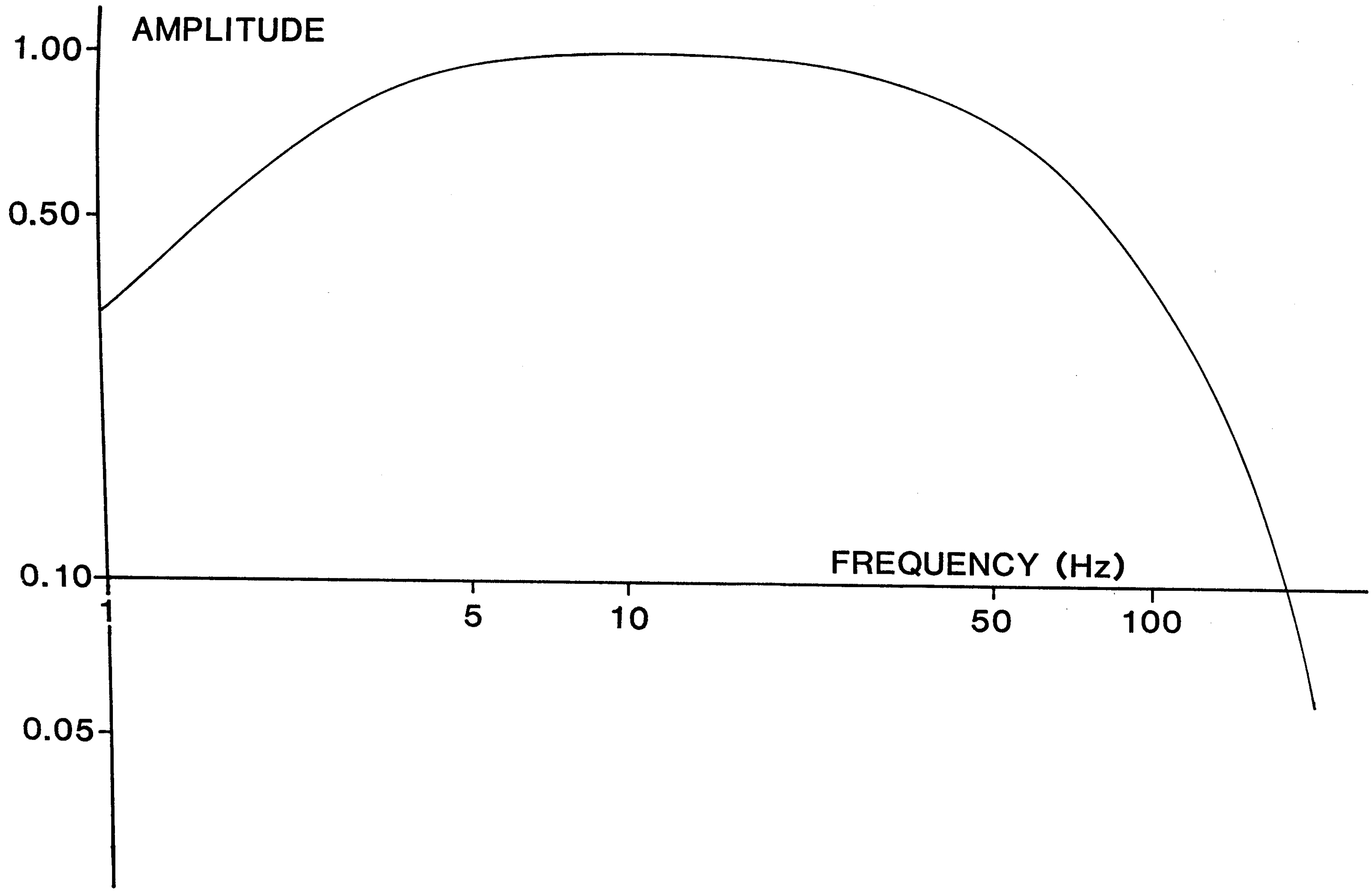

Fig.A.1 Amplitude response of the Glasgow seismic recorder.

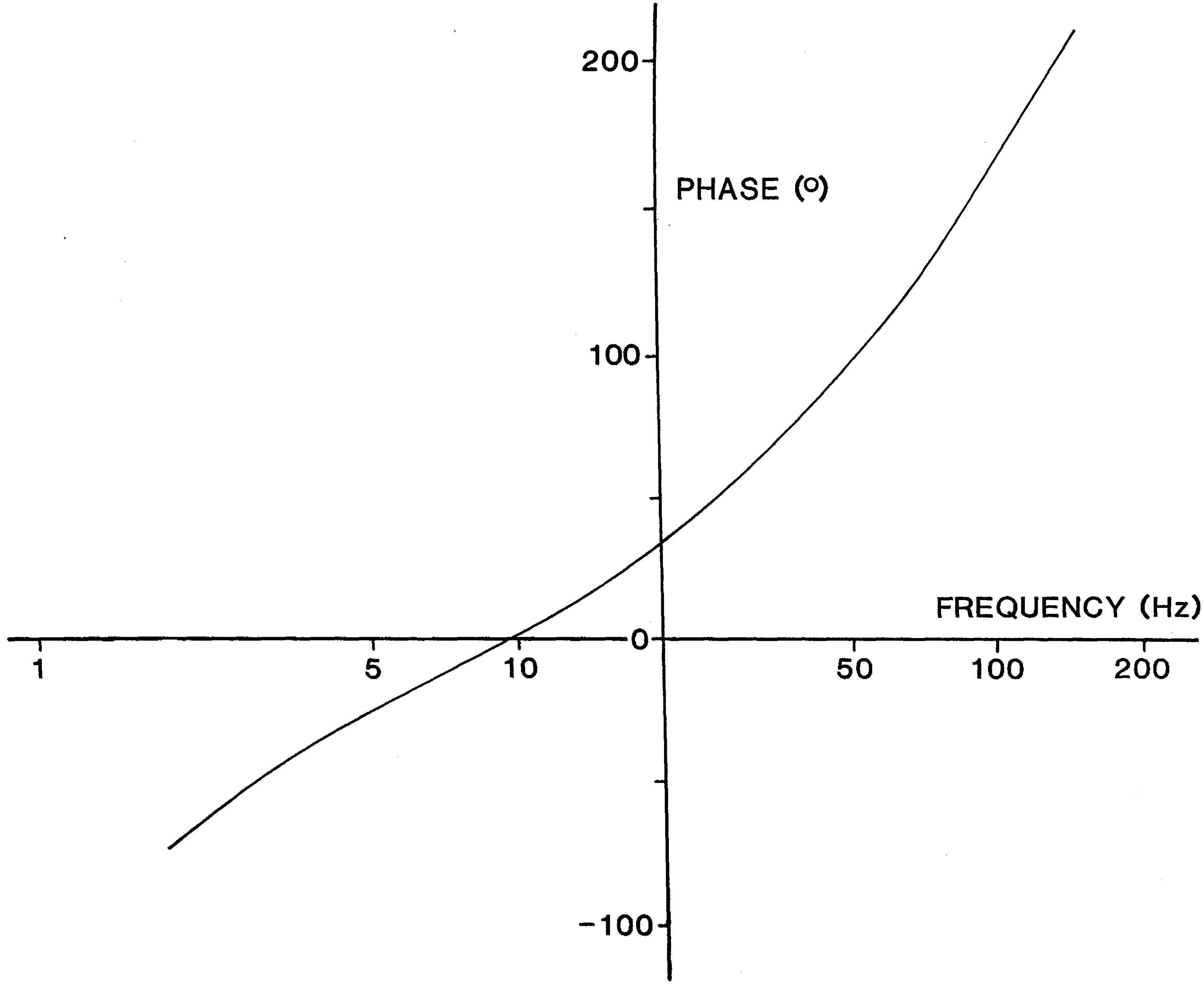

Fig.A.2 Phase response of the Glasgow seismic recorder.

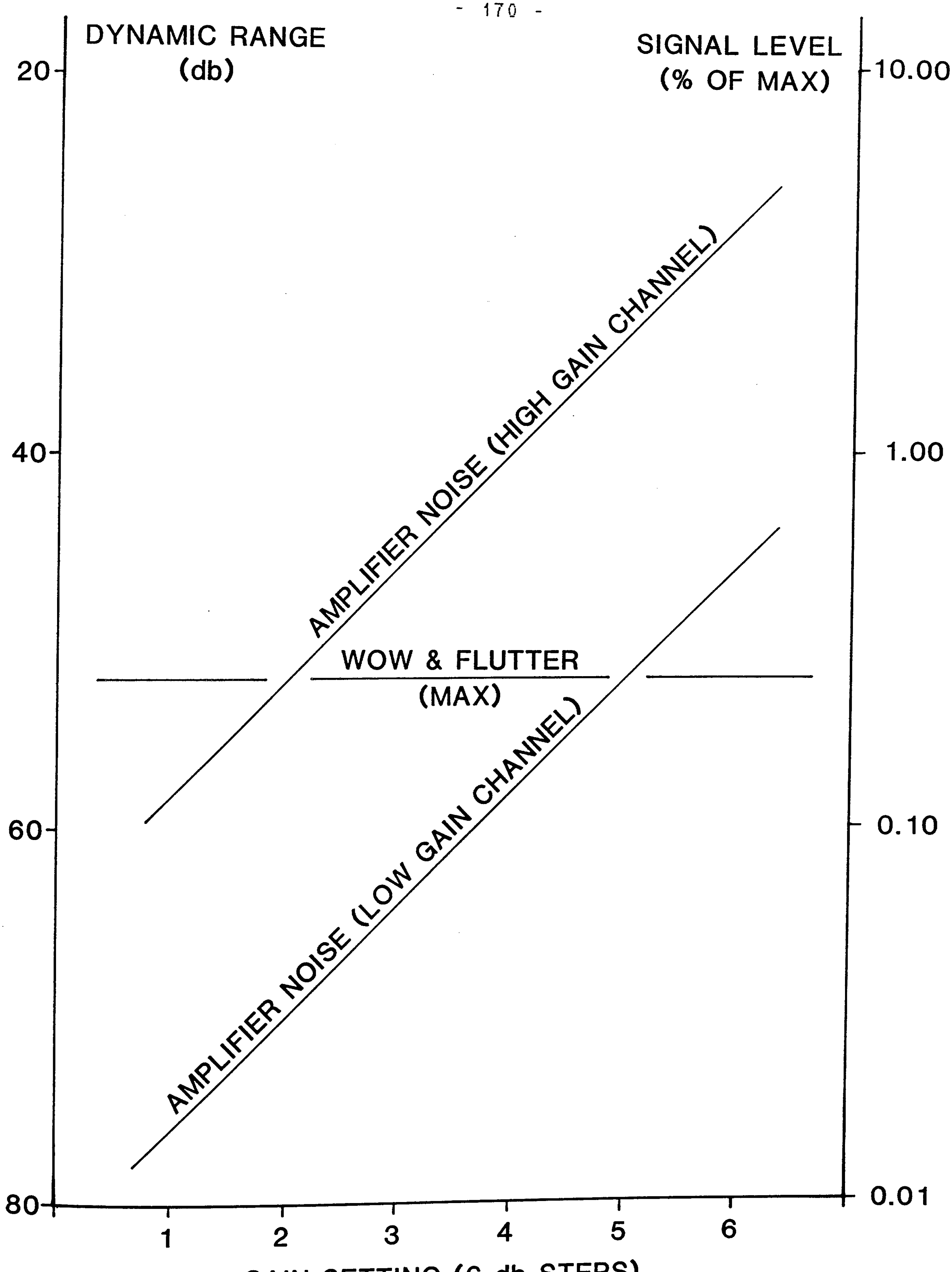

Fig.A.3 Dynamic range of the Glasgow seismic recorder.

APPENDIX 2. RECORDING SITE DETAILS

MAVIS I (SOUTH)

SITE NUMBER	SITE NAME	GRID REFERENCE km E	km N	ELEVATION km AOD	GEOPHONE COUPLING
S1	TREARNE QUARRY	236.92	653.08	0.120	ROCK
S2	THE MILL	238.62	654.55	0.120	ROCK
S3	DUNSMORE QUARRY	241.98	656.02	0.200	ROCK
S4	TOPHEAD QUARRY	244.53	656.77	0.225	ROCK
S5	FORSIDE	246.41	657.75	0.200	ROCK
S6	GATESHEAD WORKS	248.75	658.58	0.075	ROCK
S7	COWGLEN GOLF CLUB	254.27	660.48	0.050	ROCK
S8	POLLOCK GOLF CLUB	255.15	661.45	0.020	ROCK
S9	RIVER CLIFF	257.45	661.10	0.050	ROCK
S10	NECROPOLIS	260.48	665.48	0.050	ROCK
S11	PRISON	263.35	665.82	0.060	ROCK
S12	BLAIR TUMNOCK PARK	266.67	666.39	0.090	ROCK
S13	LOCKWOOD FARM	269.47	666.71	0.090	ROCK
S14	DRUMCAVEL FARM	270.53	669.21	0.080	ROCK
S15	GREENFOOT	273.16	669.01	0.110	ROCK
S16	CARTMILL	274.58	669.49	0.120	ROCK
S17	DOUGLAS GLEN	275.57	670.21	0.140	ROCK
S18	DRUMGRAY	277.43	670.24	0.170	ROCK
S19	DR WHO LANDSCAPE	278.22	669.08	0.180	ROCK
S19A	GREENCAIRS RAILWAY	278.21	670.26	0.180	ROCK
S20	FAIRNEY KNOWE	280.88	670.46	0.195	DRIFT
S21	BLACKHILL	281.42	672.28	0.160	ROCK
S22	DON'T FALL IN	283.54	672.72	0.170	ROCK
S23	SOUTHFIELD WOOD	284.66	672.32	0.190	DRIFT
S24	BALQUHATSTONE HOUSE	286.06	672.67	0.175	DRIFT
S25	GREYRIGG	287.00	672.14	0.180	ROCK
S26	NEUCKS	288.66	673.06	0.150	DRIFT
S27	WINDY YETT	290.01	673.14	0.145	DRIFT
S29	EASTER DRUMBROILER	292.31	673.87	0.170	DRIFT
S30	CANDIE HOUSE	293.53	674.11	0.175	DRIFT
S31	NETHERTON FARM	294.53	674.38	0.130	DRIFT
S32	CARRIBBER MILL	295.65	674.38	0.080	ROCK
S33	BOWDEN HILL	296.69	674.53	0.125	ROCK
S34	EASTER CARRIBBER	297.25	675.15	0.100	ROCK
S35	BELSYDE	297.93	675.45	0.120	ROCK
S36	LINLITHGOW GOLF CLUB	298.79	675.98	0.085	ROCK
S37	PRESTON HOUSE	300.00	675.94	0.110	ROCK
S38	PARKLEY CRAIGS	301.11	675.93	0.110	ROCK
S39	PARKLEY PLACE	302.87	675.99	0.110	ROCK
S40	BRIDGEND	304.14	675.94	0.080	ROCK
S41	FAIRNIEHILL WOOD	304.87	676.32	0.080	ROCK
S42	FAWNSPARK FARM	306.65	676.60	0.080	ROCK
S43	CRAIGTON QUARRY	307.67	676.88	0.080	ROCK
S44	HOPETOUN HOUSE	309.41	678.71	0.050	ROCK
S46	INCHGARVIE	311.28	678.54	0.045	ROCK
S47	PORT EDGAR	311.83	678.60	0.030	ROCK
S48	DALMENY CUTTING	314.11	677.68	0.050	ROCK
S49	LONG CRAIG GATE	314.93	678.12	0.070	ROCK
S50	DALMENY PARK	316.36	678.86	0.030	ROCK

MAVIS I (NORTH)

SITE NUMBER	SITE NAME	GRID REFERENCE km E	km N	ELEVATION km AOD	GEOPHONE COUPLING
N1	BALLIKINRAIN CURLING POND	255.94	687.11	0.120	ROCK
N2	BALLIKINRAIN CASTLE	256.98	687.43	0.095	ROCK
N3	VIOLETS WOOD	257.98	687.03	0.125	ROCK
N4	HEAD OF BAGLASS	259.37	687.39	0.105	ROCK
N5	FINTRY WOOD QUARRY	261.39	686.49	0.125	ROCK
N6	CRAIGTON MAUSOLEUM	263.23	686.60	0.150	ROCK
N7	FINTRY CASTLE	263.97	686.40	0.180	ROCK
N8	GOWK STONES	266.17	686.37	0.215	ROCK
N9	CARRON VALLEY FOREST	267.85	286.29	0.335	ROCK
N10	BOULDERS GALORE	269.23	687.09	0.320	ROCK
N11	CRINGATE MUIR	271.35	687.32	0.305	ROCK
N12	WIRELESS STATION	272.40	687.98	0.345	ROCK
N13	GROUSE BUTTS	273.51	688.09	0.275	ROCK
N14	TODHOLES	275.17	688.28	0.195	ROCK
N15	CRAIGS WOOD	275.82	687.95	0.190	ROCK
N16	SAUCHIE HOME FARM	277.12	688.02	0.155	ROCK
N17	CRAIGEND QUARRY	278.68	687.53	0.085	ROCK
N18	CROFTHILL	280.97	687.80	0.075	DRIFT
N19	SAUCHENFORD QUARRY	282.29	688.39	0.045	ROCK
N20	PLEAN	282.73	688.86	0.045	ROCK
N21	HILLHEAD	285.44	688.98	0.020	ROCK
N22	CASTLETON FARM CRAIGS	285.40	688.30	0.040	ROCK
N23	CARNOCH HOUSE CHAPEL	286.55	688.40	0.015	ROCK
N24	DUNMORE QUARRY	288.03	688.69	0.015	ROCK
N25	ST.ANDREWS CHAPEL	289.03	688.89	0.015	ROCK
N26	TULLIALLAN CASTLE	292.61	688.93	0.010	ROCK
N27	OVERTON LODGE	293.84	689.97	0.050	ROCK
N28	GARTARRY WOOD	294.24	690.54	0.080	ROCK
N29	WESTER CLASHIES	295.13	690.62	0.085	ROCK
N30	BURNBRAE	296.05	691.49	0.045	ROCK
N31	BATHMOOR PLANTATION	296.88	691.19	0.060	ROCK
N32	HALDANE	298.13	691.21	0.110	DRIFT
N33	CATTLE MOSS	299.12	691.75	0.085	ROCK
N34	STAND ALANE	300.43	692.18	0.090	ROCK
N35	KINNEDDAR QUARRY	302.18	692.06	0.115	ROCK
N36	KILLERNIE CASTLE	303.24	692.52	0.180	ROCK
N37	STEELEND QUARRY	305.00	692.56	0.215	ROCK
N38	DUNNYGASK	305.95	692.77	0.215	ROCK
N39	ROSCOBIE	307.98	693.41	0.220	ROCK
N41	CRAIGENCATS CRAIGS	310.17	695.28	0.270	ROCK
N42	BLAIRADAM	312.72	695.17	0.150	ROCK
N43	LENCHARS WOOD	314.96	696.58	0.145	ROCK
N44	BENARTY WOOD	316.57	697.49	0.230	ROCK
N45	BALLINGRY HOUSE	317.20	698.07	0.170	ROCK
N46	KIRKNESS	318.64	698.45	0.120	ROCK
N48	BOWHOUSE	323.50	697.63	0.100	DRIFT
N48A	CLUNY MAINS	324.31	696.72	0.075	DRIFT
N49	GRANTS MUIR FARM	327.70	695.59	0.085	DRIFT
N50	WEST WEMYESS	331.65	694.53	0.015	ROCK

MAVIS II (CROSS)

SITE NUMBER	SITE NAME	GRID REFERENCE km E	km N	ELEVATION km AOD	GEOPHONE COUPLING
X1	CASTLE HILL	297.54	712.65	0.125	ROCK
X2	BEN EFFREY	297.68	711.64	0.210	ROCK
X3	UPPER CLOAN QUARRY	296.82	710.67	0.230	ROCK
X4	NEAR LAKE	297.60	709.94	0.220	ROCK
X5	HAYDARN BURN	297.37	708.67	0.375	ROCK
X6	STEELE'S KNOWE	296.93	707.52	0.470	ROCK
X7	FAWNCLEUCH BURN	296.73	706.39	0.425	ROCK
X8	HILLKITTY	296.42	705.72	0.350	ROCK
X9	GLENSHERUP RESERVOIR	295.31	704.76	0.280	ROCK
X10	COWCLEUGH BURN	296.46	703.88	0.325	ROCK
X11	ROUGHCLEUGH BURN	295.28	702.78	0.375	ROCK
X12	HILLSIDE	296.49	701.42	0.510	ROCK
X13	SADDLE HILL	295.72	700.37	0.440	ROCK
X14	GLOOM HILL QUARRY	296.30	699.05	0.165	ROCK
X15	KELLYBANK	296.88	698.28	0.060	DRIFT
X16	RIVER DEVON	296.48	696.99	0.025	DRIFT
X17	BACK WOOD	296.56	695.33	0.070	DRIFT
X18	ALLACKIE	296.17	694.43	0.075	DRIFT
X19	GARTGREENIE	295.93	693.39	0.075	DRIFT
X20	HAZLEYSHAW	295.82	692.40	0.075	ROCK
X21	HANTSHAW FARM	296.05	691.49	0.045	ROCK
X22	TRACK	295.13	690.63	0.085	ROCK
X23	FORESTRY TRACK	296.14	689.34	0.070	ROCK
X24	STRUCTURE IN FORESTRY	296.19	688.68	0.070	BUILDING
X25	CLEARING IN FORESTRY	296.31	687.83	0.060	DRIFT
X26	QUARRY	295.92	687.01	0.060	ROCK
X27	MOSS WOOD	296.42	686.53	0.040	DRIFT
X28	QUARRY BY ROAD	296.61	685.68	0.010	ROCK
X28A	LONGANNET QUARRY	296.49	685.80	0.010	ROCK
X29	FIRTH OF FORTH	295.30	683.28	0.000	DRIFT
X30	INVERAVON	295.63	679.91	0.030	DRIFT
X31	AVONDALE HOUSE	295.58	679.34	0.035	DRIFT
X32	LODGE	295.25	678.85	0.055	DRIFT
X33	GILSTON	294.46	678.12	0.050	DRIFT
X34	BATTOCK	294.17	677.71	0.085	DRIFT
X35	CRAIGS FARM	293.78	677.28	0.105	DRIFT
X36	MANUEL BURN	292.98	676.50	0.130	DRIFT
X37	CRAIGEND WORKS	292.76	675.60	0.160	DRIFT
X38	EASTER BLACKRIG	291.82	675.11	0.180	DRIFT
X39	WINDY RIG	291.65	674.65	0.175	DRIFT
X40	OLD COLLIERY	291.43	674.08	0.180	DRIFT
X41	WHINNEY KNOWES	290.89	673.01	0.140	DRIFT
X42	CRAIGBANK QUARRY	290.84	672.22	0.150	ROCK
X43	LINHOUSE QUARRY	290.67	671.25	0.180	ROCK
X44	NORTH RHODENS PLANTATION	290.38	670.24	0.185	ROCK
X45	DRUMBOWIE	290.74	669.88	0.205	ROCK
X46	TAWNYCRAW HILL	290.27	669.17	0.215	ROCK
X47	EASTCRAIGS HILL	290.28	668.30	0.235	ROCK
X48	CROWNS HILL QUARRY	290.18	667.70	0.215	ROCK
X49	WESTCRAIGS QUARRY	289.88	666.66	0.185	ROCK
X50	BLAIRHILL QUARRY	288.78	665.89	0.200	ROCK

ABERUTHVEN AND DOLLAR SHOTS RECEIVED AT STATION 28
LONGANNET, AVONBRIDGE AND BLAIRHILL SHOTS RECEIVED AT STATION 28A.

MAVIS II (CAIRNYHILL QUARRY)

SITE NUMBER	SITE NAME	GRID REFERENCE km E	km N	ELEVATION km AOD	GEOPHONE COUPLING
CS1	ROADSIDE	285.70	665.81	0.235	ROCK
CS2	FORESTBURN RESERVOIR	286.21	664.80	0.235	ROCK
CS3	TREESBANK	288.04	664.30	0.225	ROCK
CS4	BLAIRMAINS	286.81	664.25	0.235	DRIFT
CS5	WESTER HASSOCKRIGG QUARRY	287.09	663.22	0.250	ROCK
CS6	RIVER ALMOND	287.87	662.58	0.240	DRIFT
CS7	BROWNHILL FARM	288.22	662.53	0.235	DRIFT
CS8	STARRYSHAW FARM	289.62	660.88	0.235	DRIFT
CS9	SOUTHFIELD COLLIERY	289.97	659.93	0.250	DRIFT
CS10	MULDRON LODGE	291.50	657.98	0.235	BUILDING
CS11	WEST CLEUGH QUARRY	291.55	657.62	0.245	ROCK
CS12	BRIDGE	291.63	657.41	0.240	DRIFT
CS13	OLD IRON MINE	292.02	656.76	0.280	DRIFT
CS14	SERGEANTS LAW	292.29	656.34	0.305	DRIFT
CN1	SNIPE QUARRY	285.16	667.63	0.185	ROCK
CN2	LOCHEND	285.39	670.29	0.220	DRIFT
CN3	SALTERHILL FARM	285.68	671.85	0.185	DRIFT
CN4	BALQUHATSTONE HOUSE	285.70	672.64	0.165	DRIFT
CN5	RIVER AVON	285.50	673.64	0.150	DRIFT
CN6	ROAD SIDE	285.38	674.78	0.180	DRIFT
CN7	NEW CRAIG COTTAGES	285.01	675.66	0.185	DRIFT
CE1	BEDLORMIE	287.44	667.29	0.205	DRIFT
CE2	BARN WOOD	288.25	667.45	0.215	DRIFT
CE3	CROWNS HILL	290.08	667.99	0.225	ROCK

CE STATION DATA WAS NOT USED

MAVIS III (INNES)

SITE NUMBER	SITE NAME	GRID REFERENCE km E	km N	ELEVATION km AOD	GEOPHONE COUPLING
I1	CALAIS	312.40	686.40	0.085	DRIFT
I2	ANNFIELD	312.86	685.38	0.085	DRIFT
I3	SUNNYBANK	312.96	684.34	0.025	DRIFT
I4	PRESTON HILL QUARRY	313.69	682.40	0.010	ROCK
I5	GARTHILL HOUSE	313.09	681.30	0.045	ROCK
I6	QUARRY	313.32	680.68	0.040	ROCK
I7	FORTH BRIDGE	313.80	678.42	0.000	ROCK
I8	NEWBIGGING	312.25	677.16	0.055	DRIFT
I9	ROAD SIDE	313.28	676.22	0.055	DRIFT
I10	CRAIGBRAE QUARRY	313.72	675.88	0.060	ROCK
I11	ALMONDHILL	312.90	675.16	0.055	DRIFT
I12	FOXHALL	313.06	674.00	0.030	DRIFT
I13	HILLYARDS CASTLE	312.90	673.56	0.030	DRIFT
I14	QUARRY	312.84	672.23	0.045	ROCK
I15	HILLWOOD	312.90	671.60	0.060	ROCK
I16	NORTON QUARRY	313.36	671.56	0.090	ROCK
I17	RATHO HALL	313.14	671.10	0.100	ROCK
I18	OLD QUARRY	313.02	670.36	0.120	DRIFT
I19	WITCHES STONE	312.97	669.76	0.135	ROCK
I20	HATTON HOUSE	312.80	669.02	0.120	ROCK
I21	SPITTALTON WOOD	312.72	668.08	0.105	DRIFT
I22	WATERLOO TOWER	312.72	667.80	0.120	DRIFT
I23	GREEN BURN	313.04	667.34	0.140	DRIFT
I24	ROAD SIDE	313.05	666.97	0.170	DRIFT
I25	QUARRY	313.35	666.22	0.190	ROCK
I26	KAIMES QUARRY	312.94	666.36	0.205	ROCK
I27	HAUGH HEAD	313.11	665.22	0.190	DRIFT
I28	TEMPLE HOUSE	313.05	664.17	0.225	DRIFT
I29	ROAD SIDE	313.43	663.35	0.250	DRIFT
I30	ROAD SIDE	313.49	662.84	0.260	DRIFT
I31	LISTONSHIELS	313.58	662.03	0.280	DRIFT
I32	MANSOON HILL QUARRY	313.10	661.28	0.360	ROCK

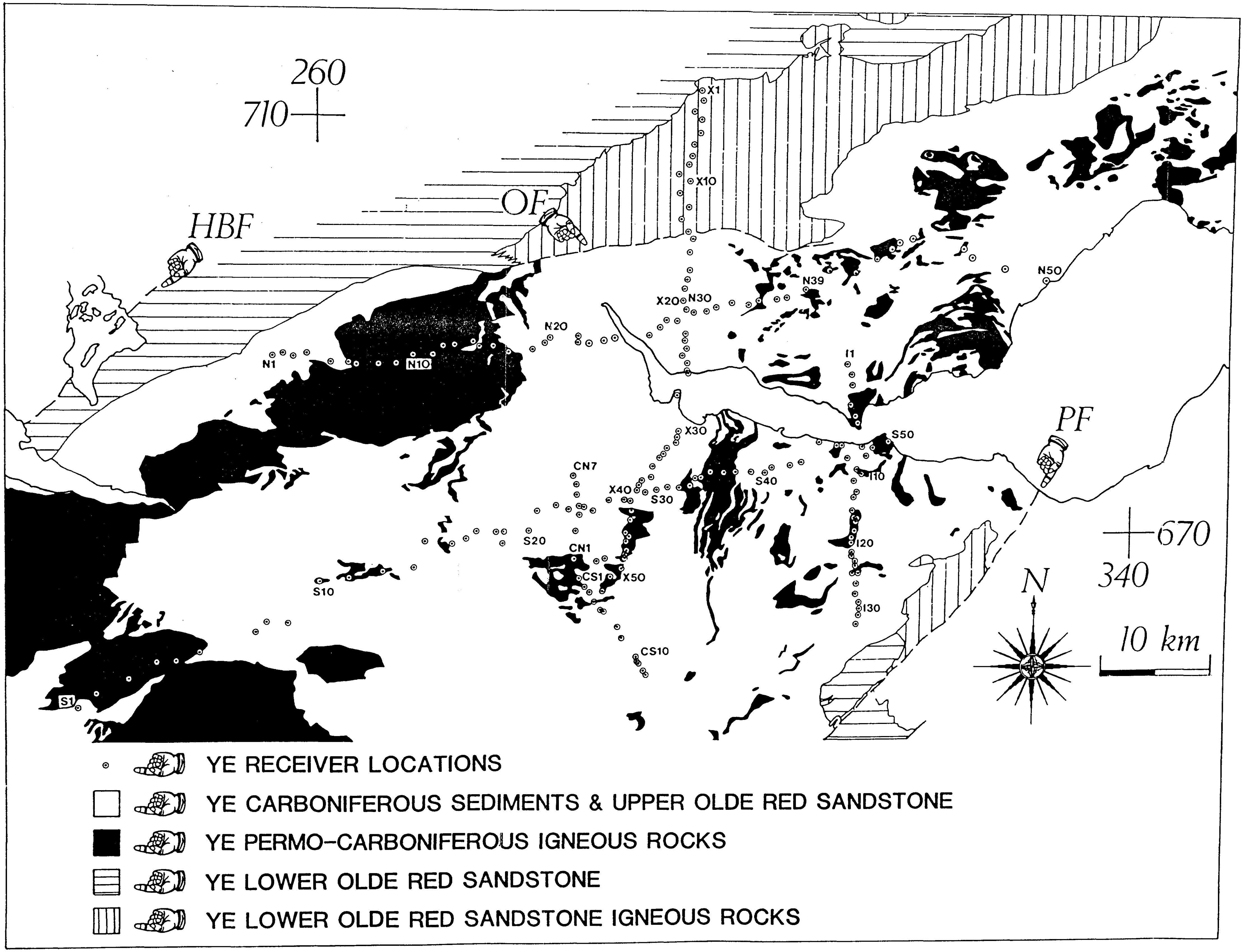

Fig.A.4 Distribution of Receiver Locations Listed in Appendix 2. HBF - Highland Boundary Fault, OF - Ochil Fault, PF - Pentland Fault.

APPENDIX 3a. OBSERVED AND CALCULATED TRAVEL TIMES: P-WAVE

Ray codes refer to Table 5.1. Reduction velocity = 6.0 km/s
A standard error in travel time of +/- 0.03 s was assumed
for data from Sola (1985).

MAVIS I: TREARNE (P WAVE)

SHOT POSITION = 0.410 KM

OBSERVED TRAVEL TIMES

RANGE (KM)	TRAVEL TIME (S)	ERROR (+) (S)	ERROR (-) (S)	RED TIME (S)
0.410	0.060	0.030	0.030	-0.008
1.850	0.490	0.030	0.030	0.182
5.450	1.130	0.030	0.030	0.222
8.050	1.800	0.050	0.050	0.458
10.170	2.310	0.030	0.030	0.615
18.460	3.920	0.030	0.030	0.843
19.650	4.140	0.030	0.030	0.865
26.220	5.300	0.050	0.030	0.930
28.930	5.870	0.050	0.050	1.048
32.190	6.380	0.030	0.030	1.015
34.880	6.780	0.030	0.030	0.967
36.870	7.250	0.030	0.030	1.105
39.180	7.480	0.030	0.030	0.950
40.670	7.740	0.030	0.030	0.962
41.870	7.910	0.030	0.030	0.932
43.590	8.140	0.030	0.030	0.875
43.890	8.270	0.030	0.030	0.955
44.320	8.360	0.030	0.030	0.973
46.870	8.760	0.030	0.030	0.948
48.060	9.010	0.050	0.050	1.000
50.180	9.330	0.030	0.050	0.967
51.070	9.470	0.030	0.030	0.958
52.500	9.660	0.050	0.050	0.910
53.180	9.790	0.030	0.030	0.927
55.060	10.110	0.050	0.050	0.933
56.350	10.280	0.050	0.030	0.888
62.070	11.240	0.050	0.050	0.895
63.100	11.350	0.050	0.050	0.833
64.560	11.670	0.050	0.050	0.910
64.560	11.490	0.050	0.050	0.730
66.690	11.990	0.050	0.050	0.875
67.730	12.070	0.050	0.050	0.782
69.410	12.310	0.050	0.050	0.742
70.600	12.550	0.050	0.050	0.783
73.190	12.940	0.050	0.050	0.742
74.240	13.090	0.050	0.050	0.717
78.200	13.720	0.050	0.050	0.687
78.740	13.790	0.050	0.050	0.667
83.120	14.490	0.050	0.050	0.637
34.880	6.880	0.050	0.050	1.067
39.180	7.600	0.050	0.050	1.070
41.870	8.020	0.050	0.050	1.042
43.890	8.410	0.050	0.050	1.095
44.320	8.500	0.050	0.050	1.113
46.870	8.820	0.050	0.050	1.008
62.070	11.140	0.050	0.050	0.795

CALCULATED TRAVEL TIMES

RAY CODE = A1

RANGE (KM)	CALC TIME (S)
0.000	0.000
1.850	0.498
0.410	0.030

RAY CODE = A3

RANGE (KM)	CALC TIME (S)
28.930	5.911
26.220	5.395
19.650	4.137
18.460	3.905
10.170	2.279
8.050	1.791
5.450	1.263
1.850	0.521

RAY CODE = A5

RANGE (KM)	CALC TIME (S)
64.560	11.660
63.100	11.415
62.070	11.236
56.350	10.292
55.060	10.082
53.180	9.791
52.500	9.683
51.070	9.453
50.180	9.302
48.060	8.952
46.870	8.768
44.320	8.354
43.890	8.280
43.590	8.231
41.870	7.953
40.670	7.757
39.180	7.514
36.870	7.134
34.880	6.811
32.190	6.364
28.930	5.816
26.220	5.362
19.650	4.237

RAY CODE = A7

RANGE (KM)	CALC TIME (S)
83.120	14.485
78.740	13.791
78.200	13.706
74.240	13.094
73.190	12.927
70.600	12.523
69.410	12.340
67.730	12.074
66.690	11.911
64.560	11.577
63.100	11.335
62.070	11.167
56.350	10.264
55.060	10.056

53,180	9,784
52,500	9,680
51,070	9,459
50,180	9,316
48,060	8,979
46,870	8,805
44,320	8,406
43,890	8,340
43,590	8,292
41,870	8,024
40,670	7,836
39,180	7,604
36,870	7,246
34,880	6,933

MAVIS I: DRUMGRAY (P WAVE)

SHOT POSITION = 43,760 KM

OBSERVED TRAVEL TIMES

RANGE (KM)	TRAVEL TIME (S)	ERROR (+) (S)	ERROR (-) (S)	RED TIME (S)
43,750	8,230	0,030	0,030	0,938
41,620	7,980	0,030	0,050	1,043
35,310	6,940	0,030	0,030	1,055
33,200	6,630	0,030	0,080	1,097
30,720	6,220	0,030	0,030	1,100
24,890	5,270	0,030	0,030	1,122
23,710	5,090	0,030	0,040	1,138
21,730	4,800	0,030	0,060	1,178
14,530	3,470	0,030	0,070	1,048
8,460	2,260	0,030	0,050	0,850
6,780	1,830	0,030	0,030	0,700
4,220	1,180	0,030	0,030	0,477
2,730	0,750	0,030	0,030	0,295
1,700	0,400	0,030	0,030	0,117
1,340	0,450	0,030	0,030	0,227
0,980	0,300	0,030	0,030	0,137
3,650	1,040	0,030	0,030	0,432
4,730	1,240	0,030	0,030	0,452
6,840	1,690	0,050	0,030	0,550
7,750	1,920	0,030	0,050	0,628
9,190	2,340	0,030	0,050	0,808
9,970	2,500	0,030	0,030	0,838
11,800	2,820	0,030	0,030	0,853
13,130	3,050	0,030	0,050	0,862
15,530	3,520	0,050	0,030	0,932
19,950	4,350	0,100	0,100	1,025
20,640	4,420	0,030	0,030	0,980
21,370	4,610	0,050	0,050	1,048
23,500	4,960	0,050	0,050	1,043
26,300	5,460	0,030	0,030	1,077
27,520	5,600	0,030	0,030	1,013
30,120	6,010	0,030	0,030	0,990
33,300	6,720	0,030	0,030	1,170
43,750	8,410	0,050	0,050	1,118
35,310	7,110	0,050	0,050	1,225

24.890	5.780	0.050	0.050	1.632
14.530	3.570	0.050	0.050	1.148
6.840	1.910	0.050	0.050	0.770
7.750	2.060	0.100	0.050	0.768
15.530	3.600	0.050	0.050	1.012

CALCULATED TRAVEL TIMES

RAY CODE = A1

RANGE (KM)	CALC TIME (S)
0.000	0.000
0.980	0.286
1.340	0.393
3.650	1.031
4.730	1.292
6.840	1.804
7.750	2.019
9.190	2.357
9.970	2.526
11.800	2.912
24.890	5.856
23.710	5.601
21.730	5.168
14.530	3.598
8.460	2.237
6.780	1.819
4.220	1.167
2.730	0.770
1.700	0.496

RAY CODE = A3

RANGE (KM)	CALC TIME (S)
26.300	5.509
23.500	4.983
21.370	4.585
20.640	4.438
19.950	4.319
15.530	3.504
13.130	3.037
11.800	2.789
9.970	2.470
9.190	2.328
7.750	2.061
6.840	1.888
24.890	5.314
23.710	5.095
21.730	4.744
14.530	3.414
8.460	2.274
6.780	1.952

RAY CODE = A5

RANGE (KM)	CALC TIME (S)
33.300	6.580
30.120	6.060

27.520	5.629
26.300	5.435
23.500	4.968
21.370	4.610
20.640	4.479
19.950	4.371
15.530	3.649
43.750	8.266
41.620	7.899
35.310	6.934
33.200	6.653
30.720	6.218
24.890	5.259
23.710	5.059
21.730	4.740
14.530	3.552

RAY CODE = A6

RANGE (KM)	CALC TIME (S)
33.200	6.770
35.310	7.051
41.620	7.987
43.750	8.343

MAVIS I: AVONBRIDGE (P WAVE)

SHOT POSITION = 58.250 KM

OBSERVED TRAVEL TIMES

RANGE (KM)	TRAVEL TIME (S)	ERROR (+) (S)	ERROR (-) (S)	RED TIME (S)
49.830	9.350	0.050	0.050	1.045
47.720	8.950	0.050	0.050	0.997
39.400	7.600	0.050	0.050	1.033
38.250	7.500	0.050	0.050	1.125
31.970	6.440	0.030	0.030	1.112
29.090	5.950	0.050	0.050	1.102
25.770	5.360	0.030	0.030	1.065
23.000	4.870	0.030	0.030	1.037
21.320	4.600	0.030	0.030	1.047
17.310	3.830	0.030	0.030	0.945
16.180	3.570	0.030	0.030	0.873
13.610	3.130	0.030	0.030	0.862
13.960	3.190	0.030	0.030	0.863
10.990	2.610	0.030	0.030	0.778
10.040	2.420	0.030	0.030	0.747
7.870	2.010	0.030	0.030	0.698
4.660	1.240	0.030	0.030	0.463
2.790	0.590	0.030	0.030	0.125
1.510	0.380	0.030	0.030	0.128
0.980	0.270	0.030	0.030	0.107
2.210	0.550	0.030	0.030	0.182
3.240	0.980	0.030	0.030	0.440
4.350	1.210	0.030	0.050	0.485
5.400	1.440	0.030	0.030	0.540

6.060	1.630	0.030	0.030	0.620
7.750	1.940	0.050	0.050	0.648
8.910	2.160	0.030	0.030	0.675
12.980	3.000	0.030	0.030	0.837
13.760	3.150	0.030	0.030	0.857
16.610	3.620	0.030	0.030	0.852
15.560	3.460	0.030	0.030	0.867
20.490	4.320	0.050	0.030	0.905
21.040	4.440	0.030	0.030	0.933
12.980	3.340	0.050	0.050	1.177
13.760	3.440	0.050	0.050	1.147
15.560	3.880	0.050	0.050	1.287

CALCULATED TRAVEL TIMES

RAY CODE = A1

RANGE (KM)	CALC TIME (S)
0.000	0.000
0.980	0.294
2.210	0.659
3.240	0.927
4.350	1.193
5.400	1.467
6.060	1.630
7.750	2.009
8.910	2.280
12.980	3.199
13.760	3.372
10.040	2.501
7.870	2.003
4.660	1.255
2.790	0.780
1.510	0.436
0.000	0.000

RAY CODE = A3

RANGE (KM)	CALC TIME (S)
21.040	4.484
20.490	4.382
15.560	3.469
16.610	3.670
13.760	3.129
12.980	2.991
8.910	2.232
7.750	2.011
6.060	1.675
5.400	1.566
25.770	5.435
23.000	4.918
21.320	4.594
17.310	3.819
16.180	3.603
13.960	3.174
13.610	3.116
10.990	2.631

10,040	2,442
7,870	2,030

RAY CODE = A5

RANGE (KM)	CALC TIME (S)
49,830	9,289
47,720	9,006
39,400	7,609
38,250	7,419
31,970	6,389
29,090	5,912
25,770	5,362
23,000	4,900
21,320	4,606
17,310	3,930

RAY CODE = A6

RANGE (KM)	CALC TIME (S)
31,970	6,539
38,250	7,514
39,400	7,702
47,720	9,060
49,830	9,342

MAVIS I: OXCARS (P WAVE)

SHOT POSITION = 91,180 KM

OBSERVED TRAVEL TIMES

RANGE (KM)	TRAVEL TIME (S)	ERROR (+) (S)	ERROR (-) (S)	RED TIME (S)
51,970	9,680	0,050	0,050	1,018
50,470	9,510	0,050	0,050	1,098
49,350	9,250	0,050	0,050	1,025
47,030	8,850	0,050	0,050	1,012
47,030	8,940	0,050	0,050	1,102
46,760	8,870	0,030	0,030	1,077
44,120	8,410	0,030	0,030	1,057
41,030	7,890	0,050	0,050	1,052
37,780	7,360	0,050	0,050	1,063
35,950	7,090	0,050	0,050	1,098
34,620	6,860	0,030	0,030	1,090
32,210	6,420	0,030	0,030	1,052
29,940	6,090	0,050	0,050	1,100
27,800	5,680	0,030	0,030	1,047
27,120	5,560	0,030	0,030	1,040
26,390	5,390	0,050	0,050	0,992
24,260	5,130	0,030	0,030	1,087
21,450	4,580	0,030	0,030	1,005
20,220	4,340	0,030	0,030	0,970
19,420	4,260	0,100	0,030	1,023
17,630	3,790	0,050	0,050	0,852
14,510	3,290	0,030	0,030	0,872
12,690	2,920	0,030	0,030	0,805
12,140	2,850	0,050	0,030	0,827
10,150	2,490	0,030	0,030	0,798
9,240	2,300	0,030	0,030	0,760

26.390	5.670	0.050	0.100	1.272
24.260	5.320	0.050	0.050	1.277
21.450	4.890	0.100	0.100	1.315
17.630	4.180	0.100	0.100	1.242

CALCULATED TRAVEL TIMES

RAY CODE = A1

RANGE (KM)	CALC TIME (S)
14.510	3.535
12.690	3.122
12.140	3.004
10.150	2.551
9.240	2.349
0.000	0.000

RAY CODE = A3

RANGE (KM)	CALC TIME (S)
26.390	5.497
24.260	5.104
21.450	4.584
20.220	4.349
19.420	4.191
17.630	3.858
14.510	3.284
12.690	2.941
12.140	2.849
10.150	2.478
9.240	2.306

RAY CODE = A5

RANGE (KM)	CALC TIME (S)
51.970	9.693
50.470	9.439
49.350	9.243
47.030	8.859
46.760	8.814
44.120	8.375
41.030	7.857
37.780	7.304
35.950	6.992
34.620	6.769
32.210	6.388
29.940	6.010
27.800	5.651
27.120	5.543
26.390	5.422
24.260	5.063
21.450	4.596
20.220	4.386
19.420	4.252
17.630	3.957

RAY CODE = A6

RANGE (KM)	CALC TIME (S)
20.220	4.712
21.450	4.895
24.260	5.308

26.390	5.635
27.120	5.753
27.800	5.848
29.940	6.180
32.210	6.541
34.620	6.895
35.950	7.112
37.780	7.416
41.030	7.947
44.120	8.451
46.760	8.871
47.030	8.920
49.350	9.300
50.470	9.481
51.970	9.728

RAY CODE = A7

RANGE (KM)	CALC TIME (S)
51.970	9.683
50.470	9.441
49.350	9.262
47.030	8.895
46.760	8.851
44.120	8.434
41.030	7.940
37.780	7.414
35.950	7.113
34.620	6.900

MAVIS I: METHIL SOUTH (P WAVE)

SHOT POSITION = 107.110 KM

OBSERVED TRAVEL TIMES

RANGE (KM)	TRAVEL TIME (S)	ERROR (+) (S)	ERROR (-) (S)	RED TIME (S)
107.100	18.690	0.030	0.030	0.840
104.990	18.420	0.030	0.030	0.922
101.320	17.780	0.030	0.030	0.893
98.670	17.470	0.030	0.030	1.025
96.570	17.150	0.050	0.050	1.055
94.090	16.780	0.030	0.030	1.098
88.250	15.750	0.050	0.050	1.042
67.570	12.580	0.030	0.030	1.318
66.070	12.380	0.030	0.030	1.368
64.900	12.190	0.050	0.050	1.373
62.810	11.870	0.030	0.030	1.402
62.400	11.770	0.030	0.030	1.370
59.830	11.350	0.030	0.030	1.378
58.690	11.180	0.050	0.050	1.398
56.550	10.850	0.030	0.030	1.425
55.640	10.740	0.030	0.030	1.467
53.590	10.300	0.030	0.030	1.368
51.640	10.070	0.030	0.030	1.463
50.360	9.900	0.030	0.030	1.507
47.950	9.490	0.030	0.030	1.498
46.730	9.340	0.030	0.030	1.552

46,730	9,220	0,030	0,030	1,432
45,700	9,110	0,030	0,030	1,493
44,670	8,880	0,030	0,030	1,435
43,660	8,760	0,030	0,030	1,483
42,900	8,620	0,030	0,030	1,470
42,150	8,490	0,030	0,030	1,465
41,160	8,270	0,030	0,030	1,410
40,060	8,140	0,030	0,030	1,463
39,050	7,980	0,030	0,030	1,472
37,430	7,690	0,030	0,030	1,452
36,310	7,520	0,030	0,030	1,468
35,480	7,390	0,030	0,030	1,477
32,730	6,920	0,030	0,030	1,465
33,770	7,090	0,030	0,030	1,462
30,350	6,490	0,050	0,050	1,432
28,760	6,250	0,030	0,030	1,457
28,250	6,160	0,030	0,030	1,452
26,750	5,900	0,030	0,030	1,442
25,820	5,740	0,030	0,030	1,437
24,220	5,290	0,030	0,030	1,253
107,100	20,010	0,050	0,100	2,160
104,990	19,740	0,050	0,100	2,242
98,670	18,620	0,050	0,050	2,175
94,090	18,460	0,050	0,100	2,778

CALCULATED TRAVEL TIMES

RAY CODE = A5

RANGE (KM)	CALC TIME (S)
40,060	8,152
39,050	7,988
37,430	7,722
36,310	7,530
35,480	7,388
32,730	6,928
33,770	7,100
30,350	6,532
28,760	6,263
28,250	6,179
26,750	5,934
25,820	5,780
24,220	5,513

RAY CODE = A7

RANGE (KM)	CALC TIME (S)
107,100	18,685
104,990	18,347
101,320	17,795
98,670	17,432
96,570	17,162
94,090	16,762
88,250	15,850
67,570	12,601
66,070	12,358
64,900	12,176
62,810	11,844
62,400	11,779
59,830	11,372

58.690	11.179
56.550	10.847
55.640	10.703
53.590	10.366
51.640	10.050
50.360	9.847
47.950	9.485
46.730	9.299
45.700	9.124
44.670	8.955
43.660	8.802

RAY CODE = A10

RANGE (KM)	CALC TIME (S)
107.100	20.020
104.990	19.730
98.670	19.010
94.090	18.470

MAVIS I: BALLIKINRAIN (P WAVE)

SHOT POSITION = 0.000 KM

OBSERVED TRAVEL TIMES

RANGE (KM)	TRAVEL TIME (S)	ERROR (+) (S)	ERROR (-) (S)	RED TIME (S)
0.230	0.090	0.030	0.030	0.052
1.290	0.400	0.030	0.030	0.185
2.190	0.620	0.030	0.030	0.255
3.610	0.980	0.030	0.030	0.378
5.620	1.420	0.030	0.030	0.483
7.450	1.780	0.030	0.030	0.538
13.440	2.980	0.030	0.030	0.740
16.640	3.560	0.030	0.030	0.787
17.760	3.760	0.030	0.030	0.800
19.430	4.070	0.030	0.030	0.832
20.060	4.180	0.030	0.030	0.837
22.900	4.680	0.030	0.030	0.863
26.540	5.340	0.030	0.050	0.917
27.010	5.430	0.030	0.030	0.928
29.640	5.920	0.030	0.030	0.980
32.290	6.400	0.030	0.030	1.018
33.300	6.560	0.030	0.030	1.010
36.870	7.190	0.030	0.050	1.045
38.170	7.400	0.050	0.050	1.038
39.510	7.710	0.030	0.030	1.125
40.520	7.760	0.030	0.030	1.007
41.330	7.980	0.050	0.050	1.092
42.560	8.180	0.050	0.050	1.087
43.600	8.360	0.050	0.050	1.093
44.950	8.580	0.080	0.050	1.088
46.670	8.900	0.030	0.030	1.122
50.500	9.500	0.030	0.030	1.083
52.590	9.850	0.030	0.030	1.085
57.520	10.600	0.030	0.030	1.013
59.950	10.930	0.030	0.030	0.938
61.690	11.220	0.030	0.030	0.938

62.410	11.320	0.030	0.030	0.918
63.900	11.520	0.030	0.080	0.870

CALCULATED TRAVEL TIMES

RAY CODE = A1

RANGE (KM)	CALC TIME (S)
0.000	0.000
1.290	0.378
2.190	0.627
3.610	0.980
5.620	1.423
7.450	1.803
13.440	3.053

RAY CODE = A3

RANGE (KM)	CALC TIME (S)
42.560	8.256
41.330	8.028
40.520	7.885
39.510	7.717
38.170	7.465
36.870	7.214
33.300	6.561
32.290	6.382
29.640	5.902
27.010	5.433
26.540	5.353
22.900	4.689
20.060	4.162
19.430	4.043
17.760	3.761
16.640	3.572
13.440	3.006
7.450	1.943

RAY CODE = A5

RANGE (KM)	CALC TIME (S)
63.900	11.541
62.410	11.320
61.690	11.206
46.670	8.871
44.950	8.595
43.600	8.375
42.560	8.207
41.330	7.990
40.520	7.851
39.510	7.692

RAY CODE = A7

RANGE (KM)	CALC TIME (S)
63.900	11.524
62.410	11.315
61.690	11.207
59.950	10.930
57.520	10.582
52.590	9.831
50.500	9.526

46.670	8.942

MAVIS I: NORTH THIRD (P WAVE)

SHOT POSITION = 19.180 KM

OBSERVED TRAVEL TIMES

RANGE (KM)	TRAVEL TIME (S)	ERROR (+) (S)	ERROR (-) (S)	RED TIME (S)
17.970	3.710	0.050	0.050	0.715
15.580	3.260	0.030	0.030	0.663
13.650	2.960	0.030	0.030	0.685
11.810	2.570	0.030	0.030	0.602
11.110	2.410	0.030	0.030	0.558
7.330	1.650	0.030	0.030	0.428
5.810	1.260	0.030	0.030	0.292
3.680	0.800	0.030	0.030	0.187
2.540	0.550	0.030	0.030	0.127
1.420	0.260	0.030	0.030	0.023
0.920	0.160	0.030	0.030	0.007
2.200	0.420	0.030	0.030	0.053
3.810	0.860	0.030	0.030	0.225
6.050	1.400	0.030	0.030	0.392
7.360	1.770	0.030	0.030	0.543
7.830	1.820	0.030	0.030	0.515
10.540	2.430	0.030	0.030	0.673
10.470	2.430	0.030	0.030	0.685
11.620	2.620	0.030	0.030	0.683
13.110	2.940	0.030	0.030	0.755
14.120	3.120	0.030	0.030	0.767
17.700	3.910	0.050	0.100	0.960
18.990	4.100	0.030	0.030	0.935
19.450	4.220	0.050	0.080	0.978
22.150	4.730	0.050	0.050	1.038
24.450	5.150	0.030	0.030	1.075
28.640	5.830	0.030	0.030	1.057
30.390	6.140	0.030	0.030	1.075
31.360	6.300	0.030	0.030	1.073
33.460	6.610	0.030	0.030	1.033
35.950	7.040	0.050	0.030	1.048
38.430	7.270	0.030	0.030	0.865
42.670	8.160	0.080	0.080	1.048
44.900	8.520	0.080	0.080	1.037
6.050	1.980	0.080	0.080	0.972
7.360	2.120	0.050	0.050	0.893
7.830	2.270	0.080	0.080	0.965
10.470	2.610	0.050	0.050	0.865
11.620	2.750	0.080	0.080	0.813
10.540	2.960	0.050	0.050	1.203
10.470	2.860	0.080	0.080	1.115
11.620	3.100	0.050	0.050	1.163
13.110	3.310	0.050	0.050	1.125
14.120	3.480	0.050	0.050	1.127
17.700	4.100	0.050	0.050	1.150
17.700	4.560	0.050	0.050	1.610
18.990	4.760	0.050	0.050	1.595
19.450	4.820	0.050	0.050	1.578

22.150	4.990	0.080	0.080	1.298
24.450	5.330	0.080	0.080	1.255
33.460	6.680	0.050	0.050	1.103
35.950	7.080	0.050	0.050	1.088

CALCULATED TRAVEL TIMES

RAY CODE = A1

RANGE (KM)	CALC TIME (S)
0.000	0.000
2.200	0.485
3.810	0.862
6.050	1.422
7.360	1.728
7.830	1.831
10.470	2.392
10.540	2.416
11.620	2.643
13.110	2.964
14.120	3.180
17.700	3.961
18.990	4.267
19.450	4.371
22.150	4.983
24.450	5.493
15.580	3.405
13.650	2.975
11.810	2.573
11.110	2.420
7.330	1.586
5.810	1.268
3.680	0.805
0.000	0.000

RAY CODE = A2

RANGE (KM)	CALC TIME (S)
24.450	5.505
22.150	5.009
19.450	4.420
18.990	4.319
17.700	4.031
14.120	3.298
13.110	3.100
11.620	2.811
10.540	2.613
10.470	2.596
7.830	2.138
7.360	2.060
6.050	1.862

RAY CODE = A4

RANGE (KM)	CALC TIME (S)
7.830	2.638
10.470	2.970
10.540	2.983
11.620	3.129
13.110	3.348

14.120	3.499
17.700	4.081
18.990	4.312
19.450	4.393
22.150	4.840

RAY CODE = A5

RANGE (KM)	CALC TIME (S)
28.660	5.865
24.450	5.131
22.150	4.722
19.450	4.246
18.990	4.154
17.700	3.907
14.120	3.250
13.110	3.074
11.620	2.804
44.900	8.423
42.670	8.091
38.430	7.419
35.950	7.054
33.460	6.635
31.360	6.310
30.390	6.165
28.660	5.932

RAY CODE = A6

RANGE (KM)	CALC TIME (S)
14.120	4.114
17.700	4.586
18.990	4.768
19.450	4.835
22.150	5.209
24.450	5.540
28.660	6.152
30.390	6.397
31.360	6.533
33.460	6.848
35.950	7.232
38.430	7.575
42.670	8.214
44.900	8.538

MAVIS I: CATTLE MOSS (P WAVE)

SHOT POSITION = 43.880 KM

OBSERVED TRAVEL TIMES

RANGE (KM)	TRAVEL TIME (S)	ERROR (+) (S)	ERROR (-) (S)	RED TIME (S)
43.710	8.400	0.030	0.030	1.115
42.650	8.210	0.050	0.050	1.102
40.270	7.820	0.030	0.030	1.108
38.370	7.560	0.030	0.030	1.165
35.830	7.150	0.030	0.030	1.178
33.660	6.740	0.030	0.030	1.130

30,520	6,210	0,030	0,030	1,123
28,390	5,820	0,030	0,030	1,088
27,260	5,690	0,030	0,030	1,147
26,150	5,450	0,030	0,030	1,092
23,880	5,070	0,030	0,030	1,090
22,580	4,950	0,030	0,050	1,187
21,130	4,600	0,030	0,030	1,078
18,830	4,210	0,050	0,050	1,072
17,430	4,080	0,050	0,050	1,175
16,910	4,030	0,050	0,050	1,212
14,220	3,450	0,030	0,030	1,080
14,400	3,500	0,030	0,030	1,100
13,250	3,260	0,030	0,030	1,052
11,750	3,000	0,030	0,030	1,042
10,730	2,810	0,030	0,030	1,022
7,300	2,000	0,030	0,030	0,783
5,800	1,600	0,030	0,030	0,633
5,280	1,520	0,030	0,030	0,640
4,400	1,320	0,030	0,030	0,587
3,380	1,040	0,030	0,030	0,477
2,570	0,770	0,030	0,030	0,342
0,380	0,130	0,030	0,030	0,067
1,190	0,370	0,030	0,030	0,172
2,800	0,860	0,030	0,030	0,393
3,940	1,130	0,030	0,030	0,473
5,670	1,640	0,030	0,030	0,695
6,640	1,820	0,030	0,030	0,713
8,750	2,240	0,050	0,050	0,782
11,380	2,790	0,030	0,030	0,893
13,780	3,120	0,030	0,030	0,823
16,330	3,670	0,030	0,030	0,948
18,150	4,010	0,030	0,030	0,985
18,940	4,130	0,030	0,030	0,973
20,420	4,390	0,030	0,030	0,987
25,420	5,440	0,030	0,030	1,203
32,360	6,780	0,030	0,030	1,387
5,670	1,720	0,050	0,050	0,775
8,750	2,340	0,050	0,050	0,882
5,800	2,250	0,050	0,050	1,283
7,300	2,430	0,100	0,100	1,213
10,730	2,990	0,050	0,050	1,202
11,750	3,210	0,050	0,080	1,252
14,400	3,610	0,050	0,050	1,210
14,220	3,560	0,050	0,050	1,190
28,390	5,910	0,050	0,050	1,178
42,650	8,270	0,050	0,050	1,162
30,520	6,330	0,050	0,050	1,243
28,390	6,110	0,050	0,080	1,378
27,260	5,900	0,050	0,080	1,357
26,150	5,760	0,050	0,050	1,402
23,880	5,410	0,050	0,050	1,430
21,130	4,920	0,050	0,050	1,398
18,830	4,480	0,100	0,100	1,342
16,910	4,620	0,050	0,100	1,802

CALCULATED TRAVEL TIMES

RAY CODE = A1

RANGE (KM)	CALC TIME (S)
0.000	0.000
1.190	0.395
2.800	0.875
3.940	1.169
5.670	1.596
6.640	1.814
8.750	2.274
11.380	2.868
13.780	3.347
26.150	5.827
23.880	5.398
22.580	5.142
21.130	4.857
18.830	4.404
17.430	4.126
16.910	4.015
14.400	3.500
14.220	3.464
13.250	3.258
11.750	2.943
10.730	2.721
7.300	1.960
5.800	1.614
5.280	1.491
4.400	1.282
3.380	1.011
2.570	0.805
0.380	0.132
0.000	0.000

RAY CODE = A2

RANGE (KM)	CALC TIME (S)
5.800	2.056
7.300	2.293
10.730	2.900
11.750	3.089
13.250	3.370
14.220	3.558
14.400	3.587
16.910	4.068
17.430	4.169
18.830	4.439
22.580	5.159
23.880	5.402
26.150	5.833

RAY CODE = A3

RANGE (KM)	CALC TIME (S)
20.420	4.366
18.940	4.121
18.150	3.999
16.330	3.673
13.780	3.267
11.380	2.895
8.750	2.432
43.710	8.453

42.650	8.266
40.270	7.855
38.370	7.544
35.830	7.118
33.660	6.740
30.520	6.172
28.390	5.816
27.260	5.631
26.150	5.426
23.880	5.035
22.580	4.829
21.130	4.587
18.830	4.202
17.430	3.967
16.910	3.886
14.400	3.453
14.220	3.424
13.250	3.264
11.750	3.018
10.730	2.857

RAY CODE = A4

RANGE (KM)	CALC TIME (S)
5.280	2.320
7.300	2.567
10.730	3.068
11.750	3.218
13.250	3.440
14.220	3.600
14.400	3.625
16.910	4.035
17.430	4.118
18.830	4.348
21.130	4.720
22.580	4.955
23.880	5.162
26.150	5.535
27.260	5.741
28.390	5.920
16.910	4.066
17.430	4.146
18.830	4.358
21.130	4.710
22.580	4.937
23.880	5.138
26.150	5.510
27.260	5.702
28.390	5.881
30.520	6.228
33.660	6.775
35.830	7.142
38.370	7.570
40.270	7.875
42.650	8.280
43.710	8.464

RAY CODE = A5

RANGE (KM)	CALC TIME (S)
32.360	6.490

25.420	5.269
20.420	4.417
18.940	4.182

43.710	8.388
42.650	8.224
40.270	7.831
38.370	7.528
35.830	7.123
33.660	6.763
30.520	6.226
28.390	5.877
27.260	5.699
26.150	5.512

RAY CODE = A6

RANGE (KM)	CALC TIME (S)
14.400	4.242
16.910	4.544
17.430	4.608
18.830	4.787
21.130	5.089
22.580	5.285
23.880	5.460
26.150	5.789
27.260	5.969
28.390	6.122
30.520	6.441

MAVIS I: WESTFIELD (P WAVE)

SHOT POSITION = 66.410 KM

OBSERVED TRAVEL TIMES

RANGE (KM)	TRAVEL TIME (S)	ERROR (+) (S)	ERROR (-) (S)	RED TIME (S)
26.130	5.390	0.050	0.050	1.035
20.130	4.260	0.030	0.030	0.905
18.970	4.060	0.030	0.050	0.898
17.310	3.770	0.050	0.050	0.885
16.350	3.610	0.030	0.030	0.885
14.230	3.120	0.030	0.030	0.748
11.520	2.640	0.030	0.050	0.720
9.180	2.420	0.030	0.030	0.890
6.570	1.520	0.030	0.050	0.425
4.750	1.200	0.030	0.030	0.408
4.000	1.010	0.030	0.030	0.343
11.410	2.870	0.030	0.030	0.968

CALCULATED TRAVEL TIMES

RAY CODE = A1

RANGE (KM)	CALC TIME (S)
0.000	0.000
11.410	2.821

14.230	3.272
11.520	2.661
9.180	2.127
6.570	1.551
4.750	1.182
4.000	1.018
0.000	0.000

RAY CODE = A3

RANGE (KM)	CALC TIME (S)
26.130	5.360
20.130	4.254
18.970	4.050
17.310	3.769
16.350	3.612
14.230	3.241
11.520	2.747

RAY CODE = A5

RANGE (KM)	CALC TIME (S)
26.130	5.355
20.130	4.310

MAVIS I: METHIL NORTH (P WAVE)

SHOT POSITION = 81.070 KM

OBSERVED TRAVEL TIMES

RANGE (KM)	TRAVEL TIME (S)	ERROR (+) (S)	ERROR (-) (S)	RED TIME (S)
80.910	14.710	0.030	0.030	1.225
77.470	14.100	0.050	0.050	1.188
75.510	13.920	0.030	0.030	1.335
72.950	13.480	0.030	0.030	1.322
72.950	13.530	0.030	0.030	1.372
70.740	13.160	0.050	0.050	1.370
67.650	12.620	0.030	0.030	1.345
65.520	12.310	0.030	0.030	1.390
64.430	12.120	0.030	0.030	1.382
63.300	11.990	0.050	0.050	1.440
61.640	11.740	0.030	0.030	1.467
61.020	11.620	0.030	0.030	1.450
59.710	11.420	0.050	0.050	1.468
58.190	11.180	0.030	0.030	1.482
56.570	10.830	0.030	0.030	1.402
54.060	10.650	0.050	0.050	1.640
51.350	10.120	0.030	0.030	1.562
51.430	10.080	0.030	0.030	1.508
51.430	10.150	0.030	0.030	1.578
50.280	9.980	0.030	0.030	1.600
48.780	9.740	0.030	0.030	1.610
47.770	9.580	0.030	0.030	1.618
44.200	9.010	0.030	0.030	1.643
42.910	8.810	0.030	0.030	1.658
42.490	8.750	0.030	0.030	1.668
41.590	8.600	0.030	0.030	1.668
40.650	8.410	0.030	0.030	1.635

39,830	8,250	0,050	0,050	1,612
37,580	7,880	0,030	0,030	1,617
34,520	7,360	0,030	0,030	1,607
33,460	7,170	0,030	0,030	1,593
31,710	6,840	0,030	0,030	1,555
30,760	6,680	0,030	0,030	1,553
28,760	6,350	0,030	0,030	1,557
26,730	6,010	0,030	0,030	1,555
24,190	5,790	0,030	0,030	1,758
22,220	5,150	0,030	0,030	1,447
20,870	4,960	0,030	0,030	1,482
19,180	4,590	0,030	0,030	1,393
13,260	3,560	0,030	0,030	1,350
9,690	2,660	0,030	0,030	1,045

CALCULATED TRAVEL TIMES

RAY CODE = A3

RANGE (KM)	CALC TIME (S)
41,590	8,632
40,650	8,459
39,830	8,311
37,580	7,906
33,460	7,172
31,710	6,875
30,760	6,716
28,760	6,364
26,730	5,996
24,190	5,515
22,220	5,148
20,870	4,890
19,180	4,612
13,260	3,595
9,690	3,027

RAY CODE = A5

RANGE (KM)	CALC TIME (S)
65,520	12,360
64,430	12,189
63,300	11,995
61,640	11,724
61,020	11,625
59,710	11,419
58,190	11,177
56,570	10,915
54,060	10,509
51,350	10,061
51,430	10,066
50,280	9,892
47,770	9,493
44,200	8,922
42,910	8,720
42,490	8,654
41,590	8,510
40,650	8,342
39,830	8,202
37,580	7,818
34,520	7,288

33.460	7.108
31.710	6.827
30.760	6.685
28.760	6.342
26.730	5.993
24.190	5.540
22.220	5.180
20.870	4.940
19.180	4.666

RAY CODE = A7

RANGE (KM)	CALC TIME (S)
80.910	14.722
77.470	14.175
75.510	13.873
72.950	13.490
70.740	13.139
67.650	12.640
65.520	12.309
64.430	12.150
63.300	11.957
61.640	11.696
61.020	11.608
59.710	11.406
58.190	11.176
56.570	10.931
54.060	10.548
51.350	10.130
51.430	10.135
50.280	9.959
48.780	9.738
47.770	9.589
44.200	9.050
42.910	8.854
42.490	8.793
41.590	8.664

MAVIS II: ABERUTHVEN (P WAVE)

SHOT POSITION = 0.000 KM

OBSERVED TRAVEL TIMES

RANGE (KM)	TRAVEL TIME (S)	ERROR (+) (S)	ERROR (-) (S)	RED TIME (S)
0.230	0.060	0.030	0.030	0.022
1.100	0.280	0.050	0.050	0.097
2.270	0.540	0.030	0.030	0.162
2.800	0.660	0.030	0.030	0.193
4.090	0.870	0.030	0.030	0.188
5.280	1.220	0.030	0.030	0.340
6.430	1.470	0.030	0.030	0.398
7.140	1.600	0.030	0.030	0.410
8.950	1.970	0.030	0.030	0.478
10.260	2.210	0.030	0.030	0.500
11.390	2.500	0.050	0.050	0.602
12.540	2.670	0.050	0.050	0.580
13.770	2.880	0.030	0.030	0.585

14,490	3,050	0,030	0,030	0,635
17,450	3,700	0,030	0,030	0,792
19,440	4,130	0,030	0,030	0,890
20,430	4,290	0,030	0,030	0,885
22,260	4,630	0,030	0,030	0,920
23,460	4,840	0,030	0,030	0,930
24,110	4,890	0,030	0,030	0,872
24,950	5,040	0,050	0,050	0,882
24,950	5,200	0,050	0,050	1,042
25,800	5,300	0,030	0,030	1,000
26,240	5,380	0,030	0,030	1,007
29,560	5,870	0,050	0,050	0,943
33,470	6,470	0,030	0,030	0,892
34,780	6,740	0,030	0,030	0,943
35,210	6,830	0,030	0,030	0,962
35,680	6,900	0,030	0,030	0,953
35,680	6,940	0,030	0,030	0,993
39,170	7,540	0,030	0,030	1,012
39,170	7,510	0,030	0,030	0,982
40,320	7,660	0,030	0,030	0,940
40,320	7,680	0,030	0,030	0,960
41,110	7,800	0,030	0,030	0,948
42,090	7,980	0,030	0,030	0,965
42,090	8,020	0,030	0,030	1,005
44,210	8,230	0,030	0,030	0,862
44,210	8,270	0,030	0,030	0,902
45,060	8,450	0,030	0,030	0,940
45,670	8,560	0,030	0,030	0,948
46,750	8,680	0,030	0,030	0,888
47,700	8,740	0,030	0,030	0,790
47,700	8,810	0,030	0,030	0,860

CALCULATED TRAVEL TIMES

RAY CODE = A3(d)

RANGE (KM)	CALC TIME (S)
0,000	0,000
1,100	0,258
2,270	0,542
2,800	0,657
4,090	0,949
5,280	1,230
6,430	1,469
7,140	1,604
8,950	1,965
10,260	2,225
11,390	2,447
12,540	2,660
13,770	2,854
14,490	3,010
17,450	3,667
19,440	4,089
20,430	4,288
22,260	4,645
23,460	4,872
24,110	4,957
24,950	5,085
25,800	5,230

26.240	5.299
29.560	5.869
33.470	6.552
34.780	6.788
35.210	6.862
35.680	6.947
36.550	7.103

RAY CODE = A5

RANGE (KM)	CALC TIME (S)
47.700	8.865
46.750	8.696
45.670	8.532
45.060	8.425
44.210	8.289
42.090	7.940
41.110	7.779
40.320	7.652
39.170	7.461
38.580	7.366
36.550	7.022
35.680	6.876
35.210	6.798
34.780	6.726
33.470	6.506
29.560	5.873
26.240	5.347
25.800	5.277
24.950	5.152
24.110	5.026

MAVIS II: DOLLAR (P WAVE)

SHOT POSITION = 16.660 KM

OBSERVED TRAVEL TIMES

RANGE (KM)	TRAVEL TIME (S)	ERROR (+) (S)	ERROR (-) (S)	RED TIME (S)
16.560	3.480	0.030	0.030	0.720
14.570	3.140	0.030	0.030	0.712
13.860	3.000	0.030	0.030	0.690
12.580	2.770	0.030	0.030	0.673
11.420	2.540	0.030	0.030	0.637
10.290	2.330	0.030	0.030	0.615
9.630	2.190	0.030	0.030	0.585
7.790	1.810	0.030	0.030	0.512
6.880	1.640	0.030	0.030	0.493
5.340	1.320	0.030	0.030	0.430
3.000	0.860	0.050	0.050	0.360
2.180	0.660	0.030	0.030	0.297
0.990	0.290	0.030	0.030	0.125
0.850	0.320	0.030	0.030	0.178
1.830	0.570	0.030	0.030	0.265
2.890	0.870	0.030	0.030	0.388
4.690	1.330	0.030	0.030	0.548
5.760	1.610	0.030	0.030	0.650
6.800	1.860	0.030	0.030	0.727

7.460	1.900	0.030	0.030	0.657
9.140	2.430	0.030	0.030	0.907
9.140	2.450	0.030	0.030	0.927
9.580	2.530	0.030	0.030	0.933
12.920	3.050	0.050	0.050	0.897
12.920	3.110	0.050	0.050	0.957
18.150	4.090	0.030	0.030	1.065
18.150	4.130	0.030	0.030	1.105
18.590	4.140	0.030	0.030	1.042
18.590	4.200	0.030	0.030	1.102
23.860	5.050	0.030	0.030	1.073
24.640	5.150	0.030	0.030	1.043
25.620	5.330	0.030	0.030	1.060
26.940	5.690	0.030	0.030	1.200
26.940	5.770	0.030	0.030	1.280
28.580	5.830	0.030	0.030	1.067
29.190	5.930	0.030	0.030	1.065
30.270	6.170	0.100	0.100	1.125
31.290	6.270	0.030	0.030	1.055

CALCULATED TRAVEL TIMES

RAY CODE = A1

RANGE (KM)	CALC TIME (S)
0.000	0.000
0.850	0.257
1.830	0.568
2.890	0.845
4.690	1.309
5.760	1.575
6.800	1.819
7.460	1.980
9.140	2.360
9.580	2.446
12.920	3.149
2.180	0.658
0.990	0.306
0.000	0.000

RAY CODE = A3

RANGE (KM)	CALC TIME (S)
25.620	5.374
24.640	5.198
23.860	5.060
18.590	4.098
18.150	4.022
12.920	3.099
9.580	2.524
9.140	2.448
16.560	3.482
15.560	3.298
14.570	3.118
13.860	2.989
12.580	2.773
11.420	2.567
10.290	2.344

9.630	2.203
8.810	2.023
7.790	1.826
6.880	1.646
5.340	1.357

RAY CODE = A5

RANGE (KM)	CALC TIME (S)
31.290	6.273
30.270	6.102
29.190	5.926
28.580	5.824
26.940	5.550
25.620	5.337
24.640	5.174
23.860	5.046
18.590	4.169
18.150	4.092

MAVIS II: LONGANNET (P WAVE)

SHOT POSITION = 26.790 KM

OBSERVED TRAVEL TIMES

RANGE (KM)	TRAVEL TIME (S)	ERROR (+) (S)	ERROR (-) (S)	RED TIME (S)
26.690	5.350	0.030	0.030	0.902
24.690	5.020	0.030	0.030	0.905
23.990	4.890	0.030	0.030	0.892
22.710	4.630	0.030	0.030	0.845
21.540	4.450	0.030	0.030	0.860
20.410	4.280	0.030	0.030	0.878
17.900	3.840	0.030	0.030	0.857
16.840	3.500	0.030	0.030	0.693
16.840	3.580	0.030	0.030	0.773
15.440	3.290	0.050	0.050	0.717
14.410	3.170	0.050	0.050	0.768
11.010	2.730	0.050	0.050	0.895
9.350	2.320	0.030	0.030	0.762
7.430	1.850	0.030	0.030	0.612
6.450	1.610	0.030	0.030	0.535
4.840	1.280	0.030	0.030	0.473
3.380	0.880	0.050	0.050	0.317
0.550	0.160	0.050	0.050	0.068
6.700	1.590	0.030	0.030	0.473
8.120	1.960	0.030	0.030	0.607
8.590	2.090	0.030	0.030	0.658
8.930	2.260	0.050	0.050	0.772
10.110	2.330	0.030	0.030	0.645
12.320	2.820	0.030	0.030	0.767
14.120	3.090	0.060	0.030	0.737
14.870	3.260	0.060	0.030	0.782
15.830	3.460	0.030	0.030	0.822
17.090	3.680	0.030	0.030	0.832
17.090	3.780	0.030	0.030	0.932
18.740	4.030	0.030	0.030	0.907
19.340	4.120	0.030	0.030	0.897

20.420	4.310	0.030	0.030	0.907
6.700	2.710	0.050	0.050	1.593
10.110	3.300	0.050	0.100	1.615
12.320	3.600	0.050	0.050	1.547
17.090	4.380	0.050	0.050	1.532
19.340	4.680	0.050	0.050	1.457
20.420	4.880	0.080	0.050	1.477

CALCULATED TRAVEL TIMES

RAY CODE = A1

RANGE (KM)	CALC TIME (S)
0.000	0.000
6.700	1.617
8.120	1.934
8.590	2.035
10.110	2.356
12.320	2.824
14.120	3.191
14.870	3.352
11.010	2.728
9.350	2.360
7.430	1.889
6.450	1.649
4.840	1.255
3.380	0.900
0.550	0.160
0.000	0.000

RAY CODE = A3

RANGE (KM)	CALC TIME (S)
20.420	4.315
19.340	4.120
18.740	4.017
17.090	3.722
15.830	3.488
14.870	3.320
14.120	3.182
12.320	2.855
10.110	2.445
8.590	2.155
8.120	2.073
21.540	4.500
20.410	4.290
17.900	3.935
16.840	3.751
15.440	3.518
14.410	3.321
11.010	2.865

RAY CODE = A5

RANGE (KM)	CALC TIME (S)
20.420	4.351
19.340	4.170
18.740	4.071
26.690	5.409

17.900   3.921

MAVIS II: AVONBRIDGE (P WAVE)

SHOT POSITION =   39.500 KM

OBSERVED TRAVEL TIMES

RANGE (KM)	TRAVEL TIME (S)	ERROR (+) (S)	ERROR (-) (S)	RED TIME (S)
39.370	7.390	0.100	0.050	0.828
37.300	6.960	0.030	0.030	0.743
36.710	6.940	0.050	0.050	0.822
36.710	7.020	0.050	0.050	0.902
35.420	6.740	0.030	0.050	0.837
34.210	6.560	0.050	0.050	0.858
33.070	6.420	0.030	0.050	0.908
32.350	6.210	0.050	0.050	0.818
31.230	6.020	0.030	0.030	0.815
31.230	6.050	0.030	0.030	0.845
30.550	5.960	0.030	0.030	0.868
29.270	5.860	0.030	0.030	0.982
28.130	5.630	0.050	0.050	0.942
26.960	5.390	0.030	0.050	0.897
22.210	4.730	0.030	0.030	1.028
20.170	4.350	0.030	0.050	0.988
19.190	4.100	0.030	0.030	0.902
18.370	3.940	0.030	0.030	0.878
17.300	3.820	0.050	0.030	0.937
16.340	3.650	0.030	0.030	0.927
15.730	3.450	0.030	0.030	0.828
15.730	3.590	0.030	0.030	0.968
14.070	3.200	0.030	0.030	0.855
13.170	2.880	0.050	0.050	0.685
6.150	1.550	0.030	0.030	0.525
5.500	1.350	0.050	0.050	0.433
5.000	1.170	0.030	0.030	0.337
4.420	1.050	0.030	0.030	0.313
1.510	0.380	0.030	0.030	0.128
1.510	0.450	0.030	0.030	0.198
1.040	0.280	0.030	0.030	0.107
0.480	0.130	0.030	0.030	0.050
0.820	0.210	0.030	0.030	0.073
1.610	0.320	0.030	0.030	0.052
2.600	0.590	0.030	0.030	0.157
3.950	0.950	0.030	0.030	0.292
4.710	1.170	0.030	0.030	0.385
5.570	1.340	0.030	0.030	0.412
6.180	1.450	0.030	0.030	0.420
7.250	1.750	0.030	0.030	0.542
8.240	1.950	0.030	0.030	0.577
28.130	5.940	0.050	0.050	1.252
26.960	5.610	0.100	0.100	1.117
22.210	5.150	0.050	0.050	1.448
20.170	4.800	0.050	0.050	1.438
19.190	4.660	0.050	0.050	1.462
18.370	4.510	0.050	0.050	1.448
17.300	4.210	0.050	0.080	1.327

16.340	4.020	0.100	0.100	1.297
15.730	4.010	0.050	0.050	1.388
14.070	3.650	0.050	0.050	1.305
13.170	3.530	0.100	0.100	1.335
3.950	1.030	0.050	0.050	0.372

CALCULATED TRAVEL TIMES

RAY CODE = A1

RANGE (KM)	CALC TIME (S)
0.000	0.000
0.820	0.220
1.610	0.429
2.600	0.675
3.950	0.987
4.710	1.166
5.570	1.356
6.180	1.490
7.250	1.725
8.240	1.944
16.340	3.713
15.730	3.579
14.070	3.215
13.170	3.012
7.150	1.692
5.500	1.327
5.000	1.216
4.420	1.088
1.510	0.406
1.040	0.279
0.480	0.132
0.000	0.000

RAY CODE = A3

RANGE (KM)	CALC TIME (S)
30.550	6.076
22.210	4.750
20.170	4.355
19.190	4.161
18.370	4.006
17.300	3.818
16.340	3.620
15.730	3.507
14.070	3.197
13.170	3.021

RAY CODE = A5

RANGE (KM)	CALC TIME (S)
39.370	7.492
37.300	7.146
36.710	7.052
31.230	6.116
30.550	6.012
29.270	5.804
28.130	5.633
26.960	5.427

RAY CODE = A6

RANGE (KM)	CALC TIME (S)
17.300	4.379
18.370	4.526
19.190	4.654
20.170	4.798
22.210	5.109
26.960	5.705
28.130	5.904
29.270	6.060

MAVIS II: BLAIRHILL (P WAVE)

SHOT POSITION = 47.680 KM

OBSERVED TRAVEL TIMES

RANGE (KM)	TRAVEL TIME (S)	ERROR (+) (S)	ERROR (-) (S)	RED TIME (S)
47.550	8.970	0.030	0.050	1.045
47.550	8.730	0.030	0.050	0.805
46.590	8.550	0.050	0.030	0.785
45.470	8.470	0.030	0.050	0.892
44.900	8.350	0.030	0.030	0.867
43.610	8.190	0.050	0.050	0.922
41.250	7.770	0.060	0.030	0.895
40.530	7.550	0.030	0.030	0.795
39.390	7.500	0.030	0.030	0.935
38.740	7.380	0.030	0.030	0.923
37.430	7.110	0.030	0.030	0.872
37.430	7.140	0.030	0.030	0.902
36.340	7.020	0.030	0.030	0.963
35.150	6.750	0.030	0.050	0.892
33.980	6.670	0.030	0.030	1.007
32.020	6.330	0.030	0.030	0.993
30.440	6.090	0.030	0.030	1.017
28.400	5.760	0.030	0.030	1.027
27.420	5.560	0.030	0.050	0.990
26.600	5.490	0.030	0.050	1.057
25.530	5.280	0.030	0.050	1.025
24.570	5.110	0.030	0.030	1.015
23.960	4.990	0.030	0.030	0.997
22.290	4.650	0.030	0.030	0.935
22.010	4.640	0.030	0.030	0.972
21.360	4.510	0.030	0.030	0.950
15.090	3.330	0.030	0.030	0.815
13.500	3.050	0.030	0.030	0.800
13.000	2.950	0.030	0.030	0.783
12.450	2.860	0.030	0.030	0.785
9.710	2.310	0.030	0.030	0.692
9.220	2.180	0.030	0.030	0.643
8.600	2.020	0.030	0.030	0.587
7.420	1.800	0.030	0.030	0.563
6.650	1.610	0.030	0.030	0.502
5.680	1.370	0.030	0.030	0.423
4.460	1.120	0.030	0.030	0.377
3.620	0.890	0.030	0.030	0.287
2.870	0.780	0.030	0.030	0.302

2.340	0.520	0.030	0.030	0.130
1.430	0.260	0.030	0.030	0.022
0.150	0.020	0.030	0.030	-0.005
32.020	6.450	0.050	0.050	1.113
30.440	6.180	0.050	0.050	1.107
28.400	5.810	0.050	0.050	1.077
12.450	3.060	0.050	0.050	0.985
12.450	3.010	0.050	0.050	0.935
8.600	2.340	0.050	0.080	0.907
7.420	2.190	0.050	0.080	0.953
6.650	2.130	0.050	0.080	1.022
5.680	2.020	0.050	0.050	1.073
4.460	1.910	0.100	0.100	1.167

CALCULATED TRAVEL TIMES

RAY CODE = A1

RANGE (KM)	CALC TIME (S)
15.090	3.395
13.500	3.068
13.000	2.955
12.450	2.839
9.710	2.264
9.220	2.158
8.600	2.022
7.420	1.762
6.650	1.592
5.680	1.373
4.460	1.105
3.620	0.917
2.870	0.735
2.340	0.605
1.430	0.381
0.000	0.000

RAY CODE = A3

RANGE (KM)	CALC TIME (S)
32.020	6.499
30.440	6.219
28.400	5.831
27.420	5.654
26.600	5.480
25.530	5.293
24.570	5.101
23.960	4.995
22.290	4.677
22.010	4.623
21.360	4.510
15.090	3.333
13.500	3.042
13.000	2.946
12.450	2.848
9.710	2.350

RAY CODE = A4

RANGE (KM)	CALC TIME (S)
3.620	1.835
4.460	1.904

5.680	2.023
6.650	2.141
7.420	2.245
8.600	2.411
9.220	2.501
9.710	2.577
12.450	2.992
13.000	3.082
13.500	3.167

RAY CODE = A5

RANGE (KM)	CALC TIME (S)
47.550	8.833
46.590	8.675
45.470	8.487
44.900	8.389
39.390	7.456
38.740	7.357
37.430	7.147
36.340	6.984
35.150	6.773
32.020	6.366
30.440	6.112
28.400	5.757
27.420	5.583
26.600	5.435
25.530	5.253
24.570	5.078
23.960	4.964
22.290	4.681
22.010	4.628
21.360	4.511
15.090	3.435

MAVIS II: CAIRNYHILL (P WAVE)

SHOT POSITION = 47.370 KM

OBSERVED TRAVEL TIMES

RANGE (KM)	TRAVEL TIME (S)	ERROR (+) (S)	ERROR (-) (S)	RED TIME (S)
1.130	0.360	0.030	0.030	0.172
3.830	1.090	0.030	0.030	0.452
5.390	1.430	0.030	0.030	0.532
6.170	1.630	0.030	0.030	0.602
7.130	1.760	0.030	0.030	0.572
8.270	2.110	0.030	0.030	0.732
9.170	2.360	0.030	0.030	0.832
12.670	3.020	0.030	0.030	0.908
12.170	2.900	0.030	0.030	0.872
11.420	2.680	0.030	0.030	0.777
11.200	2.580	0.030	0.030	0.713
11.200	2.630	0.030	0.030	0.763
10.890	2.580	0.030	0.030	0.765
8.410	2.060	0.030	0.030	0.658
7.460	1.850	0.030	0.030	0.607
5.300	1.340	0.030	0.030	0.457

5.030	1.230	0.030	0.030	0.392
4.040	1.020	0.030	0.030	0.347
3.080	0.780	0.030	0.030	0.267
2.270	0.580	0.030	0.030	0.202

CALCULATED TRAVEL TIMES

RAY CODE = A1

RANGE (KM)	CALC TIME (S)
0.000	0.000
1.130	0.300
3.830	0.960
5.390	1.310
6.170	1.490
7.130	1.710
8.270	1.960
9.170	2.150
12.670	2.950
12.170	2.840
11.420	2.690
11.200	2.640
10.890	2.580
8.410	2.050
7.460	1.840
5.300	1.330
5.030	1.270
4.040	1.030
3.080	0.790
2.270	0.600
0.000	0.000

MAVIS II: TAMSLOUP (P WAVE)

SHOT POSITION = 49.620 KM

OBSERVED TRAVEL TIMES

RANGE (KM)	TRAVEL TIME (S)	ERROR (+) (S)	ERROR (-) (S)	RED TIME (S)
11.590	2.680	0.030	0.030	0.748
10.570	2.470	0.030	0.030	0.708
9.610	2.250	0.030	0.030	0.648
8.370	2.000	0.030	0.030	0.605
4.390	1.100	0.030	0.030	0.368

CALCULATED TRAVEL TIMES

RAY CODE = A1

RANGE (KM)	CALC TIME (S)
0.000	0.000
4.390	1.105
8.370	1.992
9.610	2.263
10.570	2.471
11.590	2.695

MAVIS II: HEADLESS CROSS (P WAVE)

SHOT POSITION = 55,900 KM

OBSERVED TRAVEL TIMES

RANGE (KM)	TRAVEL TIME (S)	ERROR (+) (S)	ERROR (-) (S)	RED TIME (S)
15,070	3,160	0,030	0,030	0,648
13,820	2,970	0,030	0,030	0,667
12,290	2,610	0,030	0,030	0,562
10,200	2,240	0,030	0,030	0,540
9,750	2,140	0,030	0,030	0,515
9,510	2,100	0,030	0,030	0,515
8,710	1,980	0,030	0,030	0,528
8,640	1,960	0,030	0,030	0,520
8,430	1,920	0,030	0,030	0,515
8,020	1,840	0,030	0,030	0,503
7,780	1,800	0,030	0,030	0,503
7,540	1,770	0,030	0,030	0,513
7,320	1,630	0,030	0,030	0,410
7,110	1,610	0,030	0,030	0,425
6,550	1,600	0,030	0,030	0,508
6,450	1,510	0,030	0,030	0,435
6,430	1,510	0,030	0,030	0,438
6,150	1,470	0,030	0,030	0,445
5,920	1,430	0,030	0,030	0,443
5,890	1,350	0,030	0,030	0,368
5,770	1,360	0,030	0,030	0,398
5,640	1,300	0,030	0,030	0,360
5,510	1,300	0,030	0,030	0,382
5,410	1,260	0,030	0,030	0,358
5,250	1,260	0,030	0,030	0,385
5,140	1,280	0,030	0,030	0,423
4,880	1,260	0,030	0,030	0,447
4,630	1,200	0,030	0,030	0,428
4,480	1,170	0,030	0,030	0,423
4,260	1,130	0,030	0,030	0,420
4,050	1,090	0,030	0,030	0,415
3,670	1,020	0,030	0,030	0,408
3,470	0,970	0,030	0,030	0,392
3,240	0,880	0,030	0,030	0,340
3,140	0,840	0,030	0,030	0,317
2,870	0,790	0,030	0,030	0,312
2,700	0,750	0,030	0,030	0,300
2,660	0,740	0,030	0,030	0,297
2,580	0,710	0,030	0,030	0,280
2,540	0,700	0,030	0,030	0,277
2,430	0,700	0,030	0,030	0,295
2,300	0,660	0,030	0,030	0,277
2,300	0,670	0,030	0,030	0,287
2,280	0,630	0,030	0,030	0,250
2,200	0,620	0,030	0,030	0,253
1,930	0,580	0,030	0,030	0,258
1,710	0,510	0,030	0,030	0,225
1,490	0,440	0,030	0,030	0,192
1,360	0,390	0,030	0,030	0,163
1,160	0,340	0,030	0,030	0,147
1,130	0,320	0,030	0,030	0,132

0,950	0,300	0,030	0,030	0,142
1,440	0,450	0,030	0,030	0,210
1,950	0,590	0,030	0,030	0,265
2,840	0,820	0,030	0,030	0,347
4,690	1,230	0,030	0,030	0,448
5,020	1,310	0,030	0,030	0,473
5,590	1,460	0,030	0,030	0,528
6,230	1,610	0,030	0,030	0,572
6,470	1,610	0,030	0,030	0,532
7,820	1,890	0,030	0,030	0,587
9,260	2,230	0,030	0,030	0,687
9,400	2,230	0,030	0,030	0,663
9,450	2,330	0,030	0,030	0,755
10,580	2,490	0,030	0,030	0,727
10,670	2,580	0,030	0,030	0,802
11,160	2,630	0,030	0,030	0,770
11,590	2,780	0,030	0,030	0,848
12,350	2,850	0,030	0,030	0,792
12,900	2,950	0,030	0,030	0,800
13,260	3,040	0,030	0,030	0,830
13,830	3,120	0,030	0,030	0,815
13,830	3,120	0,030	0,030	0,815
14,160	3,210	0,030	0,030	0,850
15,330	3,360	0,030	0,030	0,805
15,620	3,440	0,030	0,030	0,837
16,150	3,540	0,030	0,030	0,848
16,790	3,620	0,030	0,030	0,822
17,250	3,710	0,030	0,030	0,835
17,790	3,810	0,030	0,030	0,845
18,050	3,880	0,030	0,030	0,872
18,500	4,000	0,030	0,030	0,917
19,140	4,020	0,030	0,030	0,830
19,850	4,170	0,030	0,030	0,862
21,500	4,380	0,030	0,030	0,797

CALCULATED TRAVEL TIMES

RAY CODE = A1

RANGE (KM)	CALC TIME (S)
0,000	0,000
1,440	0,430
1,950	0,570
2,840	0,780
4,690	1,210
5,020	1,270
5,590	1,410
6,230	1,560
6,470	1,610
7,820	1,910
9,260	2,230
9,400	2,250
9,450	2,270
10,580	2,490
10,670	2,530
11,160	2,610
11,590	2,700
12,350	2,850
12,900	2,960

13,260	3,040
13,830	3,160
13,830	3,150
14,160	3,230
15,330	3,470

5,140	1,350
4,880	1,270
4,630	1,230
4,480	1,190
4,260	1,140
4,050	1,090
3,670	1,010
3,470	0,950
3,240	0,900
3,140	0,870
2,870	0,810
2,700	0,780
2,660	0,760
2,580	0,750
2,540	0,730
2,430	0,690
2,300	0,670
2,300	0,670
2,280	0,670
2,200	0,630
1,930	0,560
1,710	0,510
1,490	0,450
1,360	0,410
1,160	0,360
1,130	0,340
0,950	0,290
0,000	0,000

RAY CODE = A3

RANGE (KM)	CALC TIME (S)
7,820	1,980
9,260	2,260
9,400	2,300
9,450	2,290
10,580	2,510
10,670	2,530
11,160	2,620
11,590	2,690
12,350	2,850
12,900	2,940
13,260	3,000
13,830	3,120
13,830	3,120
14,160	3,190
15,330	3,400
15,620	3,450
16,150	3,550
16,790	3,660
17,250	3,760
17,790	3,850
18,050	3,890
18,500	3,980

19.140	4.090
19.850	4.210
21.500	4.510
15.070	3.140
13.820	2.910
12.290	2.630
10.200	2.250
9.750	2.160
9.510	2.120
8.710	1.980
8.640	1.960
8.430	1.920
8.020	1.840
7.780	1.800
7.540	1.750
7.320	1.710
7.110	1.680
6.550	1.560
6.450	1.540
6.430	1.540
6.150	1.490
5.920	1.460
5.890	1.440
5.770	1.430
5.640	1.390
5.510	1.390
5.410	1.360
5.250	1.350
5.140	1.320
4.880	1.280
4.630	1.250
4.480	1.240

MAVIS II: CAIRNGRYFFE (P WAVE)

SHOT POSITION = 73.170 KM

OBSERVED TRAVEL TIMES

RANGE (KM)	TRAVEL TIME (S)	ERROR (+) (S)	ERROR (-) (S)	RED TIME (S)
14.670	3.000	0.030	0.030	0.555
9.210	1.920	0.030	0.030	0.385
6.890	1.410	0.030	0.030	0.262
3.140	0.700	0.030	0.030	0.177

CALCULATED TRAVEL TIMES

RAY CODE = A3(d)

RANGE (KM)	CALC TIME (S)
0.000	0.000
3.140	0.688
6.890	1.486
9.210	1.947
14.670	3.022

SOLA NORTH: MEDROX (P WAVE)

SHOT POSITION = 0.000 KM

OBSERVED TRAVEL TIMES

RANGE (KM)	TRAVEL TIME (S)	ERROR (+) (S)	ERROR (-) (S)	RED TIME (S)
1.060	0.310	0.030	0.030	0.133
2.810	0.840	0.030	0.030	0.372
3.870	1.160	0.030	0.030	0.515
4.790	1.340	0.030	0.030	0.542
5.560	1.520	0.030	0.030	0.593
7.110	1.890	0.030	0.030	0.705
7.820	2.140	0.030	0.030	0.837
9.800	2.410	0.030	0.030	0.777
11.010	2.690	0.030	0.030	0.855
11.530	2.860	0.030	0.030	0.938
13.720	3.300	0.030	0.030	1.013
15.080	3.530	0.030	0.030	1.017
15.500	3.600	0.030	0.030	1.017
15.910	3.660	0.030	0.030	1.008
18.070	4.030	0.030	0.030	1.018
18.840	4.080	0.030	0.030	0.940
20.880	4.450	0.030	0.030	0.970
22.420	4.800	0.030	0.030	1.063
25.060	5.220	0.030	0.030	1.043

CALCULATED TRAVEL TIMES

RAY CODE = A1

RANGE (KM)	CALC TIME (S)
0.000	0.000
1.060	0.320
2.810	0.850
3.870	1.120
4.790	1.350
5.560	1.540
7.110	1.900
7.820	2.070
9.800	2.500
11.010	2.750
11.530	2.860
13.720	3.330

RAY CODE = A3

RANGE (KM)	CALC TIME (S)
11.010	2.790
11.530	2.890
13.720	3.280
15.080	3.520
15.500	3.600
15.910	3.670
18.070	4.050
18.840	4.190
20.880	4.530
22.420	4.820
25.060	5.340

RAY CODE = A5

RANGE (KM)	CALC TIME (S)
20.880	4.560
22.420	4.830
25.060	5.310

SOLA SOUTH: TAMSLOUP (P WAVE)

SHOT POSITION = 0.000 KM

OBSERVED TRAVEL TIMES

RANGE (KM)	TRAVEL TIME (S)	ERROR (+) (S)	ERROR (-) (S)	RED TIME (S)
0.370	0.070	0.030	0.030	0.008
0.590	0.130	0.030	0.030	0.032
1.270	0.370	0.030	0.030	0.158
2.090	0.620	0.030	0.030	0.272
2.140	0.650	0.030	0.030	0.293
2.340	0.700	0.030	0.030	0.310
2.610	0.740	0.030	0.030	0.305
3.170	0.880	0.030	0.030	0.352
3.430	0.940	0.030	0.030	0.368
3.670	1.010	0.030	0.030	0.398
4.110	1.090	0.030	0.030	0.405
4.320	1.200	0.030	0.030	0.480
4.560	1.220	0.030	0.030	0.460
5.380	1.440	0.030	0.030	0.543
5.630	1.490	0.030	0.030	0.552
5.870	1.540	0.030	0.030	0.562
6.790	1.670	0.030	0.030	0.538
6.620	1.700	0.030	0.030	0.597
7.090	1.790	0.030	0.030	0.608
7.310	1.830	0.030	0.030	0.612
7.540	1.870	0.030	0.030	0.613
7.880	1.950	0.030	0.030	0.637
8.230	2.050	0.030	0.030	0.678
8.600	2.110	0.030	0.030	0.677
9.060	2.200	0.030	0.030	0.690
9.310	2.240	0.030	0.030	0.688
9.670	2.440	0.030	0.030	0.828
10.160	2.400	0.030	0.030	0.707
10.270	2.440	0.030	0.030	0.728
11.060	2.580	0.030	0.030	0.737
11.300	2.670	0.030	0.030	0.787
11.870	2.810	0.030	0.030	0.832
11.900	2.840	0.030	0.030	0.857
12.160	2.870	0.030	0.030	0.843
12.410	2.900	0.030	0.030	0.832
12.540	2.970	0.030	0.030	0.880
12.780	2.990	0.030	0.030	0.860
13.020	3.050	0.030	0.030	0.880
13.430	3.080	0.030	0.030	0.842
13.650	3.130	0.030	0.030	0.855
14.170	3.250	0.030	0.030	0.888
14.980	3.390	0.030	0.030	0.893
15.240	3.420	0.030	0.030	0.880
16.030	3.600	0.030	0.030	0.928

16.250	3.630	0.030	0.030	0.922
17.360	3.830	0.030	0.030	0.937
18.300	3.920	0.030	0.030	0.870
18.550	3.960	0.030	0.030	0.868
19.610	4.080	0.030	0.030	0.812
20.160	4.160	0.030	0.030	0.800
20.980	4.320	0.030	0.030	0.823
21.200	4.350	0.030	0.030	0.817
22.400	4.630	0.030	0.030	0.897
22.590	4.660	0.030	0.030	0.895
22.850	4.690	0.030	0.030	0.882

CALCULATED TRAVEL TIMES

RAY CODE = A1

RANGE (KM)	CALC TIME (S)
0.000	0.000
0.370	0.110
0.590	0.170
1.270	0.380
2.090	0.610
2.140	0.610
2.340	0.670
2.610	0.750
3.170	0.900
3.430	0.960
3.670	1.030
4.110	1.120
4.320	1.180
4.560	1.230
5.380	1.420
5.870	1.530
6.790	1.730
6.620	1.690
7.090	1.800
7.310	1.840
7.540	1.900
7.880	1.960
8.230	2.040
8.600	2.110
9.060	2.210
9.310	2.260
9.670	2.340
10.160	2.430
10.270	2.450
11.060	2.620
11.300	2.660
11.870	2.780
11.900	2.790
12.160	2.840
12.410	2.890
12.540	2.920
12.780	2.970
13.020	3.020
13.430	3.100
13.650	3.150
14.170	3.250
14.980	3.420

15.230	3.460

RAY CODE = A3

RANGE (KM)	CALC TIME (S)
11.060	2.670
11.300	2.710
11.870	2.820
11.900	2.820
12.160	2.860
12.410	2.910
12.540	2.940
12.780	2.980
13.020	3.020
13.430	3.100
13.650	3.140
14.170	3.240
14.980	3.390
15.240	3.430
16.030	3.590
16.250	3.620
17.360	3.830
18.300	4.000

RAY CODE = A5

RANGE (KM)	CALC TIME (S)
15.230	3.480
16.030	3.610
16.250	3.650
17.360	3.830
18.300	3.990
22.590	4.620
22.850	4.660

SOLA SOUTH: KAIMES (P WAVE)

SHOT POSITION = 24.860 KM

OBSERVED TRAVEL TIMES

RANGE (KM)	TRAVEL TIME (S)	ERROR (+) (S)	ERROR (-) (S)	RED TIME (S)
32.500	6.320	0.030	0.030	0.903
30.200	5.930	0.030	0.030	0.897
27.020	5.490	0.030	0.030	0.987
24.200	4.900	0.030	0.030	0.867
22.240	4.540	0.030	0.030	0.833
21.270	4.400	0.030	0.030	0.855
20.550	4.230	0.030	0.030	0.805
17.320	3.740	0.030	0.030	0.853
16.990	3.550	0.030	0.030	0.718
15.540	3.420	0.030	0.030	0.830
14.800	3.320	0.030	0.030	0.853
14.680	3.300	0.030	0.030	0.853
13.550	3.070	0.030	0.030	0.812
13.080	2.890	0.030	0.030	0.710
12.870	2.870	0.030	0.030	0.725
12.610	2.830	0.030	0.030	0.728
12.370	2.790	0.030	0.030	0.728

12.170	2.750	0.030	0.030	0.722
12.030	2.720	0.030	0.030	0.715
11.860	2.690	0.030	0.030	0.713
10.100	2.290	0.030	0.030	0.607
9.860	2.260	0.030	0.030	0.617
9.630	2.220	0.030	0.030	0.615
8.870	2.030	0.030	0.030	0.552
6.560	1.550	0.030	0.030	0.457
5.260	1.230	0.030	0.030	0.353
4.030	0.950	0.030	0.030	0.278
3.890	0.940	0.030	0.030	0.292
3.660	0.910	0.030	0.030	0.300
3.420	0.880	0.030	0.030	0.310
2.030	0.590	0.030	0.030	0.252
1.390	0.390	0.030	0.030	0.158
5.190	1.190	0.030	0.030	0.325
6.270	1.400	0.030	0.030	0.355
7.310	1.590	0.030	0.030	0.372
8.600	1.840	0.030	0.030	0.407
10.150	2.150	0.030	0.030	0.458
10.790	2.260	0.030	0.030	0.462
11.490	2.380	0.030	0.030	0.465

CALCULATED TRAVEL TIMES

RAY CODE = A1

RANGE (KM)	CALC TIME (S)
0.000	0.000
2.030	0.590
0.000	0.000
1.390	0.400

RAY CODE = A3

RANGE (KM)	CALC TIME (S)
16.990	3.710
15.540	3.410
14.800	3.270
14.680	3.240
13.550	3.000
13.080	2.910
12.870	2.870
12.610	2.810
12.370	2.760
12.170	2.720
12.030	2.690
11.860	2.650
10.100	2.290
9.860	2.250
9.630	2.190
8.870	2.040
6.560	1.530
5.260	1.230
4.030	0.990
3.890	0.960
3.660	0.910
3.420	0.860
2.030	0.570

5.190	1.200
6.270	1.410
7.310	1.620
8.600	1.880
10.150	2.140
10.790	2.260
11.490	2.380

RAY CODE = A5

RANGE (KM)	CALC TIME (S)
13.550	3.090
14.680	3.280
14.800	3.300
15.540	3.420
16.990	3.680
17.320	3.730
20.550	4.270
21.270	4.390
22.240	4.550
24.200	4.890
27.020	5.380
30.200	5.940
32.500	6.320

MAVIS III: CRUIKS (P WAVE)

SHOT POSITION = 5.000 KM

OBSERVED TRAVEL TIMES

RANGE (KM)	TRAVEL TIME (S)	ERROR (+) (S)	ERROR (-) (S)	RED TIME (S)
19.680	4.150	0.050	0.050	0.870
18.870	4.070	0.030	0.030	0.925
18.350	3.970	0.030	0.030	0.912
17.530	3.870	0.030	0.030	0.948
15.480	3.390	0.050	0.050	0.810
12.680	2.940	0.030	0.030	0.827
12.680	2.910	0.030	0.030	0.797
10.600	2.590	0.030	0.030	0.823
10.600	2.560	0.030	0.030	0.793
8.140	2.060	0.030	0.030	0.703
6.540	1.710	0.030	0.030	0.620
5.490	1.480	0.030	0.030	0.565
4.600	1.260	0.030	0.030	0.493
3.370	0.920	0.030	0.030	0.358
3.370	0.950	0.030	0.030	0.388
1.070	0.340	0.030	0.030	0.162
0.410	0.080	0.030	0.030	0.012
2.640	0.710	0.030	0.030	0.270
3.680	1.010	0.030	0.030	0.397

CALCULATED TRAVEL TIMES

RAY CODE = A1

RANGE (KM)	CALC TIME (S)
0.000	0.000

0.410	0.130
1.070	0.320
3.370	0.970
4.600	1.270
5.490	1.480
6.540	1.720
8.140	2.070
10.600	2.580
0.000	0.000
2.640	0.740
3.680	1.000

RAY CODE = A3

RANGE (KM)	CALC TIME (S)
19.680	4.190
18.870	4.040
18.350	3.940
17.530	3.790
15.480	3.400
8.140	2.110

MAVIS III: HILLWOOD (P WAVE)

SHOT POSITION = 14.920 KM

OBSERVED TRAVEL TIMES

RANGE (KM)	TRAVEL TIME (S)	ERROR (+) (S)	ERROR (-) (S)	RED TIME (S)
10.500	2.280	0.100	0.100	0.530
8.950	2.130	0.030	0.030	0.638
7.610	1.860	0.030	0.030	0.592
6.560	1.650	0.030	0.030	0.557
4.810	1.250	0.030	0.030	0.448
2.770	0.770	0.030	0.030	0.308
1.420	0.440	0.030	0.030	0.203
0.400	0.140	0.030	0.030	0.073
1.780	0.530	0.030	0.030	0.233
2.220	0.650	0.030	0.030	0.280
3.380	1.040	0.030	0.030	0.477
4.160	1.240	0.030	0.030	0.547
5.430	1.540	0.030	0.030	0.635
8.910	2.190	0.030	0.030	0.705

CALCULATED TRAVEL TIMES

RAY CODE = A1

RANGE (KM)	CALC TIME (S)
0.000	0.000
0.400	0.120
1.420	0.430
2.770	0.850
0.000	0.000
1.780	0.550

2.220	0.670
3.380	1.020
4.160	1.240
5.430	1.540
8.910	2.230

RAY CODE = A3

RANGE (KM)	CALC TIME (S)
10.500	2.410
8.950	2.090
7.610	1.820
6.560	1.600
4.810	1.240
2.770	0.790

MAVIS III: KAIMES (P WAVE)

SHOT POSITION = 20.260 KM

OBSERVED TRAVEL TIMES

RANGE (KM)	TRAVEL TIME (S)	ERROR (+) (S)	ERROR (-) (S)	RED TIME (S)
5.160	1.360	0.030	0.030	0.500
3.610	1.000	0.030	0.030	0.398
2.280	0.710	0.030	0.030	0.330
1.220	0.440	0.030	0.030	0.237
0.290	0.150	0.030	0.030	0.102
0.560	0.200	0.030	0.030	0.107
0.920	0.320	0.030	0.030	0.167
1.450	0.450	0.030	0.030	0.208
1.710	0.500	0.030	0.030	0.215
2.610	0.730	0.030	0.030	0.295
3.930	1.050	0.030	0.030	0.395
4.660	1.220	0.030	0.030	0.443
5.120	1.310	0.030	0.030	0.457
5.170	1.300	0.030	0.030	0.438
7.130	1.720	0.030	0.030	0.532
7.560	1.850	0.030	0.030	0.590
8.730	2.100	0.030	0.030	0.645
9.450	2.270	0.030	0.030	0.695
9.780	2.320	0.030	0.030	0.690
10.760	2.510	0.050	0.050	0.717
11.990	2.820	0.050	0.050	0.822
14.240	3.200	0.050	0.050	0.827
14.860	3.440	0.050	0.050	0.963
15.970	3.750	0.050	0.050	1.088
18.940	4.200	0.030	0.030	1.043
19.960	4.330	0.030	0.030	1.003
3.330	0.910	0.030	0.030	0.355

CALCULATED TRAVEL TIMES

RAY CODE = A1

RANGE (KM)	CALC TIME (S)
0.000	0.000
0.290	0.090

1,220	0,390
2,280	0,740
3,610	1,160
0,000	0,000
0,560	0,180
0,920	0,300
1,450	0,470
1,710	0,550
2,610	0,840

RAY CODE = A3

RANGE (KM)	CALC TIME (S)
5,160	1,370
3,610	1,020
2,280	0,730
1,220	0,490
11,990	2,730
10,760	2,500
9,780	2,310
9,450	2,240
8,730	2,100
7,560	1,870
7,130	1,770
5,170	1,320
5,120	1,310
4,660	1,200
3,930	1,050
3,330	0,930
2,610	0,780
1,710	0,580
1,450	0,520

RAY CODE = A5

RANGE (KM)	CALC TIME (S)
19,960	4,350
18,940	4,180
15,970	3,670

APPENDIX 3b. OBSERVED TRAVEL TIMES: S-WAVE

Ray codes refer to Table 5.1. Reduction velocity = 3.5 km/s

MAVIS I: TREARNE (S WAVE)

SHOT POSITION = 0.410 KM

OBSERVED TRAVEL TIMES

RANGE (KM)	TRAVEL TIME (S)	ERROR (+) (S)	ERROR (-) (S)	RED TIME (S)
0.410	0.290	0.060	0.060	0.173
1.850	1.290	0.060	0.060	0.761
5.450	2.670	0.060	0.060	1.113
8.050	4.050	0.060	0.060	1.750
8.050	3.520	0.060	0.060	1.220
10.170	4.140	0.060	0.060	1.234
18.460	7.100	0.100	0.100	1.826

MAVIS I: DRUMGRAY (S WAVE)

SHOT POSITION = 43.760 KM

OBSERVED TRAVEL TIMES

RANGE (KM)	TRAVEL TIME (S)	ERROR (+) (S)	ERROR (-) (S)	RED TIME (S)
8.460	4.270	0.060	0.060	1.853
6.780	3.290	0.060	0.060	1.353
4.220	2.820	0.060	0.060	1.614
2.730	1.570	0.060	0.060	0.790
1.700	1.160	0.060	0.060	0.674
1.340	1.000	0.060	0.060	0.617
0.980	0.820	0.060	0.060	0.540
3.650	1.920	0.060	0.060	0.877
4.730	2.700	0.060	0.060	1.349
6.840	3.280	0.100	0.100	1.326
7.750	3.690	0.060	0.060	1.476
9.190	4.210	0.100	0.100	1.584
11.800	5.120	0.060	0.060	1.749

MAVIS I: AVONBRIDGE (S WAVE)

SHOT POSITION = 58.250 KM

OBSERVED TRAVEL TIMES

RANGE (KM)	TRAVEL TIME (S)	ERROR (+) (S)	ERROR (-) (S)	RED TIME (S)
23.000	8.620	0.060	0.060	2.049
21.320	8.070	0.100	0.100	1.979
16.180	6.510	0.060	0.060	1.887
13.610	5.780	0.100	0.100	1.891
13.960	5.860	0.060	0.060	1.871
10.990	4.610	0.060	0.060	1.470
10.990	5.000	0.060	0.060	1.860
10.040	4.730	0.100	0.100	1.861
7.870	3.660	0.060	0.060	1.411
4.660	2.450	0.060	0.060	1.119

2.790	1.460	0.060	0.060	0.663
1.510	0.890	0.060	0.060	0.459
0.980	0.610	0.060	0.060	0.330
2.210	1.430	0.100	0.100	0.799
4.350	2.210	0.060	0.060	0.967
5.400	2.560	0.060	0.060	1.017
6.060	2.810	0.060	0.060	1.079
8.910	3.980	0.060	0.060	1.434
12.980	5.460	0.060	0.060	1.751
13.760	5.530	0.060	0.060	1.599
15.560	6.060	0.100	0.100	1.614
16.610	6.250	0.060	0.060	1.504

MAVIS I: BALLIKINRAIN (S WAVE)

SHOT POSITION = 0.000 KM

OBSERVED TRAVEL TIMES

RANGE (KM)	TRAVEL TIME (S)	ERROR (+) (S)	ERROR (-) (S)	RED TIME (S)
0.230	0.170	0.060	0.060	0.104
1.290	0.780	0.060	0.060	0.411
2.190	1.070	0.060	0.060	0.444
3.610	1.720	0.060	0.060	0.689
5.620	2.460	0.060	0.060	0.854
7.450	3.360	0.060	0.060	1.231
13.440	5.560	0.060	0.060	1.720
16.640	6.550	0.060	0.060	1.796
16.640	6.450	0.060	0.060	1.696
17.760	6.970	0.060	0.060	1.896
17.760	6.860	0.060	0.060	1.786
19.430	7.330	0.060	0.060	1.779
20.060	7.810	0.060	0.060	2.079
22.900	8.280	0.060	0.060	1.737
26.540	9.280	0.100	0.100	1.697
27.010	10.220	0.060	0.060	2.503
29.640	10.290	0.060	0.060	1.821

MAVIS I: NORTH THIRD (S WAVE)

SHOT POSITION = 19.180 KM

OBSERVED TRAVEL TIMES

RANGE (KM)	TRAVEL TIME (S)	ERROR (+) (S)	ERROR (-) (S)	RED TIME (S)
17.970	6.840	0.060	0.060	1.706
15.580	6.040	0.060	0.060	1.589
13.650	5.390	0.060	0.060	1.490
11.810	4.890	0.060	0.060	1.516
11.110	4.600	0.060	0.060	1.426
7.330	3.470	0.060	0.060	1.376
5.810	2.790	0.060	0.060	1.130
3.680	1.890	0.060	0.060	0.839
2.540	1.420	0.060	0.060	0.694
1.420	0.690	0.060	0.060	0.284

0,920	0,560	0,060	0,060	0,297
2,200	1,250	0,060	0,060	0,621
3,810	2,040	0,060	0,060	0,951
6,050	3,000	0,060	0,060	1,271
7,360	3,570	0,060	0,060	1,467
7,830	3,900	0,060	0,060	1,663
10,540	4,780	0,060	0,060	1,769

MAVIS I: CATTLE MOSS (S WAVE)

SHOT POSITION = 43,880 KM

OBSERVED TRAVEL TIMES

RANGE (KM)	TRAVEL TIME (S)	ERROR (+) (S)	ERROR (-) (S)	RED TIME (S)
16,910	6,400	0,100	0,100	1,569
11,750	5,110	0,100	0,100	1,753
10,730	4,760	0,100	0,100	1,694
7,300	3,730	0,060	0,060	1,644
5,800	2,850	0,100	0,100	1,193
5,800	3,070	0,100	0,100	1,413
5,280	2,940	0,100	0,100	1,431
4,400	2,410	0,060	0,060	1,153
3,380	2,090	0,060	0,060	1,124
2,570	1,510	0,060	0,060	0,776
0,380	0,360	0,060	0,060	0,251
1,190	0,820	0,060	0,060	0,480
2,800	1,830	0,060	0,060	1,030
3,940	2,590	0,060	0,060	1,464
6,640	3,660	0,060	0,060	1,763
8,750	4,570	0,060	0,060	2,070
11,380	5,160	0,060	0,060	1,909
13,780	5,860	0,100	0,100	1,923
16,330	6,760	0,060	0,060	2,094
18,150	7,490	0,100	0,100	2,304
20,420	8,050	0,060	0,060	2,216

MAVIS II: ABERUTHVEN (S WAVE)

SHOT POSITION = 0,000 KM

OBSERVED TRAVEL TIMES

RANGE (KM)	TRAVEL TIME (S)	ERROR (+) (S)	ERROR (-) (S)	RED TIME (S)
0,230	0,170	0,060	0,060	0,104
1,100	0,580	0,060	0,060	0,266
2,270	0,890	0,060	0,060	0,241
2,800	1,140	0,060	0,060	0,340
4,090	1,720	0,060	0,060	0,551
5,280	2,210	0,060	0,060	0,701
6,430	2,690	0,060	0,060	0,853
7,140	2,740	0,060	0,060	0,700
7,140	2,920	0,060	0,060	0,880
8,950	3,380	0,060	0,060	0,823
10,260	3,650	0,060	0,060	0,719

11.390	4.240	0.060	0.060	0.986
12.540	4.650	0.100	0.100	1.067
13.770	4.960	0.060	0.060	1.026
14.490	5.510	0.060	0.060	1.370
17.450	6.300	0.060	0.060	1.314
19.440	7.060	0.060	0.060	1.506

MAVIS II: DOLLAR (S WAVE)

SHOT POSITION = 16.660 KM

OBSERVED TRAVEL TIMES

RANGE (KM)	TRAVEL TIME (S)	ERROR (+) (S)	ERROR (-) (S)	RED TIME (S)
16.560	6.370	0.060	0.060	1.639
14.570	5.930	0.060	0.060	1.767
13.860	5.450	0.060	0.060	1.490
12.580	5.120	0.060	0.060	1.526
11.420	4.660	0.100	0.100	1.397
10.290	4.250	0.100	0.100	1.310
9.630	4.060	0.060	0.060	1.309
7.790	2.910	0.060	0.060	0.684
7.790	3.360	0.060	0.060	1.134
6.880	3.400	0.060	0.060	1.434
6.880	3.000	0.060	0.060	1.034
5.340	2.750	0.060	0.060	1.224
3.000	1.770	0.100	0.100	0.913
2.180	1.760	0.060	0.060	1.137
0.990	0.840	0.060	0.060	0.557
0.850	0.740	0.060	0.060	0.497
1.830	1.170	0.060	0.060	0.647
2.890	1.740	0.060	0.060	0.914
4.690	2.630	0.100	0.100	1.290
5.760	3.290	0.060	0.060	1.644
7.460	3.830	0.060	0.060	1.699
9.580	4.090	0.060	0.060	1.353
12.920	5.100	0.060	0.060	1.409
18.150	6.960	0.060	0.060	1.774
18.590	7.140	0.060	0.060	1.829
24.640	9.050	0.100	0.100	2.010
25.620	9.310	0.060	0.060	1.990
26.940	9.430	0.100	0.100	1.733
26.940	9.950	0.100	0.100	2.253
28.580	10.160	0.060	0.060	1.994
29.190	10.430	0.060	0.060	2.090
30.270	10.630	0.060	0.060	1.981
31.290	10.810	0.060	0.060	1.870

MAVIS II: LONGANNET (S WAVE)

SHOT POSITION = 26.790 KM

OBSERVED TRAVEL TIMES

RANGE (KM)	TRAVEL TIME (S)	ERROR (+) (S)	ERROR (-) (S)	RED TIME (S)

26,690	9,680	0,100	0,100	2,054
24,690	8,810	0,100	0,100	1,756
24,690	9,180	0,060	0,060	2,126
22,710	8,400	0,100	0,100	1,911
21,540	8,240	0,060	0,060	2,086
20,410	7,850	0,060	0,060	2,019
17,900	7,030	0,060	0,060	1,916
16,840	6,460	0,100	0,100	1,649
15,440	6,020	0,100	0,100	1,609
11,010	4,580	0,060	0,060	1,434
7,430	2,940	0,060	0,060	0,817
6,450	2,830	0,060	0,060	0,987
4,840	2,120	0,060	0,060	0,737
3,380	1,470	0,060	0,060	0,504
0,550	0,470	0,060	0,060	0,313
6,700	2,700	0,060	0,060	0,786
8,120	3,260	0,100	0,100	0,940
8,590	3,750	0,060	0,060	1,296
10,110	4,480	0,100	0,100	1,591
14,120	5,380	0,100	0,100	1,346
14,120	5,740	0,100	0,100	1,706
14,870	5,780	0,060	0,060	1,531
15,830	6,260	0,060	0,060	1,737
17,090	6,800	0,100	0,100	1,917
18,740	7,280	0,100	0,100	1,926
19,340	7,750	0,060	0,060	2,224
20,420	7,730	0,100	0,100	1,896

MAVIS II: AVONBRIDGE (S WAVE)

SHOT POSITION = 39,500 KM

OBSERVED TRAVEL TIMES

RANGE (KM)	TRAVEL TIME (S)	ERROR (+) (S)	ERROR (-) (S)	RED TIME (S)
7,150	3,380	0,060	0,060	1,337
5,500	2,810	0,100	0,100	1,239
5,000	2,550	0,060	0,060	1,121
4,420	2,180	0,060	0,060	0,917
1,510	0,790	0,100	0,100	0,359
1,040	0,510	0,060	0,060	0,213
0,480	0,420	0,060	0,060	0,283
0,820	0,770	0,060	0,060	0,536
1,610	0,940	0,100	0,100	0,480
2,600	1,450	0,100	0,100	0,707
3,950	1,990	0,060	0,060	0,861
4,710	2,250	0,060	0,060	0,904
5,570	2,900	0,060	0,060	1,309
6,180	3,450	0,060	0,060	1,684
7,250	3,440	0,100	0,100	1,369
8,240	3,880	0,060	0,060	1,526

MAVIS II: BLAIRHILL (S WAVE)

SHOT POSITION = 47,680 KM

OBSERVED TRAVEL TIMES

RANGE (KM)	TRAVEL TIME (S)	ERROR (+) (S)	ERROR (-) (S)	RED TIME (S)
15.090	6.160	0.060	0.060	1.849
13.500	5.410	0.060	0.060	1.553
13.000	5.320	0.060	0.060	1.606
12.450	4.690	0.060	0.060	1.133
9.710	4.240	0.100	0.100	1.466
7.420	3.210	0.100	0.100	1.090
6.650	2.750	0.100	0.100	0.850
5.680	2.470	0.060	0.060	0.847
4.460	1.630	0.060	0.060	0.356
3.620	1.770	0.100	0.100	0.736
2.870	1.270	0.060	0.060	0.450
2.340	1.400	0.060	0.060	0.731
1.430	0.670	0.060	0.060	0.261
0.150	0.120	0.060	0.060	0.077

APPENDIX 4. MAVIS I PLUS TIMES

MAVIS I (SOUTH)

SITE NO.	ORS REFR	REVERSED POINT?	BASEMENT REFR 6.00km/s	REVERSED POINT?	BASEMENT REFR 6.40km/s	REVERSED POINT?	BASEMENT REFR 6.53km/s	REVERSED POINT?
S1	0.35	-	0.92	-	1.37	-	1.58	-
S2	0.39	-	0.92	-	1.48	-	1.68	-
S3	0.43	-	0.92	-	1.38	-	1.57	-
S4	0.46	-	0.99	-	1.49	-	1.67	-
S5	0.48	-	0.93	-	1.50	-	1.68	-
S6	0.52	-	0.92	-	1.46	-	1.64	-
S7	0.57	-	0.92	-	1.39	-	1.55	-
S8	0.57	-	0.92	-	1.44	-	1.64	-
S9	0.62	YES	0.94	-	1.45	-	1.59	-
S10	0.59	-	0.92	-	1.45	-	1.56	-
S11	0.62	YES	0.93	-	1.47	-	1.59	-
S12	0.65	-	0.93	-	1.46	-	1.57	-
S13	0.61	-	0.91	-	1.51	-	1.61	-
S14	0.70	-	0.97	-	1.50	-	1.60	-
S15	0.69	-	0.93	YES	1.48	-	1.57	-
S16	0.64	-	0.95	YES	1.47	-	1.56	-
S17	0.66	-	0.94	YES	1.48	-	1.55	-
S18	-	-	-	-	-	-	-	-
S19	0.65	-	0.95	YES	1.47	-	1.54	-
S19	0.62	-	0.96	-	1.46	-	1.50	-
S20	0.66	-	0.97	YES	1.44	-	1.51	-
S21	0.69	-	0.95	-	1.41	-	1.46	YES
S22	0.65	-	0.99	-	1.44	-	1.49	YES
S23	0.64	-	0.93	-	1.46	-	1.51	YES
S24	0.63	-	0.93	-	1.48	-	1.48	-
S25	0.62	-	0.95	-	1.44	-	1.48	YES
S26	0.59	-	0.99	-	1.48	-	1.50	-
S27	0.56	-	0.97	-	1.45	-	1.49	YES
S29	0.53	-	1.05	YES	-	-	-	-
S30	0.52	-	1.06	-	-	-	-	-
S31	0.52	-	1.04	-	-	-	-	-
S32	0.51	-	1.03	-	1.58	-	1.61	-
S33	0.51	-	1.07	YES	1.61	-	1.65	-
S34	0.51	-	1.06	YES	1.57	-	1.61	-
S35	0.51	-	1.07	YES	1.58	-	1.62	-
S36	0.52	-	1.02	-	1.56	-	1.61	-
S37	0.53	-	1.06	YES	1.57	-	1.61	-
S38	0.53	-	1.01	-	1.55	-	1.60	-
S39	0.55	-	1.05	-	1.52	-	1.58	-
S40	0.56	YES	1.02	-	1.52	-	1.60	-
S41	0.59	YES	1.03	-	1.48	-	1.56	-
S42	0.62	YES	1.00	YES	1.50	-	1.57	-
S43	0.61	-	0.99	YES	1.49	-	1.56	-
S44	0.62	-	1.04	-	1.50	-	1.58	-
S46	0.63	-	0.99	YES	1.50	-	1.58	-
S47	0.64	-	0.98	YES	1.49	-	1.57	-
S48	0.62	-	1.06	-	1.50	-	1.60	-
S49	0.62	-	1.05	-	1.44	-	1.59	-
S50	0.64	-	1.02	-	1.50	-	1.60	-
OXCARS	0.51	-	0.92	-	1.71	-	1.83	-
METHIL	1.32	-	1.44	-	2.01	-	2.18	-

MAVIS I (NORTH)

SITE NO.	ORS REFR	REVERSED POINT?	BASEMENT REFR 6.00km/s	REVERSED POINT?	BASEMENT REFR 6.40km/s	REVERSED POINT?	BASEMENT REFR 6.53km/s	REVERSED POINT?
N1	0.61	-	1.16	-	1.75	-	1.87	-
N2	0.62	-	1.16	-	1.67	-	1.79	-
N3	0.62	-	1.17	-	1.68	-	1.80	-
N4	0.63	-	1.15	-	1.70	-	1.81	-
N5	0.64	-	1.17	-	1.71	-	1.81	-
N6	0.66	-	1.18	-	1.69	-	1.79	-
N7	0.66	-	1.21	-	1.70	-	1.80	-
N8	0.68	-	1.22	-	1.70	-	1.80	-
N9	0.69	-	1.20	-	1.72	-	1.80	-
N10	0.72	YES	1.18	-	1.70	-	1.79	-
N11	0.82	-	1.25	-	1.73	-	1.80	-
N12	0.78	YES	1.20	-	1.74	-	1.81	-
N13	0.78	YES	1.20	-	1.73	-	1.80	-
N14	0.80	-	1.21	-	1.74	-	1.80	-
N15	0.80	YES	1.22	-	1.75	-	1.81	-
N16	0.86	-	1.22	-	1.76	-	1.81	-
N17	0.80	YES	1.22	-	1.73	-	1.78	-
N18	0.89	-	1.23	-	1.79	-	1.79	-
N19	0.96	YES	1.23	-	1.77	-	1.80	-
N20	0.98	YES	1.24	-	1.77	-	1.81	-
N21	0.90	-	1.23	-	1.77	-	1.80	-
N22	0.98	YES	1.23	-	1.75	-	1.78	-
N23	0.91	-	1.23	-	1.78	-	1.81	-
N24	0.94	YES	1.22	-	1.82	-	1.82	-
N25	0.92	YES	1.22	-	1.79	-	1.81	-
N26	0.94	-	1.20	-	1.81	-	1.82	-
N27	0.96	-	1.22	YES	1.81	-	1.82	-
N28	0.96	-	1.20	-	1.81	-	1.81	-
N29	0.97	-	1.20	YES	1.80	-	1.80	-
N30	0.96	-	1.18	YES	1.80	-	1.80	-
N31	0.97	-	1.16	YES	1.80	-	1.80	-
N32	0.98	-	1.20	-	1.79	-	1.80	-
N33	0.98	-	1.18	YES	1.79	-	1.80	-
N34	1.00	-	1.04	-	1.78	-	1.80	-
N35	0.91	-	1.04	-	1.77	-	1.79	-
N36	0.92	YES	1.02	-	1.77	-	1.79	-
N37	1.02	YES	1.12	-	1.76	-	1.80	-
N38	1.08	YES	1.10	YES	1.76	-	1.80	-
N39	1.04	YES	1.10	YES	1.74	-	1.79	-
N41	-	-	1.08	-	1.73	-	1.78	-
N42	1.10	YES	-	-	1.75	-	1.81	-
N43	1.02	YES	-	-	1.71	-	1.78	-
N44	1.16	YES	1.12	-	1.75	-	1.82	-
N45	-	-	1.06	-	1.71	-	1.78	-
N46	1.18	YES	1.11	-	1.70	-	1.77	-
N48	-	-	-	-	-	-	-	-
N48a	1.18	YES	-	-	-	-	-	-
N49	-	-	-	-	-	-	-	-
N50	1.18	-	-	-	-	-	-	-
METHIL	1.32	-	1.68	-	2.14	-	2.27	-

APPENDIX 5. OBSERVED AND CALCULATED GRAVITY DATA

GRAVITY LINE 1: BATHGATE HIGH (SHALLOW SOURCE).

NO. STNS	TREND	LENGTH
51	180.00240	49.99997

COORDS OF PROFILE ENDS

EASTING 1	NORTHING 1	EASTING 2	NORTHING 2
294.00000	294.00000	705.00000	655.00000

REGIONAL GRADN	REGIONAL TREND	ERROR
-0.170	8.000	0.200
0.000	0.000	0.000

AMBIENT FIELD

DECLINATION	INCLINATION	INTENSITY
0.00000	0.00000	0.00000

FIELD DATA

STN	EASTING	NORTHING	PRO POSIT	BOUG GRAV	TOTAL MAG
1	294.01001	704.98999	0.01001	1.50000	0.000
2	294.00000	704.00000	0.99999	1.50000	0.000
3	294.00000	703.00000	2.00000	1.00000	0.000
4	294.00000	702.00000	2.99998	1.00000	0.000
5	294.00000	701.00000	4.00000	1.70000	0.000
6	294.00000	700.00000	5.00001	3.20000	0.000
7	294.00000	699.00000	6.00000	2.00000	0.000
8	294.00000	698.00000	6.99999	-1.00000	0.000
9	294.00000	697.00000	8.00000	-2.90000	0.000
10	294.00000	696.00000	8.99999	-4.20000	0.000
11	294.00000	695.00000	9.99999	-5.20000	0.000
12	294.00000	694.00000	11.00001	-4.70000	0.000
13	294.00000	693.00000	12.00000	-4.00000	0.000
14	294.00000	692.00000	13.00001	-3.60000	0.000
15	294.00000	691.00000	14.00001	-3.20000	0.000
16	294.00000	690.00000	14.99999	-2.70000	0.000
17	294.00000	689.00000	16.00000	-1.90000	0.000
18	294.00000	688.00000	16.99998	-1.10000	0.000
19	294.00000	687.00000	17.99997	-0.40000	0.000
20	294.00000	686.00000	18.99997	0.50000	0.000
21	294.00000	685.00000	19.99997	1.50000	0.000
22	294.00000	684.00000	20.99998	2.50000	0.000
23	294.00000	683.00000	21.99998	4.00000	0.000
24	294.00000	682.00000	22.99997	6.00000	0.000
25	294.00000	681.00000	23.99998	8.30000	0.000
26	294.00000	680.00000	24.99998	10.50000	0.000
27	294.00000	679.00000	25.99998	13.00000	0.000
28	294.00000	678.00000	26.99998	14.40000	0.000
29	294.00000	677.00000	27.99998	15.70000	0.000
30	294.00000	676.00000	28.99998	17.00000	0.000
31	294.00000	675.00000	30.00000	17.60001	0.000
32	294.00000	674.00000	30.99998	18.20000	0.000
33	294.00000	673.00000	31.99998	18.50000	0.000
34	294.00000	672.00000	32.99997	18.20000	0.000
35	294.00000	671.00000	33.99995	17.20000	0.000
36	294.00000	670.00000	34.99997	15.80000	0.000
37	294.00000	669.00000	35.99995	14.60000	0.000
38	294.00000	668.00000	36.99995	13.70000	0.000
39	294.00000	667.00000	37.99995	13.00000	0.000
40	294.00000	666.00000	38.99995	12.50000	0.000
41	294.00000	665.00000	39.99997	12.00000	0.000
42	294.00000	664.00000	40.99997	11.00000	0.000
43	294.00000	663.00000	41.99997	10.30000	0.000

44	294.00000	662.00000	42.99997	9.80000	0.000
45	294.00000	661.00000	43.99997	9.40000	0.000
46	294.00000	660.00000	44.99995	8.90000	0.000
47	294.00000	659.00000	45.99997	8.30000	0.000
48	294.00000	658.00000	46.99997	7.70000	0.000
49	294.00000	657.00000	47.99997	7.50000	0.000
50	294.00000	656.00000	48.99997	7.50000	0.000
51	294.01001	655.01001	49.98994	7.70000	0.000

MODEL DATA

NO. BODIES = 7

N	CORN	DENSITY	SUSC	REM DEC	REM INC	REM INT
1	16	-0.16000	0.00000	0.00000	0.00000	0.00000

CO-ORDS OF CORNERS

X	Z
5.80000	0.00000
50.00000	0.00000
60.00000	0.00000
60.00000	0.20000
50.00000	0.20000
47.10001	0.40000
46.00000	0.60000
37.00000	0.20000
33.00000	0.00000
30.39999	0.00000
25.00000	0.20000
22.00999	0.60000
22.80000	1.00000
21.70000	1.20000
10.90000	1.20000
7.01000	1.20000

N	CORN	DENSITY	SUSC	REM DEC	REM INC	REM INT
2	21	-0.16000	0.00000	0.00000	0.00000	0.00000

CO-ORDS OF CORNERS

X	Z
7.01000	1.20000
10.90000	1.20000
21.70000	1.20000
22.80000	1.00000
22.00999	0.60000
23.61000	1.40000
30.39999	1.60000
33.00000	1.60000
37.00000	1.20000
46.00000	0.60000
47.10001	0.40000
50.00000	0.20000
60.00000	0.20000
60.00000	2.00000
50.00000	2.00000
48.60001	2.00000
34.80000	2.00000
20.00000	2.00000
14.50000	3.20000
9.50000	3.30000
7.50000	1.50000

N	CORN	DENSITY	SUSC	REM DEC	REM INC	REM INT
3	23	-0.09000	0.00000	0.00000	0.00000	0.00000

CO-ORDS OF CORNERS

X	Z

```
-10.00000   1.50000
  0.00000   1.50000
  7.50000   1.50000
  9.50000   3.30000
 14.50000   3.20000
 20.00000   2.00000
 34.80000   2.00000
 48.60001   2.00000
 50.00000   2.00000
 60.00000   2.00000
 60.00000   3.90000
 50.00000   3.90000
 46.00000   3.90000
 40.00000   3.95000
 37.00000   3.95000
 32.00000   4.05000
 27.00000   4.20000
 22.00000   4.30000
 17.00000   4.40000
  9.00000   4.50000
  4.00000   6.00000
  0.00000   6.00000
-10.00000   6.00000
 N CORN DENSITY     SUSC       REM DEC     REM INC     REM INT
 4  8  -0.04000   0.00000    0.00000     0.00000     0.00000
CO-ORDS OF CORNERS
   X          Z
-10.00000   0.00000
  0.00000   0.00000
  5.80000   0.00000
  7.01000   1.20000
  7.50000   1.50000
  5.00000   1.50000
  0.00000   1.50000
-10.00000   1.50000
 N CORN DENSITY     SUSC       REM DEC     REM INC     REM INT
 5 21  -0.01000   0.00000    0.00000     0.00000     0.00000
CO-ORDS OF CORNERS
   X          Z
-10.00000   6.00000
  0.00000   6.00000
  4.00000   6.00000
  9.00000   4.50000
 17.00000   4.40000
 22.00000   4.30000
 27.00000   4.20000
 32.00000   4.05000
 37.00000   3.95000
 40.00000   3.95000
 46.00000   3.90000
 50.00000   3.90000
 60.00000   3.90000
 60.00000   7.30000
 50.00000   7.30000
 42.00000   7.45000
 32.00000   7.70000
 22.00000   7.95000
 12.00000   8.20000
  0.00000   8.45000
```

```
-10.00000   8.45000
 N CORN DENSITY    SUSC      REM DEC    REM INC    REM INT
 6 10   0.06000   0.00000   0.00000    0.00000    0.00000
CO-ORDS OF CORNERS
   X         Z
-10.00000   8.45000
  0.00000   8.45000
 12.00000   8.20000
 22.00000   7.95000
 32.00000   7.70000
 42.00000   7.45000
 50.00000   7.30000
 60.00000   7.30000
 60.00000  15.00000
-10.00000  15.00000
 N CORN DENSITY    SUSC      REM DEC    REM INC    REM INT
 7 10   0.02000   0.00000   0.00000    0.00000    0.00000
CO-ORDS OF CORNERS
   X         Z
 22.00999   0.60000
 25.00000   0.20000
 30.39999   0.00000
 33.00000   0.00000
 37.00000   0.20000
 46.00000   0.60000
 37.00000   1.20000
 33.00000   1.60000
 30.39999   1.60000
 23.61000   1.40000
TOTAL ANOMALIES
STN PRO POS  GRA ANOM(OBS) GRA ANOM(CALC)
 1   0.01001      1.49831      0.96231
 2   0.99999      1.33166      1.09919
 3   2.00000      0.66331      1.23964
 4   2.99998      0.49496      1.36205
 5   4.00000      1.02661      1.42086
 6   5.00001      2.35826      1.28549
 7   6.00000      0.98992     -0.39072
 8   6.99999     -2.17842     -2.83425
 9   8.00000     -4.24677     -4.13175
10   8.99999     -5.71512     -4.84365
11   9.99999     -6.88346     -5.19209
12  11.00001     -6.55181     -5.29782
13  12.00000     -6.02016     -5.24162
14  13.00001     -5.78851     -5.07255
15  14.00001     -5.55685     -4.81379
16  14.99999     -5.22520     -4.47387
17  16.00000     -4.59354     -4.05979
18  16.99998     -3.96189     -3.58298
19  17.99997     -3.43023     -3.05719
20  18.99997     -2.69858     -2.49435
21  19.99997     -1.86693     -1.89283
22  20.99998     -1.03527     -1.16231
23  21.99998      0.29638      0.20610
24  22.99997      2.12804      2.69976
25  23.99998      4.25969      4.94438
26  24.99998      6.29134      6.62451
27  25.99998      8.62299      7.58301
28  26.99998      9.85465      8.31016
```

29	27,99998	10,98630	8,95050
30	28,99998	12,11795	9,52891
31	30,00000	12,54961	10,04240
32	30,99998	12,98126	10,30608
33	31,99998	13,11291	10,34507
34	32,99997	12,64457	10,23877
35	33,99995	11,47622	9,59321
36	34,99997	9,90788	8,82901
37	35,99995	8,53953	7,99841
38	36,99995	7,47119	7,15525
39	37,99995	6,60284	6,36015
40	38,99995	5,93449	5,58324
41	39,99997	5,26614	4,80575
42	40,99997	4,09780	4,02216
43	41,99997	3,22945	3,23180
44	42,99997	2,56111	2,43655
45	43,99997	1,99276	1,64282
46	44,99995	1,32441	0,87170
47	45,99997	0,55607	0,22574
48	46,99997	-0,21228	-0,10110
49	47,99997	-0,58063	-0,29475
50	48,99997	-0,74897	-0,46043
51	49,98994	-0,71563	-0,61854

GRAVITY LINE 1: BATHGATE HIGH (DEEP SOURCE).

NO. STNS	TREND	LENGTH
51	180.00240	49.99997

COORDS OF PROFILE ENDS

EASTING 1	NORTHING 1	EASTING 2	NORTHING 2
294.00000	294.00000	705.00000	655.00000

REGIONAL GRADN	REGIONAL TREND	ERROR
-0.170	8.000	0.200
0.000	0.000	0.000

AMBIENT FIELD

DECLINATION	INCLINATION	INTENSITY
0.00000	0.00000	0.00000

FIELD DATA

STN	EASTING	NORTHING	PRO POSIT	BOUG GRAV	TOTAL MAG
1	294.01001	704.98999	0.01001	1.50000	0.000
2	294.00000	704.00000	0.99999	1.50000	0.000
3	294.00000	703.00000	2.00000	1.00000	0.000
4	294.00000	702.00000	2.99998	1.00000	0.000
5	294.00000	701.00000	4.00000	1.70000	0.000
6	294.00000	700.00000	5.00001	3.20000	0.000
7	294.00000	699.00000	6.00000	2.00000	0.000
8	294.00000	698.00000	6.99999	-1.00000	0.000
9	294.00000	697.00000	8.00000	-2.90000	0.000
10	294.00000	696.00000	8.99999	-4.20000	0.000
11	294.00000	695.00000	9.99999	-5.20000	0.000
12	294.00000	694.00000	11.00001	-4.70000	0.000
13	294.00000	693.00000	12.00000	-4.00000	0.000
14	294.00000	692.00000	13.00001	-3.60000	0.000
15	294.00000	691.00000	14.00001	-3.20000	0.000
16	294.00000	690.00000	14.99999	-2.70000	0.000
17	294.00000	689.00000	16.00000	-1.90000	0.000
18	294.00000	688.00000	16.99998	-1.10000	0.000
19	294.00000	687.00000	17.99997	-0.40000	0.000
20	294.00000	686.00000	18.99997	0.50000	0.000
21	294.00000	685.00000	19.99997	1.50000	0.000
22	294.00000	684.00000	20.99998	2.50000	0.000
23	294.00000	683.00000	21.99998	4.00000	0.000
24	294.00000	682.00000	22.99997	6.00000	0.000
25	294.00000	681.00000	23.99998	8.30000	0.000
26	294.00000	680.00000	24.99998	10.50000	0.000
27	294.00000	679.00000	25.99998	13.00000	0.000
28	294.00000	678.00000	26.99998	14.40000	0.000
29	294.00000	677.00000	27.99998	15.70000	0.000
30	294.00000	676.00000	28.99998	17.00000	0.000
31	294.00000	675.00000	30.00000	17.60001	0.000
32	294.00000	674.00000	30.99998	18.20000	0.000
33	294.00000	673.00000	31.99998	18.50000	0.000
34	294.00000	672.00000	32.99997	18.20000	0.000
35	294.00000	671.00000	33.99995	17.20000	0.000
36	294.00000	670.00000	34.99997	15.80000	0.000
37	294.00000	669.00000	35.99995	14.60000	0.000
38	294.00000	668.00000	36.99995	13.70000	0.000
39	294.00000	667.00000	37.99995	13.00000	0.000
40	294.00000	666.00000	38.99995	12.50000	0.000
41	294.00000	665.00000	39.99997	12.00000	0.000
42	294.00000	664.00000	40.99997	11.00000	0.000
43	294.00000	663.00000	41.99997	10.30000	0.000

44	294.00000	662.00000	42.99997	9.80000	0.000
45	294.00000	661.00000	43.99997	9.40000	0.000
46	294.00000	660.00000	44.99995	8.90000	0.000
47	294.00000	659.00000	45.99997	8.30000	0.000
48	294.00000	658.00000	46.99997	7.70000	0.000
49	294.00000	657.00000	47.99997	7.50000	0.000
50	294.00000	656.00000	48.99997	7.50000	0.000
51	294.01001	655.01001	49.98994	7.70000	0.000

MODEL DATA

NO. BODIES = 7

N	CORN	DENSITY	SUSC	REM DEC	REM INC	REM INT
1	16	-0.16000	0.00000	0.00000	0.00000	0.00000

CO-ORDS OF CORNERS

X	Z
5.80000	0.00000
50.00000	0.00000
60.00000	0.00000
60.00000	0.20000
50.00000	0.20000
47.10001	0.40000
46.00000	0.60000
37.00000	0.20000
33.00000	0.00000
30.39999	0.00000
25.00000	0.20000
22.00999	0.60000
22.80000	1.00000
21.70000	1.20000
10.90000	1.20000
7.01000	1.20000

N	CORN	DENSITY	SUSC	REM DEC	REM INC	REM INT
2	21	-0.16000	0.00000	0.00000	0.00000	0.00000

CO-ORDS OF CORNERS

X	Z
7.01000	1.20000
10.90000	1.20000
21.70000	1.20000
22.80000	1.00000
22.00999	0.60000
23.61000	1.40000
30.39999	1.60000
33.00000	1.60000
37.00000	1.20000
46.00000	0.60000
47.10001	0.40000
50.00000	0.20000
60.00000	0.20000
60.00000	2.00000
50.00000	2.00000
48.60001	2.00000
34.80000	2.00000
20.00000	2.00000
14.50000	3.20000
9.50000	3.30000
7.50000	1.50000

N	CORN	DENSITY	SUSC	REM DEC	REM INC	REM INT
3	23	-0.09000	0.00000	0.00000	0.00000	0.00000

CO-ORDS OF CORNERS

X	Z

```
-10.00000    1.50000
  0.00000    1.50000
  7.50000    1.50000
  9.50000    3.30000
 14.50000    3.20000
 20.00000    2.00000
 34.80000    2.00000
 48.60001    2.00000
 50.00000    2.00000
 60.00000    2.00000
 60.00000    3.90000
 50.00000    3.90000
 46.00000    3.90000
 40.00000    3.95000
 37.00000    3.95000
 32.00000    4.05000
 27.00000    4.20000
 22.00000    4.30000
 17.00000    4.40000
  9.00000    4.50000
  4.00000    6.00000
  0.00000    6.00000
-10.00000    6.00000
 N CORN DENSITY     SUSC      REM DEC    REM INC    REM INT
 4  8  -0.04000   0.00000    0.00000    0.00000    0.00000
CO-ORDS OF CORNERS
    X            Z
-10.00000    0.00000
  0.00000    0.00000
  5.80000    0.00000
  7.01000    1.20000
  7.50000    1.50000
  5.00000    1.50000
  0.00000    1.50000
-10.00000    1.50000
 N CORN DENSITY     SUSC      REM DEC    REM INC    REM INT
 5 21  -0.01000   0.00000    0.00000    0.00000    0.00000
CO-ORDS OF CORNERS
    X            Z
-10.00000    6.00000
  0.00000    6.00000
  4.00000    6.00000
  9.00000    4.50000
 17.00000    4.40000
 22.00000    4.30000
 27.00000    4.20000
 32.00000    4.05000
 37.00000    3.95000
 40.00000    3.95000
 46.00000    3.90000
 50.00000    3.90000
 60.00000    3.90000
 60.00000    7.30000
 50.00000    7.30000
 42.00000    7.45000
 32.00000    7.70000
 22.00000    7.95000
 12.00000    8.20000
  0.00000    8.45000
```

```
-10.00000   8.45000
 N CORN DENSITY    SUSC      REM DEC    REM INC    REM INT
 6 10   0.06000   0.00000   0.00000    0.00000    0.00000
CO-ORDS OF CORNERS
   X         Z
-10.00000   8.45000
  0.00000   8.45000
 12.00000   8.20000
 22.00000   7.95000
 32.00000   7.70000
 42.00000   7.45000
 50.00000   7.30000
 60.00000   7.30000
 60.00000  15.00000
-10.00000  15.00000
 N CORN DENSITY    SUSC      REM DEC    REM INC    REM INT
 7 10   0.02000   0.00000   0.00000    0.00000    0.00000
CO-ORDS OF CORNERS
   X         Z
 22.00999   0.60000
 25.00000   0.20000
 30.39999   0.00000
 33.00000   0.00000
 37.00000   0.20000
 46.00000   0.60000
 37.00000   1.20000
 33.00000   1.60000
 30.39999   1.60000
 23.61000   1.40000
TOTAL ANOMALIES
STN PRO POS  GRA ANOM(OBS) GRA ANOM(CALC)
 1   0.01001     1.49831      0.96231
 2   0.99999     1.33166      1.09919
 3   2.00000     0.66331      1.23964
 4   2.99998     0.49496      1.36205
 5   4.00000     1.02661      1.42086
 6   5.00001     2.35826      1.28549
 7   6.00000     0.98992     -0.39072
 8   6.99999    -2.17842     -2.83425
 9   8.00000    -4.24677     -4.13175
10   8.99999    -5.71512     -4.84365
11   9.99999    -6.88346     -5.19209
12  11.00001    -6.55181     -5.29782
13  12.00000    -6.02016     -5.24162
14  13.00001    -5.78851     -5.07255
15  14.00001    -5.55685     -4.81379
16  14.99999    -5.22520     -4.47387
17  16.00000    -4.59354     -4.05979
18  16.99998    -3.96189     -3.58298
19  17.99997    -3.43023     -3.05719
20  18.99997    -2.69858     -2.49435
21  19.99997    -1.86693     -1.89283
22  20.99998    -1.03527     -1.16231
23  21.99998     0.29638      0.20610
24  22.99997     2.12804      2.69976
25  23.99998     4.25969      4.94438
26  24.99998     6.29134      6.62451
27  25.99998     8.62299      7.58301
28  26.99998     9.85465      8.31016
```

29	27,99998	10,98630	8,95050
30	28,99998	12,11795	9,52891
31	30,00000	12,54961	10,04240
32	30,99998	12,98126	10,30608
33	31,99998	13,11291	10,34507
34	32,99997	12,64457	10,23877
35	33,99995	11,47622	9,59321
36	34,99997	9,90788	8,82901
37	35,99995	8,53953	7,99841
38	36,99995	7,47119	7,15525
39	37,99995	6,60284	6,36015
40	38,99995	5,93449	5,58324
41	39,99997	5,26614	4,80575
42	40,99997	4,09780	4,02216
43	41,99997	3,22945	3,23180
44	42,99997	2,56111	2,43655
45	43,99997	1,99276	1,64282
46	44,99995	1,32441	0,87170
47	45,99997	0,55607	0,22574
48	46,99997	-0,21228	-0,10110
49	47,99997	-0,58063	-0,29475
50	48,99997	-0,74897	-0,46043
51	49,98994	-0,71563	-0,61854

GRAVITY LINE 2: BATHGATE HIGH (SHALLOW SOURCE).

NO. STNS	TREND	LENGTH
41	90.00116	39.99998

COORDS OF PROFILE ENDS

EASTING 1	NORTHING 1	EASTING 2	NORTHING 2
275.00000	315.00000	673.00000	673.00000

REGIONAL GRADN	REGIONAL TREND	ERROR
-0.170	8.000	0.200
0.000	0.000	0.000

AMBIENT FIELD

DECLINATION	INCLINATION	INTENSITY
0.00000	0.00000	0.00000

FIELD DATA

STN	EASTING	NORTHING	PRO POSIT	BOUG GRAV	TOTAL MAG
1	275.01001	673.01001	0.01005	9.50000	0.000
2	276.00000	673.00000	1.00003	9.80000	0.000
3	277.00000	673.00000	2.00002	10.00000	0.000
4	278.00000	673.00000	3.00003	10.60000	0.000
5	279.00000	673.00000	4.00003	11.00000	0.000
6	280.00000	673.00000	5.00001	12.00000	0.000
7	281.00000	673.00000	6.00003	12.80000	0.000
8	282.00000	673.00000	7.00001	13.40000	0.000
9	283.00000	673.00000	8.00000	13.80000	0.000
10	284.00000	673.00000	9.00000	14.00000	0.000
11	285.00000	673.00000	9.99999	14.25000	0.000
12	286.00000	673.00000	10.99999	14.50000	0.000
13	287.00000	673.00000	12.00001	14.75000	0.000
14	288.00000	673.00000	12.99999	15.00000	0.000
15	289.00000	673.00000	14.00001	15.80000	0.000
16	290.00000	673.00000	15.00001	16.39999	0.000
17	291.00000	673.00000	16.00000	17.00000	0.000
18	292.00000	673.00000	17.00000	17.60001	0.000
19	293.00000	673.00000	18.00000	18.10001	0.000
20	294.00000	673.00000	18.99998	18.50000	0.000
21	295.00000	673.00000	19.99998	18.50000	0.000
22	296.00000	673.00000	20.99998	18.10001	0.000
23	297.00000	673.00000	21.99997	17.50000	0.000
24	298.00000	673.00000	22.99997	17.00000	0.000
25	299.00000	673.00000	23.99997	16.60001	0.000
26	300.00000	673.00000	24.99997	16.30000	0.000
27	301.00000	673.00000	25.99997	15.50000	0.000
28	302.00000	673.00000	26.99998	14.80000	0.000
29	303.00000	673.00000	27.99997	14.40000	0.000
30	304.00000	673.00000	28.99998	13.70000	0.000
31	305.00000	673.00000	29.99998	13.00000	0.000
32	306.00000	673.00000	30.99997	12.00000	0.000
33	307.00000	673.00000	31.99998	11.00000	0.000
34	308.00000	673.00000	32.99997	10.80000	0.000
35	309.00000	673.00000	33.99995	10.60000	0.000
36	310.00000	673.00000	34.99997	10.40000	0.000
37	311.00000	673.00000	35.99995	10.20000	0.000
38	312.00000	673.00000	36.99995	10.00000	0.000
39	313.00000	673.00000	37.99997	9.50000	0.000
40	314.00000	673.00000	38.99995	9.00000	0.000
41	314.98999	672.98999	39.98993	8.00000	0.000

MODEL DATA

NO. BODIES = 6

N	CORN	DENSITY	SUSC	REM DEC	REM INC	REM INT
1	10	-0.16000	0.00000	0.00000	0.00000	0.00000

CO-ORDS OF CORNERS

X	Z
-10.00000	0.00000
0.00000	0.00000
22.00000	0.00000
20.00000	0.10000
18.00000	0.20000
14.00000	0.60000
6.00000	0.60000
3.00000	0.96000
0.00000	0.96000
-10.00000	0.96000

N	CORN	DENSITY	SUSC	REM DEC	REM INC	REM INT
2	24	-0.16000	0.00000	0.00000	0.00000	0.00000

CO-ORDS OF CORNERS

X	Z
-10.00000	1.10000
0.00000	1.10000
6.00000	1.10000
9.00000	1.10000
10.30000	1.10000
14.00000	1.40000
17.00000	1.40000
32.00000	1.30000
27.00000	0.70000
16.00000	0.50000
18.00000	0.40000
25.00000	0.00000
40.00000	0.00000
50.00000	0.00000
50.00000	1.85000
40.00000	1.85000
30.00000	1.70000
25.00000	1.90000
20.00000	2.00000
15.00000	2.20000
10.00000	2.50000
5.00000	2.50000
0.00000	2.60000
-10.00000	2.60000

N	CORN	DENSITY	SUSC	REM DEC	REM INC	REM INT
3	21	-0.09000	0.00000	0.00000	0.00000	0.00000

CO-ORDS OF CORNERS

X	Z
-10.00000	2.60000
0.00000	2.60000
5.00000	2.50000
10.00000	2.50000
15.00000	2.20000
20.00000	2.00000
25.00000	1.90000
30.00000	1.70000
40.00000	1.85000
50.00000	1.85000
50.00000	4.30000
40.00000	4.30000
35.00000	4.26000

30.00000	4.23000
25.00000	4.20000
20.00000	4.15000
15.00000	4.10000
10.00000	4.10000
5.00000	4.10000
0.00000	4.20000
-10.00000	4.20000

N	CORN	DENSITY	SUSC	REM DEC	REM INC	REM INT
4	20	0.02000	0.00000	0.00000	0.00000	0.00000

CO-ORDS OF CORNERS

X	Z
-10.00000	0.96000
0.00000	0.96000
3.00000	0.96000
6.00000	0.60000
14.00000	0.60000
18.00000	0.20000
20.00000	0.10000
22.00000	0.00000
25.00000	0.00000
18.00000	0.40000
16.00000	0.50000
27.00000	0.70000
32.00000	1.30000
17.00000	1.40000
14.00000	1.40000
10.30000	1.10000
9.00000	1.10000
6.00000	1.10000
0.00000	1.10000
-10.00000	1.10000

N	CORN	DENSITY	SUSC	REM DEC	REM INC	REM INT
5	22	-0.01000	0.00000	0.00000	0.00000	0.00000

CO-ORDS OF CORNERS

X	Z
-10.00000	4.20000
0.00000	4.20000
5.00000	4.10000
10.00000	4.10000
15.00000	4.10000
20.00000	4.15000
25.00000	4.20000
30.00000	4.23000
35.00000	4.26000
40.00000	4.30000
50.00000	4.30000
50.00000	8.20000
40.00000	8.20000
35.00000	8.20000
30.00000	8.20000
25.00000	8.20000
20.00000	8.20000
15.00000	8.20000
10.00000	8.20000
5.00000	8.20000
0.00000	8.20000
-10.00000	8.20000

N CORN DENSITY SUSC REM DEC REM INC REM INT

6	15	0.06000	0.00000	0.00000	0.00000	0.00000

CO-ORDS OF CORNERS

X	Z
-10.00000	8.20000
0.00000	8.20000
5.00000	8.20000
10.00000	8.20000
15.00000	8.20000
20.00000	8.20000
25.00000	8.20000
30.00000	8.20000
35.00000	8.20000
40.00000	8.20000
50.00000	8.20000
50.00000	15.00000
40.00000	15.00000
0.00000	15.00000
-10.00000	15.00000

TOTAL ANOMALIES

STN	PRO POS	GRA ANOM(OBS)	GRA ANOM(CALC)
1	0.01005	9.50024	9.97403
2	1.00003	9.82366	10.17532
3	2.00002	10.04731	10.43158
4	3.00003	10.67097	10.82339
5	4.00003	11.09463	11.46125
6	5.00001	12.11828	12.23336
7	6.00003	12.94194	12.94120
8	7.00001	13.56559	13.32791
9	8.00000	13.98925	13.57004
10	9.00000	14.21291	13.80184
11	9.99999	14.48656	14.09715
12	10.99999	14.76022	14.53185
13	12.00001	15.03388	15.06680
14	12.99999	15.30753	15.62065
15	14.00001	16.13118	16.20006
16	15.00001	16.75484	16.93336
17	16.00000	17.37849	17.63391
18	17.00000	18.00215	18.09291
19	18.00000	18.52582	18.40881
20	18.99998	18.94946	18.40984
21	19.99998	18.97311	18.30992
22	20.99998	18.59679	18.17107
23	21.99997	18.02043	18.01016
24	22.99997	17.54408	17.44832
25	23.99997	17.16776	16.85379
26	24.99997	16.89140	16.22124
27	25.99997	16.11505	15.97001
28	26.99998	15.43872	15.58653
29	27.99997	15.06238	14.94328
30	28.99998	14.38603	14.20364
31	29.99998	13.70969	13.45939
32	30.99997	12.73334	12.75795
33	31.99998	11.75700	12.18553
34	32.99997	11.58066	11.80607
35	33.99995	11.40431	11.55011
36	34.99997	11.22797	11.34503
37	35.99995	11.05163	11.16096
38	36.99995	10.87528	10.98645
39	37.99997	10.39894	10.81748

40	38.99995	9.92259	10.65408
41	39.98993	8.94601	10.50082

GRAVITY LINE 2: BATHGATE HIGH (DEEP SOURCE).

NO. STNS	TREND	LENGTH
41	90.00116	39.99998

COORDS OF PROFILE ENDS

EASTING 1	NORTHING 1	EASTING 2	NORTHING 2
275.00000	315.00000	673.00000	673.00000

REGIONAL GRADN	REGIONAL TREND	ERROR
-0.170	8.000	0.200
0.000	0.000	0.000

AMBIENT FIELD

DECLINATION	INCLINATION	INTENSITY
0.00000	0.00000	0.00000

FIELD DATA

STN	EASTING	NORTHING	PRO POSIT	BOUG GRAV	TOTAL MAG
1	275.01001	673.01001	0.01005	9.50000	0.000
2	276.00000	673.00000	1.00003	9.80000	0.000
3	277.00000	673.00000	2.00002	10.00000	0.000
4	278.00000	673.00000	3.00003	10.60000	0.000
5	279.00000	673.00000	4.00003	11.00000	0.000
6	280.00000	673.00000	5.00001	12.00000	0.000
7	281.00000	673.00000	6.00003	12.80000	0.000
8	282.00000	673.00000	7.00001	13.40000	0.000
9	283.00000	673.00000	8.00000	13.80000	0.000
10	284.00000	673.00000	9.00000	14.00000	0.000
11	285.00000	673.00000	9.99999	14.25000	0.000
12	286.00000	673.00000	10.99999	14.50000	0.000
13	287.00000	673.00000	12.00001	14.75000	0.000
14	288.00000	673.00000	12.99999	15.00000	0.000
15	289.00000	673.00000	14.00001	15.80000	0.000
16	290.00000	673.00000	15.00001	16.39999	0.000
17	291.00000	673.00000	16.00000	17.00000	0.000
18	292.00000	673.00000	17.00000	17.60001	0.000
19	293.00000	673.00000	18.00000	18.10001	0.000
20	294.00000	673.00000	18.99998	18.50000	0.000
21	295.00000	673.00000	19.99998	18.50000	0.000
22	296.00000	673.00000	20.99998	18.10001	0.000
23	297.00000	673.00000	21.99997	17.50000	0.000
24	298.00000	673.00000	22.99997	17.00000	0.000
25	299.00000	673.00000	23.99997	16.60001	0.000
26	300.00000	673.00000	24.99997	16.30000	0.000
27	301.00000	673.00000	25.99997	15.50000	0.000
28	302.00000	673.00000	26.99998	14.80000	0.000
29	303.00000	673.00000	27.99997	14.40000	0.000
30	304.00000	673.00000	28.99998	13.70000	0.000
31	305.00000	673.00000	29.99998	13.00000	0.000
32	306.00000	673.00000	30.99997	12.00000	0.000
33	307.00000	673.00000	31.99998	11.00000	0.000
34	308.00000	673.00000	32.99997	10.80000	0.000
35	309.00000	673.00000	33.99995	10.60000	0.000
36	310.00000	673.00000	34.99997	10.40000	0.000
37	311.00000	673.00000	35.99995	10.20000	0.000
38	312.00000	673.00000	36.99995	10.00000	0.000
39	313.00000	673.00000	37.99997	9.50000	0.000
40	314.00000	673.00000	38.99995	9.00000	0.000
41	314.98999	672.98999	39.98993	8.00000	0.000

MODEL DATA

NO. BODIES = 7

N	CORN	DENSITY	SUSC	REM DEC	REM INC	REM INT
1	10	-0.16000	0.00000	0.00000	0.00000	0.00000

CO-ORDS OF CORNERS

X	Z
-10.00000	0.00000
0.00000	0.00000
22.00000	0.00000
20.00000	0.20000
17.00000	0.40000
14.00000	0.60000
9.00000	0.60000
5.00000	0.76000
0.00000	0.76000
-10.00000	0.76000

N	CORN	DENSITY	SUSC	REM DEC	REM INC	REM INT
2	22	-0.16000	0.00000	0.00000	0.00000	0.00000

CO-ORDS OF CORNERS

X	Z
-10.00000	1.10000
0.00000	1.10000
9.00000	1.10000
10.30000	1.00000
9.00000	0.96000
14.00000	0.96000
17.00000	0.70000
20.00000	0.50000
22.00000	0.20000
25.00000	0.00000
40.00000	0.00000
50.00000	0.00000
50.00000	1.85000
40.00000	1.85000
30.00000	1.70000
25.00000	1.90000
20.00000	2.00000
15.00000	2.20000
10.00000	2.50000
5.00000	2.50000
0.00000	2.60000
-10.00000	2.60000

N	CORN	DENSITY	SUSC	REM DEC	REM INC	REM INT
3	21	-0.09000	0.00000	0.00000	0.00000	0.00000

CO-ORDS OF CORNERS

X	Z
-10.00000	2.60000
0.00000	2.60000
5.00000	2.50000
10.00000	2.50000
15.00000	2.20000
20.00000	2.00000
25.00000	1.90000
30.00000	1.70000
40.00000	1.85000
50.00000	1.85000
50.00000	4.30000
40.00000	4.30000
35.00000	4.26000
30.00000	4.23000
25.00000	4.20000

20.00000	4.15000
15.00000	4.10000
10.00000	4.10000
5.00000	4.10000
0.00000	4.20000
-10.00000	4.20000

N	CORN	DENSITY	SUSC	REM DEC	REM INC	REM INT
4	18	0.02000	0.00000	0.00000	0.00000	0.00000

CO-ORDS OF CORNERS

X	Z
-10.00000	0.76000
0.00000	0.76000
5.00000	0.76000
9.00000	0.60000
14.00000	0.60000
17.00000	0.40000
20.00000	0.20000
22.00000	0.00000
25.00000	0.00000
22.00000	0.20000
20.00000	0.50000
17.00000	0.70000
14.00000	0.96000
9.00000	0.96000
10.30000	1.00000
9.00000	1.10000
0.00000	1.10000
-10.00000	1.10000

N	CORN	DENSITY	SUSC	REM DEC	REM INC	REM INT
5	22	-0.01000	0.00000	0.00000	0.00000	0.00000

CO-ORDS OF CORNERS

X	Z
-10.00000	4.20000
0.00000	4.20000
5.00000	4.10000
10.00000	4.10000
15.00000	4.10000
20.00000	4.15000
25.00000	4.20000
30.00000	4.23000
35.00000	4.26000
40.00000	4.30000
50.00000	4.30000
50.00000	8.20000
40.00000	8.20000
35.00000	8.20000
30.00000	8.20000
25.00000	8.20000
20.00000	8.20000
15.00000	8.20000
10.00000	8.20000
5.00000	8.20000
0.00000	8.20000
-10.00000	8.20000

N	CORN	DENSITY	SUSC	REM DEC	REM INC	REM INT
6	22	0.06000	0.00000	0.00000	0.00000	0.00000

CO-ORDS OF CORNERS

X	Z
-10.00000	8.20000

0.00000	8.20000
5.00000	8.20000
10.00000	8.20000
15.00000	8.20000
20.00000	8.20000
25.00000	8.20000
30.00000	8.20000
35.00000	8.20000
40.00000	8.20000
50.00000	8.20000
50.00000	15.00000
40.00000	15.00000
35.00000	15.00000
22.50000	15.00000
21.50000	10.00000
18.50000	10.00000
17.50000	15.00000
10.00000	15.00000
5.00000	15.00000
0.00000	15.00000
-10.00000	15.00000

N	CORN	DENSITY	SUSC	REM DEC	REM INC	REM INT
7	4	0.55000	0.00000	0.00000	0.00000	0.00000

CO-ORDS OF CORNERS

X	Z
18.50000	10.00000
21.50000	10.00000
22.50000	15.00000
17.50000	15.00000

TOTAL ANOMALIES

STN	PRO POS	GRA ANOM(OBS)	GRA ANOM(CALC)
1	0.01005	9.50024	9.69353
2	1.00003	9.82366	10.06341
3	2.00002	10.04731	10.46539
4	3.00003	10.67097	10.89465
5	4.00003	11.09463	11.35558
6	5.00001	12.11828	11.87854
7	6.00003	12.94194	12.51248
8	7.00001	13.56559	13.20235
9	8.00000	13.98925	13.89033
10	9.00000	14.21291	14.47719
11	9.99999	14.48656	14.86560
12	10.99999	14.76022	15.30824
13	12.00001	15.03388	15.87440
14	12.99999	15.30753	16.47650
15	14.00001	16.13118	17.06374
16	15.00001	16.75484	17.64240
17	16.00000	17.37849	18.14827
18	17.00000	18.00215	18.57503
19	18.00000	18.52582	18.93874
20	18.99998	18.94946	19.19124
21	19.99998	18.97311	19.25418
22	20.99998	18.59679	19.06668
23	21.99997	18.02043	18.71005
24	22.99997	17.54408	17.85281
25	23.99997	17.16776	16.96408
26	24.99997	16.89140	16.00046
27	25.99997	16.11505	15.49659
28	26.99998	15.43872	14.98368

29	27,99997	15,06238	14,46424
30	28,99998	14,38603	13,94314
31	29,99998	13,70969	13,41832
32	30,99997	12,73334	12,88826
33	31,99998	11,75700	12,36188
34	32,99997	11,58066	11,84964
35	33,99995	11,40431	11,35641
36	34,99997	11,22797	10,88422
37	35,99995	11,05163	10,43353
38	36,99995	10,87528	10,00407
39	37,99997	10,39894	9,59611
40	38,99995	9,92259	9,21102
41	39,98993	8,94601	8,85516

GRAVITY LINE 3: KINCARDINE BASIN.

NO. STNS	TREND	LENGTH
36	90.00116	34.99997

COORDS OF PROFILE ENDS

EASTING 1	NORTHING 1	EASTING 2	NORTHING 2
275.00000	310.00000	695.00000	695.00000

REGIONAL GRADN	REGIONAL TREND	ERROR
-0.170	8.000	0.200
0.000	0.000	0.000

AMBIENT FIELD

DECLINATION	INCLINATION	INTENSITY
0.00000	0.00000	0.00000

FIELD DATA

STN	EASTING	NORTHING	PRO POSIT	BOUG GRAV	TOTAL MAG
1	275.01001	694.98999	0.01002	5.50000	0.000
2	276.00000	695.00000	1.00001	5.50000	0.000
3	277.00000	695.00000	2.00001	5.50000	0.000
4	278.00000	695.00000	2.99998	5.50000	0.000
5	279.00000	695.00000	3.99998	4.50000	0.000
6	280.00000	695.00000	4.99998	3.80000	0.000
7	281.00000	695.00000	6.00000	3.20000	0.000
8	282.00000	695.00000	7.00000	2.40000	0.000
9	283.00000	695.00000	8.00000	1.50000	0.000
10	284.00000	695.00000	9.00000	0.70000	0.000
11	285.00000	695.00000	10.00001	-0.20000	0.000
12	286.00000	695.00000	10.99999	-1.40000	0.000
13	287.00000	695.00000	11.99999	-2.50000	0.000
14	288.00000	695.00000	12.99999	-3.30000	0.000
15	289.00000	695.00000	13.99999	-4.00000	0.000
16	290.00000	695.00000	14.99999	-4.25000	0.000
17	291.00000	695.00000	15.99999	-4.50000	0.000
18	292.00000	695.00000	16.99998	-4.75000	0.000
19	293.00000	695.00000	17.99998	-5.00000	0.000
20	294.00000	695.00000	18.99997	-5.20000	0.000
21	295.00000	695.00000	19.99997	-4.20000	0.000
22	296.00000	695.00000	20.99997	-3.90000	0.000
23	297.00000	695.00000	21.99997	-3.60000	0.000
24	298.00000	695.00000	22.99997	-3.40000	0.000
25	299.00000	695.00000	23.99997	-3.20000	0.000
26	300.00000	695.00000	24.99995	-3.00000	0.000
27	301.00000	695.00000	25.99995	-2.50000	0.000
28	302.00000	695.00000	26.99997	-2.00000	0.000
29	303.00000	695.00000	27.99995	-1.30000	0.000
30	304.00000	695.00000	28.99997	-0.50000	0.000
31	305.00000	695.00000	29.99998	0.40000	0.000
32	306.00000	695.00000	30.99997	1.00000	0.000
33	307.00000	695.00000	31.99998	1.20000	0.000
34	308.00000	695.00000	32.99995	1.50000	0.000
35	309.00000	695.00000	33.99995	1.20000	0.000
36	309.98999	694.98999	34.98994	1.00000	0.000

MODEL DATA

NO. BODIES = 6

N	CORN	DENSITY	SUSC	REM DEC	REM INC	REM INT
1	15	-0.16000	0.00000	0.00000	0.00000	0.00000

CO-ORDS OF CORNERS

X	Z
3.70000	0.00000

32.80000	0.00000
29.39999	0.20000
28.39999	0.40000
26.80000	0.60000
25.70000	0.80000
21.60001	1.00000
16.39999	1.40000
13.80000	1.40000
11.90000	1.20000
11.20000	1.00000
10.10000	0.80000
7.80000	0.60000
7.10000	0.40000
6.00000	0.20000

N	CORN	DENSITY	SUSC	REM DEC	REM INC	REM INT
2	29	-0.16000	0.00000	0.00000	0.00000	0.00000

CO-ORDS OF CORNERS

X	Z
-10.00000	0.25000
0.00000	0.25000
3.70000	0.25000
6.00000	0.45000
7.10000	0.65000
7.80000	0.80000
10.10000	0.80000
11.20000	1.00000
11.90000	1.20000
13.80000	1.40000
16.39999	1.40000
21.60001	1.00000
25.70000	0.80000
26.80000	0.60000
28.39999	0.40000
29.39999	0.20000
32.80000	0.00000
35.00000	0.00000
45.00000	0.00000
45.00000	1.50000
35.00000	1.50000
30.00000	1.60000
26.00000	2.95000
20.00000	3.25000
15.00000	3.25000
10.00000	2.10000
5.00000	1.40000
0.00000	1.00000
-10.00000	1.00000

N	CORN	DENSITY	SUSC	REM DEC	REM INC	REM INT
3	20	-0.04000	0.00000	0.00000	0.00000	0.00000

CO-ORDS OF CORNERS

X	Z
-10.00000	1.00000
0.00000	1.00000
5.00000	1.40000
10.00000	2.10000
15.00000	3.25000
20.00000	3.25000
26.00000	2.95000
30.00000	1.60000

35.00000	1.50000
45.00000	1.50000
45.00000	4.40000
35.00000	4.40000
30.00000	4.40000
25.00000	4.40000
20.00000	4.60000
15.00000	5.70000
10.00000	5.60000
5.00000	5.50000
0.00000	5.40000
-10.00000	5.40000

N	CORN	DENSITY	SUSC	REM DEC	REM INC	REM INT
4	15	-0.01000	0.00000	0.00000	0.00000	0.00000

CO-ORDS OF CORNERS

X	Z
-10.00000	5.40000
0.00000	5.40000
5.00000	5.50000
10.00000	5.60000
15.00000	5.70000
20.00000	4.60000
25.00000	4.40000
30.00000	4.40000
35.00000	4.40000
45.00000	4.40000
45.00000	8.60000
35.00000	8.60000
15.00000	8.60000
0.00000	8.60000
-10.00000	8.60000

N	CORN	DENSITY	SUSC	REM DEC	REM INC	REM INT
5	10	0.06000	0.00000	0.00000	0.00000	0.00000

CO-ORDS OF CORNERS

X	Z
-10.00000	8.60000
0.00000	8.60000
15.00000	8.60000
35.00000	8.60000
45.00000	8.60000
45.00000	15.00000
35.00000	15.00000
15.00000	15.00000
0.00000	15.00000
-10.00000	15.00000

N	CORN	DENSITY	SUSC	REM DEC	REM INC	REM INT
6	13	0.02000	0.00000	0.00000	0.00000	0.00000

CO-ORDS OF CORNERS

X	Z
-10.00000	0.00000
0.00000	0.00000
3.70000	0.00000
6.02000	0.20000
7.10000	0.40000
7.80000	0.60000
10.10000	0.80000
7.80000	0.80000
7.10000	0.65000
6.02000	0.45000

3.70000	0.25000
0.00000	0.25000
-10.00000	0.25000

TOTAL ANOMALIES

STN	PRO POS	GRA ANOM(OBS)	GRA ANOM(CALC)
1	0.01002	5.50024	5.43742
2	1.00001	5.52366	5.27469
3	2.00001	5.54731	5.03666
4	2.99998	5.57097	4.77030
5	3.99998	4.59462	4.43889
6	4.99998	3.91828	3.94213
7	6.00000	3.34194	3.39884
8	7.00000	2.56559	2.58203
9	8.00000	1.68925	1.57475
10	9.00000	0.91291	0.59182
11	10.00001	0.03656	-0.36094
12	10.99999	-1.13978	-1.13931
13	11.99999	-2.21612	-1.79438
14	12.99999	-2.99247	-2.36378
15	13.99999	-3.66881	-2.83330
16	14.99999	-3.89515	-3.18494
17	15.99999	-4.12150	-3.41391
18	16.99998	-4.34784	-3.53327
19	17.99998	-4.57419	-3.56426
20	18.99997	-4.75053	-3.52532
21	19.99997	-3.72687	-3.42840
22	20.99997	-3.40322	-3.28060
23	21.99997	-3.07956	-3.08586
24	22.99997	-2.85591	-2.84306
25	23.99997	-2.63225	-2.54232
26	24.99995	-2.40859	-2.16253
27	25.99995	-1.88494	-1.67441
28	26.99997	-1.36128	-1.05958
29	27.99995	-0.63763	-0.33453
30	28.99997	0.18603	0.43756
31	29.99998	1.10969	1.13533
32	30.99997	1.73334	1.63207
33	31.99998	1.95700	1.93273
34	32.99995	2.28066	2.10654
35	33.99995	2.00431	2.19842
36	34.98994	1.82773	2.22785

APPENDIX 6. COMPUTER PROGRAMS

The programs listed are available from the Department of Geology, University of Glasgow.

Program WHB10

Program for the inversion of time-distance data to velocity-depth data using the WHB and tau-p inversions (see Chapter 4).

INPUT DATA FOR PROGRAM WHB10

CARD 1 (5I5)

NPR,NCODE1,NCODE2,NCODE3

```
NPR        NUMBER OF DATA SETS
NCODE1     CONTROLS THE PLOT OF VELOCITY VS DEPTH
           1  TAU-P AND WHB VELOCITIES PLOTTED AS LINES
           2    "    "    "      "        "     AS POINTS WITH ERROR BARS
           3  WHB VELOCITIES PLOTTED AS POINTS WITH ERROR BARS
           4  TAU-P    "         "     "    "     "     "    "
           5    "      "         "     "    "      " LINES
           6  WHB      "         "     "    "     "    "
NCODE3     CONTROLS THE PLOT OF REDUCED TIME VS RANGE
           1  DATA POINTS PLOTTED
           2  DATA AND SMOOTHED CURVES PLOTTED
NCODE4     CONTROLS TYPE OF PLOT
           0  EACH PAIR OF PLOTS ARE ON SEPERATE AXES
           1  ALL PAIRS OF PLOTS USE SMAE AXES
NCODE5     CONTROLS PLOTTING OF ADITIONAL DATA ON V-Z PLOTS
           0  NO EXTRA DATA PLOTTED
           1  ADDITIONAL DATA POINTS JOINED BY STRAIGHT LINES
           2       "        "     "     PLOTTED AS SERIES OF POINTS
           3       "        "  IN 3RD ORDER POLYNOMIAL FORM
```

CARD 2 (FREE FORMAT)

ZRO2,ZMX2,VMN2,VMX2,TMN2,TMX2

```
ZRO2       MINIMUM ON DEPTH AXES WHEN NCODE4=1
ZMX2       MAXIMUM "     "     "    "     "
VMN2       MINIMUM "  VELOCITY AXES WHEN NCODE4=1
VMX2       MAXIMUM "     "       "    "     "
TMN2       MINIMUM "  REDUCED TIME AXIS WHEN NCODE4=1
TMX2       MAXIMUM "     "      "    "    "     "
```

CARD 3 (10A4)

TITLE

```
TITLE      ARBITRARY CHARACTER STRING (WHEN NCODE4=1 THE FIRST TITLE IS
           IS USED
```

CARD 4 (FREE FORMAT)

RVEL

```
RVEL       REDUCTION VELOCITY FOR REDUCED TIME VS RANGE PLOT (DEFAULT=6.00)
```

CARD 5 (FREE FORMAT)

M,N,ZRO,ZMX,VMN,VMX,TMN,TMX

```
M          NUMBER OF OBSERVED T-X POINTS
N             "     "   T-X POINTS DEFINING THE SMOOTHED T-X CURVES
ZRO        MINIMUM VALUE OF DEPTH AXIS
ZMX        MAXIMUMU  "    "    "    "
VMN        MINIMUM VALUE "  VELOCITY AXIS (WHEN NCODE4=0)
VMX        MAXIMUM VALUE "      "       "        "
TMN        MINIMUM VALUE ON REDUCED TIME AXIS "      "
TMX        MAXIMUM   "    "      "      "     "  "   "
```

CARD 6 (3F10.5)

TT(K),DIST1(K),ERROR(K),K-1,M

```
TT         OBSERVED TRAVEL TIME
DIST1      RANGE
ERROR      ERROR ON TRAVEL TIME (UNCERTAINTY = +/- ERROR)
```

CARD 7 (FREE FORMAT)

VEL0(I),I=1,5

```
VEL0       SURFACE VELOCITY
```

CARD 8 (FREE FORMAT)

T(J,M),J=1,5 DIST2(M),M=1,N

```
T          TRAVEL TIME OF SMOOTHED DATA
DIST2      RANGE OF T
```

```
      PROGRAM WHB10
C
C     PROGRAM TO INVERT TIME-DISTANCE DATA TO VELOCITY-DEPTH DATA USING
C     THE WHB AND/OR TAU-P METHODS
C
C     PROGRAM WRITTEN FOR FORTRAN 77 COMPILER WITH GHOST
C     GRAPHICS ROUTINES.
C
C     ORIGINAL PROGRAM WRITTEN BY J.HALL,
C     ADAPTED BY                  K.DAVIDSON
C     AND                         M.DENTITH
C                                 DEPT.OF GEOLOGY,
C                                 UNIVERSITY OF GLASGOW.
C
      COMMON TITLE (10)
      REAL LT
      DIMENSION VINT(5,200),VPT(5,200),Z(5,200),T(5,200),TTRED(200)
      DIMENSION DIST1(200),Q(5),VU(5,200),U(5,200),ZZ(5,200),V0(5)
      DIMENSION UTD(5,200),TAU(5,200),P(5,200),VDIFF(5,200),GRAD(5,200)
      DIMENSION TT(200), DIST2(200), ERROR(200), XINT(200), VEL0(5)
      DIMENSION TRED(5,200), UT(200), LT(200), GLOWA(200), GHIGHA(200)
      DIMENSION GLOWB(200), GLOWC(200), GHIGHB(200), GHIGHC(200)
      DIMENSION GRAF1(200),GRAF2(200),GRAF3(200),GRAF4(200),GRAF5(200)
      DIMENSION GRAF6(200),GRAF7(200),GRAF8(200),GRAF9(200),GRAF10(200)
      DIMENSION GRAF11(200),GRAF12(200),GRAF13(200),GRAF14(200)
      DIMENSION GRAF15(200)
C
```

```
      CALL PAPER (1)
C
      CALL ICL9HEMASK (64,IRES)
      ONE=1.000
      PI=ATAN(ONE)*4
C
C     READ IN DATA.
C
      READ (5,104) NPR,NCODE1,NCODE2,NCODE3,NCODE4
      READ(5,*) ZRO2,ZMX2,VMN2,VMX2,TMN2,TMX2,XMN2,XMX2
C
      OPEN(13,FILE='FNAME13')
      OPEN(3,FILE='FNAME3')
C
      DO 50 K=1,NPR
C
C
        READ (5,106) TITLE
        WRITE (6,105) K,TITLE
        READ (5,*) RVEL
        IF (RVEL.EQ.0.) RVEL=6.000
        READ (5,*) M,N,XMN,XMX,ZRO,ZMX,VMN,VMX,TMN,TMX
        READ(5,112) (TT(L), DIST1(L), ERROR(L), L=1,M)
        READ(5,*) VEL0(1),VEL0(2),VEL0(3),VEL0(4),VEL0(5)
        DO 821 J=1,N
          READ(5,*) ((T(KV,J),KV=1,5),DIST2(J))
821     CONTINUE
C
C
        DO 22 L=1,M
          TTRED(L)=TT(L)-(DIST1(L)/RVEL)
          UT(L)=(TT(L)+ERROR(L))-(DIST1(L)/RVEL)
          LT(L)=(TT(L)-ERROR(L))-(DIST1(L)/RVEL)
22      CONTINUE
C
        DO 444 IJ=1,5
C
17      UTD(IJ,1)=T(IJ,1)/DIST2(1)
        DO 15 J=2,N
          UTD(IJ,J)=(T(IJ,J)-T(IJ,J-1))/(DIST2(J)-DIST2(J-1))
          IF (UTD(IJ,J).LT.UTD(IJ,J-1)) GO TO 15
16        T(IJ,J)=T(IJ,J)-0.0001
          UTD(IJ,J)=(T(IJ,J)-T(IJ,J-1))/(DIST2(J)-DIST2(J-1))
          IF (UTD(IJ,J).LT.UTD(IJ,J-1)) GO TO 17
          GO TO 16
15      CONTINUE
C
        DO 878 IBM=1,N
          TRED(IJ,IBM)=T(IJ,IBM)-(DIST2(IBM)/RVEL)
878     CONTINUE
C
        IF(IJ.EQ.1) WRITE (6,103)
        IF(IJ.EQ.1) WRITE(6,987)
        IF(IJ.NE.1) WRITE (6,765) (IJ-1)
        WRITE(6,211)
C
C     CALCULATIONS OF VELOCITIES AND DEPTHS.
C
        VINT(IJ,1)=DIST2(1)/T(IJ,1)
```

```
      VDIFF(IJ,1)=VINT(IJ,1)
      XINT(1)=DIST2(1)
      IF (VEL0(IJ).EQ.0) THEN
        V0(IJ)=VINT(IJ,1)
      ELSE
        V0(IJ)=VEL0(IJ)
      END IF
C
      Q(IJ)=V0(IJ)/V0(IJ)**2
C
      DO 20 J=2,N
        VINT(IJ,J)=(DIST2(J)-DIST2(J-1))/(T(IJ,J)-T(IJ,J-1))
        VDIFF(IJ,J)=VINT(IJ,J)-VINT(IJ,J-1)
        XINT(J)=DIST2(J)-DIST2(J-1)
20    CONTINUE
      MM=N-1
      DO 30 J=1,MM
        VPT(IJ,J)=0.5*(VINT(IJ,J)+VINT(IJ,J+1))
        Z(IJ,J)=0.0
        GRAD(IJ,J)=0.0
        IF (VPT(IJ,J).LE.VINT(IJ,J)) GO TO 43
        DO 40 I=1,J
          X=VPT(IJ,J)/VINT(IJ,I)
          ACOSH=ALOG(X+SQRT(X**2-1.0))
          Z(IJ,J)=Z(IJ,J)+XINT(I)*ACOSH/PI
          IF (J.GT.1) GO TO 41
          ZDIFF=Z(IJ,J)
          GO TO 42
41        ZDIFF=Z(IJ,J)-Z(IJ,J-1)
42        GRAD(IJ,J)=VDIFF(IJ,J)/ZDIFF
          IF (ABS(GRAD(IJ,J)).GE.999.) GRAD(IJ,J)=999.0
40       CONTINUE
43     TAU(IJ,J)=T(IJ,J)-DIST2(J)/VPT(IJ,J)
       P(IJ,J)=(T(IJ,J)-TAU(IJ,J))/DIST2(J)
       U(IJ,J)=SQRT(P(IJ,J)**2+Q(IJ)**2)
       WRITE(6,102) Z(IJ,J),VPT(IJ,J)T(IJ,J),
     %TRED(IJ,J),DIST2(J)
30    CONTINUE
      ZZ(IJ,1)=(TAU(IJ,2)/2)/(SQRT(Q(IJ)**2-P(IJ,2)**2))
      NN=MM-1
      DO 44 J=2,NN
        ZF=SQRT(Q(IJ)**2-P(IJ,J+1)**2)
        ZG=SQRT(U(IJ,J)**2-P(IJ,J+1)**2)
        ZH=(TAU(IJ,J+1)/2)+(ZZ(IJ,J-1)*ZF)
        ZZ(IJ,J)=ZH/ZG
44    CONTINUE
C
      DO 46 J=1,NN
        VU(IJ,J)=U(IJ,J)/U(IJ,J)**2
      WRITE (6,101) DIST2(J),T(IJ,J),VPT(IJ,J)
     &,Z(IJ,J),ZZ(IJ,J)
46    CONTINUE
C
444   CONTINUE
C
C     PLOTTING SEQUENCE.
C
      IF(NCODE3.EQ.0) GO TO 497
      VMN=VMN2
```

```
      VMX=VMX2
      ZRO=ZRO2
      ZMX=ZMX2
      TMN=TMN2
      TMX=TMX2
      XMN=XMN2
      XMX=XMX2
C
497   IF(NCODE3.NE.0.AND.K.GT.1) GO TO 3333
      CALL WHBPL2(VMN,VMX,ZRO,ZMX)
      GO TO 358
3333  CALL PSPACE(0.2,0.74,0.11,0.49)
      CALL MAP(VMN,VMX,ZMX,ZMN)
C
358   DO 945 IK=1,N-1
         GRAF1(IK)=Z(1,IK)
         GRAF2(IK)=Z(2,IK)
         GRAF3(IK)=Z(3,IK)
         GRAF4(IK)=Z(4,IK)
         GRAF5(IK)=Z(5,IK)
         GRAF6(IK)=VPT(1,IK)
         GRAF7(IK)=VPT(2,IK)
         GRAF8(IK)=VPT(3,IK)
         GRAF9(IK)=VPT(4,IK)
         GRAF10(IK)=VPT(5,IK)
C
         GLOWA(IK)=MIN(Z(1,IK),Z(2,IK),Z(3,IK),Z(4,IK),Z(5,IK))
         GHIGHA(IK)=MAX(Z(1,IK),Z(2,IK),Z(3,IK),Z(4,IK),Z(5,IK))
      GLOWB(IK)=MIN(VPT(1,IK),VPT(2,IK),VPT(3,IK),VPT(4,IK),VPT(5,IK))
      GHIGHB(IK)=MAX(VPT(1,IK),VPT(2,IK),VPT(3,IK),VPT(4,IK),VPT(5,IK))
C
945    CONTINUE
       DO 123 IL=1,N-2
C
         GRAF11(IL)=ZZ(1,IL)
         GRAF12(IL)=ZZ(2,IL)
         GRAF13(IL)=ZZ(3,IL)
         GRAF14(IL)=ZZ(4,IL)
         GRAF15(IL)=ZZ(5,IL)
C
         GLOWC(IL)=MIN(ZZ(1,IL),ZZ(2,IL),ZZ(3,IL),ZZ(4,IL),ZZ
     %(5,IL))
         GHIGHC(IL)=MAX(ZZ(1,IL),ZZ(2,IL),ZZ(3,IL),ZZ(4,IL),ZZ
     %(5,IL))
C
123    CONTINUE
C
      WRITE(13,105) K,TITLE
      WRITE(13,601)
      WRITE(13,608)
      WRITE(13,*) N-1
      WRITE(13,619) (VPT(1,MII),Z(1,MII),(Z(1,MII)**2),
     &(Z(1,MII)**3),MII=1,N-1)
      WRITE(13,602)
      WRITE(13,608)
      WRITE(13,*) (N-1)*2
      WRITE(13,619) (GLOWB(MII),Z(1,MII),(Z(1,MII)**2),
     &(Z(1,MII)**3),MII=1,N-1)
      WRITE(13,619) (VPT(1,MII),GHIGHA(MII),(GHIGHA(MII)**2),
```

```
     &(GHIGHA(MII)**3),MII=1,N-1)
      WRITE(13,603)
      WRITE(13,608)
      WRITE(13,*) (N-1)*2
      WRITE(13,619) (VPT(1,MII),GLOWA(MII),(GLOWA(MII)**2),
     &(GLOWA(MII)**3),MII=1,N-1)
      WRITE(13,619) (GHIGHB(MII),Z(1,MII),(Z(1,MII)**2),
     &(Z(1,MII)**3),MII=1,N-1)
      WRITE(13,604)
C
      IF(NCODE1.NE.1.AND.NCODE1.NE.6) GO TO 825
C
      CALL PLOTNC(V0(1),0.0,44)
      CALL JOIN (VPT(1,1),Z(1,1))
      CALL BROKEN (30,15,30,15)
C
      VPLOT=MIN(V0(2),V0(3),V0(4),V0(5))
C
      CALL POSITN (VPLOT,0.0)
      CALL JOIN(GLOWB(1),GHIGHA(1))
C
      VPLOT=MAX(V0(2),V0(3),V0(4),V0(5))
C
      CALL POSITN (VPLOT,0.0)
      CALL JOIN(GHIGHB(1),GLOWA(1))
C
      CALL FULL
C
      CALL PTPLOT (GRAF6,GRAF1,1,N-1,43)
      CALL PTPLOT (GRAF6,GRAF1,1,N-1,-2)
      CALL BROKEN(30,15,30,15)
      CALL PTPLOT (GLOWB,GHIGHA,1,N-1,-2)
      CALL PTPLOT (GHIGHB,GLOWA,1,N-1,-2)
      CALL FULL
C
825   IF(NCODE1.NE.2.AND.NCODE1.NE.3) GO TO 249
C
      DO 534 LJ=1,N-1
        CALL POSITN (GRAF6(LJ),GRAF1(LJ))
        CALL CIRCLE ((VMX-VMN)/150)
        CALL POSITN (GRAF6(LJ),GLOWA(LJ))
        CALL MOVE (-1.0*((VMX-VMN)/150),0.0)
        CALL LINE (2.0*((VMX-VMN)/150),0.0)
        CALL POSITN (GRAF6(LJ),GLOWA(LJ))
        CALL JOIN (GRAF6(LJ),GHIGHA(LJ))
        CALL MOVE (-1.0*((VMX-VMN)/150),0.0)
        CALL LINE (2.0*((VMX-VMN)/150),0.0)
        CALL POSITN (GLOWB(LJ),GRAF1(LJ))
        CALL MOVE (0.0,-1.0*((VMX-VMN)/150))
        CALL LINE (0.0,2.0*((VMX-VMN)/150))
        CALL POSITN (GLOWB(LJ),GRAF1(LJ))
        CALL JOIN (GHIGHB(LJ),GRAF1(LJ))
        CALL MOVE (0.0,-1.0*((VMX-VMN)/150))
        CALL LINE (0.0,2.0*((VMX-VMN)/150))
534   CONTINUE
C
249   IF(NCODE1.EQ.1.OR.NCODE1.EQ.2) CALL BLKPEN
      IF(NCODE1.EQ.3.OR.NCODE1.EQ.6) GO TO 4
      IF(NCODE1.NE.1.AND.NCODE1.NE.5) GO TO 511
```

```
C
      CALL PLOTNC(V0(1),0.0,44)
      CALL JOIN (VPT(1,1),ZZ(1,1))
      CALL BROKEN (30,15,30,15)
C
      VPLOT=MIN(V0(2),V0(3),V0(4),V0(5))
C
      CALL POSITN (VPLOT,0.0)
      CALL JOIN(GLOWB(1),GHIGHC(1))
C
      VPLOT=MAX(V0(2),V0(3),V0(4),V0(5))
C
      CALL POSITN (VPLOT,0.0)
      CALL JOIN(GHIGHB(1),GLOWC(1))
C
      CALL FULL
      CALL PTPLOT (GRAF6,GRAF11,1,N-1,NOCHAR)
      CALL PTPLOT (GRAF6,GRAF11,1,N-2,-2)
      CALL BROKEN (30,15,30,15)
      CALL PTPLOT (GLOWB,GHIGHC,1,N-2,-2)
      CALL PTPLOT (GHIGHB,GLOWC,1,N-2,-2)
      CALL FULL
C
511   IF(NCODE1.NE.2.AND.NCODE1.NE.4) GO TO 4
C
      DO 52 IE=1,N-2
        CALL POSITN (GRAF6(IE),GRAF11(IE))
        CALL CIRCLE ((VMX-VMN)/150)
        CALL POSITN (GRAF6(IE),GLOWC(IE))
        CALL MOVE (-1.0*((VMX-VMN)/150),0.0)
        CALL LINE (2.0*((VMX-VMN)/150),0.0)
        CALL POSITN (GRAF6(IE),GLOWC(IE))
        CALL JOIN (GRAF6(IE),GHIGHC(IE))
        CALL MOVE (-1.0*((VMX-VMN)/150),0.0)
        CALL LINE (2.0*((VMX-VMN)/150),0.0)
        CALL POSITN (GLOWB(IE),GRAF11(IE))
        CALL MOVE (0.0,-1.0*((VMX-VMN)/150))
        CALL LINE (0.0,2.0*((VMX-VMN)/150))
        CALL POSITN (GLOWB(IE),GRAF11(IE))
        CALL JOIN (GHIGHB(IE),GRAF11(IE))
        CALL MOVE (0.0,-1.0*((VMX-VMN)/150))
        CALL LINE (0.0,2.0*((VMX-VMN)/150))
52    CONTINUE
C
4     CALL BLKPEN
C
605   IF(NCODE3.NE.0.AND.K.NE.NPR) GO TO 3
C
      IF(NCODE4.NE.0) CALL ADPLOT(NCODE4,K)
C
699   CONTINUE
C
C     CALL FRAME
C
3     CONTINUE
C
      IF(NCODE3.NE.0.AND.K.GT.1) GO TO 1111
      CALL WHBPL0 (RVEL,XMN,XMX,TMN,TMX)
      GO TO 2222
```

```
1111    CONTINUE
        CALL PSPACE(0.2,0.74,0.57,0.91)
        CALL MAP(XMN,XMX,TMN,TMX)
2222    DO 62 IG=1,M
          CALL POSITN (DIST1(IG),TTRED(IG))
          CALL CIRCLE ((XMX-XMN)/150)
          CALL POSITN (DIST1(IG),UT(IG))
          CALL MOVE ((-1.0*(XMX-XMN)/150),0.0)
          CALL LINE ((2.0*(XMX-XMN)/150),0.0)
          CALL POSITN (DIST1(IG),UT(IG))
          CALL JOIN (DIST1(IG),LT(IG))
          CALL MOVE ((-1.0*(XMX-XMN)/150),0.0)
          CALL LINE ((2.0*(XMX-XMN)/150),0.0)
62      CONTINUE
C
        IF(NCODE2.NE.2) GO TO 900
C
        GRAF1(1)=0.00
        GRAF2(1)=0.00
        GRAF3(1)=0.00
        GRAF4(1)=0.00
        GRAF5(1)=0.00
        GRAF6(1)=0.00
C
        DO 92 KW=2,N+1
          GRAF1(KW)=TRED(1,KW-1)
          GRAF2(KW)=TRED(2,KW-1)
          GRAF3(KW)=TRED(3,KW-1)
          GRAF4(KW)=TRED(4,KW-1)
          GRAF5(KW)=TRED(5,KW-1)
          GRAF6(KW)=DIST2(KW-1)
92      CONTINUE
C
        CALL PTPLOT(GRAF6,GRAF1,1,N+1,-2)
        CALL BROKEN(10,5,10,5)
        CALL PTPLOT(GRAF6,GRAF2,1,N+1,-2)
        CALL PTPLOT(GRAF6,GRAF3,1,N+1,-2)
        CALL PTPLOT(GRAF6,GRAF4,1,N+1,-2)
        CALL PTPLOT(GRAF6,GRAF5,1,N+1,-2)
        CALL FULL
C
900     CONTINUE
C
        IF(NCODE3.NE.0.AND.K.NE.NPR) GO TO 39
        CALL FRAME
C
39      CONTINUE
C
50      CONTINUE
C
C   FORMATS.
C
619   FORMAT(4F10.5)
201   FORMAT (F8.3,'   0.000',F8.3,'   0.000   0.000')
28    FORMAT(2I5)
921   FORMAT (3I5)
61    FORMAT(2(I5),3X,10A4)
101   FORMAT (5F8.3)
102   FORMAT (4X,F7.3,7X,F6.3,8X,F7.3,F10.3,6X,F7.3,8X
```

```
 103   FORMAT (//6X,'DETERMINATION OF VELOCITY-DEPTH FUNCTION'/6X,'BY WIE
      1CHERT-HERGLOTZ-BATEMAN INTEGRAL'//)
 987   FORMAT (1X,'BEST FIT CURVE')
 765   FORMAT (//1X,'ERROR CURVE',I3)
 432   FORMAT (1X,'ERROR CURVE 2')
 211   FORMAT (//1X,'DEPTH (KM)',2X,'VELOCITY (KM/S)',
      22X,'TIME (S)',2X,'RED.TIME',2
      3X,'DISTANCE (KM)'/)
 104   FORMAT (5I5)
 105   FORMAT (/2X,'DATASET NUMBER',I3,5X,10A4)
 106   FORMAT (10A4)
 109   FORMAT (2I3)
 110   FORMAT (2F8.3)
 111   FORMAT (9F8.3)
 112   FORMAT (3F10.5)
 73    FORMAT(6F10.5)
 113   FORMAT (3F10.5,I5)
 601   FORMAT(/,'BEST FIT WHB VELOCITY DEPTH CURVE')
 602   FORMAT(/,'MAX DEPTH, MIN VELOCITY WHB CURVE')
 603   FORMAT(/,'MIN DEPTH, MAX VELOCITY WHB CURVE')
 604   FORMAT(/,'BEST FIT TAU-P VELOCITY DEPTH CURVE')
 606   FORMAT(/,'MAX DEPTH, MIN VELOCITY TAU-P CURVE')
 607   FORMAT(/,'MIN DEPTH, MAX VELOCITY TAU-P CURVE')
 608   FORMAT(2X,'VELOCITY   DEPTH')
       CALL GREND
       STOP
       END
C
C
C      SUBROUTINE TO ANNOTATE PLOT OF VELOCITY AGAINST DEPTH.
C
       SUBROUTINE WHBPL2 (VMN,VMX,ZRO,ZMX)
       COMMON TITLE (10)
       CALL CSPACE (0.05,1.47,0.05,1.08)
       CALL PSPACE (0.2,0.74,0.11,0.49)
       CALL MAP (VMN,VMX,ZMX,ZRO)
       CALL PLACE (10,5)
       CALL TYPECS (TITLE,40)
       CALL PLACE (18,36)
       CALL TYPECS ('VELOCITY (KM/S)',15)
       CALL PLACE (5,30)
       CALL CTRORI (1.0)
       CALL TYPECS ('DEPTH (KM)',10)
       CALL CTRORI (0.0)
       CALL BORDER
       CALL CTRMAG (10)
       CALL SCALES
       CALL CTRMAG (20)
       RETURN
       END
C
C      SUBROUTINE TO ANNOTATE PLOT OF COMPUTED REDUCED TIME AGAINST RANGE
C
       SUBROUTINE WHBPL0 (RVEL,XMN,XMX,TMN,TMX)
       COMMON TITLE (10)
       CALL PSPACE (0.2,0.74,0.57,0.91)
       CALL MAP (XMN,XMX,TMN,TMX)
       CALL PLACE (18,20)
       CALL TYPECS ('RANGE (KM)',10)
```

```
      CALL PLACE (5,16)
      CALL CTRORI (1,0)
      CALL TYPECS ('REDUCED TIME',12)
      CALL CTRORI (0,0)
      CALL BORDER
      CALL CTRMAG (10)
      CALL SCALES
      CALL CTRMAG (20)
      RETURN
      END
C
      SUBROUTINE ADPLOT(NCODE4,K)
      DIMENSION Y(200), XX(200), ZZZ(50,200), ANI(200), PR(200)
      DIMENSION DATA1(200), DATA2(200)
      DIMENSION END1(50), END2(50), LIMITA(50), LIMITB(50)
      DIMENSION LIMITC(50), LIMITD(50)
C
      IF(NCODE4.NE.1.AND.NCODE4.NE.2) GO TO 628
C
      READ(5,*) MSETS
      DO 934 JHG=1,MSETS
C
        READ(5,*) NPTS
C
        DO 482 IAA=1,NPTS
          READ(5,*) DATA1(IAA),DATA2(IAA)
482     CONTINUE
C
        IF(NCODE4.NE.1) GO TO 742
C
        CALL PTPLOT(DATA1,DATA2,1,NPTS,43)
742     IF(NCODE4.NE.2) GO TO 621
        CALL PTPLOT(DATA1,DATA2,1,NPTS,-43)
621     CONTINUE
C
934   CONTINUE
C
628   IF(NCODE4.EQ.1.OR.NCODE4.EQ.2) GO TO  823
C
       READ(5,*) MSETS
       DO 832 MCD=1,MSETS
C
         READ(5,*) A,B,C,D,END1(MCD),END2(MCD),IBROKE
C
         IF(IBROKE.EQ.1) CALL BROKEN (20,10,20,10)
C
         X=0.00
         DO 517 IOTA=1,100
           Y(IOTA)=(A+B*X+C*X**2+D*X**3)
           XX(IOTA)=X
           ZZZ(MCD,IOTA)=Y(IOTA)
           X=X+0.05
           IF(X.GT.END2(MCD)) THEN
             LIMITB(MCD)=IOTA
             IOTA=100
           END IF
517      CONTINUE
      LIMITA(MCD)=NINT(END1(MCD)/0.05)
      IF(LIMITA(MCD).LT.1) LIMITA(MCD)=1.0
```

```
C
C          IF(NCODE4.NE.3) GO TO 832
          CALL PTPLOT(Y,XX,LIMITA(MCD),LIMITB(MCD),-2)
C
832     CONTINUE
C
        CALL FULL
C
C        IF(NCODE4.NE.4.AND.NCODE4.NE.5) GO TO 823
C
        READ(5,*) MSETS
        DO 513 IIO=1,MSETS
          READ(5,*) MCOMP1,MCOMP2,IBROKE
          IF(IBROKE.EQ.1) CALL BROKEN (20,10,20,10)
          IF(LIMITB(MCOMP1).GE.LIMITB(MCOMP2)) THEN
            LIMITD(IIO)=LIMITB(MCOMP2)
          ELSE
            LIMITD(IIO)=LIMITB(MCOMP1)
          END IF
       IF(LIMITA(MCOMP1).LE.LIMITA(MCOMP2)) THEN
         LIMITC(IIO)=LIMITA(MCOMP2)
       ELSE
         LIMITC(IIO)=LIMITA(MCOMP1)
       END IF
       IF(LIMITC(IIO).LT.1) LIMITC(IIO)=1.0
C
          DO 822 IIP=1,LIMITD(IIO)
            Y(IIP)=(ZZZ(MCOMP1,IIP)+ZZZ(MCOMP2,IIP))*0.5
            ANI(IIP)=(ZZZ(MCOMP1,IIP)/ZZZ(MCOMP2,IIP))
            PR(IIP)=(ANI(IIP)**2*0.5-1.0)/(ANI(IIP)**2-1.0)
822       CONTINUE
C
        IF(NCODE4.EQ.4) THEN
          CALL PTPLOT(Y,XX,LIMITC(IIO),LIMITD(IIO),-2)
        ELSE
          CALL PTPLOT(ANI,XX,LIMITC(IIO),LIMITD(IIO),-2)
          CALL PTPLOT(PR,XX,LIMITC(IIO),LIMITD(IIO),-2)
        END IF
          IF(K.EQ.1)  WRITE(3,110) (Y(IQX), XX(IQX), IQX=1,LIMITB(IIO))
110       FORMAT(2F10.5)
513     CONTINUE
C
        CALL FULL
C
823     RETURN
        END
```

Program TIMPROG

Program for the calculation of vertical and horizontal velocities through a transversely isotropic media (see chapter 4).

INPUT DATA FOR PROGRAM TIMPROG

CARD 1

NDATA

NDATA NUMBER IF T.I.M. TO BE MODELLED. CARDS 2 TO 6 REPEATED NDATA TIMES

CARD 2

TITLE CHARACTER STRING LESS THAN 40 LONG

CARD 3

NCOMP,ICAL,IUNITS,ISO

```
NCOMP     NUMBER OF COMPONENT MEDIA (INTEGER)
ICAL=0    S WAVE VELOCITY AND DENSITY CALCULATED FROM P WAVE VELOCITY
ICAL=1    S WAVE VELOCITY AND DENSITY READ IN
IUNITS=0  VELOCITY INPUT IN KM/S
IUNITS=1  VELOCITY INPUT IN FT/S
ISO=0     ALL COMPONENTS ARE ISOTROPIC
ISO=1     ONE OR MORE COMPONENTS ARE INTRINSICALLY ANISOTROPIC
```

CARD 4

READ IF(ICAL.EQ.0)
IDEN,VELO

```
DEN=1     DENSITY CALCULATED FORM P WAVE VELOCITY
DEN=2     MINIMUM DENSITY CALCULATED FROM P WAVE VELOCITY
DEN=3     MAXIMUM DENSITY CALCULATED FROM P WAVE VELOCITY
IVELO     RATIO VP:VS
```

CARD 5

IPLOT,VMIN,VMAX

```
IPLOT=0   PLOT OF VELOCITY VS THETA
IPLOT=1   PLOT OF VELOCITY ELLIPSE
VMIN      MINIMUM VELOCITY ON PLOT AXES (KM/S)
VMAX      MAXIMUM VELOCITY ON PLOT AXIS (KM/S)
```

CARD 6 (REPEATED NCOMP TIMES)

```
IF(ICAL.EQ.0.AND.ISO.EQ.0) VP,PRO
IF(ICAL.EQ.1.AND.ISO.EQ.0) VP,VS,DEN,PRO
IF(ICAL.EQ.0.AND.ISO.EQ.1) VP,FAC1,FAC2,PRO
IF(ICAL.EQ.1.AND.ISO.EQ.1) VP,FAC1,VS,FAC2,DEN,PRO
```

```
VP        P WAVE VELOCITY OF COMPONENT
VS        S WAVE VELOCITY OF COMPONENT
```

```
FAC1      RATIO VP(H):VP(V)
FAC2      RATIO VS(H):VS(V)
DEN       DENSITY OF COMPONENT (g/CC)
PRO       PROPORTION OF T.I.M (SUM OF PRO(I),I=1,NCOMP=1.0)

------------------------------------------------------------------------

        PROGRAM TIMPROG
C
C PROGRAM TO CALCULATE ANISOTROPY OF A T.I.M. (SEE APPENDIX, LEVIN 1979).
C VERTICAL AND HORIZONTAL P WAVE VELOCITIES THROUGH THE MEDIA ARE
C CALCULATED AND VELOCITY VARIATION WITH ANGLE CALCULATED ASSUMING AN
C ELLIPTICAL DEPENDENCE
C
C WHERE ALL COMPONENTS ARE ISOTROPIC EQUATIONS A-8a OF LEVIN ARE USED.
C WHERE ONE OR COMPONENTS WERE INTRINSICALLY ANISOTROPIC EQUATIONS A-8
C AND A-9 WERE USED.
C
C FORTRAN 77 WITH GHOST GRAPHICS ROUTINES
C
C MIKE DENTITH 1987

      COMMON TITLE(3)
      DIMENSION X(160),V(160),FAC1(1000),FAC2(1000),VX(1000)
      DIMENSION VP(1000),VS(1000),DEN(1000)
      REAL PRO(1000),NN,N,LL,L,P,Q,R,S,PROTOT
C
      READ(5,*) NDATA
C
      DO 99 J=1,NDATA
C
C INPUT MEDIA DETAILS
C
      READ(5,27) TITLE
      WRITE(6,27) TITLE
      WRITE(6,93)
93    FORMAT('COMPONENT PROPERTIES')
      WRITE(6,31)
31    FORMAT('     VP(H)        VP(V)         VS(H)         VS(V)     DENSITY
     %   PROPORTION')
      READ(5,*) NCOMP,ICAL,IUNITS,ISO
      IF(ICAL.EQ.0)READ(5,*) IDEN, VELO
      READ(5,*) IPLOT,VMIN,VMAX
C
C SET ELASTIC CONSTANTS AND INTERMEDIATE VARIABLES TO ZERO
      A=0.0
      C=0.0
      F=0.0
      N=0.0
      L=0.0
      D=0.0
      F1=0.0
      F2=0.0
      A1=0.0
      A2=0.0
      A3=0.0
C
      PROTOT=0.0
C
```

```
C LOOP TO CALCULATE ELASTIC CONSTANTS A,C,F,L,N OF COMPONENTS
C
      DO 10 I=1,NCOMP
C
C INPUT COMPONENT DETAILS
C
27      FORMAT(3A4)
C
        IF(ICAL.EQ.0.AND.ISO.EQ.0) READ(5,*) VP(I),PRO(I)
        IF(ICAL.EQ.1.AND.ISO.EQ.0) READ(5,*) VP(I),VS(I),DEN(I),PRO(I)
        IF(ICAL.EQ.0.AND.ISO.EQ.1) READ(5,*) VP(I),FAC1(I),FAC2(I),PRO(I)
        IF(ICAL.EQ.1.AND.ISO.EQ.1) READ(5,*) VP(I),FAC1(I),VS(I),FAC2(I)
     & ,DEN(I),PRO(I)
C
        PROTOT=PROTOT+PRO(I)
C
        IF(IUNITS.EQ.0) VP(I)=(VP(I)/0.3048)*1000.0
        IF(IUNITS.EQ.0.AND.ICAL.EQ.1) VS(I)=(VS(I)/0.3048)*1000.0
C
C SELECT VP DENSITY FUNCTION AND CALC VS (IF.ICAL.EQ.0)
C
        IF(ICAL.NE.0) GO TO 92
C
        VX(I)=(VP(I)*0.3048)/1000.0
C
        IF(IDEN.EQ.1) THEN
        DEN(I)=((0.006*VX(I)**3)+(-0.086*VX(I)**2)+(0.557*VX(I))+1.132)
        ELSE IF (IDEN.EQ.2) THEN
        DEN(I)=((0.007*VX(I)**3)+(-0.122*VX(I)**2)+(0.767*VX(I))+0.677)
        ELSE
        DEN(I)=((-0.006*VX(I)**3)+(0.062*VX(I)**2)+(-0.009*VX(I))+2.029)
        END IF
C
        VS(I)=VP(I)/VELO
C
92      CONTINUE
        IF(ISO.EQ.0) THEN
          FAC1(I)=1.0
          FAC2(I)=1.0
        END IF
C
        WRITE(6,43) VP(I)*0.3048,(VP(I)*0.3048)/FAC1(I),VS(I)*0.3048,
     %(VS(I)*0.3048)/FAC2(I),DEN(I),PRO(I)*100.0
43      FORMAT(1F9.2,'M/S',1F9.2,'M/S',F9.2,'M/S',
     %1F9.2,'M/S',1F6.2,'g/CC',1F9.2,'%')
C
        IF(I.EQ.NCOMP) WRITE(6,117) PROTOT*100
117     FORMAT(20X,'                                  TOTAL:',1F8.2,'%')
C
C
C CALCULATE ELASTIC CONSTANTS
C
      IF(ISO.EQ.0) THEN
         AA1=(4*DEN(I)*VS(I)**2*(1-(VS(I)**2/VP(I)**2)))*PRO(I)
         AA2=((1-(2*VS(I)**2/VP(I)**2))*PRO(I))
         AA3=(1/(DEN(I)*VP(I)**2))*PRO(I)
         A1=A1+AA1
         A2=A2+AA2
         A3=A3+AA3
```

```
            CC=(1/(DEN(I)*VP(I)**2))*PRO(I)
            C=C+CC
            FF1=(1-(2*VS(I)**2/VP(I)**2))*PRO(I)
            FF2=(1/(DEN(I)*VP(I)**2))*PRO(I)
            F1=F1+FF1
            F2=F2+FF2
            NN=(DEN(I)*(VS(I)**2))*PRO(I)
            N=N+NN
            LL=(1/(DEN(I)*VS(I)**2))*PRO(I)
            L=L+LL
          ELSE
            Q1=DEN(I)*VP(I)**2
            Q2=DEN(I)*VS(I)**2
            Q3=DEN(I)*(VP(I)**2-2*VS(I)**2)
            Q4=DEN(I)*(VP(I)/FAC1(I))**2
            Q5=DEN(I)*(VS(I)/FAC2(I))**2
            AA1=(Q1-Q3**2*(1/Q4))*PRO(I)
            AA2=(1/Q4)*PRO(I)
            AA3=Q3*(1/Q4)*PRO(I)
            A1=A1+AA1
            A2=A2+AA2
            A3=A3+AA3
            CC=(1/Q4)*PRO(I)
            C=C+CC
            FF1=(1/Q4)*PRO(I)
            FF2=Q3*(1/Q1)*PRO(I)
            F1=F1+FF1
            F2=F2+FF2
            NN=Q5*PRO(I)
            N=N+NN
            LL=(1/Q2)*PRO(I)
            L=L+LL
          END IF
C
            DD=DEN(I)*PRO(I)
            D=D+DD
C
10      CONTINUE
C
C CONVERT ELASTIC CONSTANTS FROM COMPONENTS TO THOSE OF T.I.M
C
          IF(ISO.EQ.0) THEN
            L=1/L
            F=F1/F2
            C=1/C
            A=A1+((A2**2)/A3)
          ELSE
            L=1/L
            F=(1/F1)*F2
            C=1/C
            A=A1+(1/A2)*A3**2
          END IF
C
C WRITE MODEL PARAMETERS TO FILE
C
        WRITE(6,94)
94      FORMAT('T.I.M. PROPERTIES')
        WRITE(6,29) D
29      FORMAT('DENSITY',1F8.2,'g/CC')
```

```
      WRITE(6,21)
21    FORMAT('ELASTIC CONSTANTS * 10exp-6.0 ')
      WRITE(6,22)
22    FORMAT('    A          C          F          L          N          ')
C
      WRITE(6,20) A*0.000001,C*0.000001,F*0.000001,L*0.000001,
     &N*0.000001
C
20    FORMAT(5F10.5)
C
C CALCULATE VERTICAL AND HORIZONTAL P-WAVE VELOCITIES
C
      VV=(C/D)**0.5
      VH=(A/D)**0.5
      AN=VH/VV
C
      WRITE(6,37)
37    FORMAT('    VP(VERT)      VP(HORIZ)       VP(H)/VP(V)  ANISO',
     &'TROPY')
C
      WRITE(6,34) VV*0.3048,VH*0.3048,VH/VV,((VH-VV)/VV)*100
34    FORMAT(F10.2,'M/S ',F10.2,'M/S ',F10.2,7X,F6.2,'%')
C
C CALCULATE VELOCITY AT ANGLE X FROM THE VERTICAL ASSUMING ELLIPTICAL
C
      X(1)=0.00
      WRITE(6,303)
303   FORMAT('VELOCITY AS A FUNCTION OF ANGLE FROM VERTICAL')
      WRITE(6,101)
101   FORMAT('  THETA(RADS) VELOCITY')
C
      DO 100 K=1,158
C
        R=(VV*VH)**2
        S=(VV**2)*(SIN(X(K))**2)
        T=(VH**2)*(COS(X(K))**2)
        V(K)=(R/(S+T))**0.5
C
        WRITE(6,102) X(K),V(K)*0.3048
        X(K+1)=X(K)+0.01
102     FORMAT(F10.3,2X,F10.3)
C
100   CONTINUE
C
       VMIN=VMIN*1000
       VMAX=VMAX*1000
C
       IF(IPLOT.NE.1) GO TO 44
C
       CALL AXPL(VMAX,VMIN)
       CALL POSITN(X(1),V(1)*0.3048)
       DO 88 M=2,158
       CALL JOIN(X(M),V(M)*0.3048)
88     CONTINUE
       CALL FRAME
C
44     IF(IPLOT.NE.0) GO TO 99
C
       CALL AXPL2
```

```
      CALL ARCELL(1.00,0.0,1.57,VH/VV)
      CALL FRAME
C
99    CONTINUE
C
      CALL GREND
      STOP
      END
C
C SUBROUTINE TO ANNOTATE PLOT OF VELOCITY VS ANGLE
C
      SUBROUTINE AXPL (VMAX,VMIN)
      COMMON TITLE (3)
      CALL CSPACE (0.05,1.1,0.05,0.82)
      CALL PSPACE (0.2,1.1,0.2,0.76)
      CALL MAP (0.00,1.57,VMIN,VMAX)
      CALL PLACE (20,1)
      CALL TYPECS (TITLE,40)
      CALL PLACE (30,24)
      CALL TYPECS ('ANGLE (RADS)',12)
      CALL PLACE (4,17)
      CALL CTRORI (1.0)
      CALL TYPECS ('VELOCITY (M/SEC)',16)
      CALL CTRORI (0.0)
      CALL BORDER
      CALL CTRMAG (10)
      CALL SCALES
      CALL CTRMAG (20)
      RETURN
      END
C
C SUBROUTINE TO ANNOTATE PLOT OF VELOCITY VS VELOCITY
C
      SUBROUTINE AXPL2
      COMMON TITLE (3)
      CALL CSPACE (0.05,1.1,0.05,0.82)
      CALL PSPACE (0.2,0.76,0.2,0.76)
      CALL MAP (0.00,1.00,0.0,1.00)
      CALL PLACE (20,1)
      CALL TYPECS (TITLE,40)
      CALL PLACE (17,24)
      CALL TYPECS ('HORIZONTAL VELOCITY',19)
      CALL PLACE (4,17)
      CALL CTRORI (1.0)
      CALL TYPECS ('VERTICAL VELOCITY',17)
      CALL CTRORI (0.0)
      CALL BORDER
      CALL CTRMAG (10)
      CALL SCALES
      CALL CTRMAG (20)
      RETURN
      END
```

Program MD2D

Program for the calculation two-dimension gravity and magnetic anomalies (see Chapter 6).

INPUT DATA FOR PROGRAM MD2D

THE PROGRAM CALCULATES GRAVITY AND/OR MAGNETIC ANOMALIES ALONG A PROFILE AND PLOTS THE RESULTS AGAINST OBSERVED DATA.

STATIONS ARE EXTRAPOLATED ON TO THE PROFILE AT 90' TO THE PROFILE TREND. IF STATIONS LIE OUTSIDE THE PROFILE THEY ARE PLACED ON TO THE EXTRAPOLATION OF THE PROFILE.

SET IGRAF TO 7 ON INITIAL RUN TO CHECK PROFILE POSITIONING.

IF REGIONAL GRADIENTS ARE SPECIFIED THESE ARE REMOVED FROM OBSERVED DATA

ALL DATA IS READ IN FREE FORMAT EXCEPT CARD 1.
IF PARAMETERS ARE NOT USED THEY SHOULD BE SET TO ZERO.
ALL DISTANCES ARE IN KM

CARD 1

IGRAF,TITLE   FORMAT(I3,104)

IGRAF   CONTROLS GRAPHICAL OUTPUT

= 1   ONLY THE MODEL IS PLOTTED
= 2   ONLY THE CALCULATED AND OBSERVED MAGNETICS ARE PLOTTED
= 3   ONLY THE CALCULATED AND OBSERVED GRAVITY ARE PLOTTED
= 4   MODEL AND OBS AND CALC GRAVITY ARE PLOTTED
= 5   MODEL AND OBS AND CALC MAGNETICS ARE PLOTTED
= 6   MODEL AND BOTH OBS AND CALC GRAVITY AND MAGNETICS ARE PLOTTED
= 7   MAP OF STATIONS AND PROFILE IS PLOTTED

TITLE   CHARACTER STRING OF LENGTH LESS THAN 41 APPEARING ON ALL PLOTS

CARD 2

NSTN

NSTN   NUMBER OF STATIONS (INTEGER)

CARD 3

END1E,END1N,END2E,END2N

END1E   THE EASTING OF THE ORIGIN OF THE PROFILE
END1N   THE NORTHING OF THE ORIGIN OF THE PROFILE
END2E   EASTING OF THE OTHER END OF PROFILE
END2N   NORTHING OF THE OTHER END OF PROFILE

NOTE THAT A STATION MUST NOT LIE AT THE PROFILE ENDS SINCE THE COSINE RULE IS USED TO EXTRAPOLATE ONTO THE PROFILE AND A ZERO DISTANCE TO ONE OF THE PROFILE ENDS CAUSES A ZERO DIVIDE

CARD 4

GGRAD,GTREN,ERRG,GCONS

GGRAD	THE REGIONAL GRAVITY GRADIENT
GTREN	TREND OF THE ABOVE GRADIENT
ERRG	ERROR IN OBSERVED GRAVITY DATA
GCONS	CONSTANT ADDED TO CALCULATED GRAVITY

ERRG IS SHOWN AS AN ERROR BAR ON THE CALCULATED DATA

CARD 5

MGRAD,MTREN,ERRM,MCONS

MGRAD	AS CARD 4 FOR MAGNETIC DATA
MTREN	
ERRM	
MCONS	

CARD 6

DECA,INCA,INTA

DECA	DECLINATION OF AMBIENT FIELD (354 IN SCOTLAND)
INCA	INCLINATION OF AMBIENT FIELD (+70.0 IN SCOTLAND)
INTA	INTENSITY OF AMBIENT FIELD (45000 IN SCOTLAND)

CARD 7

ISTN,GREFE,GREFN,BOANOM,TOTMAG (REPEATED NSTN TIMES)

ISTN	ARBITUARY STATION NUMBER
GREFE	STATION EASTING
GREFN	STATION NORTHING
BOANOM	BOUGUER GRAVITY AT STATION
TOTMAG	TOTAL MAGNETIC FIELD AT STATION

CARD 8

NBOD

NBOD	NUMBER OF BODIES IN MODEL (INTEGER)

CARDS 9 AND 10 ARE REPEATED NBOD TIMES

CARD 9

LNO,NPT,RHO,SUS,DECR,RINC,RINT

LNO	ARBITARY BODY NUMBER (INTEGER)
NPT	NUMBER OF CORNERS TO BODY (INTEGER). THE 1ST POINT IS NOT REPEATED POINTS INPUT IN CLOCKWISE ORDER.
RHO	DENSITY OF BODY (g/cm**3)
SUS	SUSCEPTIBILTY OF BODY
DECR	DECLINATION OF REMANENT MAGNETISM IN BODY (DEGREES)
RINC	INCLINATION OF REMANENT MAGNETISM IN BODY (DEGREES)
RINT	INTENSITY OF REMANENT MAGNETISM (AMP/METRE)

CARD 10

```
X,Y

X              X CO-ORD OF CORNER RELATIVE TO PROFILE ORIGIN
Y              Z CO-ORD OF CORNER RELATIVE TO GROUND LEVEL (+VE DOWNWARDS)

CARD 11

EMAX,EMIN,NMAX,NMIN

EMAX           MAXIMUM EASTING WHEN PLOTTING MAP
EMIN           MINIMUM    "      "      "     "
NMAX           MAXIMUM NORTHING  "      "     "
NMIN           MINIMUM    "      "      "     "

CARD 12

ZMAX,ZMIN,ZINT

ZMAX           MAXIMUM DEPTH WHEN PLOTTING MODEL
ZMIN           MINIMUM DEPTH  "       "       "
ZINT           INTERVAL AT WHICH AXIS IS LABELLED

CARD 13

MMAX,MMIN,MINT

MMAX           |
MMIN           | AS ABOVE FOR MAGNETIC DATA
MINT           |

CARD 14

GMAX,GMIN,GINT

GMAX           |
GMIN           | AS ABOVE FOR GRAVITY DATA
GINT           |

CARD 15

XINT

XINT           INTERVAL AT WHICH RANGE AXIS IS LABELLED ON ABOVE PLOTS

---------------------------------------------------------------------------

      PROGRAM MD2D
C
C PROGRAMME TO CALCULATE 2D GRAVITY AND MAGNETIC ANOMALIES
C FORTRAN 77 WITH GHOST GRAPHICS ROUTINES
C
C
C MIKE DENTITH JUNE 1987
C GRAVITY PROGRAMME ADAPTED FROM PROGRAMME T2D BY W.SOWERBUTTS
C MAGNETIC PROGRAMME ADAPTED FROM PROGRAMME BY D.WATTS
C
      COMMON TITLE(10),D(200),ISTN(200),GREFE(200),GREFN(200)
      COMMON BOANOM(200),TOTMAG(200)
      COMMON LNO(200),NPT(200),RHO(200),SUS(200),X(200,200),Y(200,200)
```

```
      COMMON DECR(200),RINC(200),RINT(200)
      COMMON RESG(200),RESM(200),SSELZ(200),PDELZ(200,200)
      COMMON CALM(200),CMBOD(200,200)
      REAL INTA,INCA,MCONS,MGRAD,MTREN
C
C READ CONTROL PARAMETERS
C
      READ(5,11) IGRAF,TITLE
11    FORMAT(I3,10A4)
C
C CALL SUBROUTINES
C
      CALL DATIN(DIST,NSTN,TREND,END1E,END1N,END2E,END2N
     &  ,GGRAD,GTREN,ERRG,GCONS,MGRAD,MTREN,ERRM,MCONS,DECA,INCA,INTA)
      CALL GRADN(TREND,DIST,NSTN,GGRAD,GTREN,MGRAD,MTREN)
      CALL MODIN(NBOD)
      CALL GRANOM(NSTN,NBOD,GCONS)
      CALL MAANOM(TREND,NBOD,NSTN,INTA,INCA,DECA,MCONS)
      CALL DATAPL(IGRAF,DIST,NSTN,NBOD,GGRAD,MGRAD,ERRG,ERRM,END1E,END1N
     &,END2E,END2N,TREND,MTREN,GTREN)
      CALL DATOUT(DIST,NSTN,TREND,END1E,END1N,END2E,END2N
     &  ,GGRAD,GTREN,ERRG,GCONS,MGRAD,MTREN,ERRM,MCONS,DECA,INCA,INTA,
     &  NBOD)
      CALL GREND
C
      STOP
      END
C
C ***********************************************************************
C
C SUBROUTINE TO READ IN DATA AND CONSTRUCT PROFILE
C
      SUBROUTINE DATIN(DIST,NSTN,TREND,END1E,END1N,END2E,END2N
     &  ,GGRAD,GTREN,ERRG,GCONS,MGRAD,MTREN,ERRM,MCONS,DECA,INCA,INTA)
C
      COMMON TITLE(10),D(200),ISTN(200),GREFE(200),GREFN(200)
      COMMON BOANOM(200),TOTMAG(200)
      COMMON LNO(200),NPT(200),RHO(200),SUS(200),X(200,200),Y(200,200)
      COMMON DECR(200),RINC(200),RINT(200)
      COMMON RESG(200),RESM(200),SSELZ(200),PDELZ(200,200)
      REAL INTA,INCA,MCONS,MGRAD,MTREN
C
      READ(5,*) NSTN
      READ(5,*) END1E,END1N,END2E,END2N
      READ(5,*) GGRAD,GTREN,ERRG,GCONS
      READ(5,*) MGRAD,MTREN,ERRM,MCONS
      READ(5,*) DECA,INCA,INTA
C
      DO 13 I=1,NSTN
        READ(5,*) ISTN(I),GREFE(I),GREFN(I),BOANOM(I),TOTMAG(I)
13    CONTINUE
C
C CALC LENGTH AND TREND OF PROFILE
C
      PI=3.141593
      DIST=((END1E-END2E)**2+(END1N-END2N)**2)**0.5
      IF(END1N.EQ.END2N.OR.END1E.EQ.END2E) GO TO 18
      ANGLE=(ATAN((END1E-END2E)/(END1N-END2N)))/PI*180
C
```

```
 18     IF(END1E.GT.END2E.AND.END1N.GT.END2N) THEN
          TREND=180.00+ANGLE
        ELSE IF(END1E.LT.END2E.AND.END1N.GT.END2N) THEN
          TREND=180.00+ANGLE
        ELSE IF(END1E.LT.END2E.AND.END1N.LT.END2N) THEN
          TREND=0.0+ANGLE
        ELSE IF(END1E.GT.END2E.AND.END1N.LT.END2N) THEN
          TREND=360.00+ANGLE
        ELSE IF(END1E.EQ.END2E.AND.END1N.NE.END2N) THEN
          IF(END1N.GT.END2N) TREND=180.00
          IF(END1N.LT.END2N) TREND=0.00
        ELSE
          IF(END1E.GT.END2E) TREND=270.0
          IF(END1E.LT.END2E) TREND=90.0
        END IF
C
        DO 14 J=1,NSTN
C
          DA=((GREFE(J)-END1E)**2+(GREFN(J)-END1N)**2)**0.5
          DB=((GREFE(J)-END2E)**2+(GREFN(J)-END2N)**2)**0.5
C
C
          COSA=(DA**2-DB**2-DIST**2)/(-2.0*DB*DIST)
          COSB=(DB**2-DA**2-DIST**2)/(-2.0*DA*DIST)
C
          D1=DA*COSB
          D2=DIST-(DB*COSA)
          D(J)=(D1+D2)/2
C
14      CONTINUE
C
        RETURN
        END
C
C ******************************************************************
C
C SUBROUTINE TO READ IN MODEL
C
        SUBROUTINE MODIN(NBOD)
C
        COMMON TITLE(10),D(200),ISTN(200),GREFE(200),GREFN(200)
        COMMON BOANOM(200),TOTMAG(200)
        COMMON LNO(200),NPT(200),RHO(200),SUS(200),X(200,200),Y(200,200)
        COMMON DECR(200),RINC(200),RINT(200)
        COMMON RESG(200),RESM(200),SSELZ(200),PDELZ(200,200)
C
        READ(5,*) NBOD
C
        DO 19 K=1,NBOD
C
          READ(5,*) LNO(K),NPT(K),RHO(K),SUS(K),DECR(K),RINC(K),
     &    RINT(K)
C
          DO 20 MN=1,NPT(K)
          READ(5,*) X(K,MN),Y(K,MN)
20        CONTINUE
C
19      CONTINUE
C
```

```
      RETURN
      END
C
C ***********************************************************************
C
C SUBROUTINE TO PLOT DATA
C
      SUBROUTINE DATAPL(IGRAF,DIST,NSTN,NBOD,GGRAD,MGRAD,ERRG,ERRM,END1E
     &,END1N,END2E,END2N,TREND,MTREN,GTREN)
C
      COMMON TITLE(10),D(200),ISTN(200),GREFE(200),GREFN(200)
      COMMON BOANOM(200),TOTMAG(200)
      COMMON LNO(200),NPT(200),RHO(200),SUS(200),X(200,200),Y(200,200)
      COMMON DECR(200),RINC(200),RINT(200)
      COMMON RESG(200),RESM(200),SSELZ(200),PDELZ(200,200)
      COMMON CALM(200),CMBOD(200,200)
      DIMENSION XMOD(200),YMOD(200)
      REAL MMAX,MMIN,MGRAD,MINT,NMIN,NMAX,MTREN
C
C READ IN PLOT CONTROL PARAMETERS
C
      READ(5,*) EMAX,EMIN,NMAX,NMIN
      READ(5,*) ZMAX,ZMIN,ZINT
      READ(5,*) MMAX,MMIN,MINT
      READ(5,*) GMAX,GMIN,GINT
      READ(5,*) XINT
C
C MAP WINDOW AND SELECT LABELLING
C
      CALL CSPACE(0.05,1.1,0.05,0.82)
      CALL PSPACE(0.2,1.1,0.2,0.78)
      CALL PLACE(20,1)
      CALL TYPECS(TITLE,40)
      CALL PLACE(30,24)
      IF(IGRAF.EQ.7) THEN
        CALL TYPECS('EASTING (KM)',12)
      ELSE
        CALL TYPECS('RANGE (KM)',10)
      END IF
C
      IF(IGRAF.EQ.1.OR.IGRAF.EQ.2.OR.IGRAF.EQ.3) THEN
        CALL PLACE(4,14)
        CALL CTRORI(1.0)
        IF(IGRAF.EQ.1) CALL TYPECS('DEPTH (KM)',10)
        IF(IGRAF.EQ.2) CALL TYPECS('ANOMALY (NT)',12)
        IF(IGRAF.EQ.3) CALL TYPECS('ANOMALY (MGAL)',14)
      ELSE IF(IGRAF.EQ.4.OR.IGRAF.EQ.5) THEN
        CALL PLACE(4,20)
        CALL CTRORI(1.0)
      IF(IGRAF.EQ.4) CALL TYPECS('DEPTH (KM)       ANOMALY (MGAL)',30)
        IF(IGRAF.EQ.5) CALL TYPECS('DEPTH (KM)         ANOMALY (NT)',30)
      ELSE IF(IGRAF.EQ.6) THEN
        CALL PLACE(4,22)
        CALL CTRORI(1.0)
        CALL TYPECS('DEPTH (KM)   ANOM (NT)   ANOM (MGAL)',36)
      ELSE
        CALL PLACE(4,14)
        CALL CTRORI(1.0)
        CALL TYPECS('NORTHING (KM)',13)
```

```
      END IF
C
      CALL CTRORI(0,0)
C
C SELECT PLOT
C
      IF(IGRAF.EQ.1.OR.IGRAF.EQ.4.OR.IGRAF.EQ.5.OR.IGRAF.EQ.6) THEN
        IF(IGRAF.EQ.4.OR.IGRAF.EQ.5) CALL PSPACE(0.2,1.1,0.2,0.47)
        IF(IGRAF.EQ.6) CALL PSPACE(0.2,1.1,0.2,0.36)
        CALL MAP(0.00,DIST,ZMAX,ZMIN)
        CALL BORDER
        CALL CTRMAG(10)
        CALL SCALSI(XINT,ZINT)
        CALL CTRMAG(20)
        DO 21 II=1,NBOD
          DO 22 JJ=1,NPT(II)
            XMOD(JJ)=X(II,JJ)
            YMOD(JJ)=Y(II,JJ)
22        CONTINUE
          ICOUNT=NPT(II)
          CALL PTPLOT(XMOD,YMOD,1,ICOUNT,-1)
21      CONTINUE
      END IF
C
      IF(IGRAF.EQ.2.OR.IGRAF.EQ.5.OR.IGRAF.EQ.6) THEN
        IF(IGRAF.EQ.5) CALL PSPACE(0.2,1.1,0.51,0.78)
        IF(IGRAF.EQ.6) CALL PSPACE(0.2,1.1,0.41,0.57)
        CALL MAP(0.00,DIST,MMIN,MMAX)
        CALL BORDER
        CALL CTRMAG(10)
        CALL SCALSI(XINT,MINT)
        CALL CTRMAG(20)
        IF(MGRAD.EQ.0.0) GO TO 30
        CALL BROKEN(10,10,10,10)
        CALL PTPLOT(D,TOTMAG,1,NSTN,-2)
30      CALL FULL
        CALL PTPLOT(D,RESM,1,NSTN,-2)
        DO 43 JJ=1,NSTN
          CALL PLOTNC(D(JJ),CALM(JJ),57)
          CALL MOVE(0.00,ERRM)
          CALL LINE(0.00,-2.0*ERRM)
43      CONTINUE
      END IF
C
      IF(IGRAF.EQ.3.OR.IGRAF.EQ.4.OR.IGRAF.EQ.6) THEN
        IF(IGRAF.EQ.4) CALL PSPACE(0.2,1.1,0.51,0.78)
        IF(IGRAF.EQ.6) CALL PSPACE(0.2,1.1,0.62,0.78)
        CALL MAP(0.00,DIST,GMIN,GMAX)
        CALL BORDER
        CALL CTRMAG(10)
        CALL SCALSI(XINT,GINT)
        CALL CTRMAG(20)
        IF(GGRAD.EQ.0.0) GO TO 31
        CALL BROKEN(10,10,10,10)
        CALL PTPLOT(D,BOANOM,1,NSTN,-2)
31      CALL FULL
        CALL PTPLOT(D,RESG,1,NSTN,-2)
        DO 40 KK=1,NSTN
          CALL PLOTNC(D(KK),SSELZ(KK),57)
```

```
            CALL MOVE(0.00,ERRG)
            CALL LINE(0.00,-2.0*ERRG)
40        CONTINUE
       END IF
C
        IF(IGRAF.EQ.7) THEN
          CALL MAP(EMIN,EMAX,NMIN,NMAX)
          CALL BORDER
          CALL CTRMAG(10)
          CALL SCALES
          CALL CTRMAG(20)
          CALL PLOTNC(EMAX-((EMAX-EMIN)/10),NMAX-((NMAX-NMIN)/10),24)
          CALL MOVE(0.0,(NMAX-NMIN)*(-0.05))
          CALL CTRORI(2.0)
          CALL TYPENC(32)
          CALL CTRORI(0.0)
          CALL LINE(0.0,(NMAX-NMIN)*(-0.1))
          CALL POSITN(END1E,END1N)
          CALL CIRCLE(0.1)
          CALL JOIN(END2E,END2N)
          CALL CIRCLE(0.1)
          IF(GGRAD.NE.0.0) THEN
            CALL POSITN(EMIN+(EMAX-EMIN)*0.2,NMAX-(NMAX-NMIN)*(0.2))
            CALL TYPENF(GGRAD,2)
            CALL TYPECS(' MGAL/KM',8)
            CALL MOVE(0.0,(NMAX-NMIN)*(0.05))
        CALL LINE((EMAX-EMIN)*0.1*SIN(GTREN),(NMAX-NMIN)*0.1*COS(GTREN))
             CALL TYPENC(43)
         END IF
         IF(MGRAD.NE.0.0) THEN
            CALL POSITN(EMIN+(EMAX-EMIN)*0.5,NMAX-(NMAX-NMIN)*(0.2))
            CALL TYPENF(MGRAD,2)
            CALL TYPECS(' NT/KM',6)
            CALL MOVE(0.0,(NMAX-NMIN)*(0.05))
        CALL LINE((EMAX-EMIN)*0.1*SIN(MTREN),(NMAX-NMIN)*0.1*COS(MTREN))
            CALL TYPENC(43)
       END IF
       CALL POSITN(EMIN+(EMAX-EMIN)*(0.1),NMIN+(NMAX-NMIN)*(0.1))
       CALL TYPECS('STATIONS ',9)
       CALL TYPENC(45)
       CALL BROKEN(5,5,5,5)
       DO 101 M=1,NSTN
        CALL POSITN((END1E+(D(M)*SIN(TREND))),END1N+(D(M)*COS(TREND)))
         CALL JOIN(GREFE(M),GREFN(M))
         CALL TYPENC(45)
101    CONTINUE
       CALL FULL
       END IF
C
      RETURN
      END
C
C ******************************************************************
C
C SUBROUTINE TO REMOVE REGIONAL GRADIENT
C
       SUBROUTINE GRADN(TREND,DIST,NSTN,GGRAD,GTREN,MGRAD,MTREN)
C
      COMMON TITLE(10),D(200),ISTN(200),GREFE(200),GREFN(200)
```

```
      COMMON BOANOM(200),TOTMAG(200)
      COMMON LNO(200),NPT(200),RHO(200),SUS(200),X(200,200),Y(200,200)
      COMMON DECR(200),RINC(200),RINT(200)
      COMMON RESG(200),RESM(200),SSELZ(200),PDELZ(200,200)
      REAL MGRAD,MTREN,MPROGR,MCON
C
      TREND=TREND/57.295
      GTREN=GTREN/57.295
      MTREN=MTREN/57.295
C
      GPROGR=GGRAD*COS(ABS(TREND-GTREN))
      MPROGR=MGRAD*COS(ABS(TREND-MTREN))
C
      DO 24 II=1,NSTN
        RESG(II)=BOANOM(II)-GPROGR*D(II)
        RESM(II)=TOTMAG(II)-MPROGR*D(II)
24    CONTINUE
C
       RETURN
       END
C
C ********************************************************************
C
C SUBROUTINE TO CALCULATE GRAVITATIONAL EFFECT OF MODEL
C
      SUBROUTINE GRANOM(NSTN,NBOD,GCONS)
C
      COMMON TITLE(10),D(200),ISTN(200),GREFE(200),GREFN(200)
      COMMON BOANOM(200),TOTMAG(200)
      COMMON LNO(200),NPT(200),RHO(200),SUS(200),X(200,200),Y(200,200)
      COMMON DECR(200),RINC(200),RINT(200)
      COMMON RESG(200),RESM(200),SSELZ(200),PDELZ(200,200)
      DIMENSION FX(200),FZ(200)
C
      PI=3.141593
C
      DO 451 K=1,NSTN
        FZ(K)=0.00
         FX(K)=D(K)
  451 CONTINUE
  520 CONTINUE
      DO 53 K=1,NSTN
      SSELZ(K)=GCONS
   53 CONTINUE
       DO 430 IZ=1,NBOD
      DO 420 K=1,NSTN
      SDELZ=0.0
      I=1
205   CONTINUE
      IF(I.EQ.NPT(IZ)+1) THEN
        EXXX=X(IZ,1)-FX(K)
        ZEEE=Y(IZ,1)-FZ(K)
      ELSE
      EXXX=X(IZ,I)-FX(K)
      ZEEE=Y(IZ,I)-FZ(K)
      END IF
      RR=EXXX**2+ZEEE**2
      IF(EXXX)210,240,280
  210 IF(ZEEE)220,230,230
```

```
  220 THETB=ATAN(ZEEE/EXXX)-PI
      GO TO 300
  230 THETB=ATAN(ZEEE/EXXX)+PI
      GO TO 300
  240 IF(ZEEE)250,260,270
  250 THETB=-1.57080
      GO TO 300
  260 THETB=0.0
      GO TO 300
  270 THETB=1.57080
      GO TO 300
  280 THETB=ATAN(ZEEE/EXXX)
  300 IF(I-1)3001,3002,3001
 3002 EXX=EXXX
      ZEE=ZEEE
      R=RR
      THETA=THETB
      IF(I-1)205,200,205
  200 I=2
      GO TO 205
 3001 CHECK=EXX*ZEEE-ZEE*EXXX
      IF(CHECK)320,310,320
  310 DELZ=0.0
      GO TO 400
  320 OMEGA=THETA-THETB
      IF(OMEGA)3201,3202,3202
 3202 IF(OMEGA-PI)330,330,340
 3201 IF(OMEGA+PI)340,330,330
  330 DTHET=OMEGA
      GO TO 370
  340 IF(OMEGA)350,360,360
  350 DTHET=OMEGA+6.28319
      GO TO 370
  360 DTHET=OMEGA-6.28319
  370 A=CHECK/((EXXX-EXX)**2+(ZEEE-ZEE)**2)
      B=(EXXX-EXX)*DTHET
      C=0.5*(ZEEE-ZEE)*ALOG(RR/R)
      DELZ=A*(B+C)
  400 SDELZ=SDELZ+DELZ
      IF(I-(NPT(IZ)+1))3003,3005,3005
 3003 I=I+1
      GO TO 3002
 3005 PDELZ(IZ,K)=13.34*RHO(IZ)*SDELZ
      SSELZ(K)=SSELZ(K)+PDELZ(IZ,K)
  420 CONTINUE
  430 CONTINUE
  24        CONTINUE
C
      RETURN
      END
C
C *******************************************************************
C
C SUBROUTINE TO CALCULATE MAGNETIC ANOMALY
C
      SUBROUTINE MAANOM(TREND,NBOD,NSTN,INTA,INCA,DECA,MCONS)
C
      COMMON TITLE(10),D(200),ISTN(200),GREFE(200),GREFN(200)
      COMMON BOANOM(200),TOTMAG(200)
```

```
      COMMON LNO(200),NPT(200),RHO(200),SUS(200),X(200,200),Y(200,200)
      COMMON DECR(200),RINC(200),RINT(200)
      COMMON RESG(200),RESM(200),SSELZ(200),PDELZ(200,200)
      COMMON CALM(200),CMBOD(200,200)
      DIMENSION IX(51),IZ(51),IXN(200,51),STORM(200)
      REAL MAGZ(200),MAGX(200),MAGT(200)
      REAL INTA,INCA,MCONS,JXR,JZR,JXI,JZI,JXT,JZT,JI,HFIELD
C
       PI=3.141593
C
C INITIALISE MAGNETIC PROFILE VARIABLES
C
       DATA MAGZ/200*0./
       DATA MAGX/200*0./
       DATA MAGT/200*0./
       DATA STORM/200*0./
C
       TRENDD=TREND/PI*180
C
       IF(TRENDD.LT.360.AND.TRENDD.GE.180) THEN
         STRIKE=TRENDD-90.0
       ELSE
         STRIKE=TRENDD+90.0
       END IF
C
       STRIKE=STRIKE*PI/180
C
       HFIELD=(INTA*1.E-9)/(4.0*PI*1.0E-7)
       DECA=DECA*PI/180.0
       INCA=INCA*PI/180.0
C
       DO 55 III=1,NBOD
C
       DO 99 JJJ=1,NSTN
       MAGZ(JJJ)=0.00
       MAGX(JJJ)=0.00
99     CONTINUE
C
       DO 54 JJ=1,NPT(III)
       IX(JJ)=X(III,JJ)*1000
       IZ(JJ)=Y(III,JJ)*1000
54     CONTINUE
C
       DECR(III)=DECR(III)*PI/180
       RINC(III)=RINC(III)*PI/180
C
       JI=SUS(III)*HFIELD
C CALCULATE PROJECTION OF MAGNETIC VECTORES IN PLANE OF BODY
C
       JXR=RINT(III)*(COS(RINC(III))*COS(PI/2.0+STRIKE-DECR(III)))
       JZR=RINT(III)*(SIN(RINC(III)))
       JXI=JI*(COS(INCA)*COS(PI/2.0+STRIKE-DECA))
       JZI=JI*(SIN(INCA))
       JXT=JXI+JXR
       JZT=JZI+JZR
C
       IX(NPT(III)+1)=IX(1)
       IZ(NPT(III)+1)=IZ(1)
C
```

```
C TRANSFORM CO-ORDS OF POLYGON TO ORIGIN AT EACH STATION
C
      DO 300 J=1,NSTN
        DO 400 J1=1,NPT(III)+1
        IXN(J,J1)=(IX(J1)-(D(J)*1000))
400     CONTINUE
300   CONTINUE
C
C CALCULATE ANOMALY
C
      DO 500 J=1,NSTN
      ZMAG=0.0
      XMAG=0.0
        DO 600 J1=1,NPT(III)
        IX1=IXN(J,J1)
        IX2=IXN(J,J1+1)
        IZ1=IZ(J1)
        IZ2=IZ(J1+1)
        Z1=REAL(IZ1)
        Z2=REAL(IZ2)
        X1=REAL(IX1)
        X2=REAL(IX2)
        IF(IX1.EQ.0.AND.IZ1.EQ.0) THEN
          IZ1=1
          Z1=1.0
        END IF
        IF(IX2.EQ.0.AND.IZ2.EQ.0) THEN
          IZ2=1
          Z2=1.0
        END IF
        IF(IX1.EQ.0) THEN
          THETA1=PI/2
        ELSE
          THETA1=ATAN(Z1/X1)
        END IF
        IF(IX2.EQ.0) THEN
          THETA2=PI/2
        ELSE
          THETA2=ATAN(Z2/X2)
        END IF
        IF(THETA1.LT.0.0) THETA1=PI+THETA1
        IF(THETA2.LT.0.0) THETA2=PI+THETA2
        X12=X1-X2
        Z21=Z2-Z1
        R1=SQRT(X1**2+Z1**2)
        R2=SQRT(X2**2+Z2**2)
        PCHAR=(Z21**2/(Z21**2+X12**2))*(THETA1-THETA2)+
     &        (Z21*X12/(Z21**2+X12**2))*ALOG(R2/R1)
        QCHAR=(Z21*X12/(Z21**2+X12**2))*(THETA1-THETA2)-
     &        (Z21**2/(Z21**2+X12**2))*ALOG(R2/R1)
        ZMAG=2.0*(JXT*QCHAR-JZT*PCHAR)
        XMAG=2.0*(JXT*PCHAR+JZT*QCHAR)
          MAGZ(J)=MAGZ(J)+ZMAG
          MAGX(J)=MAGX(J)+XMAG
600     CONTINUE
      MAGT(J)=MAGZ(J)*SIN(INCA)+MAGX(J)*(COS(INCA)*COS(PI/2.0+
     &    STRIKE-DECA))
      MAGT(J)=MAGT(J)*1.0E2
      CMBOD(III,J)=MAGT(J)
```

```
      STORM(J)=STORM(J)+MAGT(J)
500   CONTINUE
      IF(III.EQ.NBOD) THEN
        DO 67 I=1,NSTN
          CALM(I)=STORM(I)+MCONS
67      CONTINUE
      END IF
55    CONTINUE
C
      RETURN
      END
C
C **********************************************************************
C
C SUBROUTINE TO FORMAT AND OUTPUT DATA
C
      SUBROUTINE DATOUT(DIST,NSTN,TREND,END1E,END1N,END2E,END2N
     & ,GGRAD,GTREN,ERRG,GCONS,MGRAD,MTREN,ERRM,MCONS,DECA,INCA,INTA,
     & NBOD)
C
      COMMON TITLE(10),D(200),ISTN(200),GREFE(200),GREFN(200)
      COMMON BOANOM(200),TOTMAG(200)
      COMMON LNO(200),NPT(200),RHO(200),SUS(200),X(200,200),Y(200,200)
      COMMON DECR(200),RINC(200),RINT(200)
      COMMON RESG(200),RESM(200),SSELZ(200),PDELZ(200,200)
      COMMON CALM(200),CMBOD(200,200)
      REAL INTA,INCA,MCONS,MGRAD,MTREN
C
      WRITE(6,10) TITLE
      WRITE(6,21)
      TREND=TREND/3.141593*180
      WRITE(6,11) NSTN,TREND,DIST
      WRITE(6,19)
      WRITE(6,22)
      WRITE(6,12) END1E,END2E,END1N,END2N
      WRITE(6,24)
      GTREN=GTREN/3.141593*180
      MTREN=MTREN/3.141593*180
      WRITE(6,18) GGRAD,GTREN,ERRG
      WRITE(6,18) MGRAD,MTREN,ERRM
      WRITE(6,25)
      WRITE(6,26)
      WRITE(6,13) DECA/3.14159*180,INCA/3.14159*180,INTA
      WRITE(6,27)
      WRITE(6,28)
      WRITE(6,14) (ISTN(K),GREFE(K),GREFN(K),D(K),BOANOM(K),TOTMAG(K),
     &        K=1,NSTN)
C
      WRITE(6,29)
      WRITE(6,15) NBOD
      DO 98 J=1,NBOD
        WRITE(6,31)
        DECR(J)=DECR(J)/3.141593*180
        RINC(J)=RINC(J)/3.141593*180
        WRITE(6,16) LNO(J),NPT(J),RHO(J),SUS(J),DECR(J),RINC(J),RINT(J)
        WRITE(6,32)
        WRITE(6,33)
        WRITE(6,17) (X(J,JJ),Y(J,JJ),JJ=1,NPT(J))
98    CONTINUE
```

```
C
      WRITE(6,34)
      DO 85 L=1,NBOD
        WRITE(6,35) L
        WRITE(6,36)
        DO 84 LL=1,NSTN
          WRITE(6,37) ISTN(LL),D(LL),CMBOD(L,LL),PDELZ(L,LL)
84      CONTINUE
85    CONTINUE
C
      WRITE(6,38)
      WRITE(6,39)
      WRITE(6,40) (ISTN(KK),D(KK),RESM(KK),CALM(KK),RESG(KK),
     & SSELZ(KK),KK=1,NSTN)
10    FORMAT(10A4)
11    FORMAT(I5,2(10X,F10.5))
12    FORMAT(4(F10.5,5X))
13    FORMAT(2(5X,F10.5),5X,F15.5)
14    FORMAT(I5,4F10.5,F15.3)
15    FORMAT('NO. BODIES =',I3)
16    FORMAT(2I3,5F10.5)
17    FORMAT(2F10.5)
18    FORMAT(3(F15.3,2X))
21    FORMAT(' NO. STNS        TREND                    LENGTH')
19    FORMAT(' COORDS OF PROFILE ENDS')
22    FORMAT('  EASTING 1     NORTHING 1     EASTING 2      NORTHING 2
     & ')
24    FORMAT('      REGIONAL GRADN REGIONAL TREND          ERROR    ')
25    FORMAT(' AMBIENT FIELD')
26    FORMAT('      DECLINATION     INCLINATION         INTENSITY')
27    FORMAT(' FIELD DATA')
28    FORMAT('   STN EASTING   NORTHING  PRO POSIT BOUG GRAV     TOTAL
     & MAG')
29    FORMAT(' MODEL DATA')
30    FORMAT('BODY NO.',I3)
31    FORMAT('  N CORN DENSITY    SUSC      REM DEC    REM INC    REM INT
     &')
32    FORMAT(' CO-ORDS OF CORNERS')
33    FORMAT('     X            Z')
34    FORMAT(' ANOMALY DUE TO EACH BODY')
35    FORMAT('BODY NUMBER',I3)
36    FORMAT(' STN PRO POS       MAG ANOM         GRAV ANOM')
39    FORMAT(' STN PRO POS  MAG ANOM (OBS) MAG ANOM (CALC) GRA ANOM(OBS
     &) GRA ANOM(CALC)')
37    FORMAT(I3,F10.5,2F15.5)
38    FORMAT(' TOTAL ANOMALIES')
40    FORMAT(I3,F10.5,2F15.5,F12.5,F15.5)
C
      RETURN
      END
```

GEOPHYSICAL CONSTRAINTS ON UPPER CRUSTAL STRUCTURE IN THE MIDLAND VALLEY OF SCOTLAND

MICHAEL C. DENTITH

Thesis submitted for the degree of Philosophiae Doctorem
at the University of Glasgow, 1987.

VOL. II

CONTENTS (Vol I)

CONTENTS (Vol II - List of Figures)

CHAPTER 4 - SEISMIC VELOCITY DETERMINATION AND INTERPRETATION

CHAPTER 5 - INTERPRETATION OF SEISMIC DATA

APPENDIX 1 (Figs in Vol. I)

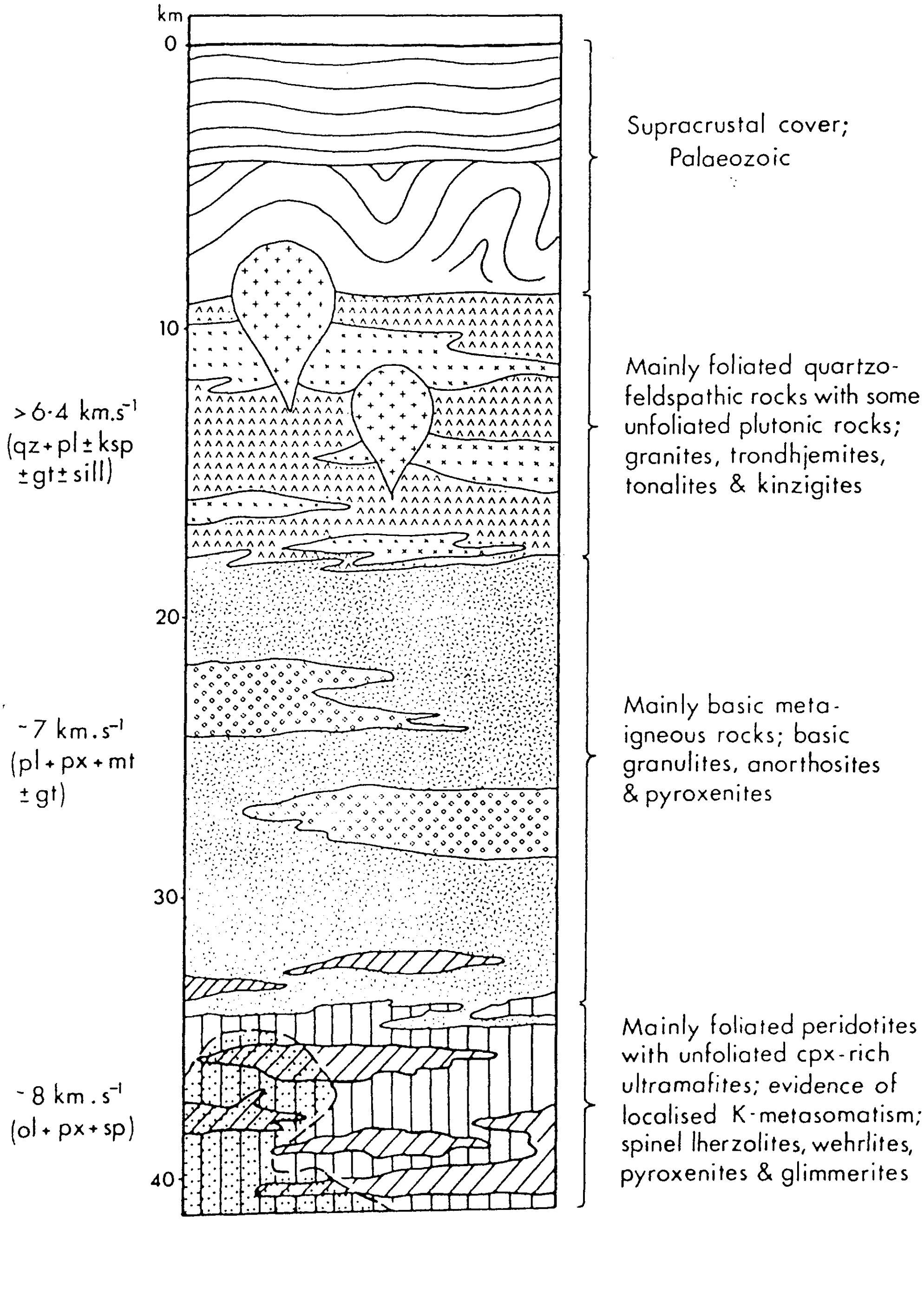

Fig. 1.1 Schematic section through the upper lithosphere beneath the Midland Valley of Scotland (after Upton et al. 1984).

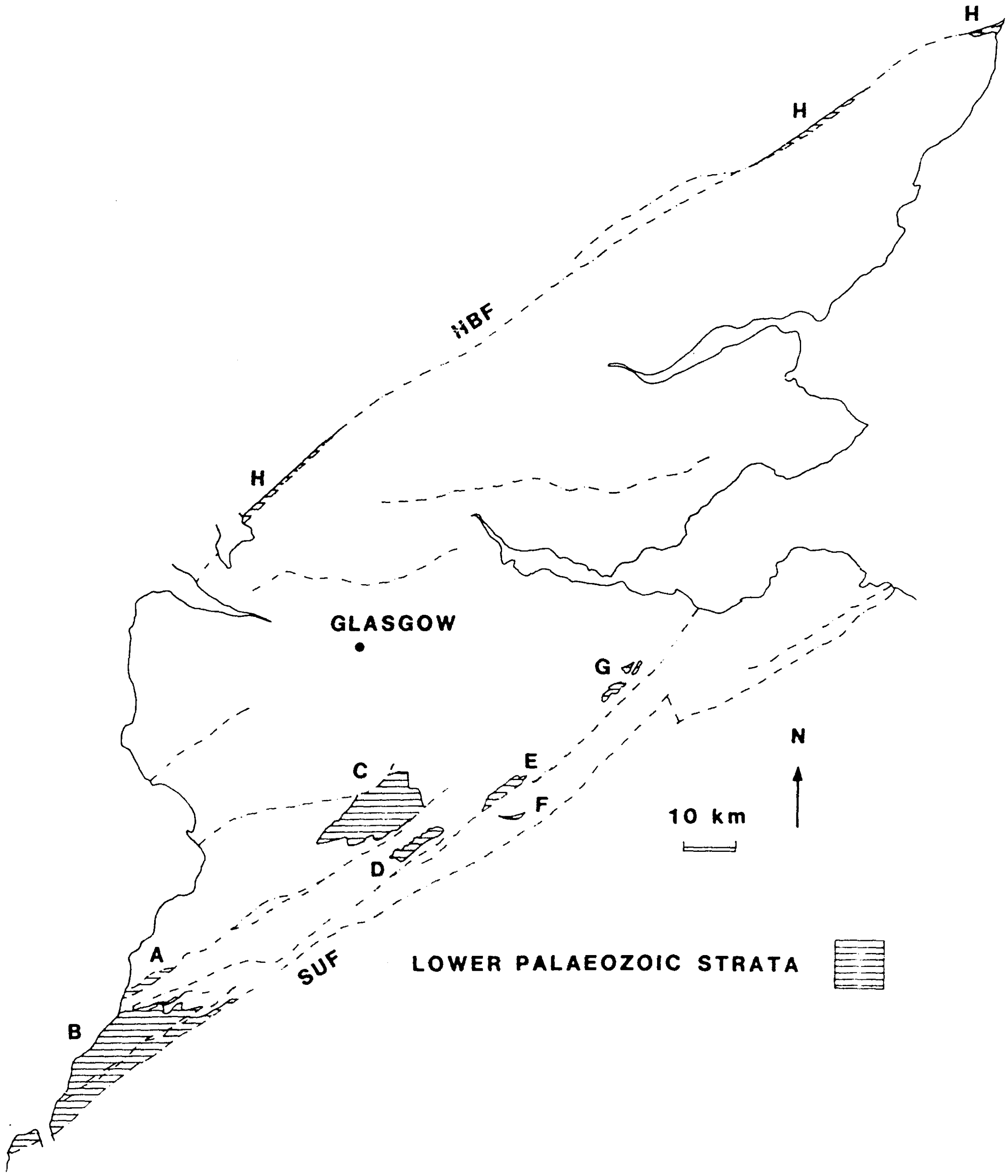

Fig.1.2 Outcrop of Lower Palaeozoic rocks in the Midland Valley of Scotland. A - Craighead, B - Girvan, C - Lesmahagow, D - Hagshaw Hills, E - Carmichael, F - Eastfield, G - Pentland Hills, H - Highland Border, HBF - Highland Boundary Fault, SUF - Southern Uplands Fault.

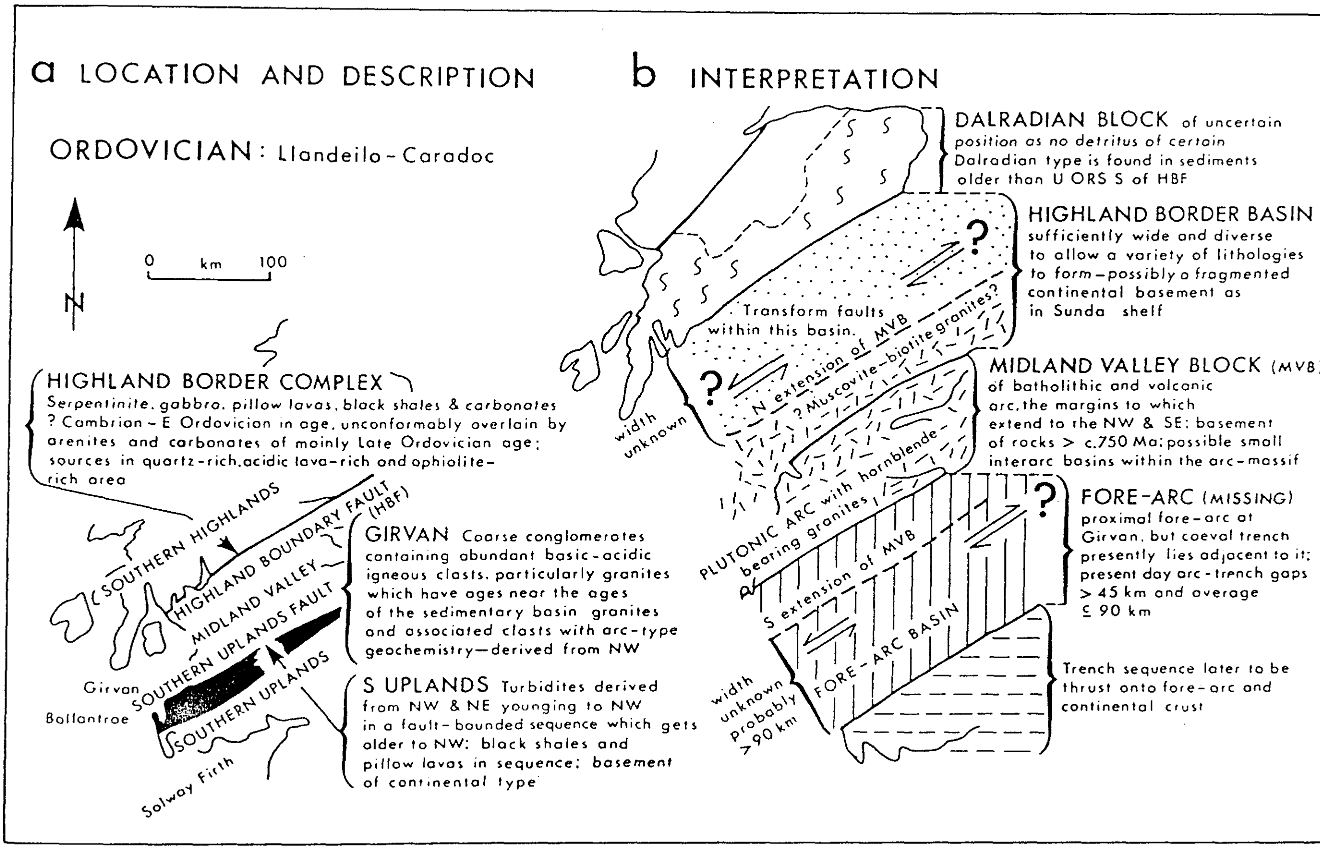

Fig.1.3 Tectonic setting of the Midland Valley of Scotland during the Ordovician (after Bluck 1984)

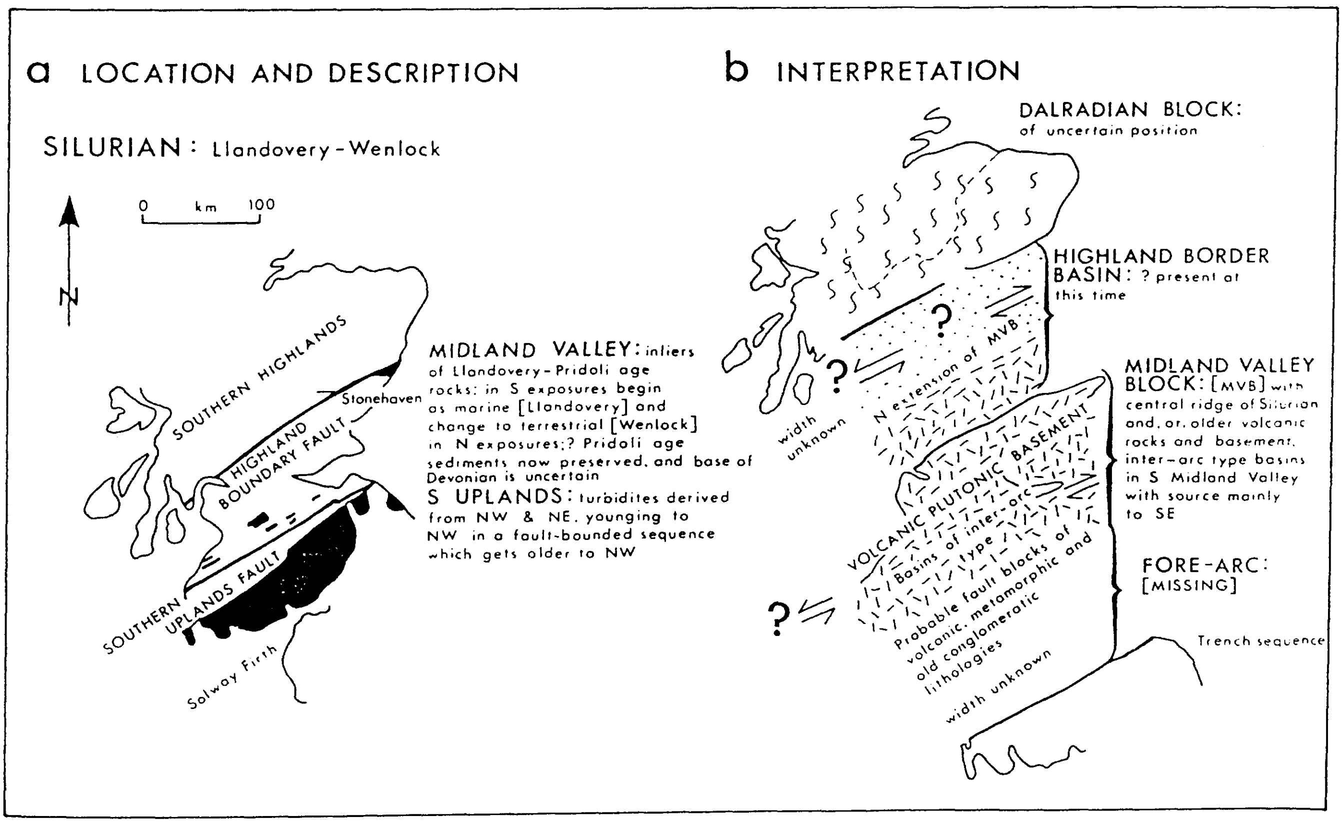

Fig.1.4 Tectonic setting of the Midland Valley of Scotland during the Silurian (after Bluck 1984).

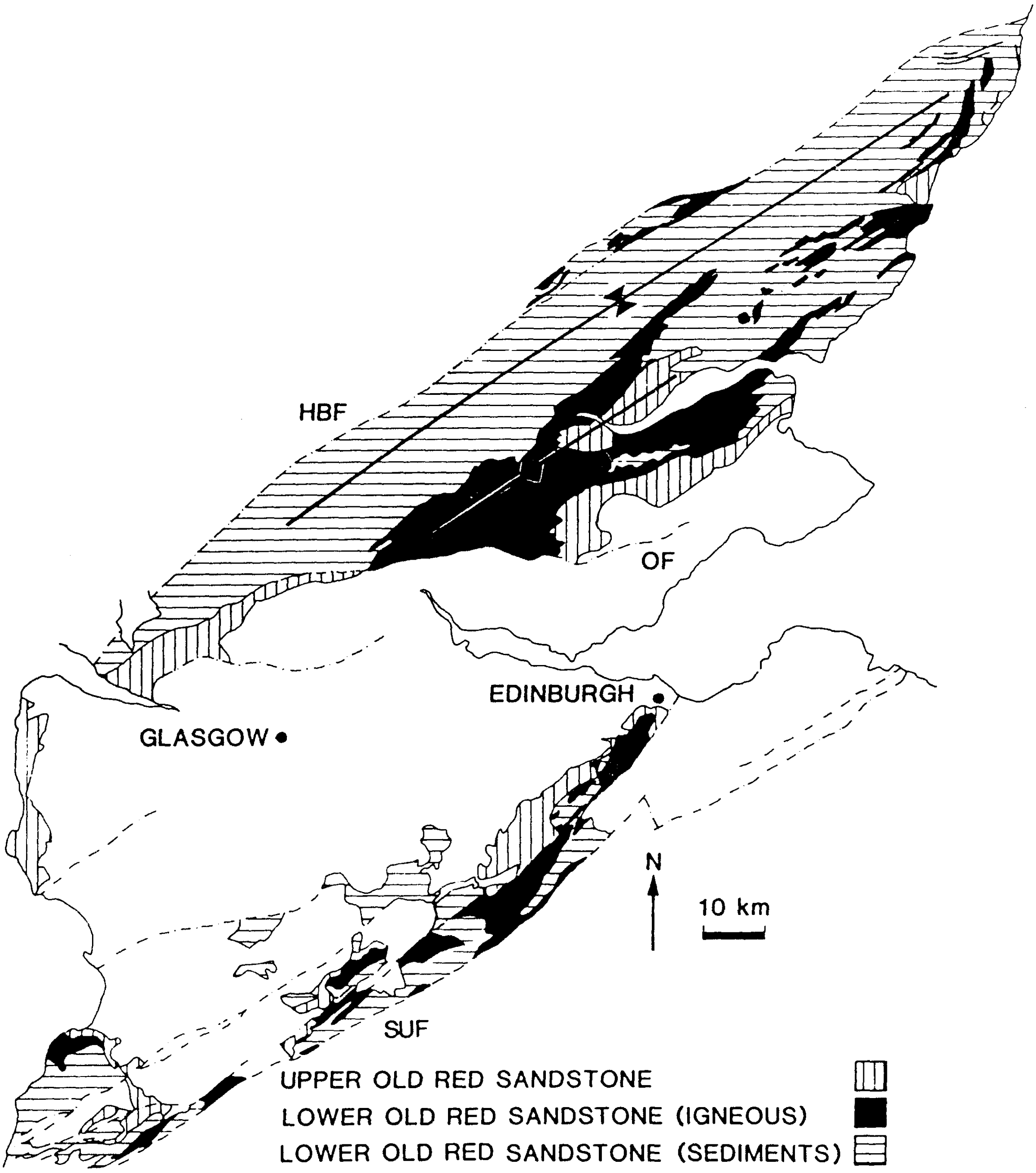

Fig. 1.5 Distribution of ORS strata in the Midland Valley of Scotland. HBF - Highland Boundary Fault, OF - Ochil Fault, SUF - Southern Uplands Fault. The Strathmore Syncline and Ochil-Sidlaw Anticline trend parallel to the HBF.

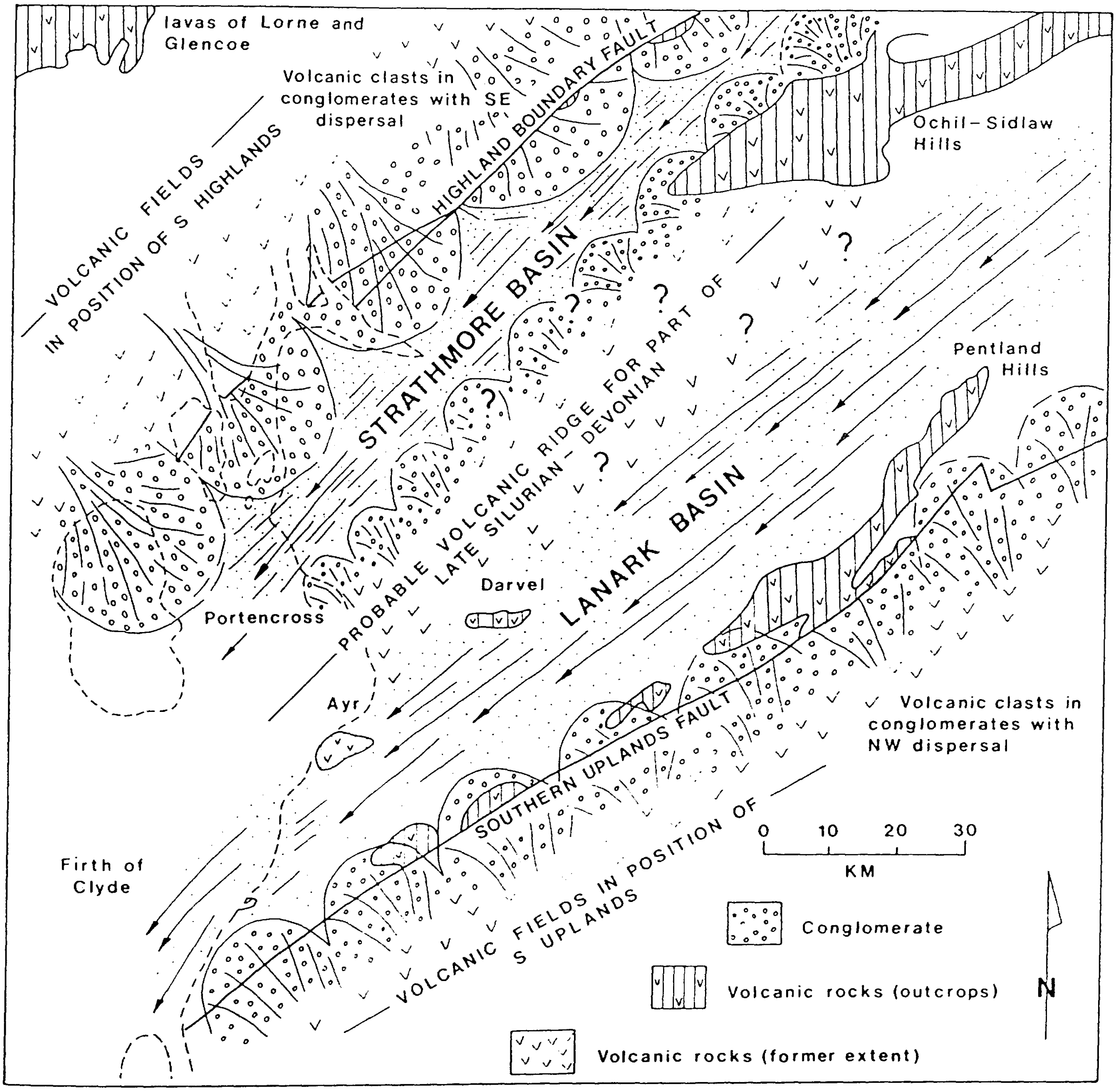

Fig.1.6 Palaeogeography of the Midland Valley during the late Silurian and early Devonian (after Bluck 1983).

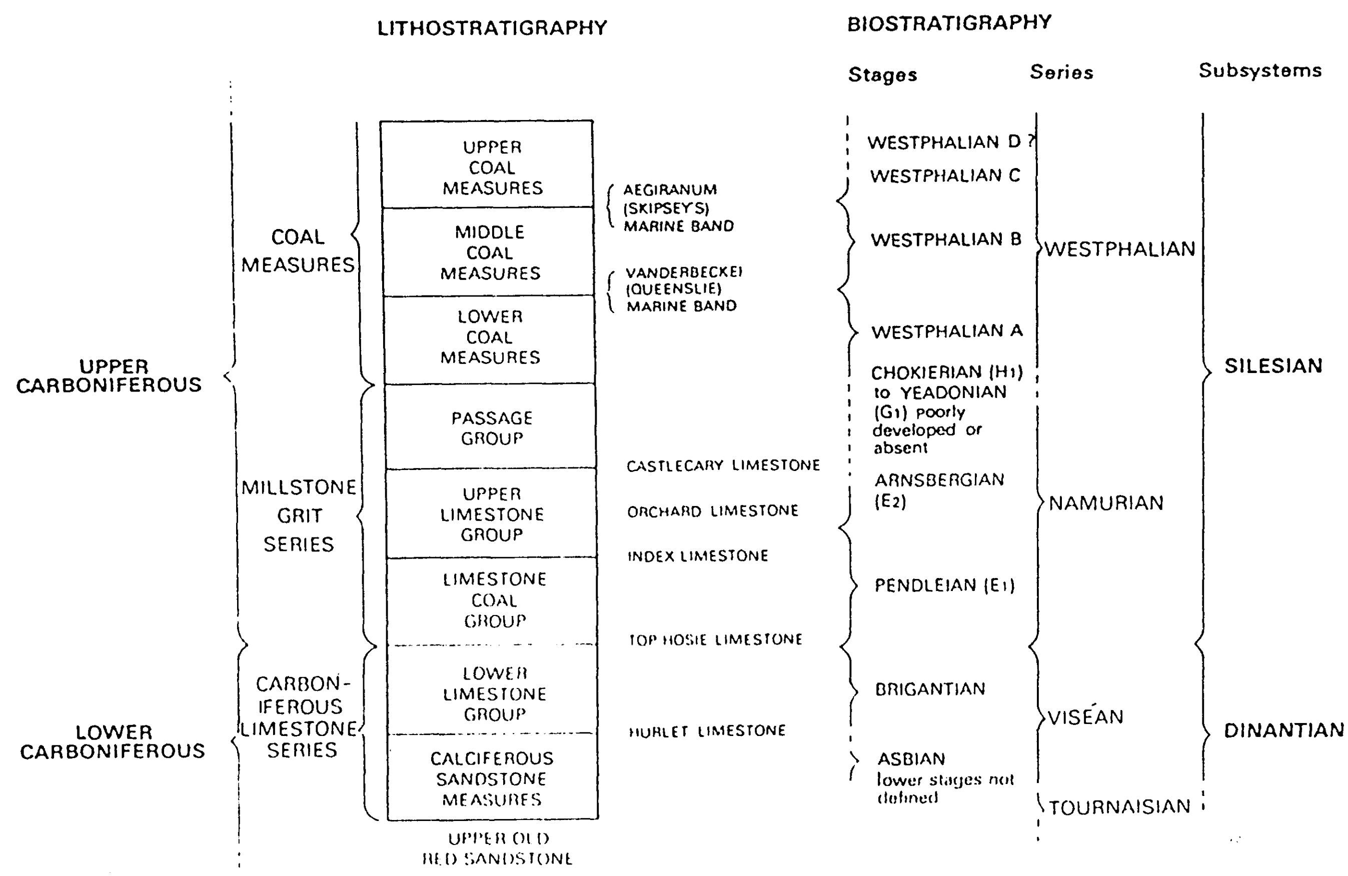

Fig.1.7 Carboniferous stratigraphy of the Midland Valley of Scotland (after Cameron & Stephenson 1985).

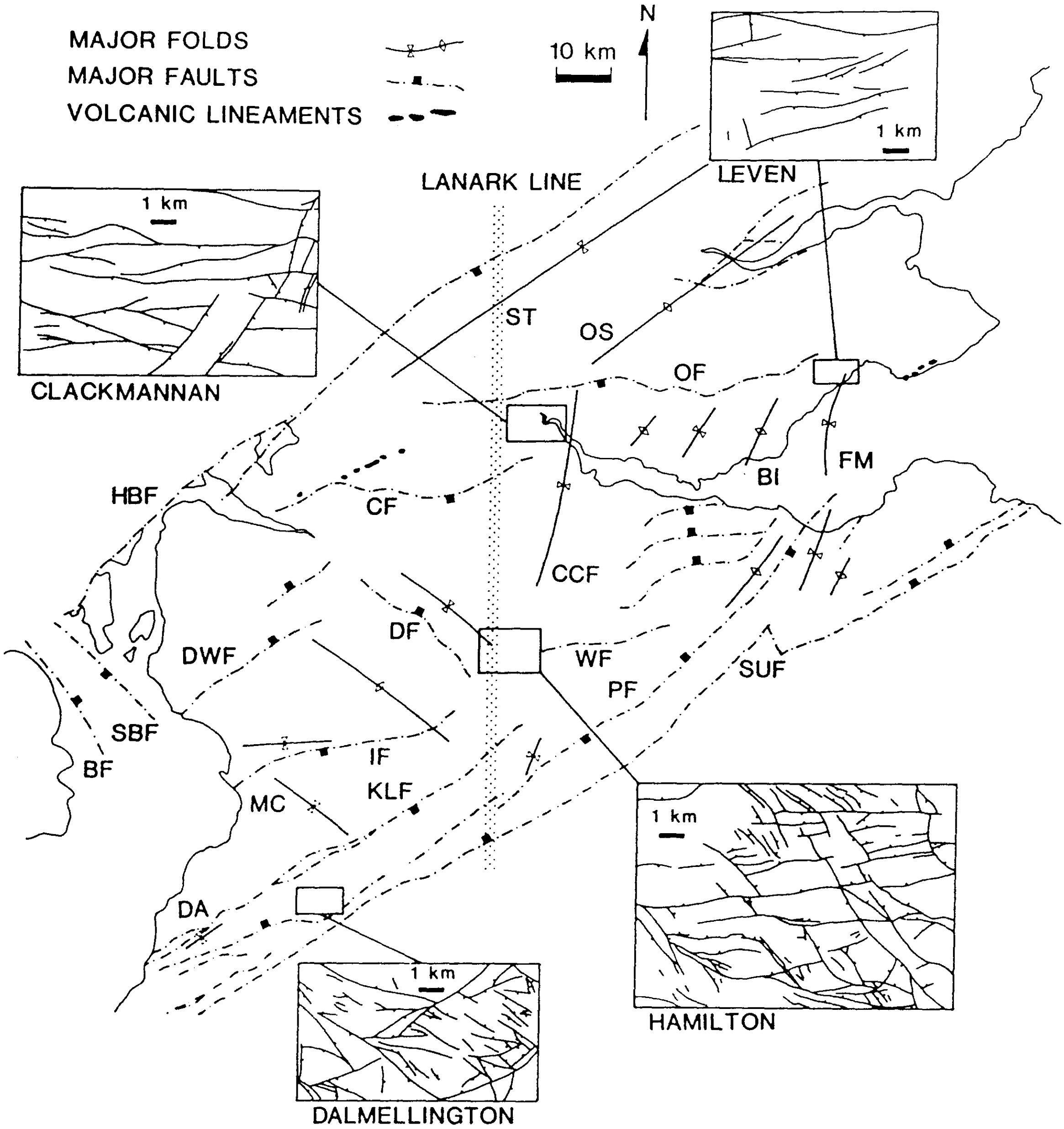

Fig.1.8 Structural map of the Midland Valley of Scotland. Insets show local fault patterns. Ticks are on down-thrown side of faults. BF - Brodick Bay Fault, BI - Burntisland Anticline, CCF - Central Coalfield Syncline, CF - Campsie Fault, DA - Dailly Anticline, DF - Dechmont Fault, DWF - Dusk Water Fault, FM - Fife-Midlothian Syncline, HBF - Highland Boundary Fault, IF - Inchgotrick Fault, KLF - Kerse Loch Fault, MC - Mauchline Basin, PF - Pentland Fault, OS - Ochil-Sidlaw Anticline, OF - Ochil Fault, SBF - Sound of Bute Fault, ST - Strathmore Syncline, SUF - Southern Uplands Fault, WF - Wilsontown Fault.

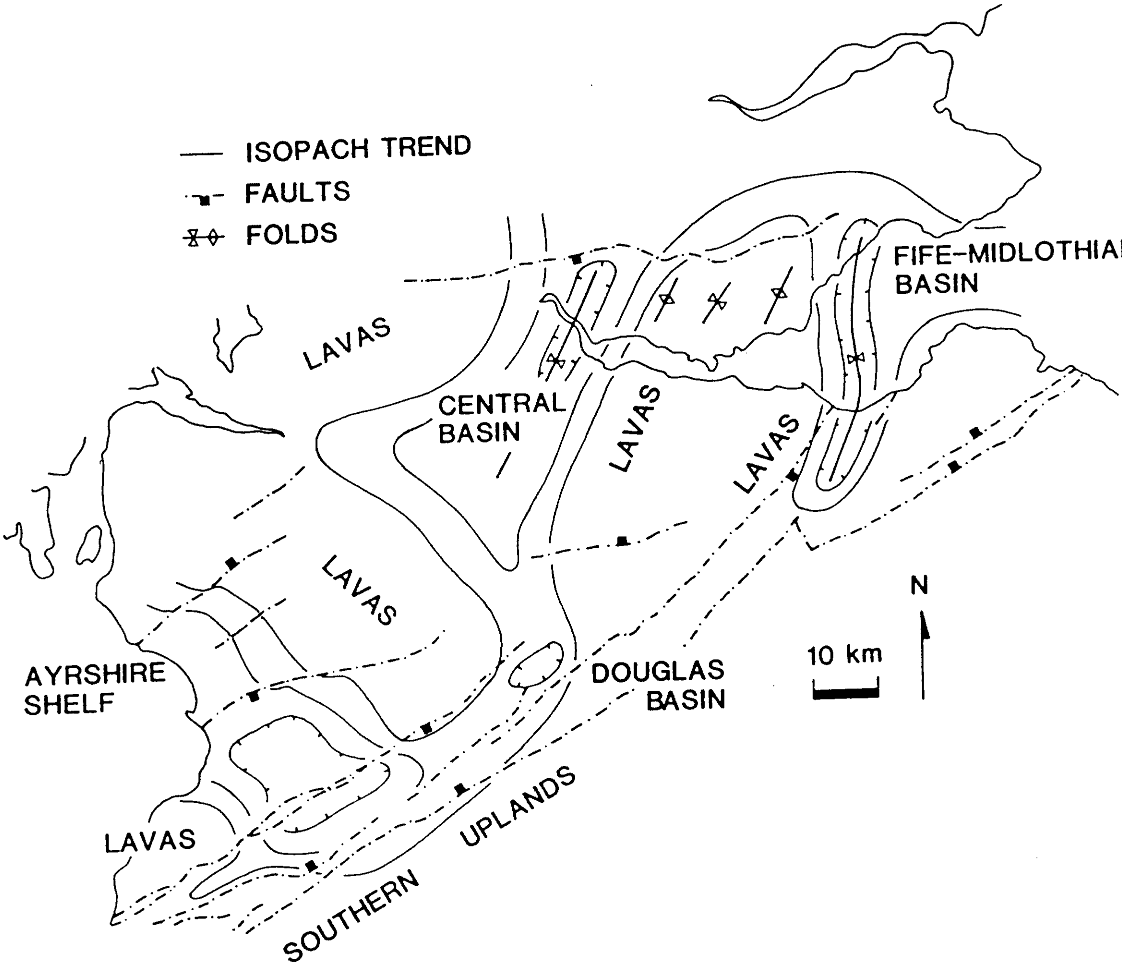

Fig.1.9 Controls on sedimentation within the Midland Valley of Scotland. Ticks are on downthrown side of faults.

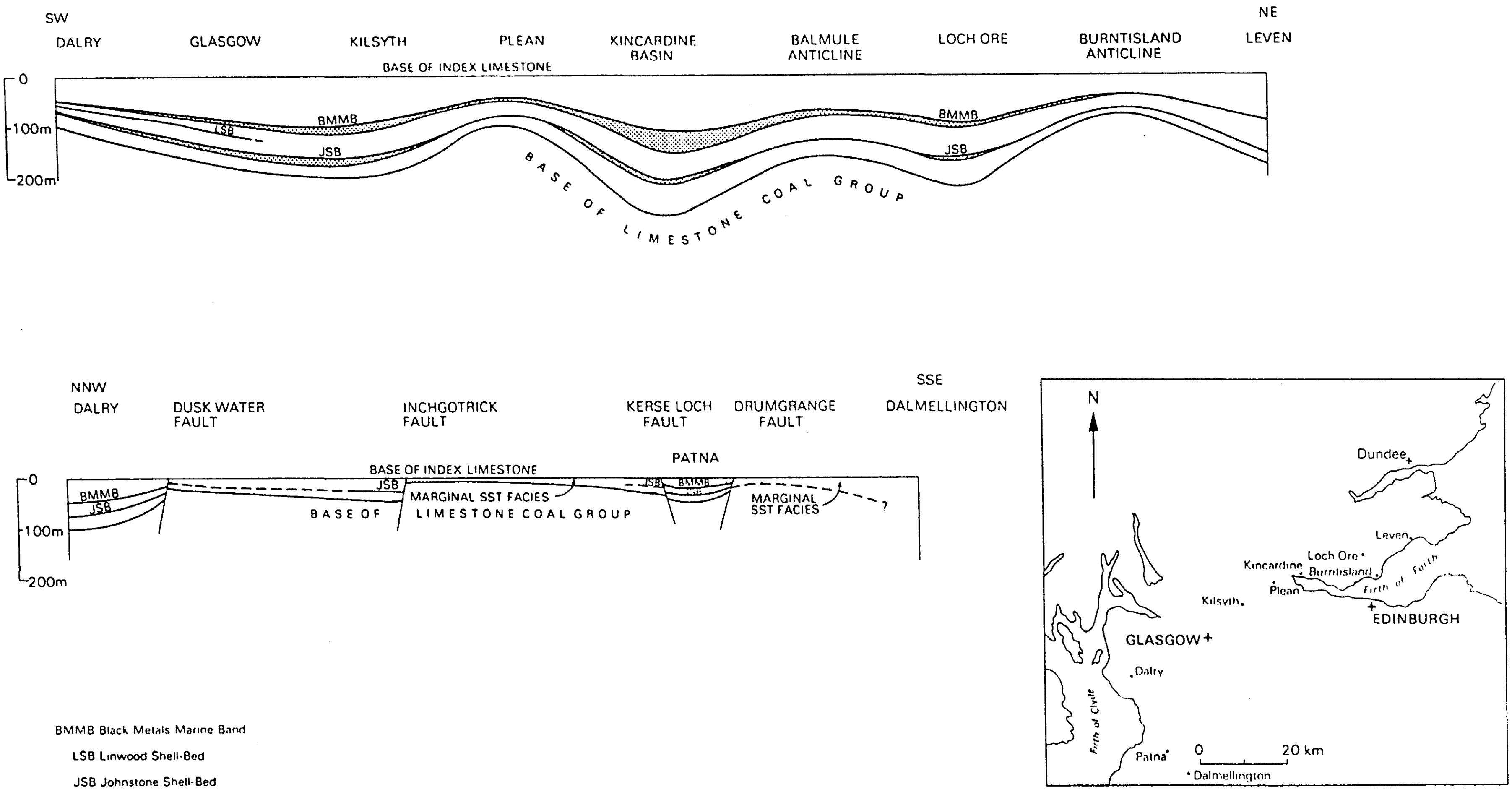

Fig.1.10 Schematic cross-sections illustrating variations in thickness of the Limestone Coal Group within the Midland Valley (after Cameron & Stephenson 1985).

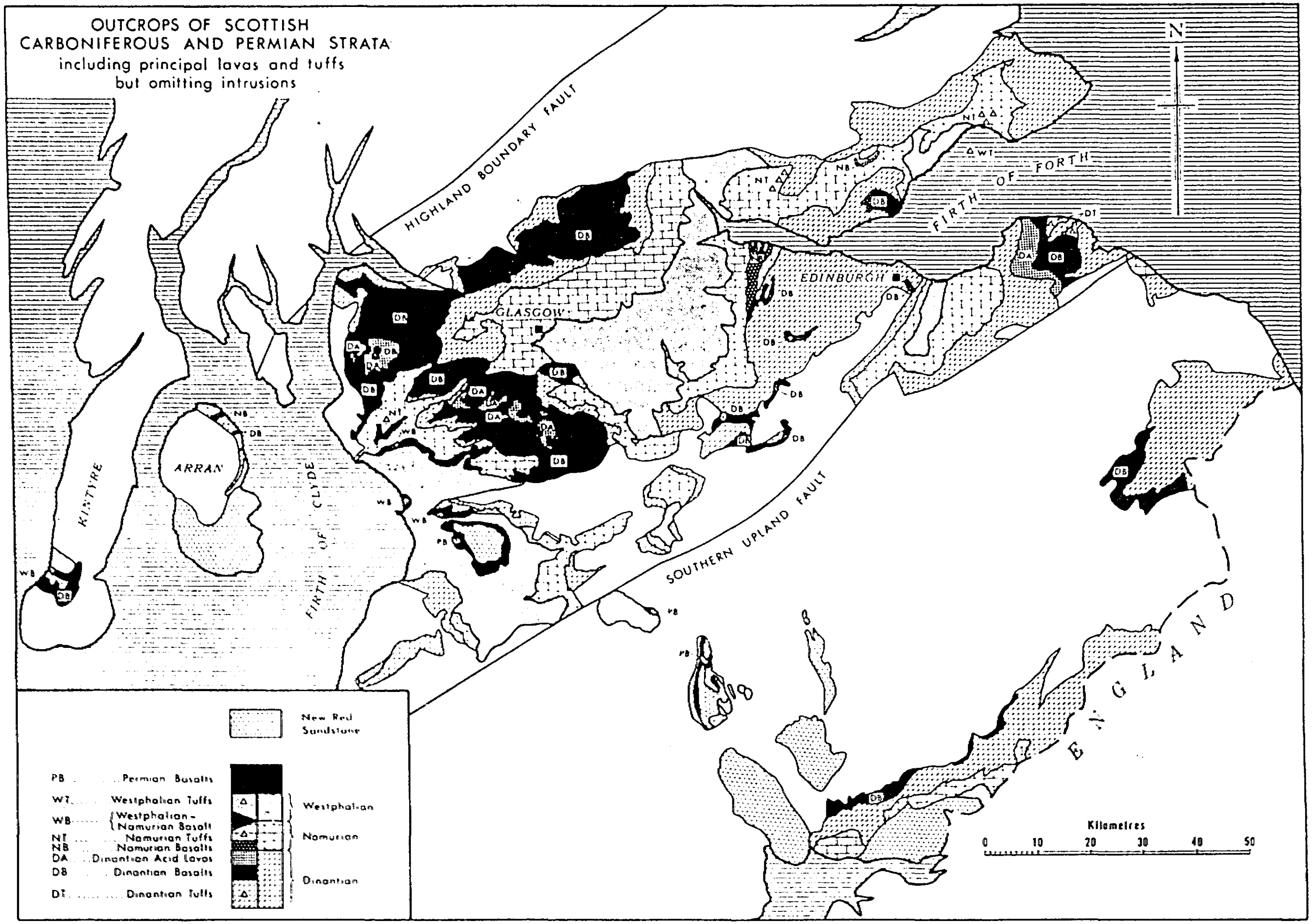

Fig.1.11 Distribution of Permo-Carboniferous volcanic rocks in southern Scotland (after Francis 1983).

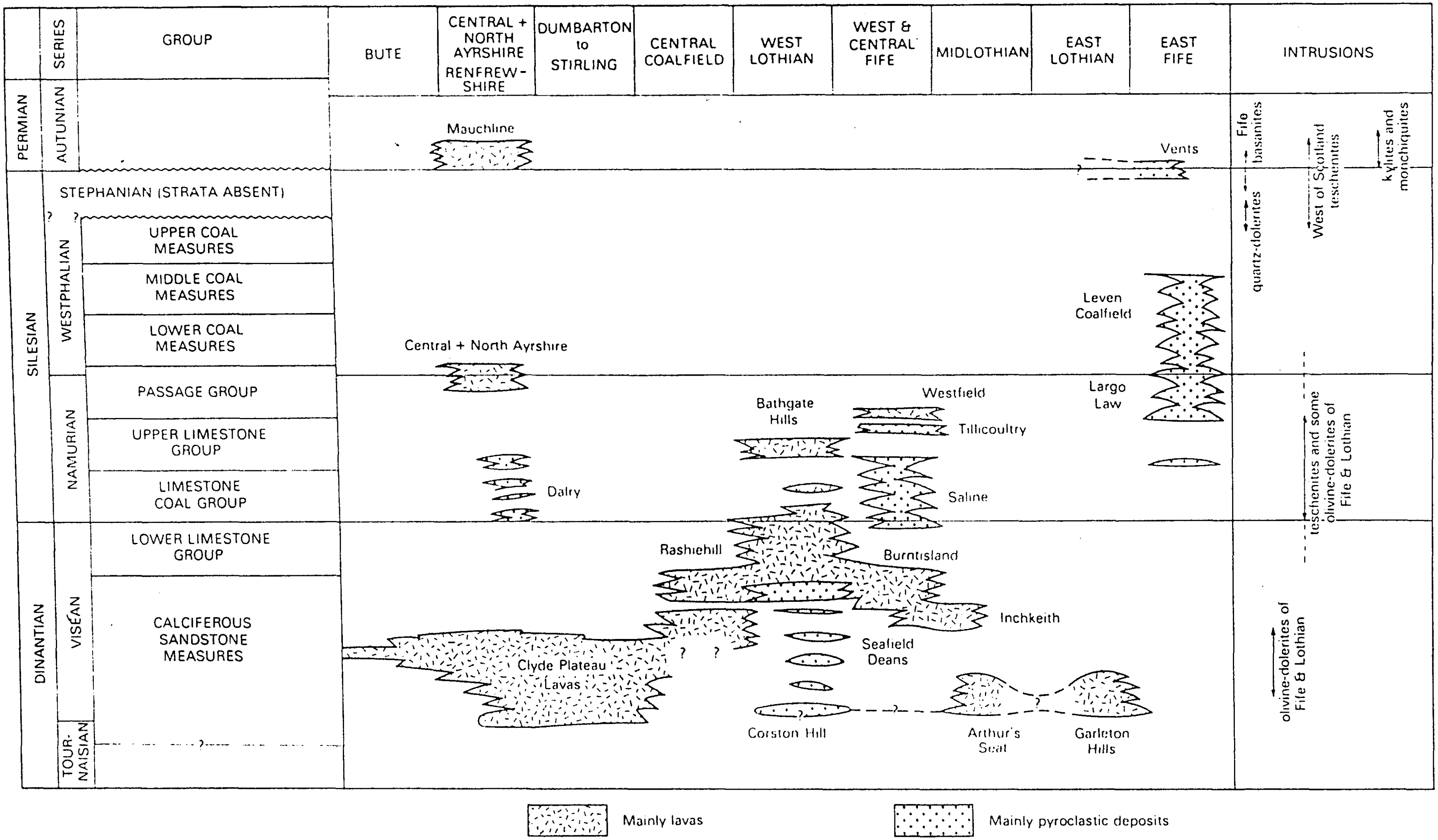

Fig.1.12 Spatial and temporal distribution of Permo-Carboniferous igneous rocks in the Midland Valley of Scotland (after Cameron & Stephenson 1985).

A) B)

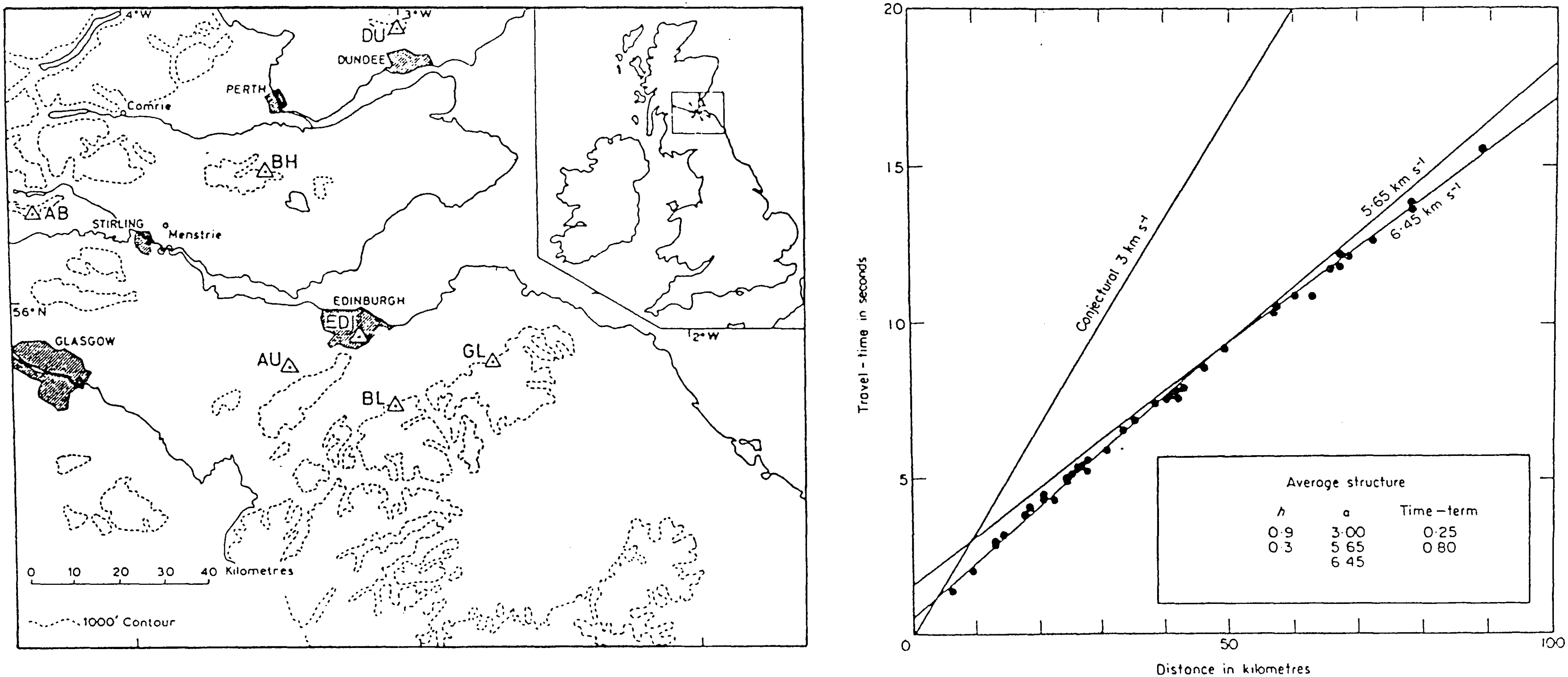

Fig.2.1 LOWNET: A) Location of seismic arrays. AB - Aberfoyle, AU - Auchinoon Hill, BH - Black Hill, BL - Broad Law, DU - Craigowl Hill, Dundee, EDI - Royal Observatory Edinburgh, GL - Gala Law. B), Travel-time data and interpretation. (after Crampin et al. 1970).

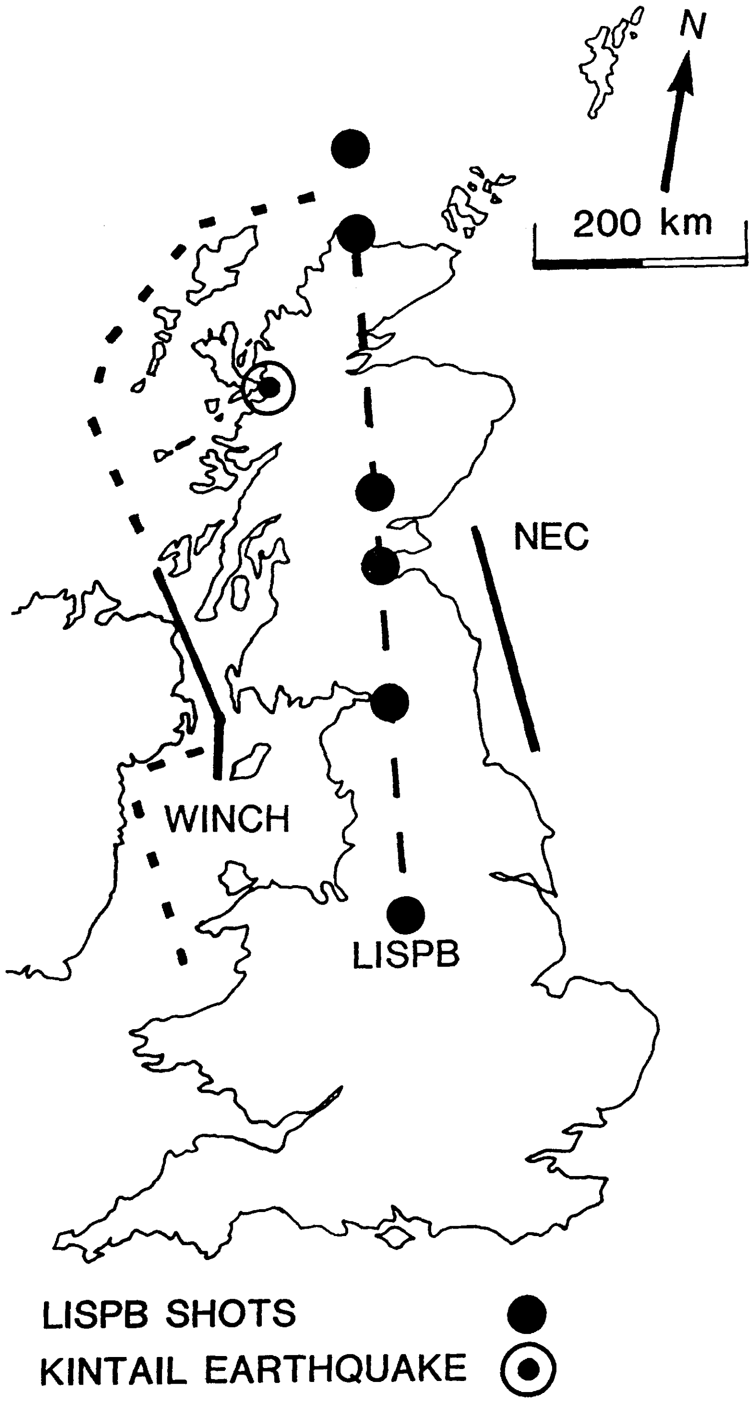

Fig.2.2 Location map for regional seismic lines crossing the Midland Valley. The section of the WINCH line drawn solid is shown in Fig.2.11.

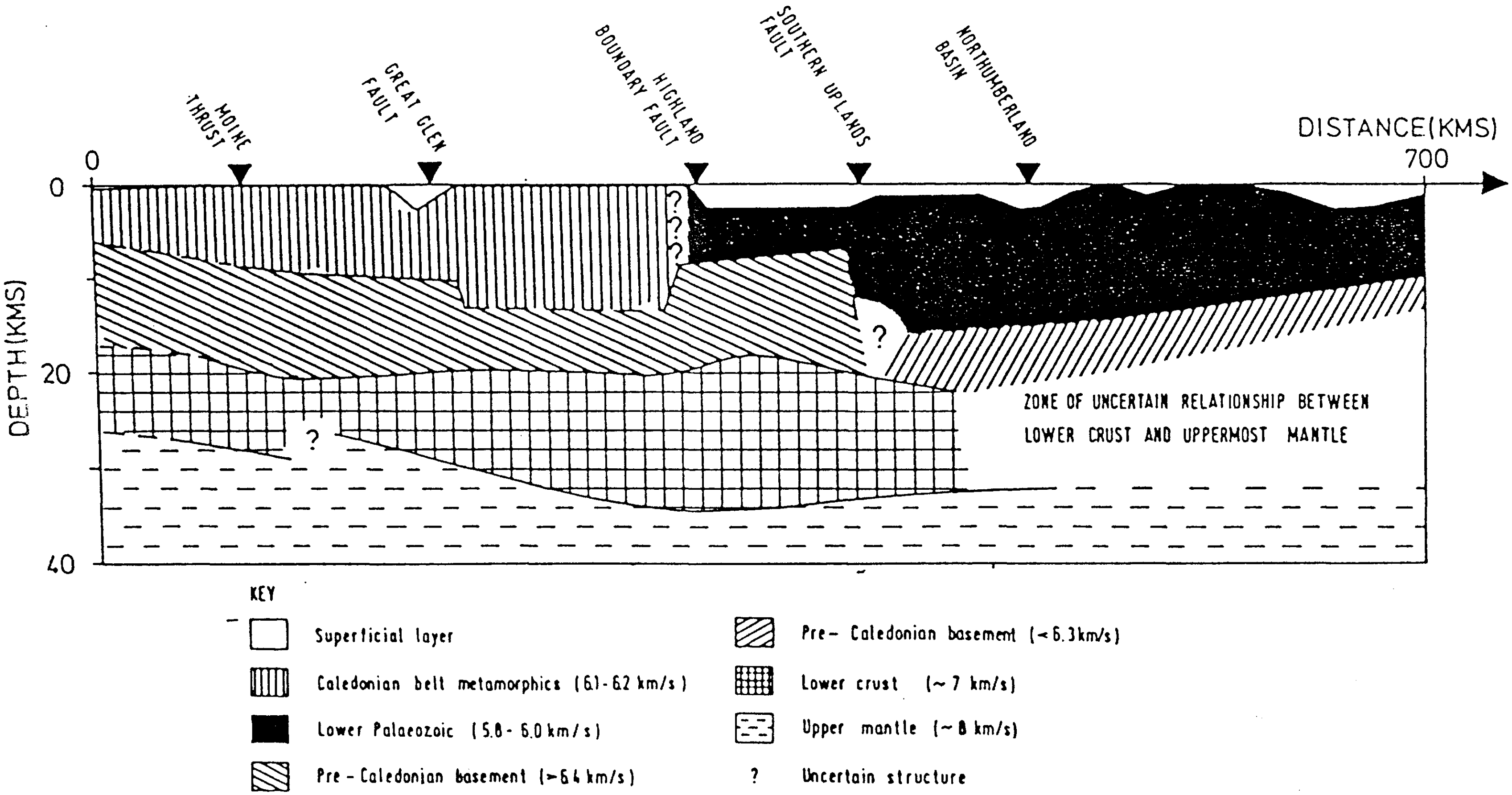

Fig.2.3 Cross-section of the crust and Moho of northern Britain from the LISPB profile (after Bamford 1979).

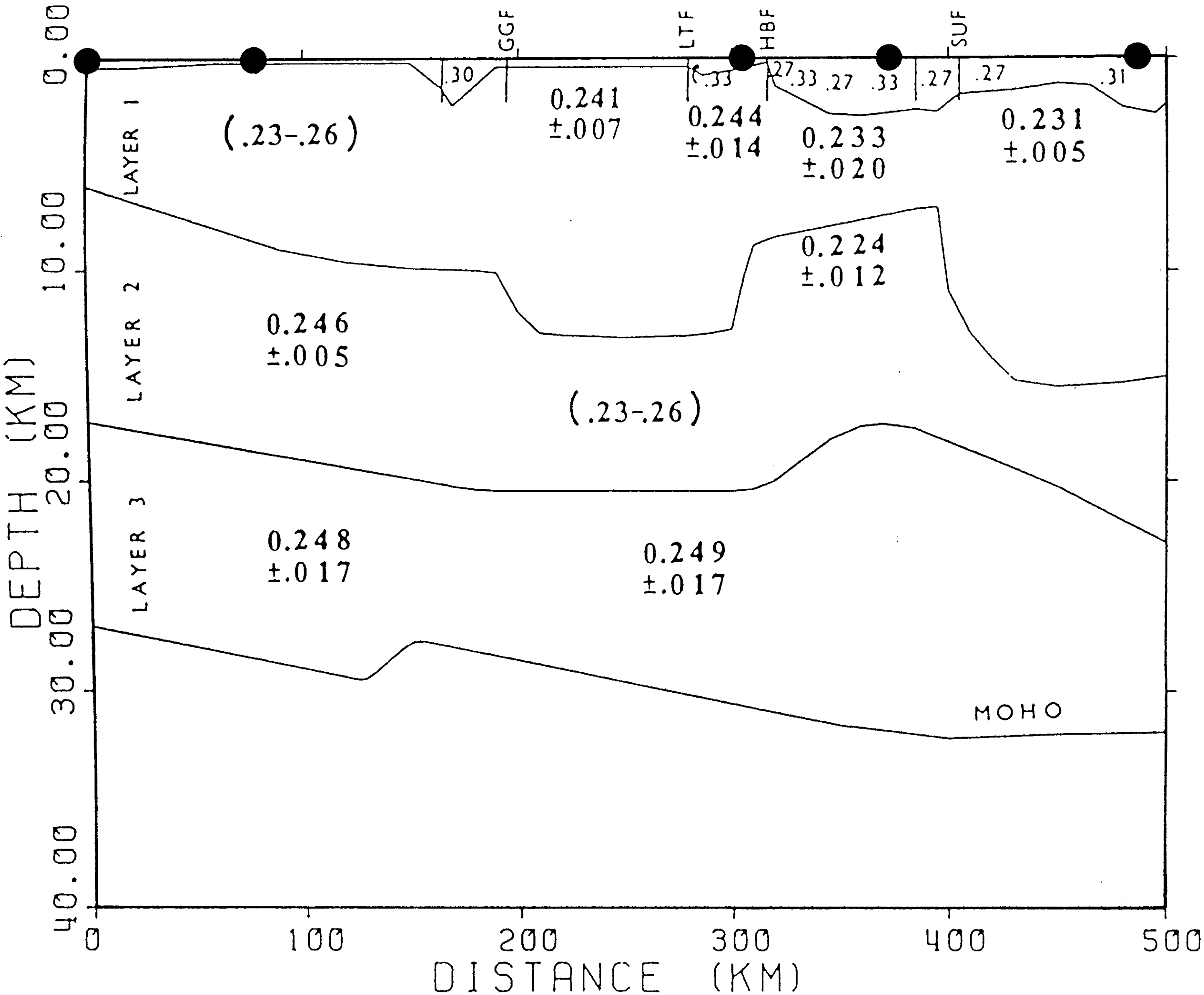

Fig.2.4 Poisson's ratio structure of the crust of northern Britain. GGF - Great Glen Fault, HBF - Highland Boundary Fault, LTF - Loch Tay Fault, SUF - Southern Uplands Fault. Dots are shot locations (after Assumpcao & Bamford 1978).

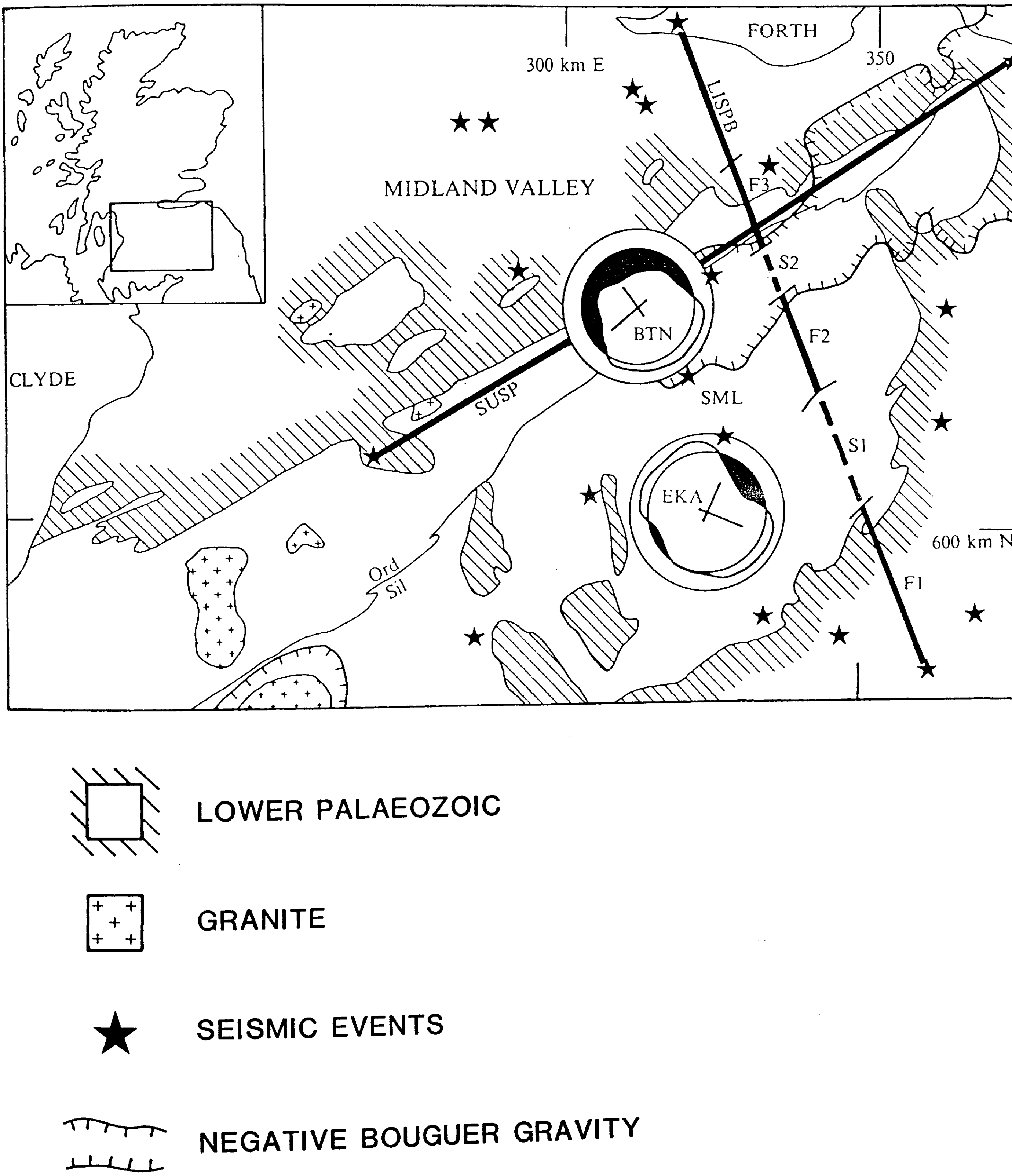

Fig.2.5 Location of previous seismic work in southern Scotland. On LISPB F1-3 and S1-2 locate high and low velocity blocks. BTN - Broughton seismic array, EKA - Eskdalemuir seismic array, SML - Saint Mary's Loch, SUSP - Southern Uplands Seismic Profile. Polar plots are of apparent velocity vs direction with scale rings at 5.5 km/s (outer) and 6.0 km/s (inner) so black area represents area where velocity is greater than 6.0 km/s (redrawn from Hall et al. 1983).

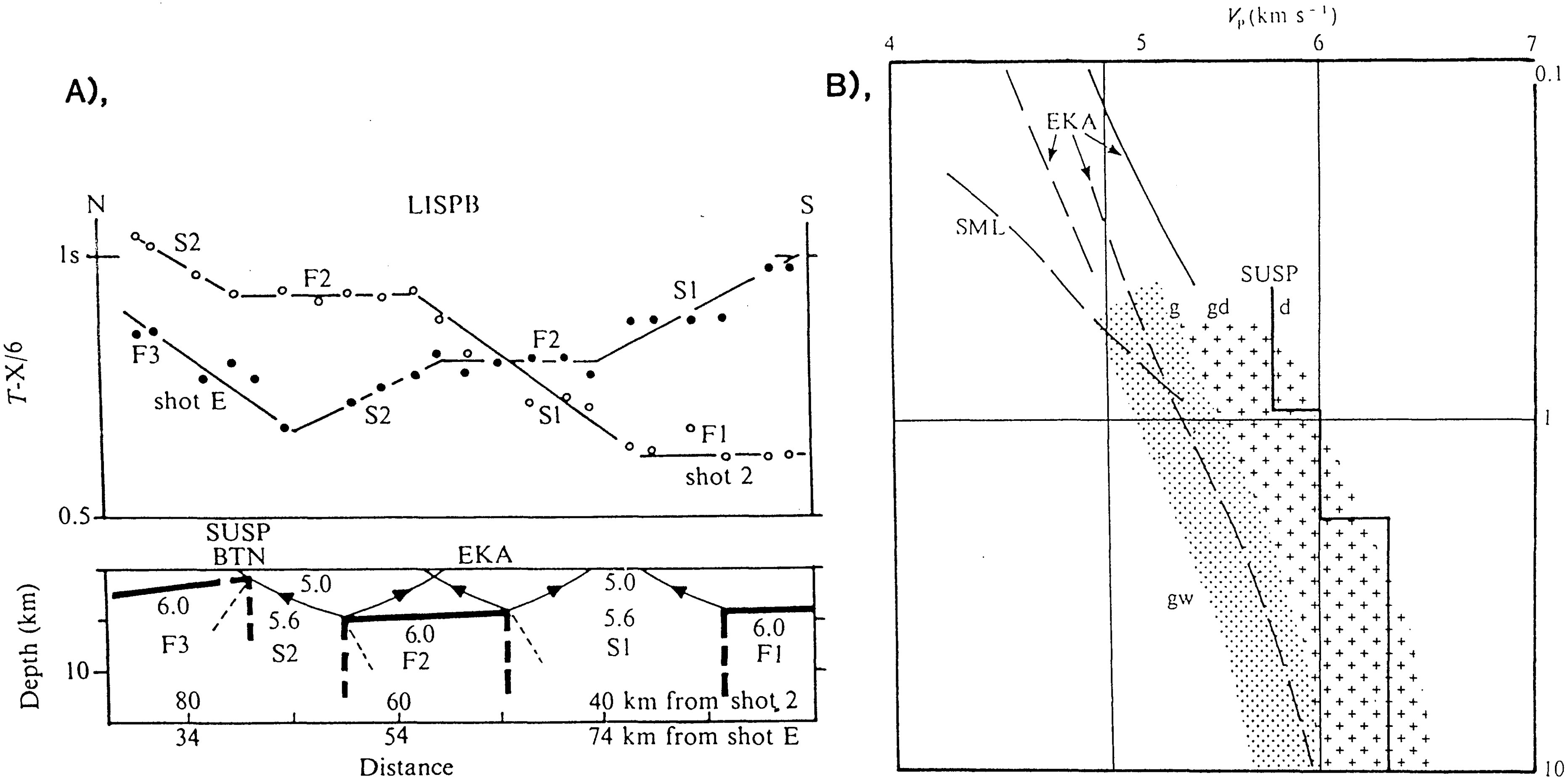

Fig.2.6 A), LISPB time-distance data from the Southern Uplands, reduction velocity is 6.0 km/s. Structural model shows velocity distribution containing fast (F) and slow (S) blocks which give rise to the corresponding segments on the time-distance plot. B), Velocity-depth plot for the Southern Uplands. Solid lines show along-strike velocities and dashed lines across-strike velocities. EKA - Eskdalemuir seismic array, SML is an array study at Saint Mary's Loch in the S2 slow block. Dotted area, (gw), represents velocity field for Lower Palaeozoic greywackes. Plusses indicate velocity field for plutonic rocks, g - granite, gd - granodiorite, d - diorite. SUSP - Southern Uplands Seismic Profile, (after Hall et al. 1983).

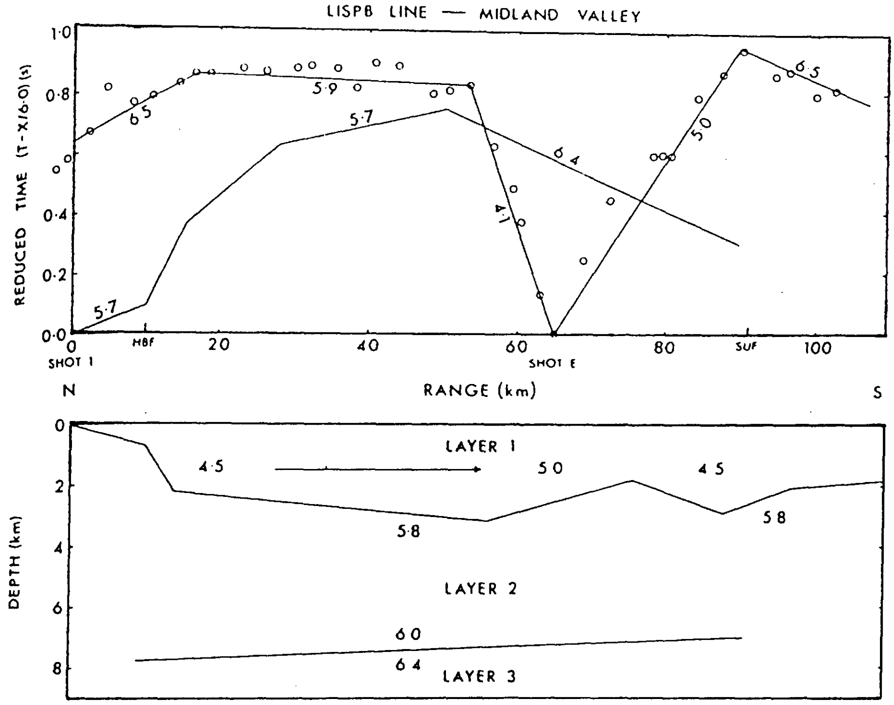

Fig.2.7 The LISPB model across the Midland Valley with time-distance data and interpretation (after Davidson et al. 1984).

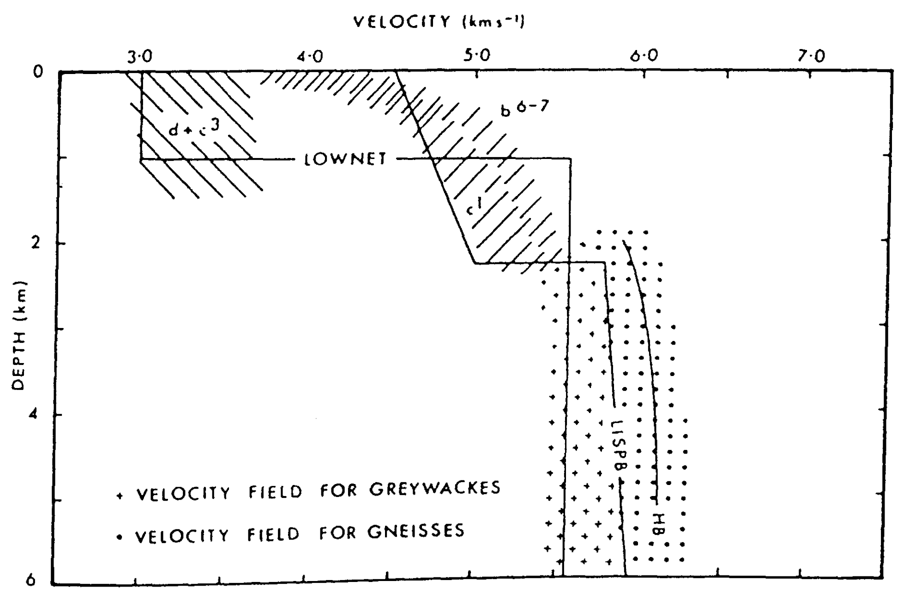

Fig.2.8 Velocity-depth plot for Midland Valley lithologies. The velocity-depth models of LISPB and LOWNET are shown for comparison. d - Carboniferous, c3 - Upper ORS, c1 - Lower ORS, b6-7 - Silurian. HB is velocity of basement refractor (after Davidson et al. 1984).

A)

B)

C)

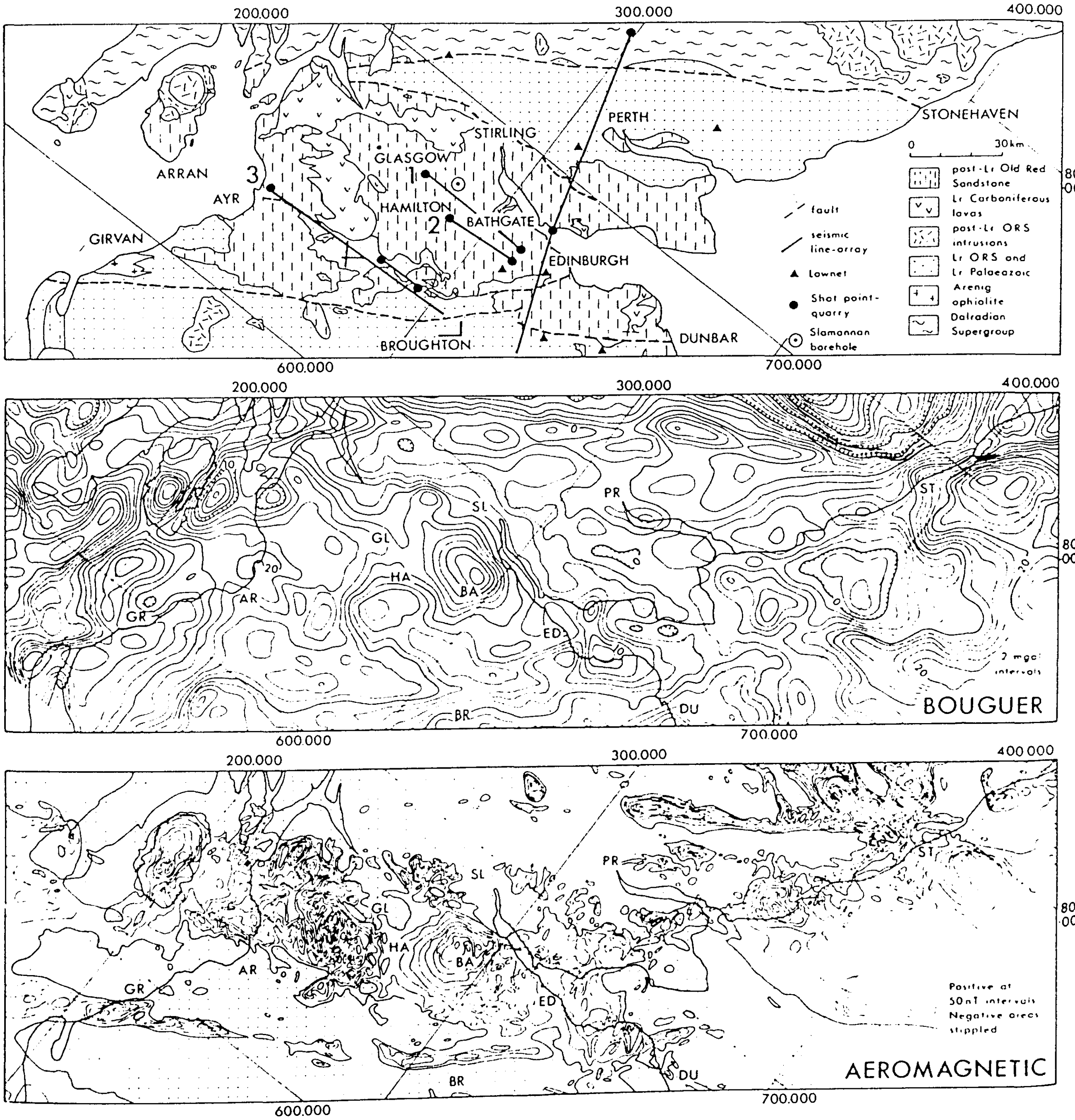

Fig.2.9 A), Simplified geological map of the Midland Valley. Numbers refer to seismic lines. B), Bouguer gravity map of the Midland Valley (redrawn from Hussain & Hipkin 1981). Locality names abbreviated from (A). C), Aeromagnetic map of the Midland Valley (redrawn from I.G.S. 1972). Locality names abbreviated from a). Negative contours omitted. (after Davidson et al. 1984).

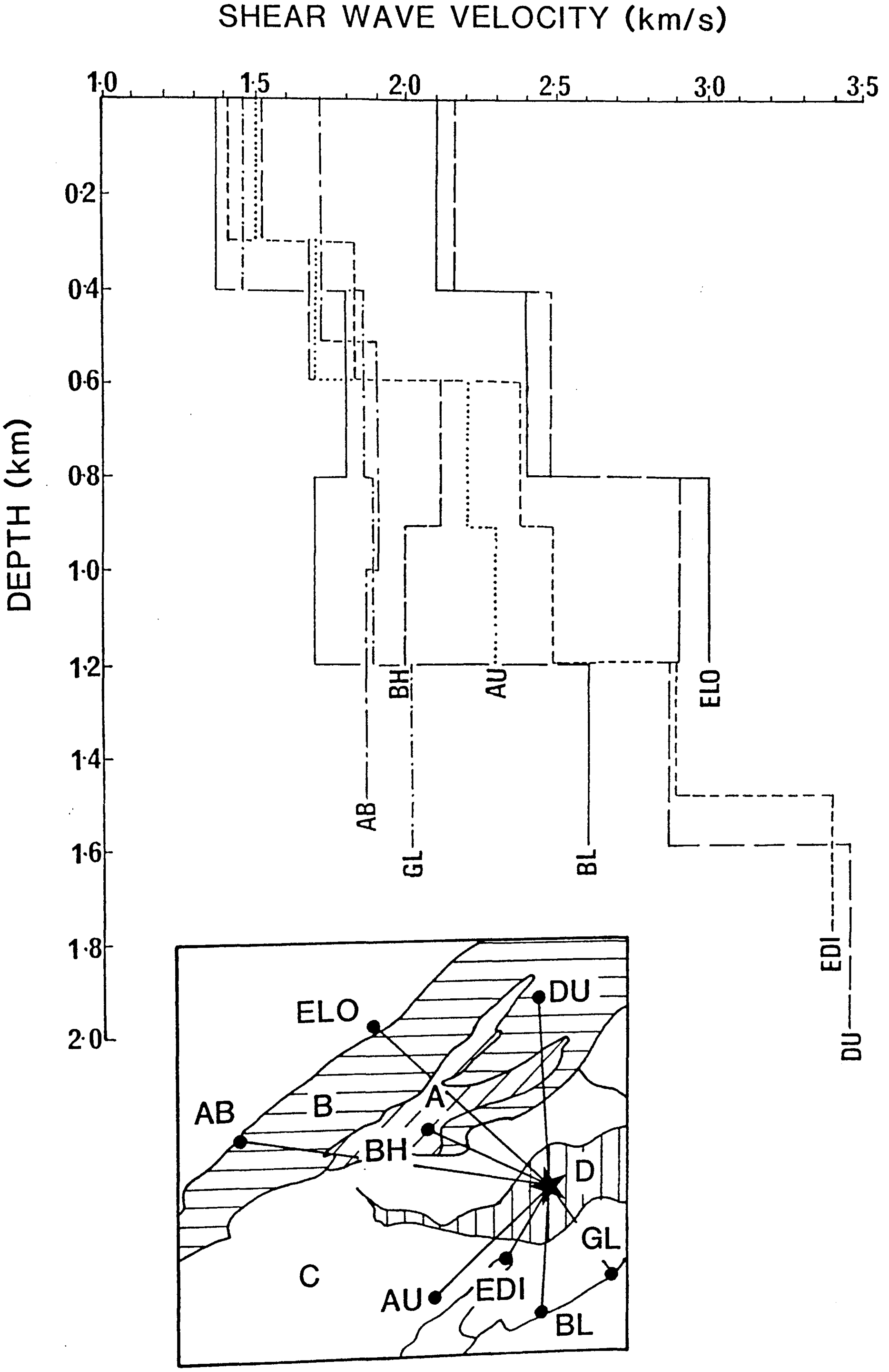

Fig.2.10 Shear wave velocity-depth plot obtained by inversion of surface wave group velocity data. Letters refer to LOWNET stations (see Fig.2.1). A - ORS lavas, B - ORS sediments, C - Carboniferous, D - Carboniferous beneath the Firth of Forth (redrawn from MacBeth & Burton 1986).

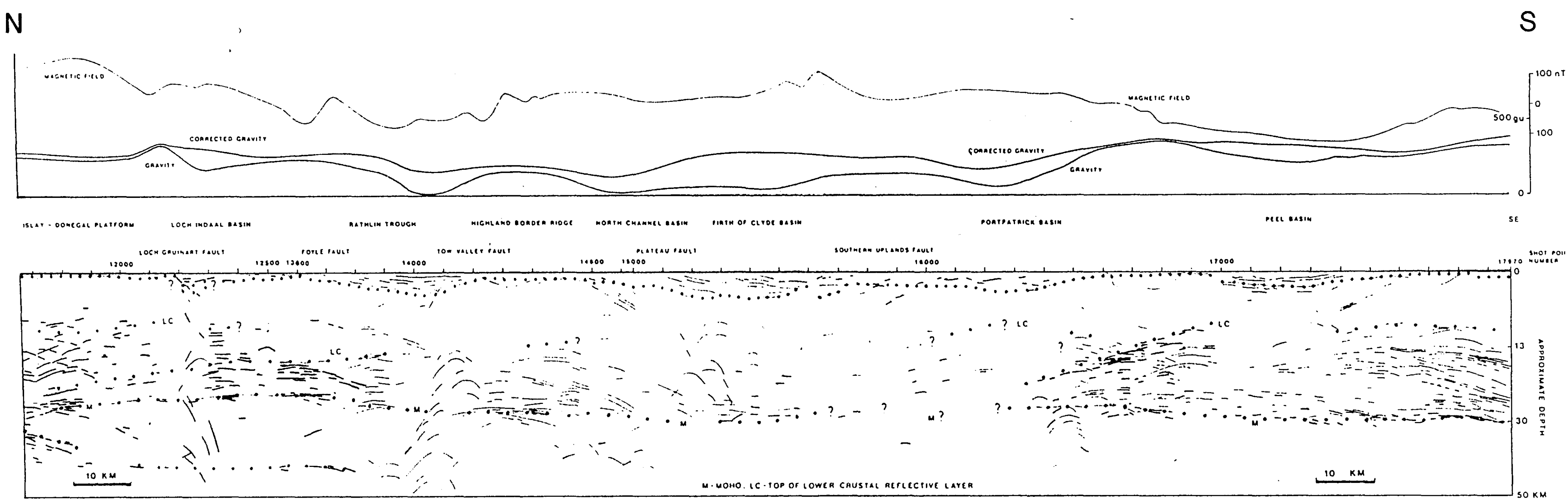

Fig.2.11 Line drawing of WINCH section shown in Fig.2.2. The magnetic and Bouguer gravity fields with corrected gravity, obtained by one-dimensional correction for the thickness of sedimentary rocks above basement, are also shown (after Hall et al. 1984).

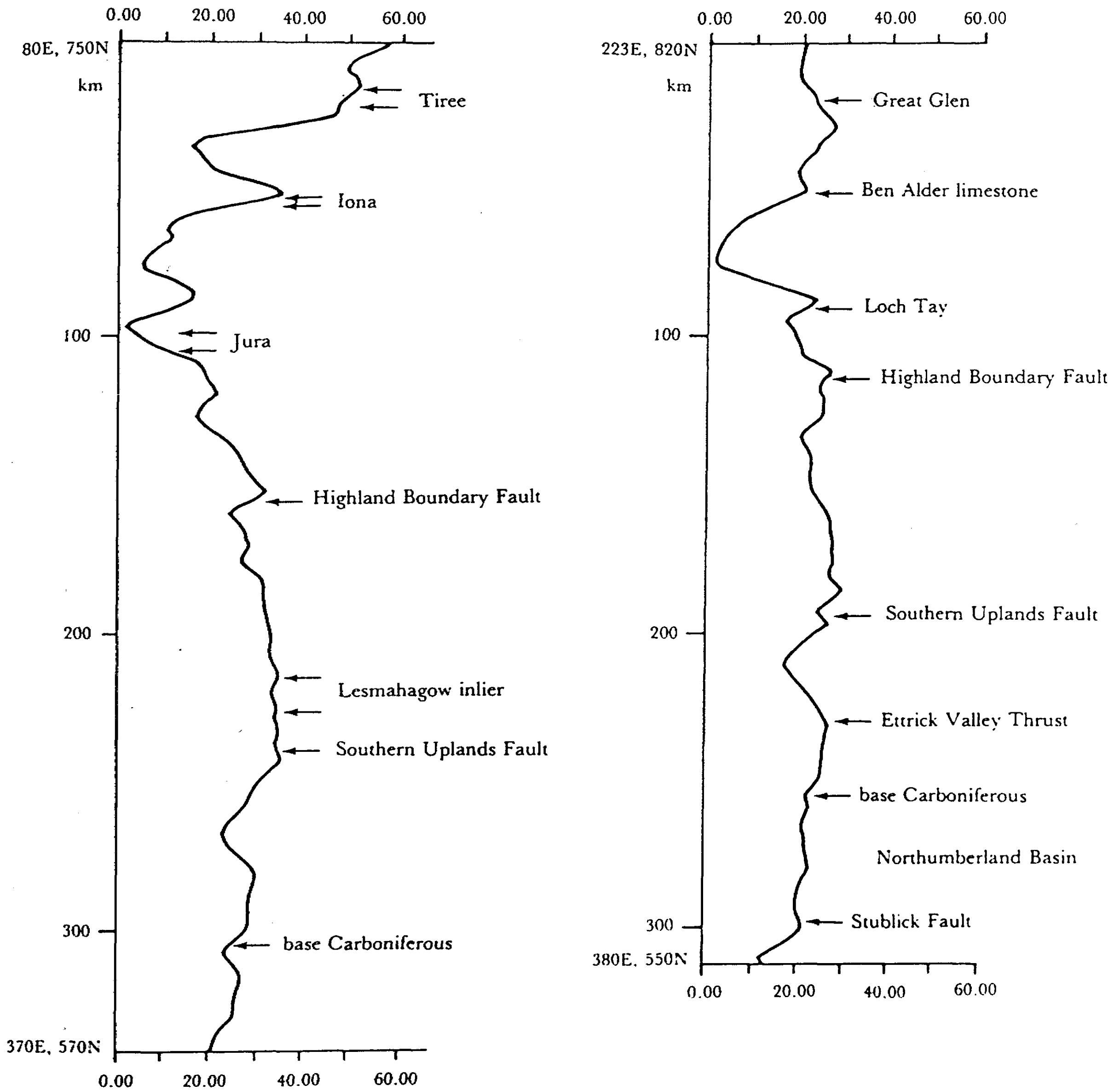

Fig.2.12 Stripped isostatic anomaly profiles (in mgals) across the Midland Valley (after Hipkin & Hussain 1983).

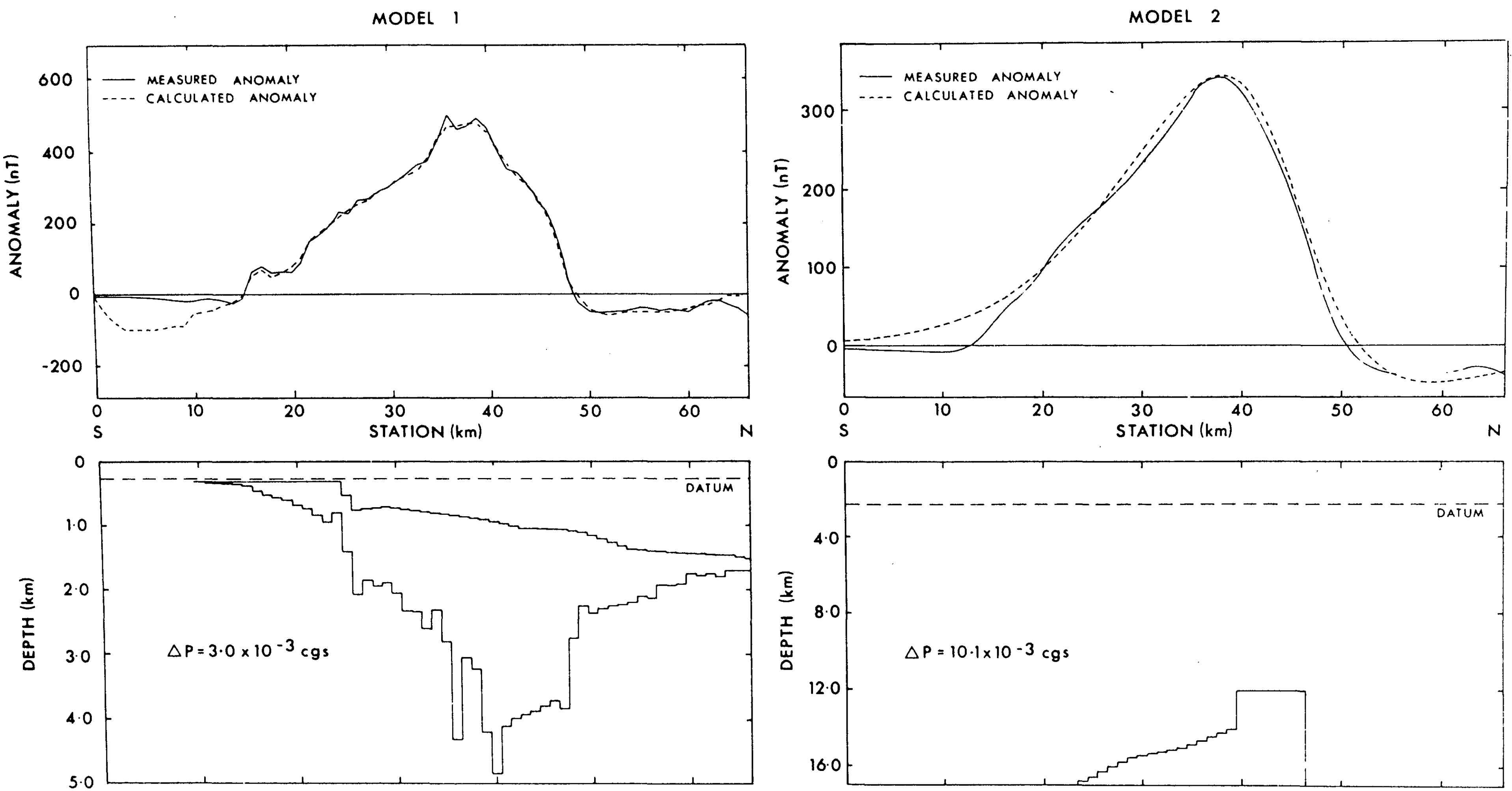

Fig.2.13 Alternative models of the Bathgate magnetic anomaly (after Hossain 1976).
ΔP = Polarisation contrast

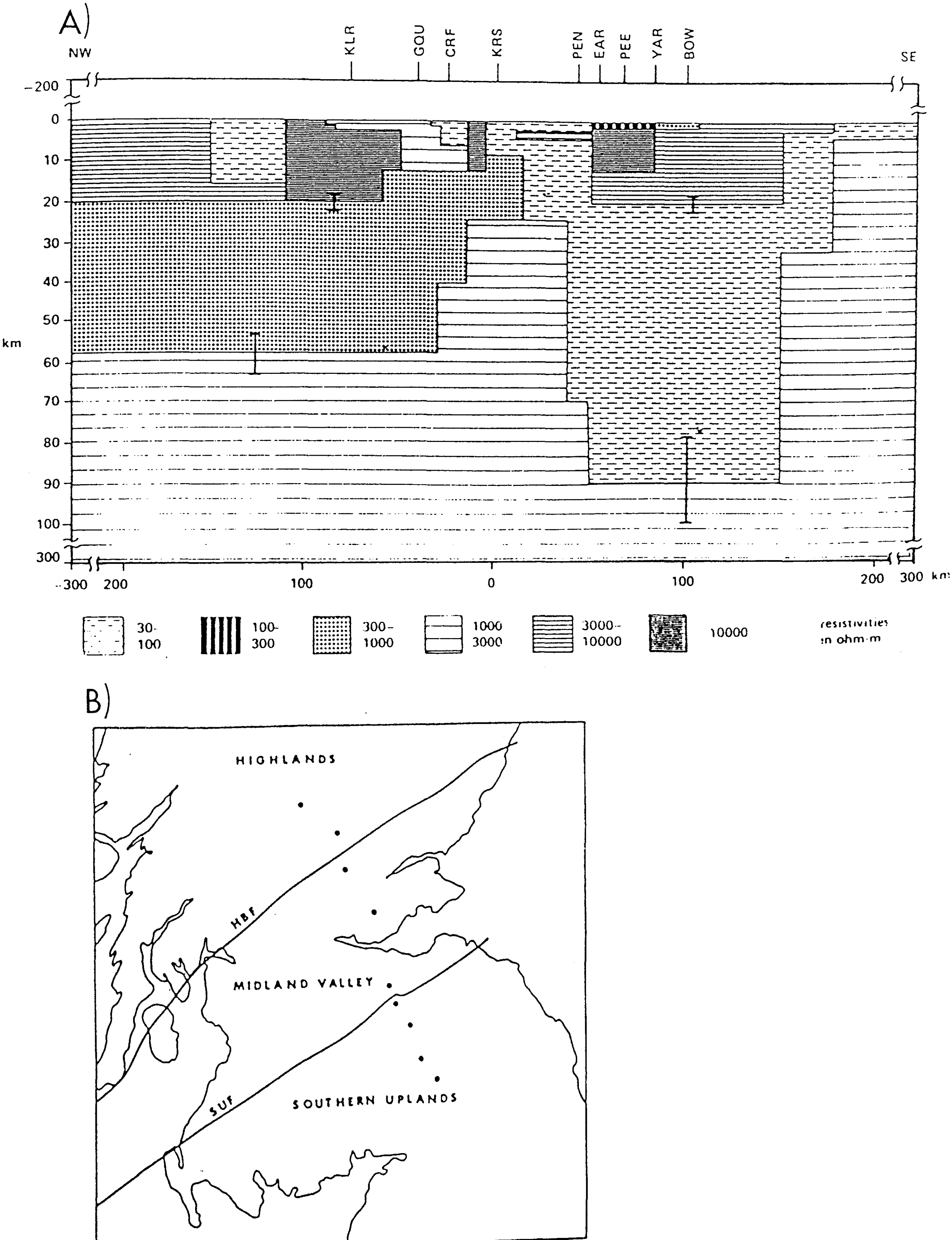

Fig.2.14 A), Generalised resistivity section for southern Scotland. Abbreviations refer to stations in (B). B), Location map of magnetotelluric sites (circles) (after Ingham & Hutton 1982).

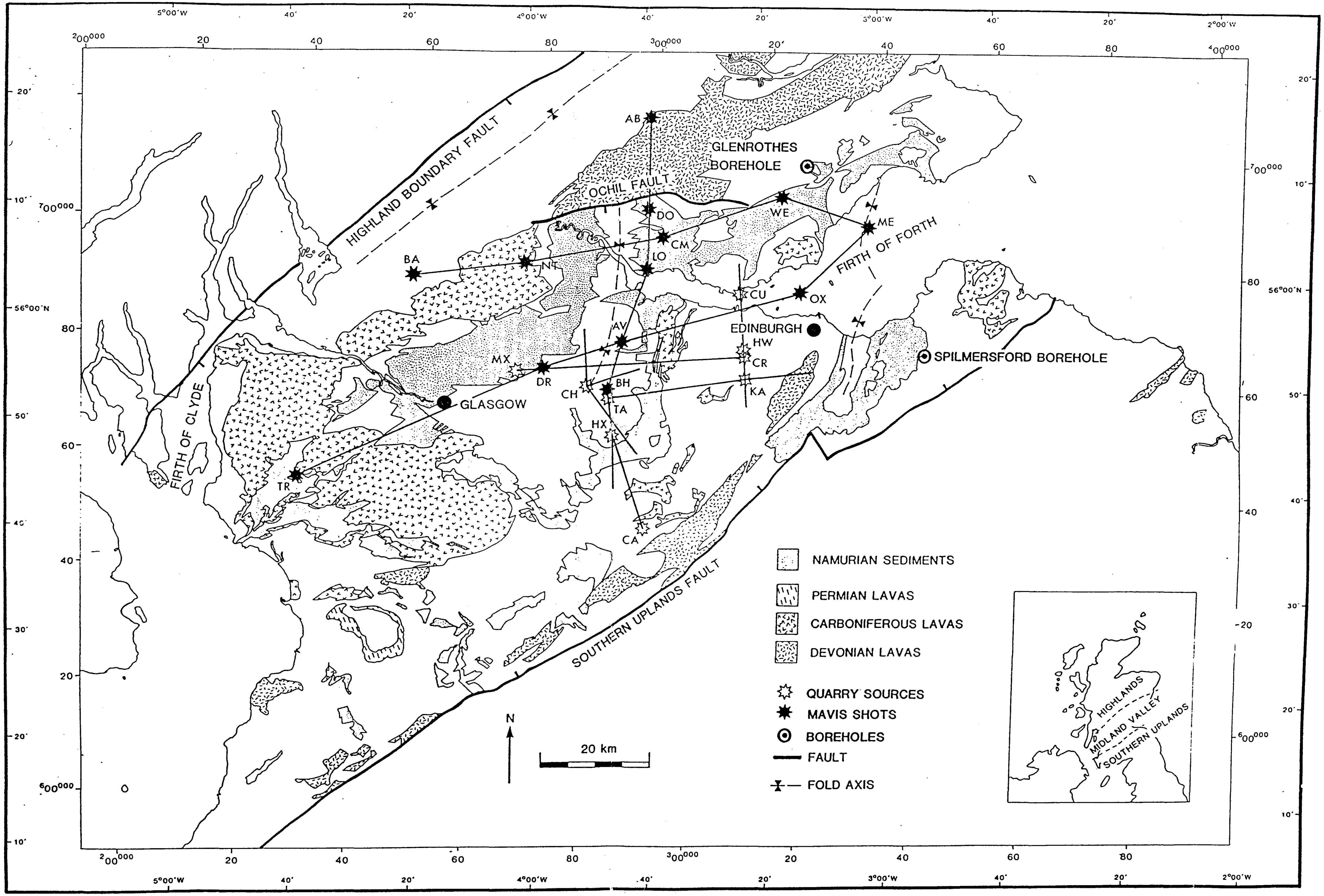

Fig.3.1 MAVIS location map. MAVIS I (South): TR - Trearne, DR - Drumgray, AV - Avonbridge, OX - Oxcars, ME - Methil. MAVIS I (North): BA - Ballikinrain, NT - North Third, CM - Cattlemoss, WE - Westfield, ME - Methil. MAVIS II: AB - Aberuthven, DO - Dollar, LO - Longannet, AV - Avonbridge, CH - Cairnyhill, BH - Blairhill TA - Tamsloup, HX - Headless Cross, CA - Cairngryffe. MAVIS III: CU - Cruiks, HW - Hillwood, KA - Kaimes. Sola (North): MX - Medrox, CR - Craigpark. Sola (South): TA - Tamsloup, KA - Kaimes.

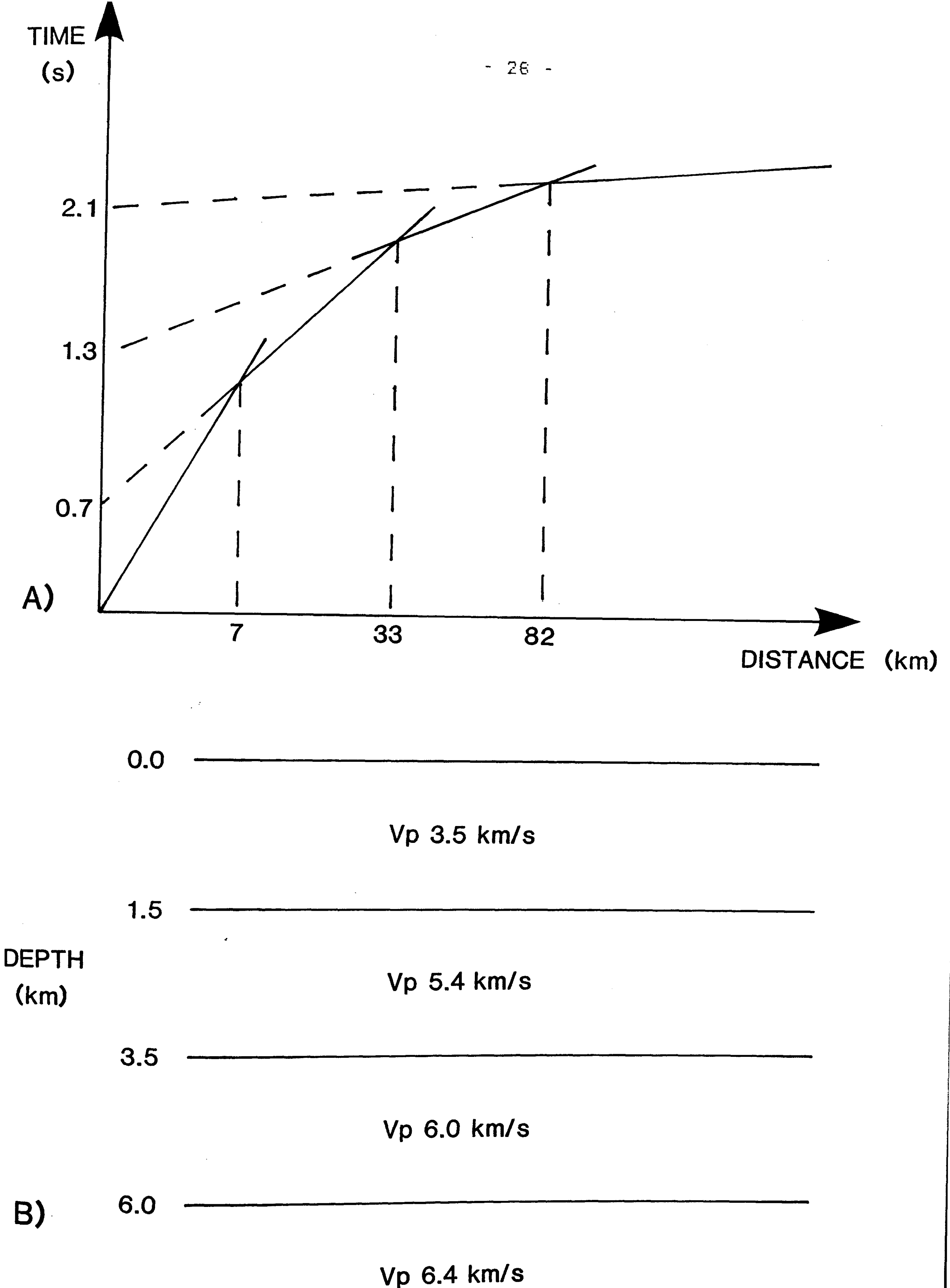

Fig.3.2 Crustal model assumed in the planning of MAVIS; A), time-distance graph B), crustal model (not to scale).

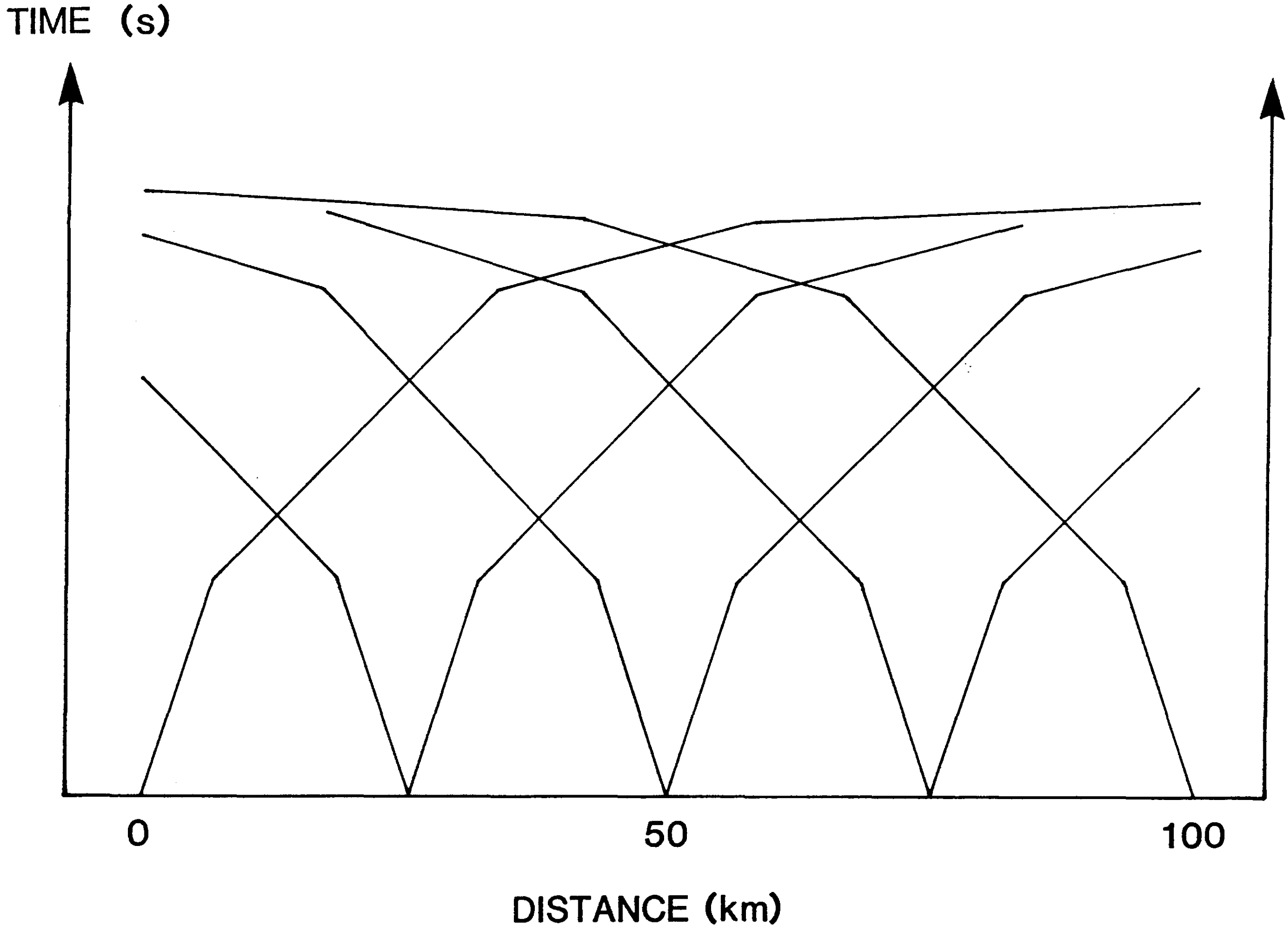

Fig.3.3 Schematic first arrival coverage of MAVIS based on Fig.3.2.

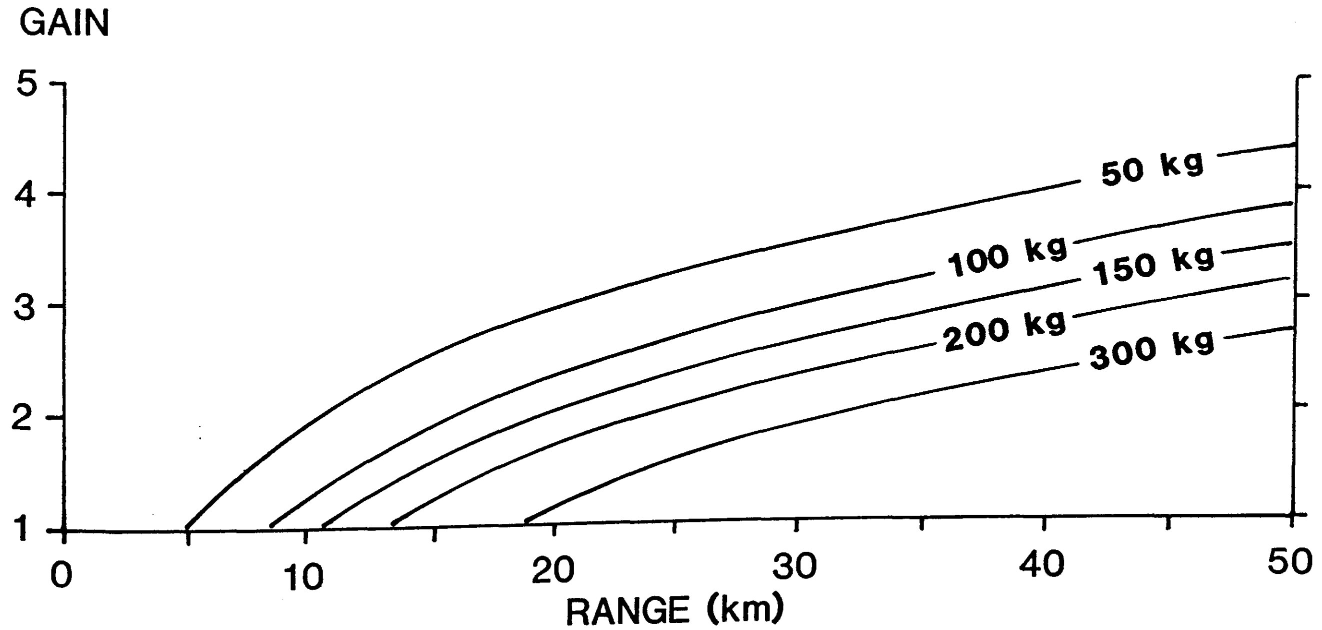

Fig.3.4 Seismograph gain versus range for charges of different size.

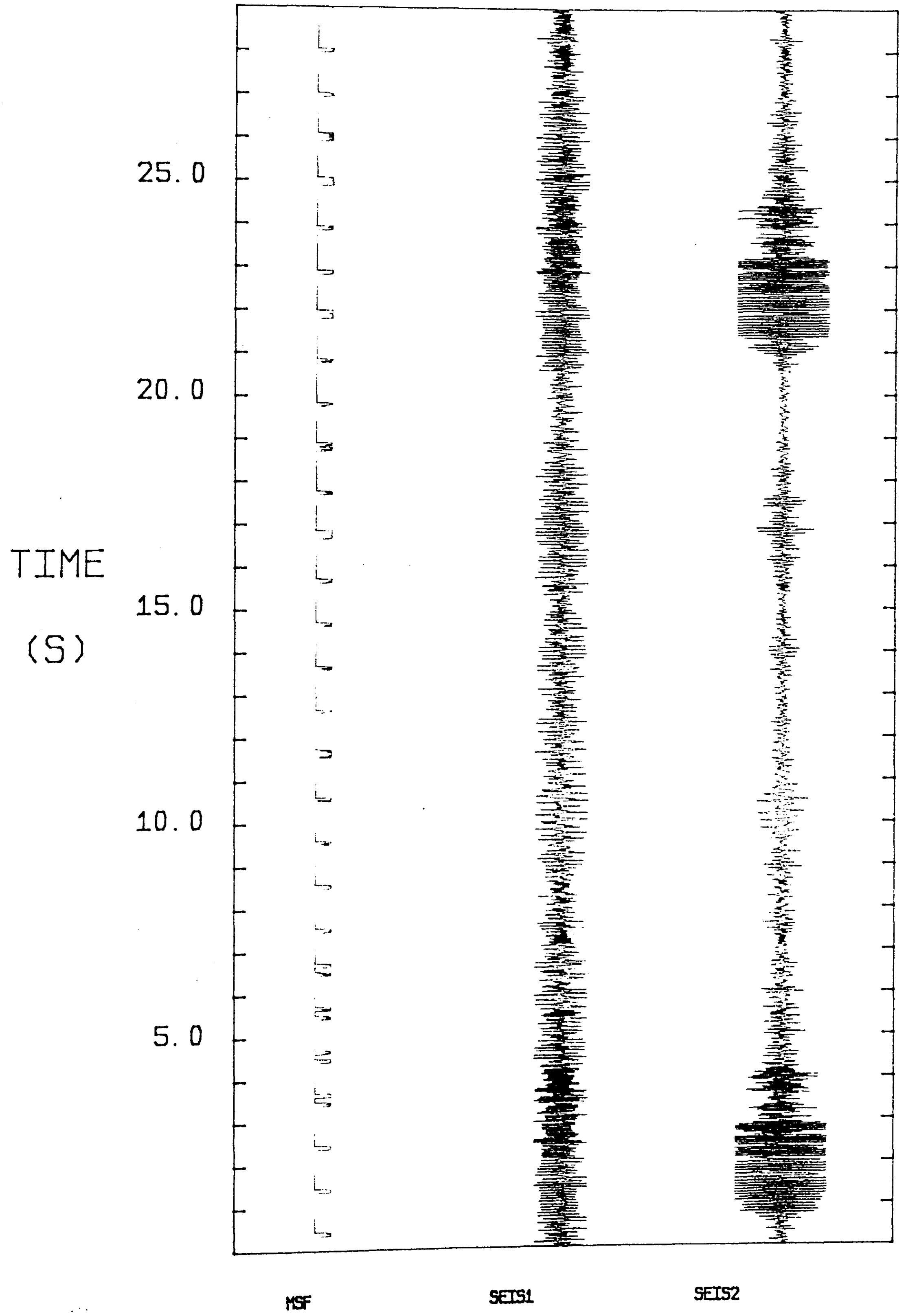

Fig.3.5 Uncorrelated Vibroseis data recorded by the Glasgow seismic recorder.

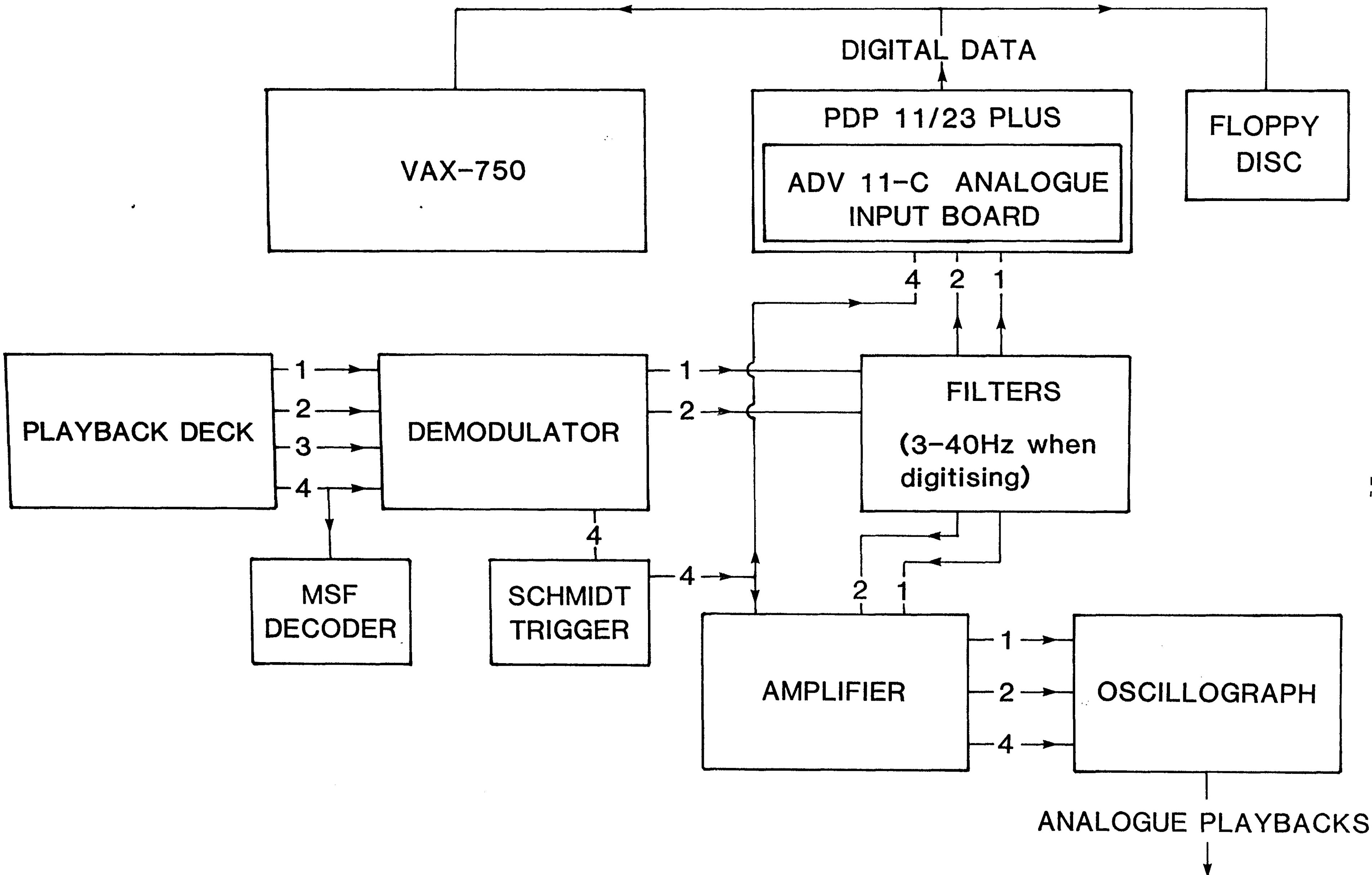

Fig.3.6 Schematic diagram of Glasgow playback system.

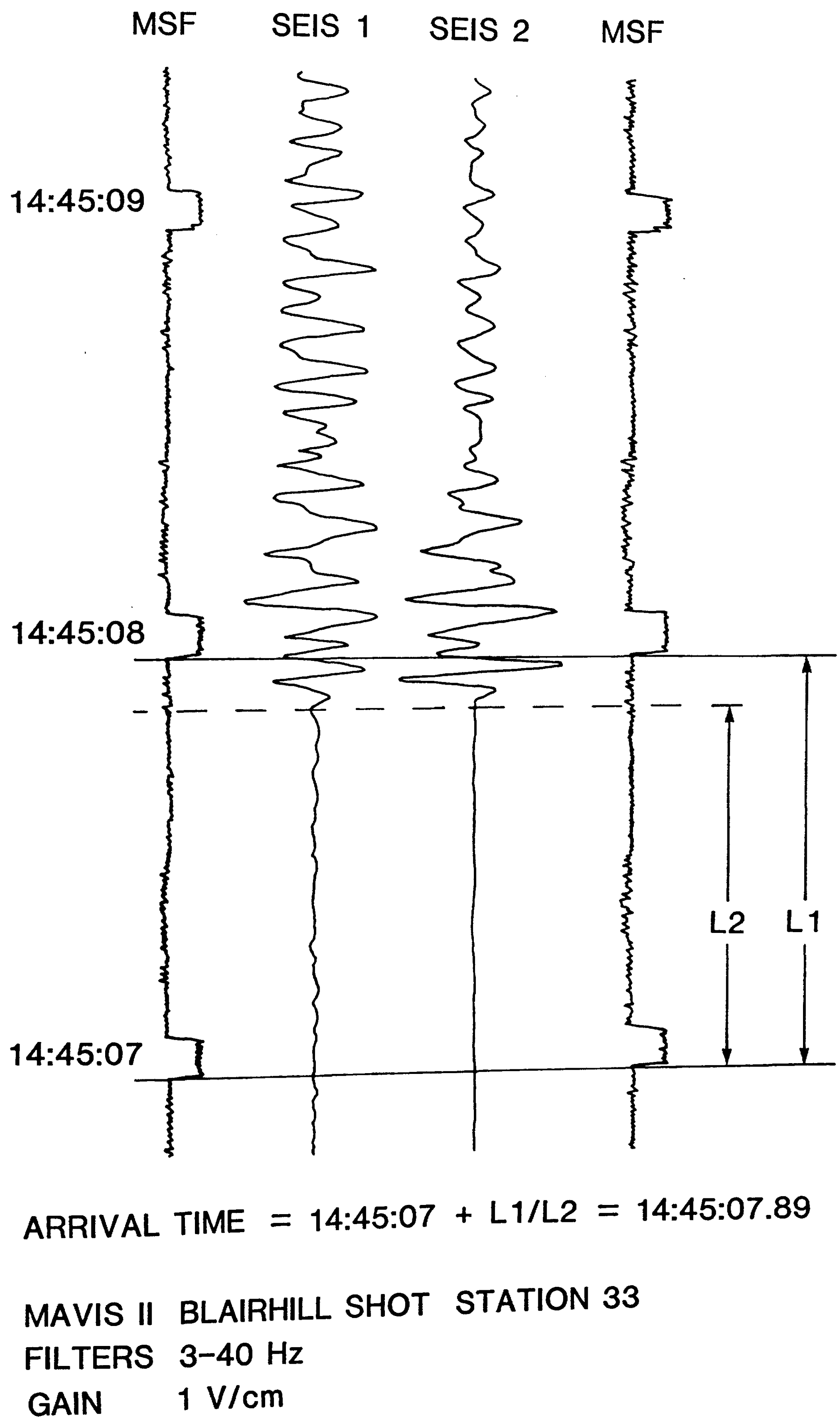

Fig.3.7 Calculation of arrival time from analogue playbacks.

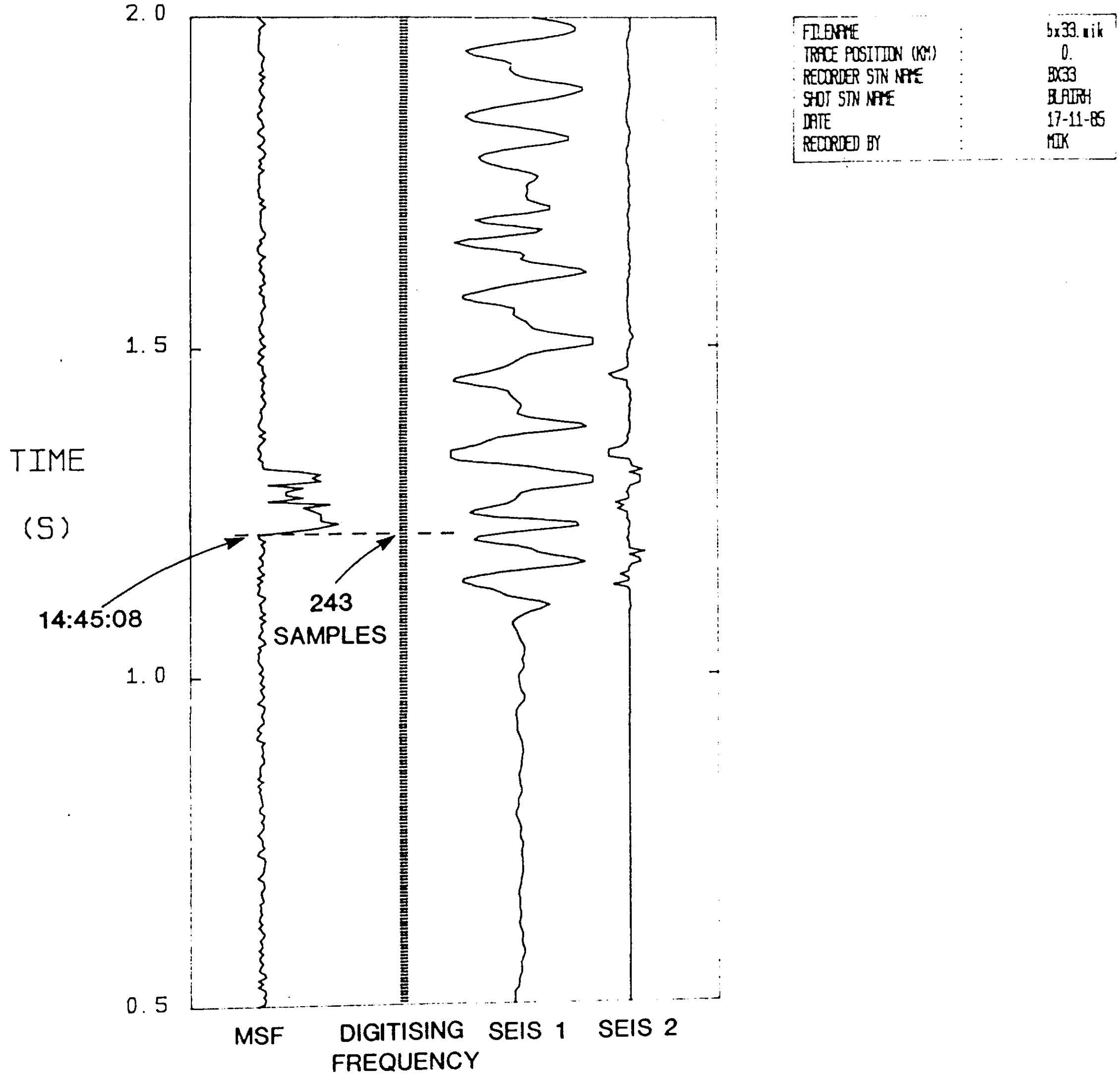

SHOT TIME	14:45:04.82
ARRIVAL TIME	14:45:07.89
DIGITISING FREQUENCY	200 SAMPLES/s
FILE START TIME	14:45:08 − 243 x 1/200 = 14:45:06.785
SHOT TIME − FILE START TIME	−1.965 s =−393 SAMPLES

Fig.3.8 Example of output from program MSFPLOT and the calculation of file start time.

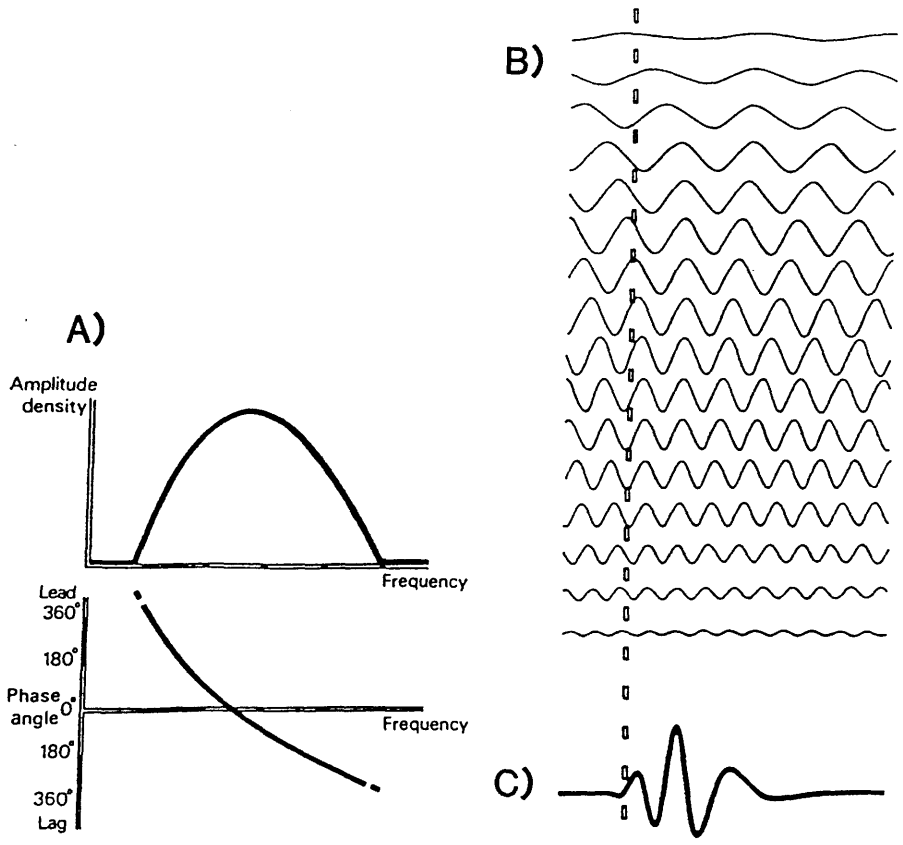

Fig.3.9 Fourier representation of seismic waveform; A), amplitude and phase spectra B), sinusoidal waves having amplitudes and time shifts corresponding to the spectra in (A) C), synthesis of the waveform by summation of the waves in (B), (after Anstey 1970).

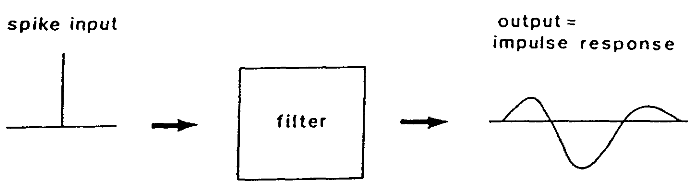

Fig.3.10 The impulse response of a filter (after Kearey & Brooks 1984).

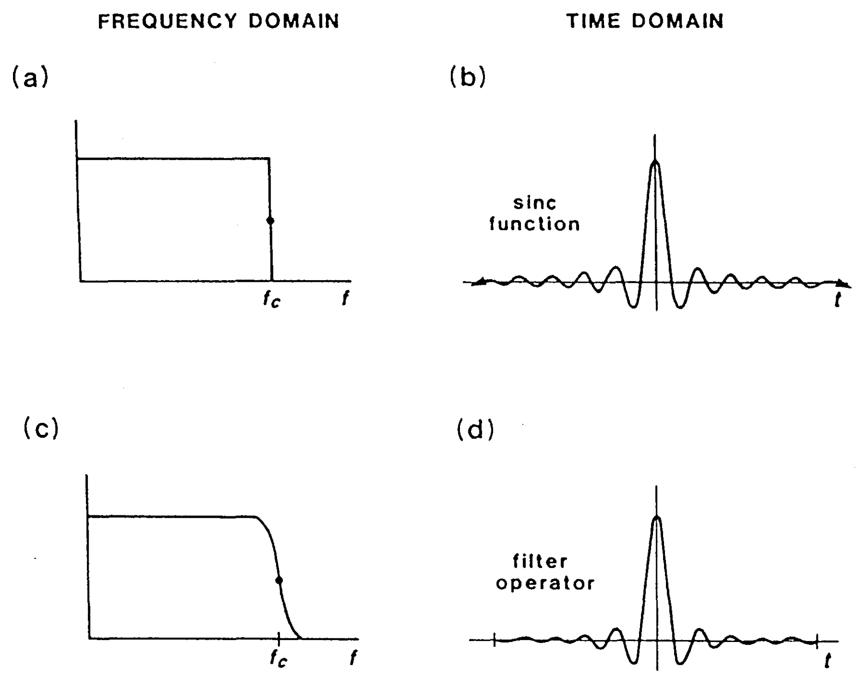

Fig.3.11 Design of a low-pass filter (after Kearey & Brooks 1984).

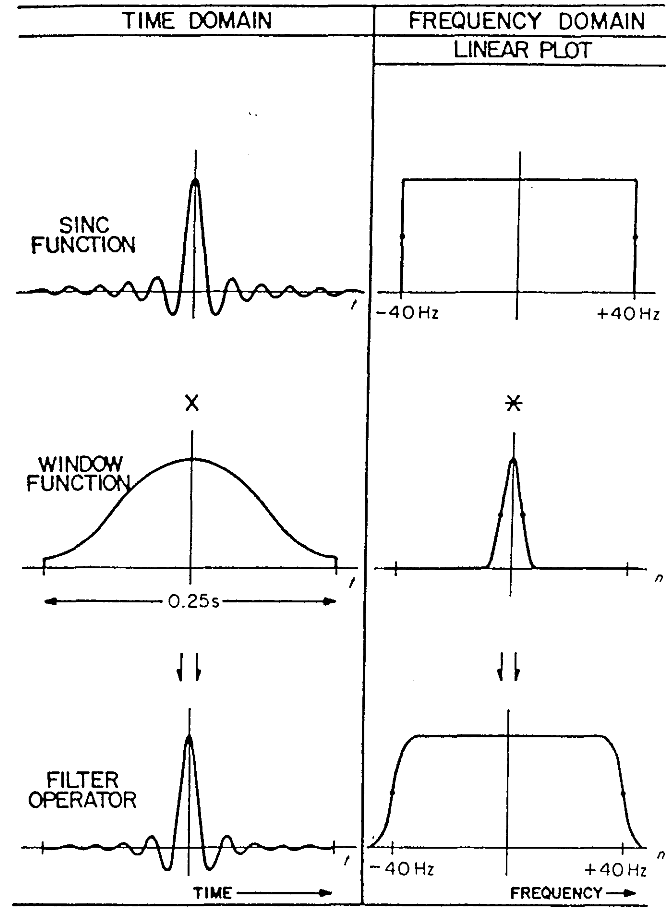

Fig.3.12 Truncation of a filter operator by a windowing function (after Peterson & Dobrin 1966).

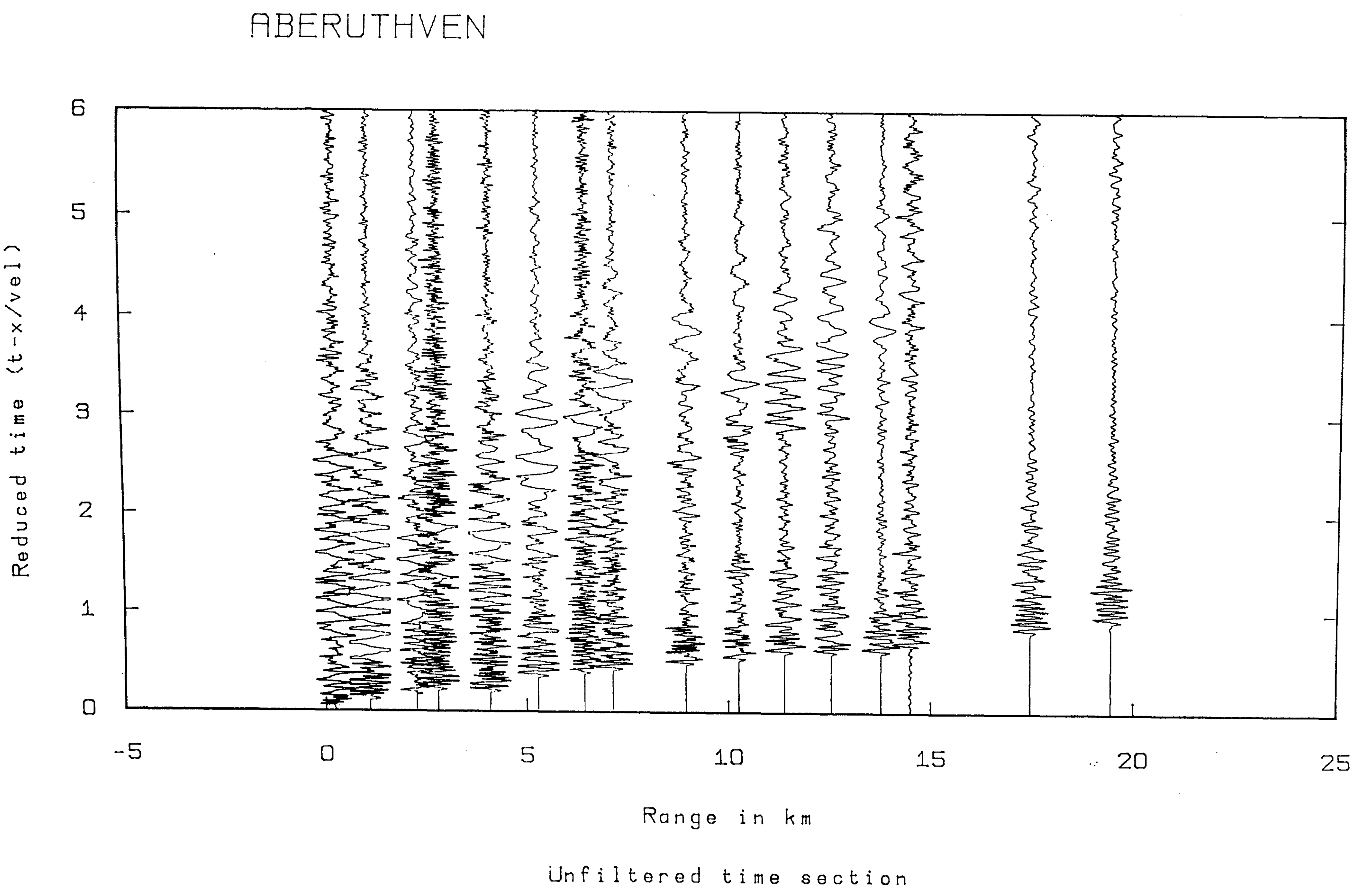

Fig.3.13 Data recorded from the MAVIS II Aberuthven shot used to ascertain the optimum filter parameters.

ABERUTHVEN (P WAVE)

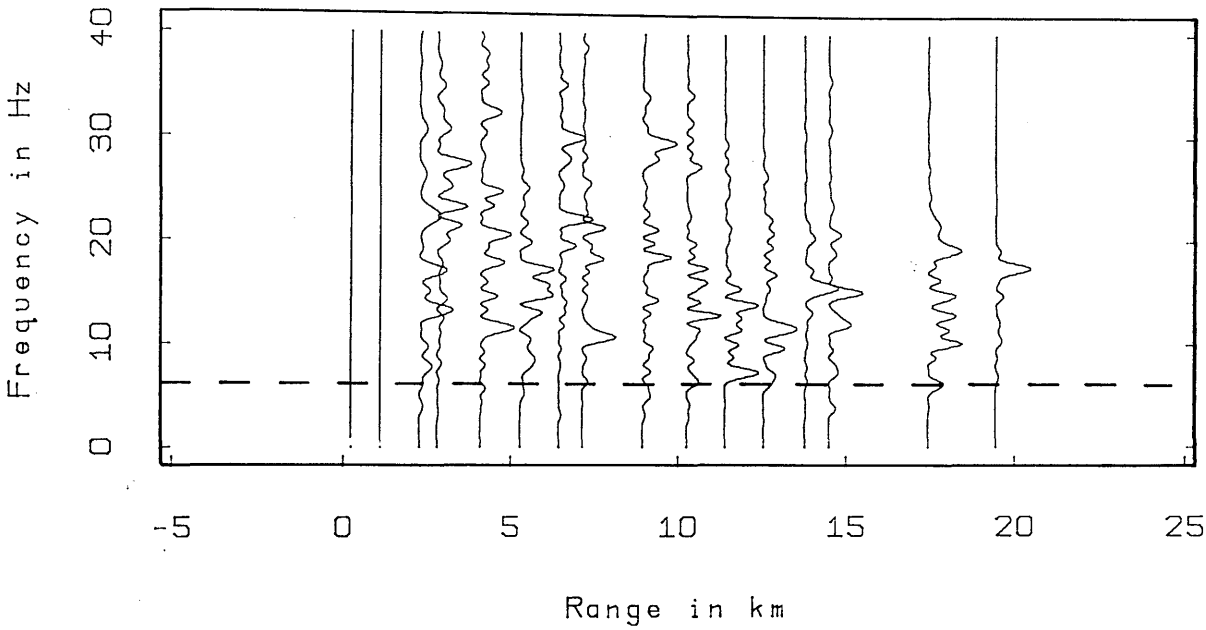

Spectral analysis plot

ABERUTHVEN (S WAVE)

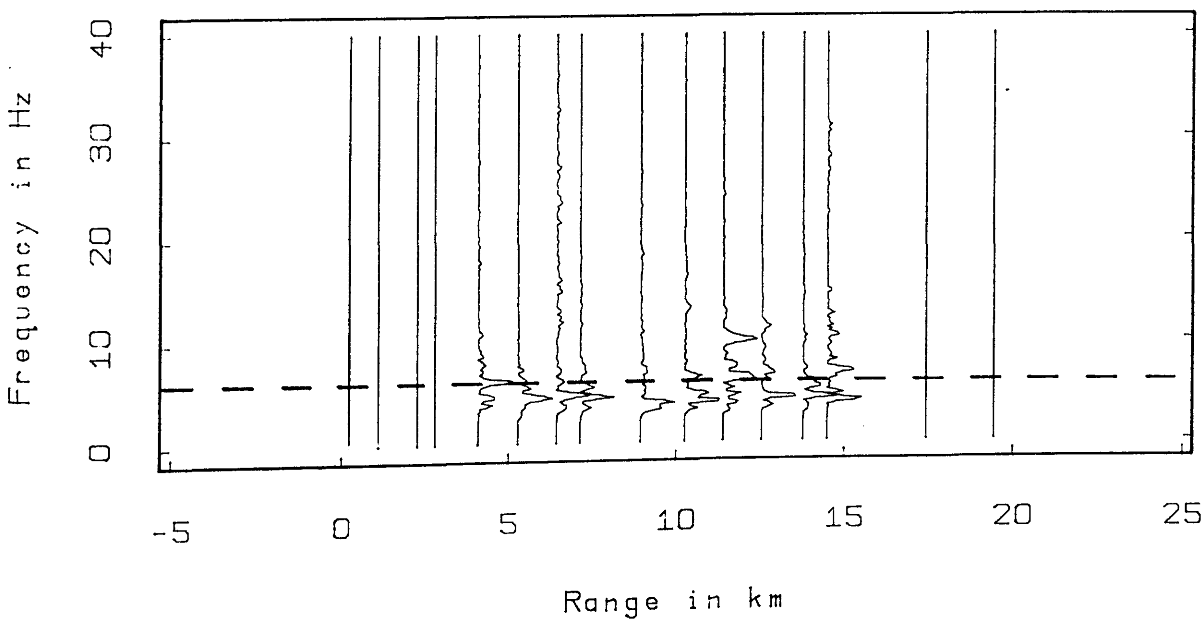

Spectral analysis plot

Fig.3.14 Frequency spectra of P- and S-wave arrivals in Fig.3.13. Dashed line is at 6 Hz.

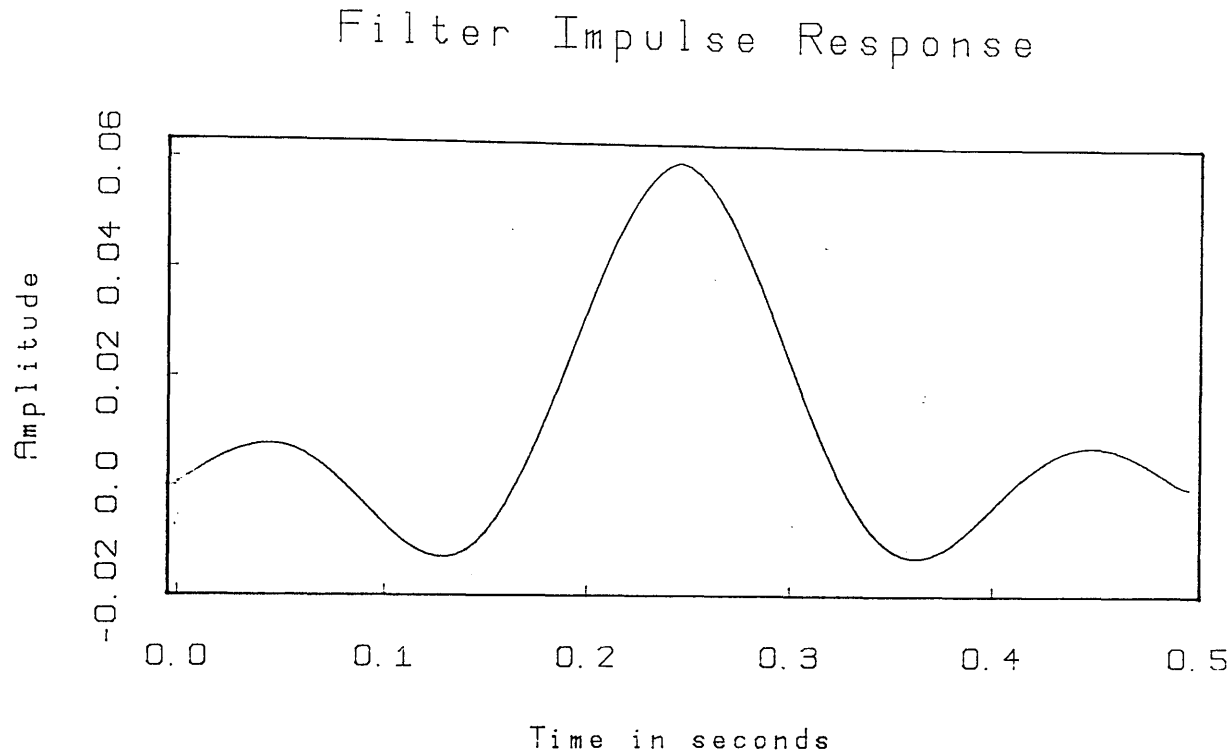

Zero-phase, lowpass filter 6.0Hz and length 0.50 s
with a rectangular window

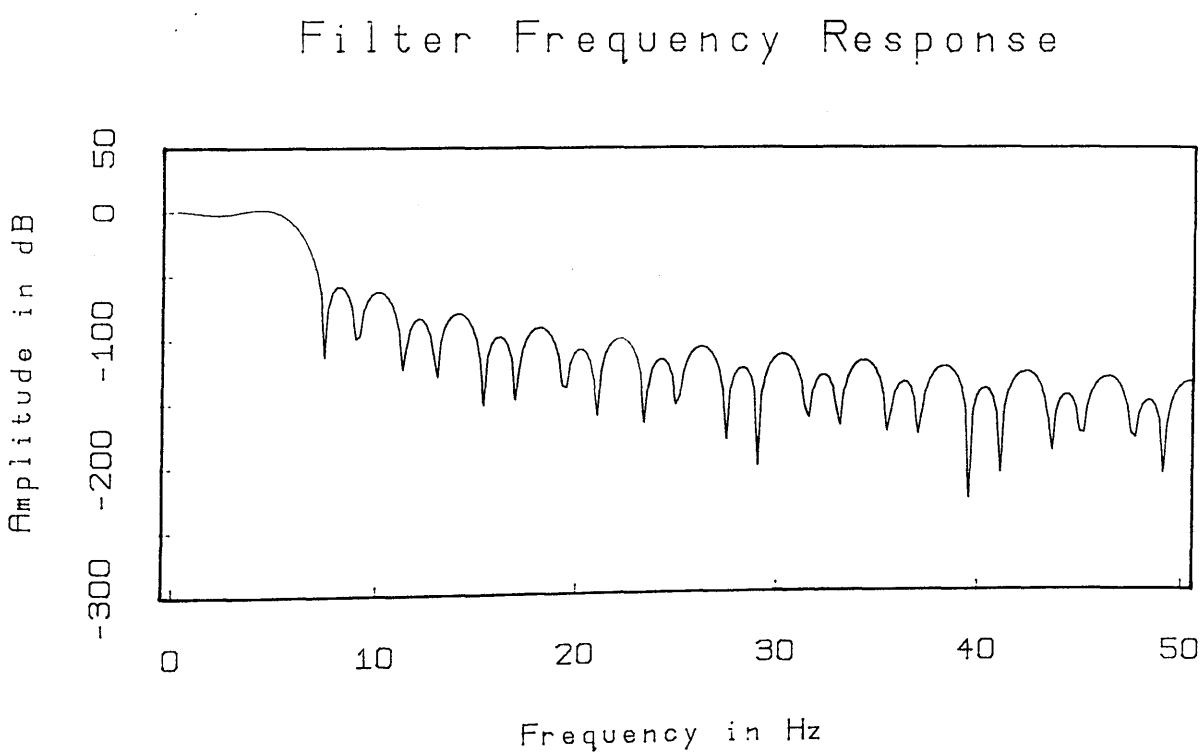

Zero-phase, lowpass filter 6.0Hz and length 0.50 s
with a rectangular window

Fig.3.15 Filter response with rectangular window.

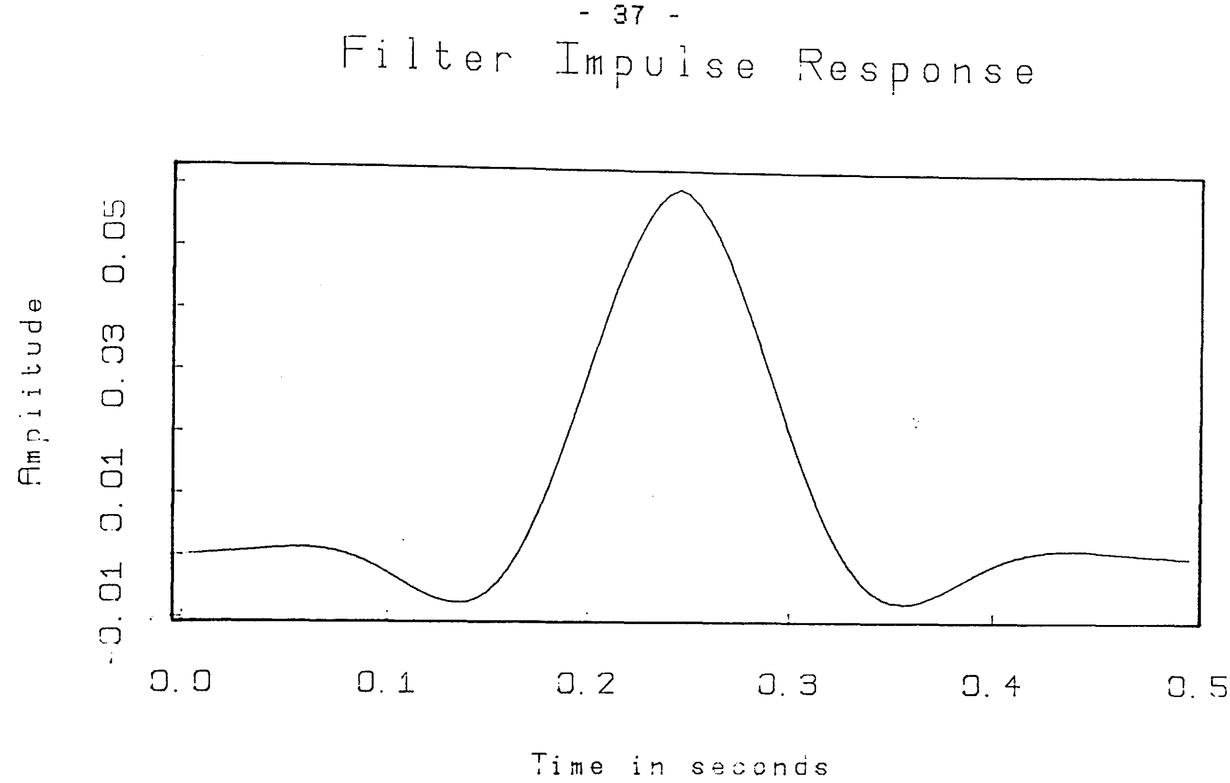

Zero-phase, lowpass filter 6.0Hz and length 0.50 s
with a Hamming window

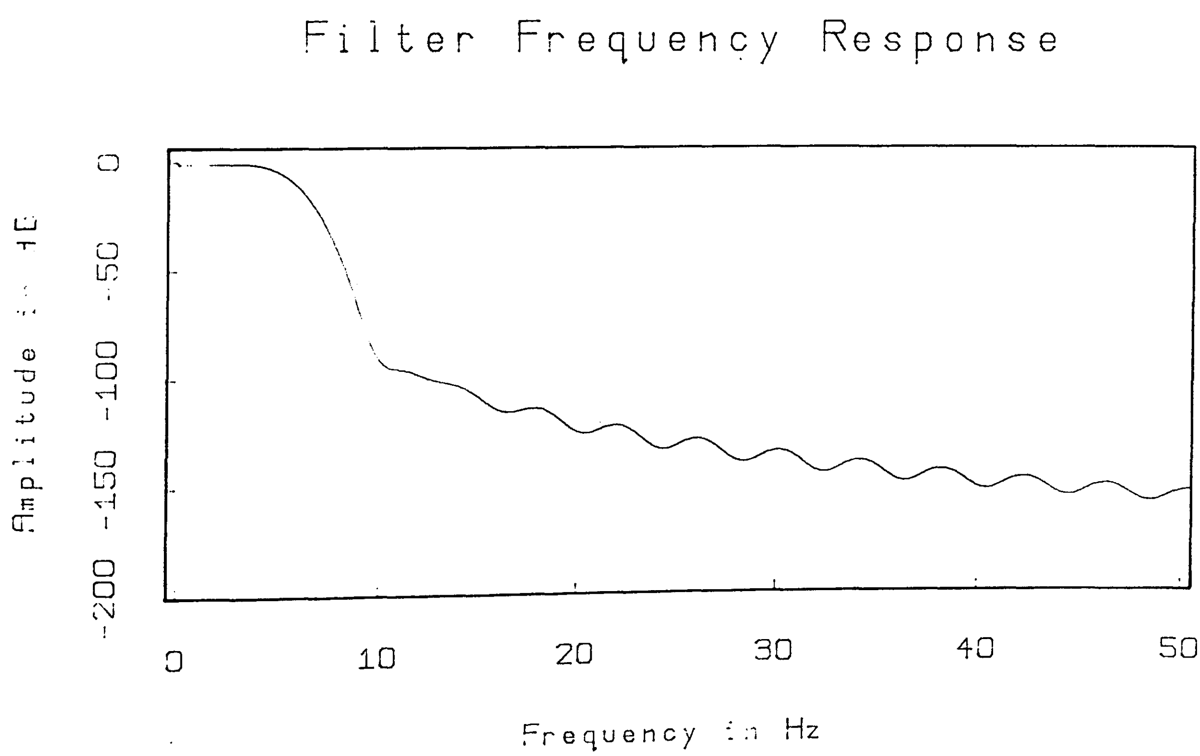

Zero-phase, lowpass filter 6.0Hz and length 0.50 s
with a Hamming window

Fig.3.16 Filter response with Hamming window.

Filter Impulse Response

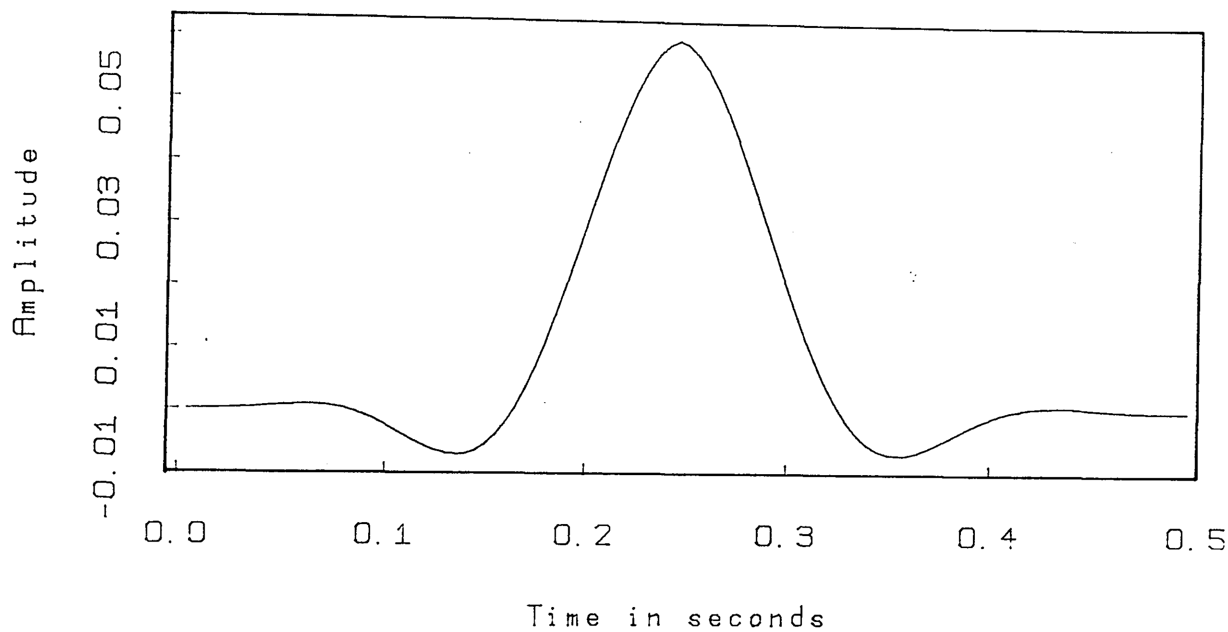

Zero-phase, lowpass filter 6.0Hz and length 0.50 s
with a generalised Hamming window

Filter Frequency Response

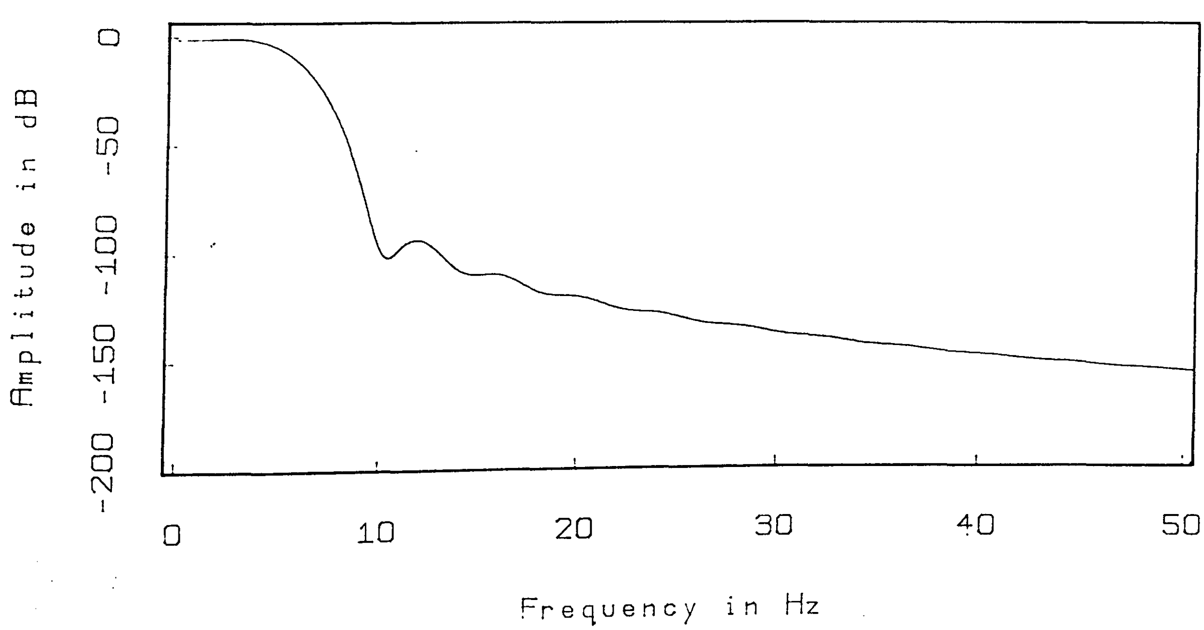

Zero-phase, lowpass filter 6.0Hz and length 0.50 s
with a generalised Hamming window

Fig.3.17 Filter response with generalised Hamming window.

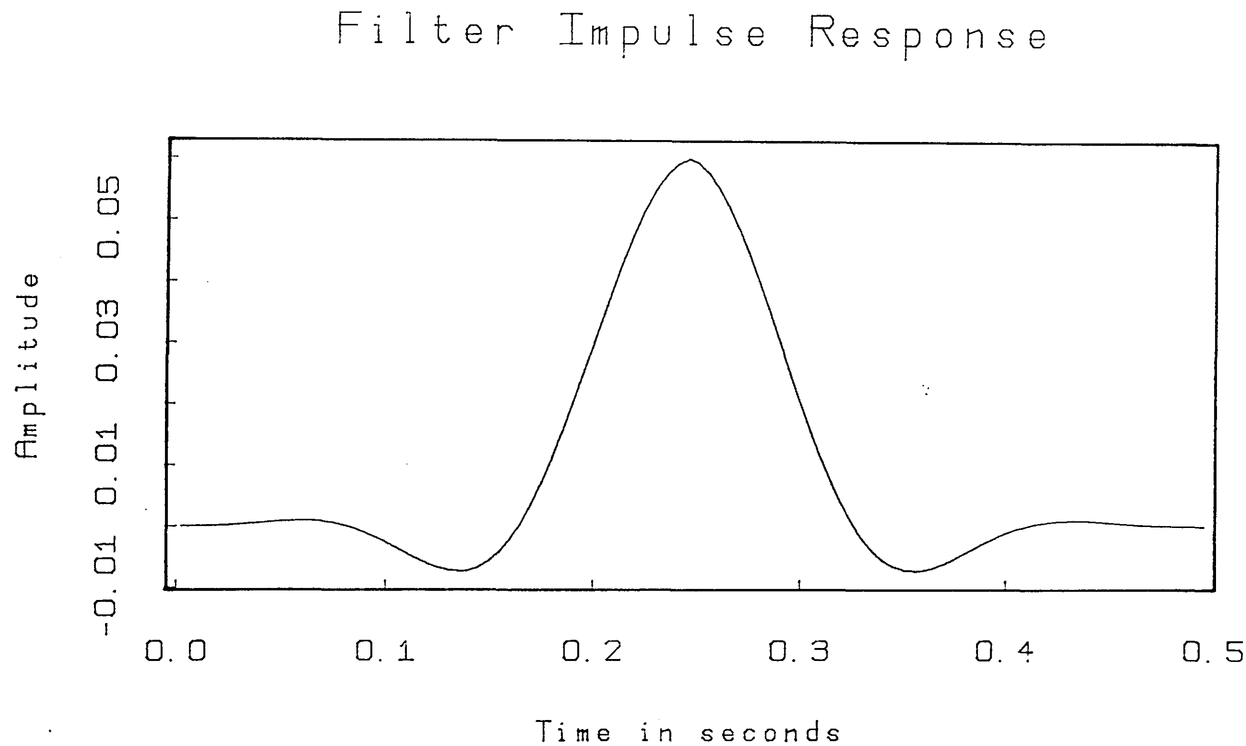

Zero-phase, lowpass filter 6.0Hz and length 0.50 s
with a Hanning window

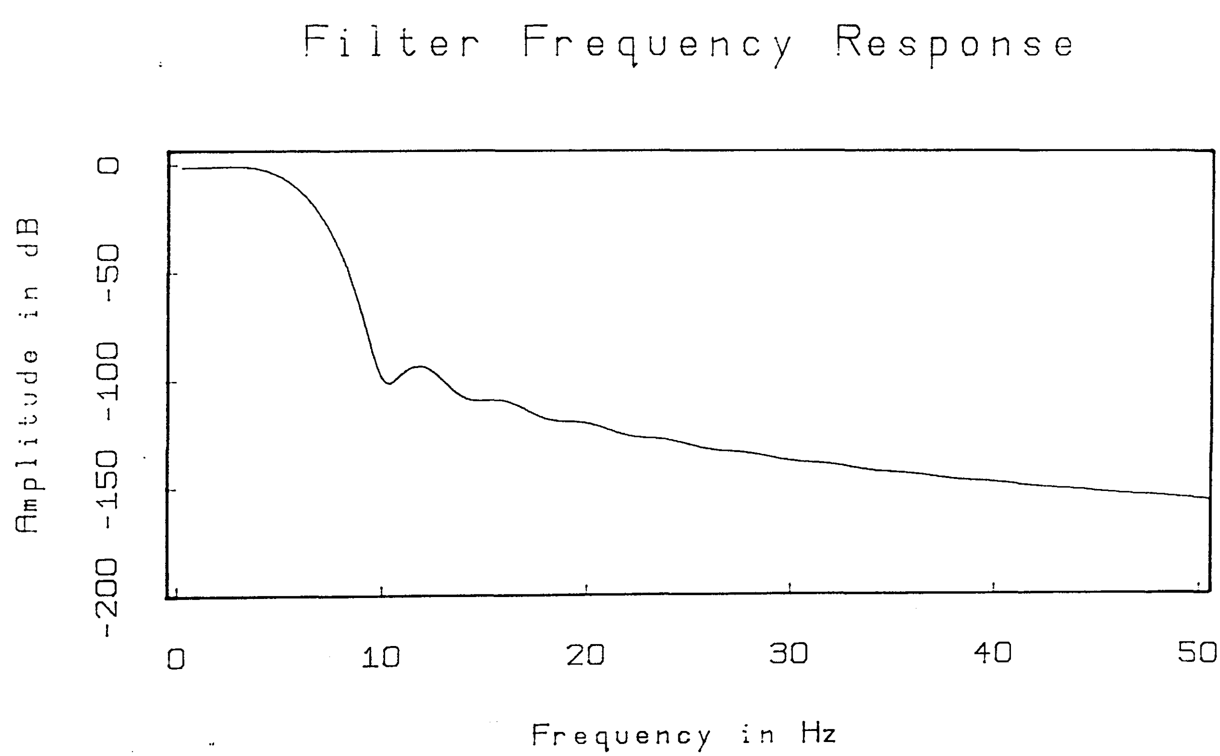

Zero-phase, lowpass filter 6.0Hz and length 0.50 s
with a Hanning window

Fig.3.18 Filter response with Hanning window.

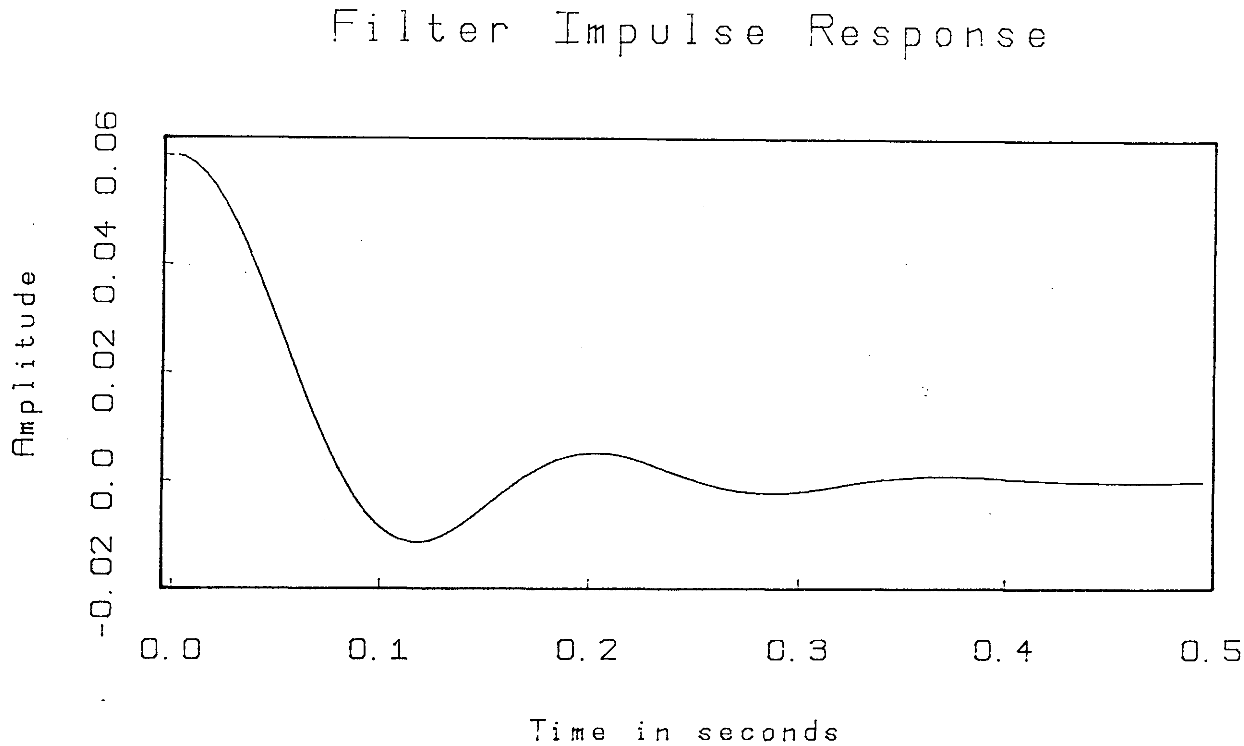

Minimum-phase, lowpass filter 6.0Hz and length 0.50 s
with a Hamming window

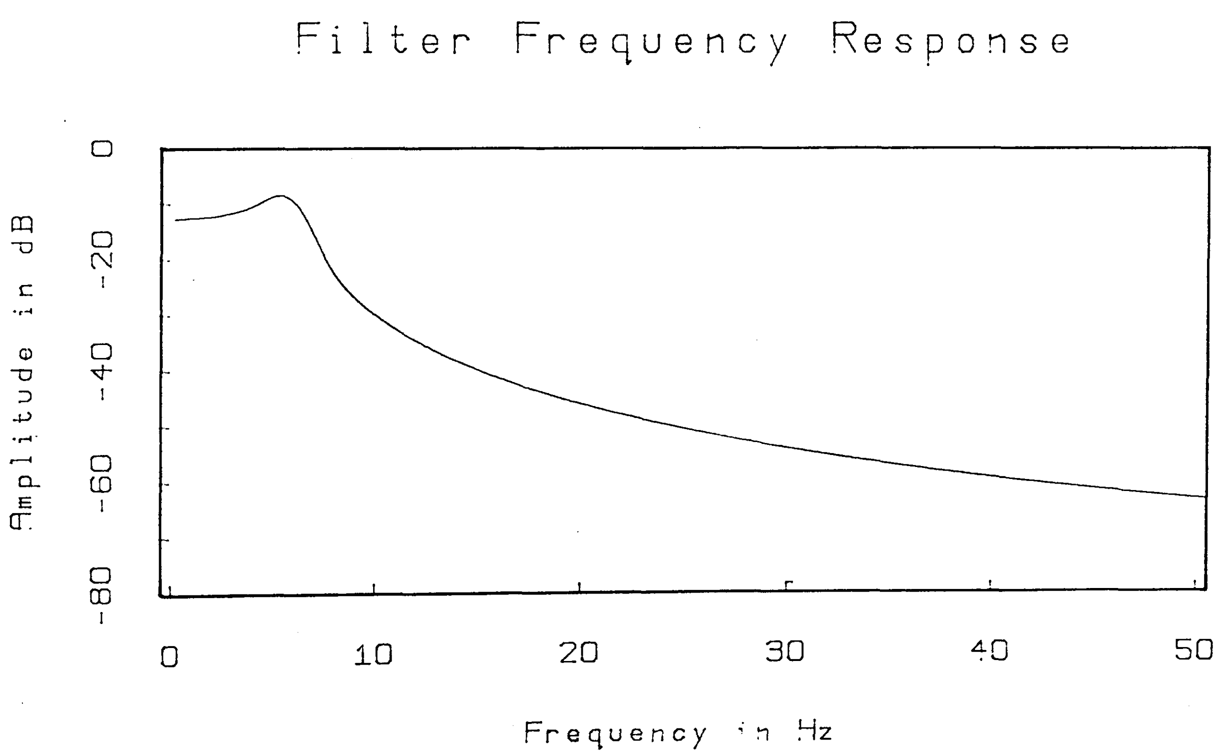

Minimum-phase, lowpass filter 6.0Hz and length 0.50 s
with a Hamming window

Fig.3.19 Filter response with Hamming window (minimum phase).

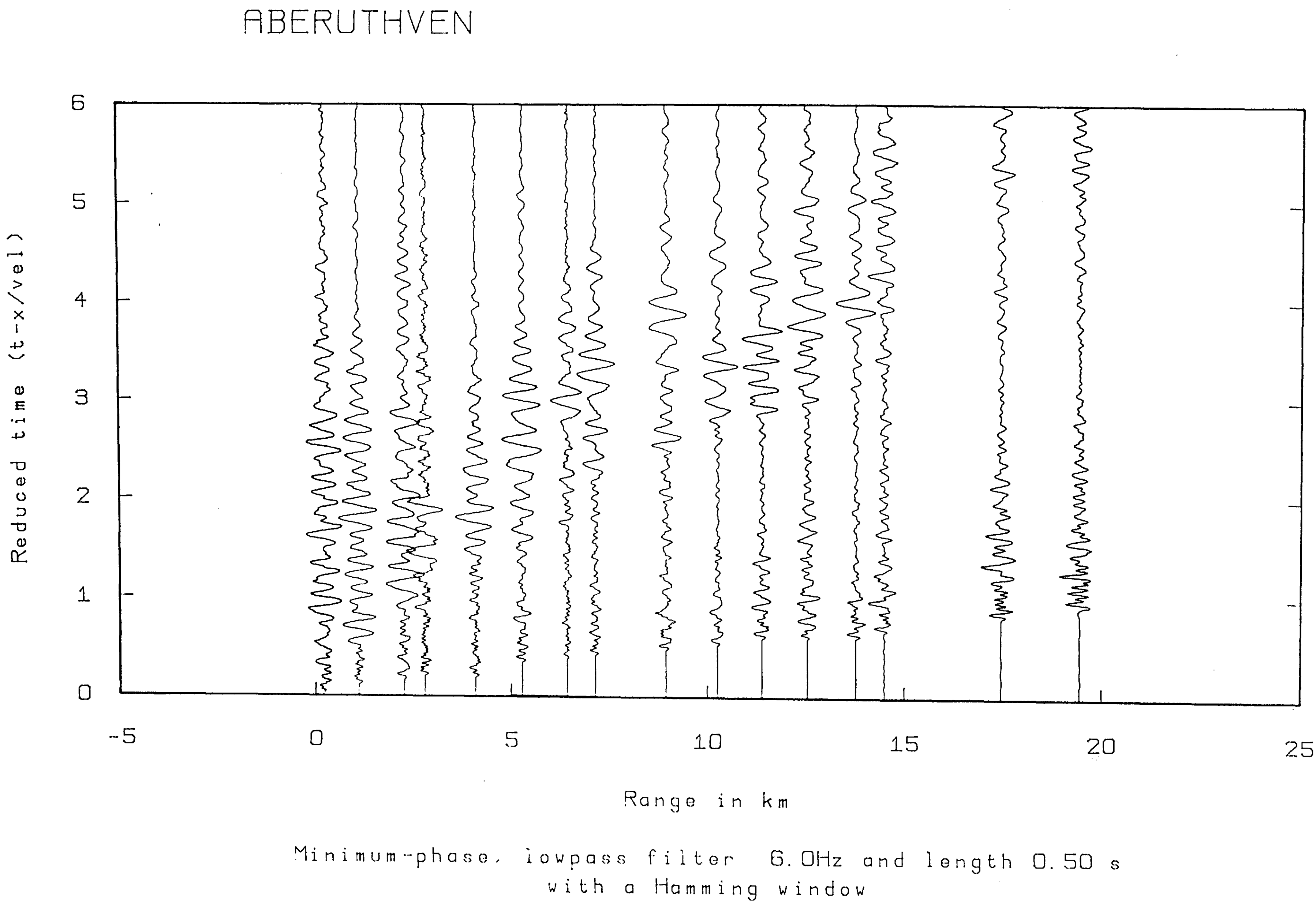

Fig.3.20 Effect of minimum phase filter with Hamming window.

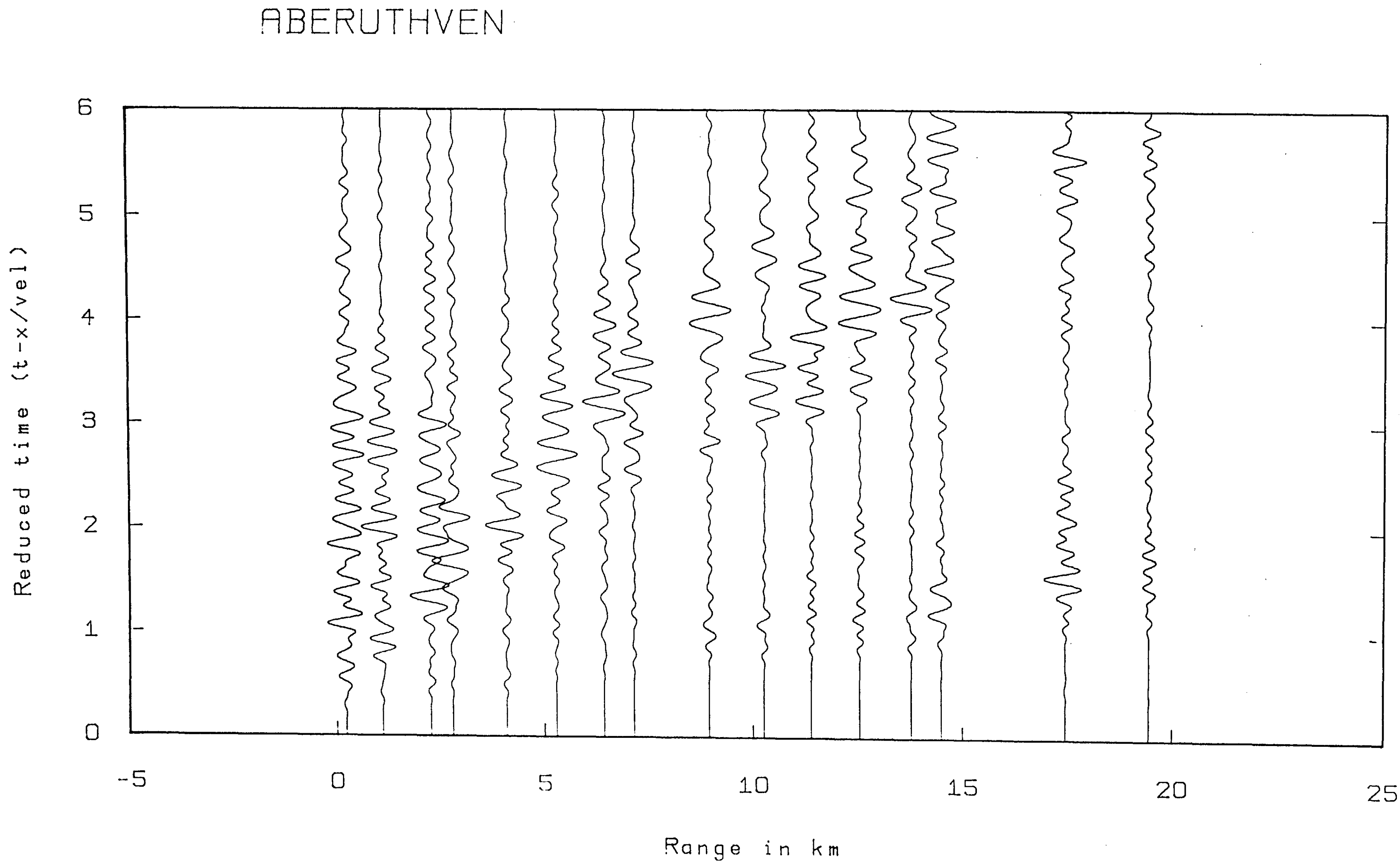

Zero-phase, lowpass filter 6.0Hz and length 0.50 s
with a Hamming window

Fig.3.21 Effect of zero phase filter with Hamming window.

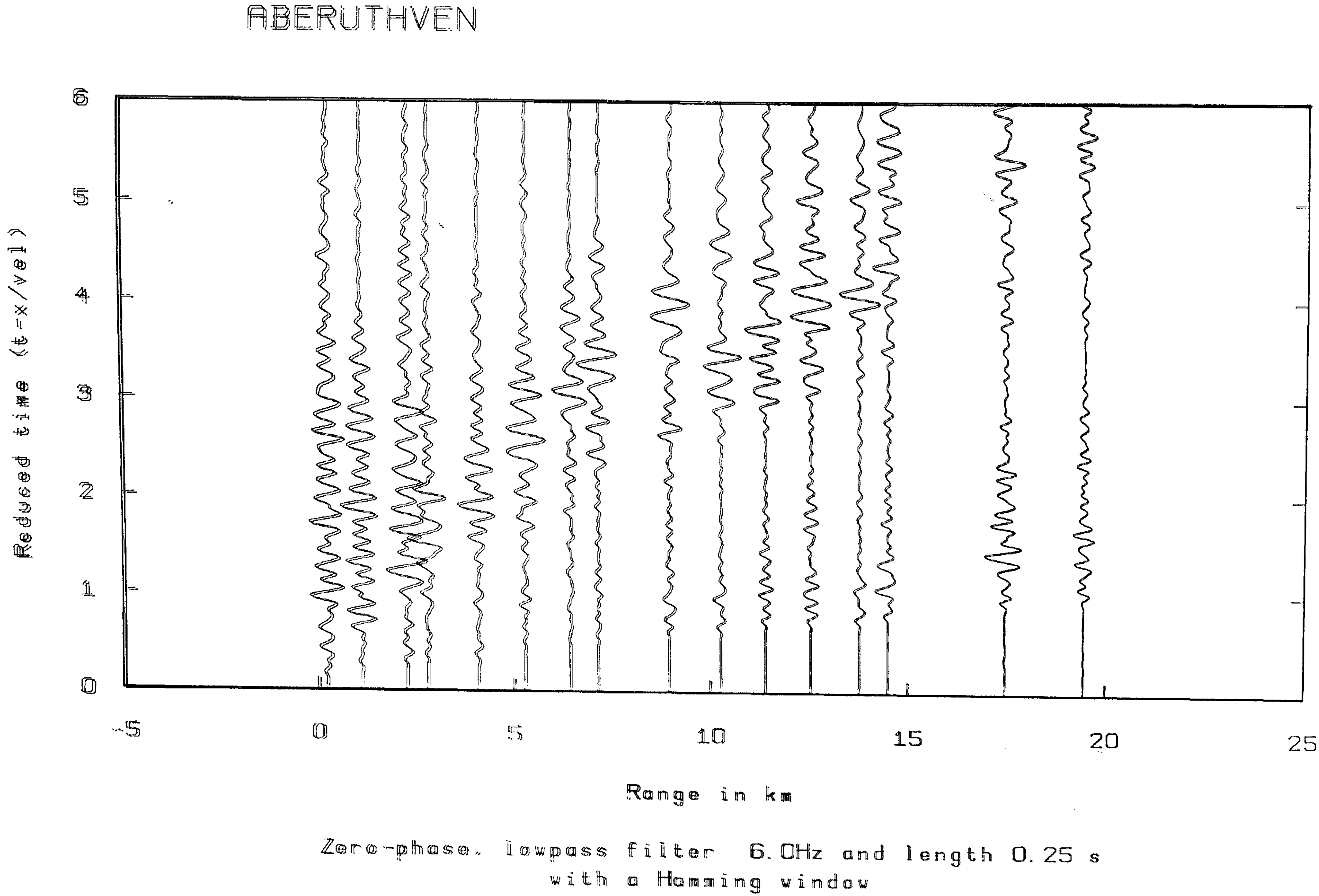

Fig.3.22 Effect of filter length (0.25 s).

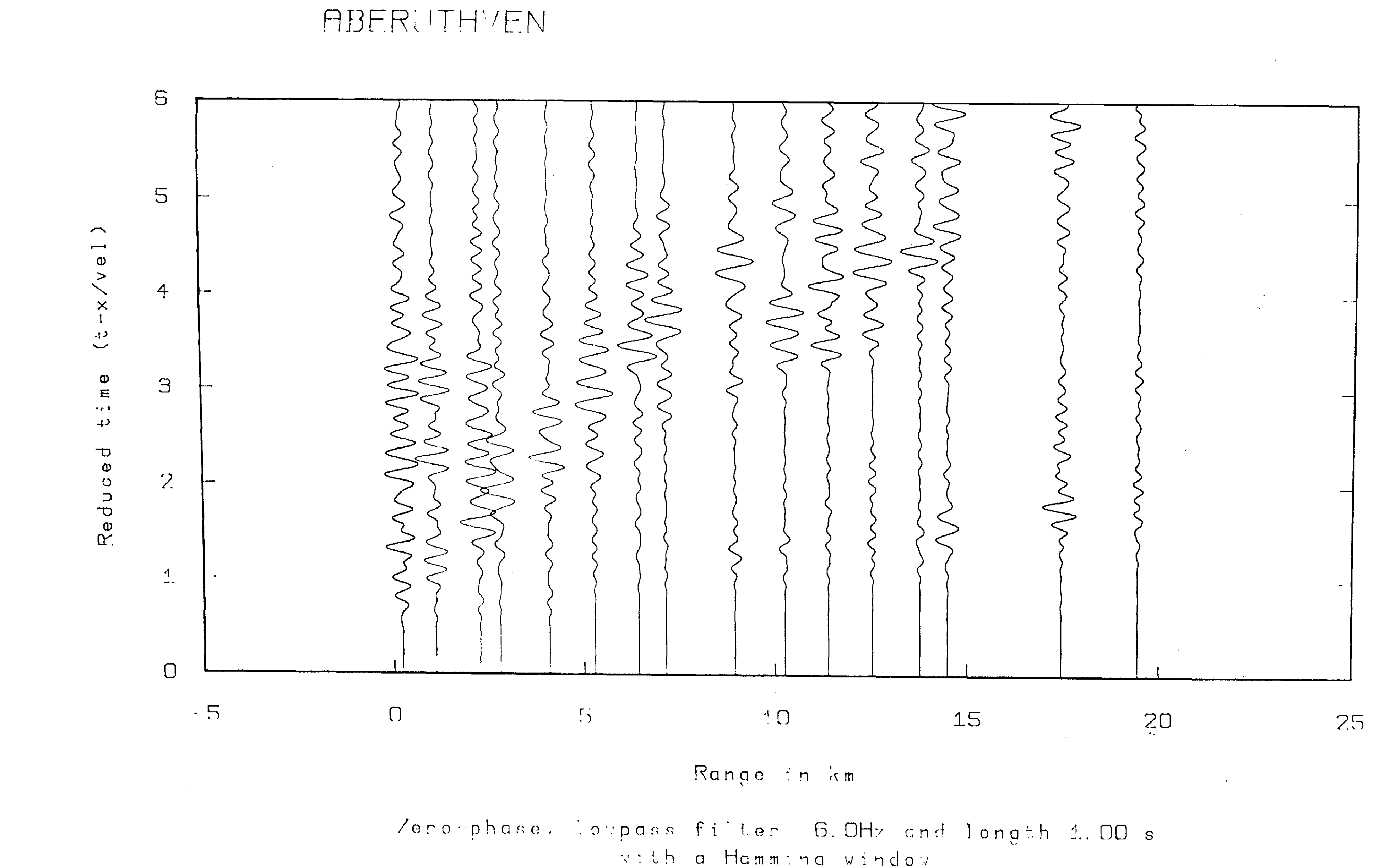

Fig.3.23 Effect of filter length (1.00 s).

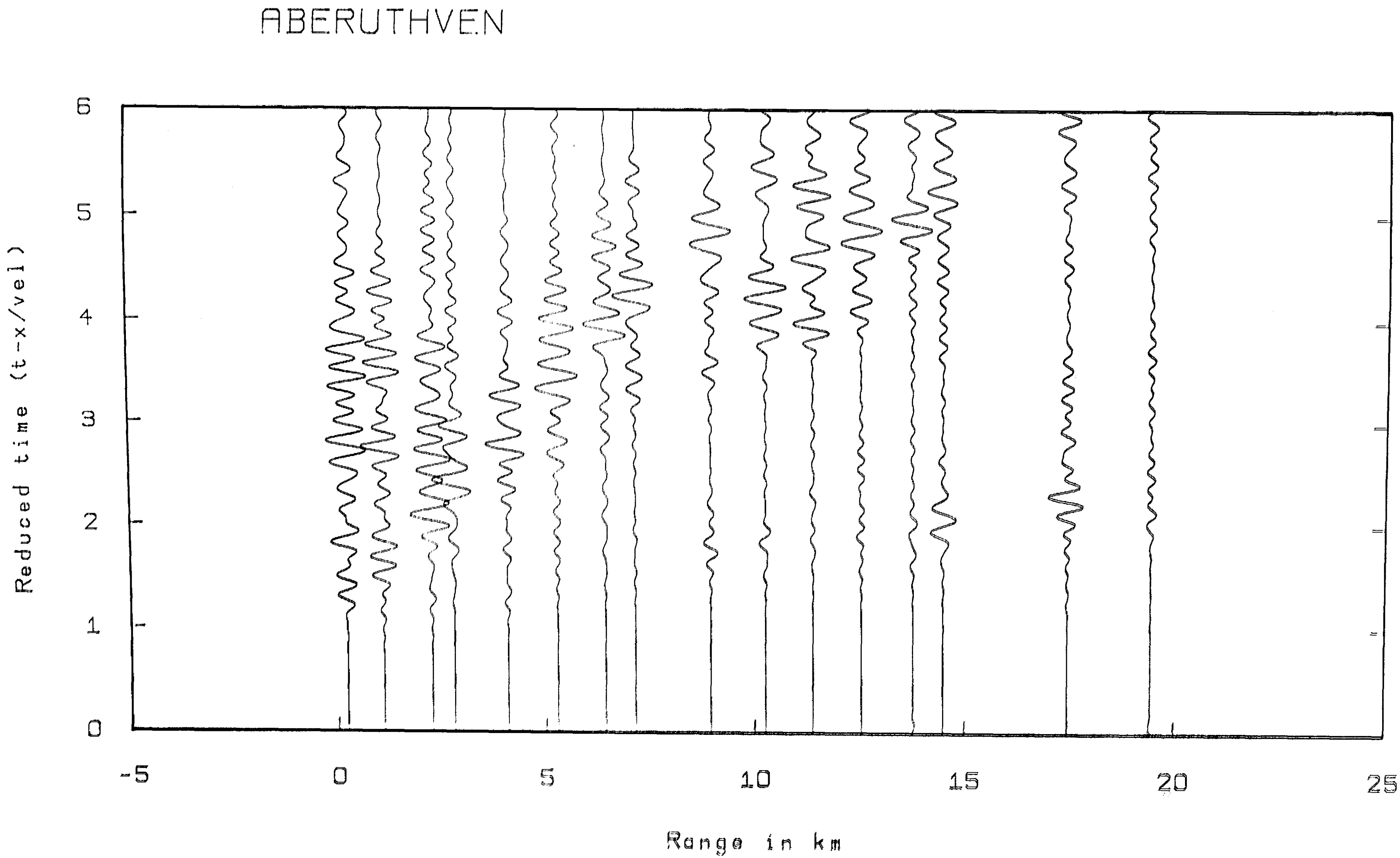

Zero-phase, lowpass filter 6.0Hz and length 2.00 s
with a Hamming window

Fig.3.24 Effect of filter length (2.00 s).

Figs.3.25 to 3.50:

Where possible the following data are presented; A), unfiltered data, B), unfiltered data with P- and S-wave picks C), data filtered to enhance P-wave arrivals D), data filtered to enhance S-wave arrivals (if any were identified). All traces are normalised with respect to the maximum amplitude within the trace. Also shown are; E), time-distance graphs of the P-wave arrivals and, where appropriate, F), time-distance graphs of the S-wave arrivals. All are plotted at a reduction velocity of 6.0 km/s, except (D) and (F) which are at 3.5 km/s. Both first and second arrival picks are shown.

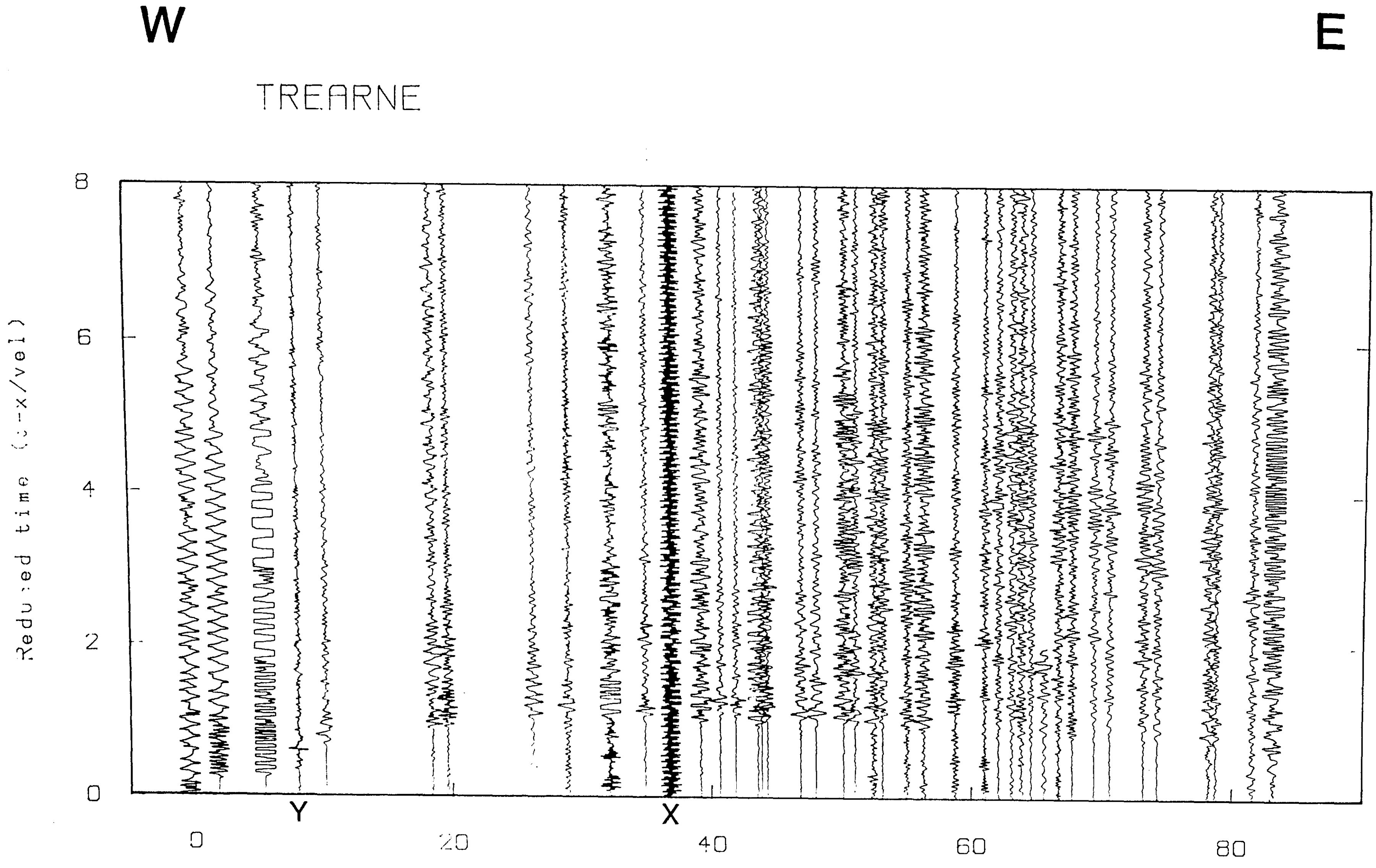

Fig.3.25a Unfiltered time section

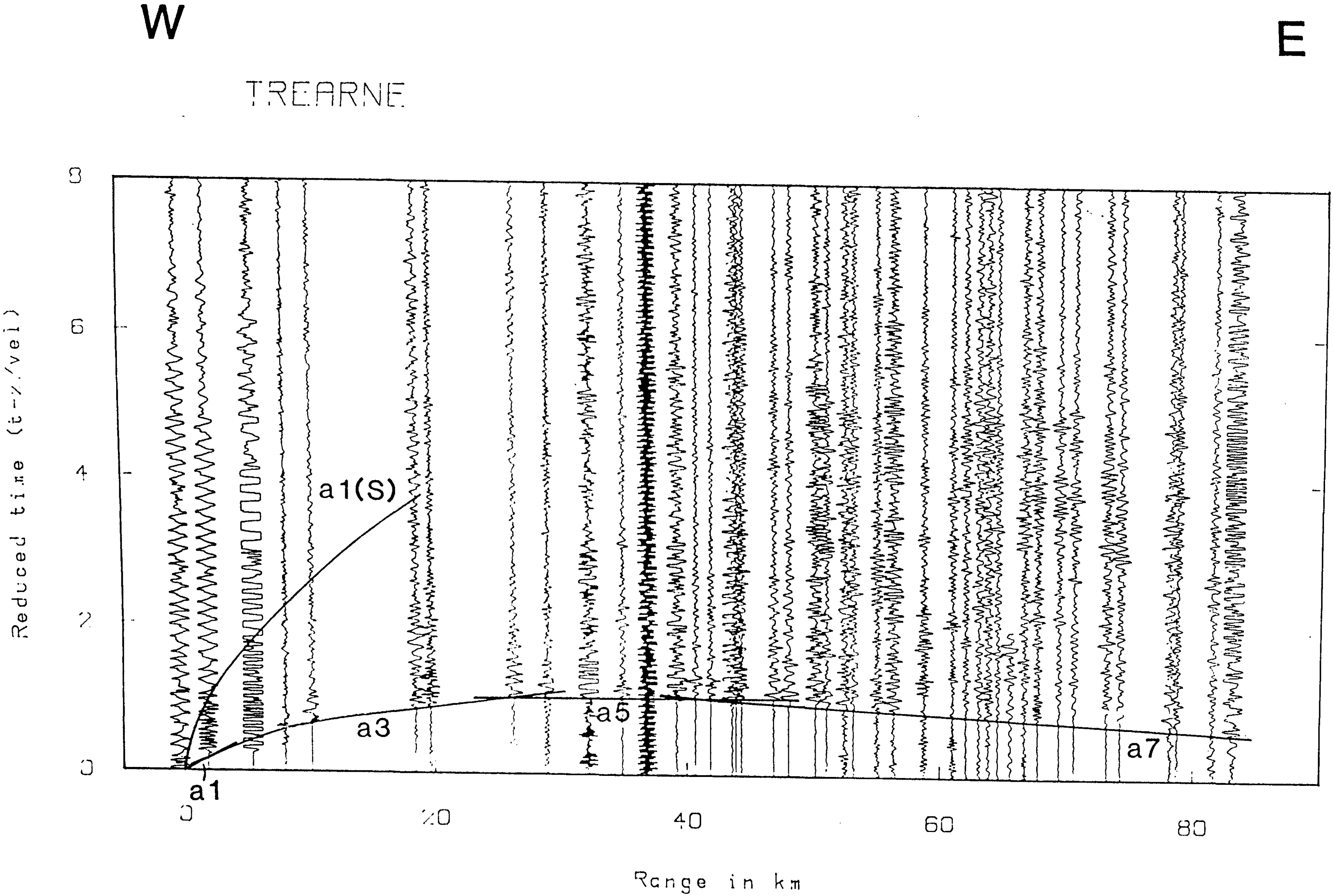

Fig.3.25b Unfiltered time section

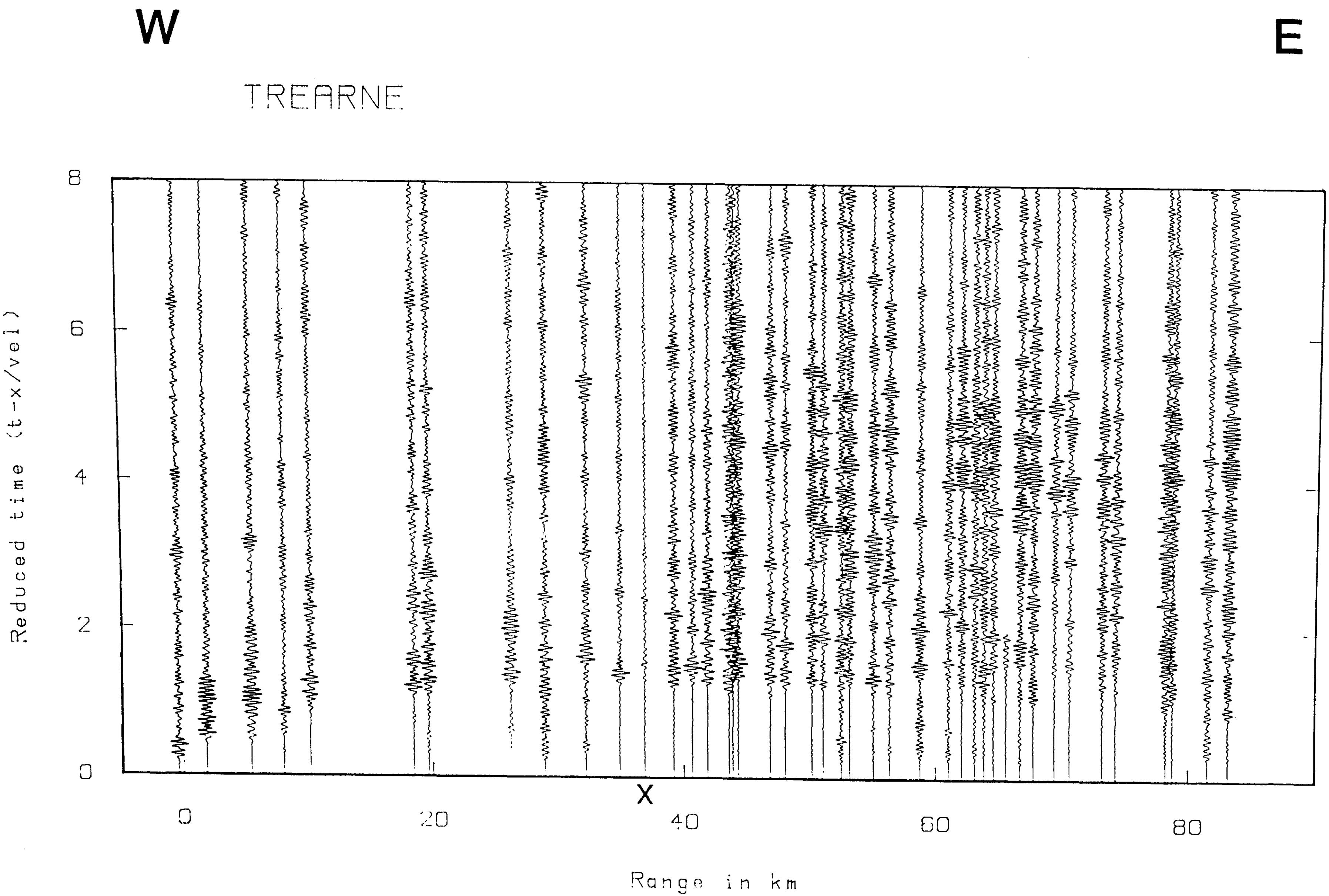

Fig.3.25c Zero-phase, bandpass filter 10.0- 20.0Hz and length 0.50 s with a Hamming window

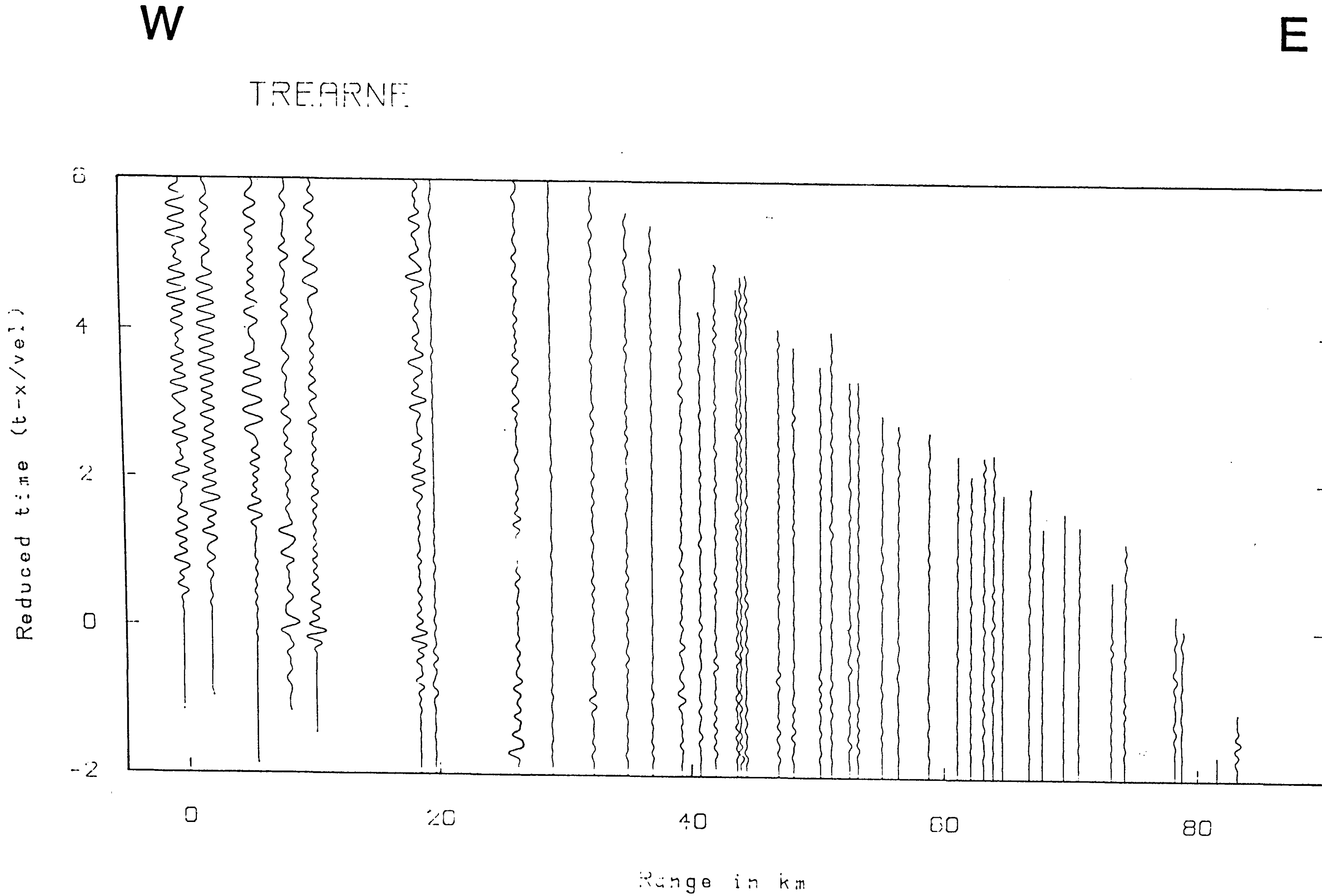

Fig.3.25d Zero-phase lowpass filter 6.0Hz and length 0.50 s with a Hamming window

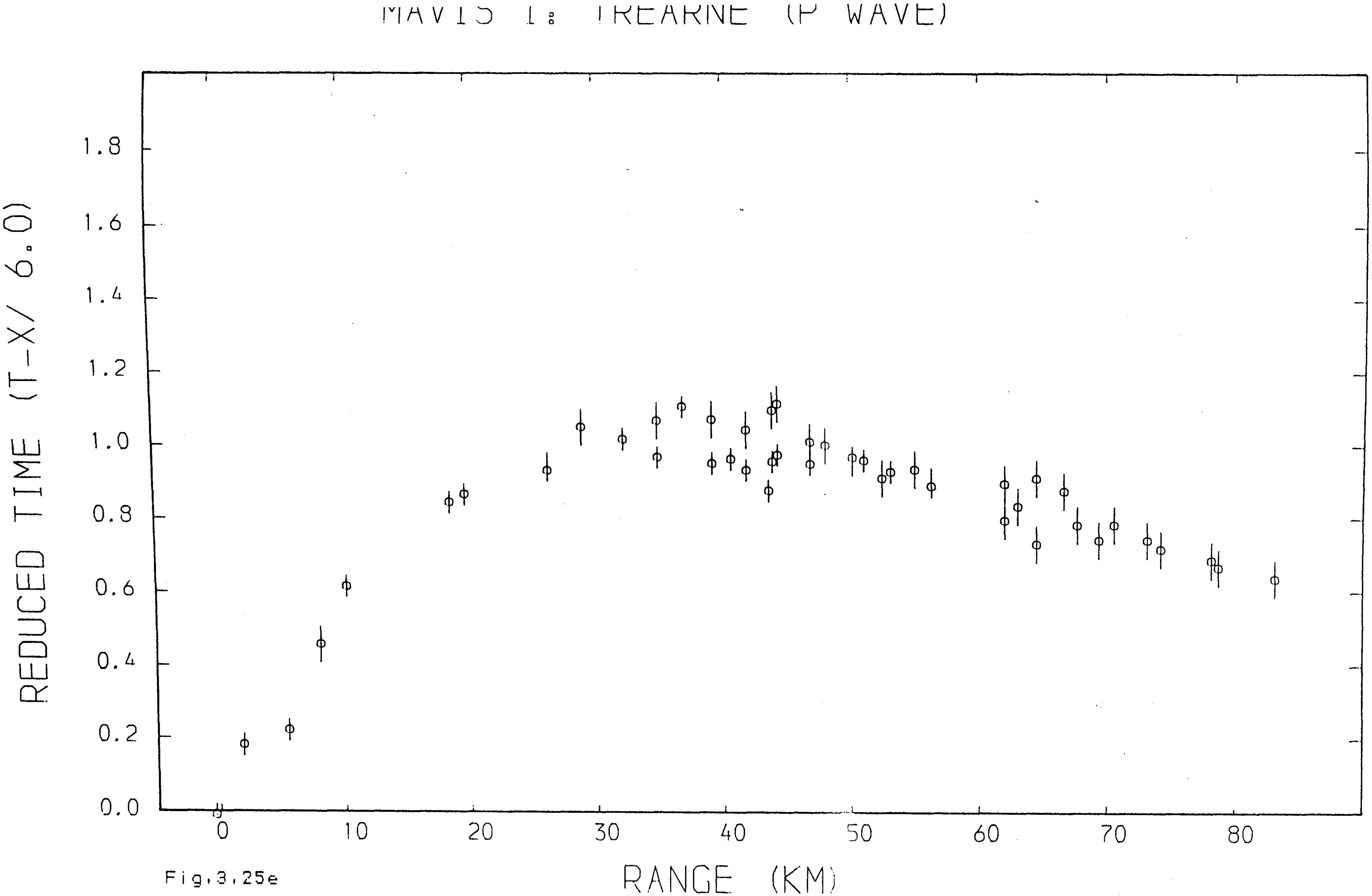
MAVIS 1: TREARNE (P WAVE)
REDUCED TIME (T-X/ 6.0)
1.8
1.6
1.4
1.2
1.0
0.8
0.6
0.4
0.2
0.0
0
10
20
30
40
50
60
70
80
RANGE (KM)

Fig.3.25e

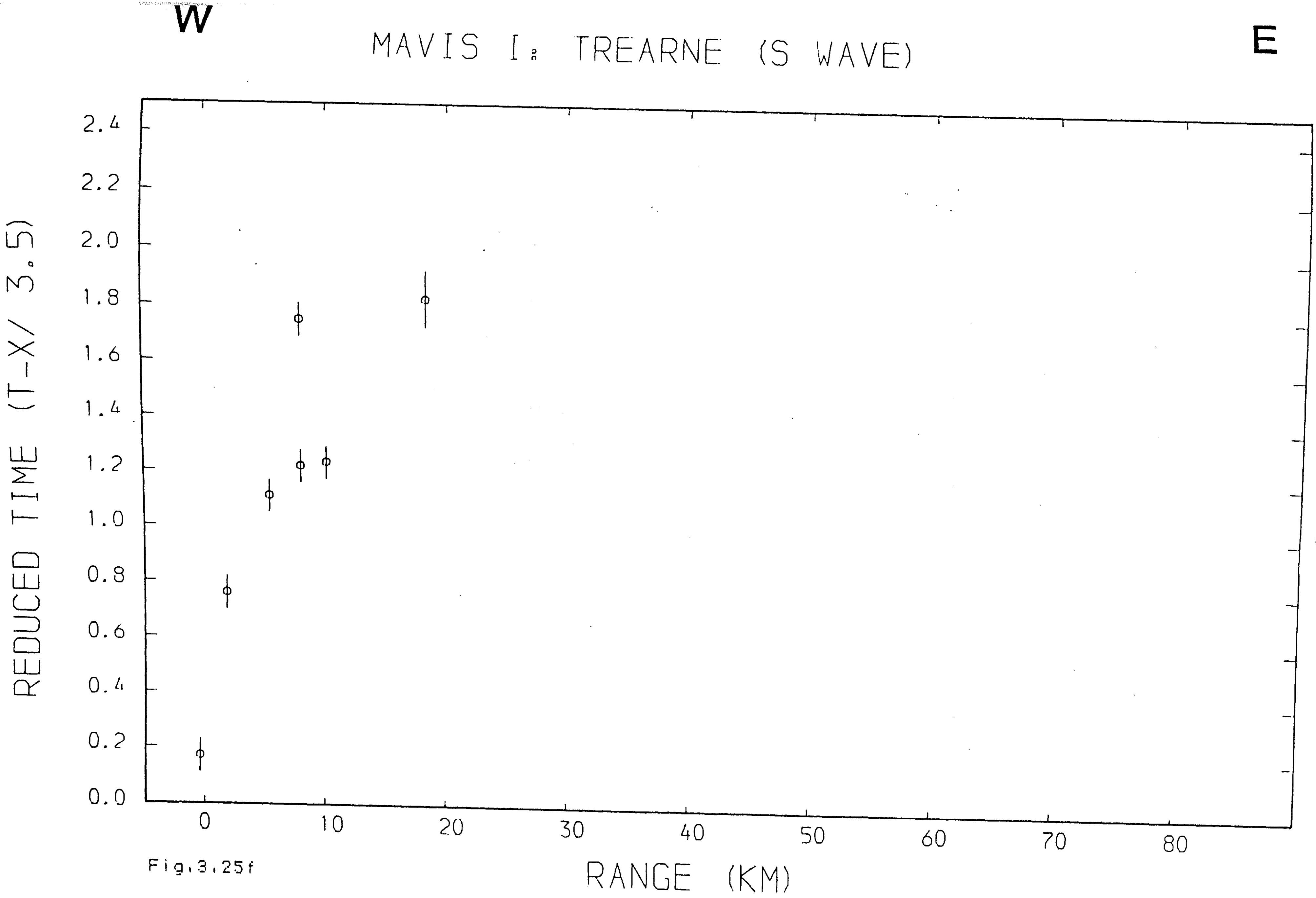
W
E
MAVIS I: TREARNE (S WAVE)
REDUCED TIME (T-X/ 3.5)
2.4
2.2
2.0
1.8
1.6
1.4
1.2
1.0
0.8
0.6
0.4
0.2
0.0
0
10
20
30
40
50
60
70
80
RANGE (KM)

Fig.3.25f

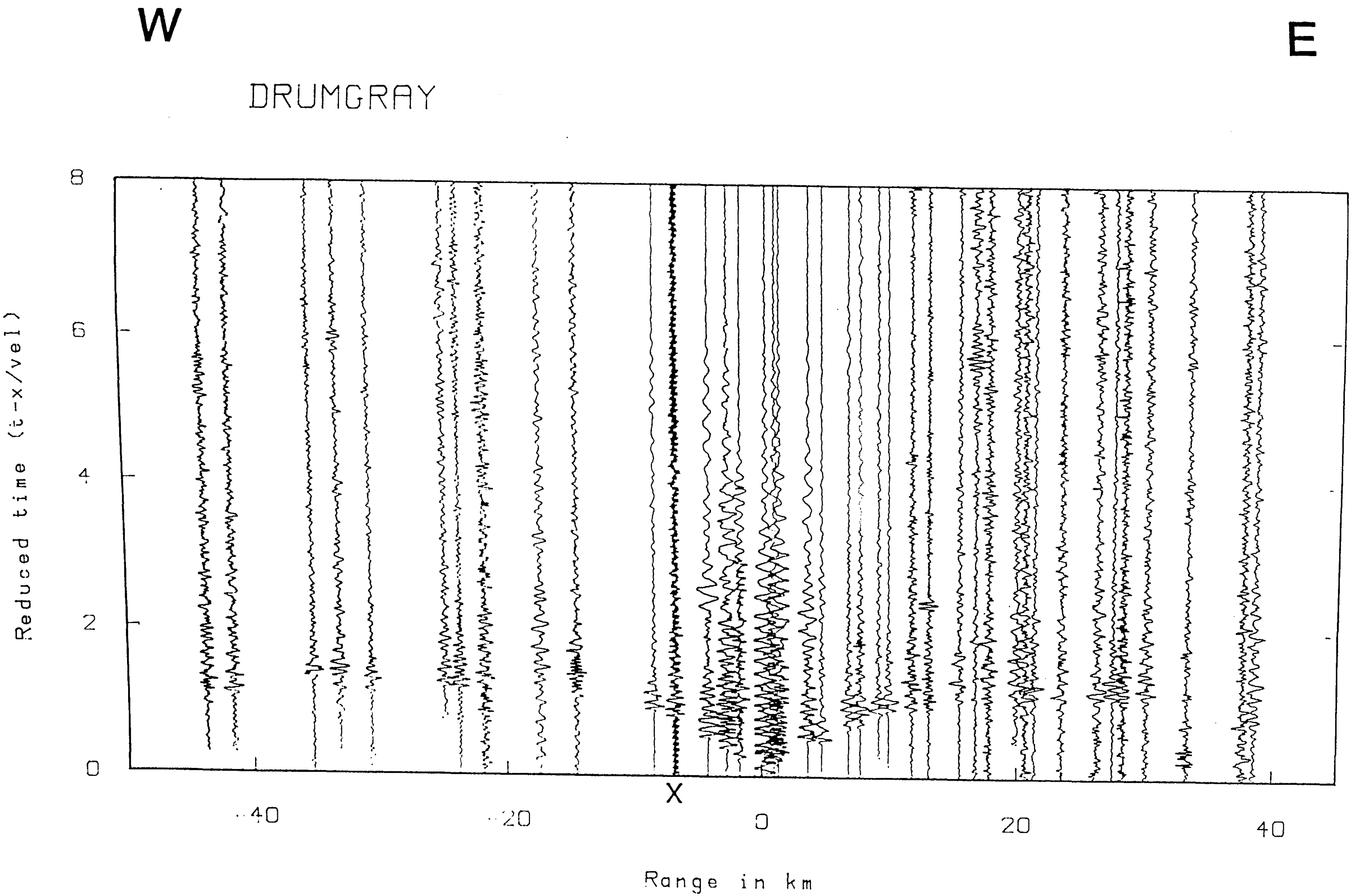

Fig.3.26a

Unfiltered time section

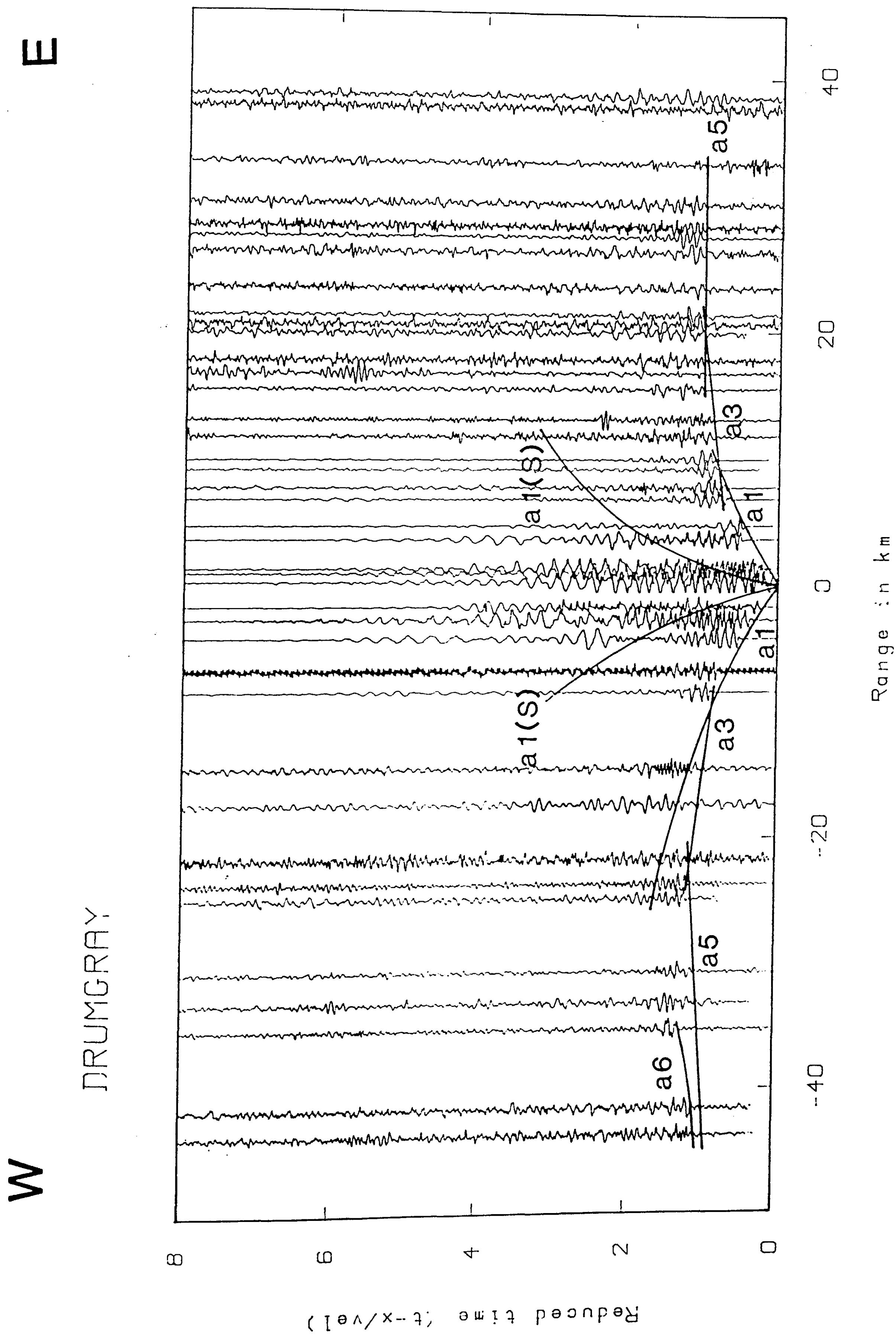

Unfiltered time section

Fig.3.26b

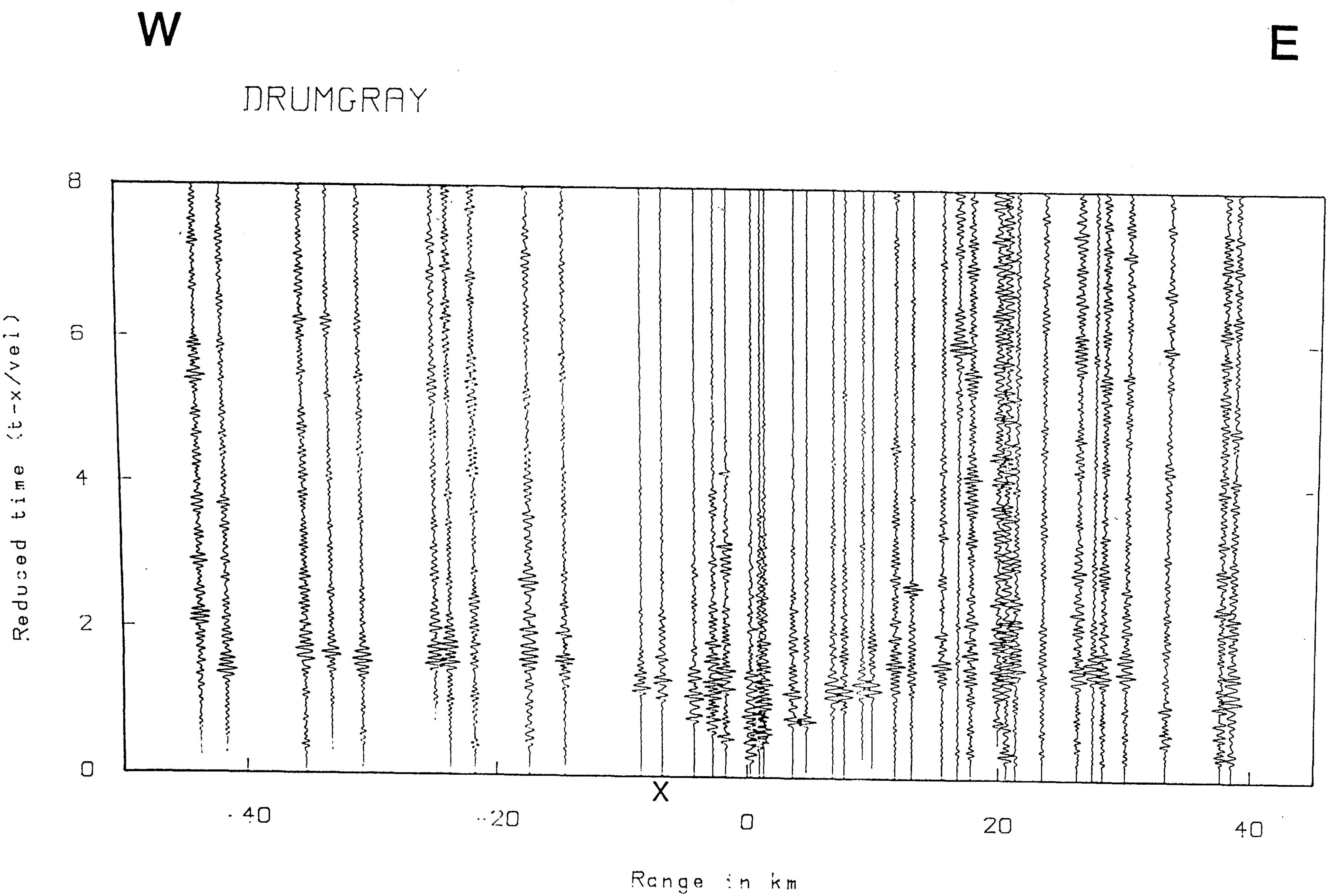

Fig.3.26c Zero-phase, bandpass filter 8.0- 18.0Hz and length 0.50 s with a Hamming window

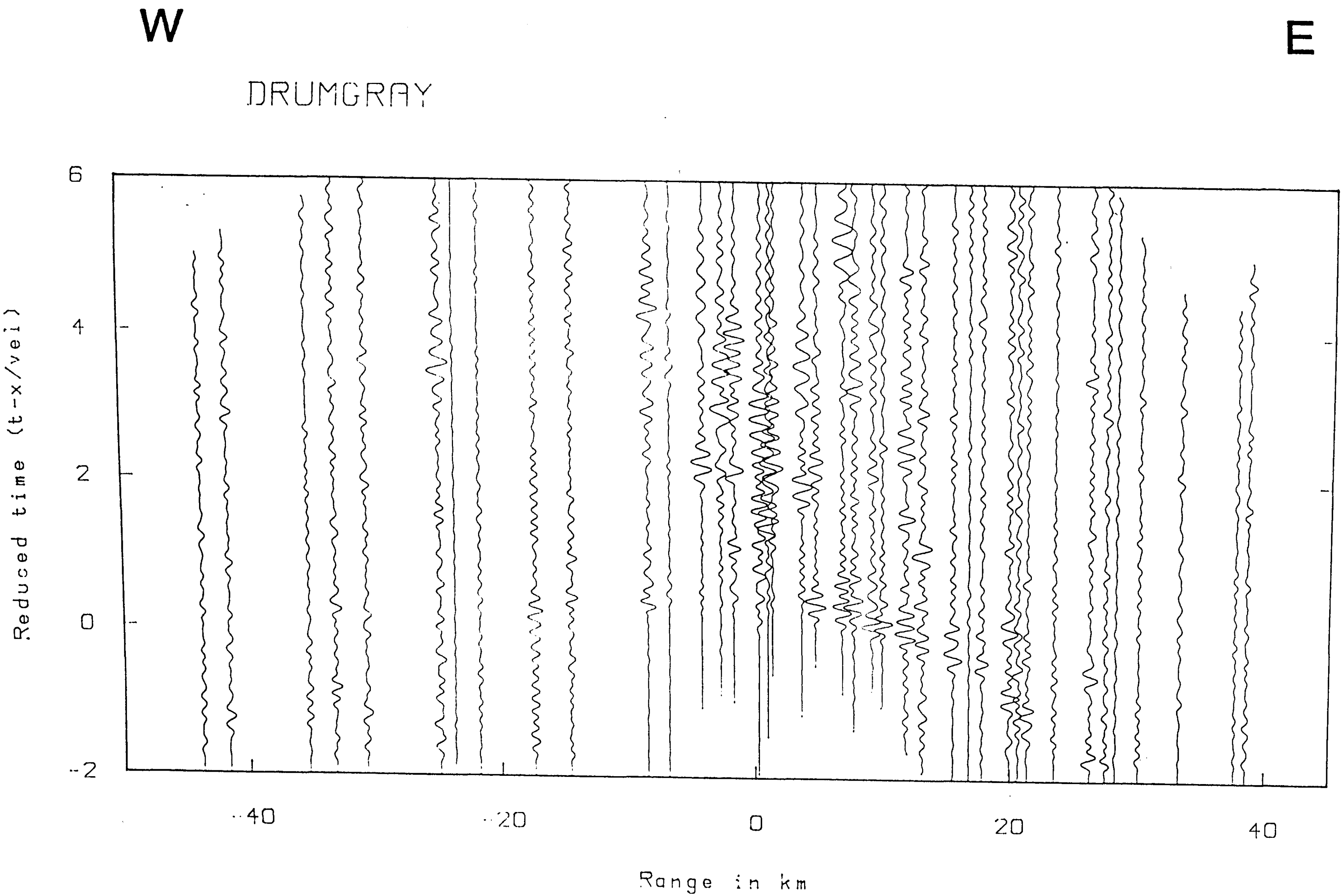

Fig.3.26d Zero-phase, lowpass filter 6.0Hz and length 0.50 s with a Hamming window

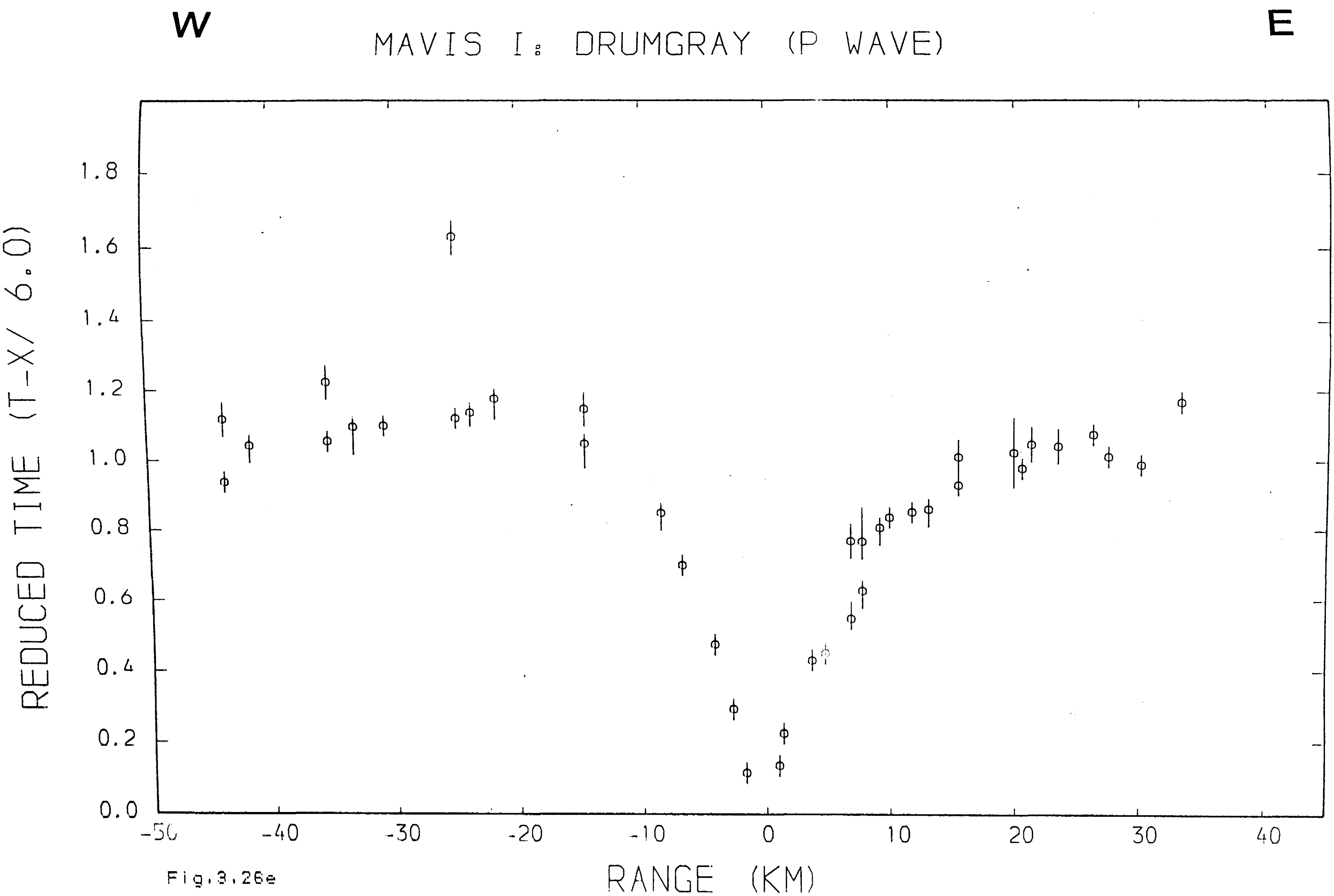
W
E
MAVIS I: DRUMGRAY (P WAVE)
REDUCED TIME (T-X/ 6.0)
1.8
1.6
1.4
1.2
1.0
0.8
0.6
0.4
0.2
0.0
-50
-40
-30
-20
-10
0
10
20
30
40
RANGE (KM)

Fig.3.26e

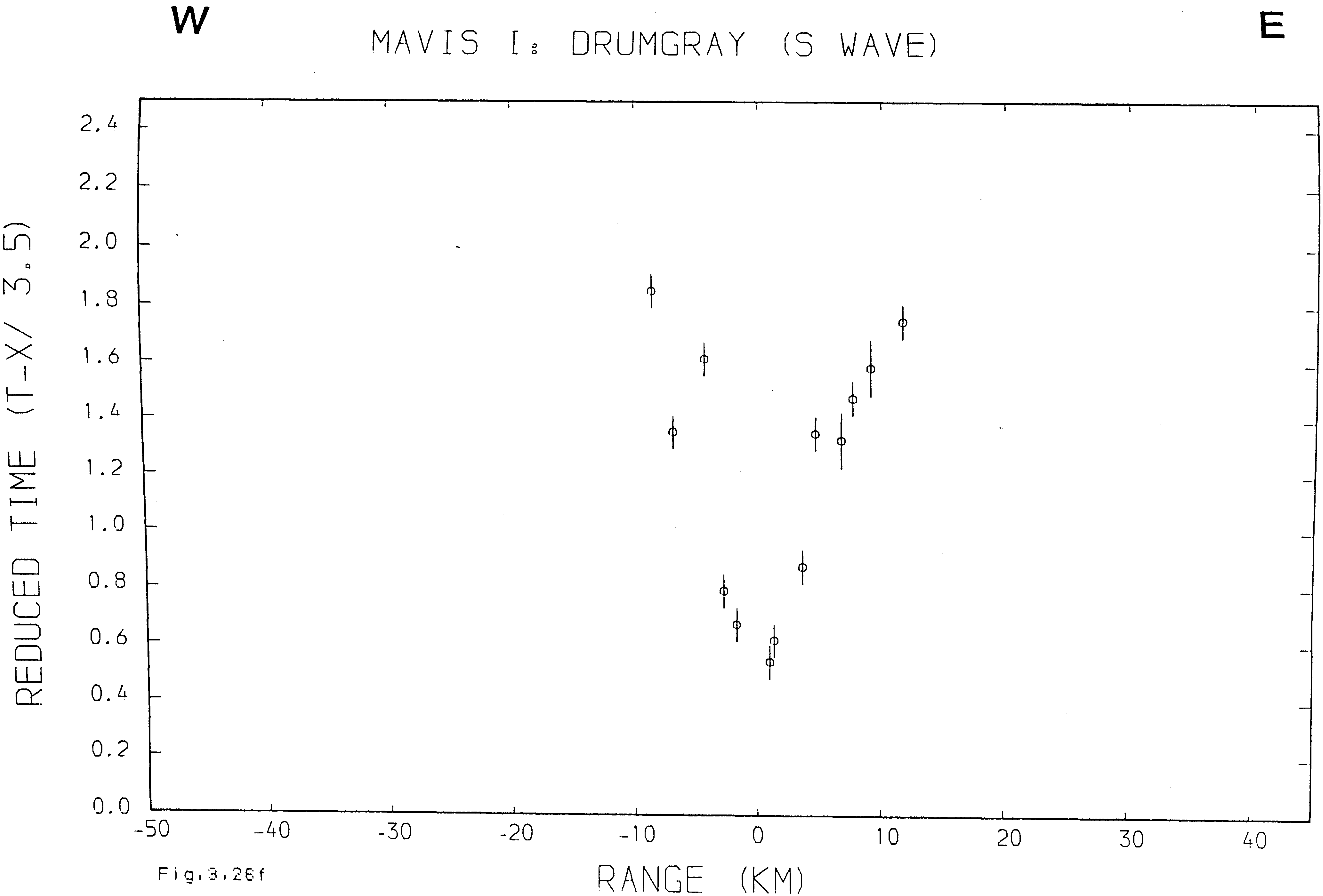
W
E
MAVIS I: DRUMGRAY (S WAVE)
REDUCED TIME (T-X/ 3.5)
2.4
2.2
2.0
1.8
1.6
1.4
1.2
1.0
0.8
0.6
0.4
0.2
0.0
-50
-40
-30
-20
-10
0
10
20
30
40
RANGE (KM)

Fig.3.26f

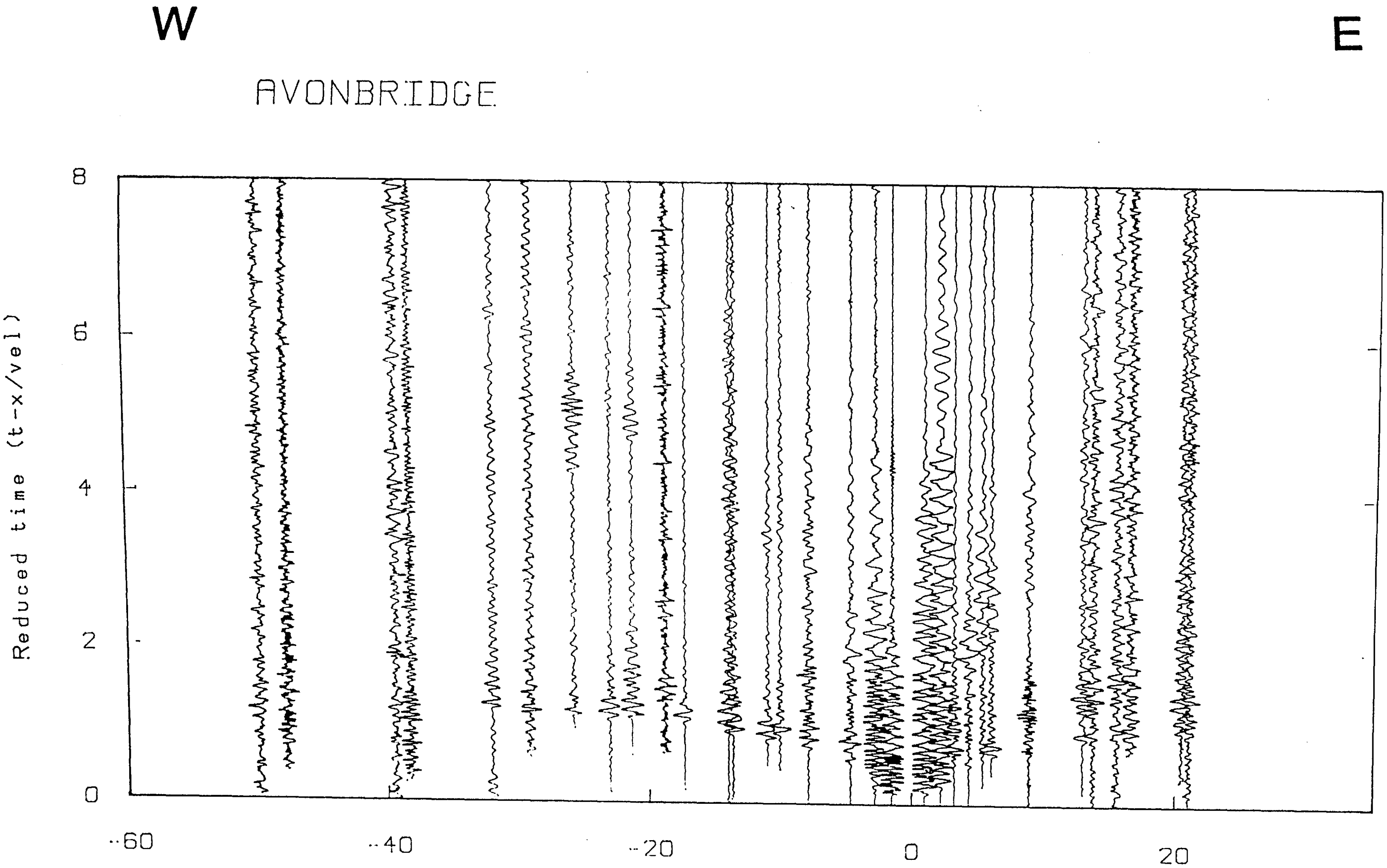

Fig.3.27a Unfiltered time section

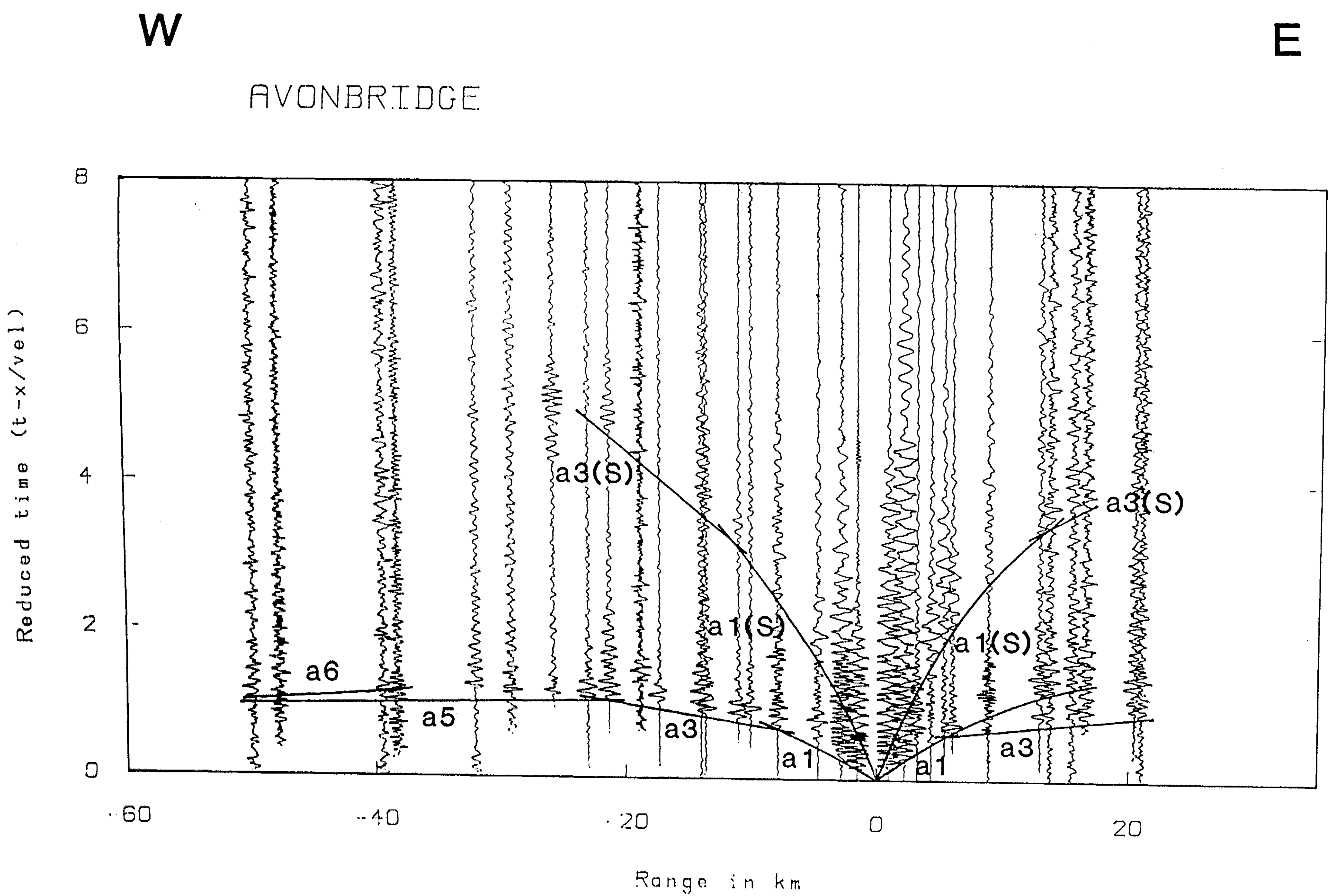

Fig.3.27b

Unfiltered time section

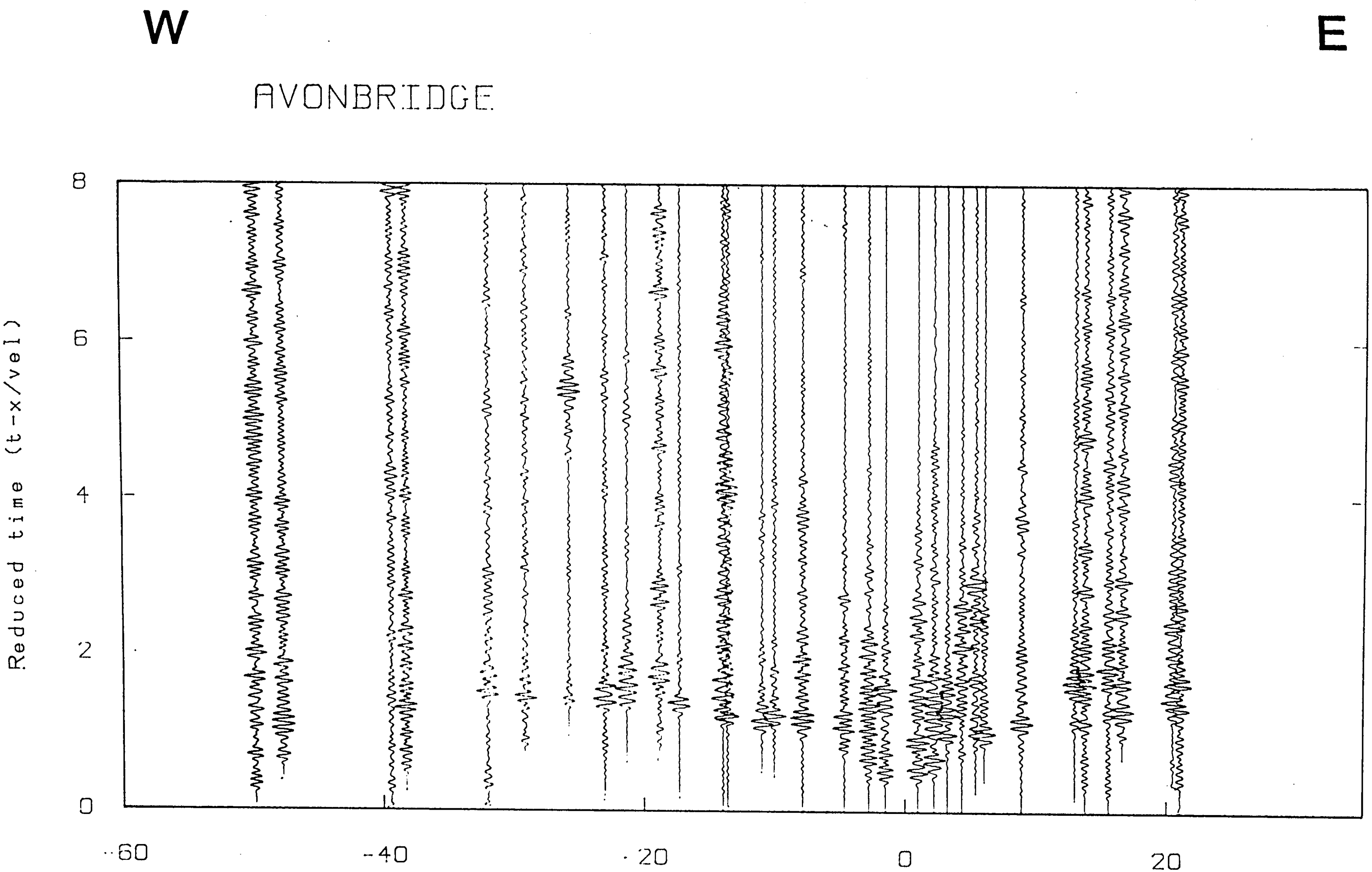

Zero-phase. bandpass filter 8.0- 15.0Hz and length 0.50 s with a Hamming window

Fig.3.27c

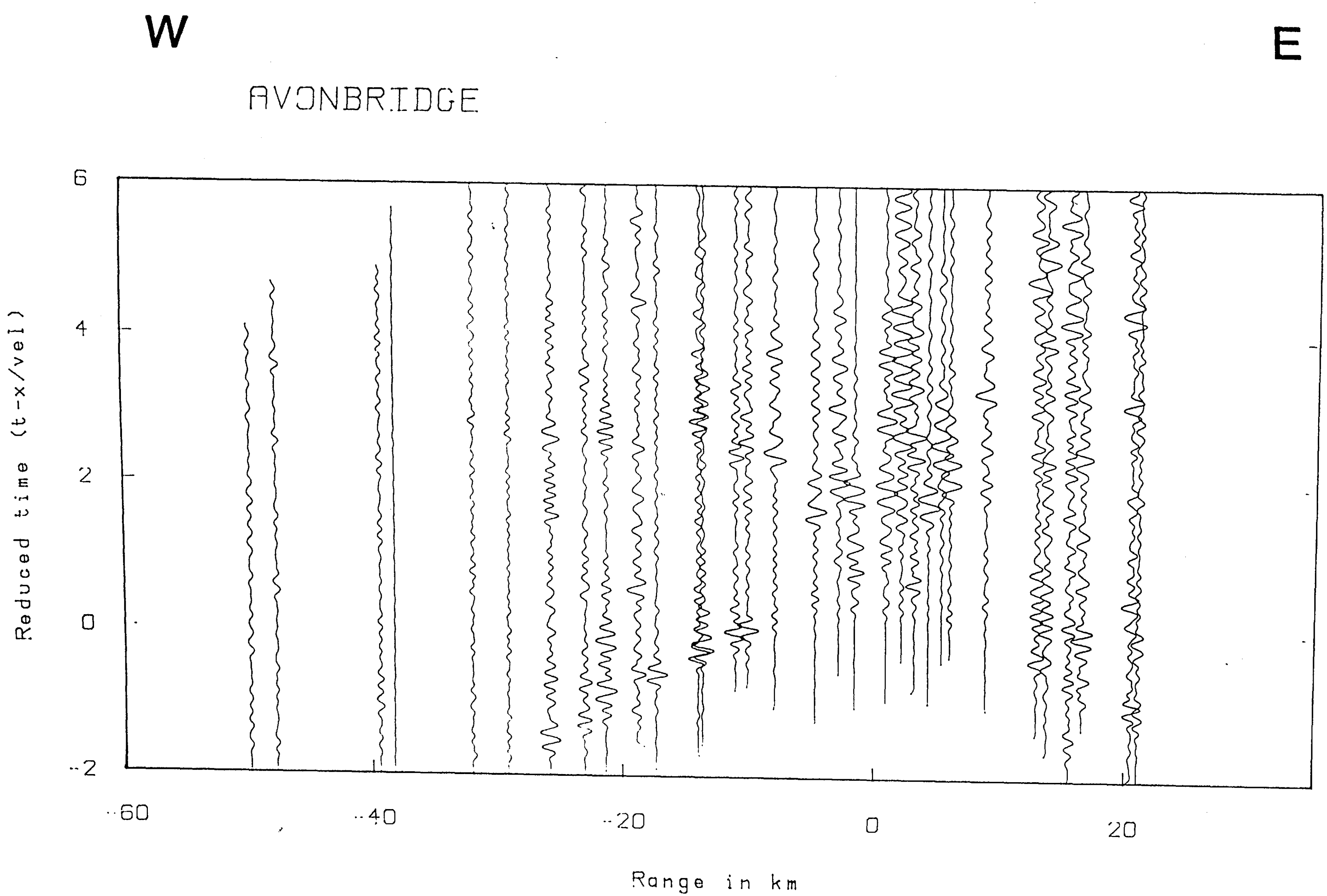

Fig.3.27d Zero-phase, lowpass filter 6.0Hz and length 0.50 s with a Hamming window

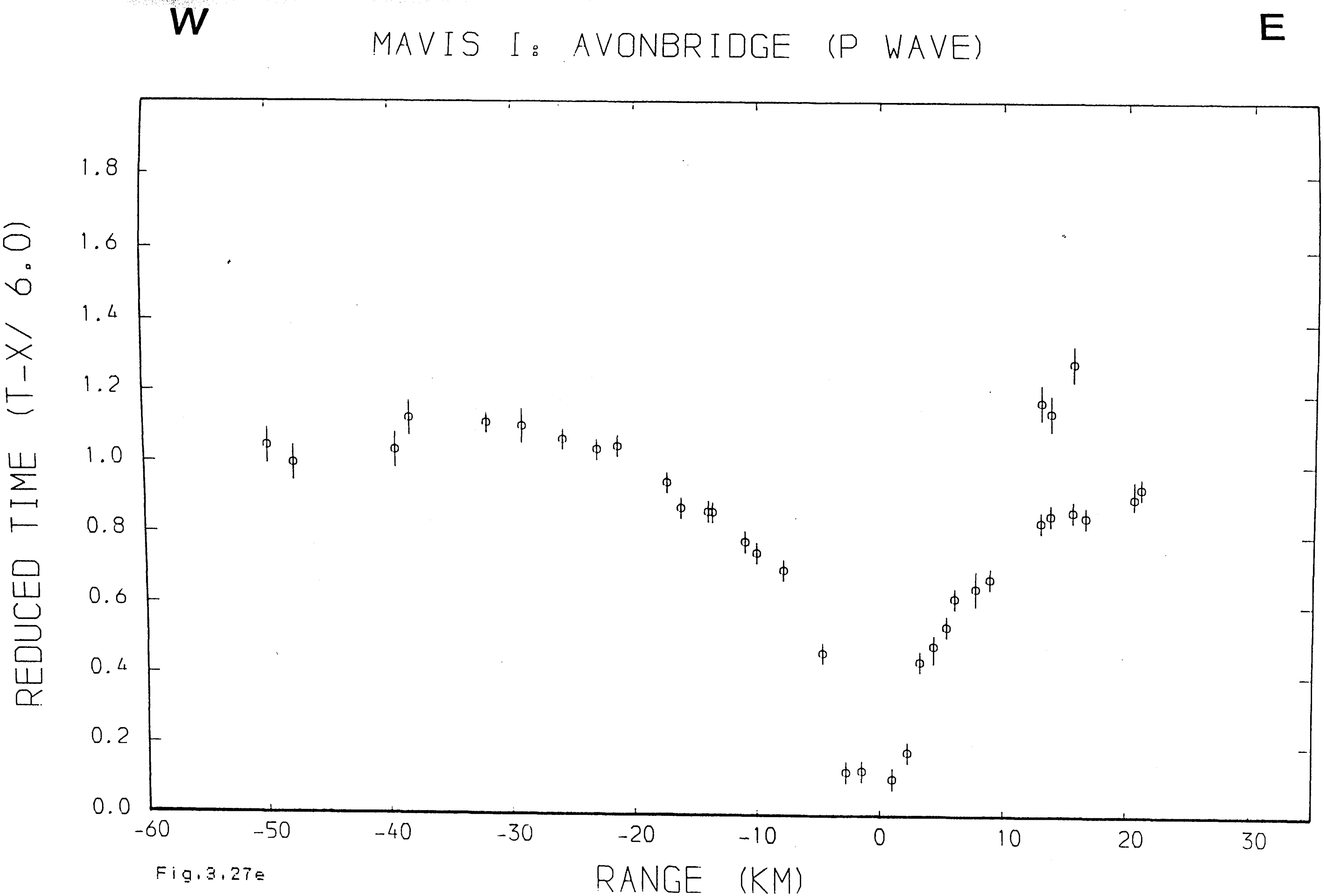
W
E
MAVIS I: AVONBRIDGE (P WAVE)
REDUCED TIME (T-X/ 6.0)
1.8
1.6
1.4
1.2
1.0
0.8
0.6
0.4
0.2
0.0
-60
-50
-40
-30
-20
-10
0
10
20
30
RANGE (KM)

Fig.3.27e

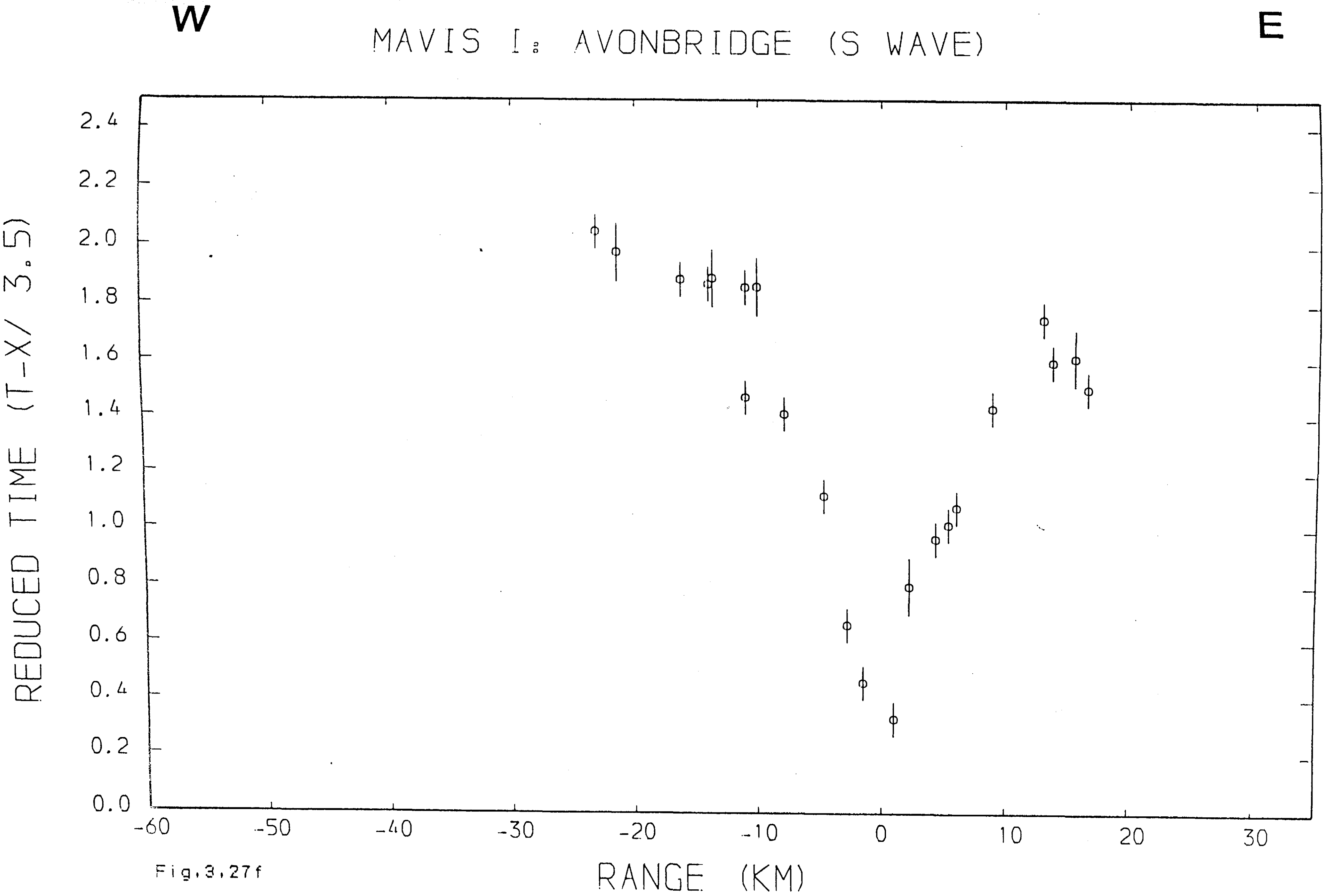
W
E
MAVIS I: AVONBRIDGE (S WAVE)
REDUCED TIME (T-X/ 3.5)
2.4
2.2
2.0
1.8
1.6
1.4
1.2
1.0
0.8
0.6
0.4
0.2
0.0
-60
-50
-40
-30
-20
-10
0
10
20
30
RANGE (KM)

Fig.3.27f

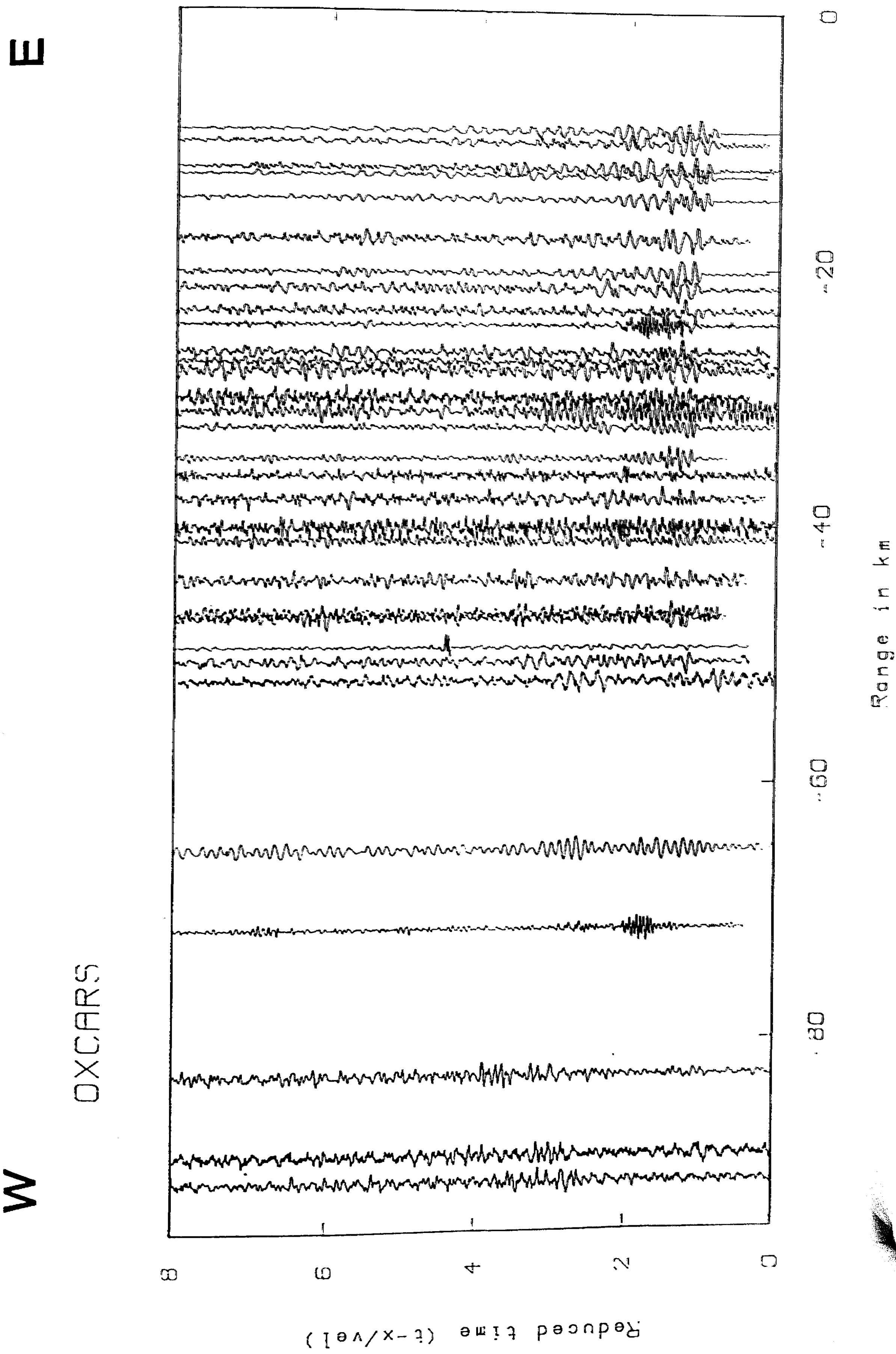

Fig.3.28a Unfiltered time section

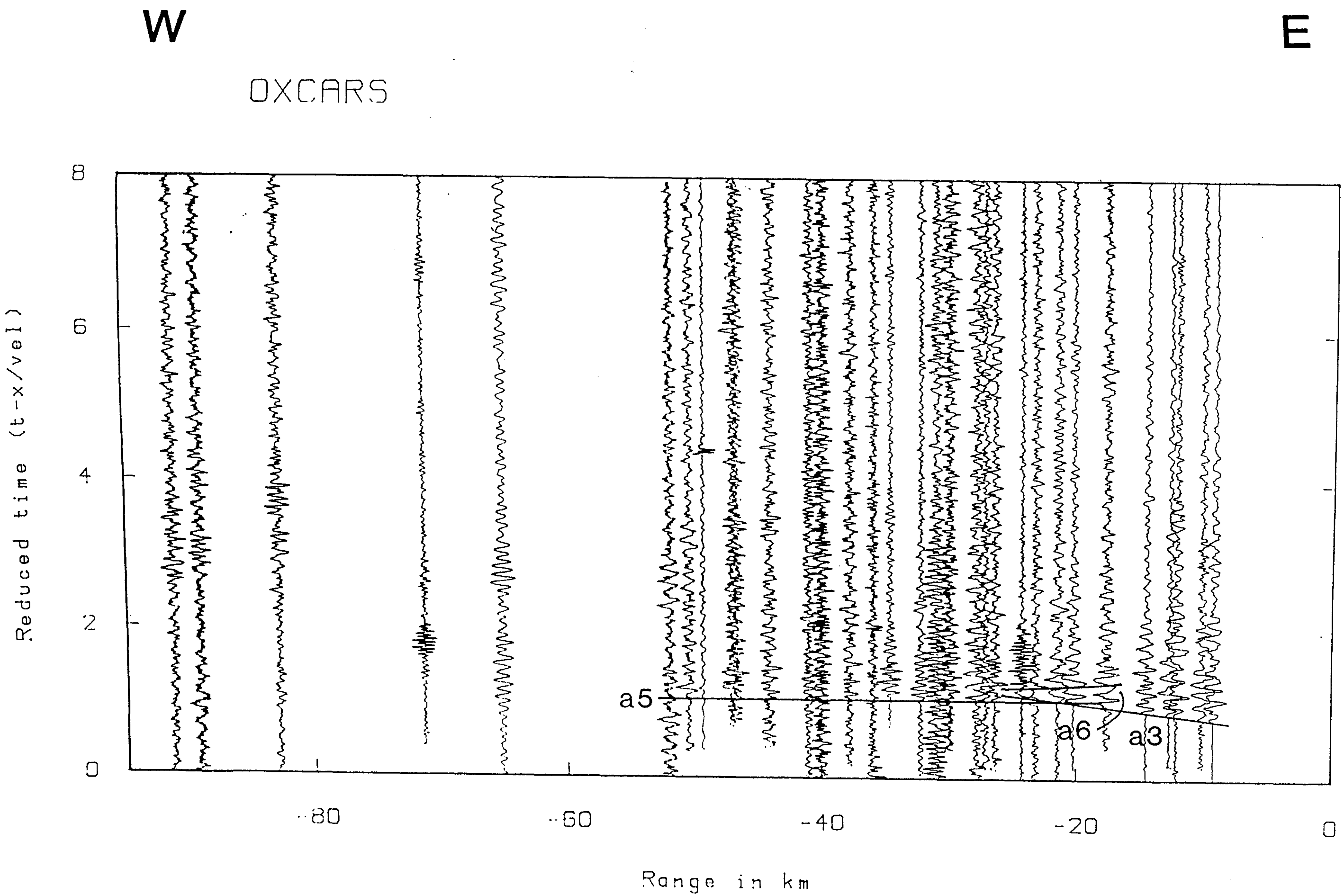

Fig.3.28b Unfiltered time section

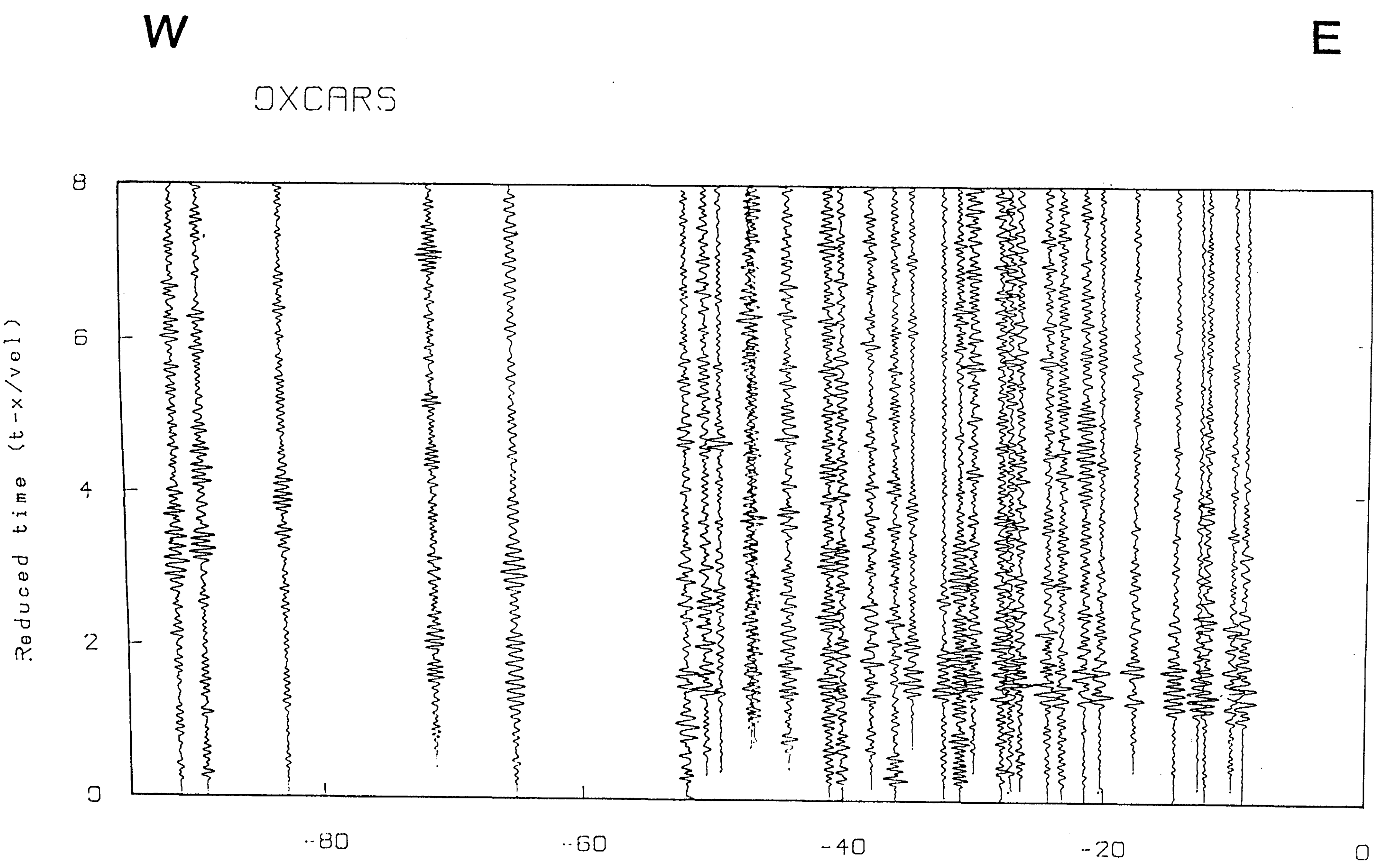

Fig.3.28c Zero-phase, bandpass filter 6.0- 16.0Hz and length 0.50 s with a Hamming window

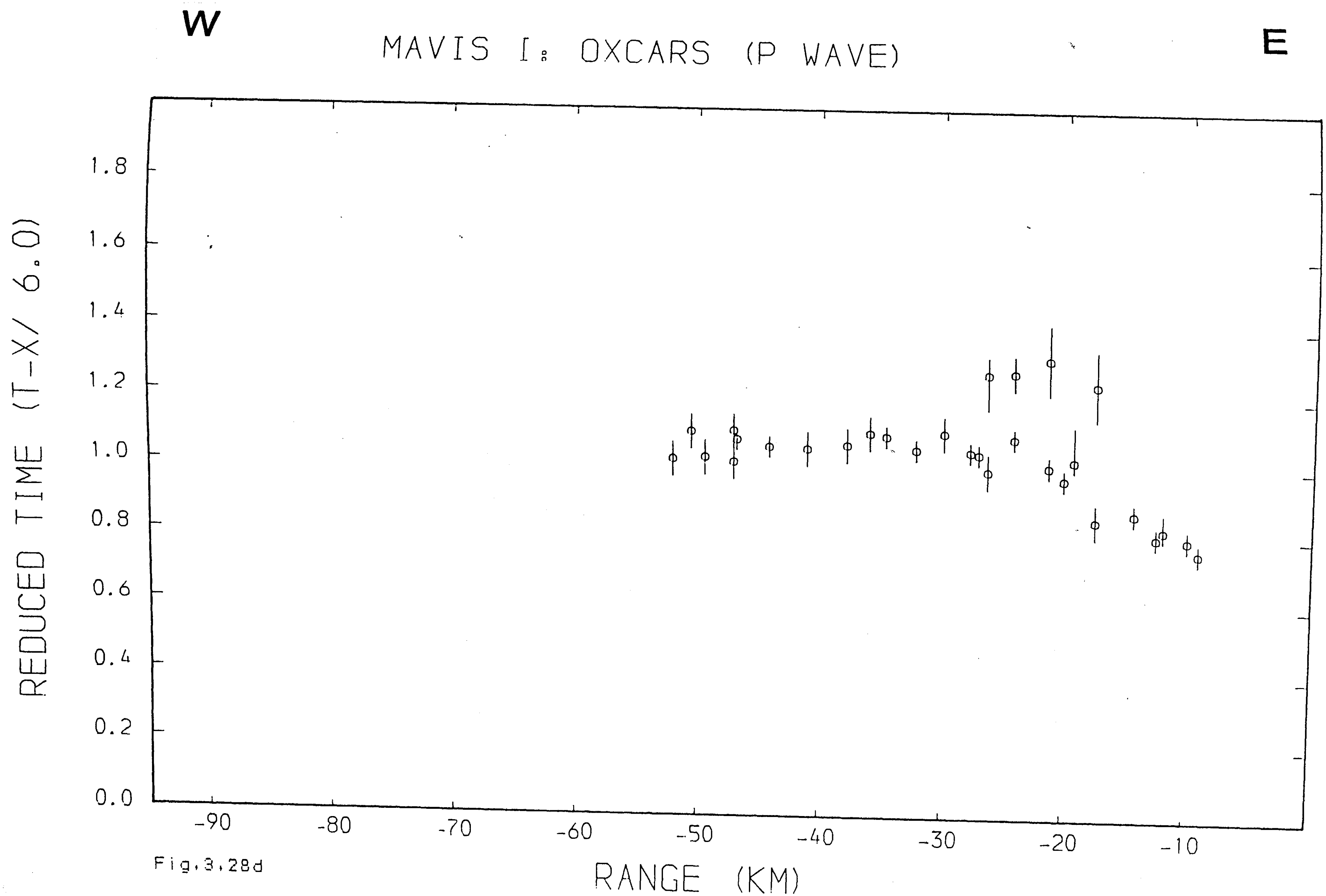
W
E
MAVIS I: OXCARS (P WAVE)
REDUCED TIME (T-X/ 6.0)
1.8
1.6
1.4
1.2
1.0
0.8
0.6
0.4
0.2
0.0
-90
-80
-70
-60
-50
-40
-30
-20
-10
RANGE (KM)

Fig.3.28d

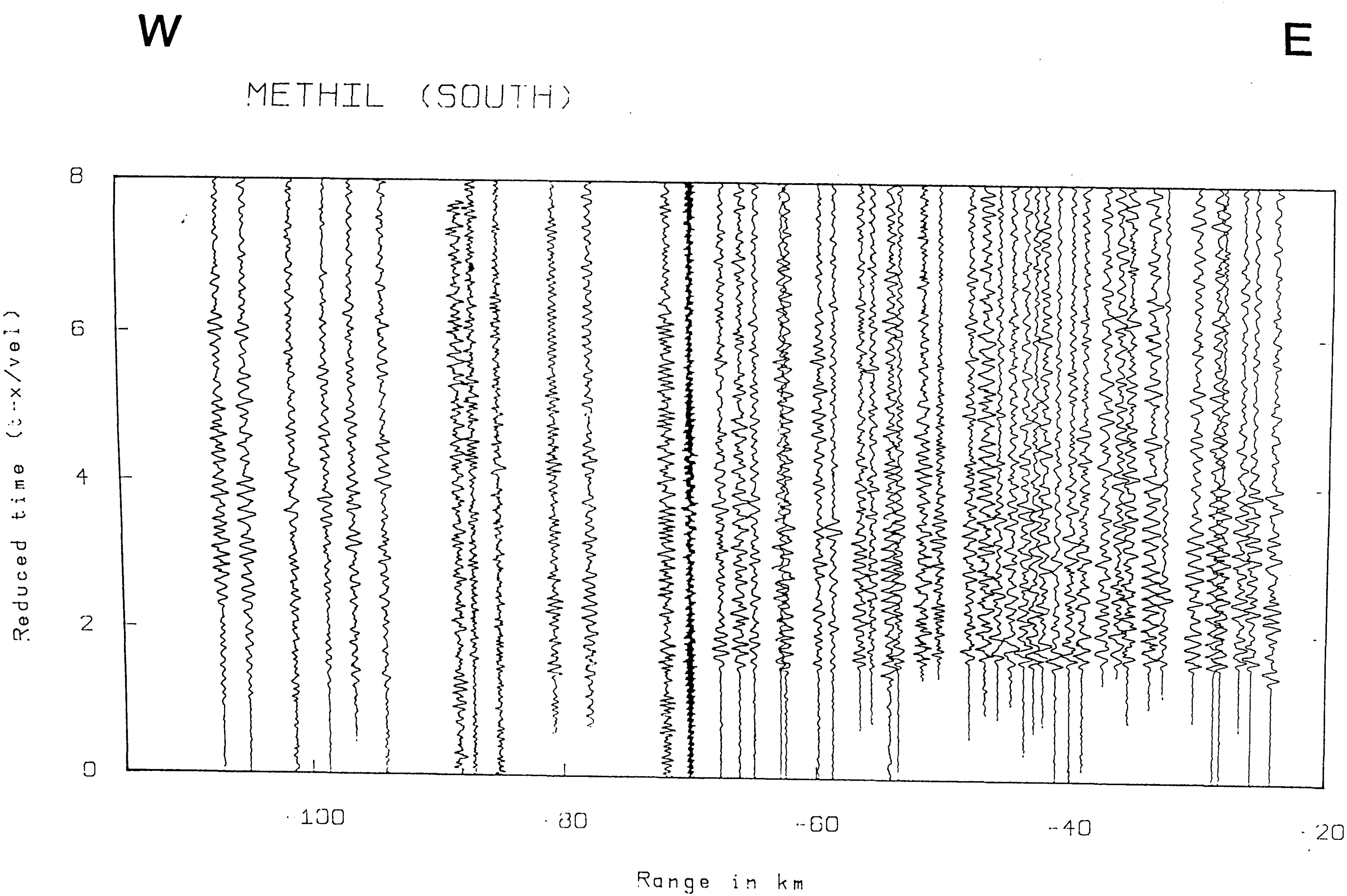

Fig.3.29a Unfiltered time section

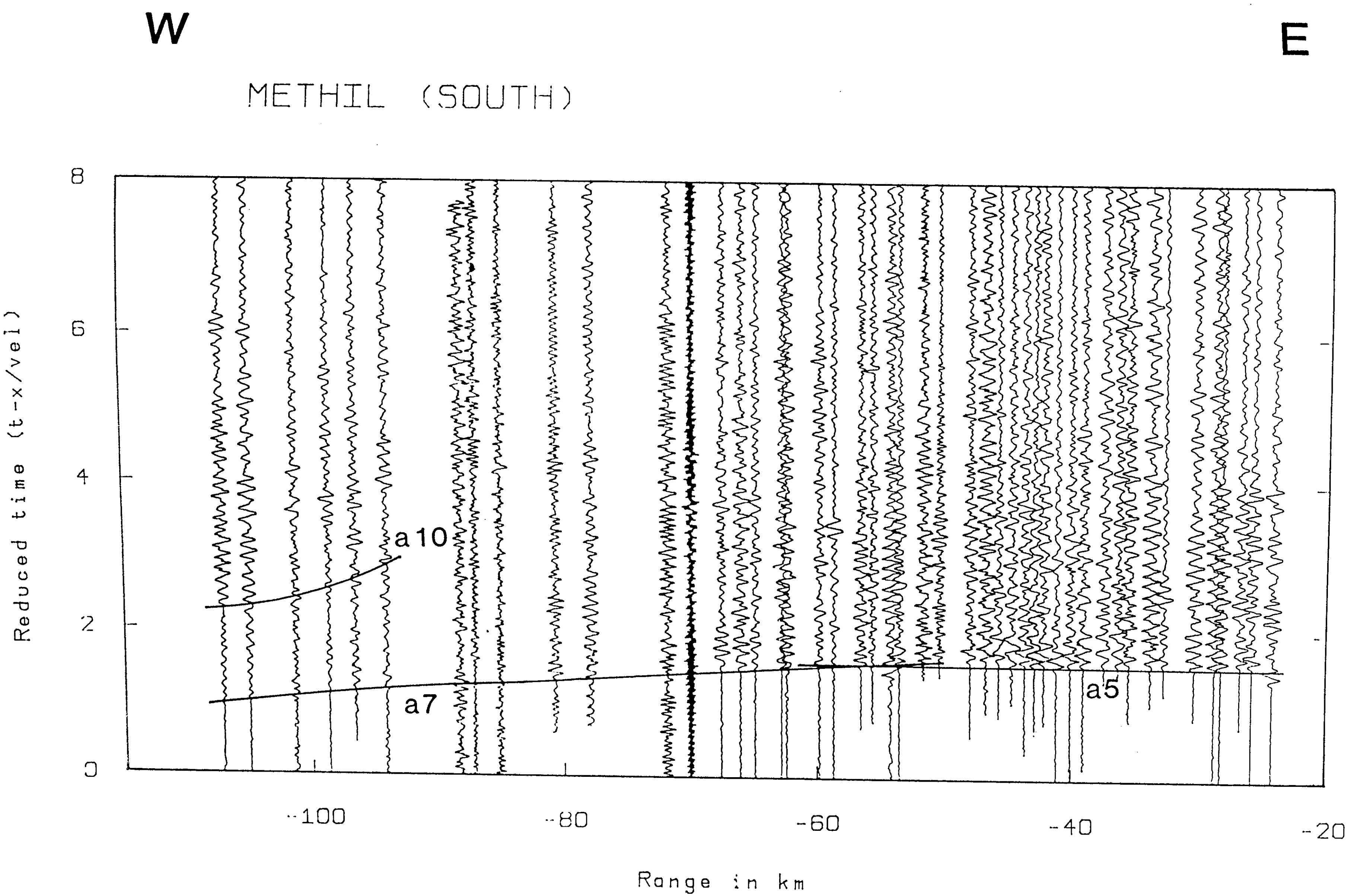

Fig.3.29b

Unfiltered time section

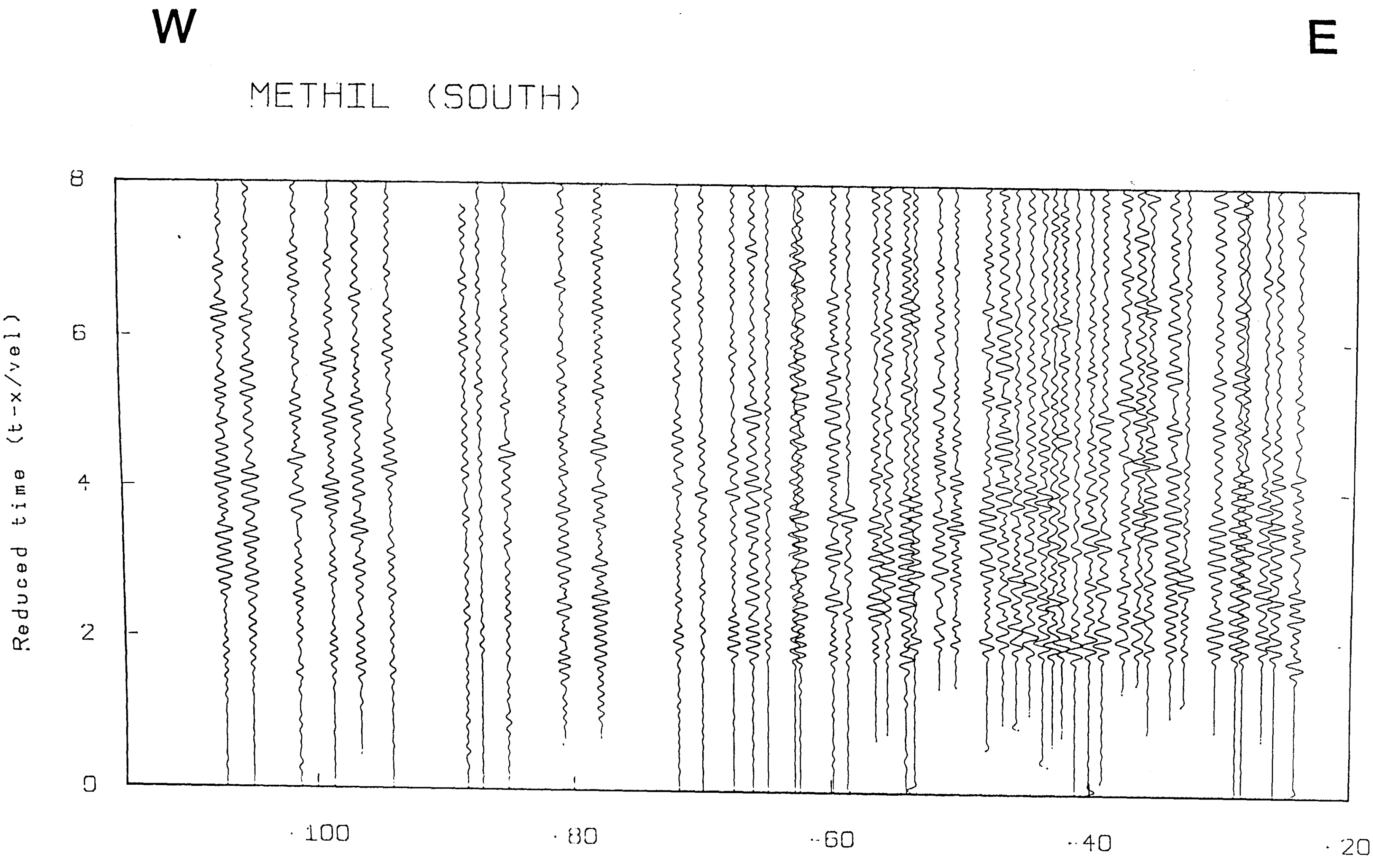

Fig.3.29c Zero-phase. bandpass filter 4.0- 8.0Hz and length 0.50 s with a Hamming window

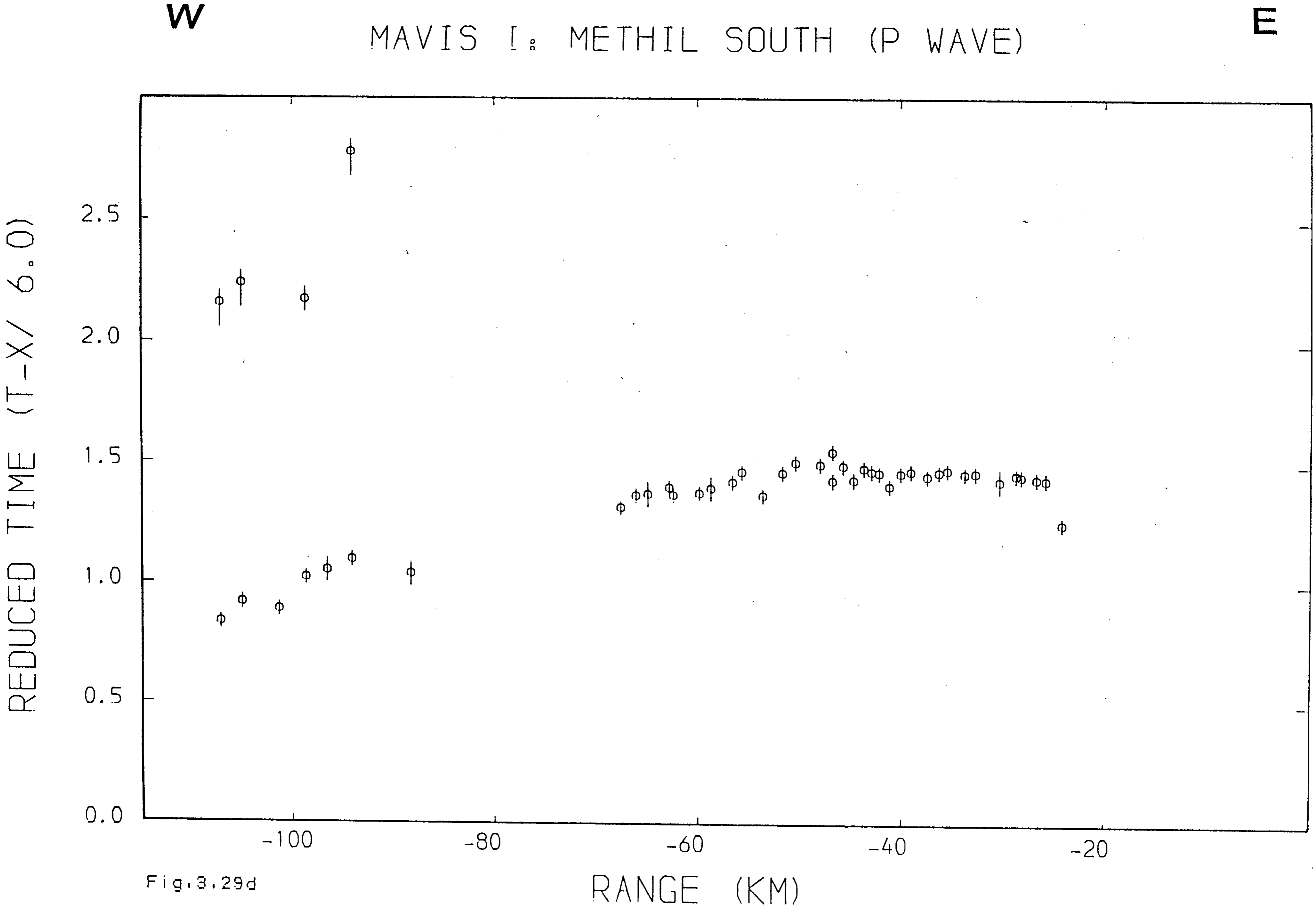
W
E
MAVIS I: METHIL SOUTH (P WAVE)
REDUCED TIME (T-X/ 6.0)
2.5
2.0
1.5
1.0
0.5
0.0
-100
-80
-60
-40
-20
RANGE (KM)

Fig.3.29d

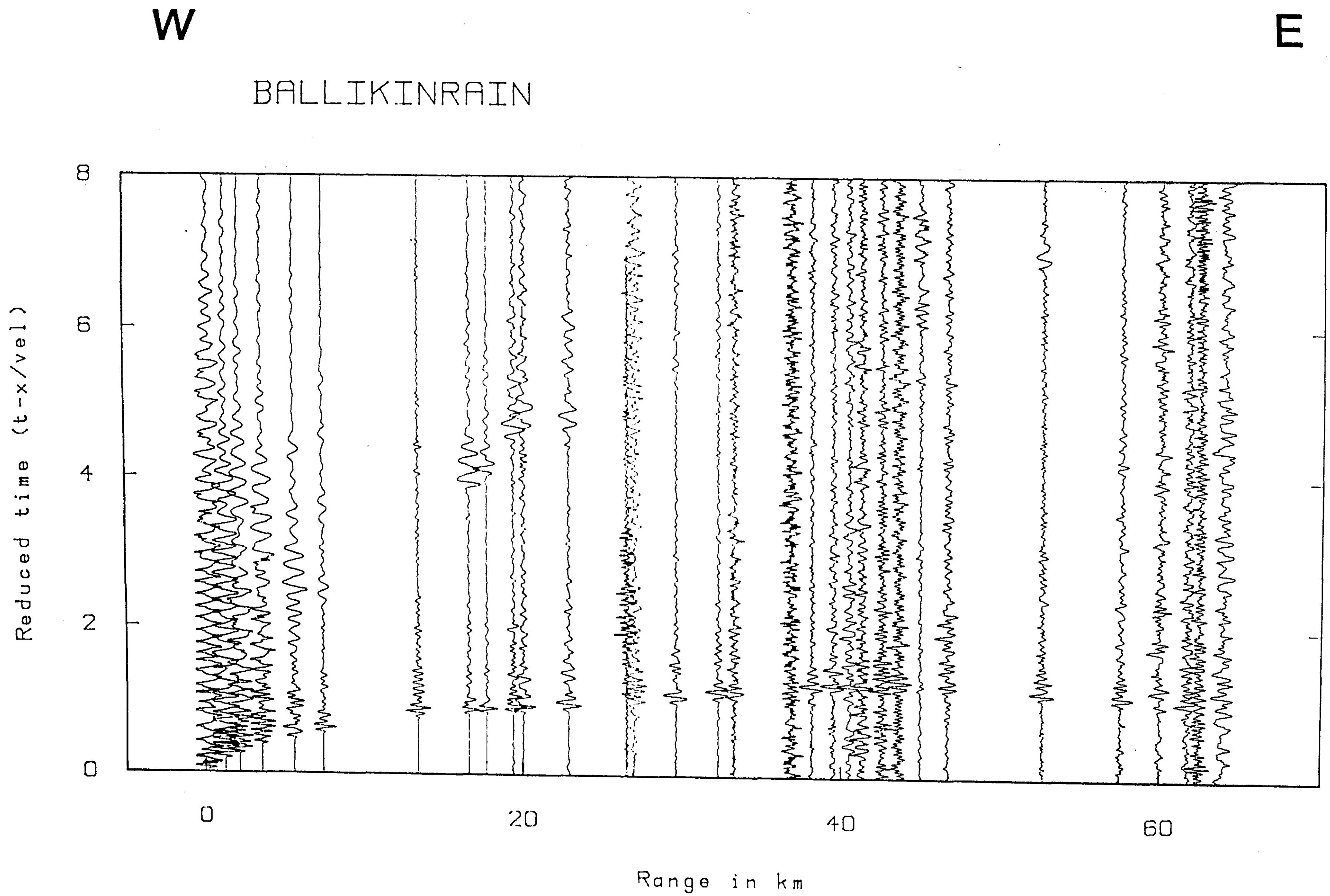

Fig.3.30a Unfiltered time section

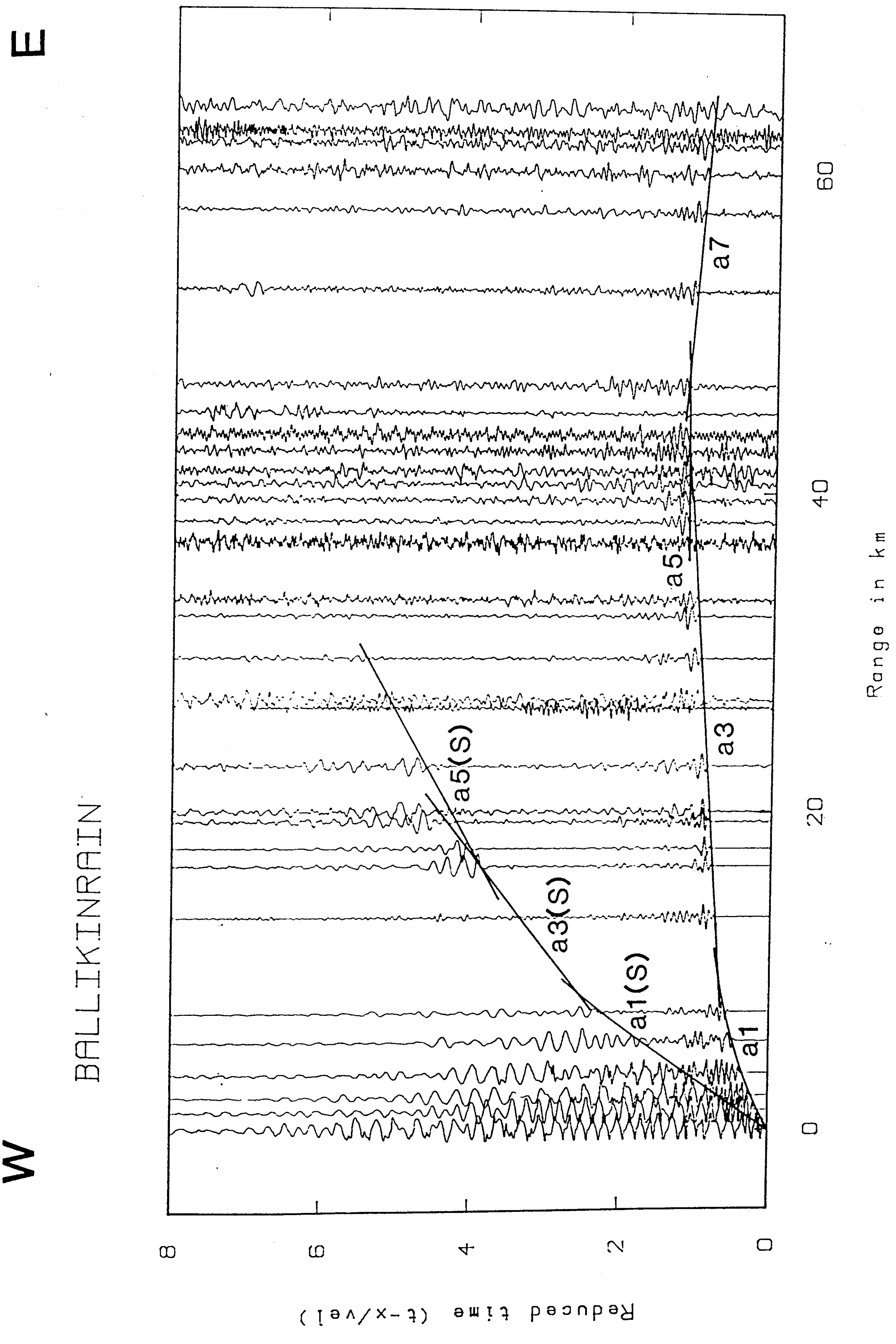

Fig.3.30b

Unfiltered time section

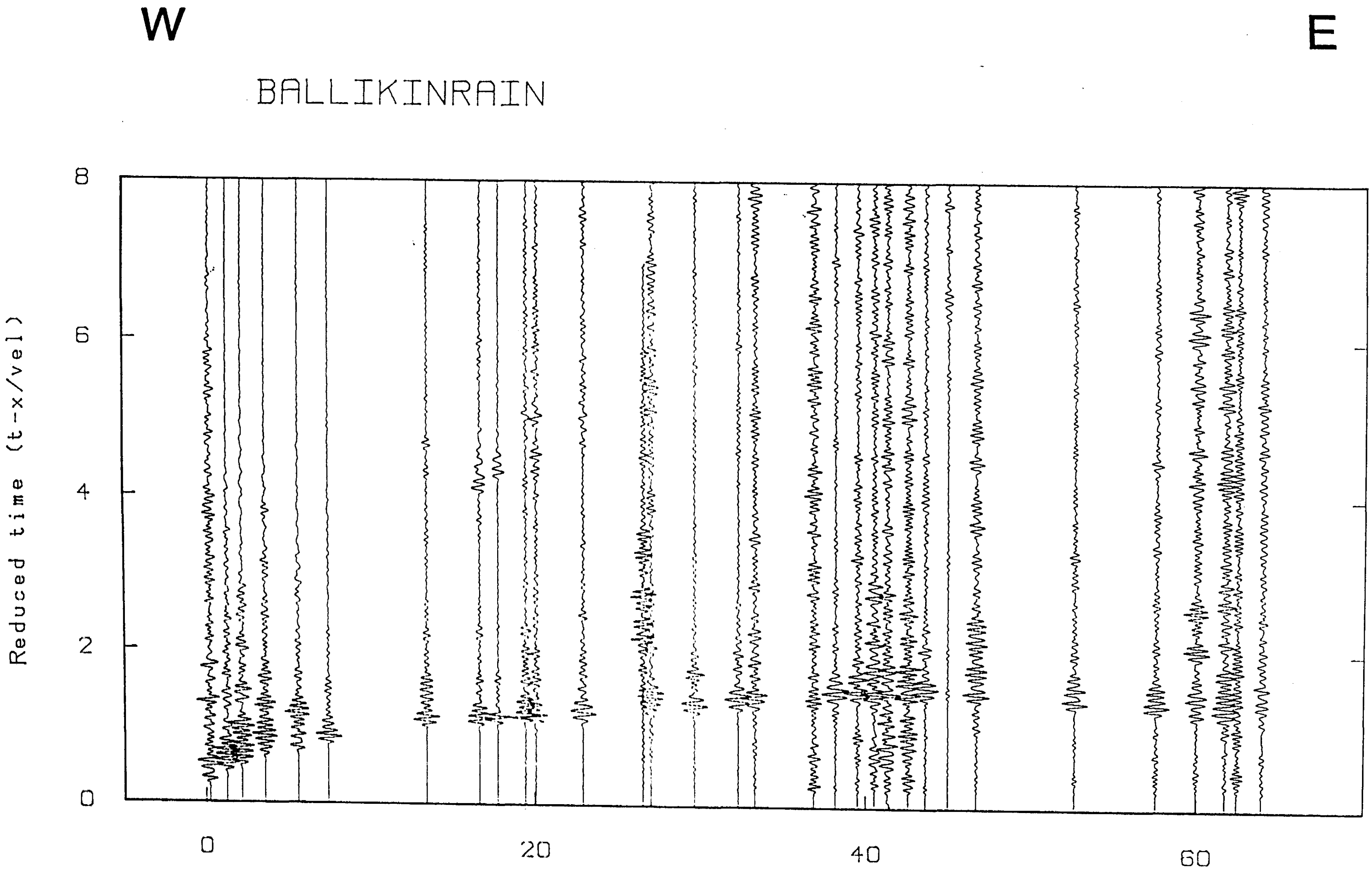

Fig.3.30c Zero-phase, bandpass filter 8.0- 18.0Hz and length 0.50 s with a Hamming window

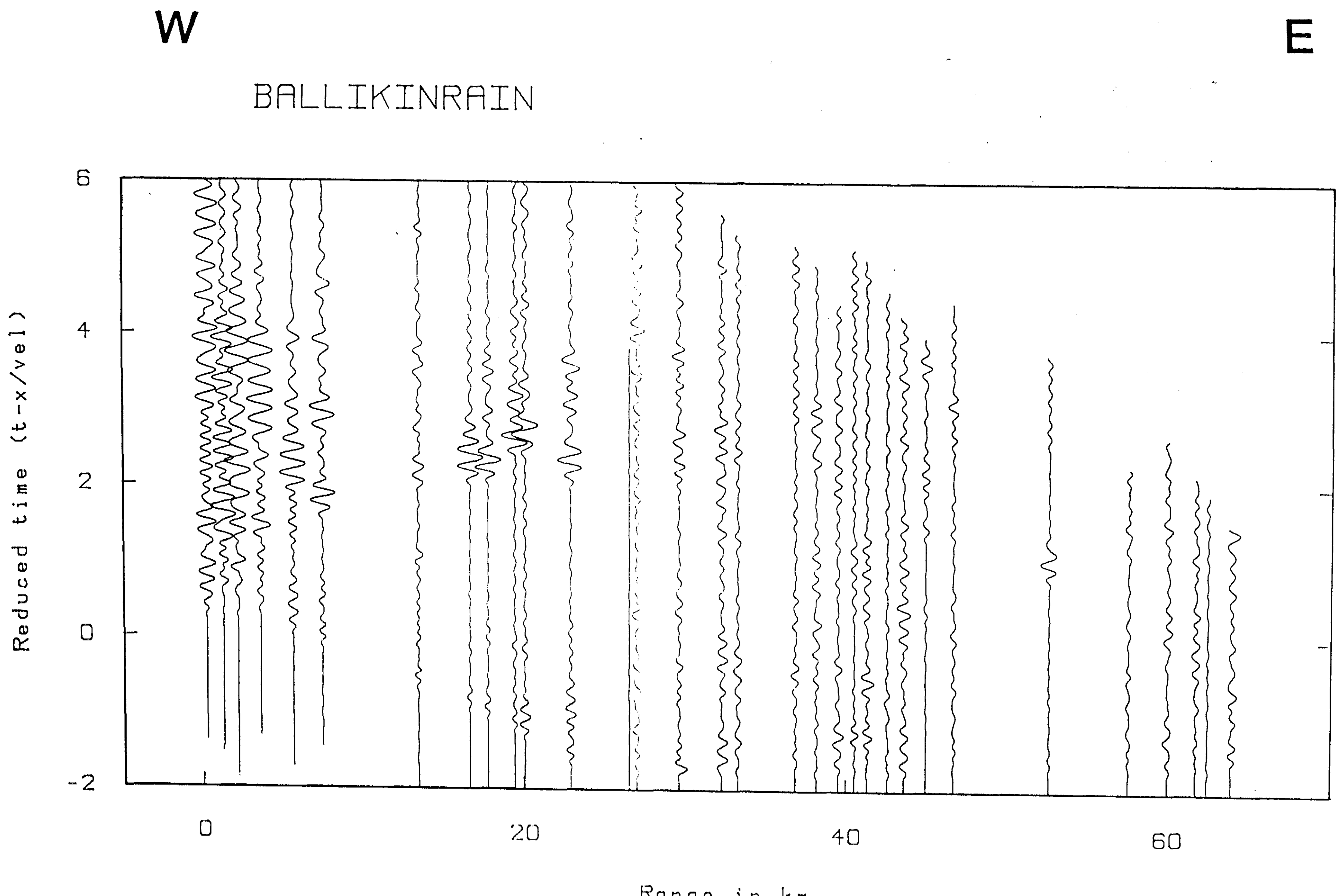

Fig.3.30d Zero-phase, lowpass filter 6.0Hz and length 0.50 s with a Hamming window

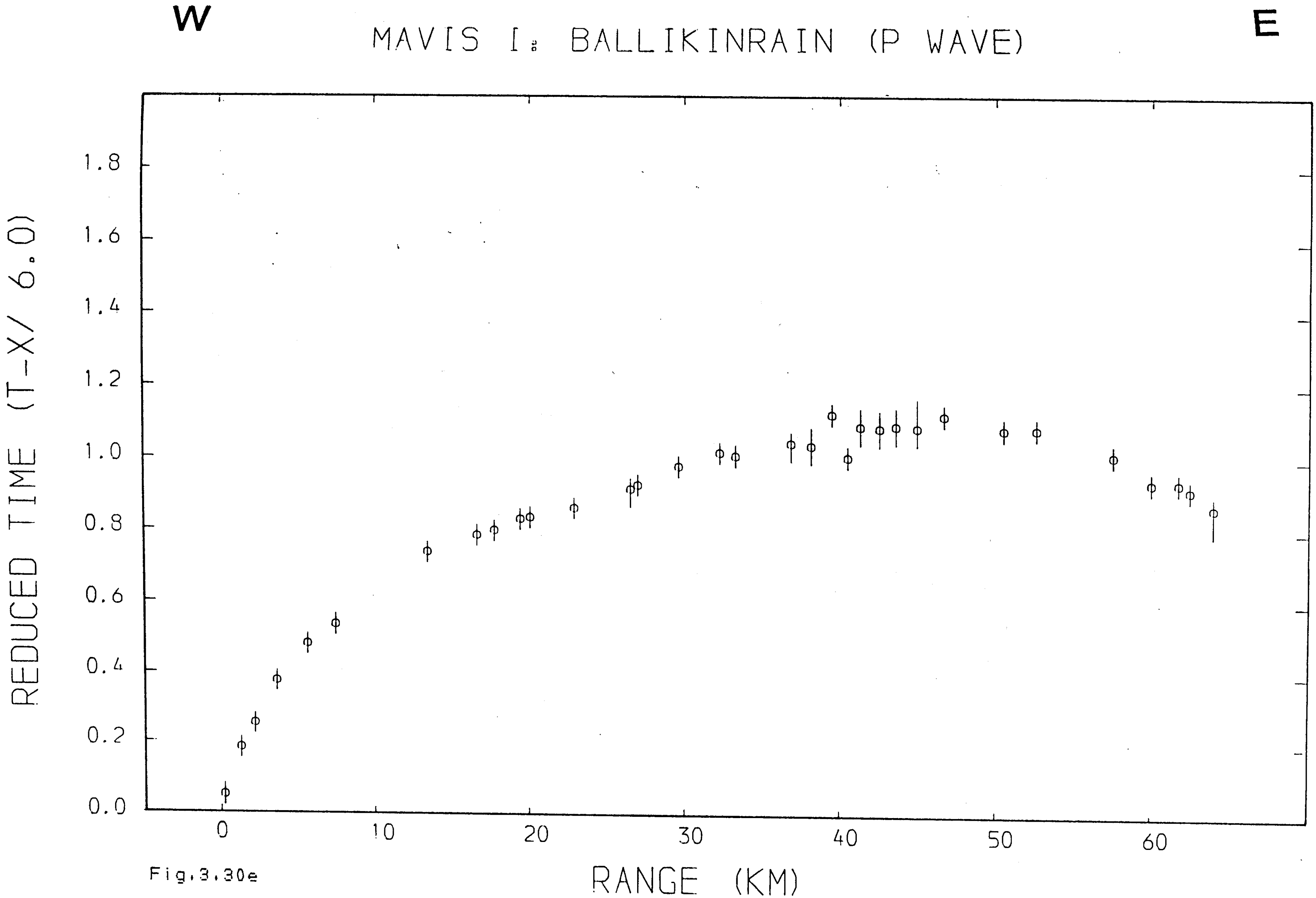
W
E
MAVIS I: BALLIKINRAIN (P WAVE)
REDUCED TIME (T-X/ 6.0)
1.8
1.6
1.4
1.2
1.0
0.8
0.6
0.4
0.2
0.0
0
10
20
30
40
50
60
RANGE (KM)

Fig.3.30e

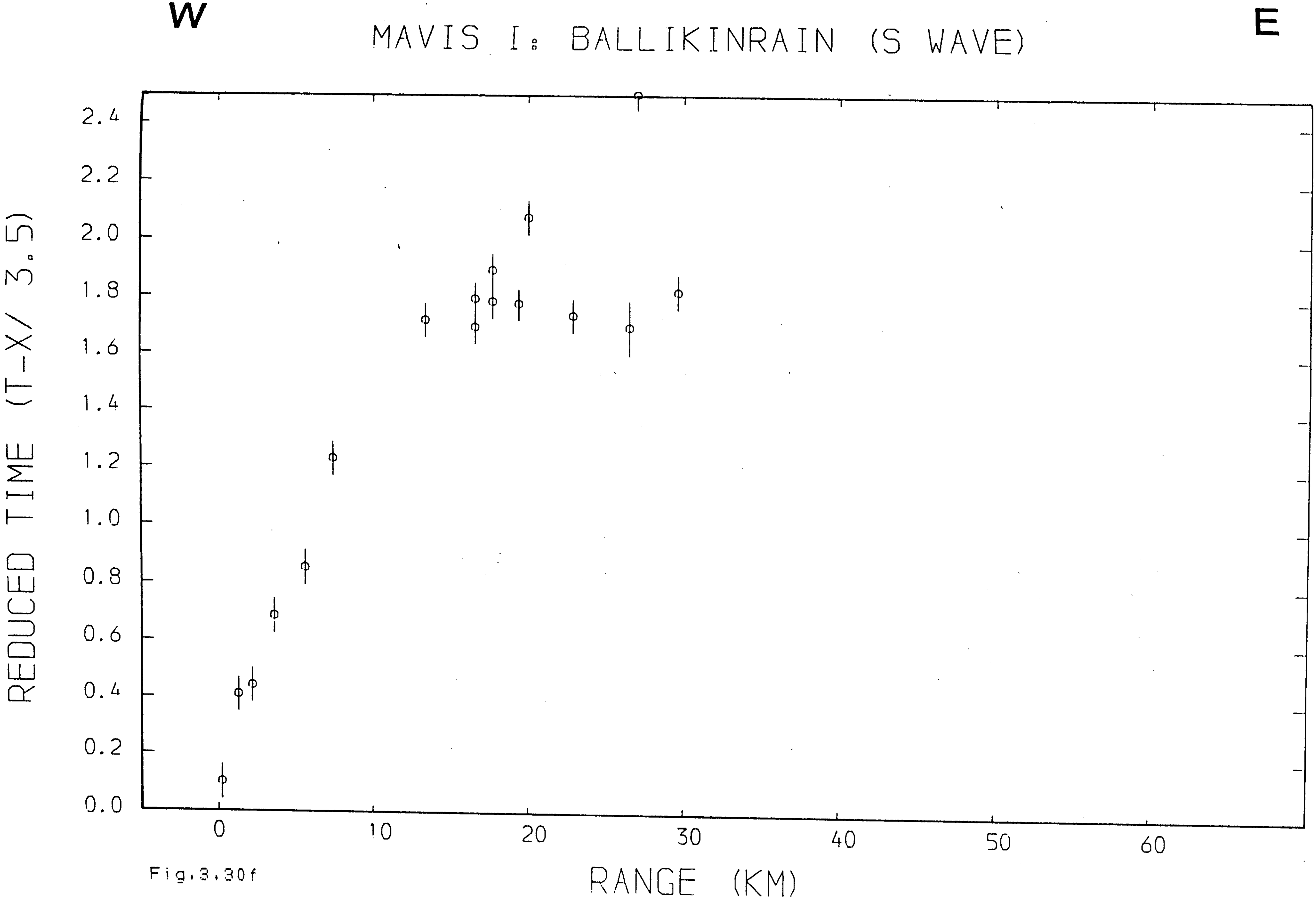
W
E
MAVIS I: BALLIKINRAIN (S WAVE)
REDUCED TIME (T-X/ 3.5)
2.4
2.2
2.0
1.8
1.6
1.4
1.2
1.0
0.8
0.6
0.4
0.2
0.0
0
10
20
30
40
50
60
RANGE (KM)

Fig.3.30f

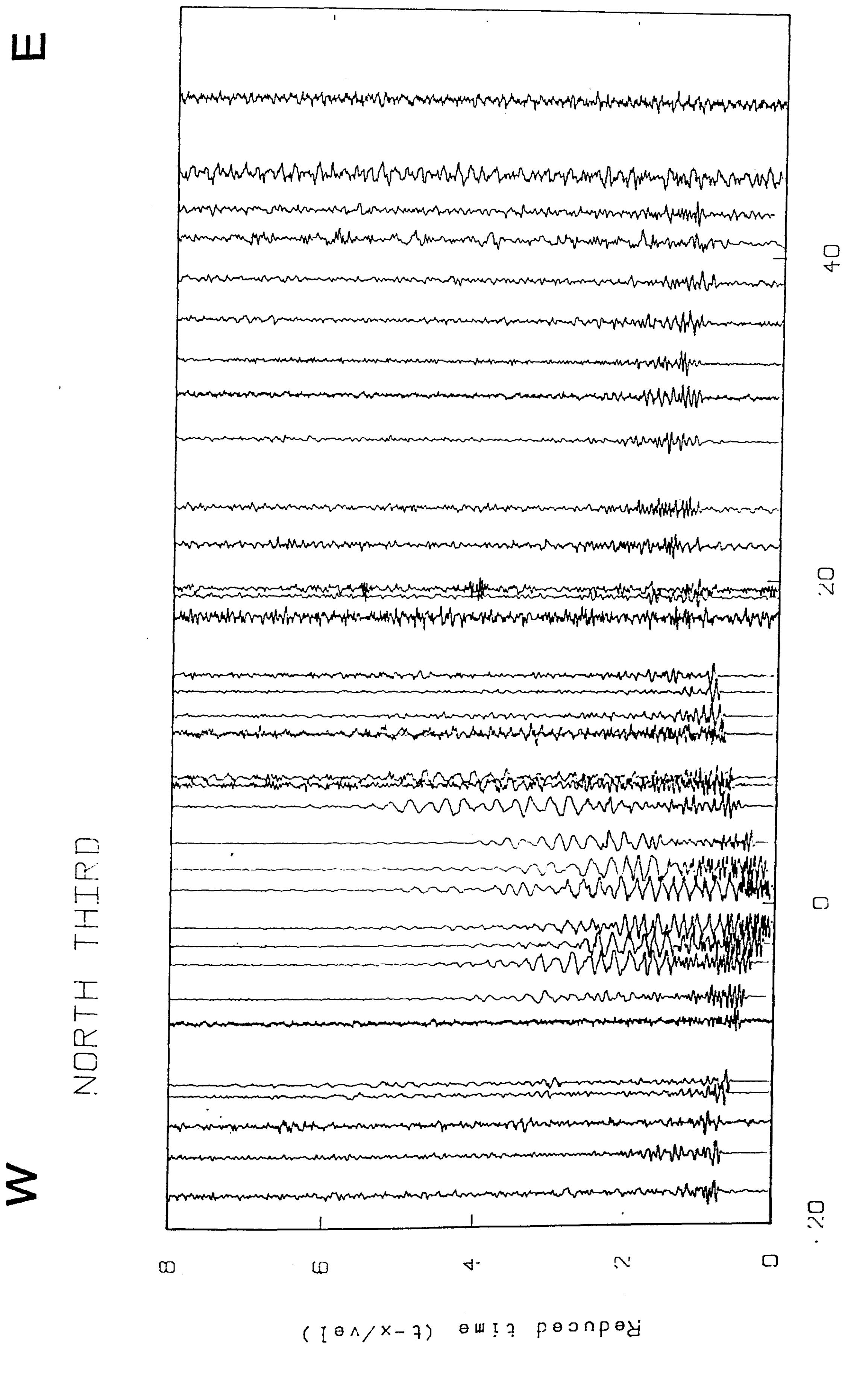

Fig.3.31a

Unfiltered time section

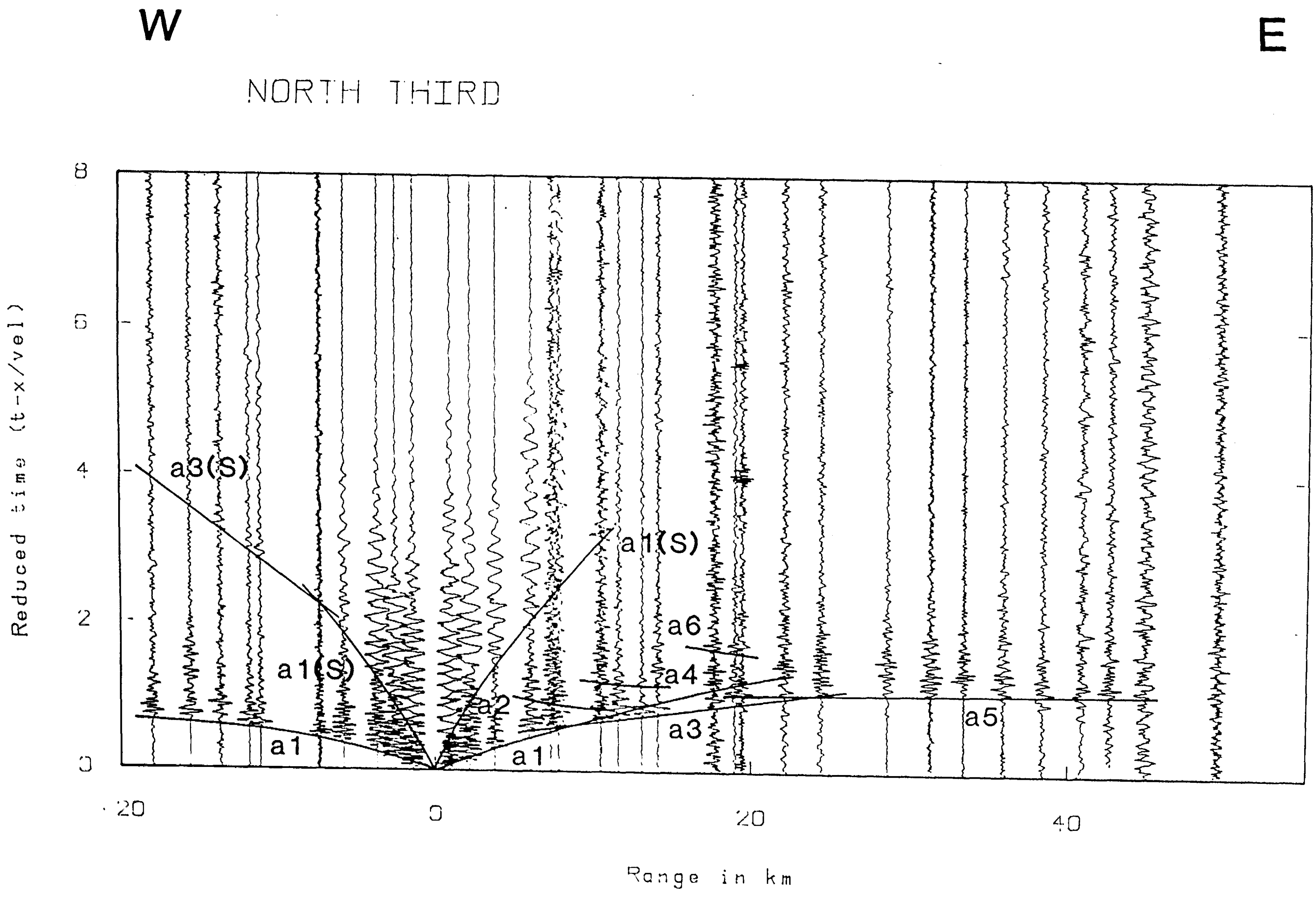

Fig.3.31b Unfiltered time section

W E

NORTH THIRD

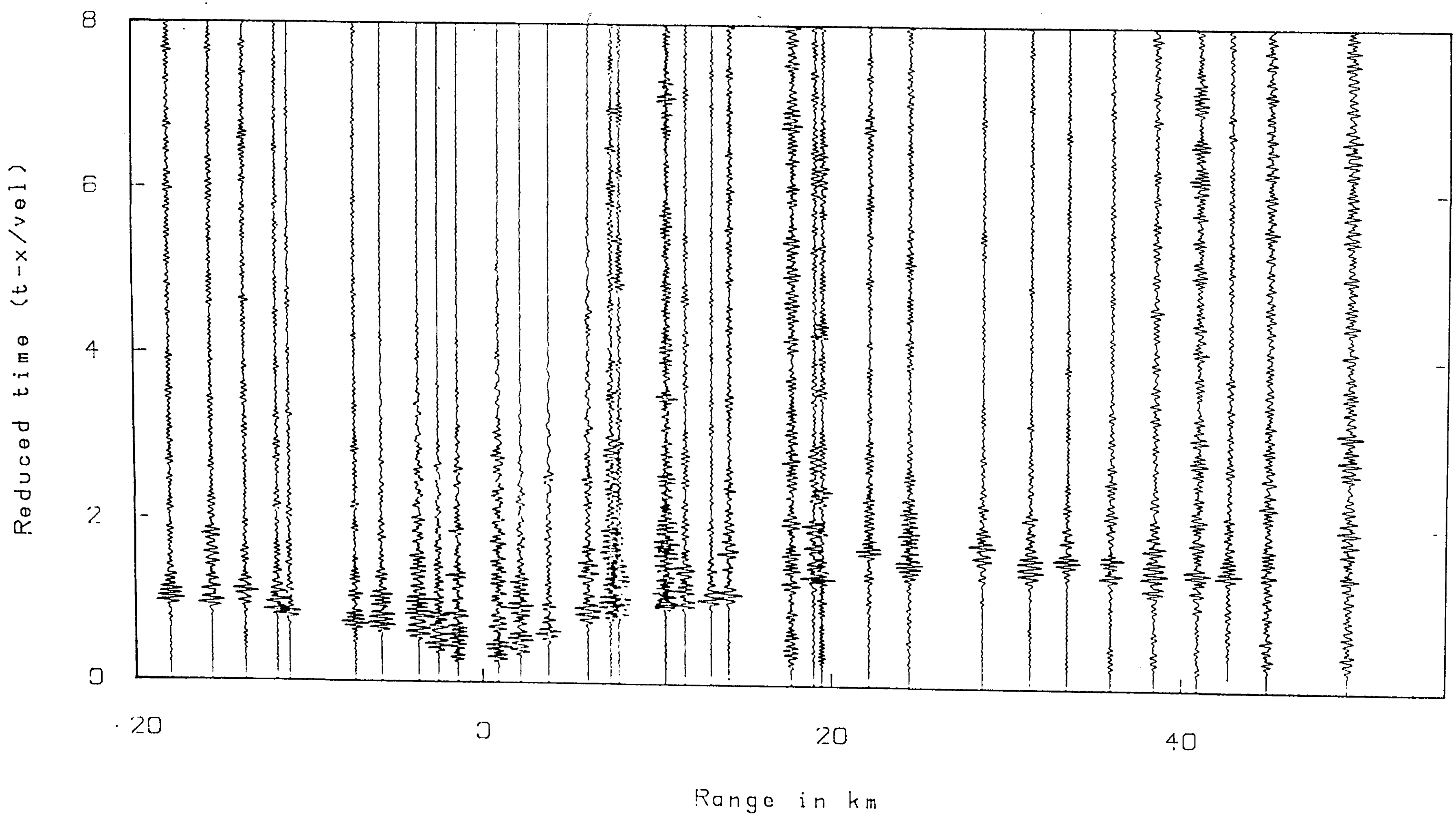

Fig.3.31c Zero-phase, bandpass filter 10.0- 22.0Hz and length 0.50 s with a Hamming window

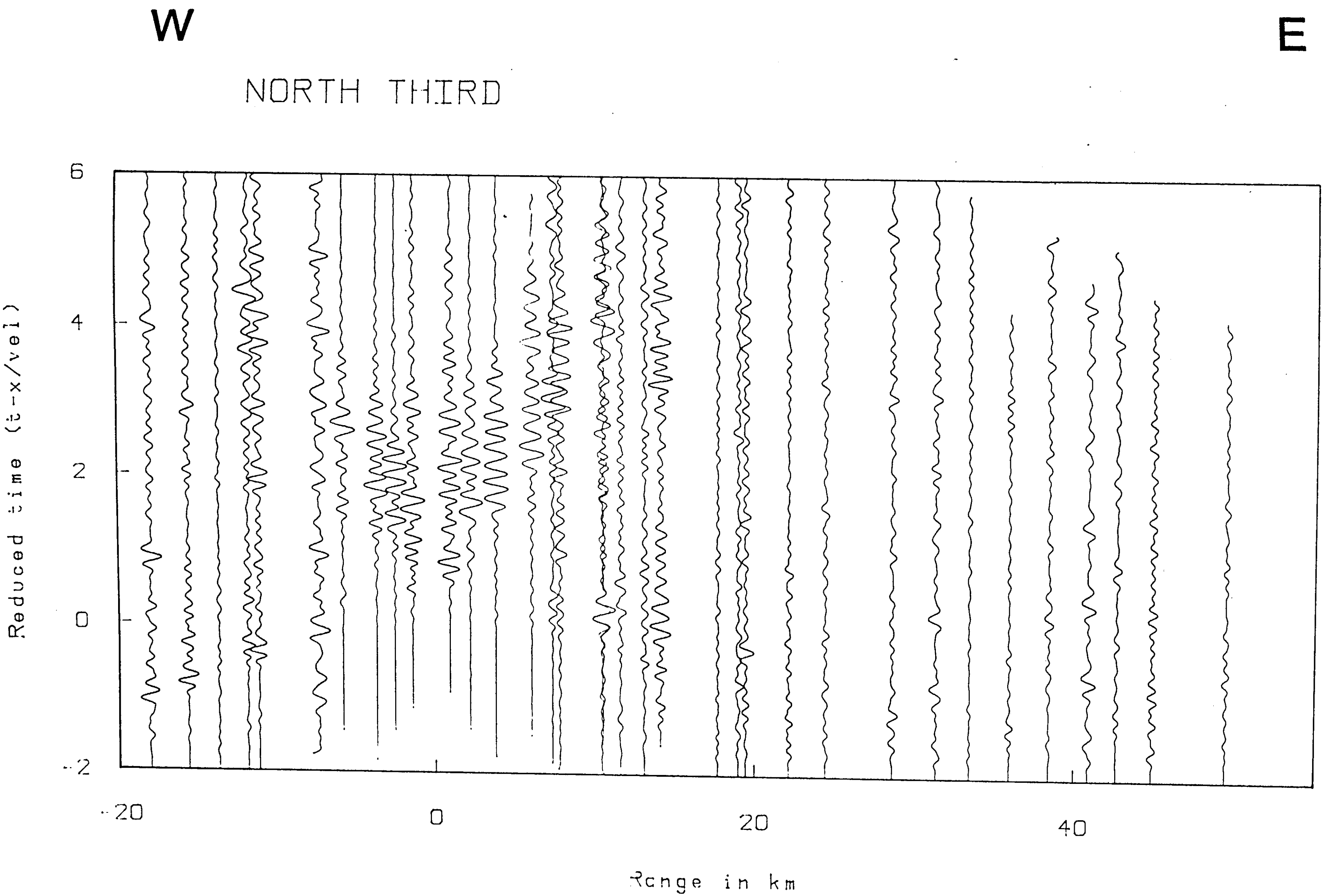

Fig.3.31d Zero-phase, lowpass filter 6.0Hz and length 0.50 s with a Hamming window

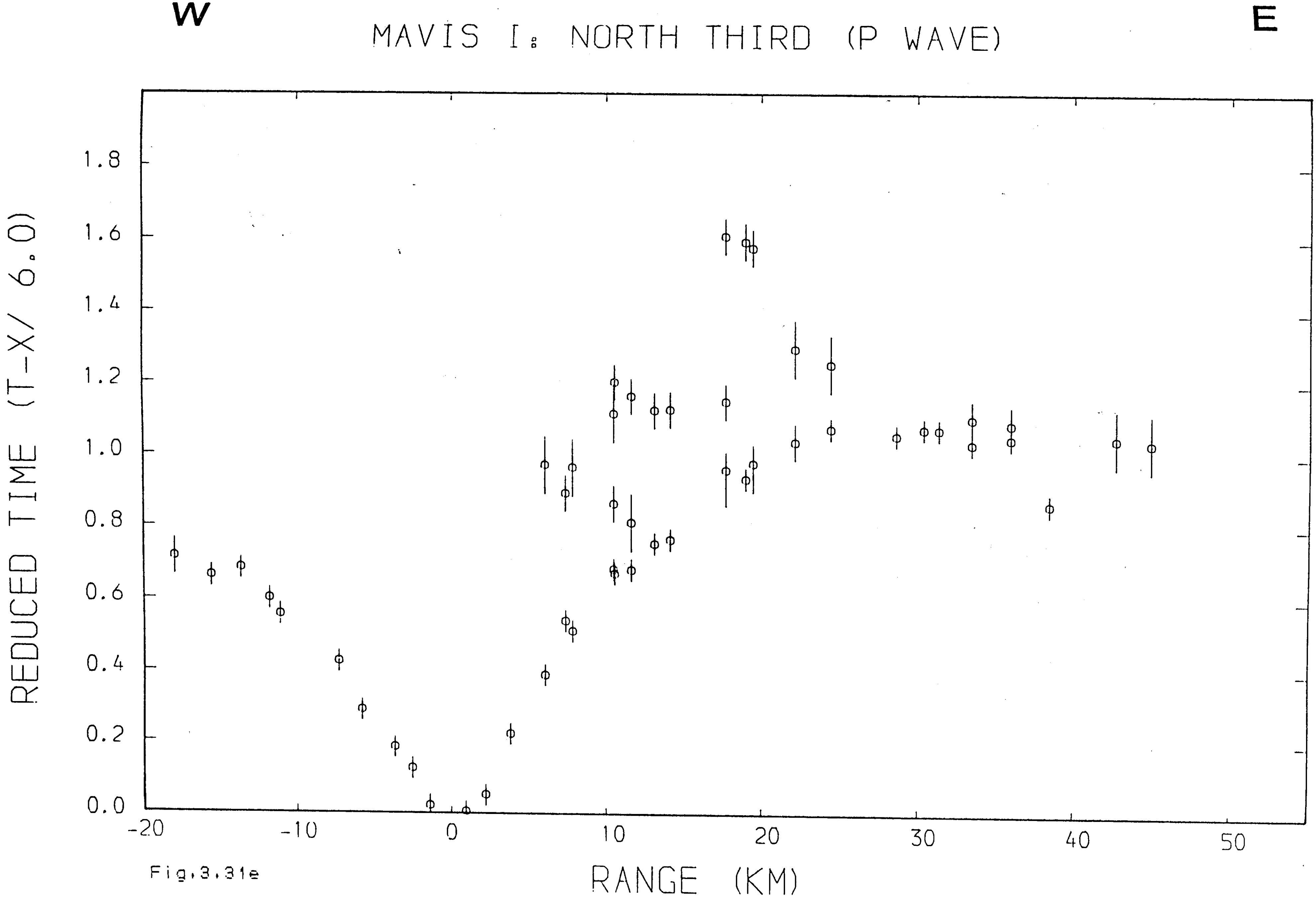
W
E
MAVIS I: NORTH THIRD (P WAVE)
REDUCED TIME (T-X/ 6.0)
1.8
1.6
1.4
1.2
1.0
0.8
0.6
0.4
0.2
0.0
-20
-10
0
10
20
30
40
50
RANGE (KM)

Fig.3.31e

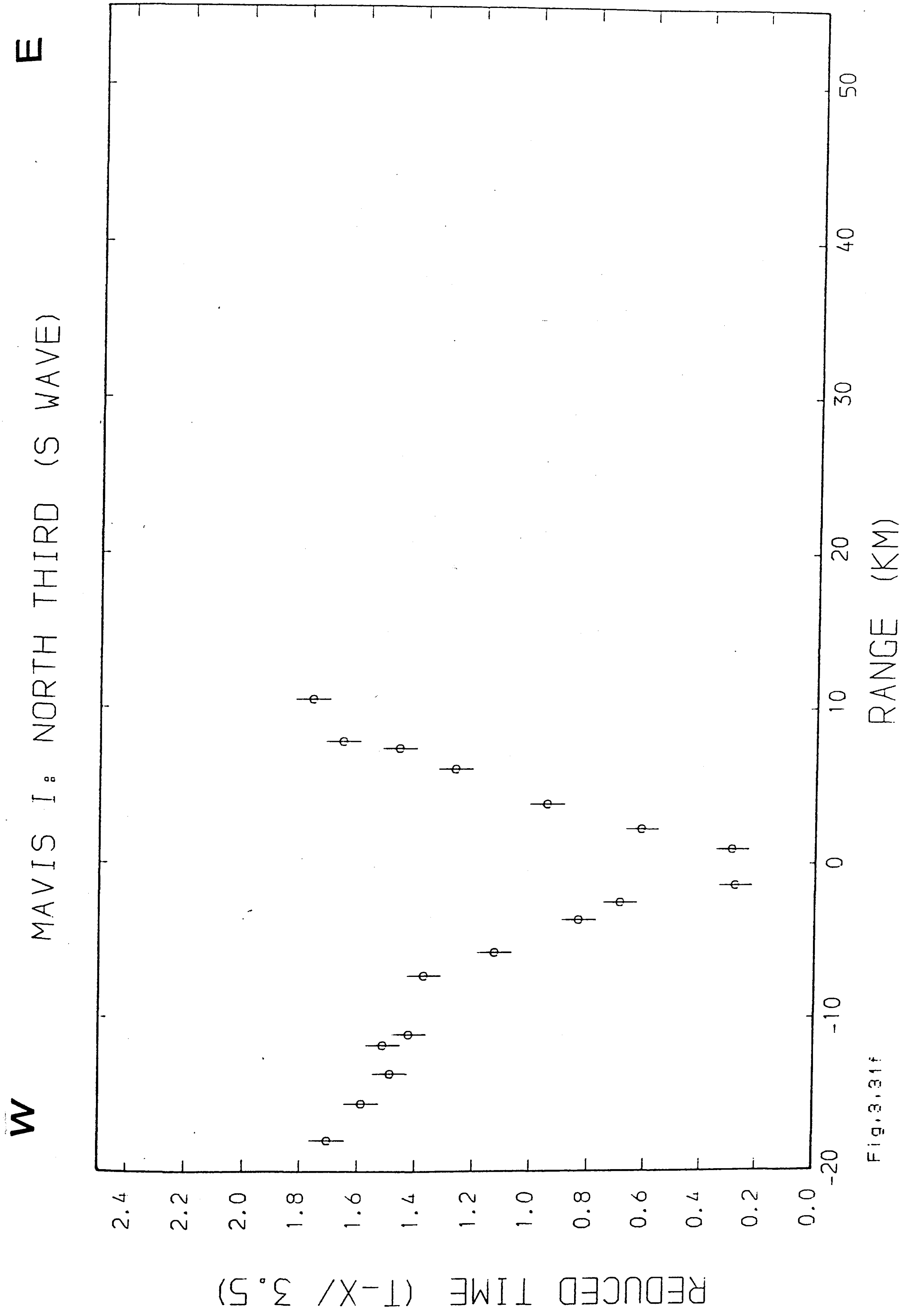
MAVIS I: NORTH THIRD (S WAVE)
W
E
REDUCED TIME (T-X/ 3.5)
2.4
2.2
2.0
1.8
1.6
1.4
1.2
1.0
0.8
0.6
0.4
0.2
0.0
RANGE (KM)
-20
-10
0
10
20
30
40
50

Fig.3.31f

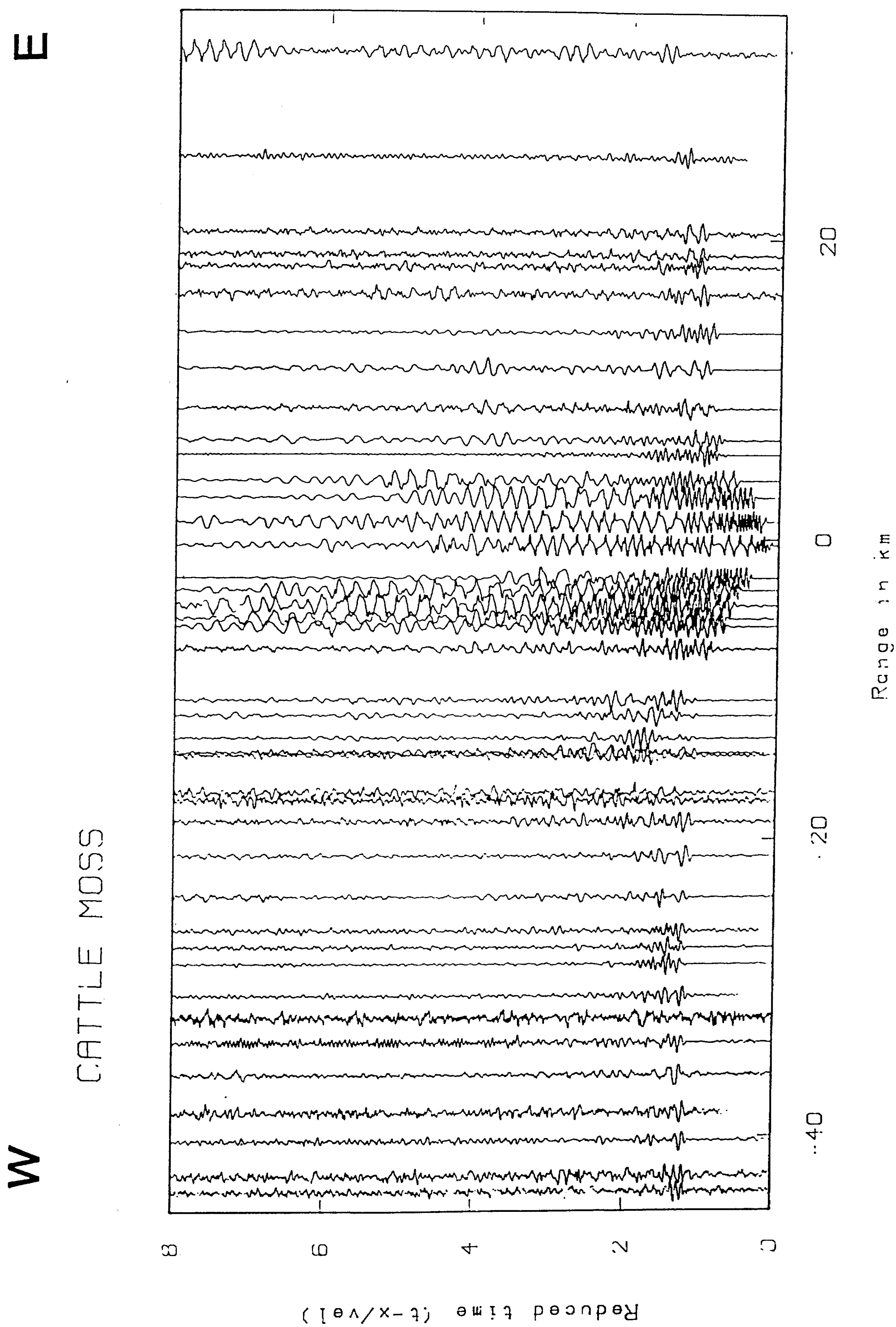

Fig.3.32a. Unfiltered time section

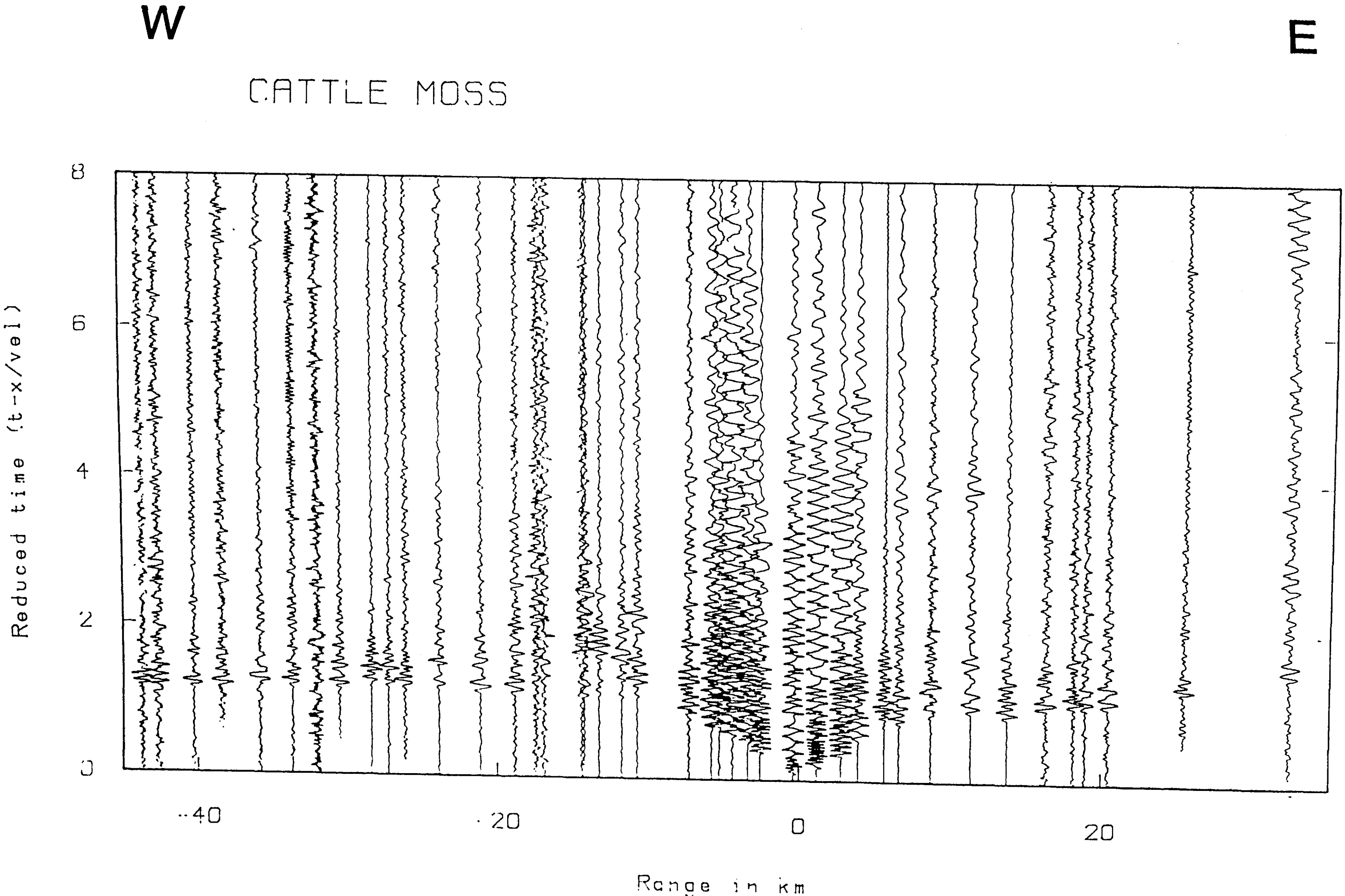

Fig.3.32a. Unfiltered time section

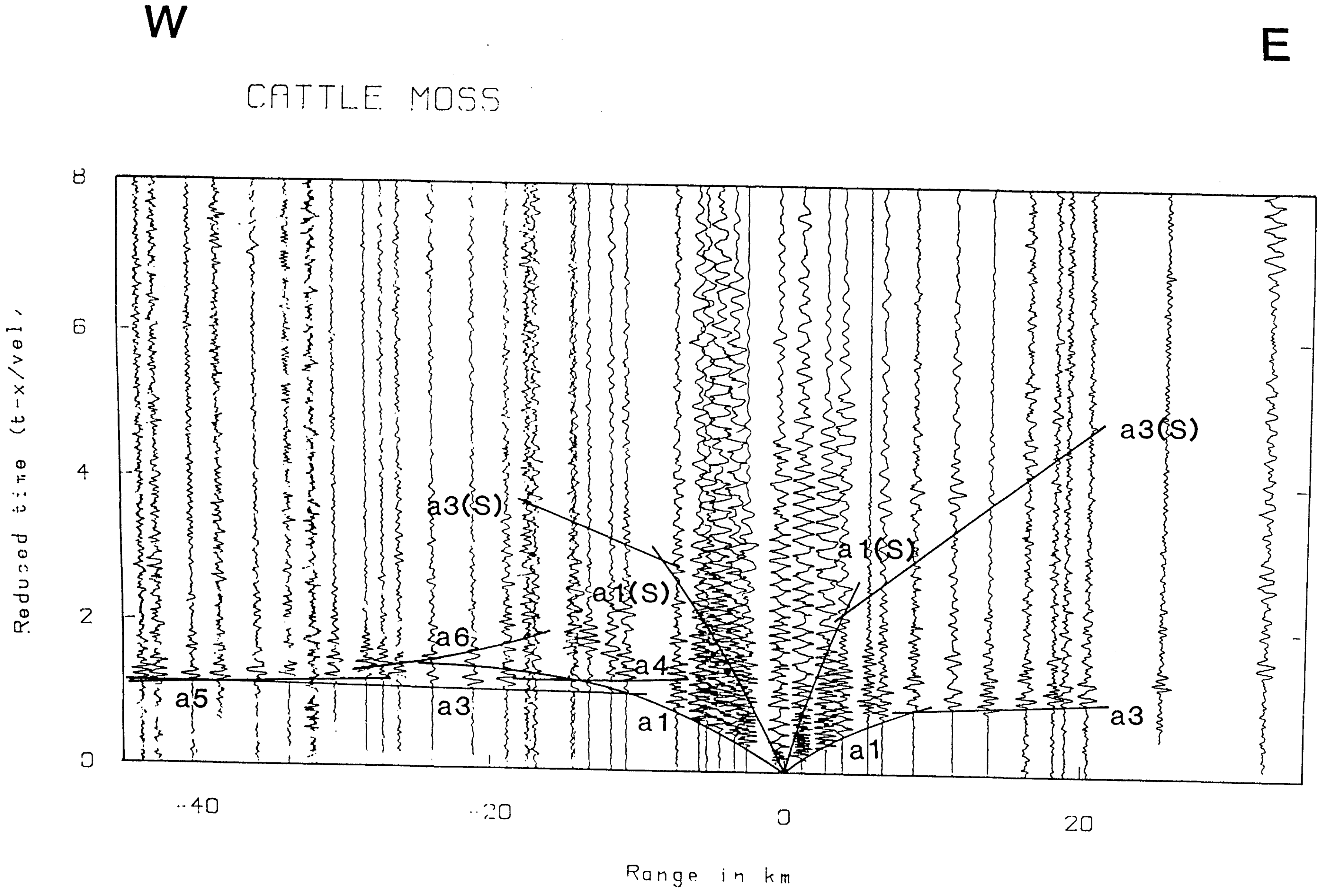

Fig.3.32b Unfiltered time section

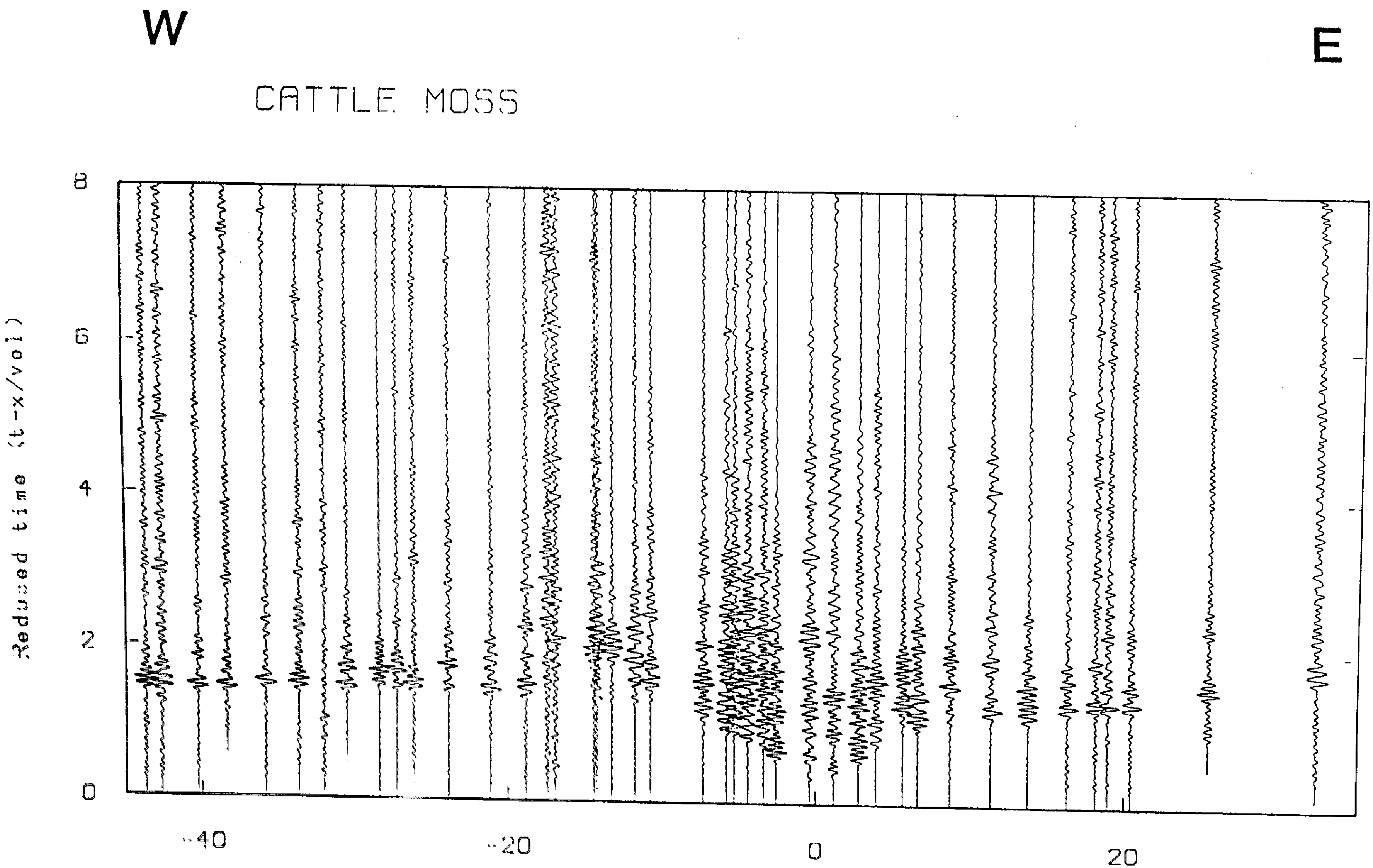

Fig.3.32c Zero-phase, bandpass filter 6.0- 16.0Hz and length 0.50 s with a Hamming window

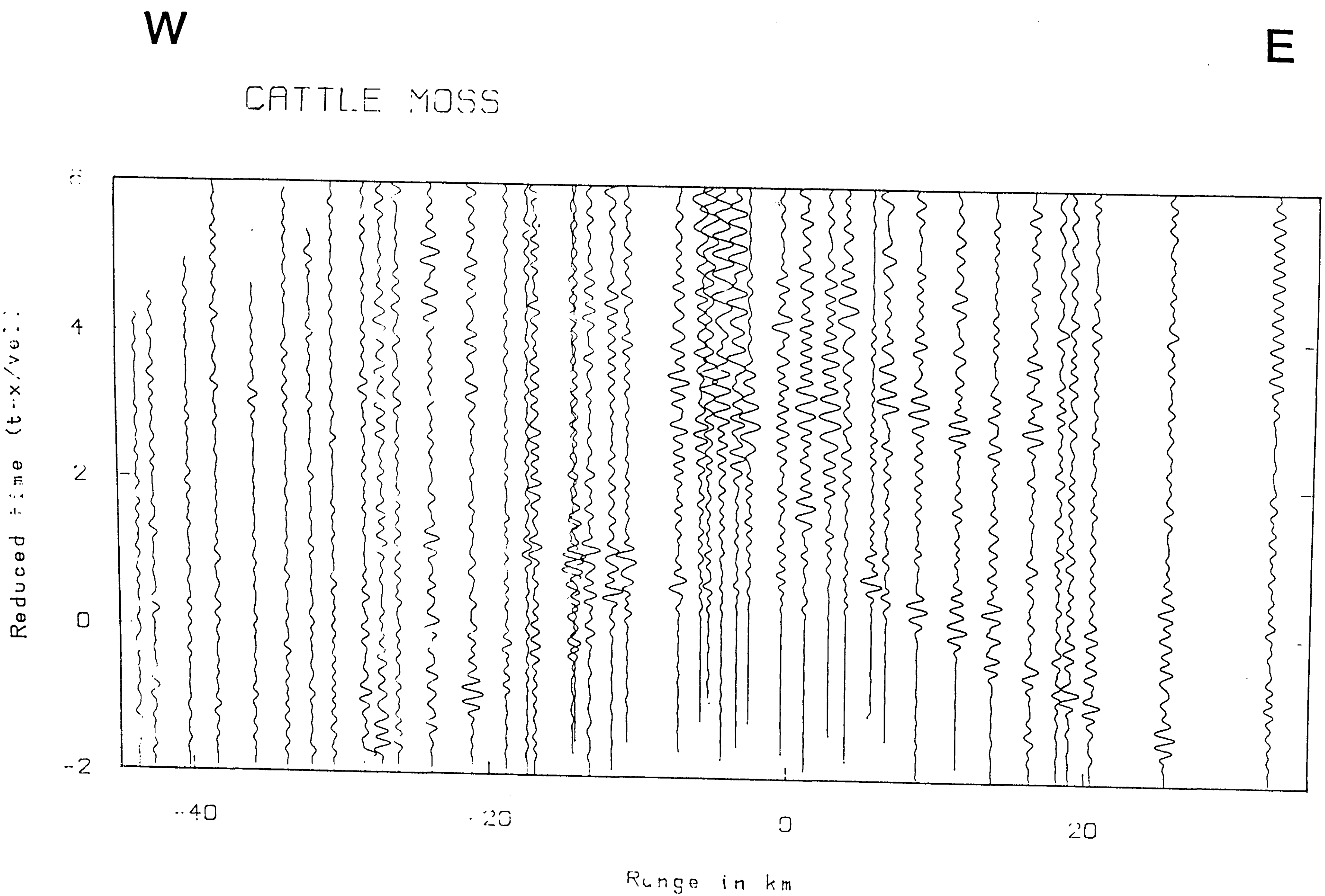

Fig.3.32d Zero-phase, lowpass filter 6.0Hz and length 0.50 s with a Hamming window

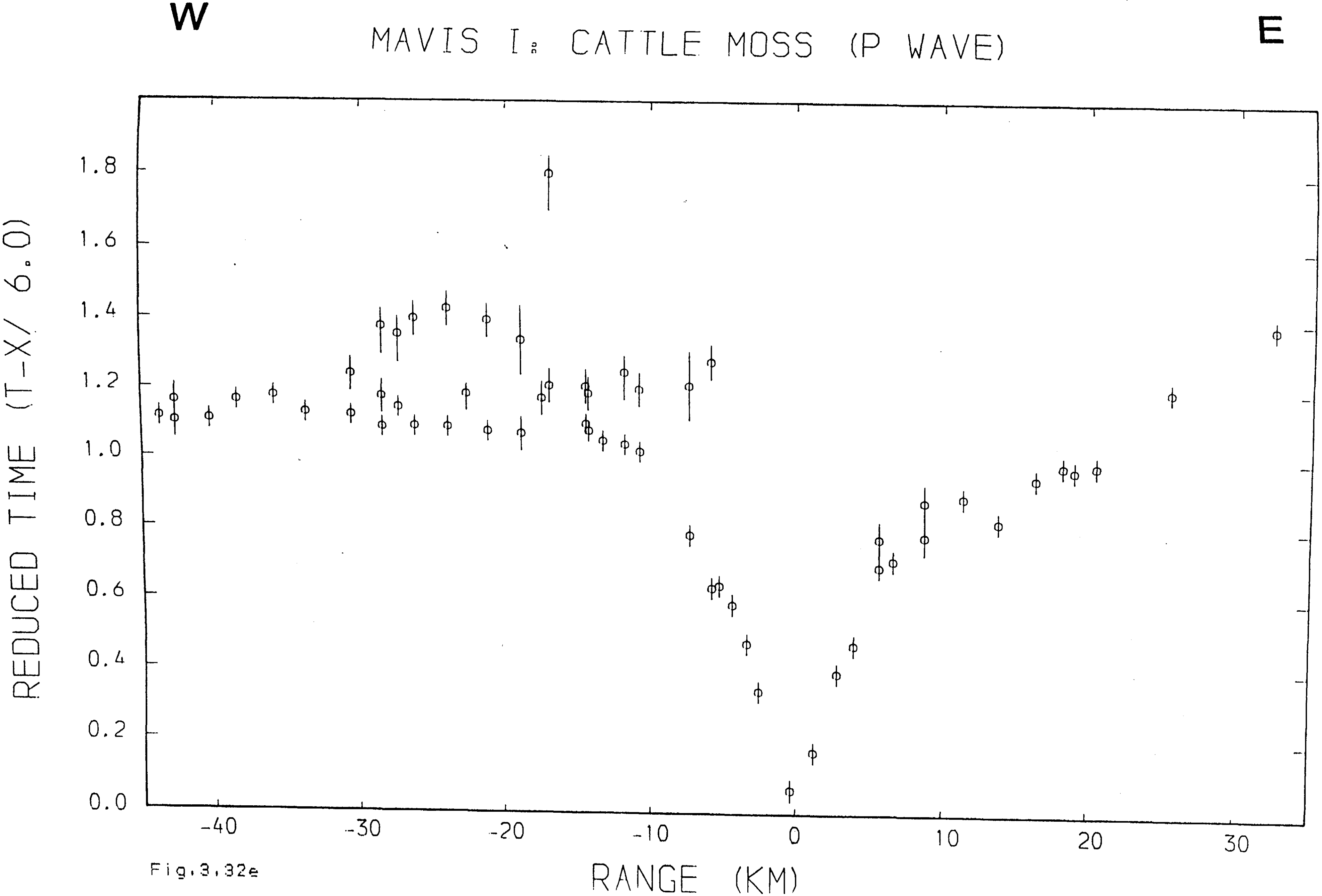
W
MAVIS I: CATTLE MOSS (P WAVE)
E
REDUCED TIME (T-X/ 6.0)
1.8
1.6
1.4
1.2
1.0
0.8
0.6
0.4
0.2
0.0
-40
-30
-20
-10
0
10
20
30
RANGE (KM)

Fig.3.32e

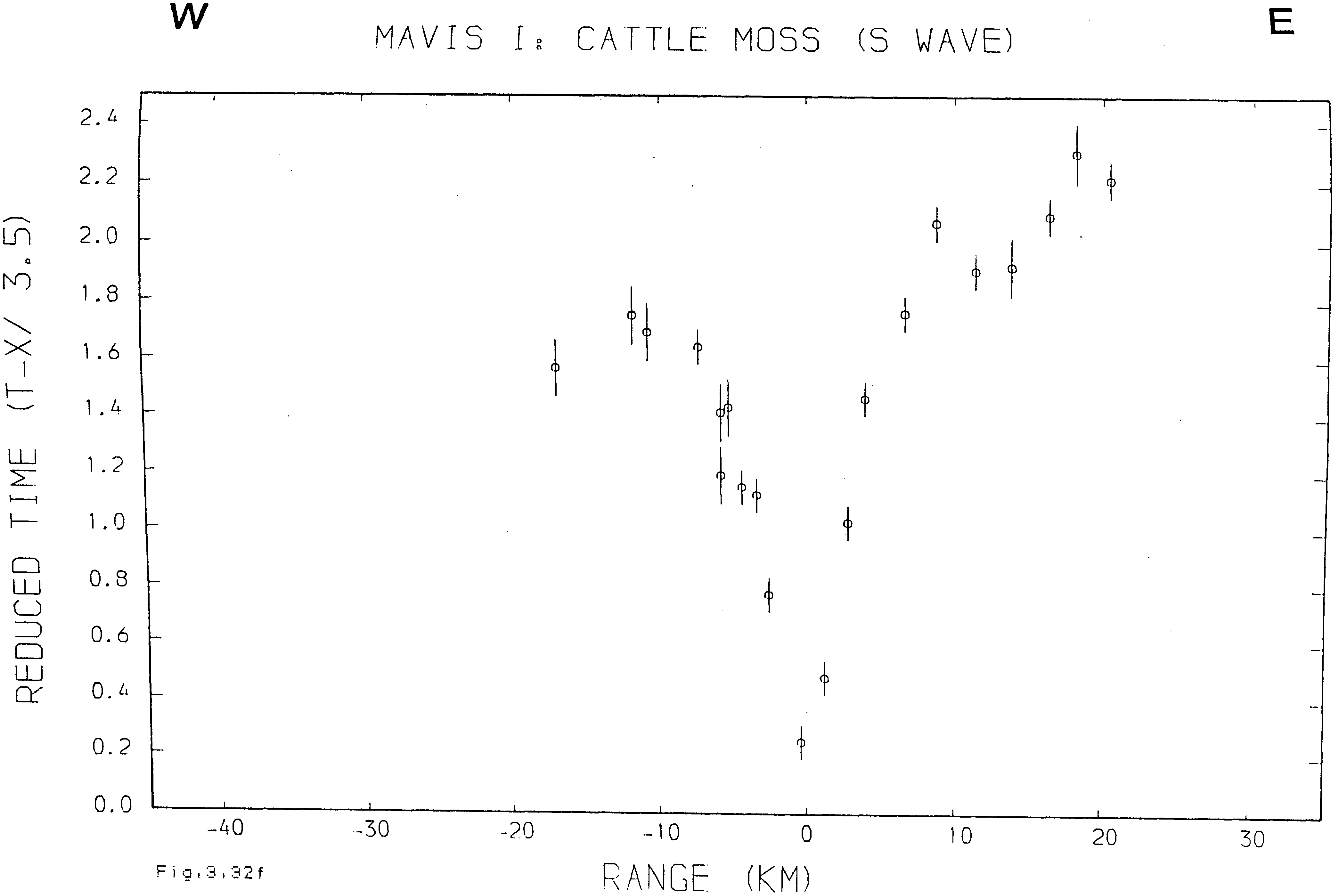
W
E
MAVIS I: CATTLE MOSS (S WAVE)
REDUCED TIME (T-X/ 3.5)
2.4
2.2
2.0
1.8
1.6
1.4
1.2
1.0
0.8
0.6
0.4
0.2
0.0
-40
-30
-20
-10
0
10
20
30
RANGE (KM)

Fig.3.32f

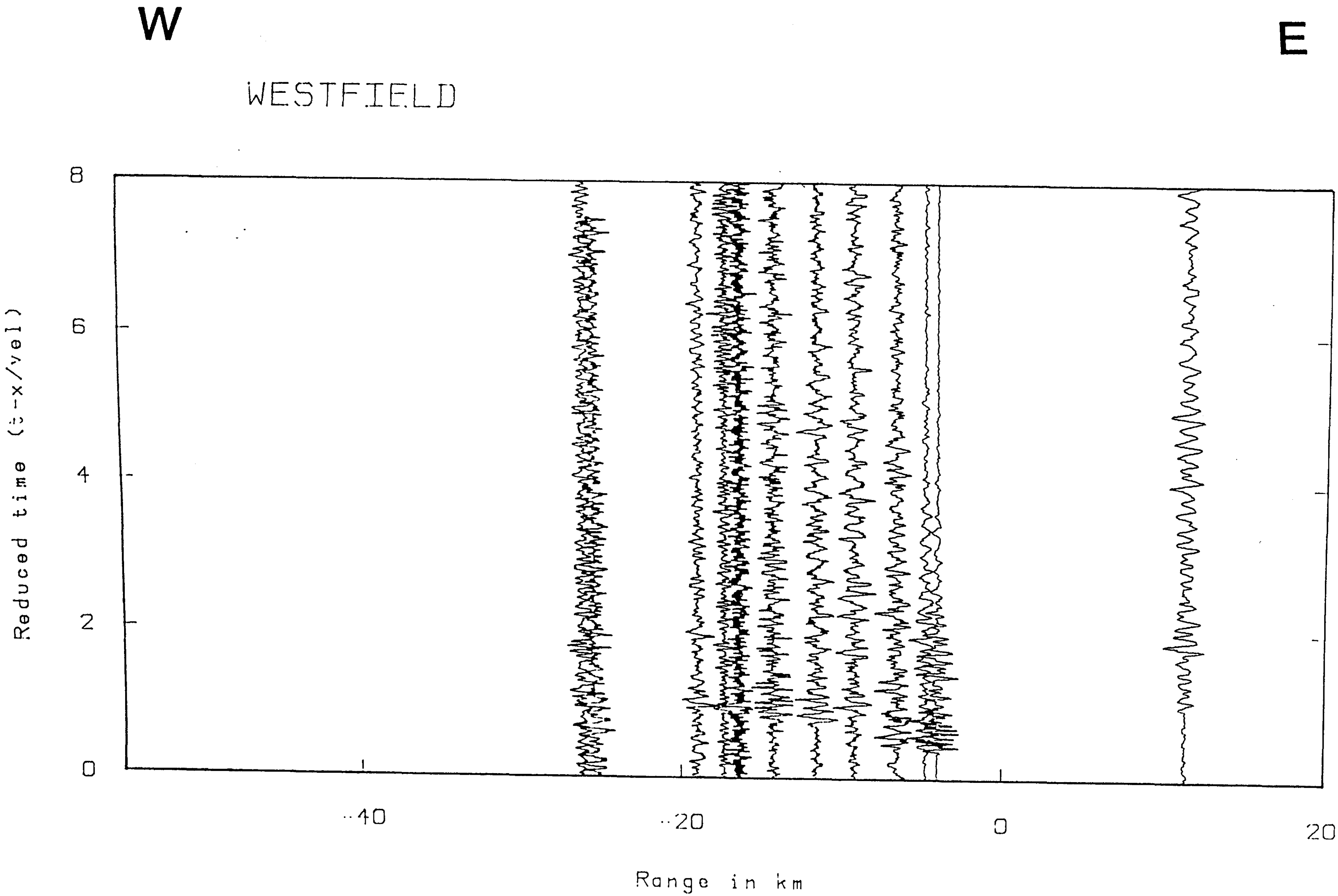

Fig.3.33a Unfiltered time section

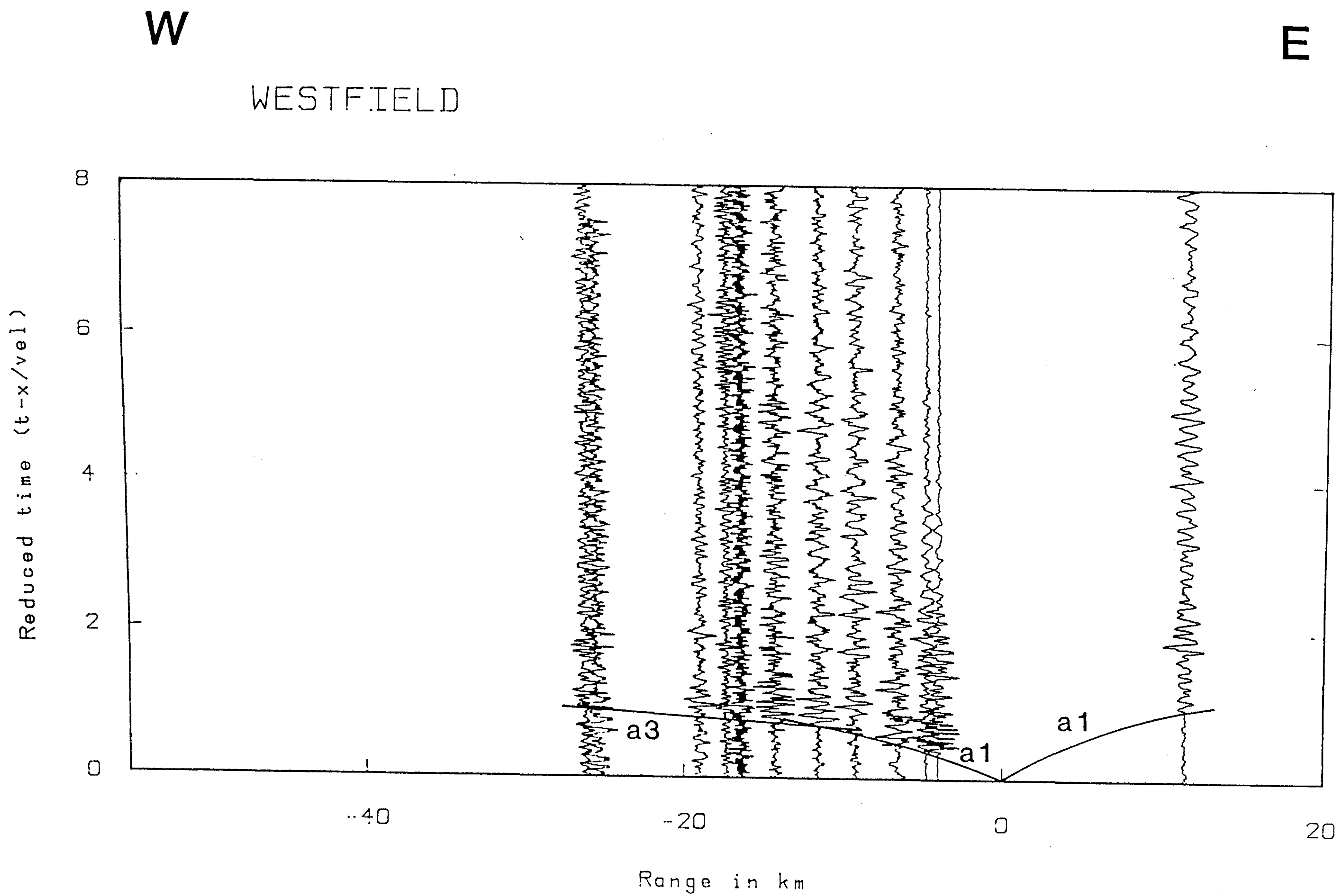

Fig.3.33b

Unfiltered time section

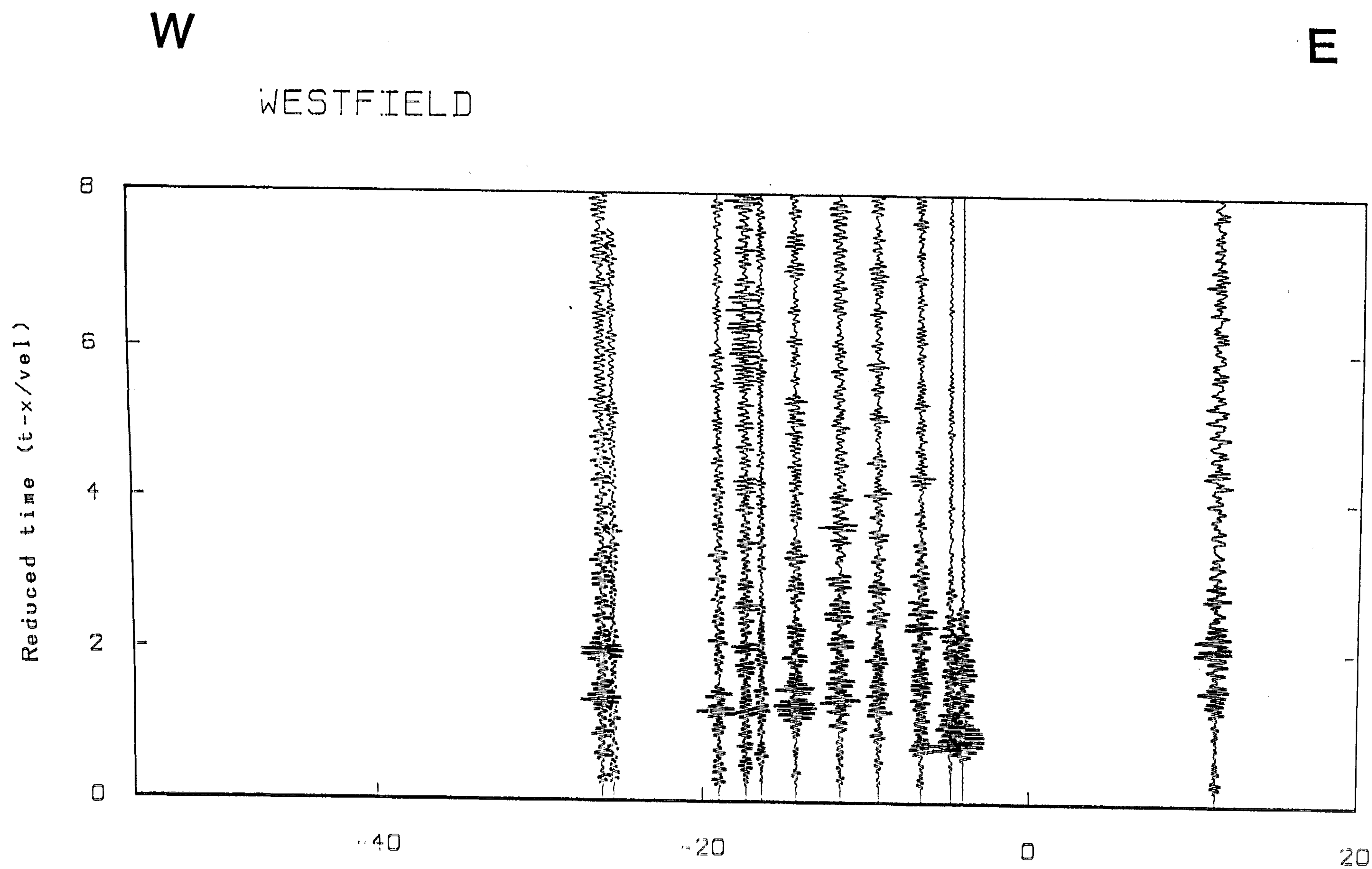

Fig.3.33c Zero-phase, bandpass filter 10.0- 20.0Hz and length 0.50 s with a Hamming window

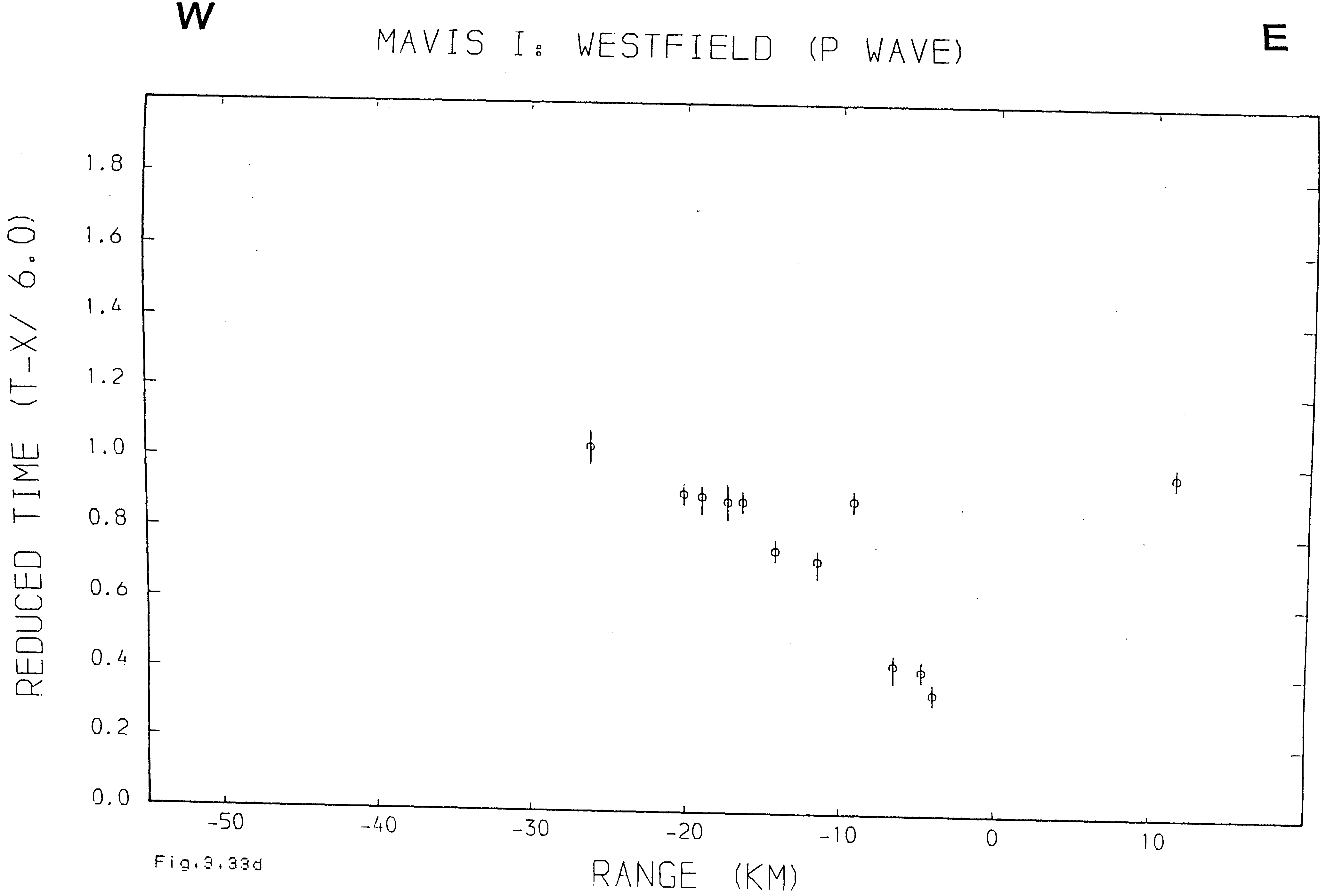
W
MAVIS I: WESTFIELD (P WAVE)
E
REDUCED TIME (T-X/ 6.0)
1.8
1.6
1.4
1.2
1.0
0.8
0.6
0.4
0.2
0.0
-50
-40
-30
-20
-10
0
10
RANGE (KM)

Fig.3.33d

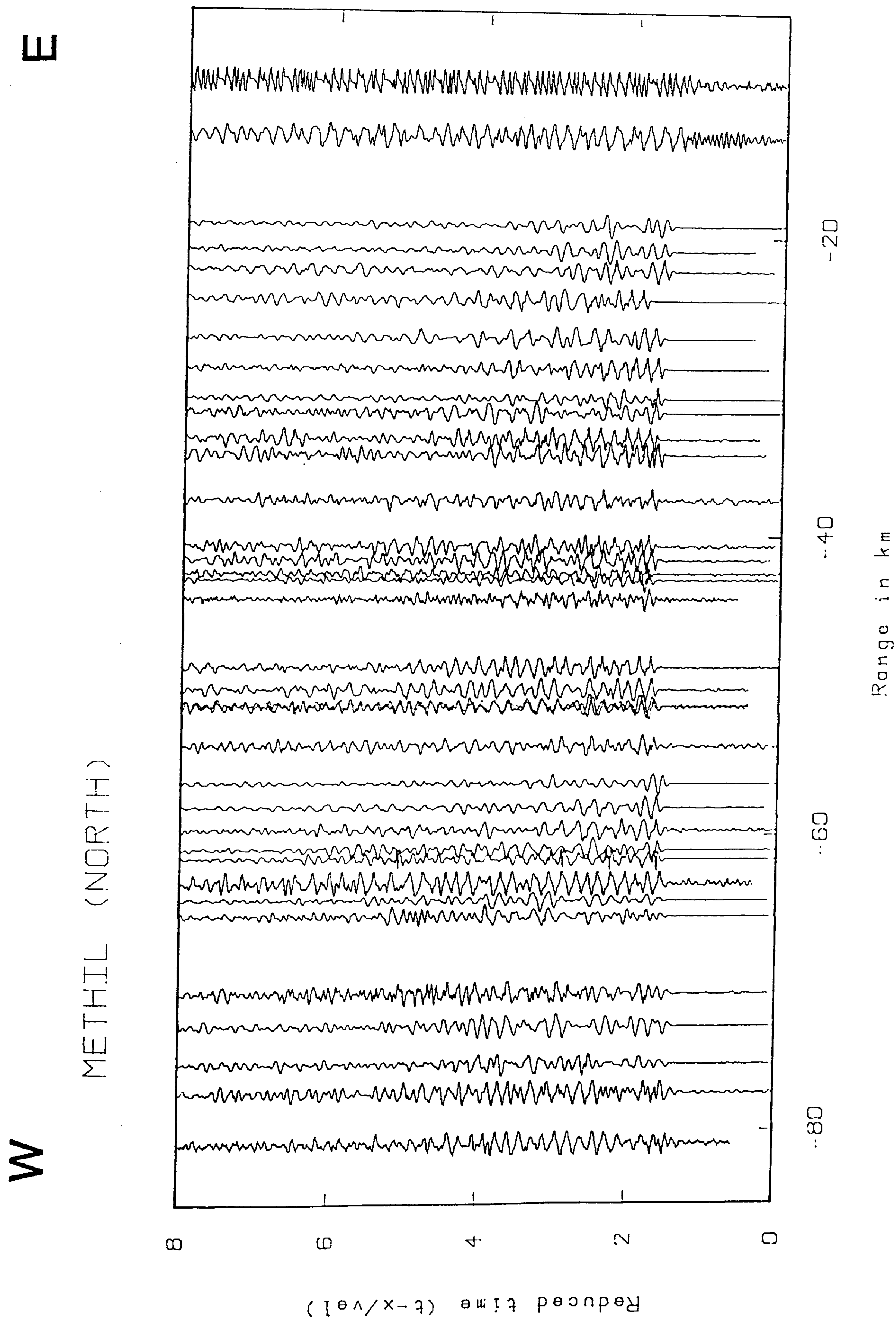

Unfiltered time section

Fig.3.34a

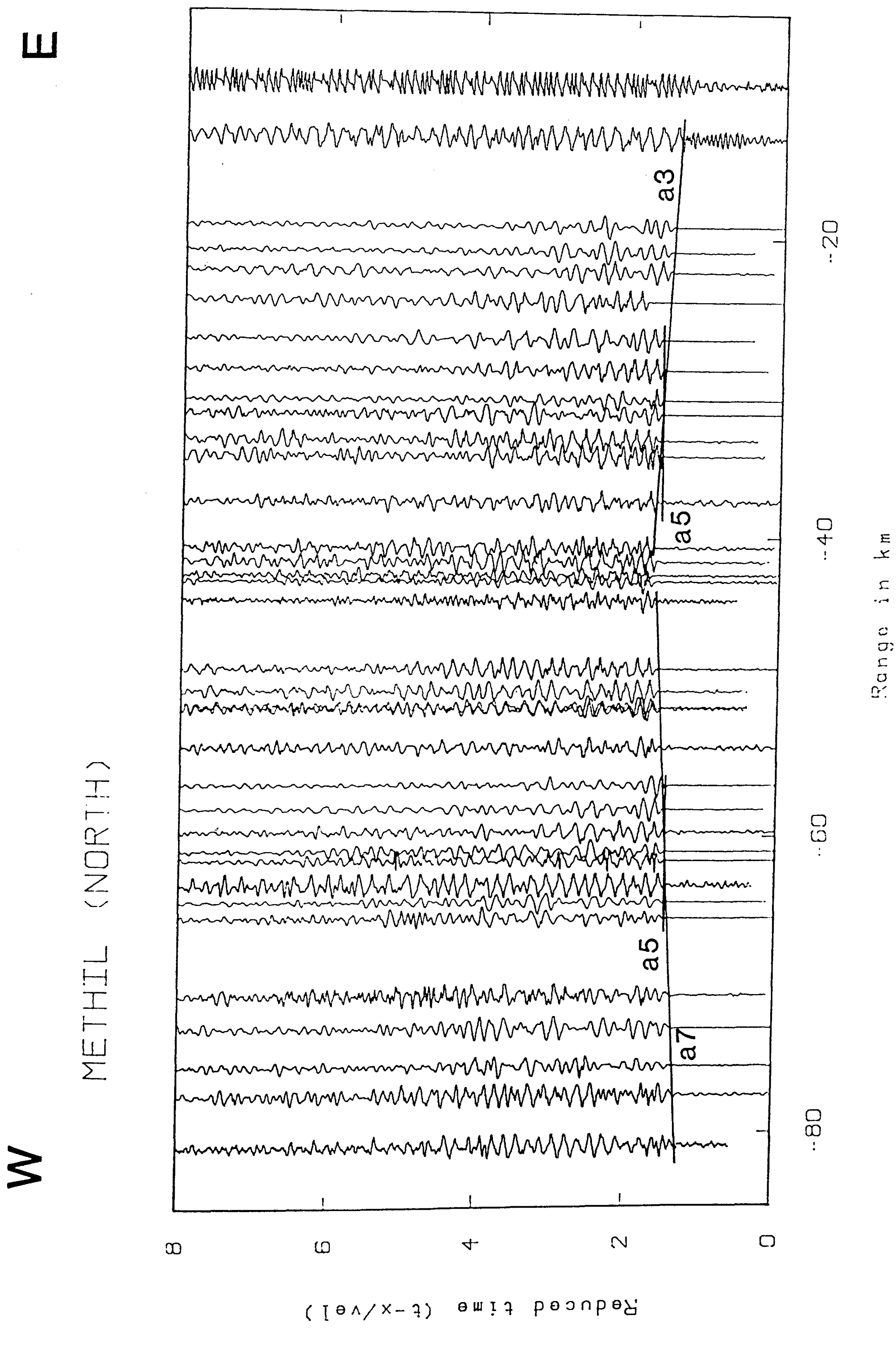

Unfiltered time section

Fig.3.34b

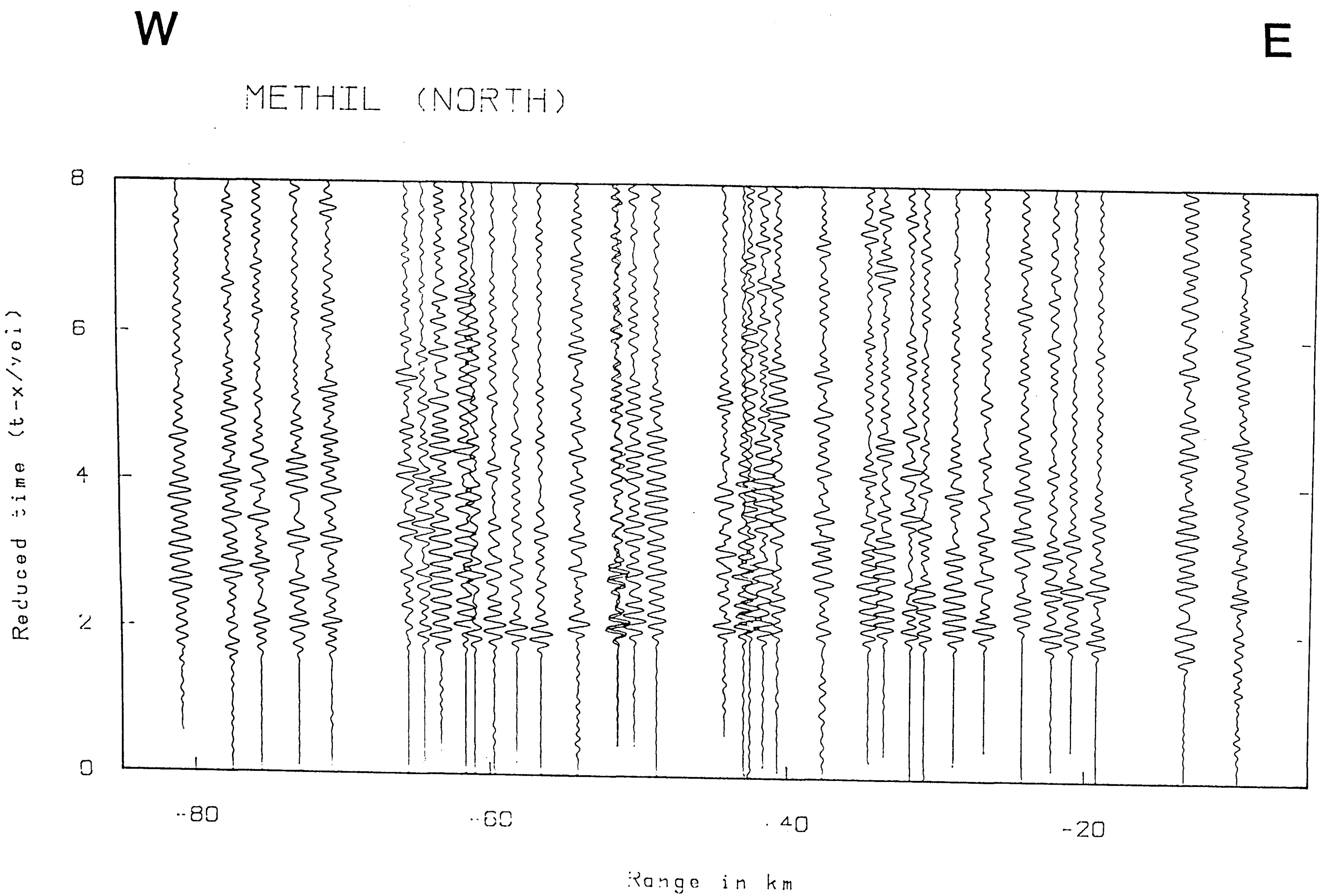

Fig.3.34c Zero-phase. bandpass filter 4.0- 8.0Hz and length 0.50 s with a Hamming window

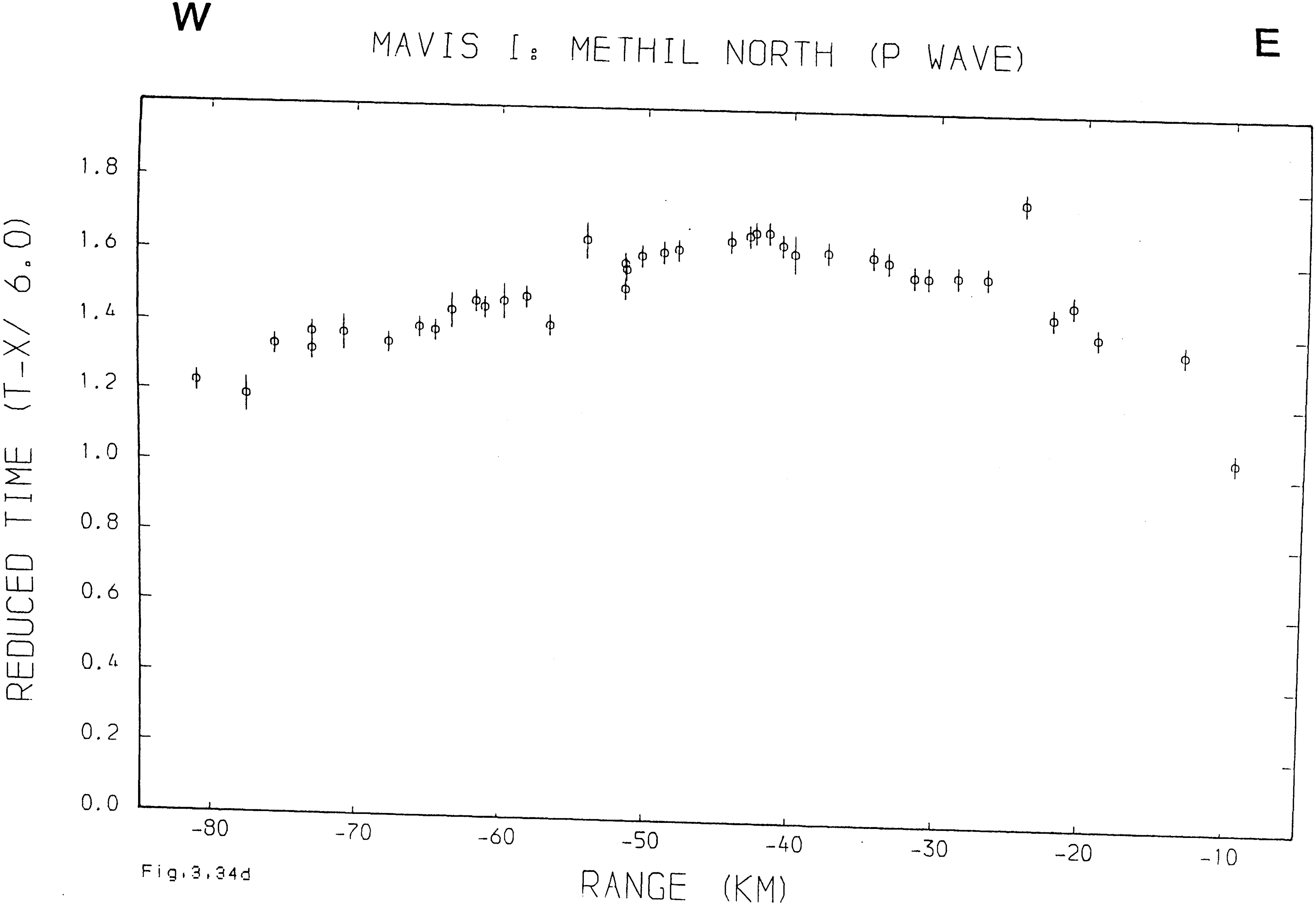
W
MAVIS I: METHIL NORTH (P WAVE)
E
REDUCED TIME (T-X/ 6.0)
1.8
1.6
1.4
1.2
1.0
0.8
0.6
0.4
0.2
0.0
-80
-70
-60
-50
-40
-30
-20
-10
RANGE (KM)

Fig.3.34d

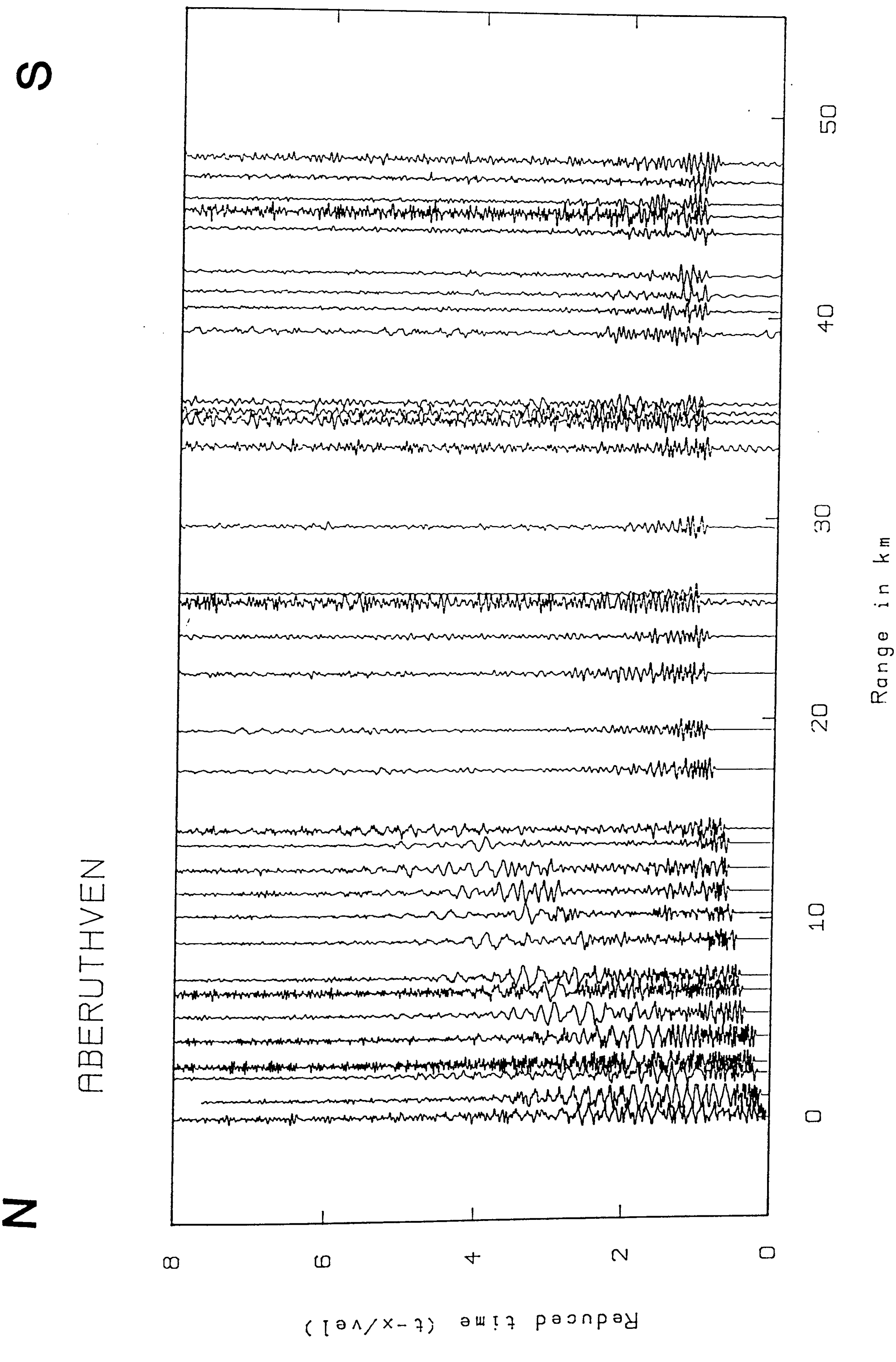

Unfiltered time section

Fig.3.35a

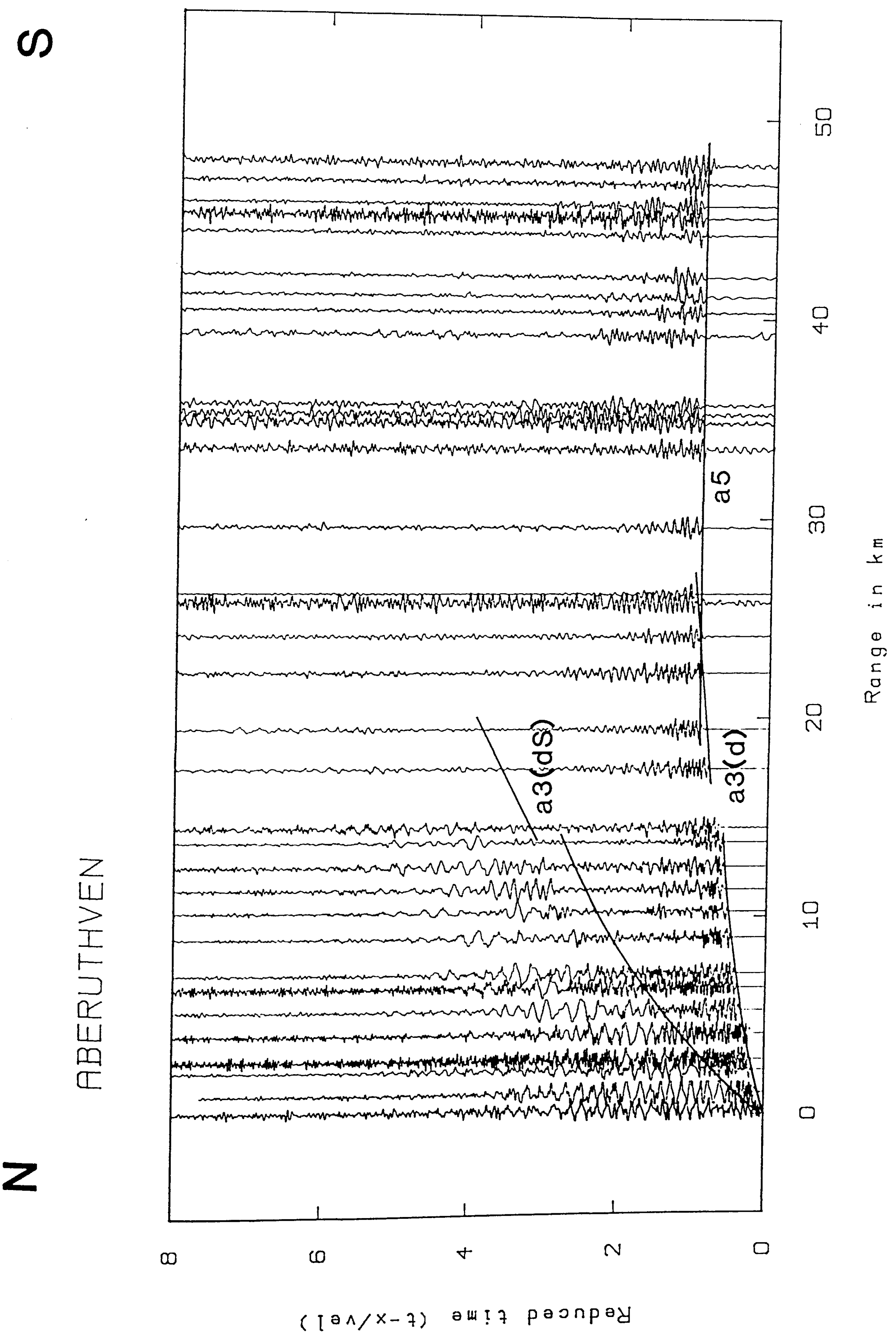

Unfiltered time section

Fig.3.35b

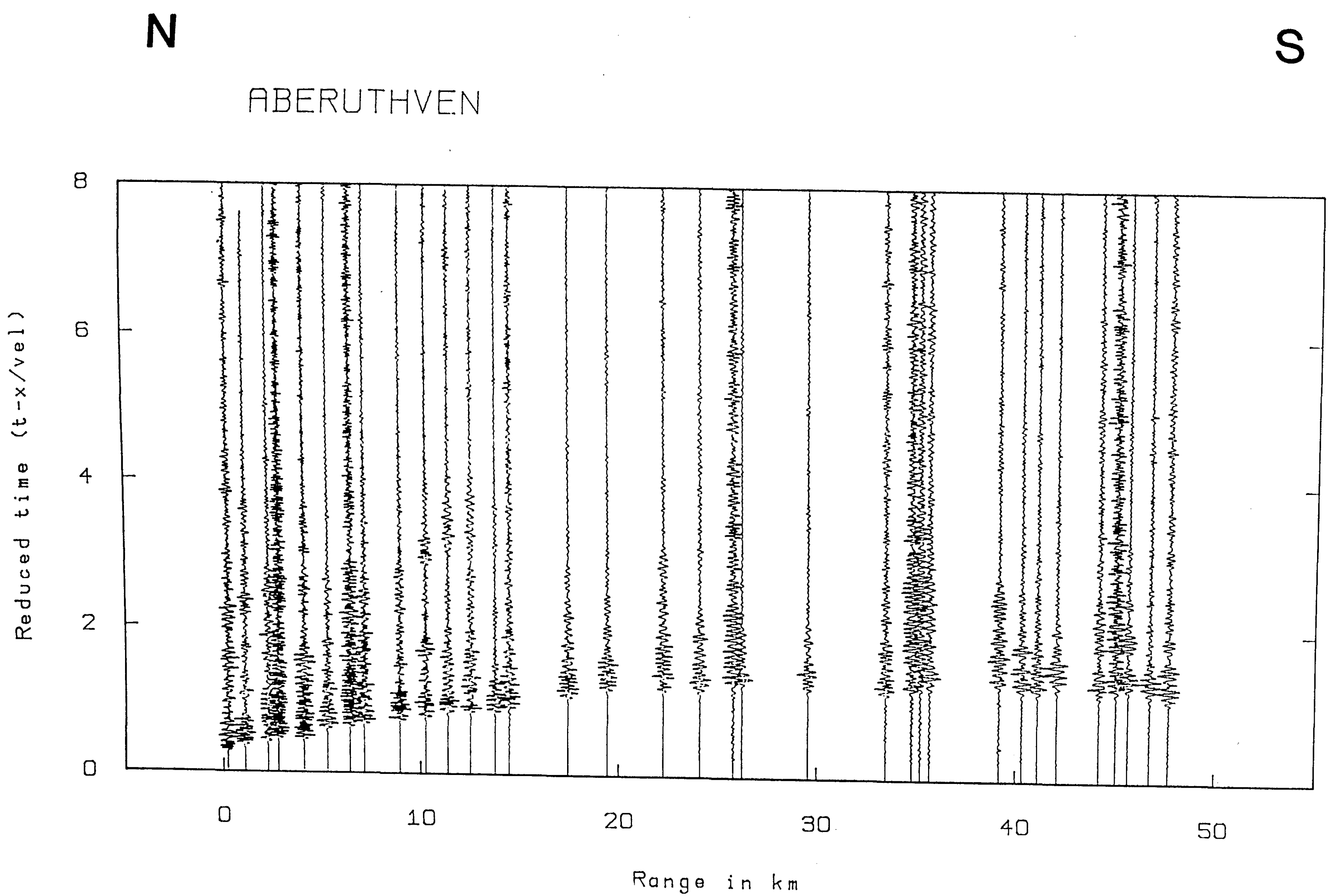

Fig.3.35c Zero-phase, highpass filter 10.0Hz and length 0.50 s with a Hamming window

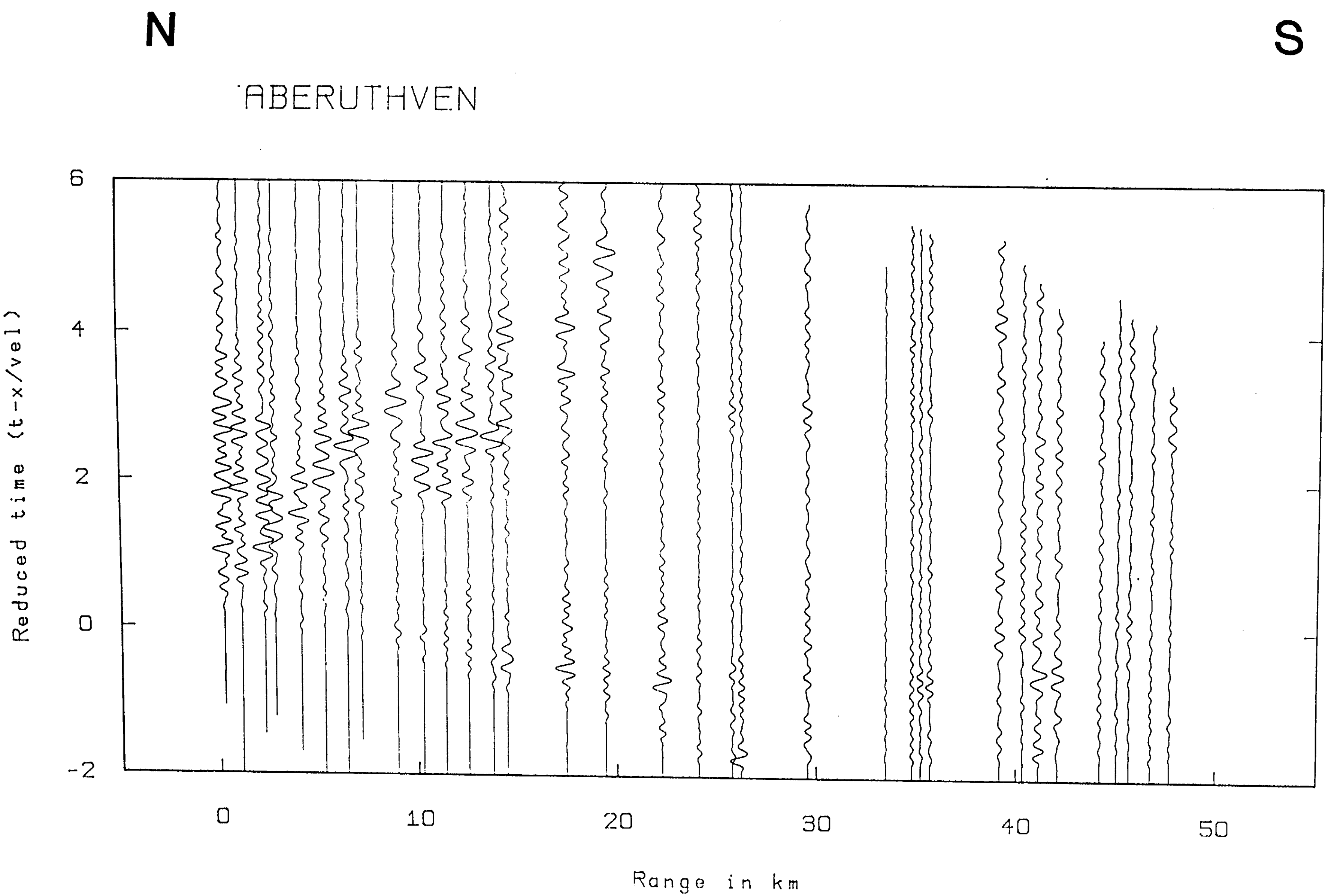

Fig.3.35d Zero-phase, lowpass filter 6.0Hz and length 0.50 s with a Hamming window

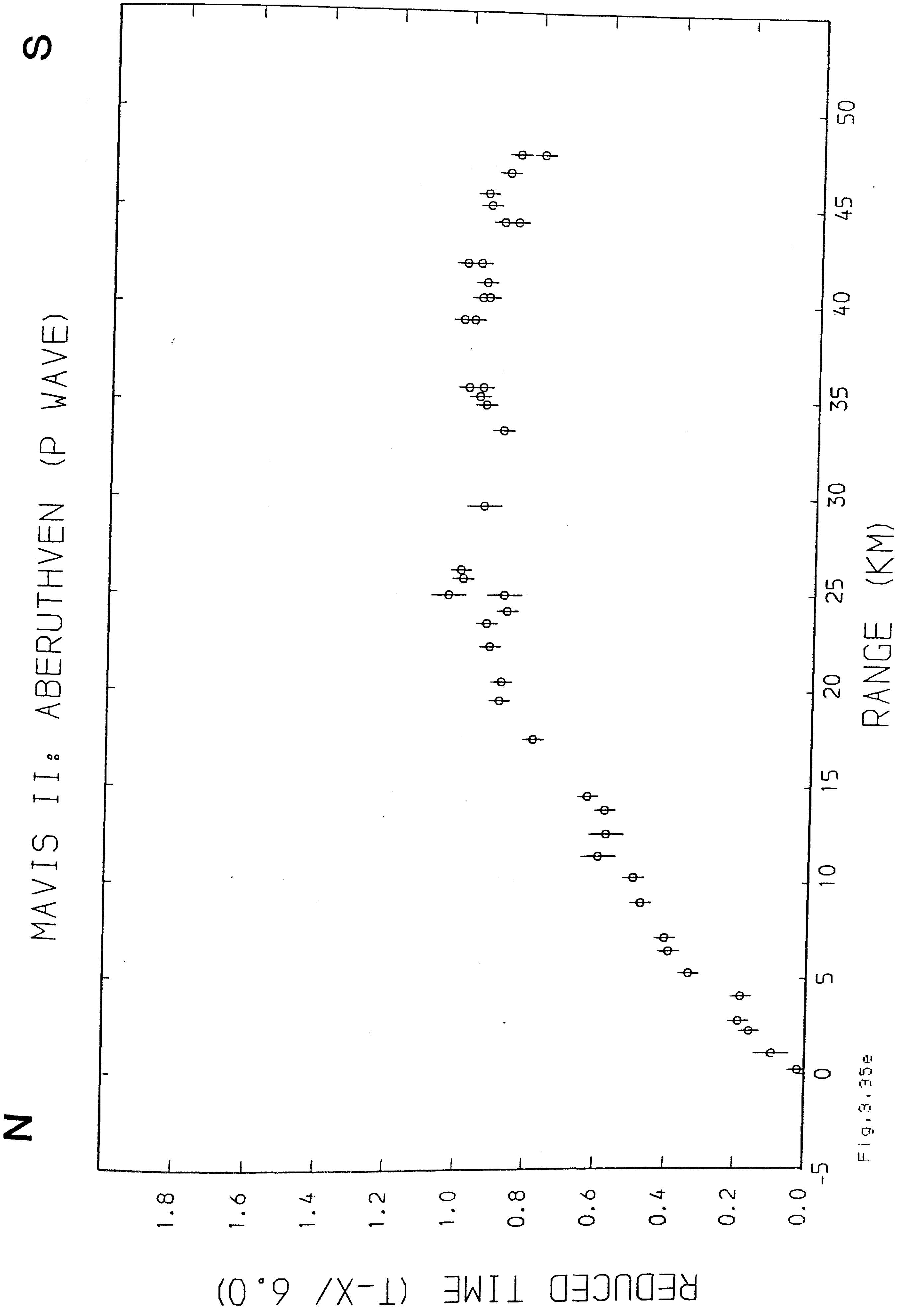
MAVIS II: ABERUTHVEN (P WAVE)
N
S
RANGE (KM)
REDUCED TIME (T-X/ 6.0)
-5
0
5
10
15
20
25
30
35
40
45
50
0.0
0.2
0.4
0.6
0.8
1.0
1.2
1.4
1.6
1.8

Fig.3.35e

MAVIS II: ABERUTHVEN (S WAVE)

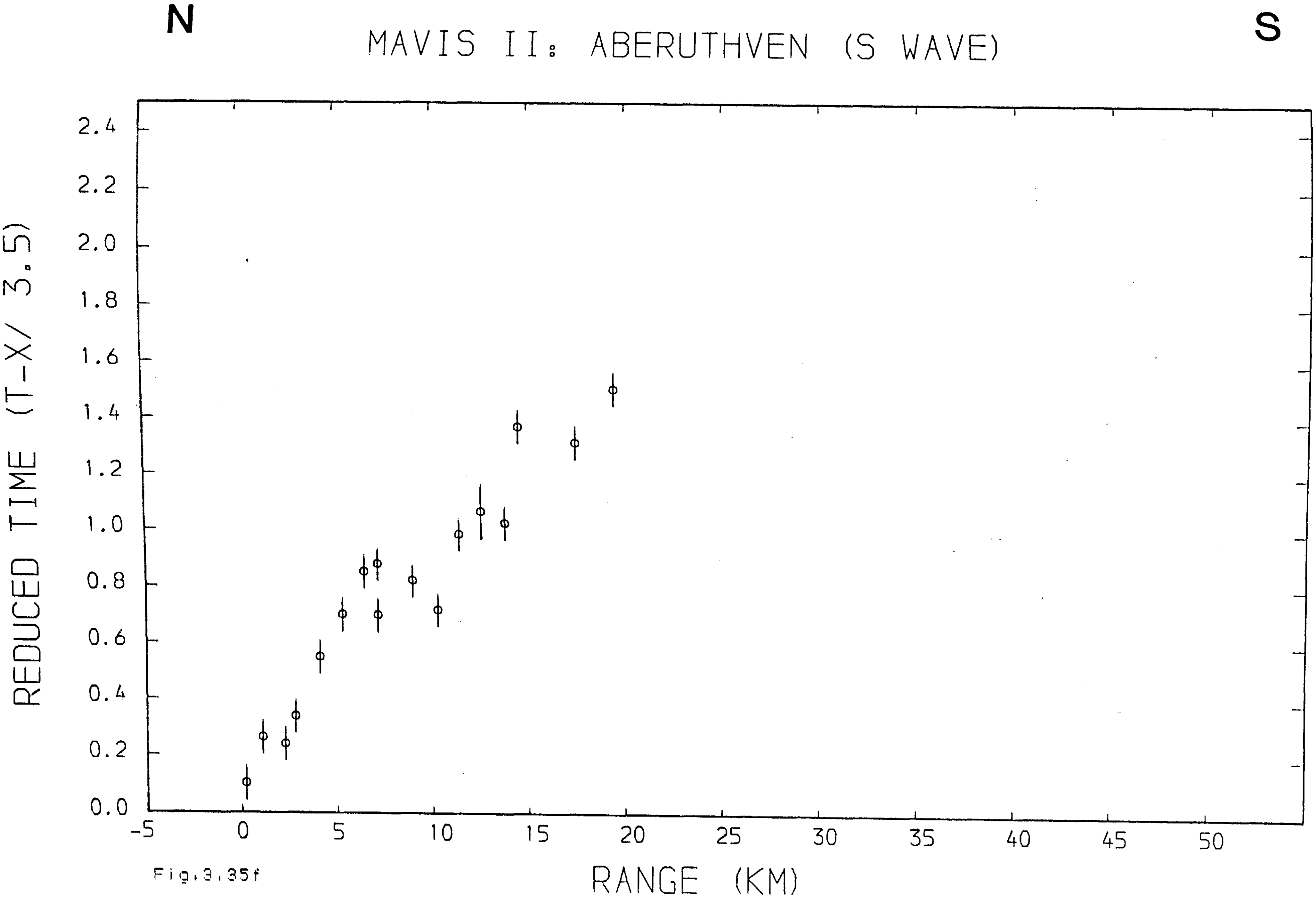

Fig.3.35f

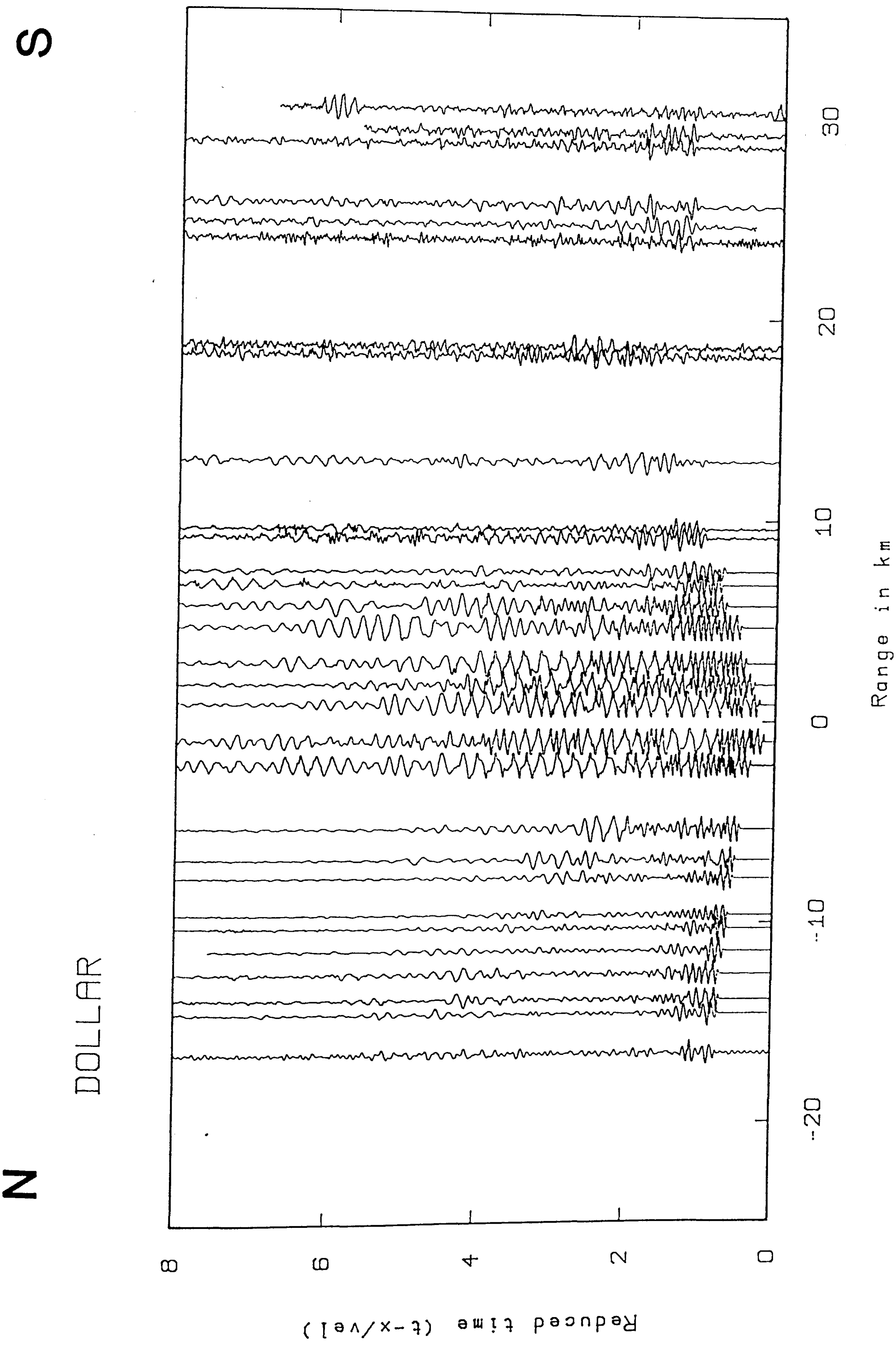

Unfiltered time section

Fig.3.36a

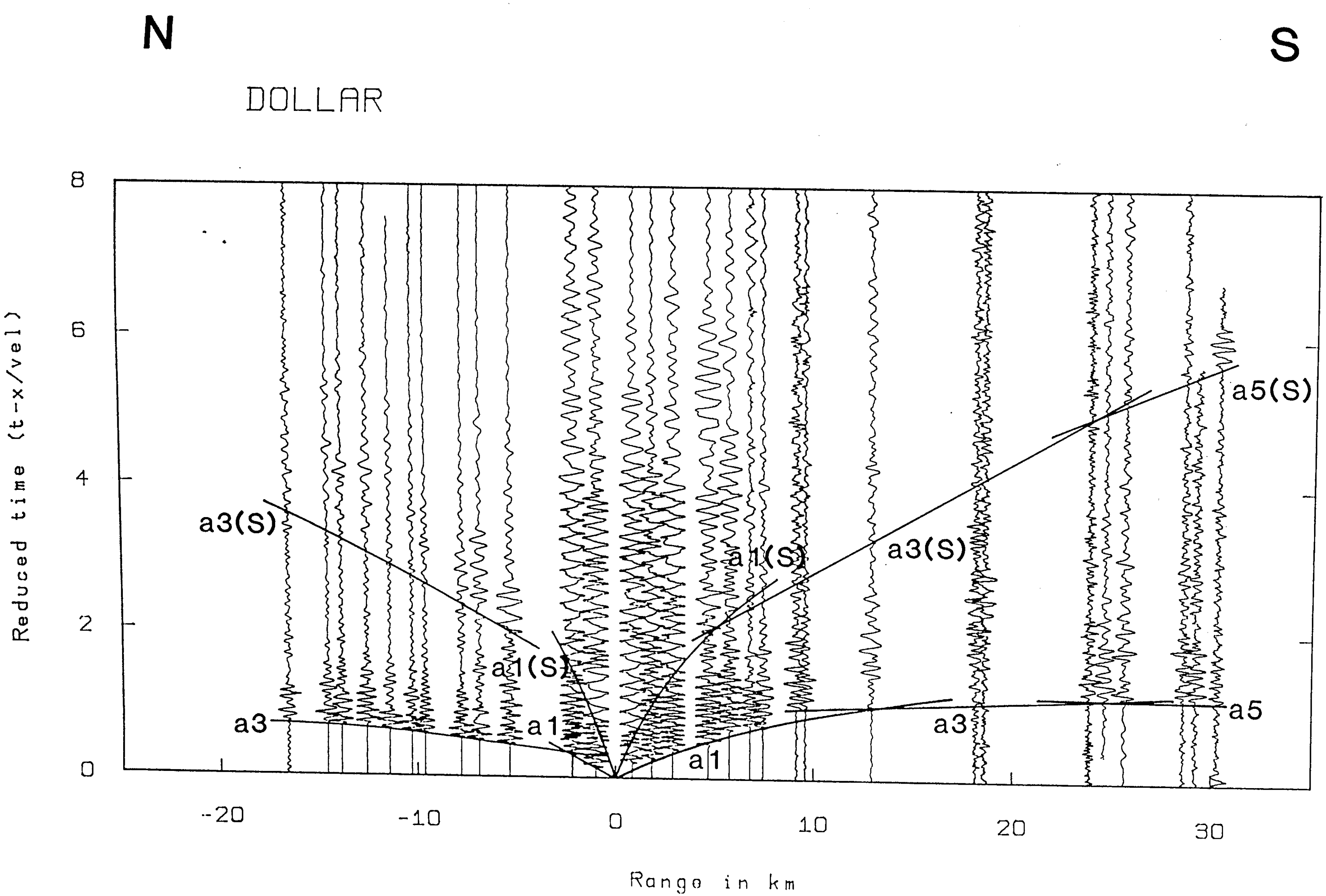

Fig.3.36b

Unfiltered time section

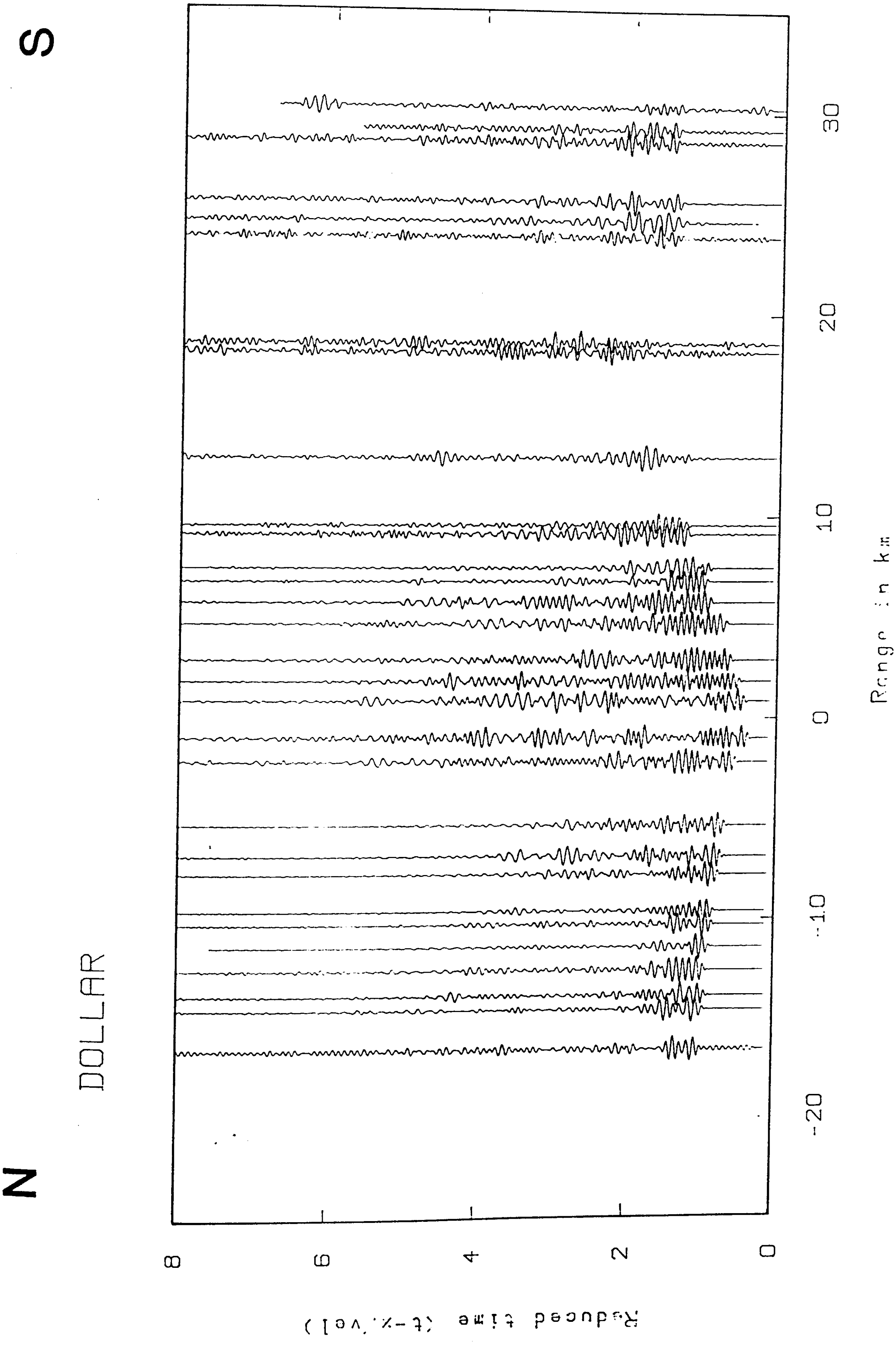

Fig.3.36c Zero-phase, bandpass filter 6.0- 16.0Hz and length 0.50 s with a Hamming window

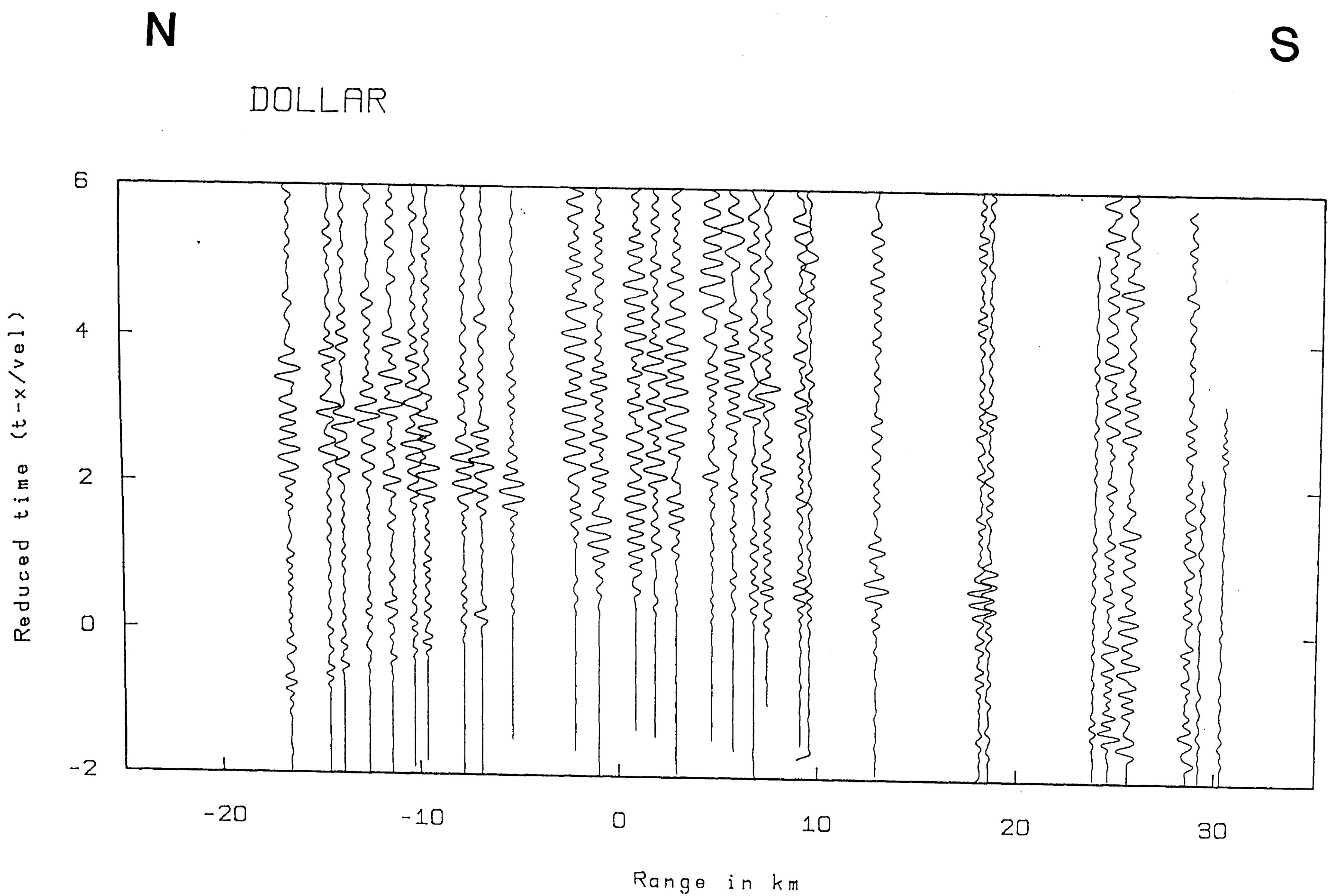

Fig.3.36d Zero-phase, lowpass filter 6.0Hz and length 0.50 s with a Hamming window

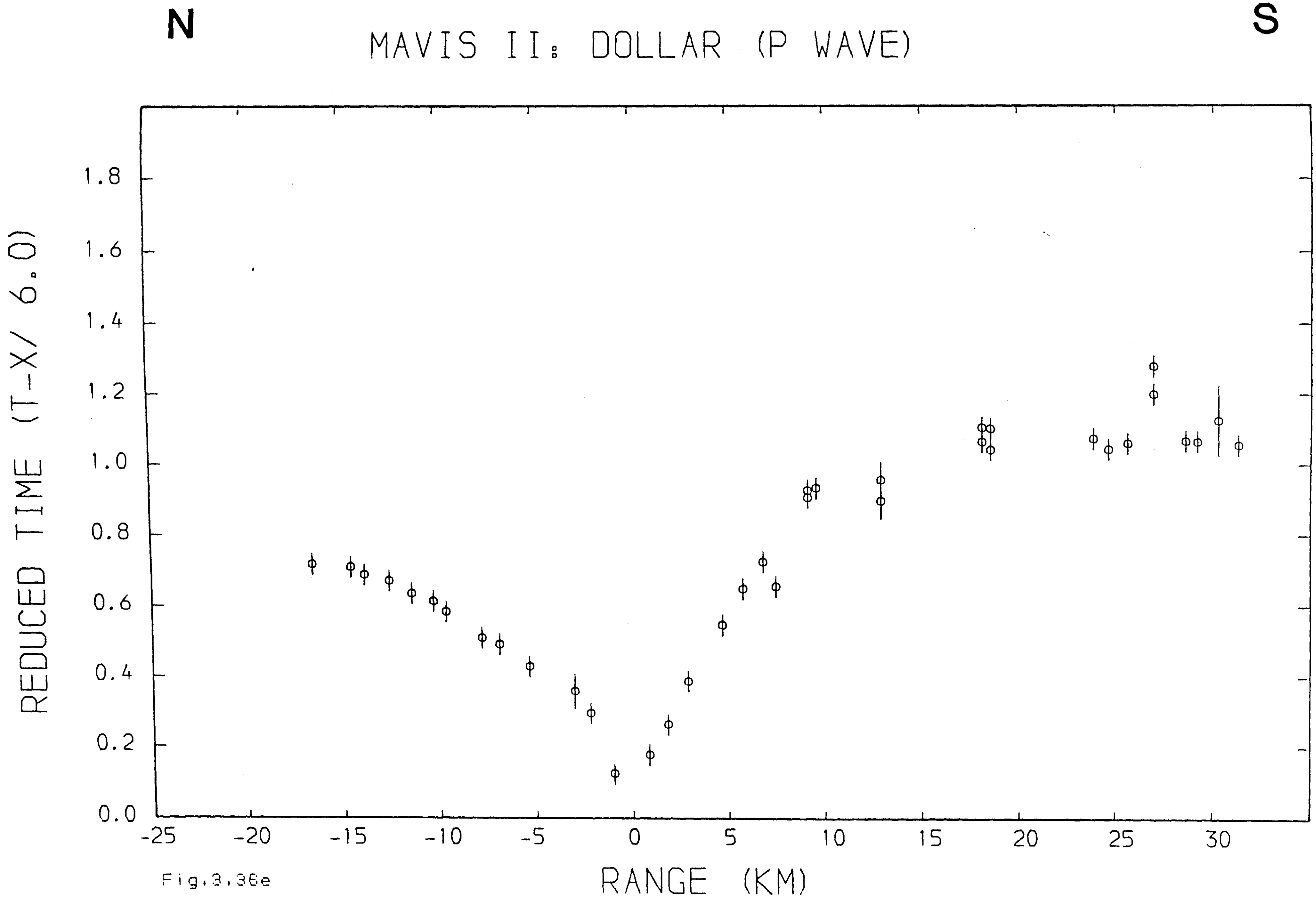
N
S
MAVIS II: DOLLAR (P WAVE)
REDUCED TIME (T-X/ 6.0)
1.8
1.6
1.4
1.2
1.0
0.8
0.6
0.4
0.2
0.0
-25
-20
-15
-10
-5
0
5
10
15
20
25
30
RANGE (KM)

Fig.3.36e

MAVIS II: DOLLAR (S WAVE)

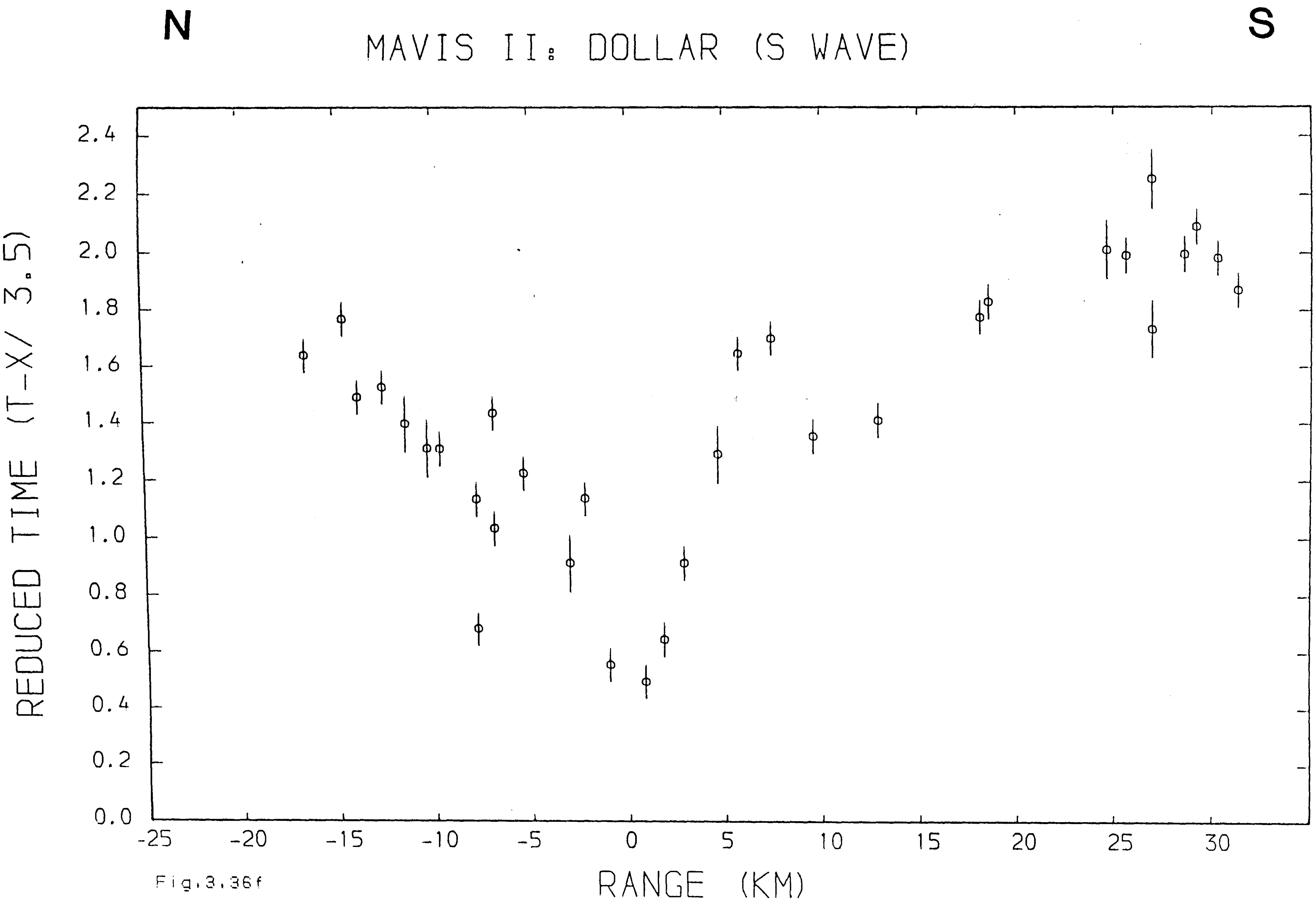

Fig.3.36f

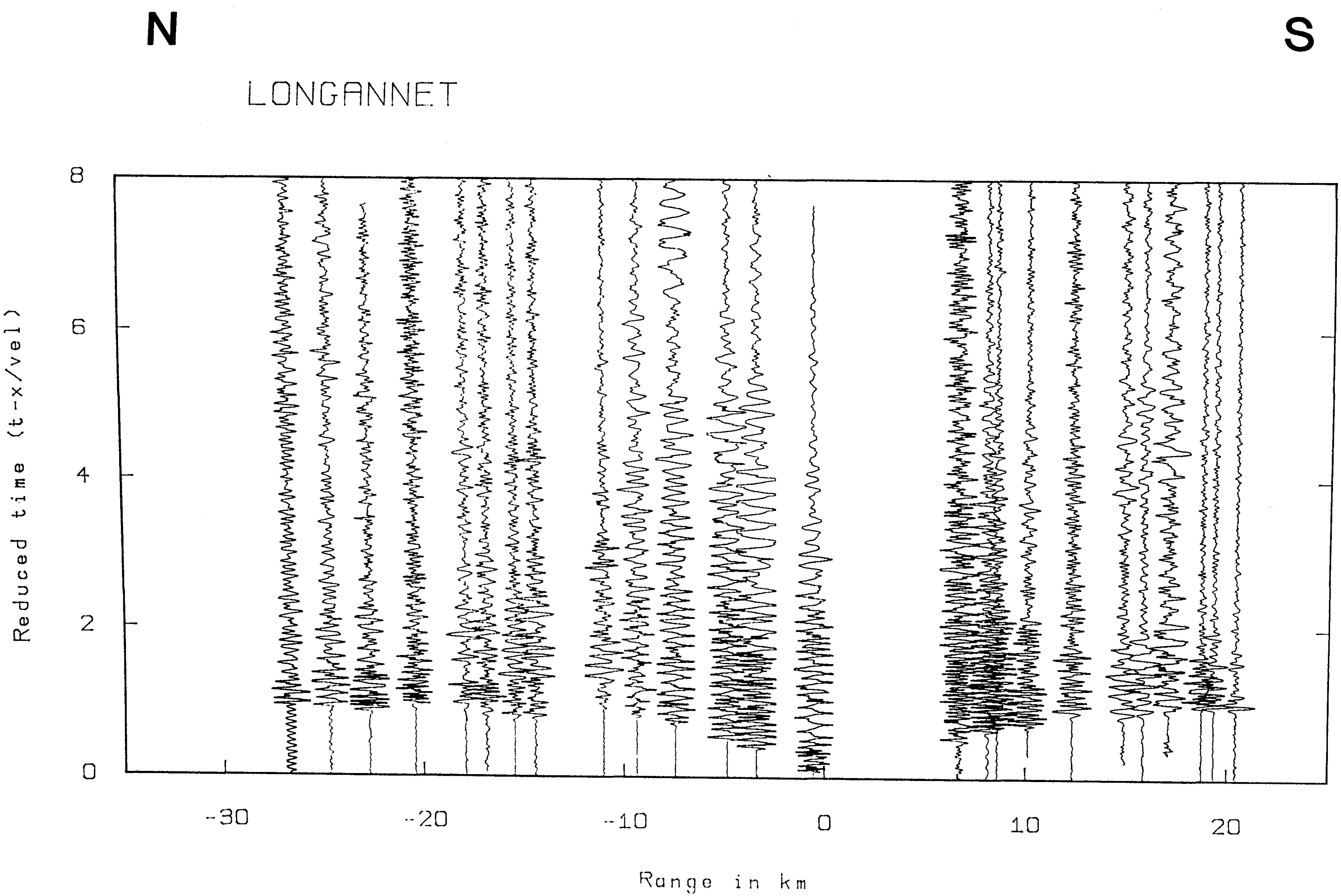

Fig.3.37a Unfiltered time section

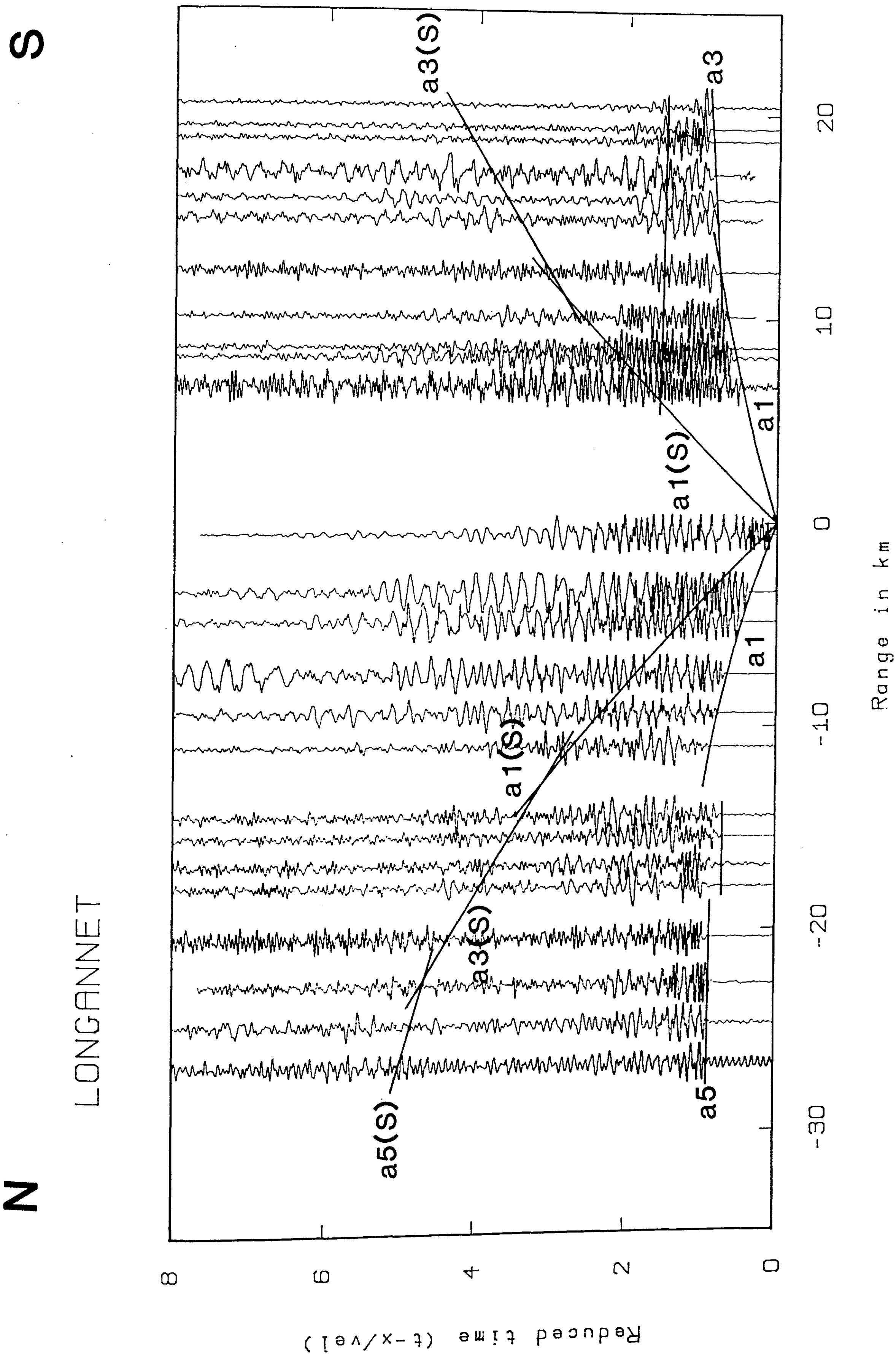

Unfiltered time section

Fig.3.37b

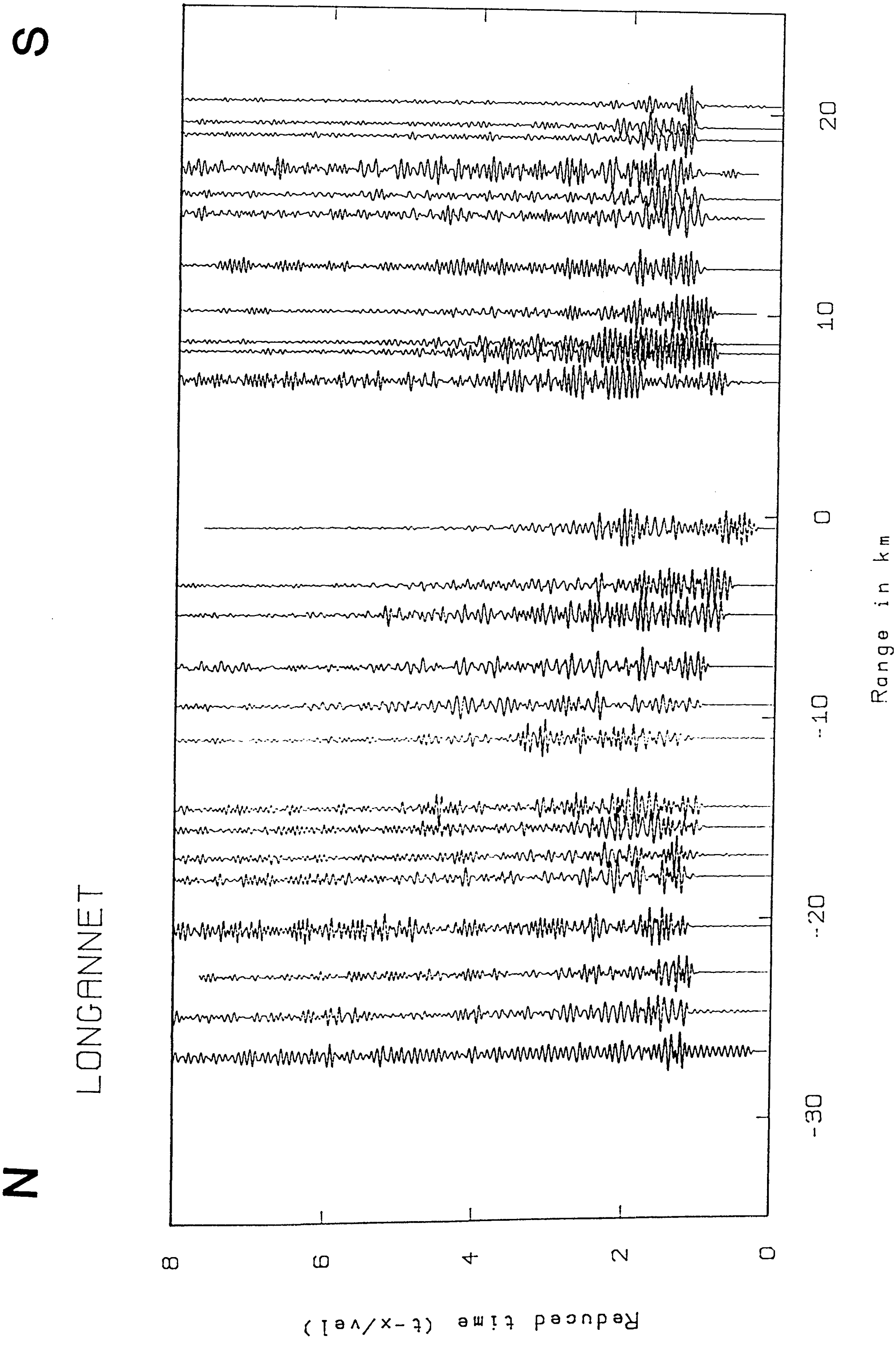

Fig.3.37c Zero-phase, bandpass filter 8.0- 18.0Hz and length 0.50 s with a Hamming window

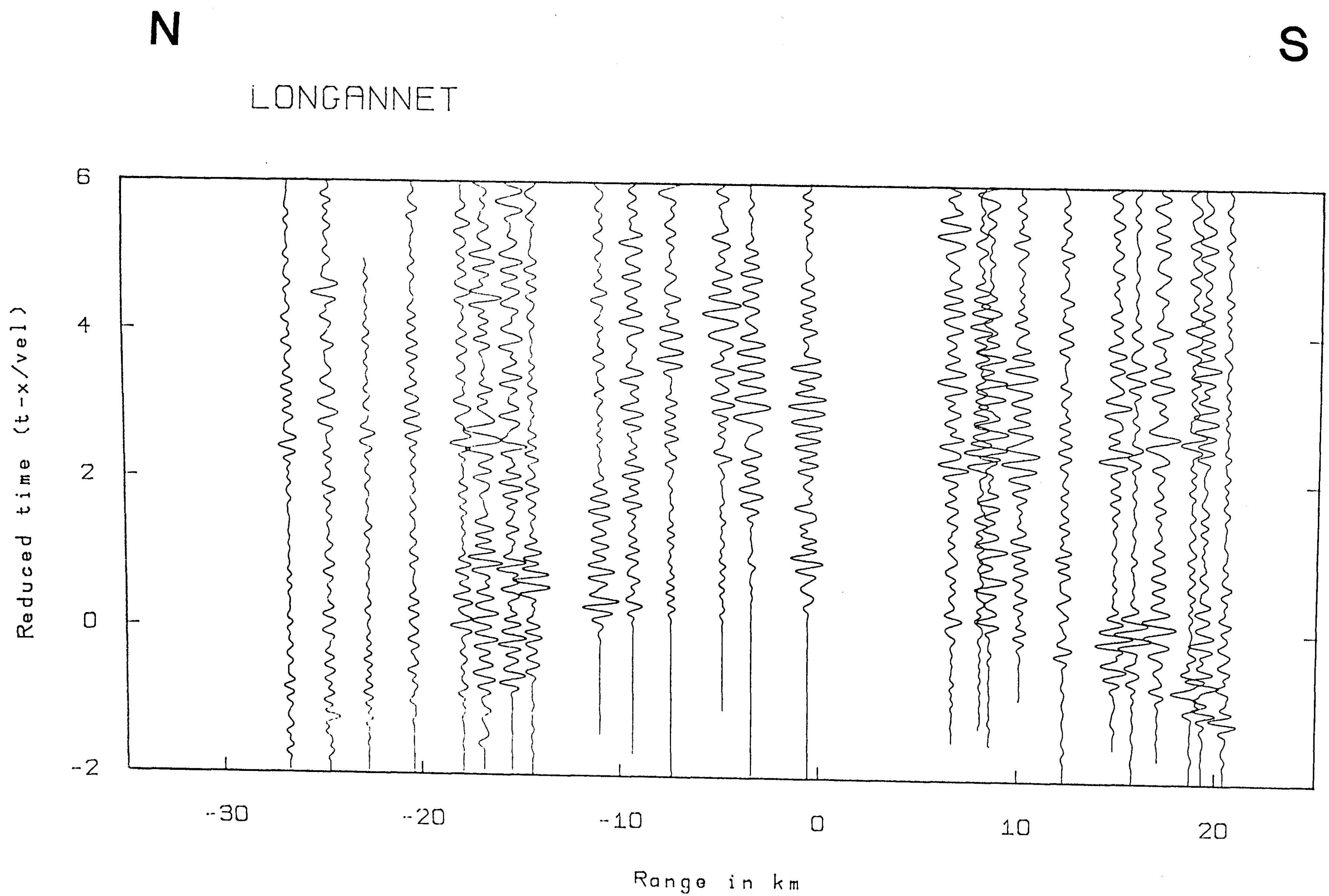

Fig.3.37d Zero-phase, lowpass filter 6.0Hz and length 0.50 s with a Hamming window

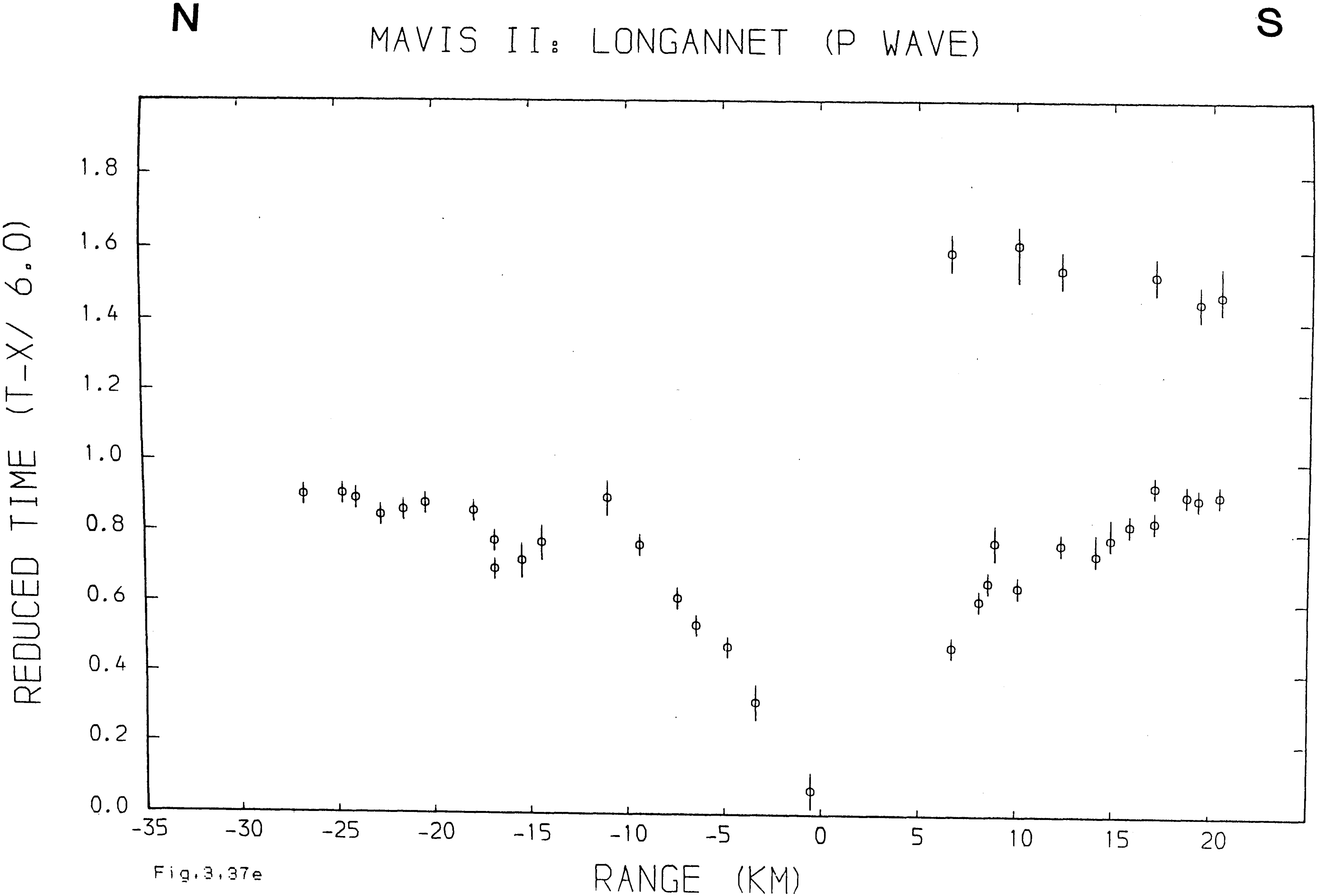
N
S
MAVIS II: LONGANNET (P WAVE)
REDUCED TIME (T-X/ 6.0)
1.8
1.6
1.4
1.2
1.0
0.8
0.6
0.4
0.2
0.0
-35
-30
-25
-20
-15
-10
-5
0
5
10
15
20
RANGE (KM)

Fig.3.37e

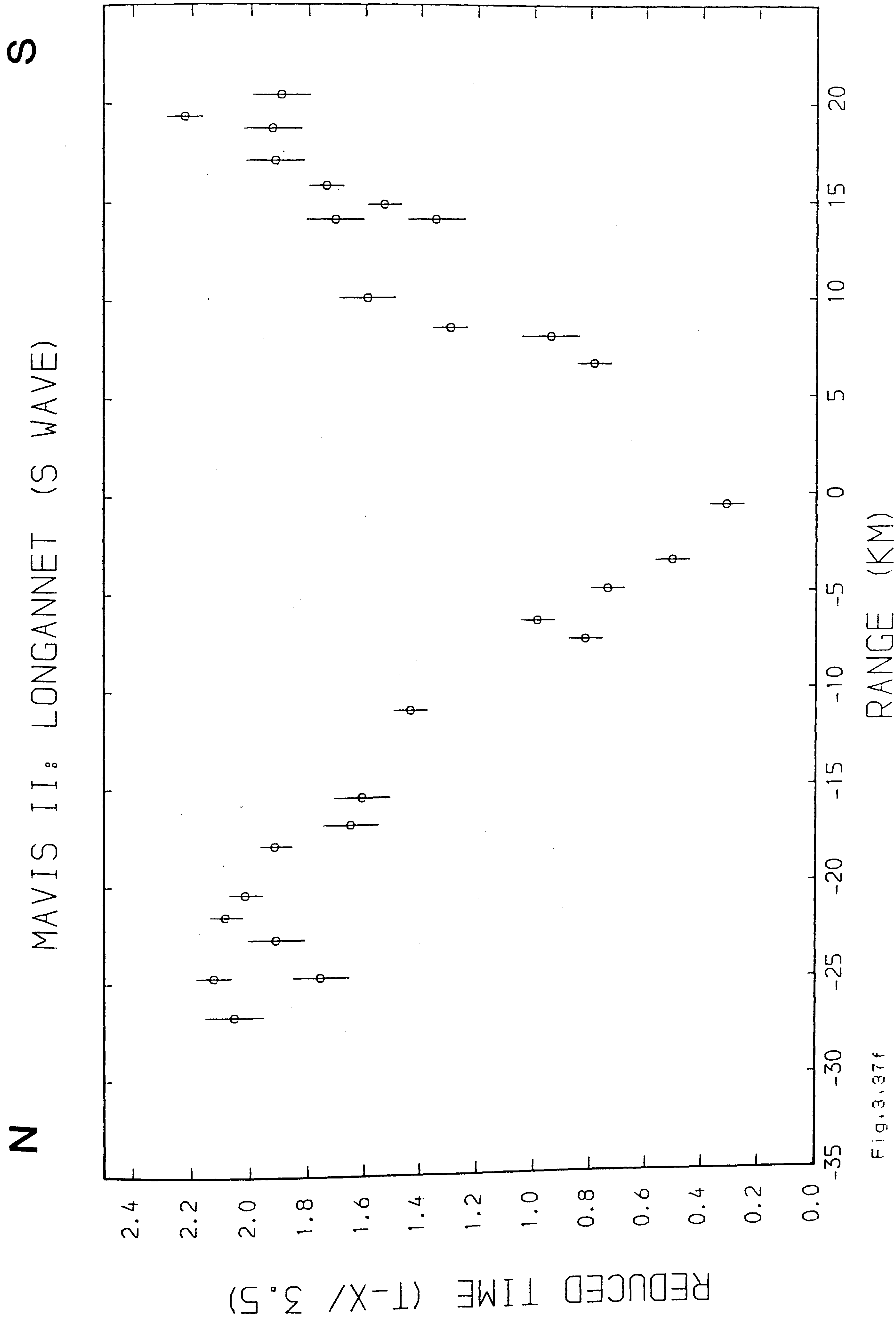
N
S
MAVIS II: LONGANNET (S WAVE)
RANGE (KM)
-35
-30
-25
-20
-15
-10
-5
0
5
10
15
20
REDUCED TIME (T-X/ 3.5)
0.0
0.2
0.4
0.6
0.8
1.0
1.2
1.4
1.6
1.8
2.0
2.2
2.4

Fig.3.37f

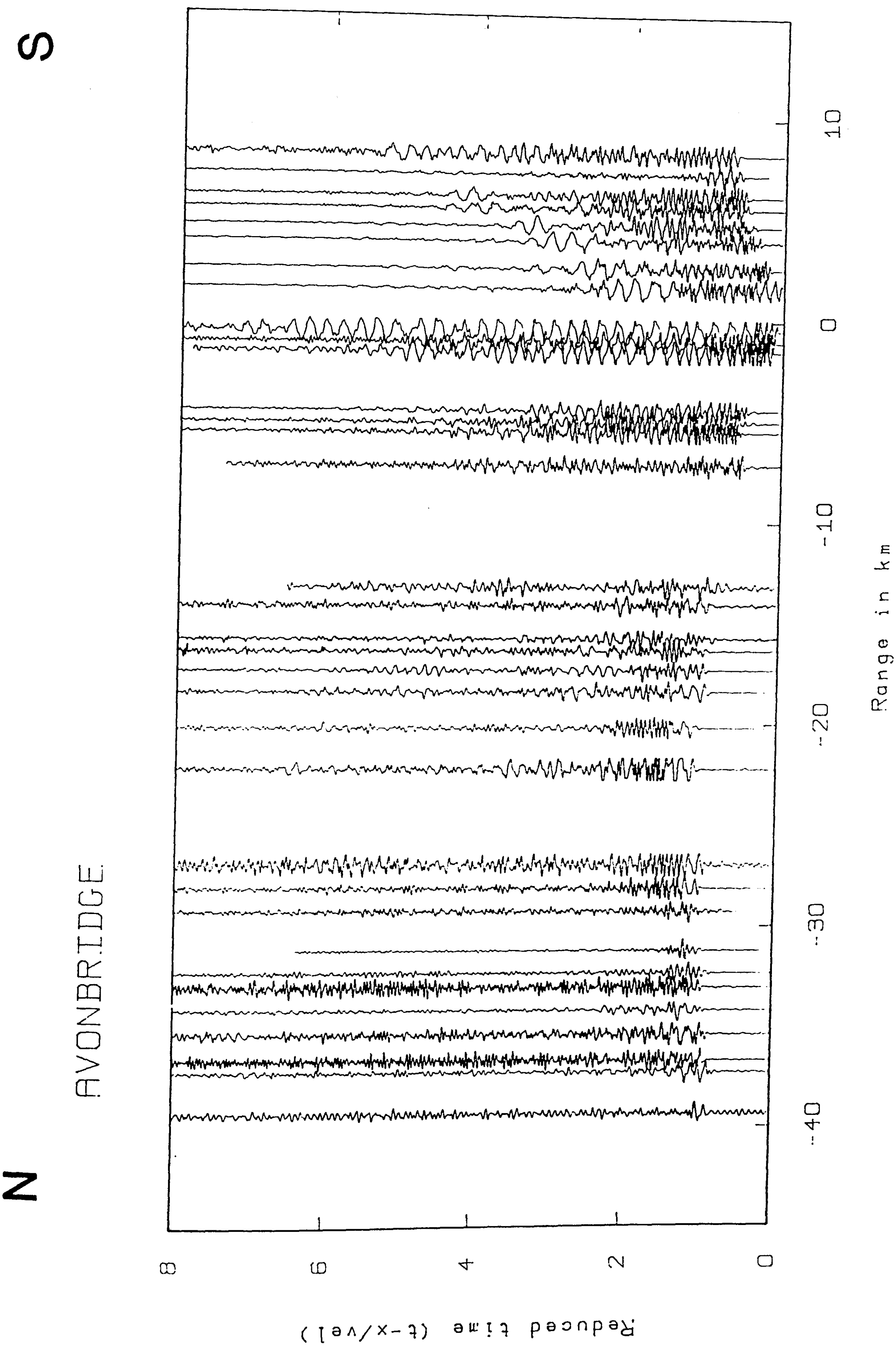

Unfiltered time section

Fig.3.38a

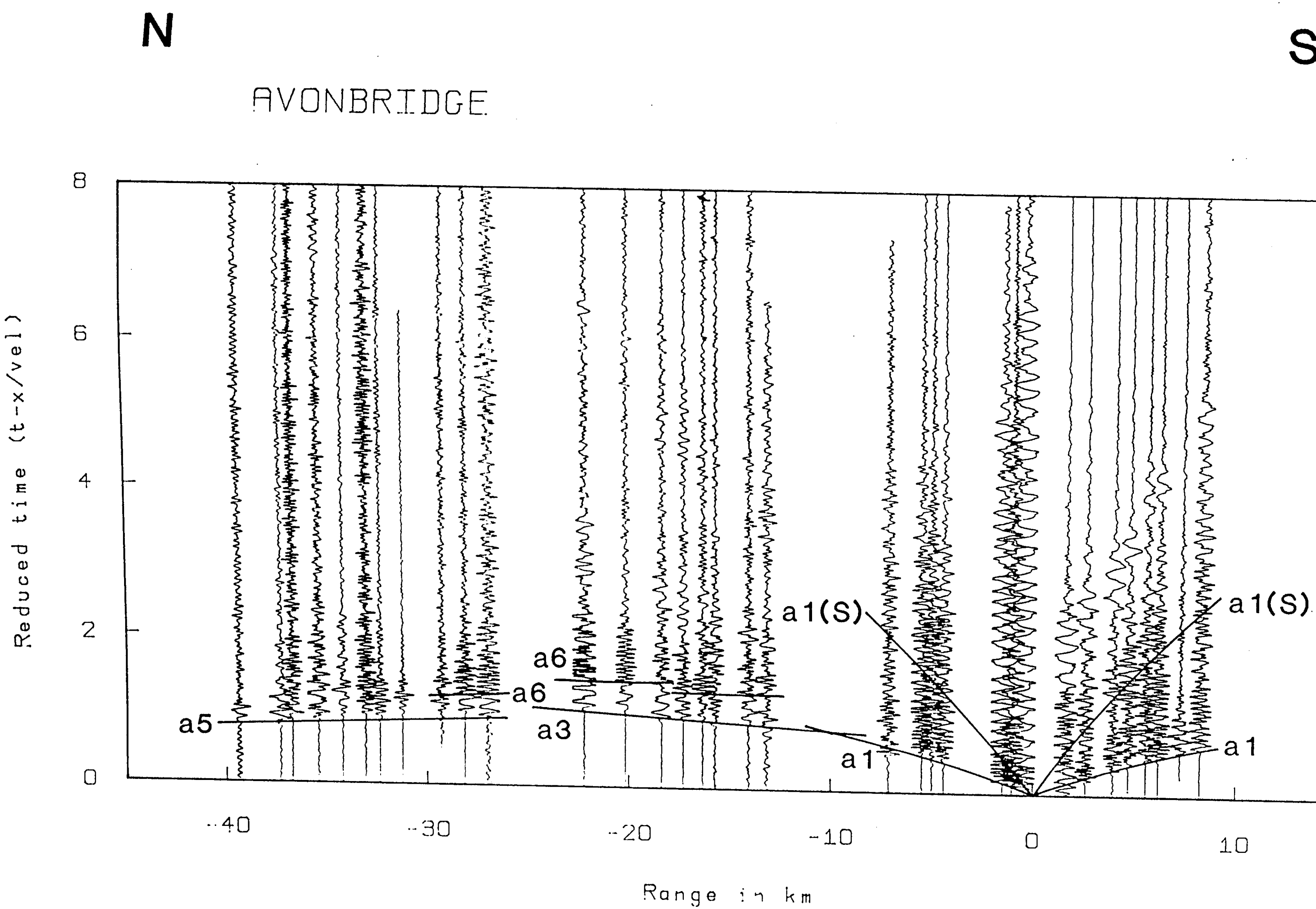

Fig.3.38b

Unfiltered time section

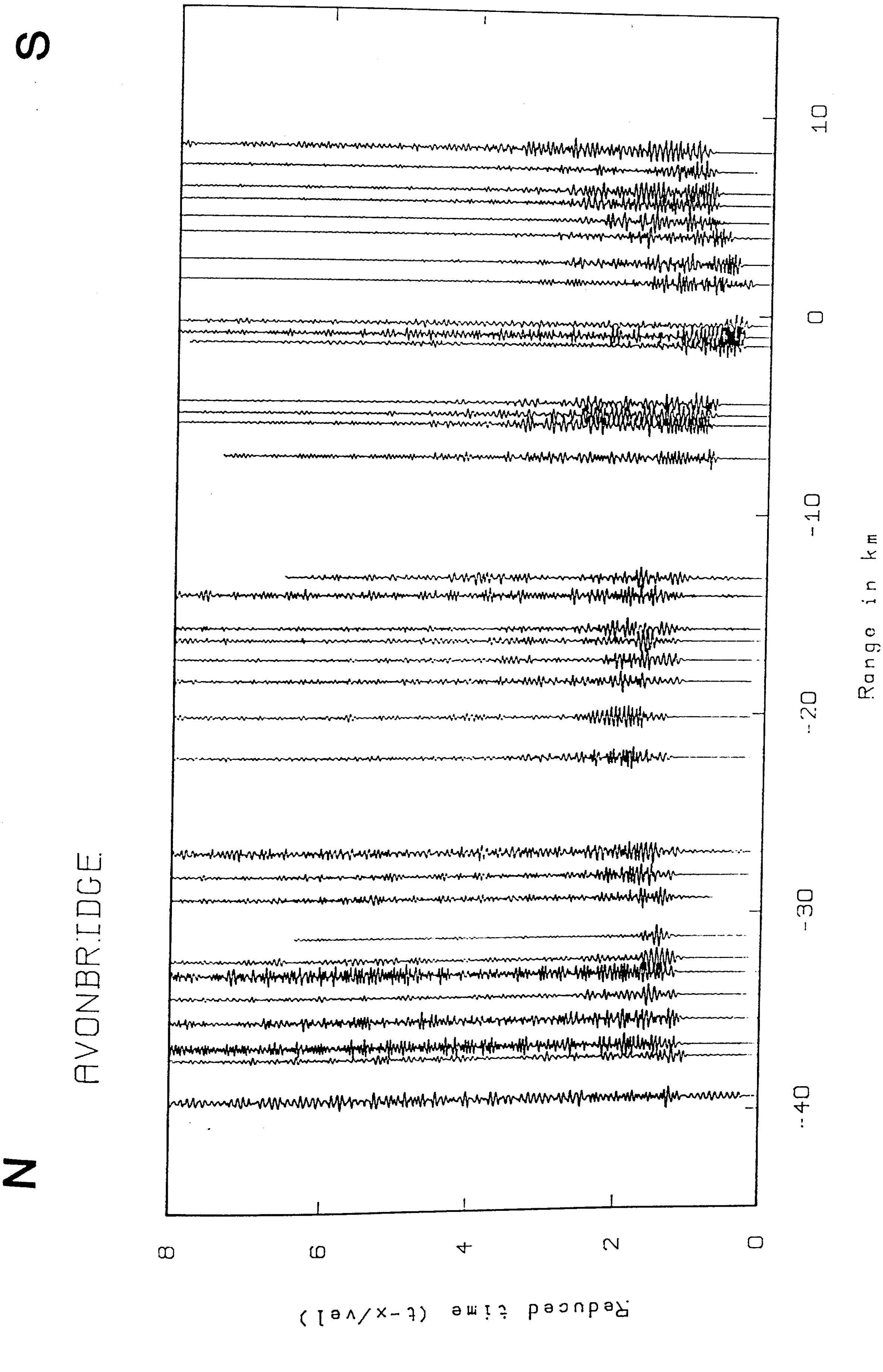

Fig.3.38c Zero-phase, highpass filter 10.0Hz and length 0.50 s with a Hamming window

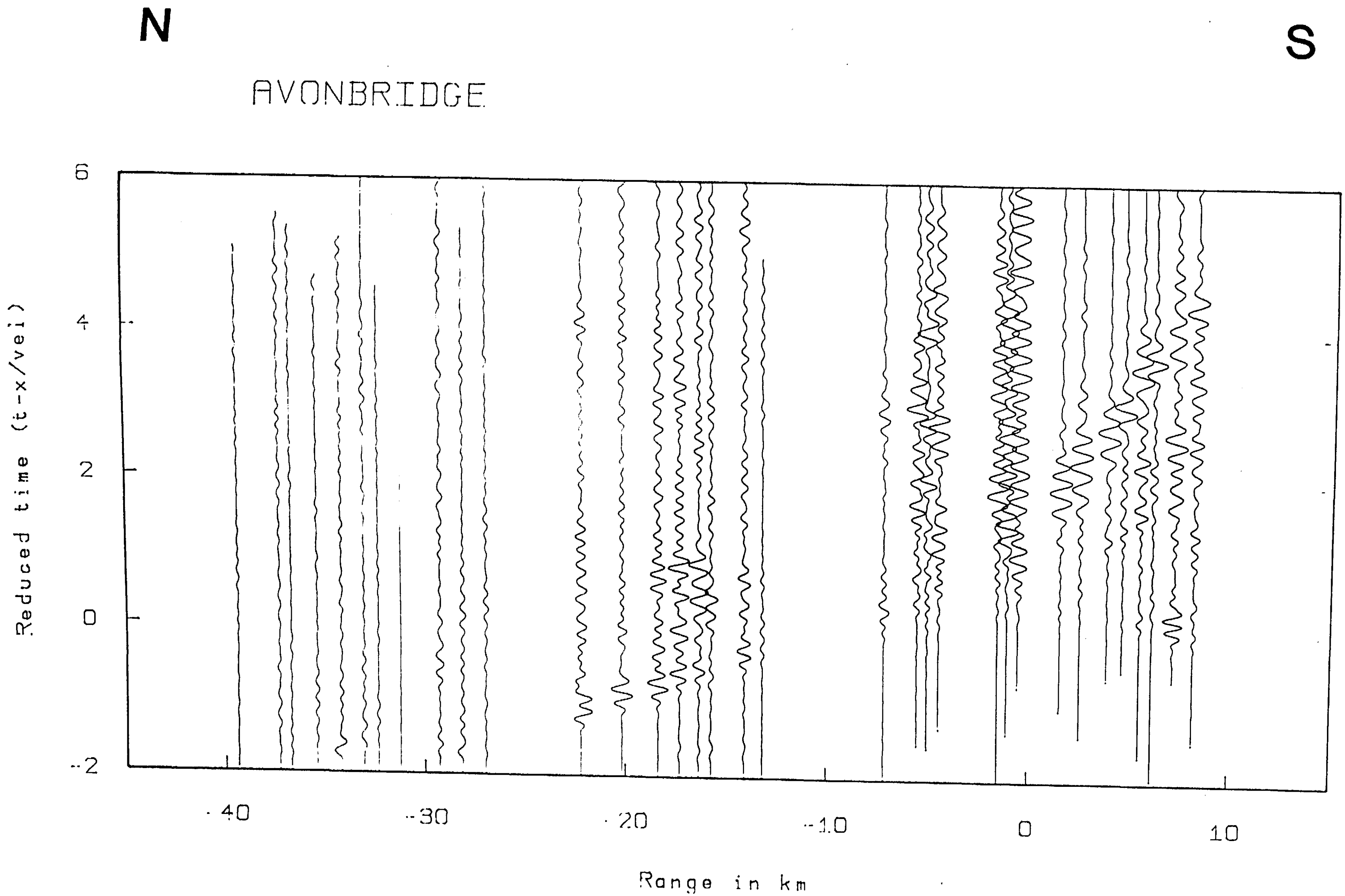

Fig.3.38d Zero-phase lowpass filter 5.0Hz and length 0.50 s with a Hamming window

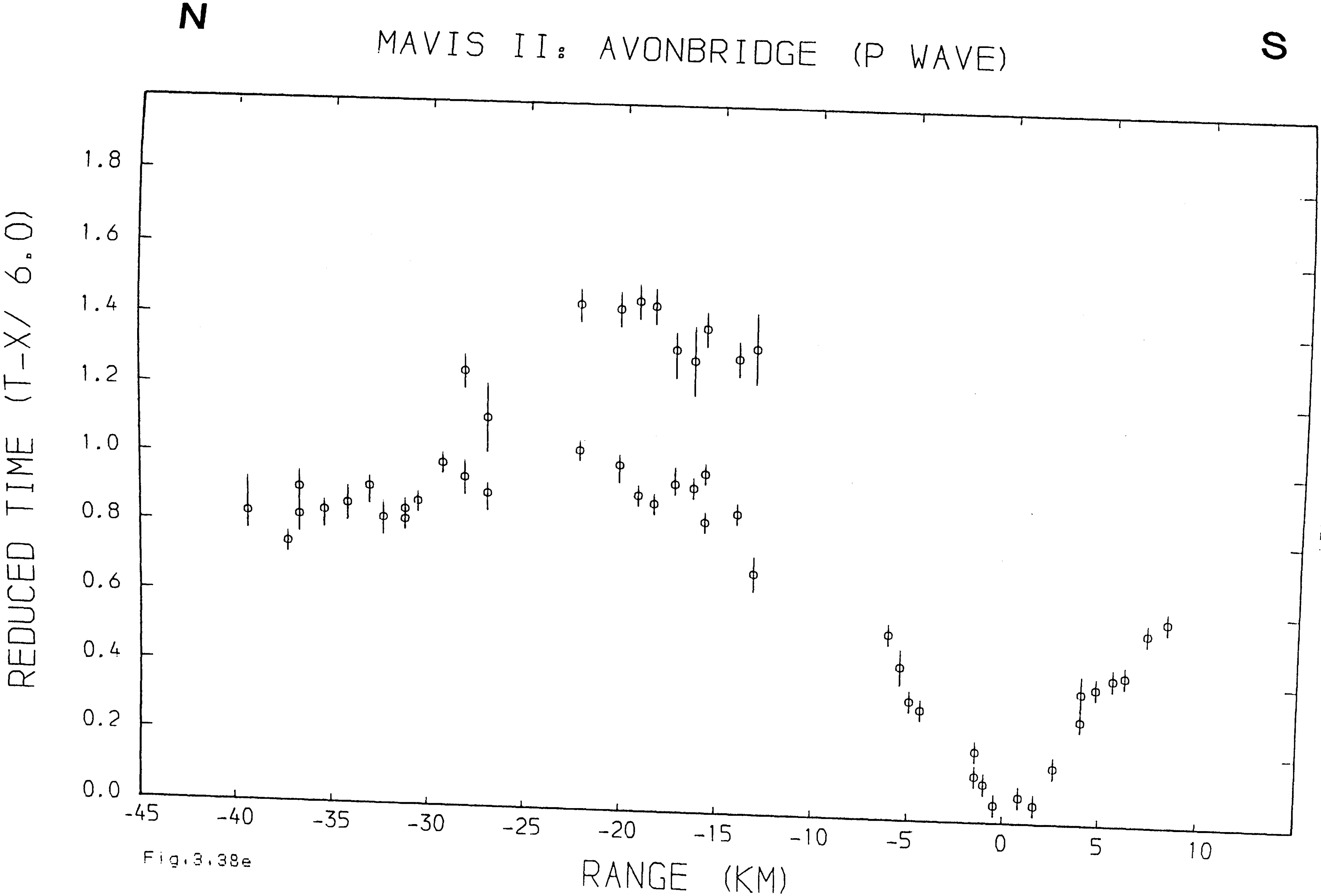
N
MAVIS II: AVONBRIDGE (P WAVE)
S
REDUCED TIME (T-X/ 6.0)
1.8
1.6
1.4
1.2
1.0
0.8
0.6
0.4
0.2
0.0
-45
-40
-35
-30
-25
-20
-15
-10
-5
0
5
10
RANGE (KM)

Fig.3.38e

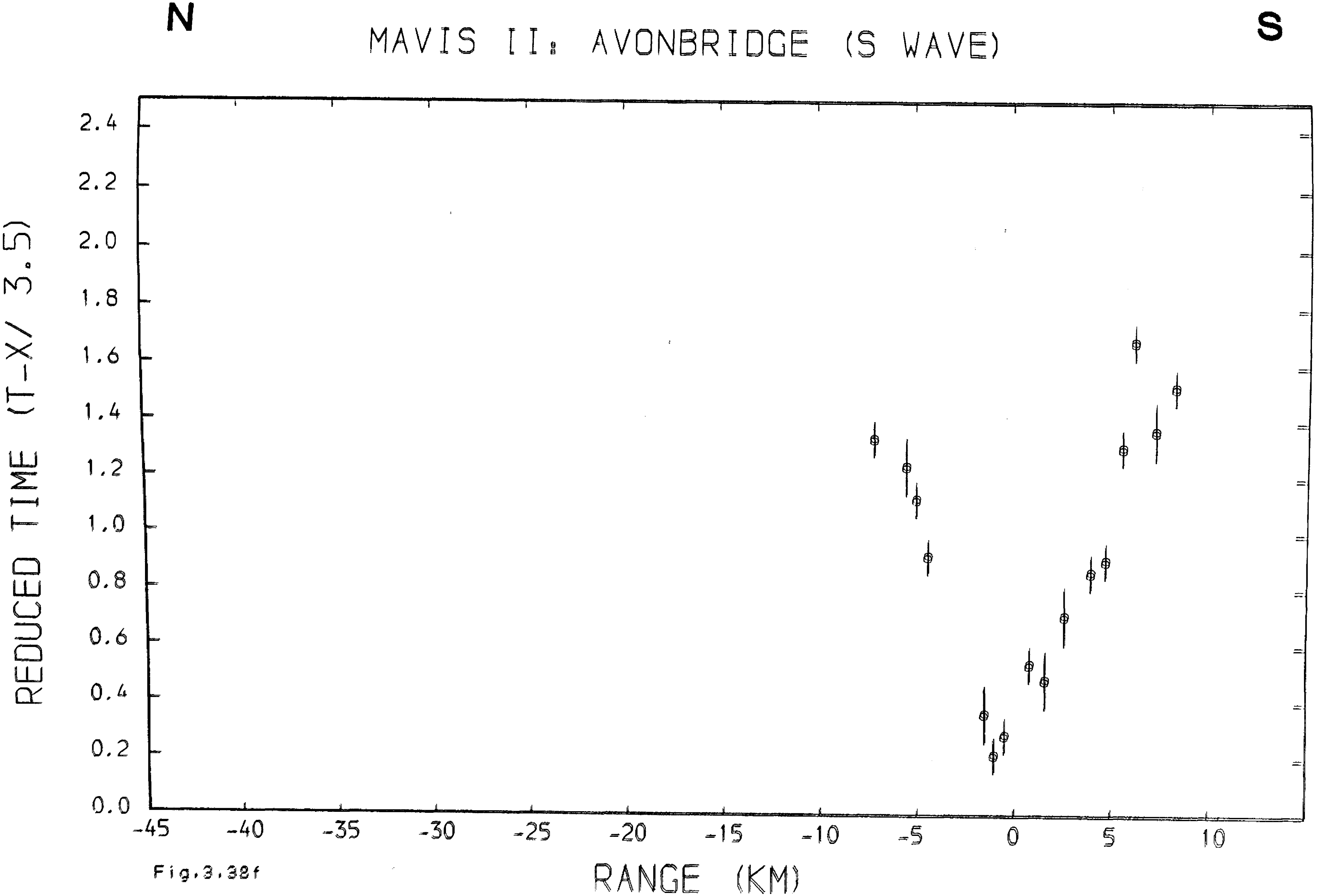
N
S
MAVIS II: AVONBRIDGE (S WAVE)
REDUCED TIME (T-X/ 3.5)
2.4
2.2
2.0
1.8
1.6
1.4
1.2
1.0
0.8
0.6
0.4
0.2
0.0
-45
-40
-35
-30
-25
-20
-15
-10
-5
0
5
10
RANGE (KM)

Fig.3.38f

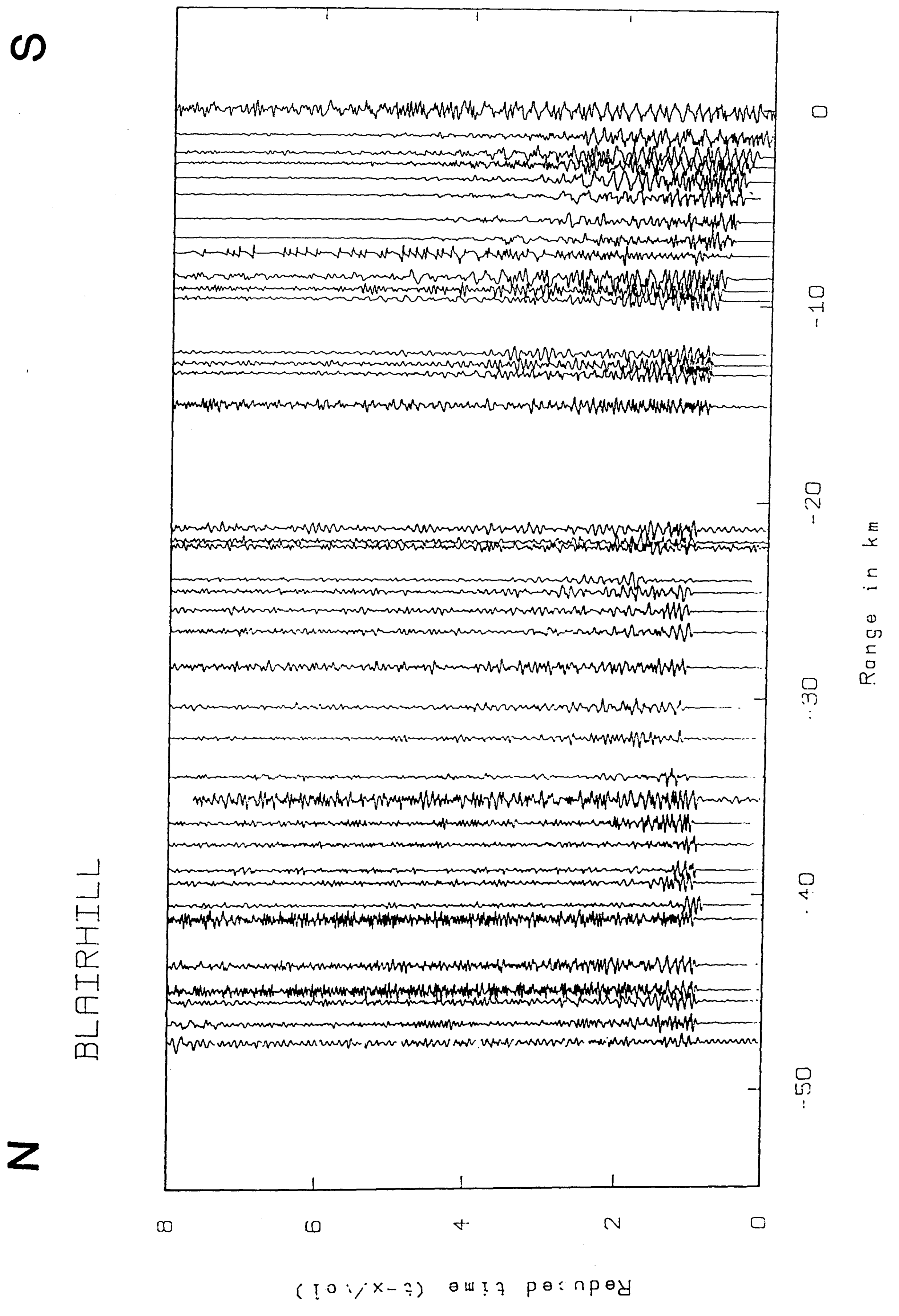

Unfiltered time section

Fig.3.39a

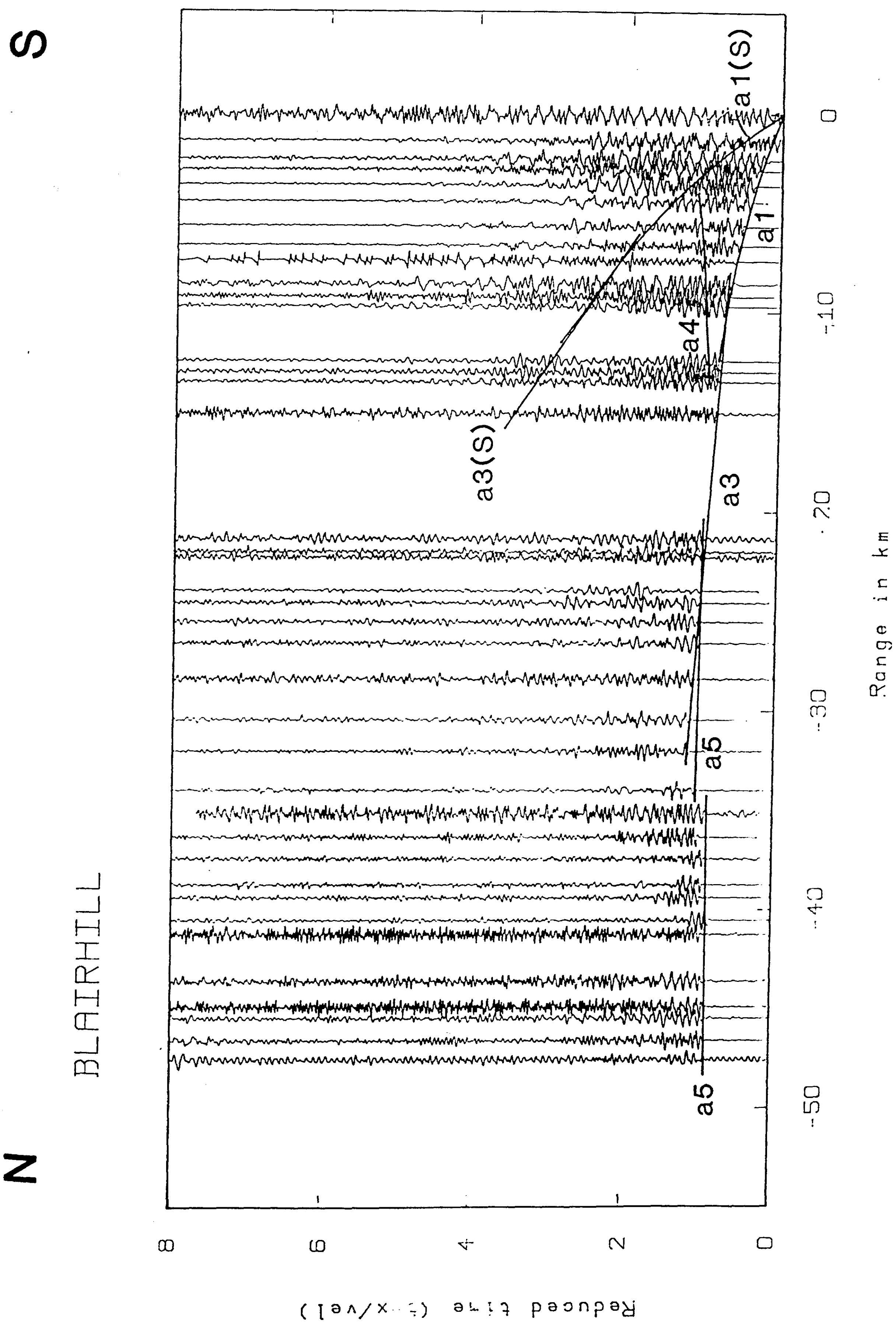

Unfiltered time section

Fig.3.39b

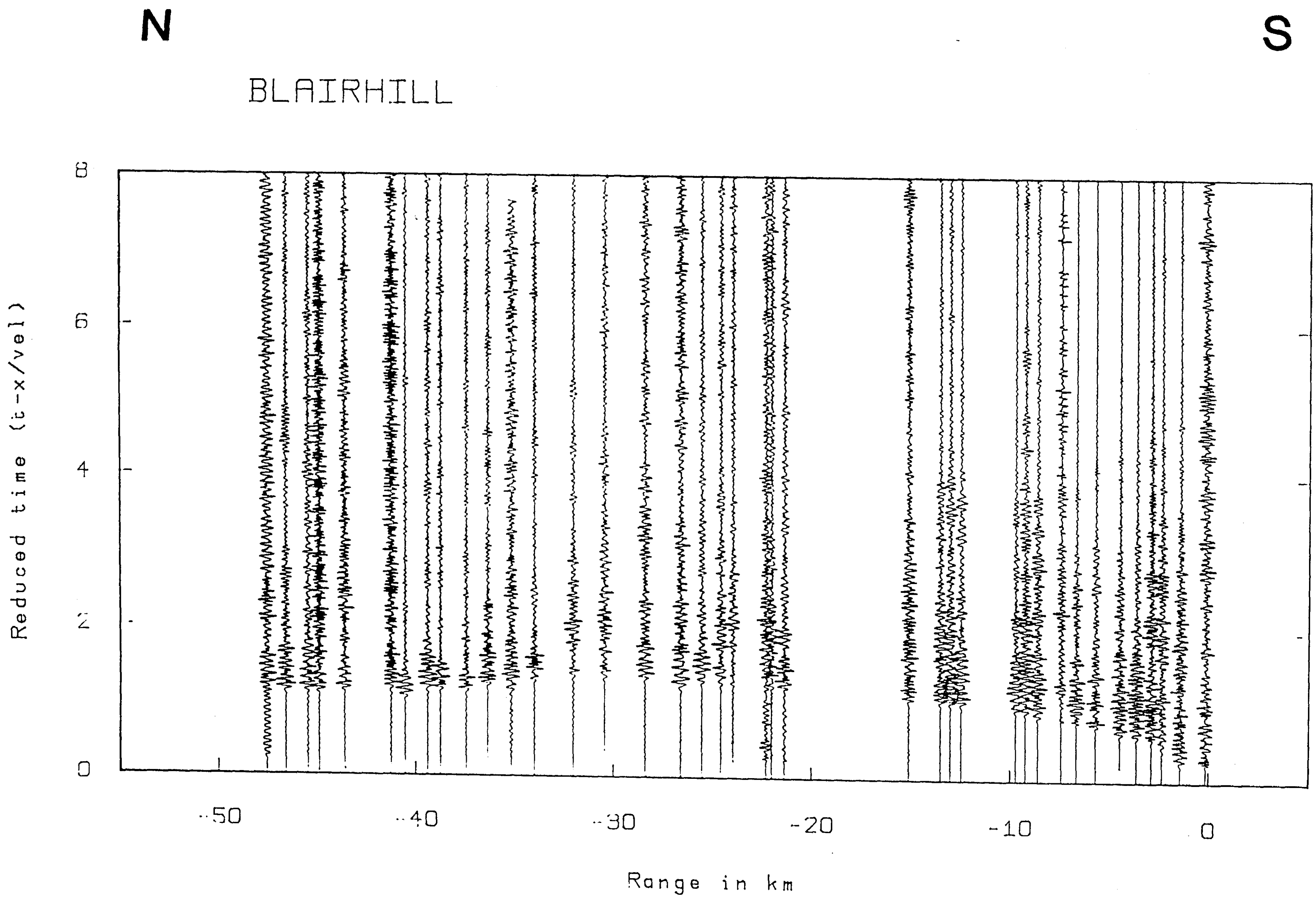

Fig.3.39c Zero-phase, highpass filter 10.0Hz and length 0.50 s with a Hamming window

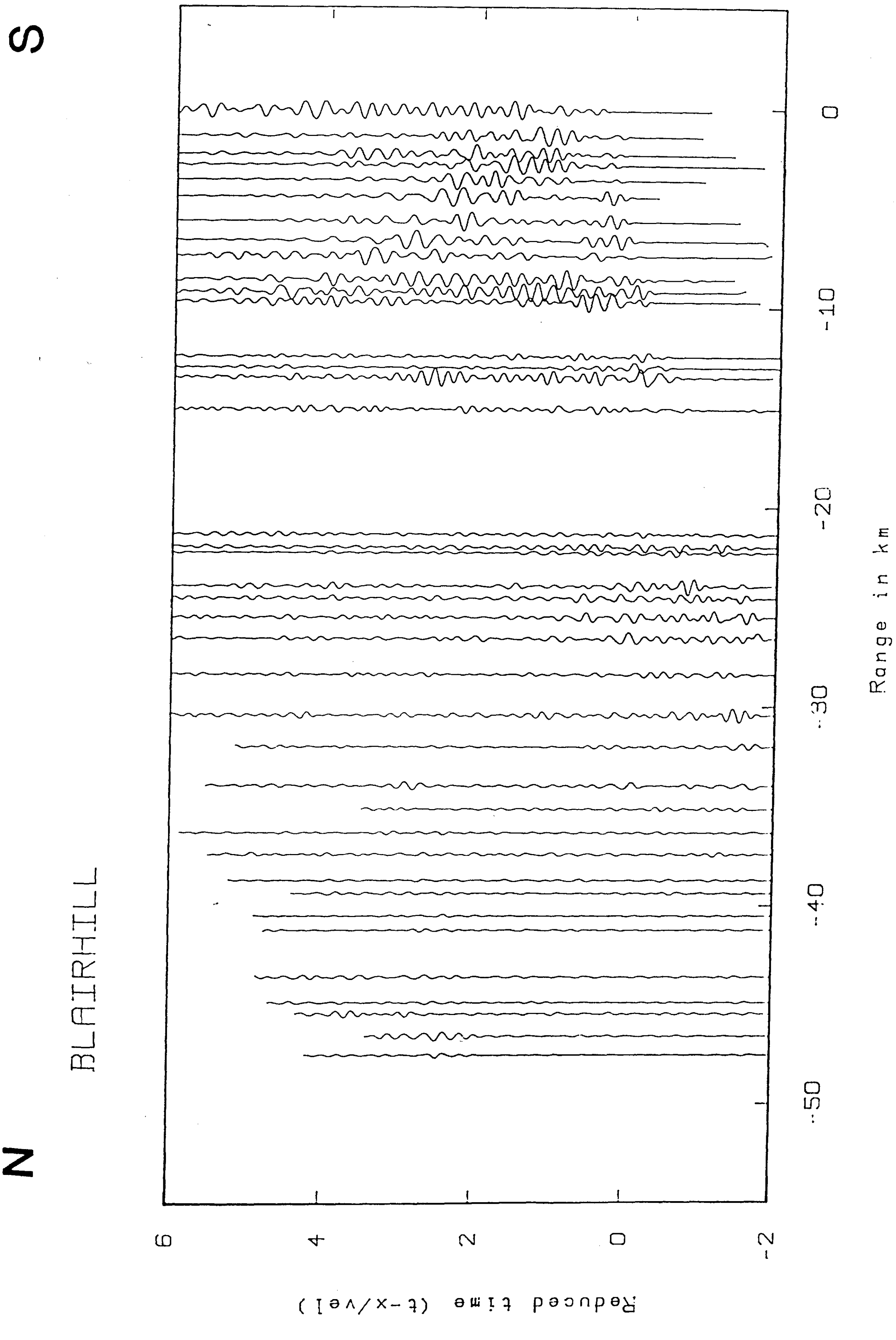

Fig.3.39d Zero-phase lowpass filter C.0Hz and length 0.50 s with a Hamming window

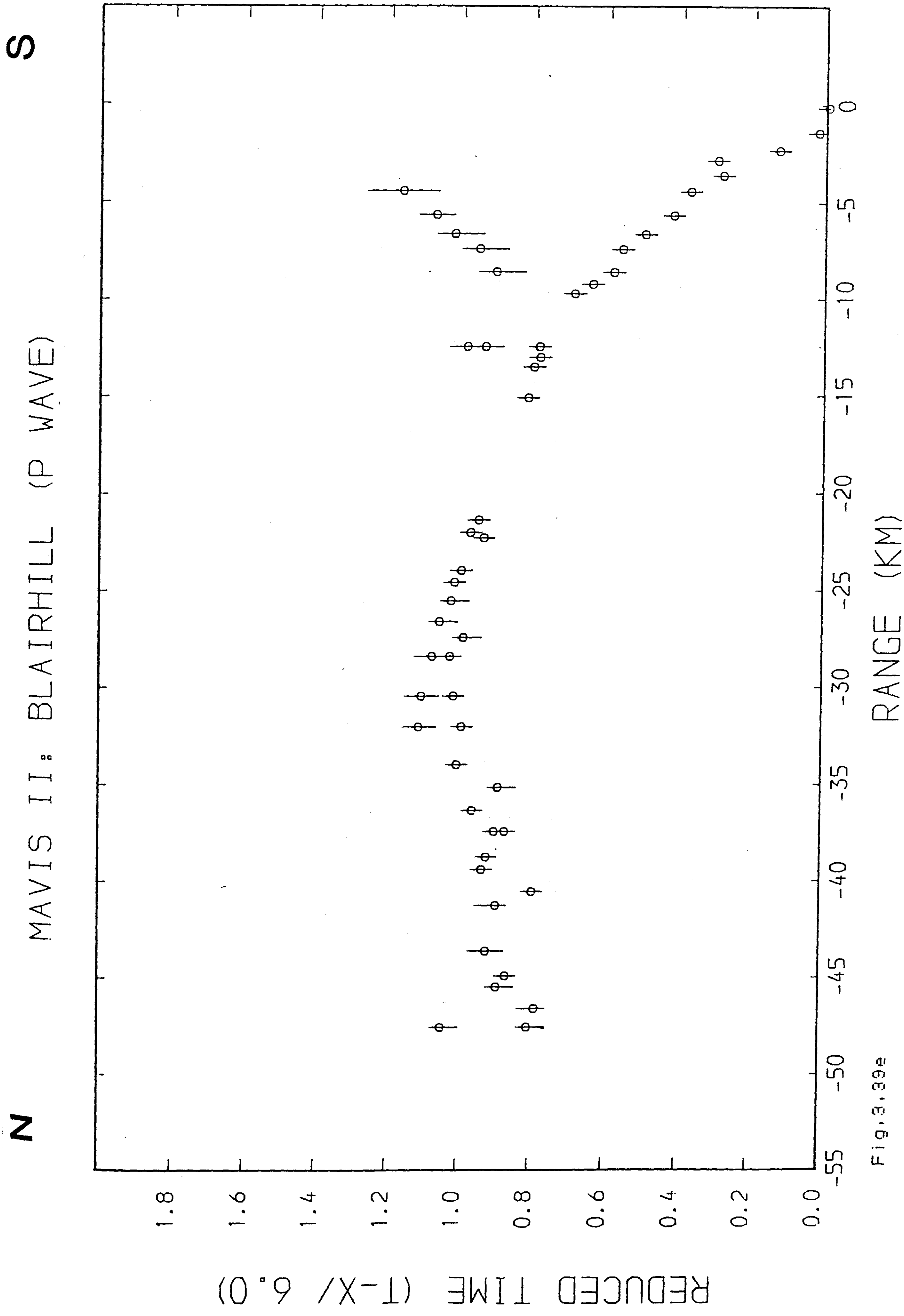
N
S
MAVIS II: BLAIRHILL (P WAVE)
0
-5
-10
-15
-20
-25
-30
-35
-40
-45
-50
-55
RANGE (KM)
0.0
0.2
0.4
0.6
0.8
1.0
1.2
1.4
1.6
1.8
REDUCED TIME (T-X/ 6.0)

Fig.3.39e

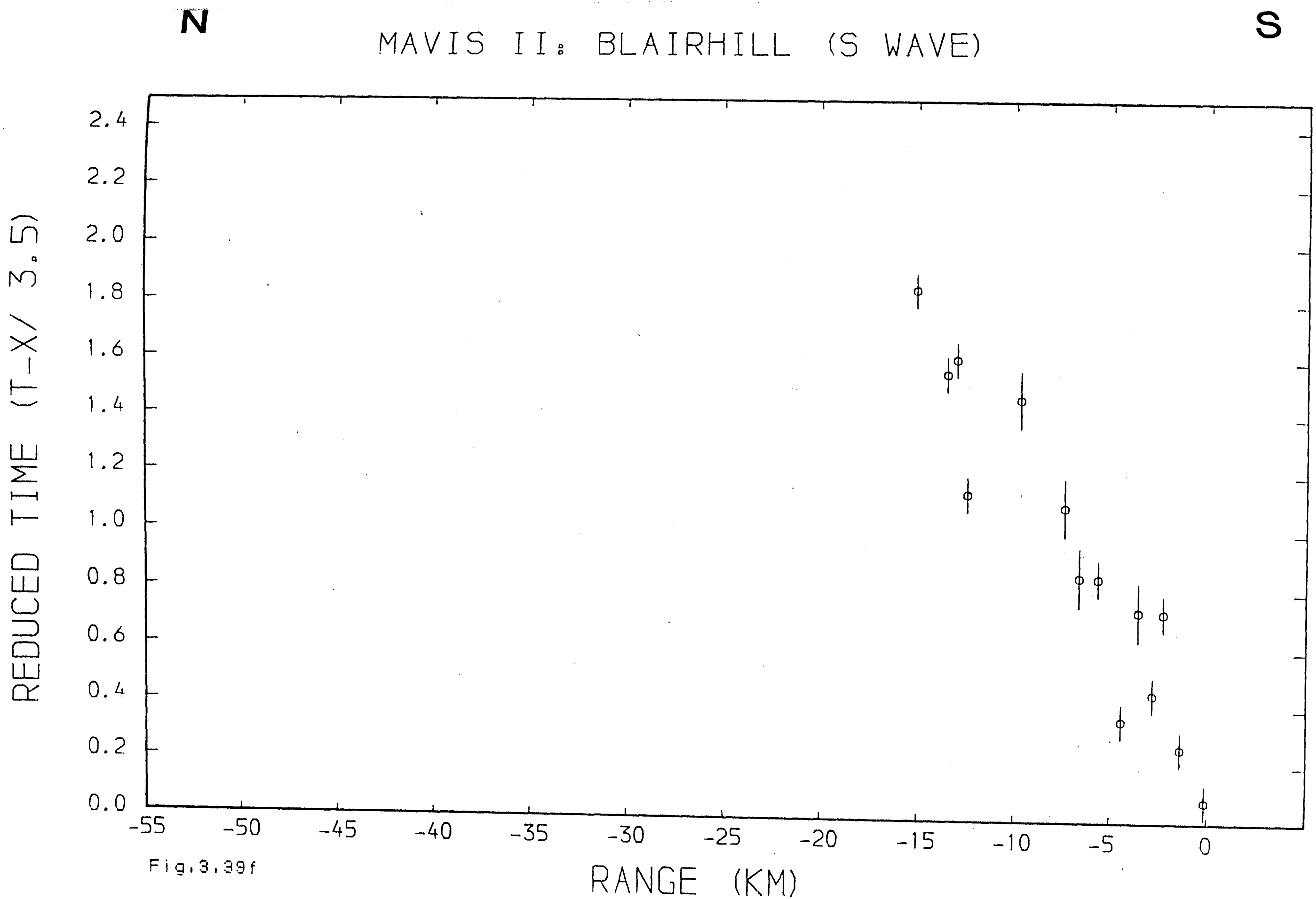
N
S
MAVIS II: BLAIRHILL (S WAVE)
REDUCED TIME (T-X/ 3.5)
2.4
2.2
2.0
1.8
1.6
1.4
1.2
1.0
0.8
0.6
0.4
0.2
0.0
-55
-50
-45
-40
-35
-30
-25
-20
-15
-10
-5
0
RANGE (KM)

Fig.3.39f

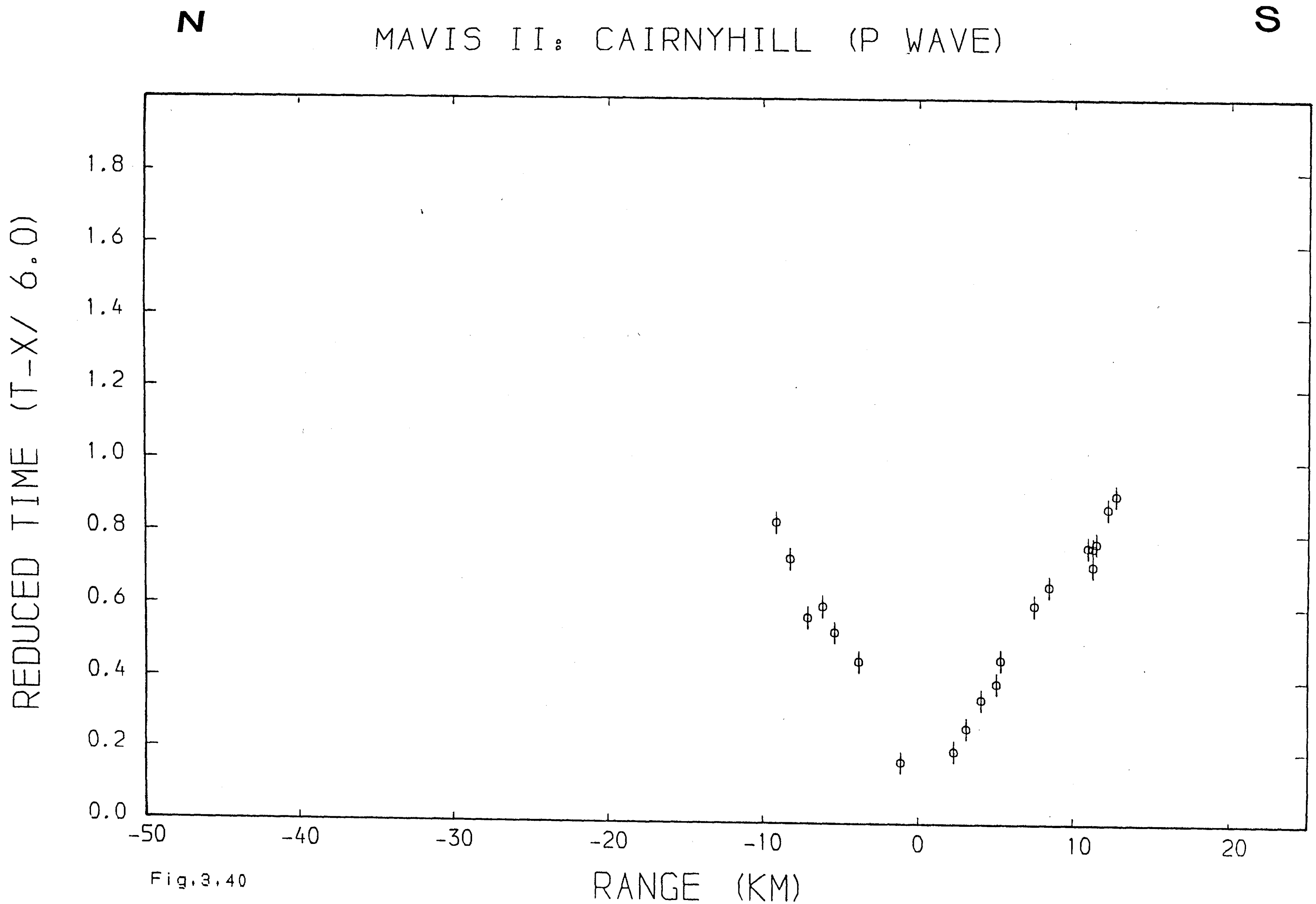
N
S
MAVIS II: CAIRNYHILL (P WAVE)
REDUCED TIME (T-X/ 6.0)
0.0
0.2
0.4
0.6
0.8
1.0
1.2
1.4
1.6
1.8
-50
-40
-30
-20
-10
0
10
20
RANGE (KM)

Fig.3.40

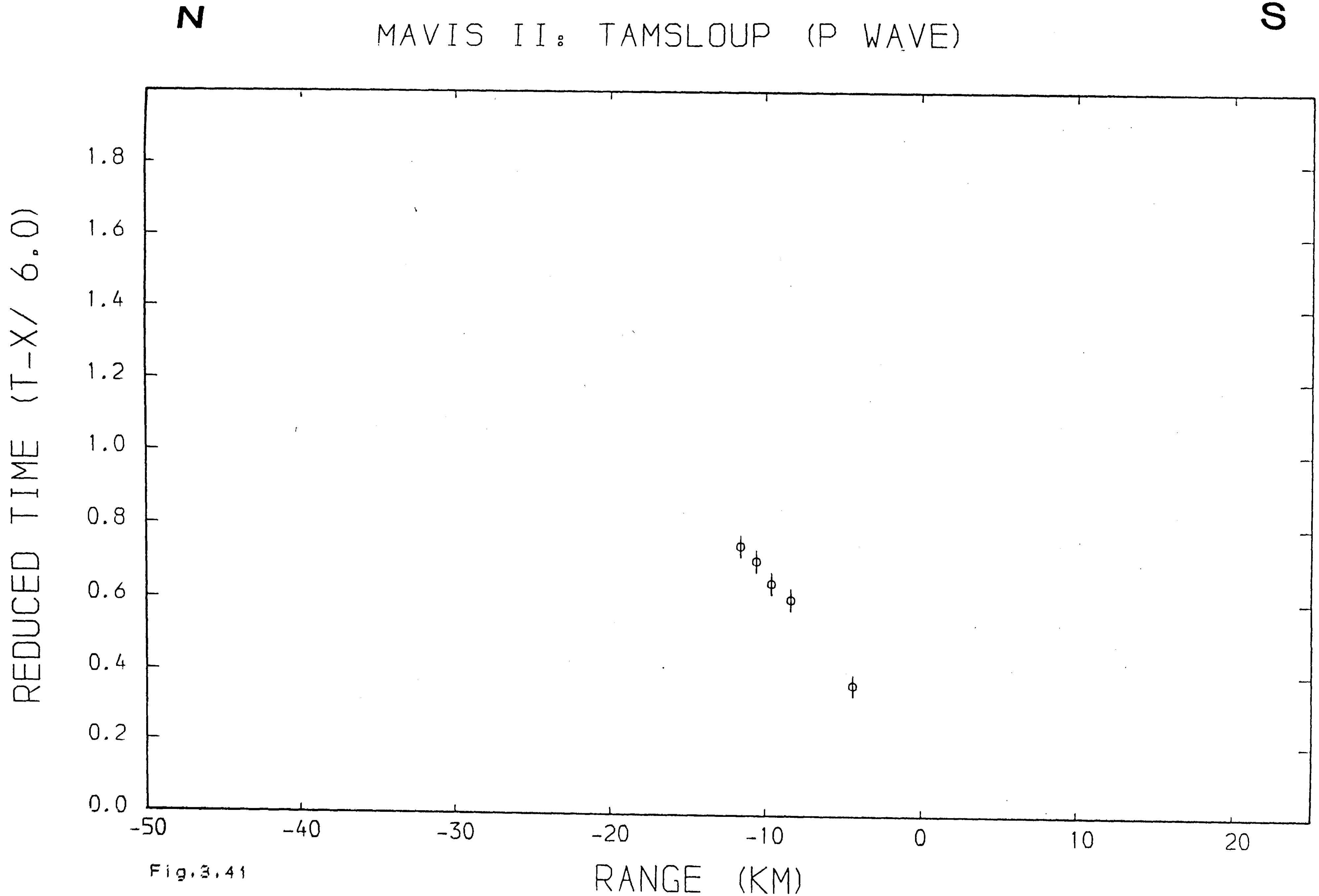
N
S
MAVIS II: TAMSLOUP (P WAVE)
REDUCED TIME (T-X/ 6.0)
1.8
1.6
1.4
1.2
1.0
0.8
0.6
0.4
0.2
0.0
-50
-40
-30
-20
-10
0
10
20
RANGE (KM)

Fig.3.41

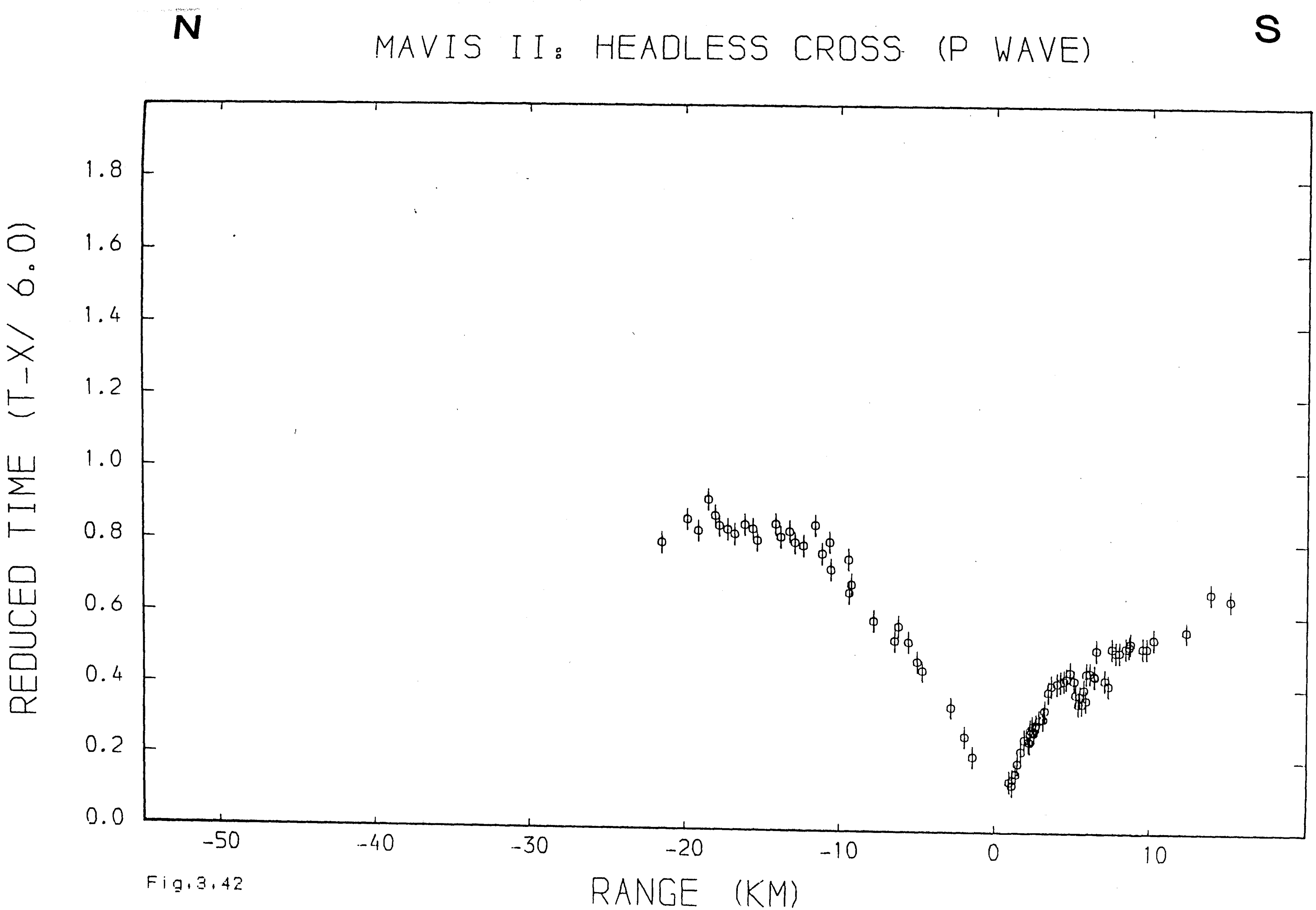
N
S
MAVIS II: HEADLESS CROSS (P WAVE)
REDUCED TIME (T-X/ 6.0)
1.8
1.6
1.4
1.2
1.0
0.8
0.6
0.4
0.2
0.0
-50
-40
-30
-20
-10
0
10
RANGE (KM)

Fig.3.42

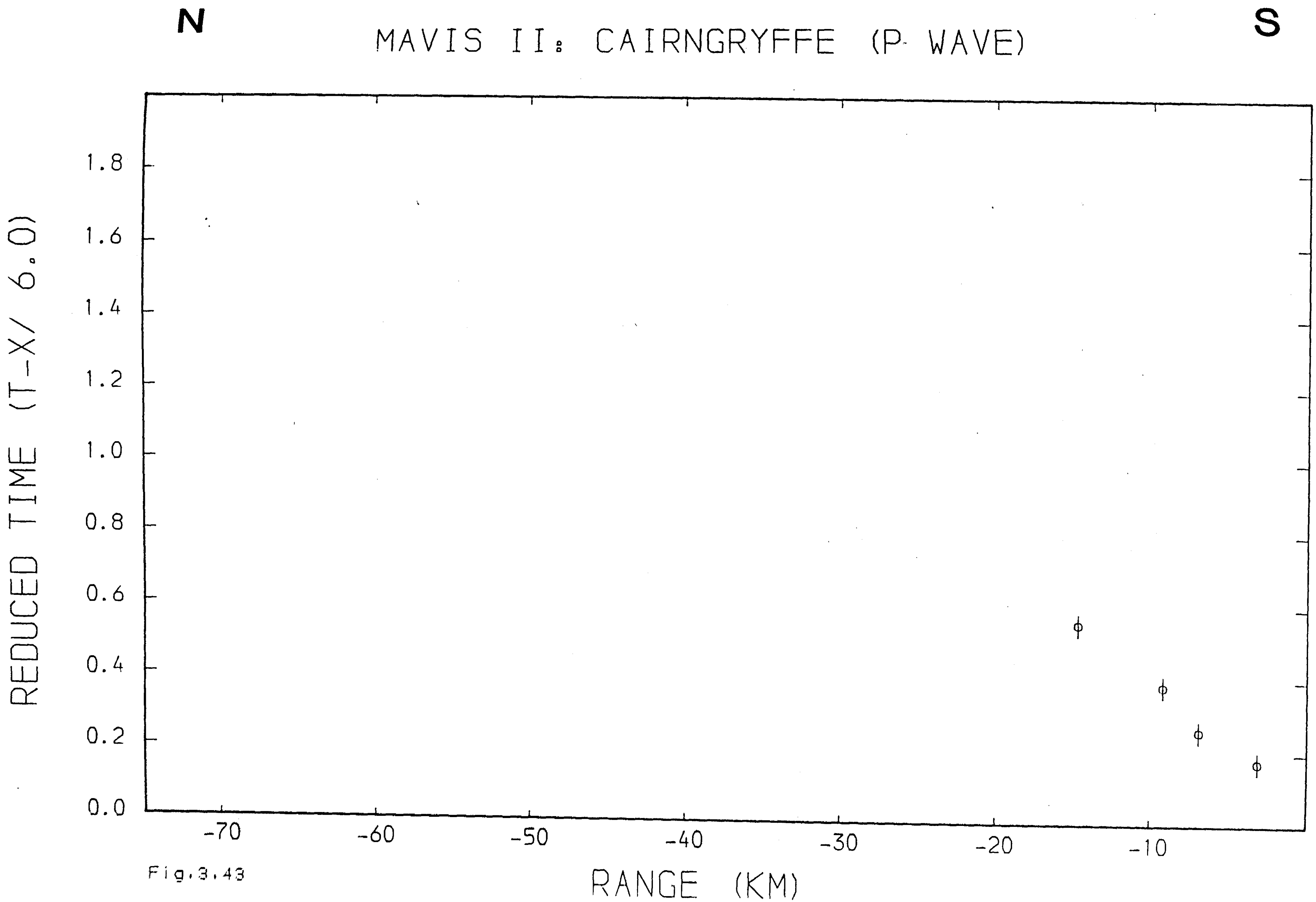
N
S
MAVIS II: CAIRNGRYFFE (P WAVE)
REDUCED TIME (T-X/ 6.0)
1.8
1.6
1.4
1.2
1.0
0.8
0.6
0.4
0.2
0.0
-70
-60
-50
-40
-30
-20
-10
RANGE (KM)

Fig.3.43

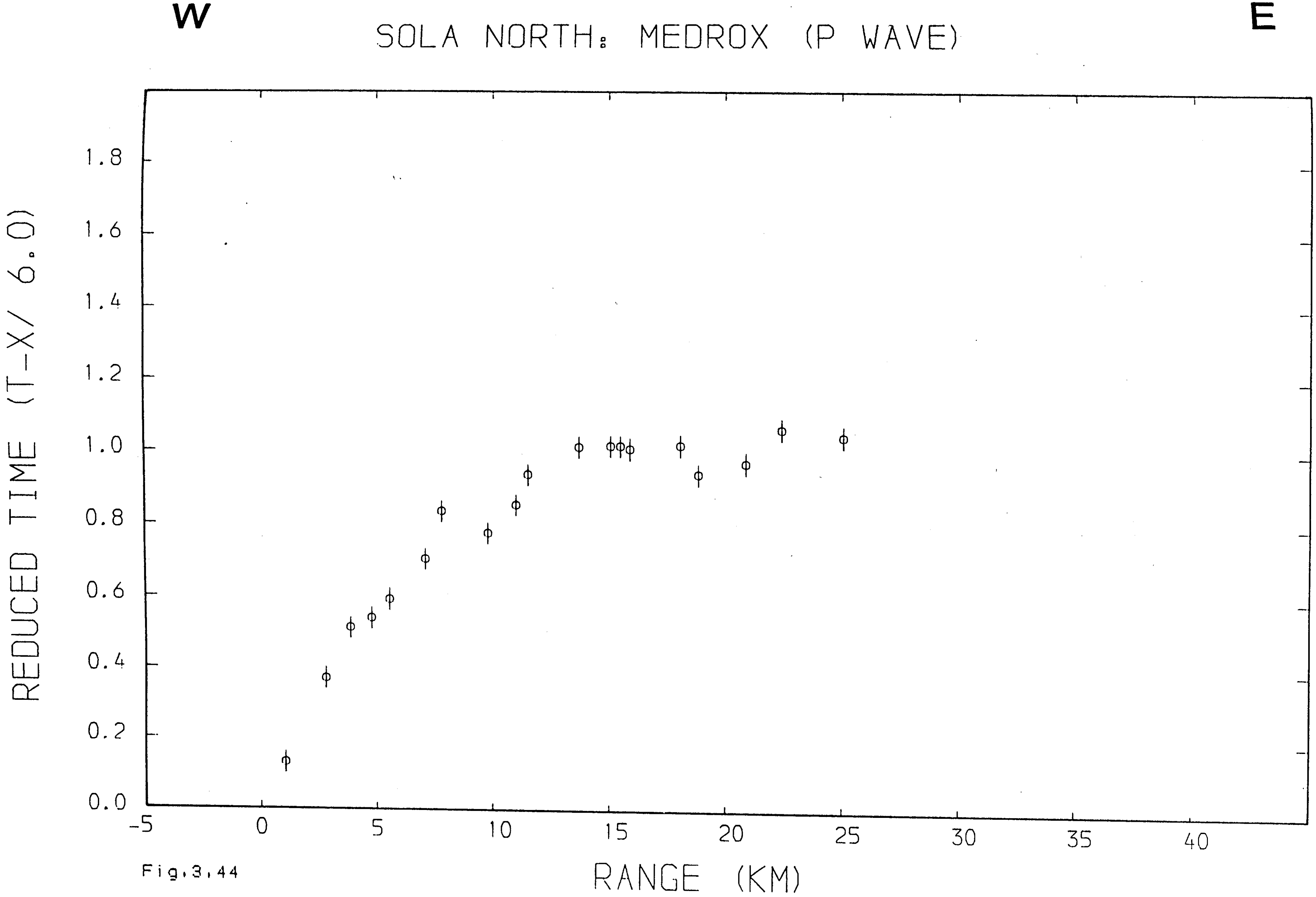
W
E
SOLA NORTH: MEDROX (P WAVE)
REDUCED TIME (T-X/ 6.0)
1.8
1.6
1.4
1.2
1.0
0.8
0.6
0.4
0.2
0.0
-5
0
5
10
15
20
25
30
35
40
RANGE (KM)

Fig.3.44

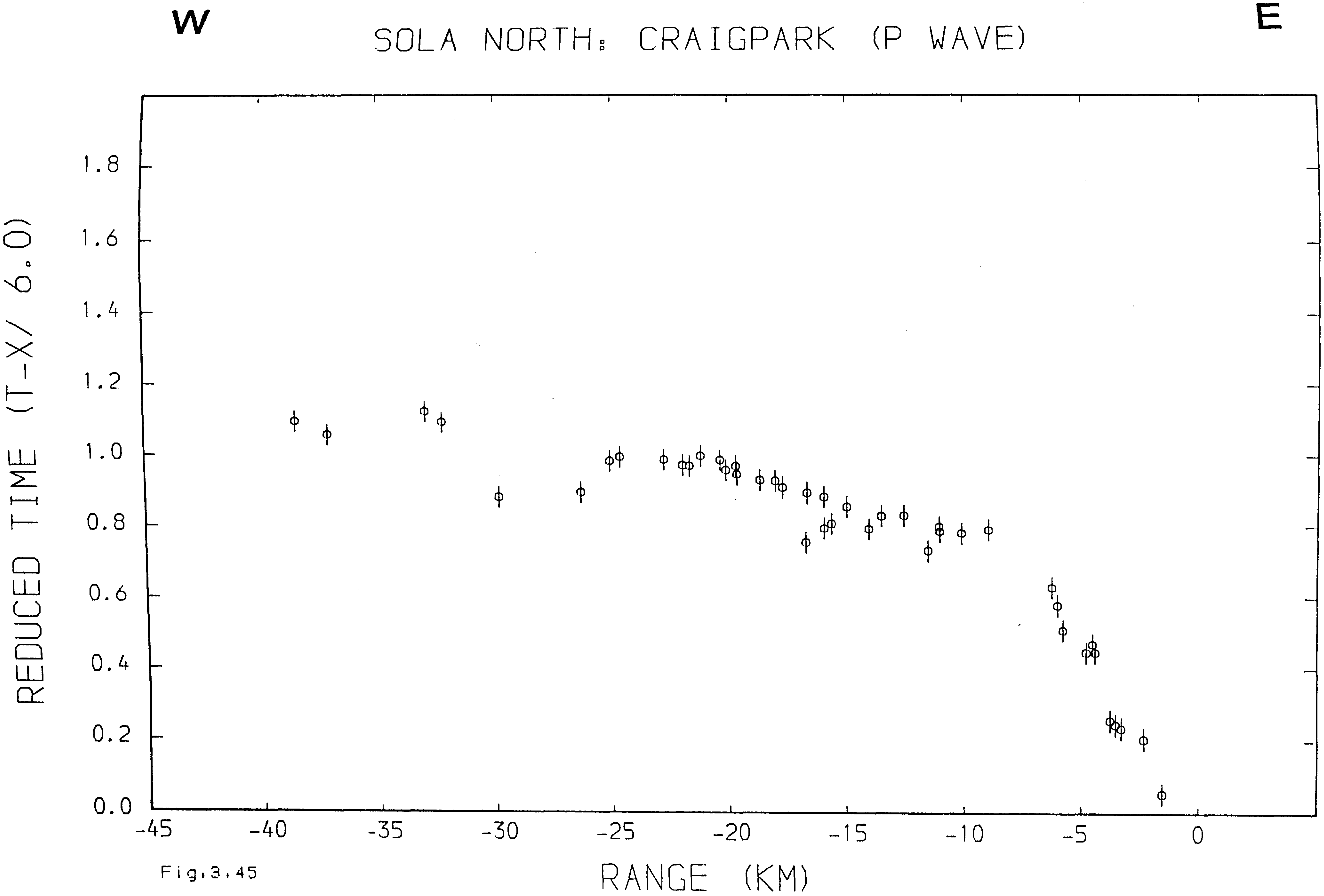
W
E
SOLA NORTH: CRAIGPARK (P WAVE)
REDUCED TIME (T-X/ 6.0)
0.0
0.2
0.4
0.6
0.8
1.0
1.2
1.4
1.6
1.8
-45
-40
-35
-30
-25
-20
-15
-10
-5
0
RANGE (KM)

Fig.3.45

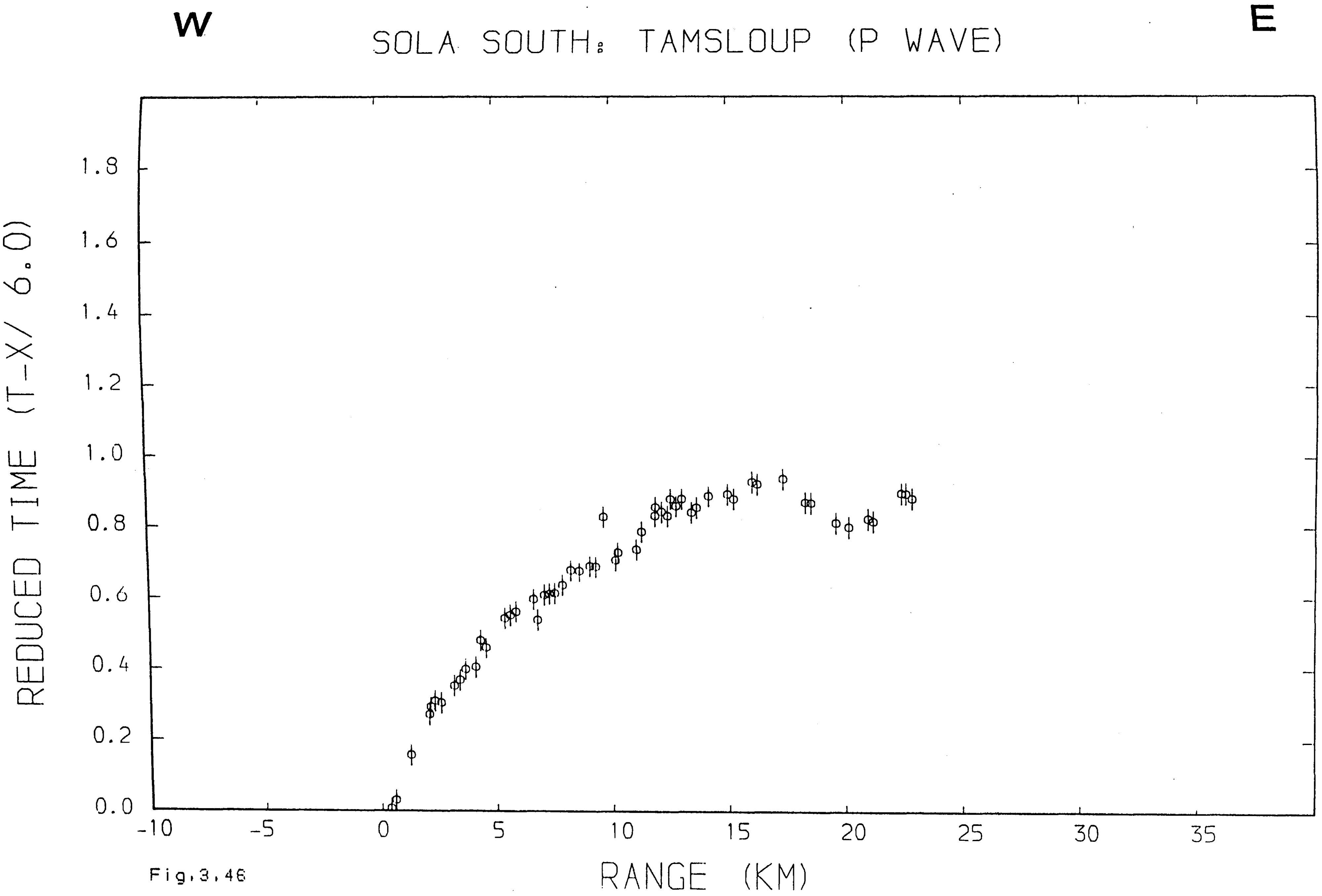
W
E
SOLA SOUTH: TAMSLOUP (P WAVE)
REDUCED TIME (T-X/ 6.0)
0.0
0.2
0.4
0.6
0.8
1.0
1.2
1.4
1.6
1.8
-10
-5
0
5
10
15
20
25
30
35
RANGE (KM)

Fig.3.46

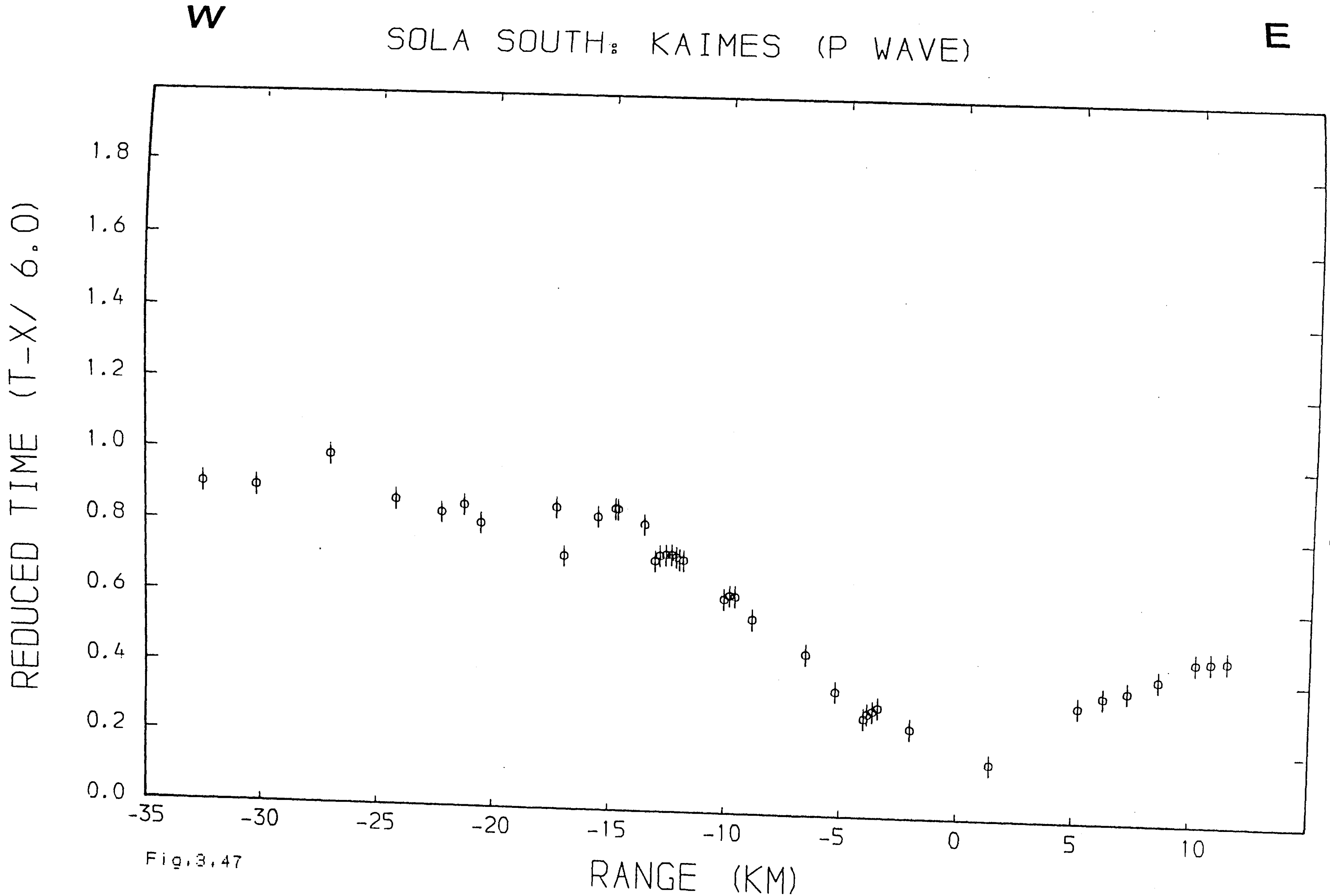
W
SOLA SOUTH: KAIMES (P WAVE)
E
REDUCED TIME (T-X/ 6.0)
1.8
1.6
1.4
1.2
1.0
0.8
0.6
0.4
0.2
0.0
-35
-30
-25
-20
-15
-10
-5
0
5
10
RANGE (KM)

Fig.3.47

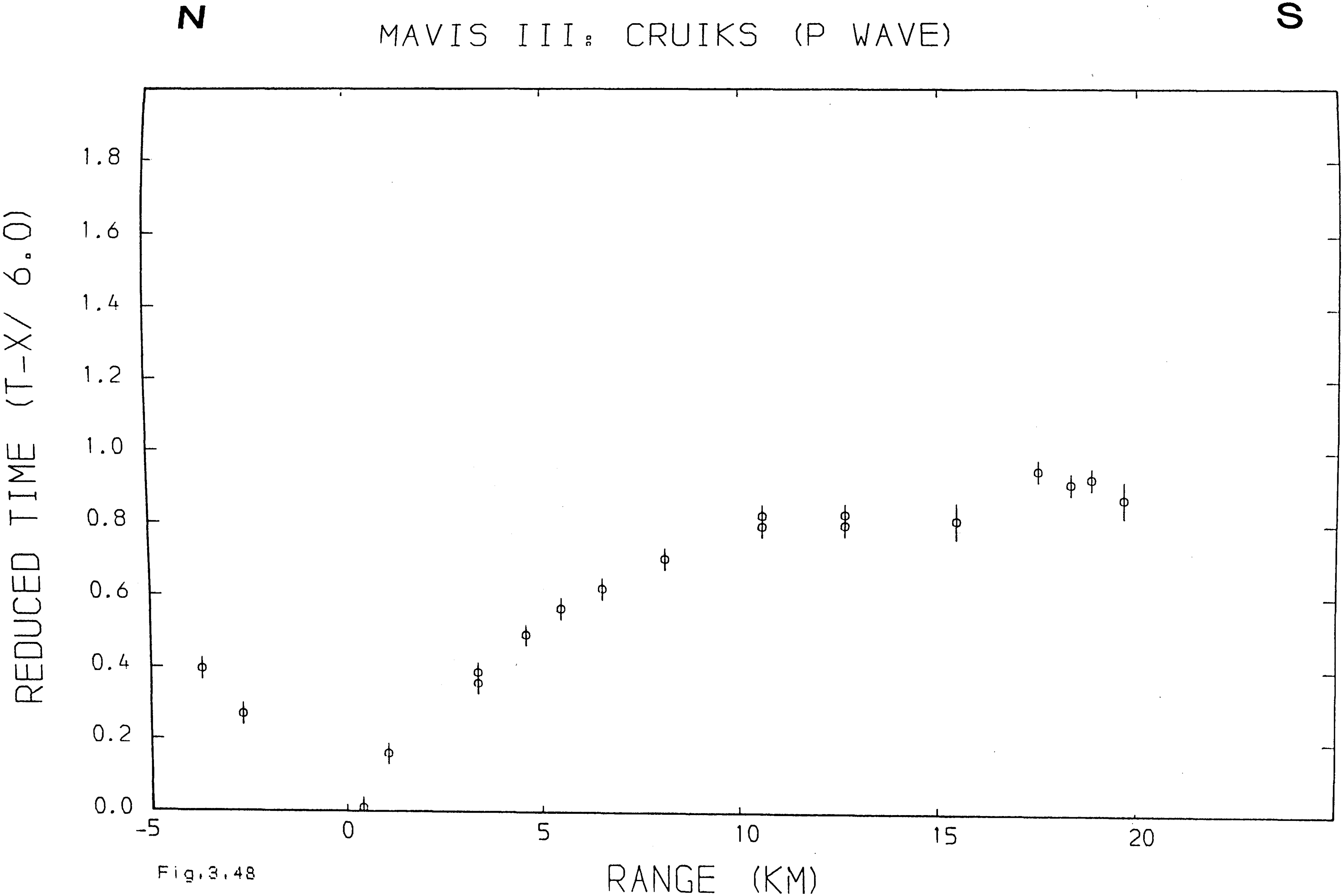
N
S
MAVIS III: CRUIKS (P WAVE)
REDUCED TIME (T-X/ 6.0)
0.0
0.2
0.4
0.6
0.8
1.0
1.2
1.4
1.6
1.8
-5
0
5
10
15
20
RANGE (KM)

Fig.3.48

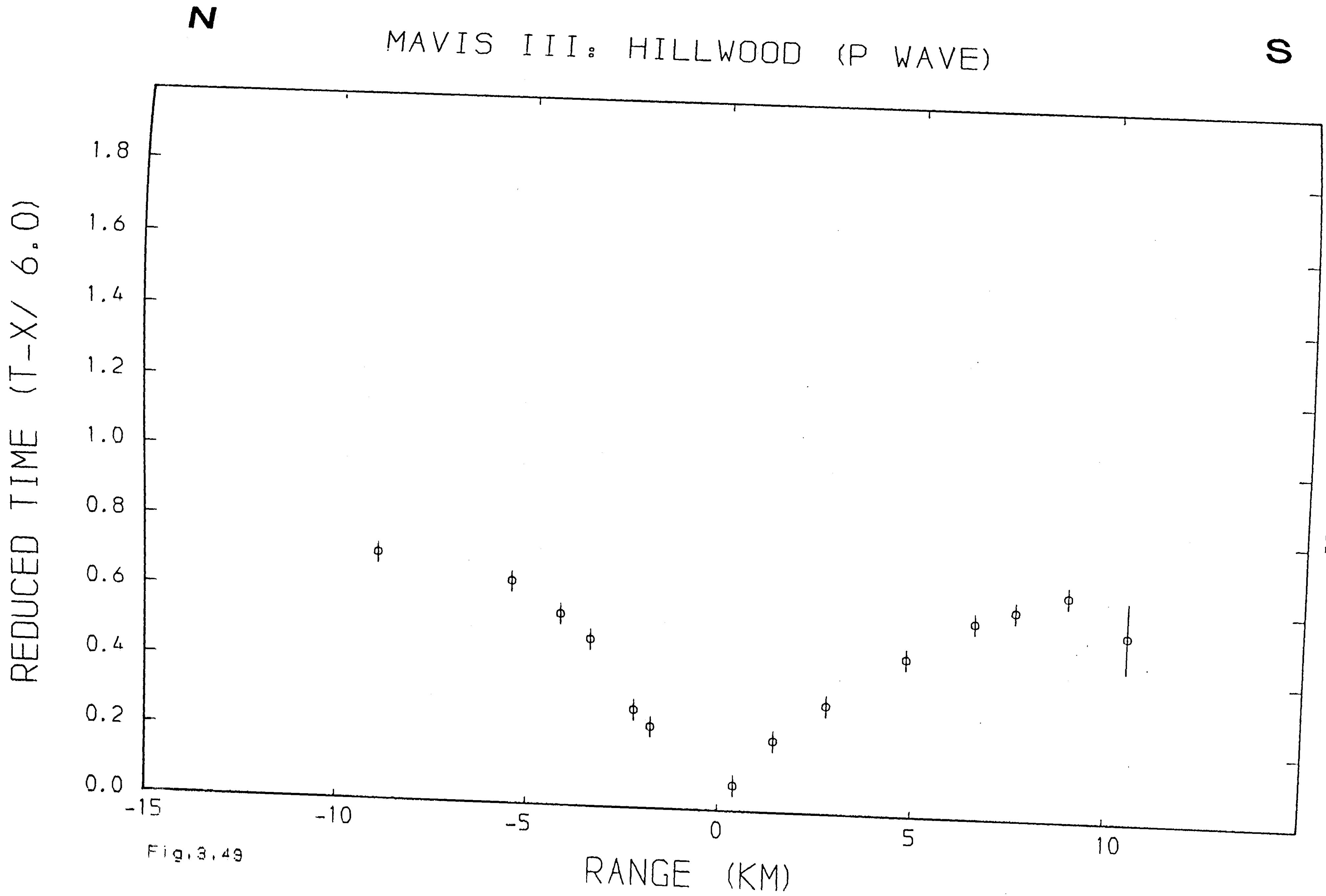
N
MAVIS III: HILLWOOD (P WAVE)
S
REDUCED TIME (T-X/ 6.0)
1.8
1.6
1.4
1.2
1.0
0.8
0.6
0.4
0.2
0.0
-15
-10
-5
0
5
10
RANGE (KM)

Fig.3.49

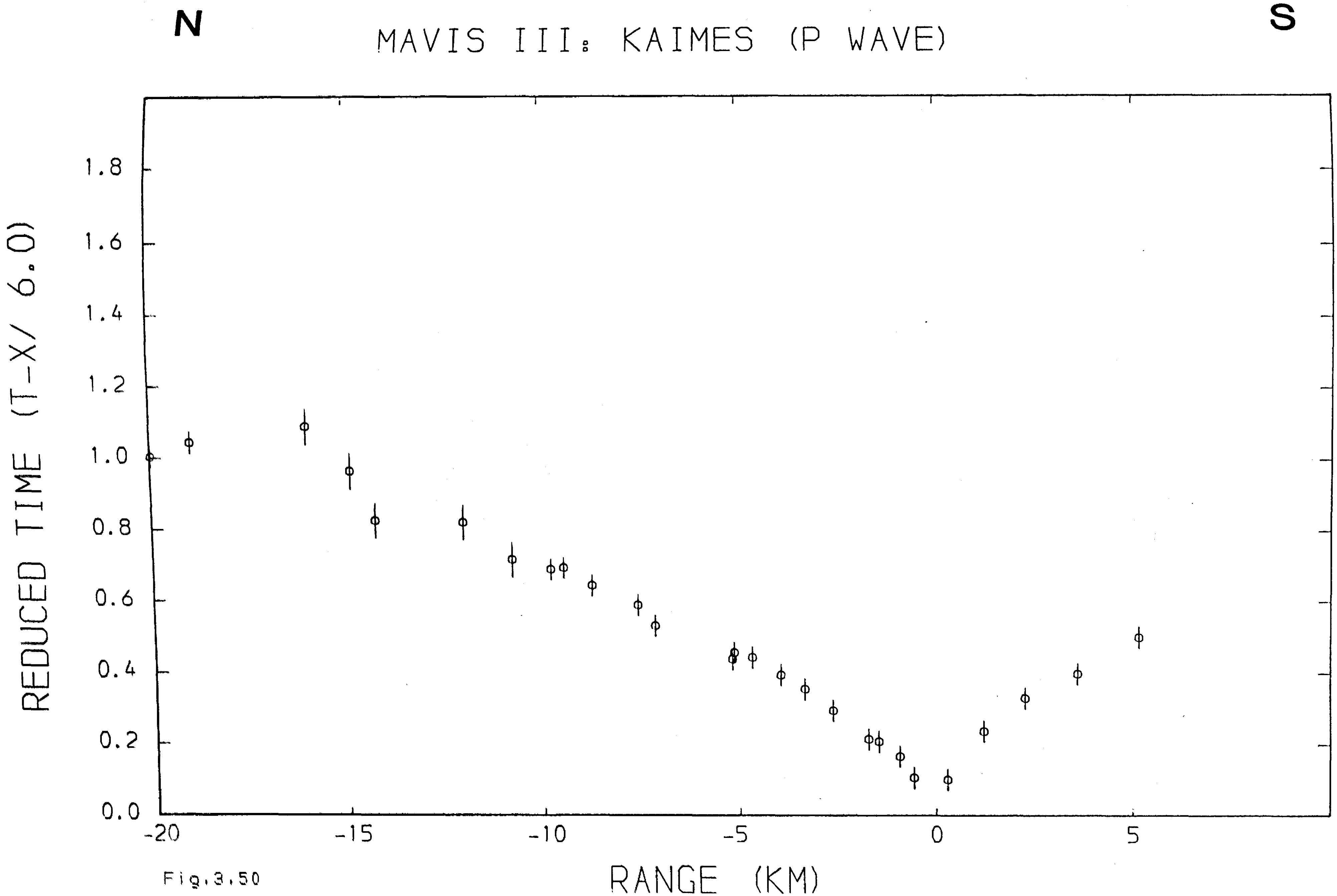
N
S
MAVIS III: KAIMES (P WAVE)
REDUCED TIME (T-X/ 6.0)
1.8
1.6
1.4
1.2
1.0
0.8
0.6
0.4
0.2
0.0
-20
-15
-10
-5
0
5
RANGE (KM)

Fig.3.50

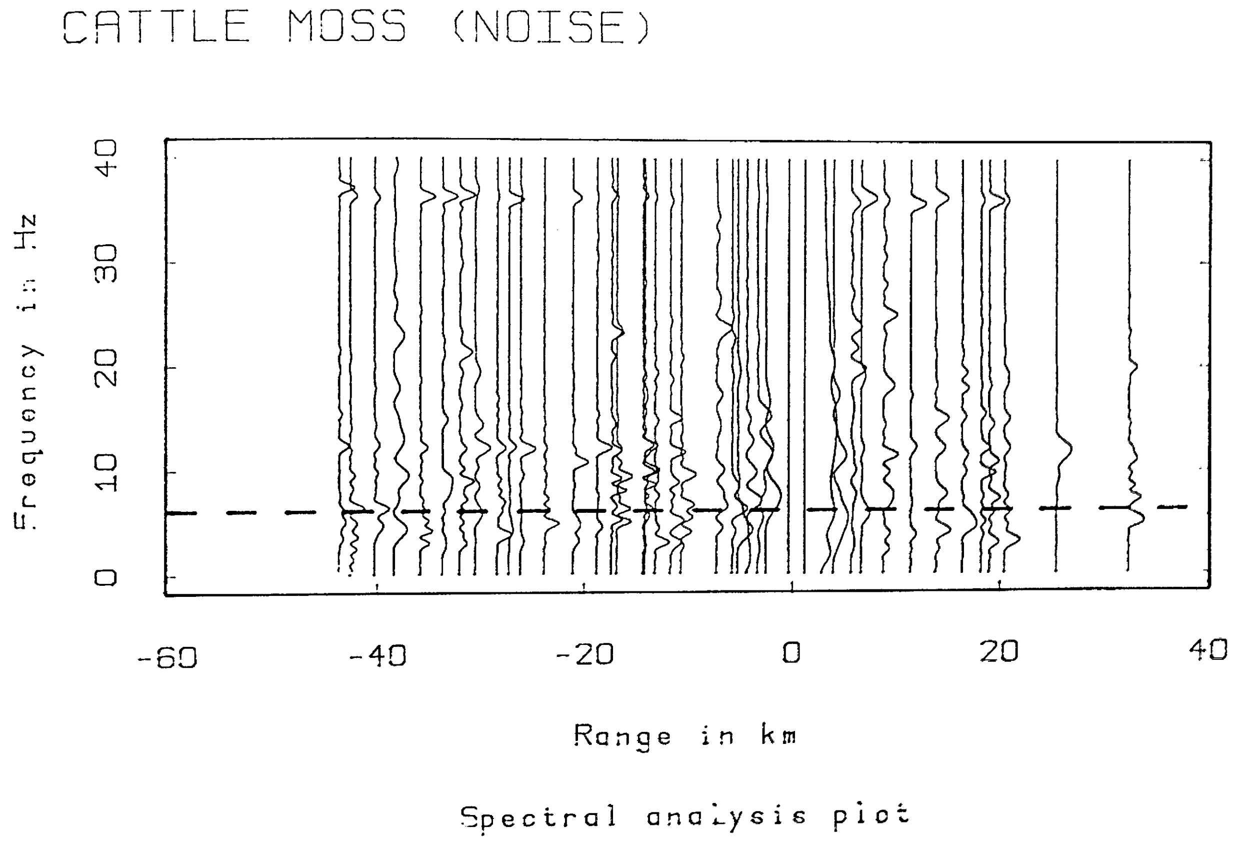

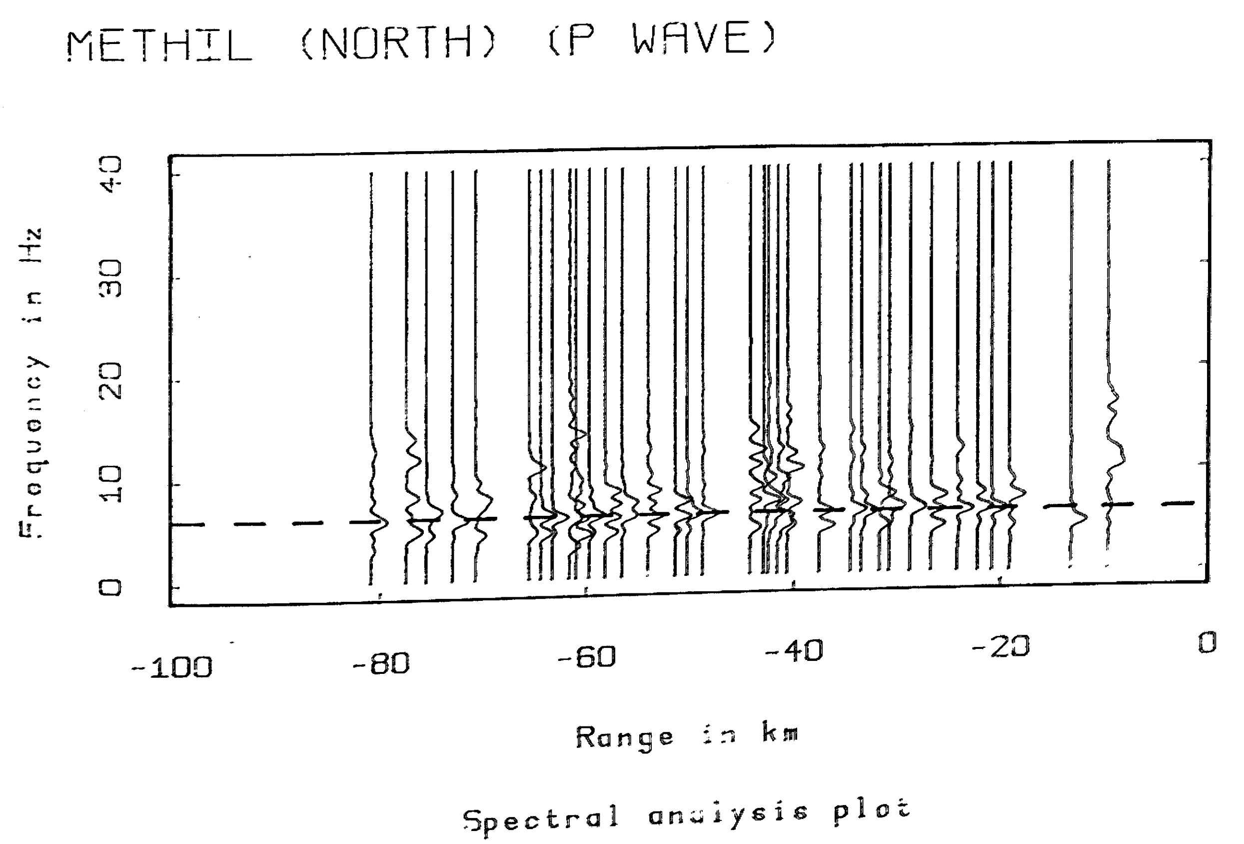

Fig.3.51 Representative frequency spectra of noise and marine shot P-wave arrivals. Dashed line is at 6 Hz.

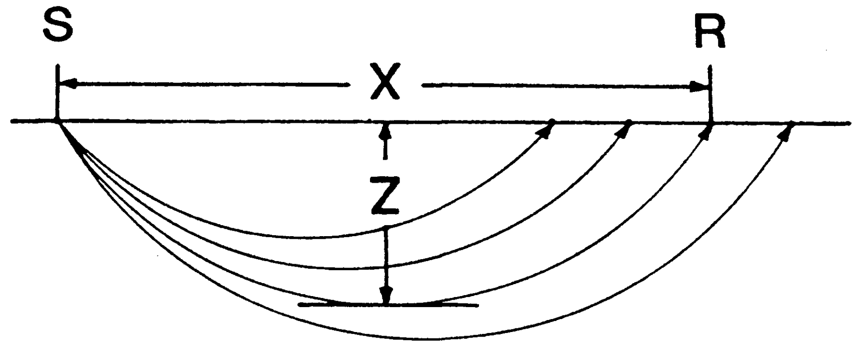

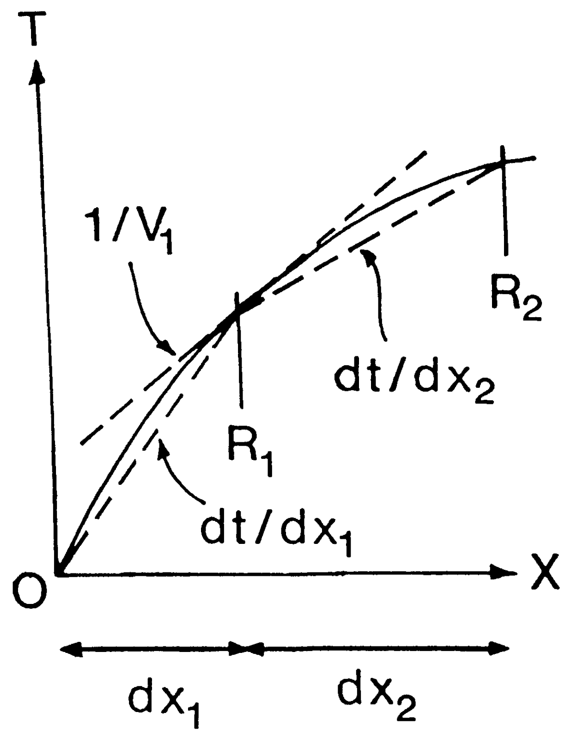

$$Z(V) = \frac{1}{\pi} \int_{x=0}^{x=X} \cosh^{-1}(V \cdot dt/dx)\,dx$$

WHERE $V = (dx/dt)_{x=X}$

Fig.4.1 WHB inversion of time-distance data.

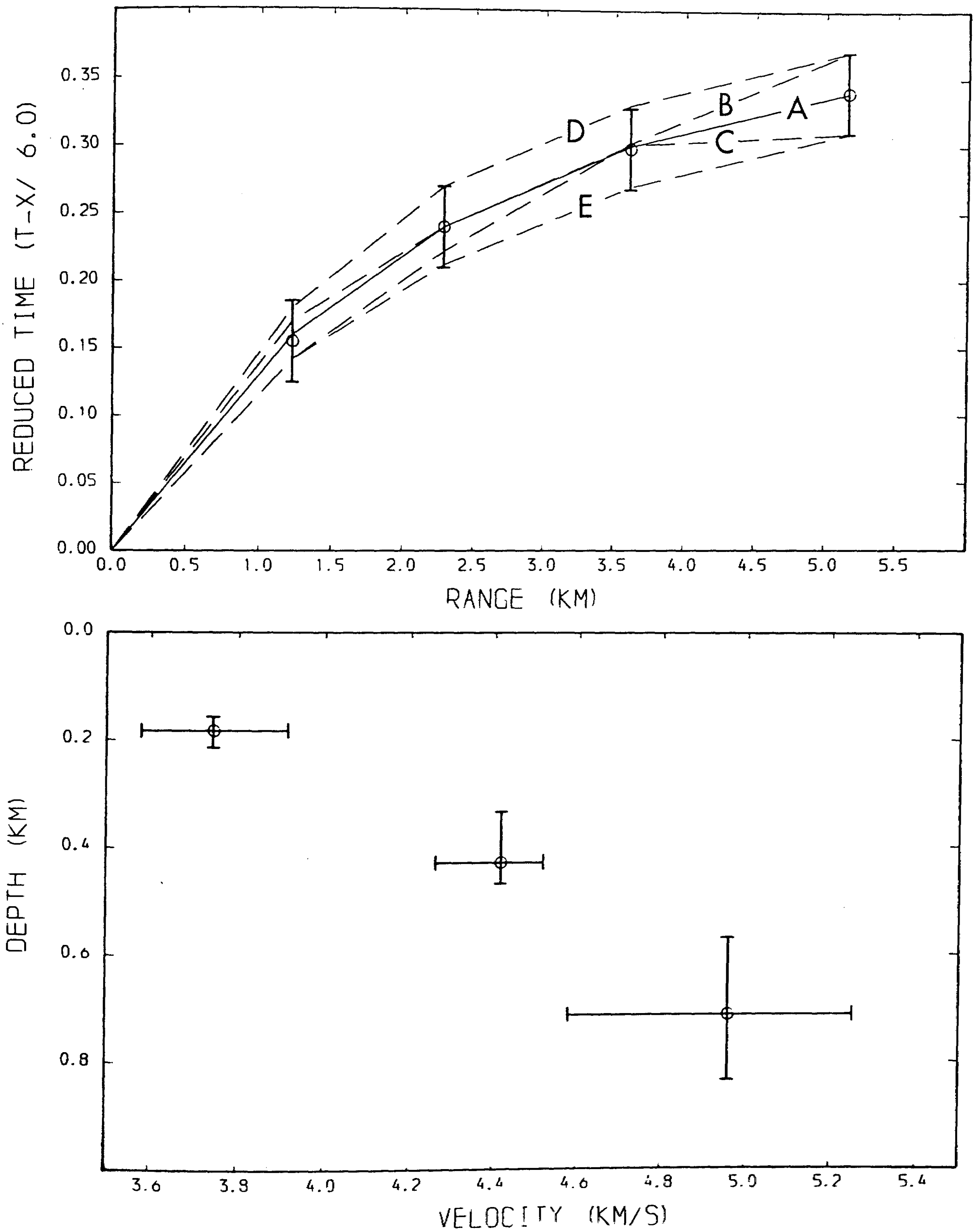

Fig.4.2 WHB inversion of the five time-distance curves (A to E) representing the best-fit, and maximum variation within errors, of the data.

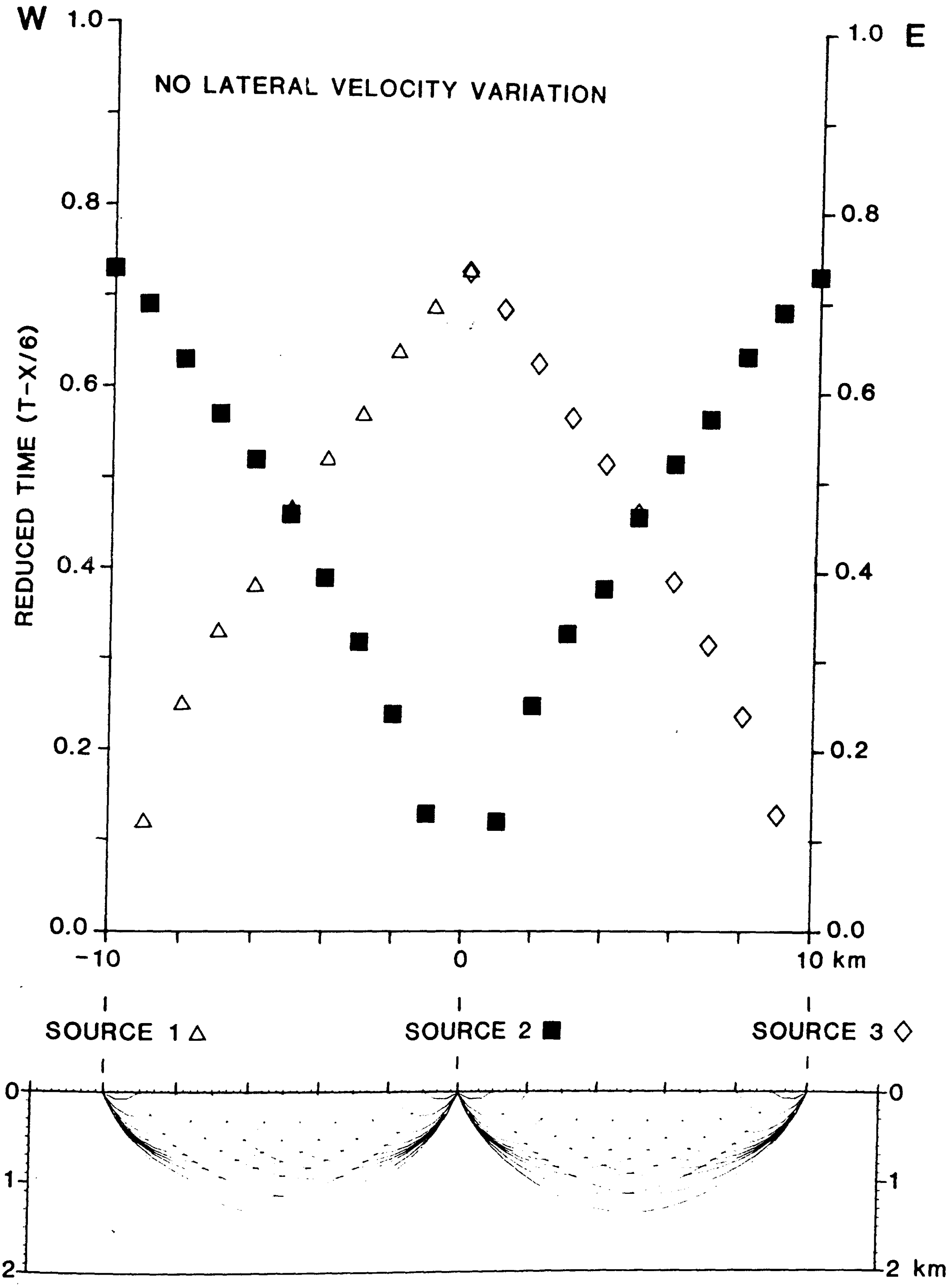

Fig.4.3 Model, plus time-distance data and ray-paths calculated by SEIS81.

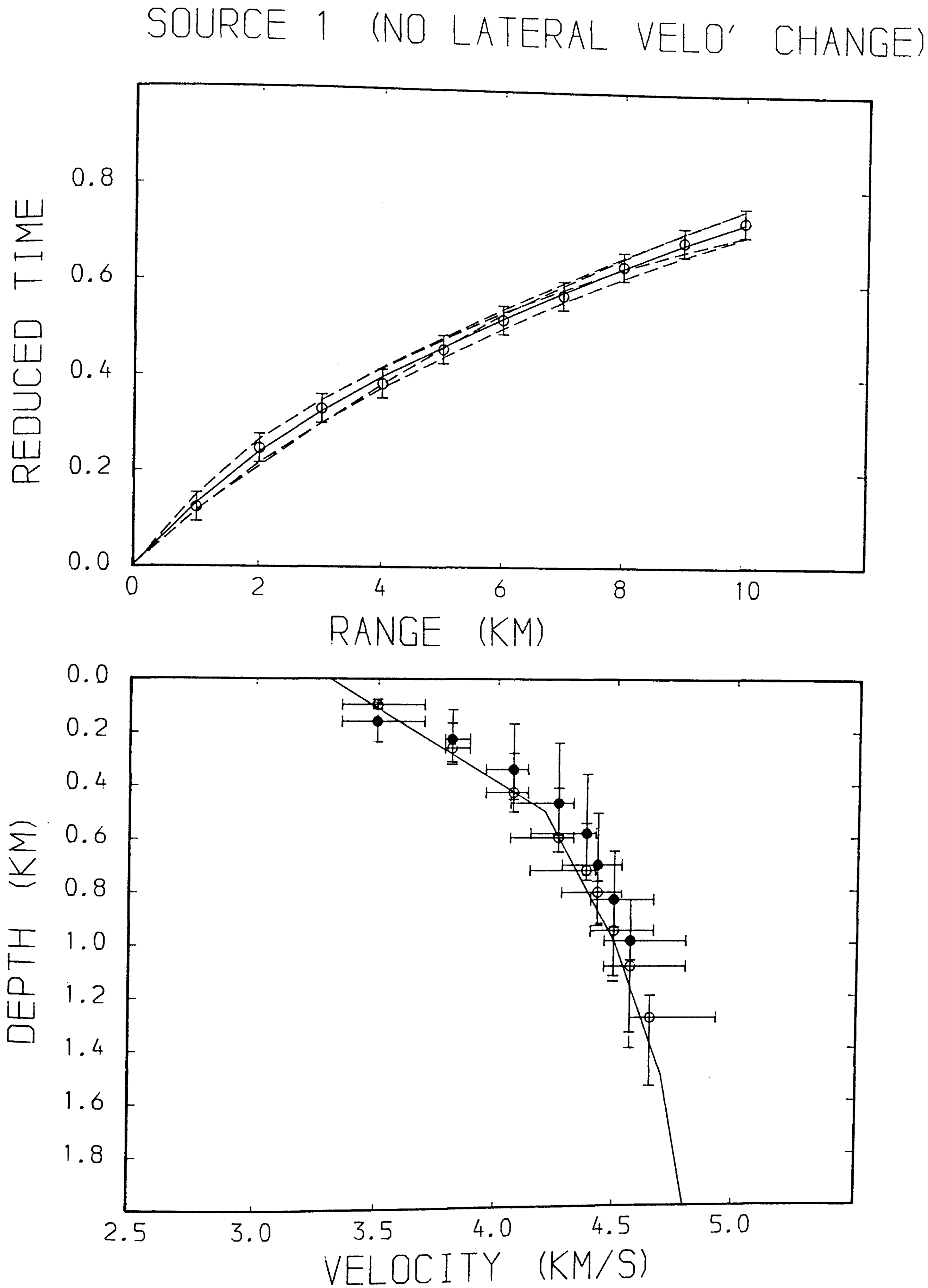

Fig.4.4a Comparison of model and calculated velocity-depth data; source 1. Reduction velocity is 6.0 km/s. WHB data open circles, tau-p data solid circles. The model curve is shown for comparison.

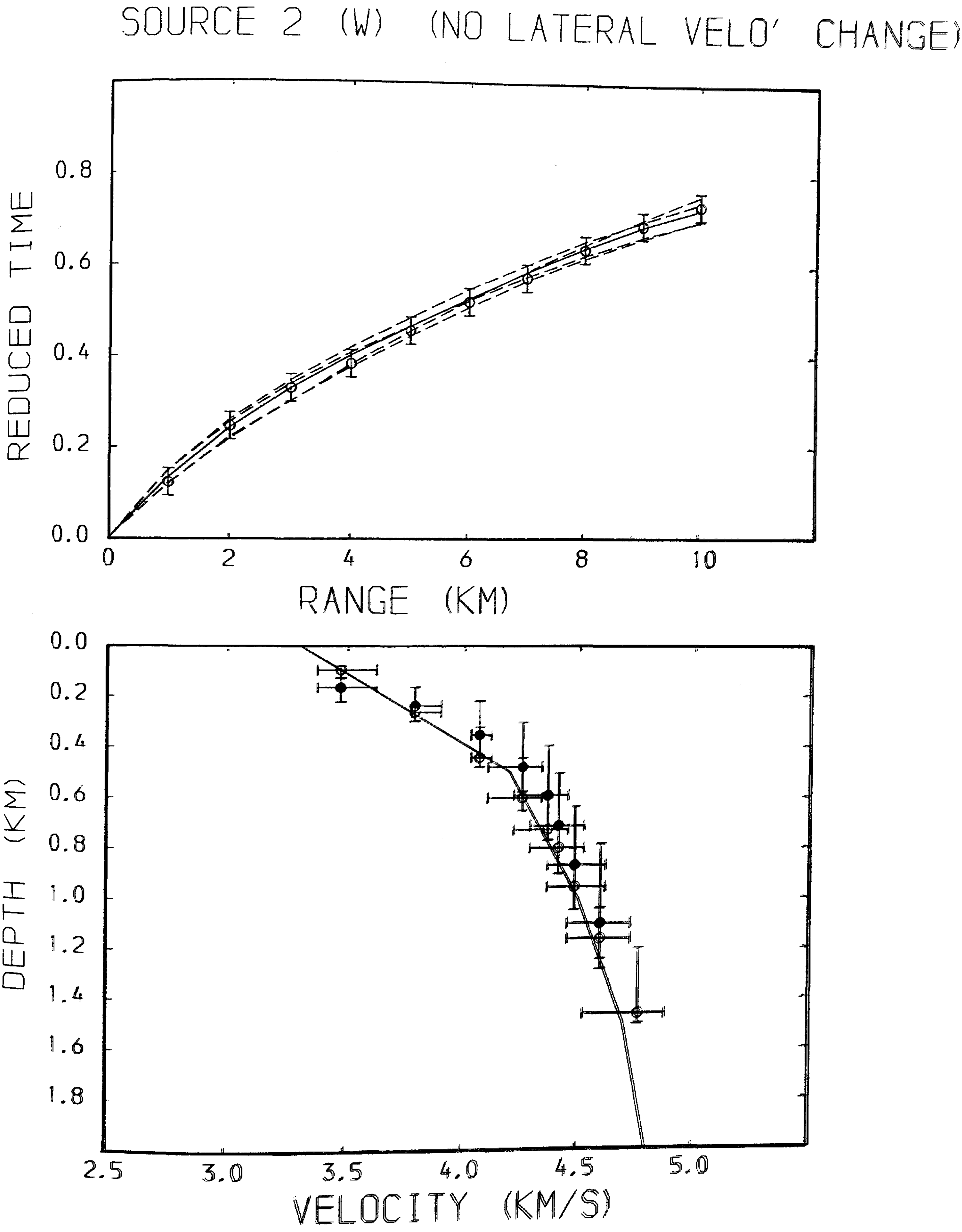

Fig.4.4b Comparison of model and calculated velocity-depth data; source 2 (west). Reduction velocity is 6.0 km/s. WHB data open circles, tau-p data solid circles. The model curve is shown for comparison.

SOURCE 2 (E) (NO LATERAL VELO' CHANGE)

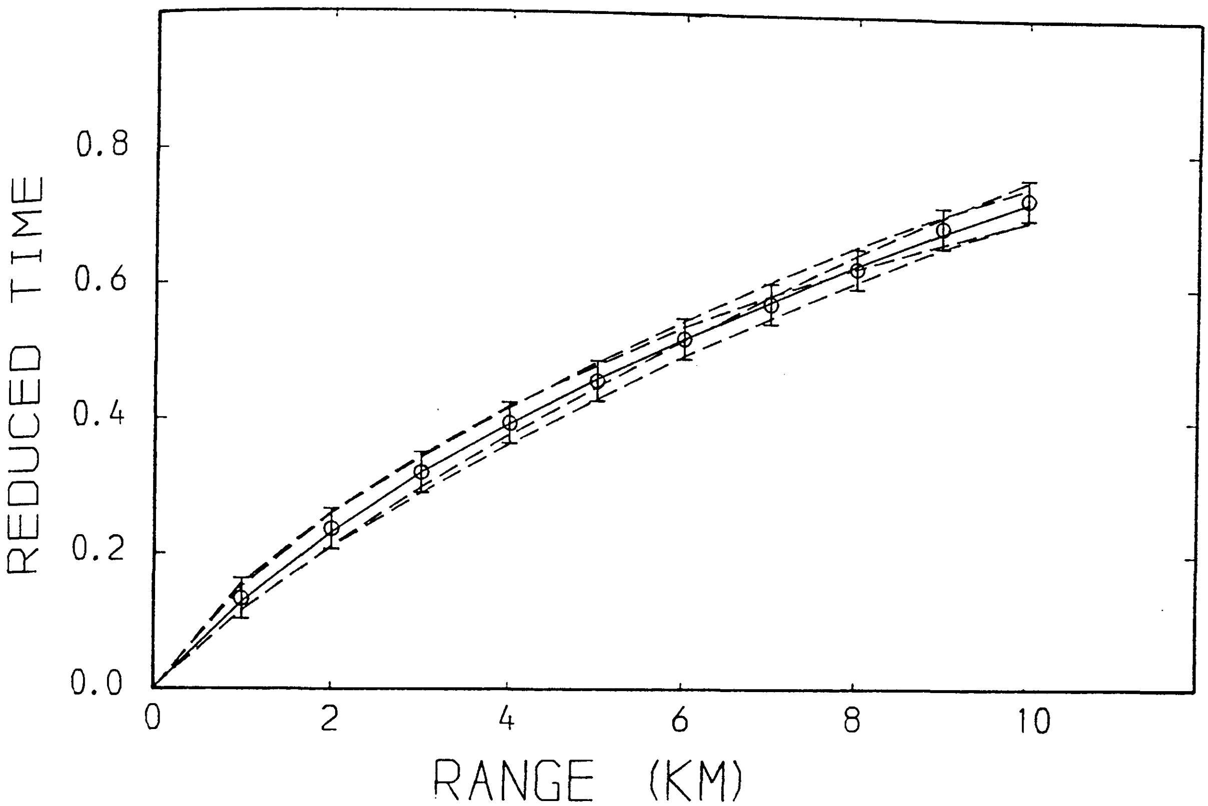

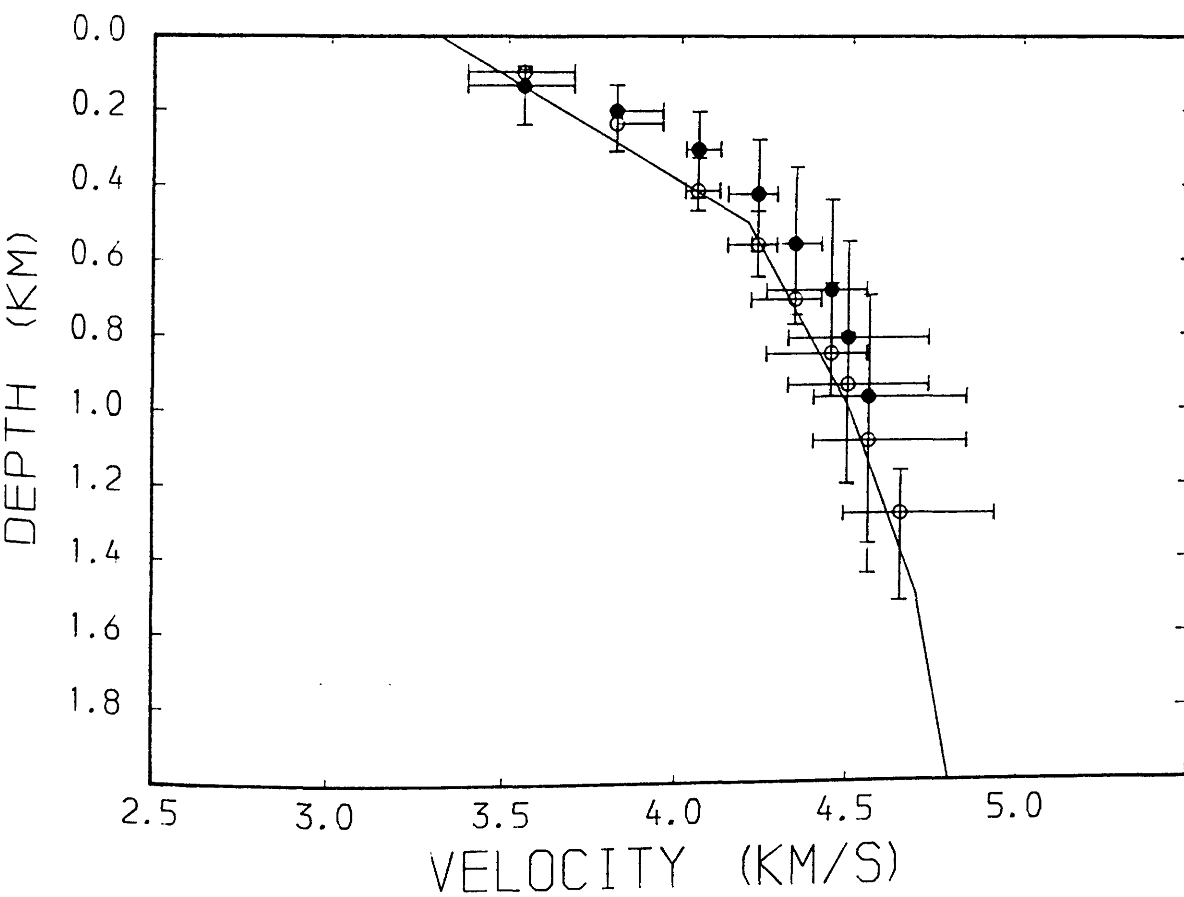

Fig.4.4c Comparison of model and calculated velocity-depth data; source 2 (east). Reduction velocity is 6.0 km/s. WHB data open circles, tau-p data solid circles. The model curve is shown for comparison.

SOURCE 3 (NO LATERAL VELO' CHANGE)

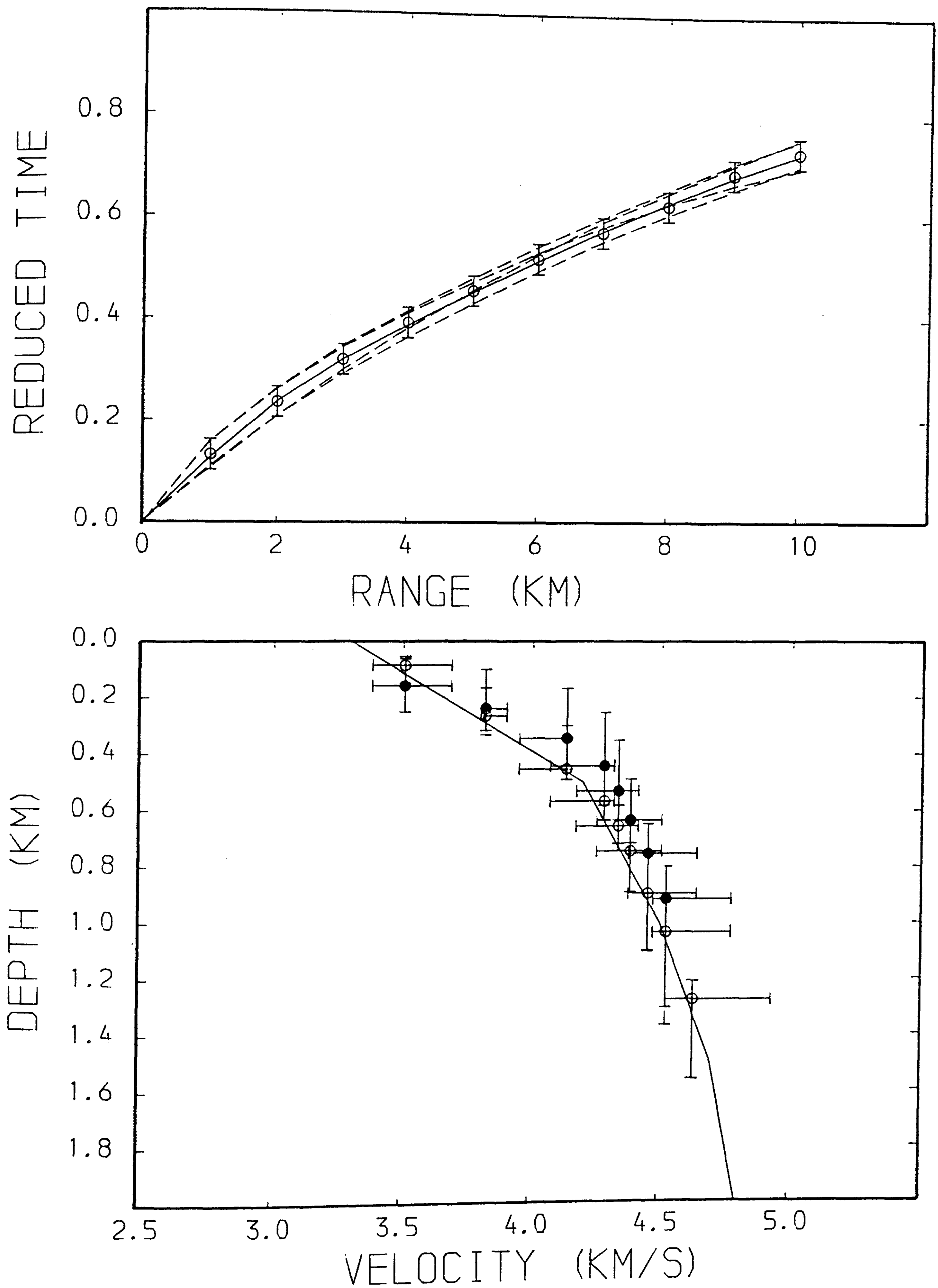

Fig.4.4d Comparison of model and calculated velocity-depth data,; source 3. Reduction velocity is 6.0 km/s. WHB data open circles, tau-p data solid circles. The model curve is shown for comparison.

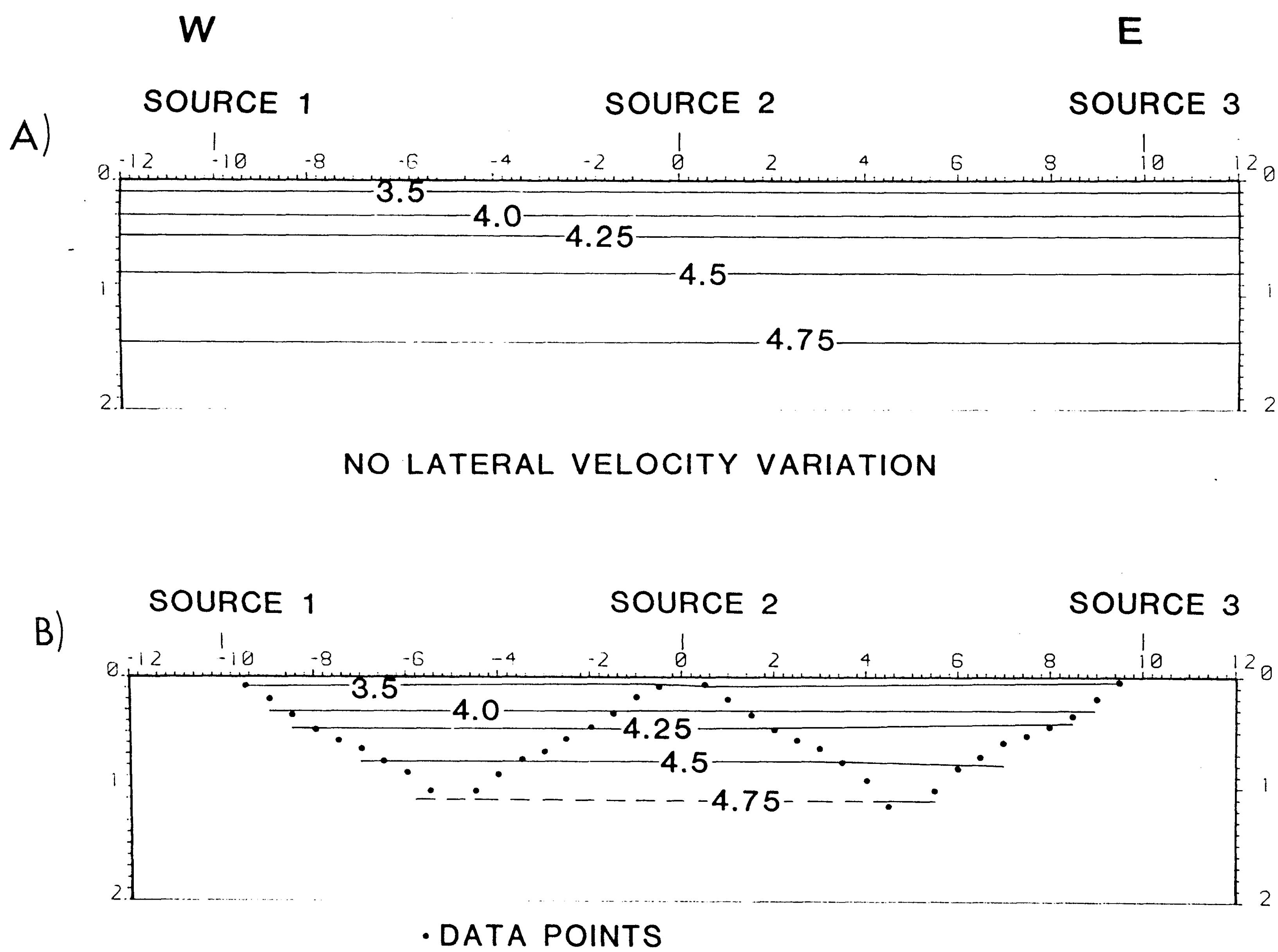

Fig.4.5 Input (A) and derived (B) velocity model using the WHB inversion. Velocity contours in km/s.

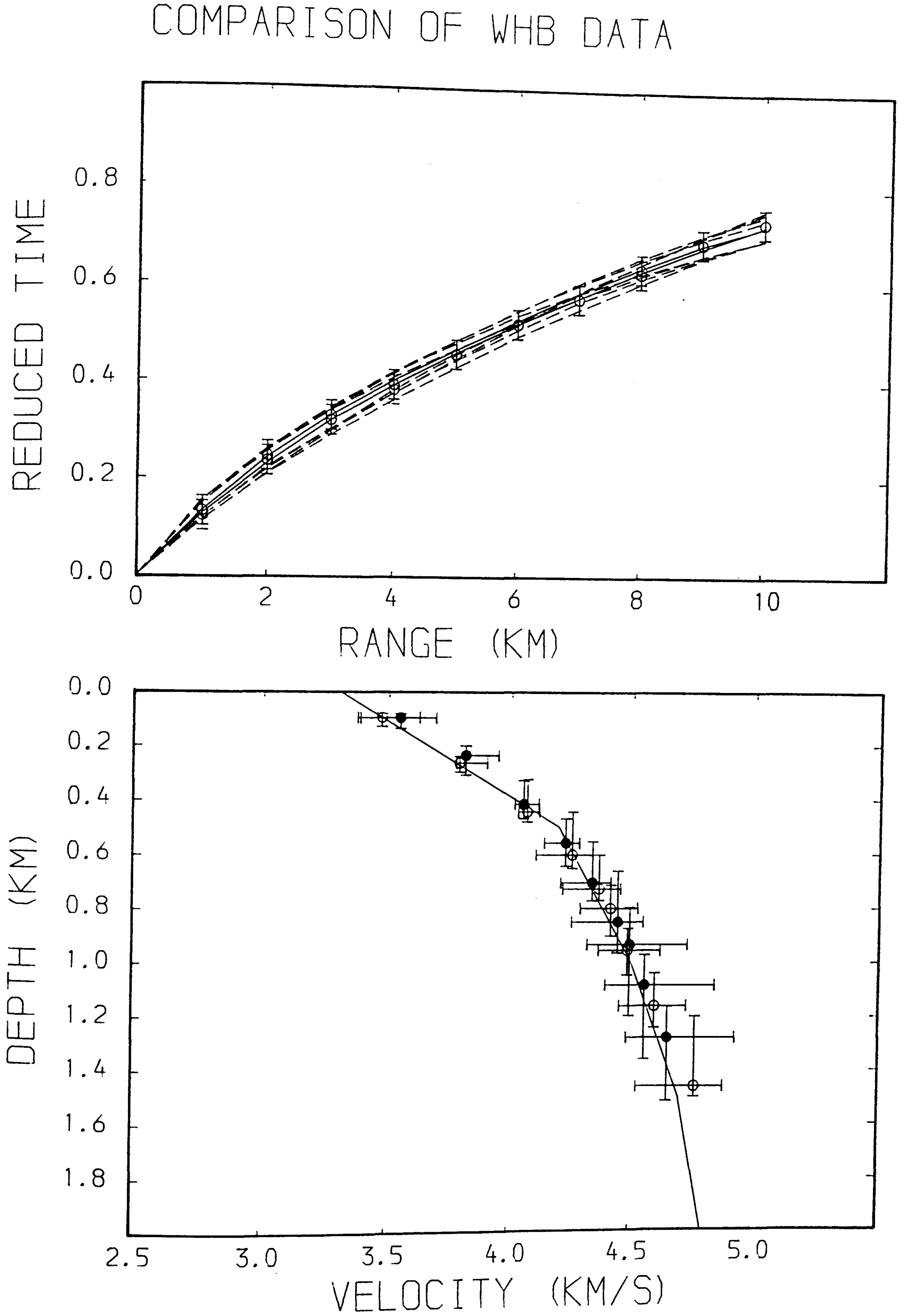

Fig.4.6a Comparison of data derived using the WHB inversion technique. Reduction velocity is 6.0 km/s. Data are from source 2, east solid circles, west open circles. The model curves is shown for comparison.

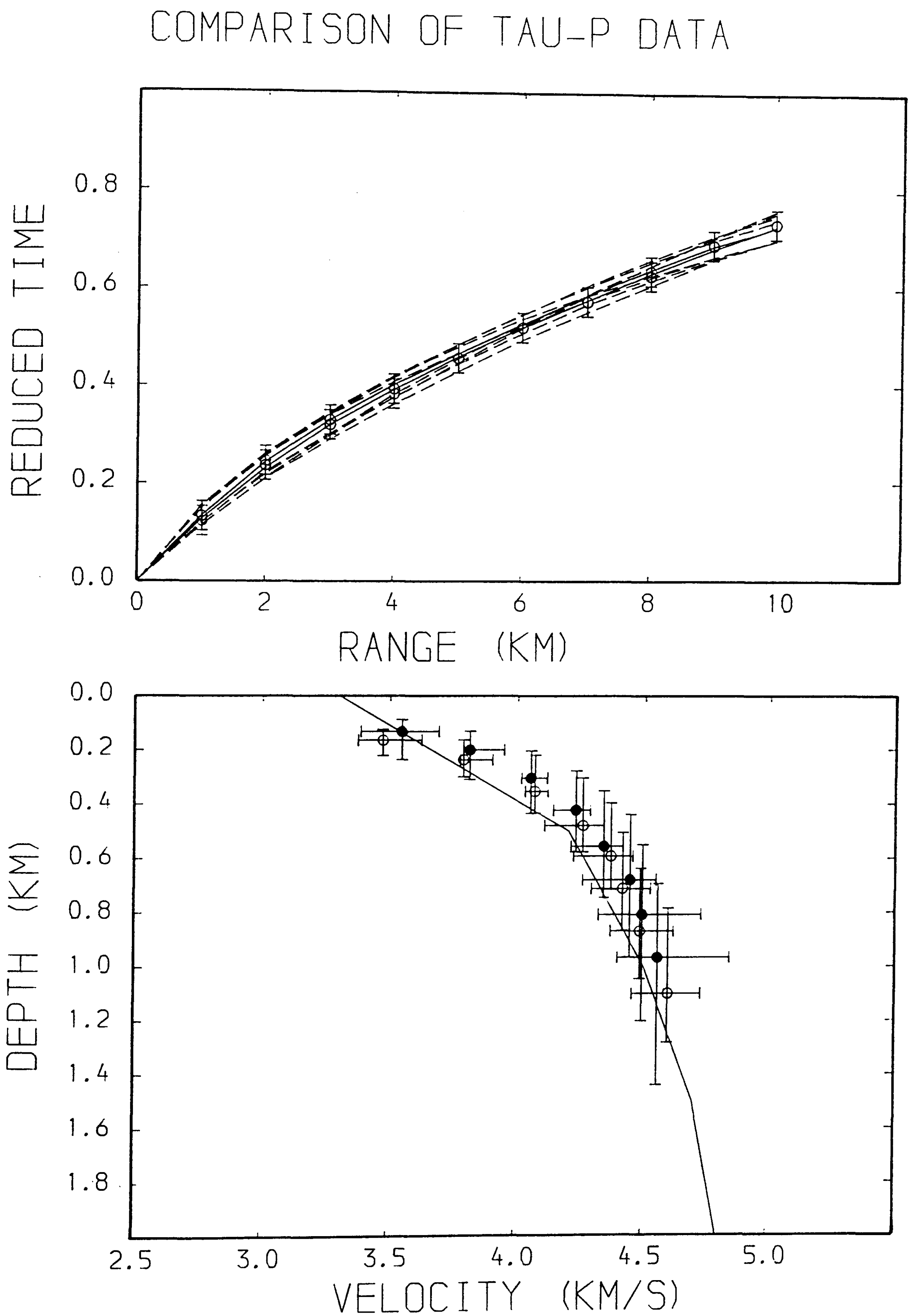

Fig.4.6b Comparison of data derived using the tau-p inversion technique. Reduction velocity is 6.0 km/s. Data are from source 2, east solid circles, west open circles. The model curves is shown for comparison.

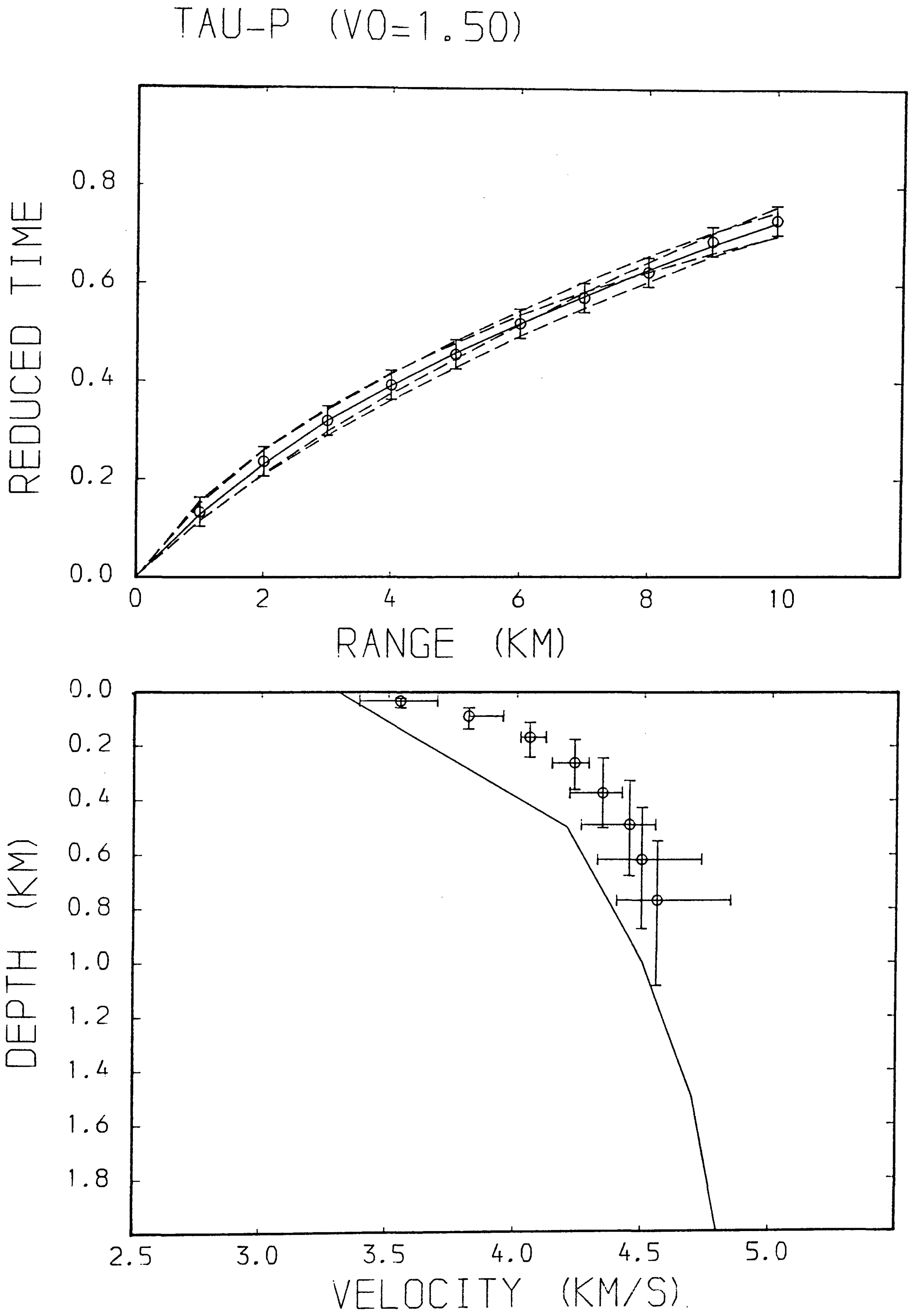

Fig.4.7a The effect of V0 on the tau-p method, V0 = 1.50 km/s. Reduction velocity is 6.0 km/s. The model curve is shown for comparison.

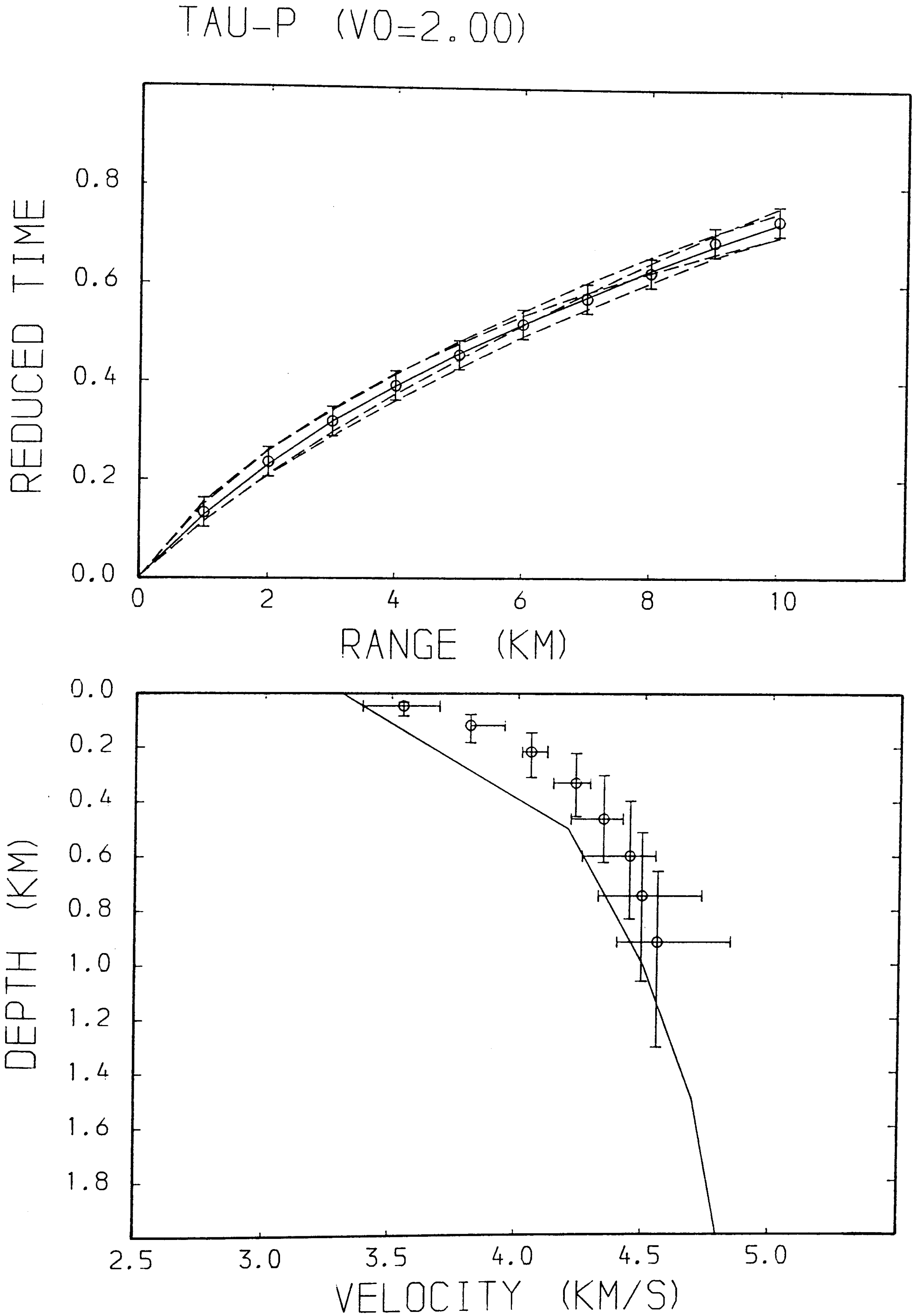

Fig.4.7b The effect of V0 on the tau-p method, V0 = 2.00 km/s. Reduction velocity is 6.0 km/s. The model curve is shown for comparison.

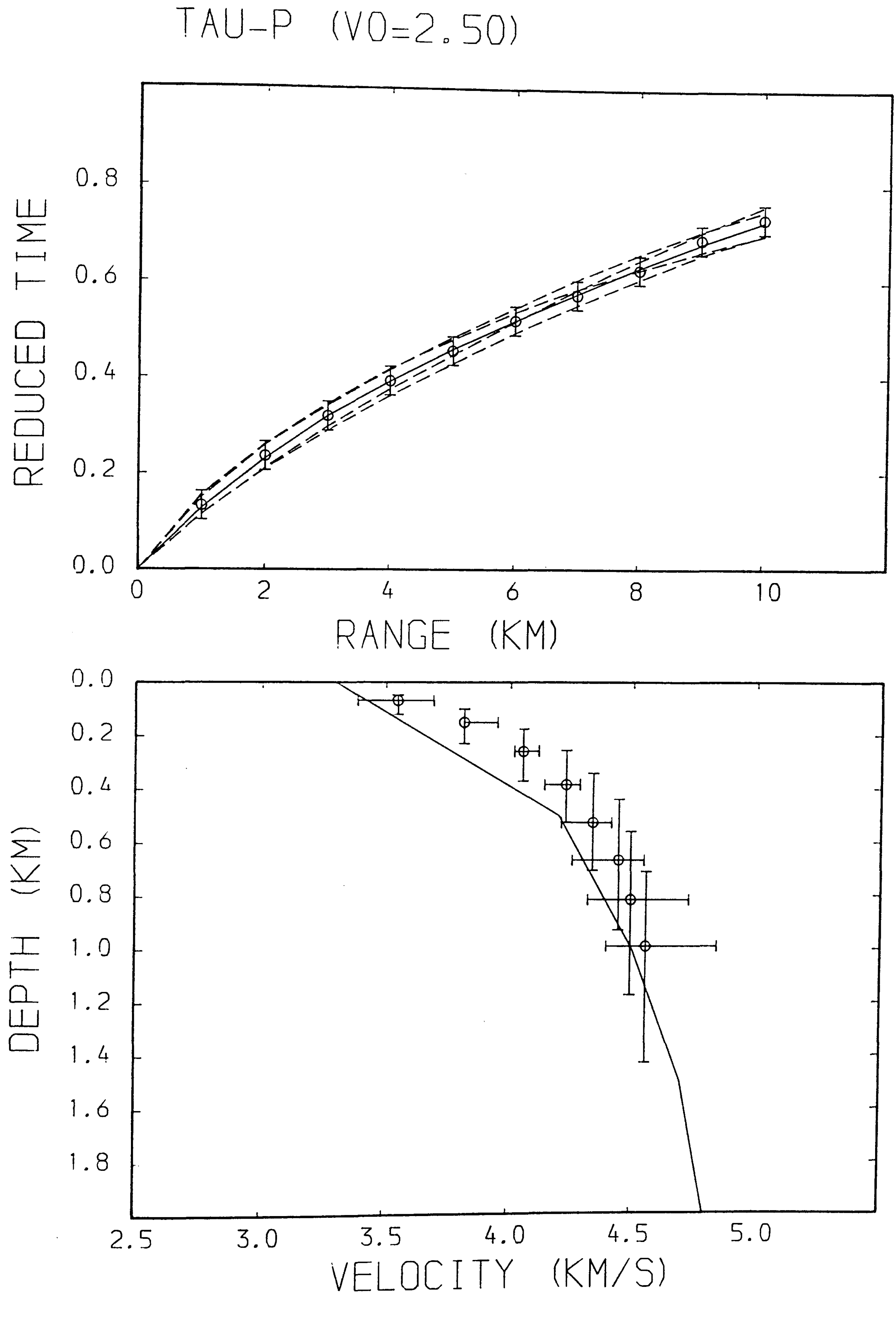

Fig.4.7c The effect of V0 on the tau-p method, V0 = 2.50 km/s. Reduction velocity is 6.0 km/s. The model curve is shown for comparison.

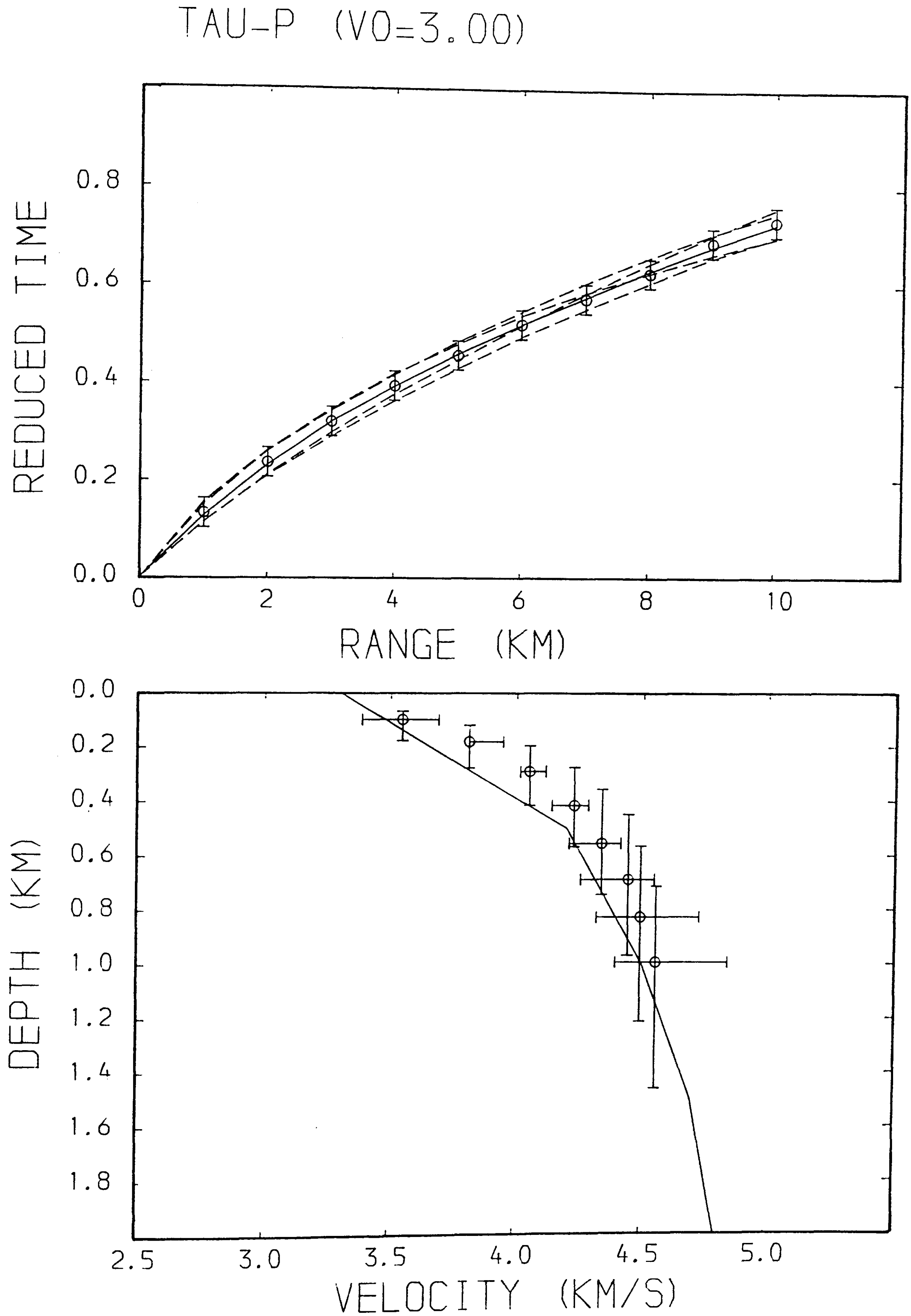

Fig.4.7d The effect of V0 on the tau-p method, V0 = 3.00 km/s. Reduction velocity is 6.0 km/s. The model curve is shown for comparison.

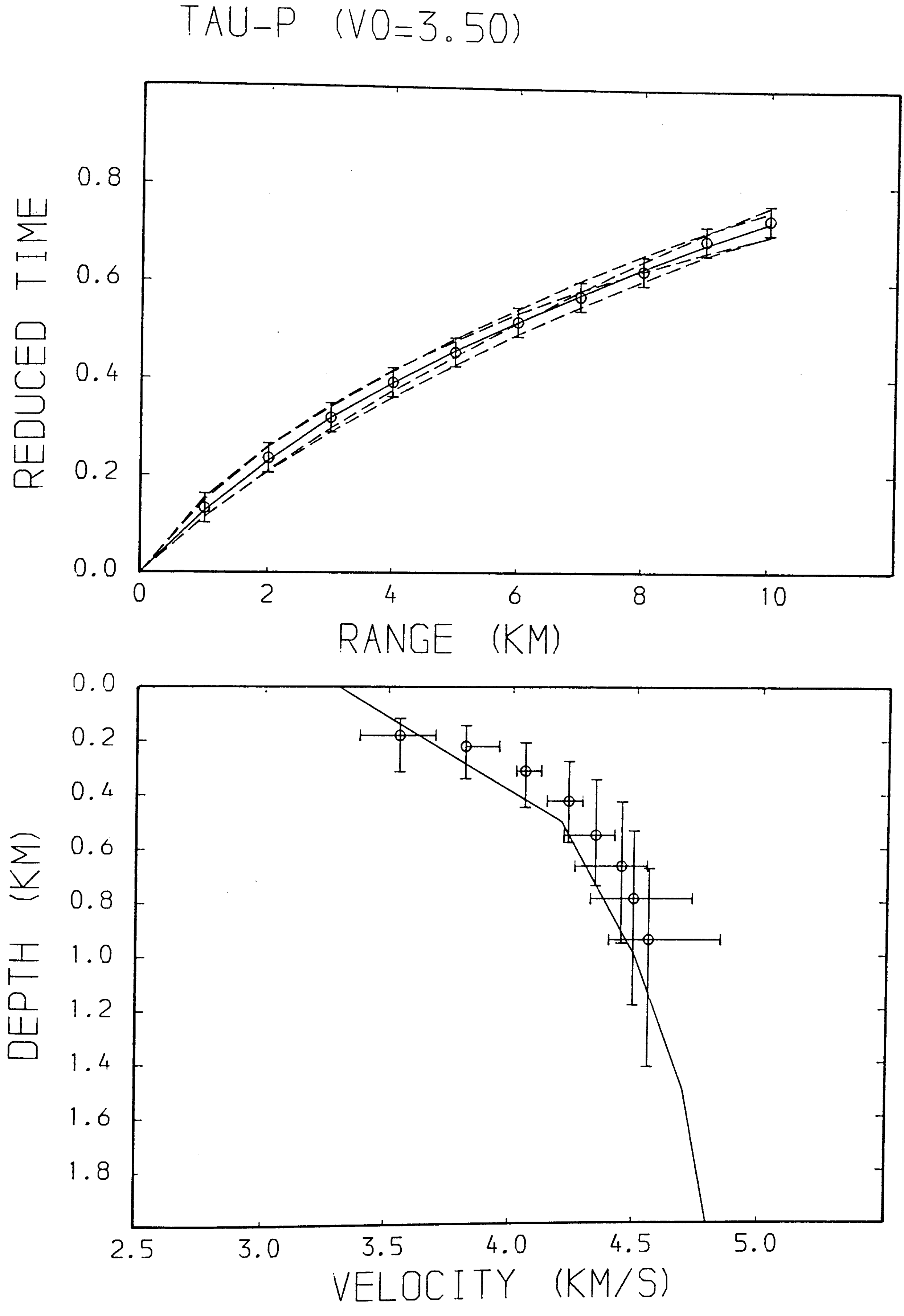

Fig.4.7e The effect of V0 on the tau-p method, V0 = 3.50 km/s. Reduction velocity is 6.0 km/s. The model curve is shown for comparison.

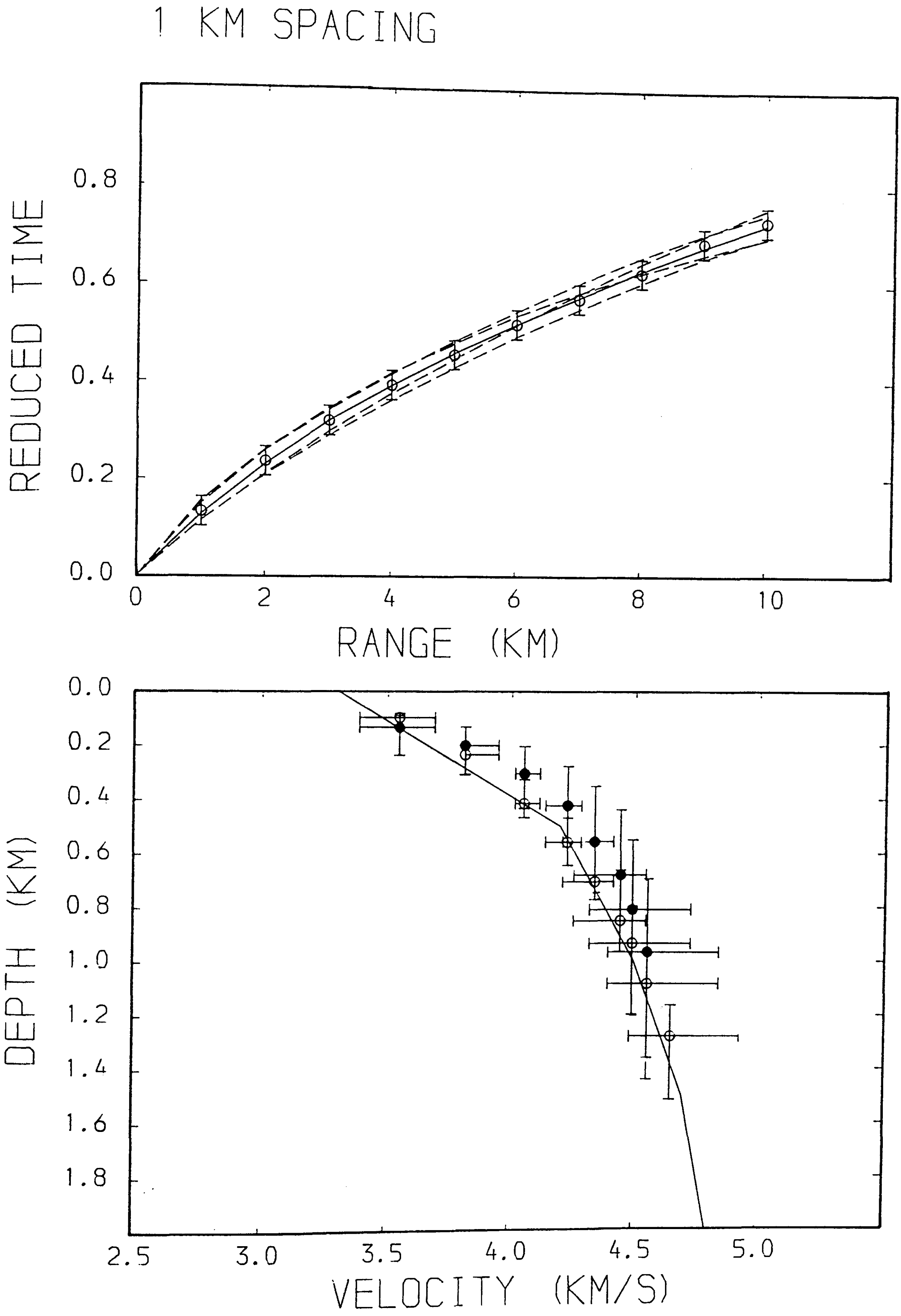

Fig.4.8a Effect of receiver spacing, 1 km spacing. Reduction velocity is 6.0 km/s. WHB data open circles, tau-p data solid circles. The model curve is shown for comparison.

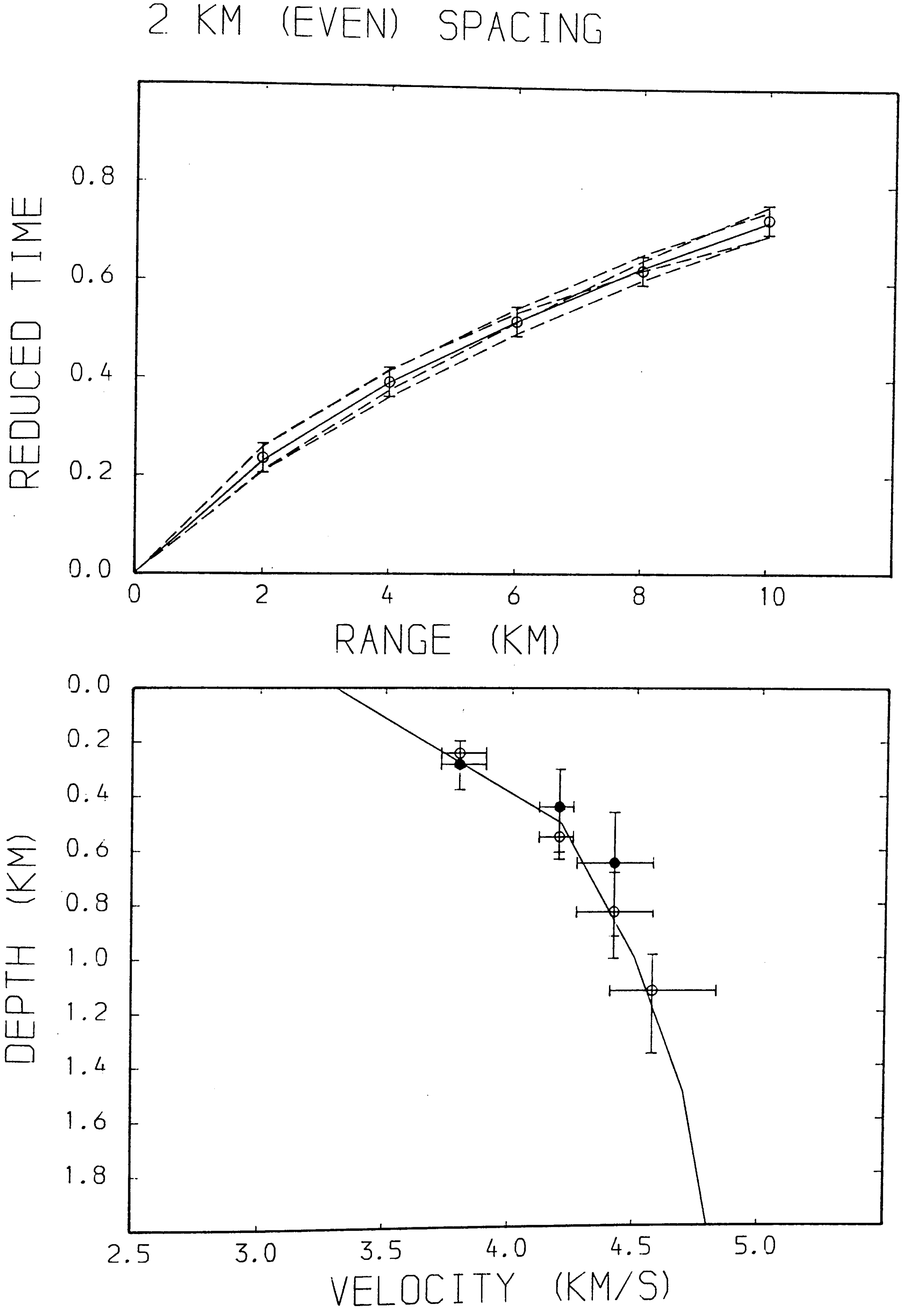

Fig.4.8b Effect of receiver spacing, 2 km (even) spacing. Reduction velocity is 6.0 km/s. WHB data open circles, tau-p data solid circles. The model curve is shown for comparison.

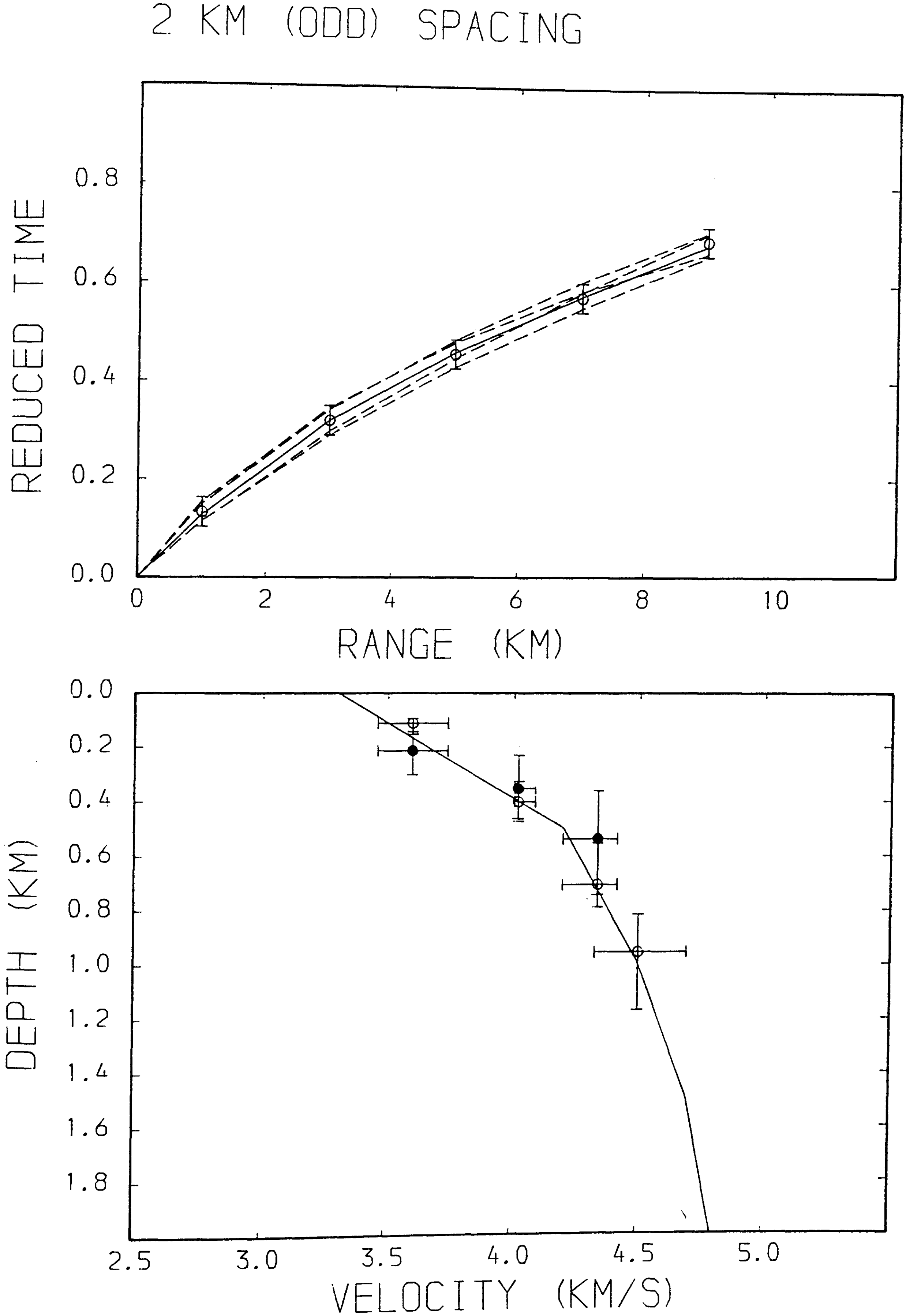

Fig.4.8c Effect of receiver spacing, 2 km (odd) spacing. Reduction velocity is 6.0 km/s. WHB data open circles, tau-p data solid circles. The model curve is shown for comparison.

3 KM (1, 4, 7, 10) SPACING

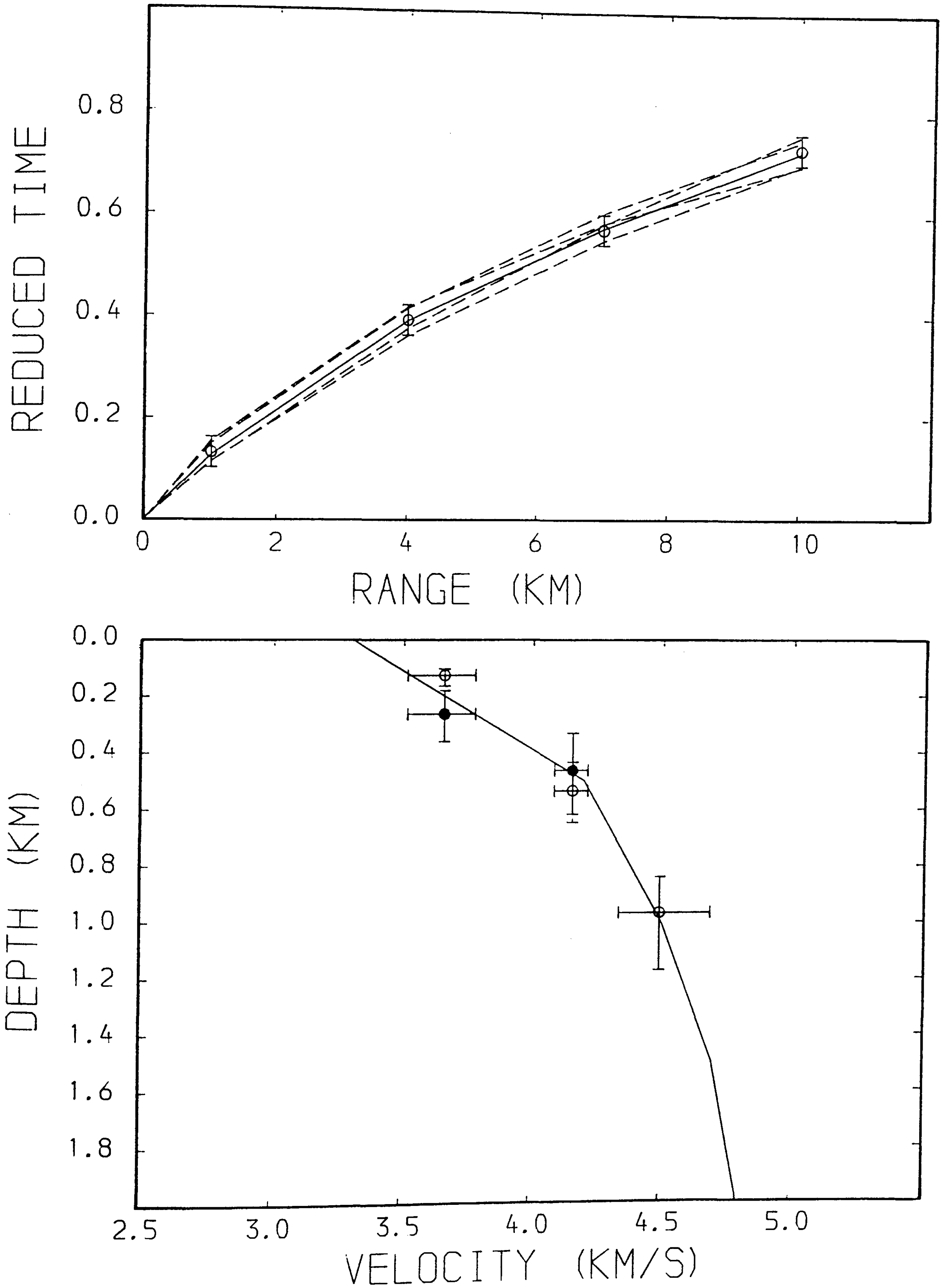

Fig.4.8d Effect of receiver spacing, 3 km (1,4,7,10) spacing. Reduction velocity is 6.0 km/s. WHB data open circles, tau-p data solid circles. The model curve is shown for comparison.

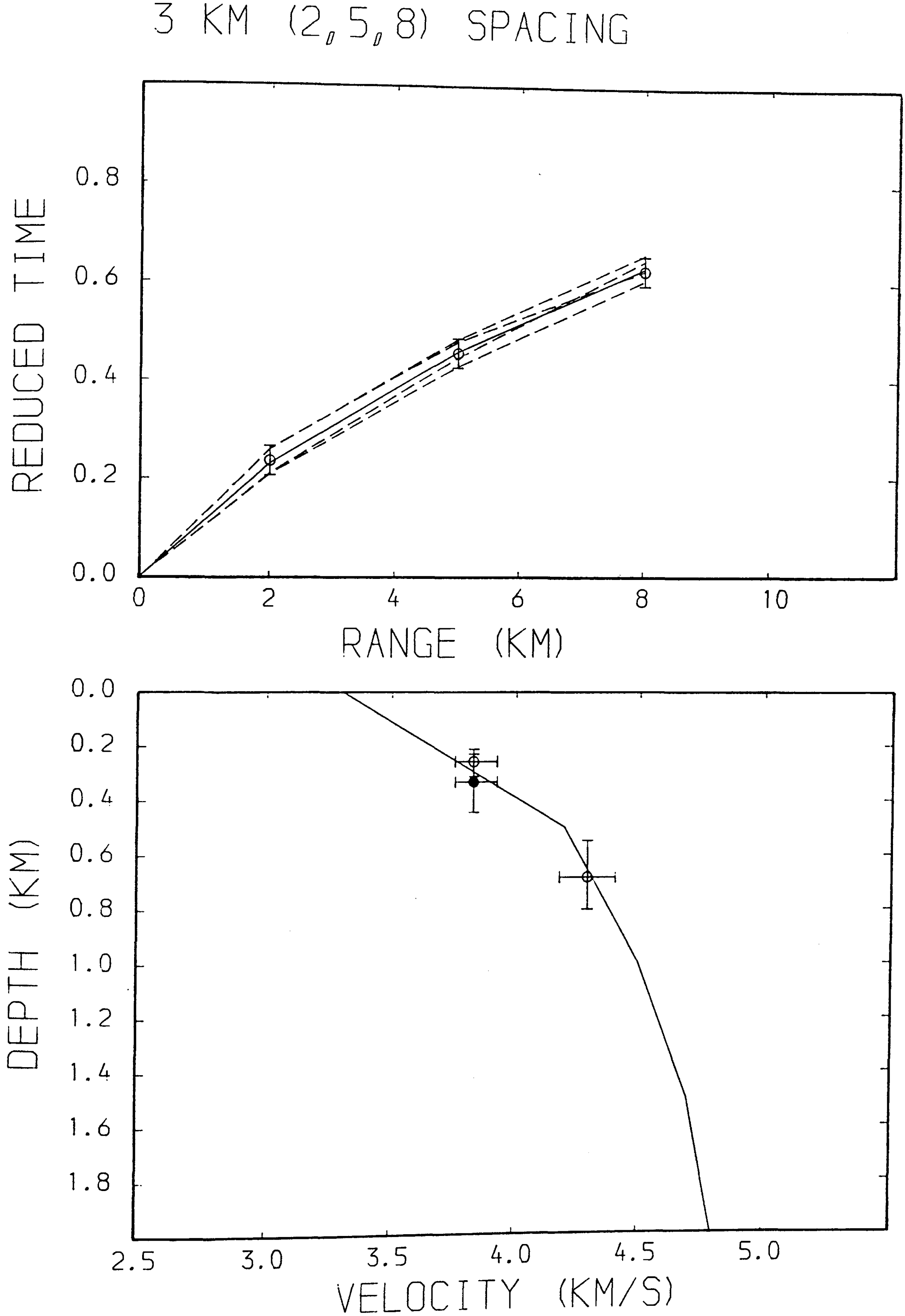

Fig.4.8e Effect of receiver spacing, 3 km (2,5,8) spacing. Reduction velocity is 6.0 km/s. WHB data open circles, tau-p data solid circles. The model curve is shown for comparison.

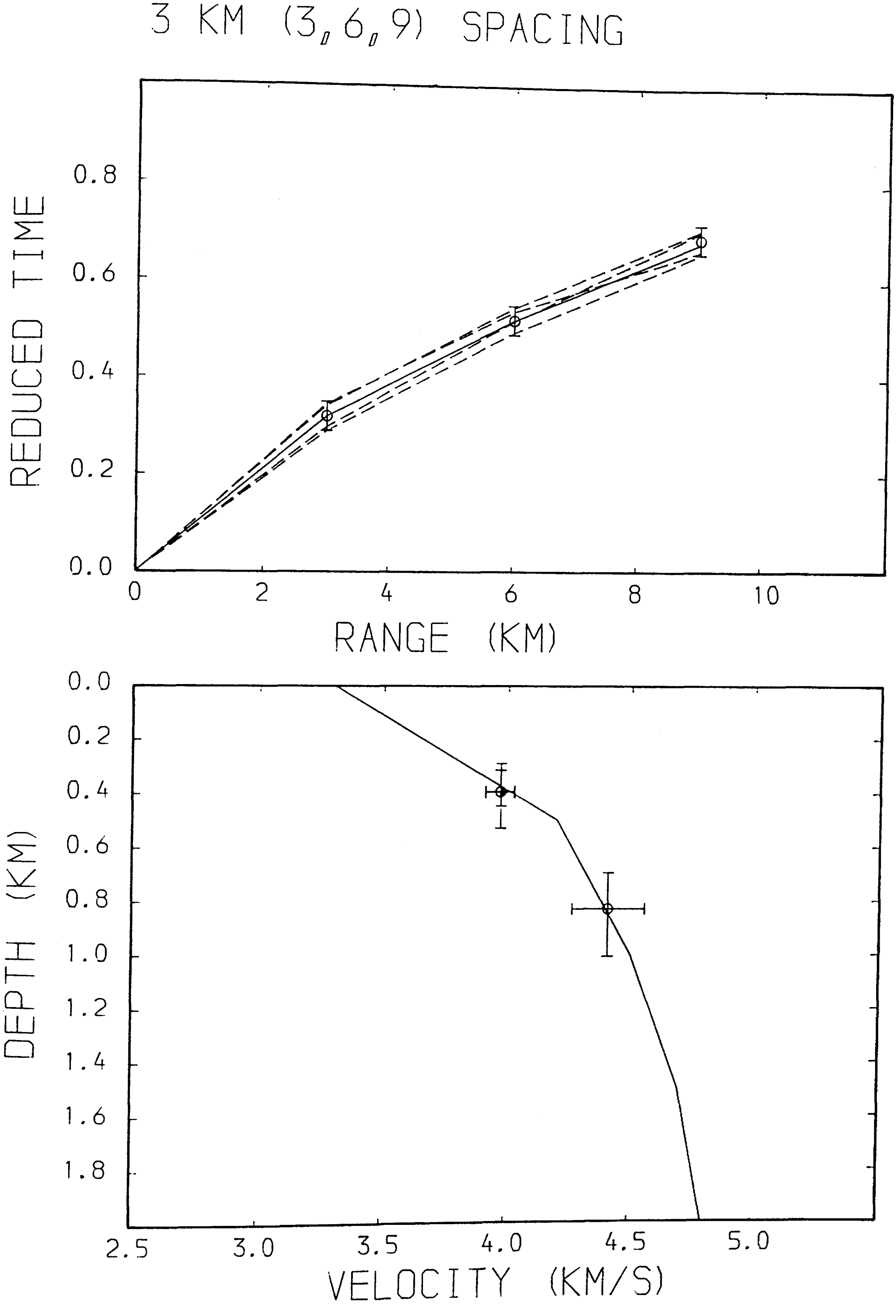

Fig.4.8f Effect of receiver spacing, 3 km (3,6,9) spacing. Reduction velocity is 6.0 km/s. WHB data open circles, tau-p data solid circles. The model curve is shown for comparison.

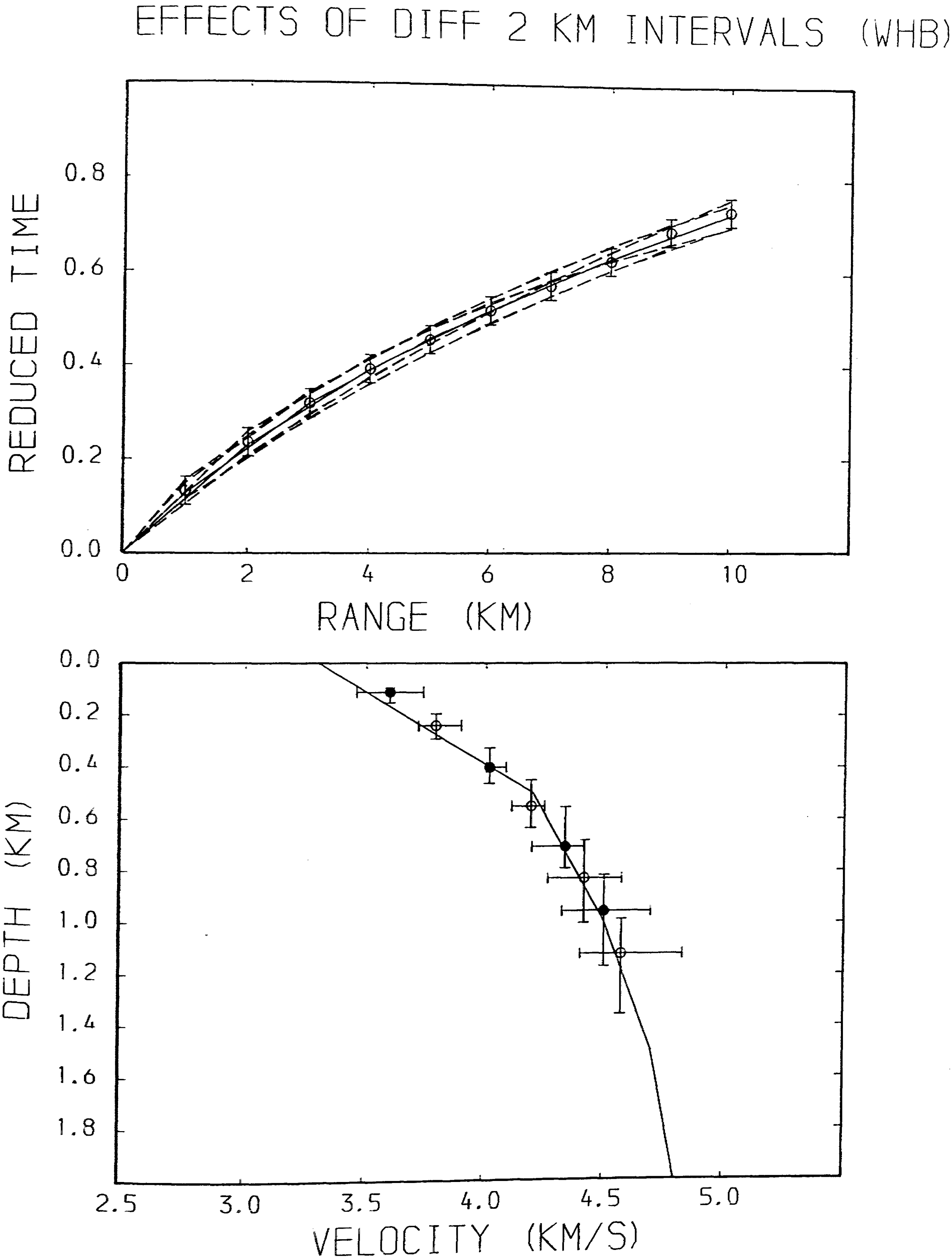

Fig.4.9a Effect of receiver geometry, 2 km spacing WHB data. Reduction velocity is 6.0 km/s. The model curve is shown for comparison. Even spacing open circles, odd spacing solid circles.

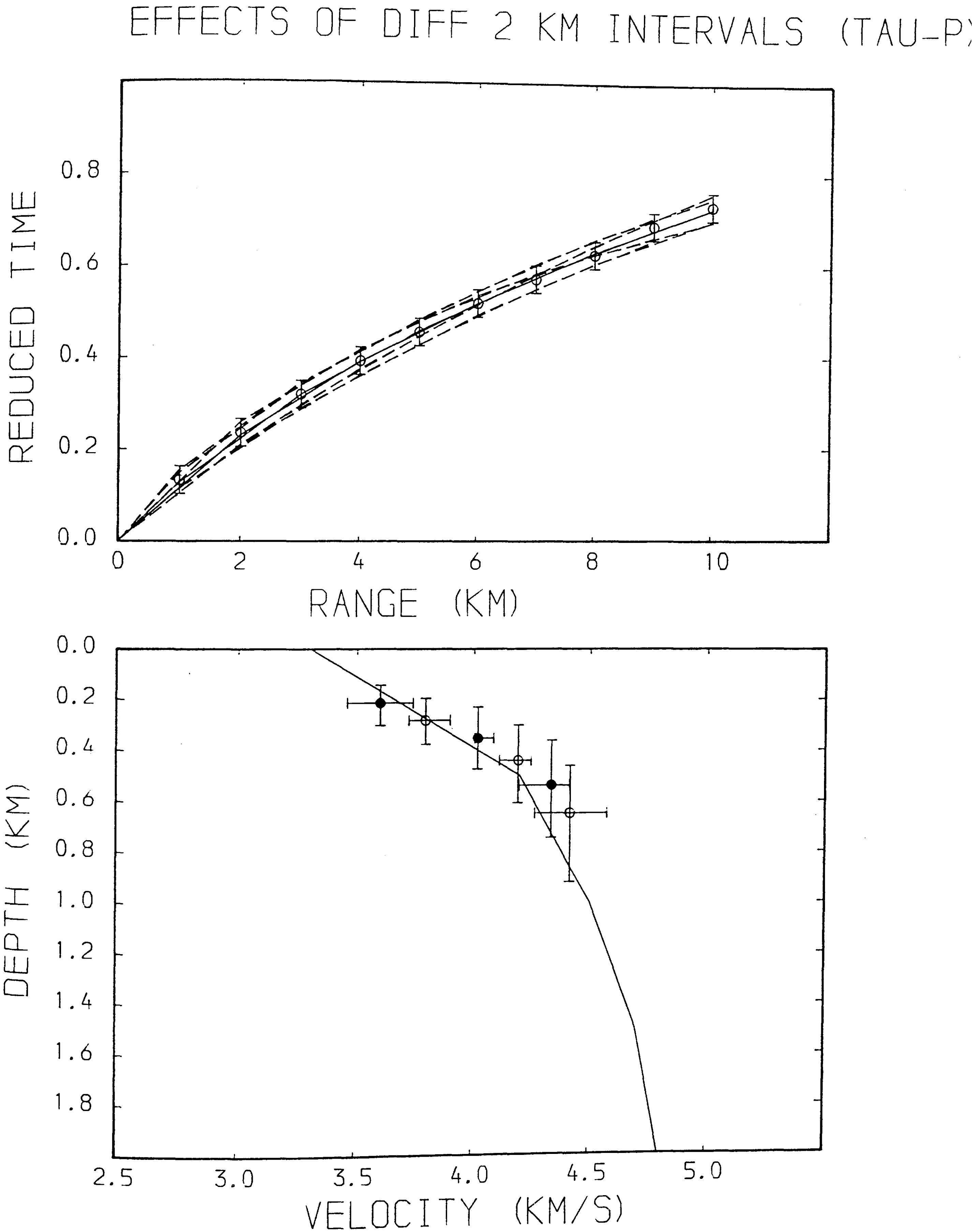

Fig.4.9b Effect of receiver geometry, 2 km spacing tau-p data. Reduction velocity is 6.0 km/s. The model curve is shown for comparison. Even spacing open circles, odd spacing solid circles.

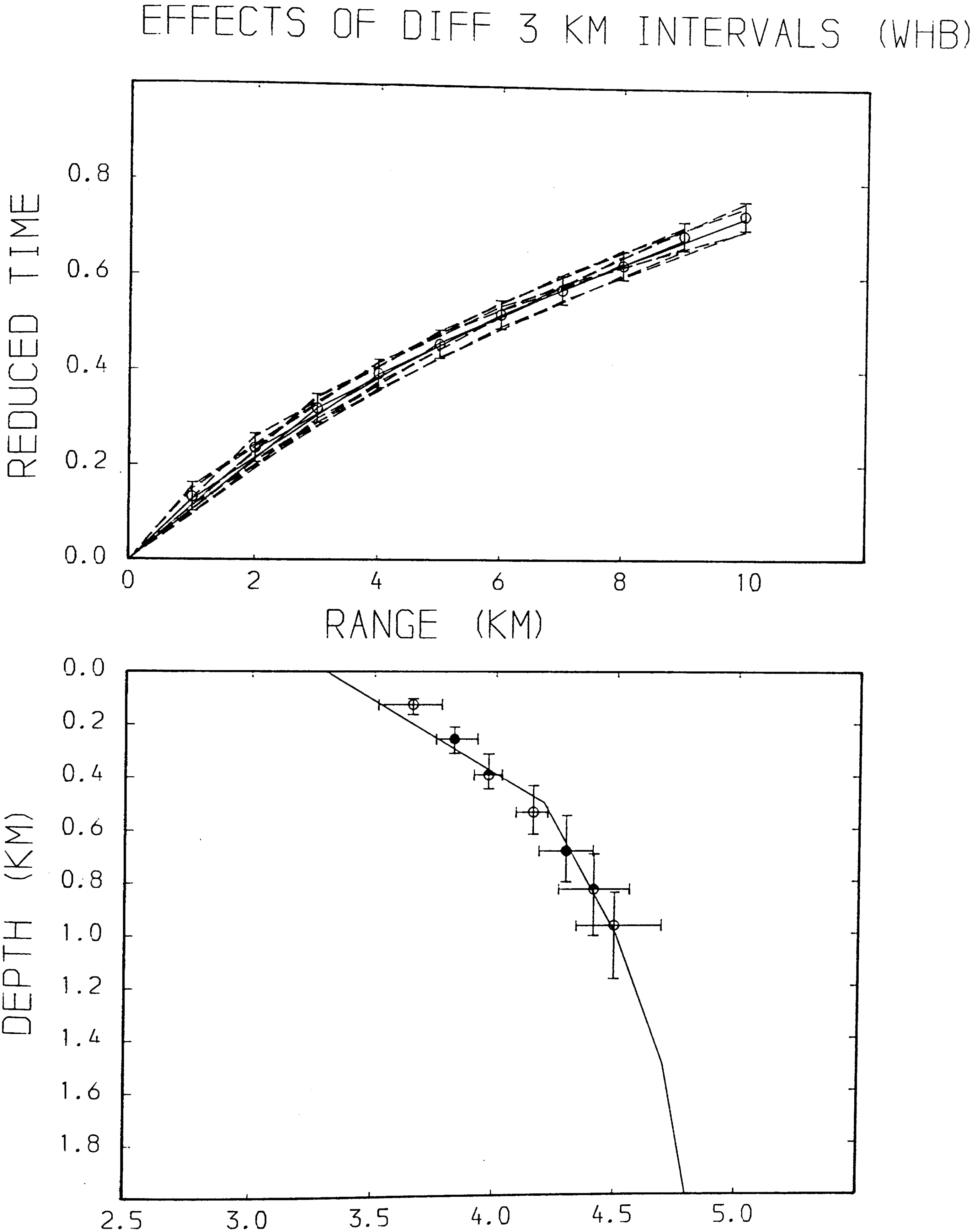

Fig.4.9c Effect of receiver geometry, 3 km spacing WHB data. Reduction velocity is 6.0 km/s. The model curve is shown for comparison. 1,4,7,10 open circles, 2,5,8 solid circles, 3,6,9 half circles.

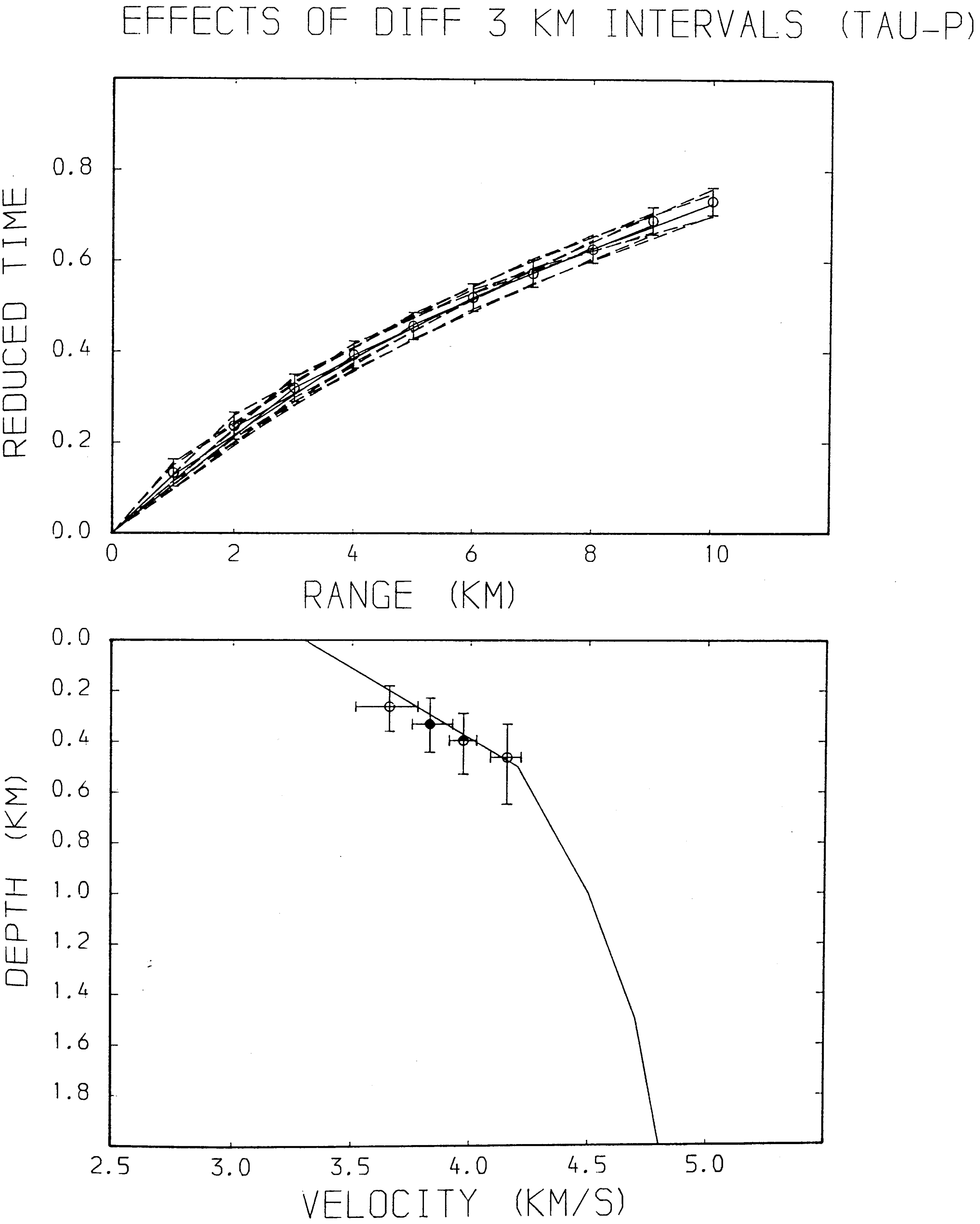

Fig.4.9d Effect of receiver geometry, 3 km spacing tau-p data. Reduction velocity is 6.0 km/s. The model curve is shown for comparison. 1,4,7,10 open circles, 2,5,8 solid circles, 3,6,9 half circles.

EFFECTS OF SAMPLE INTERVAL (WHB)

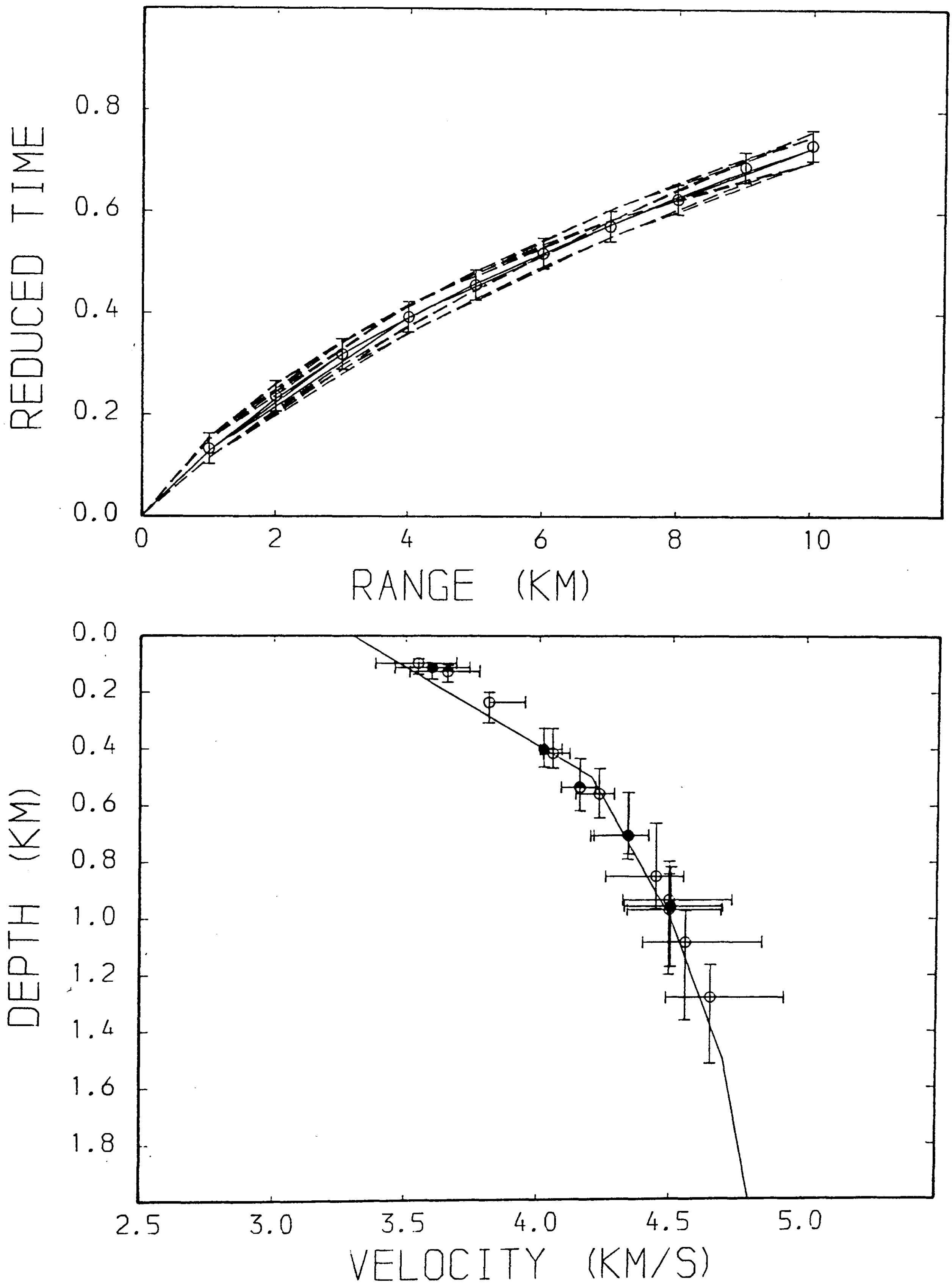

Fig.4.10a Effect of receiver interval, WHB data. Reduction velocity is 6.0 km/s. 1 km spacing open circles, 2 km (odd) spacing solid circles, 3 km (1,4,7,10) spacing half circles. The model curve is shown for comparison.

EFFECTS OF SAMPLE INTERVAL (TAU-P)

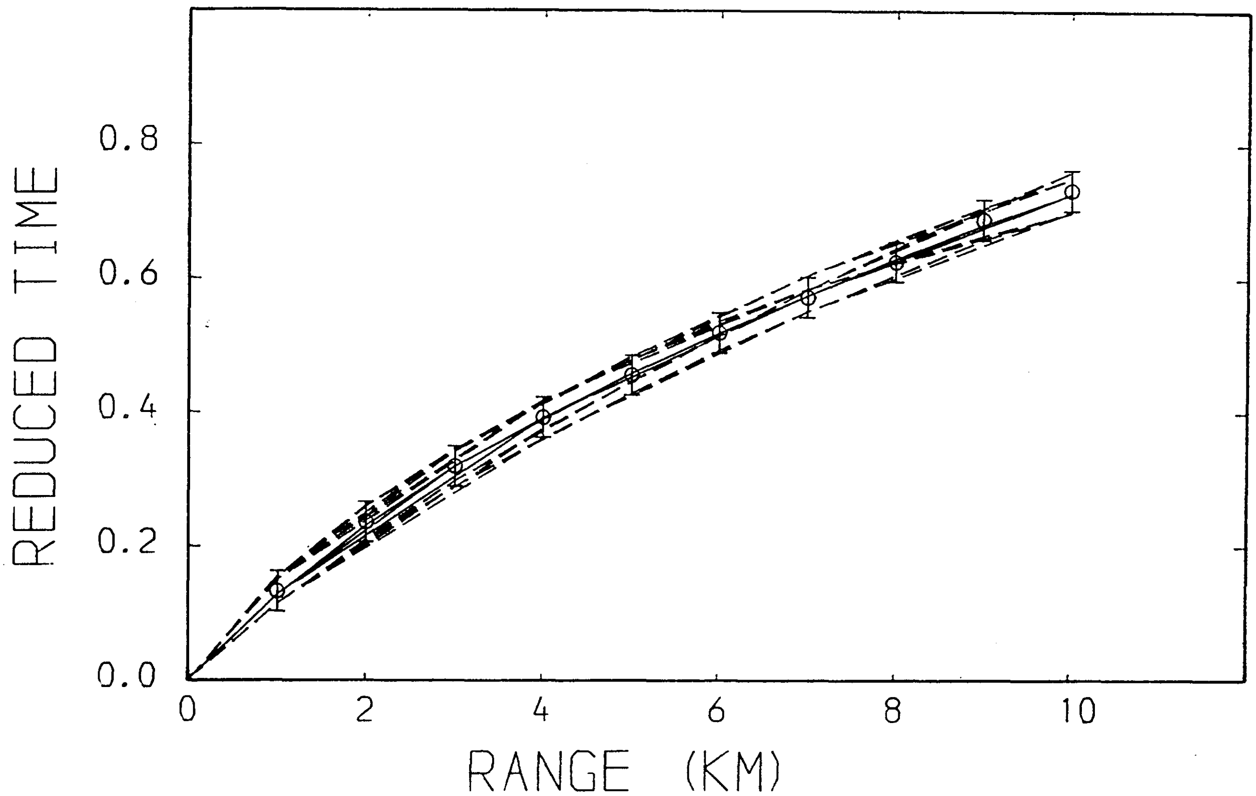

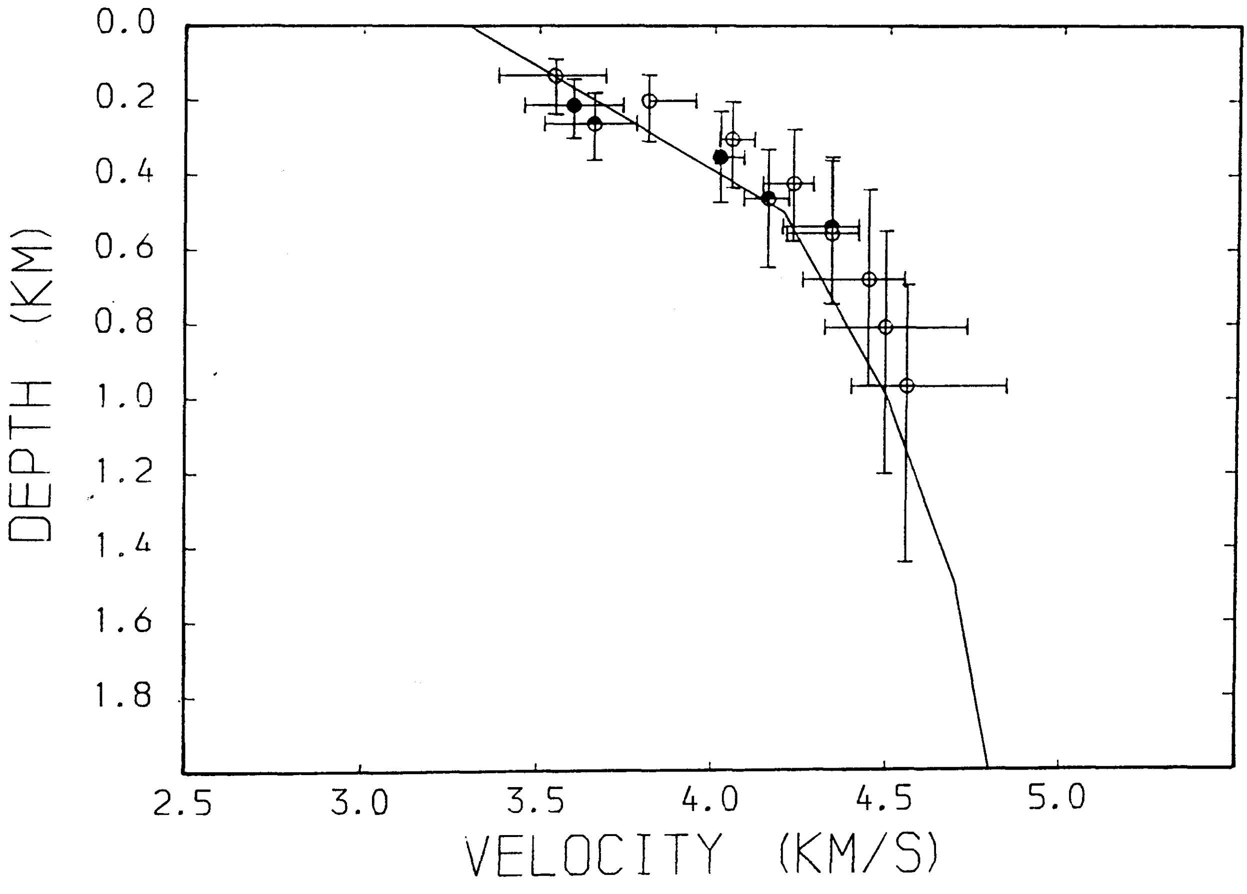

Fig.4.10b Effect of receiver interval, tau-p data. Reduction velocity is 6.0 km/s. 1 km spacing open circles, 2 km (odd) spacing solid circles, 3 km (1,4,7,10) spacing half circles. The model curve is shown for comparison.

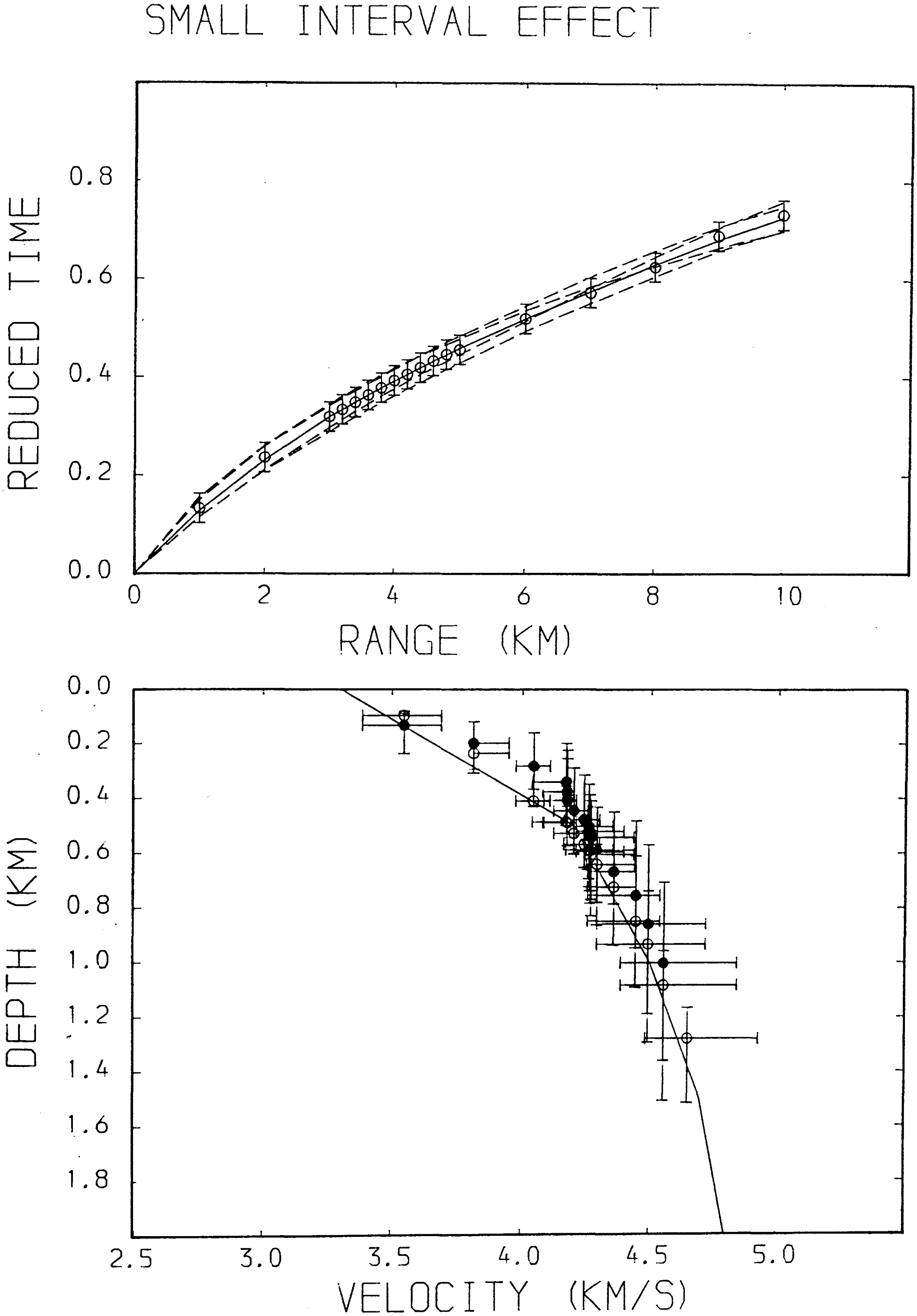

Fig.4.11 The effect of small receiver spacing. Reduction velocity is 6.0 km/s. WHB data open circles, tau-p data solid circles. The model curve is shown for comparison.

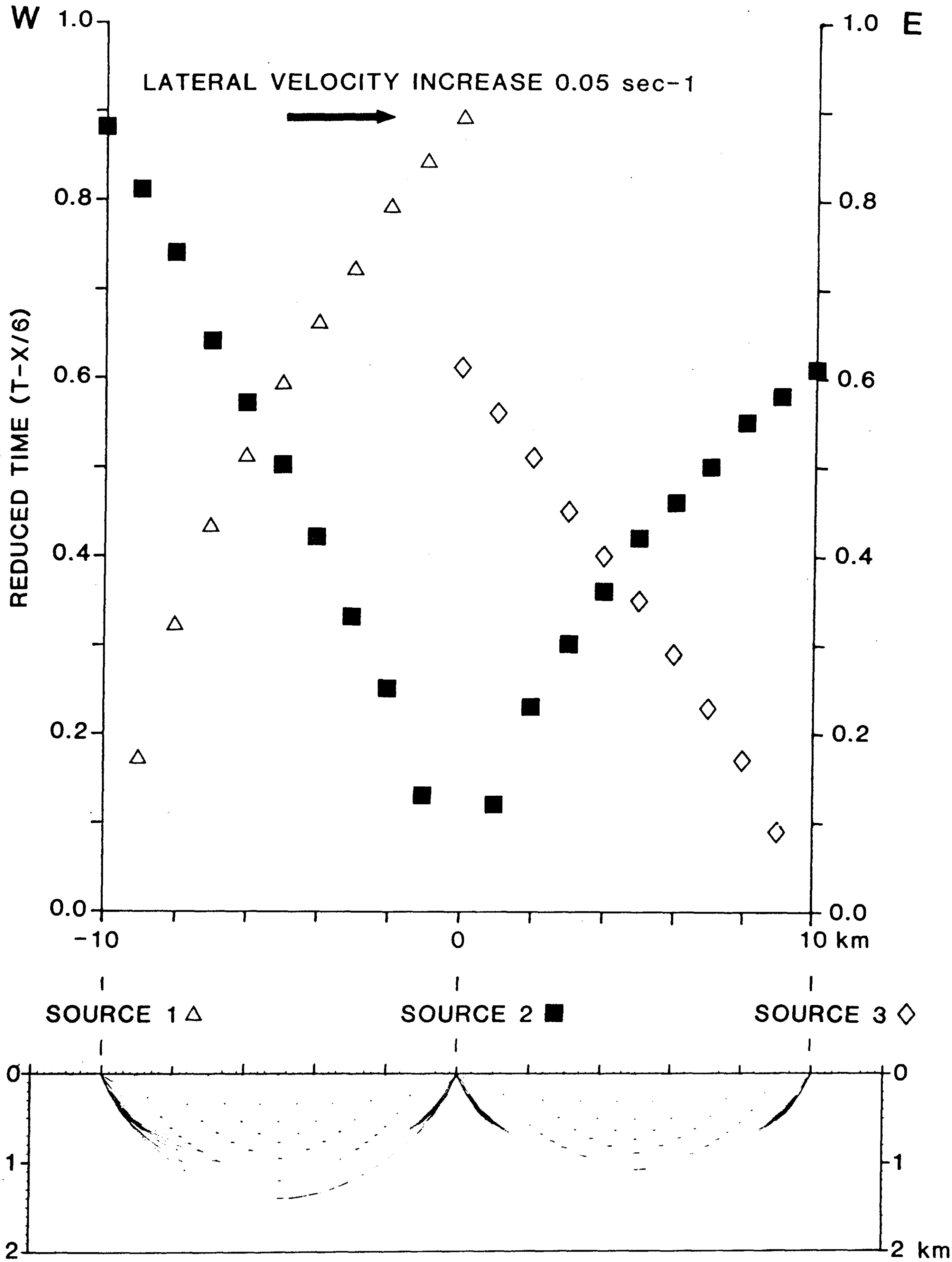

Fig.4.12 Model with lateral velocity change, plus time-distance data and ray-paths calculated by SEIS81.

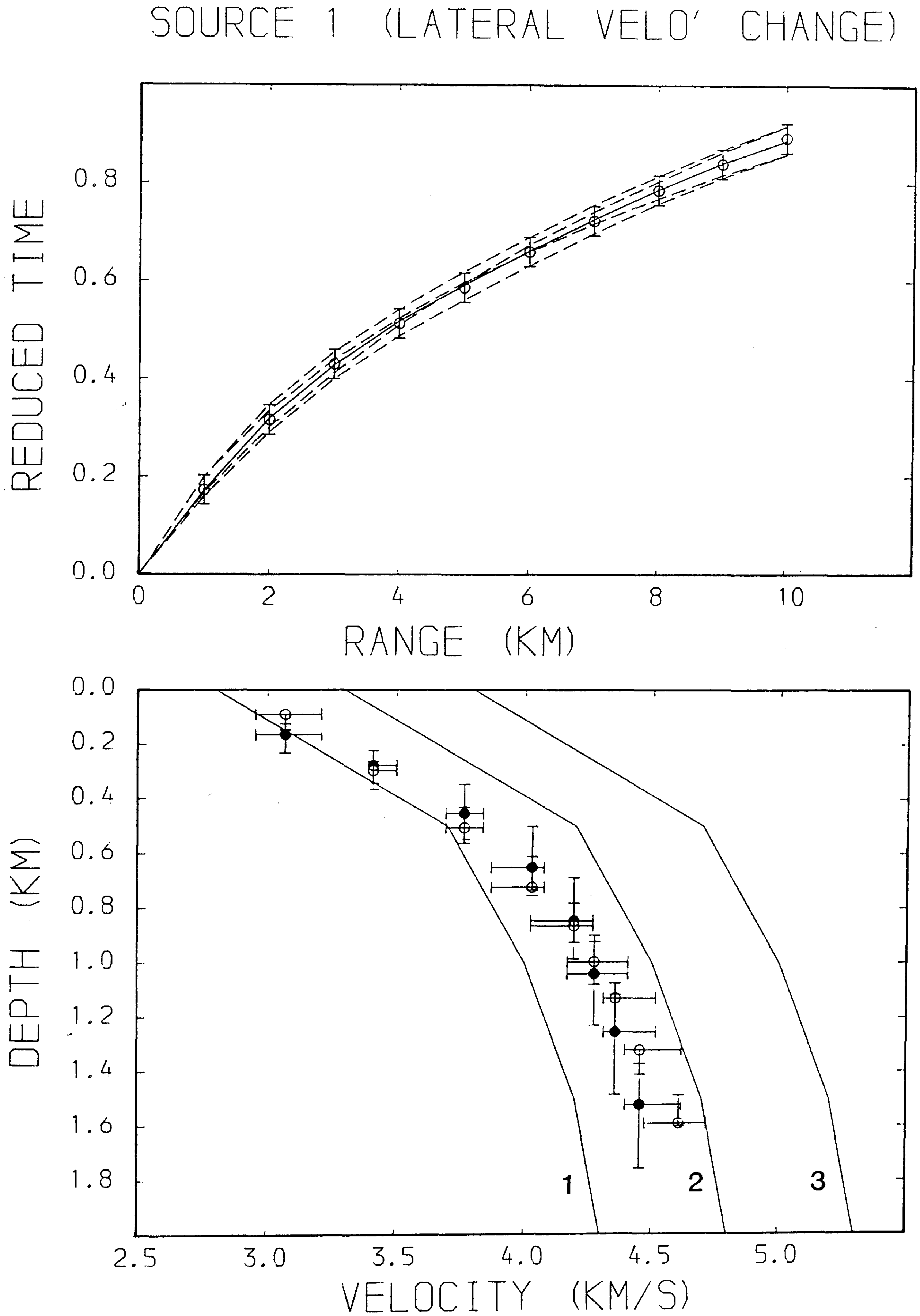

Fig.4.13a Comparison of model and calculated velocity-depth data, source 1. Reduction velocity is 6.0 km/s. WHB data open circles, tau-p data solid circles. The model curves beneath each shot point are shown for comparison.

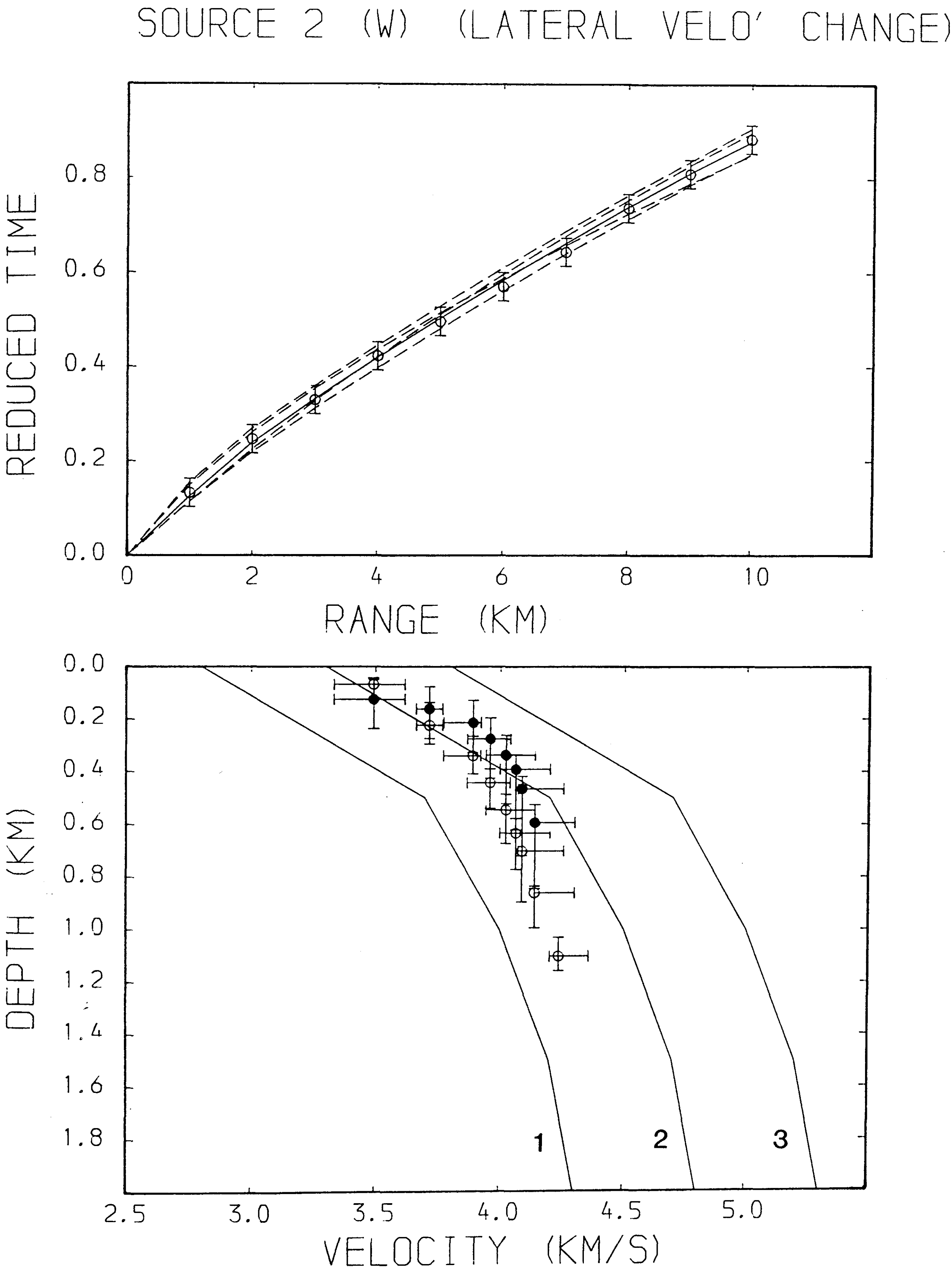

Fig.4.13b Comparison of model and calculated velocity-depth data, source 2 (west). Reduction velocity is 6.0 km/s. WHB data open circles, tau-p data solid circles. The model curves beneath each shot point are shown for comparison.

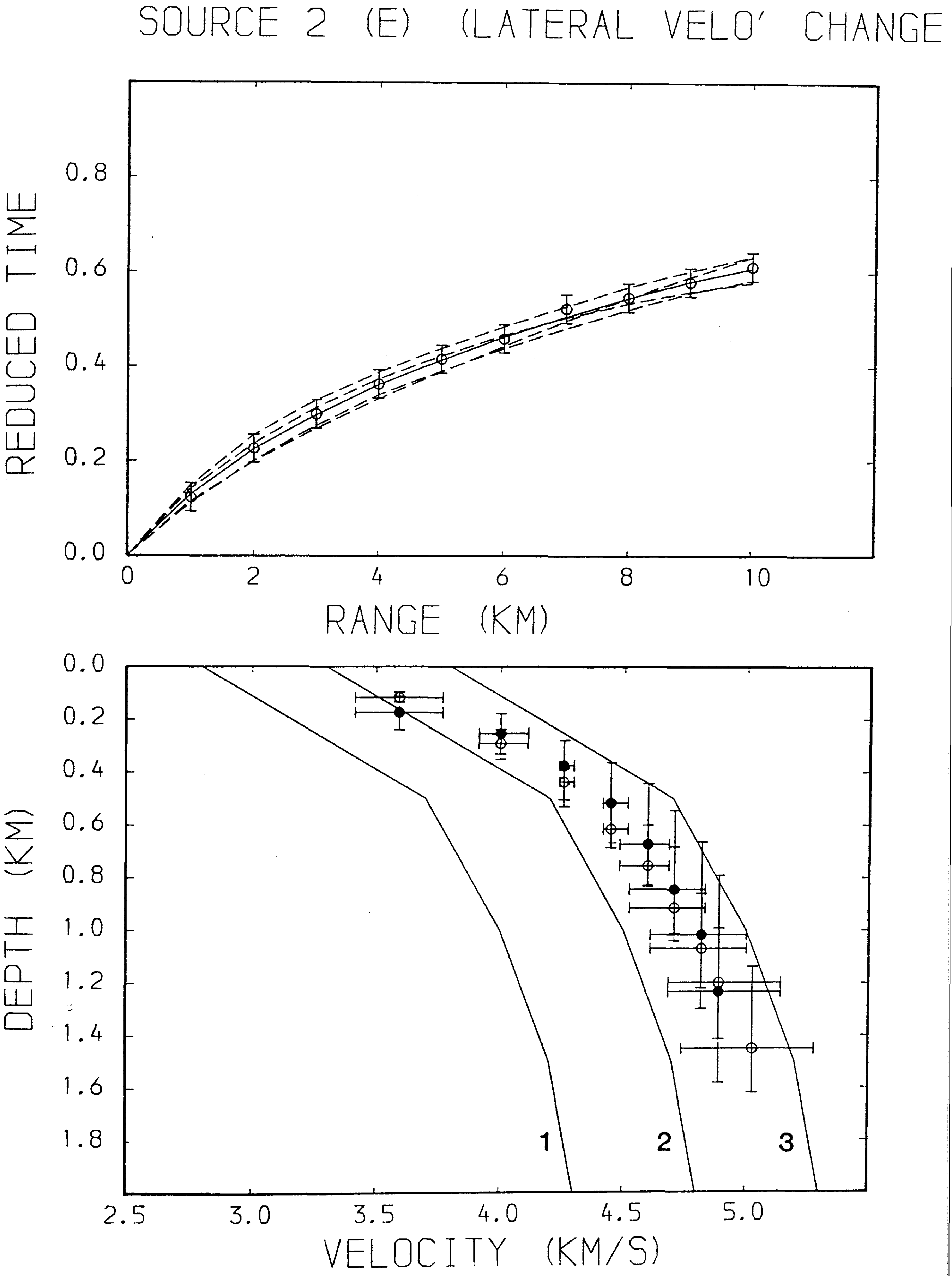

Fig.4.13c Comparison of model and calculated velocity-depth data, source 2 (east). Reduction velocity is 6.0 km/s. WHB data open circles, tau-p data solid circles. The model curves beneath each shot point are shown for comparison.

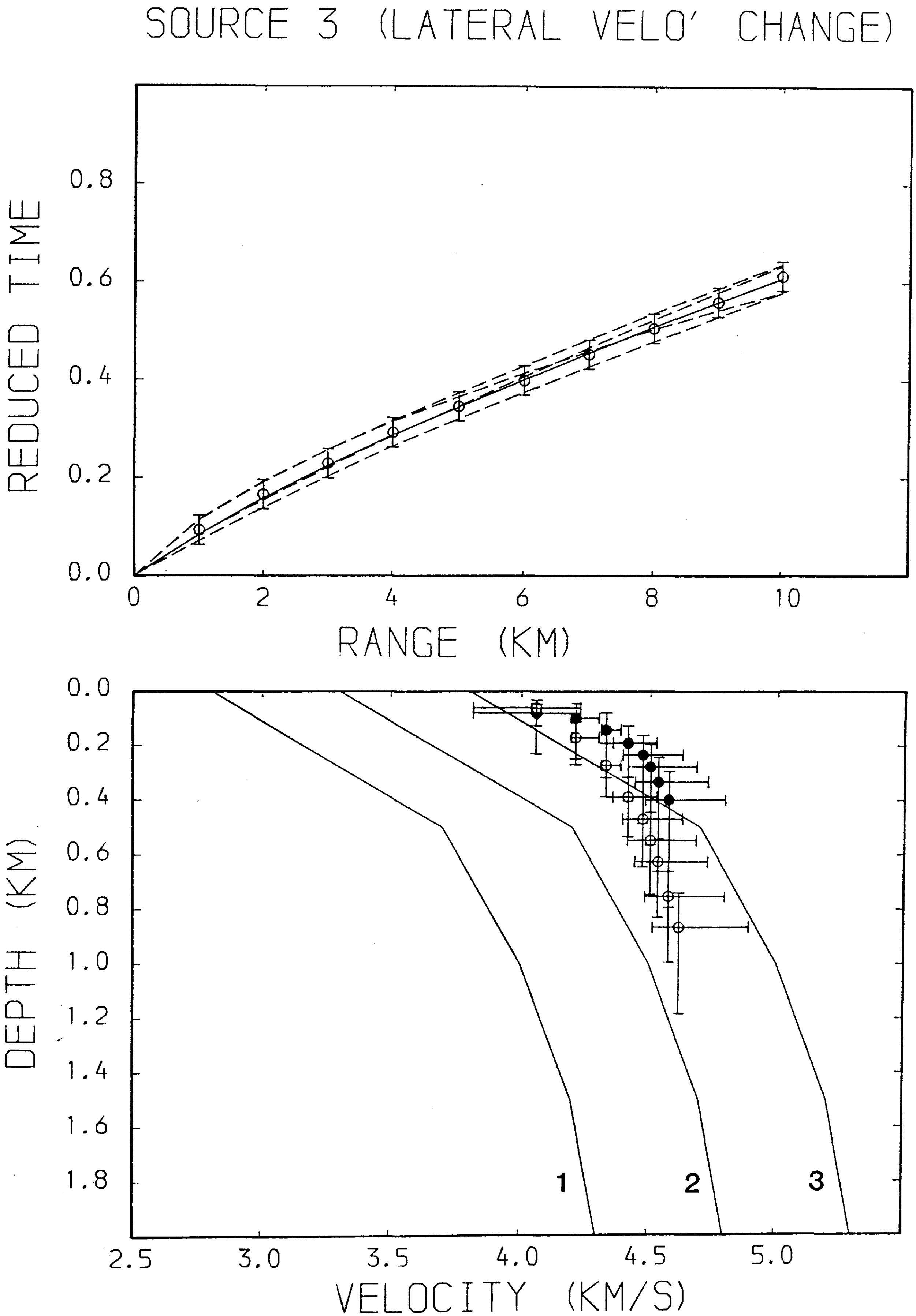

Fig.4.13d Comparison of model and calculated velocity-depth data, source 3. Reduction velocity is 6.0 km/s. WHB data open circles, tau-p data solid circles. The model curves beneath each shot point are shown for comparison.

SOURCE 2 (LATERAL VELO' CHANGE)

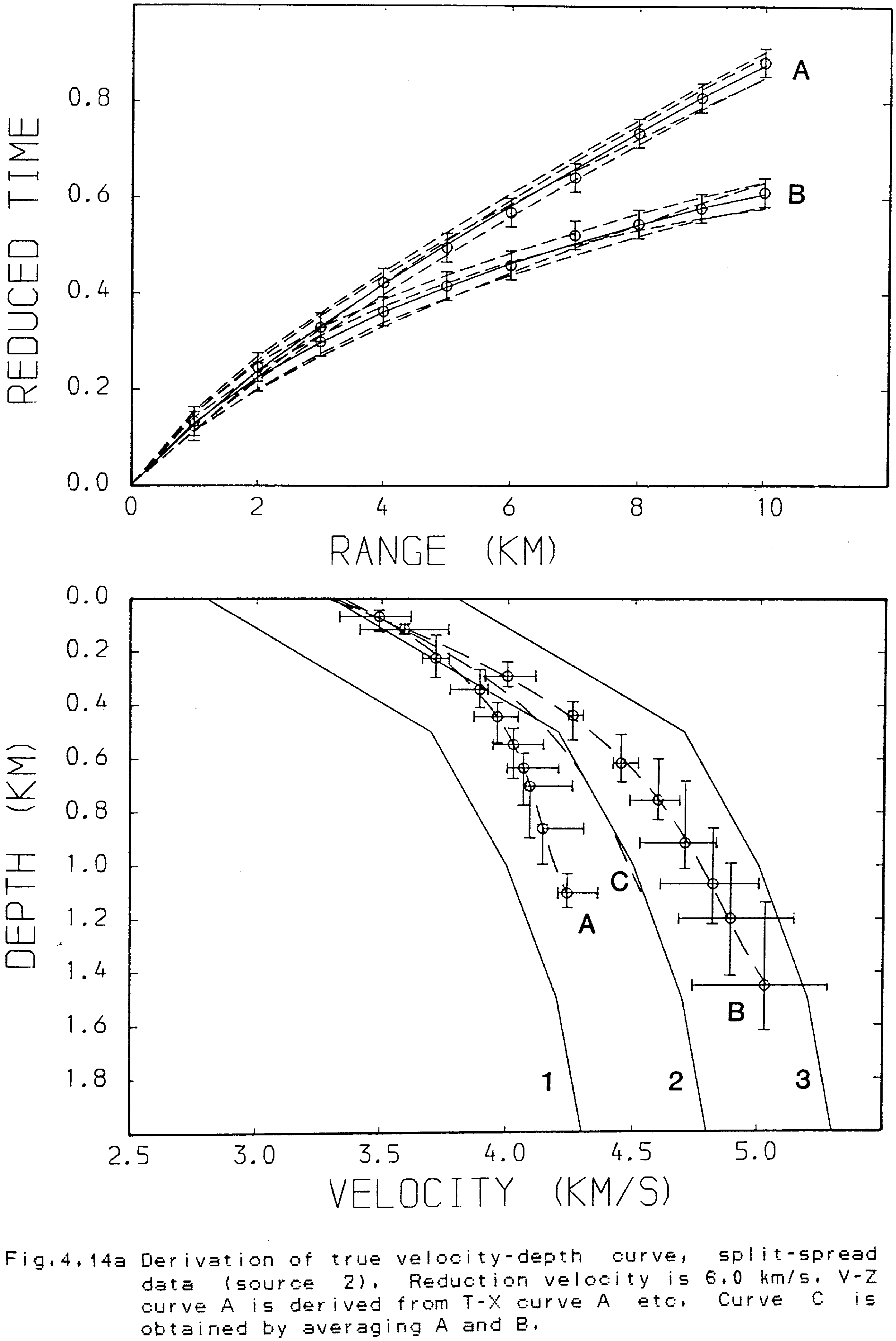

Fig.4.14a Derivation of true velocity-depth curve, split-spread data (source 2). Reduction velocity is 6.0 km/s. V-Z curve A is derived from T-X curve A etc. Curve C is obtained by averaging A and B.

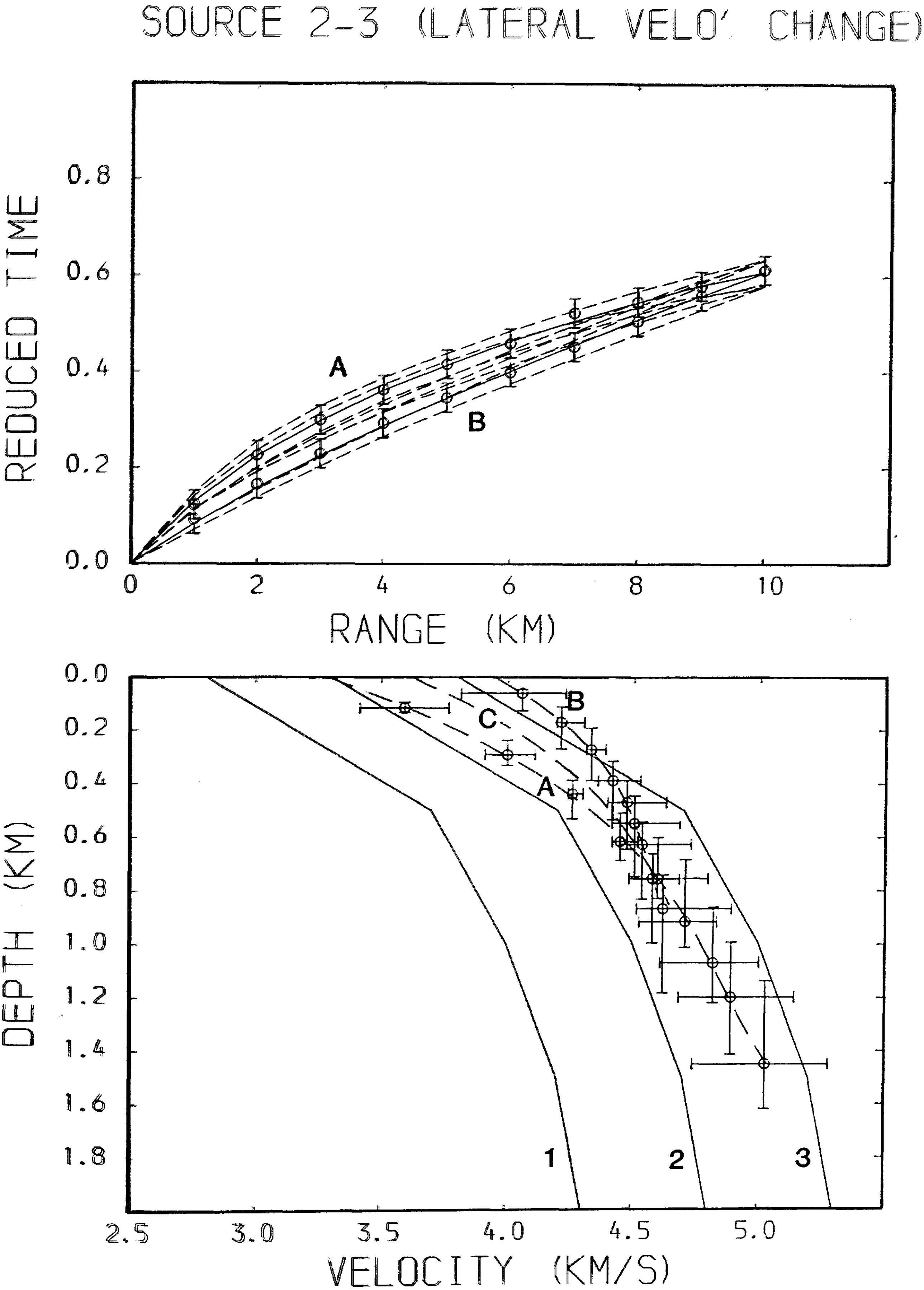

Fig.4.14b Derivation of true velocity-depth curve, reversed data (sources 2 & 3). Reduction velocity is 6.0 km/s. V-Z curve A is derived from T-X curve A etc. Curve C is obtained by averaging A and B. a), split-spread data.

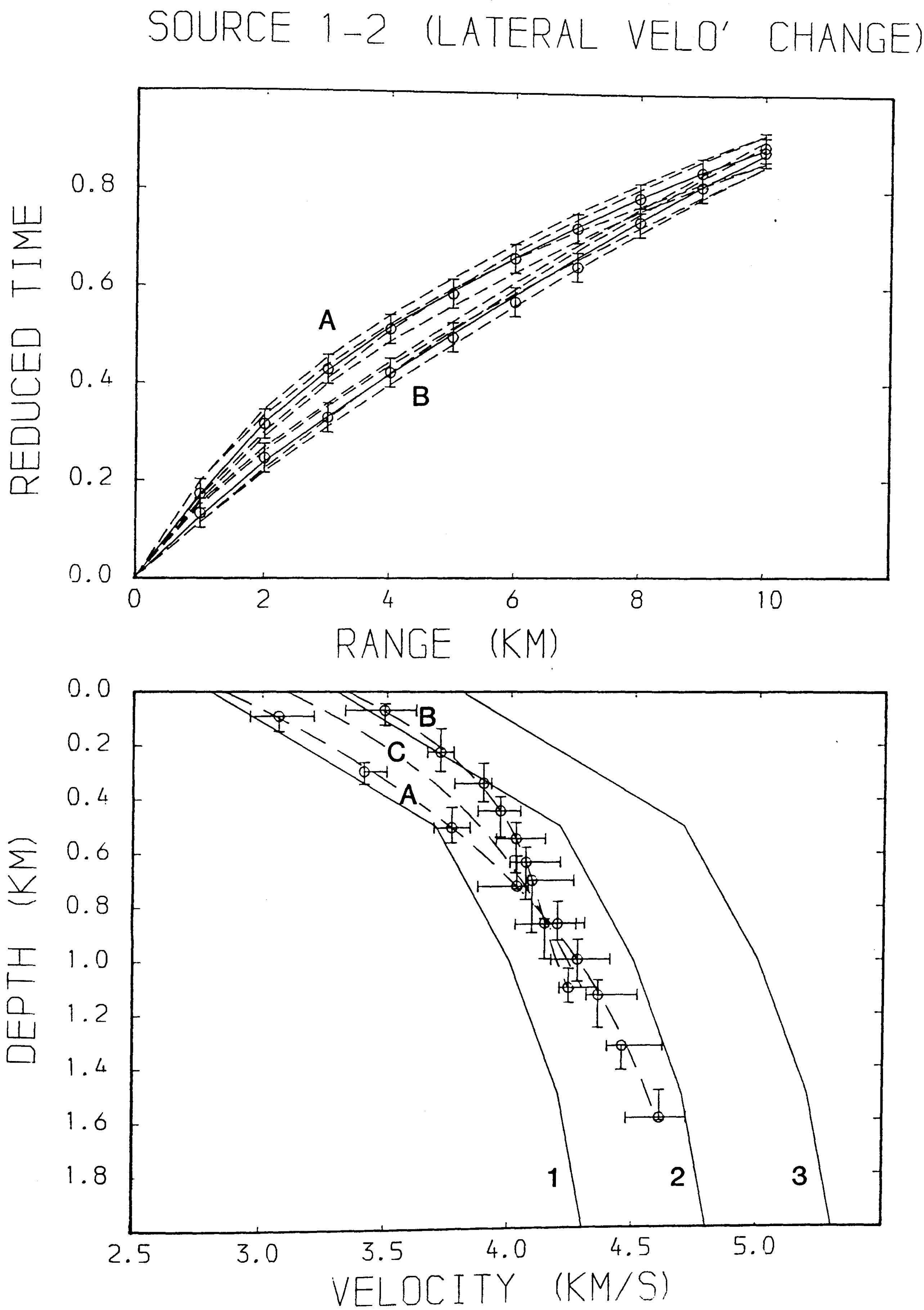

Fig.4.14c Derivation of true velocity-depth curve, reversed data (sources 1 & 2). Reduction velocity is 6.0 km/s. V-Z curve A is derived from T-X curve A etc. Curve C is obtained by averaging A and B.

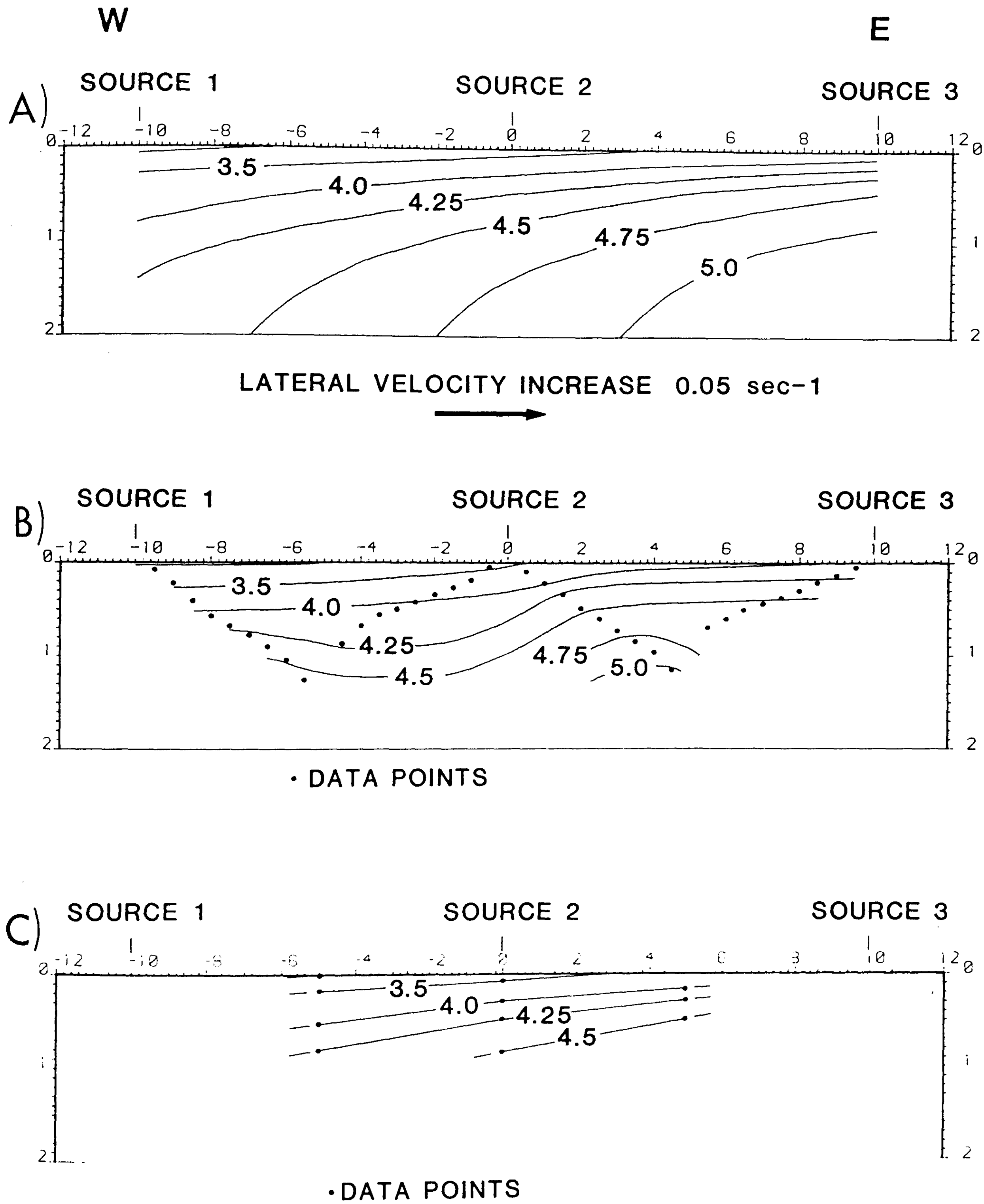

Fig.4.15 Input (A) and derived (B & C) velocity models using the WHB inversion. Velocity contours in km/s. A), without compensation for lateral velocity variation. c), with compensation for lateral velocity variation.

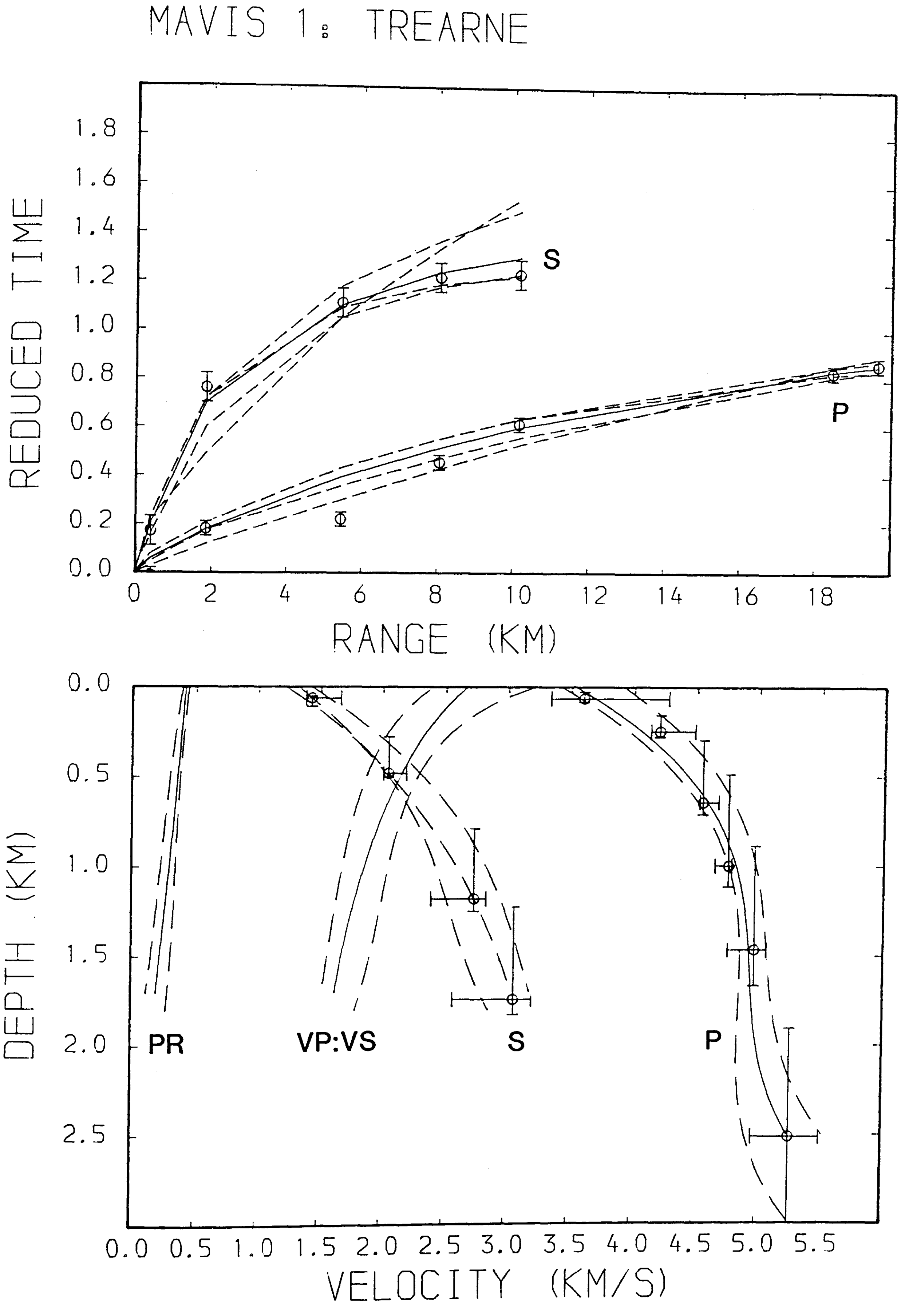

Fig.4.16 Time-distance and velocity-depth data from WHB inversion; Trearne shot. S - shear wave data, P - compressional wave data, VP:VS - ratio of P- and S-wave velocities, PR - Poisson's ratio. Reduction velocity is 6.0 km/s for P-wave data and 3.5 km/s for S-wave data.

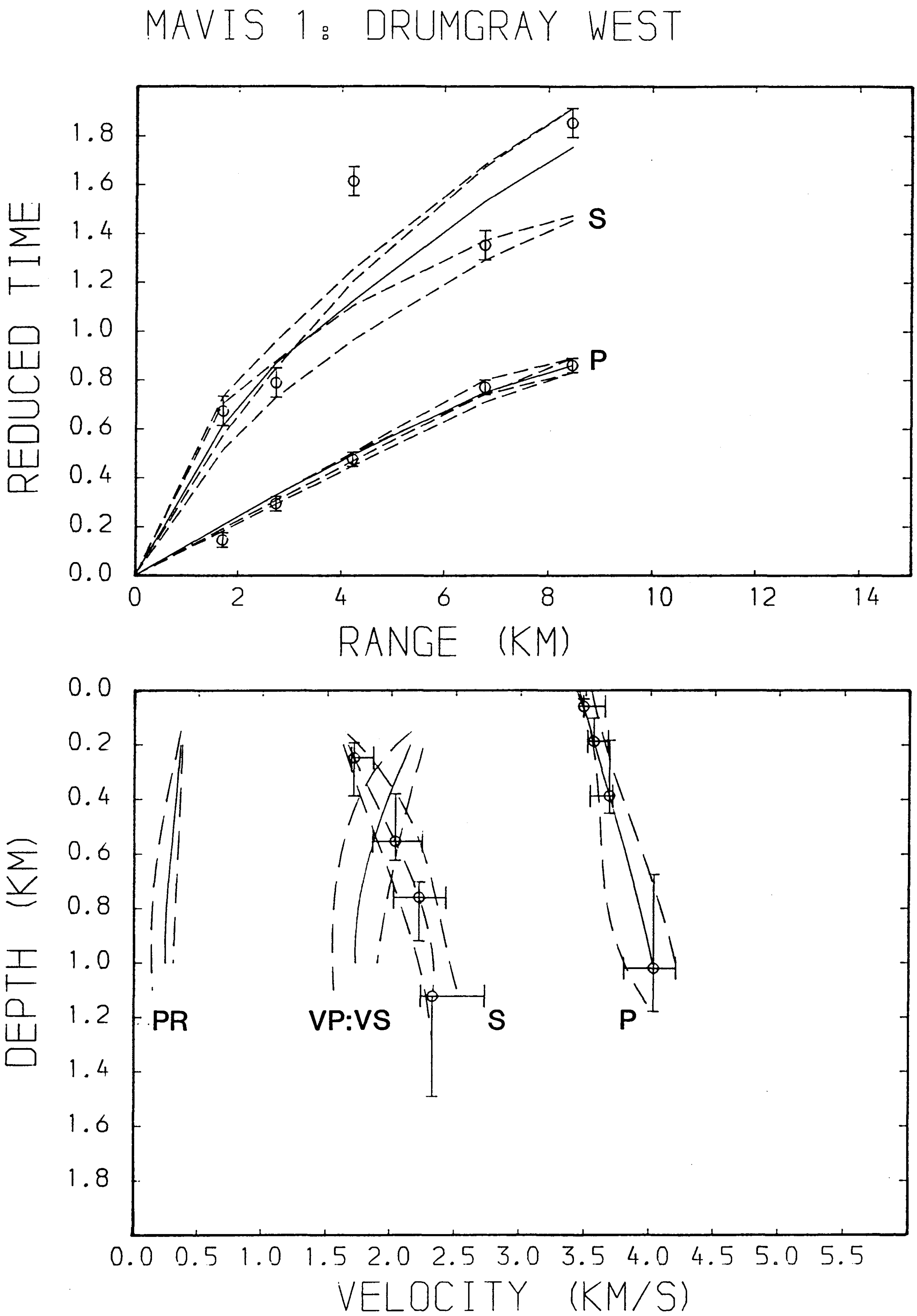

Fig.4.17 Time-distance and velocity-depth data from WHB inversion; Drumgray shot (west). S - shear wave data, P - compressional wave data, VP:VS - ratio of P- and S-wave velocities, PR - Poisson's ratio. Reduction velocity is 6.0 km/s for P-wave data and 3.5 km/s for S-wave data.

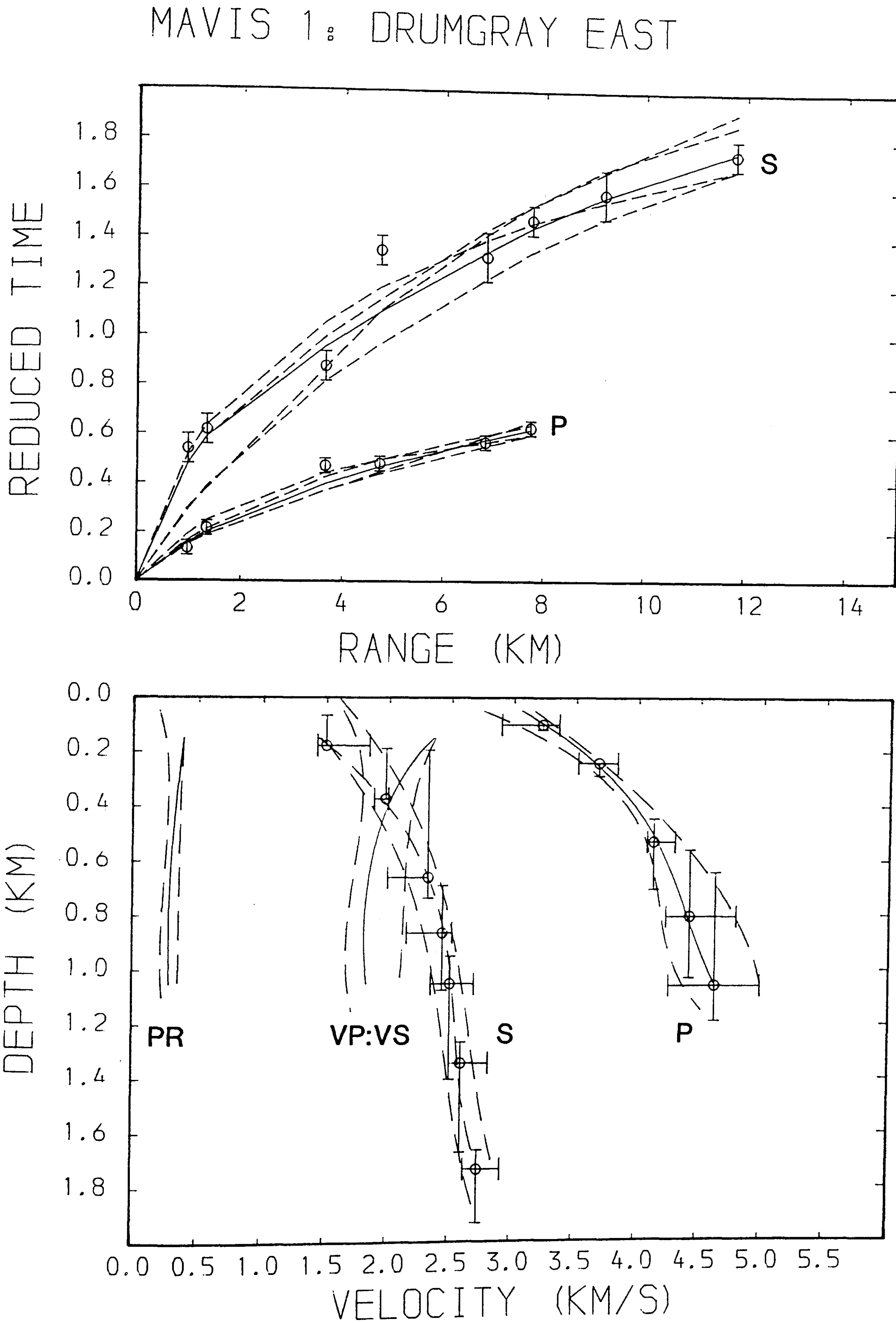

Fig.4.18 Time-distance and velocity-depth data from WHB inversion; Drumgray shot (east). S - shear wave data, P - compressional wave data, VP:VS - ratio of P- and S-wave velocities, PR - Poisson's ratio. Reduction velocity is 6.0 km/s for P-wave data and 3.5 km/s for S-wave data.

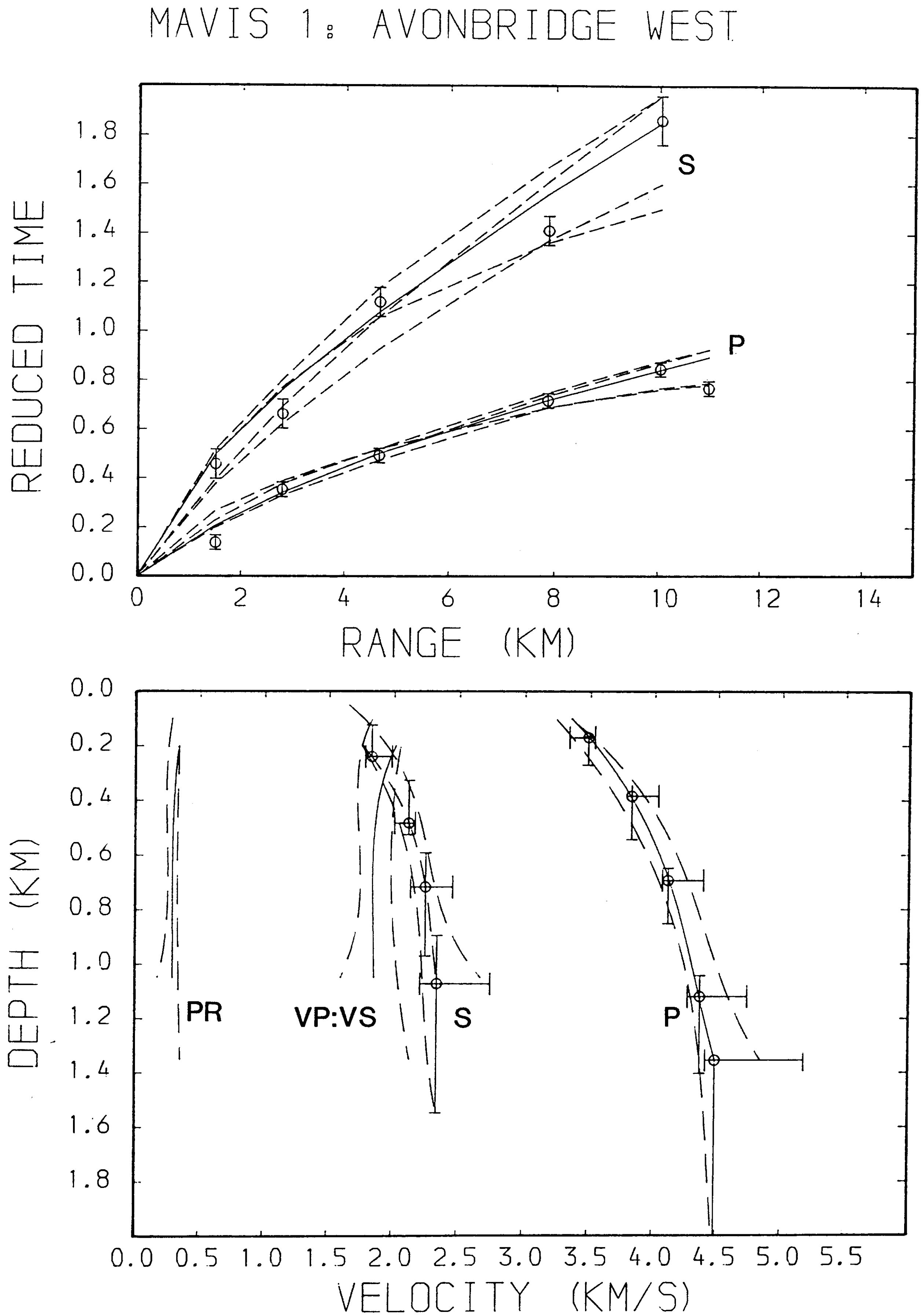

Fig.4.19 Time-distance and velocity-depth data from WHB inversion; Avonbridge shot (west). S - shear wave data, P - compressional wave data, VP:VS - ratio of P- and S-wave velocities, PR - Poisson's ratio. Reduction velocity is 6.0 km/s for P-wave data and 3.5 km/s for S-wave data.

MAVIS 1: AVONBRIDGE EAST

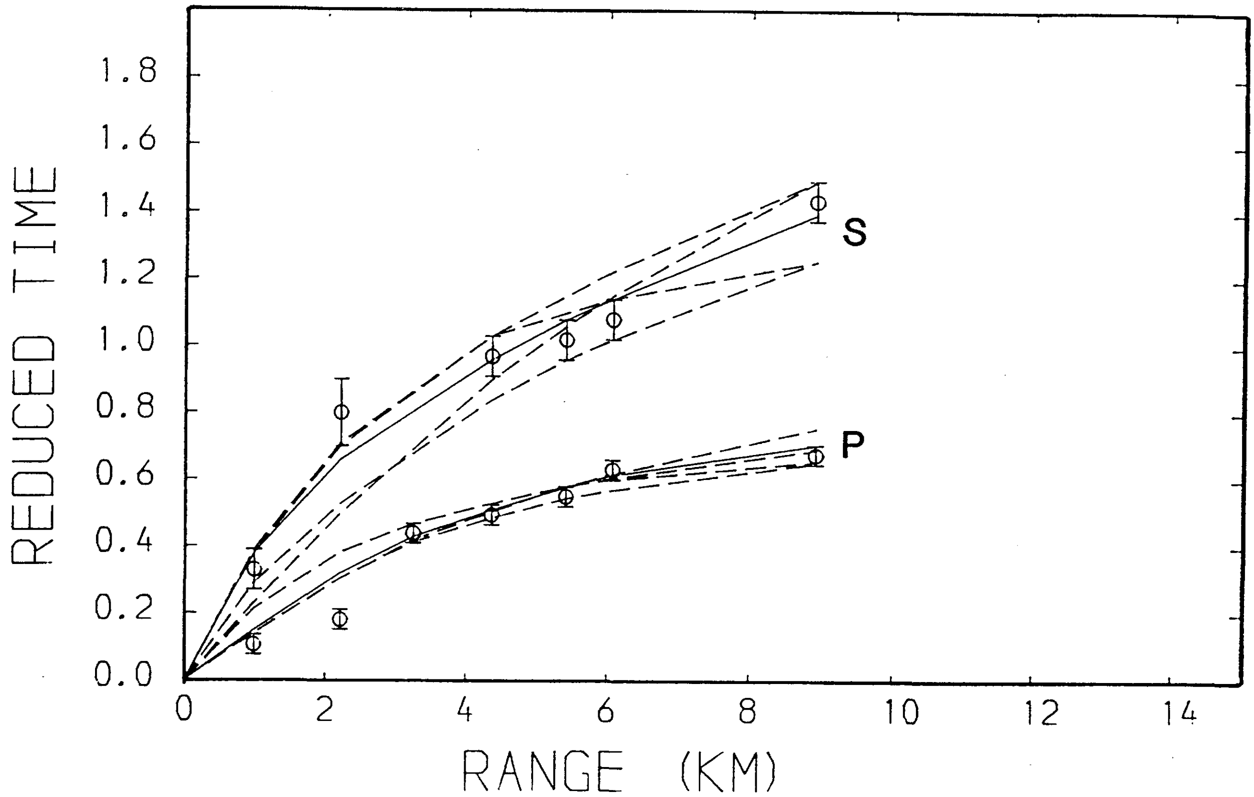

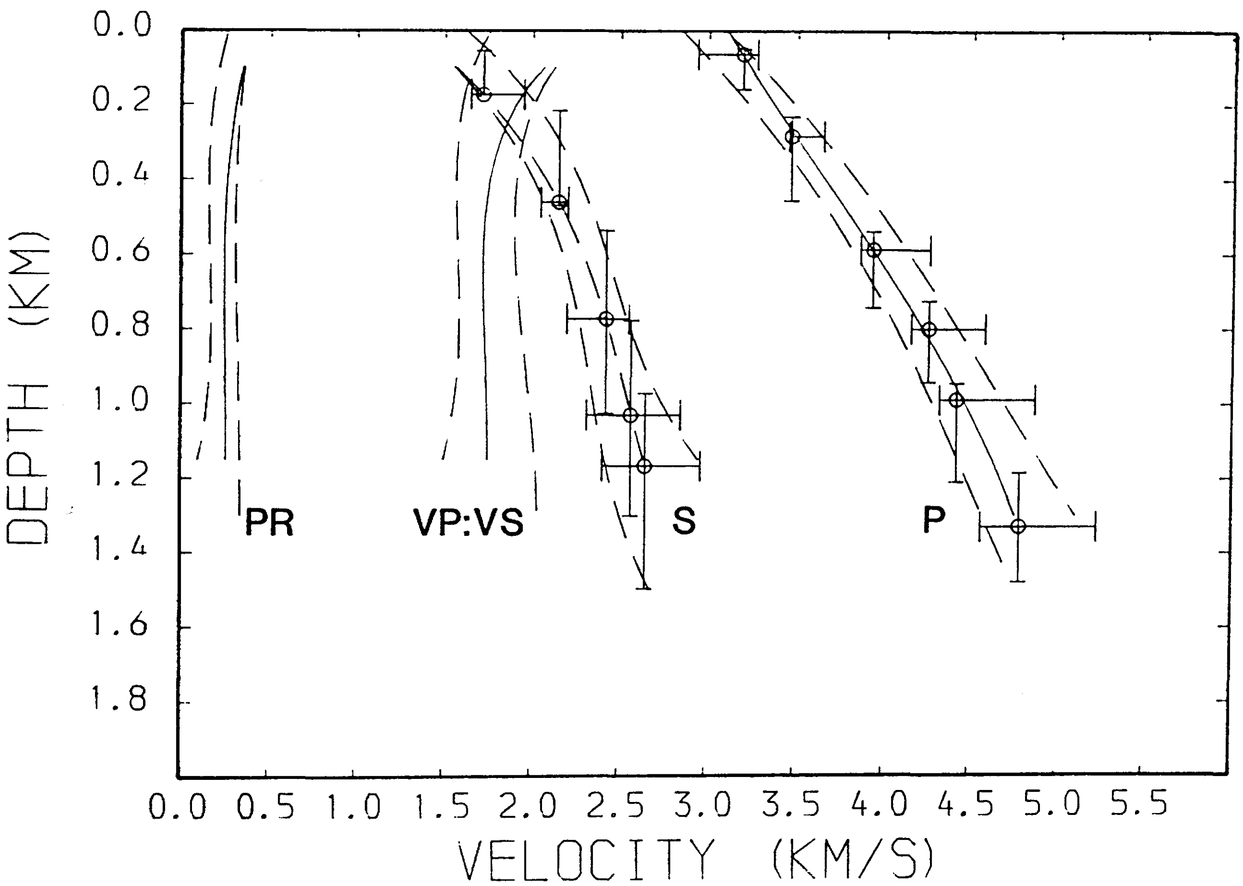

Fig.4.20 Time-distance and velocity-depth data from WHB inversion; Avonbridge shot (east). S - shear wave data, P - compressional wave data, VP:VS - ratio of P- and S-wave velocities, PR - Poisson's ratio. Reduction velocity is 6.0 km/s for P-wave data and 3.5 km/s for S-wave data.

MAVIS 1: BALLIKINRAIN

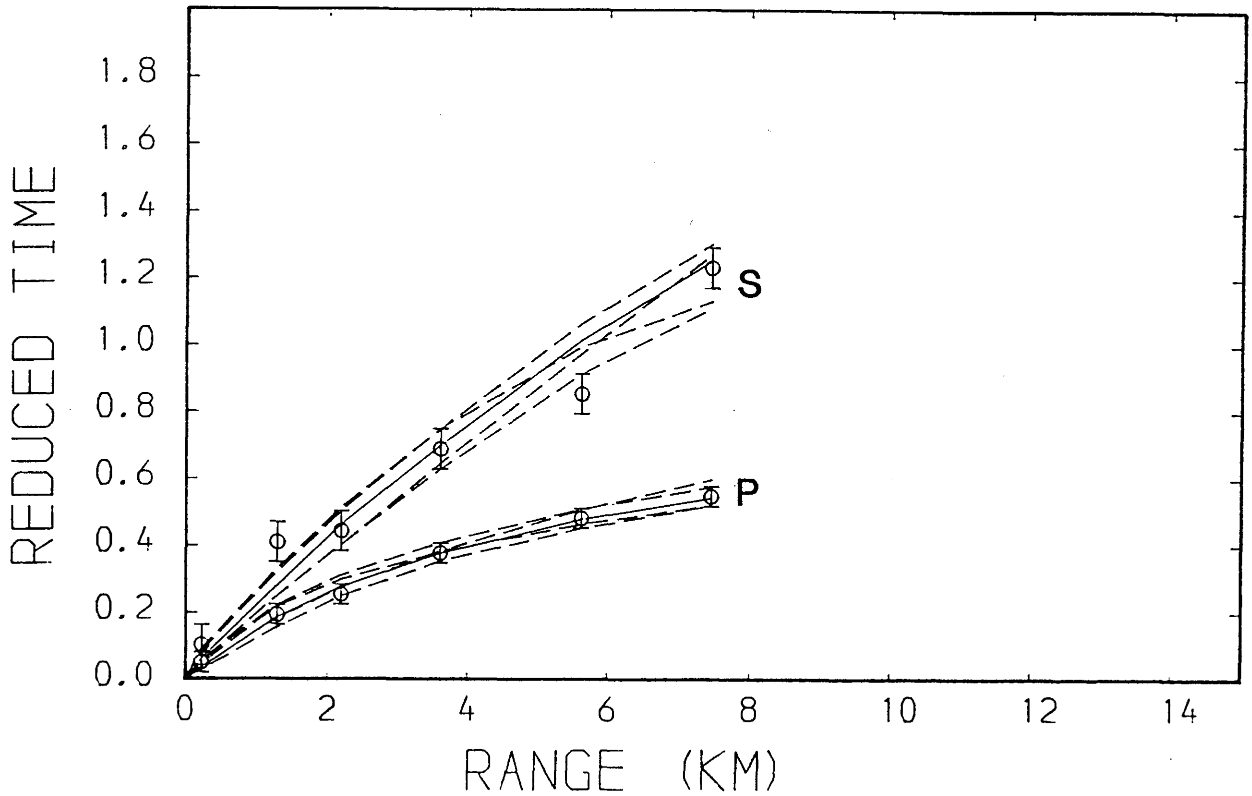

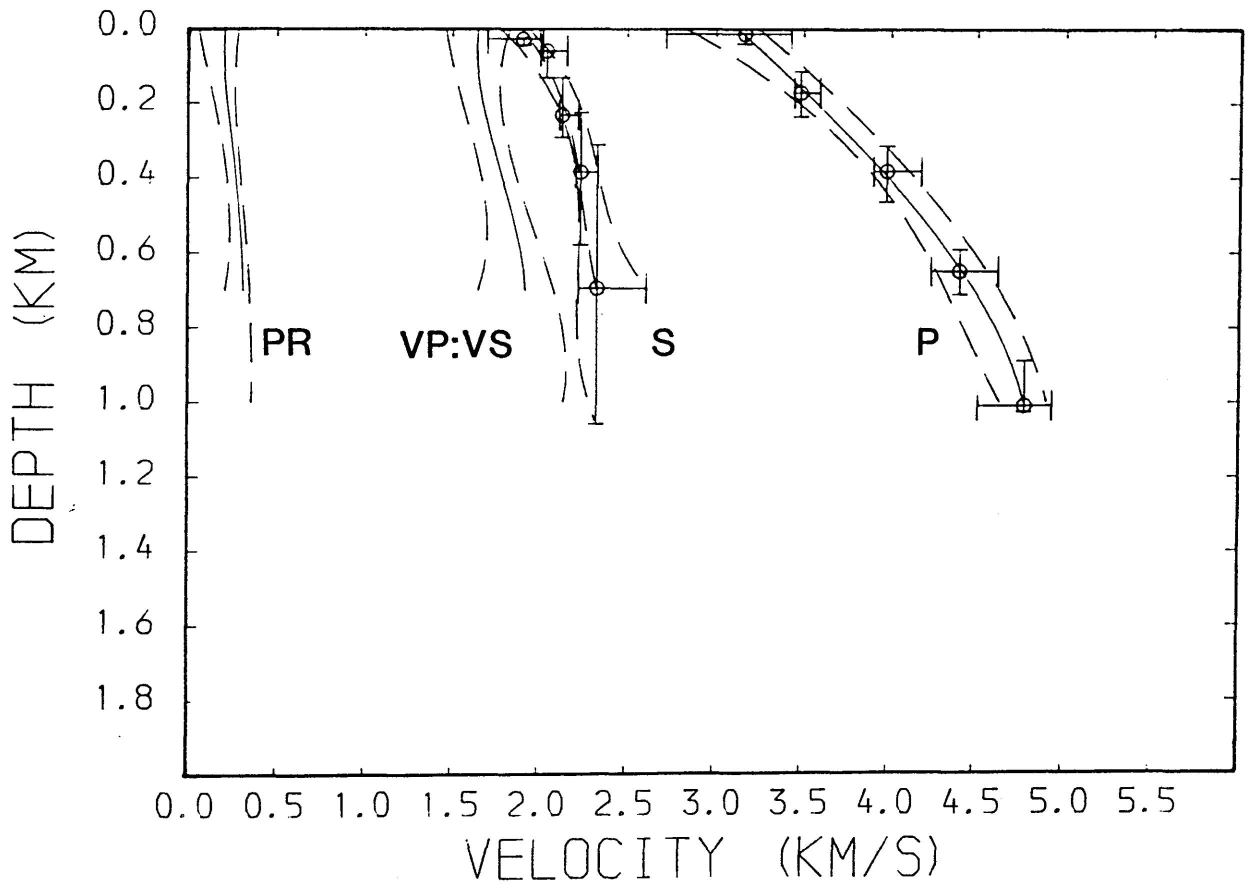

Fig.4.21 Time-distance and velocity-depth data from WHB inversion; Ballikinrain shot. S - shear wave data, P - compressional wave data, VP:VS - ratio of P- and S-wave velocities, PR - Poisson's ratio. Reduction velocity is 6.0 km/s for P-wave data and 3.5 km/s for S-wave data.

MAVIS 1: NORTH THIRD WEST

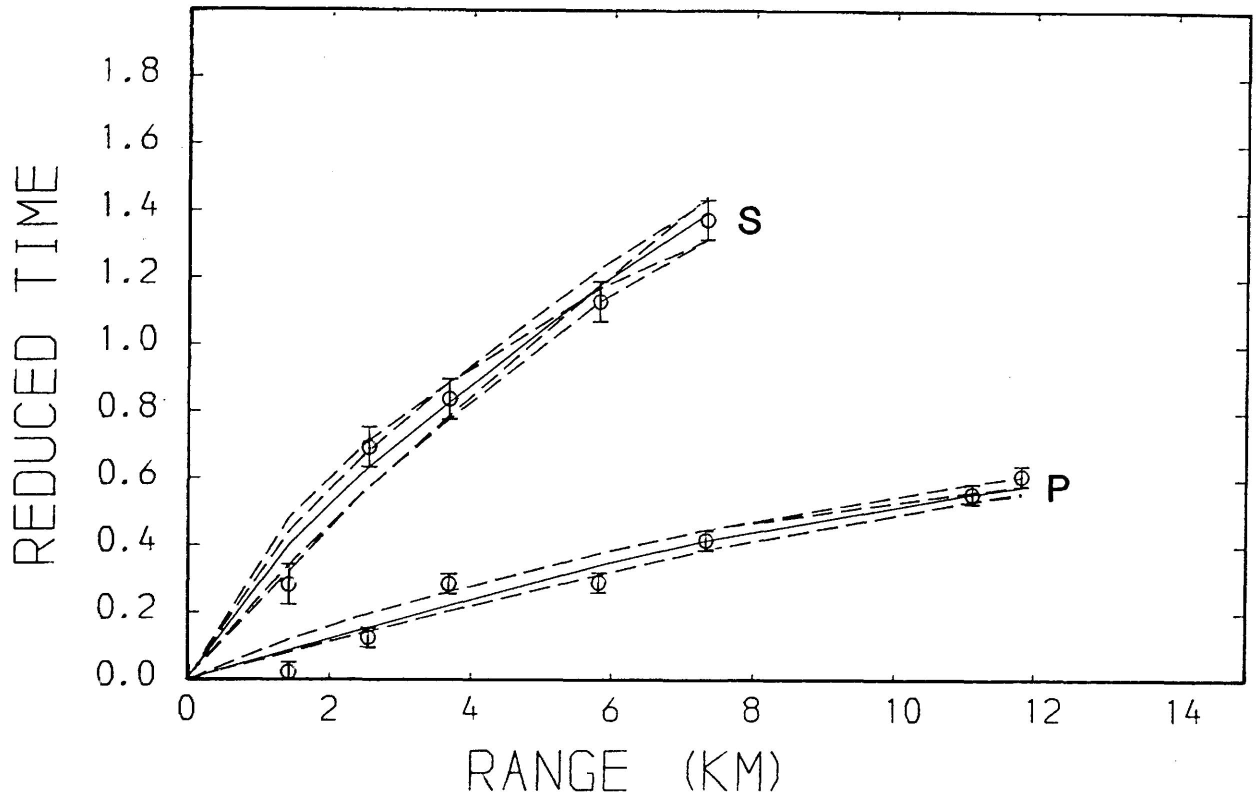

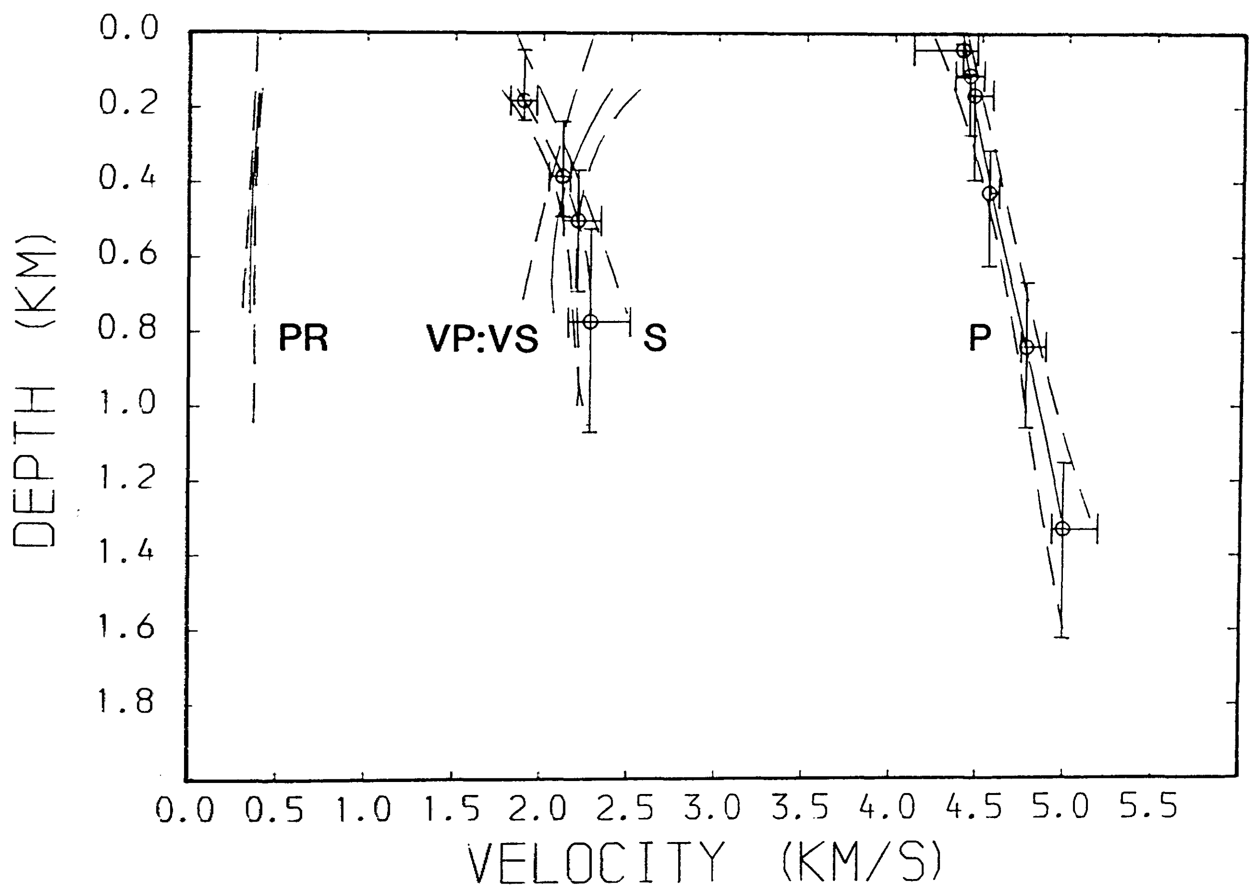

Fig.4.22 Time-distance and velocity-depth data from WHB inversion; North Third shots (west). S - shear wave data, P - compressional wave data, VP:VS - ratio of P- and S-wave velocities, PR - Poisson's ratio. Reduction velocity is 6.0 km/s for P-wave data and 3.5 km/s for S-wave data.

MAVIS 1: NORTH THIRD EAST

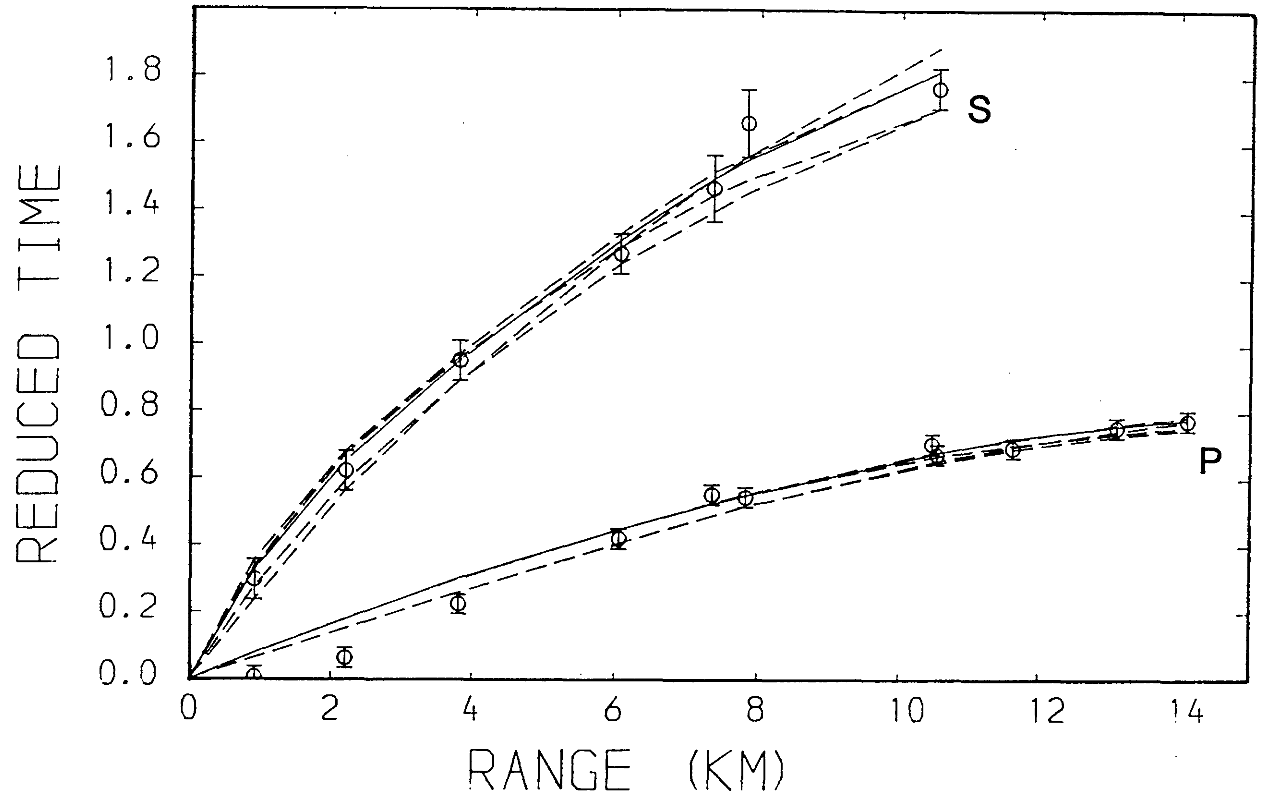

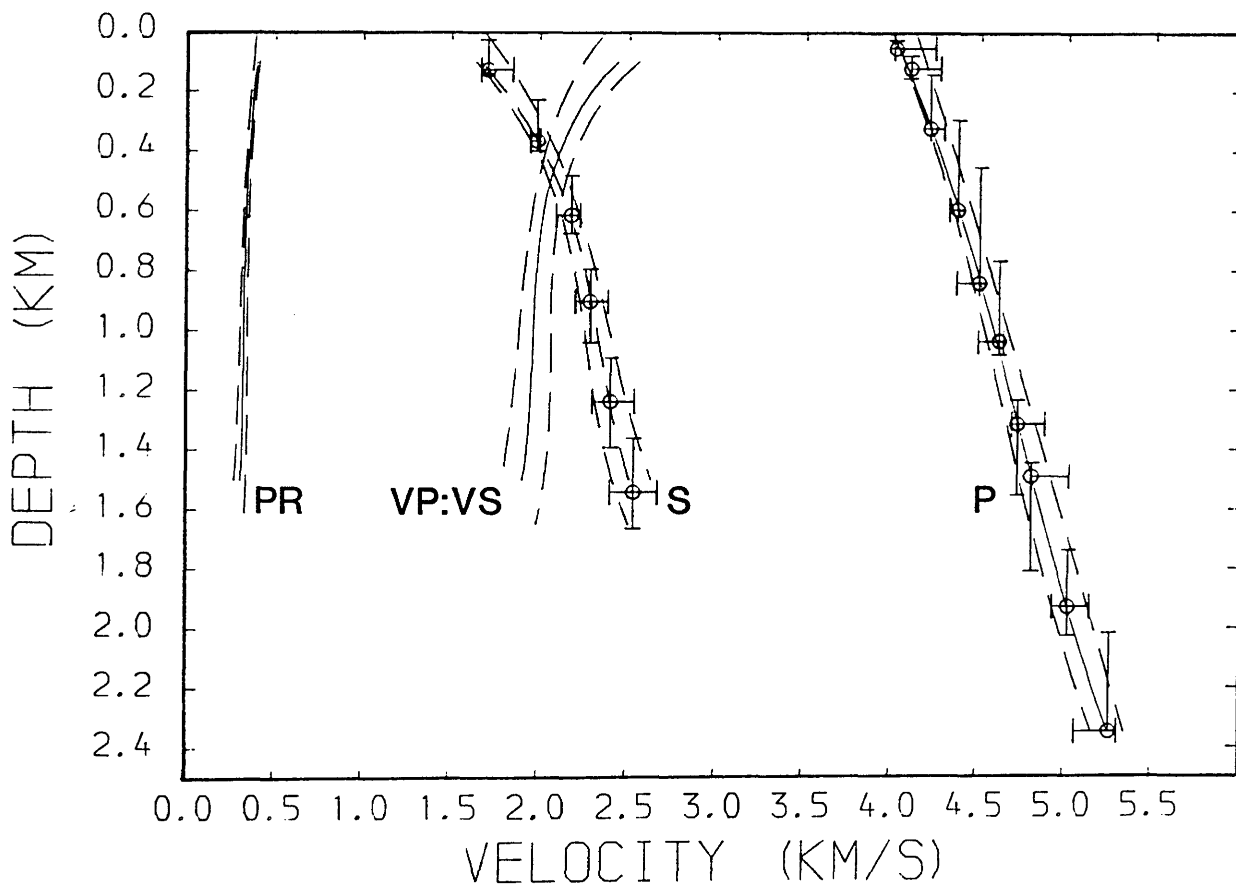

Fig.4.23 Time-distance and velocity-depth data from WHB inversion; North Third shot (east). S - shear wave data, P - compressional wave data, VP:VS - ratio of P- and S-wave velocities, PR - Poisson's ratio. Reduction velocity is 6.0 km/s for P-wave data and 3.5 km/s for S-wave data.

MAVIS 1: CATTLEMOSS WEST

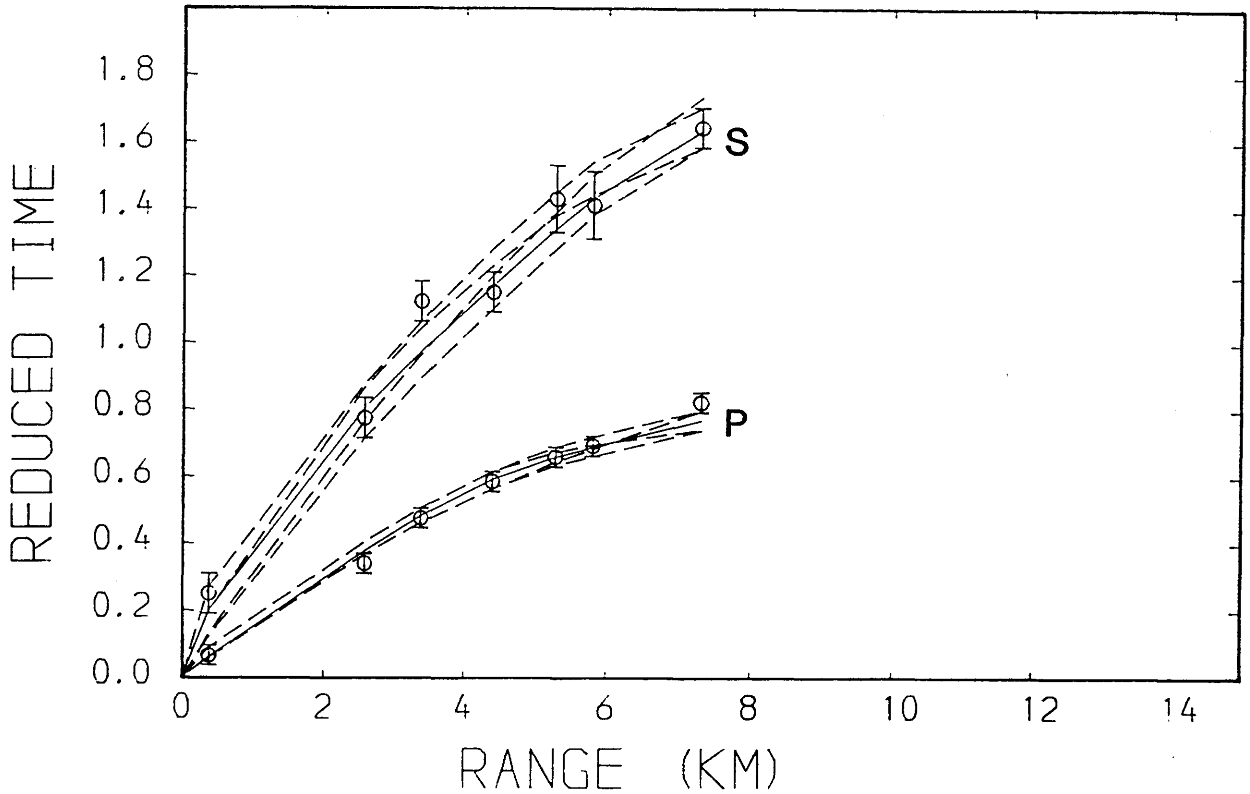

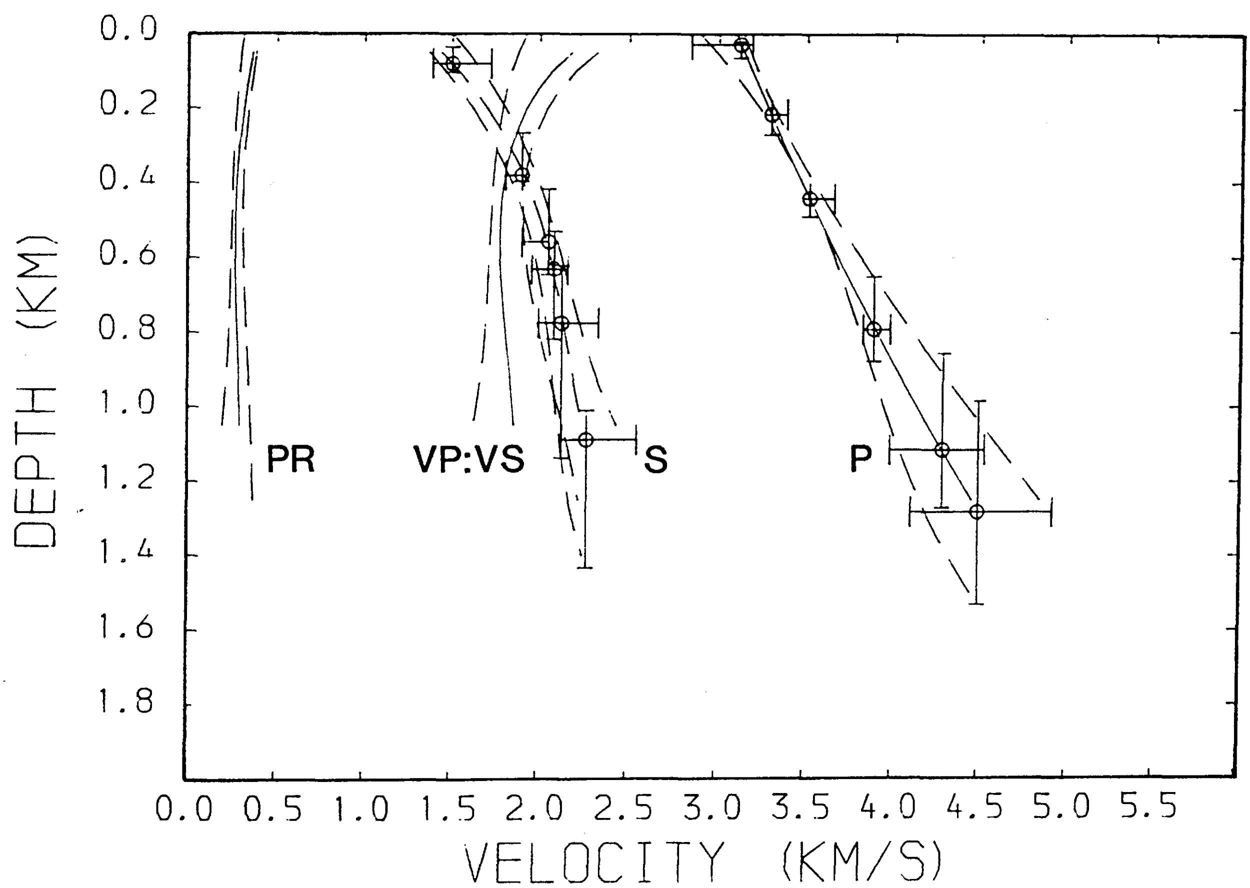

Fig.4.24 Time-distance and velocity-depth data from WHB inversion; Cattlemoss shot (west). S - shear wave data, P - compressional wave data, VP:VS - ratio of P- and S-wave velocities, PR - Poisson's ratio. Reduction velocity is 6.0 km/s for P-wave data and 3.5 km/s for S-wave data.

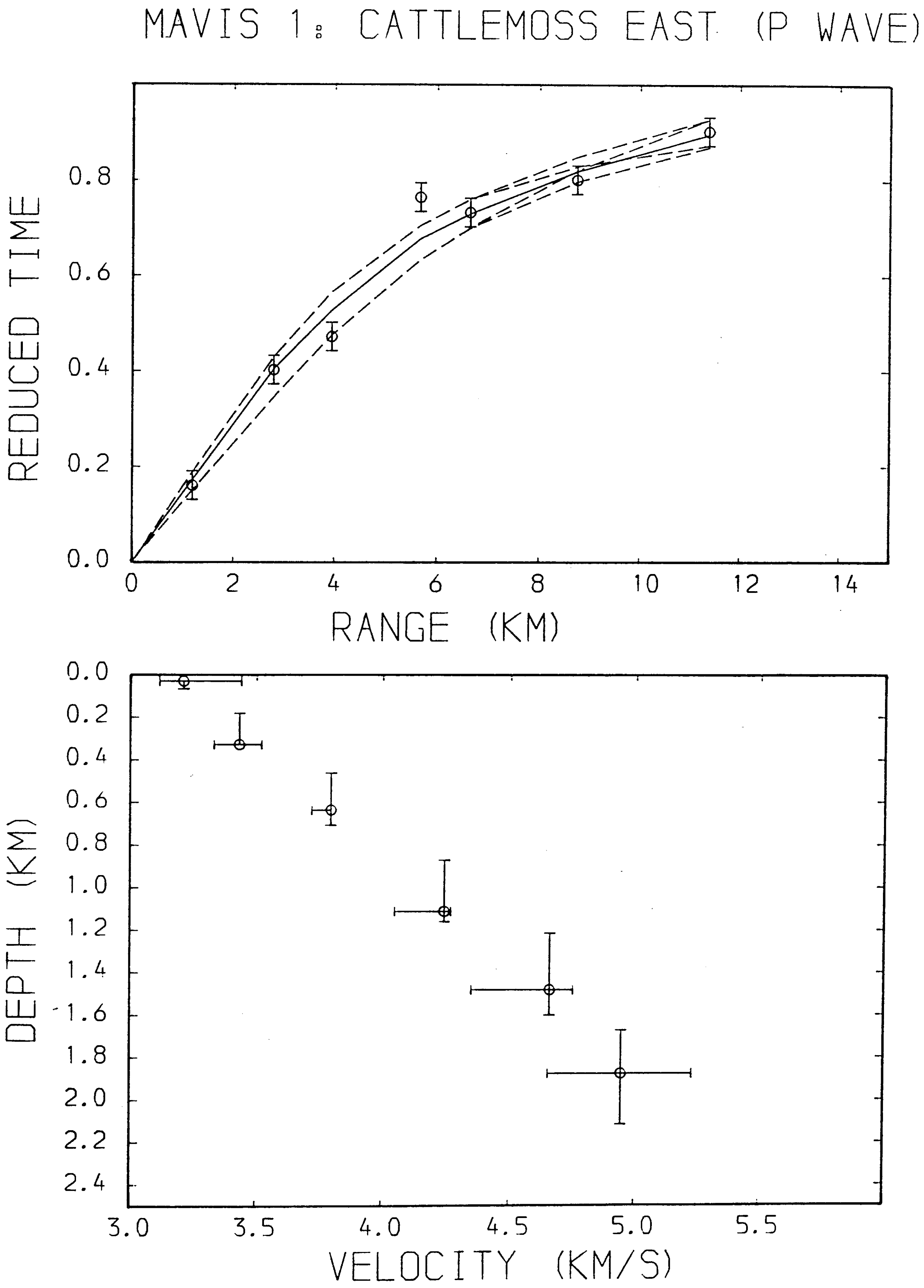

Fig.4.25 Time-distance and velocity-depth data from WHB inversion; Cattlemoss shot (east). Reduction velocity is 6.0 km/s.

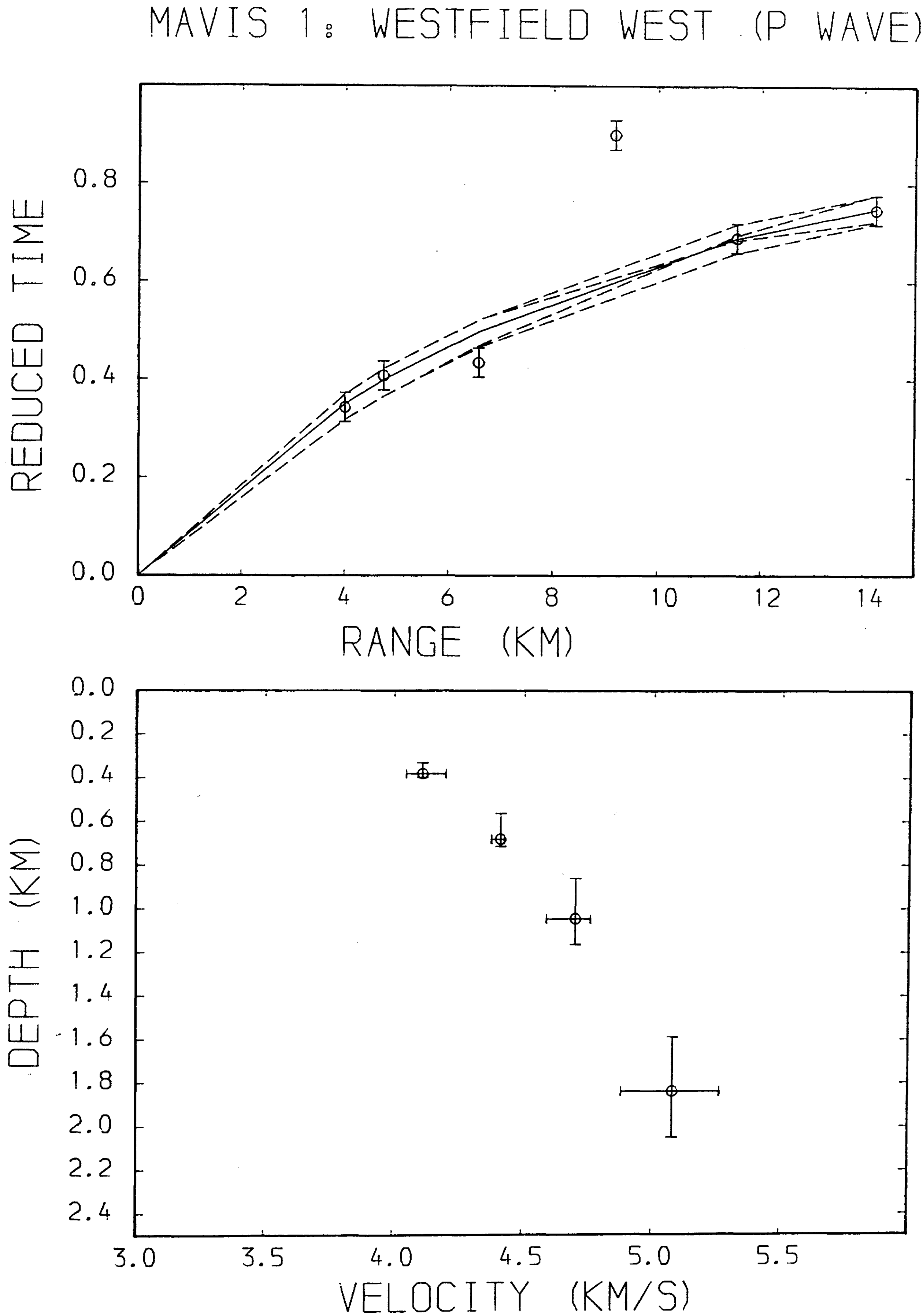

Fig.4.26 Time-distance and velocity-depth data from WHB inversion; Westfield shot (west). Reduction velocity is 6.0 km/s.

MAVIS 2: ABERUTHVEN

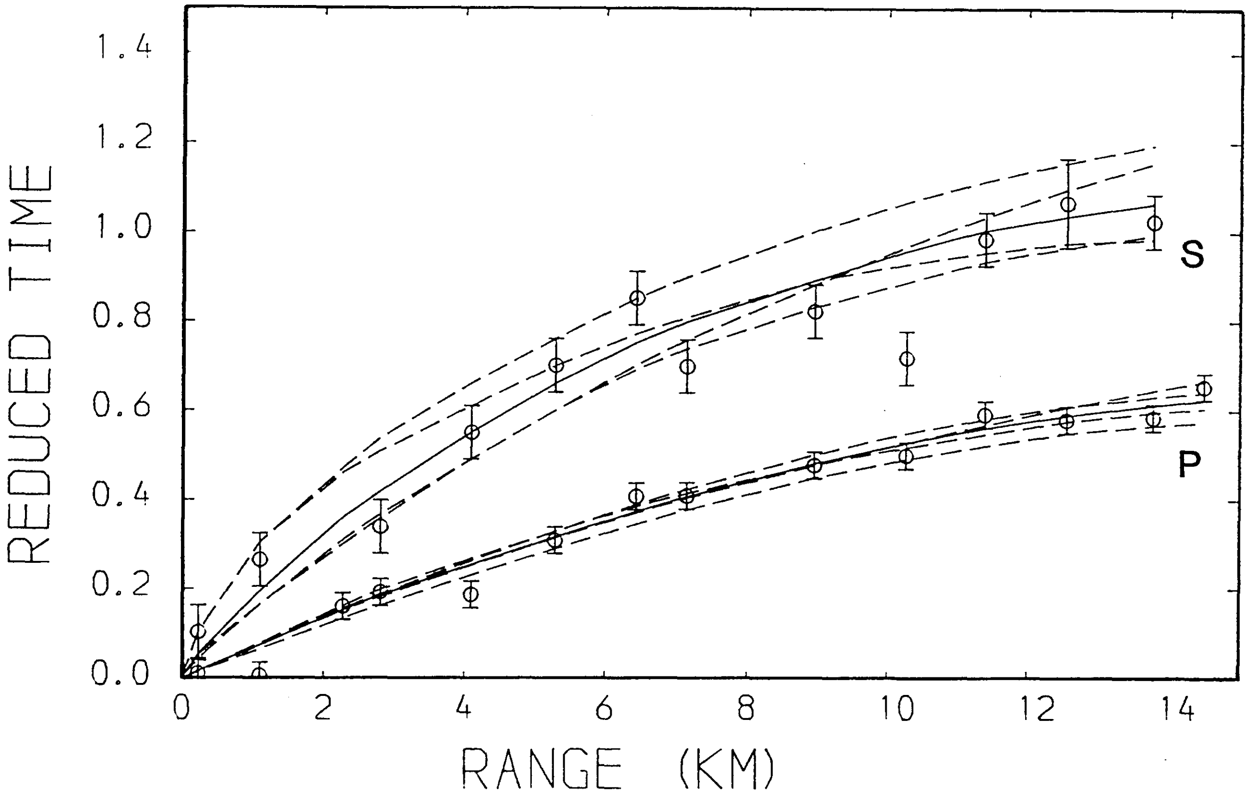

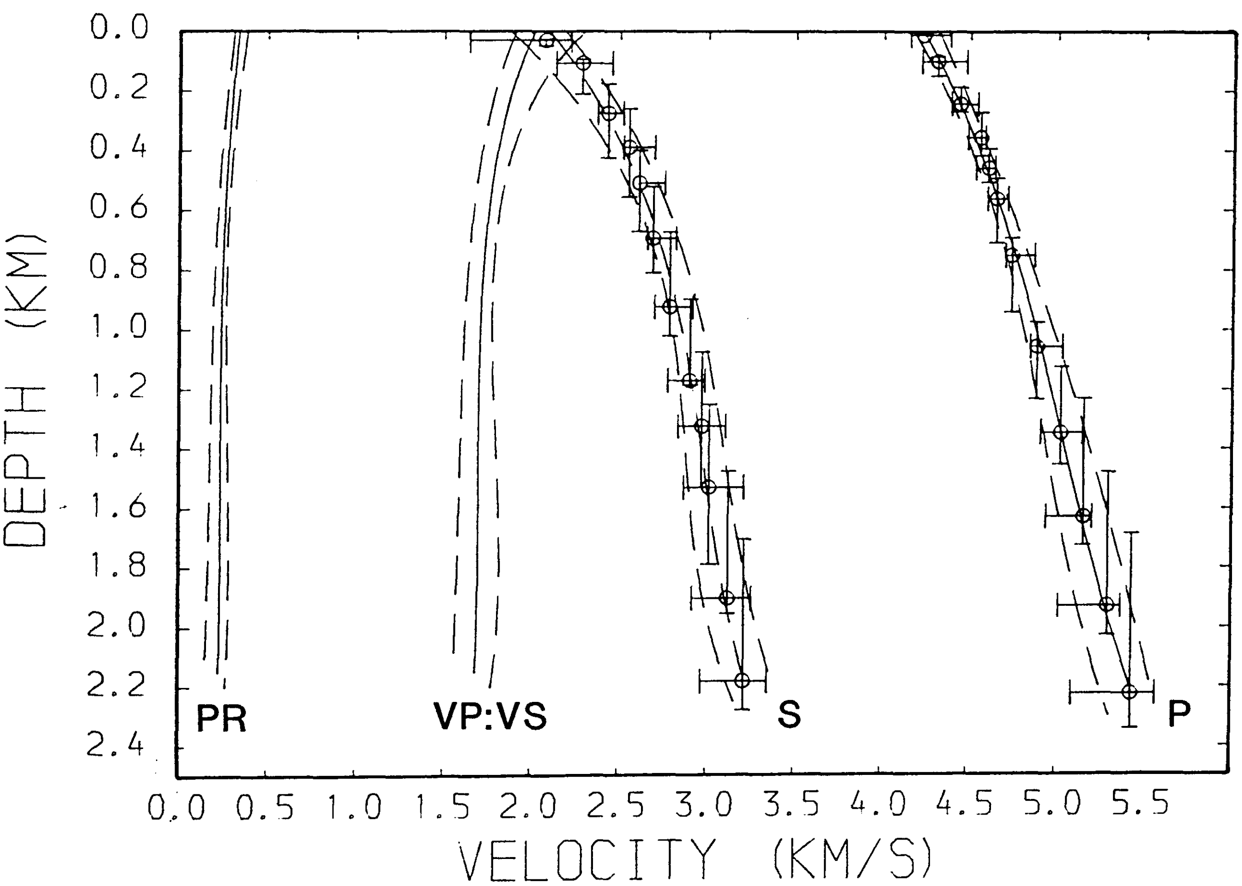

Fig.4.27 Time-distance and velocity-depth data from WHB inversion; Aberuthven shot, S - shear wave data, P - compressional wave data, VP:VS - ratio of P- and S-wave velocities, PR - Poisson's ratio. Reduction velocity is 6.0 km/s for P-wave data and 3.5 km/s for S-wave data.

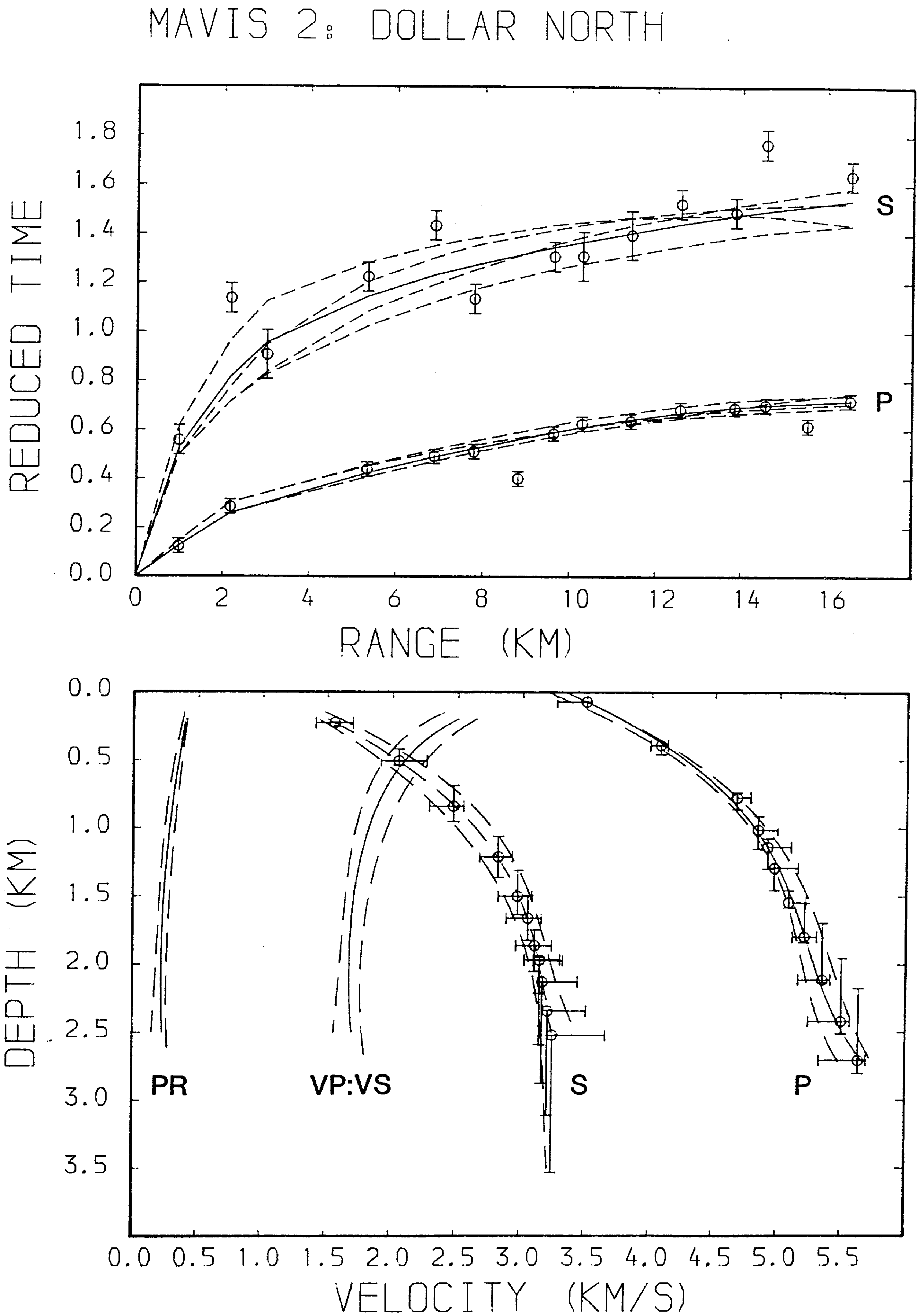

Fig.4.28 Time-distance and velocity-depth data from WHB inversion; Dollar shot (north). S - shear wave data, P - compressional wave data, VP:VS - ratio of P- and S-wave velocities, PR - Poisson's ratio. Reduction velocity is 6.0 km/s for P-wave data and 3.5 km/s for S-wave data.

MAVIS 2: DOLLAR SOUTH

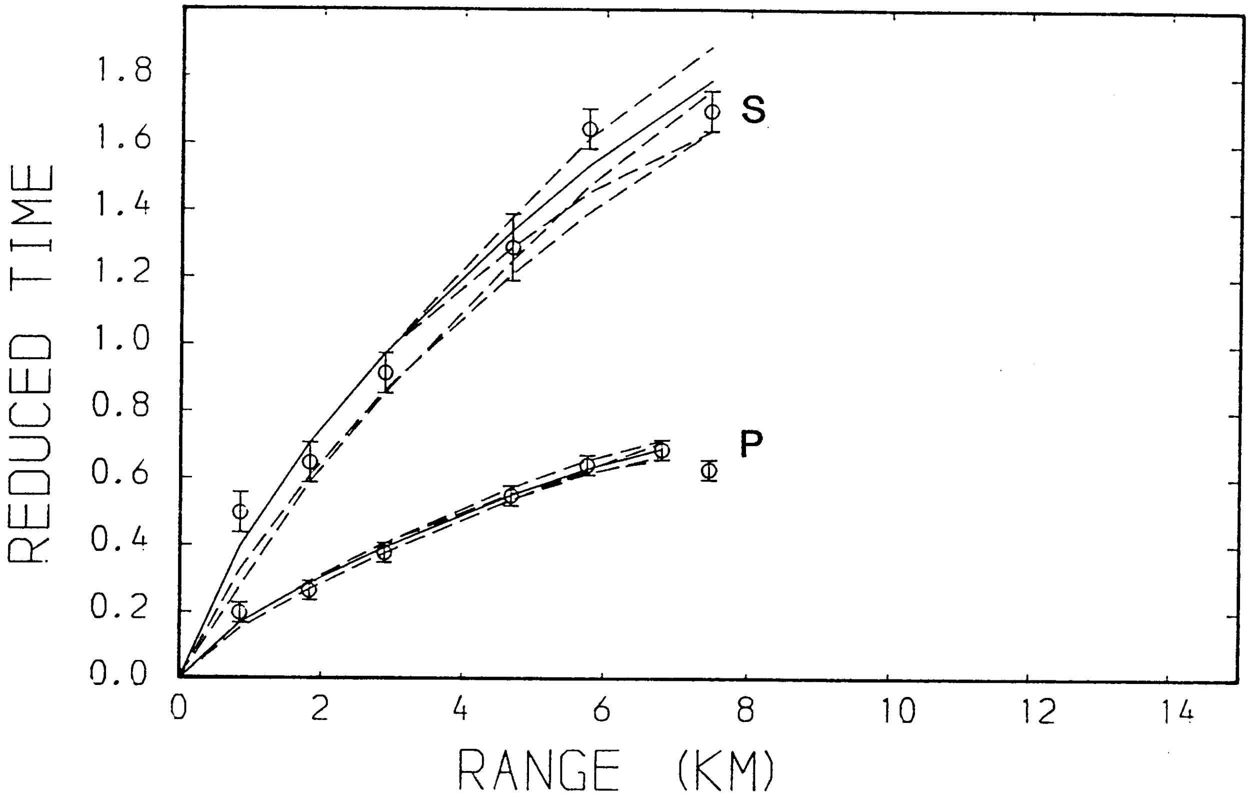

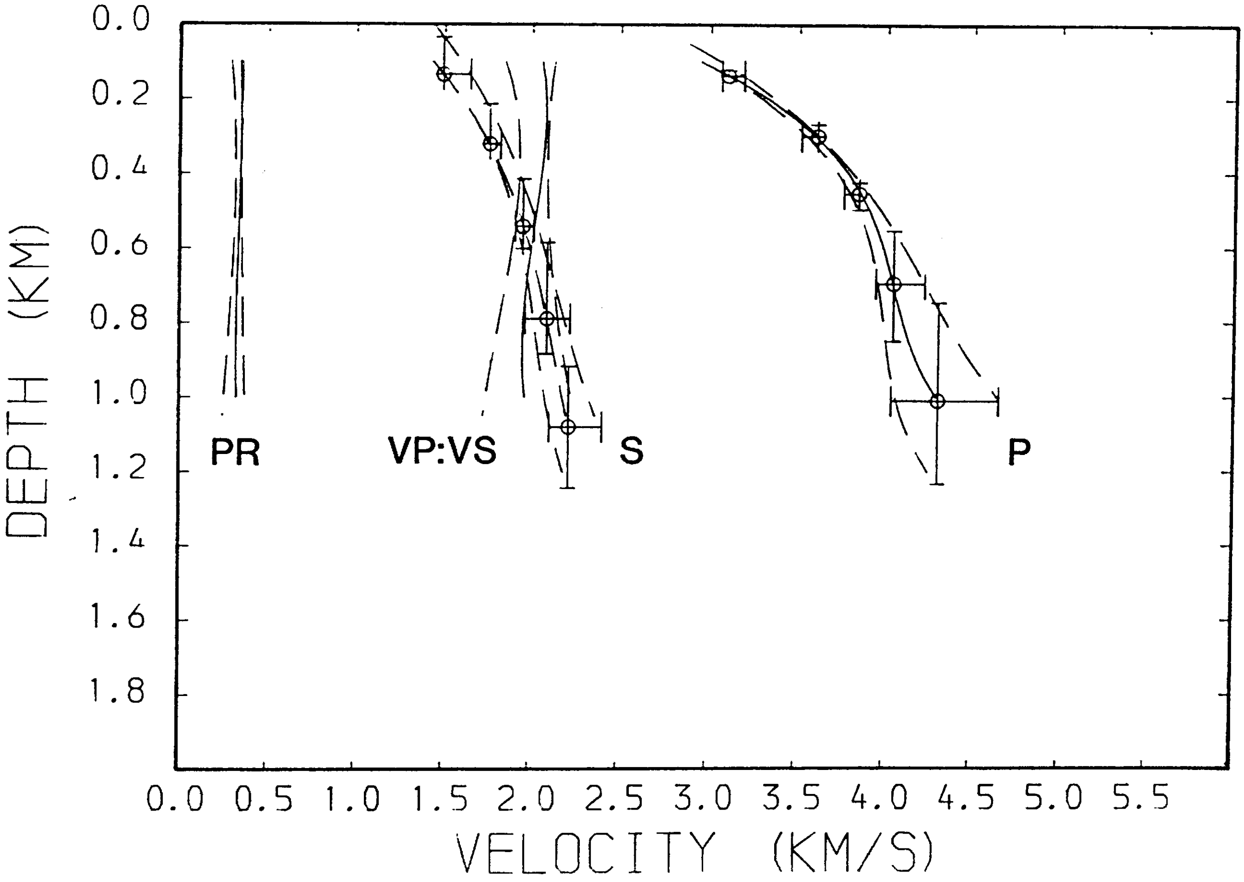

Fig.4.29 Time-distance and velocity-depth data from WHB inversion; Dollar shot (south). S - shear wave data, P - compressional wave data, VP:VS - ratio of P- and S-wave velocities, PR - Poisson's ratio. Reduction velocity is 6.0 km/s for P-wave data and 3.5 km/s for S-wave data.

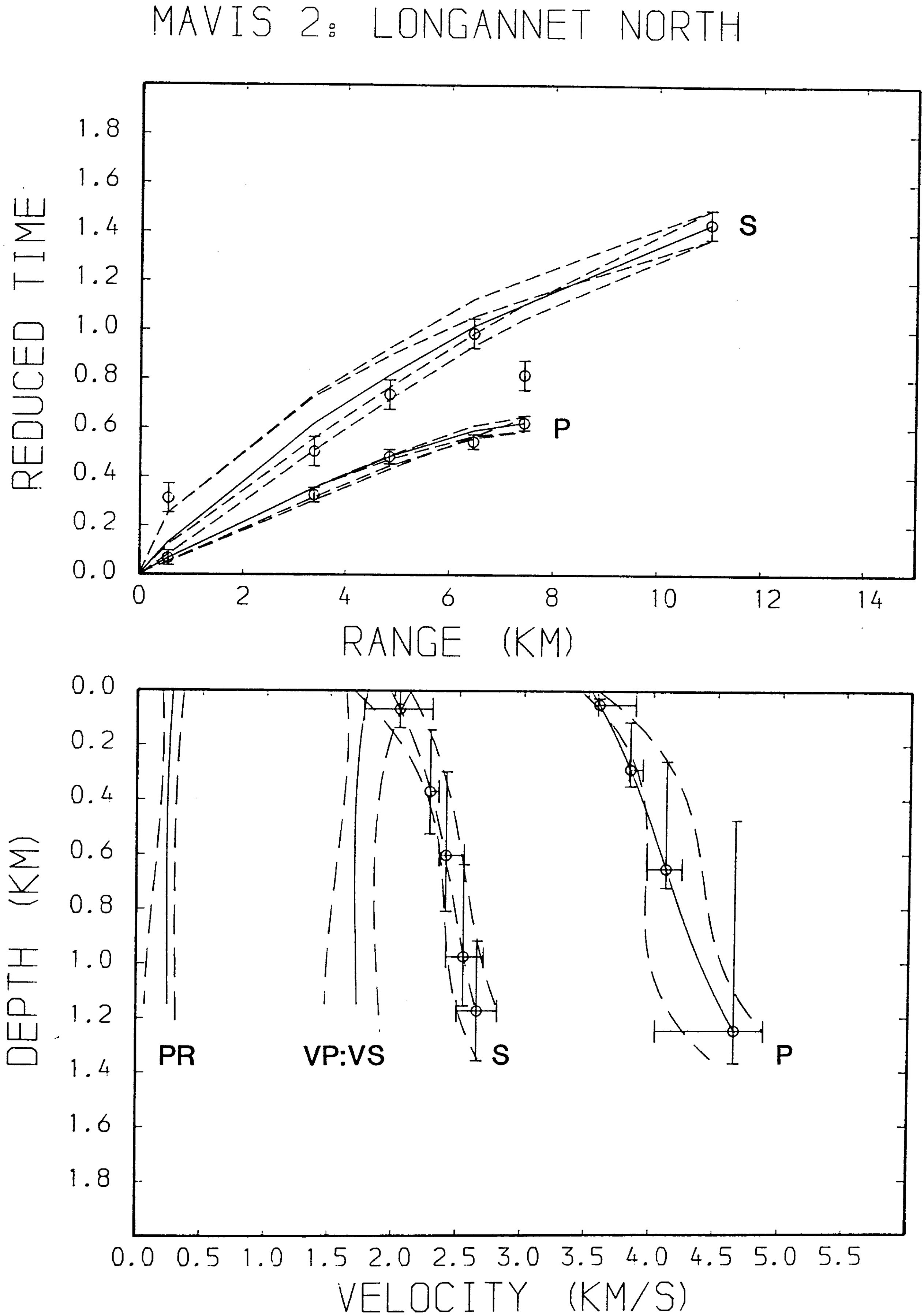

Fig.4.30 Time-distance and velocity-depth data from WHB inversion; Longannet shot (north). S - shear wave data, P - compressional wave data, VP:VS - ratio of P- and S-wave velocities, PR - Poisson's ratio. Reduction velocity is 6.0 km/s for P-wave data and 3.5 km/s for S-wave data.

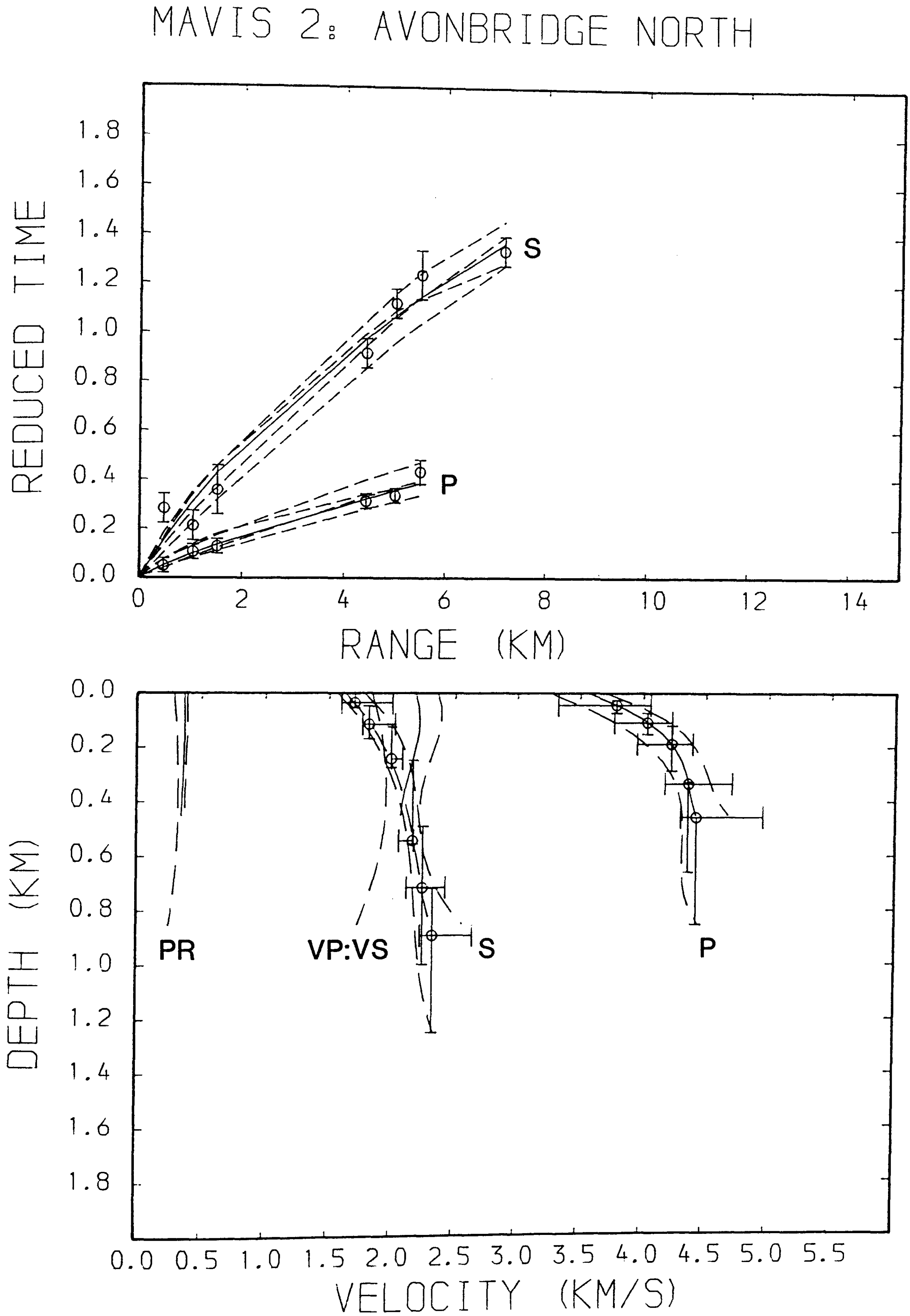

Fig.4.31 Time-distance and velocity-depth data from WHB inversion; Avonbridge shot (north). S - shear wave data, P - compressional wave data, VP:VS - ratio of P- and S-wave velocities, PR - Poisson's ratio. Reduction velocity is 6.0 km/s for P-wave data and 3.5 km/s for S-wave data.

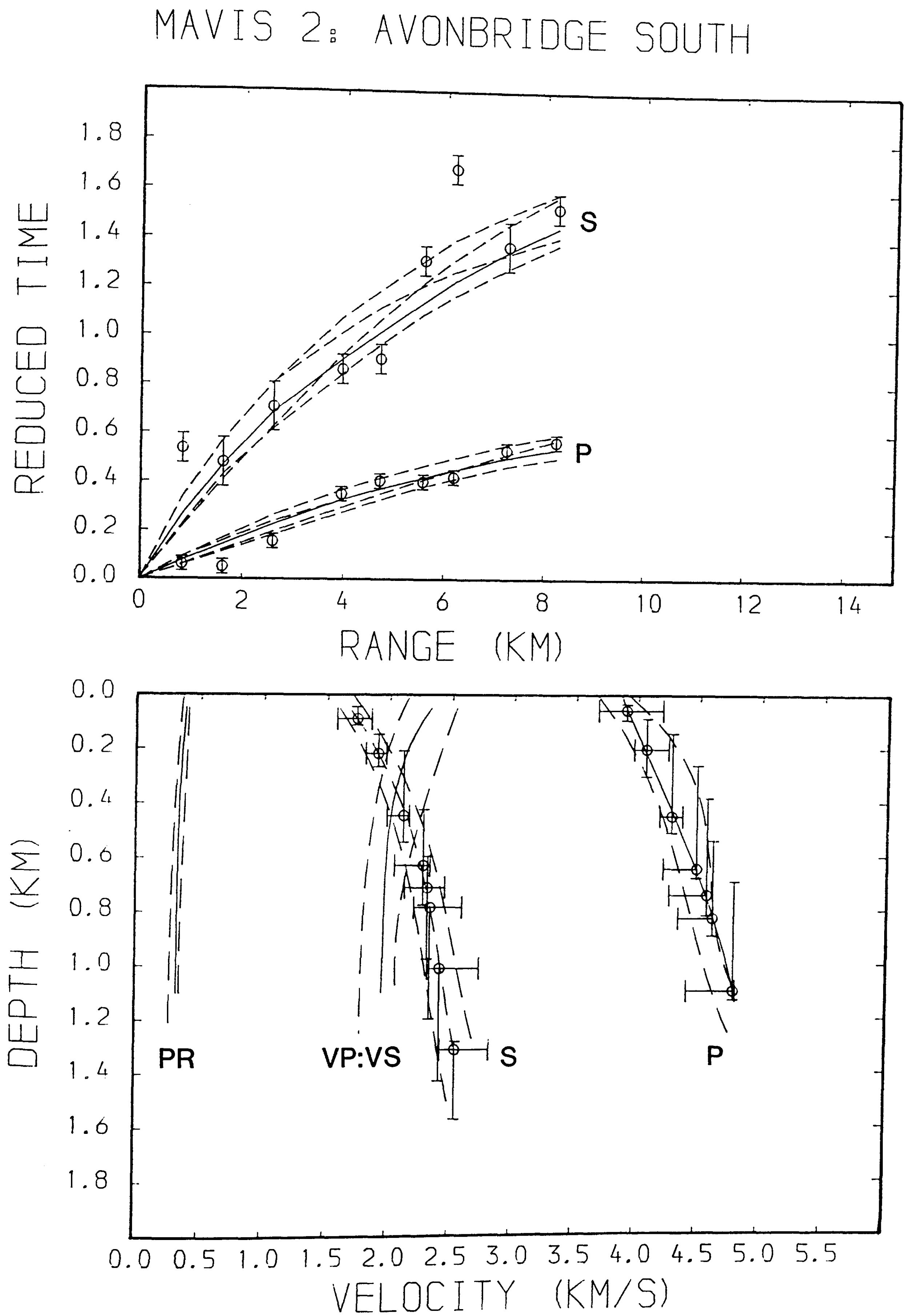

Fig.4.32 Time-distance and velocity-depth data from WHB inversion; Avonbridge shot (south). S - shear wave data, P - compressional wave data, VP:VS - ratio of P- and S-wave velocities, PR - Poisson's ratio. Reduction velocity is 6.0 km/s for P-wave data and 3.5 km/s for S-wave data.

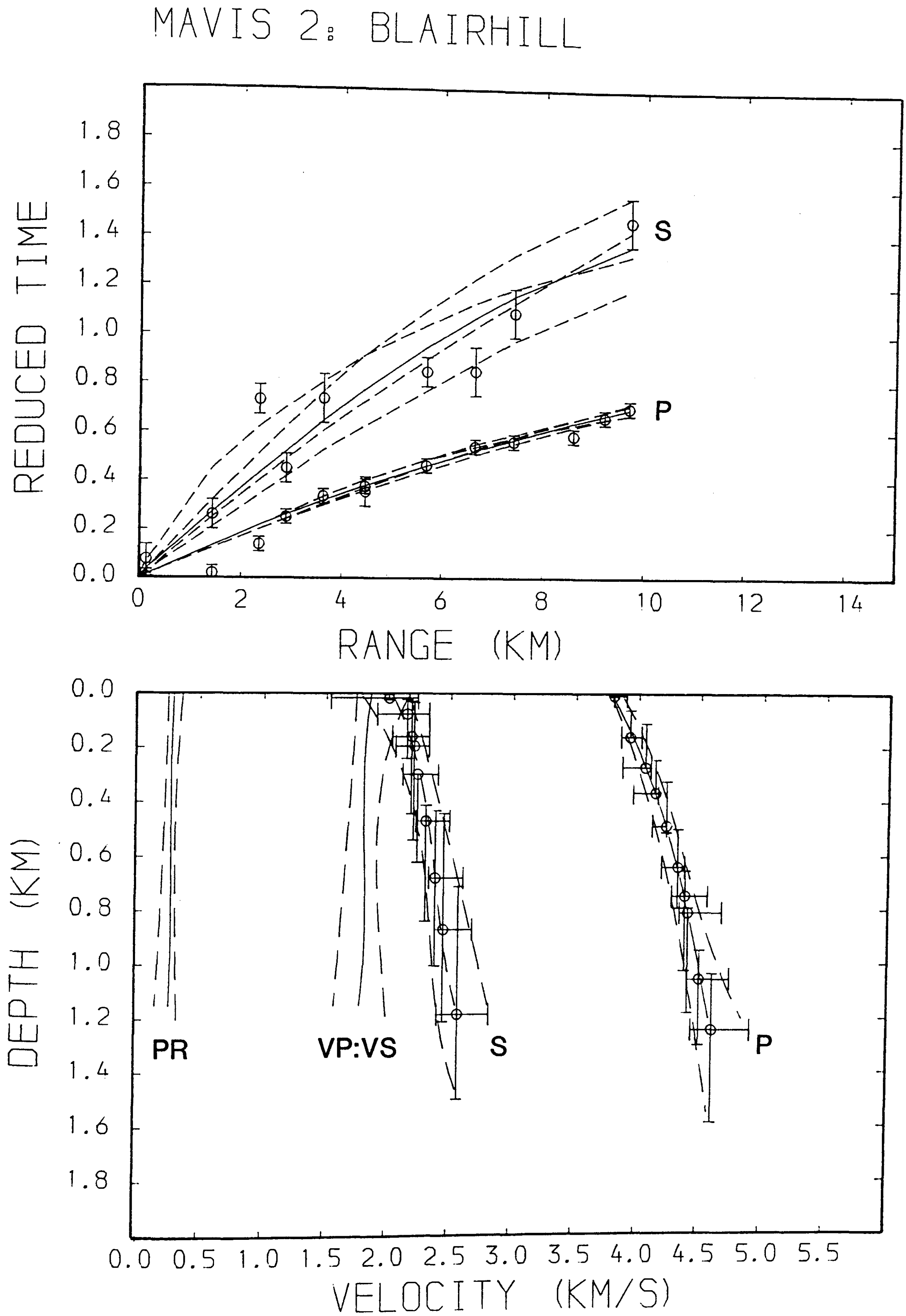

Fig.4.33 Time-distance and velocity-depth data from WHB inversion; Blairhill shot. S - shear wave data, P - compressional wave data, VP:VS - ratio of P- and S-wave velocities, PR - Poisson's ratio. Reduction velocity is 6.0 km/s for P-wave data and 3.5 km/s for S-wave data.

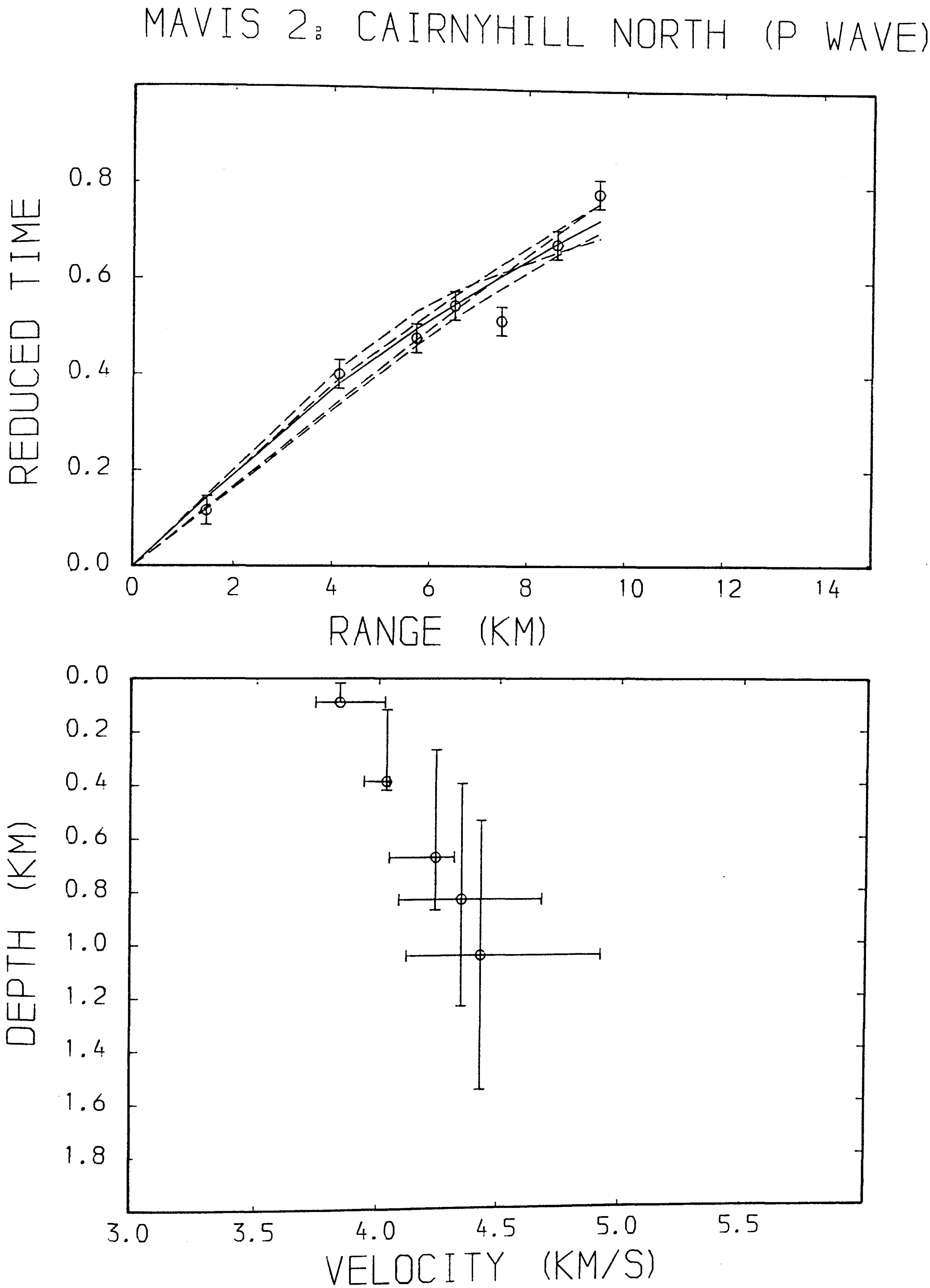

Fig.4.34 Time-distance and velocity-depth data from WHB inversion; Cairnyhill shot (north). Reduction velocity is 6.0 km/s.

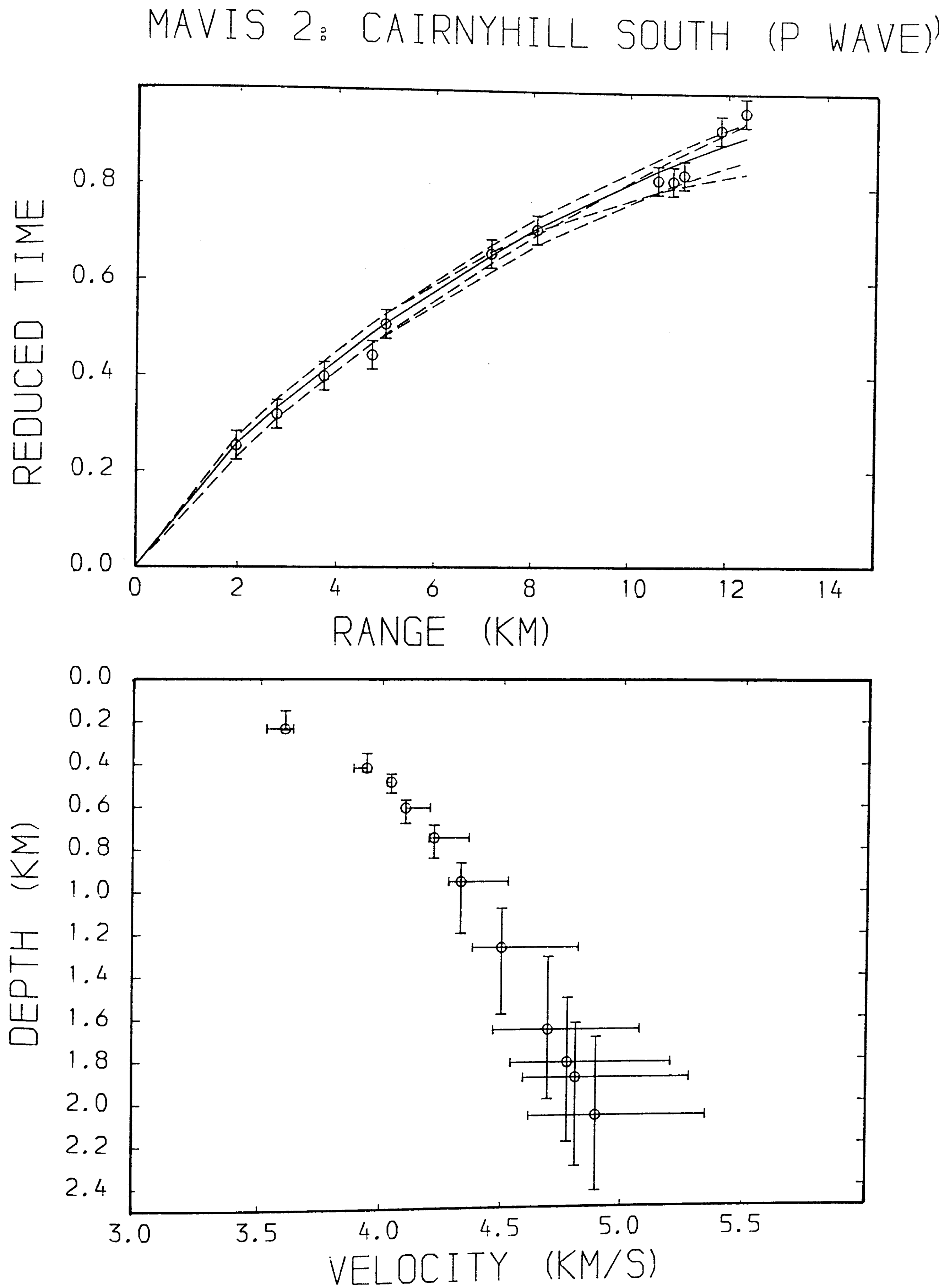

Fig.4.35 Time-distance and velocity-depth data from WHB inversion; Cairnyhill shot (south). Reduction velocity is 6.0 km/s.

MAVIS 2: TAMSLOUP NORTH (P WAVE)

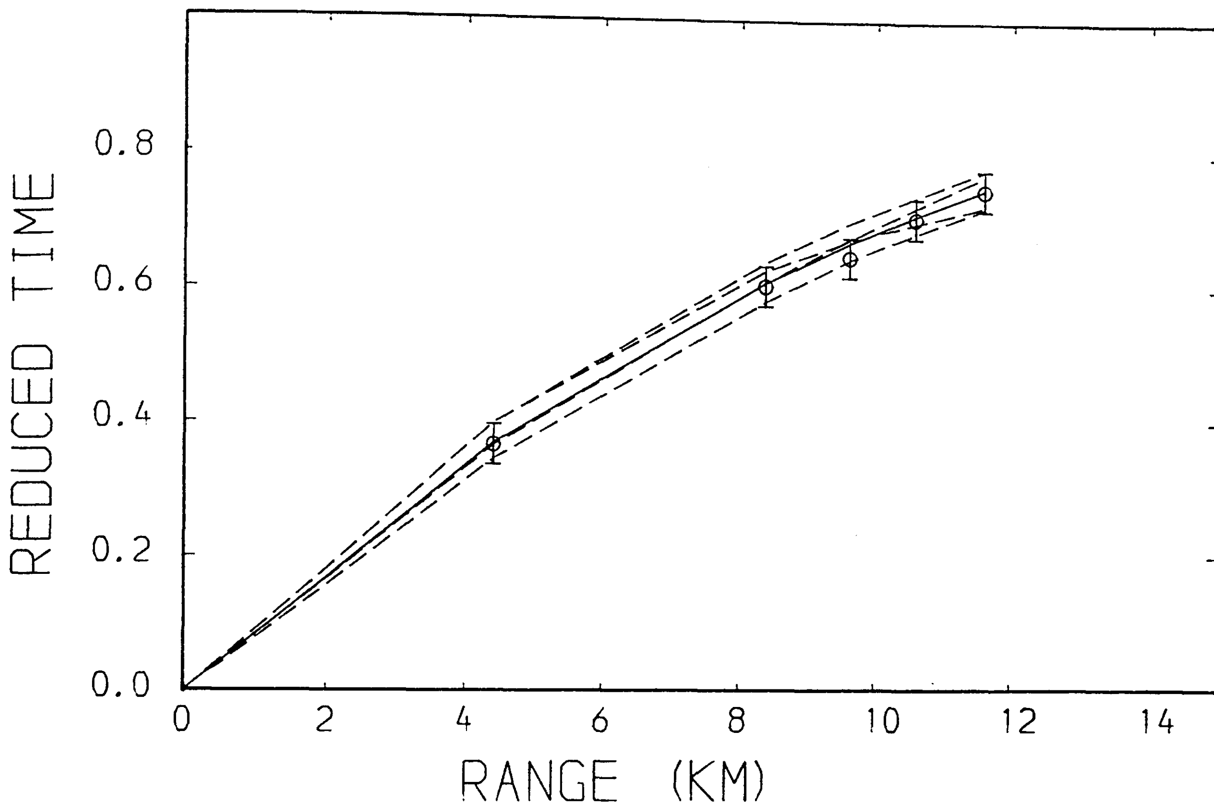

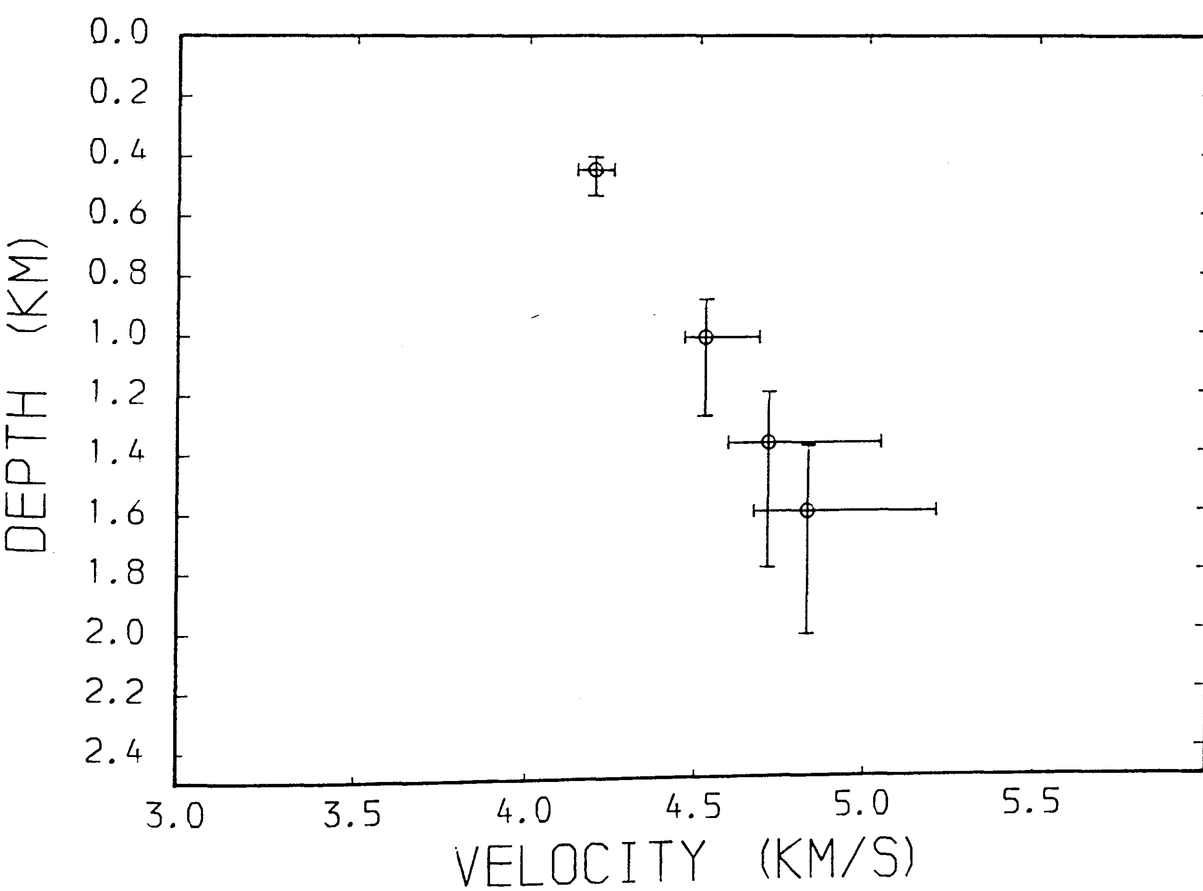

Fig.4.36 Time-distance and velocity-depth data from WHB inversion; Tamsloup shot (north). Reduction velocity is 6.0 km/s.

MAVIS 2: HEADLESS CROSS NORTH (P WAVE)

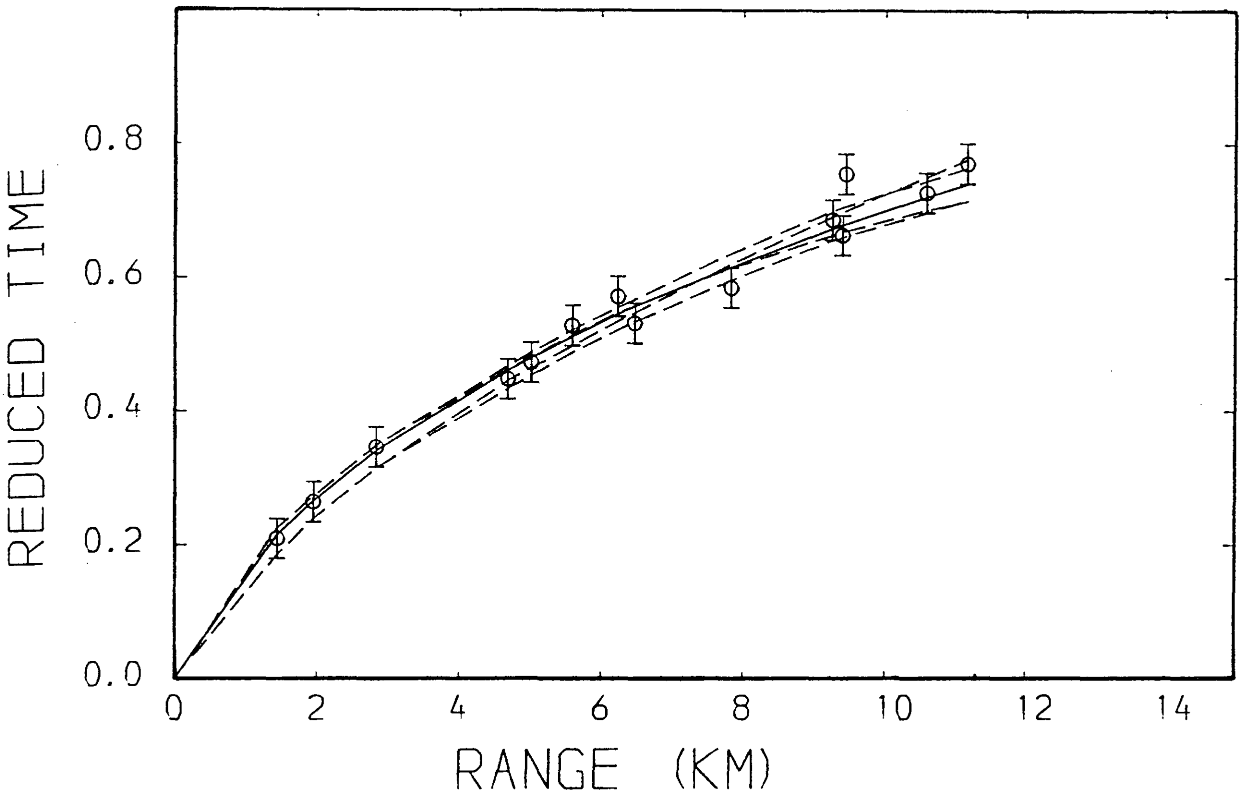

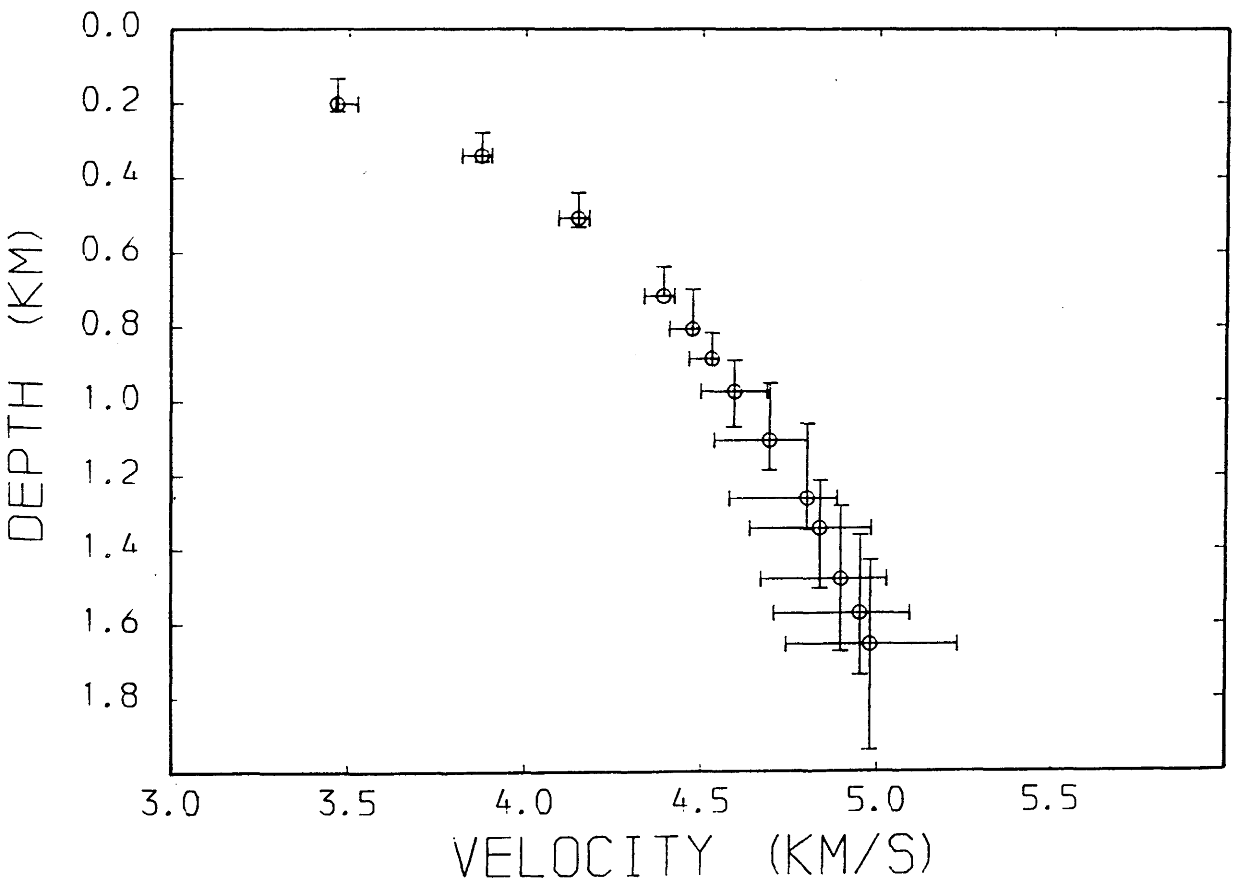

Fig.4.37 Time-distance and velocity-depth data from WHB inversion; Headless Cross shot (north). Reduction velocity is 6.0 km/s.

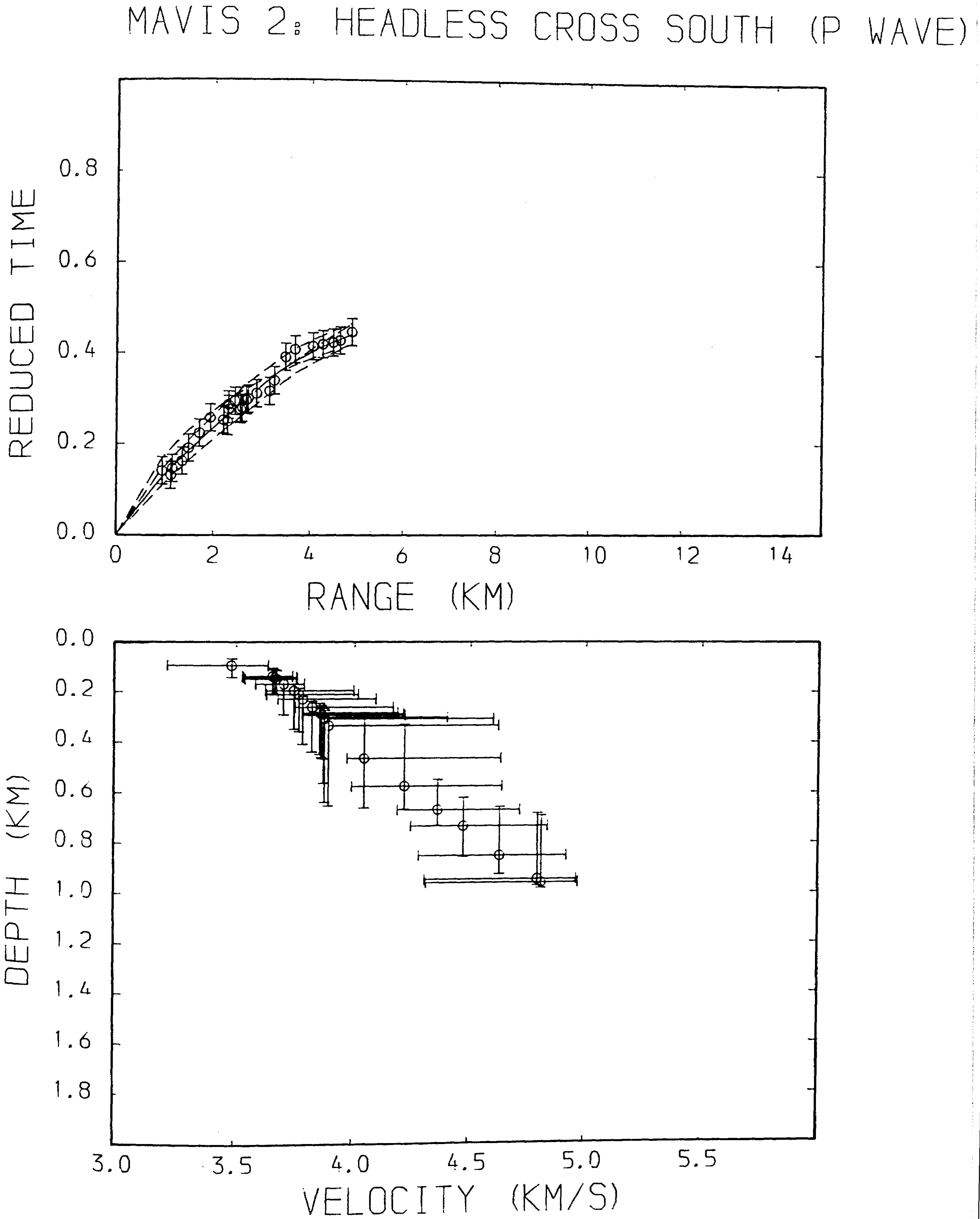

Fig.4.38 Time-distance and velocity-depth data from WHB inversion; Headless Cross shot (south). Reduction velocity is 6.0 km/s.

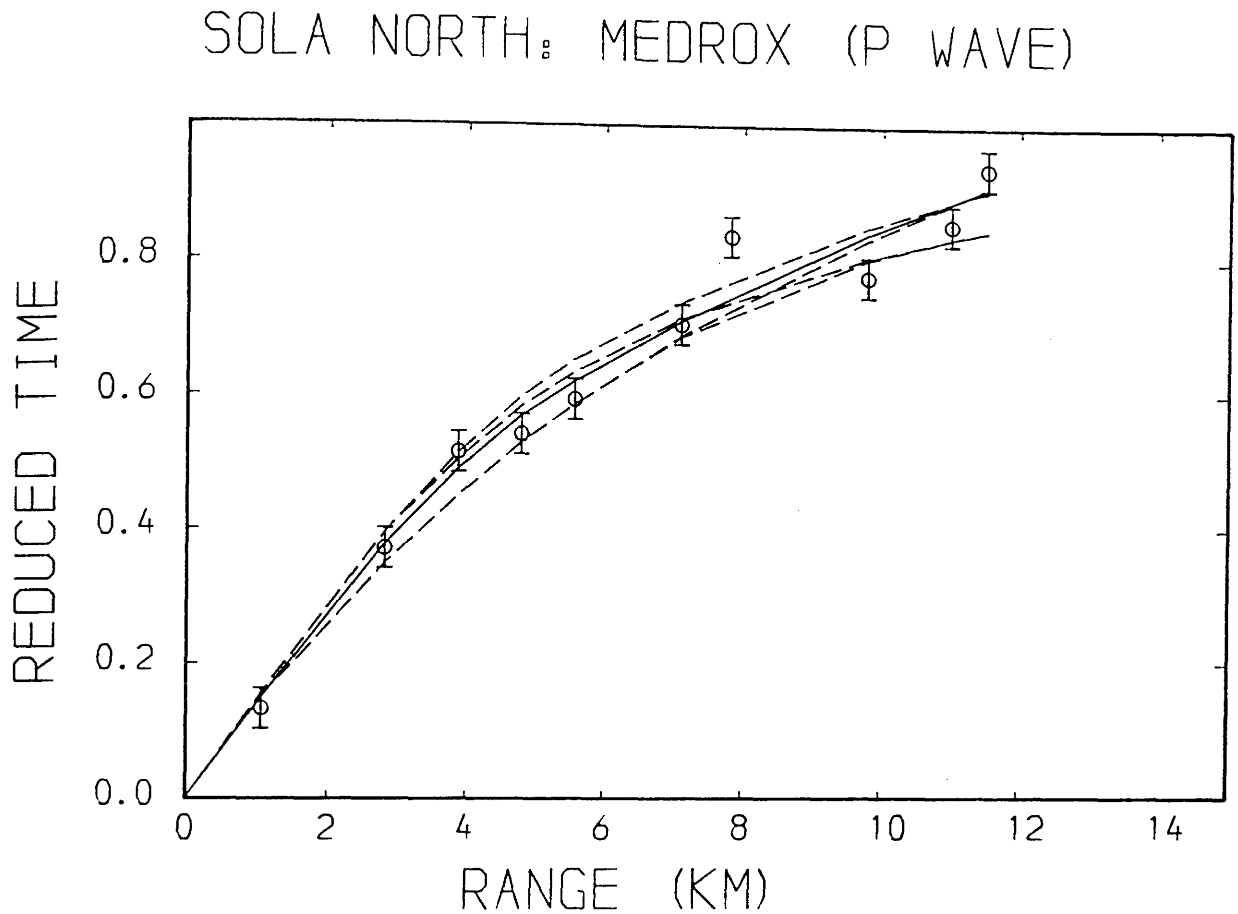

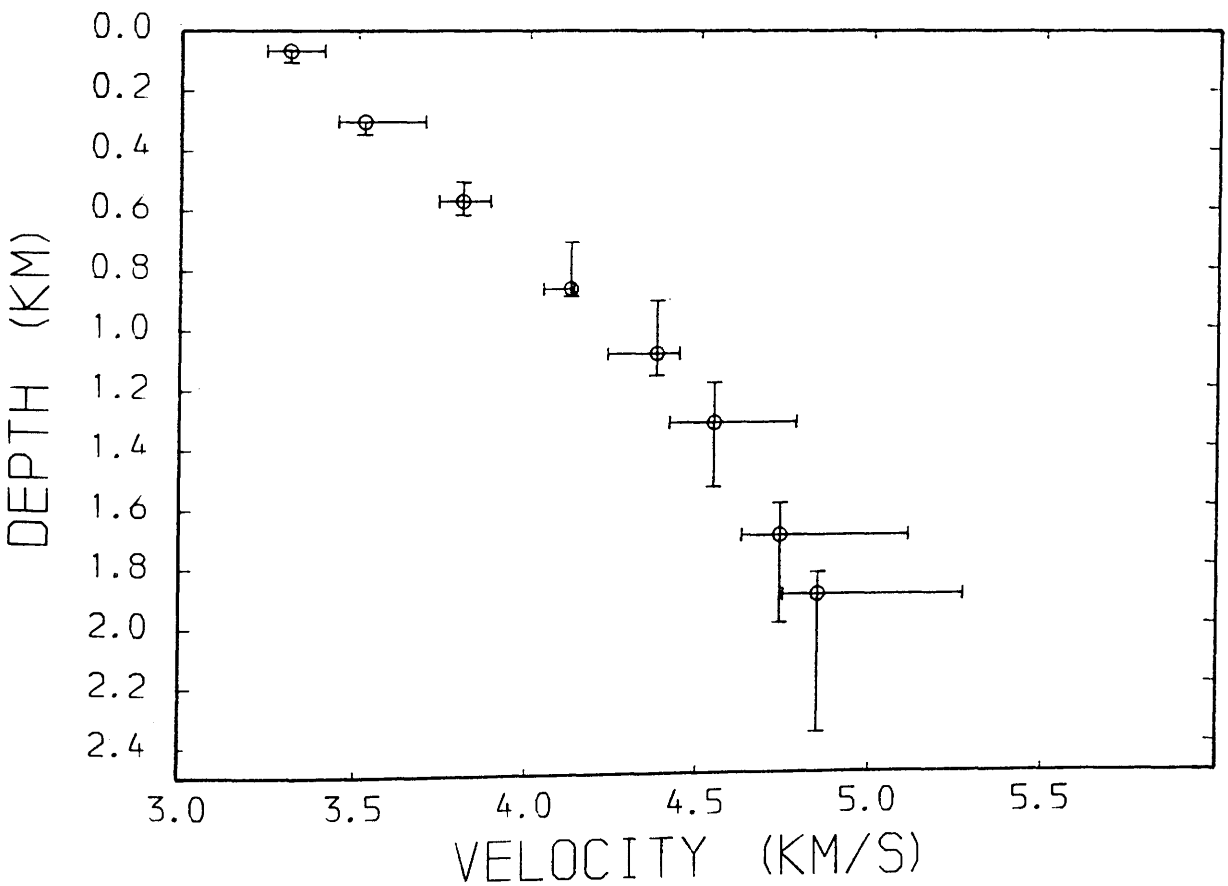

Fig.4.39 Time-distance and velocity-depth data from WHB inversion; Medrox shot. Reduction velocity is 6.0 km/s.

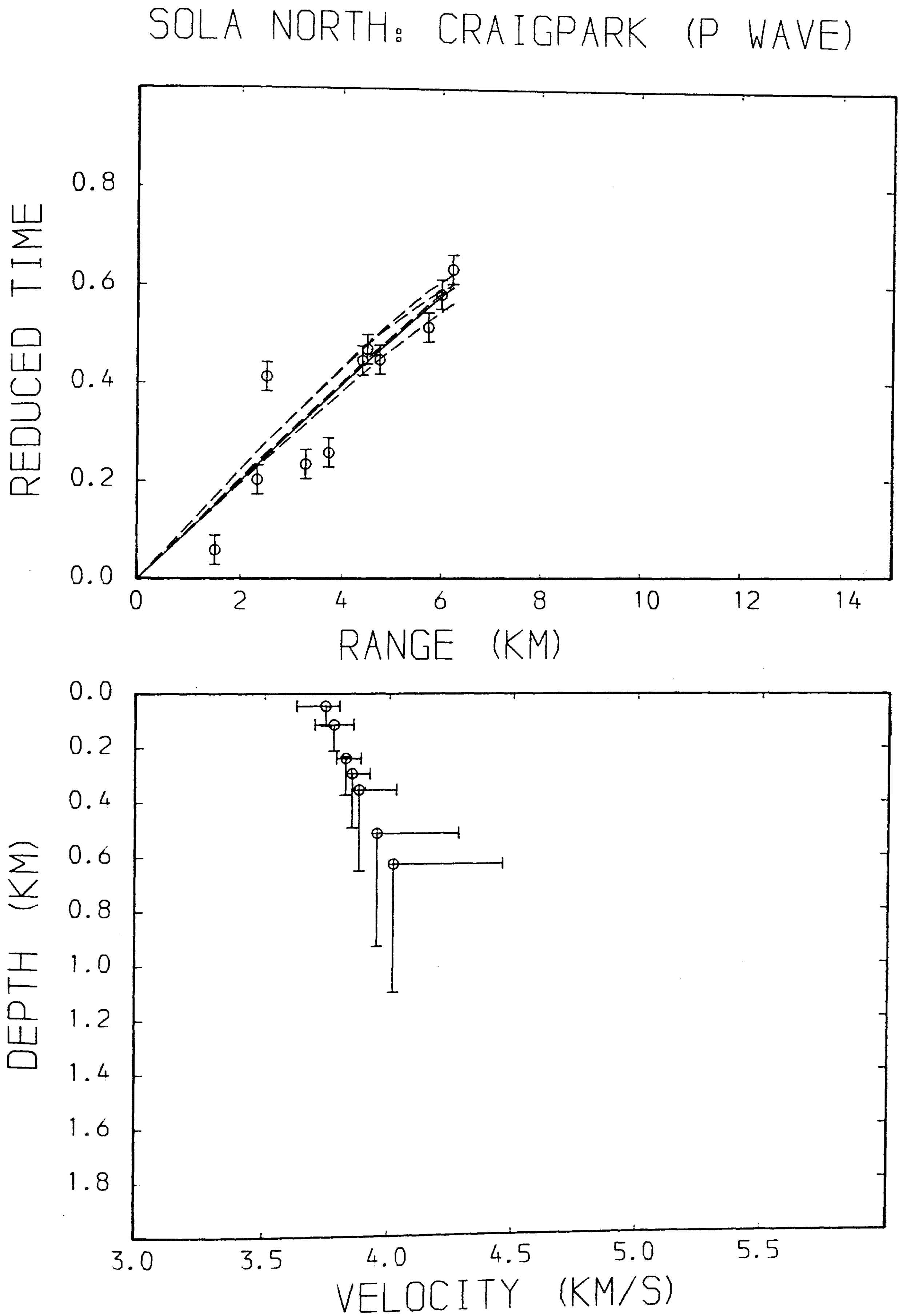

Fig.4.40 Time-distance and velocity-depth data from WHB inversion; Craigpark shot. Reduction velocity is 6.0 km/s.

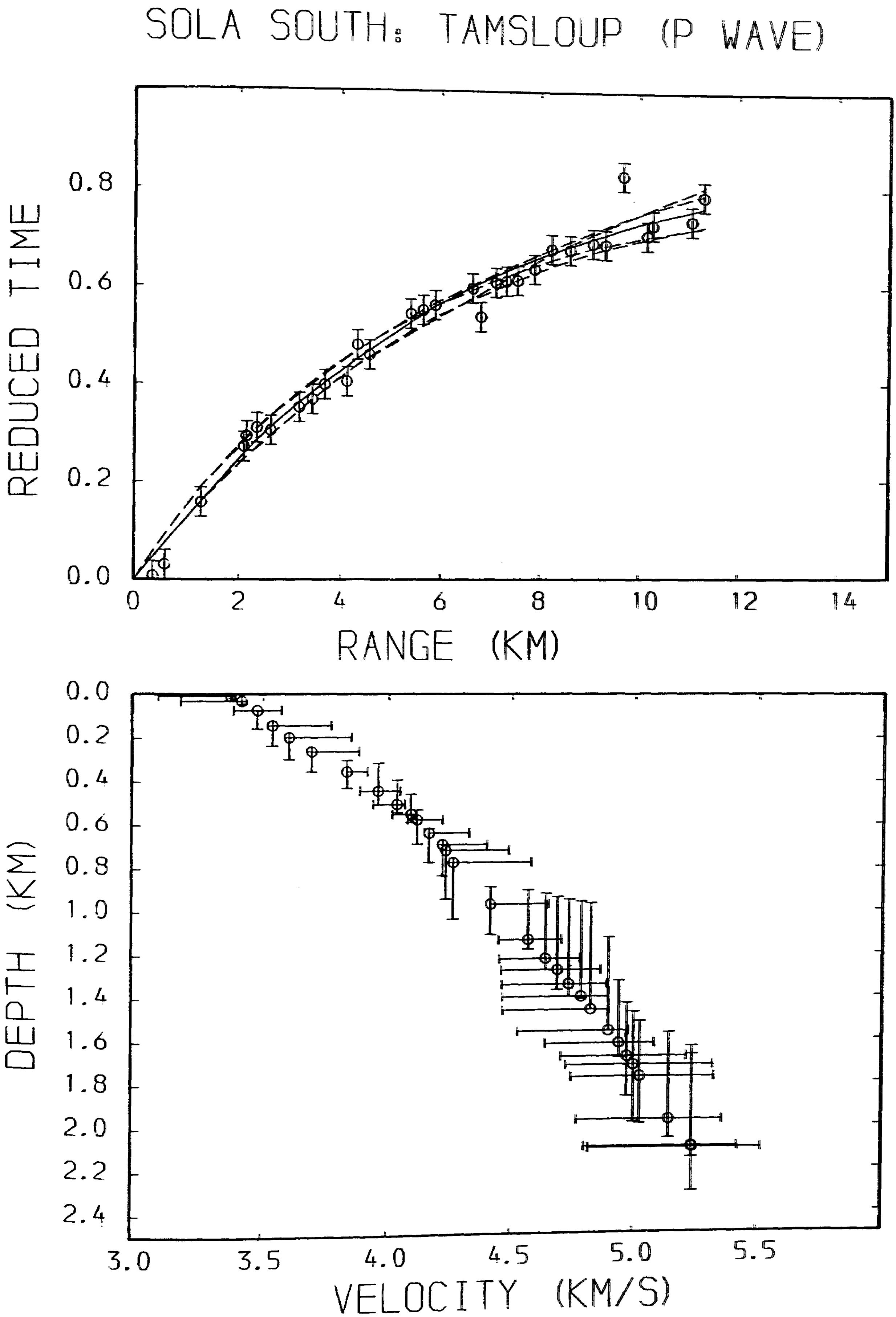

Fig.4.41 Time-distance and velocity-depth data from WHB inversion; Tamsloup shot (east). Reduction velocity is 6.0 km/s.

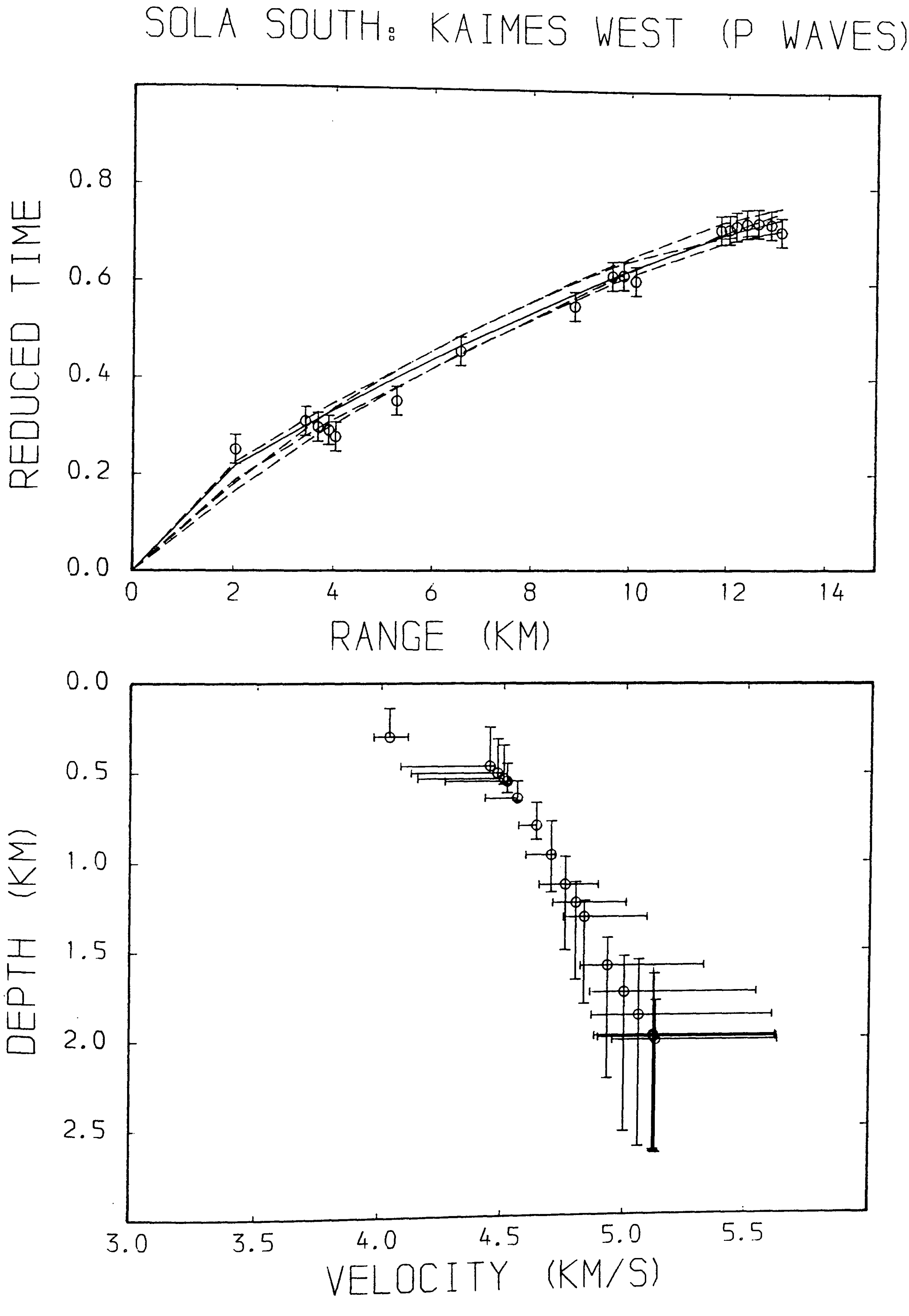

Fig.4.42 Time-distance and velocity-depth data from WHB inversion; Kaimes shot (west). Reduction velocity is 6.0 km/s.

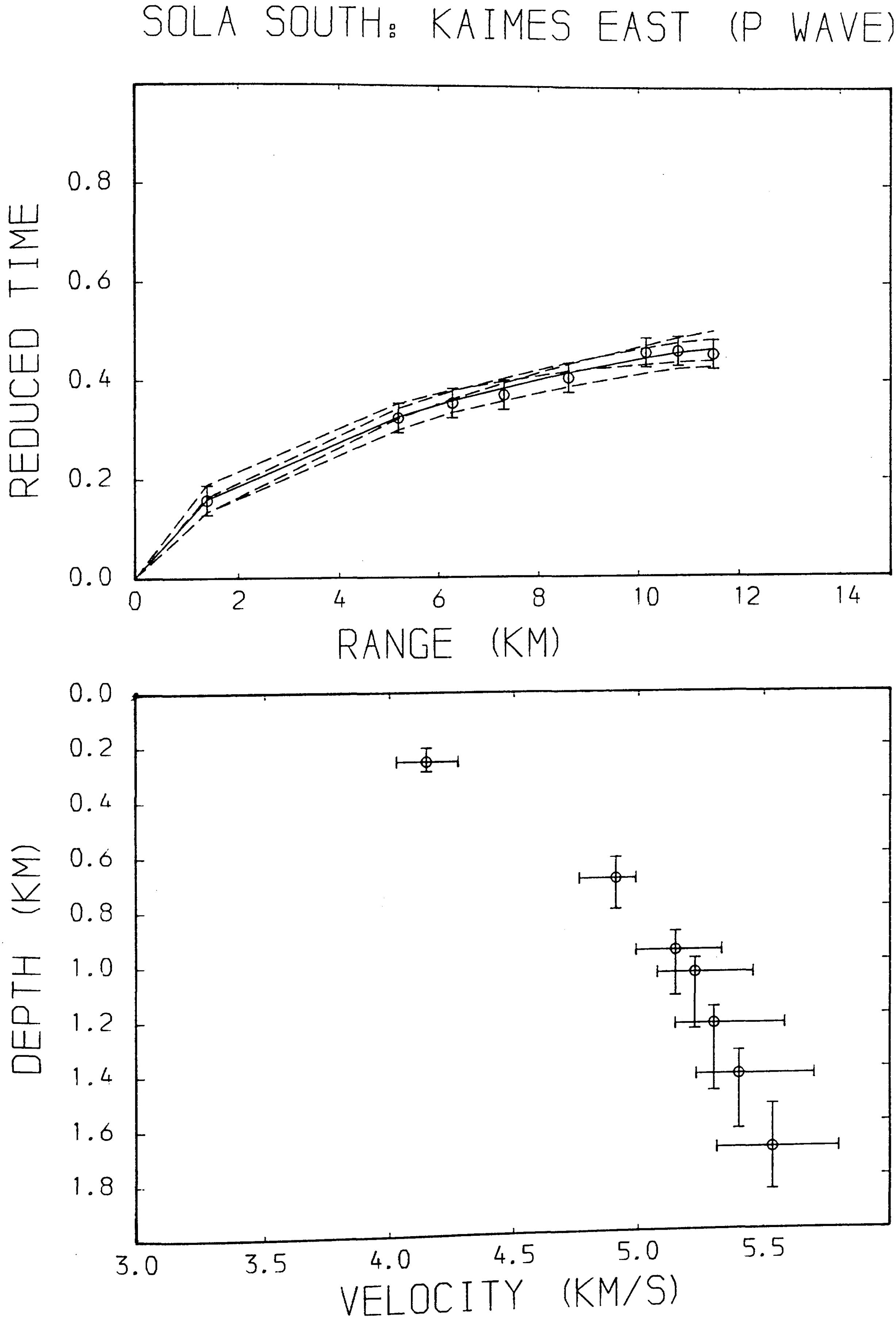

Fig.4.43 Time-distance and velocity-depth data from WHB inversion; Kaimes shot (east). Reduction velocity is 6.0 km/s.

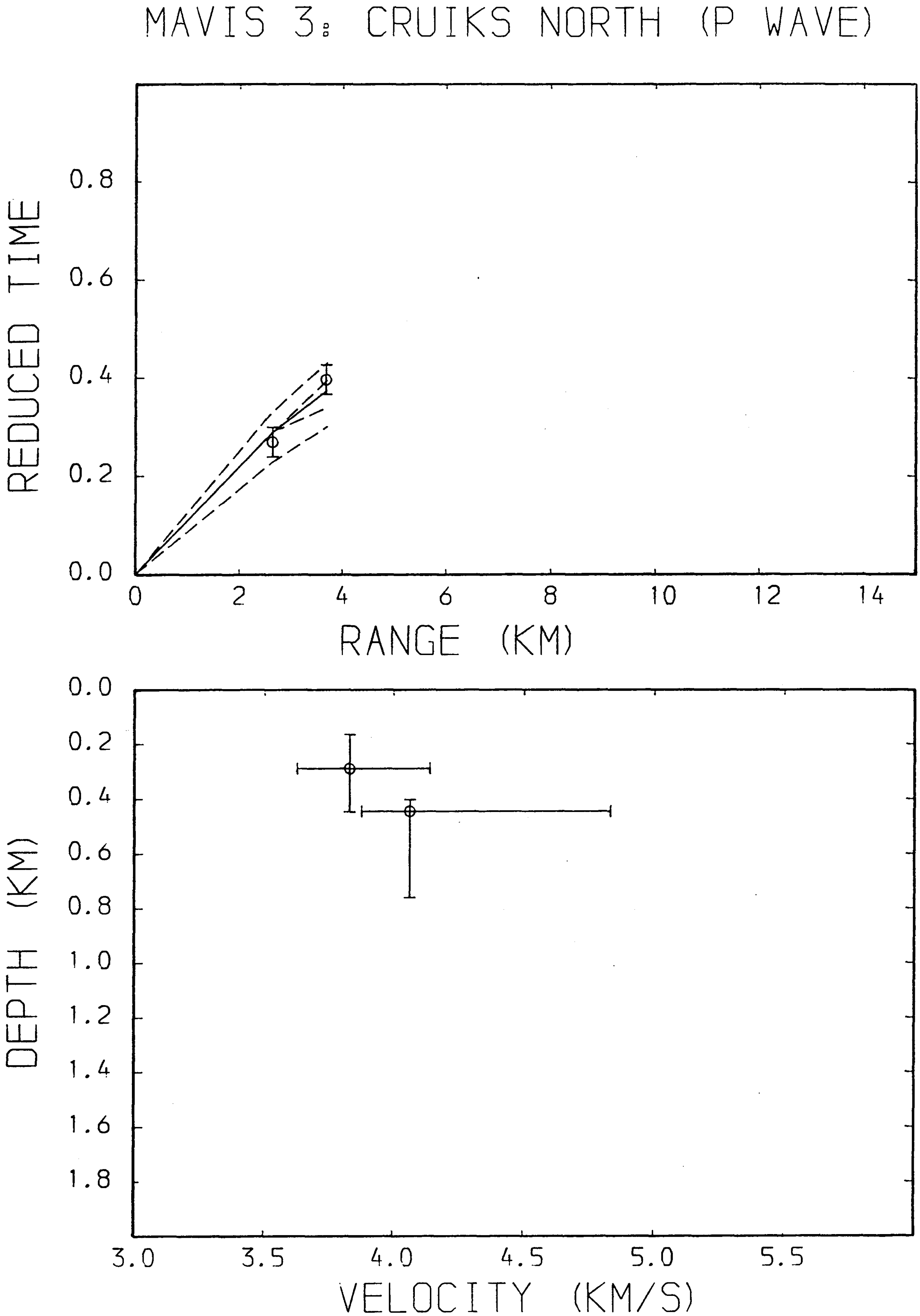

Fig.4.44 Time-distance and velocity-depth data from WHB inversion; Cruiks shot (north). Reduction velocity is 6.0 km/s.

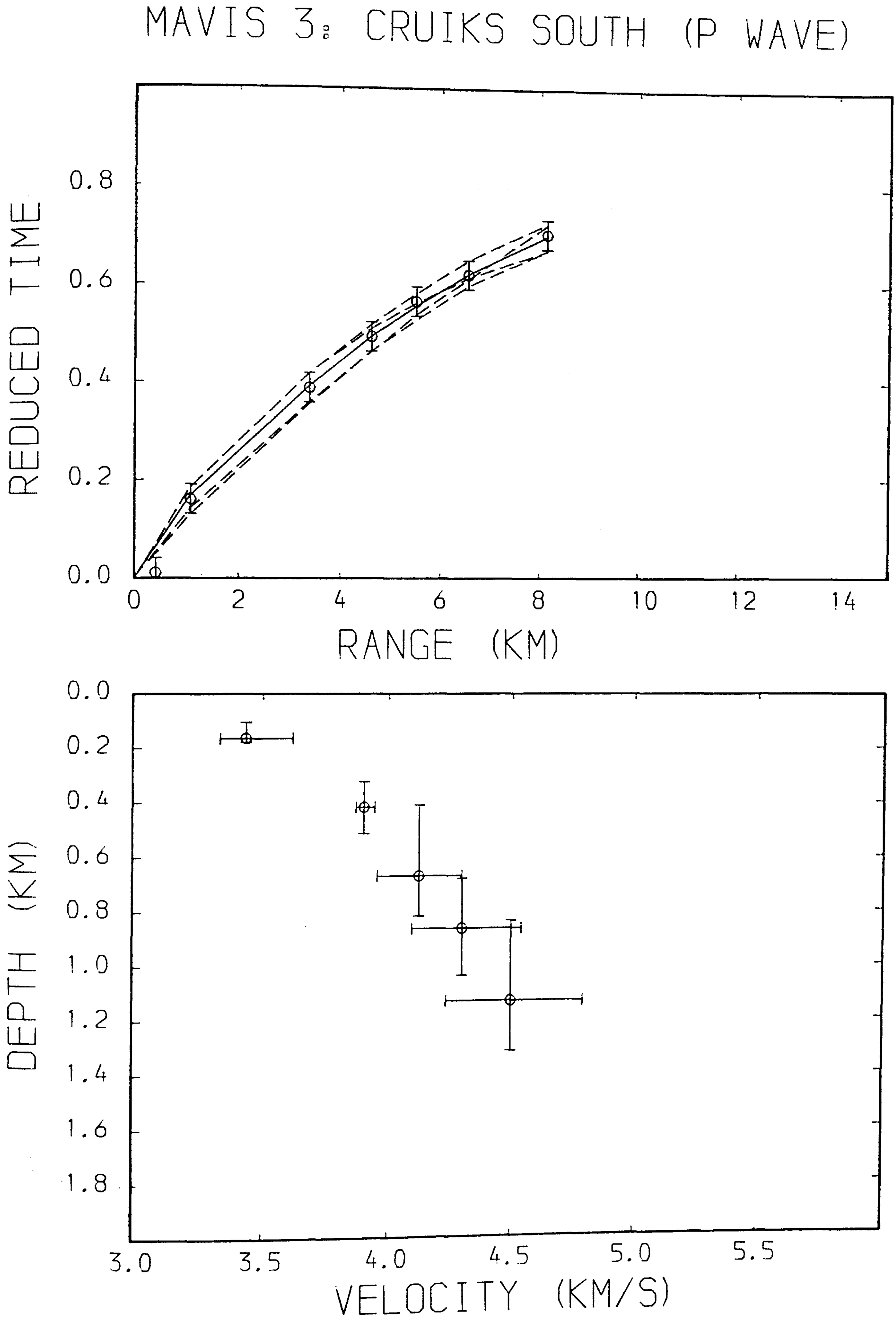

Fig.4.45 Time-distance and velocity-depth data from WHB inversion; Cruiks shot (south). Reduction velocity is 6.0 km/s.

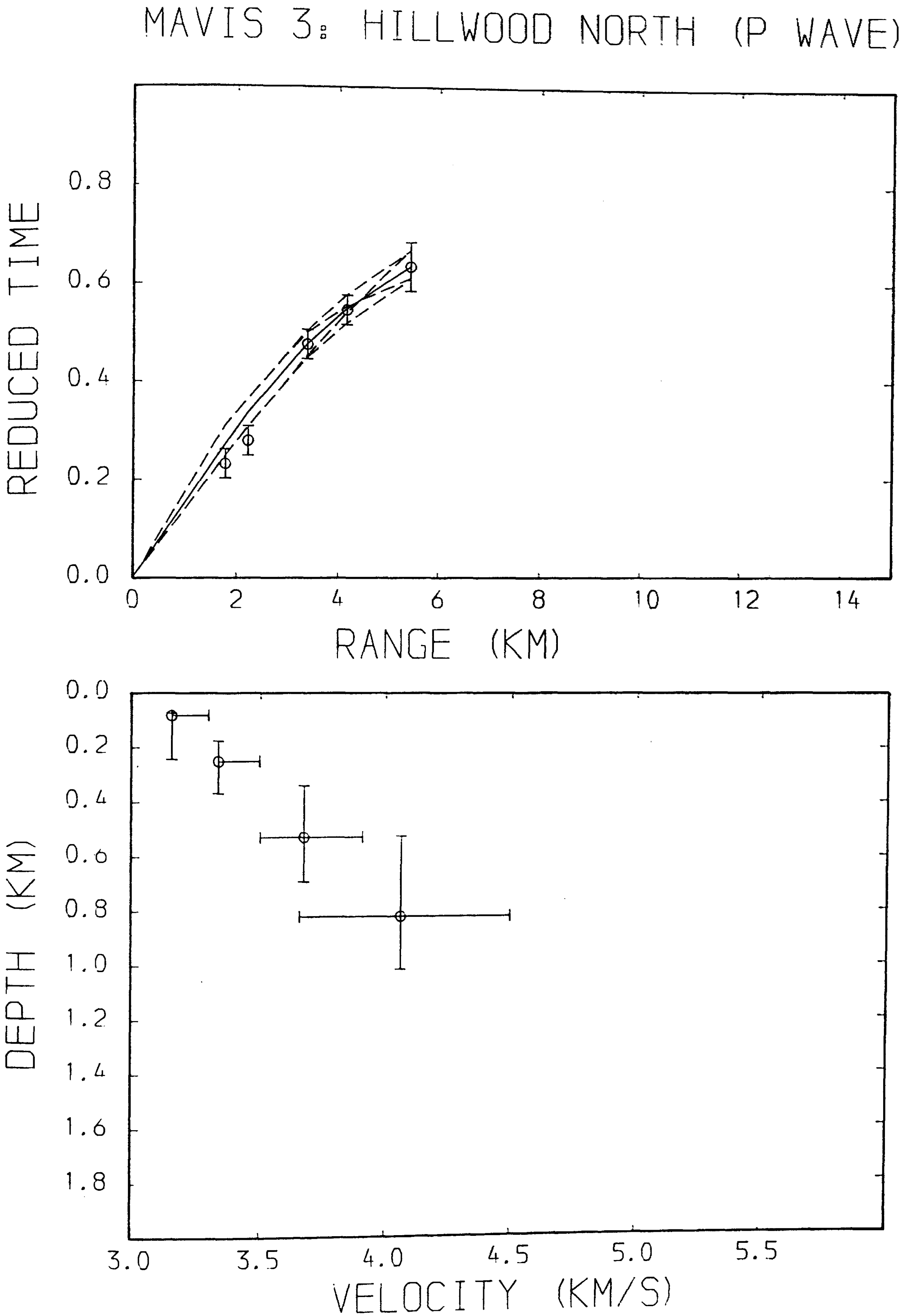

Fig.4.46 Time-distance and velocity-depth data from WHB inversion; Hillwood shot (north). Reduction velocity is 6.0 km/s.

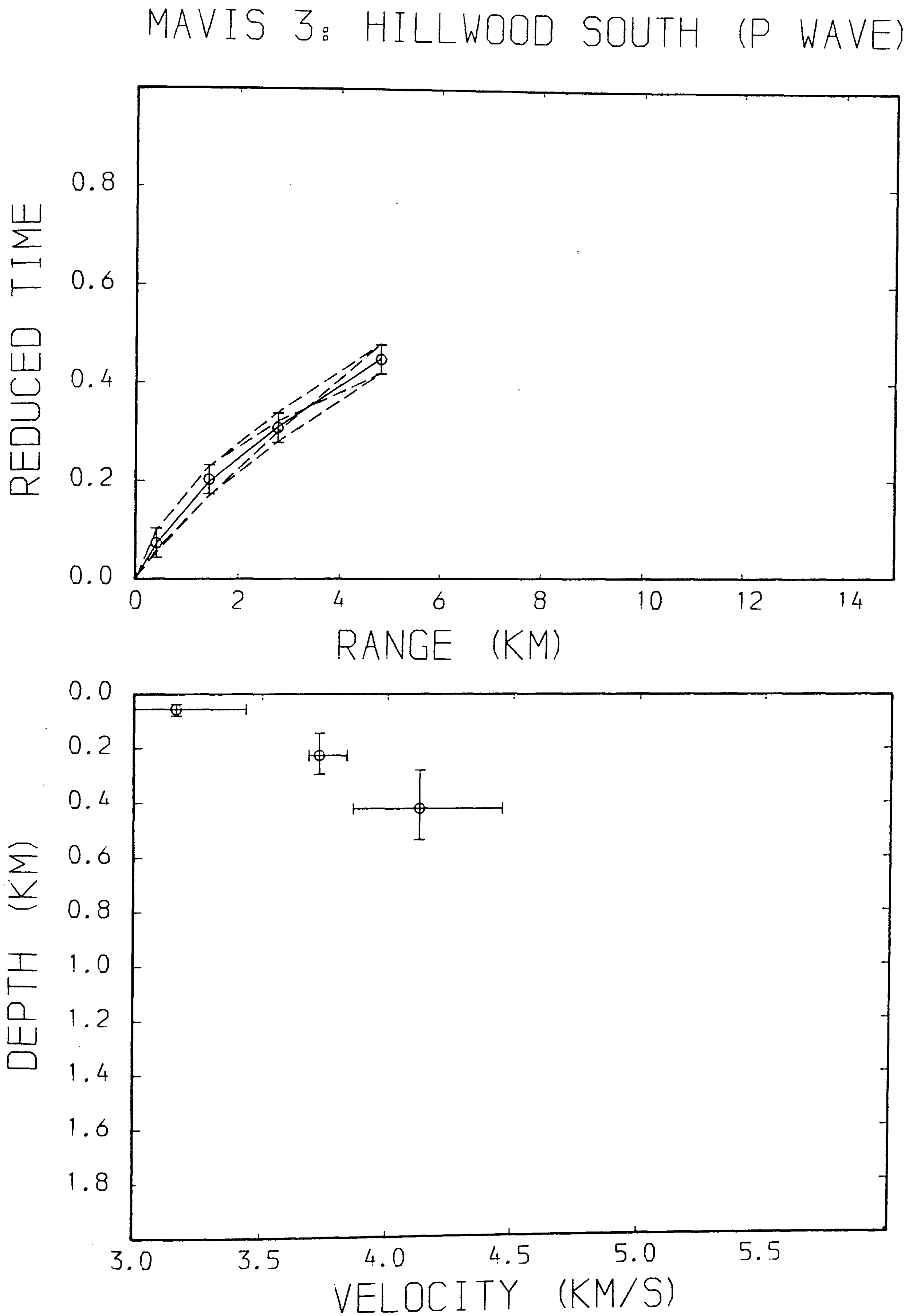

Fig.4.47 Time-distance and velocity-depth data from WHB inversion; Hillwood shot (south). Reduction velocity is 6.0 km/s.

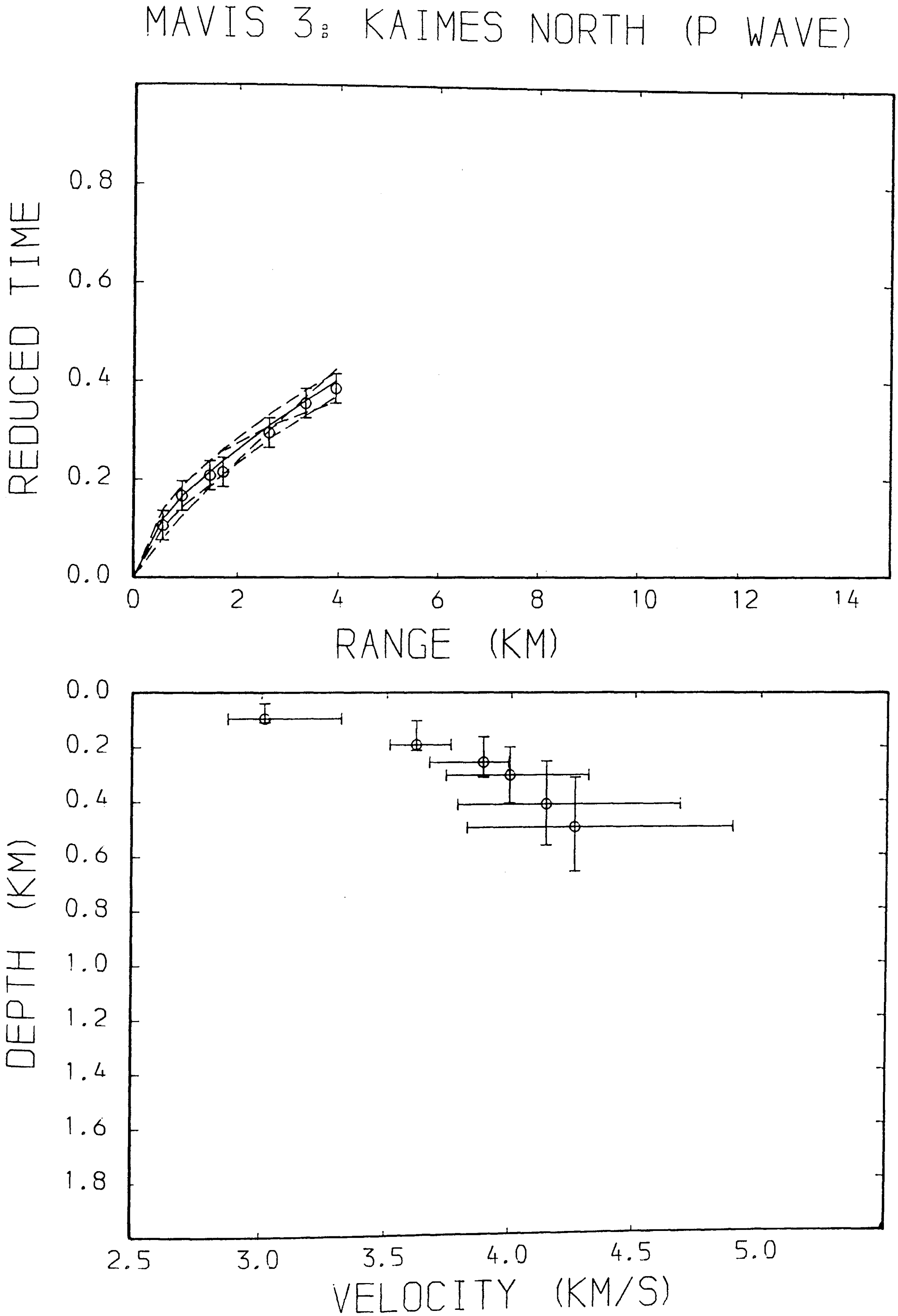

Fig.4.48 Time-distance and velocity-depth data from WHB inversion; Kaimes shot (north). Reduction velocity is 6.0 km/s.

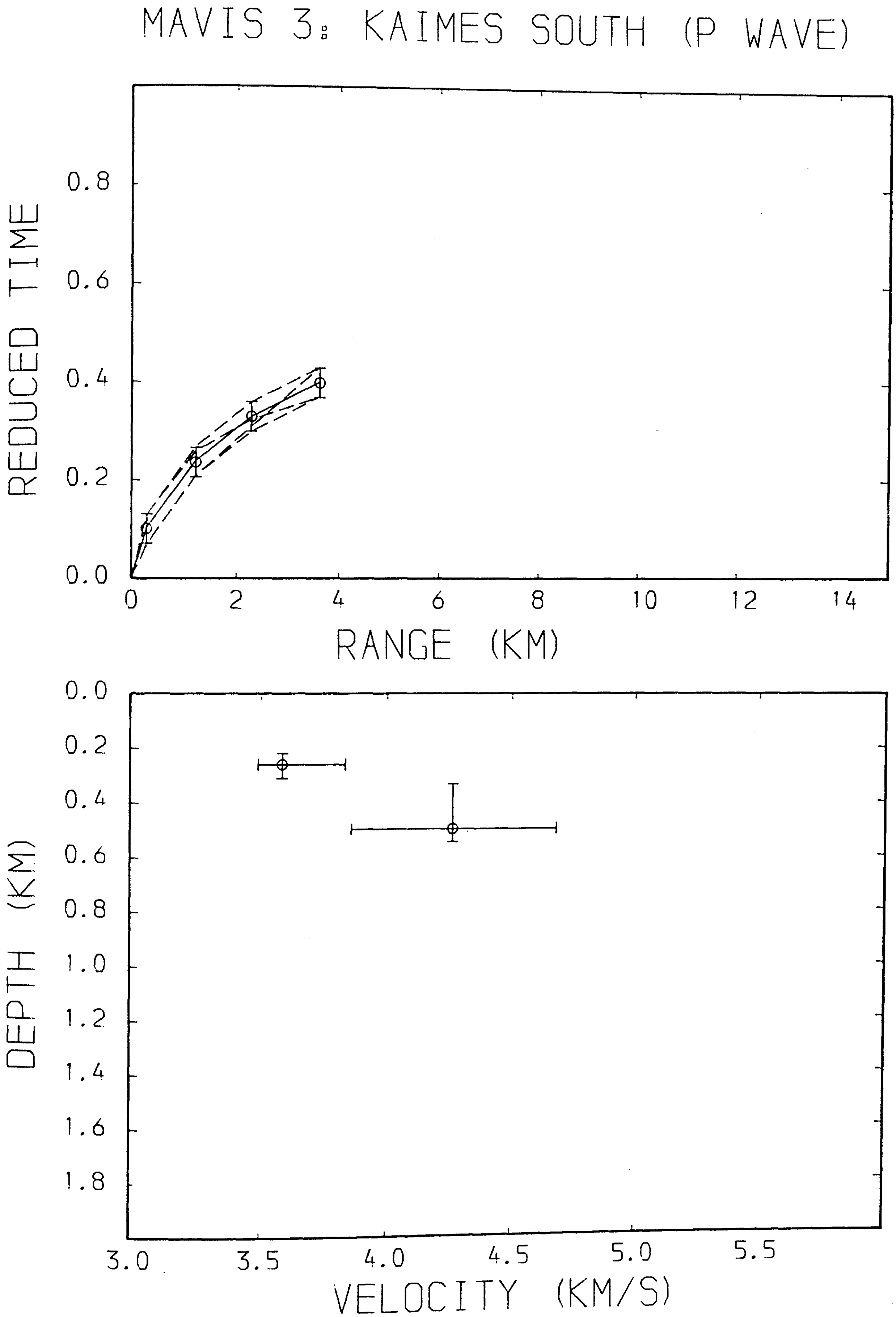

Fig.4.49 Time-distance and velocity-depth data from WHB inversion; Kaimes shot (south). Reduction velocity is 6.0 km/s.

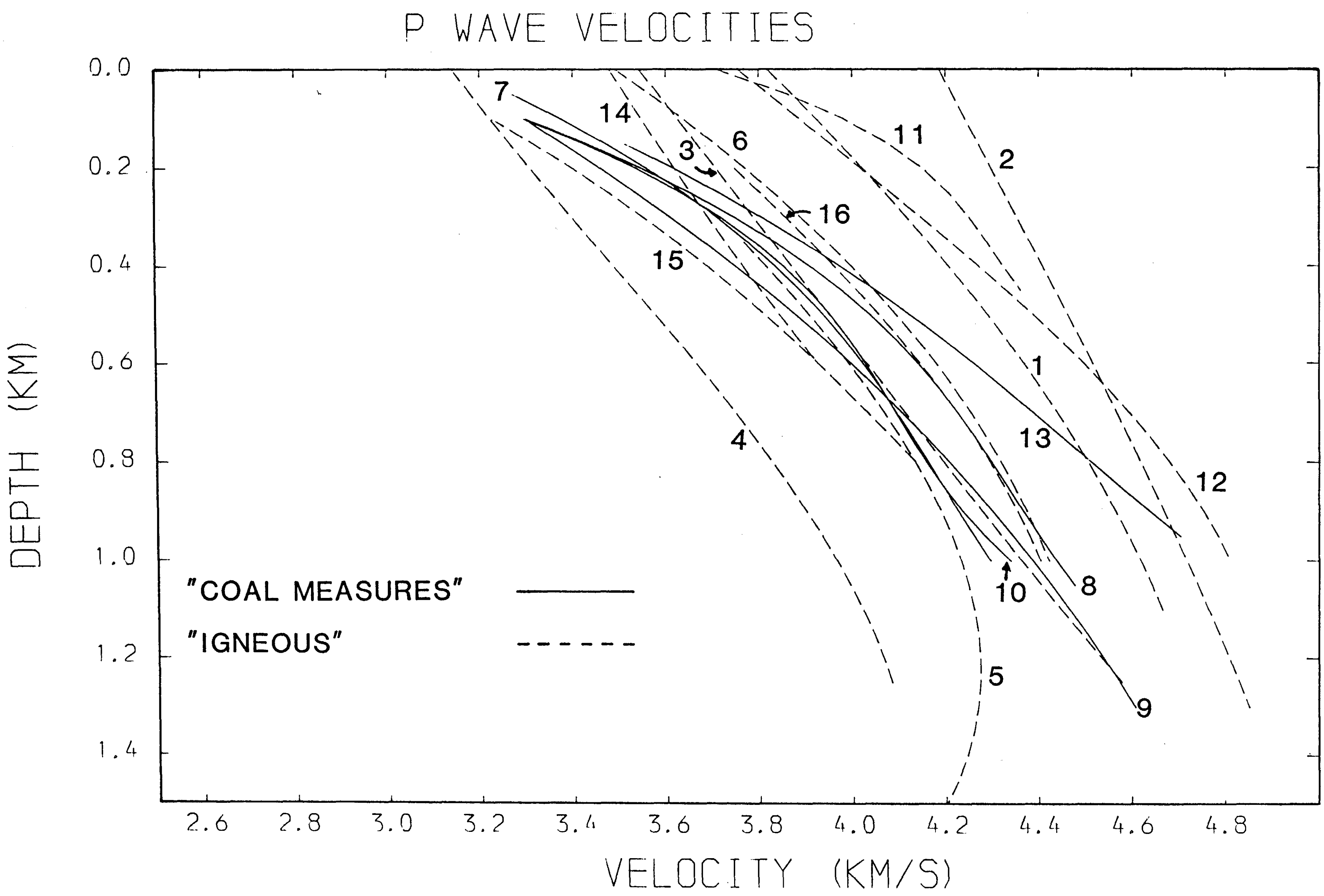

Fig.4.50 P-wave velocity-depth data from WHB inversion using shot pairs listed in Table 4.1. Numbers refer to pairs listed in the Table 4.1.

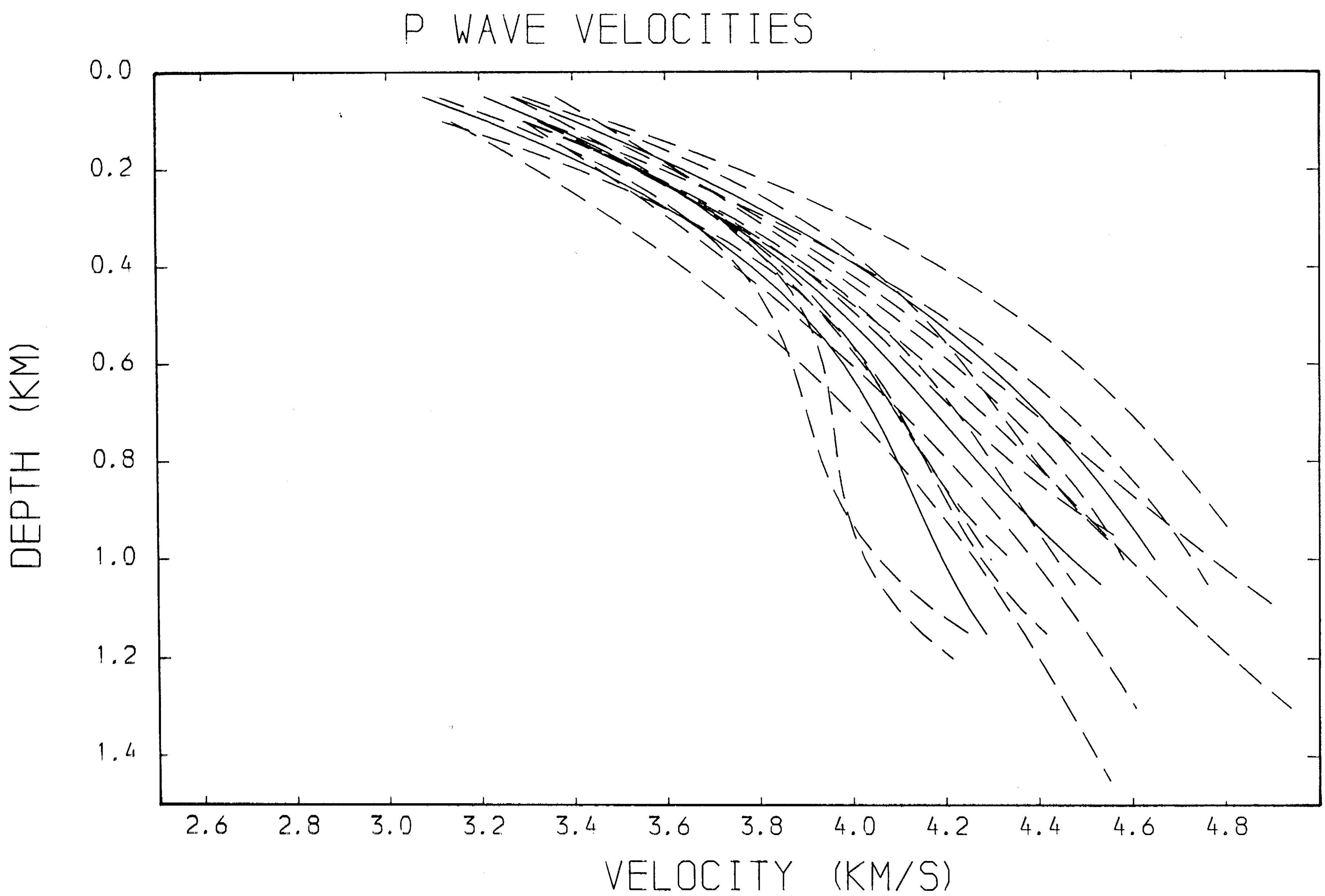

Fig.4.51 P-wave velocity-depth data from WHB inversion using shot pairs 7, 8, 9, 10, 13 (dashed lines). Best-fit lines are shown solid, numbers refer to Table 4.1.

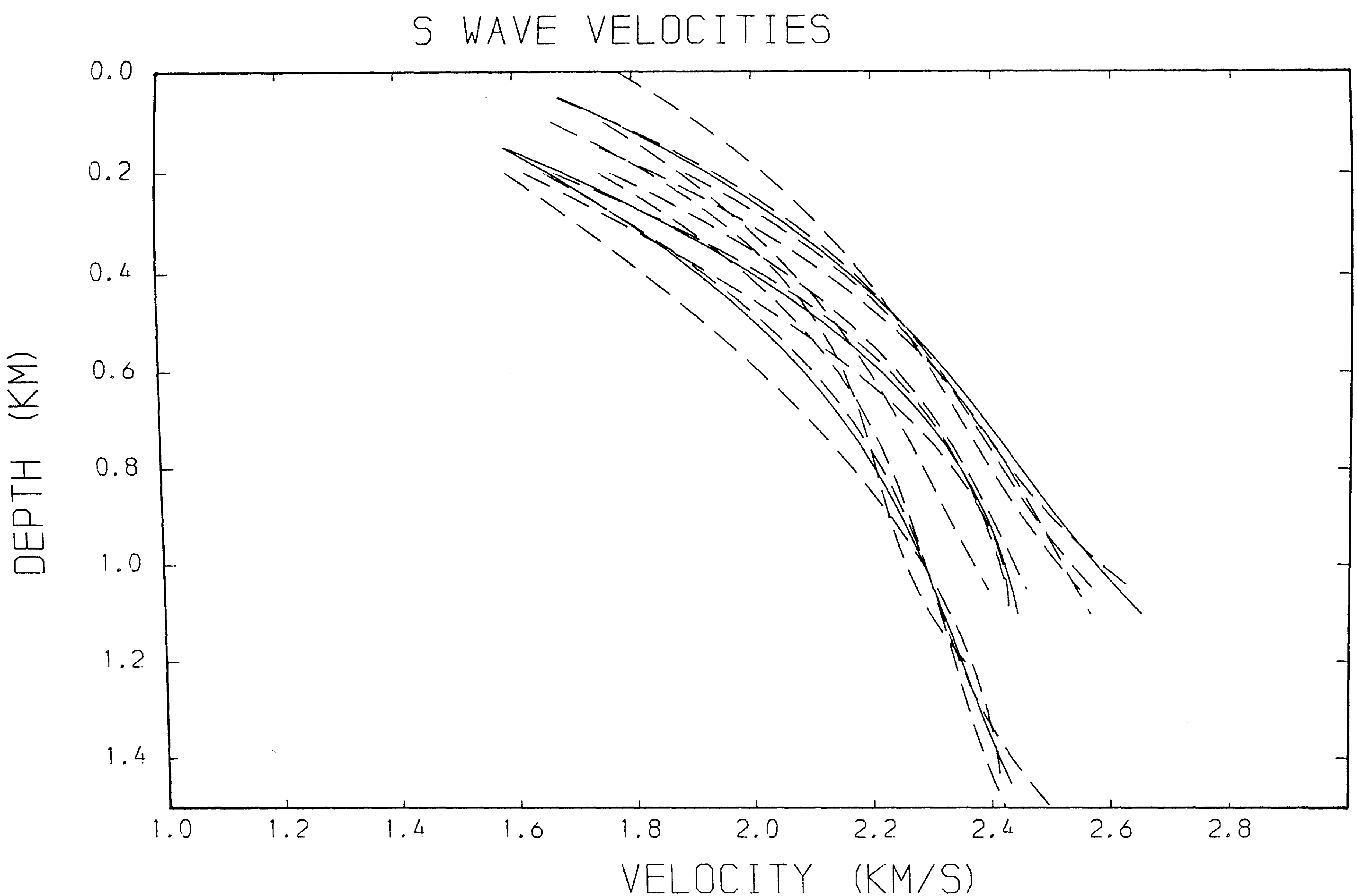

Fig.4.52 S-wave velocity-depth data from WHB inversion using shot pairs 7, 8, 9 (dashed lines). Best-fit lines are shown solid, numbers refer to Table 4.1.

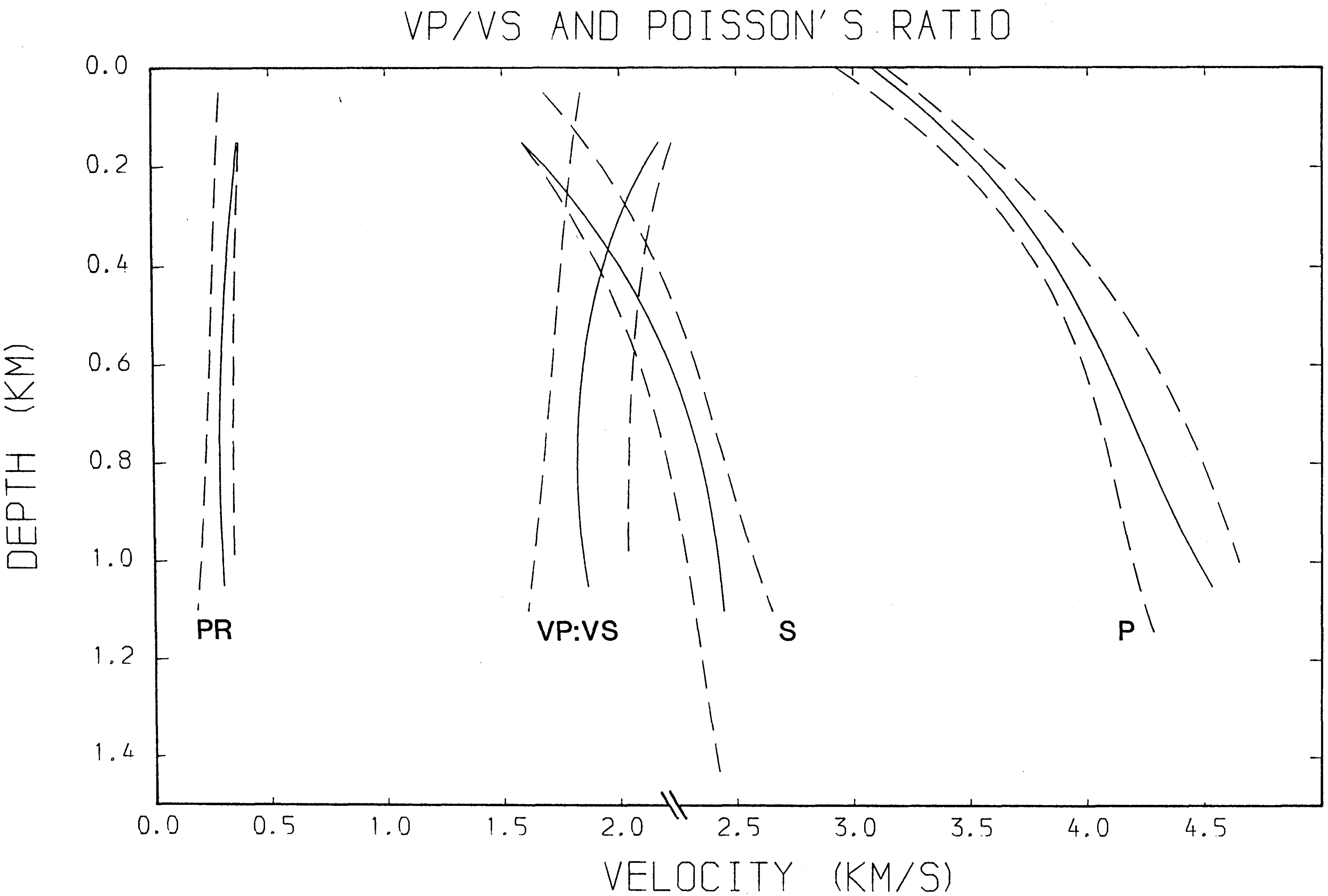

Fig.4.53 Vp:Vs and Poisson's ratio (PR) from the best-fit data of Fig.4.51 and 4.52.

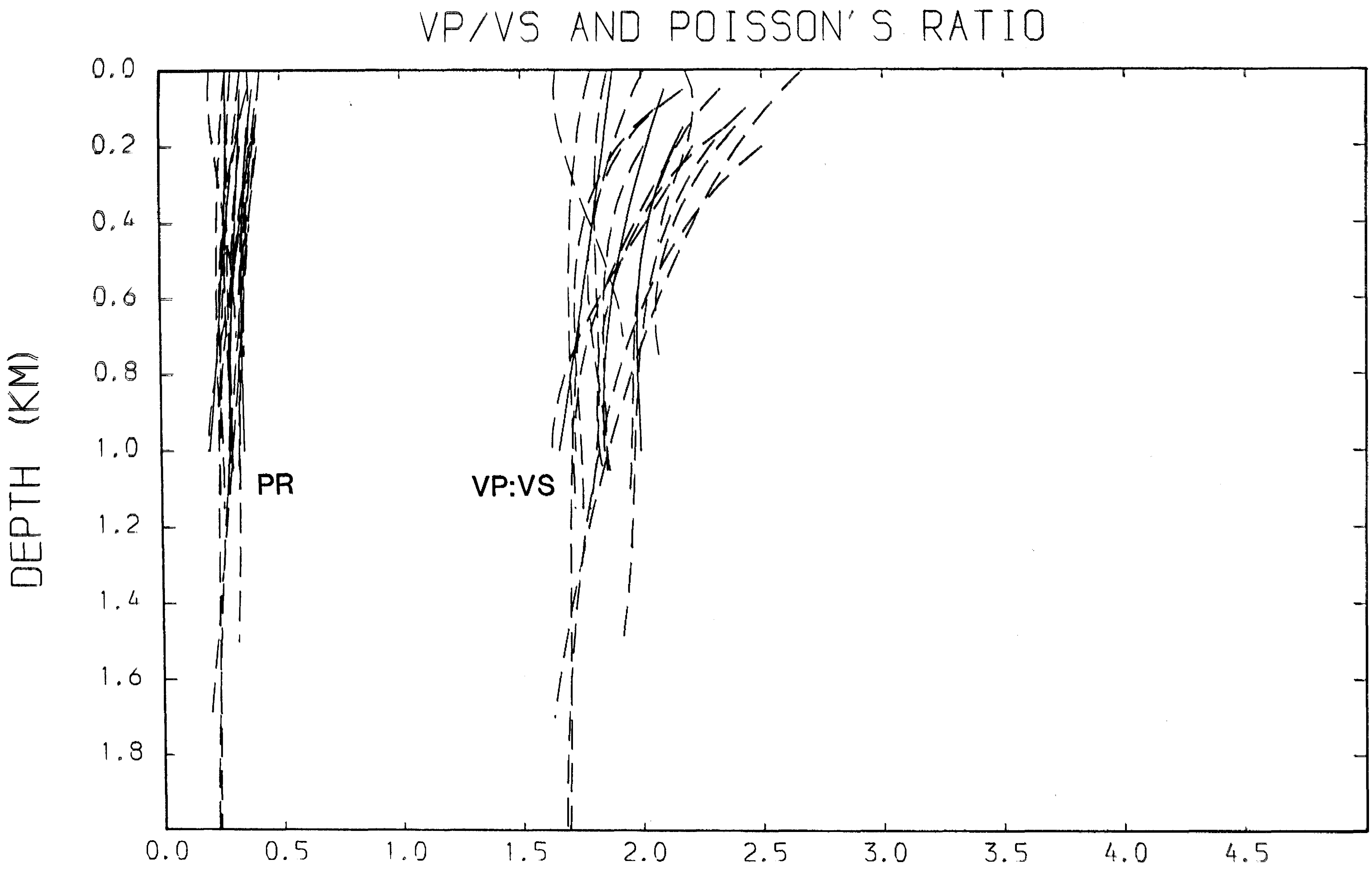

Fig.4.54 Vp:Vs and Poisson's ratio from all available data (dashed lines). Best-fit lines shown solid.

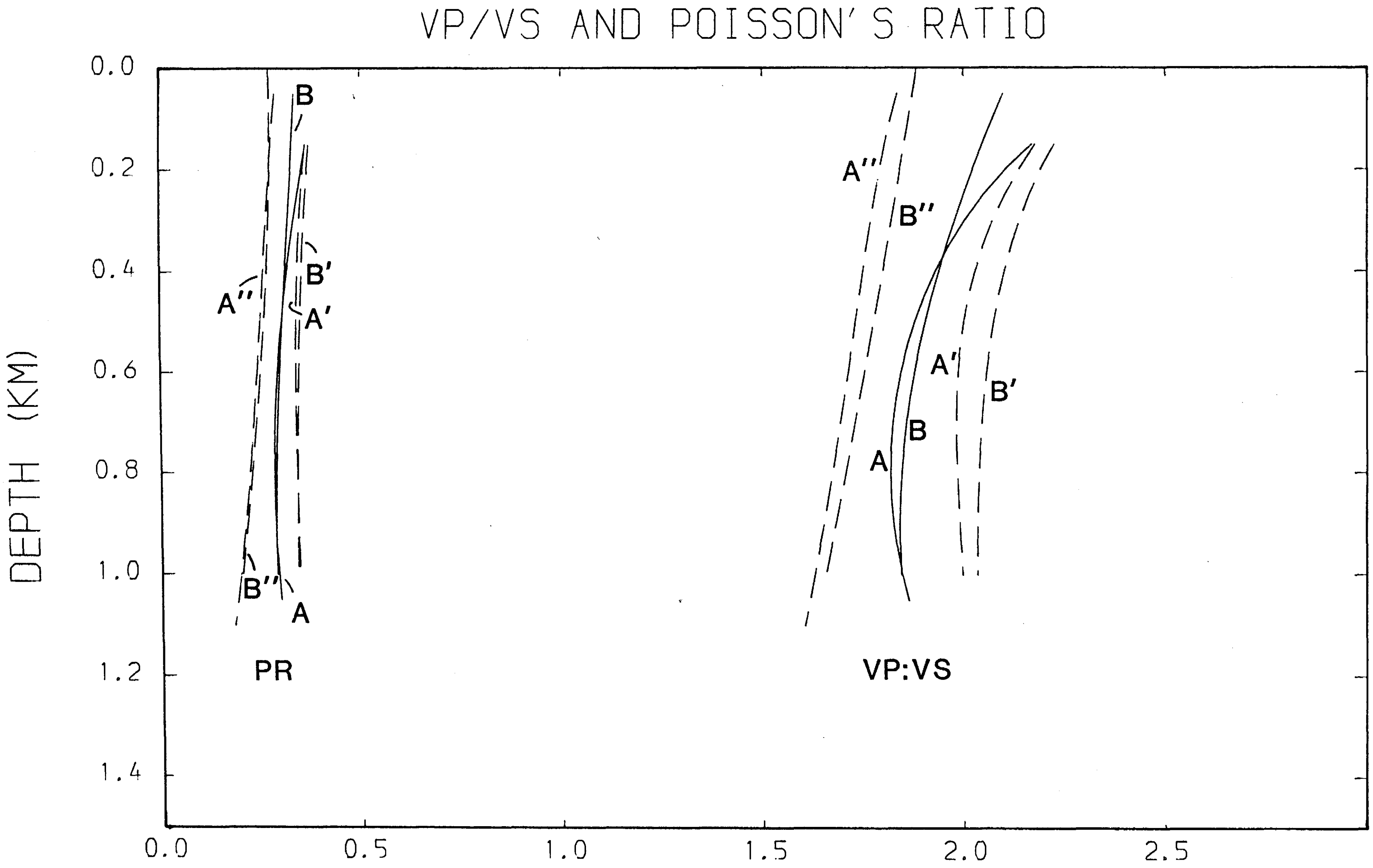

Fig.4.55 Vp:Vs and Poisson's ratio. A, A' and A'' are best-fit and confidence limit curves from Fig.4.53. B, B' and B'' are best-fit and confidence limit curves from Fig.4.54.

A)

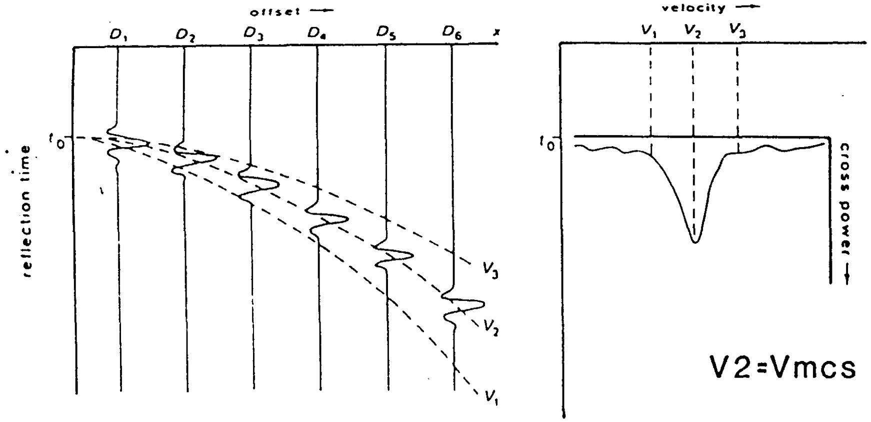

B)

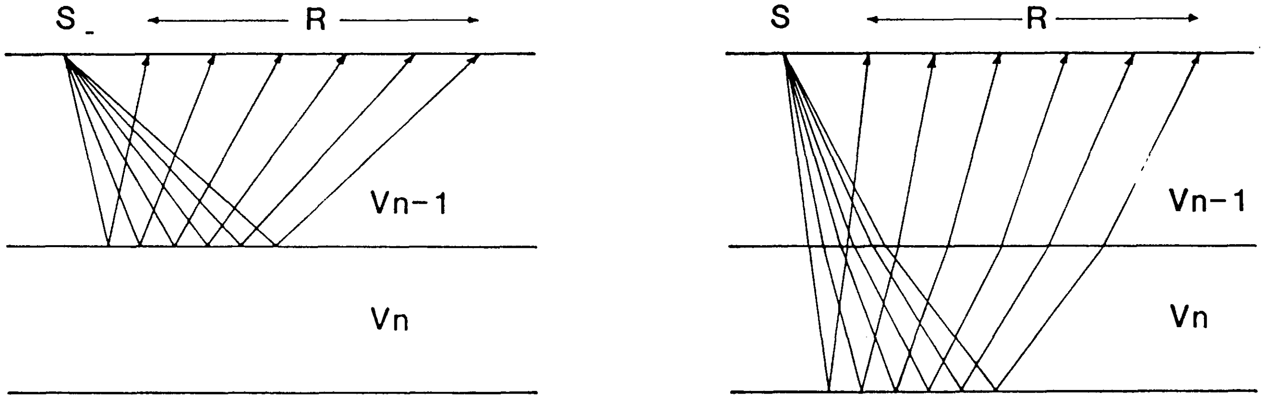

ASSUME Vmcs=Vrms =Vactual

$$V_{int}^2 = \frac{V_n^2 . t_n - V_{n-1}^2 . t_{n-1}}{t_n - t_{n-1}}$$

Fig.4.56 Derivation of interval velocities from seismic reflection data. A), reflection events in a CDP gather are corrected for NMO using velocities v1, v2 and v3. v2 is found to produce the maximum coherency between the events (redrawn from Taner & Koehler 1969). B), derivation of interval velocity from two sets of reflections.

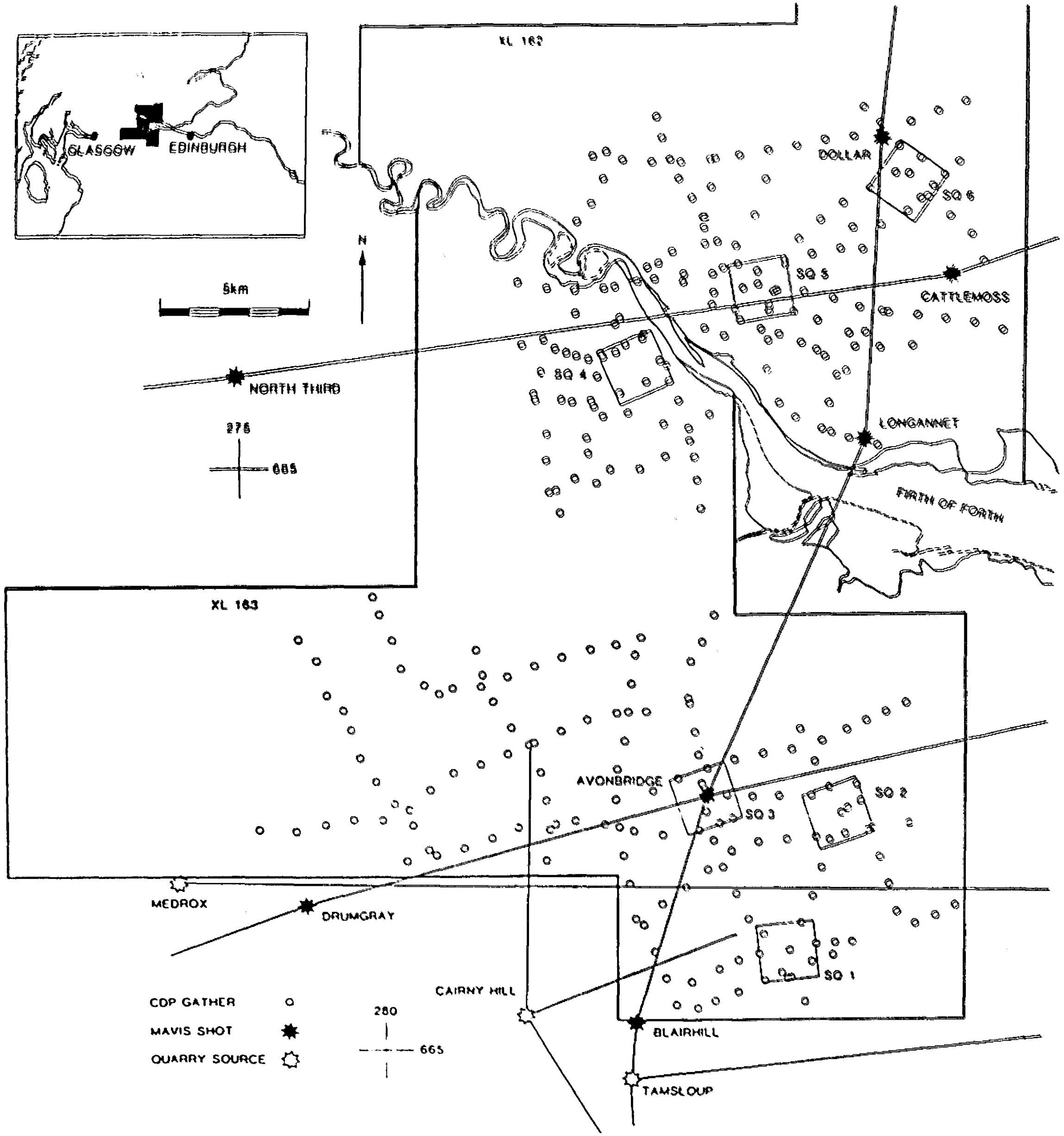

Fig.4.57 Distribution of CDP gathers and areas used in error analysis.

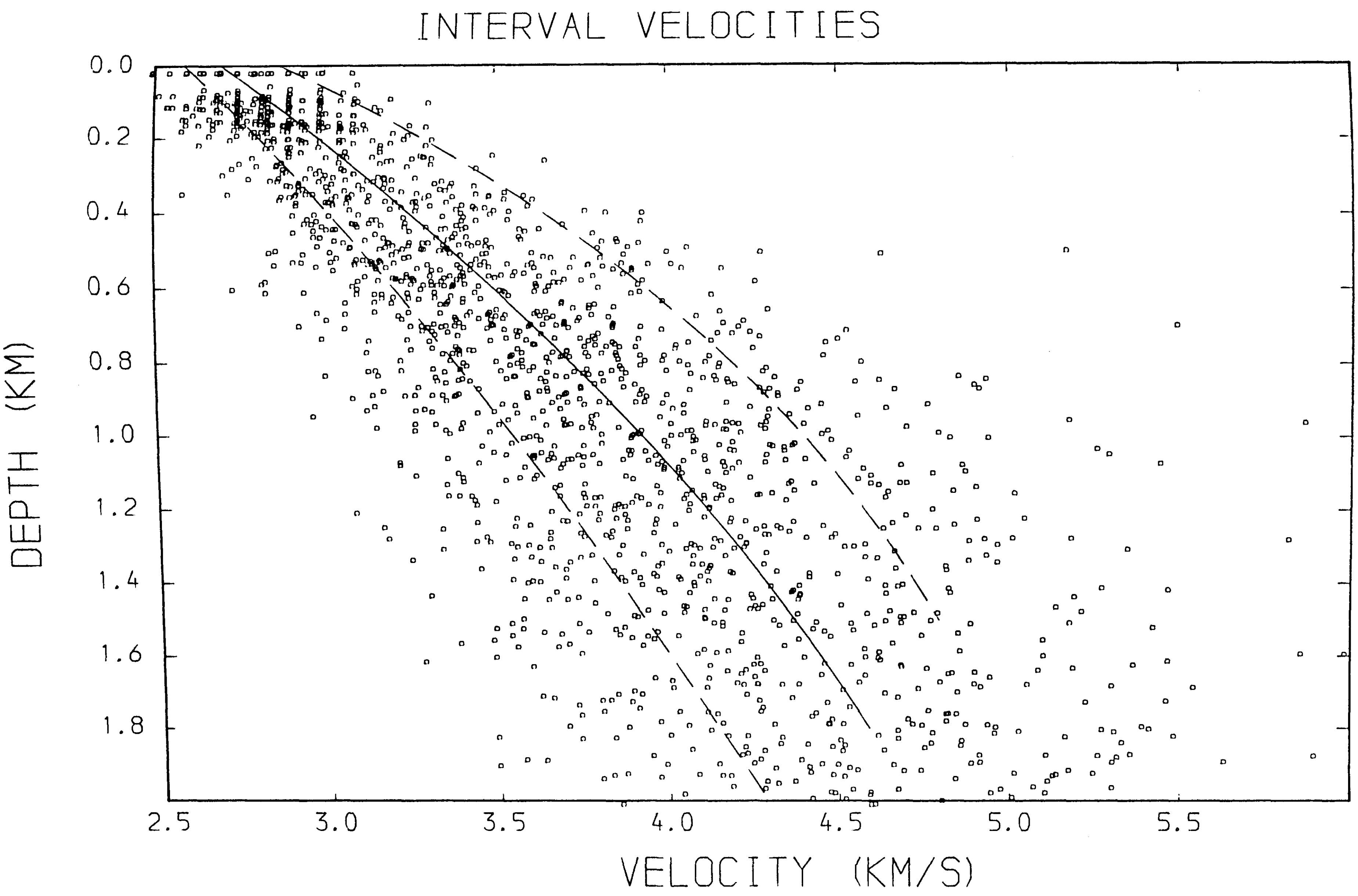

Fig.4.58 Interval velocity versus interval mid-point depth from seismic reflection data with best-fit (solid line) and error (dashed lines) curves.

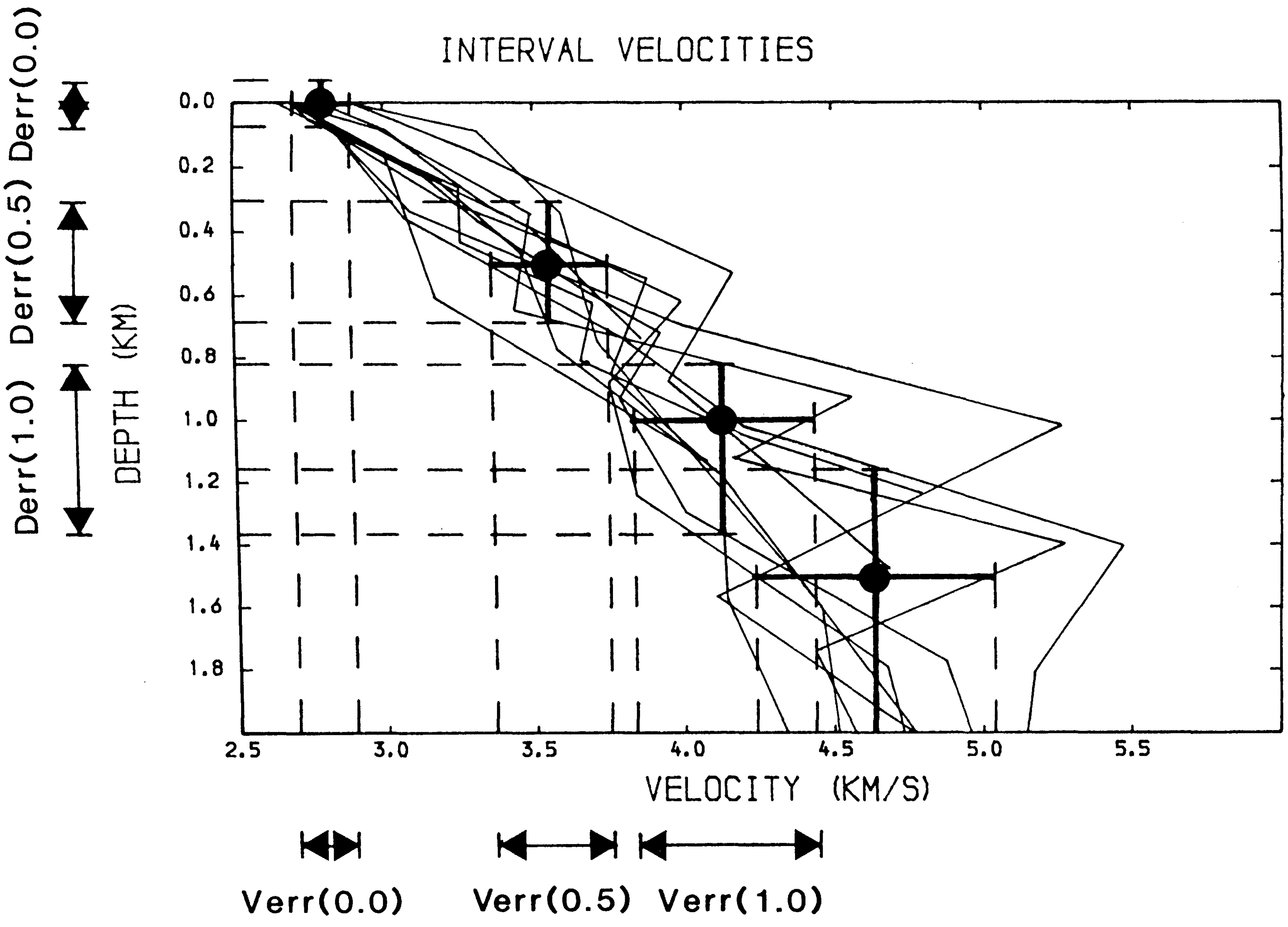

Fig.4.59 Estimation of interval velocity errors from area 2 data (see Fig.4.57).

A)

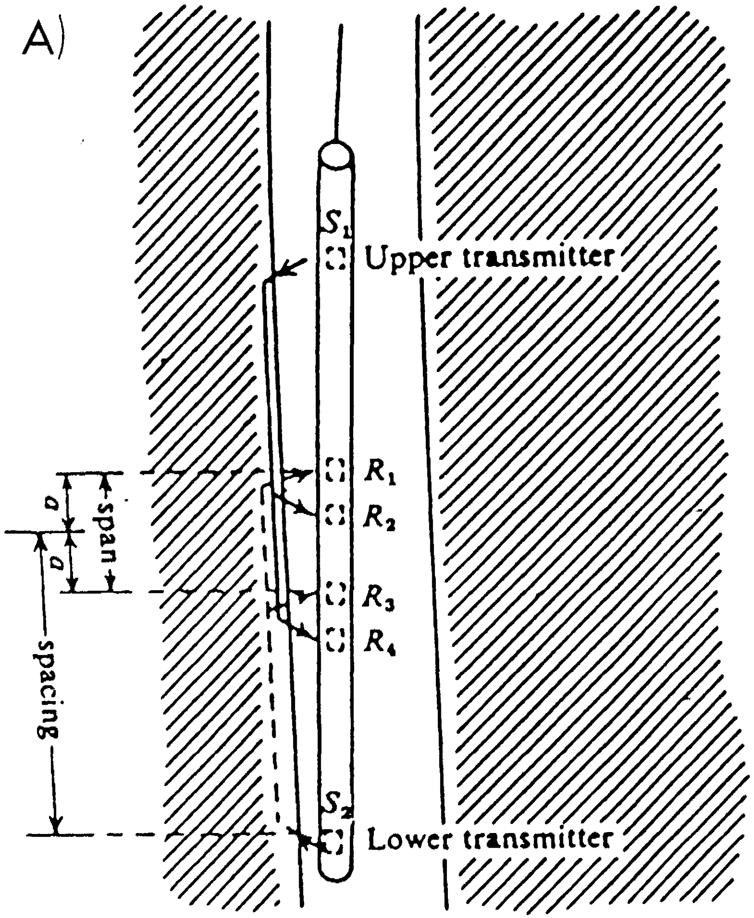

B)

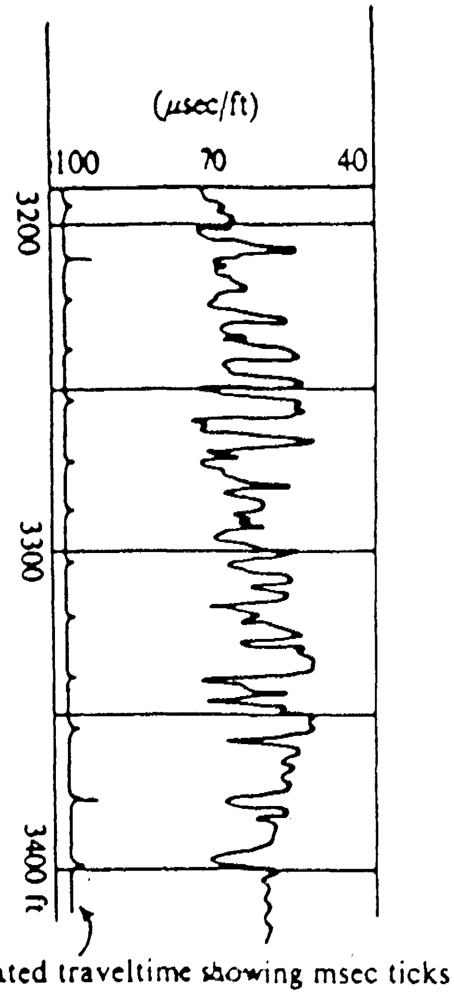

Fig.4.60 A), Borehole compensated logging sonde B), velocity log (after Telford et al. 1976).

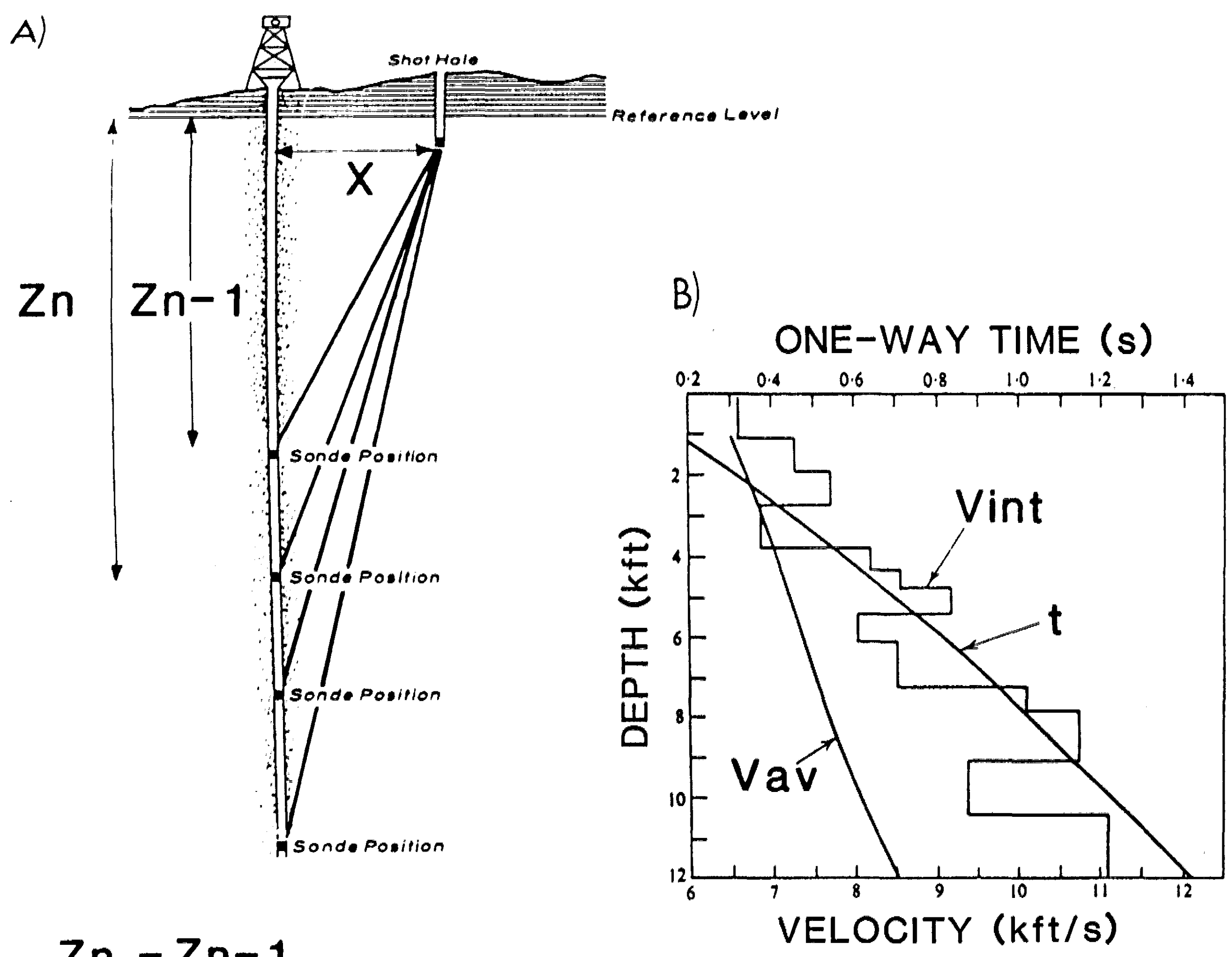

$$Vint = \frac{Zn - Zn-1}{tn - tn-1}$$

t=VERTICAL TIME

Fig.4.61 A), Schematic diagram of well-shooting survey (redrawn from Waters 1978). B), data from well-shooting survey. Vav - average velocity, Vint - interval velocity, t - time (after Telford et al. 1976).

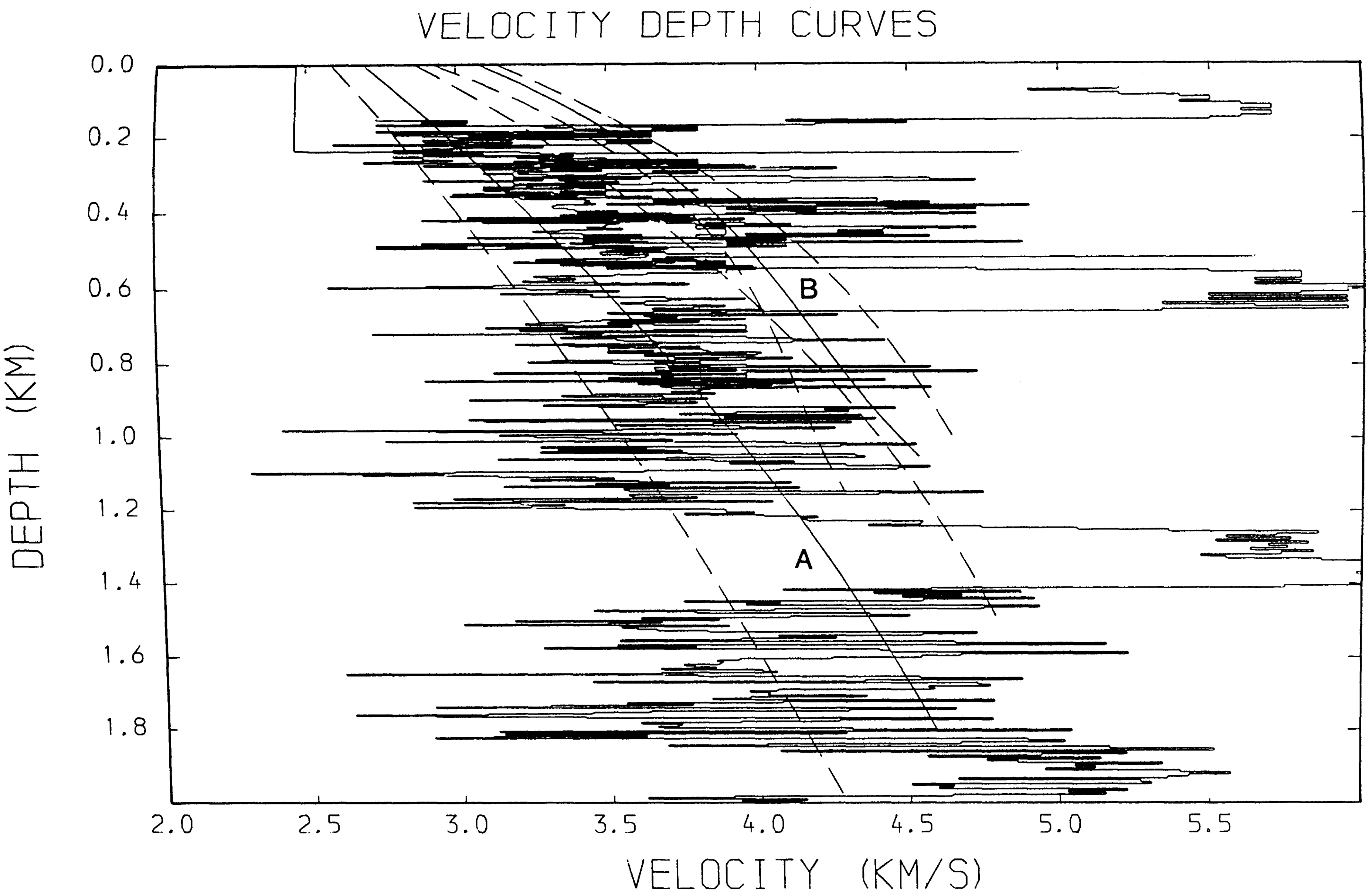

Fig.4.62 Velocity-depth curves from velocity logs. The reflection (A) and refraction (B) derived curves are shown for comparison. Best-fit lines are solid, confidence limited dashed.

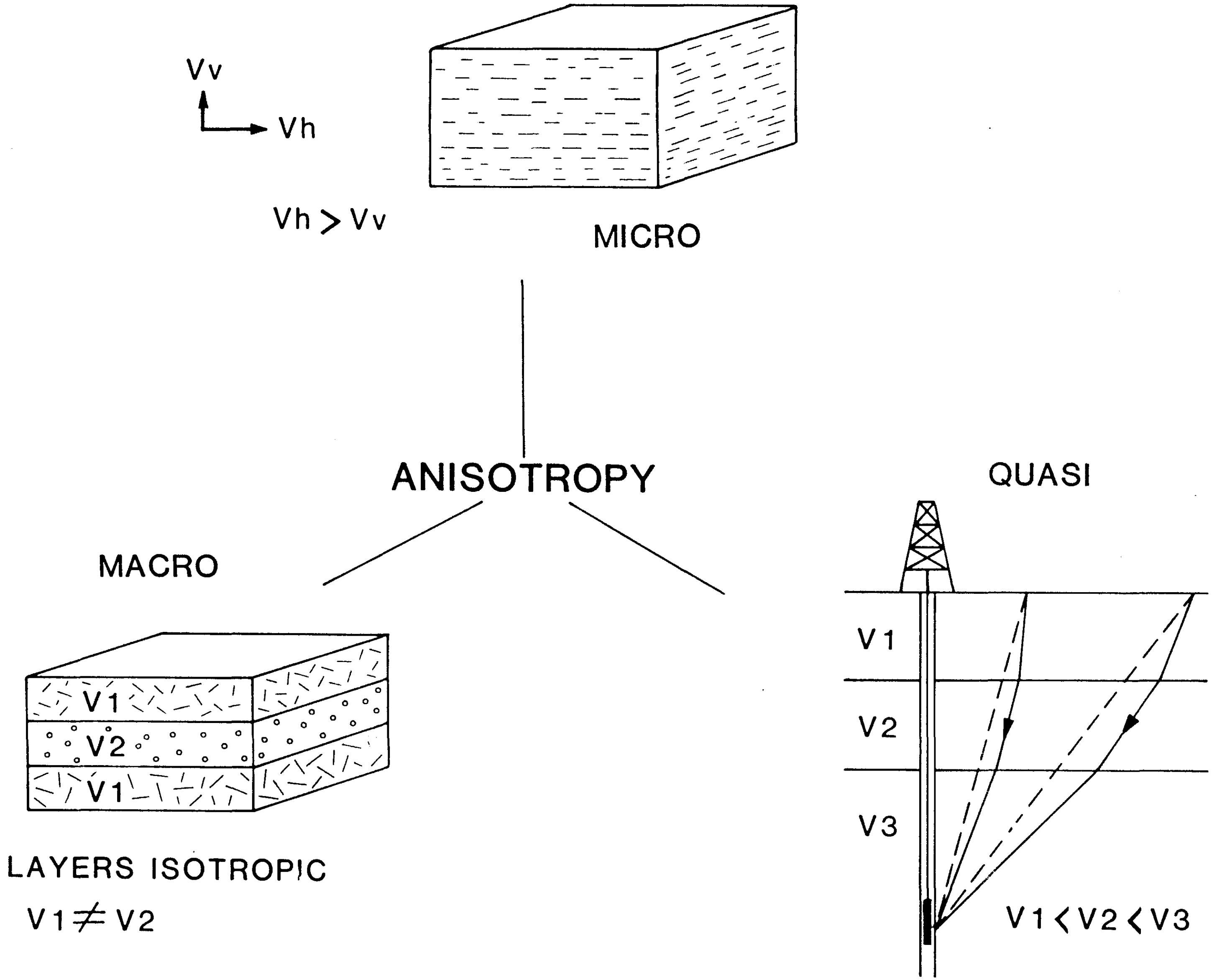

Fig.4.63 Schematic diagram illustrating different types of seismic velocity anisotropy.

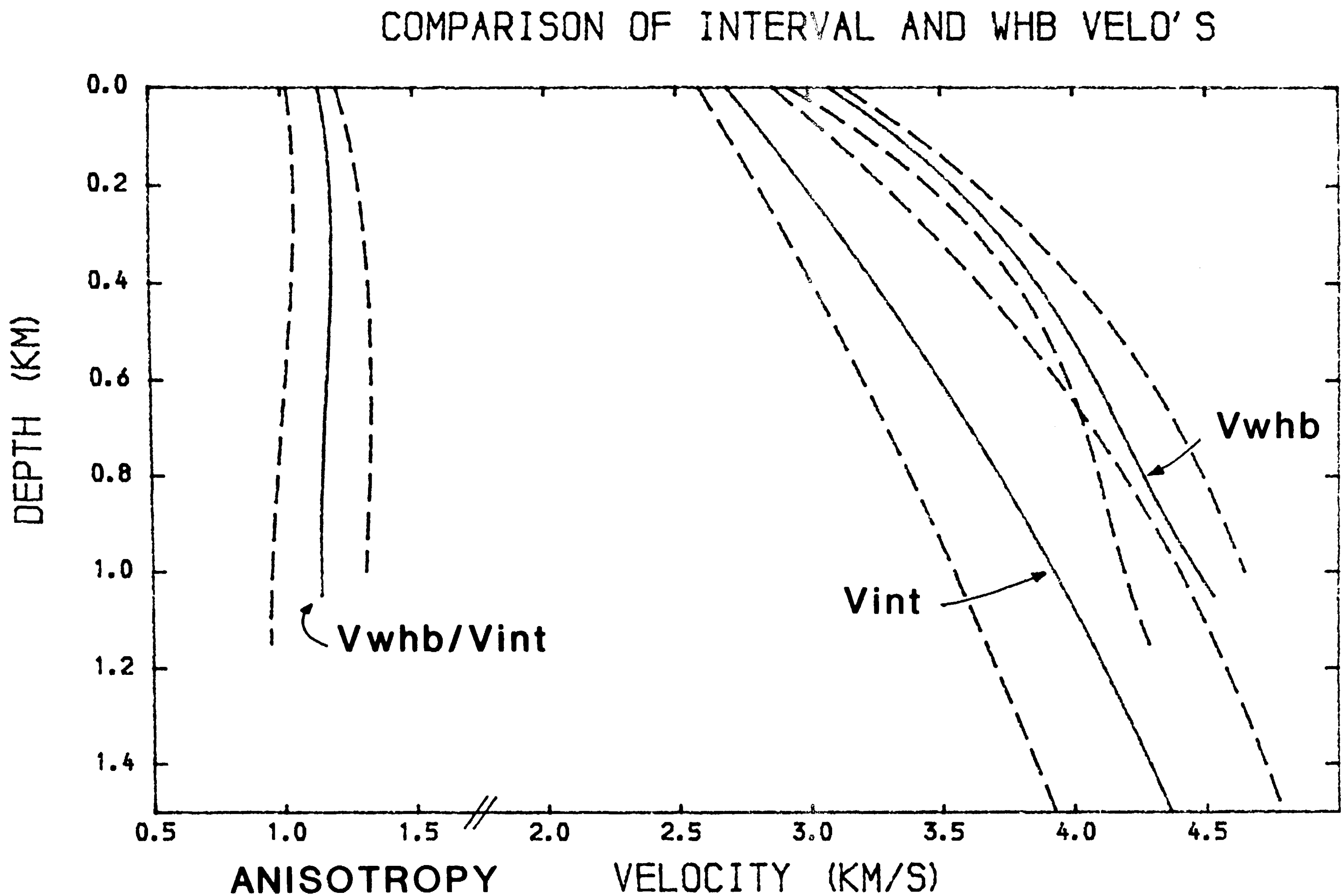

Fig.4.64 Estimation of velocity anisotropy by comparison of reflection (Vint) and refraction (Vwhb) derived velocities. Best-fit data are shown solid, confidence limits dashed.

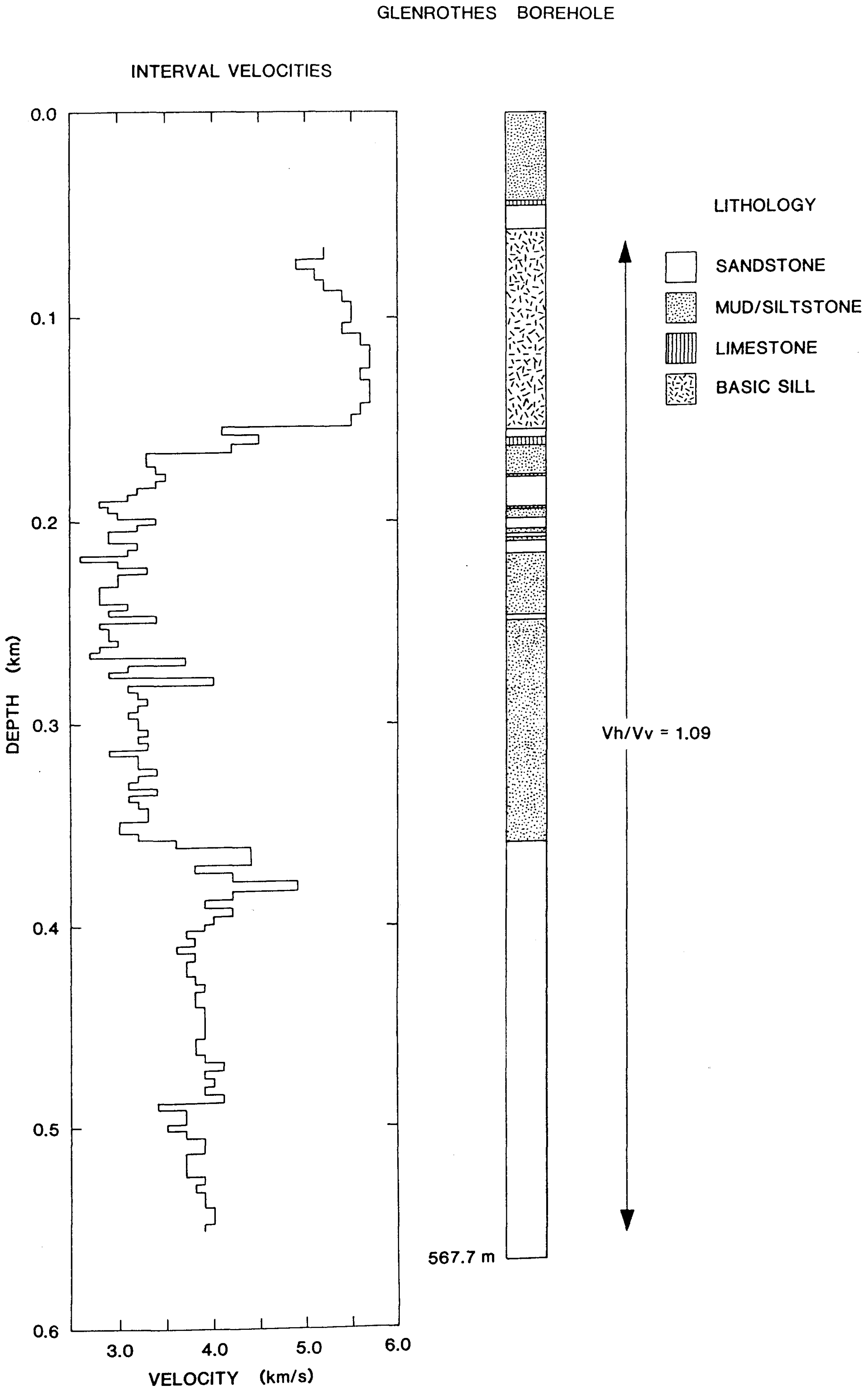

Fig.4.65 Interval velocities, from velocity log, and lithology of the Glenrothes borehole.

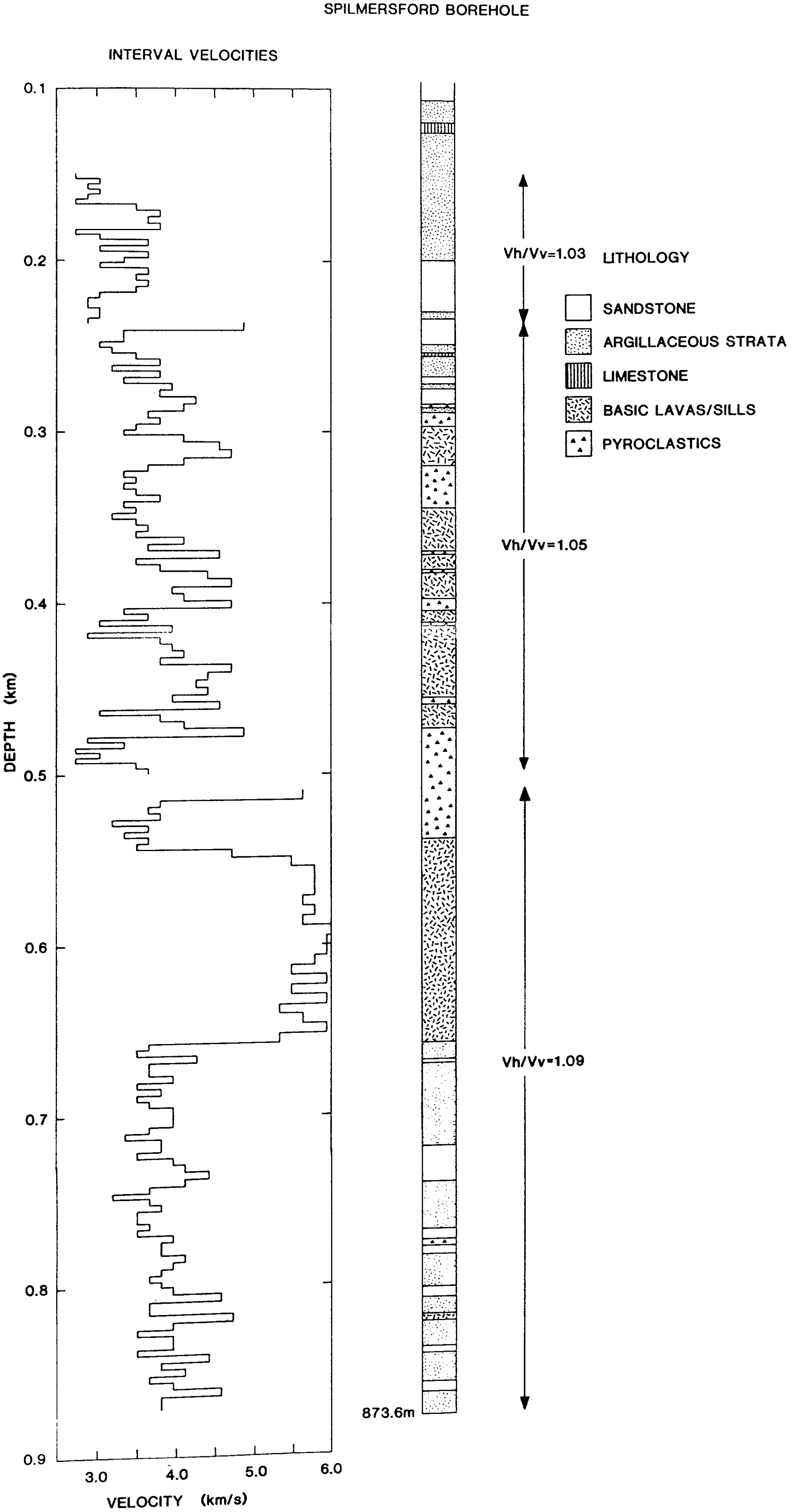

Fig.4.66 Interval velocities, from velocity logs, and lithology of the Spilmersford borehole.

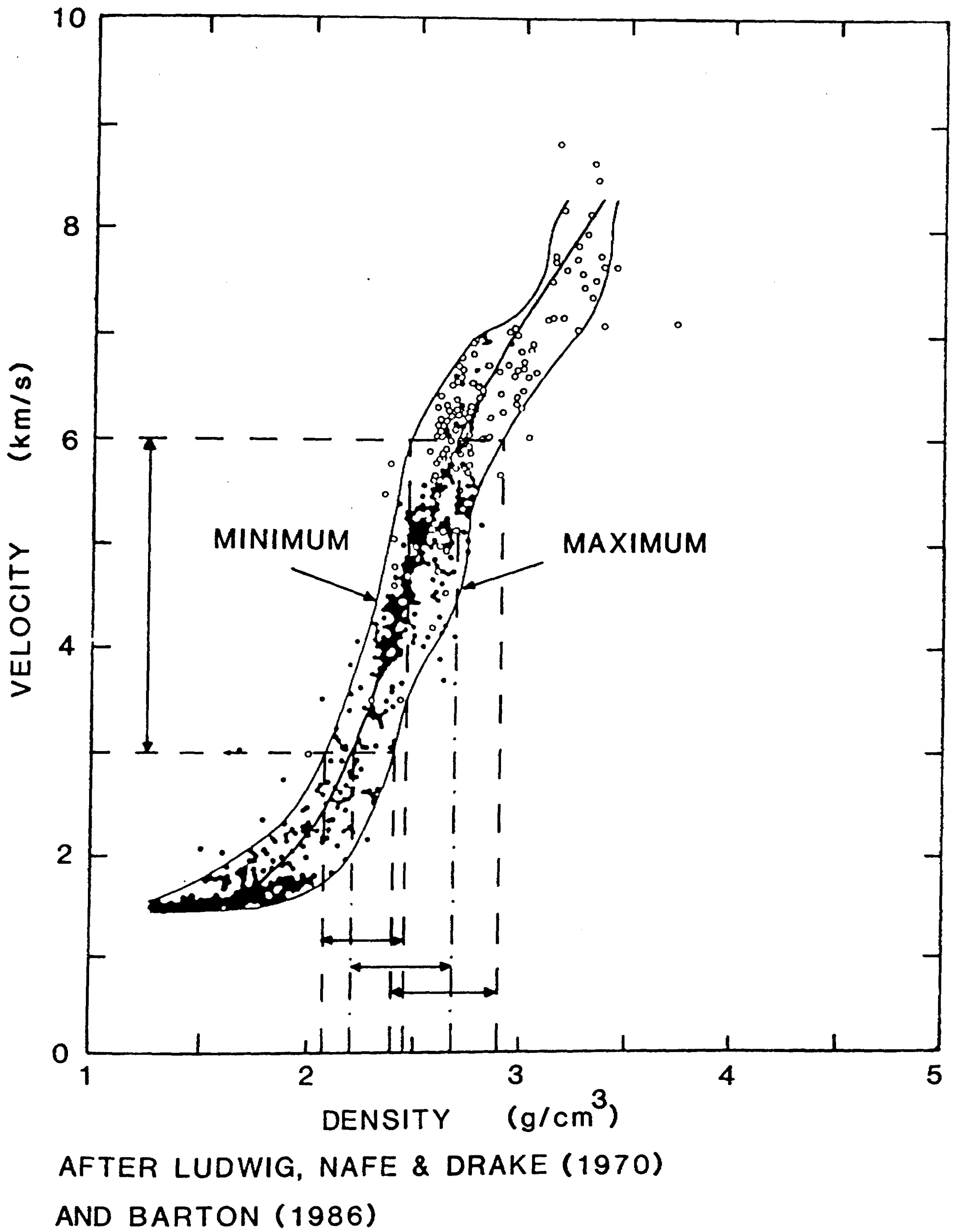

Fig.4.67 Velocity-density plot with best-fit, maximum and minimum density curves. (redrawn from Ludwig, Nafe & Drake 1970, Barton 1986)

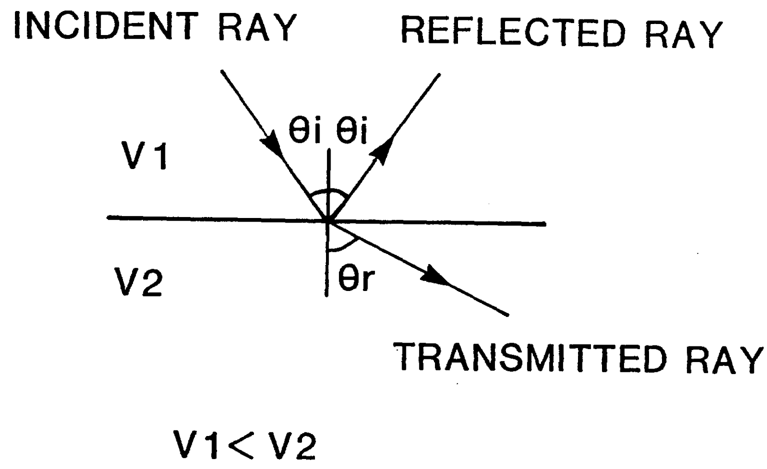

Fig.5.1 Reflected and refracted rays resulting from oblique incidence of a ray on an interface of acoustic impedance contrast.

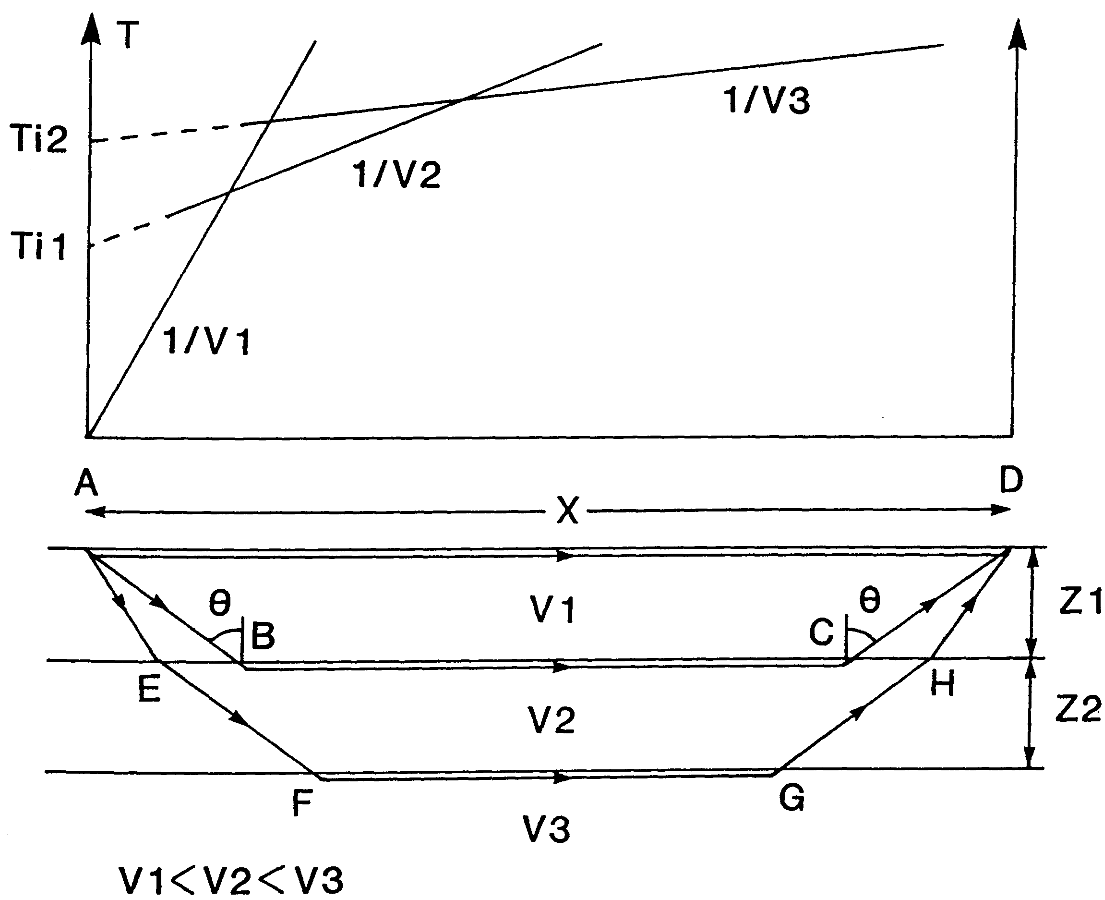

Fig.5.2 Travel-time curves and ray-paths resulting from the critical refraction of rays at interfaces between constant velocity horizontal layers.

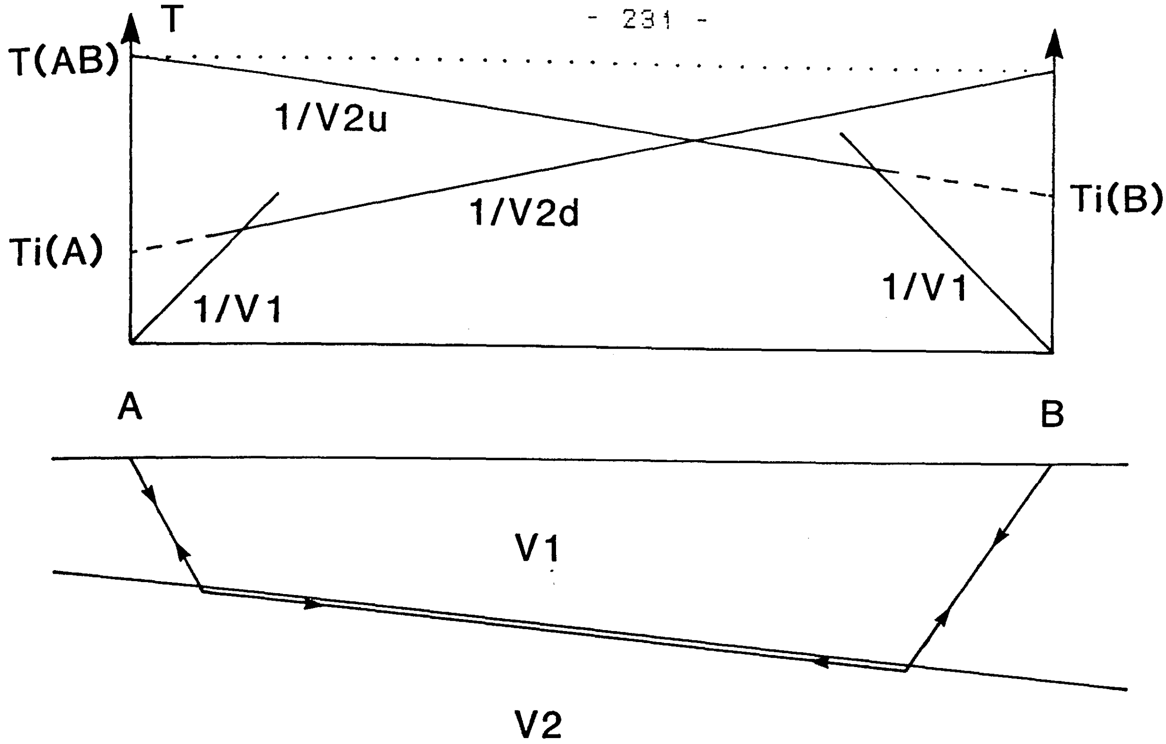

Fig.5.3 Travel-time curves and ray-paths resulting from the critical refraction of rays at a dipping interface between constant velociy layers.

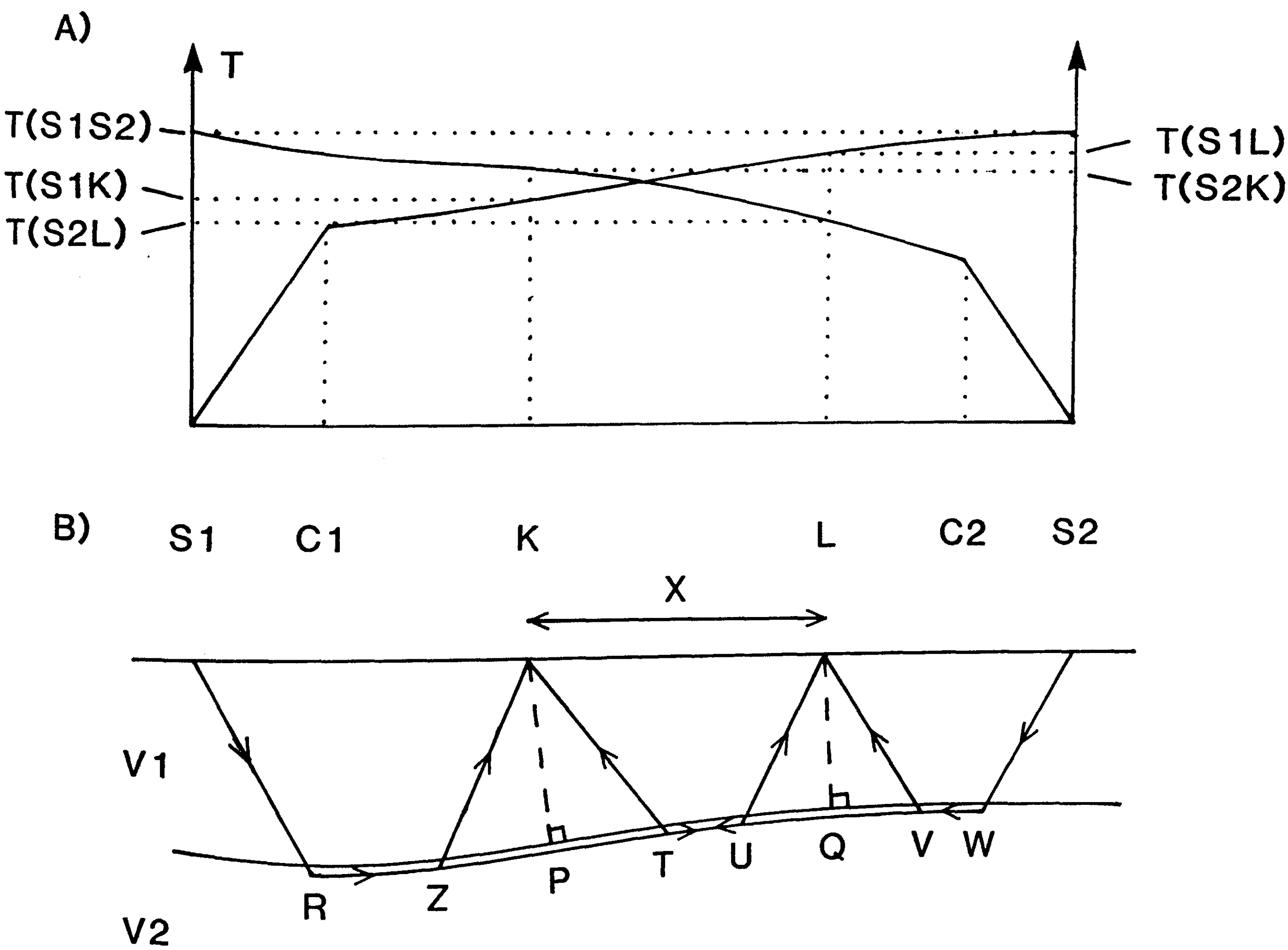

Fig.5.4 The plus-minus method of refraction interpretation; A), travel-time curves B), ray-paths from end shots (S1, S2) to intermediate receivers (K, L).

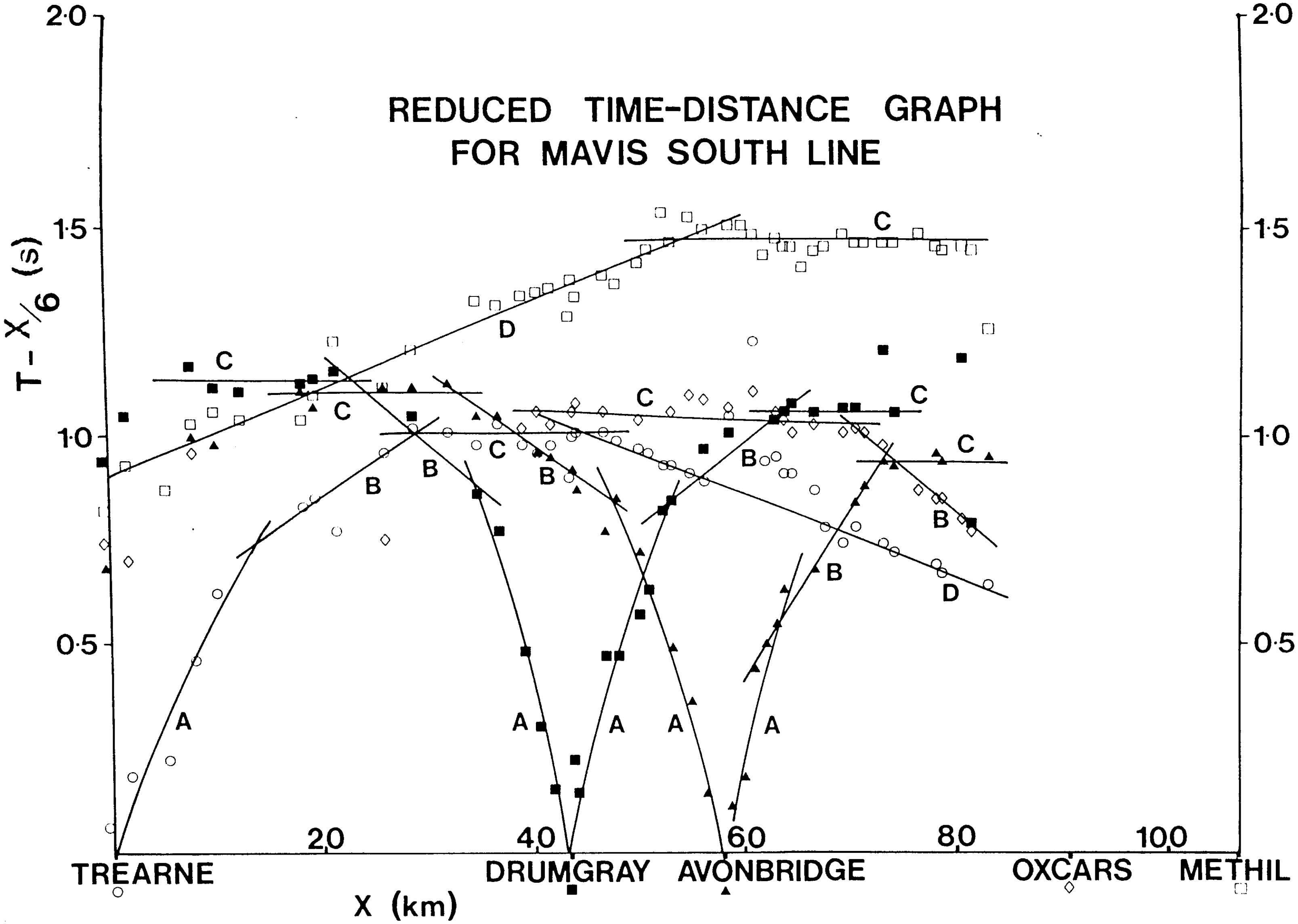

Fig.5.5 Reduced time-distance graph for the MAVIS I south line. Branches A to D correspond to the four layers used in the plus-minus interpretation.

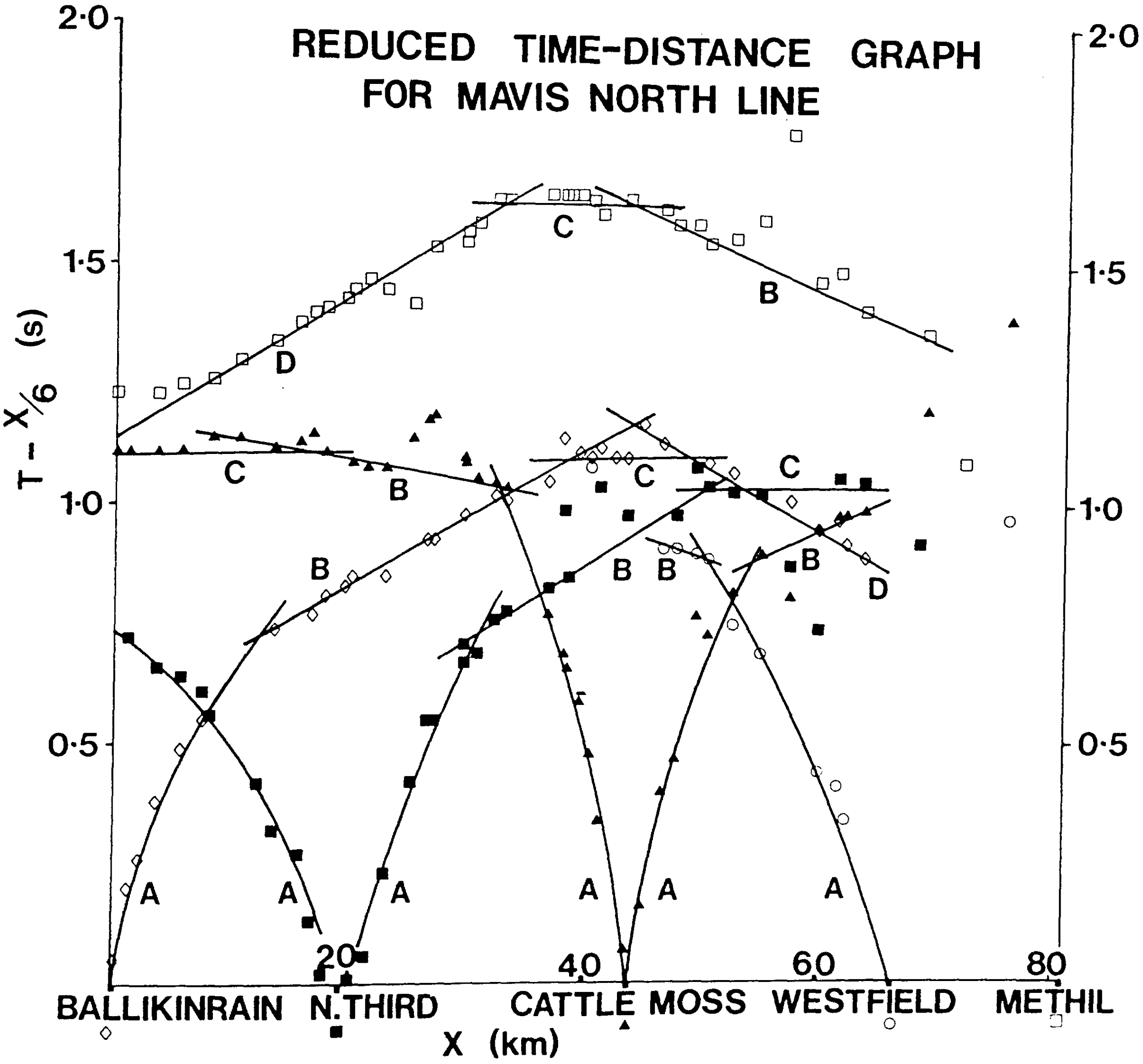

Fig.5.6 Reduced time-distance graph for the MAVIS I north line. Branches A to D correspond to the four layers used in the plus-minus interpretation.

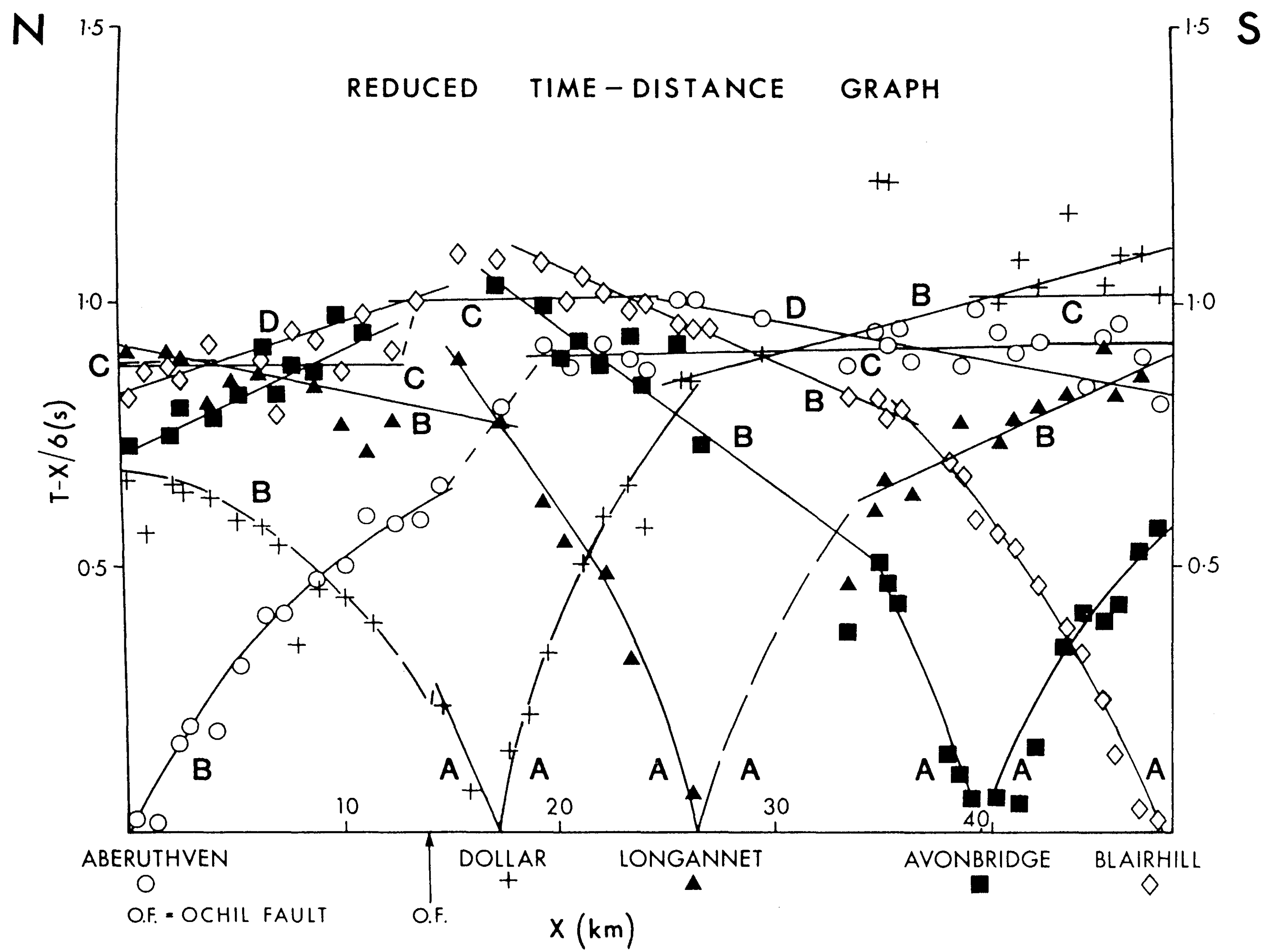

Fig.5.7 Reduced time-distance graph for the MAVIS II line. Branches A to D correspond to the four layers used in the delay-time interpretation.

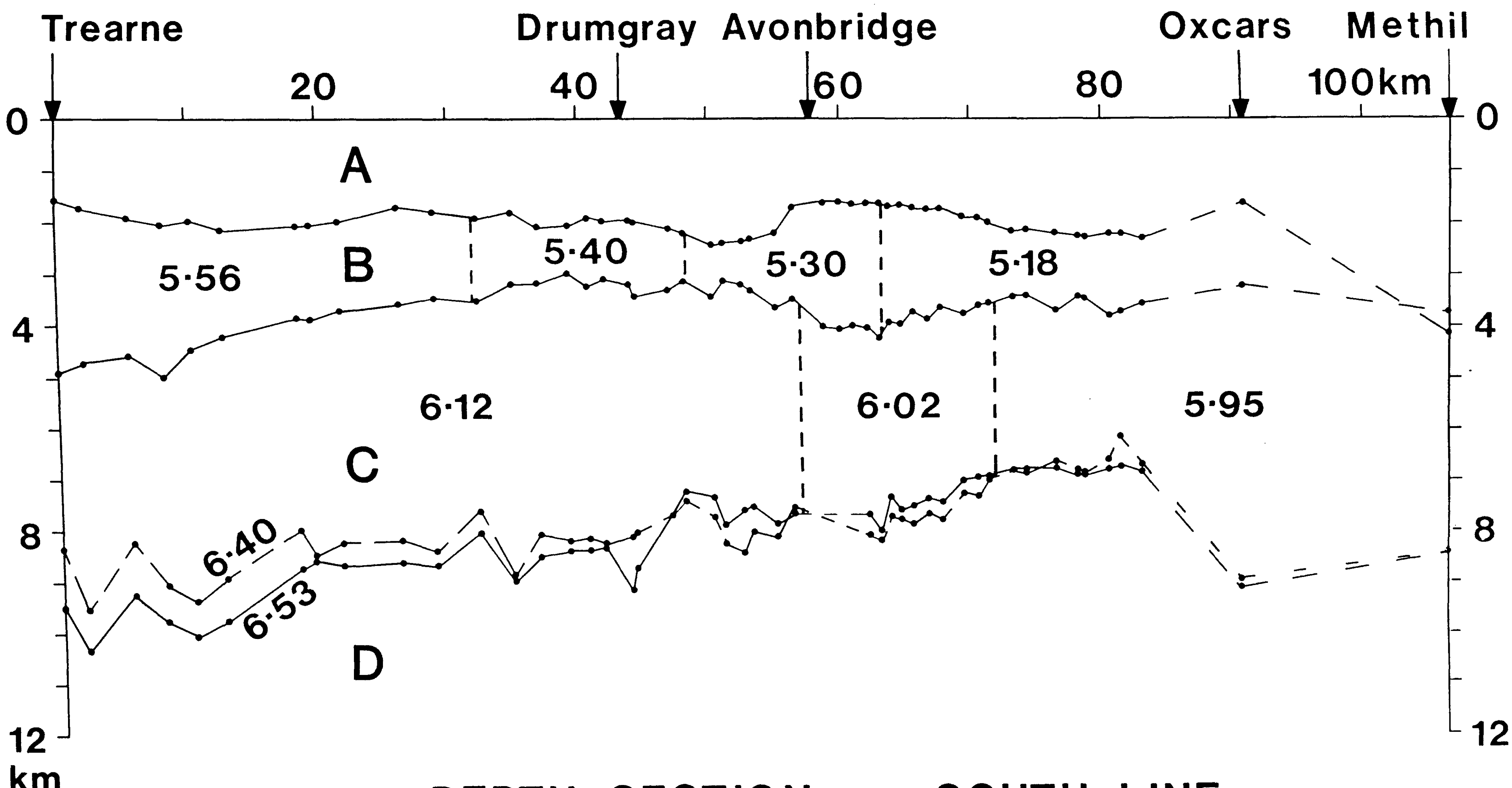

DEPTH SECTION SOUTH LINE

Fig.5.8a Plus-minus interpretation of the MAVIS I south line. Layers A to D correspond to the four time-distance branches in Fig.5.5.

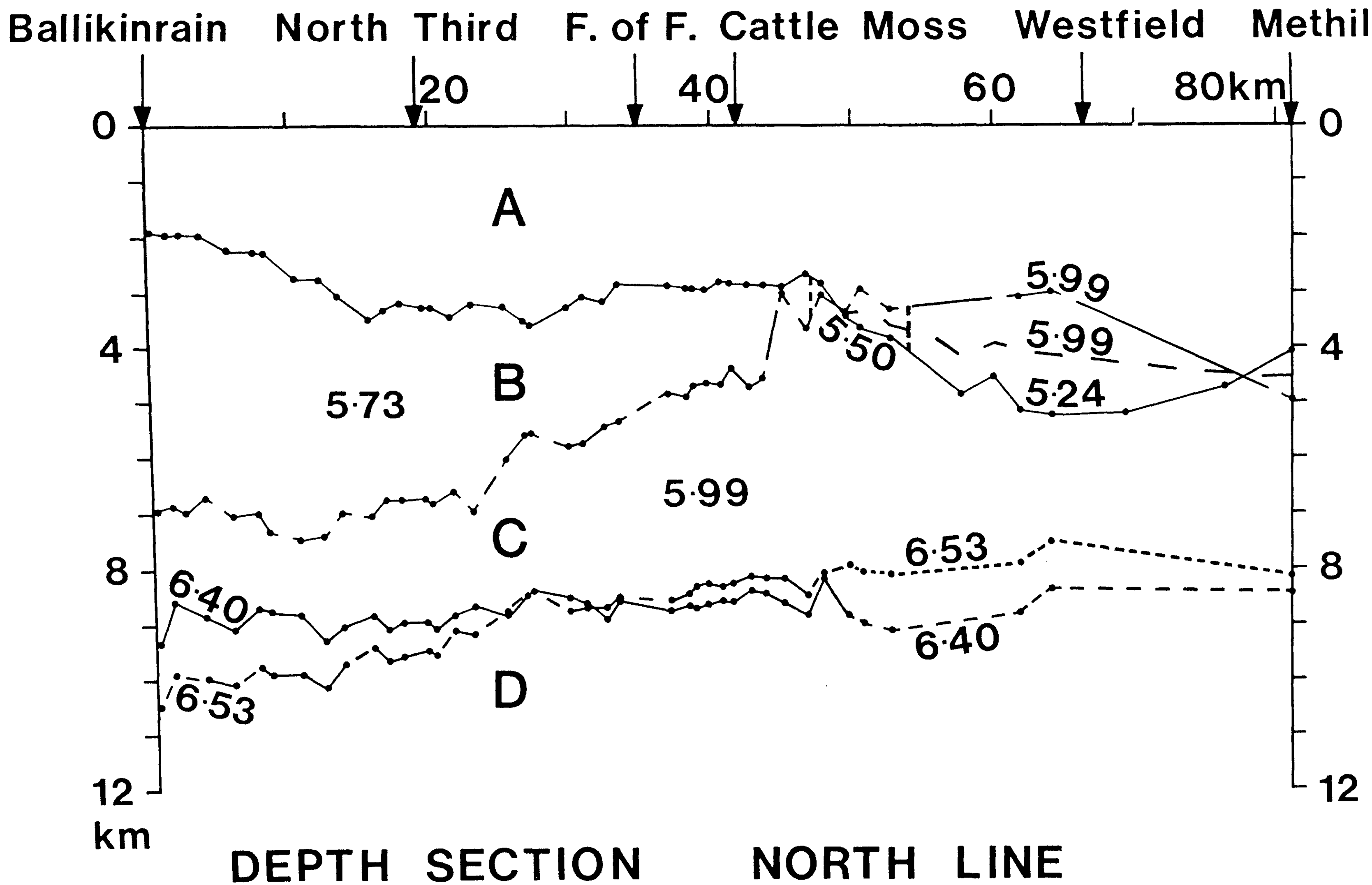

Fig.5.8b Plus-minus interpretation of the MAVIS I north line. Layers A to D correspond to the four time-distance branches in Fig.5.6.

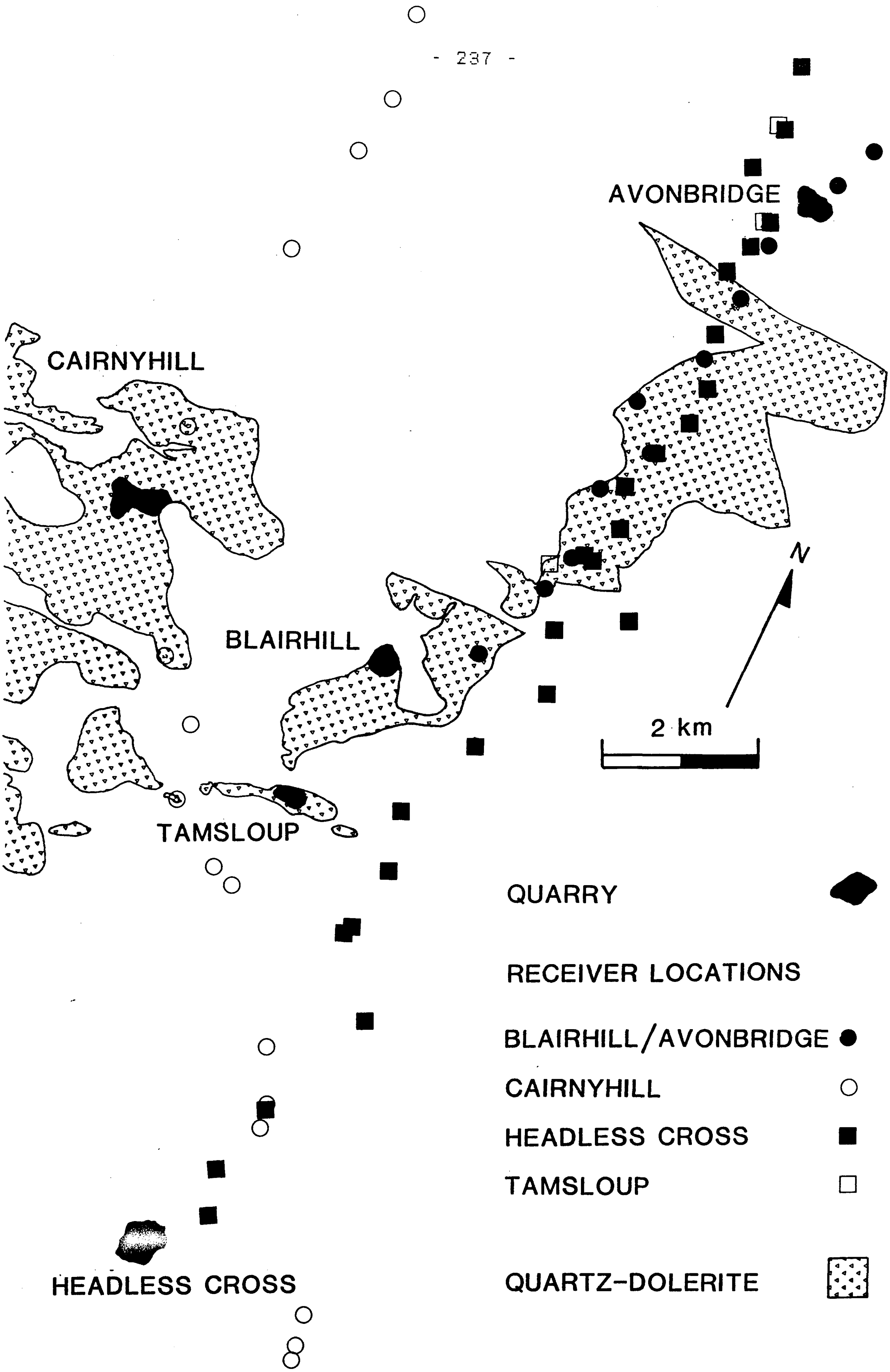

Fig.5.9 Location map of seismic sources and receivers for part of the MAVIS II line.

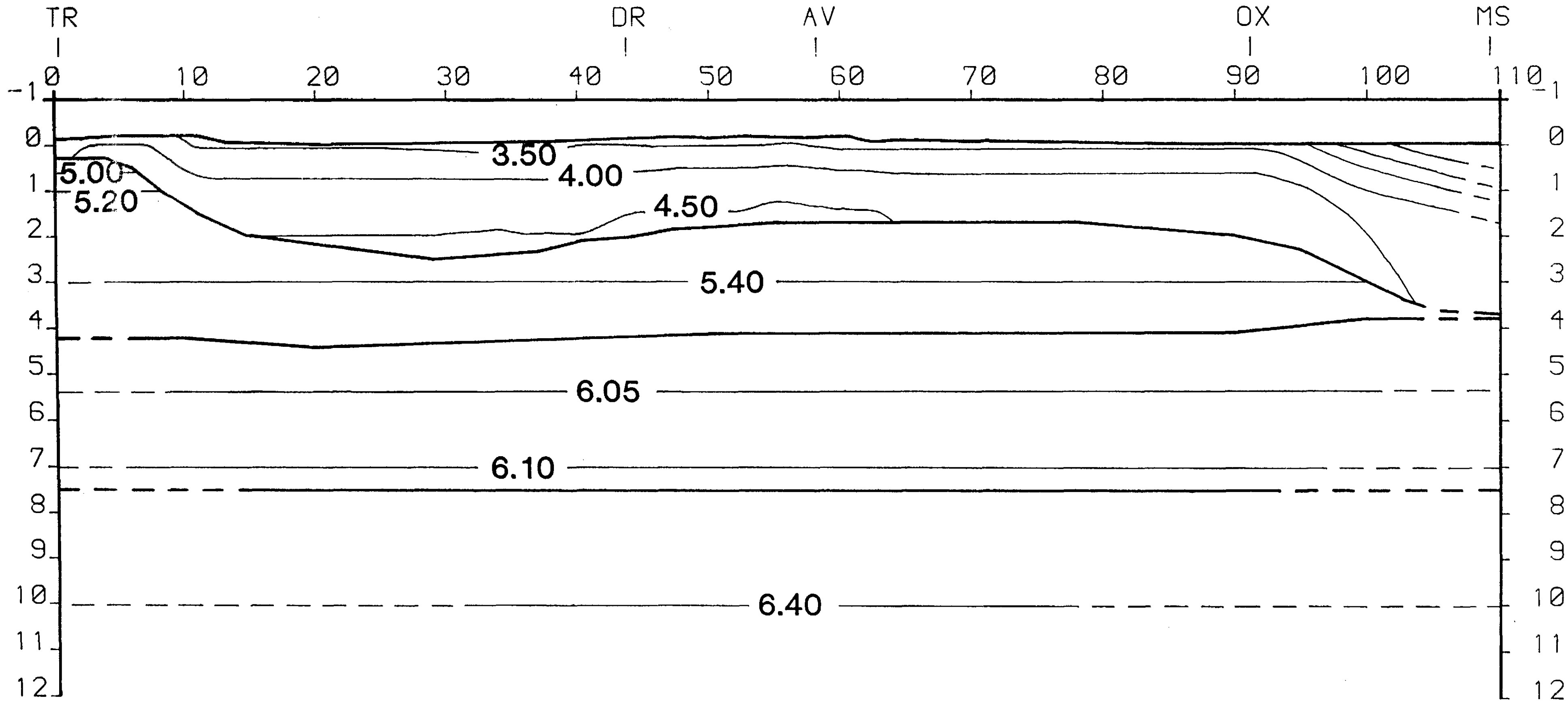

Fig.5.10 Ray-traced model of the MAVIS I south line; TR - Trearne, DR - Drumgray, AV - Avonbridge, OX - Oxcars, MS - Methil. Interfaces shown by thick lines, seismic velocity contours, in km/s, by thin lines. Scales are in km.

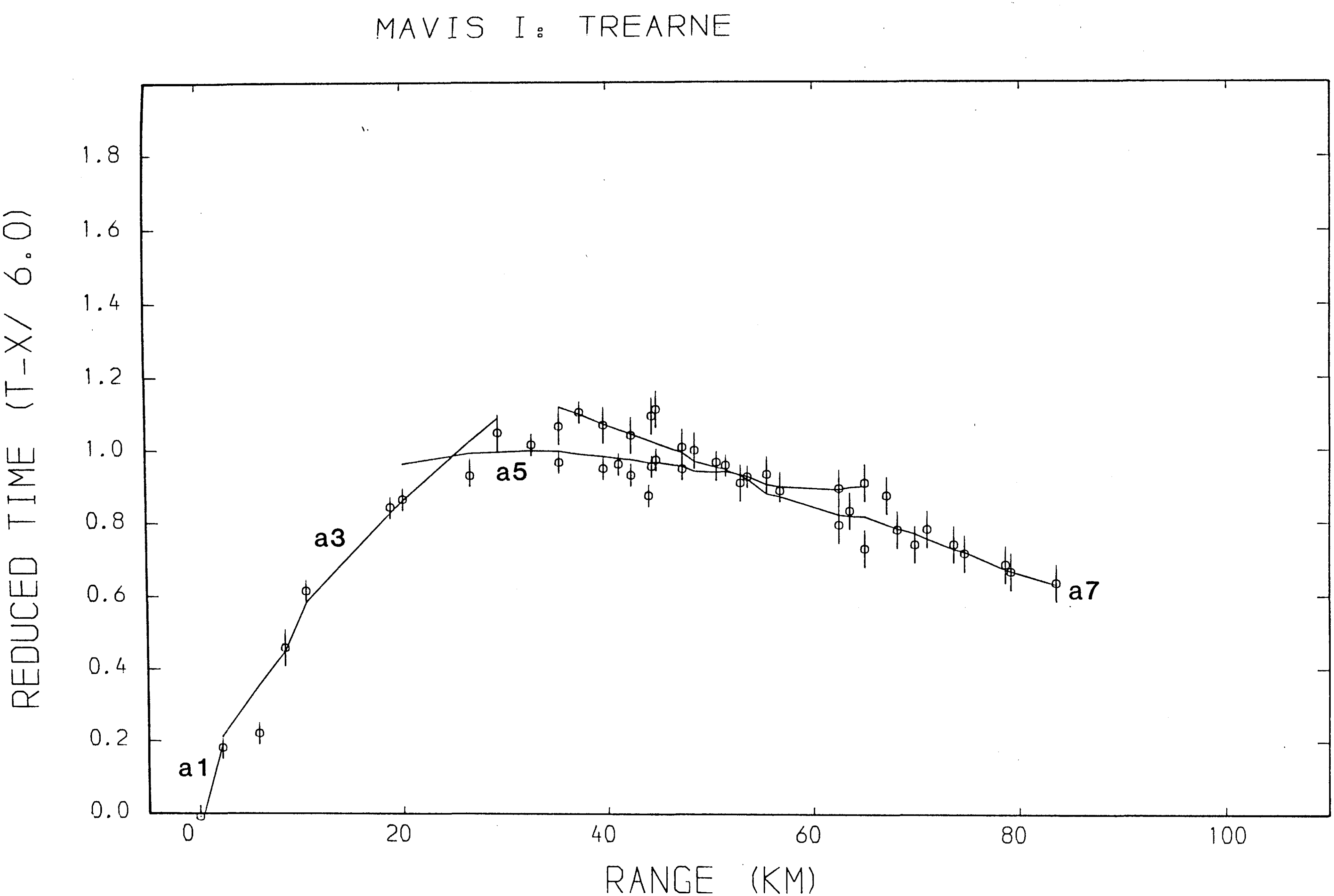

Fig.5.11 Observed (circles with error bars) and calculated (lines) travel-times; Trearne shot. See Table 5.1 for classification of travel-time branches.

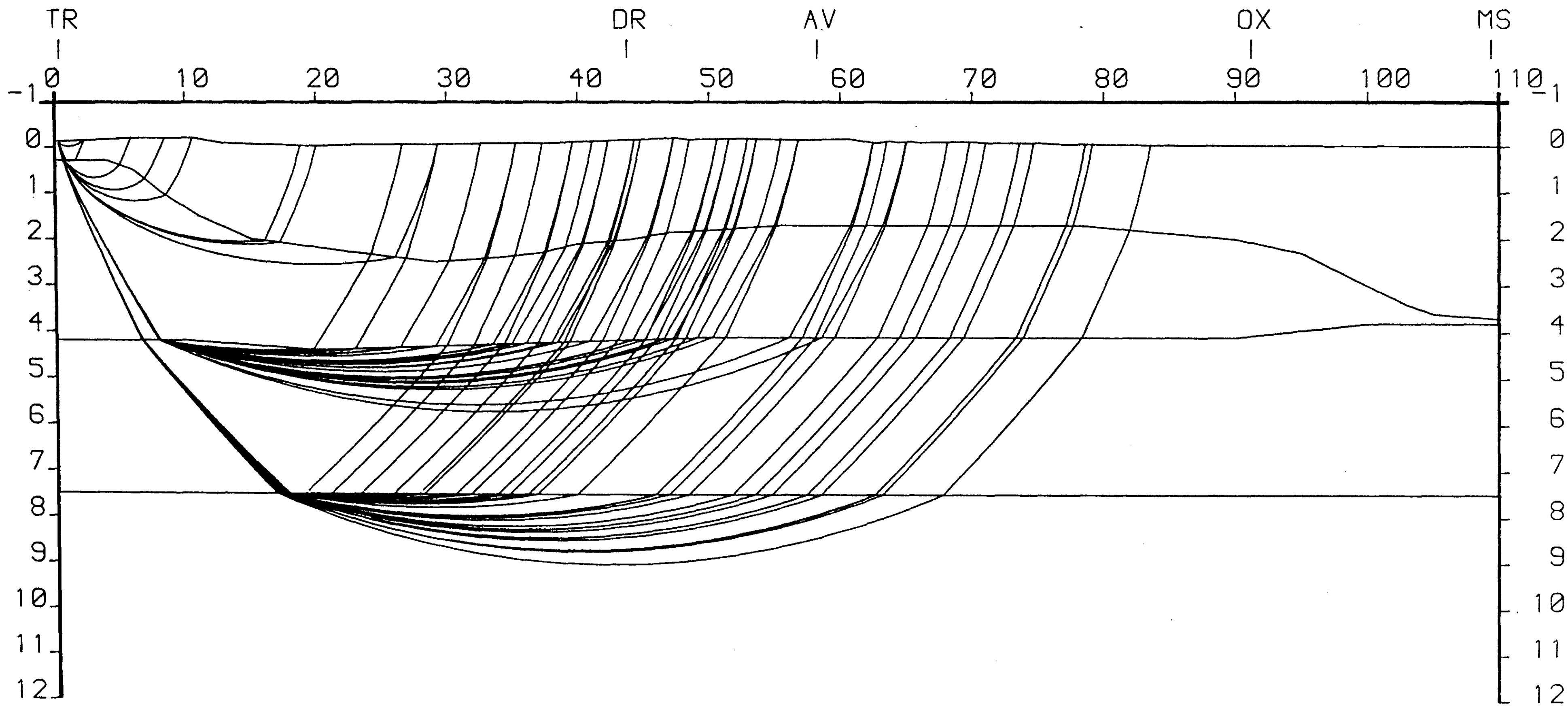

Fig.5.12 Ray-paths used in the calculation of travel-times shown in Fig.5.11. See Fig.5.10 for abbreviations. Scales are in km.

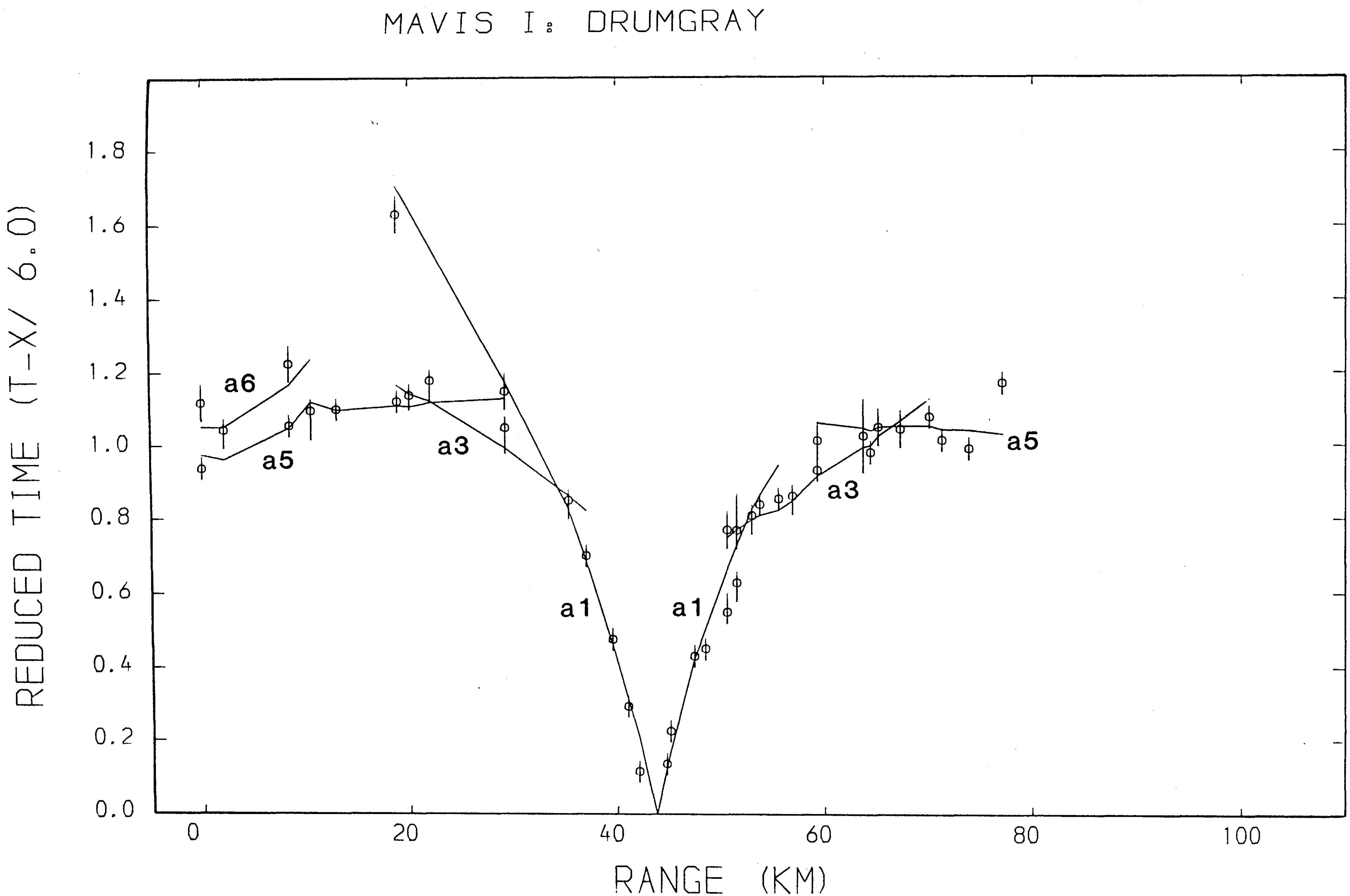

Fig.5.13 Observed (circles with error bars) and calculated (lines) travel-times; Drumgray shot. See Table 5.1 for classification of travel-time branches.

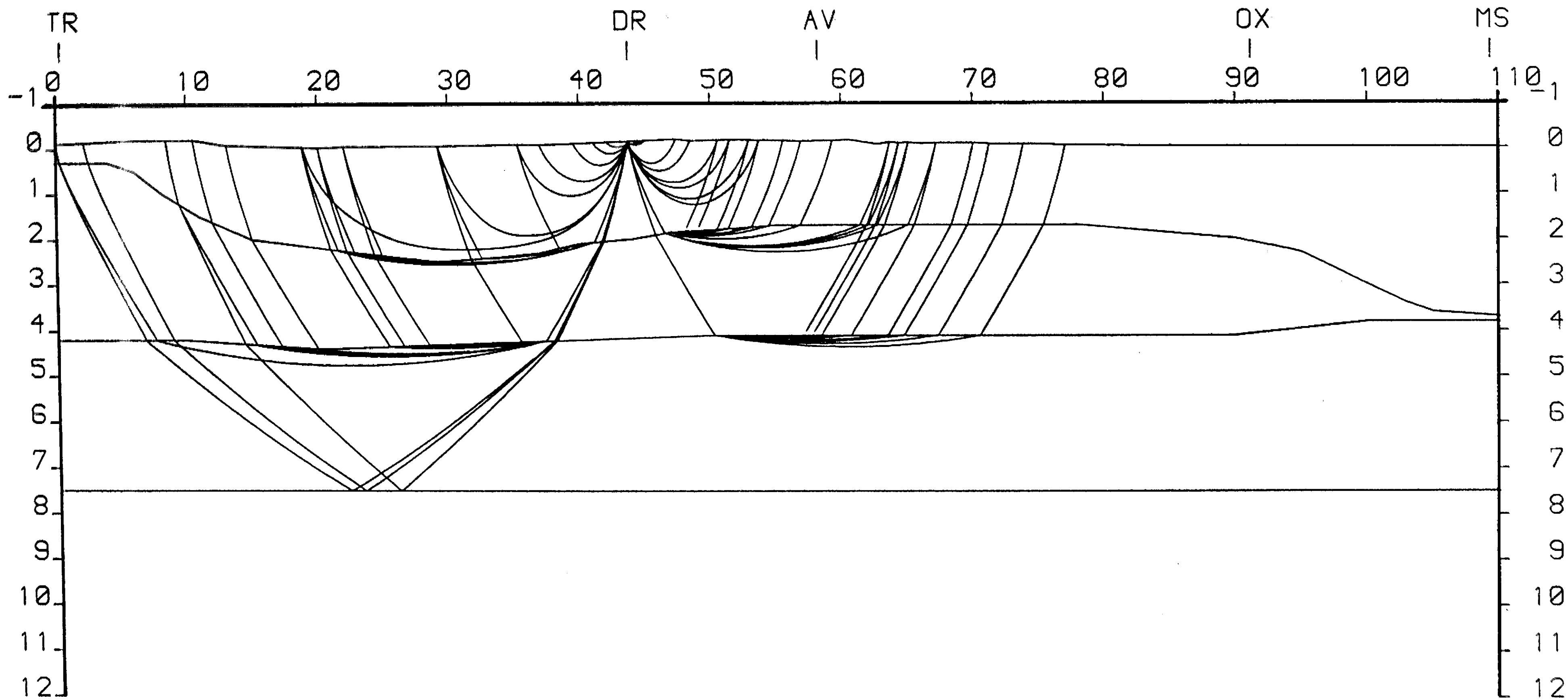

Fig.5.14 Ray-paths used in the calculation of travel-times shown in Fig.5.13. See Fig.5.10 for abbreviations. Scales are in km.

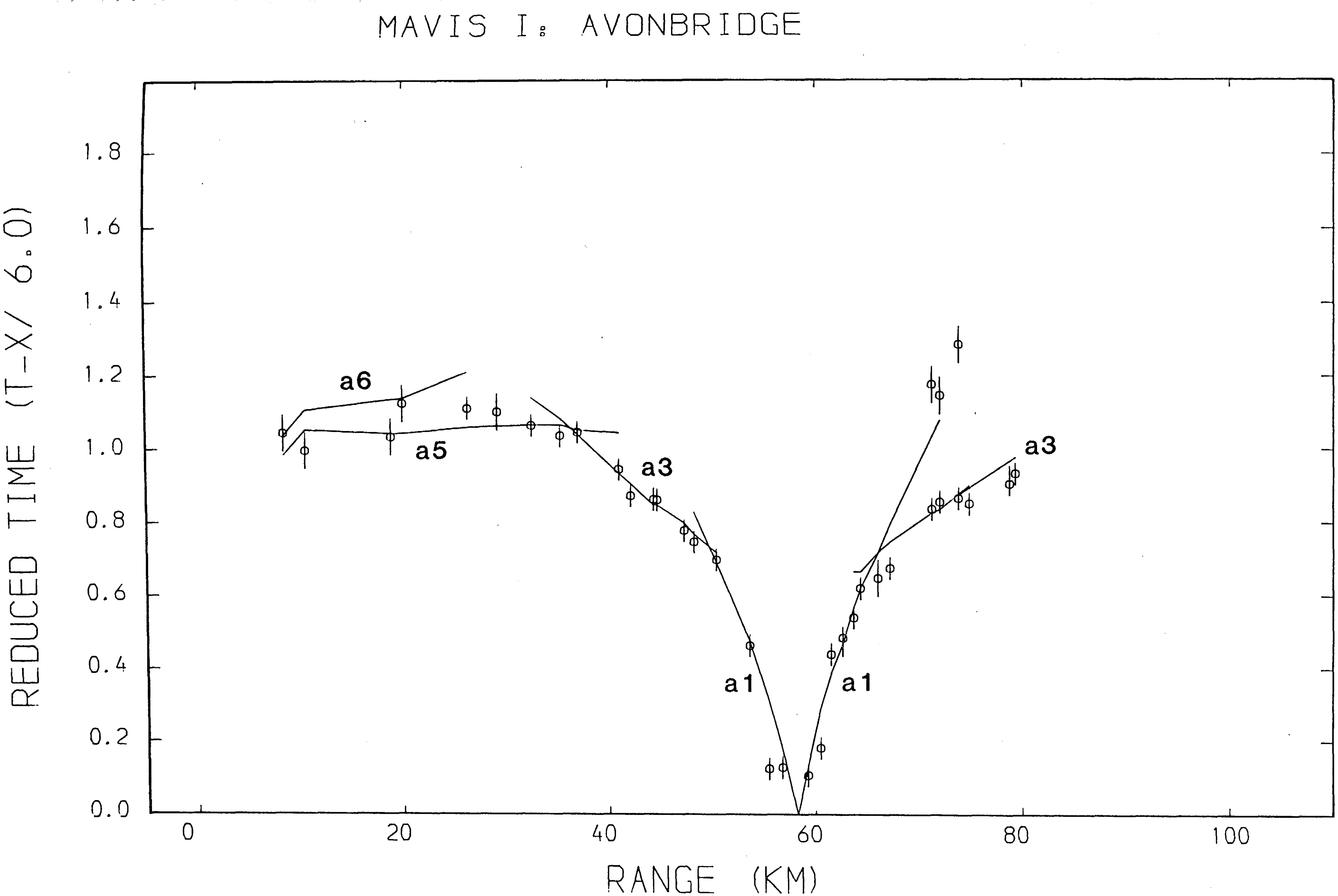

Fig.5.15 Observed (circles with error bars) and calculated (lines) travel-times; Avonbridge shot. See Table 5.1 for classification of travel-time branches.

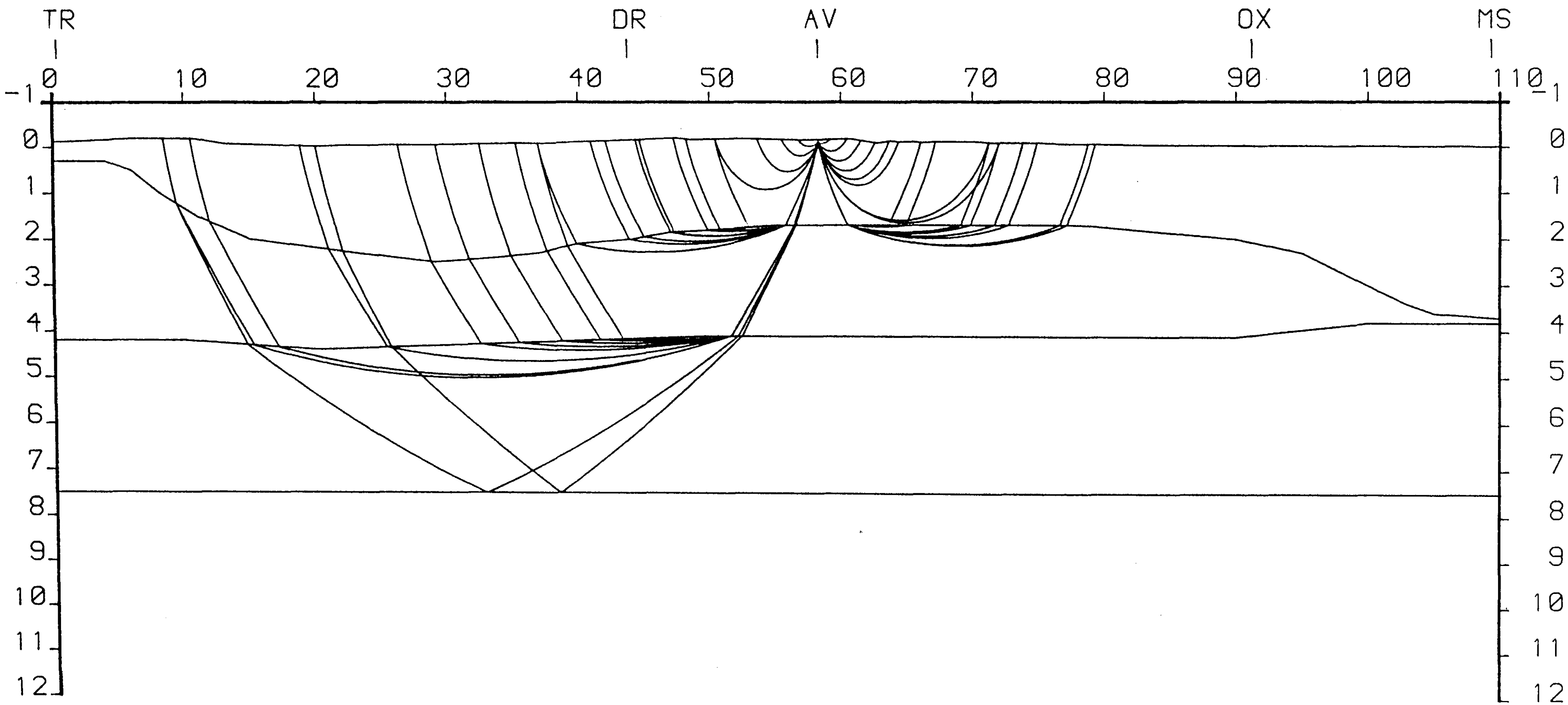

Fig.5.16 Ray-paths used in the calculation of travel-times shown in Fig.5.15. See Fig.5.10 for abbreviations. Scales are in km.

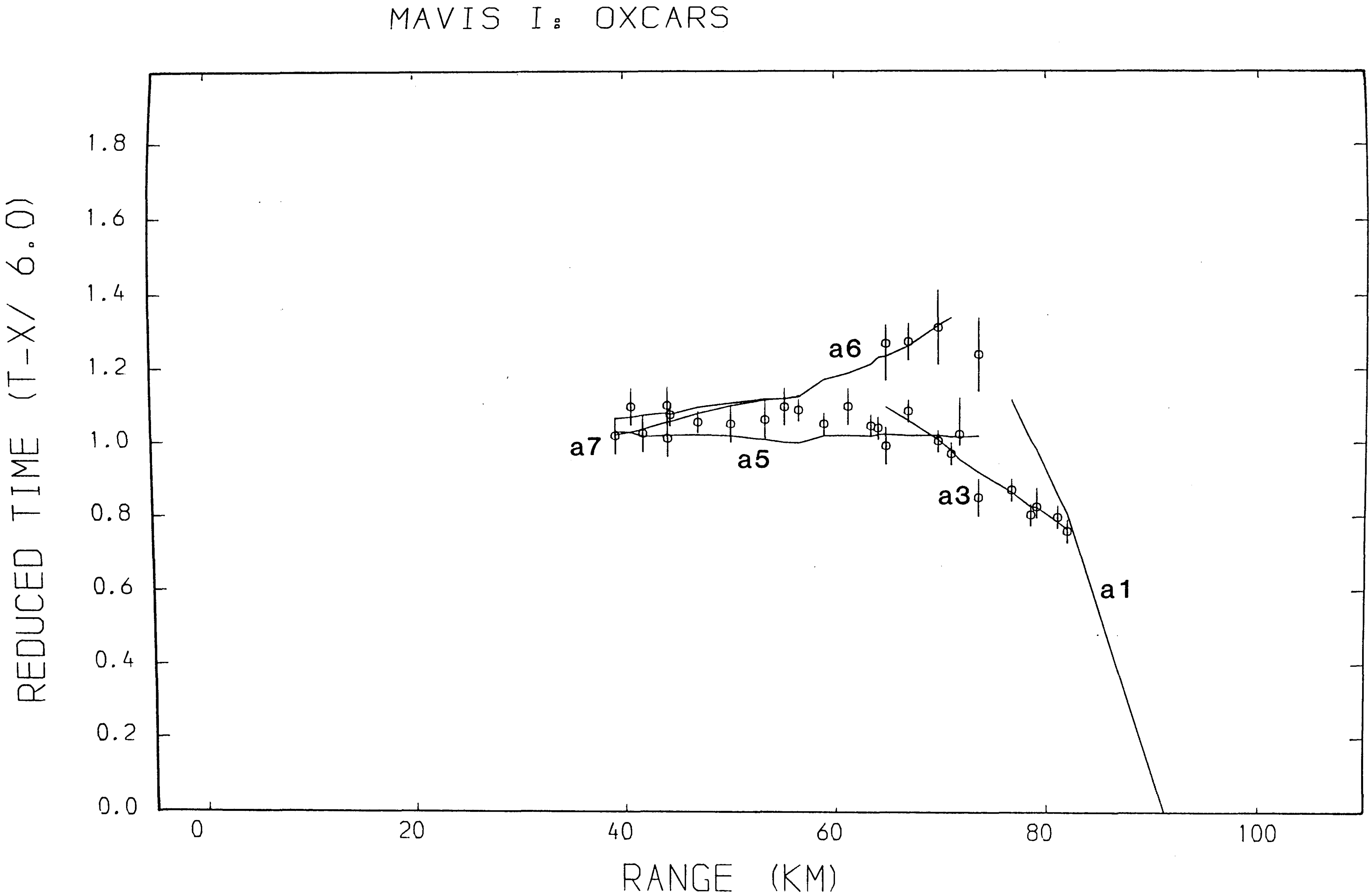

Fig.5.17 Observed (circles with error bars) and calculated (lines) travel-times; Oxcars shot. See Table 5.1 for classification of travel-time branches.

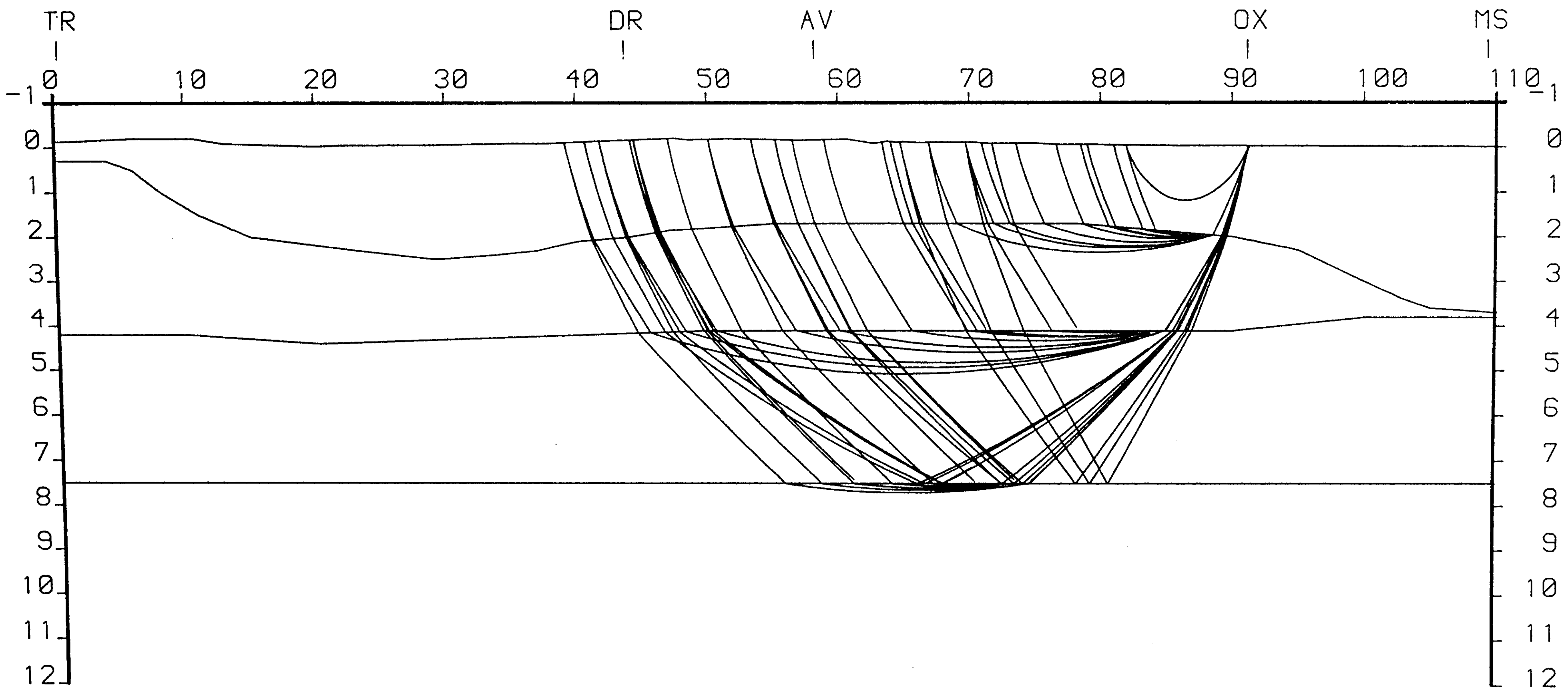

Fig.5.18 Ray-paths used in the calculation of travel-times shown in Fig.5.17. See Fig.5.10 for abbreviations. Scales are in km.

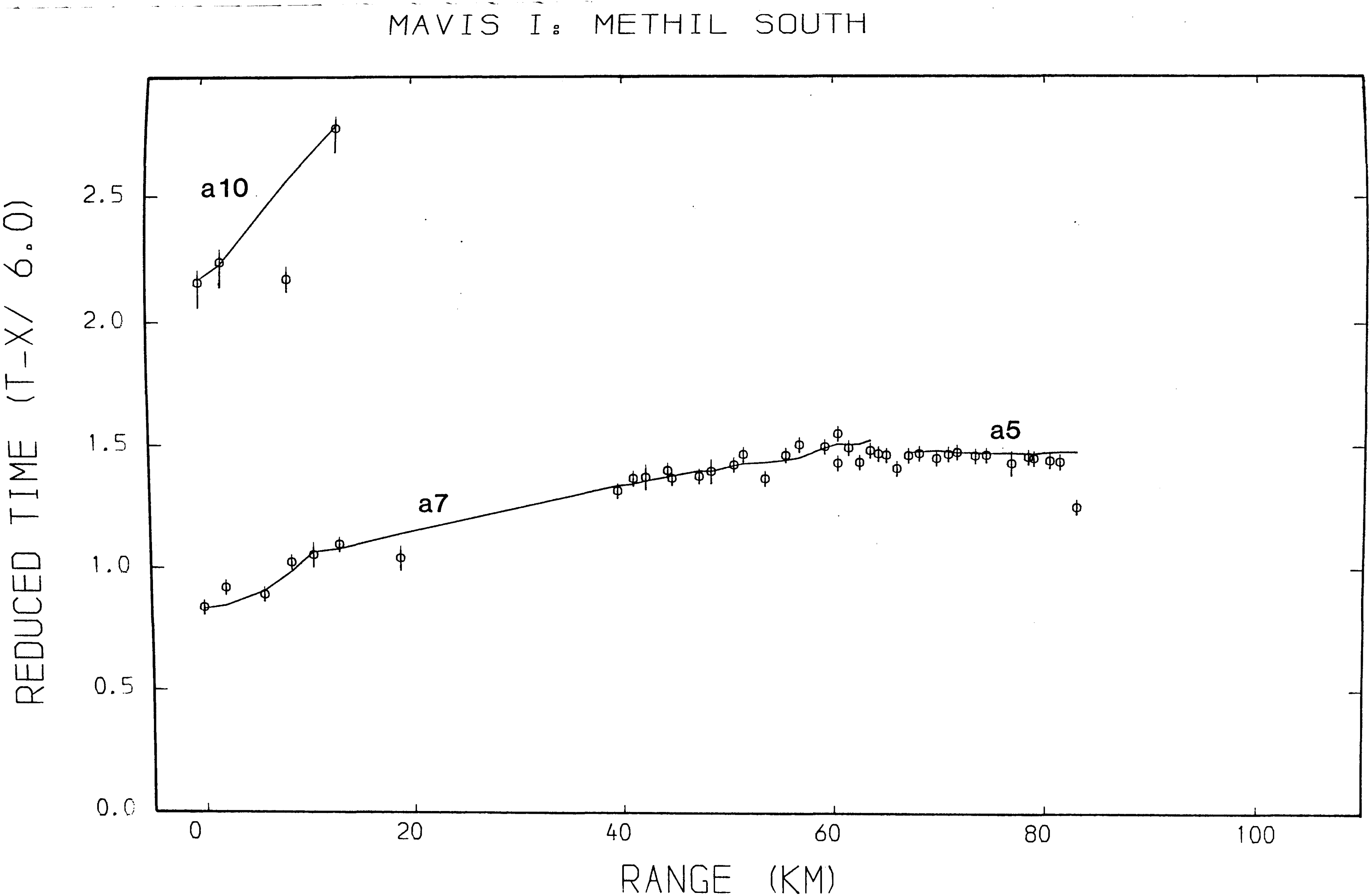

Fig.5.19 Observed (circles with error bars) and calculated (lines) travel-times; Methil shot. See Table 5.1 for classification of travel-time branches.

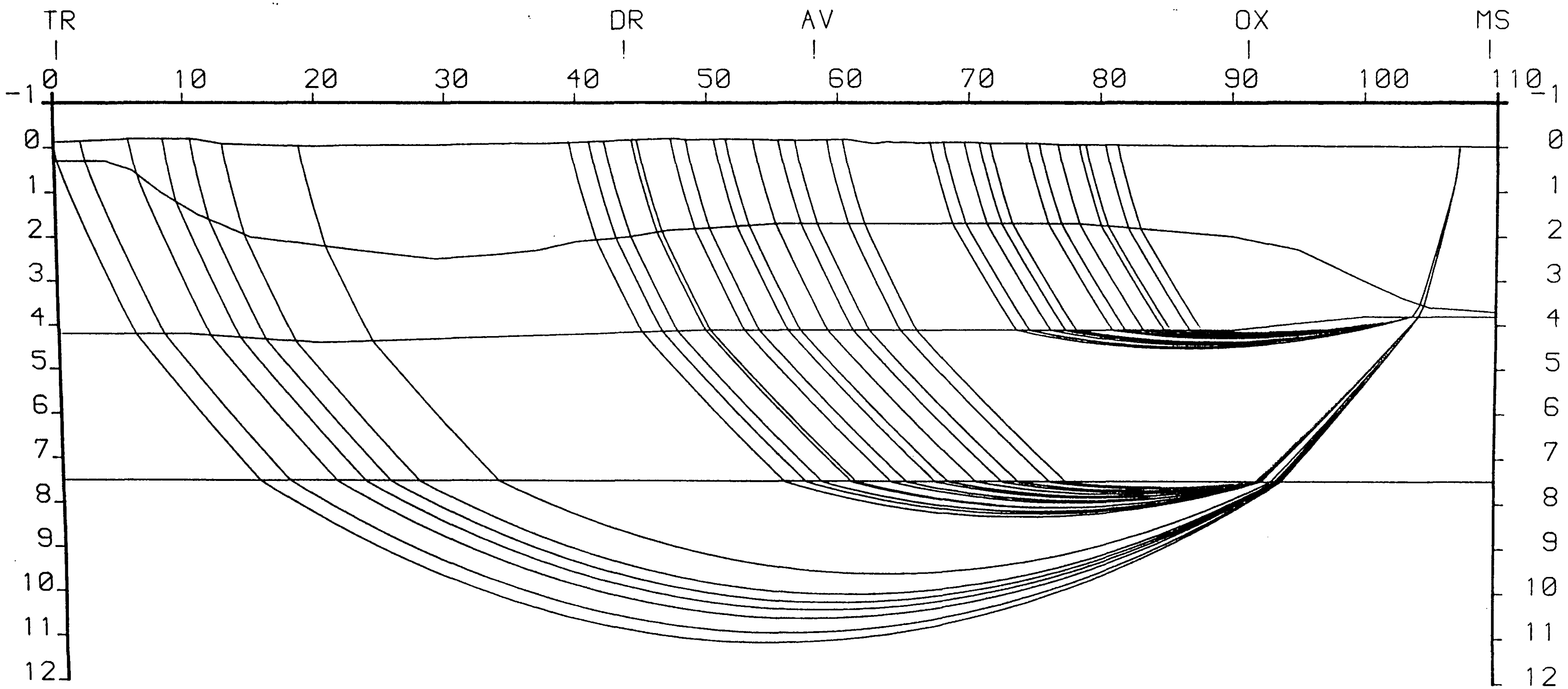

Fig.5.20 Ray-paths used in the calculation of travel-times of a5 and a7 arrivals shown in Fig.5.19. See Fig.5.10 for abbreviations. Scales are in km.

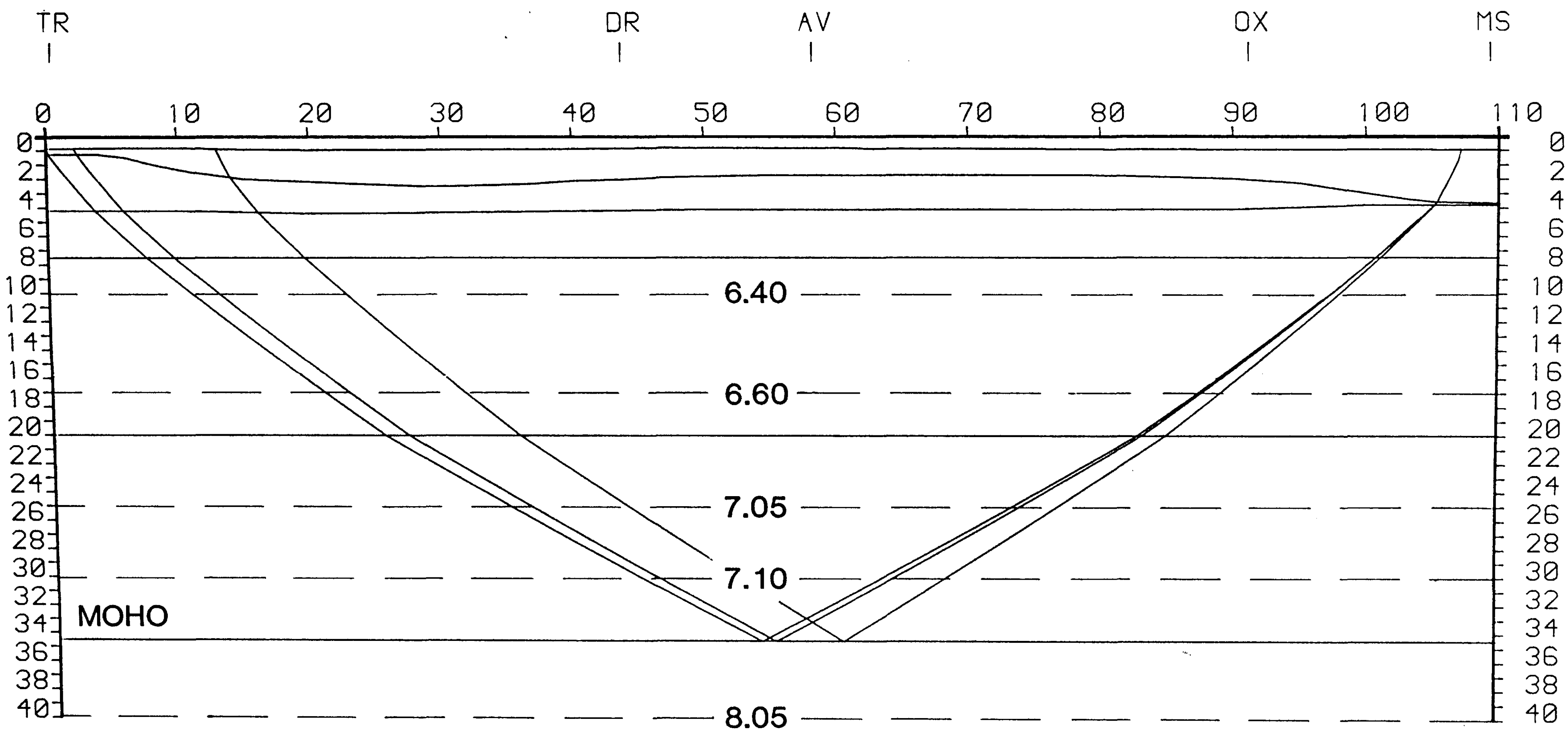

Fig.5.21 Ray-paths used in the calculation of travel-times of a10 arrivals shown in Fig.5.19. See Fig.5.10 for abbreviations. Scales are in km.

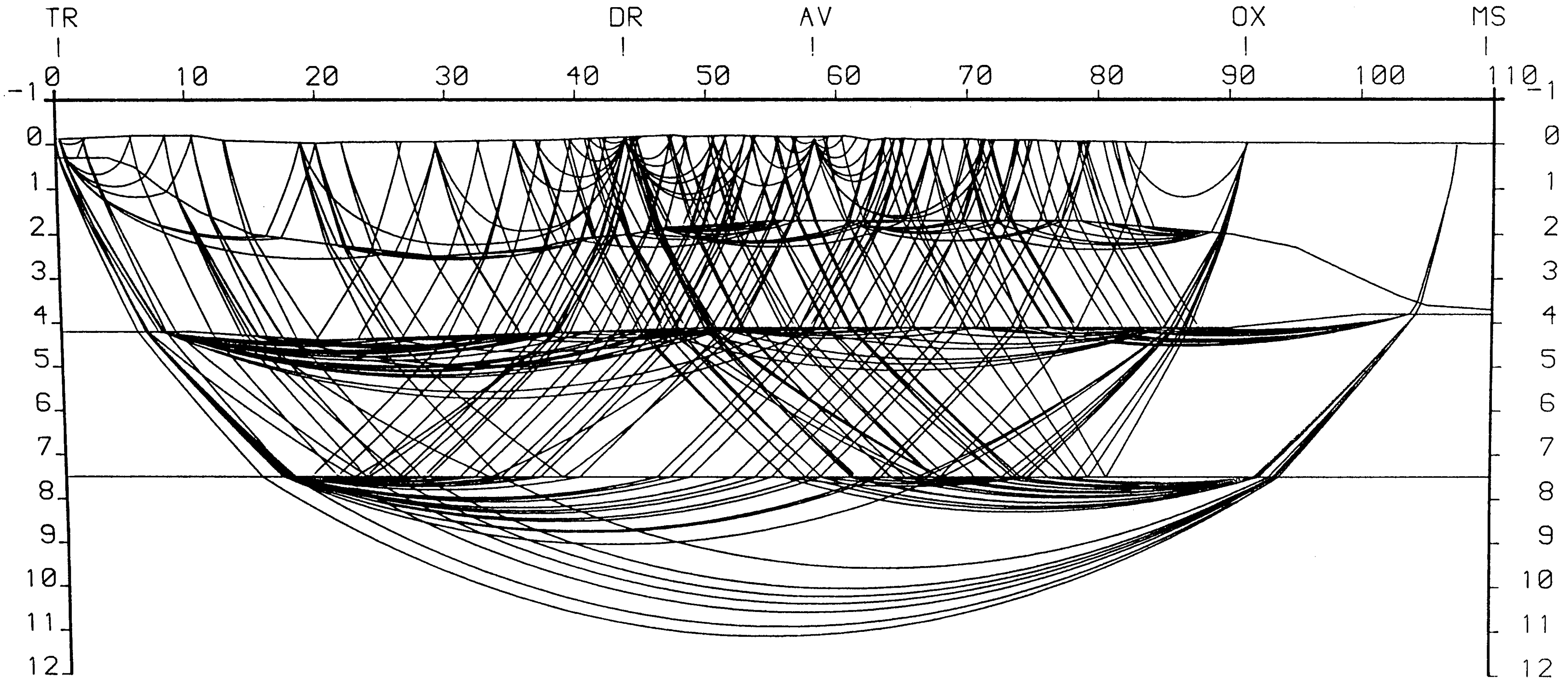

Fig.5.22 Ray-diagram showing all ray-paths used in the calculation of travel-times from MAVIS I south line sources. See Fig.5.10 for abbreviations. Scales are in km.

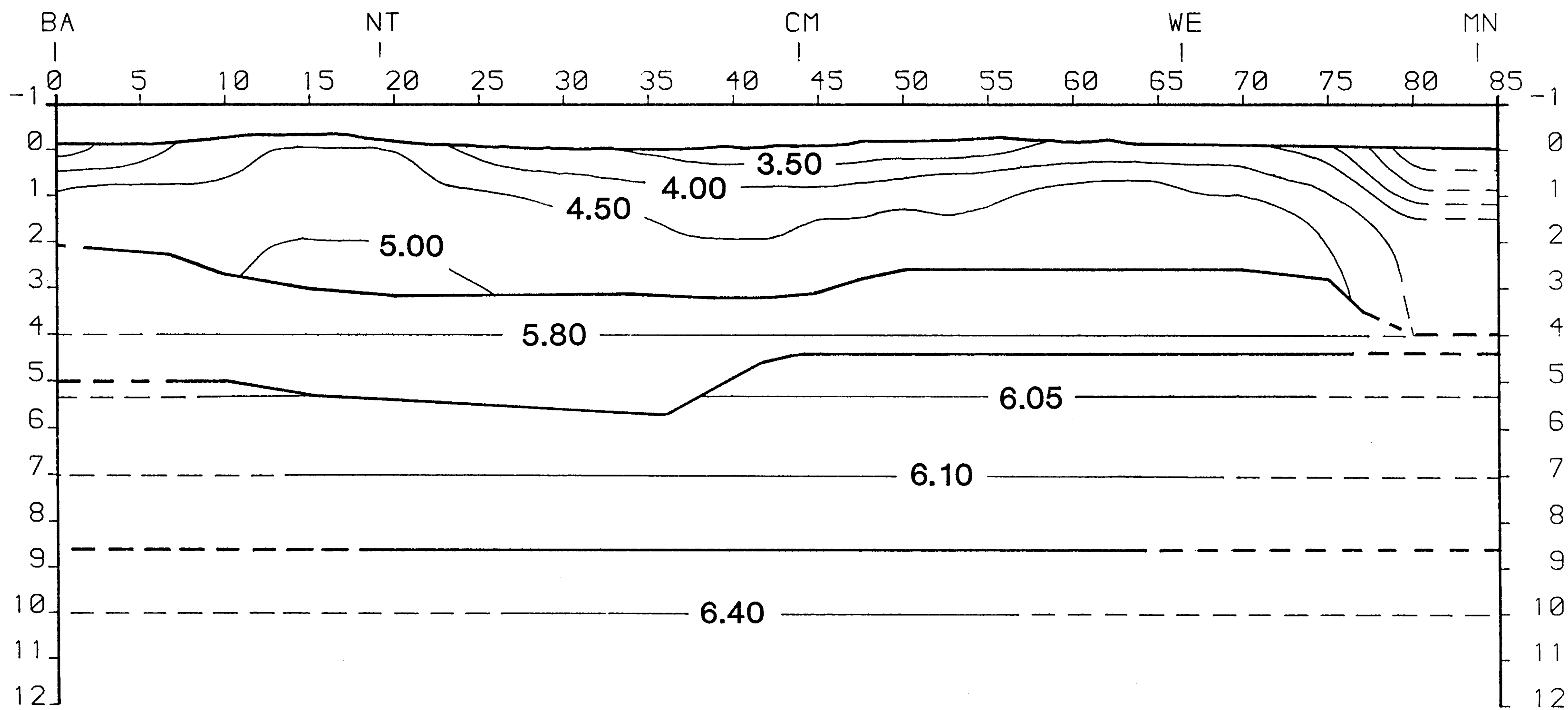

Fig.5.23 Ray-traced model of the MAVIS I north line; BA - Ballikinrain, NT - North Third, CM - Cattlemoss, WE - Westfield, MN - Methil. Interfaces shown by thick lines, seismic velocity contours, in km/s, by thin lines. Scales are in km.

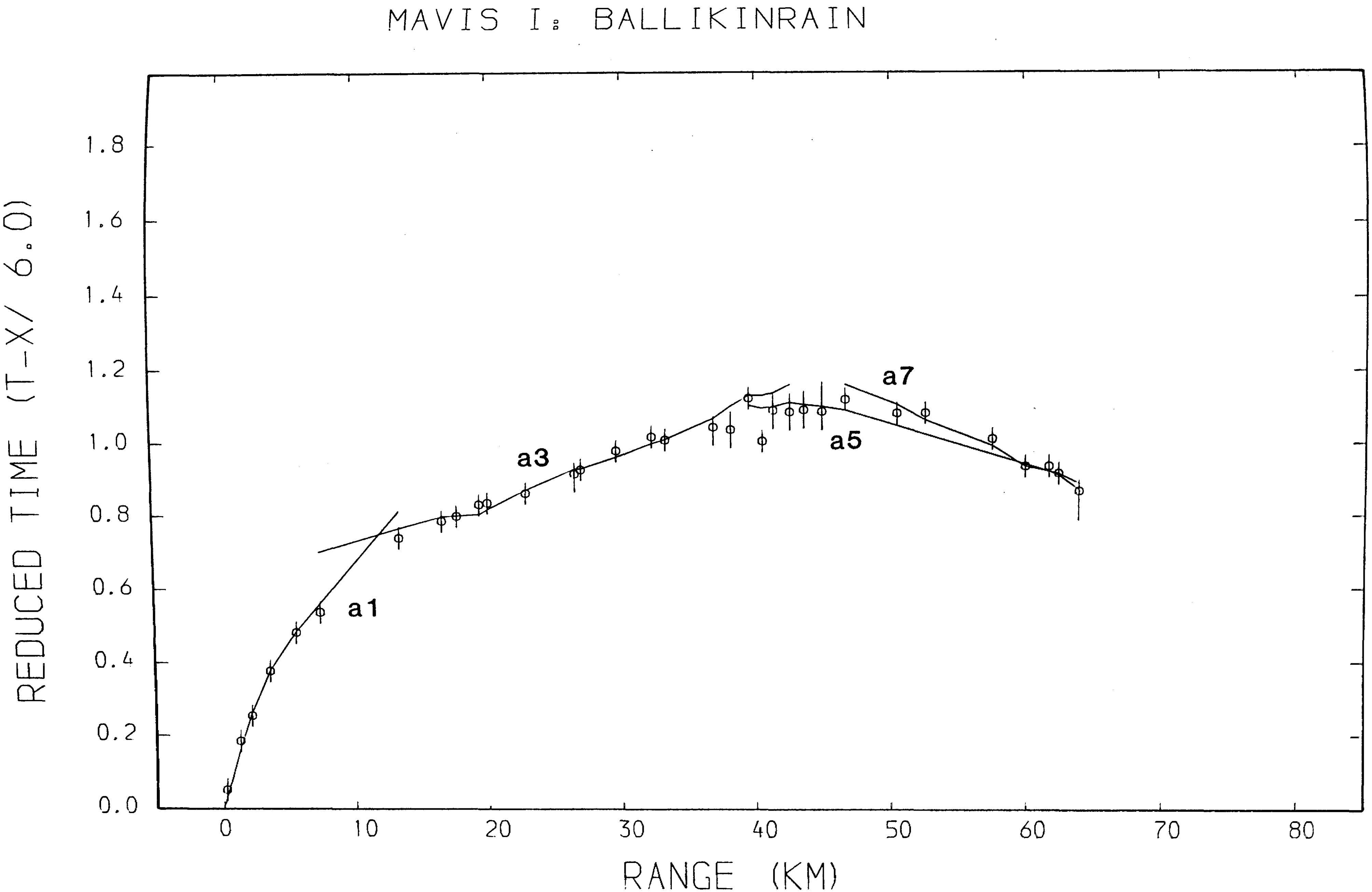

Fig.5.24 Observed (circles with error bars) and calculated (lines) travel-times; Ballikinrain shot. See Table 5.1 for classification of travel-time branches.

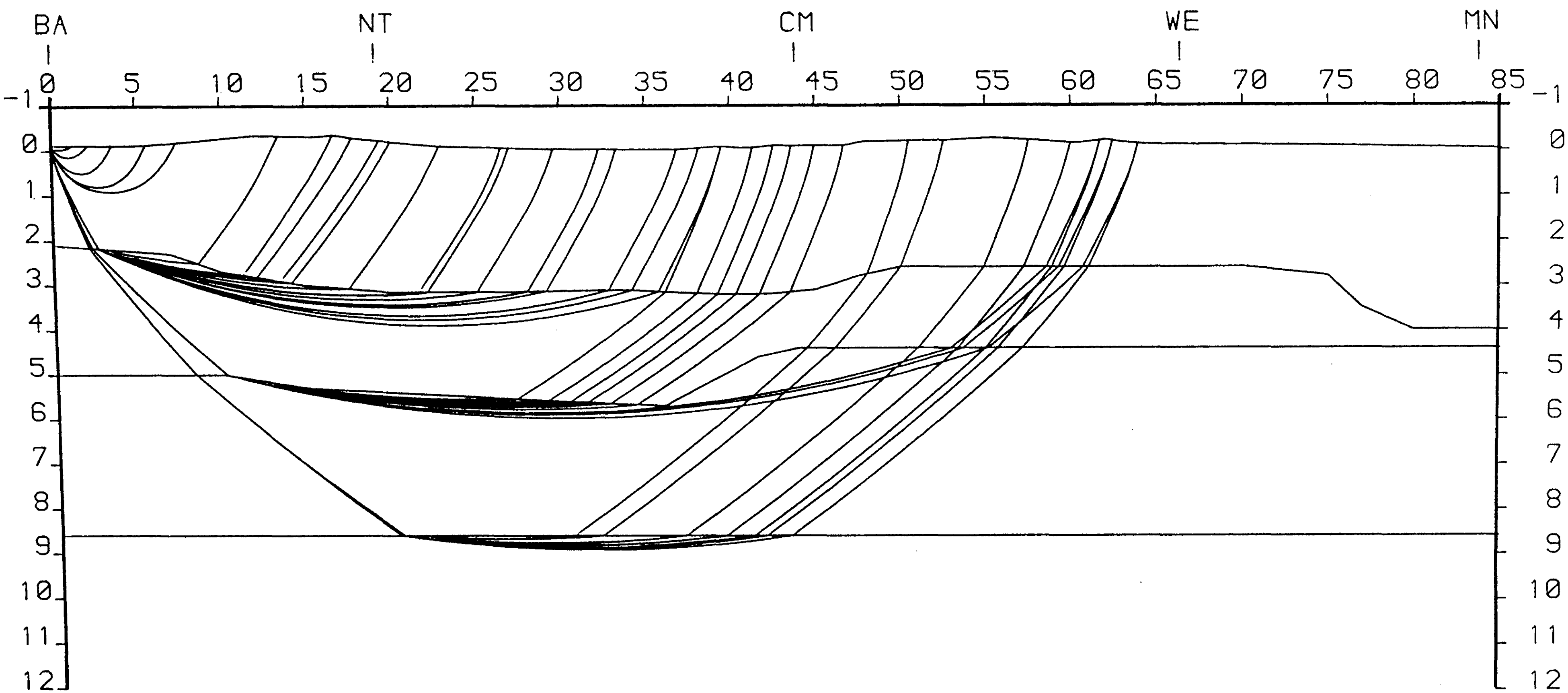

Fig.5.25 Ray-paths used in the calculation of travel-times shown in Fig.5.24. See Fig.5.23 for abbreviations. Scales are in km.

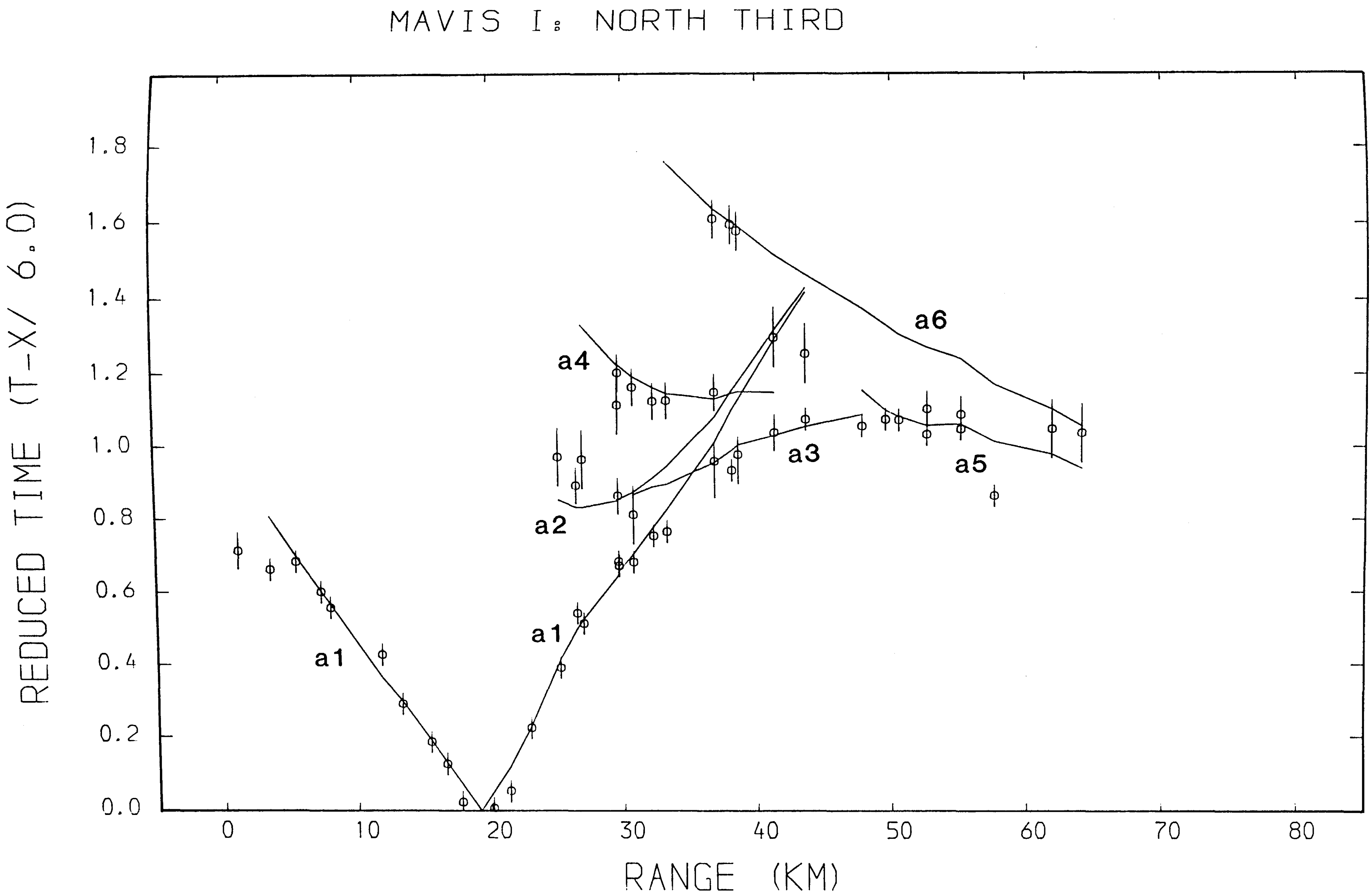

Fig.5.26 Observed (circles with error bars) and calculated (lines) travel-times; North Third shot. See Table 5.1 for classification of travel-time branches.

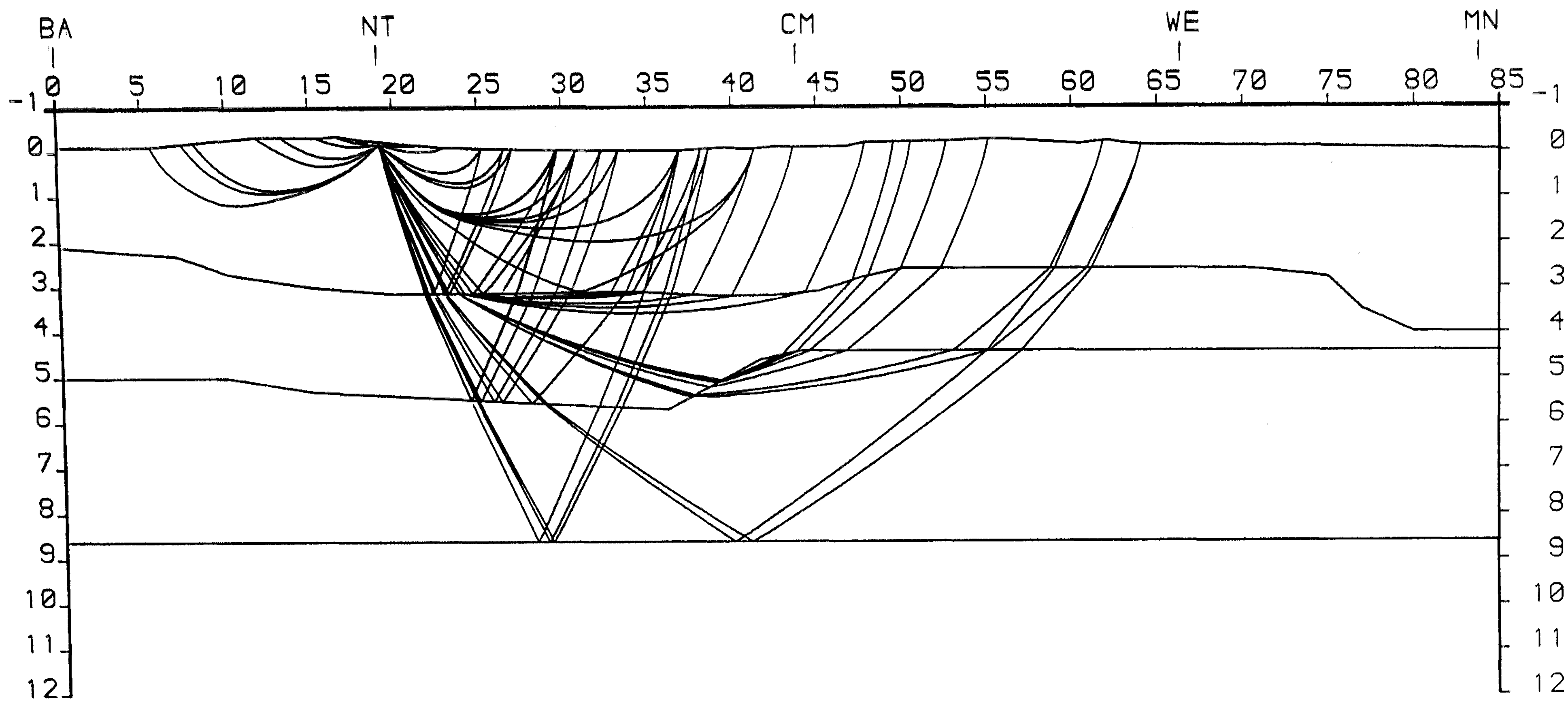

Fig.5.27 Ray-paths used in the calculation of travel-times shown in Fig.5.26. See Fig.5.23 for abbreviations. Scales are in km.

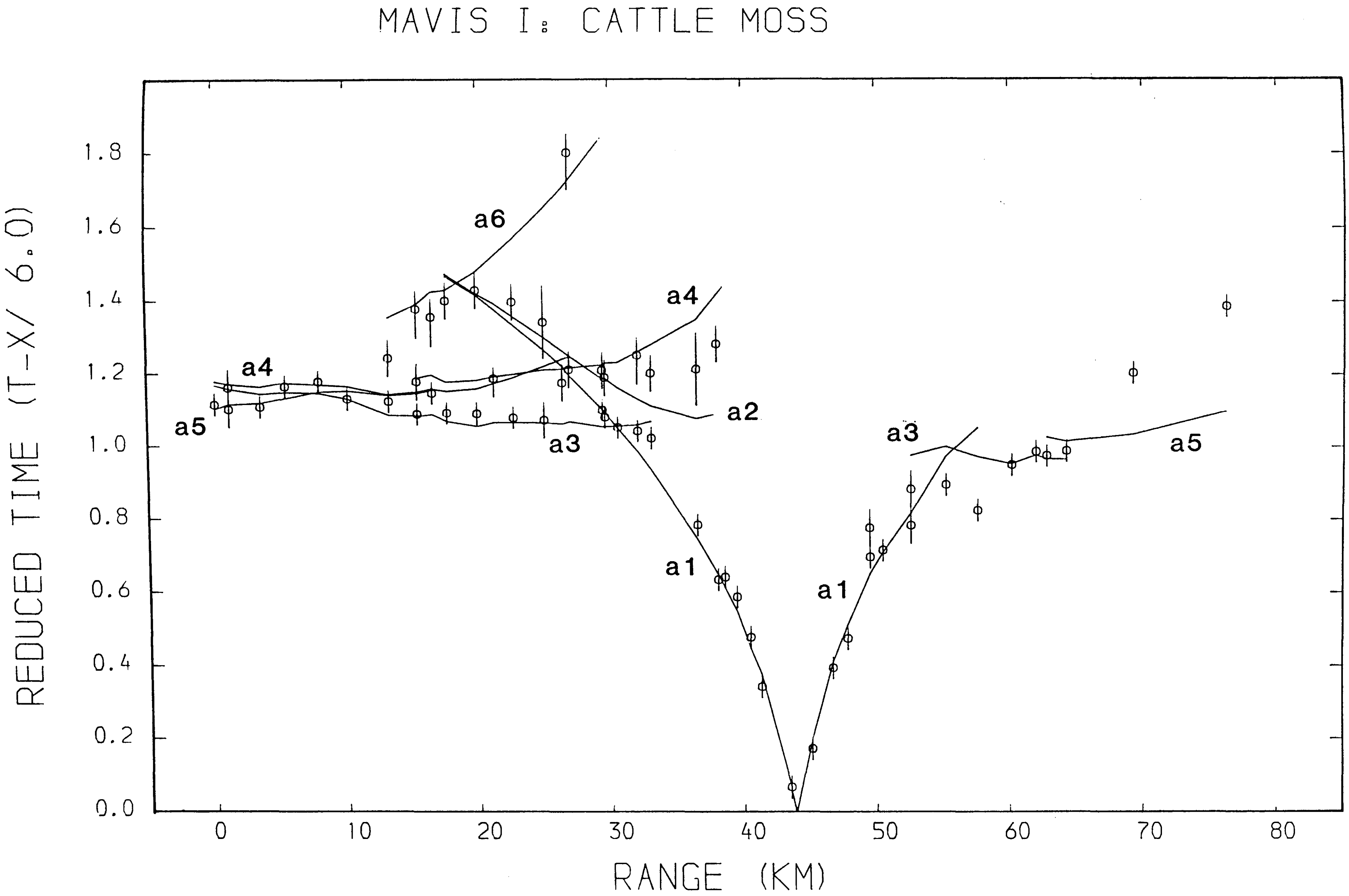

Fig.5.28 Observed (circles with error bars) and calculated (lines) travel-times; Cattlemoss shot. See Table 5.1 for classification of travel-time branches.

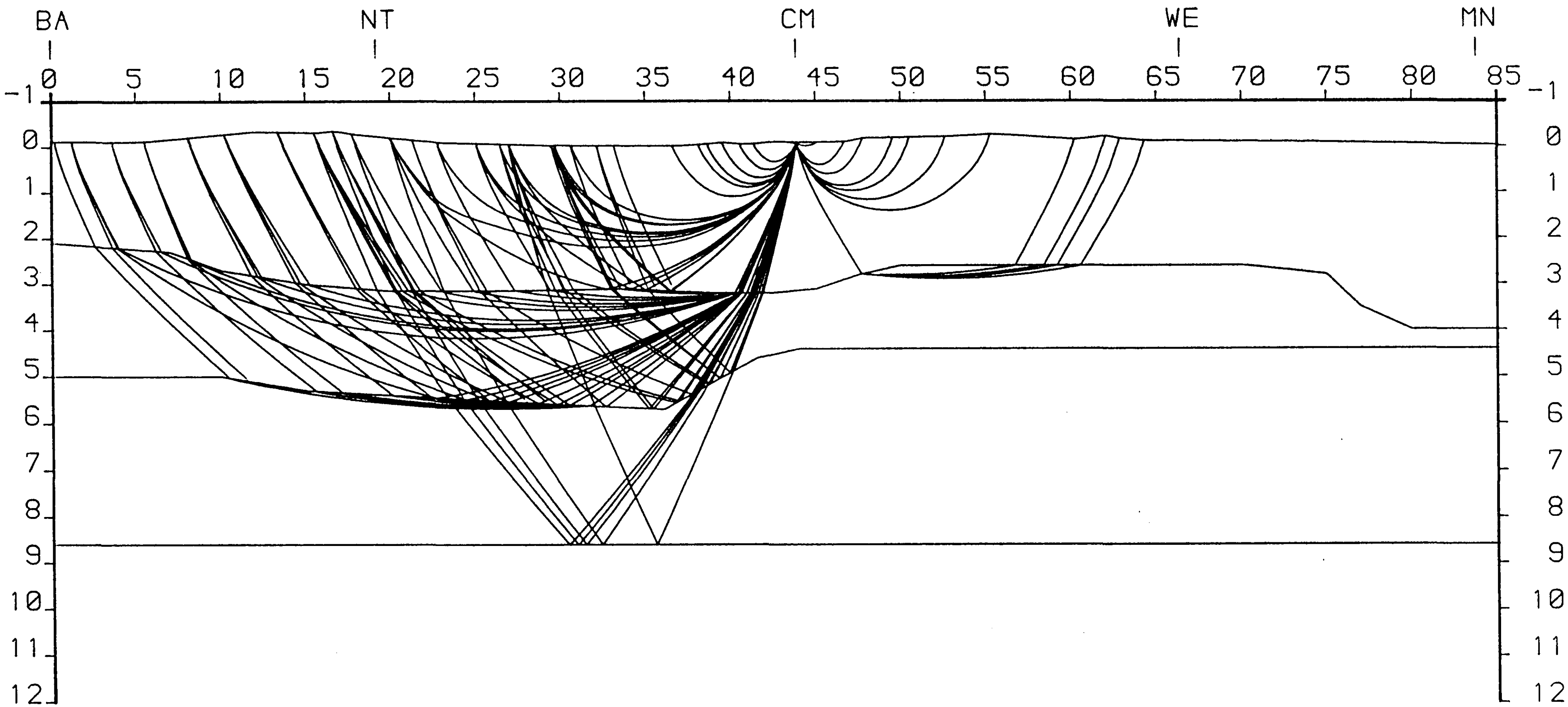

Fig.5.29 Ray-paths used in the calculation of travel-times shown in Fig.5.28. See Fig.5.23 for abbreviations. Scales are in km.

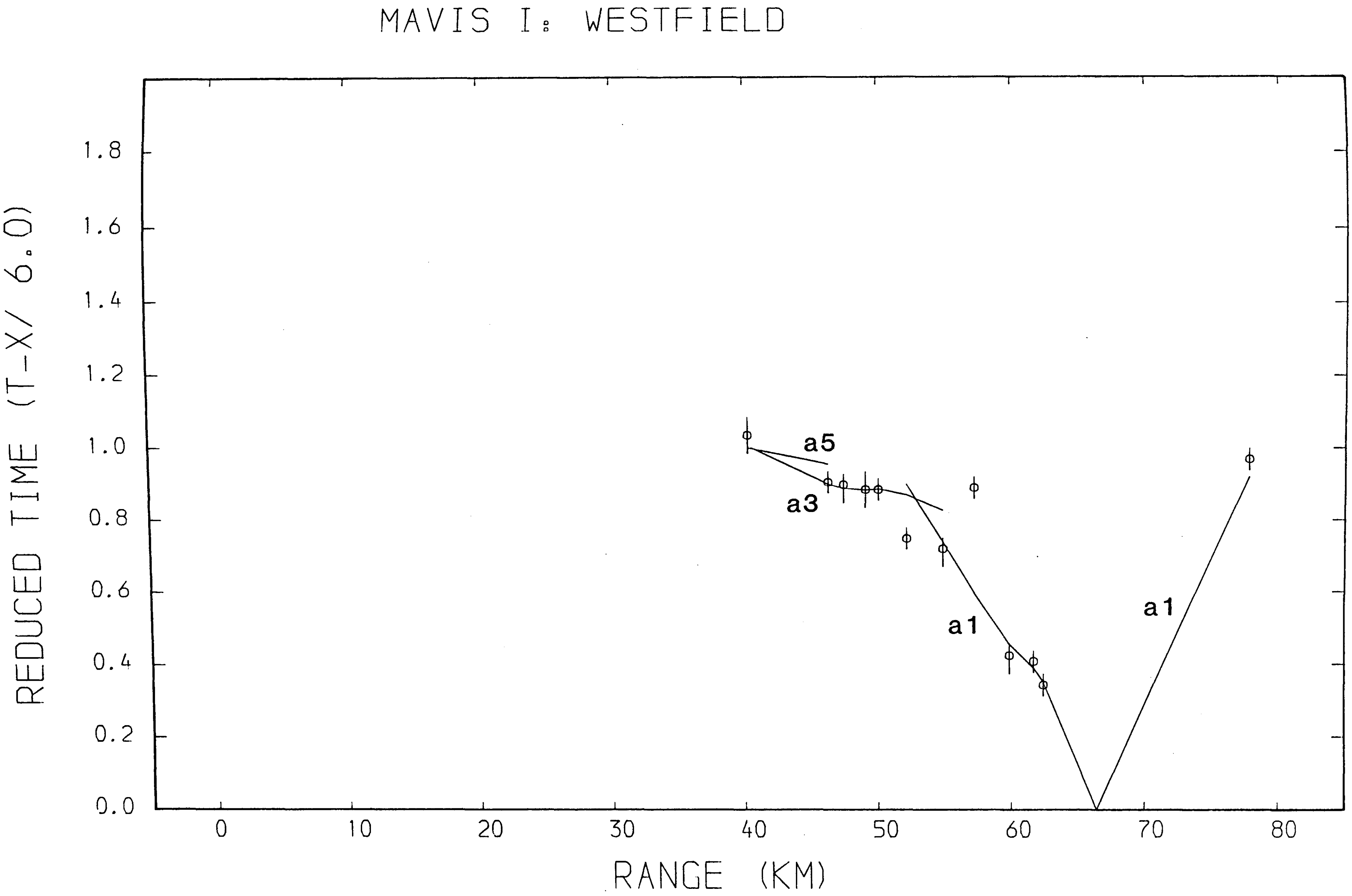

Fig.5.30 Observed (circles with error bars) and calculated (lines) travel-times; Westfield shot. See Table 5.1 for classification of travel-time branches.

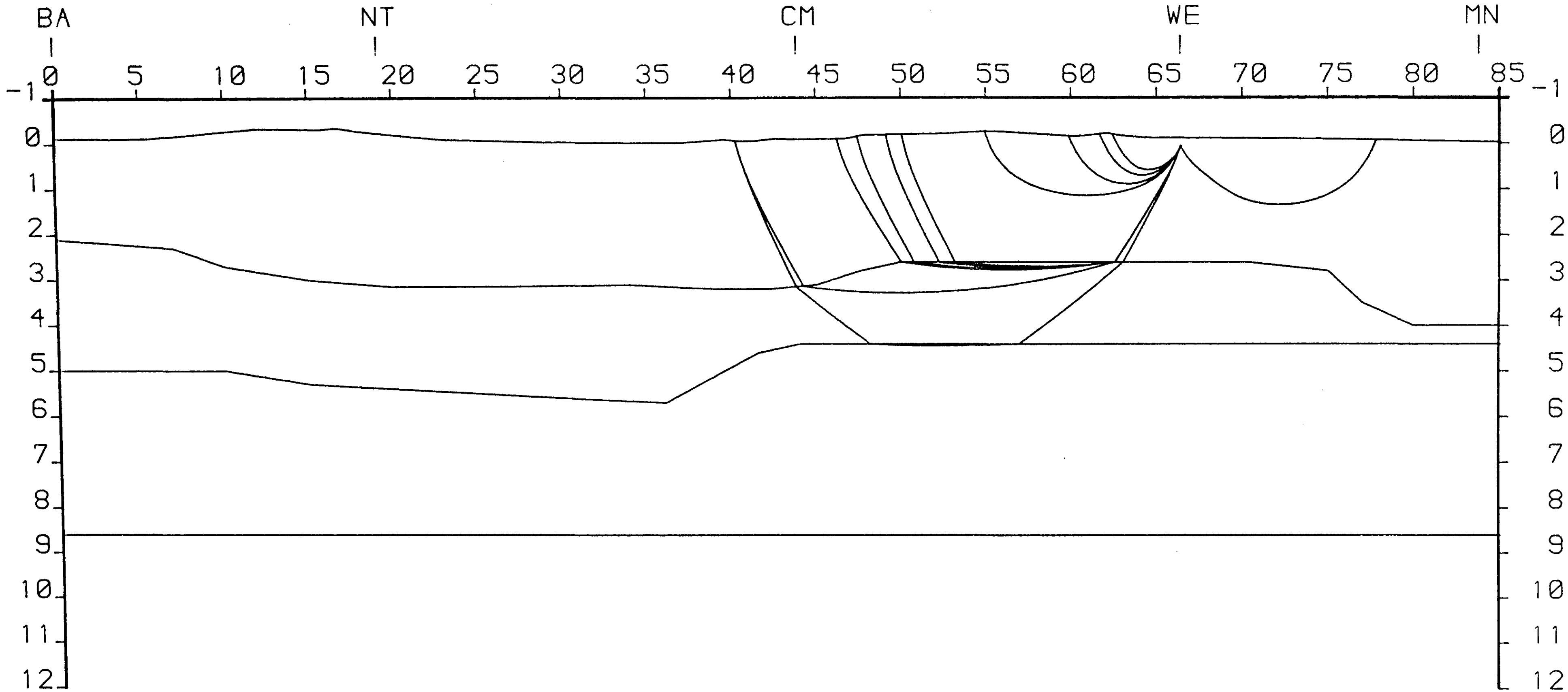

Fig.5.31 Ray-paths used in the calculation of travel-times shown in Fig.5.30. See Fig.5.23 for abbreviations. Scales are in km.

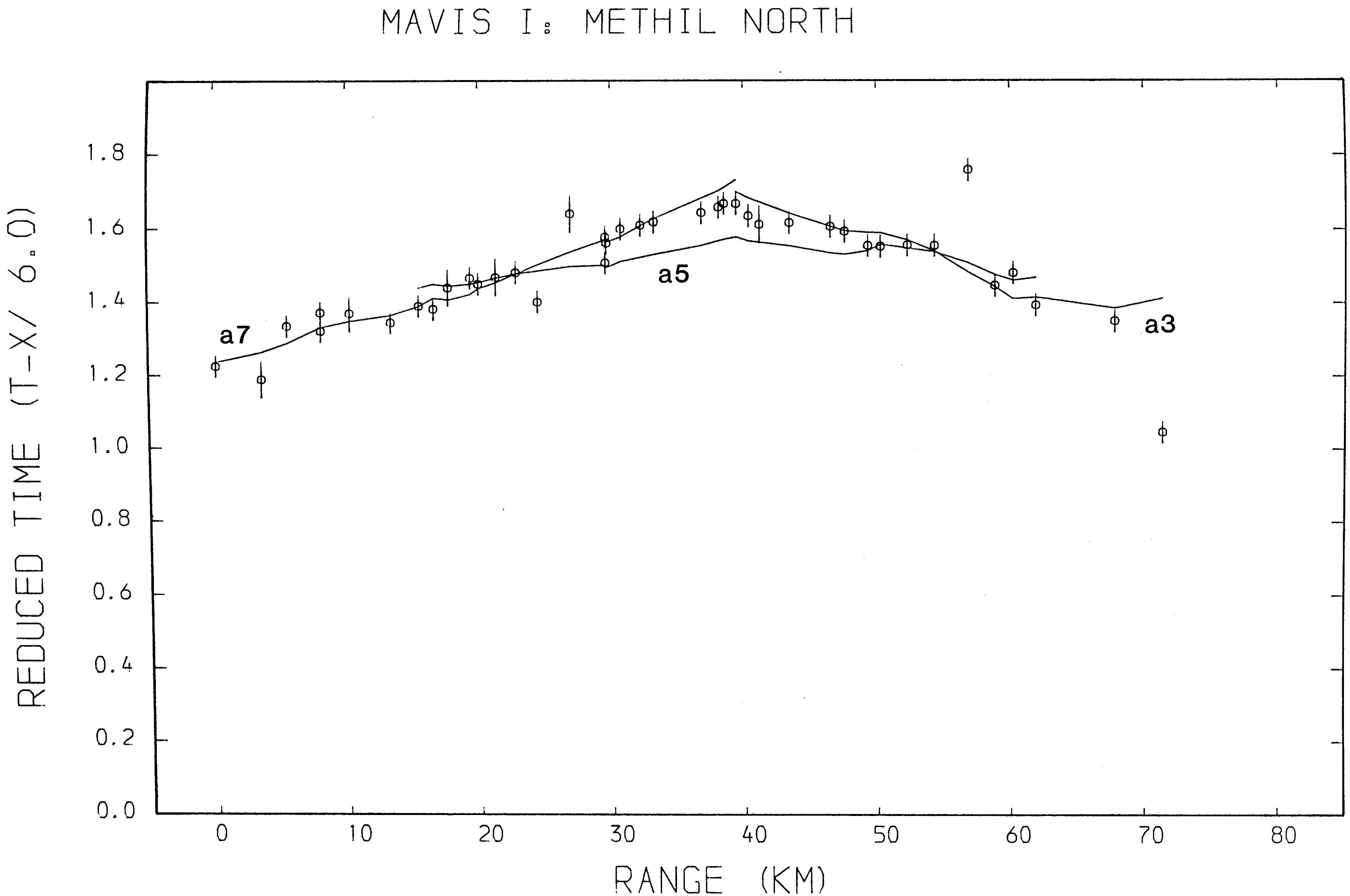

Fig.5.32 Observed (circles with error bars) and calculated (lines) travel-times; Methil shot. See Table 5.1 for classification of travel-time branches.

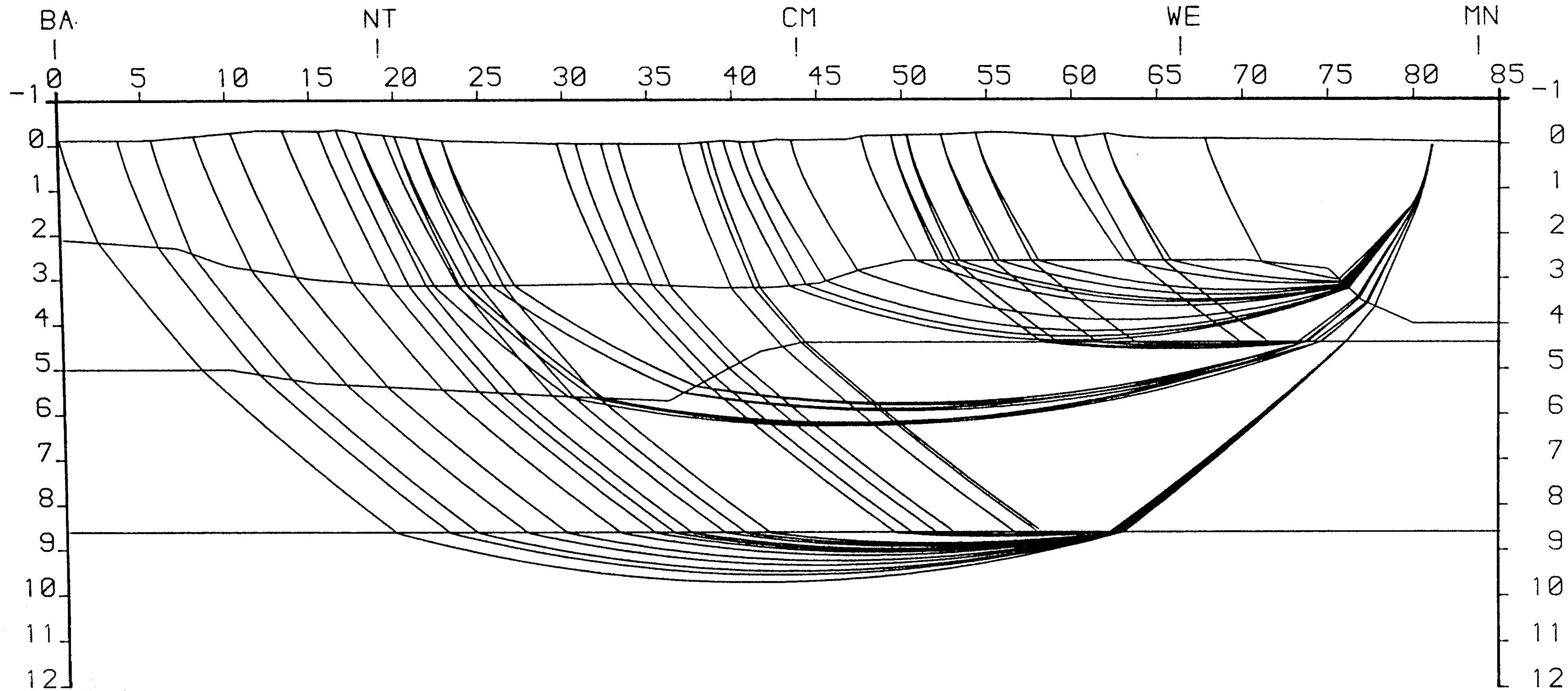

Fig.5.33 Ray-paths used in the calculation of travel-times shown in Fig.5.32. See Fig.5.23 for abbreviations. Scales are in km.

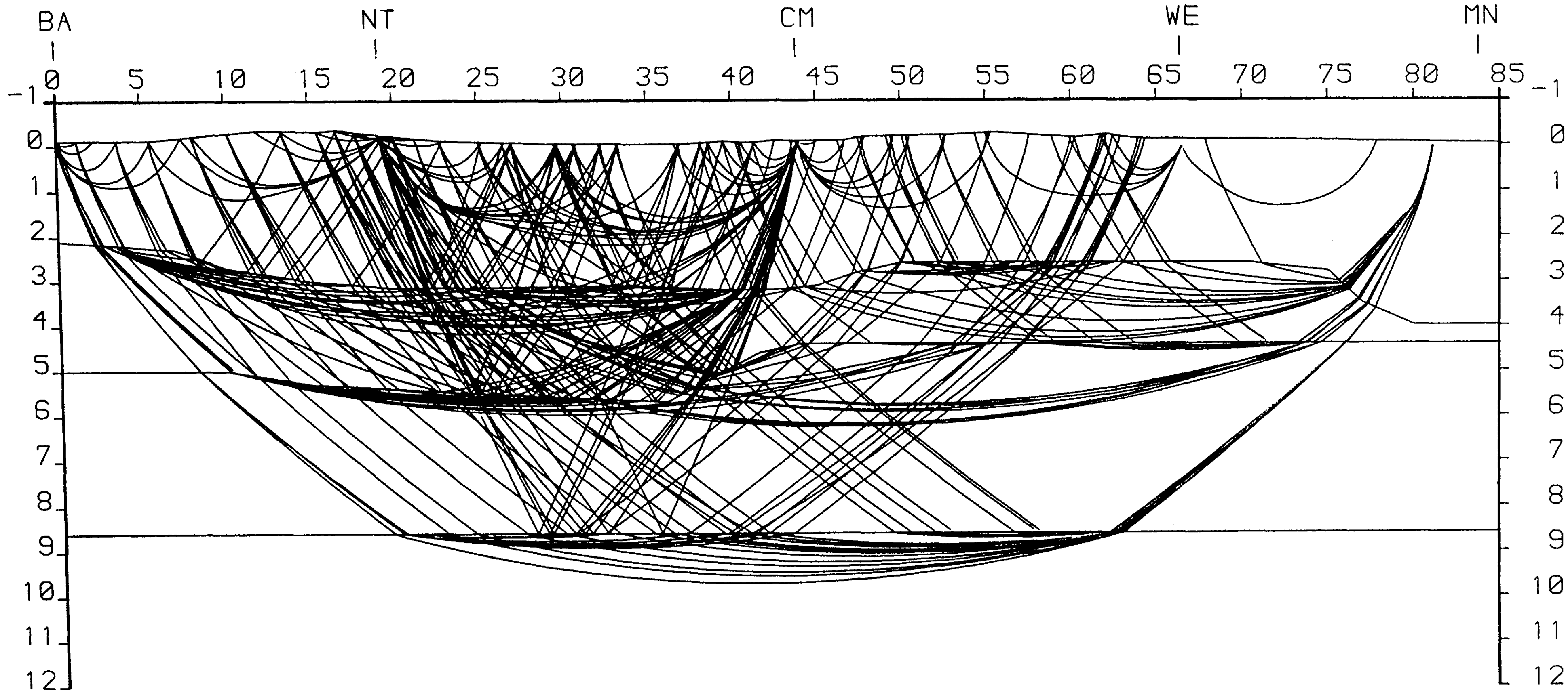

Fig.5.34 Ray-diagram showing all ray-paths used in the calculation of travel-times from MAVIS I north line sources. See Fig.5.23 for abbreviations. Scales are in km.

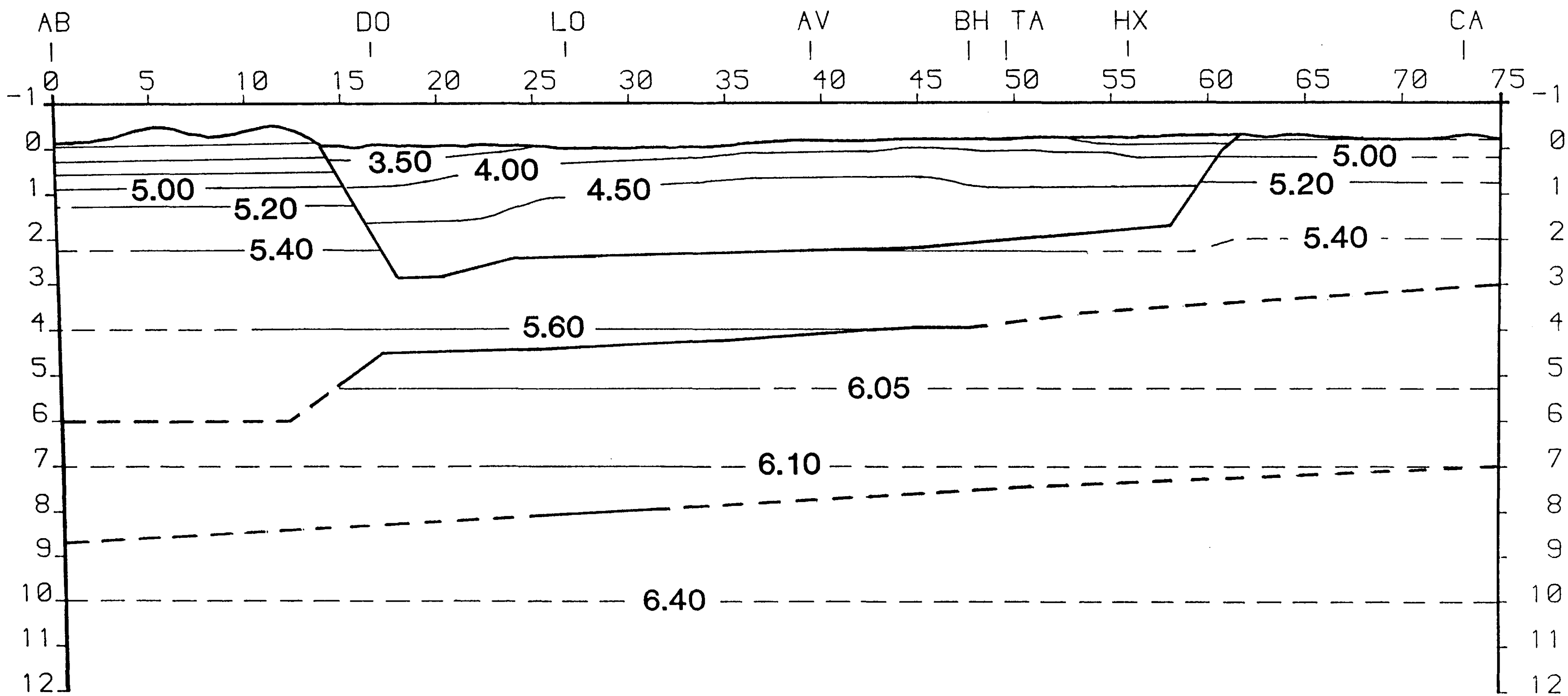

Fig.5.35 Ray-traced model of the MAVIS II line; AB - Aberuthven, DO - Dollar, LO - Longannet, AV - Avonbridge, BH - Blairhill, TA - Tamsloup, HX - Headless Cross, CA - Cairngryffe. Interfaces shown by thick lines, seismic velocity contours, in km/s, by thin lines. Scales are in km.

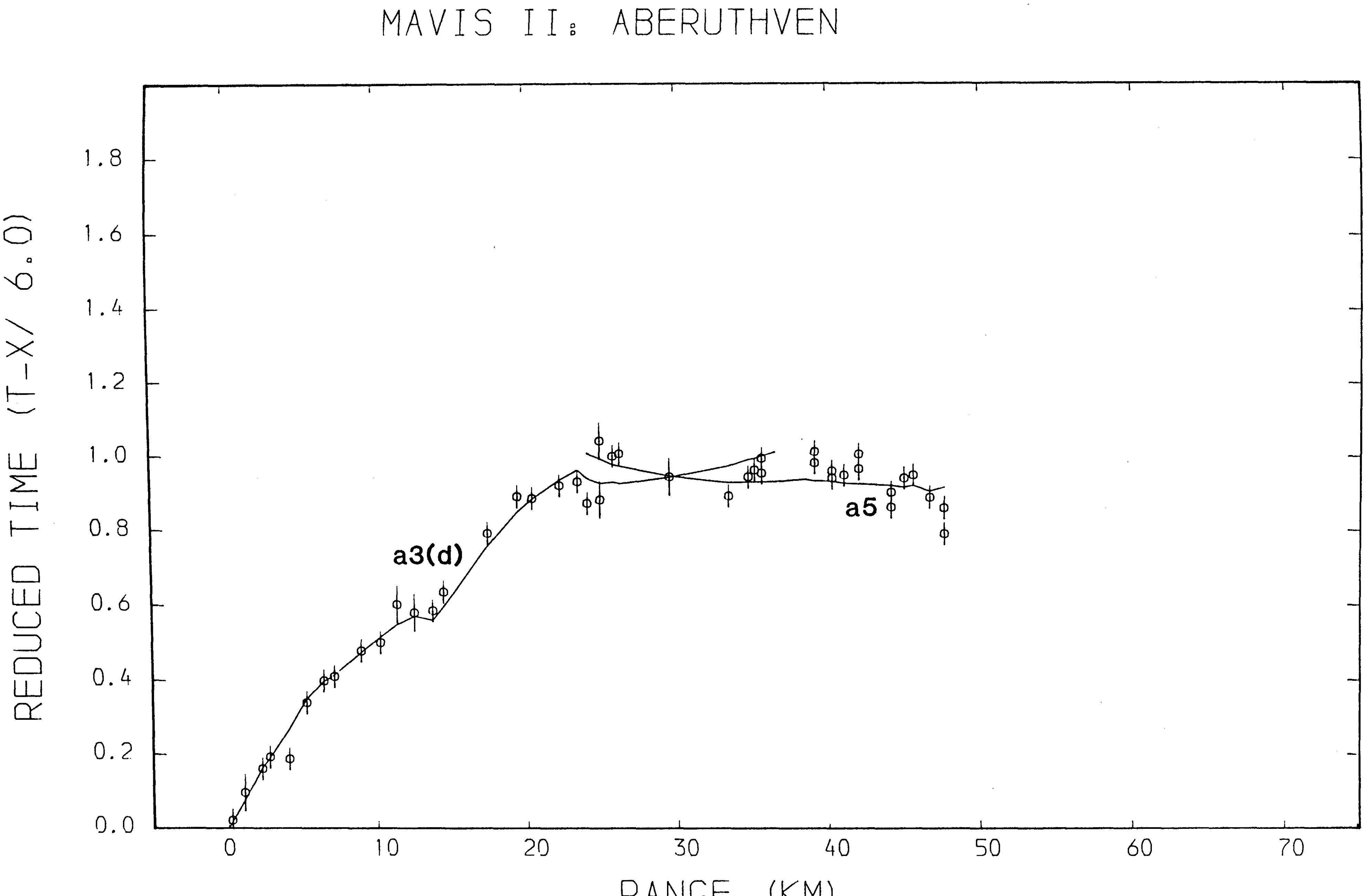

Fig.5.36 Observed (circles with error bars) and calculated (lines) travel-times; Aberuthven shot. See Table 5.1 for classification of travel-time branches.

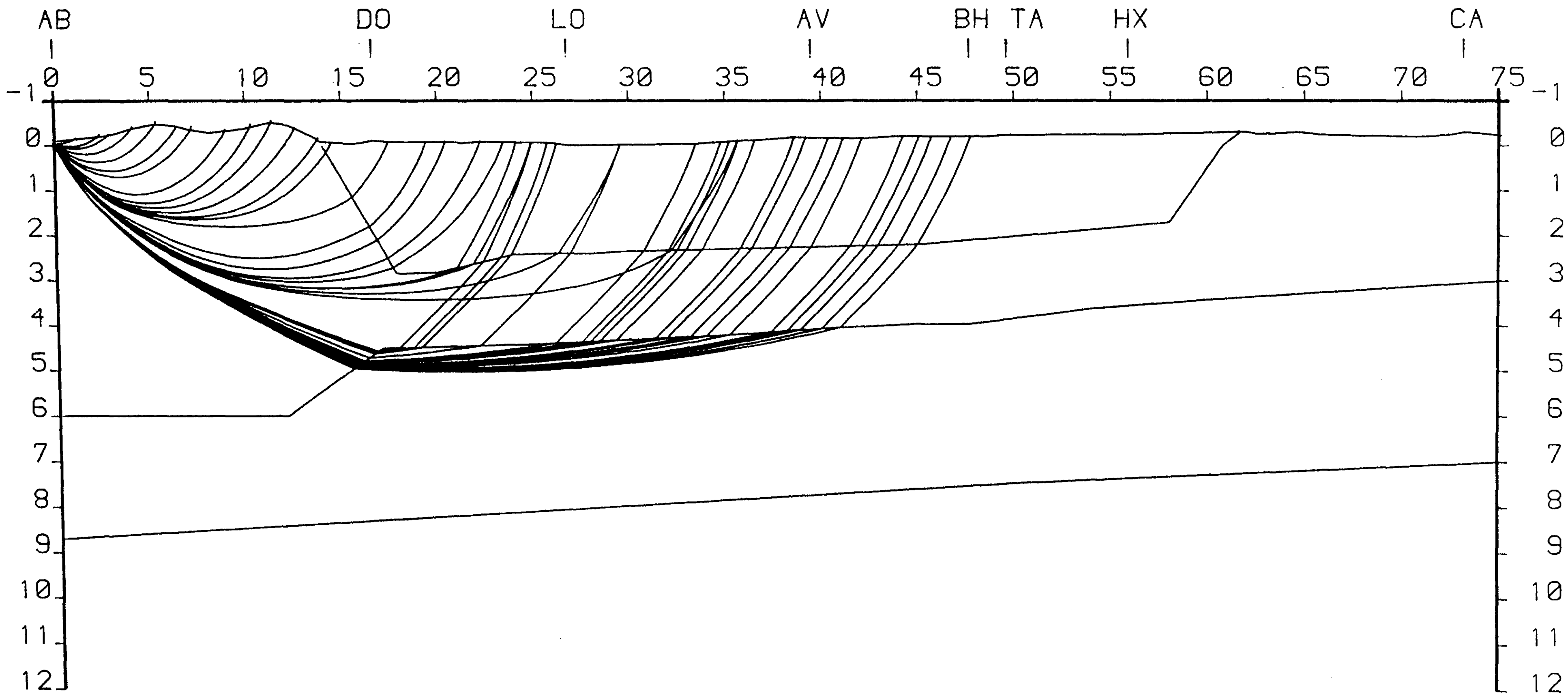

Fig.5.37 Ray-paths used in the calculation of travel-times shown in Fig.5.36. See Fig.5.35 for abbreviations. Scales are in km.

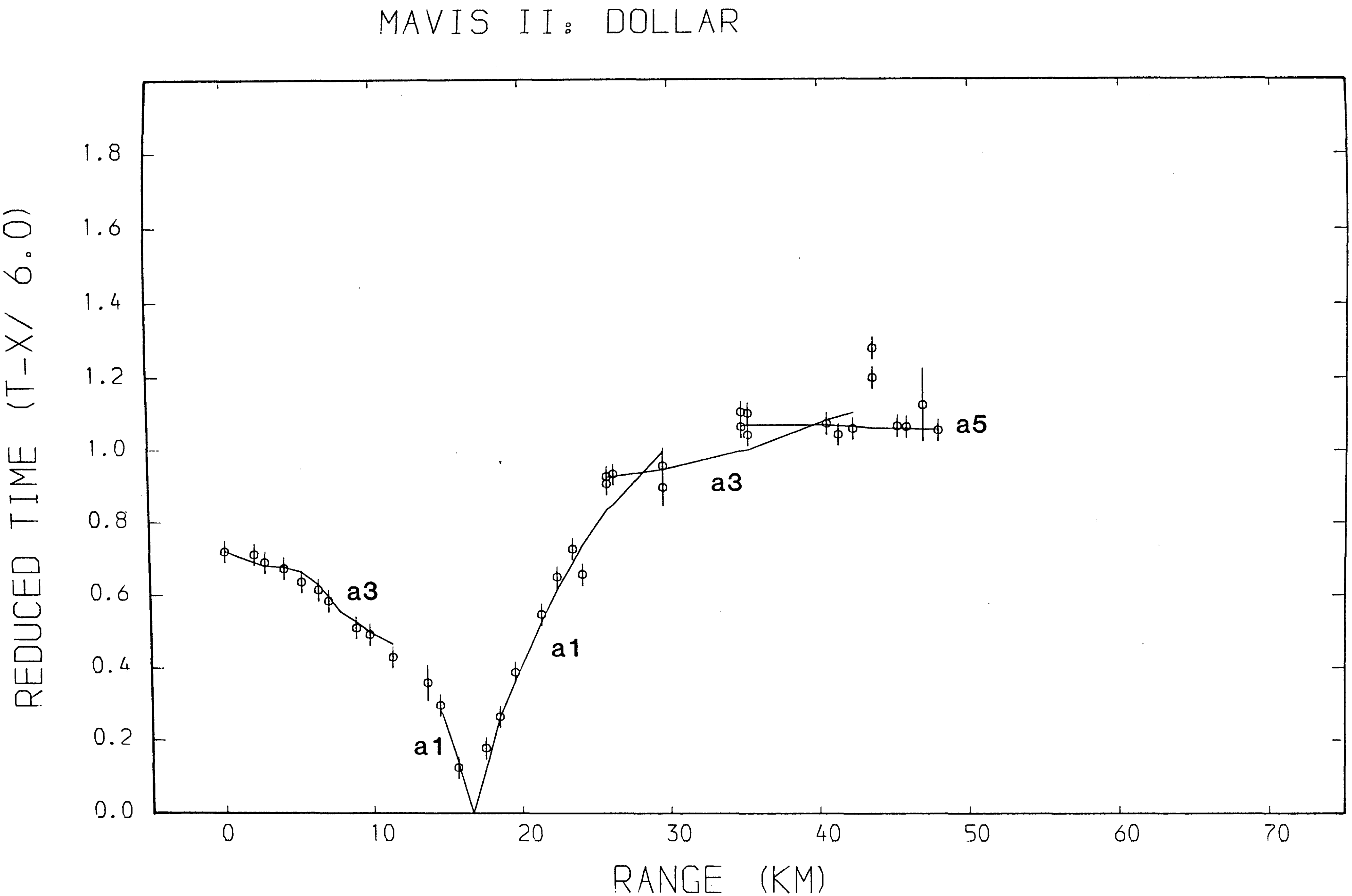

Fig.5.38 Observed (circles with error bars) and calculated (lines) travel-times; Dollar shot. See Table 5.1 for classification of travel-time branches.

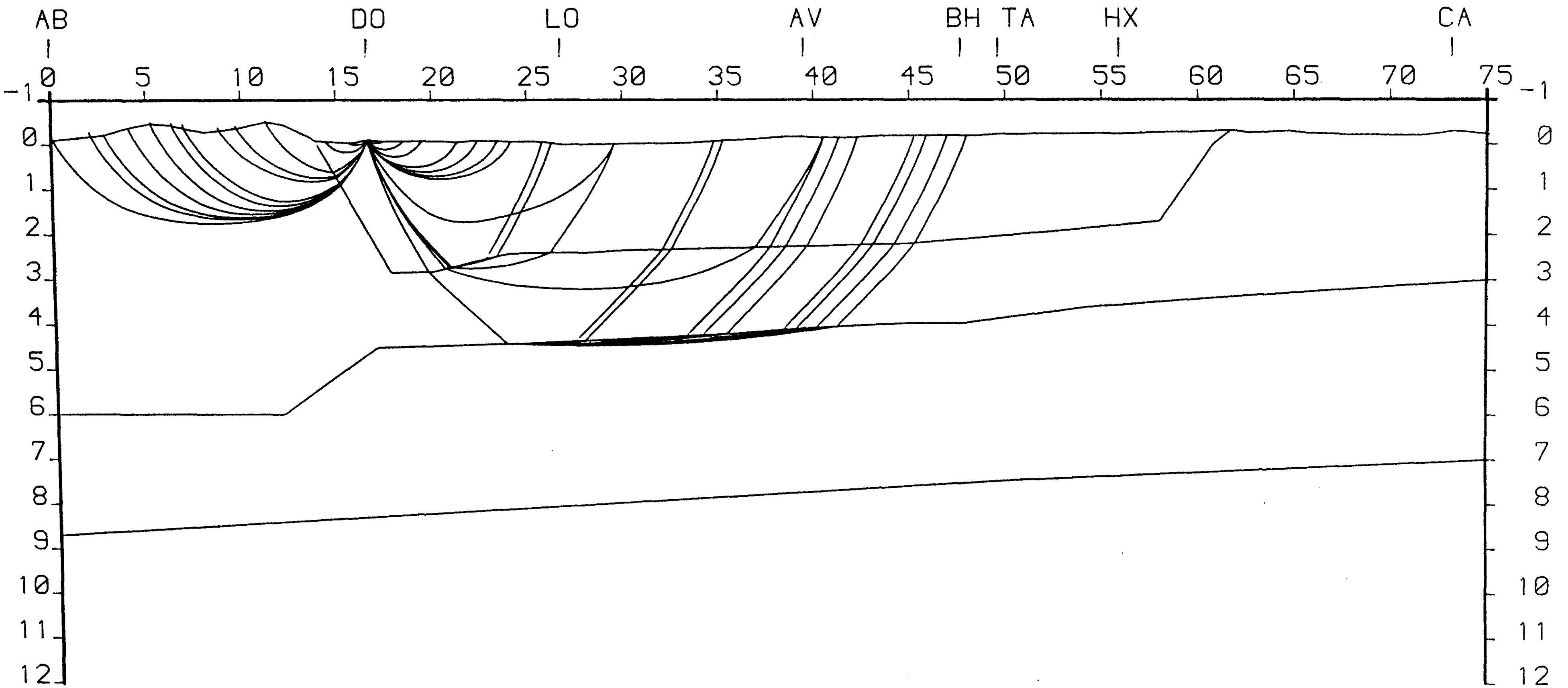

Fig.5.39 Ray-paths used in the calculation of travel-times shown in Fig.5.38. See Fig.5.35 for abbreviations. Scales are in km.

MAVIS II. LONGANNET

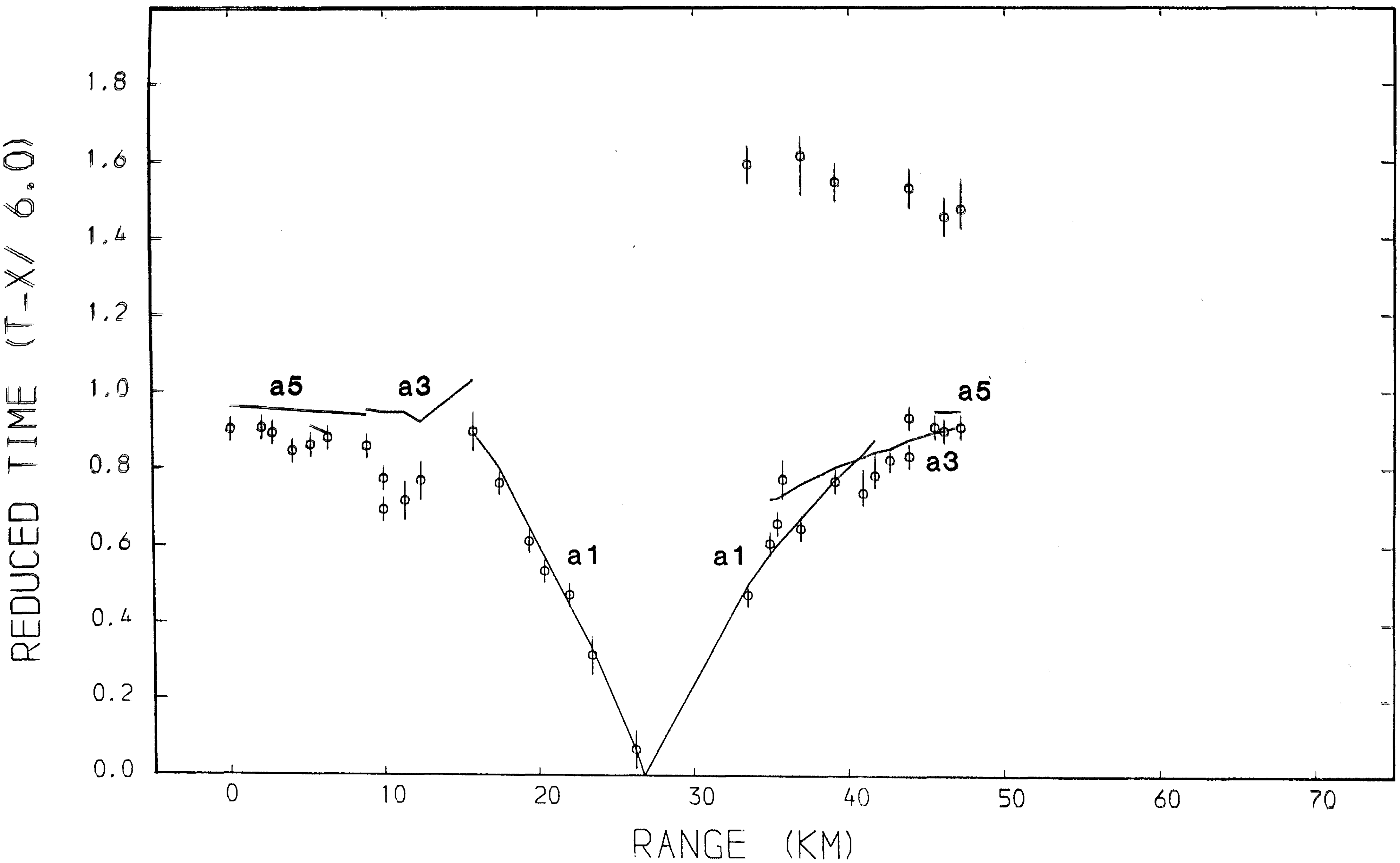

Fig.5.40 Observed (circles with error bars) and calculated (lines) travel-times; Longannet shot. See Table 5.1 for classification of travel-time branches.

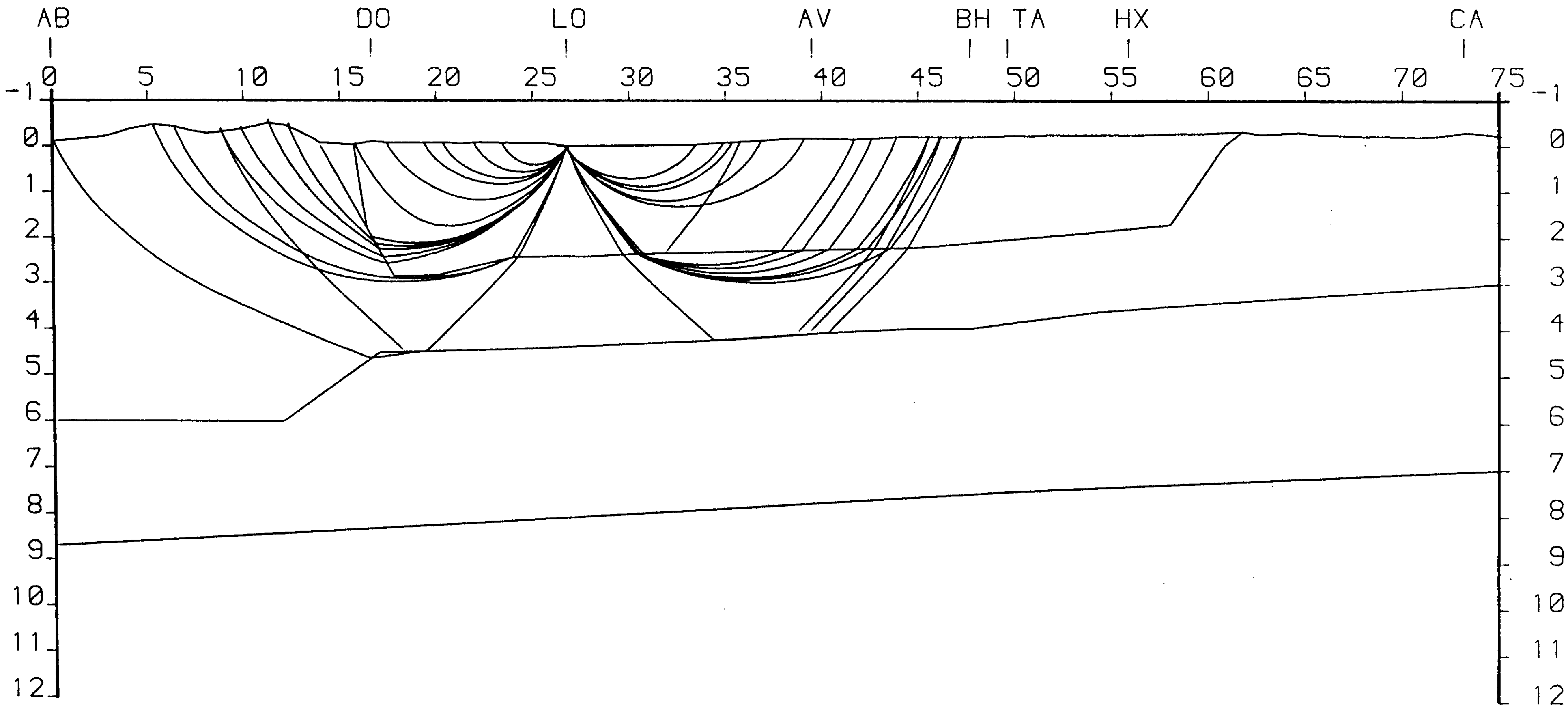

Fig.5.41 Ray-paths used in the calculation of travel-times shown in Fig.5.40. See Fig.5.35 for abbreviations. Scales are in km.

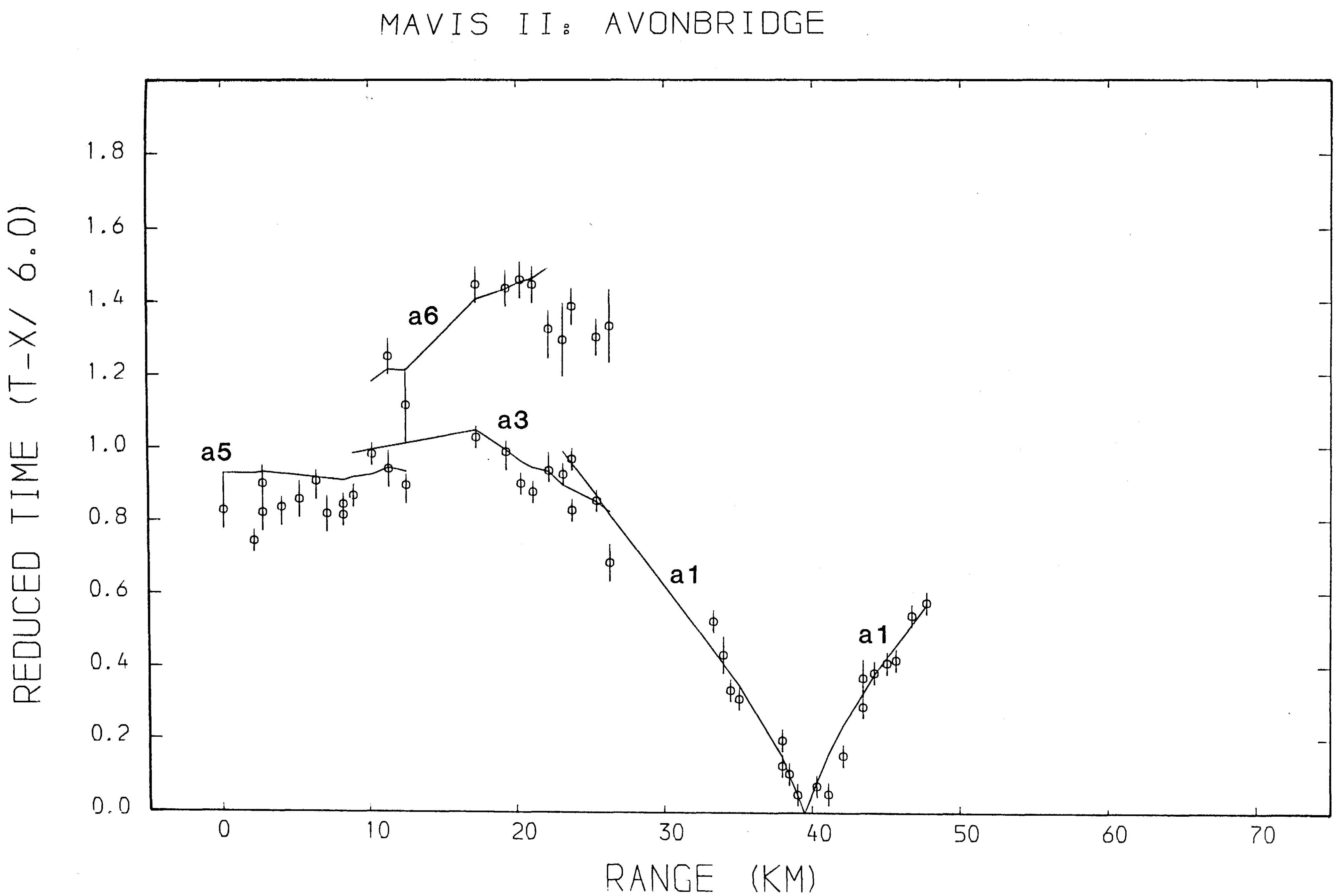

Fig.5.42 Observed (circles with error bars) and calculated (lines) travel-times; Avonbridge shot. See Table 5.1 for classification of travel-time branches.

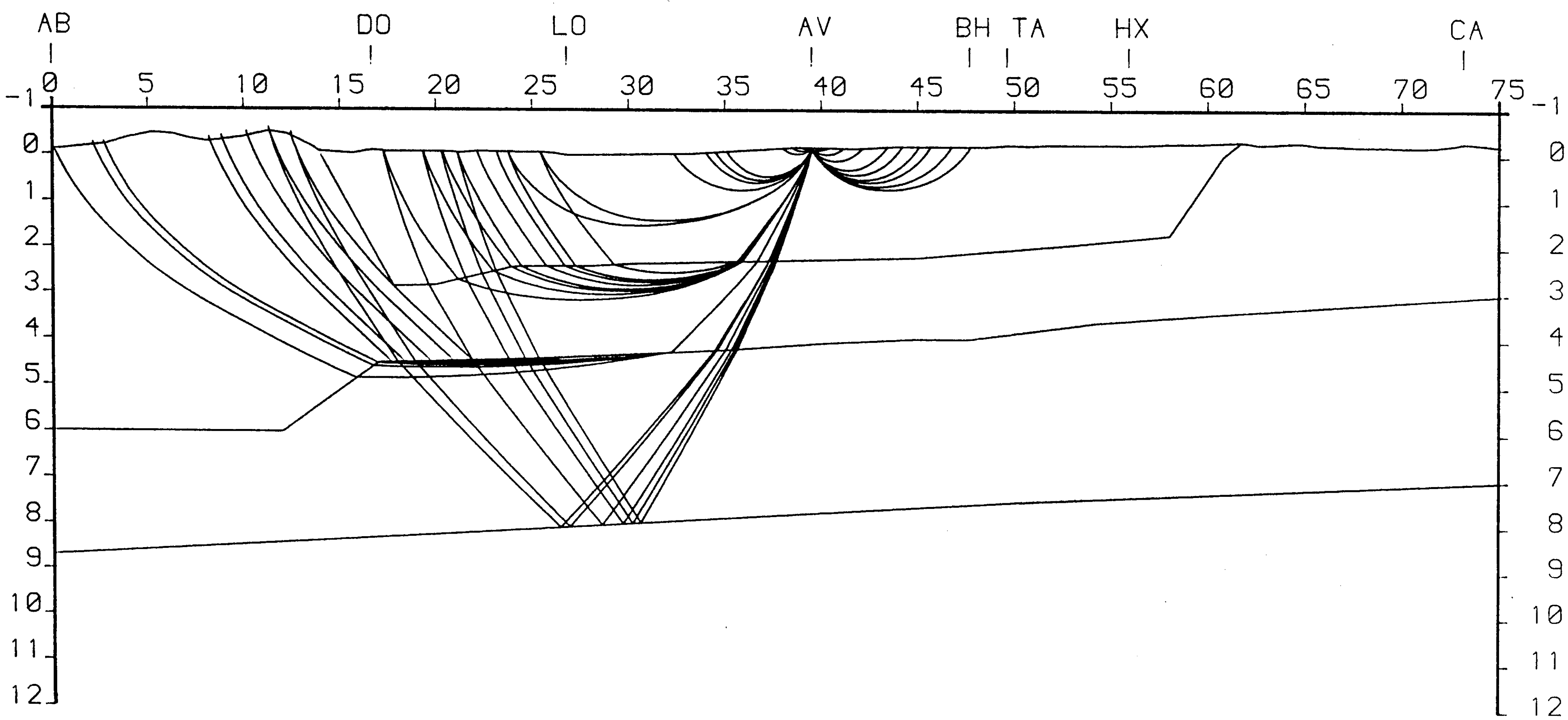

Fig.5.43 Ray-paths used in the calculation of travel-times shown in Fig.5.42. See Fig.5.35 for abbreviations. Scales are in km.

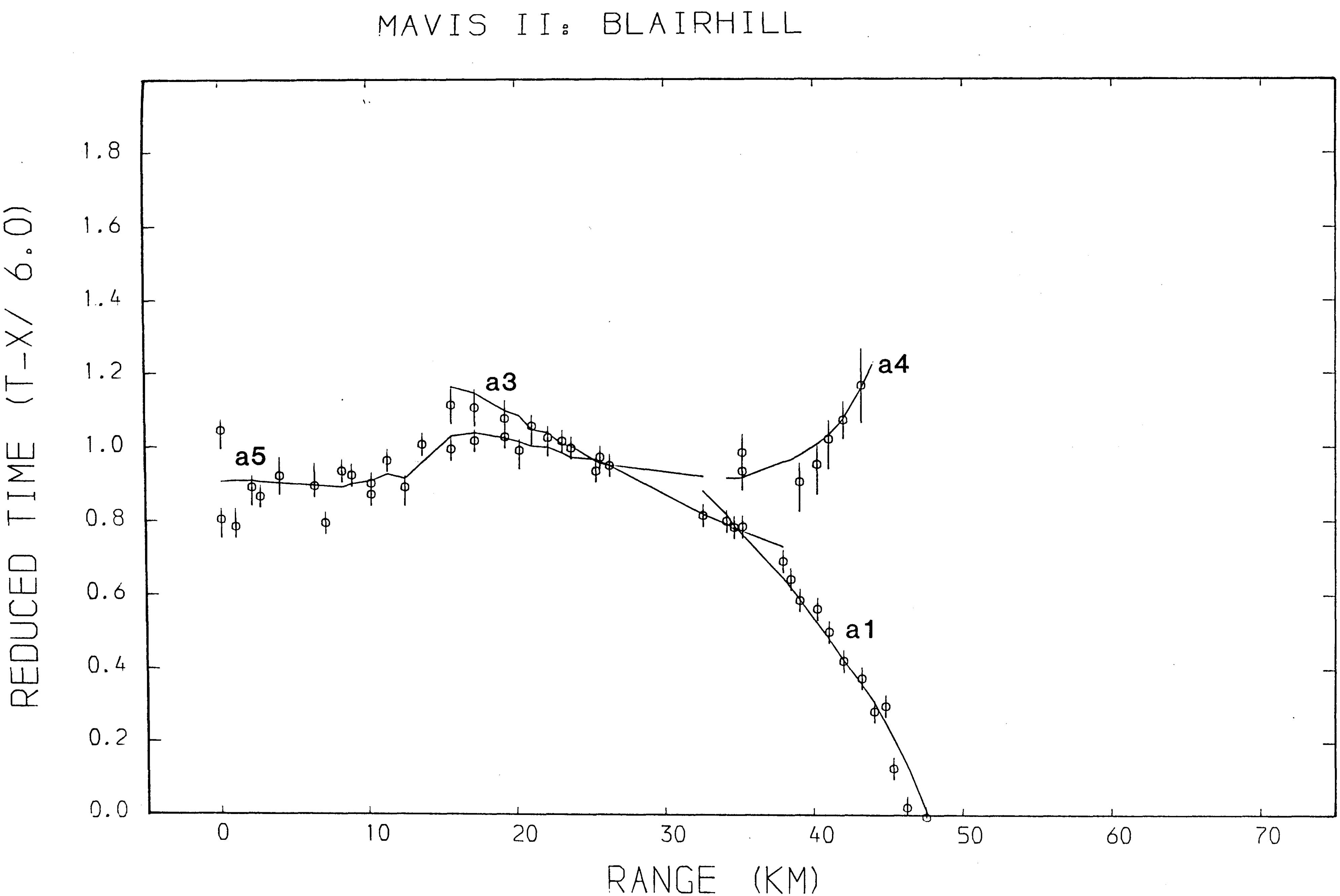

Fig.5.44 Observed (circles with error bars) and calculated (lines) travel-times; Blairhill shot. See Table 5.1 for classification of travel-time branches.

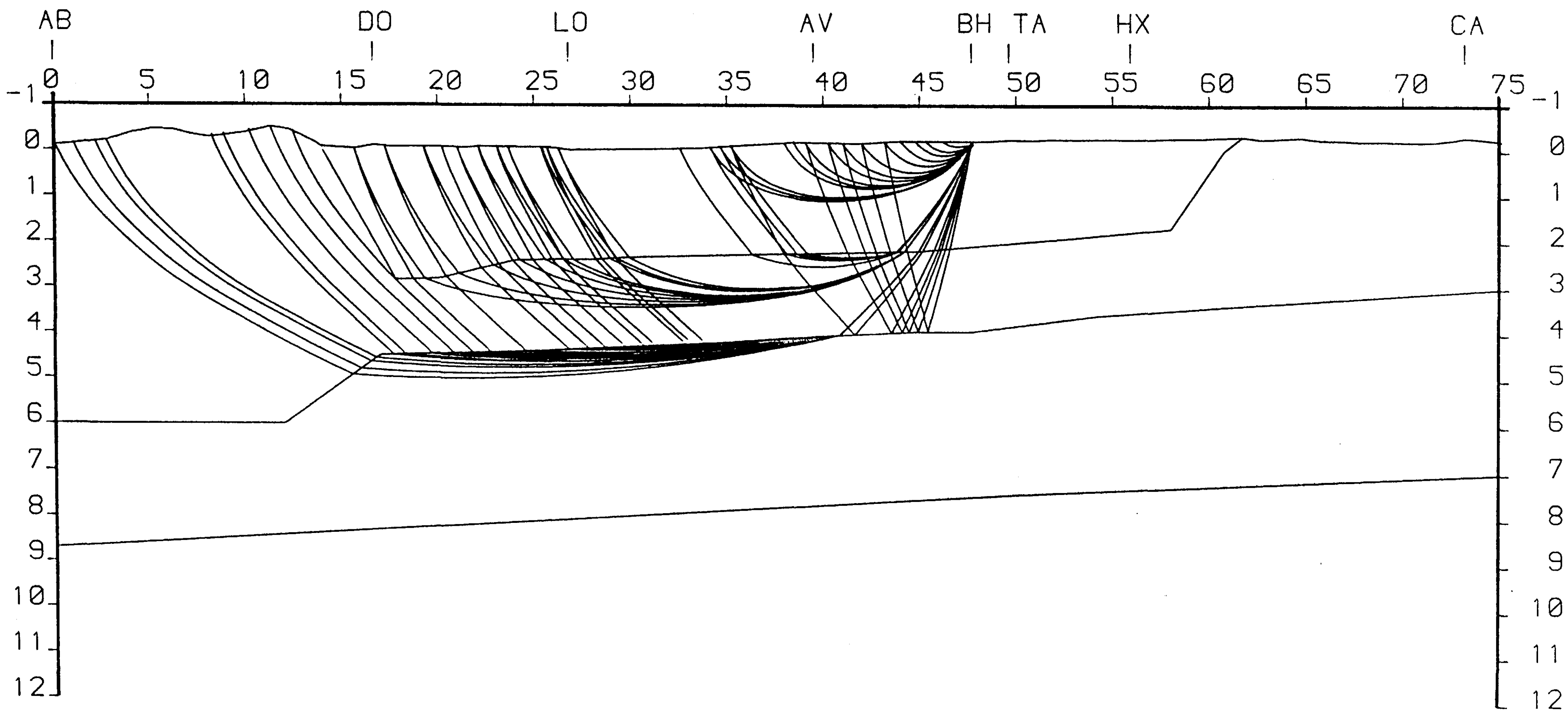

Fig.5.45 Ray-paths used in the calculation of travel-times shown in Fig.5.44. See Fig.5.35 for abbreviations. Scales are in km.

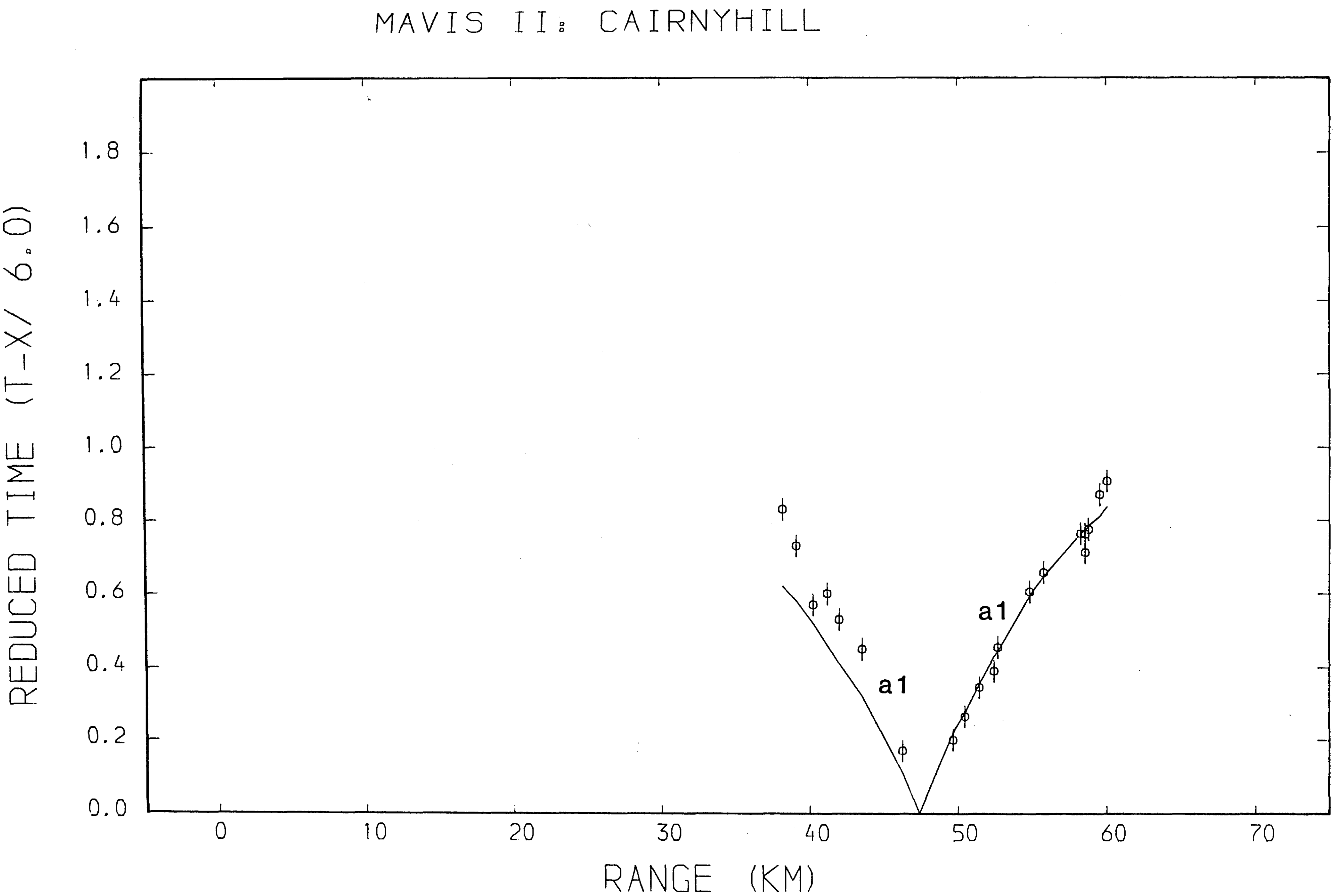

Fig.5.46 Observed (circles with error bars) and calculated (lines) travel-times; Cairnyhill shot. See Table 5.1 for classification of travel-time branches.

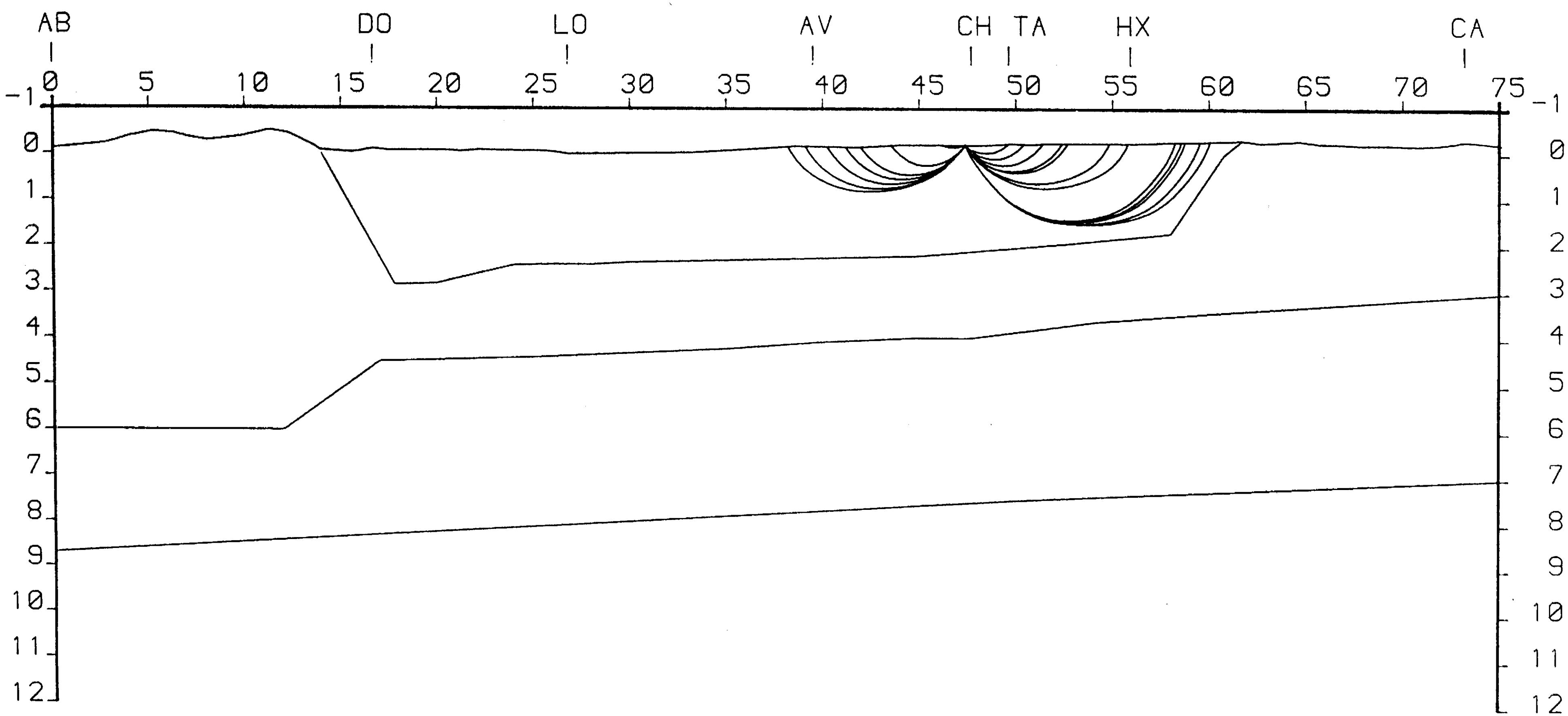

Fig.5.47 Ray-paths used in the calculation of travel-times shown in Fig.5.46. CH - Cairnyhill, see Fig.5.35 for other abbreviations. Scales are in km.

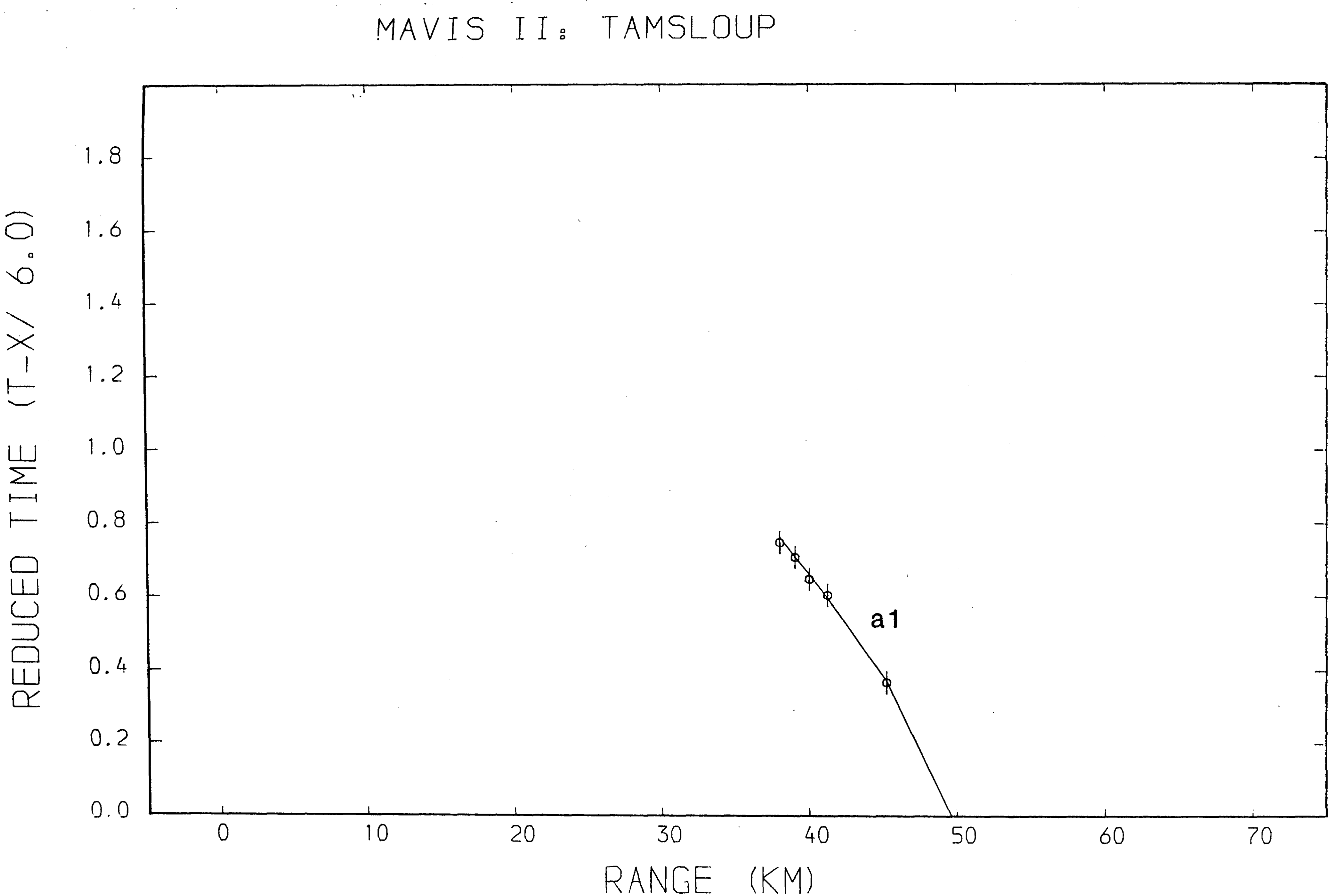

Fig.5.48 Observed (circles with error bars) and calculated (lines) travel-times; Tamsloup shot. See Table 5.1 for classification of travel-time branches.

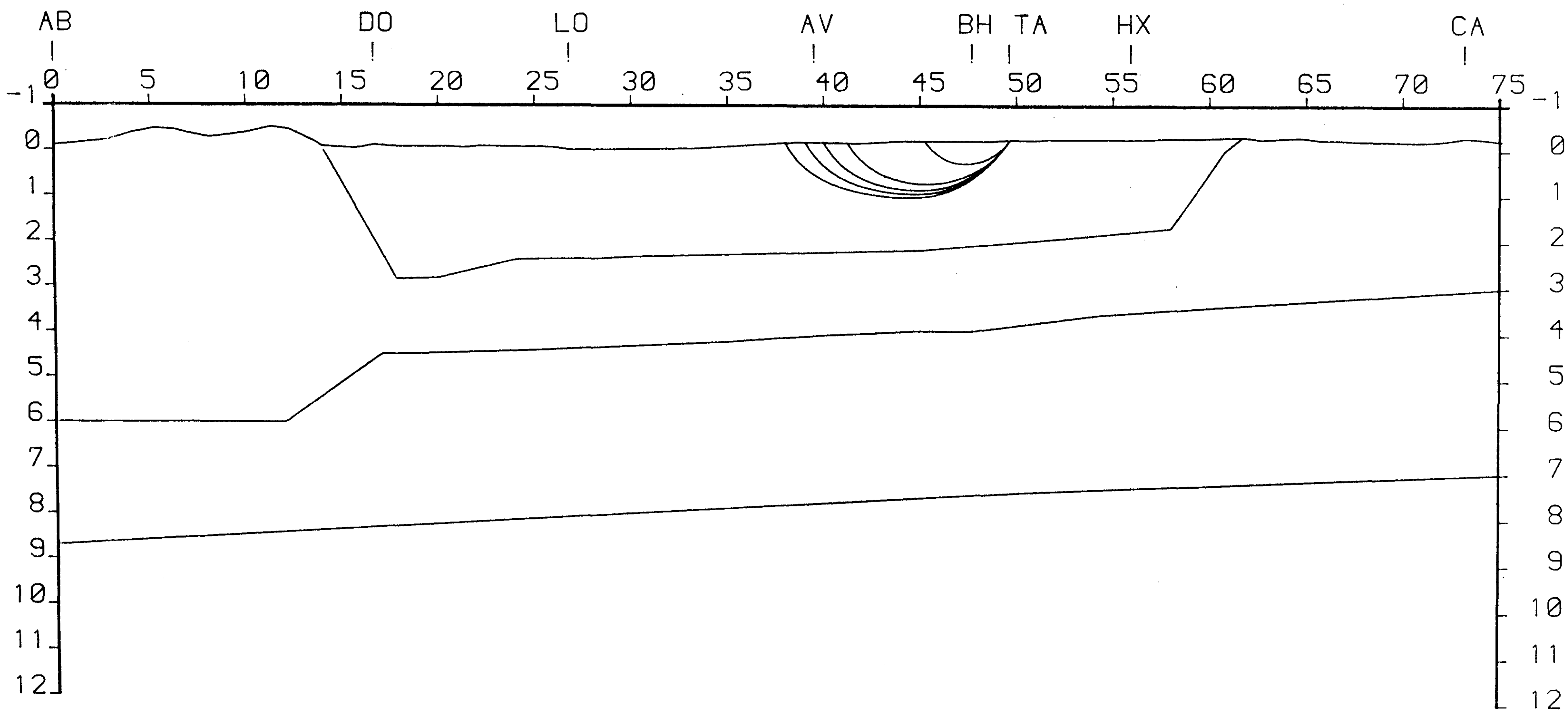

Fig.5.49 Ray-paths used in the calculation of travel-times shown in Fig.5.48. See Fig.5.35 for abbreviations. Scales are in km.

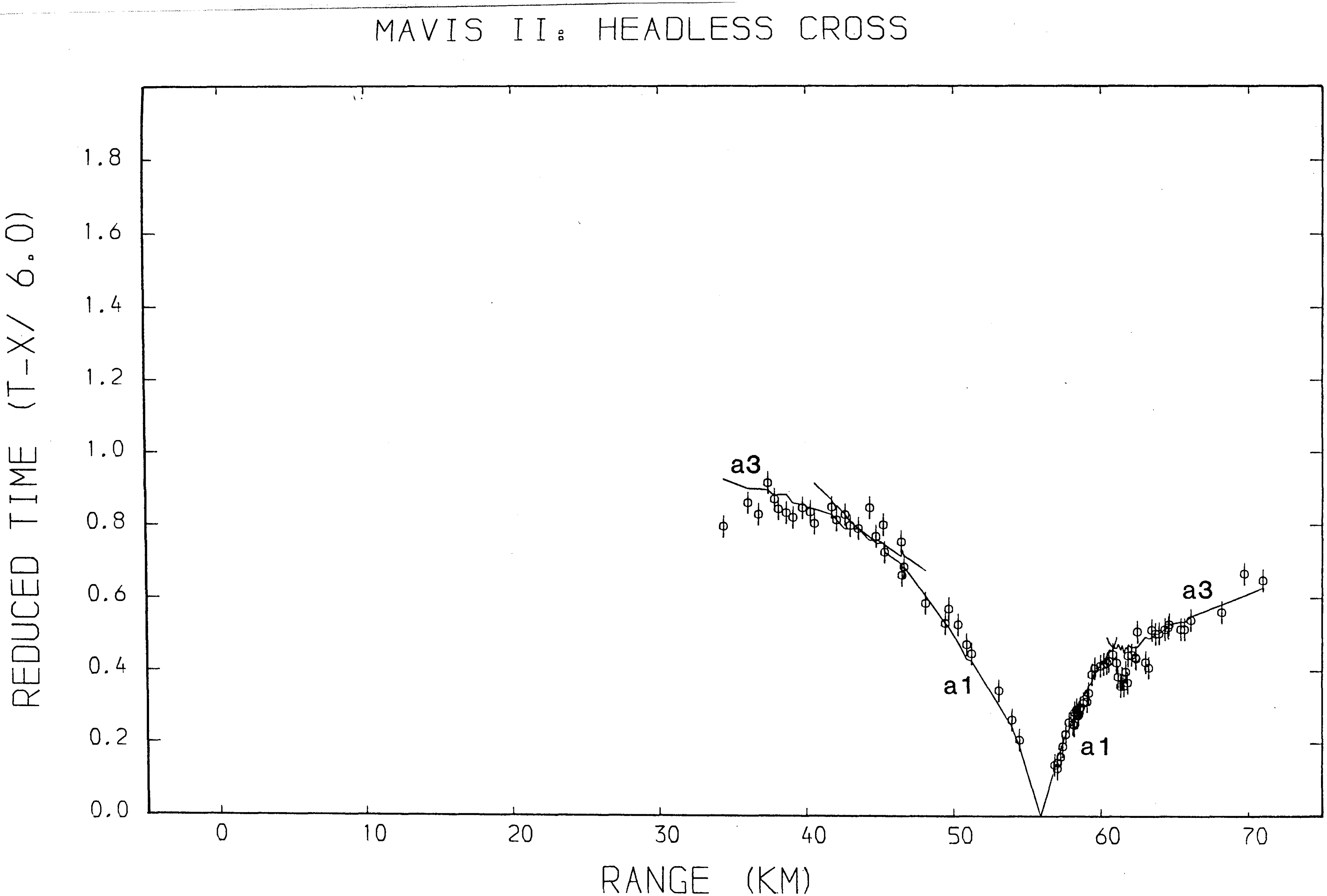

Fig.5.50 Observed (circles with error bars) and calculated (lines) travel-times; Headless Cross shot. See Table 5.1 for classification of travel-time branches.

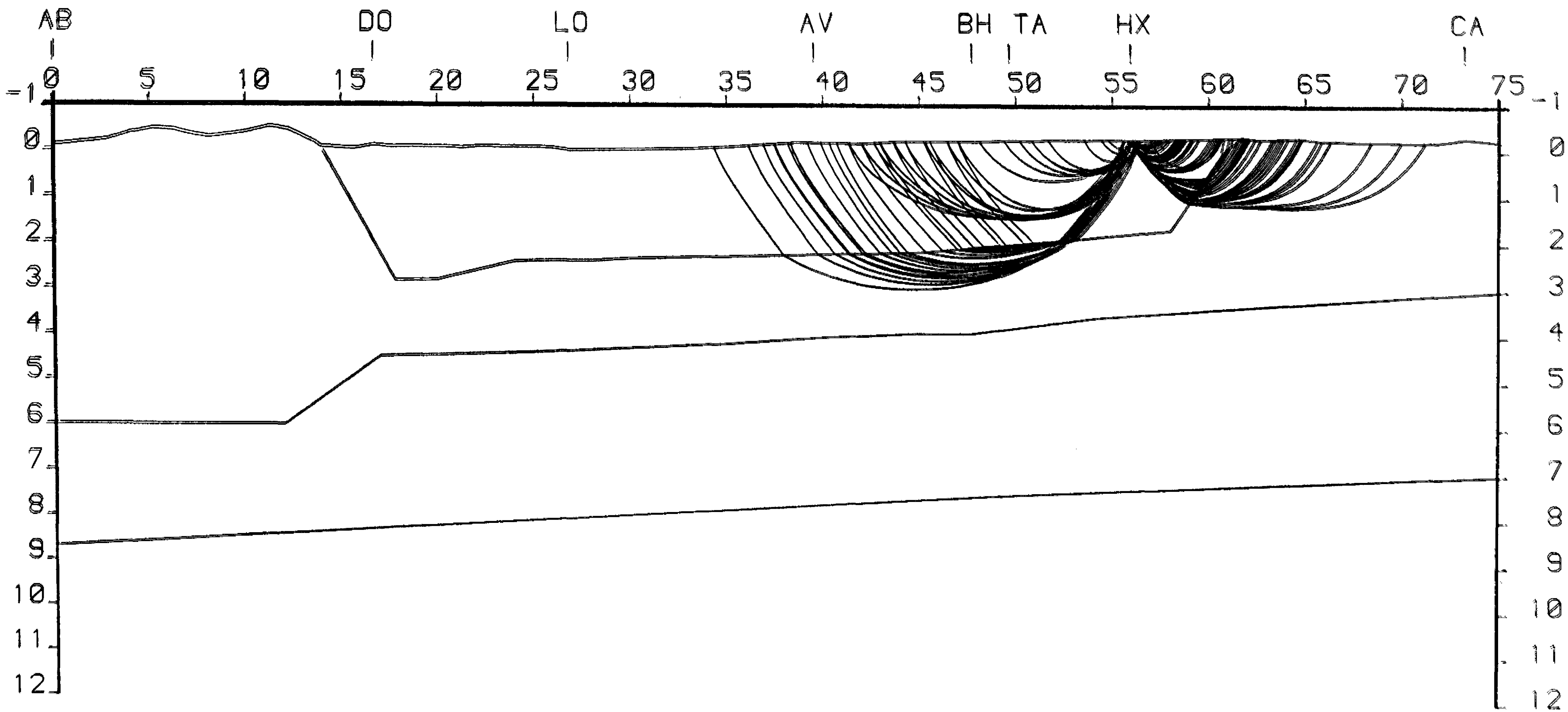

Fig.5.51 Ray-paths used in the calculation of travel-times shown in Fig.5.50. See Fig.5.35 for abbreviations. Scales are in km.

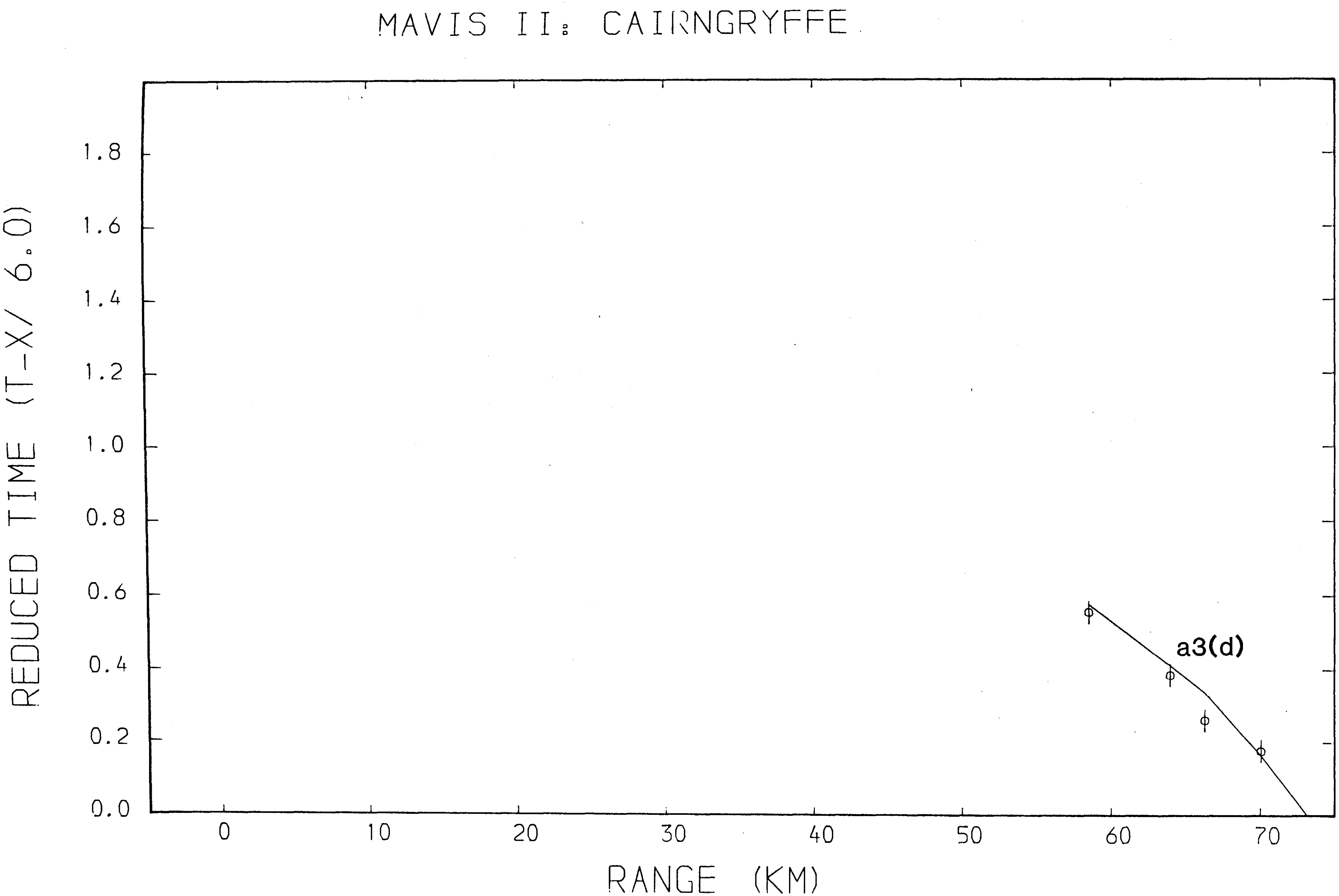

Fig.5.52 Observed (circles with error bars) and calculated (lines) travel-times; Cairngryffe shot. See Table 5.1 for classification of travel-time branches.

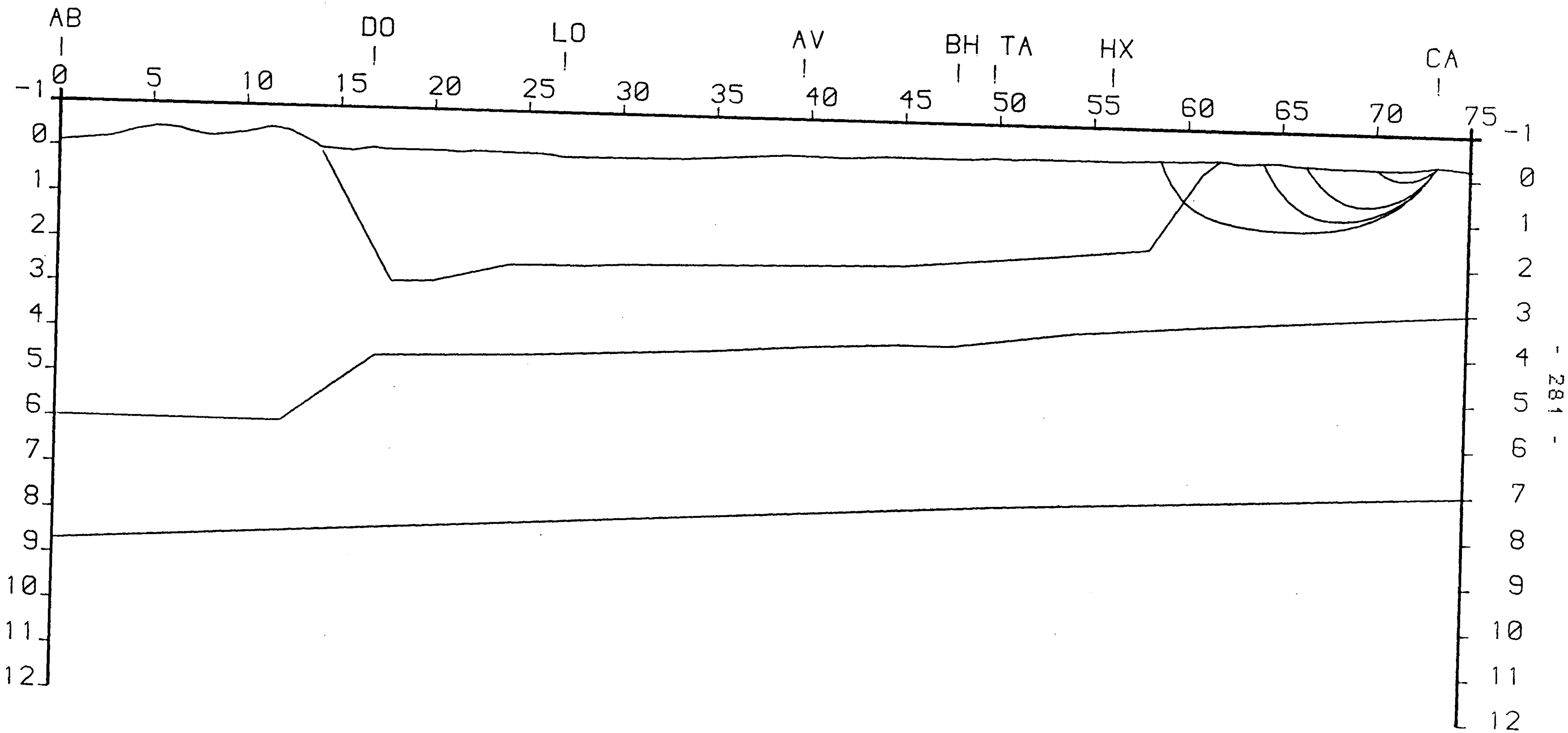

Fig.5.53 Ray-paths used in the calculation of travel-times shown in Fig.5.52. See Fig.5.35 for abbreviations. Scales are in km.

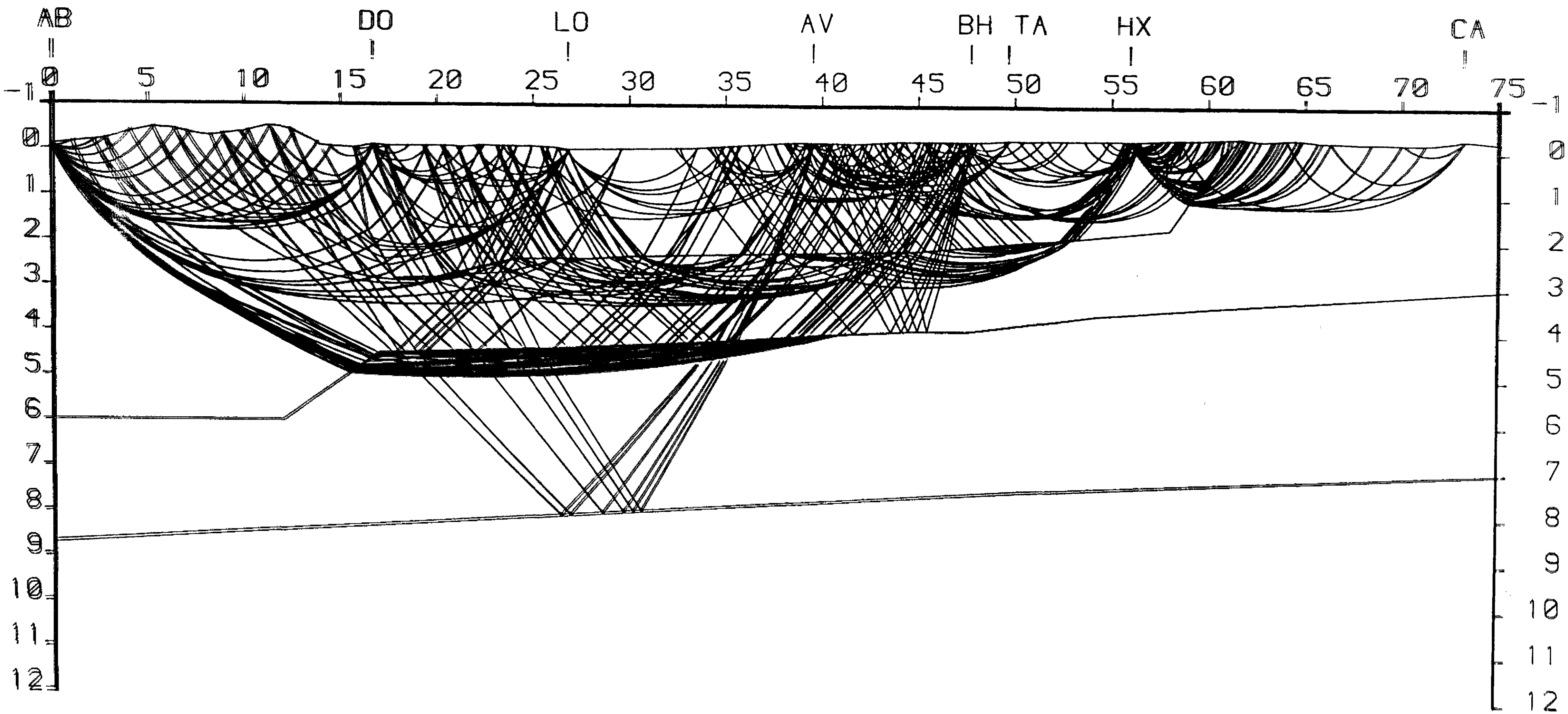

Fig.5.54 Ray-diagram showing all ray-paths used in the calculation of travel-times from MAVIS II line sources. See Fig.5.35 for abbreviations. Scales are in km.

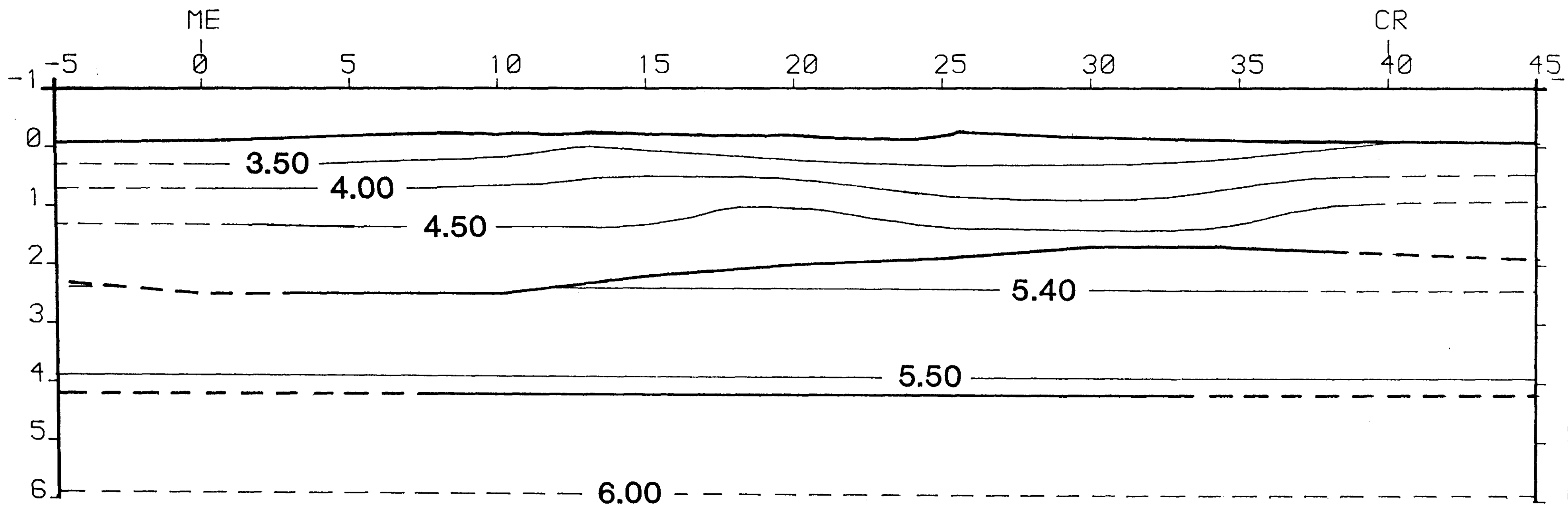

Fig.5.55 Ray-traced model of the Sola north line; ME - Medrox, CR - Craigpark. Interfaces shown by thick lines, seismic velocity contours, in km/s, by thin lines. Scales are in km.

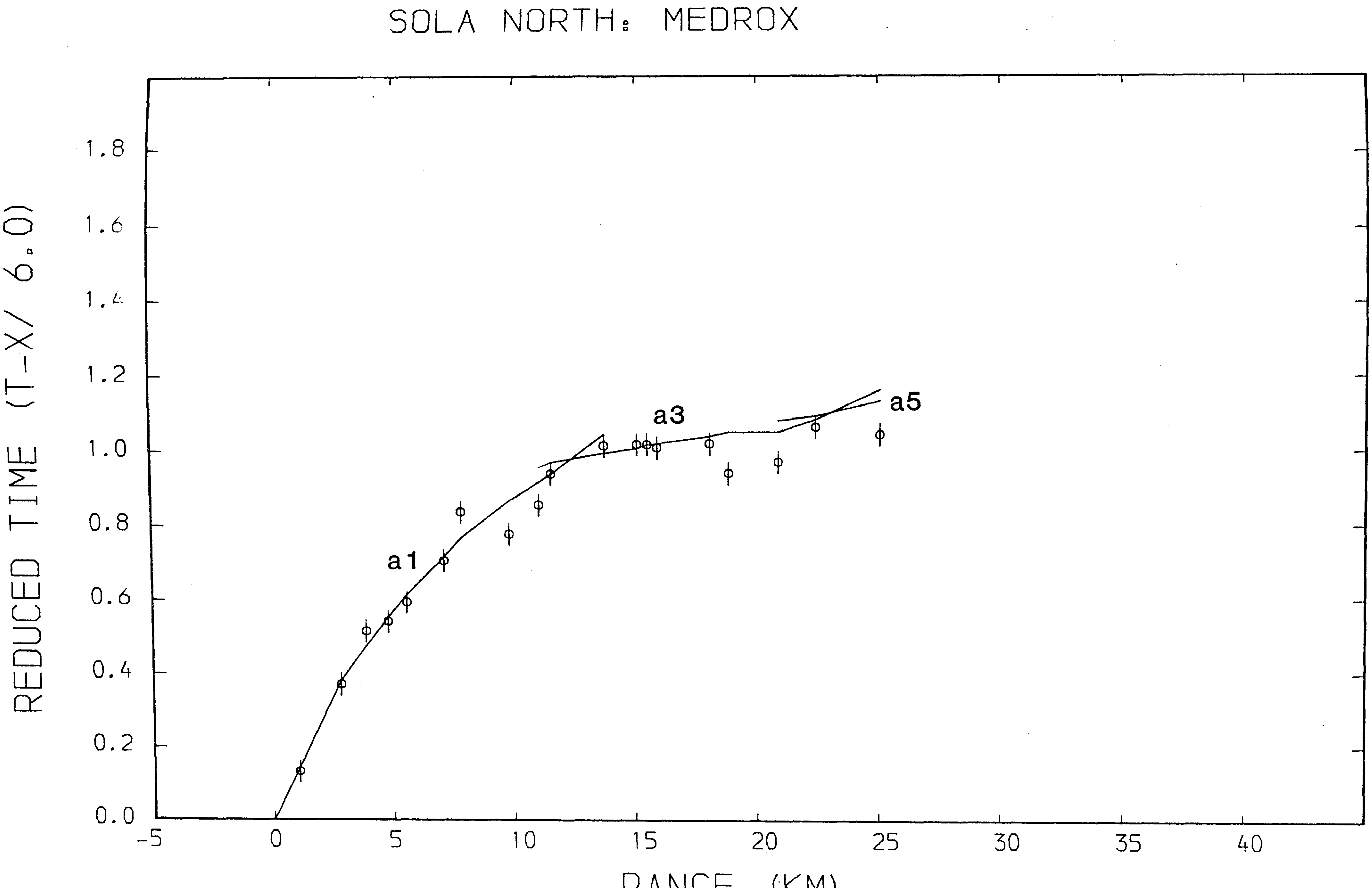

Fig.5.56 Observed (circles with error bars) and calculated (lines) travel-times; Medrox shot. See Table 5.1 for classification of travel-time branches.

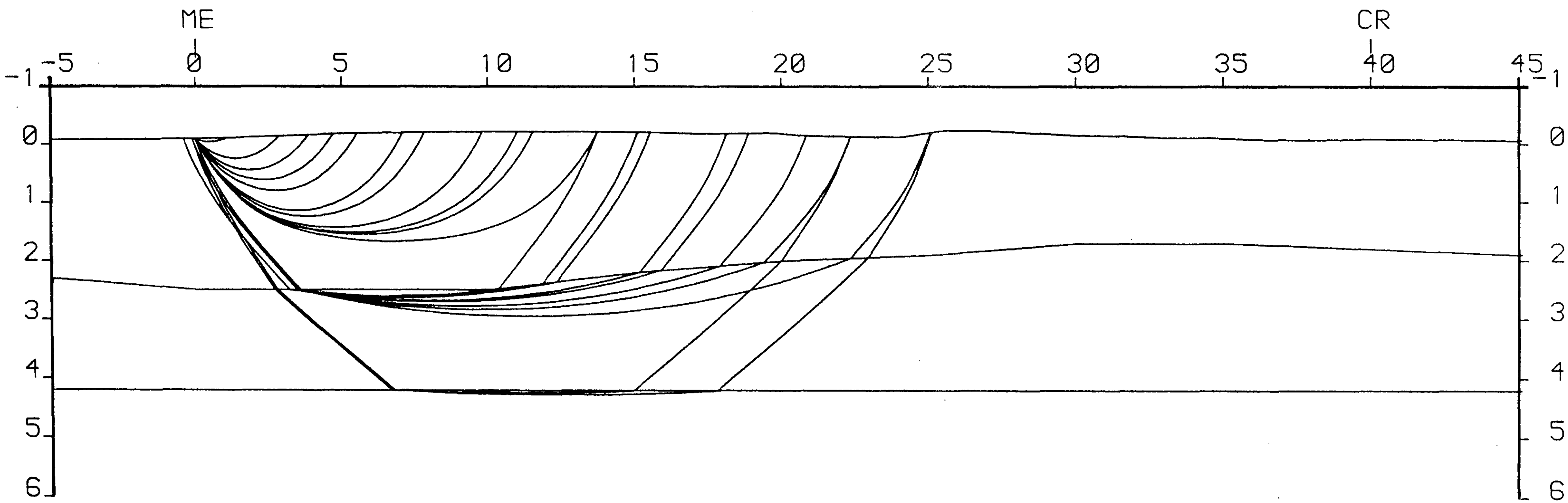

Fig.5.57 Ray-paths used in the calculation of travel-times shown in Fig.5.56. See Fig.5.55 for abbreviations. Scales are in km.

SOLA NORTH: CRAIGPARK

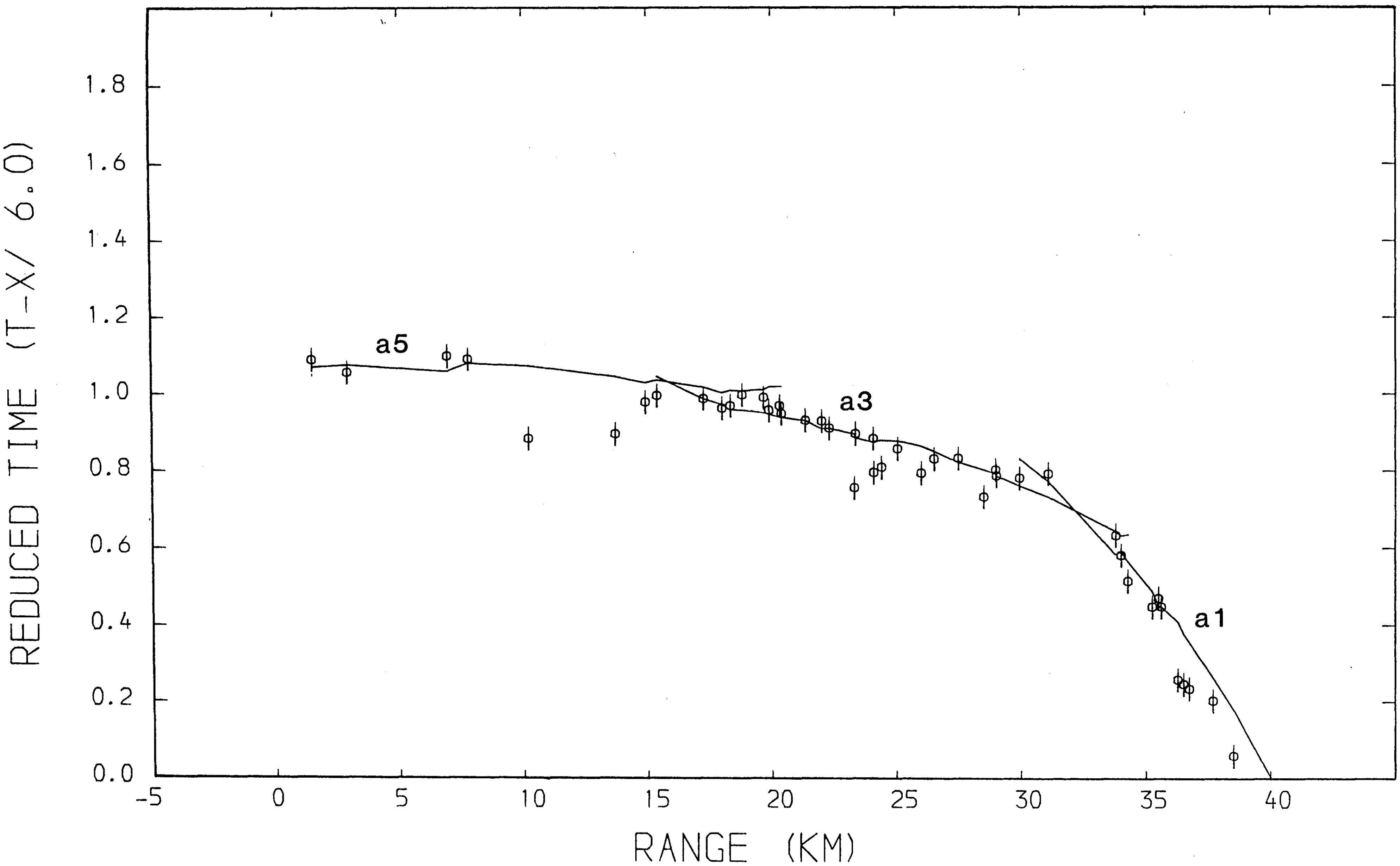

Fig.5.58 Observed (circles with error bars) and calculated (lines) travel-times; Craigpark shot. See Table 5.1 for classification of travel-time branches.

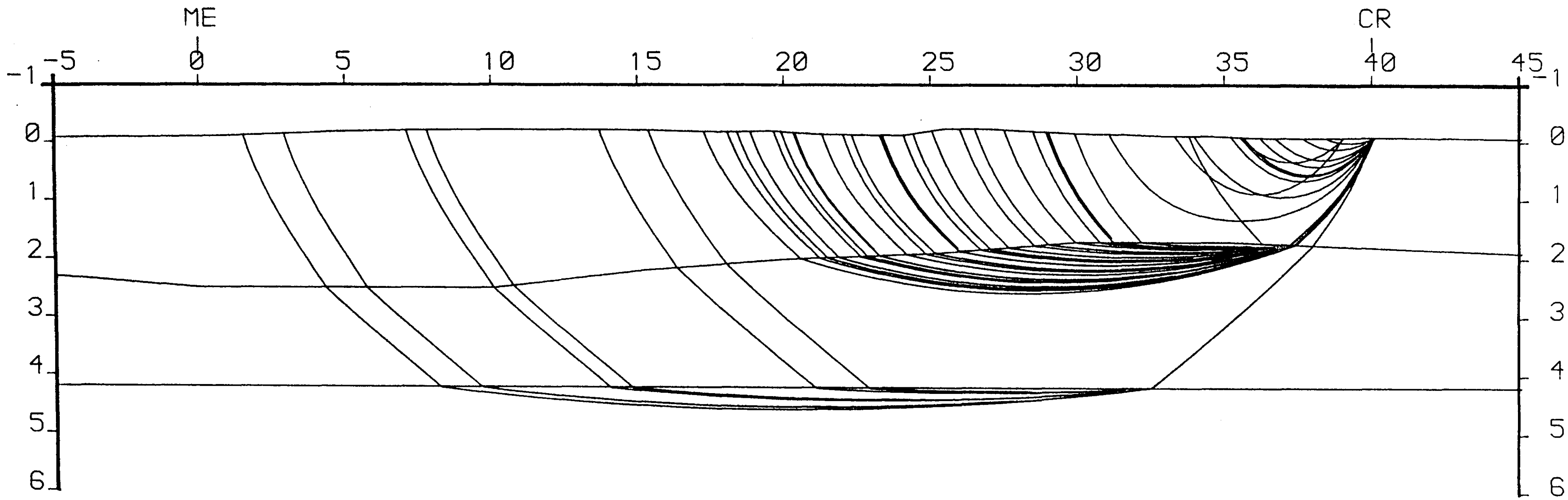

Fig.5.59 Ray-paths used in the calculation of travel-times shown in Fig.5.58. See Fig.5.55 for abbreviations. Scales are in km.

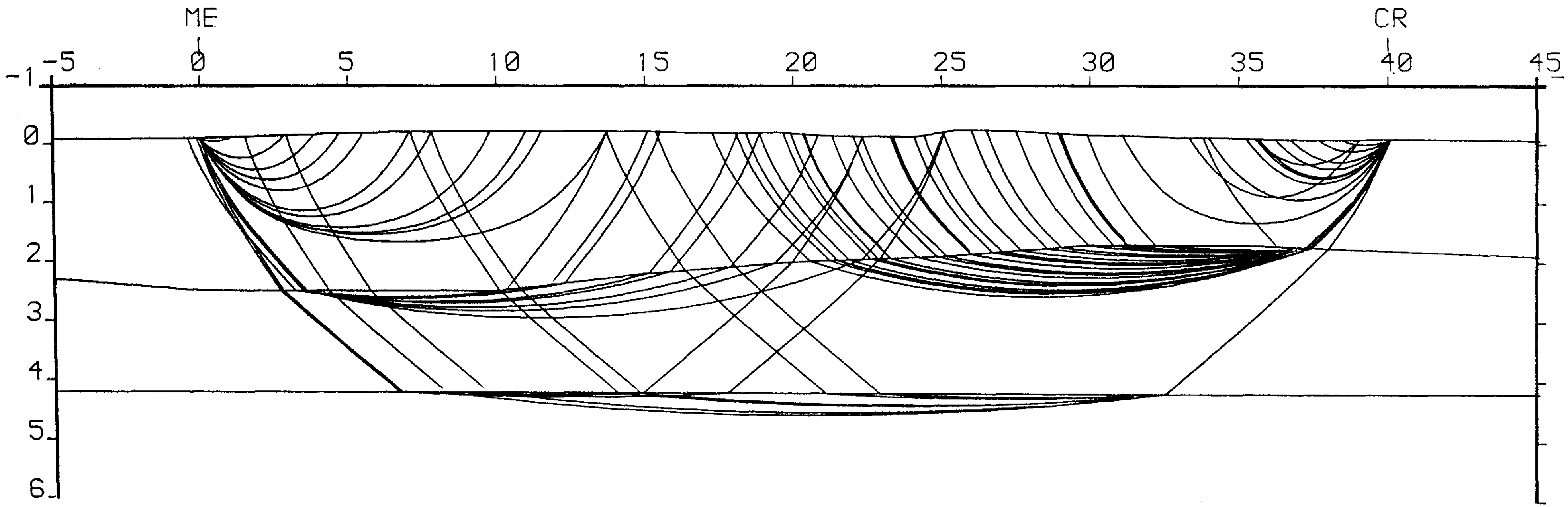

Fig.5.60 Ray-diagram showing all ray-paths used in the calculation of travel-times from Sola north line sources. See Fig.5.55 for abbreviations. Scales are in km.

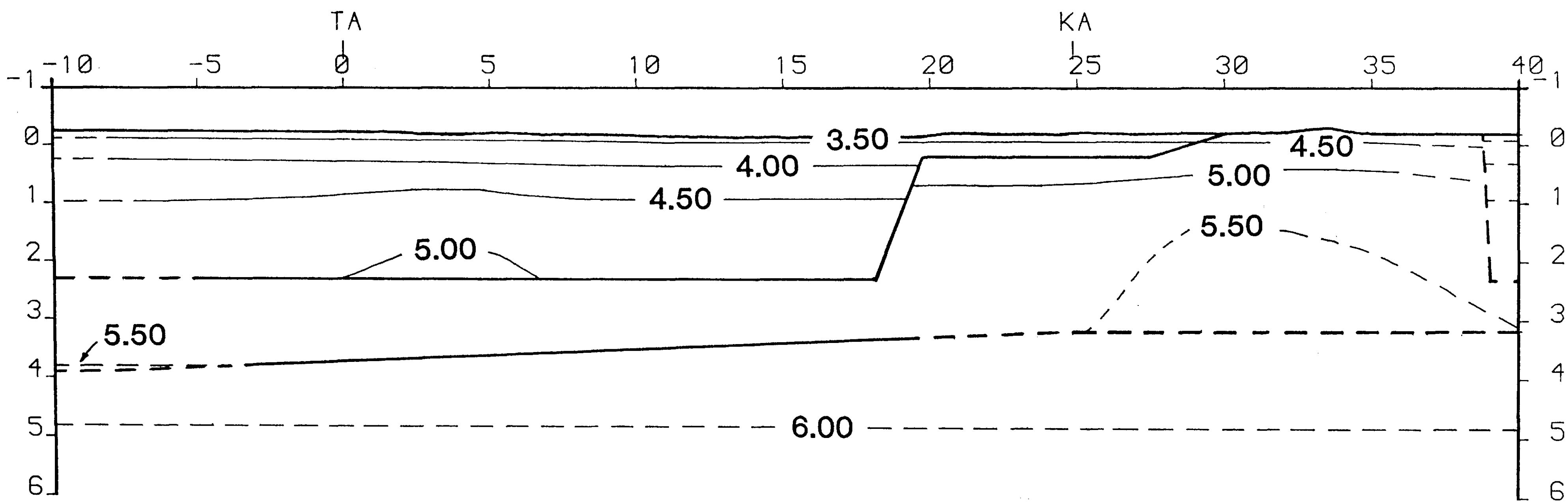

Fig.5.61 Ray-traced model of the Sola south line; TA - Tamsloup, KA - Kaimes. Interfaces shown by thick lines, seismic velocity contours, in km/s, by thin lines. Scales are in km.

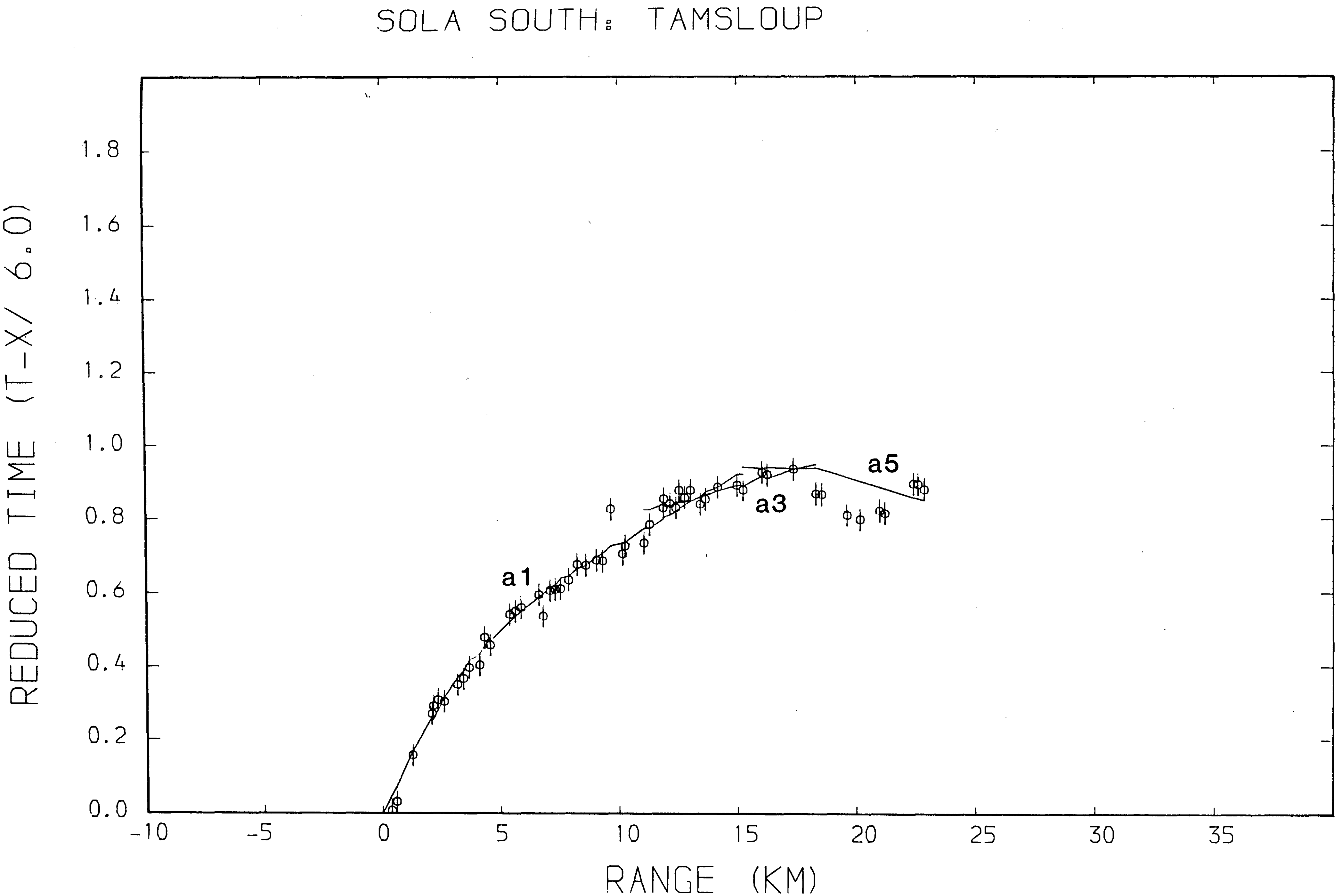

Fig.5.62 Observed (circles with error bars) and calculated (lines) travel-times; Tamsloup shot. See Table 5.1 for classification of travel-time branches.

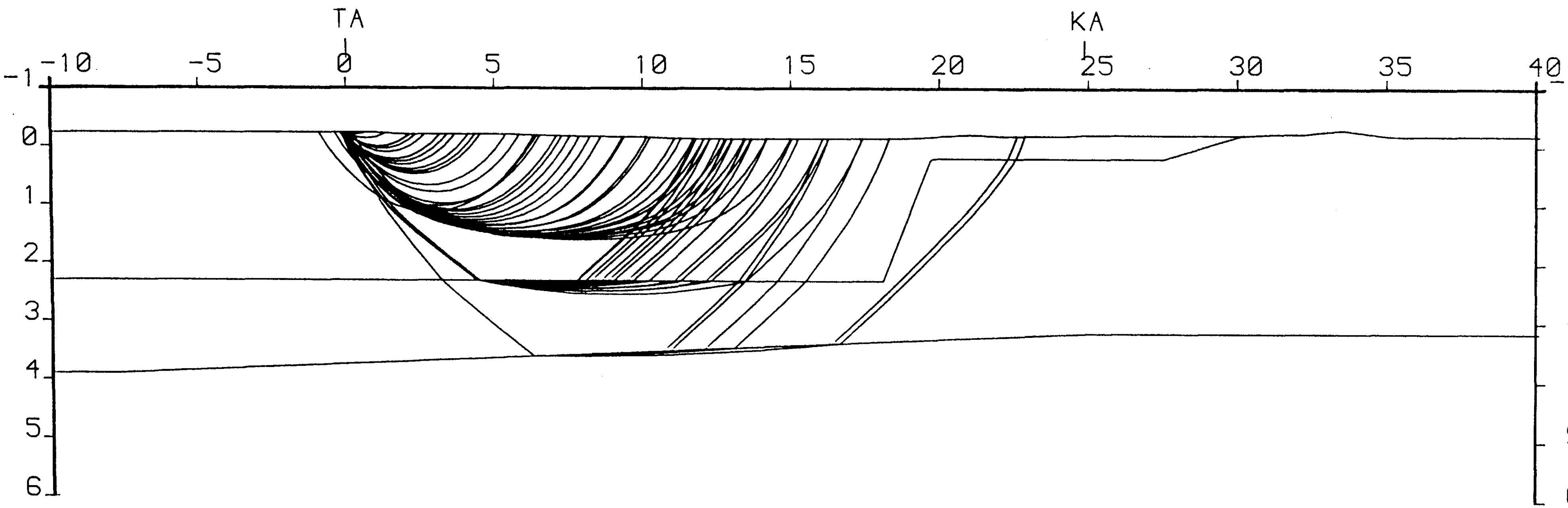

Fig.5.63 Ray-paths used in the calculation of travel-times shown in Fig.5.62. See Fig.5.61 for abbreviations. Scales are in km.

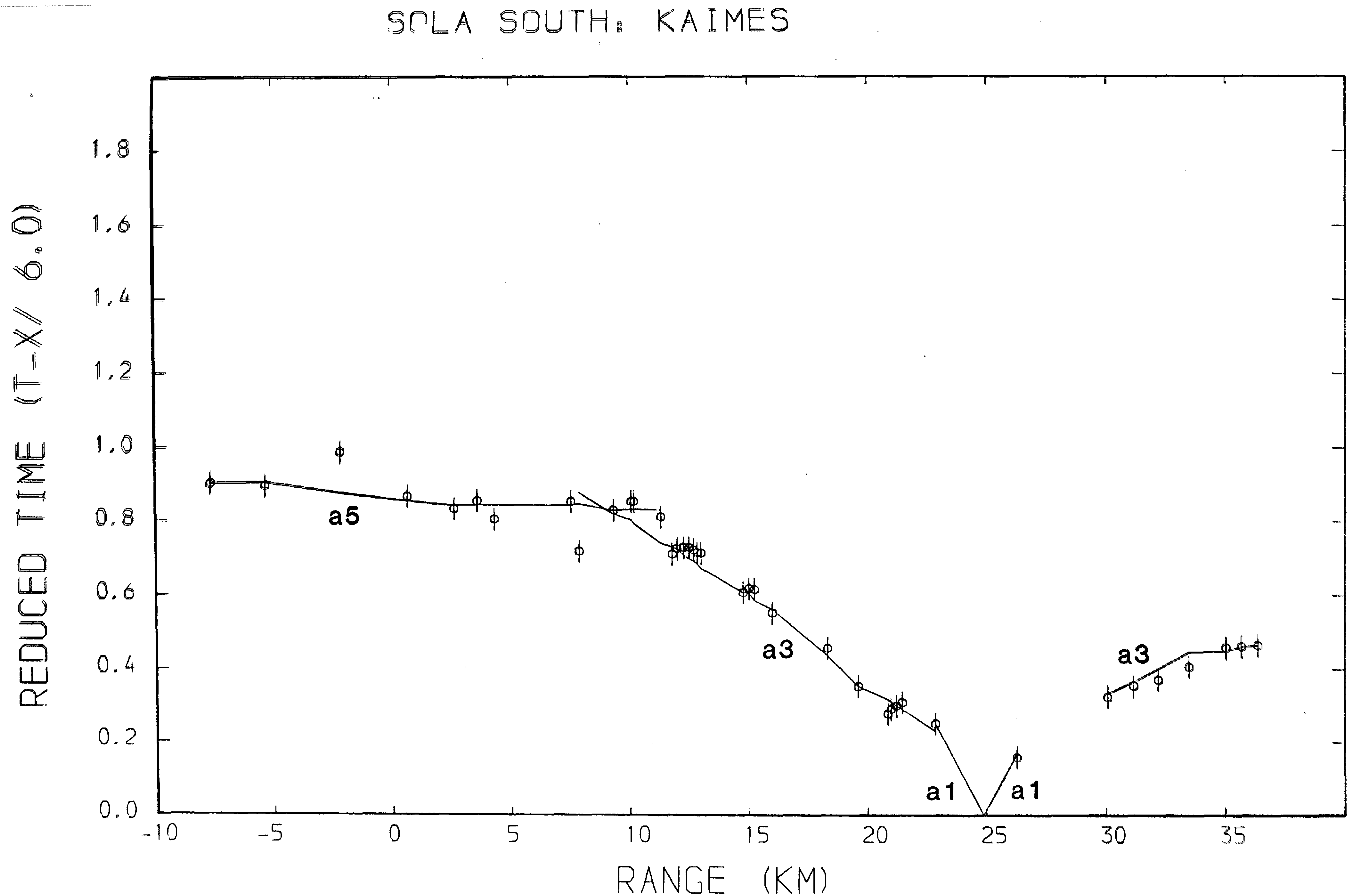

Fig.5.64 Observed (circles with error bars) and calculated (lines) travel-times; Kaimes shot. See Table 5.1 for classification of travel-time branches.

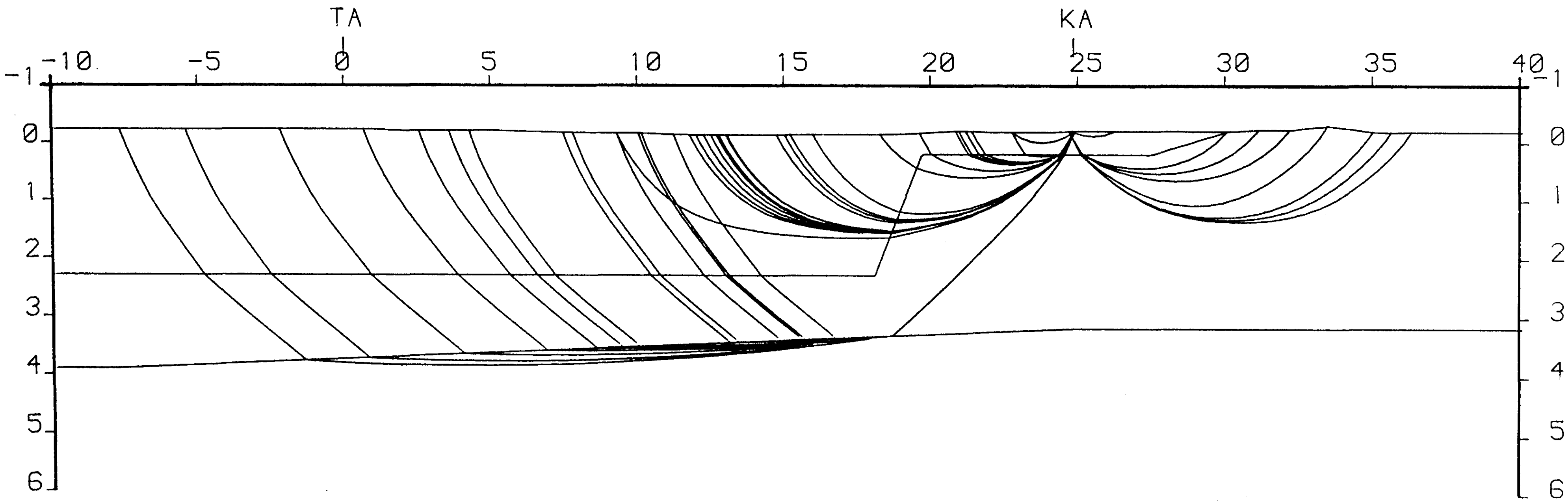

Fig.5.65 Ray-paths used in the calculation of travel-times shown in Fig.5.64. See Fig.5.61 for abbreviations. Scales are in km.

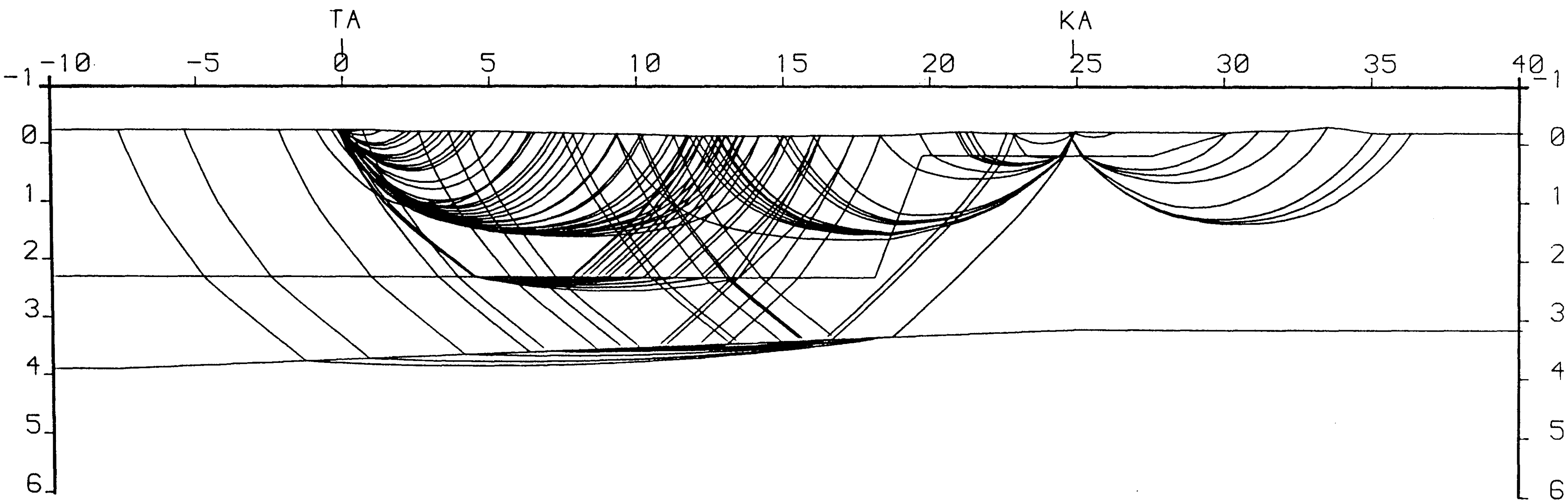

Fig.5.66 Ray-diagram showing all ray-paths used in the calculation of travel-times from Sola south line sources. See Fig.5.61 for abbreviations. Scales are in km.

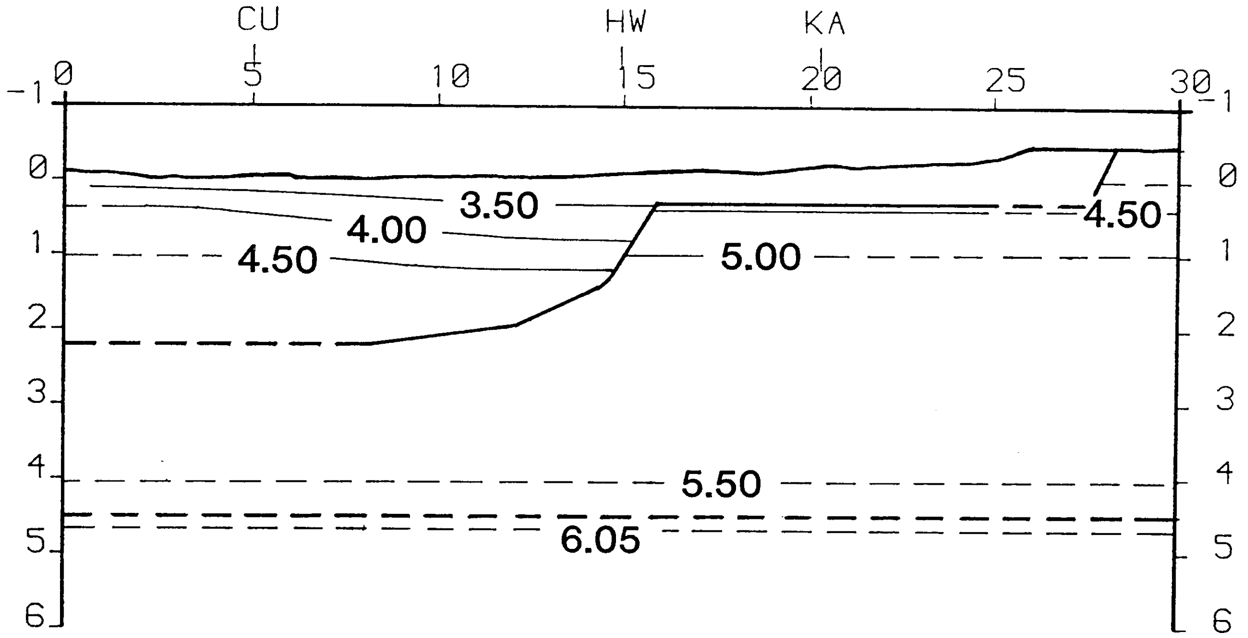

Fig.5.67 Ray-traced model of the MAVIS III line; CU - Cruiks, HW - Hillwood, KA - Kaimes. Interfaces shown by thick lines, seismic velocity contours, in km/s, by thin lines. Scales are in km.

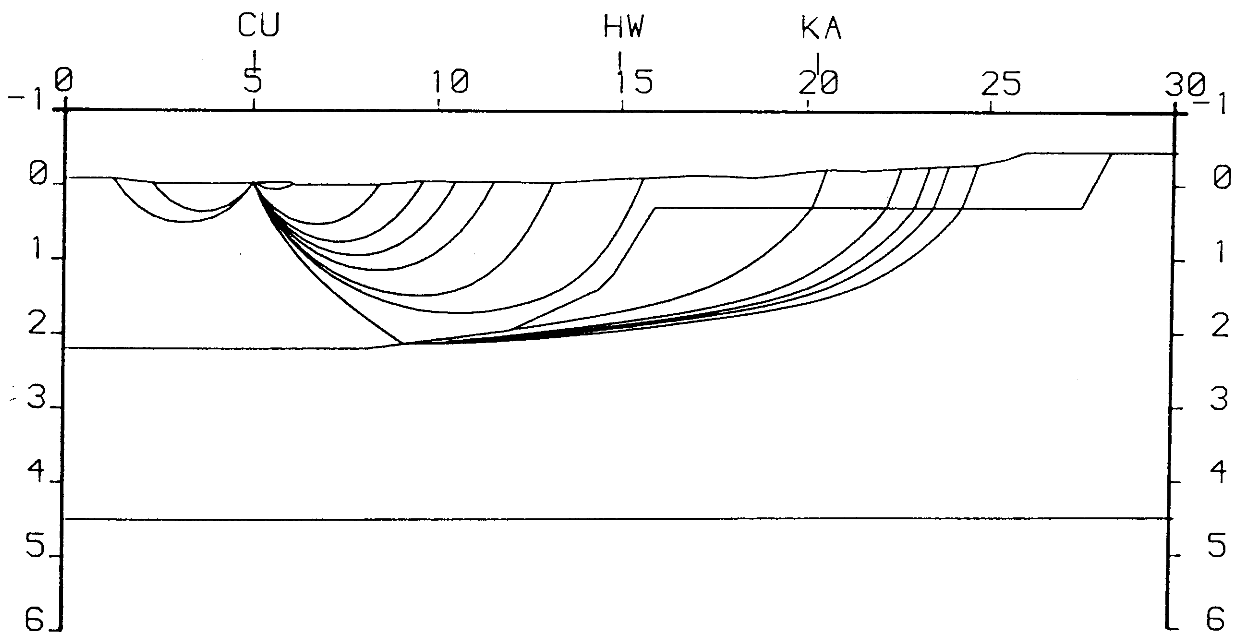

Fig.5.68 Ray-paths used in the calculation of travel-times shown in Fig.5.69. See Fig.5.67 for abbreviations. Scales are in km.

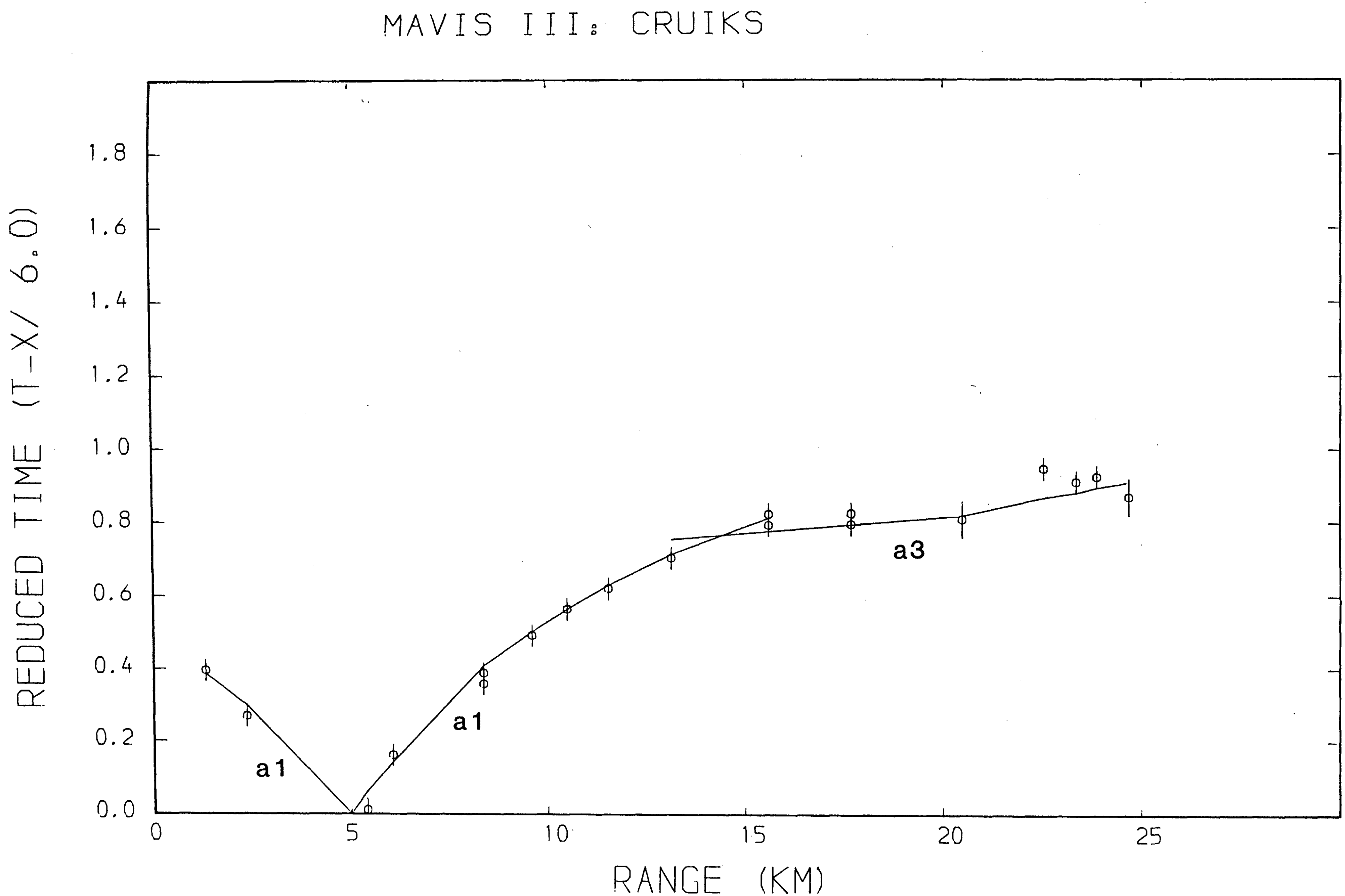

Fig.5.69 Observed (circles with error bars) and calculated (lines) travel-times; Cruiks shot. See Table 5.1 for classification of travel-time branches.

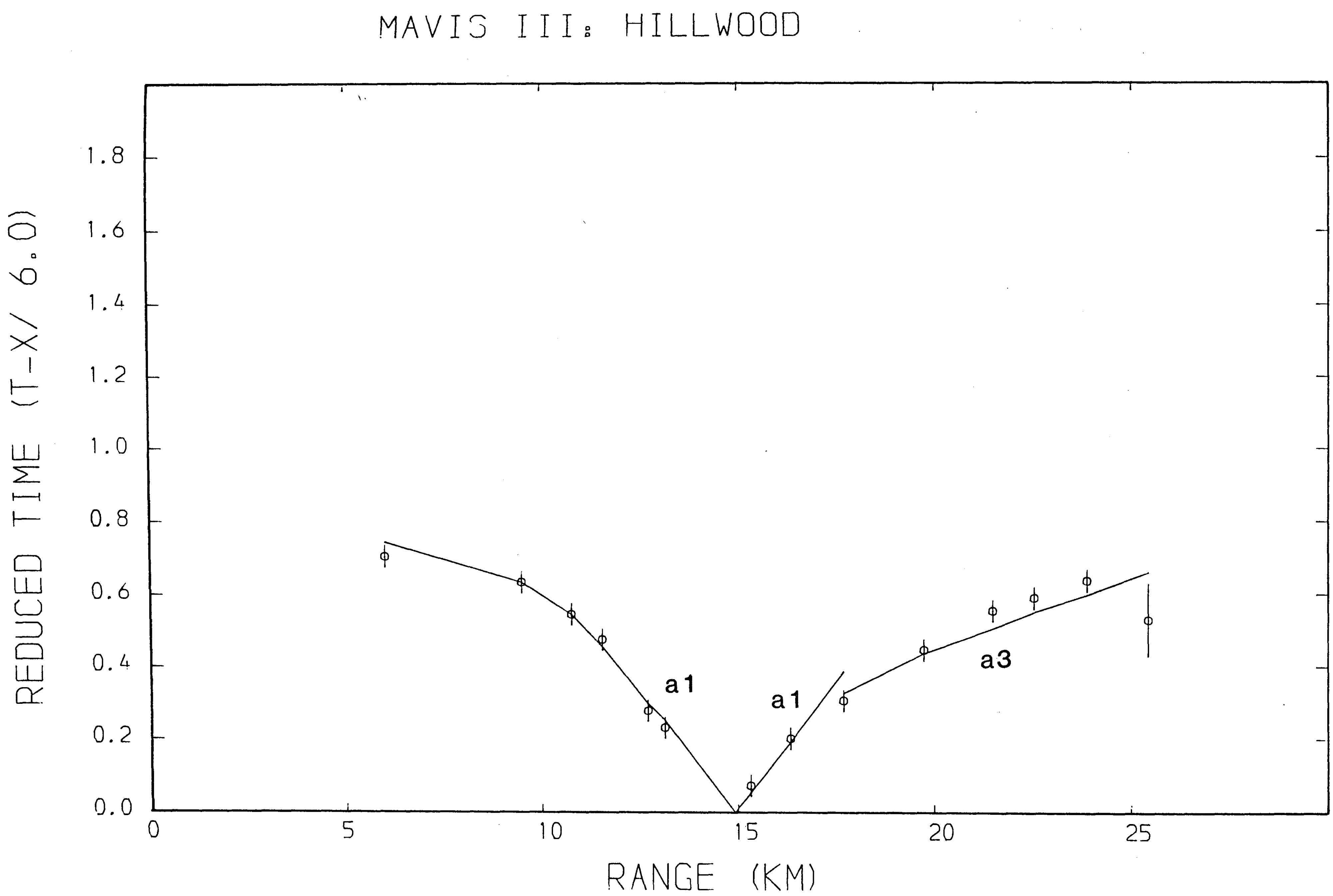

Fig.5.70 Observed (circles with error bars) and calculated (lines) travel-times; Hillwood shot. See Table 5.1 for classification of travel-time branches.

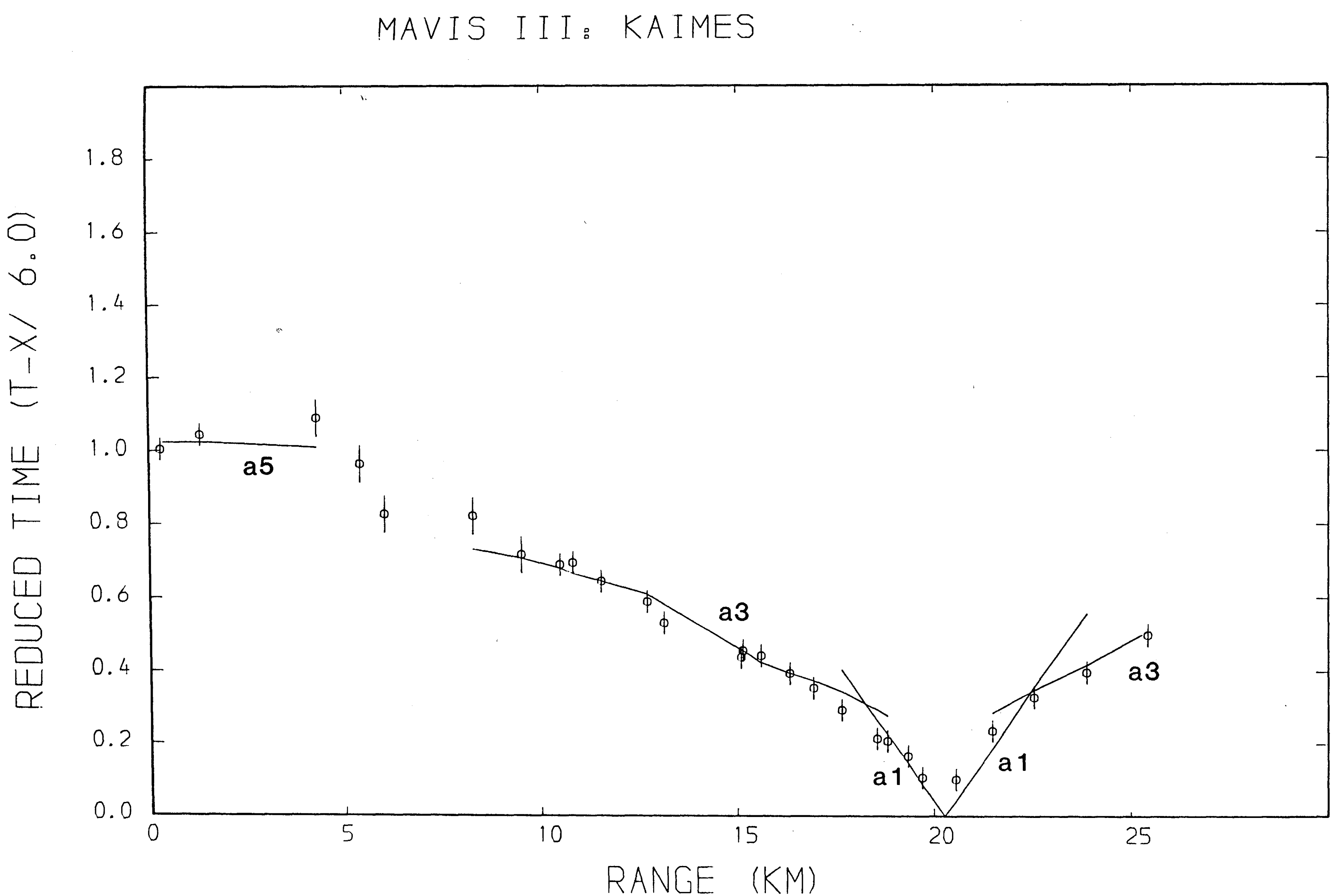

Fig.5.71 Observed (circles with error bars) and calculated (lines) travel-times; Kaimes shot. See Table 5.1 for classification of travel-time branches.

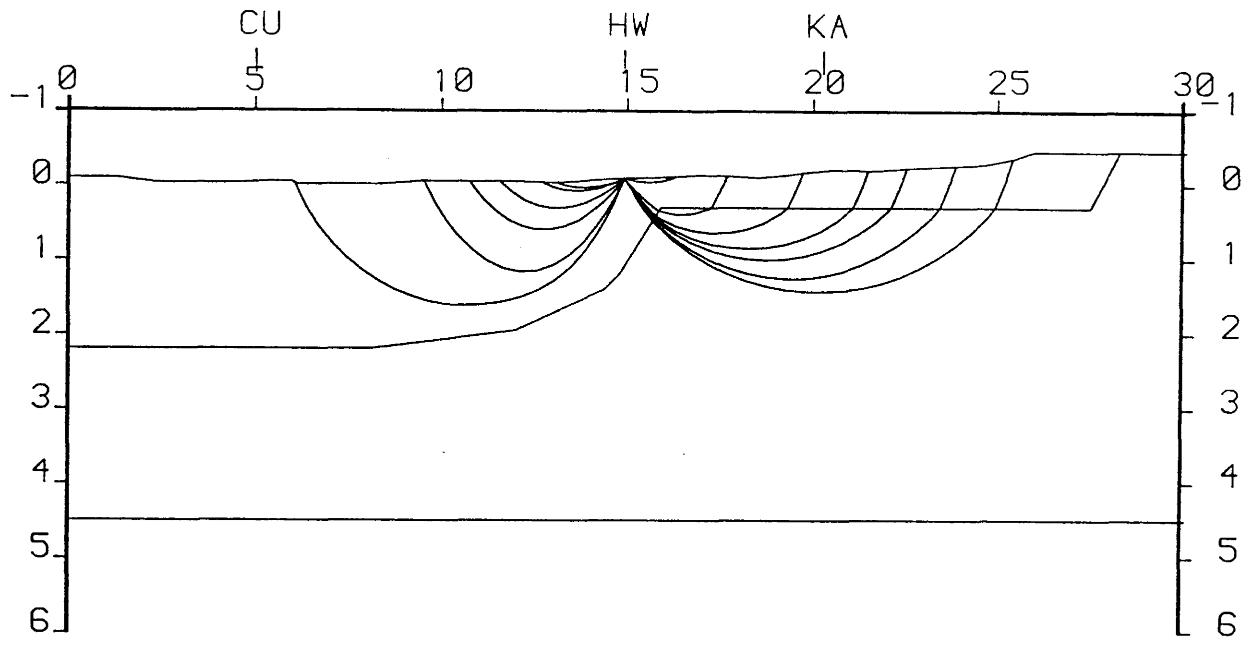

Fig.5.72 Ray-paths used in the calculation of travel-times shown in Fig.5.70. See Fig.5.67 for abbreviations. Scales are in km.

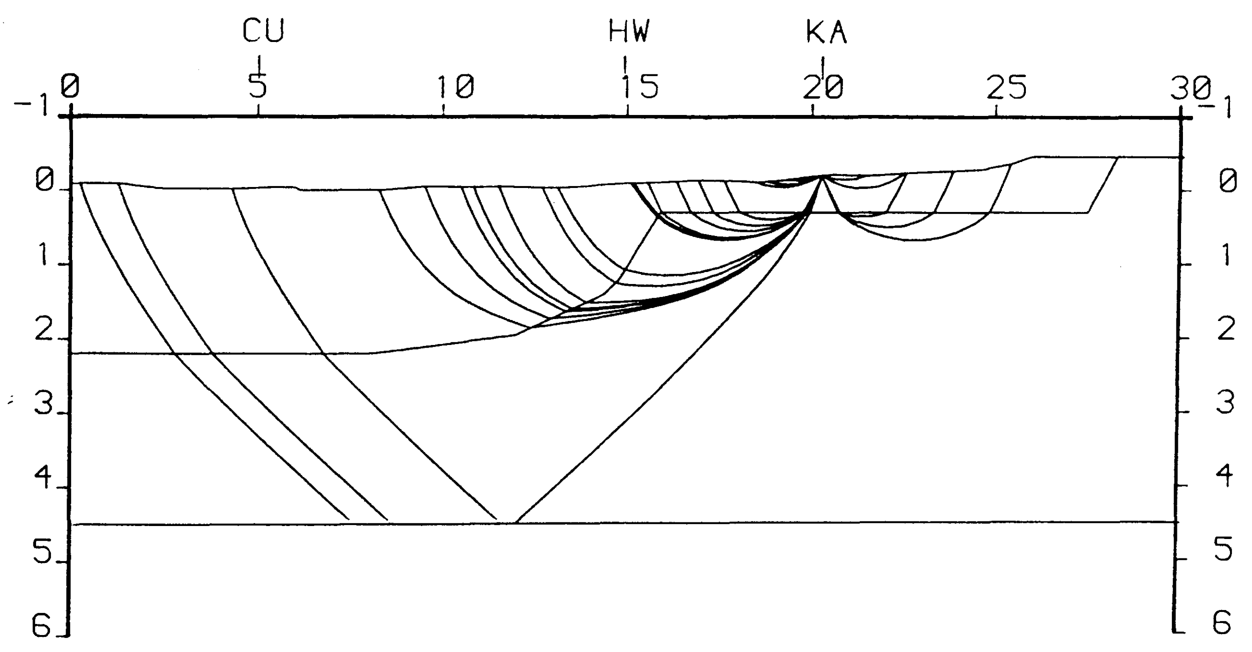

Fig.5.73 Ray-paths used in the calculation of travel-times shown in Fig.5.71. See Fig.5.67 for abbreviations. Scales are in km.

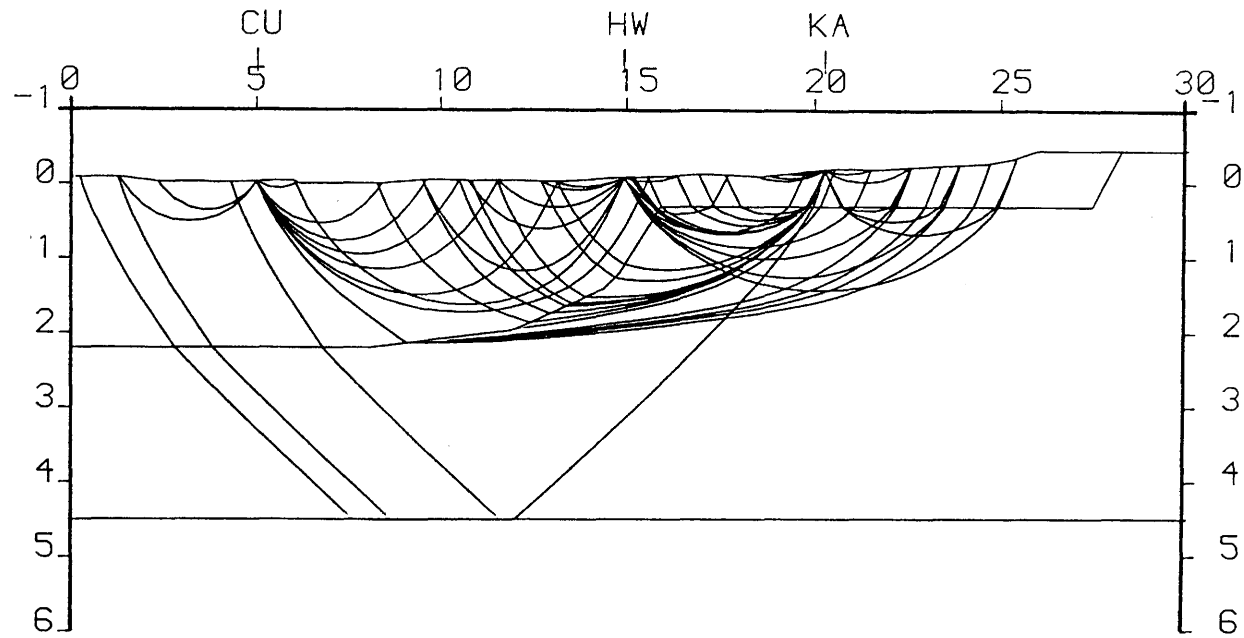

Fig.5.74 Ray-diagram showing all ray-paths used in the calculation of travel-times from MAVIS III line sources. See Fig.5.67 for abbreviations. Scales are in km.

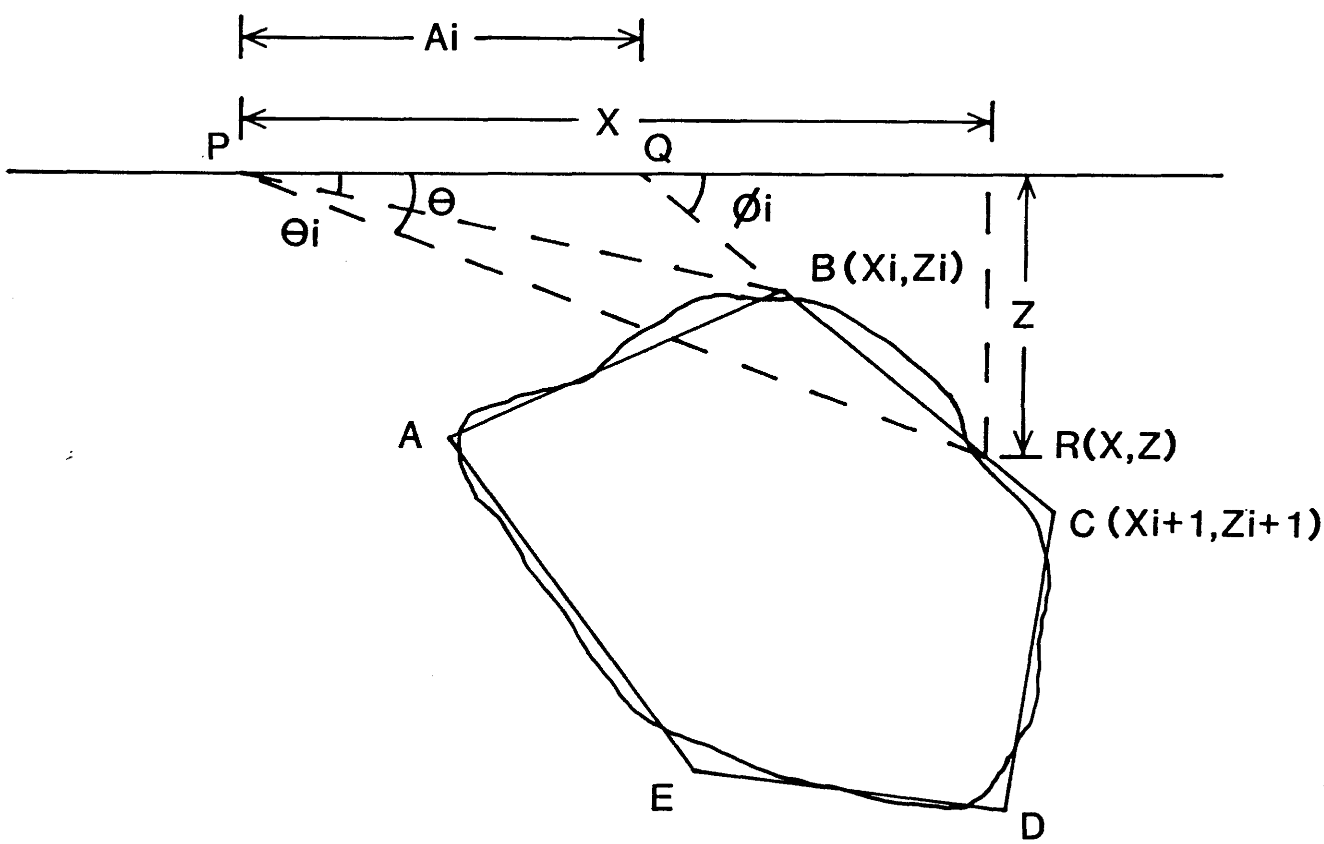

Fig.6.1 Polygonal approximation of an irregular body to calculate its gravity effect, see text for explanation of symbols (after Telford et al. 1976).

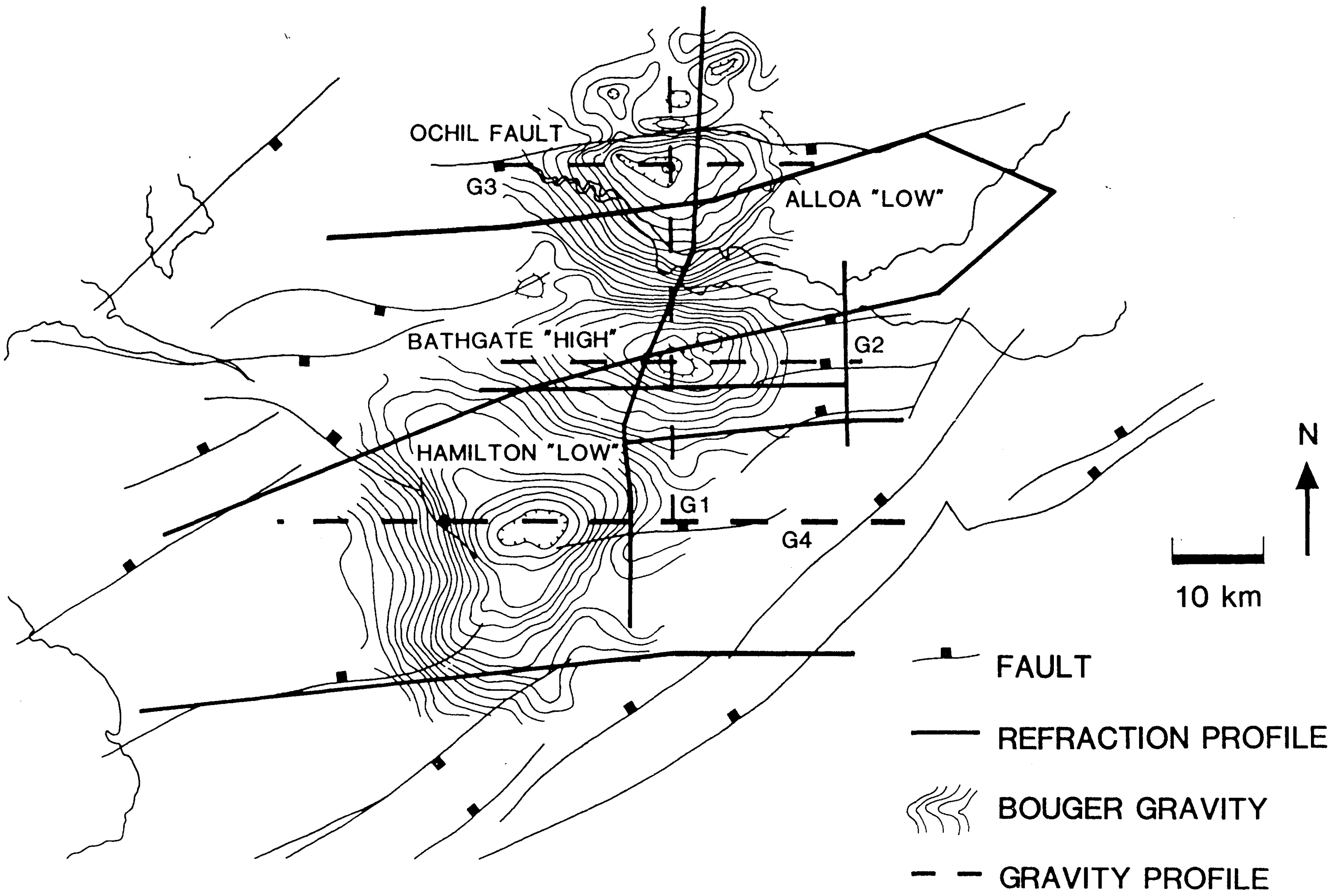

Fig.6.2 Relationship between Bouguer gravity anomalies, the MAVIS refraction lines and the gravity profiles G1, G2, G3 and G4. Gravity data are from Hussain & Hipkin (1981). Contours are in mgals. Ticks are downthrown sides of faults.

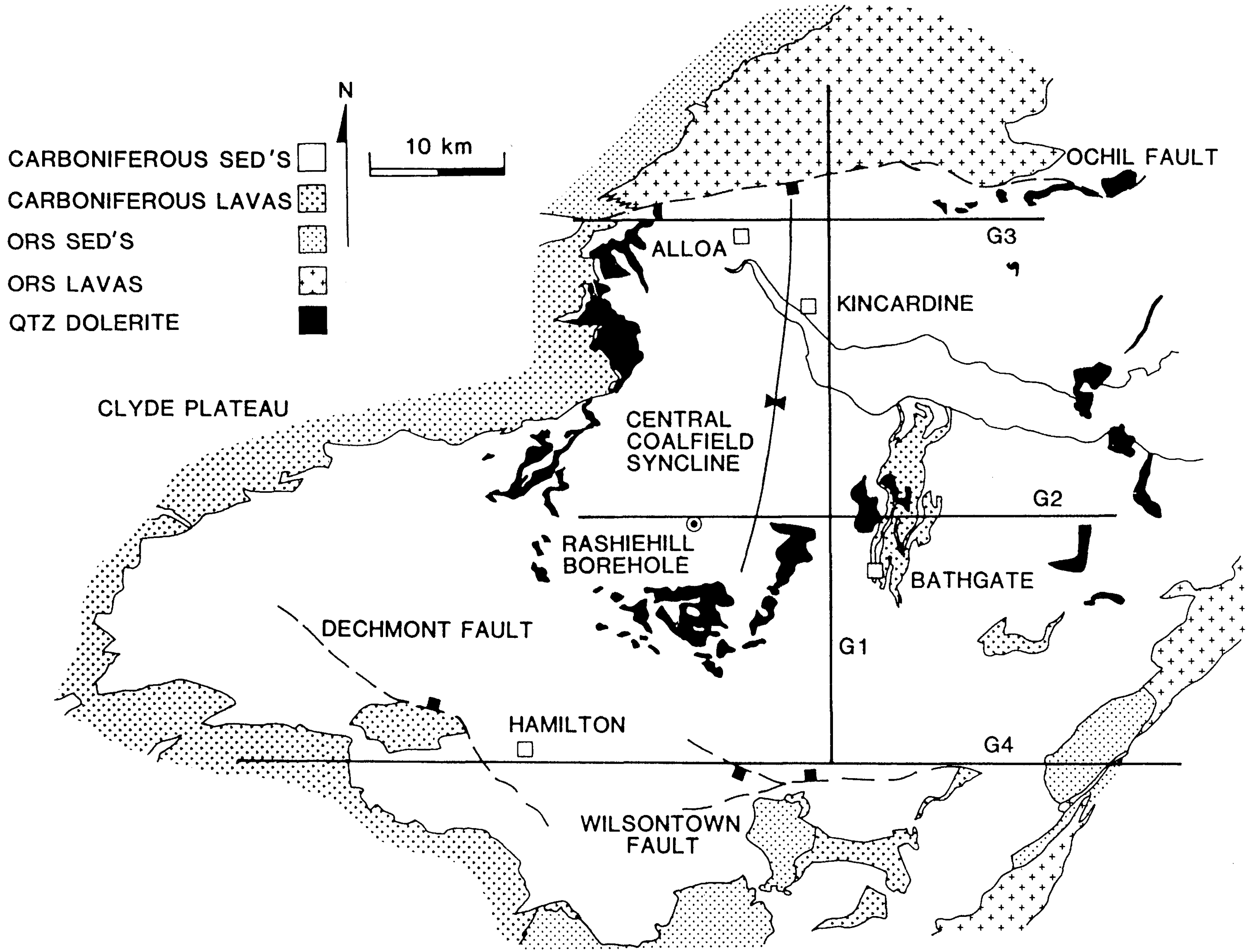

Fig.6.3 Distribution of igneous rocks within the central Midland Valley of Scotland.

	LAYER	DENSITY
	CARBONIFEROUS & UPPER ORS	2.54 g/cm3
A	CARBONIFEROUS LAVAS	2.72 g/cm3
	LOWER ORS & LOWER PALAEOZOIC	2.61 g/cm3 (2.66 g/cm3 G3)
B	LOWER ORS LAVAS	2.66 g/cm3
	BASEMENT (6.0 km/s)	2.69 g/cm3
	BASEMENT (6.4 km/s)	2.76 g/cm3
C	BASIC INTRUSION	3.25 g/cm3

Fig.6.4 Key to gravity models shown in Figs.6.5 and 6.6 and 6.8 to 6.10.

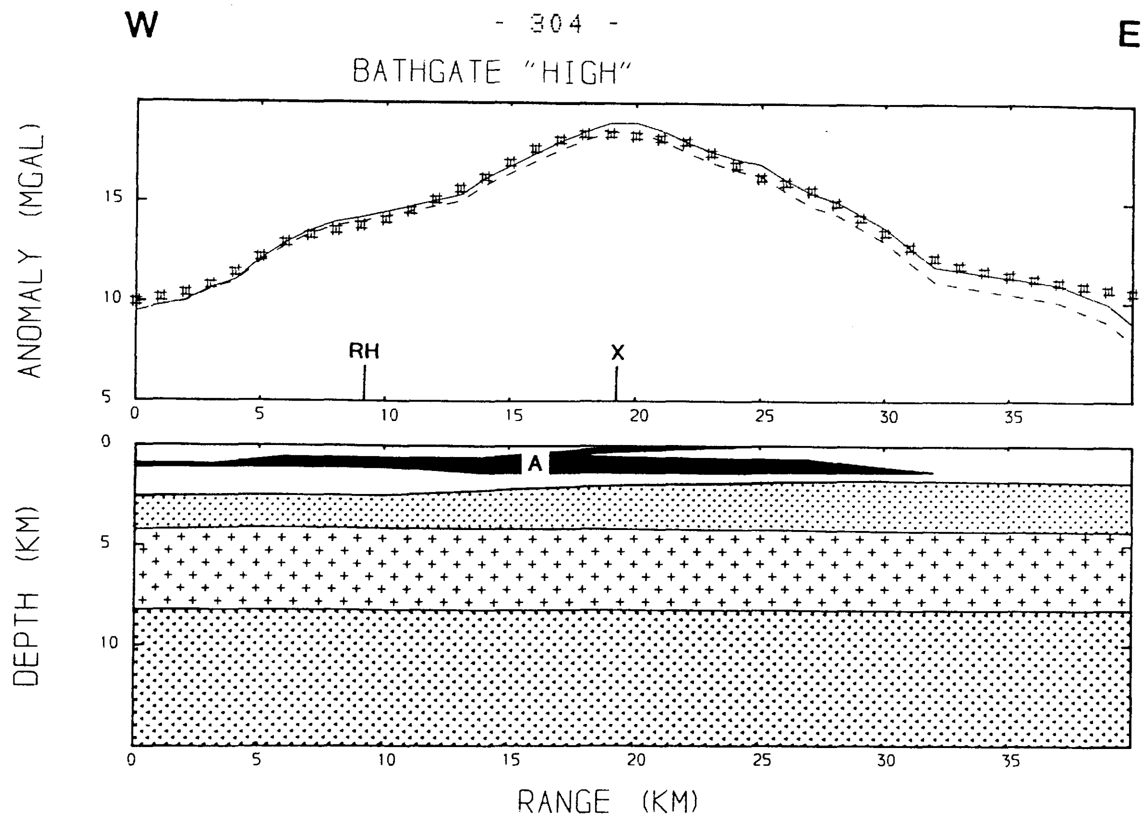

Fig.6.5 Gravity model of the Bathgate "high" (G3). Anomaly modelled using a shallow lava source. - - - - observed Bouguer gravity, ——— residual Bouguer gravity, # calculated gravity. RH, Rashiehill borehole, X, intercept with G1 profile.

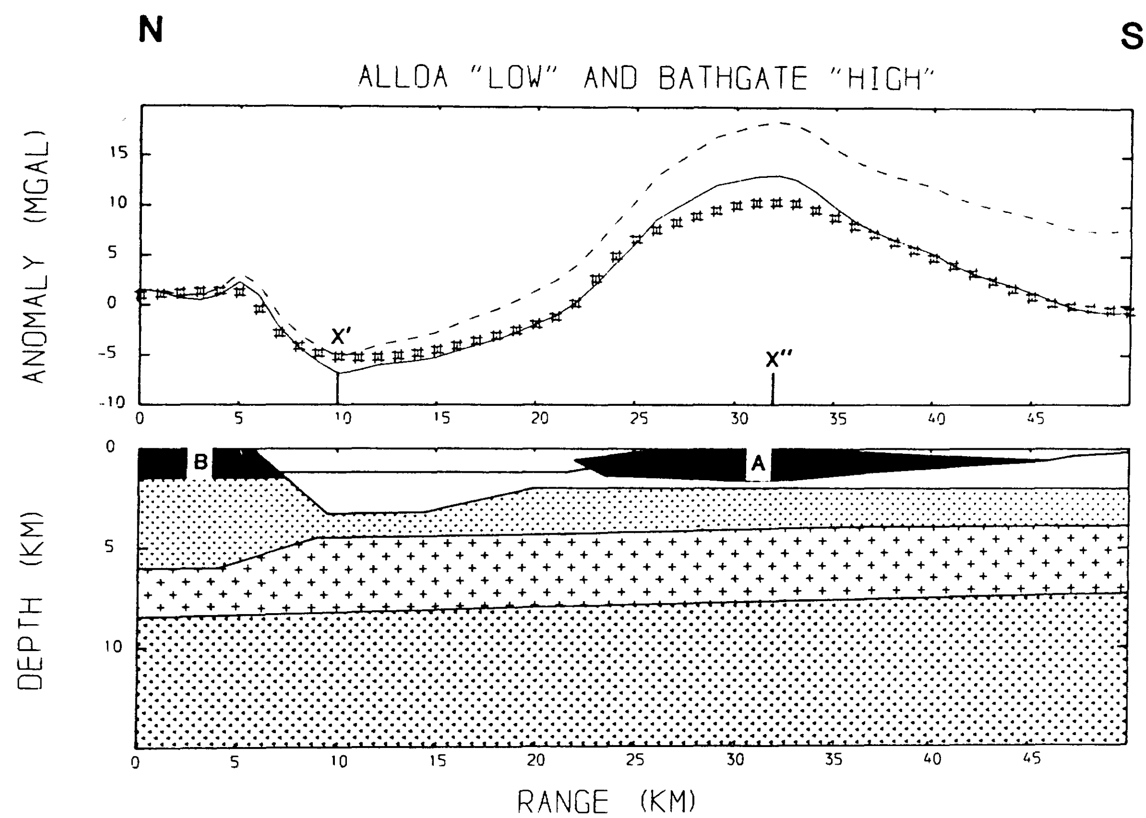

Fig.6.6 Gravity model of the Bathgate "high" and Alloa "low" (G1). Bathgate anomaly modelled using a shallow lava source. - - - - observed Bouguer gravity, ——— residual Bouguer gravity, # calculated gravity. X', intercept with G3 profile, X'' intercept with G2 profile.

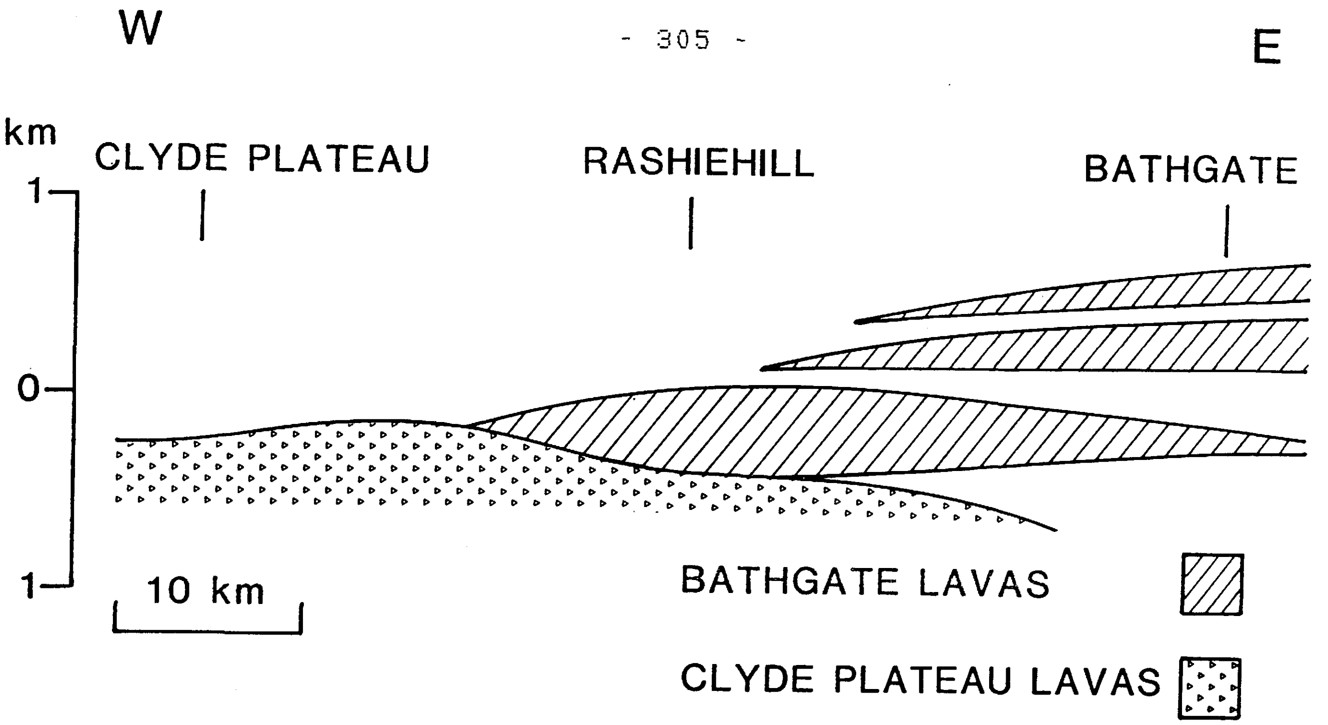

Fig.6.7 Schematic cross-section of the relationship between the lavas of the Clyde Plateau and Bathgate Hills (redrawn from Anderson 1963).

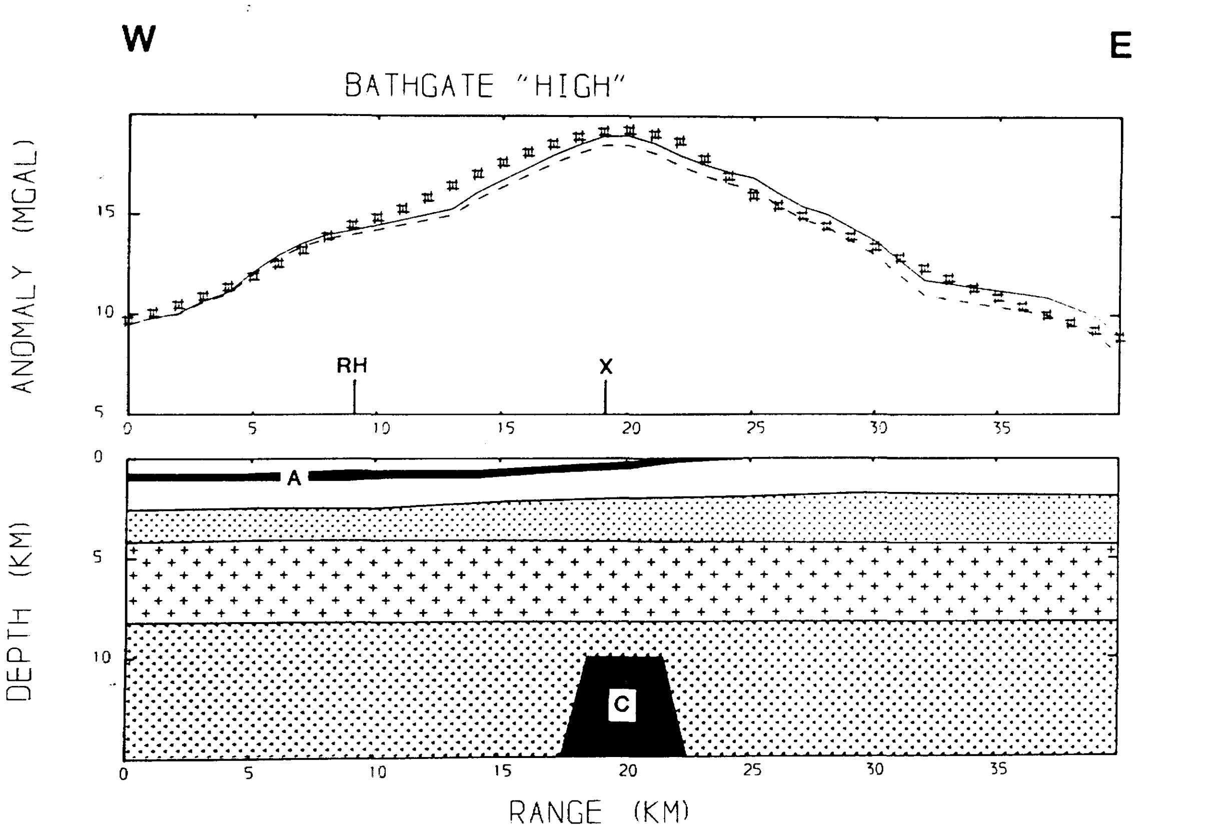

Fig.6.8 Gravity model of the Bathgate "high" (G3). Anomaly modelled using shallow lava and deep intrusive sources. - - - - observed Bouguer gravity, ——— residual Bouguer gravity, # calculated gravity. RH, Rashiehill borehole, X, intercept with G1 profile.

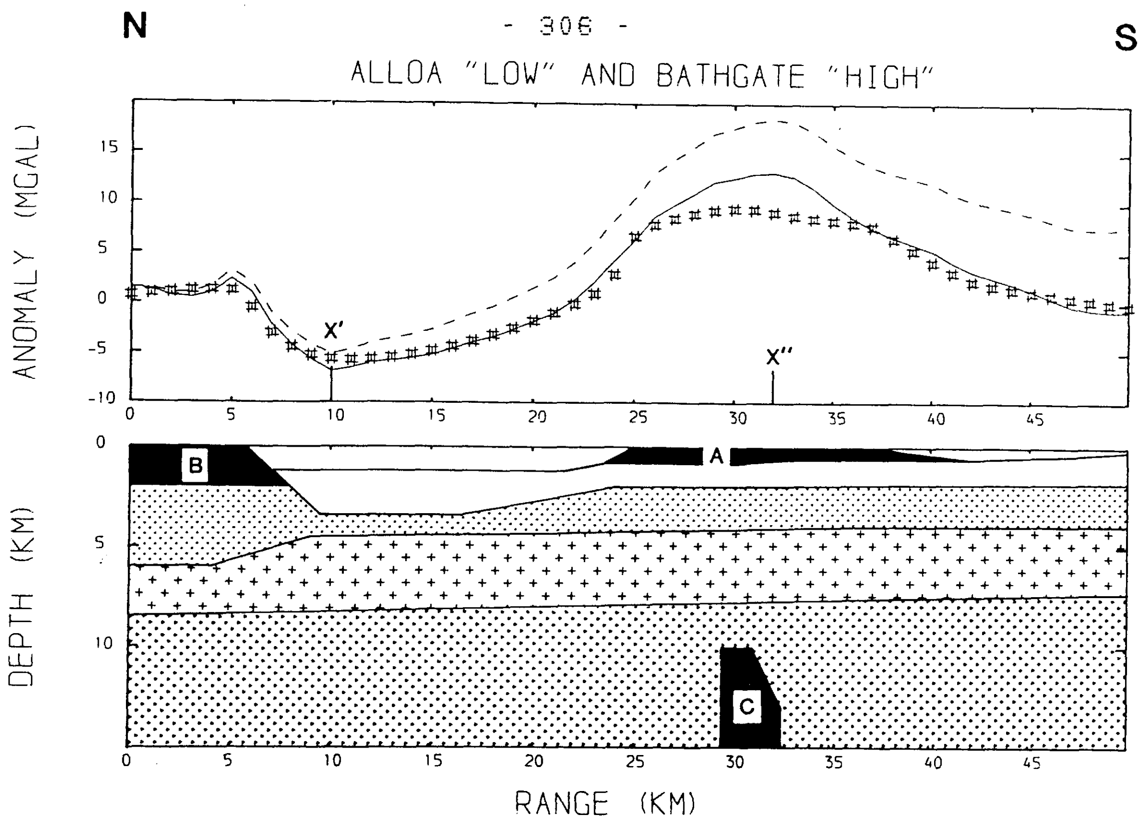

Fig.6.9 Gravity model of the Bathgate "high" and Alloa "low" (G1). Bathgate anomaly modelled using shallow lava and deep intrusive sources. - - - - observed Bouguer gravity, ——— residual Bouguer gravity, # calculated gravity. X', intercept with G3 profile, X'' intercept with G2 profile.

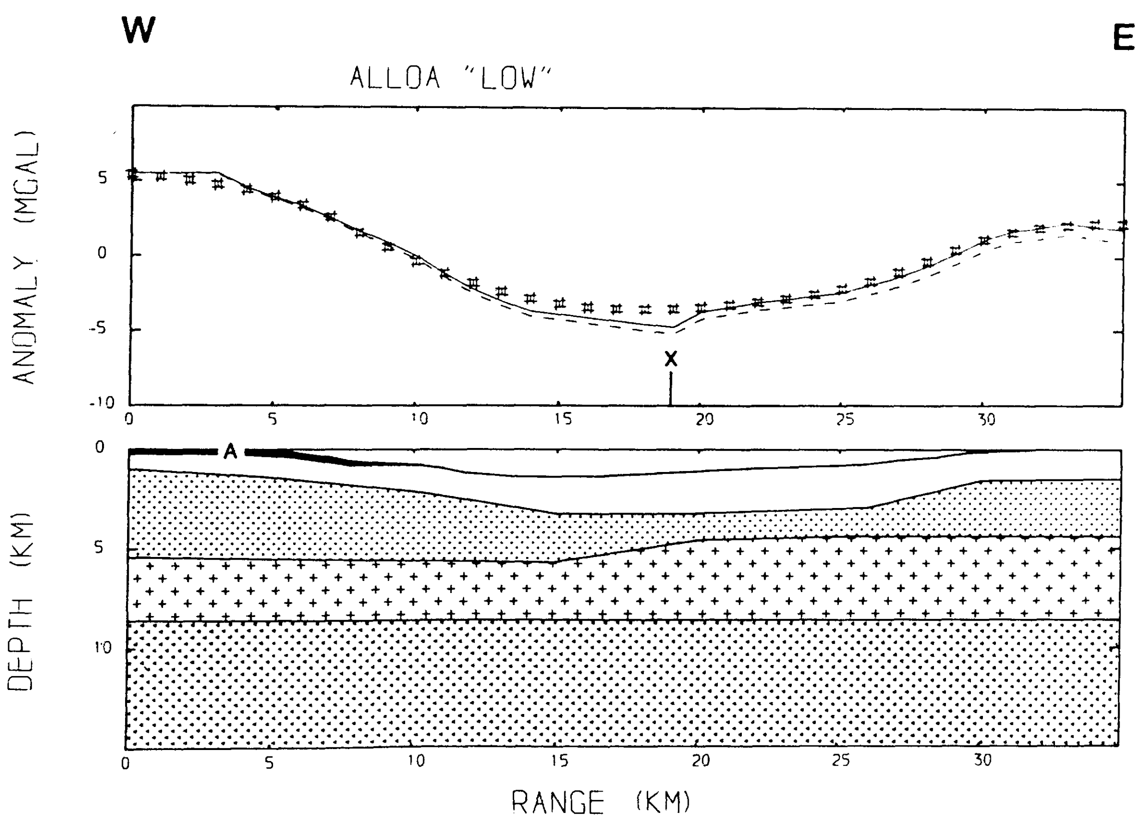

Fig.6.10 Gravity model of the Alloa "low". - - - - observed Bouguer gravity, ——— residual Bouguer gravity, # calculated gravity. X, intercept with G1 profile.

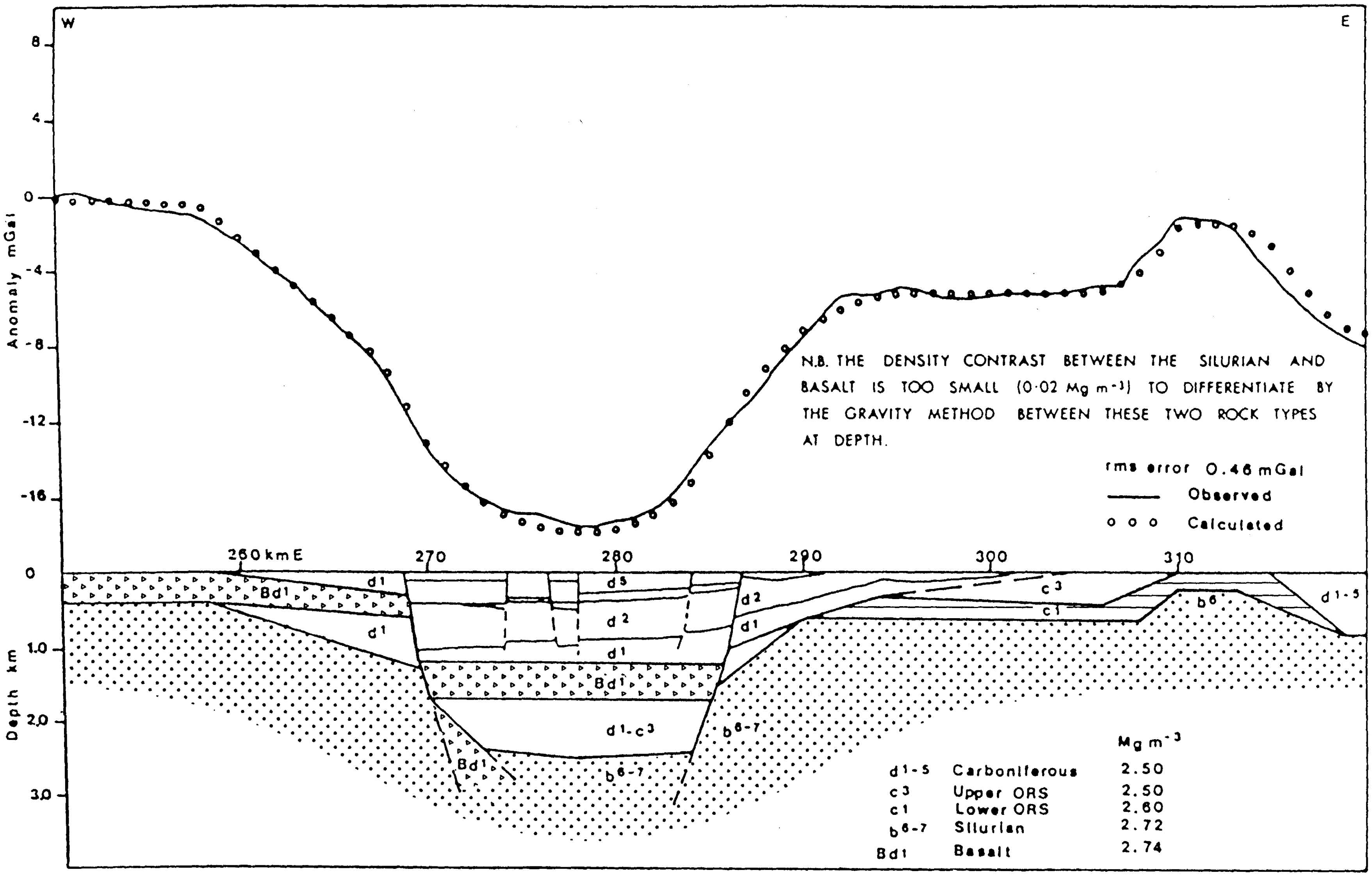

Fig.6.11 Gravity model of the Hamilton "low" (redrawn from Browne et al, 1987).

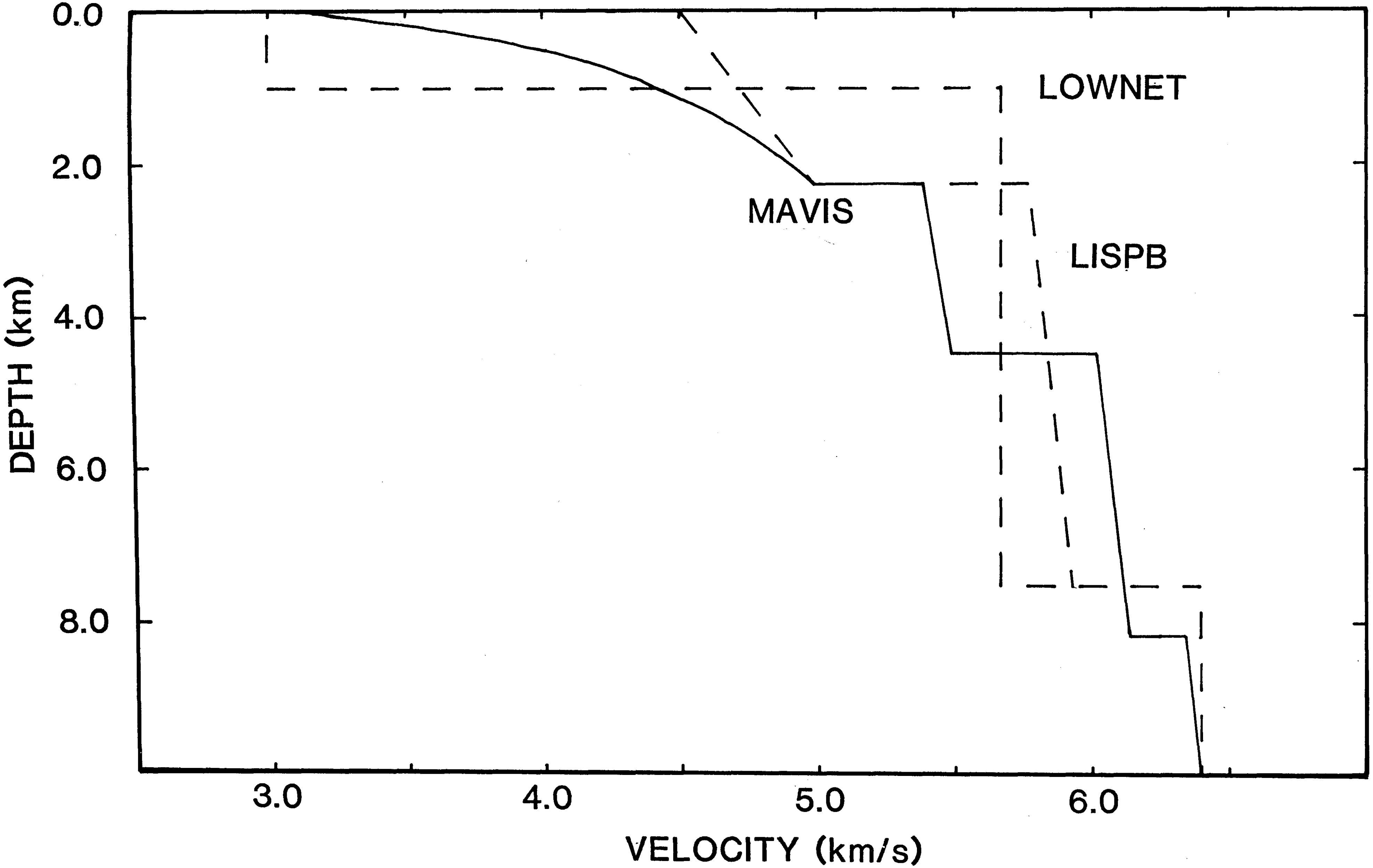

Fig.7.1 Comparison of velocity-depth curves from the Midland Valley of Scotland.

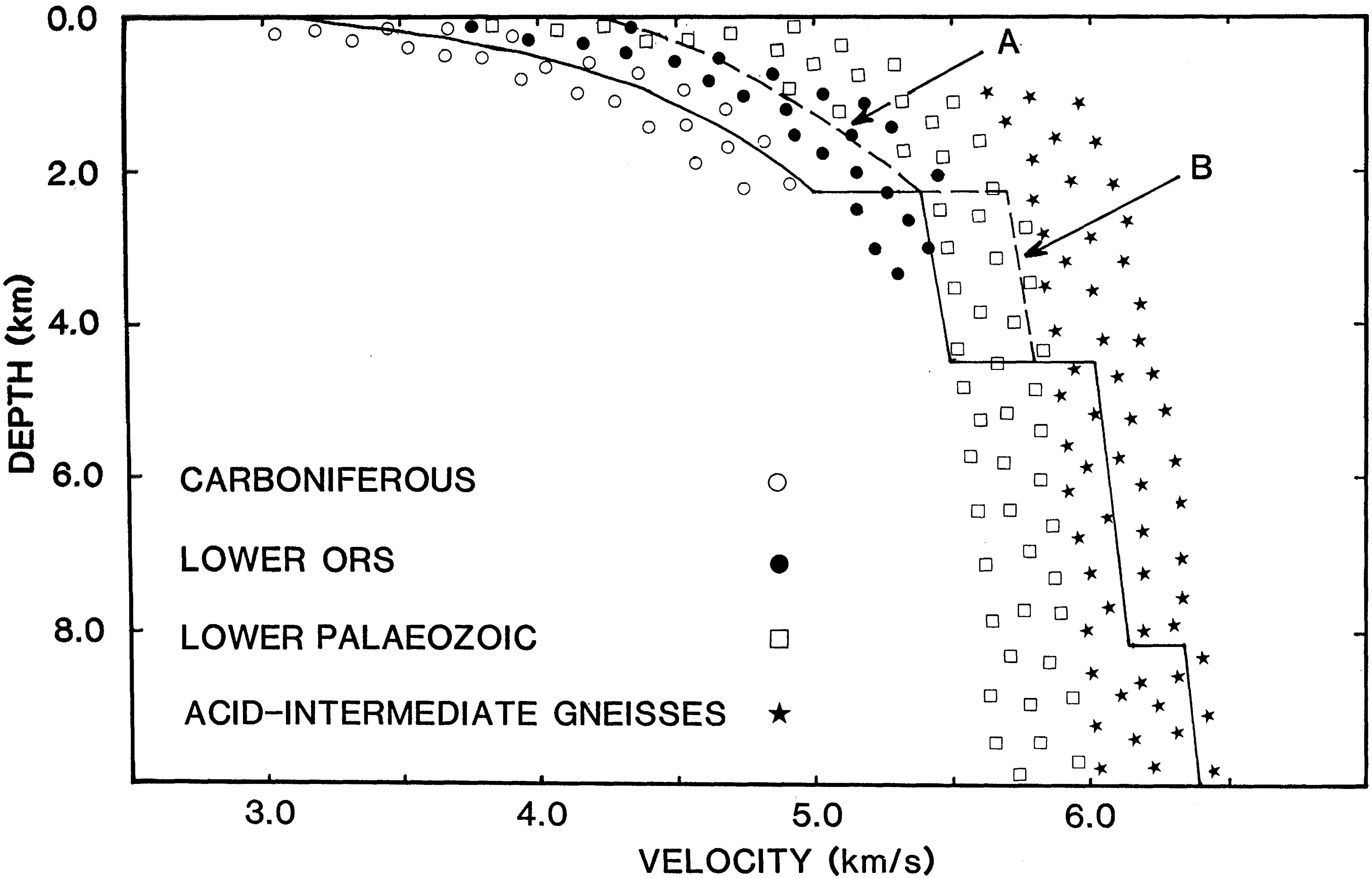

Fig.7.2 Comparison of MAVIS velocity-depth curves with the velocity fields of Midland Valley lithologies.

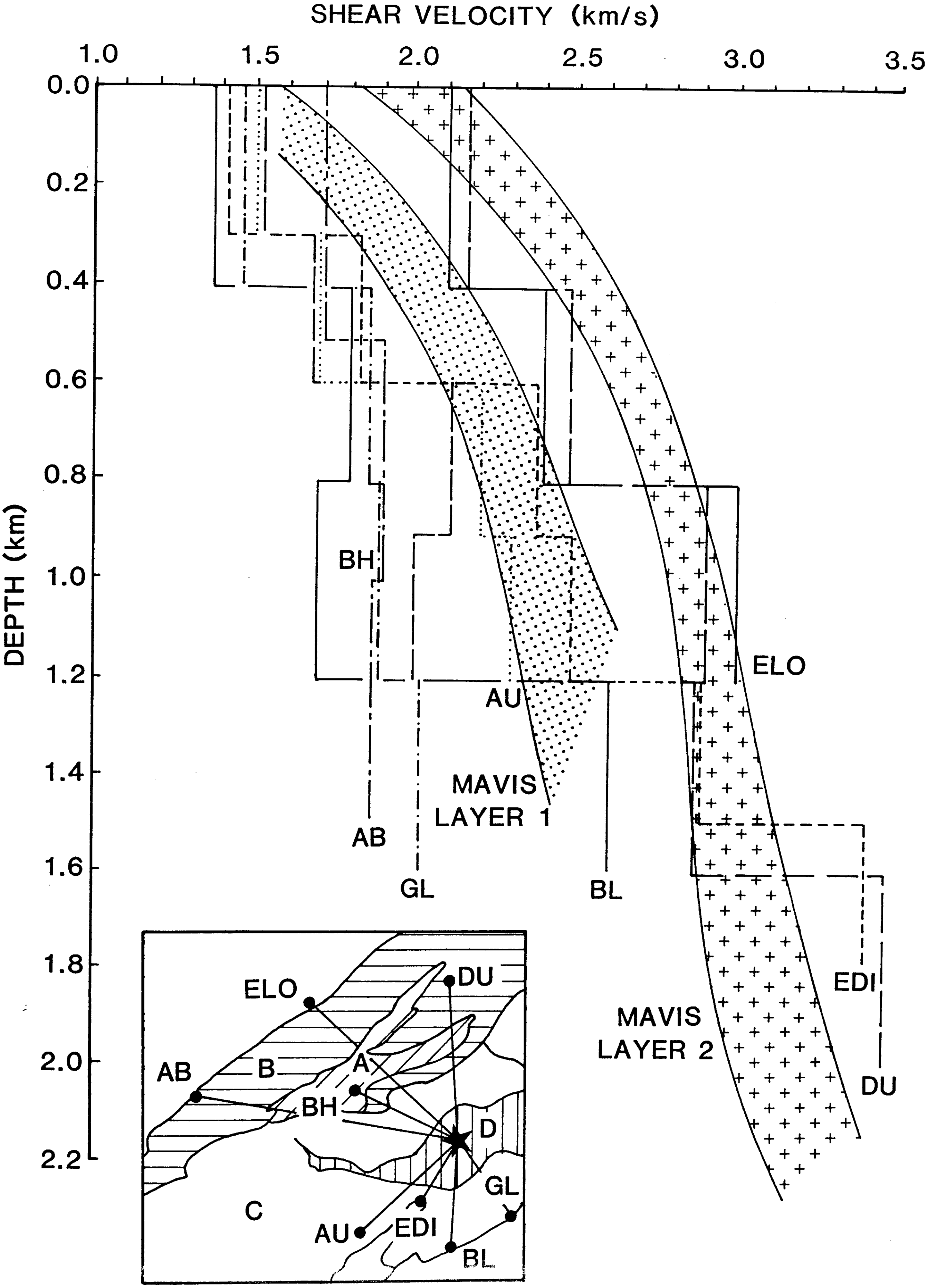

Fig.7.3 Comparison of shear wave velocity-depth curves from the Midland Valley of Scotland. Inset; A - ORS lavas, B - ORS sediments, C - Carboniferous, D - Carboniferous beneath the Firth of Forth. See Fig.2.1 for other abbreviations (Redrawn from MacBeth & Burton 1986).

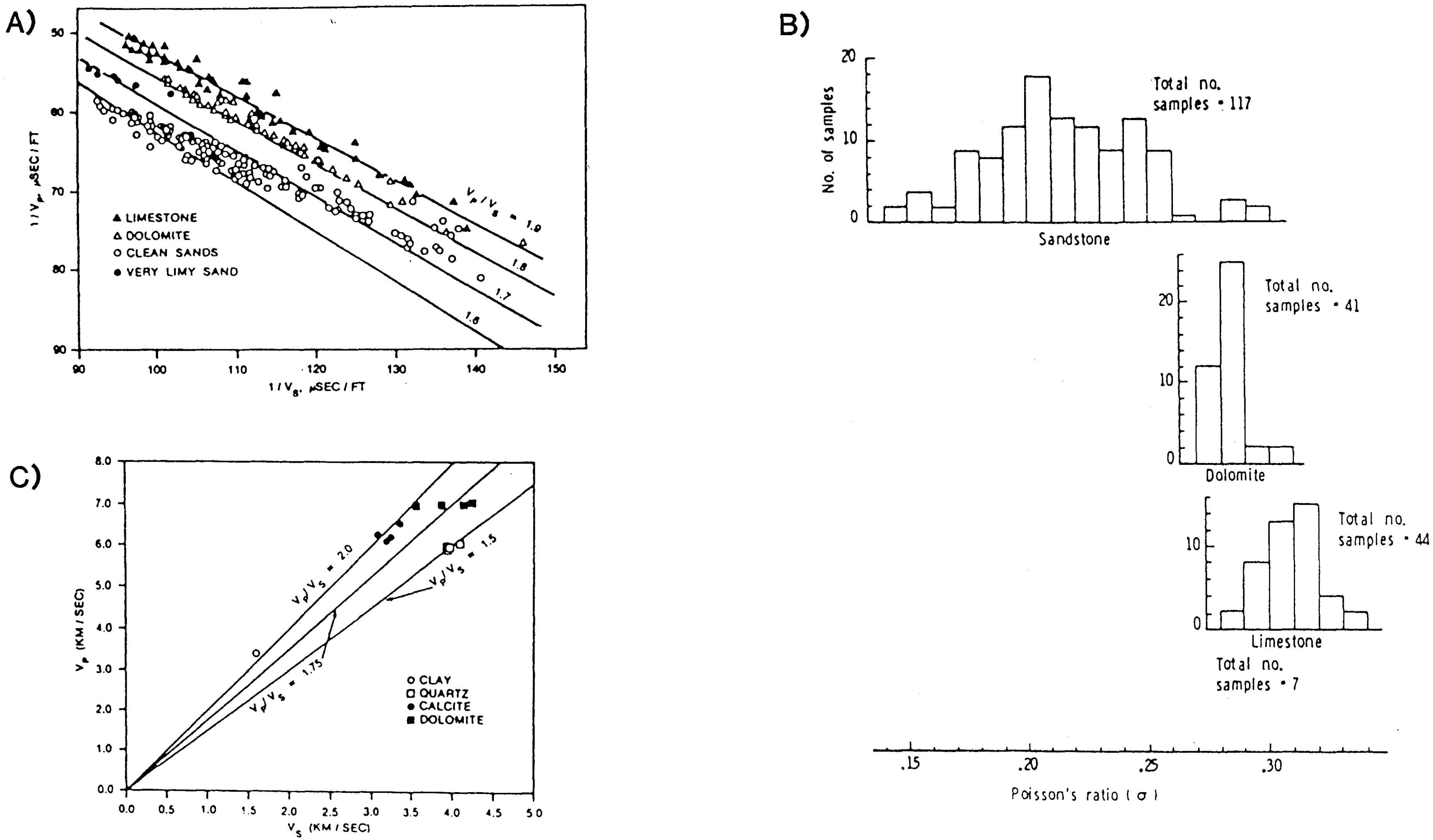

Fig.7.4 A), Vp/Vs from laboratory measurements on cores of different lithology (after Pickett 1963) B), Poisson's ratio from the measurements in (A) (redrawn from Domenico 1984), C), Vp/Vs from laboratory measurements on different minerals (after Castagna et al, 1985).

Depth in km

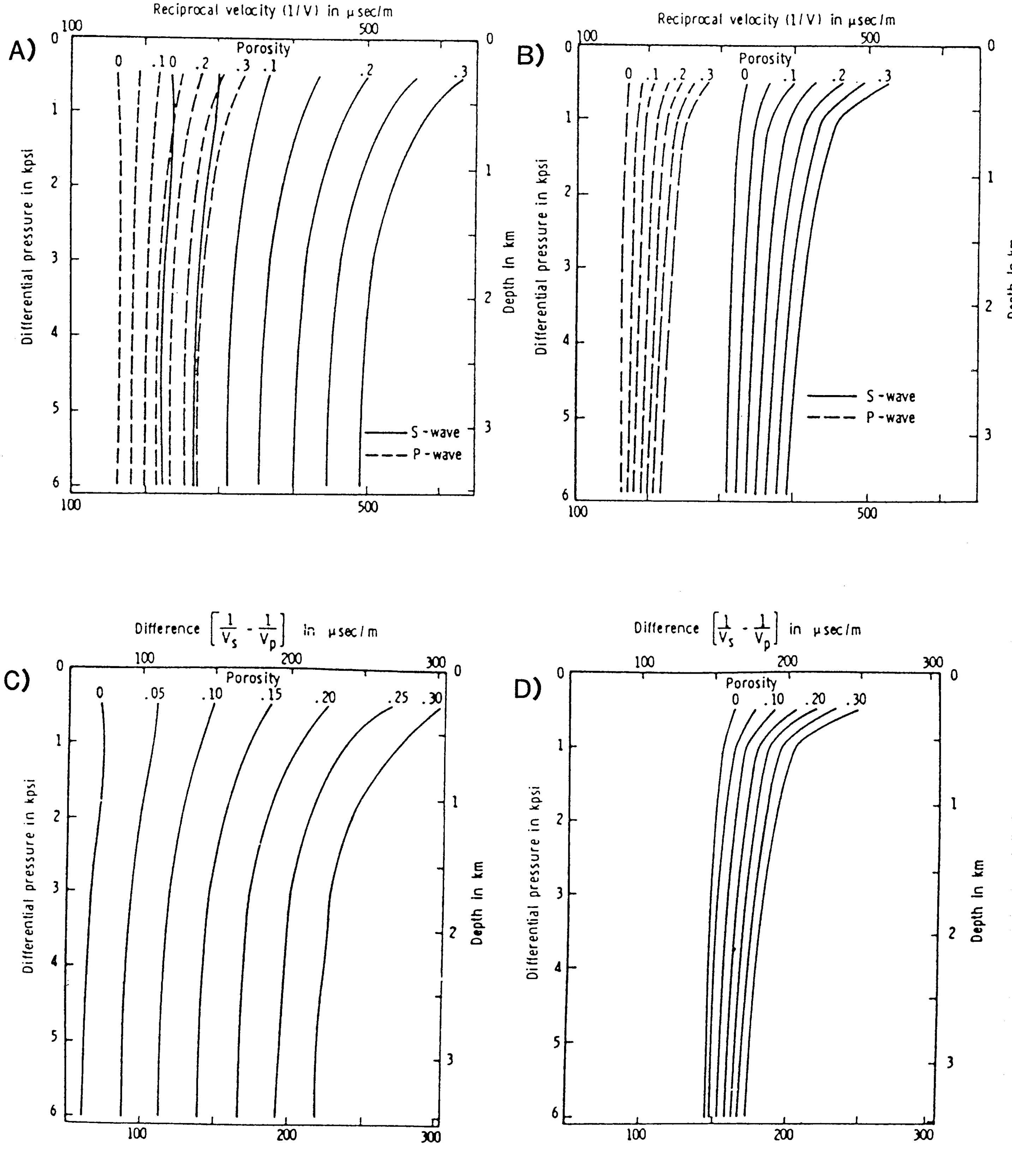

Fig.7.5 A), Sandstone reciprocal velocity versus differential pressure at constant porosity. B), Limestone reciprocal velocity versus differential pressure at constant porosity. C), Difference between limestone P-and S-wave reciprocal velocity at constant pressure. D), Difference between sandstone P-and S-wave reciprocal velocity at constant pressure. (after Domenico 1984).

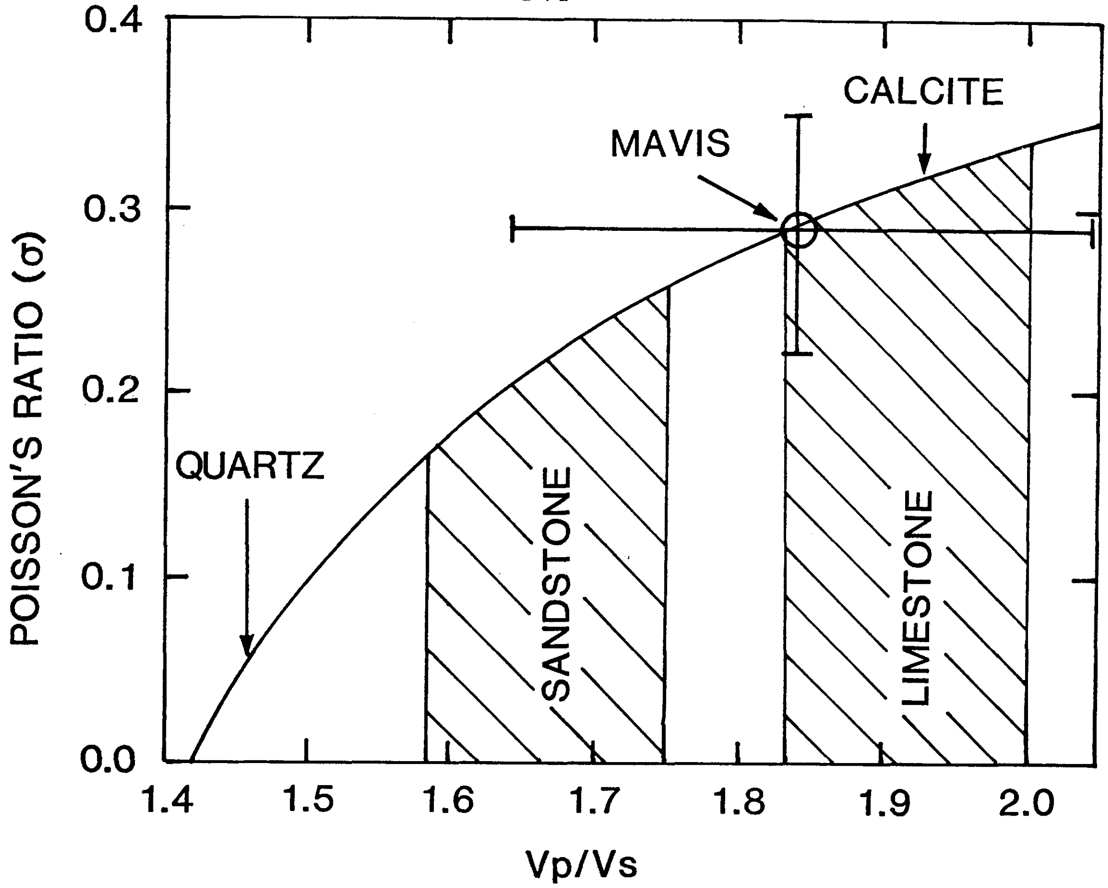

Fig.7.6 Vp/Vs and Poisson's ratio for sandstone, limestone, quartz and calcite. The MAVIS data from depths greater than about 0.5 km shown for comparison. (redrawn from Domenico 1984).

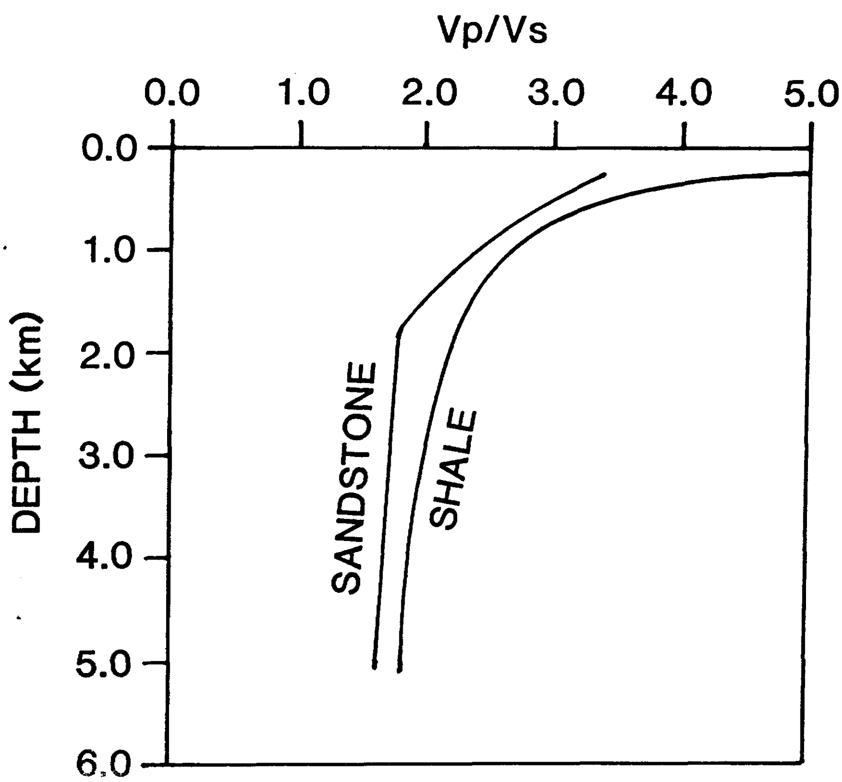

Fig.7.7 Vp/Vs as a function of depth for selected Gulf Coast shales and water saturated sands (after Castagna et al. 1985).

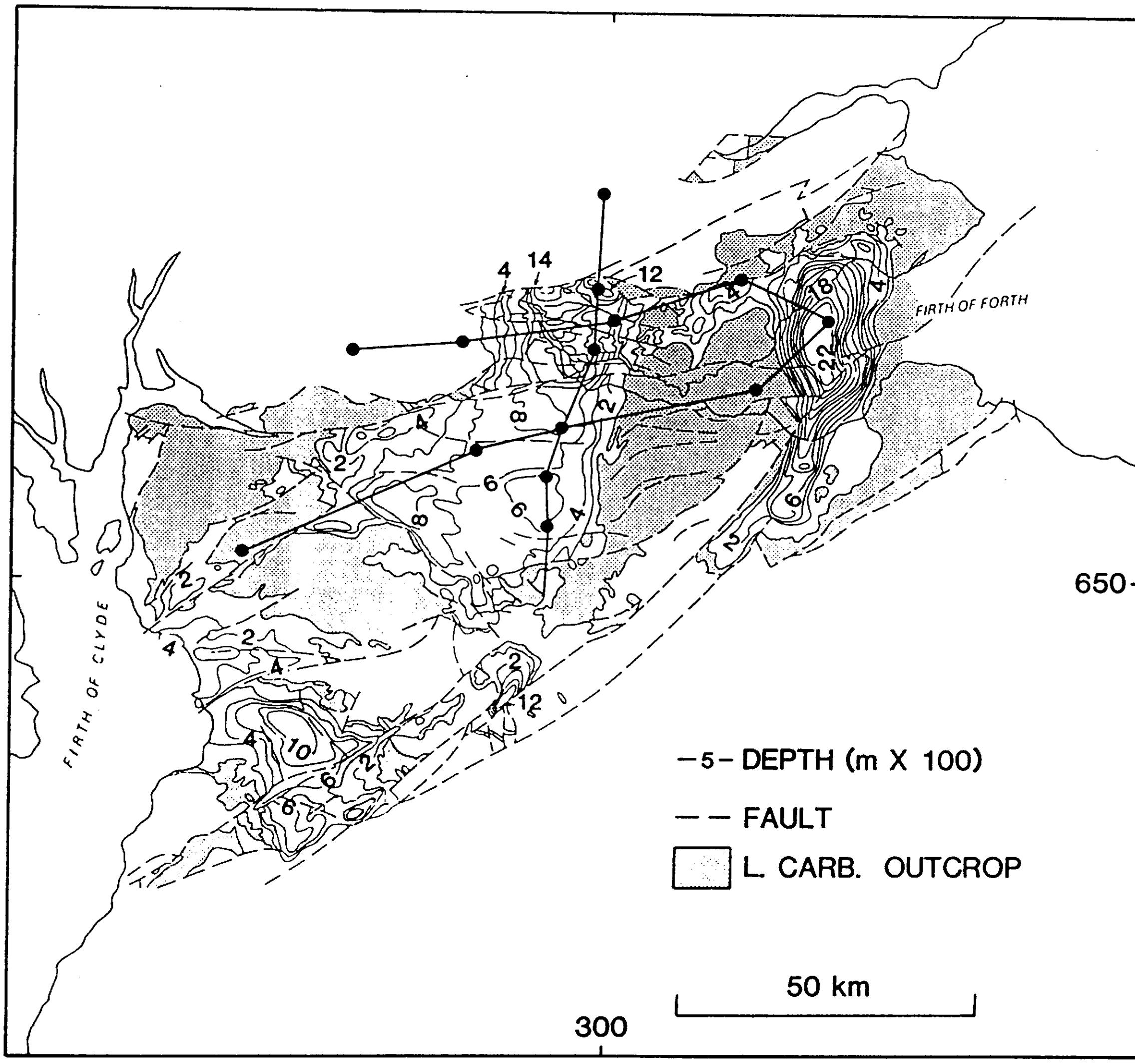

Fig.7.8 Depth contours on the base of the Upper Carboniferous (redrawn from Browne et al, 1985).

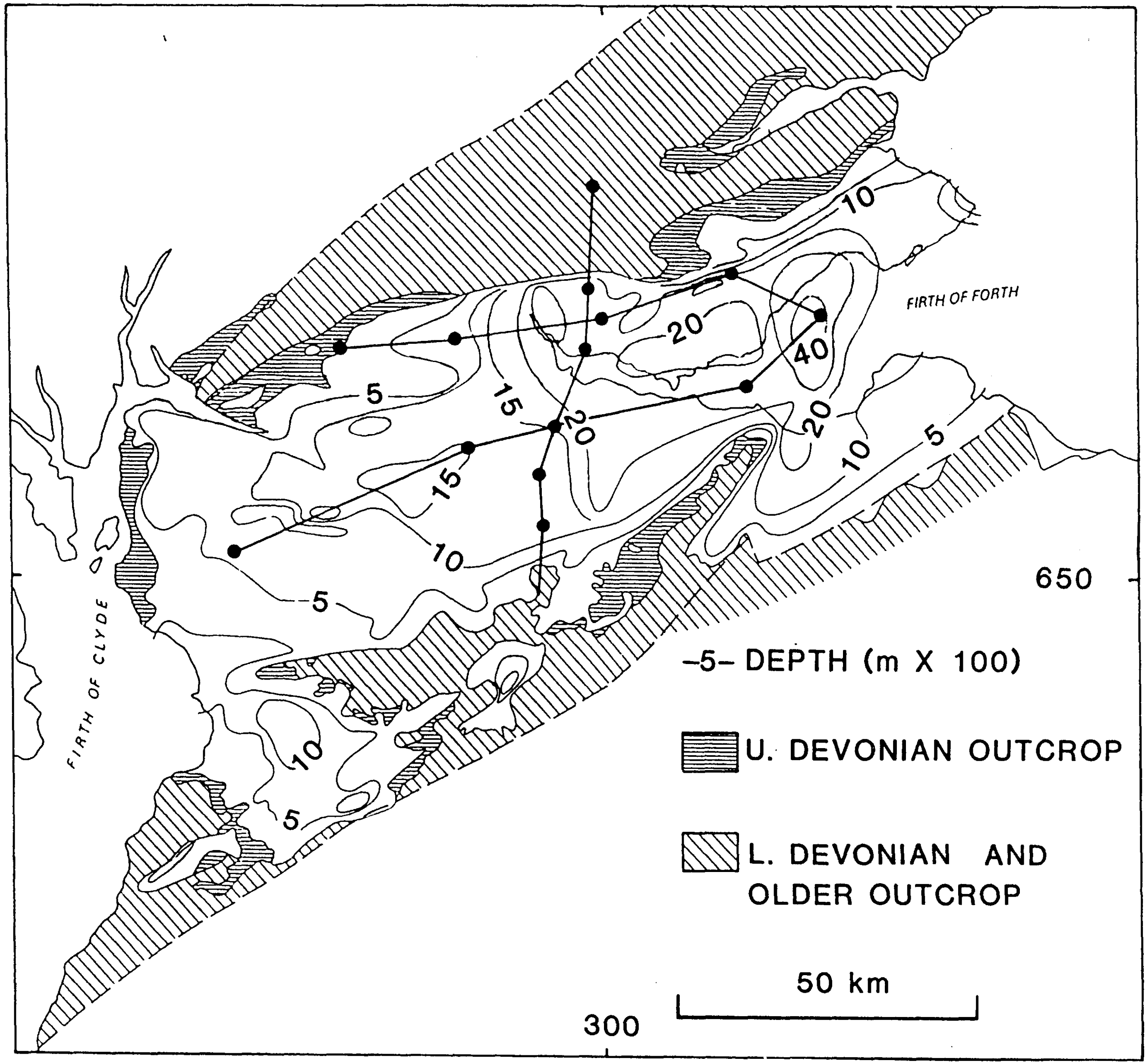

Fig.7.9 Depth contours on the base of the Carboniferous (redrawn from Browne et al, 1985).

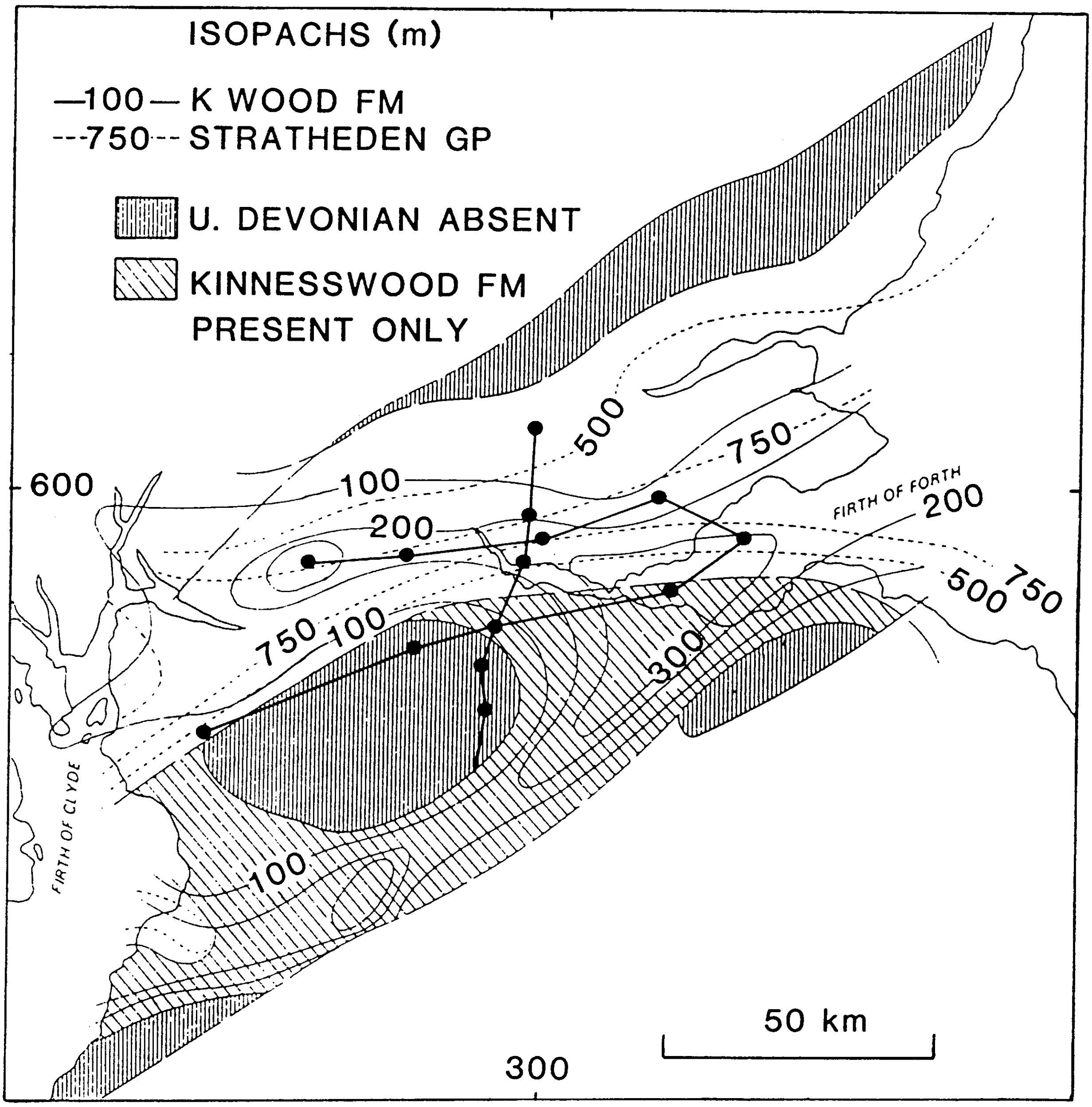

Fig.7.10 Isopach map of the Stratheden Group and Kinnesswood Formations of the Upper ORS (redrawn from Browne et al. 1985).

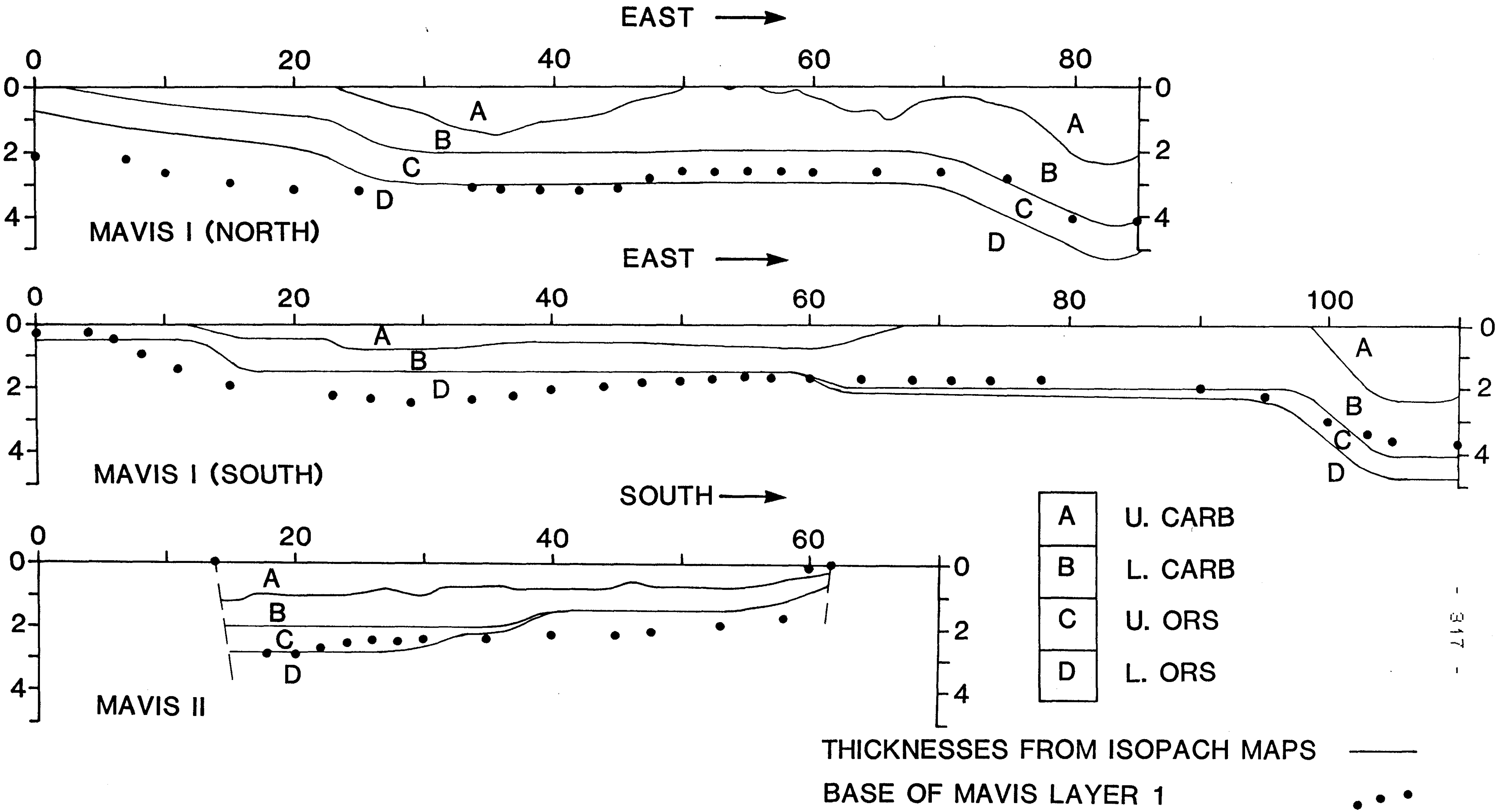

Fig.7.11 Comparison of the thickness of MAVIS layer 1 with the Carboniferous and Upper ORS isopach data of Browne et al. (1985). Scales are in km.

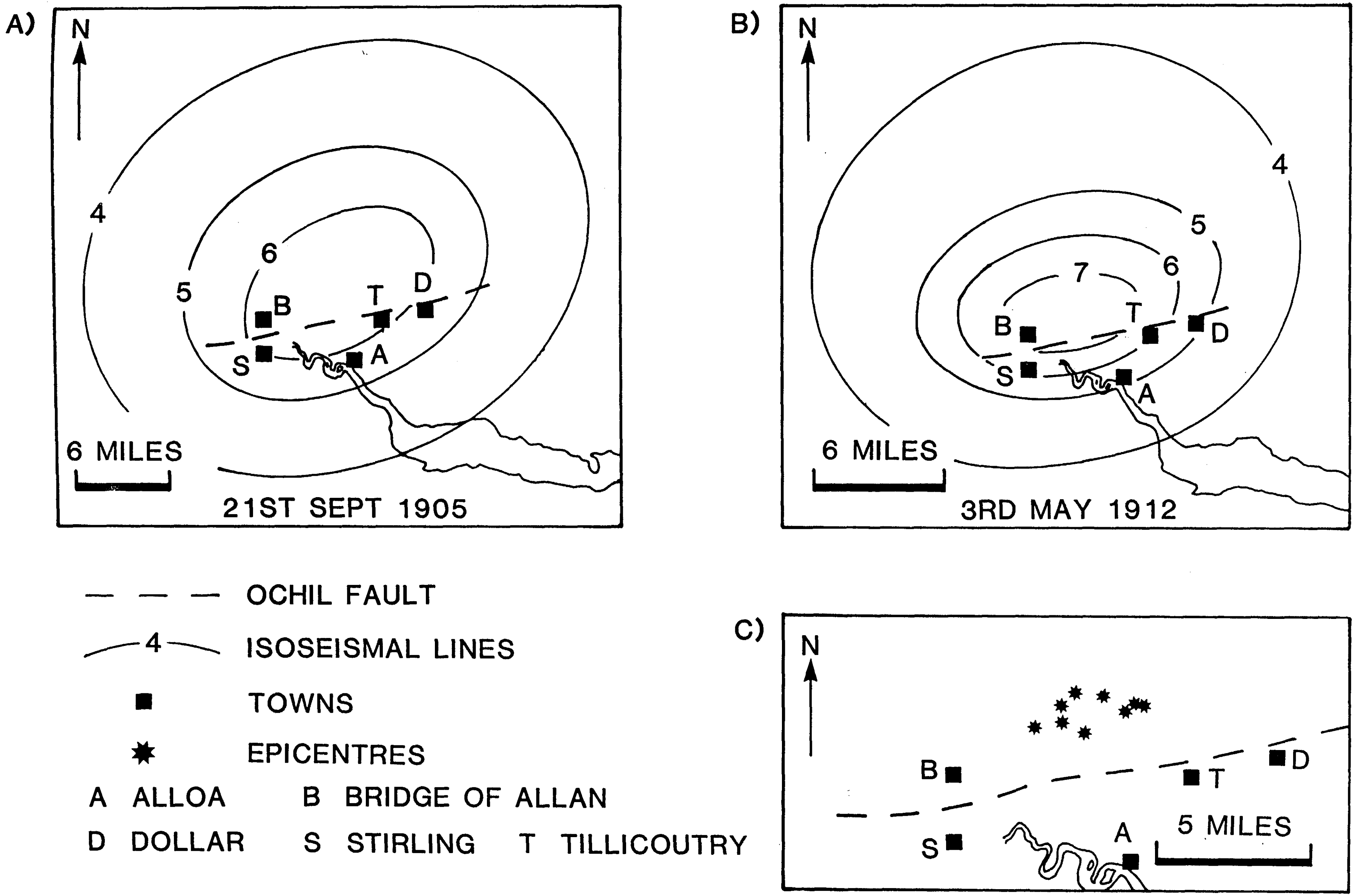

Fig.7.12 Earthquakes associated with the Ochil fault, A) and B), distribution of isoseismal lines for two earthquakes, C) distribution of known epicentres (redrawn from Davison 1924).

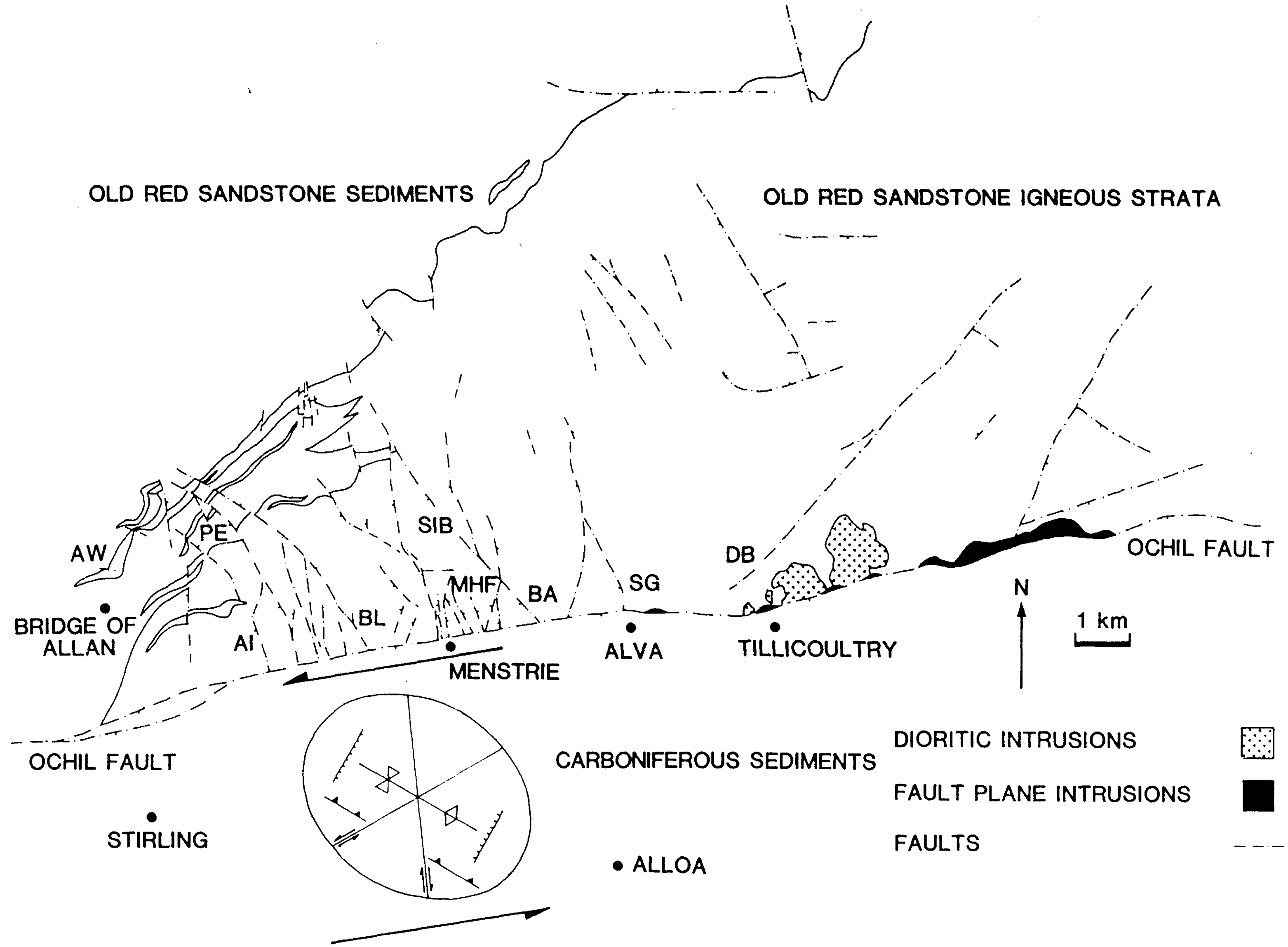

Fig.7.13 Geological map of the area of the Ochil Fault. Strain ellipse after Harding (1974). AI - Airthrey, AW - Allan Water, BA - Balquhan Burn, BL - Blairlogie, DB - Daiglen Burn, MHF - Myreton Hill Fault, PE - Pendreich, SIB - Second Inchna Burn, SG - Silver Glen.

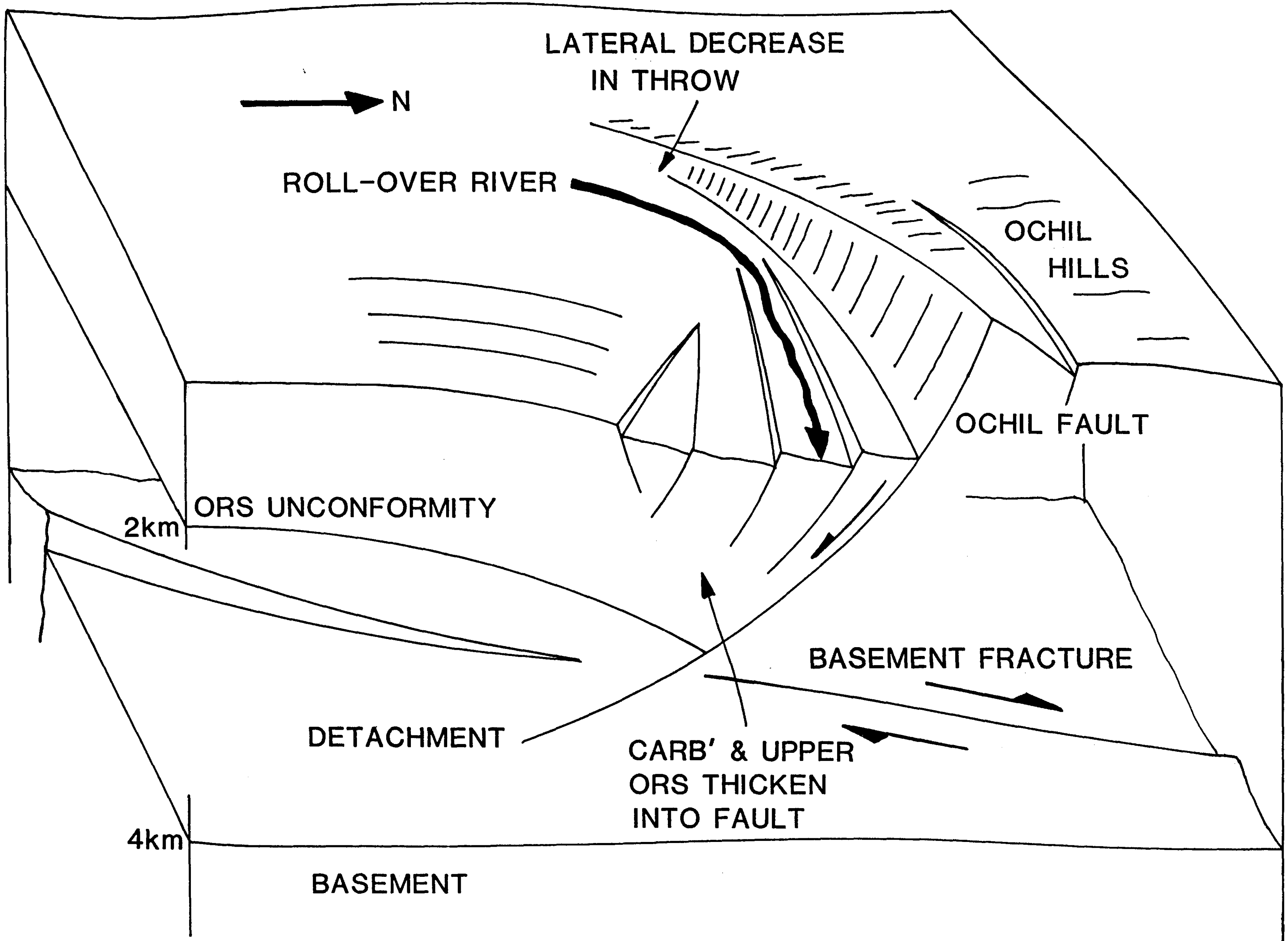

Fig.7.14 Schematic structural model for the Ochil Fault and underlying basement.

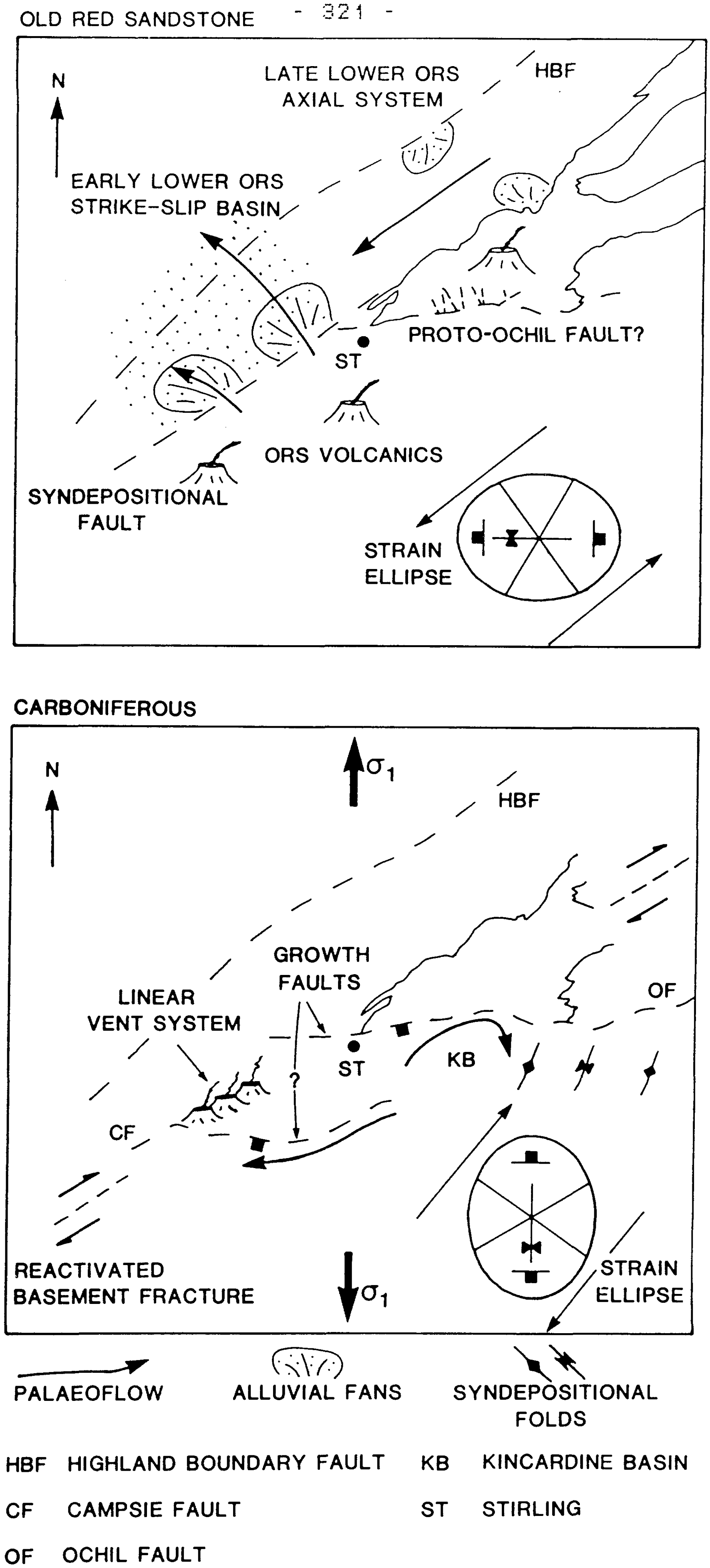

Fig. 7.15 Tectonic model for the evolution of the area around the Ochil Fault.

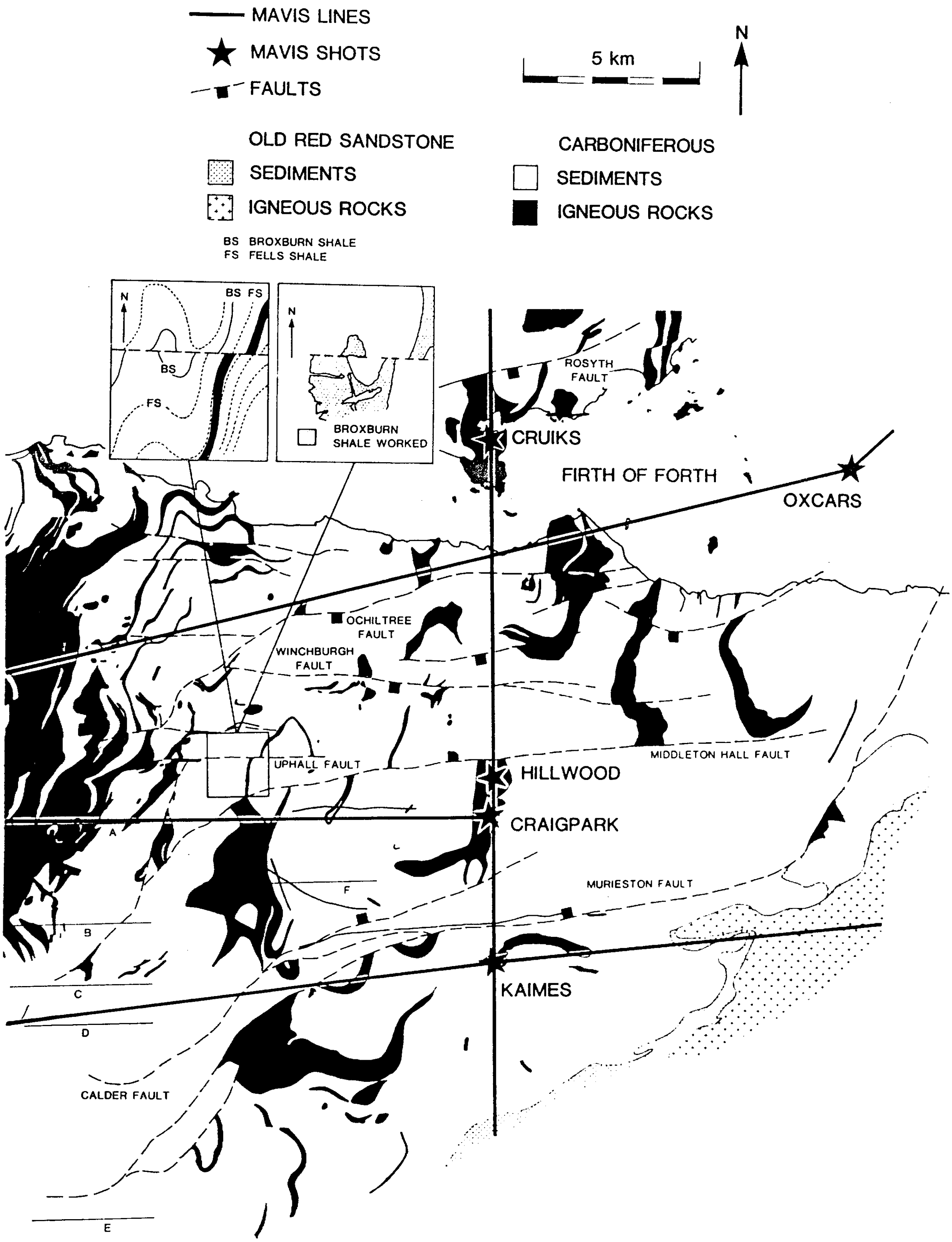

Fig.7.16 Geological map of the Lothian oil-shale fields. Insets; demonstration of lateral movements on the Uphall Fault (redrawn from Kennedy 1944).

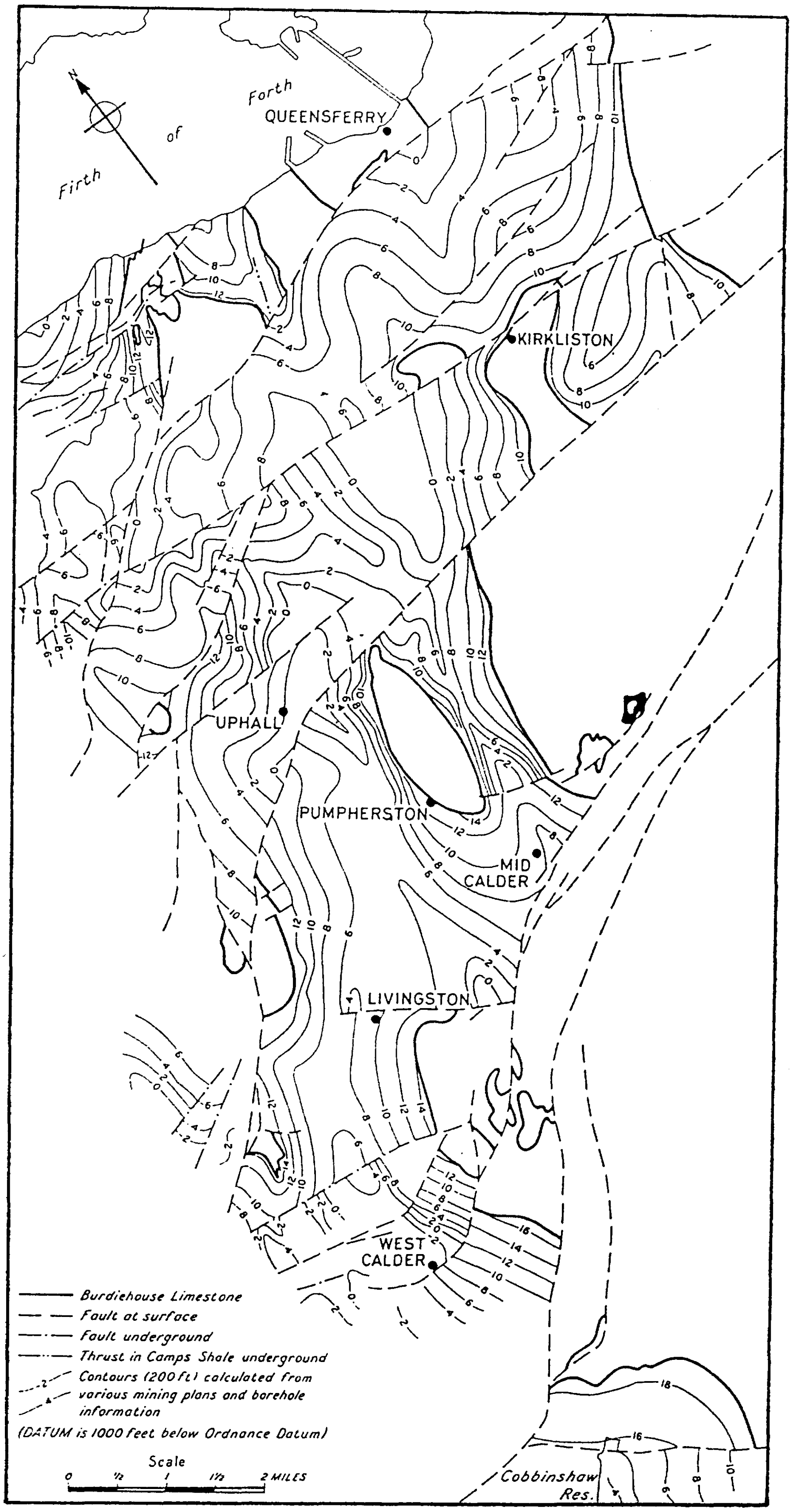

Fig.7.17 Structural map of the Burdiehouse Limestone in West Lothian (after Mitchell & Mykura 1962).

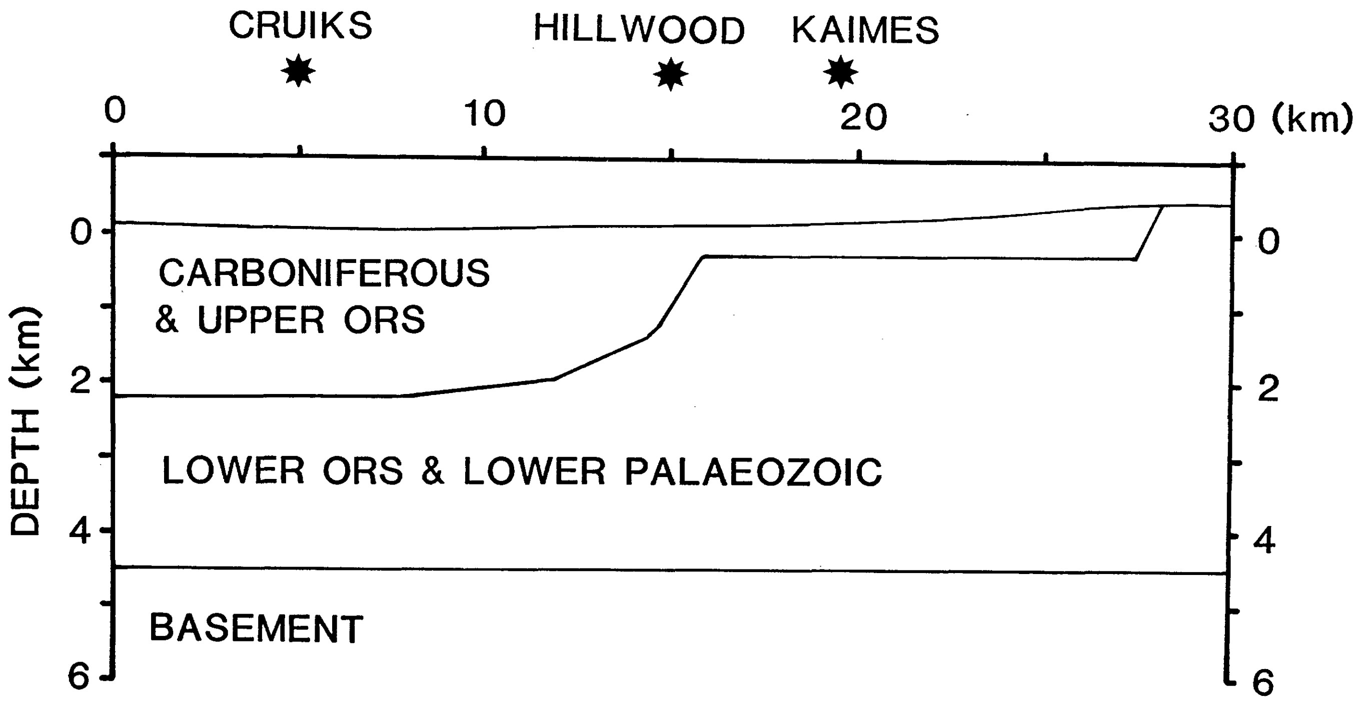

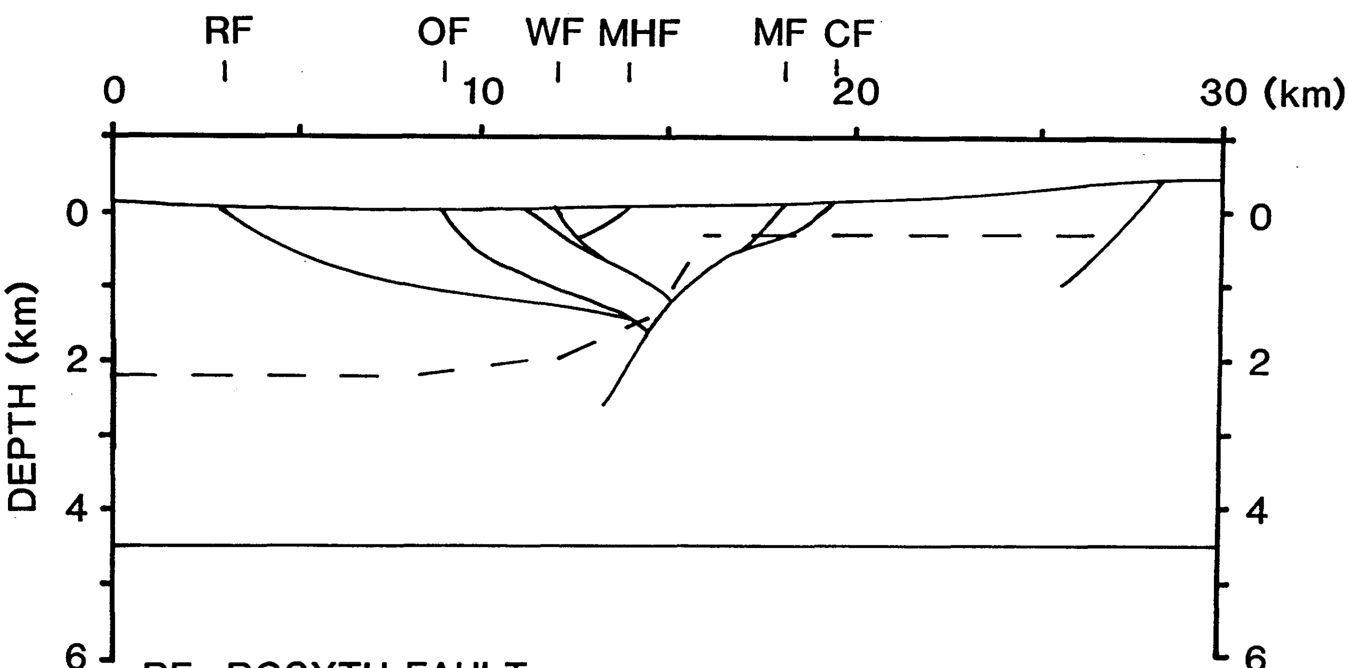

RF ROSYTH FAULT

OF OCHILTREE FAULT

WF WINCHBURGH FAULT

MHF MIDDLETON HALL FAULT

MF MURIESTON FAULT

CF CALDER FAULT

Fig.7.18 MAVIS III ray-traced profile and its structural interpretation. Stars show the location of shot points.

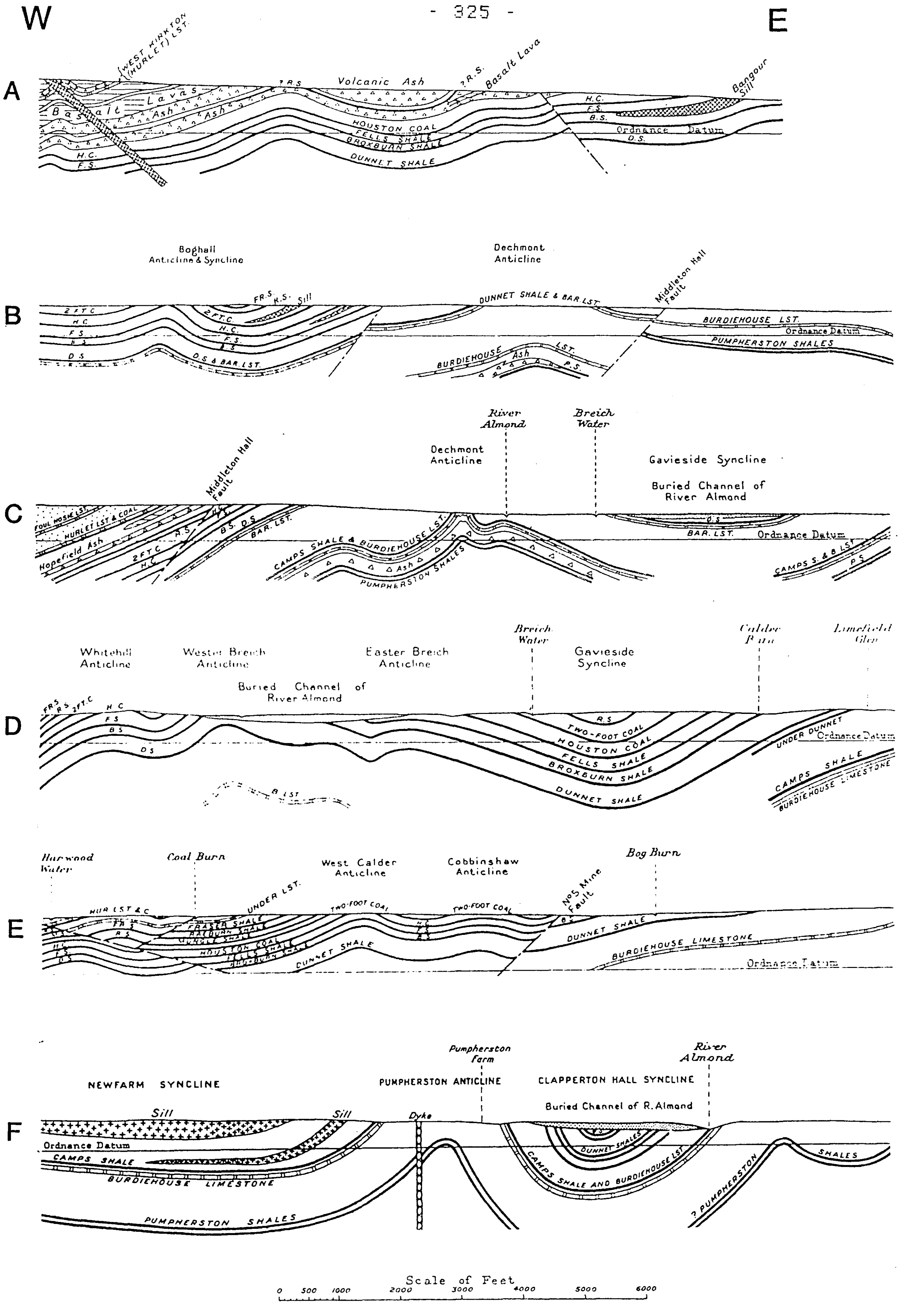

Fig.7.19 Cross-sections of the Lothian oil-shale fields (after Anderson 1942, Kennedy 1943, Richey 1942) see Fig.7.16 for locations.

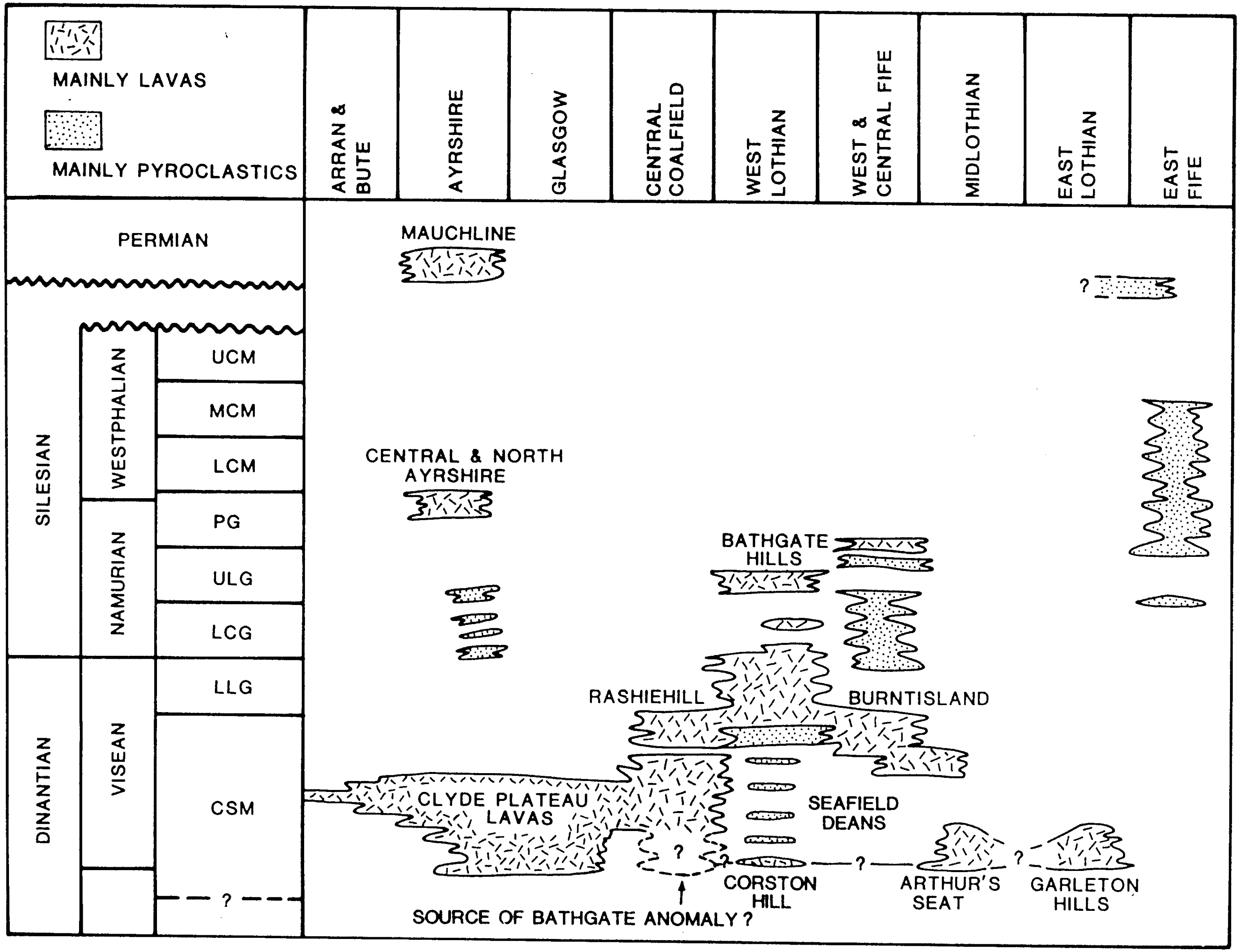

Fig.7.20 Schematic representation of the temporal and spatial distribution os Permo-Carboniferous igneous rocks in the Midland Valley of Scotland (redrawn from Cameron & Stephenson 1985, Francis 1983b).

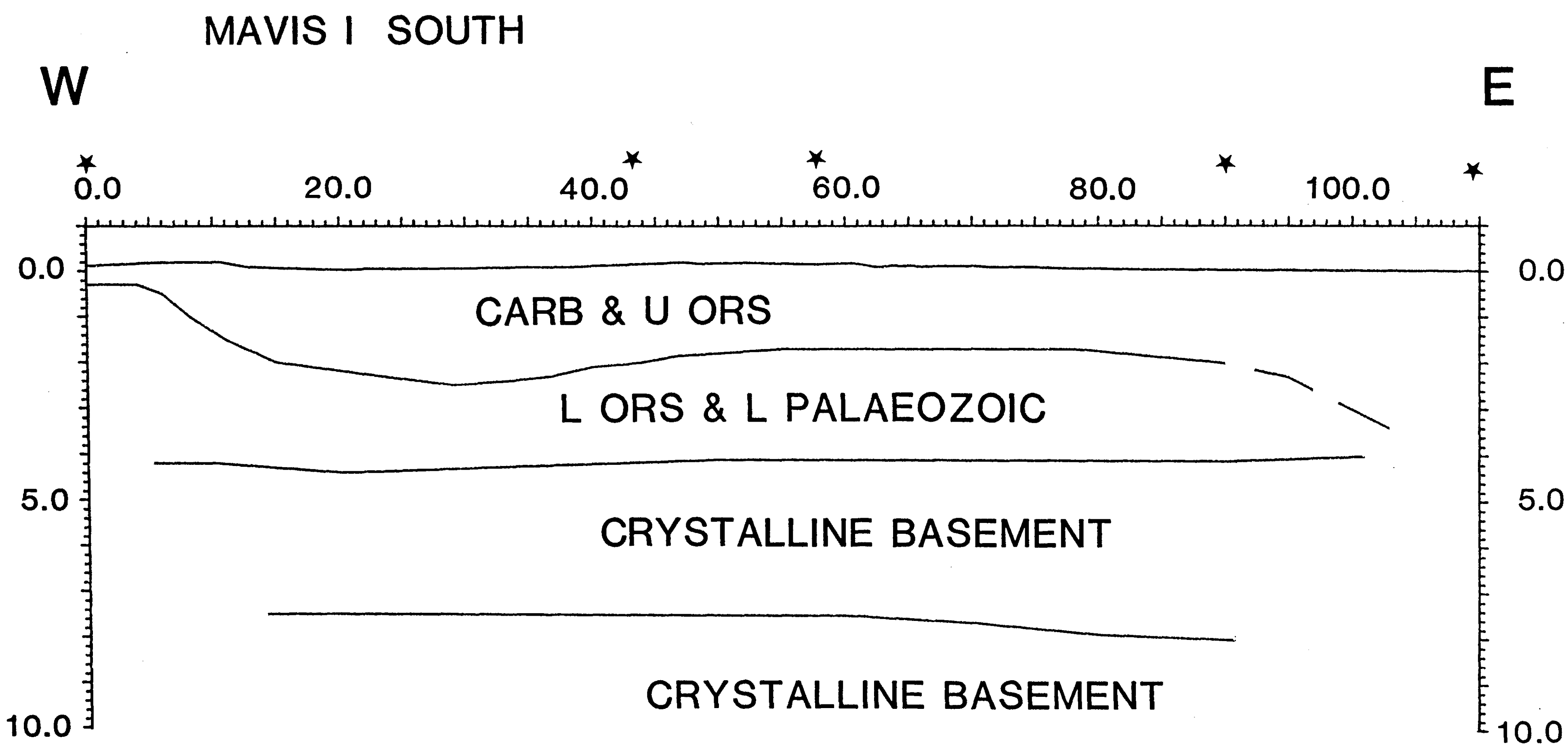

Fig.7.21 Summary of the structure of the MAVIS I south line and its geological interpretation. Stars show the location of shot points, scales in km.

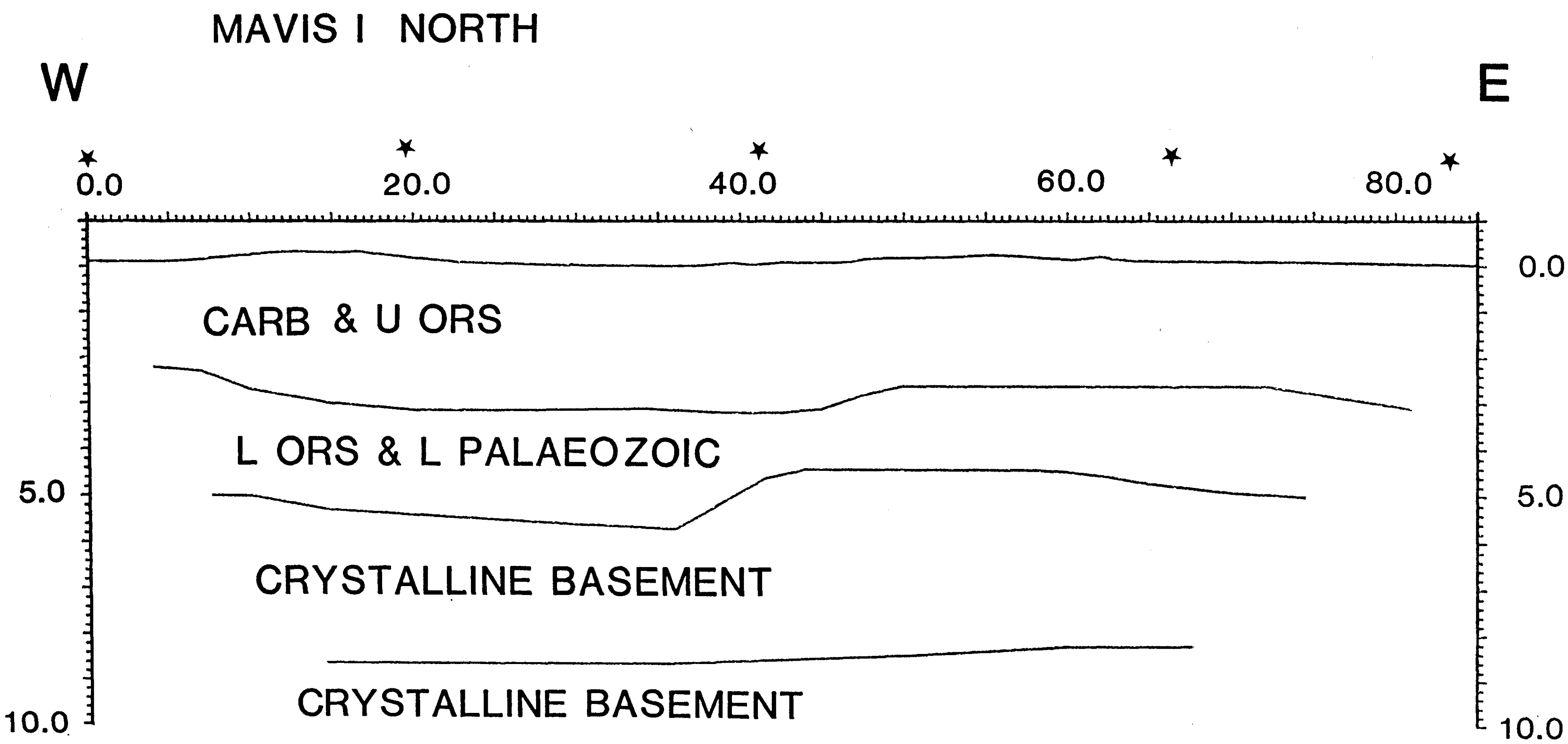

Fig.7.22 Summary of the structure of the MAVIS I north line and its geological interpretation. Stars show the location of shot points, scales in km.

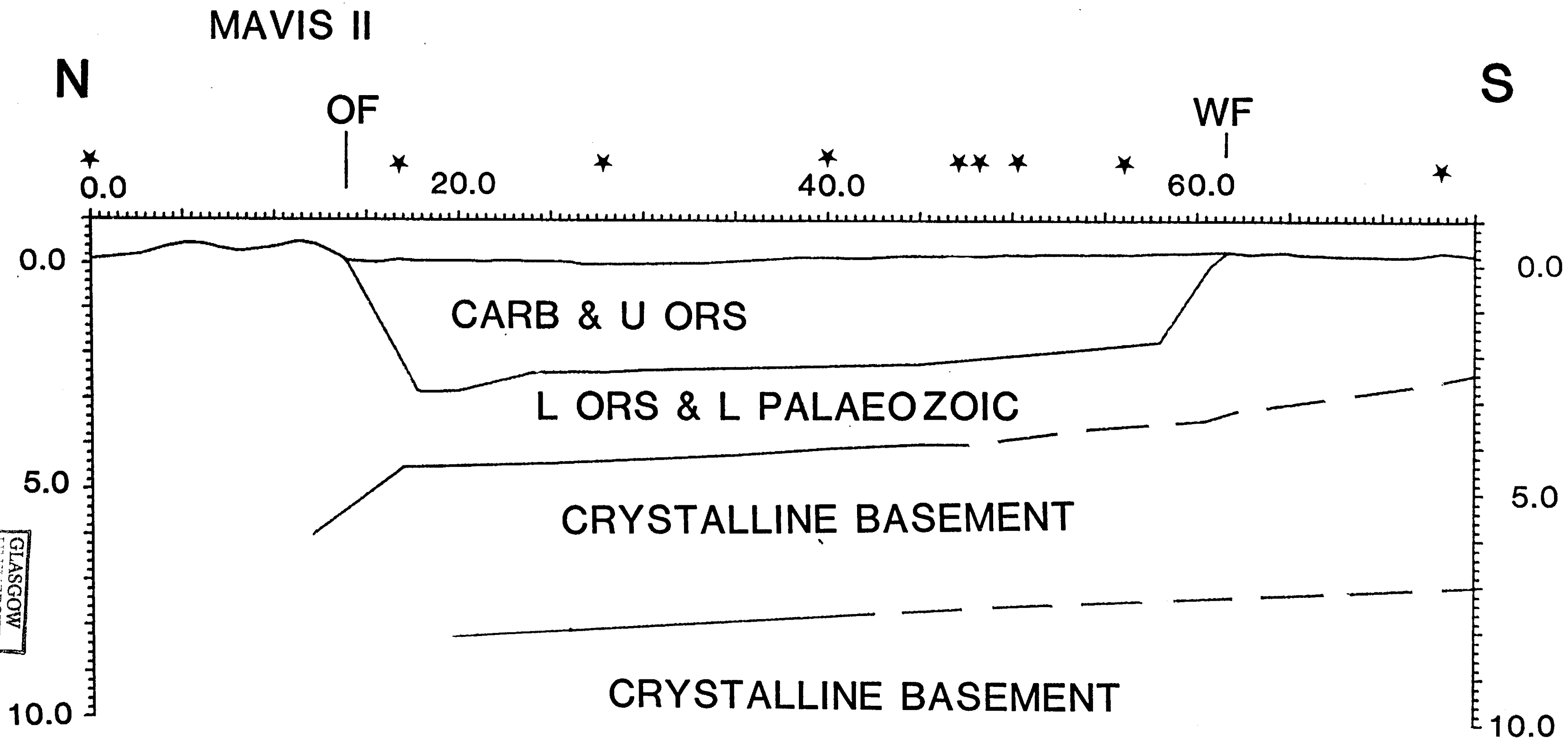

Fig.7.23 Summary of the structure of the MAVIS II line and its geological interpretation. Stars show the location of shot points, OF - Ochil Fault, WF - Wilsontown Fault, scales in km.

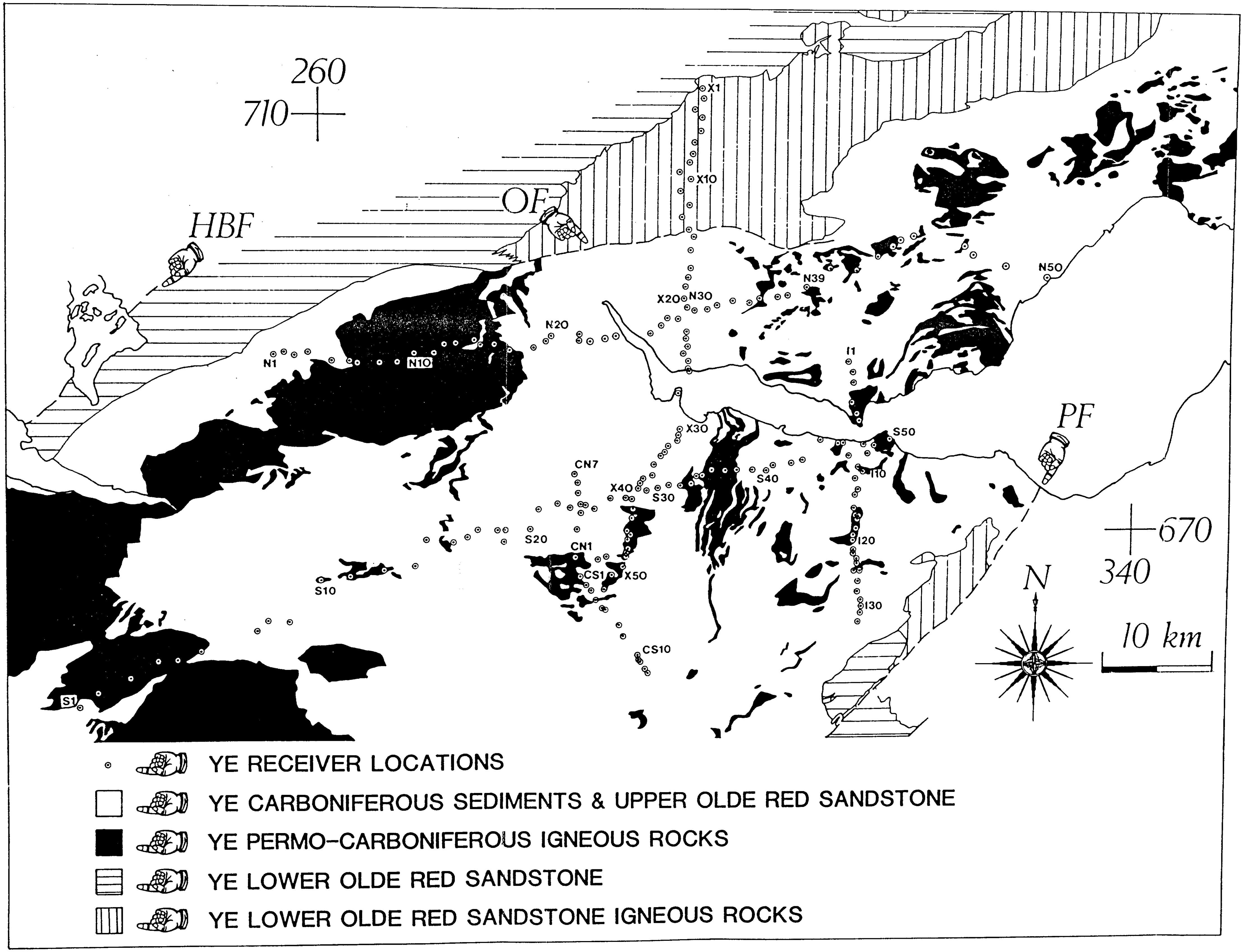

Fig.A.4 Distribution of Receiver Locations Listed in Appendix 2. HBF - Highland Boundary Fault, OF - Ochil Fault, PF - Pentland Fault.